

REPORT DOCUMENTATION PAGE				Form Approved OMB No. 0704-0188	
Public reporting burden for this collection of information is estimated to average 1 hour per response, including the time for reviewing instructions, searching existing data sources, gathering and maintaining the data needed, and completing and reviewing the collection of information. Send comments regarding this burden estimate or any other aspect of this collection of information, including suggestions for reducing the burden, to Department of Defense, Washington Headquarters Services, Directorate for Information Operations and Reports (0704-0188), 1215 Jefferson Davis Highway, Suite 1204, Arlington, VA 22202-4302. Respondents should be aware that notwithstanding any other provision of law, no person shall be subject to any penalty for failing to comply with a collection of information if it does not display a currently valid OMB control number. <b>PLEASE DO NOT RETURN YOUR FORM TO THE ABOVE ADDRESS.</b>					
<b>1. REPORT DATE (DD-MM-YYYY)</b> 13-02-2002		<b>2. REPORT TYPE</b> Conference Proceedings		<b>3. DATES COVERED (From - To)</b> 6 August 2001 - 10 August 2001	
<b>4. TITLE AND SUBTITLE</b> Meteoroids 2001				<b>5a. CONTRACT NUMBER</b> F61775-01-WF032	
				<b>5b. GRANT NUMBER</b>	
				<b>5c. PROGRAM ELEMENT NUMBER</b>	
				<b>5d. PROJECT NUMBER</b>	
<b>6. AUTHOR(S)</b> Conference Committee				<b>5d. TASK NUMBER</b>	
				<b>5e. WORK UNIT NUMBER</b>	
<b>7. PERFORMING ORGANIZATION NAME(S) AND ADDRESS(ES)</b> Swedish Institute of Space Physics (IRF) Kauppinen Kiruna SE-981 28 Sweden				<b>8. PERFORMING ORGANIZATION REPORT NUMBER</b>  N/A	
<b>9. SPONSORING/MONITORING AGENCY NAME(S) AND ADDRESS(ES)</b>  EOARD PSC 802 BOX 14 FPO 09499-0014				<b>10. SPONSOR/MONITOR'S ACRONYM(S)</b>	
				<b>11. SPONSOR/MONITOR'S REPORT NUMBER(S)</b> CSP 01-5032	
<b>12. DISTRIBUTION/AVAILABILITY STATEMENT</b> Approved for public release; distribution is unlimited.					
<b>13. SUPPLEMENTARY NOTES</b>					
<b>14. ABSTRACT</b>  The Final Proceedings for Meteoroids 2001, 6 August 2001 - 10 August 2001  This conference will cover: Historical observations and perspectives on meteoroids; Dynamics, sources and spatial distribution of meteoroids including sporadic, swarm and interstellar meteoroids; Physics and chemistry of meteoroid interaction process in the atmosphere including both head echo and trail effects; Impacts of meteoric constituents on atmospheric phenomena; Hypervelocity impact effects on spacecraft; Leonids - meteor storms and their short-term environmental effects.					
<b>15. SUBJECT TERMS</b> EOARD, Electromagnetics, Ionosphere, Atmospheric Transmission, Meteors					
<b>16. SECURITY CLASSIFICATION OF:</b>			<b>17. LIMITATION OF ABSTRACT</b> UL	<b>18. NUMBER OF PAGES</b> 683	<b>19a. NAME OF RESPONSIBLE PERSON</b> David M. Burns, Lt Col, USAF
<b>a. REPORT</b> UNCLAS	<b>b. ABSTRACT</b> UNCLAS	<b>c. THIS PAGE</b> UNCLAS			<b>19b. TELEPHONE NUMBER (Include area code)</b> +44 (0)20 7514 4955

**SP-495**  
November 2001

# **Proceedings of the Meteoroids 2001 Conference**

6 – 10 August 2001  
Swedish Institute of Space Physics  
Kiruna, Sweden

**DISTRIBUTION STATEMENT A**

Approved for Public Release  
Distribution Unlimited

20020531 115

**European Space Agency  
Agence spatiale européenne**

AQ F02-08-1615

## Scientific Organising Committee

Prof. W.J. Baggaley,	University of Canterbury, New Zealand
Prof. Oleg Belkovich	Kazan State University, Russia
Dr. Gerhard Drolshagen	European Space Agency, Netherlands
Prof. Eberhard Grün	Max-Planck-Institut für Kernphysik, Germany
Dr. Robert Hawkes	Mount Allison University, Canada
Dr. Peter Jenniskens	NASA Ames Research Center, USA
Dr. Ingrid Mann	European Space Agency, Netherlands, and the University of Münster, Germany
Prof. David D. Meisel	State University of New York, USA
Dr. Edmond Murad	Air Force Research Laboratory, USA
Dr. Asta Pellinen-Wannberg,	Swedish Institute of Space Physics, Sweden
Dr. Vladimir Porubcan	Astronomical Institute SAV, Slovakia
Dr. Junichi Watanabe	National Astronomical Observatory of Japan, Japan
Prof. Iwan Williams	University of London, UK

## Local Organising Committee

Asta Pellinen-Wannberg, Diego Janches, Eivor Jonsson, Christina Jurén, Rick McGregor, Birgitta Määttä

## Sponsors

European Space Agency  
 European Office of Aerospace Research and Development  
 Air Force Office of Scientific Research  
 United States Air Force Research Laboratory  
 Swedish Space Corporation, Esrange  
 The Municipality of Kiruna  
 Umea University, Department of Space Physics  
 Luleå University of Technology, Department in Kiruna  
 The Wenner-Gren Foundations  
 The Långman Entrepreneurial Foundation  
 County Administrative Board of Norrbotten  
 The Swedish Research Council

<i>Publication</i>	Proceedings of the Meteoroids 2001 Conference, 6-10 August 2001, Swedish Institute for Space Physics, Kiruna, Sweden (ESA-SP 495)
<i>Published by</i>	ESA Publications Division ESTEC, Noordwijk, the Netherlands
<i>Printed in</i>	the Netherlands
<i>Editor</i>	Barbara Warmbein
<i>Price</i>	60 Euro
<i>ISBN</i>	92-9092-805-0
<i>ISSN</i>	0379-6566
<i>Copyright</i>	© 2001 European Space Agency

# Meteoroids 2001 – Contents

## *Dynamics and Manifestation of Meteor Streams*

<i>Visual and Radar Observations of the Perseid Meteor Stream 1953-83</i> <b>B.A. Lindblad</b>	3
<i>Millimeter Continuum Observations of Parent Comets of Meteor Storms</i> <b>H. Hasegawa et al.</b>	9
<i>Meteoroid Stream Impacts on the Moon: Information of Duration of the Seismograms</i> <b>O.B. Khavroshkin, V.V. Tsyplakov</b>	13
<i>The Discrete Solution of a Quasi-Thomography Problem for Construction of Radiant Distribution of Meteors by Results of Radar Goniometer Measurements</i> <b>V. Sidorov, S. Kalabanov</b>	21
<i>Thin Space Structure of Meteor Flux Irregularities in Large Meteor Showers in 1986-1999</i> <b>A.V. Karpov</b>	27
<i>The Determination of the Ejection Velocity of Meteoroids from Cometary Nuclei</i> <b>I.P. Williams</b>	33
<i>Resonance Structure of Meteoroid Streams</i> <b>V.V. Emel'yanenko</b>	43
<i>Constraining Cometary Ejection Models from Meteor Storm Observations</i> <b>M. Mueller et al.</b>	47
<i>Parent Objects of Alpha Capricornid Meteor Stream</i> <b>I. Hasegawa</b>	55
<i>Asteroid (1620) Geographos as a Possible Parent Body for a Meteor Stream</i> <b>G.O. Ryabova</b>	63
<i>The IAU Meteor Data Center</i> <b>B.A. Lindblad</b>	71
<i>The Updated Version of the IAU MDC Database of Photographic Meteor Orbits</i> <b>B.A. Lindblad et al.</b>	73
<i>Mathematical Model of the Geminid Meteor Stream Formation</i> <b>G.O. Ryabova</b>	77
<i>Forecast for the Remainder of the Leonid Storm Season</i> <b>P. Jenniskens</b>	83

<i>Comparative Analysis of Meteor Shower Observations Processed by Three Different Methods</i> <b>O.I. Belkovich et al.</b>	91
<i>Temporal Structure of Meteoroid Stream and Lunar Seismicity according to Nakamura's Catalogue</i> <b>O.B. Khavroshkin, V.V. Tsyplakov</b>	95
<i>On a Fine Structure of Perseid Meteoroid Stream. Method of Indices</i> <b>J. Svoren et al.</b>	105
<i>The New Meteor Shower, eta Eridanids</i> <b>K. Ohtsuka et al.</b>	109
<i>Comparison among the Keplerian-Orbit-Diversity Criteria in Major-Meteor-Shower Separation</i> <b>L. Neslusan, P.G. Welch</b>	113
<i>Extreme Beginning Heights for Non-Leonid Meteors</i> <b>P. Koten et al.</b>	119
<i>TV Observations of the 1998 Giacobinid Meteor Shower in Japan</i> <b>Y. Fujiwara et al.</b>	123

## ***The Leonids Meteor Shower***

<i>Orbital Perturbations on Dust Trails: Predicting Meteor Storms</i> <b>David Asher</b>	131
<i>Common Ground-Based Optical and Radiometric Detections within Czech Fireball Network</i> <b>P. Spurny et al.</b>	135
<i>Prediction and Observations of Leonid Meteor Shower in China</i> <b>G. Wu</b>	141
<i>Theoretical Leonid Entry Modeling</i> <b>D.O. ReVelle</b>	149
<i>Periodic Activity Variations during the 1999 Leonid Meteor Storm in Various Data Sets</i> <b>J. Rendtel</b>	155
<i>Five-year Cooperative Observations of the Leonid Shower by the BLM Forward Scatter Radio System</i> <b>V. Porubcan et al.</b>	161
<i>Meteor Observations from Israel</i> <b>N. Brosch et al.</b>	165
<i>The Activity Profile of Comet 55P/Tempel-Tuttle in 1998 Return: Meteoroid Release Concentration on Perihelion</i> <b>J. Watanabe et al.</b>	175

<i>Large Leonid Entry Modeling: Application to the Bolide of 11/17/1998</i> <b>D.O. ReVelle</b>	179
<i>Radioseismology as a New Method of Investigations of Meteor Streams on the Moon and Planets</i> <b>A.A. Berezhnoi et al.</b>	185
<i>The Global Monitor of Meteor Streams by Radio Meteor Observation all over the World</i> <b>H. Ogawa et al.</b>	189
<i>Results of 1999 Leonids Daytime Observation in Japan</i> <b>H. Serizawa, M. Toda</b>	193
<i>Ground-based Observations of the Leonids 1999-2000</i> <b>M. Campbell et al.</b>	197
<i>Video Spectra of Leonids and Other Meteors</i> <b>J. Borovicka</b>	203
<i>Leonid Meteors Found in Chinese Historical Records</i> <b>Y. Fujiwara, I. Hasegawa</b>	209
<i>Persistent Leonid Meteor Trails: Types I and II</i> <b>J.D. Drummond et al.</b>	215
<i>Radar Observations of the 1999 and 2000 Leonid Meteor Storms at Middle Europe and Northern Scandinavia</i> <b>W. Singer et al.</b>	221

### ***Physics and Chemistry of Meteors***

<i>Physics and Chemistry of Meteoroids in the Upper Atmosphere</i> <b>E. Murad</b>	229
<i>Formation of Disturbed Area around Fast Meteor Body</i> <b>O.P. Popova et al.</b>	237
<i>Meteors as a Delivery Vehicle for Organic Matter to the Early Earth</i> <b>P. Jenniskens</b>	247
<i>The Model of the Quasi-Continuous Fragmentation</i> <b>V.L. Kuznetsov, G.G. Novikov</b>	255
<i>Light Curves of Faint Meteors</i> <b>P. Koten, J. Borovicka</b>	259
<i>Fragmentation and Initial Radius</i> <b>M. Campbell, J. Jones</b>	265
<i>On the Variable Meteor Parameters</i> <b>P. Pecina</b>	271

<i>Techniques for High Resolution Meteor Light Curve Investigations</i> <b>R.L. Hawkes et al.</b>	281
<i>About Pulsation Brightness of the Bright Meteors</i> <b>G.G. Novikov, O.V. Sokolov</b>	287
<i>Kinetic Simulation of Magnetic Field Effects on Wakes of Meteoroids: Imaginary Emission Method</i> <b>M. Ponomarev</b>	295

## ***Optical Observations of Meteors***

<i>Lidar Observations of Meteor Trails: Evidence for Fragmentation of Meteoroids and their Subsequent Differential Ablation</i> <b>U. von Zahn</b>	303
<i>The AKM Video Meteor Network</i> <b>S. Molau</b>	315
<i>Double Station TV Meteors and Analysis of their Trajectories</i> <b>R. Stork</b>	319
<i>Results of Double-station TV Observations during 1998 and 2000</i> <b>M. Ueda et al.</b>	325
<i>ALIS (Auroral Large Imaging System) Used for Optical Observations of the Meteor Impact Process</i> <b>U. Brändström et al.</b>	331
<i>Some Features of Digital Kinematic and Photometrical Processing of Faint TV Meteors</i> <b>P.M. Kozak et al.</b>	337

## ***Impacts of Meteoroids on the Atmosphere***

<i>The Dispersion of the Swarm of Fragments of Large Meteoroids due to Aerodynamic Forces</i> <b>Y. Su</b>	345
<i>Thermal Explosions of Meteoroids in the Earth Atmosphere</i> <b>V.G. Kruchynenko</b>	351
<i>The Effective Diffusion Coefficient of Meteor Trails above 100 km</i> <b>W.G. Elford, M.T. Elford</b>	357
<i>Theory and Simulations of Field-Aligned Irregularities in Meteor Trails</i> <b>M.M. Oppenheim et al.</b>	361
<i>The Computer Model 'KAMET': The New Generation Version</i> <b>A. Karpov et al.</b>	367

<i>On the Atmospheric Dynamics of the Tunguska Cosmic Body</i> <b>L. Foschini et al.</b>	371
<i>The Measurement of Ozone Concentration by Kazan Radar Observations</i> <b>A. Karpov, A. Konnov</b>	377
<i>Meteor Trains as a Probe for Measuring the Dynamics of the Upper Atmosphere</i> <b>S.H. Marsh, W.J. Baggaley</b>	381

## ***Classical Radar Observations of Meteors***

<i>Features of the Enhanced AMOR facility: The Advanced Meteor Orbit Radar</i> <b>W.J. Baggaley et al.</b>	387
<i>Interferometric Radar Observations of Meteors at Widely Separated Locations</i> <b>A.R. Webster et al.</b>	393
<i>Relation between the Optical and Radar Characteristics of Meteors: Perseids 1998 and 1999</i> <b>P. Pecina et al.</b>	399
<i>Observations of the Structure of Meteor Trails at Radio Wavelengths Using Fresnel Holography</i> <b>W.G. Elford</b>	405
<i>Results of Forward-Scatter Radio Echo Observations in 2000</i> <b>M. Ueda, K. Maegawa</b>	413
<i>Effects of Meteoroid Fragmentation on Radar Observations of Meteor Trails</i> <b>W.G. Elford, L. Campbell</b>	419
<i>Simultaneous Optical and Radar Observations of Meteors: Another Criterion of Commonness</i> <b>P. Pecina et al.</b>	425
<i>The Motion of Radio Meteor Reflection Point of Geminids</i> <b>K. Ohnishi et al.</b>	429
<i>The Earth Rotation and Revolution Effect on the Daily and Annual Variation of Sporadic Meteor Echo</i> <b>K. Ohnishi et al.</b>	435

## ***Observations of Meteors Using Large Aperture Radars***

- The High Power Large Aperture Radar Method for Meteor Observations* 443  
**A. Pellinen-Wannberg**
- Two-frequency Meteor Observations Using the Advanced Research Project Agency Long Range Tracking and Instrumentation Radar (ALTAIR)* 451  
**S. Hunt et al.**
- Meteor Head Echo Observations Using the Millstone Hill UHF Incoherent Scatter Radar System* 457  
**P.J. Erickson et al.**
- Interpretation of Non-Specular Radar Meteor Trails* 465  
**L. Dyrud et al.**
- Astronomical and Physical Data for Meteoroids Recorded by the ALTAIR Radar* 469  
**P. Brown et al.**

## ***Fireballs, Bolides and Meteorites***

- On the Relationship between Asteroids, Fireballs and Meteorites* 477  
**A.E. Rosaev**
- Global Infrasonic Monitoring of Large Bolides* 483  
**D.O. ReVelle**
- Bolide Fragmentation Processes: Single-Body Modeling Versus the Catastrophic Fragmentation Limit* 491  
**D.O. ReVelle**
- The Tagish Lake Meteorite Fall: Interpretation of Fireball Physical Characteristics* 497  
**P. Brown et al.**
- Bolide Physical Theory with Application to PN and EN Fireballs* 507  
**D.O. ReVelle, Z. Ceplecha**
- Bolide Dynamics and Luminosity Modeling: Comparisons between Uniform Bulk Density and Porous Meteoroid Models* 513  
**D.O. ReVelle**
- EN310800 Vimperk Fireball: Probable Meteorite Fall of an Aten-Type Meteoroid* 519  
**P. Spurny, J. Borovicka**
- Modeling the Dynamical and Photometric Behaviours of Faint Meteors in the Earth's Atmosphere* 525  
**L.R. Bellot Rubio et al.**

## ***Hypervelocity Impact Effects on Spacecraft***

<i>Hypervelocity Impact Effects on Spacecraft</i> <b>G. Drolshagen</b>	533
<i>Comparison of Meteoroid and Space Debris Fluxes to Spacecraft in Earth Orbit</i> <b>V. Ekstrand, G. Drolshagen</b>	543
<i>Calculations of Shape Change and Fragmentation Parameters Using Very Precise Bolide Data</i> <b>D.O. ReVelle, Z. Ceplecha</b>	551
<i>On the very high velocity Meteors</i> <b>A. Hajduk</b>	557

## ***Physical Properties of Interplanetary Dust***

<i>Is the Problem of Sporadic Meteoroids Space Distribution Solving Correct?</i> <b>O.I. Belkovich</b>	603
<i>Probing the Structure of the Interplanetary Dust Cloud Using the AMOR Meteoroid Orbit Radar</i> <b>D.P. Galligan, W.J. Baggaley</b>	609
<i>Modelling of the Sporadic Meteoroid Sources</i> <b>J. Jones et al.</b>	615
<i>Lifetimes of Meteoroids in Interplanetary Space: The Effect of Erosive and Planetary Perturbations</i> <b>S. Nikolova, J. Jones</b>	621
<i>Clues to the Structure of Meteoroids, from Dust Light Scattering Properties</i> <b>A.Ch. Levasseur-Regourd, E. Hadamcik</b>	627
<i>Interplanetary Dust Observation in the Earth-Mars Region by Mars Dust Counter (MDC) on Board NOZOMI: Three-Year Results</i> <b>S. Sasaki et al.</b>	635
<i>Io Revealed in the Jovian Dust Streams</i> <b>A.L. Graps et al.</b>	641
<i>Interplanetary Dust Model: From Micron-Sized Dust to Meteors</i> <b>V. Dikarev et al.</b>	649
<i>Microswarm Structure of a Meteoric Complex Beyond an Ecliptic Plane</i> <b>S. Kalabanov et al.</b>	657
<i>Development of a New Reflectron Type TOF Mass Spectrometer for Dust Analysis in Space</i> <b>Y. Hamabe et al.</b>	661

## ***Interstellar Meteors and Dust***

<i>Contemporary Interstellar Meteoroids in the Solar System – In-situ Measurements and Clues on Composition</i> <b>M. Landgraf</b>	667
<i>Properties of Interstellar Dust derived from Remote Astronomical Observatories, Laboratory Analyses and In Situ Measurements</i> <b>H. Kimura et al.</b>	673
<i>Interstellar Particle Detection and Selection Criteria of Meteor Streams</i> <b>B.L. Kashcheyev, S. V. Kolomiyets</b>	683
<i>Dust Astronomy: A New Approach to the Study of Interstellar Dust</i> <b>E. Gruen et al.</b>	691
<i>Mapping the Interstellar Dust Flow into the Solar System</i> <b>W.J. Baggaley, D.P. Galligan</b>	703
<i>Expected Distribution of Interstellar Meteoroids in the Vicinity of the Earth's Orbit</i> <b>A.R. Bagautdinova, O.I. Belkovich</b>	707
<i>Possibility of Meteor Path Determination by Records in Ancient Chinese Local Gazetteers</i> <b>N. Nagatoshi</b>	711

## ***Participants***

<b>Participants list</b>	715
<b>Group Picture</b>	723

# **Dynamics and Manifestation of Meteor Streams**

## VISUAL AND RADAR OBSERVATIONS OF THE PERSEID METEOR STREAM 1953-83

B.A. Lindblad

*Lund Observatory, Box 43, SE-221 00 Lund, Sweden*

*e-mail: linasu@gemini ldc.lu.se*

### ABSTRACT

This paper describes a long term, high-resolution study of the activity of the Perseid meteor stream based on visual and radar observations at the Onsala Space Observatory in Sweden. The data consists of 147 visual hourly rates and 1368 radar hourly rates. In a previous paper (Lindblad 2000) a high-resolution study of the visual zenithal hourly rates of bright Perseid meteors versus solar longitude was described. The study revealed that the Perseid activity curve has a multi-peak structure. A preliminary analysis of 1368 mid-August radar hourly rates obtained in 1953-75 is presented. The activity curve of the Perseid meteor stream based on radar data indicates a similar multi-peak structure of the Perseid meteor stream.

### 1. INTRODUCTION

The Perseid meteor shower is one of the most frequently observed annual meteor showers in the Northern Hemisphere. Since its documentation by Herrick (1838) and Quetelet (1839) numerous reports have been published by visual observers describing the activity of the meteor stream. For references to these reports see Olivier (1925), Lovell (1954), Kronk (1988) and Hasegawa (1993).

One of the first long-term visual studies of the Perseid activity profile was made by Denning (1899 a, b), who in the period 1869-98 recorded 2409 Perseids observed between July 11 and August 19. In order to study the Perseid radiant in detail Denning plotted all observed meteors on star maps. In doing this he discovered the daily motion of the Perseid radiant. Unfortunately Denning (and his contemporaries) described the activity curve of a meteor stream by listing mean observed hourly rates versus date, thereby introducing unnecessary smoothing of the Perseid activity profile. During the 20<sup>th</sup> century extensive studies of the activity of the Perseid meteor stream were carried out both by single observers and by several observing teams (Ahnert-Rohlfs 1952, Zvolankova 1984, Lindblad 1986). In most of the modern studies the activity profile of the stream was described by listing mean zenithal hourly rates versus solar longitude. This procedure reduced the scatter in the hourly rate data, but it did not give much new information.

A problem in all of the studies of the Perseid activity profile is that the Northern Hemisphere observing window for Perseids is very short, i.e. one can only observe Perseid meteors during a few hours of darkness each night. This implies that for any given station and year the observer can only record some 20-40 % of the total diurnal activity of the shower. In order to get a complete record of the Perseid activity profile by visual observations one must continue the observing program for many years. The present paper describes one such investigation carried out in the period 1953-83 using both visual and radar techniques.

### 2. PRELIMINARY STUDIES

A long-term visual and radar study of the Perseid stream was carried out at the Onsala Space Observatory in Sweden (longitude = 0°48' E, latitude 57°24' N) in the period 1953-83. A preliminary study of the activity profile of the Perseid stream based on visual observations was presented in Lindblad (1986a). This study which covered the period 1953-79 was carried out by a team of three experienced meteor observers plus a timekeeper. Two of the observers watched the beamed sky area of the radar, the third observer watched the adjacent field extending to the zenith. Owing to the restricted field of each observer the total hourly rate count of the team was similar to that of a single observer who recorded all meteors he sees. The team members were either professional astronomers or senior graduate students.

Fig. 1A shows the Perseid activity profile obtained by plotting team one-hour zenithal rates for the period 1953-79 versus solar longitude (1950). A very large scatter in the hourly rate data is evident. Fig. 1B shows the resulting smoothed Perseid activity profile obtained by using a sliding mean of 5 data points. Fig. 1C shows the corresponding activity profile for sporadic meteors. It is evident that the sliding mean process produces a smooth mean activity profile for visual Perseids peaking at solar longitude 139.20° (Equinox 1950). Similar activity profiles based on radar studies of Perseid activity have been obtained in other studies (Lindblad and Šimek 1986, Šimek and McIntosh 1986).

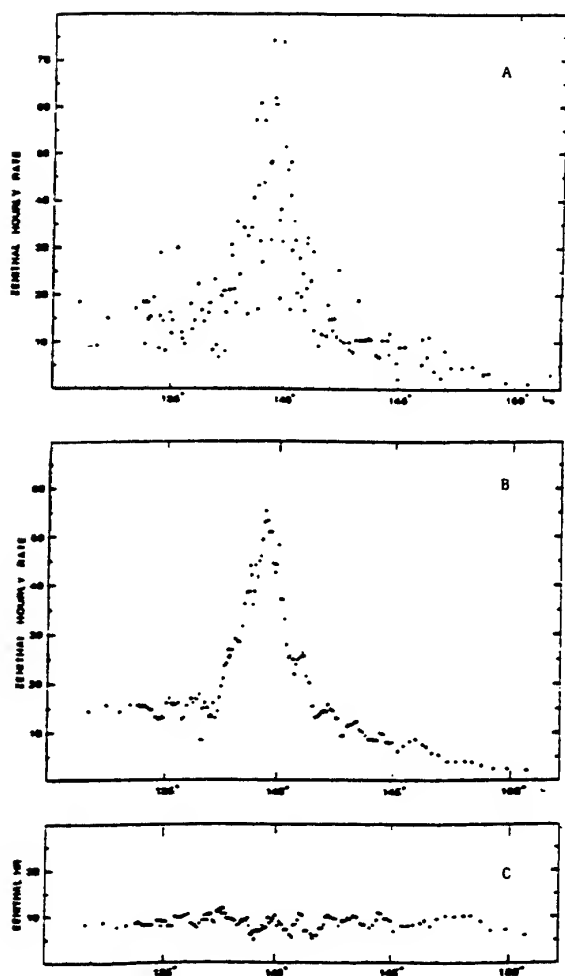


Fig. 1

- A. Perseid zenithal hourly rate vs solar longitude  
 B. Perseid smoothed zenithal hourly rate vs solar longitude  
 C. Sporadic zenithal hourly rate vs solar longitude

### 3. SPURIOUS MAXIMA AND MINIMA

Inspection of Fig. 1C reveals a wave-like structure in the sporadic count rate. To a lesser extent the same phenomena is evident also in the wings of the Perseid activity curve (Fig. 1B). Rather similar wave-like structures have appeared in previous meteor studies. In Lindblad (1985) a comparison was made of night-time and daytime Perseid *radar* activity profiles for the period 1960-75. The radar rate data were first subject to a background subtraction (see section 7.3) and then smoothed using an iterative process which produces an average stream profile (Simek 1985). The result of this study showed that the maxima and minima at the wings of the derived Perseid distributions were spurious. Similar problems have appeared in numerous

geophysical and meteorological studies where smoothing of day to day data based on sliding means is sometimes attempted. For a discussion of this problem see Martyn (1965). The reason for these spurious maxima and minima in the meteor data is that meteor hourly rates are serially correlated, i.e. sporadic meteor rates recorded a given day show a strong correlation with sporadic meteor rates recorded on the following day, etc. For a discussion about serial correlations in meteor hourly rate data see Lindblad (1980).

### 4. GLOBAL NETWORK STUDIES

An interesting alternative to the long-term single station visual observations of a meteor shower is to organise recordings by a chain of visual observers widely spread out in geographical longitude, thereby considerably extending the daily observing window for Perseid meteors. One of the first attempts to organise such a global network for Perseid studies was made by a large group of amateur meteor observers (Roggemans 1989). An interesting result of this study was that a double Perseid peak was detected in the activity profile. A similar double peak in the traditional Perseid maximum is also evident in our visual data 1953-83 (Lindblad 2000).

A problem in the global network studies is to co-ordinate the observing techniques of the various visual groups. The occurrence at some stations of Perseid counts made at very large zenith distances of the radiant is also a serious problem, since the hourly rates critically depend on the choice of the exponent  $n$  in the  $(\sec z_R)^n$  correction.

### 5. LONG TERM STUDIES OF THE PERSEID ACTIVITY CURVE

As mentioned above a long-term study of the Perseid meteor stream was carried out in 1953-83 at the Onsala Space Observatory in Sweden using both radar and visual observing techniques. The radar observing program covered a two-week period in mid-August each year. It was supplemented by one or two control runs in late August and/or in September. The standard diurnal radar observing period was 22 hrs to 04 hrs (night-time recordings) plus 08 hrs to 14 hrs (daytime recordings). All times are Mid-European time = UT + 1 hour. A short description of the radar equipment is given in the Appendix.

Owing to the size of the collected observational material it has taken many years to complete the data reduction. The data reduction process for radar recordings involved the reading of about 150 hours of

film recordings per Perseid campaign plus an additional 50 hours of background film recordings. From these data we have thus obtained about 200 raw hourly rates per year. These raw hourly rates were next corrected for gaps in the records and converted to zenithal hourly rates, assuming a simple  $\sec z_R$  law.

## 6. VISUAL DATA

### 6.1 Visual Observations and Visual Hourly Rates

Visual meteor observations were carried out every clear night during the August radar campaign by a team of three observers plus a timekeeper. During the night runs the observers watched the beamed-sky area of the receiving antenna and plotted all meteors observed in this restricted field. The standard visual observing period was (weather permitting) from 22 hrs to 02.45 hours MET. The observing window for visual observations was thus much shorter than that of the radar recordings.

In the period 1953-83 a total of 8705 visual meteors were recorded and plotted on star maps. Of these meteors 5974 were Perseids, 458 were Aquarids, 47 were members of various minor August showers and 2226 were classified as sporadic meteors. For each plotted meteor all relevant data was put on a 80 col. card, and later read into a computer file. From these files raw visual hourly rates were computed. A computer program later corrected the raw visual rate data for gaps in the records, for varying seeing conditions and converted the observed hourly rates to zenithal hourly rates. For further details of the data reduction process see Lindblad (2000). A total of 570 visual zenithal hourly rates recorded in 1953-83 were then used to obtain a high-resolution activity profile of the Perseid stream. The activity profile was studied for

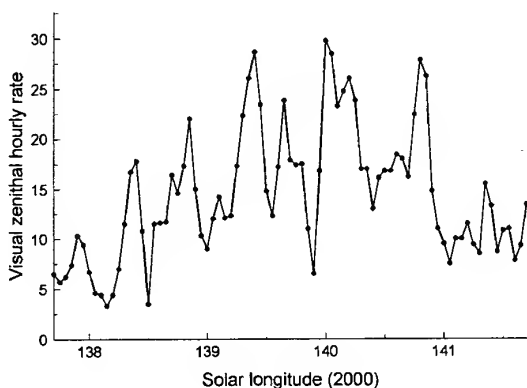


Fig. 2

three different magnitude groups (magn.  $\leq 2.5$ ,  $= 3.0$  and  $\geq 3.5$ ). In Lindblad (2000) the central part of the activity profile ( $137.70^\circ$  to  $143.05^\circ$  in solar long.) was studied in considerable detail. For bright visual meteors ( $m \leq 2$ ) the study revealed that the Perseid maximum consists of 4 separate peaks of about the same size. A similar result has previously been found based on an analysis of photographic data (Lindblad and Porubcan 1994). The activity profile for the Perseid maximum period based on bright Perseids is shown in Fig. 2. The number of Perseid visual hourly rates averaged in each bin of Fig. 2 varied between 1 and 10 with a mean of 5.2.

### 6.2 Radar-Visual Time Coincidences

The Onsala visual recordings were co-ordinated in time with the radar recordings thus allowing identification of time coincidences between visual meteors and radar echoes. In Lindblad (1963) the relation between log echo duration and absolute (zenithal) visual magnitude for 688 Perseid meteors was found to be

$$\log \tau = -0.50 M_z + 1.08 \quad (1)$$

## 7. RADAR DATA

### 7.1 Radar Observations and Radar Hourly Rates

The radar activity profile of the Perseid meteor stream has been discussed in several earlier publications (Lindblad 1986b, Lindblad and Šimek 1986). In these studies the radar meteor echoes recorded by the Onsala radar have been divided into three echo duration groups:  $> 1$  sec,  $1.0$ - $0.5$  sec and  $< 0.5$  sec. From eq. (1) we find that the above three Perseid echo duration groups correspond approximately to Perseid visual absolute magnitudes 1) brighter than  $1.0^m$ , 2) visual magnitudes  $1.0^m$  -  $1.5^m$  and 3) fainter than  $1.5^m$ .

The Perseid activity curve based on radar recordings 1953-75 (note that 1976-83 is not yet completely reduced) has recently been re-studied for several combinations of data. Here we present a preliminary, long-term high-resolution study of the radar night-time data based on one hour radar rate counts made between 22-04 MET leaving the discussion of the corresponding daytime rates (08-14 MET) for a later paper. The reason for this choice is that the daytime data in some years appears to be slightly contaminated by the activity of an unidentified daytime radiant.

## 7.2 High Resolution Study of Radar Rates

A high resolution long-term study of the zenithal hourly rates of long-duration meteor echoes ( $\tau > 0.5$  sec) versus solar longitude has been made. The study covers the interval  $137^\circ - 142^\circ$  in solar longitude and involves 356 individual hourly rates. In the study the night-time zenithal hourly rates were sorted into a bin of width  $0.10^\circ$  in solar longitude, which bin was moved forward using a step length of  $0.05^\circ$  in solar longitude. A mean hourly rate was computed for each step. The input file consisted of 356 night-time radar hourly rates observed in the period 1953-75. The 1953-75 night-time data are plotted in Fig. 3 versus solar longitude (2000). The number of radar hourly rates averaged in each bin of Fig. 3 varied between 5 and 16 with a mean of 11.0. As previously found for both short duration and long duration echoes the distribution peaks at solar longitude  $139.20^\circ$ .

## 7.3 Background Subtraction

For a long enduring meteor shower, there is no entirely reliable method to estimate the background (sporadic) level, i.e. it is not possible to separate the sporadic and shower components of the total meteor radar rates. An often used procedure is to subtract from the observed total hourly rates an assumed constant background rate. If this subtraction produces a negative rate the rate value is discarded. This background rate is usually determined from observations made a few days before or after the shower period. Since the beginning date of the Perseid shower is difficult to pinpoint and the period of activity in late July and early August is known to contain considerable activity from other showers such as the  $\delta$  Aquarids, Capricornids and Cygnids, we have determined the background rate from numerous radar measurements made in late August and during the first three weeks of September. The available background rate measurements are summarized in Table 1. We note that the mean background rate in late August for echoes of duration  $> 0.5^s$  is  $6.4+8.0=14.4$ . Inspection of Fig. 3 shows that for echo durations  $> 0.5^s$  no negative hourly rates will be produced by the background subtraction process. At the time of writing this report the use of the background subtraction procedure is being further studied.

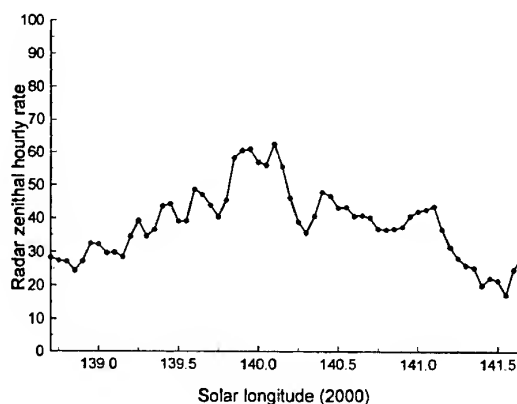


Fig. 3

Table 1. Observed zenithal h.r. of background

	N	$\tau > 1^s$	1-0.5 s	$< 0.5^s$	Total
Aug. 25-31	123	6.4	8.0	94.9	109.3
Sept. 1-20	564	6.6	7.2	110.2	124.1
Oct.	36	8.5	7.9	118.2	134.6

N = Number of observing hours

$\tau$  = Echo duration in seconds

## 8. PLANNED FUTURE STUDIES

A comparison of the visual and radar Perseid hourly rate curves shows that for bright meteors and persistent echo durations ( $\tau > 0.5^s$ ) the derived Perseid activity profiles are very similar. A more detailed comparison of the visual and radar stream profiles is planned as soon as the radar data for 1976-83 are fully reduced. A second planned study is to make a re-analysis of the relation between log echo duration and absolute visual magnitude. This study will be based on 2748 time coincidences between visual meteors and radar echoes recorded in the period 1953-75.

## 9. ACKNOWLEDGEMENTS

The author wants to thank members of the Lund and Onsala Observatory staffs for kind assistance during various phases of the observing program at Onsala. In particular thanks go to Leif Andréasson for his constant help and interest in all instrumental aspects of the project. The author is deeply indebted to Dr. Petr Janeček for his constant help in writing and later modifying numerous large and complicated Fortran programs.

The meteor observing program at the Onsala Space Observatory 1953-83 was supported by grants from the Swedish Natural Science Research Council and from Wallenbergsstiftelsen, both in Stockholm. The data reduction process in Lund has been supported by grants from Helge Ax:son Johnsons Stiftelse, Stockholm and from Crafoordstiftelsen and Kgl. Fysiografiska Sällskapet in Lund. The author is deeply indebted to these agencies and foundations for continued support during a period of several decades.

## 10. REFERENCES

- Ahnert-Rohlfs, E., *Veröffentl. der Sternwarte in Sonnenberg*, Akad. Verlag Berlin, 2, 2, 5 1952.
- Denning, W.F., *Mem. Roy. Astron. Soc.*, 53, 203, 1899a.
- Denning, W.F., *Astron. Nachricht.*, 148, 284, 1899b.
- Hasegawa, L., Historical records of meteor showers, in *Meteoroids and their Parent Bodies*, (edited by J. Stohl and I.P. Williams), Slovak Acad. Sciences, Bratislava, 209, 1993.
- Herrick, E.C., *Am.J. Sci.*, 33, 176, 354, 1838.
- Kronk, G.W., *Meteor Showers*, A Descriptive Catalog, Enslow Publishers, New Jersey, 1988.
- Lindblad, B.A., *Smithson. Contr. Astrophys.*, Vol. 7, 27, 1963.
- Lindblad, B.A., Serial correlation of meteor radar rates, in *Solid Particles in the Solar System*, (edited by I. Halliday and B.A. McIntosh), 105, Dordrecht, 1980.
- Lindblad, B.A., Structure and activity of the Perseid meteor stream from visual observations 1953-81, in *Asteroids, Comets and Meteors II* (edited by C.-I. Lagerkvist, H. Rickman, B.A. Lindblad and H. Lundstedt), 531 Reprocentralen, Uppsala, 1986a.
- Lindblad, B.A., Spurious Maxima and Minima in Meteor Stream Profiles, *Asteroids, Comets and Meteors II* (edited by C.-I. Lagerkvist, H. Rickman, B.A. Lindblad and H. Lundstedt), 545, Reprocentralen, Uppsala, 1986b.
- Lindblad, B.A., *Planet. Space Sci.*, Vol. 45, 1997.
- Lindblad, B.A., *Planet. Space Sci.*, Vol. 48, 905, 2000.
- Lindblad, B.A. and Porubčan, V., *Planet. Space Sci.*, Vol. 42, 117, 1984.
- Lindblad, B.A. and Šimek, M. in *Asteroids, Comets and Meteors II* (edited by C.-I. Lagerkvist, B.A. Lindblad, H. Lundstedt and H. Rickman), 1986.
- Lindblad, B.A. and Šimek, M., The activity curve of the Perseid meteor stream from Onsala radar observations 1953-78, *Ibid.*, 537, 1986.
- Martyn, D.F., *Austr. J. Sci.*, Vol. 27, 249, 1965.
- Lovell, A.C.B., *Meteor Astronomy*, Oxford University Press, Oxford, 1954.
- Olivier, C.P., *Meteors*, Williams and Wilkins, Baltimore, 1925.
- Quetelet, A., *Catalogue der Principales, Apparitions d'Etoile Filiantes*, Bruxelles, 1839.
- Roggemans, P., *WGN*, Vol. 17, 127, 1988.
- P., *Sky and Telescope*, Vol.,
- Šimek, M., *WGN*, Vol. 21, 13, 1993
- Šimek, M., and McIntosh, B.A., *Bull. Astron. Inst. Czech.*, Vol. 37, 146, 1986.
- Zvolankova, J., *Contr. Astron. Obs. Skalnaté Pleso*, Vol. 12, 45, 1984.

## APPENDIX

The radar transmitter at Onsala operated at a frequency of 32.6 MHz. The transmitter sent out 20  $\mu$ sec pulses with a PRF = 50. The transmitting antenna was a half-wave dipole mounted a quarter wavelength above ground. The radar receiver was located about 400 m from the transmitter. The receiver was equipped with range-time and amplitude-time displays, which were simultaneously photographed on 35 mm moving film using a Shakman and Sons oscilloscope-recording camera. The receiving antenna consisted of an array of four three-element Yagis, which was fully steerable in both azimuth and elevation angle. During the Perseid recordings the antenna beam was pointed to a direction which differed by 180° in azimuth and 90° in elevation from that of the Perseid radiant. The receiving antenna was changed in elevation each hour during both night and day runs. The observing window for Perseid radar recording was 12 hours per day. For further details of the visual and radar observing techniques see Lindblad (2000).

# MILLIMETER CONTINUUM OBSERVATIONS OF PARENT COMETS OF METEOR STORMS

Hitoshi Hasegawa<sup>1</sup>, Nobuharu Ukita<sup>2</sup>, and Ryosuke Nakamura,<sup>3</sup>

<sup>1</sup>ASTEC, Inc., 1-3-11 Koishikawa Bunkyo-ku Tokyo 112-0002, Japan

<sup>2</sup>Nobeyama Radio Observatory, Minamimakimura Nagano 384-1305, Japan

<sup>3</sup>Earth Observation Research Center NASDA, 1-8-10 Harumi, Chuo-ku, Tokyo 104-6023, Japan

## ABSTRACT

The 2 millimeter continuum observations of parent comets of meteor storms, 55P/Tempel-Tuttle and 21P/Giacobini-Zinner, were made with a bolometer array installed on the 45m radio telescope at the Nobeyama Radio Observatory. 55P/Tempel-Tuttle was observed on January 16 1998, near its closest approach to the earth, and 21P/Giacobini-Zinner was observed November 5 and 8 1998. The maps obtained showed no signal from these comets greater than 12.0 mJy for 55P/Tempel-Tuttle and 17.4 mJy for 21P/Giacobini-Zinner ( $3\sigma$ ). We estimated that the mass upper limits in the 12 arcsec beam were  $7.5 \times 10^9$  kg and  $6.2 \times 10^{10}$  kg for 55P/Tempel-Tuttle and 21P/Giacobini-Zinner respectively. We estimated total mass of these meteor streams from the observed upper limits. The derived total mass upper limits of the meteor streams are compared to those of meteor streams.

## 1. INTRODUCTION

Meteoroids in meteor storms are submillimeter to centimeter size dust grains which are ejected from the cometary nuclei by their out gassing process. Millimeter and submillimeter continuum observations are suitable to detect thermal emissions from such larger dust particles, while optical and infrared observations are difficult to observe large size particles, because of contaminations by gas emission lines in visible wavelength region and by thermal emissions from much abundant small grains in the coma at mid-infrared region. On the other hand, the radio wavelength, the thermal emissions from submicron to micron size dust particles are relatively weak due to their low thermal emissivity. We would like to introduce our 2 mm continuum observations of two meteor storm parents (Hasegawa *et al.* 2000), 21P/Giacobini-Zinner and 55P/Tempel-Tuttle and the estimates of the total mass production rate from these comets. Comet 55P/Tempel-Tuttle is known to the parent comet of the Leonid meteor storm and comet 21P/Giacobini-Zinner is known to the parent of the Giacobinid (or Draconid) meteor storm.

The Leonid meteor storm was observed in 1999 (Jenniskens *et al.* 2000), and the Giacobinid showed mod-

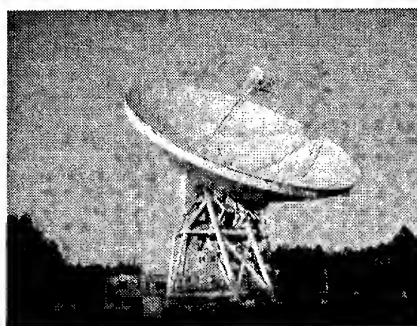


Figure 1. 45m radio telescope of the Nobeyama Radio Observatory.

eratory activity in 1998 (Watanabe *et al.* 1999), in association with their recent returns. These meteor observations provide mass distribution indices of the dust streams. On the other hand, radio continuum observations at different wavelengths can provide information about the dust size distributions ejected from the nuclei just before the observations. To compare with these size distributions, we can discuss the evolutions of cometary dusts to meteor streams.

## 2. OBSERVATIONS

Our millimeter continuum observations were made with the Nobeyama Bolometer Array (NOBA) (Kuno *et al.* 1993) mounted on the focus of the 45 m radio telescope (fig. 1) of the Nobeyama Radio Observatory, Nagano Japan. The frequency of the NOBA (fig. 2) is 150 GHz ( $\lambda = 2$ mm) and the band width is 30 GHz. The NOBA is consisted of 7 bolometers whose individual beam size is 12 arcsec in FWHM and their separation is 16 arcsec. The telescope can track solar system objects from orbital elements within 1 arcseconds RMS. The telescope linearly scanned the predicted position of the comets in azimuth and elevation directions. The observation logs are summarized in Table 1.

Name of comet	Date (UT)	$\Delta$ (AU)	$R$ (AU)	$S_\lambda$ (mJy)	$M$ (kg)
55P/Tempel-Tuttle	1998 Jan 16.6-16.8	0.36	1.20	$< 12.0$	$< 7.5 \times 10^9$
21P/Giacobini-Zinner	1998 Nov 5.3-5.4, 8.4-8.5	0.90	1.06	$< 17.4$	$< 6.2 \times 10^{10}$

Table 1. Observational parameters.

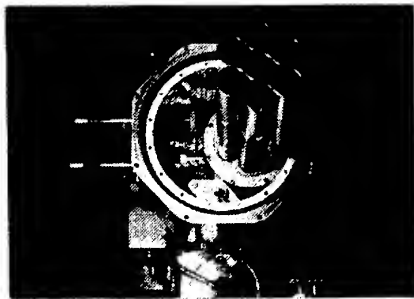


Figure 2. NOBA, seven elements bolometer array.

### 2.1. Comet 55P/Tempel-Tuttle

We observed comet 55P/Tempel-Tuttle on January 16, 1998. The heliocentric distance of the comet was 1.20 AU, and the geocentric distance was 0.36 AU at our observation. The total on source integration time was 2.9 hours. We combined the individual scans and finally obtained an integrated map whose field of view was 37 arc-sec square. Absolute calibration was performed using the radio source 3C84 whose flux density was  $4.0 \pm 0.4$  Jy at 150 GHz. The NRO is monitoring 3C84 as a calibration source, and we used the value of early 1998. The  $3\sigma$  r.m.s. noise level of the map was 12.0 mJy and we could not find any flux concentrations vicinity of the predicted position of the comet.

### 2.2. Comet 21P/Giacobini-Zinner

Comet 21P/Giacobini-Zinner was observed on November 5 and 8, 1998. The heliocentric distances were 1.06 and 1.05 AU, and the geocentric distances were 0.90 and 0.89 AU. The same linear scanning mode was the used as 55P/Tempel-Tuttle. We totally scanned the comet 3.4 hours in both dates. The absolute calibrations were performed using NGC7027 whose flux density was 4.4 Jy (Sandell, 1994). The obtained radio continuum map showed no cometary signals brighter than the  $3\sigma$  upper limit of 17.4 mJy.

## 3. UPPER LIMITS OF THE DUST MASSES AND THE DUST PRODUCTION RATES

We estimated the mass upper limit of the dusts in the beam from the observed flux density upper limit, using

a simple flux model by Jewitt and Mathews (1997). According to their model,  $S_\lambda$  the flux density from the dusts within the beam at a wavelength  $\lambda$  is defined by,

$$S_\lambda = B_\lambda(T_{BB}) \frac{\kappa(\lambda_0)M}{\Delta^2(\lambda/\lambda_0)^\beta}, \quad (1)$$

where,  $B_\lambda(T)$  is the Plank function,  $T_{BB}(=278/\sqrt{R})$  is the equilibrium blackbody temperature of the dust grain at the heliocentric distance  $R$ ,  $\kappa$  is the opacity at  $\lambda$ ,  $\lambda_0(=1\text{mm})$  is the reference wavelength,  $\beta$  is the the opacity index.  $M$  is the total dust mass in the beam, and  $\Delta$  is the geocentric distance. We assumed  $\kappa(\lambda_0) = 0.05\text{m}^2\text{kg}^{-1}$  and  $\beta = 0.89$ , the same value determined from the sub-millimeter observations of C/Hyakutake (1996B6) by Jewitt and Mathews. The resulting dust mass upper limits using the above definition are  $7.5 \times 10^9$  kg and  $6.2 \times 10^{10}$  kg for 55P/Tempel-Tuttle and 21P/Giacobini-Zinner respectively.

The dust production rate  $Q_d$  at the geocentric distance  $\Delta$  is given by

$$Q_d = \frac{2VM}{\Delta\phi}, \quad (2)$$

where  $M$  is the dust mass in the radio beam,  $V$  is the dust ejection velocity, and  $\phi$  is the beam width. Following Jewitt (1996), we assumed the typical ejection velocity of 5m/s. The derived upper limits of the dust production rates are  $2.4 \times 10^4$  kg/s and  $7.9 \times 10^4$  kg/s for 55P/Tempel-Tuttle and 21P/Giacobini-Zinner, respectively. These production rate upper limits are 2 orders lower than that of C/Hale-Bopp (Jewitt and Mathews 1999). Integrating these production rates over their single orbital periods assuming that the dust production rate was assumed to be proportional to  $R^{-2}$  (Gehrz and Ney 1992), we can estimate the mass loss rates per orbit.

$$M_{total} = \int^{1rot} Q_d(t)dt \quad (3)$$

The total dust masses released over their single orbital periods  $M_{total}$  are less than  $5.9 \times 10^{11}$  kg for 55P/Tempel-Tuttle and  $1.3 \times 10^{12}$  kg for 21P/Giacobini-Zinner (Table 2). The estimated total masses upper limit for 21P/Tempel-Tuttle is several orders larger than the total masses which were estimated from Leonids and Giacobinids meteor storms (Jenniskens 1995). On the other hand, the mass upper limit derived from the 55P/Tempel-Tuttle observation is comparable to the mass of the massive dust remnant estimated from recent Leonid observations (Jenniskens and Betlem 2000). For the reference

Meteor storm	Parent comet	$M_{\text{meteor}}$ (kg)	$M_{\text{radio}}$ (kg)	$Q_d$ (kg/s)
Leonids	55P/Tempel-Tuttle	$1 \times 10^{12}$	$< 5.9 \times 10^{11}$	$< 2.4 \times 10^4$
Giacobinids	21P/Giacobini-Zinner	$7 \times 10^9$	$< 1.3 \times 10^{12}$	$< 7.9 \times 10^4$
Perseids	109P/Swift-Tuttle	$1 \times 10^{10}$	$1.5 \times 10^{12}$	$5 \times 10^4$

Table 2. The estimated mass of the Leonids are estimated from meteor outbursts  $M_{\text{meteor}}$  (Jenniskens and Betlem 2000). The mass upper limits derived from the radio observations  $M_{\text{radio}}$ . The dust production rates  $Q_d$  are estimated by assuming the dust ejection velocity of 5 m/s. The dust production rate of 109P/Swift-Tuttle is taken from Jewitt (1996).

purpose, the mass loss of 109P/Swift-Tuttle the parent of the Perseid shower, over its orbit is also calculated using the sub-millimeter observations by Jewitt (1996), and its mass in the orbit is  $1.5 \times 10^{12}$  kg and still larger than the mass of the storm. Farther radio continuum observations are needed to reduce these difference.

#### 4. COMPARISON TO THERMAL-INFRARED SPECTRA

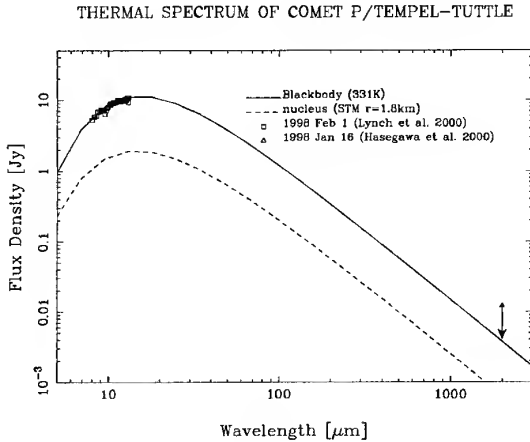


Figure 3. Combined thermal spectrum of 55P/Tempel-Tuttle.

It is worth to compare our flux density upper limits at the millimeter wavelength to thermal-infrared observations. Lynch et al. (2000) made thermal-infrared observations of 55P/Tempel-Tuttle on 8th and 9th February 1998, about a half month after our observation. The infrared fluxes are scaled to those of observed at the same heliocentric distance and geocentric distance of our millimeter observation. Combining (1) and (2),

$$S = B_{\lambda}(T_{BB}) \frac{\kappa(\lambda_0) Q_d(R(t)) \phi}{2V \Delta (\lambda/\lambda_0)^{\beta}}. \quad (4)$$

As assumed previously, the dust production rate  $Q_d(t)$  is proportional to  $R^{-2}$ , the observed flux can be scaled using

$$S \propto \frac{\phi}{\Delta R^2}. \quad (5)$$

THERMAL SPECTRUM OF COMET P/GIACOBINI-ZINNER

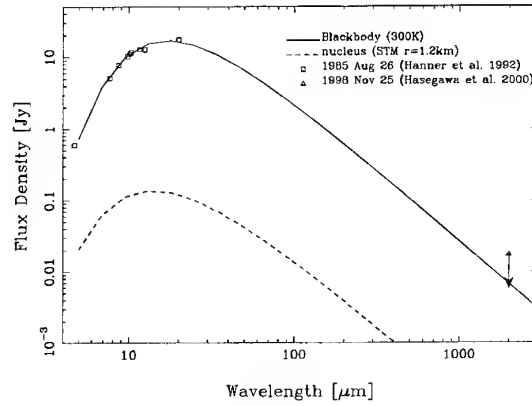


Figure 4. Combined thermal spectrum of 21P/Giacobini-Zinner.

Fig. 3 shows comparison of both infrared and radio observations. The solid line indicates 330K black body curve. This color temperature is fitted by the mid-infrared spectrum.

We used the mid-infrared data for 21P/Giacobini-Zinner, taken at two rotations before the recent 1998 return (Hanner et al. 1992), because there have not been published mid-infrared observations of the current return. Fig. 4 shows the thermal spectrum of the comet. Because, observations at different apparitions may not be expected to have the same flux variation to heliocentric distance, note this comparison as a reference only.

It founds that our millimeter upper limit is located just above the fitted blackbody curves, if the cometary dust spectrum are close to the blackbody spectrum.

For the reference, we also plot the flux density curves from the nuclei using the standard thermal model of asteroids (Lebofsky et al. 1986). The size of the nuclei used in the calculations are 1.8 km for 55P/Tempel-Tuttle (Hainaut et al., 1998) and 1.2 km for 21P/Giacobini-Zinner (Landaberry et al. 1991). As shown in these figures, fluxes from the dust coma are expected to be one or two orders higher than those from nuclei.

## 5. OPACITY INDEX AND SIZE DISTRIBUTION

The opacity index have been determined for only two long period comets, C/Hakutake and C/Hale-Bopp (Jewitt and Mathews 1997, Jewitt and Mathews 1999). Opacity index for a short period comet, such that make a meteor streams, have not been determined yet. The  $\beta$ , however can take a value between 0.0 to 2.0. For  $\beta = 0.0$ , the spectrum is identical to the blackbody curve. Approaching the  $\beta$  to 2.0, the spectrum is close to Rayleigh limit which represents a thermal emission spectrum from dust particles composed of small dust particles relative to the wavelengths. Figure 5 is an example of model emission spectra of 55P/Tempel-Tuttle for different dust size distributions using a Mie model. The optical constant of an astronomical silicate (Drain 1985) is used and a power law size distribution function is assumed. The dust size range is  $1\mu\text{m}$  to  $10\text{ mm}$ . It is found that a higher power index has a steeper spectrum. Because of no silicate excess (see the model spectrum for index = -4) was observed in the mid-infrared spectrum, the dusts of 55P/Tempel-Tuttle is expected to be consist of large particles.

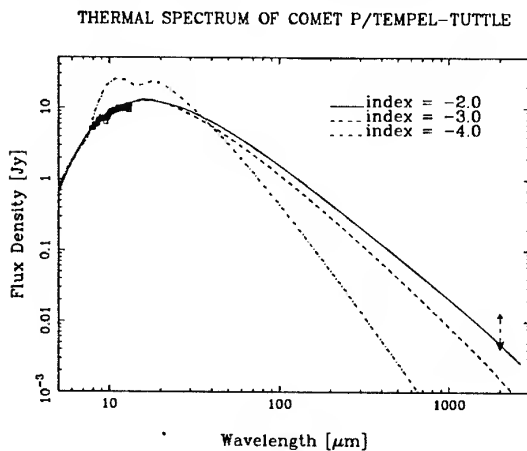


Figure 5. Model dust spectra of 55P/Tempel-Tuttle for difference dust size distributions.

If we could observe radio emissions from the comets, we are able to estimate the size distribution index comparing with the model. Mass distribution index of meteor shower were estimated from optical or radar observations. These mass distribution does not represents originally ejected distribution, because initial ejection velocity and radiation pressure affect on the dust particles would modify their size distributions in time. To understand the evolution of a meteor stream, farther radio continuum observations of a meteor parent comet at millimeter to submillimeter wavelengths are needed.

## ACKNOWLEDGMENTS

We thank NRO staffs for the assistance of our observations. We also thank J. Watanabe, S. Abe, S. Yokogawa and T. Sekiguchi for their helpful discussions.

## REFERENCES

- Drain, B.T., Tabulated optical properties of graphite and silicate grains, *Astrophys. J. Suppl.*, 57, 587-594, 1985
- Gehrz, R.D. and Ney, P., 0.7- to 23-micron photometric observations of P/Halley 1986 III and six recent bright comets, *Icarus* 100, 162-186, 1992
- Hainaut, O.R., Meech, K.J., Boehnhardt, H., West, R.M., Early recovery of Comet 55P/Tempel-Tuttle *Astron. Astrophys* 333, 746-752, 1998
- Hanner, M. S., Veeder, G. J., Tokunaga, A. T., The dust coma of Comet P/Giacobini-Zinner in the infrared *Astron. J.* 104, 386-393, 1992
- Hasegawa, H., Ukita, N., Matsuo, H., Kuno, N., Saitoh, T., Sekiguchi, T., Fuse, T., Nakamura, R., Yokogawa, S., Millimeter Continuum Observations of Parent Comets of Meteor Storms, *Astron. J.* 119, 417-418, 2000
- Jenniskens, P., Meteor stream activity. II: Meteor outbursts, *Astron. & Astrophys.*, 295, 206-235, 1995
- Jenniskens, P., Betlem, H., Massive remnant of evolved cometary dust trail detected in the orbit of Halley-type comet 55P/Tempel-Tuttle, *Astrophys. J.* 531, 1161-1167, 2000
- Jenniskens, P., Butow, S.J., Fonda, M., The 1999 Leonid multi-instrument air craft campaign 0 an early review, Halley-type comet 55P/Tempel-Tuttle, *Earth, Moon & Planets* 82-83, 2000
- Jewitt, D., Debris from comet P/Swift-Tuttle, *Astron. J.* 111, 1713-1717, 1996
- Jewitt, D., Mathews, H.E., Submillimeter continuum observations of comet Hyakutake (1996B2), *Astron. J.* 113, 1145-1151, 1997
- Jewitt, D., Mathews, H.E., Particle mass loss from comet Hale-Bopp, *Astron. J.* 117, 1056-1062, 1999
- Kuno, N., Matsuo, H., Mizumoto, Y., Lange, A.E., Bee-man, J.W., Haller, E.E., Seven matched bolometers for millimeter wave observations, *Int. J. of Infrared and Millimeter-Waves* 14, 749-762, 1993
- Landaberry, S.J.C, Singh, P.D., de Freitas Pacheco, J.A., Ground-based observations of comets Giacobini-Zinner (1984e) and Hartley-Good (1985) *Astron. Astrophys* 246, 597-602, 1991
- Lebofsky, L.A., Skykes, M.V., Tedesco, E.F., Veeder, G.J., Matson, D.L., Brown, R.H., Gradie, J.C., Feierberg, M.A., Rudy, R.J., A refined "standard" thermal model for asteroids based on observations of 1 Ceres and 2 Pallas, *Icarus* 68, 239-251, 1986,
- Lynch, D.K., Russell, R., Sitko, M.L., 3- to 14-um spectroscopy of comet 55P/Tempel-Tuttle, parent body of the Leonid meteors, *Icarus* 144, 187-190, 2000
- Sandell, G., Secondary calibrators at submillimeter wavelengths *MNRAS*, 271, 75-80, 1994
- Watanabe, J., Abe, S., Takanashi, M., Hashimoto, T., Iiyama, O., Ishibashi, Y., Morishige, K., Yokogawa, S., HD TV observation of the strong activity of the Giacobinid meteor shower in 1998, *Geophys. Res. Lett.* 26, 1117, 1999

# METEOROID STREAM IMPACTS ON THE MOON: INFORMATION OF DURATION OF THE SEISMOGRAMS

O.B.Khavroshkin, V.V.Tsyplakov

Schmidt United Institute of Physics of the Earth, Russian Academy of  
Sciences, B.Gruzinskaya 10, 123885 Moscow D242 Russia

The seismograms of meteoroid stream impacts on the Moon have brought important information about inside structure of the Moon any years ago. This work is a new attempt of using records of "Apollo" seismic network for receiving further information about dynamic processes on the Moon. The Nakamura Catalogue is employed for research of these problems. We have built up some histograms from seismic data of Catalogue. The duration of impact  $\tau_{imp}$  in minutes was a general parameter for our analysis. Preliminary conclusions of processing histograms is as follows: the increase of energy of impact from 1imp/day to 3imp/day moves a maximum of histograms to shorter duration, this is especially evident in the case of 4-8 impacts per day; every histogram contains significant picks which are 58-56; 40; 38; 25; 19-20; 16 minutes, but 6; 10,13 minute picks existe only for 4-8 imp/day histogram. We expect that physical models for explaining these picks might be discussed at the meeting.

The seismograms of meteoroid stream impacts on the Moon have brought important information about inside structure of the Moon many years ago [1-3]. This work is a new attempt of using records of "Apollo" seismic network for receiving further information about dynamic processes on the Moon and a logical continuation of our research cycle on blancet lunar seismicity. The Nakamura Catalogue is employed for research of these problems.

Results on sapidity of seismogram duration of moonquakes were obtained

preliminary. The analysis of the Catalogue data revealed the seismic wave response of the Moon to solar processes, specific features of the Moon as an astrophysical detector [4]. As the next step some histograms from seismic data of the Catalogue have been built up. The duration of impact  $\tau_{imp}$  in minutes was a general parameter for our analysis. The impact duration was plotted on the horizontal axe of histogram and sum number of impacts  $\Sigma n_i$  for every impact duration was plotted on its vertical axe. In other words, these histograms are the graphic images of

relationships between  $\Sigma n_i$  and  $\tau_{imp}$ .

Following kinds of functions  $\Sigma n_i = \Sigma n_i(\tau_{imp})$  are analysed: (1)— one impact of a meteoroid per Earth day; (2) — two impacts per day; (3) — three impacts per day; (4) — (four-eight) impacts per day; functions (1)-(3) have been built up only within 1974 ; function (4) have been built up for every year within 1974-1977 and for their sum also (Fig 1-8).

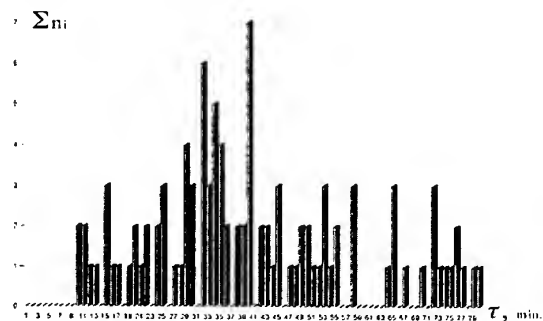


Fig. 1.

Annual histograms (distributions) of durations of seismograms of meteoroid streams (1974) with intensity of one impact per day.

$\Sigma n_i$  — number of seismograms which have the duration in minutes  $\tau$  in the period of one year (1974).

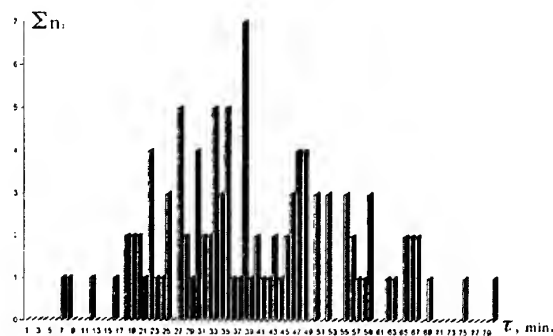


Fig. 2

Figure is similar to fig. 1, but intensity of meteoroid stream is two impacts per day.

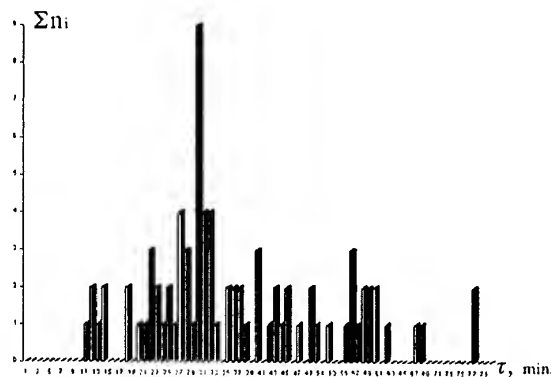


Fig. 3

Annual histograms (distributions) of durations of seismograms of meteoroid streams (1974) with intensity of three impact per day.  $\Sigma n_i$  — number of seismograms which have the duration in minutes  $\tau$  in the period of one year (1974).



Fig. 4

Figure is similar to fig. 3, but intensity of meteoroid stream is 4-8 impacts per day.

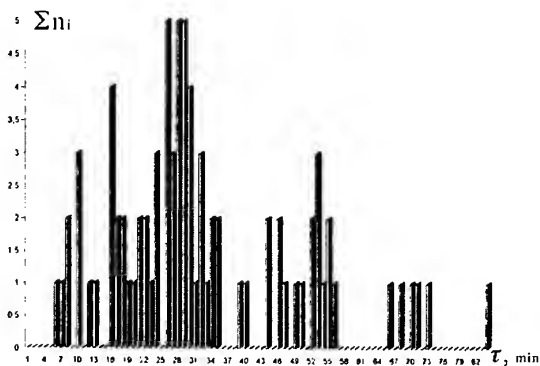


Fig. 5

Annual histograms (distributions) of durations of seismograms of meteoroid streams (1975) with intensity of 4-8 impact per day.

$\Sigma n_i$  — number of seismograms which have the duration in minutes  $\tau$  in the period of one year (1975).

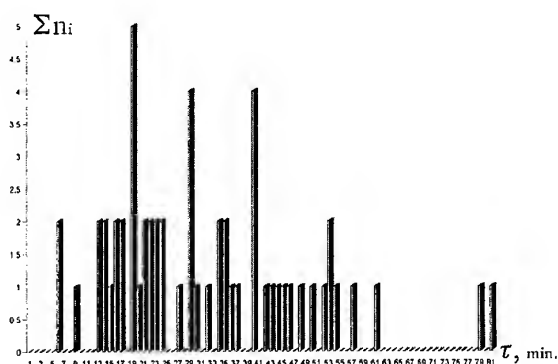


Fig. 6

Figure is similar to fig. 5, but for period of the year 1976.

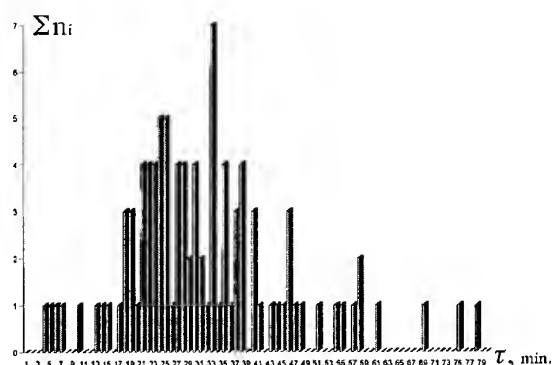


Fig. 7

Annual histograms (distributions) of durations of seismograms of meteoroid streams (1977) with intensity of 4-8 impact per day.

$\Sigma n_i$  – number of seismograms which have the duration in minutes  $\tau$  in the period of one year (1977).

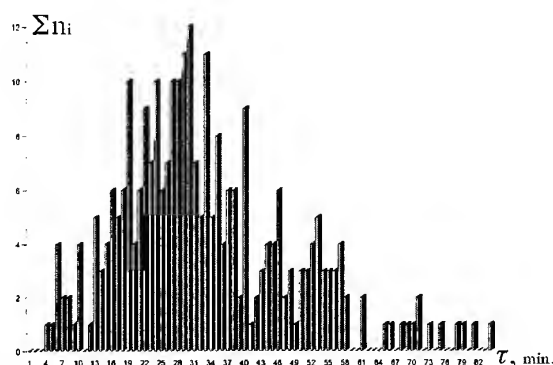


Fig. 8

Figure is similar to fig. 7, but for period of four years (1974 – 1977).

Every histogram distribution of Fig. 1-8 has peculiarities. These peculiarities are picks at  $T_i$ . All the picks were used for creating the General Table, which contains information about different physical events, for example, optical ones. Preliminary conclusions of processing histograms are as follows: the increase of energy of impact from (1) to (3) moves a maximum of histograms to shorter duration, this is especially evident in the case of 4-8 impacts per day; every histogram contains significant picks which are 56-58; 40; 38; 25; 19-20; 16 minutes, but 6; 10, 13, 16, 18- minute picks existed only for 4-8 imp/day histograms. The periodicity of 6-8 minutes corresponds to spectra components of lunar free oscillation. Such interpretation and shift of the histogram pick when the number of meteoroid impacts per day is increased show experimentally the possibilities of excitation of principle wave modes by meteoroid impact energy.

Similar periodicities are detected under analysis of durations of seismograms of so-called "thermal" moonquakes. But features of these moonquakes conflict with the thermal mechanism of its arising. One part of "thermal" moonquakes are possibly induced by interaction between dust-gas plasma of meteoroid stream and lunar surface, because this interaction are able to excite eigenous oscillations of the Moon (Fig.9).

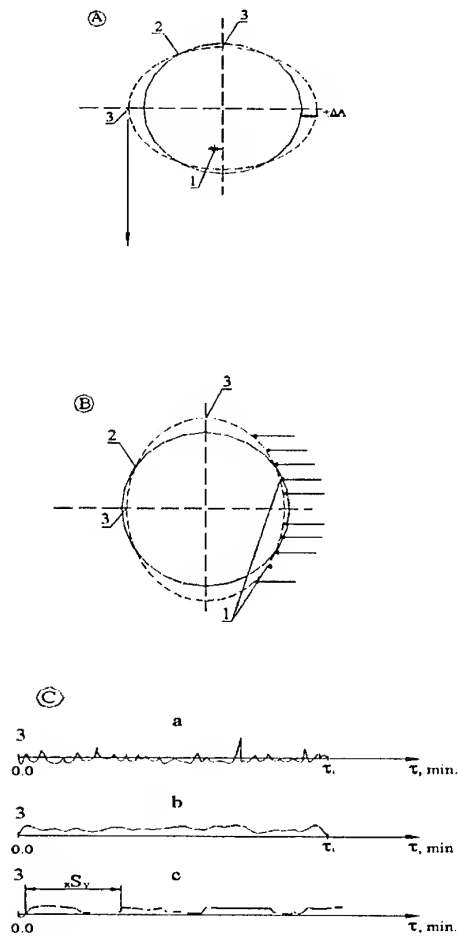


Fig.9. Arising of lunar oscillations caused by impacts of individual meteoroid (A) or shock waves of the dust-gas plasma related to the meteoroid stream (B) which acts on the surface of the Moon and is modulated by free oscillations of the Sun:

- 1 - point of the meteoroid impact at the lunar surface (A) or the surface of impacts (B) caused by the dust-gas shock wave;
- 2 - rods of the deformation wave of the free oscillation;
- 3 - crest of the deformation wave of the oscillation;

(C) - picture of generating the train of seismic waves (cases A and B) derived from lunar oscillations at the zones of maximum deformation (crest of free oscillation):

- a - original high frequency train of the waves;
- b - the envelope of the train of waves (a);
- c - a few envelopes (b) which have free oscillation of the Moon with a period  $xS_v$ ;
- $\tau$  - duration of the packet of waves in the seismogram.

Under analysis of the General Table we have compared the values of maximal periodicity picks for the processes of different nature. The results are a few common picks (25; 30; 40; 45 min) which coincide with eigenious oscillations of the

Sun [6]. It shows the informativity of durations of impact seismograms. It is necessary to note that professor B.A.Lindblad (2000) [7] pointed multiply to the importance of durations which relate with the processes of meteoroid streams.

#### General Table

Maxima  $\sum n_i = \sum n_i(\tau_i)$  of annual histograms (distributions) of durations for meteoroid impact signals (seismograms) as a dependence of numbers of impacts per day (1974), maxima of annual histograms for 4-8 impacts per day (1975-1977); data of maximums of durations of optic signals observed by Moore P. (1967-1971).

Years	Impact/day	Maxima of distributions (histograms) of impact durations (min)
1974	1	10-11 15 25 29-30 32 40 45 53 58 65 72
	2	22 25 27 30 33 35 38 47-48 50 52 55 59
	3	23 27-28 30 40 57
	4-8	15 27 30 33 36-38 45 52 56-57
1975	4-8	10 16 24 26 28-29 33 53
1976	4-8	19 29 40
1977	4-8	18-19 24-25 33 38 40 46
1974-1977	4-8	6 10 13 16 19 22 24 29-30 33 35 37-38 40 46 53 58
Maxima of histograms of optic event durations from data observed by Moore (in min)		
1967-1971	120	1 5 7 10 15 18 20 25 28 30 35 40 45 60
Maxima of histograms of impact durations which more often than 50% are frequent in all histograms (min) to within accuracy of the analysis 1 min.		
1974-1977		23 25 28 30 33 40 46 53 58
Maxima of histograms of seismic events durations which more often than 50% are frequent in all histograms (min) to within accuracy of the analysis 0 min.		
1970-1977	55	8 12 15 18 22 25 27 30 33 35 40 45 50
Maxima of histograms of processes durations which are frequent in all histograms (min)		
1967-1977		25 30 40 45

The revealed coincidence of the solar free oscillation periods and meteoroid seismogram durations indicates modulation of meteoroid streams by the processes on the Sun while

the examination of the temporal (time) structure of the series derives mainly orbital rhythms of giant-planets satellites [8].

These features may be explained by the motion of dust particles. The streams of bulky particles move from the edge of Solar System to its center and are modulated first of all by the giant-planet satellites. In the neighbourhood of the Sun there are processes of destruction from bulky particles into the small ones. These smaller particles originate oppositely directed streams which are named streams of B-meteoroids. Streams of B-meteoroids are initially modulated by wave processes on the Sun and in the neighbourhood of the Sun.

The investigation of meteoroid streams has caused the creation "dust telescope" [10]. In the light of obtained results the Moon is a nature dust and astrophysical megadetector which also may considerably broaden the scope for the progress in dust astronomy.

Implicitly proposed conclusions take into account revealed earlier information which contents data of durations of moonquake seismograms, expected connections between optical events and tidal deformations of the Moon and the following peculiarities of lunar seismicity: the ratio between seismicity energy and heat stream is  $10^{-9}$ ; because the ratio of the energy of the Earth seismic noise to heat stream is  $10^{-4}$ , the energy of lunar seismic noise is more than the energy of seismicity by the factor of 105.

Preliminary conclusions

Comparative analysis of durations of meteoroid impacts indicates the following.

1. This is also bound up with deformational processes in the lithosphere.

2. Maximum of histograms moves to shorter duration with increasing energy of action on the Moon by meteoroids.

3. Histogram of intensive meteoroid stream (4-8 impacts per day) contains the part of durations which correspond to the periods of the free oscillations of the Moon.

4. Some picks of durations of all lunar processes which constantly existing on the histograms correspond to periods of the free oscillations of the Sun.

5. Several seismograms, for example, of "the heat moonquakes" are probably results of action on the Moon surface by dust-gas plasma of meteoroid stream.

6. Dust-gas plasma of meteoroid stream may be modulated by the wave field of the free oscillations of the Sun.

7. The Moon is the global dust telescope.

## REFERENCES

1. Latham G. et al Rezul'taty passivnogo seismicheskogo eksperimenta po programme "apollo". Kosmokhimiya luny i planet (Results of Passive Seismic Experiment under the Apollo Program: Cosmochemistry of the Moon and Planets), Moscow, Publishing House "Nauka", 209-301, 1975.

2. Nakamura Y. et al, SCIENCE. Vol. 181, 49-51, 1973.

3. Galkin I.N. et al, IZV.AKAD.NAUK SSSR, FIZ.ZEMLI, Vol.7, 82-85, 1980

4. Khavroshkin O.B. and Tsyplakov V.V., Information Content of the Catalogue of Lunar Seismicity, DOKLADY EARTH SCIENCES, Vol.377A, 368-373, 2001. Translated from DOKLADY AKADEMII NAUK, Vol.377, 687-692, 2001.

5. Moore P. J.BRIT.ASTR.ASSOC., Vol.81 365-390, 1971.

6.Christensen-Dalsgaard J. in Seismology of the Sun and the Distant Stars, Ed. D.O.Gough (Dordrecht: Reidel) p.23, 1986.

7. Lindblad B.A., Visual and Radar Observations of the Perseid Meteor Stream 1953-83. Proceedings of the Conference METEORIDS 2001, Swedish Institute of Space Physics, Kiruna, Sweden, 6-10 August 2001.

8. Khavroshkin O.B. and Tsyplakov V.V., Temporal Structure of Meteoroid Streams and Lunar Seismicity ccordind to Nakamura's Catalogue, ibid.

9. Mann I.N. et al. Cosmic Dust near 1AU, ibid.

10. Grun E., Dust Astronomy, ibid.

# THE DISCRET SOLUTION OF A QUASY-THOMOGRAPHY PROBLEM FOR CONSTRUCTION OF RADIANT DISTRIBUTION OF METEORS BY RESULTS OF RADAR GONIOMETER MEASUREMENTS

Vladimir Sidorov<sup>(1)</sup>, Sergey Kalabanov<sup>(1)</sup>,

<sup>(1)</sup>Kazan State University, Russia, 420008, Kremlevskaya, 18, Physic Department,

Email: [Vladimir.Sidorov@ksu.ru](mailto:Vladimir.Sidorov@ksu.ru)

## ABSTRACT

It is the first submission of the new solution of a quasi-thomography problem of determination of spatial distribution of a meteoric complex constructed on the goniometer data of the meteoric radar. The previous solution obtained by Belkovich, Sidorov and Filimonova [1] was based on submission about a ceaseless radiant distribution of sporadic meteors on a celestial sphere. In that solution the number of unknowns grew quadratically with increase of the angular measurement accuracy. Therefore stable solution was possible to receive only for the angular measurement accuracy  $10^\circ \times 10^\circ$ . Such accuracy is not enough for majority of problems of a meteoric astronomy.

The new solution is obtained because of hypothesis about a discretization of angular radiant distribution of meteors. It assumes all meteor flux is submitted by not single meteors, but by system of showers and microshowers with identical velocities and angular parameters of meteors in each one.

The method is based on a computer selection of such radiant distribution on a celestial sphere, which does not contradict a microshower hypothesis, to a mirror condition of reflection and is confirmed by independent measurements. The method is realized as computer technology for the goniometer processing for the discretization  $2^\circ \times 2^\circ$ , and it have used for determination of meteor radiant parameters at one day of radar observation at December 13, 1993.

## INTRODUCTION AND HISTORY

Hey and Steward [2] for the first time used two position of the narrow beam antenna of the radar for radiant determination of a large meteor shower.

Yu. Papishev [3] used the rotated antenna and has given the first solution of quasy thomography problem by deciding a return problem of radiant distribution determination by diurnal changes of observable number of meteors in different azimuths. The use of an antenna beam as the measuring tool did not provide high accuracy, therefore Papishev's maps of radiant distribution had accuracy  $30^\circ \times 30^\circ$  degree.

The low accuracy of measurements is common fault of methods, using a beam of the directional antenna.

V. Sidorov, L. Karukina and A. Fahrutdinova [4] have solved a problem of precision radiant measurement of

the large meteor showers by using phase goniometer measurements and idea of a fitting of reflecting points of one plane moved owing to rotation of the Earth. The position of this plane was determined by a method of least squares.

Morton and Jones [5] solved that problem originally by taking advantage a central projection of reflecting points coordinates to a horizontal plane standing much higher than meteoric zone. On this plane of a projection of reflecting points of meteors were drawn up in a line, which equations determined coordinates of meteor shower radiants.

Unfortunately problem of selection of meteors, which are inherent to a shower, in the last two methods was not solved up to the end and consequently it could be used only for very large meteor showers.

O. Belkovich, V. Sidorov and T. Filimonova [1] have formulated a problem radiant distribution measurement as quasy thomography problem. The essence of the task and principles of the solution were similar to statement of a problem of Ju. Papishev. The higher accuracy of the measuring tool has allowed to increase the accuracy. However it was not possible to reach the accuracy better, than  $10^\circ \times 10^\circ$ .

The matter is with an increase of accuracy the number of unknowns grows quadratically and for best accuracy there was no stable solution at use of a method of successive approximations.

V. Sidorov and A. Rassim [6] were able in frameworks of thomography solution to return from a statistical problem to almost determined solution and to distribute registered meteors on their most probable arrangement on a celestial sphere. On this basis the distributions of a meteor velocities on a celestial sphere were obtained.

V. Sidorov, T. Filimonova and other [7,8] used the posterior probability to get the meteor radiant in given area for searching thin radiant structure. It was revealed, that in maxima of rate distribution there is a plenty of meteors with identical velocities.

The hope has appeared the obtained thomography results will have value for astronomy, if it is possible to increase accuracy of the solution. The basis for this hope is given by rather high accuracy of angle measurements of the meteoric radar

Therefore problem of an accuracy increasing of the quasy thomography solution of a problem of determination of radiant distribution of radar meteors on a celestial orb remains actual now.

It is especially important for the Kazan university, in which by a 1979 the meteoric radar with goniometer was constructed [9] and after 1986 this radar worked in an almost continuous mode and the huge data including about 10 million of meteor reflections was accumulated.

## BASIC EQUATIONS

In a classical tomography problem the internal structure of object is restored under the characteristics of numerous projections. In our case, each registered meteoric reflection gives us projection to a celestial sphere as a line of a possible radiant position.

Let  $A_j$  is a single vector of reflecting point position of j-meteor on a celestial sphere;

let  $R_j$  is a single vector of radiant position of that meteor on celestial sphere.

$$\text{Let } A_j(A, Z) \Rightarrow A_j(\varepsilon, \psi) \quad (1)$$

$$\text{and } R_j(A, Z) \Rightarrow R_j(\varepsilon, \psi) \quad (2)$$

are a transitions from horizontal to ecliptic coordinate system in which one from axes coincides with apex of Earth motion. In such system the visible radiant distribution is deformed by motion of the Earth, but the angular position of meteoric radiant is not changed because of errors in determination of velocity of a meteor.

$$A_j * R_j = 0 \quad (3)$$

is the mirror condition of scattering of radio waves by a meteoric trail.

$$R_j = \bigcup_l R_{j,l} \quad (4)$$

$$\text{and } \sum_l P(R_{j,l}) = 1, \quad l = 1, 2, \dots, k \quad (5)$$

is logic equations of a fittings of a j-meteor to one from k radiants on line of possible position on celestial sphere.

$$P(R_{j,l}) = L_{j,l} * \beta_{j,l} \quad (6)$$

is the probability that radiant of a meteor number j belongs to a site number l on a line of a radiant position,  $L_{j,l}$  is length of a line of a position inside of a site number l,  $\beta_{j,l}$  is a factor which is taking into account non-uniformity of sensitivity distribution of the radar for different meteor radiants along a line of a position.

$$P\{R_j(\varepsilon, \psi)\} \Rightarrow F[P\{A_j(A, Z)\}] \quad (7)$$

is a connection between function of radiant distribution and function of angle positions distribution.

The set of equations [1-7] in which number of equations are determined by number of measurements, and the number of unknowns is equal to number of elementary segments on a celestial sphere is an object of the solution of a quasy tomography problem.

## IDEA OF NEW METHOD

It was unexpected that tomography method has detected sharp irregular radiant distribution of meteors on a celestial sphere. The acute peaks, ridges and large segments almost of full absence radiant were observed [8].

This result appeared quite unexpectedly to confirm the previously unpopular Southworth hypothesis which postulated that the sporadic background consists of barely distinguishable showers.

The new solution is obtained because of hypothesis about a discretization of angular radiant distribution of meteors. Such solution assumes, that dropping flow of meteors is submitted by not single meteors, but by system of microshowers with close speeds and close angular parameters.

The method is based on a computer selection of such radiant distribution on a celestial sphere, which does not contradict to a microshower hypothesis, to a mirror condition of reflection and is confirmed by independent measurements

Let's consider two independent measurements  $A_j$  and  $A_k$  of angular coordinates of two different meteoric reflections divided by the slice of time  $t_{j,k} = t_k - t_j$ .

Let's consider that both measurements have close equal velocity of meteors. The lines of a position of these two meteors will be crossed in two points on a celestial sphere, one of its will be higher than horizon.

Three versions here are possible a) both reflections belong to meteors of one meteoric shower, b) they belong to different one, c) they belong to a sporadic background, i.e. have random radiants. Intersection of their line position in case a) will characterize an angular radiant position of a meteoric shower, and in cases b) and c) the cross point will be a random point on a celestial sphere.

If the second pair of reflections belongs to the same meteoric shower, its radiant coordinates will be measured twice, and the outcome of measurements will coincide within a measurement error of the radar goniometer.

The random coordinates also can be coincided in a random way. Repeating such measurements we will receive true shower radiants on a celestial sphere, if they are in act at this time, and random, as an outcome of random combinations. A problem is how to distinguish one from other. The complexity of this problem is that number of random point on a celestial sphere grows as number of combinations among two measurements, and the number of true meteor radiants will grow linearly inside of area of shower radiation.

### BASIC EQUATIONS OF DISCRETE SOLUTION

The realization of the discrete approach implements additions to Eq.(1-7) procedural ratios (8-10):

$$P_N(\varepsilon_{jk}, \psi_{jk}) = P_N^0(\varepsilon_{jk}, \psi_{jk}) + P_N^r(\varepsilon_{jk}, \psi_{jk}), \quad (8)$$

$$P_M(\varepsilon_{jk}, \psi_{jk}) = P_M^0(\varepsilon_{jk}, \psi_{jk}) + P_M^r(\varepsilon_{jk}, \psi_{jk}), \quad (9)$$

where  $P_N$  and  $P_M$  are distributions on selected discrete intervals  $\varepsilon_{j,k}, \psi_{j,k}$  for each  $j, k$ -para on a celestial sphere accordingly of  $M$  and  $N$  independent measurements.  $P^0$  - distribution of true shower radiants,  $P^r$  is distribution of false random radiants on a celestial sphere. Result of logical combine of two series of independent measurements give us:

$$P_{M+N} = P_M \cap P_N = P_{M+N}^0 + P_{M \cap N}^r, \quad \text{or}$$

$$P_{M+N}^0 = P_M \cap P_N - P_{M \cap N}^r, \quad (10)$$

here  $P_{M+N}^0$  - unknown quantity of shower radiant distribution,  $P_{M \cap N}^r$  - are false or sporadic radiants.

The series application of a procedure (10) for different ways of a partition of experimental data on  $M$  and  $N$  allows to reduce  $P_{M \cap N}^r$  up to a level below threshold.

The threshold is selected like in technical radiolocation depending on what we select probabilities not to detect a genuine microshower and to detect false one. At the first stage we have preferred to have small probability of false radiants.

It is achieved by decreasing of number of meteors treated simultaneously in one cycle. The maximum permissible number is determined by a method of computer simulation. The methods and outcomes of simulation are shown in [11]

Parameters of computer technology now are: accuracy -  $2 \times 2$  deg., the rate threshold - 4-5 meteors on day with equal velocities, probability to get false radiant - 5 %,

probability not to get the real radiant with threshold rate - 50%.

### METEOR RADAR OF KAZAN UNIVERSITY

The meteor radar of Kazan university [9] works on frequencies 32 MHz till 1995 and 32,8 MHz. since 1997.

Impulse power of the transmitter varies from 150 kW in a pulse till 1995 to 20 kW since 1997, with duration of a pulse 100 microsecond and frequency of pulse sending is 400 pulses per second.

The transmitter aerial system has two parallel five-element wave channels placed on the rotating basis. The aerial has computer controller and can be automatically focused in one of four azimuths N, E, S, W.

Five 3-element receiving aerals also are established on the rotating bases and can change the orientation under the control of the computer. The aerals formed phase goniometer with base lines oriented on North and on East and sizes of adjacent bases are 4 and 4,5 lengths of waves.[10].

The aerial system is equipped with system of calibration allowing automatically to support of a phase ratio in measuring aerals so that an error of measurement of corners was no more than 1 degree with range no more than 300 km.

After detection of meteor reflection on an output of each of five receiving devices the amplitude and phase for each pulse is measured. The amplitude changing range is 40 dB. In result we receive an opportunity to measure angular coordinates of each accepted pulse, and to measure amplitude - temporary and phase - temporary of the characteristic of each meteor reflection with amplitude of the established level. The level gets out proceeding of a required signal/noise ratio for the worst conditions of measurements.

Except measurement of amplitude and the phase a meteoric radio echo, were measured:

- horizontal coordinates of reflecting points on meteor trails ,
- velocity of flight of a meteoric particle (not for each meteor),
- meanings of diffusion factor (not for each meteor),
- radial velocity component of wind moving of a meteoric trail,
- time of occurrence of a meteor - day, hours, minute, second..

## PRACTICAL REALIZATION OF A METHOD

The discrete method was used for analysis micro shower structure meteors with results of observation of meteor shower Geminid in December 1993 from Kazan meteor radar data.

In Fig.1 is seen only one meteoric shower Geminid for intervals of measured velocity: 32-35 km/s. The same picture we have for intervals of velocity: 29-32 km/s and 35-38 km/s.

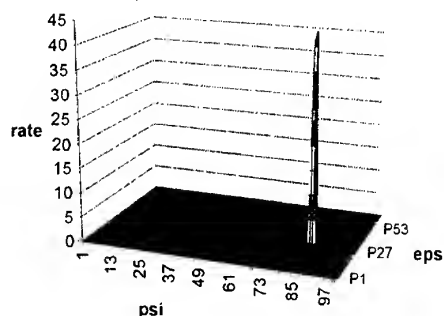


Fig.1 Microshower radiant distribution on celestial sphere, December 13, 1993, 33km/s < V < 35km/s

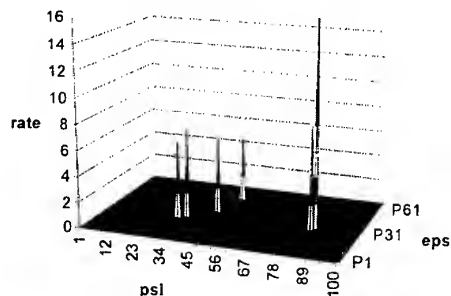


Fig.2 Microshower radiant distribution on celestial sphere, December 13, 1993, 44km/s < V < 47km/s

In Fig 2 for intervals of velocity 44-47 km/s we have 4 micro showers and again Geminids. Five microshowers is seen for interval 47-50 km/s (Fig 3) and again Geminid.

Groups of meteors with Geminid radiants is seen almost in all intervals of speed from 20 up to 62 km/s. It can not be true. Obviously the method of measurement of velocity with diffraction pictures which used in Kazan radar is very bad.

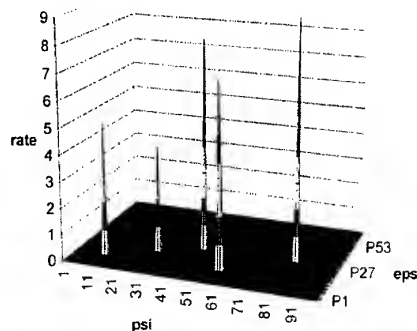


Fig.3 Microshower radiant distribution on celestial sphere, December 13, 1993, 47km/s < V < 50km/s

Nevertheless from a comparison of microshowers in Fig 4 and Fig 5 we can see in different intervals of velocity is observed the microshowers in ranges with different elongation angle from apex. It is a natural outcome of motion of the Earth.

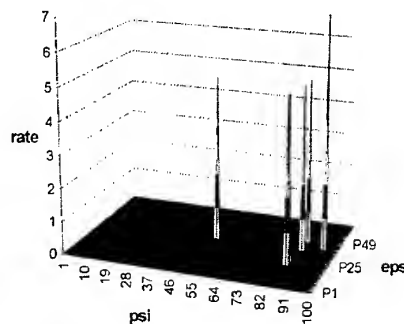


Fig.4 Microshower radiant distribution on celestial sphere, December 13, 1993, 23km/s < V < 26km/s

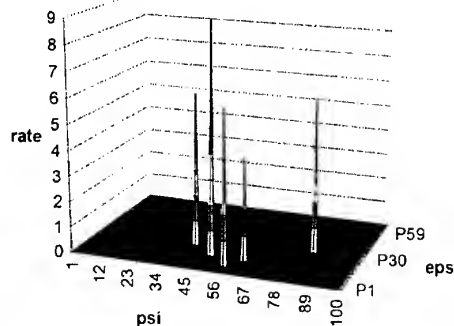


Fig.5 Microshower radiant distribution on celestial sphere, December 13, 1993, 59 < V < 62 km/s

In fact for one day of measurement we have got 37 microshowers including 200 meteors (not counting

Geminid). Distribution of these microshowers on a longitude have been given in the diagram Fig 6.

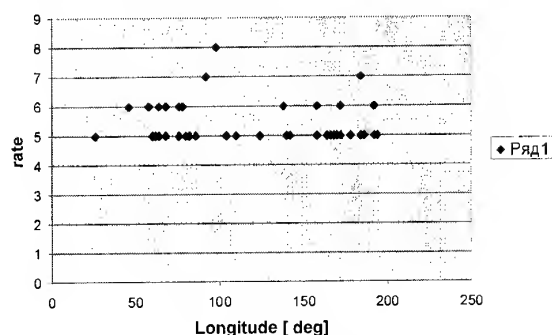


Fig 6 Rate of microshowers for different radiant longitude [meteors per day]

We can see, two areas of increased radiant density are observed: 60-75 degrees and 165-185 degrees. The same we can see in ecliptic longitude distribution of radiant density on 9-15 December 1993 which have been obtained by quasy tomography method [ ] Apparently extremums on tomography maps are concentration of rate of microshowers.

### STRUCTURE OF GEMINID RADIATION AREA

As fact we have small accuracy of measurement of meteor velocity but is possible to use that for check of efficiency of a method for detection of weak meteoric showers. So on Fig 1-5 we see a Geminid meteoric shower on all velocity intervals. Certainly in an interval of 59 -62 km/s we have got these meteors owing to errors of the velocity measurer, however they had similar angular coordinates and were perceived by us as meteoric showers with rate of 5 and more meteors per one day as it is shown in Fig 5.

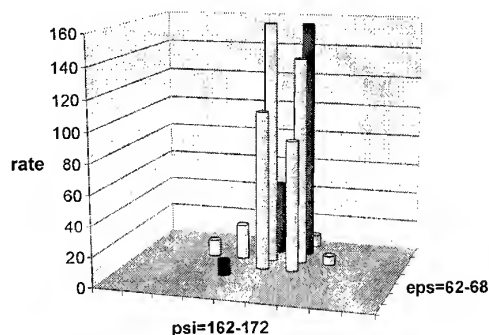


Fig 7 Radiant structure of Geminid

The fact is Geminid is stable observed in many intervals of velocity gives us a capability to select reliably a large

part of meteors of this shower and to apply a new method of the solution to the analysis of a structure of area of radiation of Geminid shower and to calculate mean velocity of meteors of a shower for each elementary segment (2x2 deg) in a radiant structure

We can see a structure of area of radiation of a meteoric shower Geminid in Fig 7. As we see, the area size of radiation is less than it was measured by other methods. The edges of area are very sharp.

We have also more compact distribution of mean velocities on area of radiation (Fig 8)

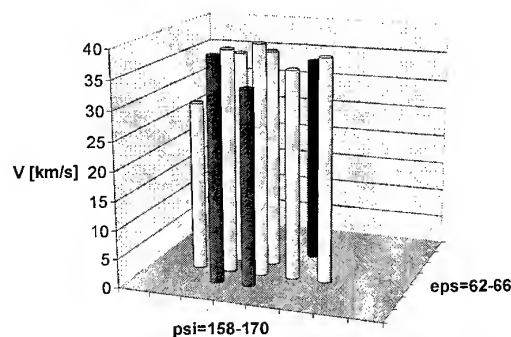


Fig.8 Distribution of mean velocity of meteors on radiation area for Geminid shower.

We also can see in an example of December 13 1994 during a maximum of an operation of a meteoric shower Geminid and other days, many microshowers have more compact angular radiant distributions, than angular distributions of large meteoric shower

### CONCLUSION

The new method of the analysis of the goniometer data of the meteoric radar ensuring high accuracy of measurement of radiant coordinates and rate of meteoric showers and microshowers with number of registered meteors more than 5 for day of observation is developed.

This method allows reliably to divide observable reflections into their fittings to different showers and microshowers for the consequent analysis (altitude, density and other)

The method is based on the concept of a microshower structure of an meteoric complex. Its success is the valid proof of justice of a microshower hypothesis for the some part of meteor complex.

Already first outcomes of measurements generate new problems:

What are a microshowers that we have observed? For today it is a group of more than 5 meteors in one day

which have identical velocity and an identical angular radiant position.

Why they have got small angular sizes? Aren't their parent bodies the very small comets, which in big quantities intersect orbit of the Earth, but can not be remarked by modern optical methods?

May be we must to take in account not only showers, sporadic meteors but and sporadic showers.

It is possible to hope, that a new method will allow to give to radar observations a new life in interests of a meteoric astronomy.

**Acknowledge:** This work has been supported by Russia Fund of Fundamental Investigations and American Meteor Society. Authors thanks Anatoli Stepenov for his efforts to support of equipment activity

## REFERENCES

1. Belkovich O.I., Sidorov V.V. and Filimonova T.K. *Calculation of meteor radiant distribution by using one meteor radar with goniometer*, Astronomical Vestnik M., Nauka, 1991.- V. 25.- N 2.- pp. 225-232.
2. Hey J.S., Stewart G.S., *Radar observations of meteors*, Proc. Phys.Soc., 59, 858-883, 1947
3. Sidorov V.V., Andrianov N.S., Pupysev Y.A. *The distribution of orbit parameters and the changes in meteor particle flux density*, Mon. Not. R. Astr. Soc., 1970.- N 48, 1970
4. V. Sidorov, L. Karukina and A. Fahrutdinova. *The using of goniometer of meteor radar for determination of coordinates of meteor shower radiants*, Meteor Wave Propagation, Вып 5-6. pp 3-5, KSU publishing company, Kazan, 1969.
5. Jones, J., Morton J.D., *The determination of meteor stream radiants from single station observations* //Bull. Astron. Ins. Czech., Vol. 28, N 5, 267-272, 1977
6. Sidorov V.V., Rassim Amer Ali. *Distribution of velocities of meteors on a celestial orb on observations on one radar station with goniometer*, Astronomical Vestnik, Vol. 28 - N1, 81-92, 1994.
7. Sidorov V.V., Filimonova T.K., Rassim Amer Ali, Ganin V.A. *Research of the thin structure of meteor falling flux in locality of Earth by radar tomographic method*, Astronomical Society of the Pacific conference series, Vol.3, p. 154-160, San Francisco, California, 1994.
8. Evdokimov O.I., Filimonova T.K., Sidorov V.V., Rasim Amer Ali, *Investigation of micro streams and associations by the data of radar meteor observations in plane Kazan*, J. Earth, Moon and Planets, Vol. 68, Kluwer Academic Publishers, Dordrecht, 1995.
9. Sidorov V.V., Pupysev Yu. A., and other, *The automatic complex - KSU-M5 for meteor researches* P1, Meteor Radio Wave Propagation. V.14- KSU publishing company, Kazan 1979.
10. Makarov, V.A., Nesterov, V.Yu., Pupysev, Yu.A., Sidorov, V.V., Stepanov A.M., Fahrutdinova, A.N., Shuvarikov, V.A., *Radar complex KGU-M5 for measuring of reflecting parts coordinates on meteor trail*, Meteor Radio Wave Propagation, V.17, P 96-100 KSU publishing company, Kazan 1981
11. Kalabanov S, Sidorov, V.V., Filimonova T.K., *Microswarm structure of a meteoric complex beyond an ecliptic*

## THIN SPACE STRUCTURE OF METEOR FLUX IRREGULARITIES IN LARGE METEOR SHOWERS IN 1986 -1999

Arkady Karpov

*Russia 420110 Kazan st. Zorge53 – 54, Email: Arkadi.Karpov@ksu.ru*

### ABSTRACT

Meteoric observations obtained with the radar KGU-M5 (1986 - 2000), have been archived in an Oracle 8 relational database. An advanced statistical method of searching for fine spatial structure of meteoric showers has been applied to the database and information on the distribution of particles in the Quadrantid, Geminid and Perseid showers has been obtained. For the Geminid meteor shower, evidence of grouping was found in 49% of the intervals of observation (similarly for the Quadrantid and Perseid showers 39% and 63 % were obtained, respectively). The results also had a dependence on signal level. Groupings were detected in 79 % of cases only at low signal level, in 17 % of cases the groupings were detected at both high and low levels detection, and in 4 % of cases groupings were found only at high signal levels and they were absent at low levels. The prevalence of groupings observed at low signal levels corresponds qualitatively well to that of a Poisson-Poisson model of particles distribution.

### INTRODUCTION

It is believed that the meteoric complex in the solar system is, mainly, a group of meteoric bodies that move on random orbits (sporadic meteors) and there are several showers against this background – gigantic combination of particles that move on practically the same orbits. This classification is rather relative since numerous investigations conducted lately have shown that a significant part of the sporadic component of the complex can also be a group of micro-showers not discovered earlier.

The meteoric matter is distributed extremely irregularly in the near-Earth space of the solar system. All possible observation methods (visual, photographic, radio-location) reveal the effect of the meteor emergence in groups with time intervals of several seconds and average inter-group intervals of hundreds of seconds inside the groups.

In this paper we do not consider the issues of the grouping emergence. The connection of the grouping phenomenon with the peculiarities of the meteoric matter ejection from comet cores when comets pass perihelions of their orbits [1] needs experimental and theoretical confirmations. Obviously, there are other

mechanisms that cause the heterogeneous distribution of meteoric bodies in shower sections and, consequently, cause the effect of meteor grouping. The grouping phenomenon in case of sporadic meteors observation may be the evidence of the fact that the sporadic complex of meteors is the group of micro-flows.

If meteoric particles invaded the Earth's atmosphere somehow, separately one from another, the distribution of registration numbers per a time unit (observation interval  $\Delta T$ ) would obey the Poisson law. Several experimental works have been published where there is no mention of great deviations in properties of the registered showers from that of Poisson [2-5]. Based on this, a conclusion was made that the shower that invades the Earth's atmosphere (input flow) satisfies the properties of the Poisson flow and is unstructured. In the meantime, many articles have been published that reveal deviations in the properties of the registration flow from those of the Poisson flow [6-11].

The unique technical characteristics of the radio-locator and the obtained results distinguish the article [6]. In 1957-58 radar observations of sporadic meteors up to  $+15^m$  were conducted at Stanford University. The experiment was conducted using the equipment unique for meteoric research. The antenna system consisted of 96 antennas of "yagi" type; the impulsive capacity of the transmitter was 70 kilowatt. The angular dimensions of the antenna directivity diagram were  $1,5^\circ$  by azimuth and  $60^\circ$  in height. This provided for the registration of trace reflections with the linear density of  $\alpha > 10^{10}$  el/m. Over 2 000 meteors, on average, were registered per 1 hour. We should note that in other similar experiments mentioned above the energy was much lower and the number of registered meteors was much less. The standard deviation was not  $13.6 = \sqrt{185}$  as it could be said in the assumption of the lack of space-time groupings but 55. Hence, the authors have come to the conclusion that in reality meteors are distributed in the variety of small flows and the change in the number of meteors is stipulated by the change in the number of micro-flows that can be registered by the radio-locator at a certain moment. On average, every moment  $(185/55)^2 = 11$  showers are observed. The duration of each flow's action is from several hours to a day.

# 1. THE METHOD OF INVESTIGATING THE FINE STRUCTURE

In this paper the data of experiments conducted from 1986 to 1998 in azimuthal regime employed for the investigation of meteoric activity distribution over the celestial sphere were used to study the thin structure of the shower. The radar "KGU-M5" has the following characteristics:

- frequency – 32,6 MHz
- transmitter power – 20-120 kilowatt
- radar's receiving antenna - three-element "yagi" and transmitting antenna - five-element "yagi".

In the course of the observations the antennas were orientating themselves in the four cardinal points one after another at intervals of fifteen minutes. The radar was operating in the mode of radiating impulses with the duration of 100 microseconds and the repetition rate of 400 Hz.

The complex research of the fine spatial structure was conducted only after the creation of the relational database "Meteor". The huge amount of the experimental data obtained over the last two decades is constantly used for later investigations. Here it takes to make extracts on several criteria from the available data, obtain statistical data over a certain period, and search data by the terms. The use of the up-to-date database management systems, e.g. Oracle 8, for the database development, besides the above-mentioned basic requirements, also provides for the remote access to the database, its corporate use and high fault tolerance. The use of the relational base "Meteor" has significantly facilitated the access to the unique experimental data and provided for the complex research of fundamental problems directly or indirectly related to the information obtained at radio-observations of meteors.

The statistical method of investigating the fine spatial structure has been developed taking into account the specificity of the database management system. The diagram of investigation method is given in the fig.1.

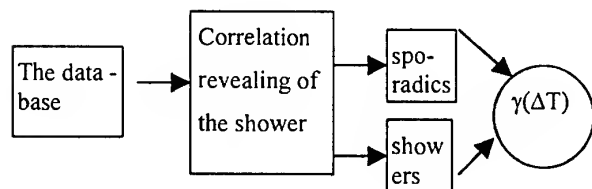


Fig. 1 The diagram of investigation method

After restoring and ordering of the observation archive, conducted using the meteoric radio-location complex "KGU-M5", the block "Results of angular observations" is formed from the archive of the relational da-

tabase controlled by the database management system Oracle 8. In the block "Correlation detection" the separation of meteor shower from the sporadic background based on the methods, proposed in the paper [12], takes place.

The grouping identification takes place with the use of statistical  $\gamma(\Delta T)$  - criterion

$$\gamma = \frac{\sum_{i=1}^p n_i^2 - k_1 - \frac{k_1 \cdot (k_1 - 1)}{p}}{\sigma} \quad (1)$$

$$k_1 = \sum_{i=1}^p n_i \quad \sigma^2 = \frac{2 \cdot (p-1)}{p} \cdot k_1 \cdot (k_1 - 1)$$

$n_i$  - number of registration a meteoric radioecho received in time  $\Delta T$ ;

$p$  - number of intervals of supervision of length  $\Delta T$ .

$\gamma$  is asymptotically normal (0,1) and the proposed criterion is the most powerful for the differences Poia, Poisson and binomial distributions. Thus, the large value  $\gamma$  ( $\gamma > 3$ ) indicates the significant deviation from the Poisson distribution.

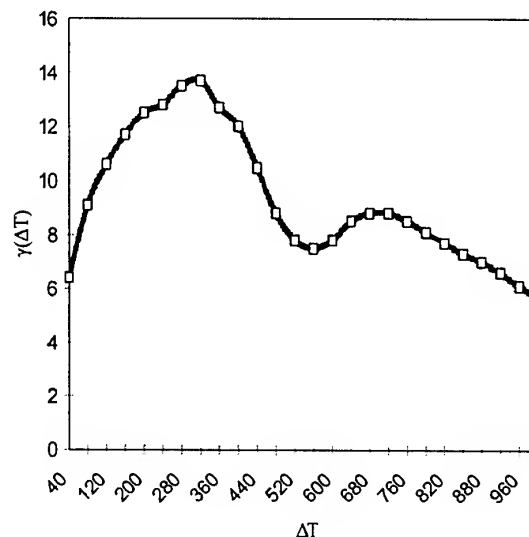


Fig.2. A model example of identification of groupings

Let us consider the time series of registrations with the length  $T_I$ . For any  $\Delta T < T_I$  we may calculate the parameter  $\gamma$  and come to the consideration of  $\gamma(\Delta T)$ -

function. The modeling of groupings with the average length  $T_0$  showed that  $\gamma(\Delta T)$ -function takes the maximal value when  $(\Delta T) = T_0$ . The fig. 2 shows the results of a model experiment in which the groupings with the length  $T_0 = 300$  c and  $T_0 = 700$  c were generated against the background of the Poisson flow. Hence comes the possibility to interpret observation results through the contraposition of maximum  $\gamma(\Delta T)$ -function with characteristic dimensions of groupings. When we know the velocity of shower particles  $V_0$ , we can come to a more vivid characteristic  $L$  – characteristic length of groupings  $L = \Delta T \cdot V_0$ .

## 2. THE ANALYSIS OF EXPERIMENTAL DATA

It the course of this research it was determined that it takes at least seven registrations (at the upper level of registration) per an observation integral to obtain reliable values  $\gamma$ . In order to provide sufficient statistics for later investigations the analysis of information stored in the database was conducted. The hourly numbers meteors distribution over the celestial sphere in time was constructed. The values of hourly numbers higher than 250 were in the focus. Later there was the selection of the chosen data regarding their attachment to main showers. As a result of this selection the following showers were marked out as having sufficient statistics for research: the Geminid (1986, 1987, 1988 and 1989), the Quadrantid (1988, 1990), the Perseid (1986, 1987) and some other observations conducted in 1976 and 1983.

The analysis of experimental data is conducted in two directions:

1. investigating the fine structure in different areas of the flow section,
2. investigating variations of  $\gamma$  parameter depending on the value of the observation interval  $\Delta T$ .

We will consider the fine structure investigation in different areas of the flow section using the example of the 1983 Geminid. In the shower periphery the values  $\gamma$  insignificantly differ from zero and even the maximum value  $\gamma_{\max} < 3$ . This is a unique evidence of the practical absence of groupings during the period of the observations from December 10 to 13. On December 14 during the peak activity of the shower the share of grouped particles increases significantly ( $\gamma_{\max}$  reaches  $\gamma_{\max} = 12$ ) and the characteristic length of groupings reaches 9000 km and more. On December 15, on the contrary, most groupings have the length up to 7000 km. The grouping degree is lower that the day before.

The fig 3 shows the changes of the parameter  $\gamma$  in the shower section. The results obtained in this research are rather steadily repeated for all observation intervals  $\Delta T$ . The fig 3 also gives the results for  $\Delta T = 500$  sec. Particle groupings become apparent in the shower peak (December 14-15, the solar longitude Sun  $\lambda_{\odot} = (262^\circ - 263^\circ)$ ), and there is also an additional peak, much lower than the main one, when  $\lambda_{\odot} = 259^\circ$ .

The experimental data of 1976 were processed using the  $\gamma(\Delta T)$ -function calculated for the two registration levels, which at the first level corresponded to the registered masses higher than  $10^{-5}$  gr. and at the second level -  $5 \cdot 10^{-5}$  gr. The figs. 4 and 5 give the  $\bullet$  sign for the results of the first-level registration and  $\Delta$  sign for the results of the second-level registration.

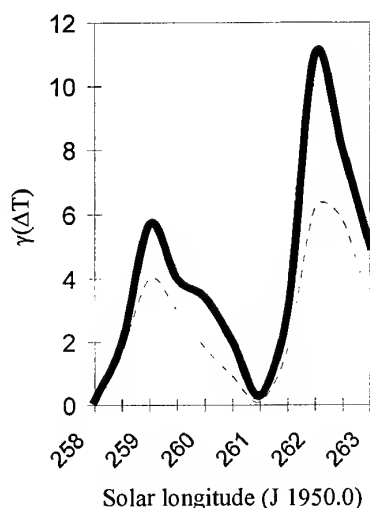


Fig. 3. Structure of the 1976 Geminid

For the 1976 Geminid (fig 4) at the lower registration level the main part of the groupings has the length from 450 to 14000 km. Two peaks of  $\gamma(\Delta T)$ -function when  $L_0 = 6125$  km ( $T_0 = 175$  sec) and  $L_0 = 10500$  km ( $T_0 = 300$  sec) are well expressed. At a higher registration level the groupings of length from  $L_0 = 9000$  km to  $L_0 = 21000$  km with the peak when  $L_0 = 19250$  become evident.

For the 1976 Quadrantid (fig 5) the groupings are expressed not so distinctly. At the lower registration level the presence of the weakly expressed groupings with the continuous spectrum from  $L_0 = 500$  km ( $T_0 = 12.5$  sec) to  $L_0 = 19000$  km ( $T_0 = 475$  sec) was revealed.

The fact calls to our attention that in the both cases at the lower registration level the deviation degree is higher than that of Poisson.

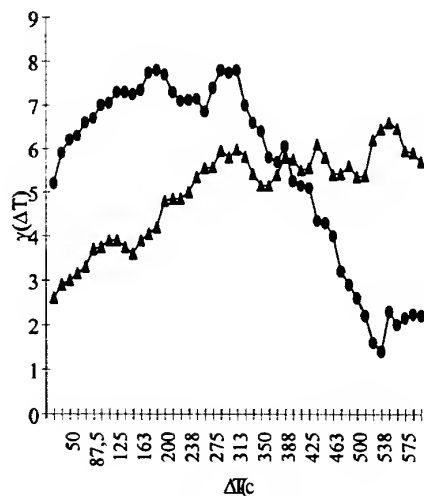


Fig.4. Thin structure of the 1976 Geminid

Here is also the contraposition of results obtained at Stanford University with those obtained using relatively low-powered radar. The significant rule becomes evident: the degree of the observed grouping depends on the energy of the meteoric radar.

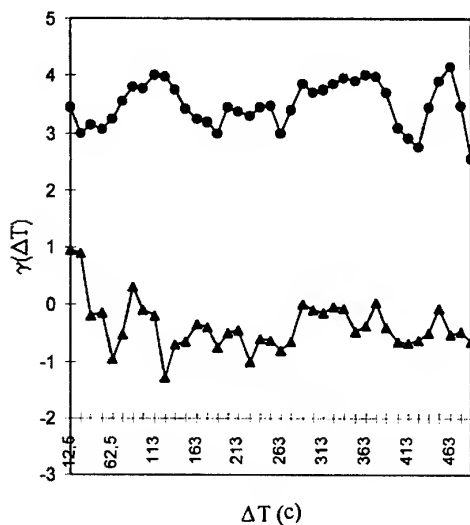


Fig.5 Thin structure of the 1976 Quadrantid

One of the probable explanations of this phenomenon is the existence of various kinds of groupings. "Light" particle groupings are smaller and their number significantly exceeds the number of "heavy" particle groupings. This phenomenon calls for the further detailed investigation. In the meantime, it is obvious that the conduction of the registration at several boundaries increases the method's self-descriptiveness.

The examples of the characteristic realizations of the function  $\gamma(\Delta T)$  are given on the fig. 6 – 8.

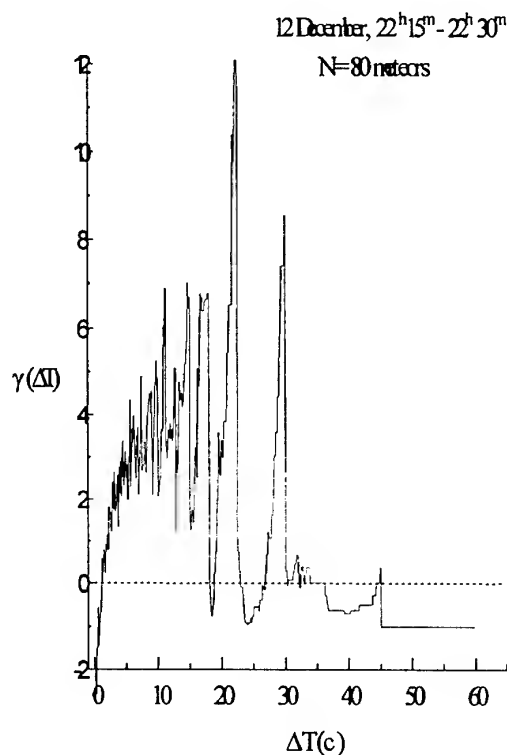


Fig.6. An example of functions describing presence of groupings.

The significant peaks of the value  $\gamma(\Delta T)$  on the graphs demonstrate the presence of the groupings in the meteor registrations on December 7, 12 and in the period 22<sup>h</sup> 15<sup>m</sup> - 22<sup>h</sup> 30<sup>m</sup> UT. However, on the boundaries of the observations time domain (until 21<sup>h</sup> and after 0<sup>h</sup> UT) the groupings did not show (fig. 8). It might be caused by the shift of the Geminid radiant and, consequently, flow meteors were registered at the radar's lower sensitivity. As a result, this led to the increase of minimally registered masses of meteoric bodies. The similar relation of the presence of meteoric bodies groupings depending on their masses for the Geminid

was noted before [1]. In these investigations conducted using the same equipment meteoric bodies groupings showed more clearly for smaller particles. Revealed deviations of the registration flow properties cannot be explained by the change in the number of registered meteors. They might be caused by the presence of the complex structure of the shower.

The given graphs of the realization of the function  $\gamma(\Delta T)$  also point at the presence of large-scale rules in the change of the structure of the Geminid – the available peaks in the original spectrum  $\gamma(\Delta T)$  shift from 150-200 sec (December 7) to 200-300 sec (December 12) and 120 sec (December 14). Analyzing the distribution of the function  $\gamma(\Delta T)$  calculated over the period of the flow observations under the same conditions of its surveillance we may find out characteristic peculiarities in dimensions of particle groupings in various parts of the shower.

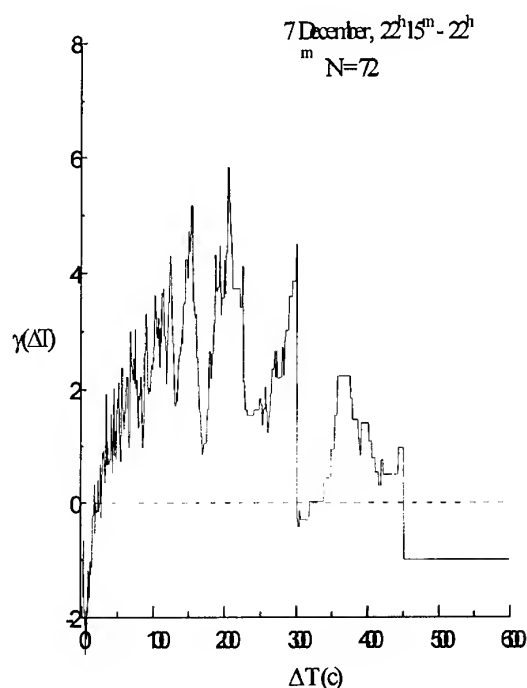


Fig.7. An example of functions describing presence of groupings.

Most grouping dimensions are observed on December 12 (fig. 7) which corresponds to the central part of the flow in the area of the greatest density of the particle flow. On other days of the observations the tendency to the decrease of grouping dimensions is distinctly observed on the periphery.

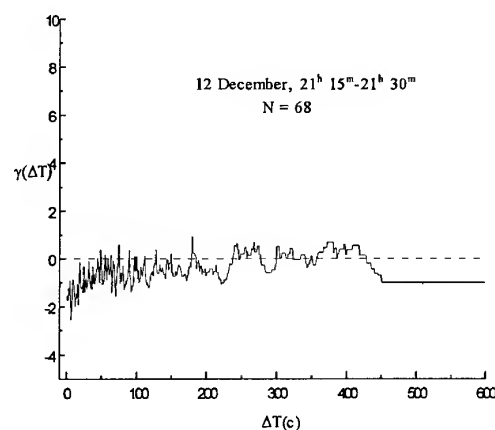


Fig.7. An example of functions describing absence of groupings.

Undoubtedly, the conduction of the research at several different registration levels is of a certain interest. We dwelled on the two levels believing that the lower level corresponds to the "light" particle registration while the upper level corresponds to the "heavy" particle registration. The lower level is determined by the minimal registration level of the receiving equipment. The choice of the upper level is a rather subjective procedure. On the one hand, the levels should be fairly scattered while, on the other hand, the sufficient statistics of no less than 7 registrations over the observation period should be provided at the upper level. The table 1 gives the main generalized results of the statistical processing of the experimental data.

Table 1. Generalized results of the statistical processing of the experimental

	Geminid 1988	Geminid 1989	Quadrantid 1988
1	46	31	13
2	0.75	0.78	0.33
3	0.22	0.11	0.5
4	0.03	0.11	0.17
	Quadrantid 1988	Quadrantid 1988	Perseid 1987
1	33	32	
2	0.55	0.5	0.5
3	0.18	0.5	0.4
4	0.27	0	0.1

Table 1: Generalized results of the statistical processing of the experimental data.

In the first line of the table:

1. The number of fifteen-minute intervals

2. The share of intervals with groupings only at the lower registration level
3. The share of intervals with groupings at the both registration levels
4. The share of intervals with groupings only at the upper registration level

## CONCLUSIONS

In the course of the statistical analysis of the experimental data the following main results were obtained. For the Geminid groupings were revealed in 49% of the observation intervals. In cases of the grouping observations they were distributed as follows: 79% - groupings observed at the lower registration level, 17% - at the both registration levels and 4% - groupings were observed at the upper registration level and were not available at the lower level. For the Quadrantid groupings were revealed in 39% of the observation intervals. In cases of the grouping observations they were distributed as follows: 48% - groupings observed at the lower registration level, 35% - at the both registration levels and 17% - groupings were observed at the upper registration level and were not available at the lower level. For the Perseid groupings were revealed in 63% of the observation intervals. In cases of the grouping observations they were distributed as follows: 50% - groupings observed at the lower registration level, 40% - at the both registration levels and 10% - groupings were observed at the upper registration level and were not available at the lower level. The prevalence of the groupings at the lower registration level was observed which qualitatively well corresponds to the Poisson-Poisson model of the particle distribution. In this model, smaller particles group around larger ones (the interval distribution among large particles obeys the exponential law). Smaller particles in the groupings are distributed according to the Poisson law with another distribution parameter. The above-mentioned results explain the absence of the groupings in experiments when low-sensitivity radars were used and the presence of the groupings when high-sensitivity radars were engaged.

## ACKNOWLEDGMENTS

This work was funded by the Russian Foundation for Fundamental Research (Project № 00-02-16845)

## REFERENCES

1. Karpov A.V., et al., Study of meteoric flux properties by means of statistical modeling methods, *Solar System Research*, Vol. 17, 44-51, 1984.
2. Belkovich O.I. *Astronomy Repots*, Vol. 38, 532 - 535, 1961.
3. Briggs B.H. Observation short bursts of signal from a distant, *J. Atm. Terr. Phys.*, Vol. 8, 171-178, 1956.
4. Keary T.J., Wirth H.J. *The random occurrence of meteors in the upper atmosphere*, *J. Geoph. Res.*, Vol. 63, 67-75, 1958.
5. Keay C.S., Ellyett C.D. Absence of unusual periodicity's in radar meteor rates, *J. Geoph. Res.*, Vol. 71, 1409-1411, 1966.
6. Gallagher P.B., Eshelman V.R. Sporadic shower properties of very small meteors, *J. Geoph. Res.*, Vol. 65, 1846-1847, 1960.
7. Poole L.M.G., Kaiser T.R. The detection of shower structure in the sporadic meteor background, *Mon. Not. Roy. Astron. Soc.*, Vol. 156, 283-290, 1972.
8. Kresak L., Slancikova I. On the structure of the Geminid meteor shower, *Bull. Astron. Inst. Czechosl.*, Vol. 26, 327-342, 1975.
9. Simek M. Some characteristics of the Geminid meteor shower, *Bull. Astron. Inst. Czechosl.*, Vol. 29, 331-340, 1978.
10. Porubcan V. On the grouping of meteors in meteor streams, *Bull. Astron. Inst. Czechosl.*, Vol. 19, 316-323, 1968.
11. Porubcan V. On the structure of the 1969 Leonid meteor shower, *Bull. Astron. Inst. Czech.*, Vol. 25, 353-361, 1974.
12. Jones J., Morton J.D. The determination of meteor streams from single station observation, *Bull. Astron. Inst. Czech.*, Vol. 28, 267-272, 1977.

# THE DETERMINATION OF THE EJECTION VELOCITY OF METEOROIDS FROM COMETARY NUCLEI

I. P. Williams

Astronomy Unit, Queen Mary, University of London, Mile End Rd London E1 4NS, UK

## ABSTRACT

The value of the ejection velocity of meteoroids from cometary nuclei is determined by the physical processes that are ongoing there. In broad terms, this is well-understood: as the comet approaches the Sun, the increasing solar radiation falling on the nucleus heats it up until ices sublime causing an outflow of gas. This gas outflow drags out and accelerates meteoroids away from the nucleus. The details of the processes and values of the parameters involved are less well determined. Hence a fairly wide range of ejection velocity values can be obtained depending on the detailed choices made, ranging from a few meters per second to a few hundred meters per second. Reversing the argument, if the value of the ejection velocity is known, then it helps to constrain the value of parameters relevant to the nucleus and details of the physical processes. From the view-point of understanding meteor stream evolution, the initial velocity is also important. Both the initial velocity and gravitational perturbations cause a dispersal of stream meteoroids and a precise determination of one allows the other to be quantified. Here, as well as discussing the general problem, we concentrate on situations where the final outcome is very sensitive to the assumed initial velocity and hence, by reversing the argument, if the final outcome is observed, then the ejection velocity must have been within a narrow permitted range. Most of the arguments lead to values of the ejection velocity of the order of  $75 \text{ m s}^{-1}$  - rather close to the values obtained for one millimeter sized grains by Whipple half a century ago.

Key words: Meteoroids, Cometary nuclei.

## 1. INTRODUCTION

An association between comets and meteoroid streams was first suggested in the second half of the nineteenth century, probably by Schiaparelli (1867). The suggestion was based on the similarity between the orbits of certain meteoroid streams and comets, in particular the Perseids and comet 109P/Swift-Tuttle and the Leonids and comet 55P/Tempel-Tuttle. Since then, comet-meteoroid stream pairs have been identified, based of the similarity in the orbital elements, for virtually all recognizable significant

streams, the only exception being the Quadrantids where some debate over its parent is still ongoing. In order to verify such a pairing, some objective measure of the differences between the orbits, such as that proposed by Southworth & Hawkins (1963) or Drummond (1981) is usually used. A discussion of this topic can be found in Neslušan & Welch (2002). The same objective measure is used to identify new meteoroid members of the stream.

Until about half a century ago, it was a subject of some considerable, and heated, debate as to what the physical processes that lead to meteoroids and comets moving on similar orbits were. There was debate as to whether meteoroids were accumulating to form comets or were comets disintegrating to form meteoroid streams. It is important to remember that the prevailing view regarding the structure of comets at this time was the *flying sand-bank* model in which a loose aggregation of grains were usually held together by their own mutual gravitational field but became affected by the tidal effect of the Sun when close to perihelion, possibly with each grain moving on independent heliocentric orbits. On such a model, the transition of a grain from comet member to a meteoroid stream member, or *vice-versa* only needed a small perturbation to the individual orbits. The question that we are addressing in this contribution, namely the value of the ejection velocity of meteoroids from comets hardly had any relevance. As observations of comets became more numerous and detailed, it became apparent that this *flying sand-bank* model had a number of serious difficulties in explaining these. When Whipple (1950) proposed a new model for comets in which a single icy cometary nucleus existed, this was widely accepted by almost all workers. The basic model, called the *icy conglomerate model* or more popularly as the *dirty snowball model*, is still generally accepted today and indeed the *Giotto* fly-by of the nucleus of comet 1P/Halley verified its main assumptions.

In this model, the comets consists of a single solid nucleus rather than a swarm of individual small particles. This nucleus was assumed to be composed primarily of an icy matrix within which dust grains of varying sizes were embedded. As the comet nucleus approached the Sun, the increased heating from solar radiation would cause the ice to sublime, and flow away from the nucleus to first form a coma and also the plasma tail. The embedded grains would also be freed and these would be dragged outwards against the gravitational field of the

cometary nucleus, by the outflowing gas. The motion of very small grains would soon be dominated by Solar radiation pressure and flow nearly radially outwards to form the well known dust tail. Very larger grains would remain bound to the cometary nucleus since the gravitational force from the nucleus would be greater than gas drag. Intermediate sized grains would escape with some finite velocity relative to the cometary nucleus. The gravitational field of the Sun soon dominates the motion of the meteoroids and they move on Keplerian orbits that are fairly similar to the comet cometary orbit since the meteoroid velocity relative to the nucleus will almost certainly be much less than the orbital velocity and so in a heliocentric reference frame the velocity and position of a meteoroid is very similar to those of the comet. Hence what is called a meteoroid stream is formed, that is a collection of meteoroids moving on nearly identical orbits.

The basic physical processes involved in the above scenario is very straight forward. Solar radiation heats up the nucleus at an increasing rate as the comet approaches the Sun. When the surface temperature of the nucleus reaches a sufficiently high value, the ice will sublimate resulting in an outflow of gas from the nucleus. A drag force due to this outflow will exist on all loose grains and, if this drag force exceeds the gravitational field of the nucleus, the grains will also flow outwards, being continually accelerated by the gas drag. It is thus self-evident that the grains can not have a greater velocity than the gas and that the gas speed will be in the general region of the mean thermal velocity, in the region of  $1 \text{ km s}^{-1}$ . Since the orbital velocity of the parent comet is in the region of  $40 \text{ km s}^{-1}$ , the contention that the ejection velocity is much less than the orbital velocity is obviously true and the ejected dust will also have a velocity in the heliocentric frame of the order of  $40 \text{ km s}^{-1}$  and we should expect meteoroid streams to be formed by this physical process. The aim is to produce a more quantifiable model than the qualitative one described. This was considered by Whipple (1951) who derived the following formula for the ejection speed  $v$ , in  $\text{cm s}^{-1}$  of the meteoroids relative to the nucleus,

$$v^2 = 4.3 \times 10^5 R_c \left( \frac{1}{b\rho r^{2.25}} - 0.013 R_c \right), \quad (1)$$

where  $R_c$  is the radius of the nucleus in kilometers,  $r$  the heliocentric distance in AU,  $b$  the meteoroid radius and  $\rho$  its bulk density, both in cgs units. Insertion of typical values for the parameters in equation (1), namely  $R_c = 5$ ,  $\rho = 0.8$  gives the ejection speed of a meteoroid of radius one millimeter as  $50 \text{ m s}^{-1}$ . For centimeter sized grains this reduces by a factor of three, while possible variations in the size of the nucleus also can change the value by a similar factor. Thus, the Whipple formula predicts ejection velocities in the general range from a few meters to a few hundred meters per second.

In deriving this formula, Whipple made a number of assumptions, amongst them being

(a) that the nucleus was not a great sink of energy so that the energy carried out by the outflow was directly proportional to the energy input from the Sun

(b) that the nucleus surface would be heated uniformly

and that the outflow occurred uniformly from all the surface of the nucleus

(c) that the outflowing gas was in an approximately equilibrium state so that the velocity distribution of the escaping molecules was approximately Maxwellian

(d) that the grains were approximately spherical

(e) that the cometary nucleus was predominantly water ice.

Some of these assumptions have been questioned, leading to some authors suggesting modifications to the Whipple formula. Probst (1968) suggested that the ejection velocity should be increased by a factor of 2 to take into account the fact that the gas is not in equilibrium but rather expanding adiabatically into vacuum, while a lightly larger factor of 2.5 was obtained by Jones (1995) to compensate for essentially the same effect. A factor of similar order was also suggested by Crifo (1995) and Hughes (2000) to compensate for the fact that, as we now know, cometary nuclei tend to have active vents from which most of the outflow of gas takes place so that the area over which energy is lost is not the same as the area over which it is gained from Solar radiation. Gustafson (1989) considered meteoroids that were non-spherical and suggested an increase in the ejection velocity by an other factor of order two. Hence, if all of these corrections are adopted, the theoretical value for the ejection velocity could be increased to  $0.5\text{--}1 \text{ km s}^{-1}$ , still much less than the orbital velocity of the parent.

Assumption (e) above mainly affects the heliocentric distance at which outgassing starts and has been discussed by many authors. (See O'Ceallaigh *et al.*, 1995 and references therein).

Steel (1994) pointed out that meteoroids could be composed of both ice and the more traditional non-volatile component and that the ice could remain within the meteoroid for some considerable time. The sublimation of this ice would cause outgassing from the meteoroid and hence there would be a reaction force on the meteoroid, a *rocket effect*, which could accelerate the meteoroid, giving it a velocity that was significantly higher in value than the original ejection velocity generated by gas drag. This was quantified by Hughes (2000) who obtained velocities relative to the comet for the meteoroids of the order of  $500 \text{ m s}^{-1}$  through this *rocket effect*.

Hajduk (1986) consider the detected flux of material from comet 1P/Halley by the Giotto experiments and concluded that the ejection velocity of centimeter sized grains could only have been a few  $\text{m s}^{-1}$ . It is important to recognize that this value is a deduction from the measured outflow rate and the implied mass distribution index and not a direct measurement of the velocity of any meteoroid by Giotto. Various theories thus predict a wide range of values for the ejection velocity!

Determination of the ejection velocity from direct observations of the dust close to cometary nuclei has also proved difficult. In essence, the effects of dust that can be detected through ground based observations is dominated by bodies that are much smaller than meteoroids.

those grains whose motion are seriously affected by radiation pressure. It thus requires much extrapolation to obtain meteoroid velocities. Similarly, *in situ* measurements from space craft also to focus on grains of sizes that are an order of magnitude smaller than stream meteoroid in this case simple because there are many more of these grains. Hence, very little information is obtained about the ejection velocity of stream meteoroids through direct measurements of dust near comets.

The aim of this paper is to consider what limits can be placed on the value of the ejection velocity of meteoroids from cometary nuclei by considering data from the observations of meteor showers.

Determination of this velocity is important for two reasons. First, it is necessary to know this if detailed models of stream evolution are to be produced in order to predict meteor outbursts such as the recent ones in the Leonid shower for example. Second, it produces a valuable constraint on the nucleus parameters and a check on our understanding of our models for cometary nuclei.

The main intention is to discuss the methodology that can be used on data from individual streams rather than the determination of specific values for specific observations. Nevertheless, it is useful to obtain typical values and so we will derive values based on published data for a number of stream. for the purposes of this derivation, the following values for the orbital parameters  $q$  (perihelion distance in astronomical units),  $e$  (eccentricity),  $i$  (inclination),  $\omega$  (argument of perihelion) and  $\Omega$  (longitude of the ascending node) will be assumed. All other parameters, including  $a$ , the semi-major axis are calculated from this set. (The problem is that while for each meteoroid, the inverse of the semi-major axis can be determined directly from observations, for a whole set of meteoroids the mean value of  $a$  is not the same as the inverse of the mean value of  $1/a$ . Hence, while for each individual orbit,  $q = a(1 - e)$ , when the mean value of each of these quantities is obtained for a set of meteoroids, these means do not satisfy this equation. So since the mean orbit should be elliptical, one of these mean values has to be discarded, we have chosen to discard the mean value of  $a$  obtained from the mean of  $1/a$  and use instead for the mean value of  $a$  the value obtained from  $q = a(1 - e)$ ). We do not enter into any discussion of whether these are the best or most appropriate values for any given stream, they are used only as a means to deriving some typical values of the ejection velocity from comets and not to produce a definitive value for any given stream.

For the Geminid stream we take the values of the orbital parameters from Betlem *et al.* (1997), namely,  $q = 0.142$ ,  $e = 0.893$ ,  $i = 23^\circ.77$ ,  $\omega = 324^\circ.53$  and  $\Omega = 262^\circ.02$ . The corresponding values for the assumed parent of the Geminids, namely asteroid 3200 *Phaethon*, are taken from Williams & Wu (1993) and are  $q = 0.1395$ ,  $e = 0.8903$ ,  $i = 22^\circ.04$ ,  $\omega = 321^\circ.67$  and  $\Omega = 265^\circ.51$ .

The meteoroid stream that is associated with comet 1P/Halley produces two observable meteor showers on Earth, the  $\eta$  Aquarids and the Orionids. The reason for this is simple, both nodes of the orbit of 1P/Halley are

fortuitously close to the orbit of the Earth. The orbital elements of comet 1P/Halley, are taken from Williams *et al.* (1993) and are  $q = 0.587$ ,  $e = 0.967$ ,  $i = 162^\circ.24$ ,  $\omega = 111^\circ.85$  and  $\Omega = 58^\circ.15$ . In principle, being part of one stream, one should expect the orbits of the meteors from the two showers to be the same. In practice, since the earth passes through a slightly different part of the stream on the two occasions, they are not. For the  $\eta$  Aquarids, Lindblad (1990) gives  $q = 0.603$ ,  $e = 0.939$ ,  $i = 165^\circ.6$ ,  $\omega = 99^\circ.63$  and  $\Omega = 45^\circ.7$ , while Lindblad & Porubčan (1999) obtained  $q = 0.580$ ,  $e = 0.963$ ,  $i = 163^\circ.9$ ,  $\omega = 81^\circ.38$  and  $\Omega = 27^\circ.1$  for the Orionids.

The orbital elements for the Perseid meteoroid stream are given also by Betlem *et al.* (1997) as  $q = 0.951$ ,  $e = 0.967$ ,  $i = 113^\circ.36$ ,  $\omega = 151^\circ.34$  and  $\Omega = 139^\circ.48$ . The parent comet is 109P/Swift-Tuttle and Marsden & Williams (1996) give orbital elements for this comet as  $q = 0.9582$ ,  $e = 0.9636$ ,  $i = 113^\circ.4$ ,  $\omega = 153^\circ.0$  and  $\Omega = 139^\circ.44$ .

The Leonids present a slight problem in that many good observations of the activity profile were derived in 1999, leading to a very accurate value of  $\Omega$  of  $235^\circ.29$ , but very few double station observations were obtained so that the other orbital elements are not well determined for the 1999 outburst. For the the remaining orbital elements we have therefore taken the mean of the values given by Lindblad, Porubčan & Stohl (1993) and Suzuki *et al.* (1999), namely  $q = 0.982$ ,  $e = 0.899$ ,  $i = 162^\circ.2$ ,  $\omega = 172^\circ.1$ , and is a mean value for meteors seen over a number of recent years. The parent comet of this stream is also well known and is 55P/Tempel-Tuttle. Its orbital elements are taken from Yeomans *et al.* (1996) and are  $q = 0.9766$ ,  $e = 0.9055$ ,  $i = 162^\circ.48$ ,  $\omega = 172^\circ.50$  and  $\Omega = 235^\circ.26$ .

In this review we shall also from time to time quote results for the ejection velocity obtained by other authors. These values are those given by these authors as given in the literature and not the values that would have been obtained had we used their methodology but with our assumed orbits for either the parent comet or the mean meteoroid stream.

## 2. CHANGES IN THE SEMI-MAJOR AXIS

Any ejection velocity given to a meteoroid changes the velocity of that meteoroid in a heliocentric frame compared to that of the parent comet. Hence there is also a change in the the kinetic energy per unit mass of that meteoroid relative to that of the parent comet. However, at the instant of ejection the position of both meteoroid and comet are the same and so there has been no change in potential energy. Consequently, the total orbital energy per unit mass,  $U$ , is changed by the same amount as the kinetic energy per unit mass. To a reasonable approximation, meteoroids move on Keplerian ellipses about the Sun, so that standard theory gives us

$$U = -\frac{GM_\odot}{2a}, \quad (2)$$

where  $G$  is the gravitational constant and  $M_{\odot}$  the mass of the Sun. Hence, if meteoroids are ejected from a cometary nucleus with any finite velocity, causing a change in  $U$ , there must be a corresponding change in  $a$ , the semi-major axis.

Assuming that the changes are small, we can obtain to first order,

$$\frac{\Delta U}{U} = -\frac{\Delta a}{a}. \quad (3)$$

If we denote the component of the ejection velocity in the orbital plane of the comet by  $v$ , then it is convenient to consider this in two components, along the direction of the parent body's motion and perpendicular to this as  $v \cos \theta$  and  $v \sin \theta$ , so that  $\theta$  is the angle between the tangent to the parent's orbit and the direction of the ejection velocity component in the orbital plane. Hence, in a heliocentric frame, twice the kinetic energy of the meteoroid is given by

$$\begin{aligned} & (v \sin \theta)^2 + (V + v \cos \theta)^2, \\ & = V^2 + v^2 + 2vV \cos \theta, \end{aligned} \quad (4)$$

where  $V$  is the orbital speed of the parent comet at the time of meteoroid ejection. Since, as we have said, the location of the parent body and the meteoroid is the same at the instant of ejection, there is no change in potential energy per unit mass, hence,

$$2\Delta U = v^2 + 2Vv_{\parallel} \quad (5)$$

represents the change in orbital energy per unit mass between the parent body and the meteoroid.

As mentioned already  $v$  is likely to be much less than  $V$  and so for most streams it is convenient to denote the velocity component along the direction of motion of the comet,  $v \cos \theta$ , by  $v_{\parallel}$  and,

$$\Delta U = Vv_{\parallel}. \quad (6)$$

Remembering that

$$V^2 = GM_{\odot}(2/r - 1/a), \quad (7)$$

where  $r$  is the heliocentric distance, we obtain

$$\frac{\Delta a}{a} = 2 \frac{v_{\parallel}}{V} \left( \frac{2a}{r} - 1 \right) \quad (8)$$

If additionally we assume that most meteoroids are ejected when the parent comet is close to perihelion, so that  $r = a(1 - e)$ , equation (8) becomes

$$\frac{\Delta a}{a} = 2 \frac{(1 + e)}{(1 - e)} \frac{v_{\parallel}}{V} \quad (9)$$

and we have a linear relationship between the ejection velocity and the difference between the semi-major axes of the meteoroid and parent comet. Hence, if the differences between the semi-major axes of meteoroids and their parent comet can be quantified through observations, then the ejection velocity of those meteoroids can be determined.

A slight variant on this method was used by Harris and Hughes (1995) where they interpreted  $\Delta a$  as being the standard deviation in the observed distribution of  $a$  in the stream rather than the difference between the mean value of  $a$  for the meteoroid stream and the value of  $a$  for the parent body. They obtained an ejection velocity in excess of  $600 \text{ m s}^{-1}$  for the Perseid stream. This variant of the method was also used by Williams (1996) to determine the ejection velocity for six well known streams, the Quadrantids, Geminids, Perseids, Taurids,  $\eta$  Aquarids and Orionids. The following values for the ejection velocities were found (in the order as above) 880, 200, 750, 340, 170 and  $160 \text{ m s}^{-1}$ . The value for the Perseids is in agreement with that obtained by Harris and Hughes (1995). One advantage of using this variation is that the method can be used for a stream such as the Quadrantids where there exists some doubt over the identity of the parent body.

Using the method strictly as described above, that is, substituting our assumed values for the orbital elements into equation (9), noting that we can not now obtain a value for the Quadrantid stream because of uncertainties over the parent, we obtain the following values for  $v_{\parallel}$ . The Geminids,  $140 \text{ m s}^{-1}$ ; Perseids,  $38 \text{ m s}^{-1}$ ;  $\eta$  Aquarids,  $200 \text{ m s}^{-1}$ ; Orionids  $58 \text{ m s}^{-1}$  and the Leonids  $66 \text{ m s}^{-1}$ . The most obvious discrepancy between our estimate for the ejection velocity and those obtained previously is for the Perseids. The reason for the discrepancy is obvious, the Perseids is a fairly broad stream (large standard deviation in  $a$ , but with the mean values being very close to that of the comet. This highlights again the difficulty of this method- one can argue for a long time over the most appropriate measure of  $\Delta a$  to take.

Unfortunately, there are problems with both variations of this method of determining the ejection velocity. First, as was pointed out by Jones (1995), Brown and Jones (1998), the determination, from observations, of the mean semi-major axis of a meteoroid orbit is a very difficult task for reasons already explained in the introduction. Second, unless the stream is young, the effects of radiation pressure and gravitational perturbations will both tend to increase the spread in the values of the semi-major axis of meteoroids in a stream. This second problem is present in all methods for determining the value of the ejection velocity of meteoroids from observations of meteor showers. Hence, as both difficulties tend to increase  $\Delta a$  over the true initial value, this method produces a fairly reliable upper limit to the value of the ejection velocity. How close to this upper limit the real value is depends primarily on the age of the stream and the number of meteoroid orbits actually used, the larger the number of accurate orbits used, the better determines  $\Delta a$  will be. At present this number is rather small (at most a few tens) for most streams so more data is required.

### 3. CHANGES TO THE ORBITAL SEMI-PARAMETER

In the same way as the orbital energy  $U$  is proportional to  $1/a$  only, so the square of the angular momentum per unit

mass,  $h$ , is proportional to the semi-parameter,  $p$ , with

$$h^2 = GM_{\odot}p. \quad (10)$$

Thus, apart from the singular case when the meteoroid is ejected directly along the Solar or anti-Solar direction, any finite ejection velocity will also cause a change in the angular momentum per unit mass,  $h$  and thus in the semi-parameter  $p$ . Hence it seems logical to consider changes in this parameter next since, as in the case of the semi-major axis, we have a one-to-one relationship between the geometric orbital parameter  $e$  and the physical parameter  $h$ .

The semi-parameter of a cometary orbit is the heliocentric distance of the comet when the radius vector from the Sun to the comet is perpendicular to the major axis. In terms of the other orbital parameters, it is given by

$$p = a(1 - e^2) = q(1 + e). \quad (11)$$

where  $q$  is the perihelion distance. Also, from the definition of orbital angular momentum per unit mass, equation (10) above, provided again changes are small, it is easy to obtain to first order

$$\frac{2\Delta h}{h} = \frac{\Delta p}{p}. \quad (12)$$

If the ejection takes place close to perihelion, then  $v_{\parallel}$  is essentially orthogonal to the radius vector so that

$$\frac{\Delta h}{h} = \frac{v_{\parallel}}{V}. \quad (13)$$

with  $v_{\parallel}$  and  $V$  as previously defined. Hence we obtain a relationship between the changes in the semi-parameter  $p$  and  $v_{\parallel}$  as

$$\frac{\Delta p}{p} = 2 \frac{v_{\parallel}}{V}. \quad (14)$$

Thus again, if  $\Delta p$  is obtained from observations of meteor showers, then the ejection velocity can be deduced by using equation (14).

This method has not been in general use, partially because it can be regarded as only a variant on the first method. Applying this method for the five streams that we have assumed data for, we obtain the following ejection velocities; for the Geminids,  $820 \text{ m s}^{-1}$ ; Perseids,  $120 \text{ m s}^{-1}$ ;  $\eta$  Aquarids,  $330 \text{ m s}^{-1}$ ; Orionids,  $380 \text{ m s}^{-1}$  and the Leonids  $44 \text{ m s}^{-1}$ . There is excellent agreement between this value and that obtained in the previous section for the Leonids and tolerable agreement for the Perseids,  $\eta$  Aquarids and Orionids, but a very large discrepancy for the Geminids. The deduced values are also generally higher than those obtained in the preceding section despite the fact that those were regarded as an upper limit.

In addition to the difficulties mentioned in the last section, a significant problem with applying this method is that if the location of the point of ejection is not close to perihelion then  $v_{\parallel}$  is not orthogonal to the radius vector and calculating the change in angular momentum is more complex. The relevant equations for the general situation can be found in Williams (2001), but now there

are two free parameters, the ejection velocity and the true anomaly of the ejection point so that no unique solution can be found the ejection velocity. It is interesting to note that the largest discrepancy over values was for the Geminids, where, because of the very small orbit, ice sublimation and thus meteoroid ejection could be taking place over a significant fraction of the orbit.

#### 4. CHANGES IN THE NODAL DISTANCE

Considering the nodal distance has a distinct advantage over the above two methods in that the nodal distance for a meteoroid stream is known very accurately, it is the distance of the Earth from the Sun at the time when the meteor was observed. It thus seems obvious to consider next this situation where observational error, which is in effect what causes problems with the previous two methods, is essentially zero. The two nodal distances are derived from the standard equation for an ellipse with the true anomaly being taken as  $\pi - \omega$  or  $-\omega$ , that is

$$(1 - e \cos \omega) r_N = p$$

and

$$(1 + e \cos \omega) r_N = p.$$

Hence, we can obtain (see Williams, 2001 )

$$(1 - e \cos \omega) \frac{\Delta r_N}{r_N} = \frac{1 - e^2}{2e} \cos \omega \frac{\Delta a}{a} - \frac{(e^2 \cos \omega + \cos \omega - 2e) \Delta p}{2e p} - e \sin \omega \Delta \omega, \quad (15)$$

from the first of these two equations and a similar equation from the second.

From the fact that the point where the change occurred must be on both the old and the new orbit, we can obtain

$$e \cos(f_0 + \Delta \omega) - e \cos f_0 = \frac{(2e + e^2 \cos f_0 + \cos f_0) \Delta p}{2e p} - \frac{1 - e^2}{2e} \cos f_0 \frac{\Delta a}{a}. \quad (16)$$

from which  $\Delta \omega$  can be determined for a given situation. If we make the usual assumption that ejection was at perihelion, the  $\Delta \omega$  is zero, resulting in a considerable simplification. Substituting also for  $\frac{\Delta a}{a}$  and  $\frac{\Delta p}{p}$ , from equations (9) and (14), we obtain

$$(1 - e \cos \omega) \frac{\Delta r_N}{r_N} = 2 \frac{v_{\parallel}}{V} (1 + \cos \omega) \quad (17)$$

for one nodal distance and

$$(1 + e \cos \omega) \frac{\Delta r_N}{r_N} = 2 \frac{v_{\parallel}}{V} (1 - \cos \omega) \quad (18)$$

for the other nodal distance.

Inserting the selected numerical values for the orbital parameters of the five streams that we are considering but taking  $r_N$  to be the heliocentric distance of the Earth gives for the Geminids  $9 \text{ km s}^{-1}$ ; the Perseids  $330 \text{ m s}^{-1}$ ; the  $\eta$  Aquarids  $12 \text{ km s}^{-1}$ ; the Orionids  $4.7 \text{ km s}^{-1}$  and for the Leonids  $38 \text{ km s}^{-1}$ . All these values are absurdly high and the reason for this is not hard to find.

First, all the comments made in the other two sections apply, but in addition  $1 \pm \cos \omega$  tends to be small and division by this quantity takes place. Thus the answer is very sensitive to  $\omega$  and the mean value of this quantity for a stream is not very well defined. Secondly, small changes in the orbital parameters causes significant changes in the nodal distances. Thus, between the time the meteoroids were ejected and the value when the stream was seen can be significant, probably larger than the value calculated for  $\Delta r_N$  for both the stream and the comet. As an illustration, had we used the orbit of comet 55P/Temple-Tuttle in 1833 rather than its current orbit for the calculations on the Leonids, the ejection velocity would change from  $38 \text{ km s}^{-1}$  to  $2 \text{ km s}^{-1}$ .

Third, in the equations we have used, it is assumed that ejection of the meteoroids took place exactly at perihelion. If this is not the case, then  $\Delta \omega$  is not zero as we have assumed in the above calculation. With  $\Delta \omega$  at  $3^\circ$  the omitted term is in fact equal to  $\Delta r_N$ . The mathematics gets significantly more difficult if this assumption is not made and, to make progress then, it is necessary to specify the location of the ejection point. Doing this is beyond the scope of this review but all the necessary equations are given above.

This method may in fact be of more use in determining the location of the ejection point, that is determining  $\Delta \omega$  and then  $f_0$ , after the ejection velocity has been determined by some other means.

## 5. CHANGES IN THE LONGITUDE OF THE NODE

A second quantity that is very reliably determined is the time at which a meteor was observed. Since this meteor was at the same position as the Earth when observed and Earth's position is known, then determining the time of observation in effect determines the position at which the meteoroid crosses the ecliptic, in other words, the longitude of the node,  $\Omega$ . The line of nodes is the intersection line between the orbital plane and the ecliptic and to change the position of the node thus requires the orbital plane to change. To generate any such change, it is necessary to change the angular momentum per unit mass of the orbiting body. To consider such a change, we use the Cartesian heliocentric-ecliptic frame with the Sun at the origin, the x-axis towards the first point of Aries and the z-axis orthogonal to the ecliptic. This has the advantage of being an inertial frame. In this frame the angular momentum per unit mass,  $\mathbf{h}$ , is given by

$$\begin{aligned} \mathbf{h} &= (h_x, h_y, h_z) = \mathbf{r} \times \mathbf{V} \\ &= (y\dot{z} - z\dot{y}, z\dot{x} - x\dot{z}, x\dot{y} - y\dot{x}). \end{aligned} \quad (19)$$

Also, in terms of the orbital parameters,

$$\pm h_x = h \sin i \sin \Omega, \quad (20)$$

$$\mp h_y = h \sin i \cos \Omega, \quad (21)$$

and

$$h_z = h \cos i, \quad (22)$$

where  $i$  is the inclination of the orbit,  $\Omega$  the longitude of the ascending node and  $h$  the magnitude of  $\mathbf{h}$ .

Hence

$$\tan \Omega = -\frac{h_x}{h_y}. \quad (23)$$

From this equation, it is easy to obtain

$$\begin{aligned} \sec^2 \Omega \Delta \Omega &= -\left(\frac{\Delta h_x}{h_y} - \frac{h_x \Delta h_y}{h_y^2}\right) \\ &= \tan \Omega \left(\frac{\Delta h_x}{h_x} - \frac{\Delta h_y}{h_y}\right), \end{aligned} \quad (24)$$

where again  $\Delta$  represents the change in the relevant quantity between the meteoroid orbit and the parent orbit.

Thus

$$\begin{aligned} \Delta \Omega &= \sin \Omega \cos \Omega \left(\frac{\Delta h_x}{h_x} - \frac{\Delta h_y}{h_y}\right) \\ &= -\frac{1}{h^2 \sin^2 i} (h_y \Delta h_x - h_x \Delta h_y), \end{aligned} \quad (25)$$

on making use of equations (20) and (21).

But

$$\Delta h_x = y \Delta \dot{z} - z \Delta \dot{y}, \quad (26)$$

$$\Delta h_y = z \Delta \dot{x} - x \Delta \dot{z}, \quad (27)$$

since only the velocity of the meteoroid, but not its position, is changed through the ejection process.

Substituting  $\Delta h_x$  and  $\Delta h_y$  into equation (25), we have

$$\Delta \Omega = \frac{z}{h^2 \sin^2 i} (\mathbf{h} \cdot \Delta \mathbf{V}) = \frac{r \sin(\omega + f)}{h \sin i} v_{\perp}. \quad (28)$$

Here,  $f$  is the true anomaly of the point at which the ejection of the meteoroid occurred,  $r$  is the corresponding heliocentric distance,  $\Delta \Omega$  represents the difference in the ascending node between the orbit of the meteoroid and that of the parent and  $v_{\perp}$  is the component of the ejection velocity perpendicular to the orbital plane of the parent comet.

The equation of the cometary orbit (that is the relationship between heliocentric distance,  $r$ , and true anomaly,  $f$ ) is

$$r = \frac{q(1 + e)}{1 + e \cos f}, \quad (29)$$

where eccentricity and  $q$  is perihelion distance of the orbit. Hence equation (28) becomes

$$\Delta \Omega = \frac{q(1 + e)}{h \sin i} F(f) v_{\perp}. \quad (30)$$

where

$$F(f) = \frac{\sin(\omega + f)}{1 + e \cos f}, \quad (31)$$

a function of true anomaly only. Equation (30) indicates that, as one might expect, the longitude of the node of the new meteoroid orbit is affected by three almost independent factors, the orbit of the parent body, the location of the ejection point on that orbit and the component of the ejection velocity ( $v_{\perp}$ ) perpendicular to the orbital plane of the parent.

The term that depends on the orbital parameters will be constant for a given stream, though some variation from stream to stream might be expected. Thus for example for the Leonids equation (30) becomes

$$\Delta\Omega = 8.726 \times 10^{-3} F(f) v_{\perp} \quad (\Delta\Omega \text{ in degrees}), \quad (32)$$

while the Perseids gives

$$\Delta\Omega = 2.884 \times 10^{-3} F(f) v_{\perp} \quad (\Delta\Omega \text{ in degrees}) \quad (33)$$

or for streams associated with comet Halley

$$\Delta\Omega = 6.775 \times 10^{-3} F(f) v_{\perp} \quad (\Delta\Omega \text{ in degrees}). \quad (34)$$

If again it is assumed that meteoroids are ejected at perihelion so that we can substitute  $f = 0$  into the above equations,  $F(f)$  becomes unity and the above three equations for example become, for the Leonids,

$$\Delta\Omega = 5.977 \times 10^{-4} v_{\perp} \quad (\Delta\Omega \text{ in degrees}), \quad (35)$$

while the Perseids gives

$$\Delta\Omega = 6.656 \times 10^{-4} F(f) v_{\perp} \quad (\Delta\Omega \text{ in degrees}) \quad (36)$$

or for streams associated with comet Halley

$$\Delta\Omega = 3.197 \times 10^{-3} F(f) v_{\perp} \quad (\Delta\Omega \text{ in degrees}). \quad (37)$$

Since  $\Delta\Omega$  is given by observations we can thus derive an estimate for  $v_{\perp}$  from the above. For example, Arlt *et al.* (1999) found that for the Leonids in 1999,  $\Delta\Omega$  was  $0^{\circ}.03$ . Hence  $v_{\perp}$  is  $50.2 \text{ ms}^{-1}$ , while for 1833 according to Brown & Jones (1999),  $\Delta\Omega$  was only  $0^{\circ}.02$ , giving the corresponding ejection velocity as  $34 \text{ ms}^{-1}$ . For the Perseids, Rendtl & Brown (1997) gives  $\Delta\Omega$  in 1992 as  $0^{\circ}.04$ , yielding  $v_{\perp}$  as  $60 \text{ ms}^{-1}$ .

We have not used this method for either the Geminids or the two streams associated with comet 1P/Halley because they are both fairly old and gravitational perturbations, which have a rapid effect on the node, have obviously caused very significant changes.

An additional problem is that meteoroids may not be ejected at perihelion and  $F(f)$  is a sensitive function of the true anomaly. Indeed, it is obvious that at  $f = -\omega$  and  $\pi - \omega$ , that is at the two nodes of the cometary orbit,  $F(f)$  is zero so that  $\Delta\Omega$  is also zero. Hence if meteoroids are ejected at the nodes, irrespective of how large or small  $v_{\perp}$  is, there is no change in  $\Omega$ . This is of course the obvious consequence of the fact that the ejection point of

the meteoroid must be on both the old and the new orbit so that if ejection is at the node, the position of the node can't change. In this event of course, we can not use the above method to determine  $v_{\perp}$ .

Ma & Williams (2001) investigated the effects on the calculated value of the ejection of variations in  $F(f)$  that could arise from assuming realistic ejection locations for the meteoroids. They found that for the Leonids and the Perseids variations in the observed  $\Delta\Omega$  from year to year could be explained through the variations in  $F(f)$  alone, thus allowing  $v_{\perp}$  to be constant for all the ejections. The deduced values for  $v_{\perp}$  were about  $70 \text{ ms}^{-1}$  for the Leonids and about  $80 \text{ ms}^{-1}$  for the Perseids. In reality it is likely that the value of the ejection velocity also depends on the location of the ejection point. However investigating the situation with both being variable is much more complex, and, to our knowledge has not so far been done. In reality one might expect that the mean ejection velocity would be somewhere between the two extremes discussed here.

## 6. PECULIAR FEATURES OBSERVED IN SOME METEOR SHOWERS

The four methods discussed so far all involve calculating the variations that are caused by a finite ejection velocity in some orbital parameter. A particular value of the ejection velocity could cause some other effect. For example, Asher *et al.* (1999) suggested that the unexpected outburst of Leonid meteors seen in 1998 was caused by meteoroids ejected from 55P/Tempel-Tuttle in 1333 and captured into mean-motion resonance with Jupiter. This requires a well determined change in the semi-major axis which, by using the first method that we described can be translated into a specific value of  $v_{\parallel}$ . They found that this required an ejection velocity of the order of  $10 \text{ m s}^{-1}$ .

The April Lyrid shower also has a very significant outbursts in activity. These outbursts in activity have been recorded at time intervals that are multiples of twelve years. The first recorded outburst was in 1803 and a list of outburst events by Lindblad & Porubčan (1991) covers a period from AD1803 to AD1982. The parent of the stream is comet C/1861 G1 Thatcher which has an orbital period in excess of 400 years and, as its name suggests, was seen near the Earth in 1861. Hence, unlike the Leonid outbursts for example, these outbursts can not be associated with the return of the parent comet to the vicinity of the Earth. Arter & Williams (1995) have given an account of some of the theories that have been proposed to explain these outburst, but none of those appear to fully explain the observations. Arter & Williams (1997) offered a solution based on the results from a large computer simulation of the stream. The simulation used in Arter & Williams (1997) was based upon a model by Williams & Wu and used by them to investigate several streams, for example the Persid shower in Williams & Wu (1994). In this model meteoroids were assumed to be ejected from a cometary nucleus into a cone about the solar direction. This was modelled by assuming that the number of meteoroids ejected as a function of angle about

the Solar direction satisfied a Gaussian distribution with the mean as the Solar direction and the standard deviation as  $22^\circ.5$ .

The model also assumed that meteoroids would be ejected once sublimation of ices could take place, increase towards perihelion and decrease again until sublimation ceases. The heliocentric distance at which sublimation of the ices starts seems to be slightly variable from comet to comet. Comet C1/1861 G1 (Thatcher) is probably more similar to comet 1P/Halley than to other comets that have been studied and so Arter & Williams (1997) used a value determined by West & Jorgensen (1989) for comet 1P/Halley, namely 8.5 AU. The number of ejected meteoroids as a function of true anomaly was assumed to satisfy a Gaussian distribution with the mean at zero (that is at perihelion) and a standard deviation of  $48^\circ$ .

Arter & Williams (1997) found that gravitational perturbations (mostly from Jupiter) caused the stream to take the form of a hollow tube rather than a filled one. This is not the first time that simulations have suggested such a form for meteoroid streams, Jones (1985) found that in his simulation, the Geminid stream also took on form of a hollow tube as a consequence of gravitational perturbations. The intersection of the stream with the ecliptic thus forms a ring rather than a disk. Individual meteoroids of course follow a Keplerian orbit that forms a single strand in the structure of the stream and cross the ecliptic at a single point in the ring. However the orbital periods of meteoroids on different orbits are slightly different and (not surprising since the differences are caused by Jupiter), meteoroids in the ring span a twelve year interval. Since the Earth intersects this ring at a point outbursts are also seen with this time interval. In the simulation, Arter & Williams (1997) assumed an ejection velocity at 1AU of  $75 \text{ m s}^{-1}$ .

Arter & Williams (2001) investigated the importance of the value of the ejection velocity in preserving or destroying the above mentioned ring structure. Hence they investigate five additional models with differing ejection velocities, all other parameters of the model have been kept exactly the same as in the model of Arter & Williams (1997). In each the ejection velocity is given by  $V_\infty = Cr^{-1.125}$  and the coefficient  $C$  is assigned the following values 23, 180, 860, 1050 and 1220. In addition,  $C = 75$  corresponds to the previously investigated model. (The slightly peculiar set of values arise because in reality parameters in the original Whipple expression given as equation (1) were changed which then gave rise to values of the constant  $C$  as indicated.) Hence, in all, six sets of results were obtained, corresponding to ejection velocities at 1AU of 23, 75, 180, 860, 1050 and  $1220 \text{ m s}^{-1}$  respectively, and the previously published data is the second set. Figure 1, shows the median position of all the meteoroids that crossed the ecliptic in a given single year for thirty such years between 1800 and 1830 for the first four of these models.

It can be seen that a ring structure is present, producing an intersection with the Earth every 12 years, for the two models with the lowest ejection velocity and may also be present for the third lowest, but is completely lost in the fourth model with an ejection velocity of  $1050 \text{ m s}^{-1}$ .

For this reason, we do not show the results from the models with even higher ejection velocities. They can be found in Arter & Williams (2001). Arter & Williams (2001) also considered whether meteoroids would continue to reach Earth in the latter half of the twentieth century, given that the parent comet and any meteoroids on an identical orbit was close to aphelion at that time, and concluded that this required an ejection velocity in excess of  $25 \text{ m s}^{-1}$ , to sufficiently change the orbital period. Hence, their final conclusion was that the ejection velocity from comet Thatcher in order to produce the pattern of frequency for the April Lyrid outbursts had to be in the range of  $25\text{--}150 \text{ m s}^{-1}$ , with some bias towards values at the lower end of the range.

## 7. CONCLUSIONS

We have discussed the various methods of determining the value of the ejection velocities of meteoroids from cometary nuclei, through observations of meteoroid streams. The first considered the differences in the semi-major axes of the parent and stream since this parameter depends only on the meteoroid velocity. The main difficulty with this is that of determining the mean value of the semi-major axis of the stream. The problem has been discussed in some detail by Voloshchuk (1999), but in essence the problem centers on the fact that values of  $1/a$  are determined from observations, while the mean of  $1/a$  is not the same as the inverse of the mean of  $a$ . This results in the mean values satisfying  $q = a(1 - e)$  even though individual values do. The semi-major axes also change with time so that more false values are determined for older streams. Nevertheless a reasonable upper bound may be obtained. The average value for the five streams that we considered is  $100 \text{ m s}^{-1}$ . If the Geminids are left out, both because of its rather peculiar small orbit and possible large age, the average value for the ejection velocity becomes  $90 \text{ m s}^{-1}$ .

The second method considered the changes in the semi-parameter since this is directly related to the angular momentum, again determined from the meteoroid velocity though now the angle between the velocity direction and the solar direction is important, introducing slightly more room for error. In consequence, the method gave, on average, slightly larger ejection velocities, the mean for the five streams considered being  $340 \text{ m s}^{-1}$ . Again, for the same reasons as above, the Geminids are excluded, then the mean for the other four streams becomes  $240 \text{ m s}^{-1}$ .

The third method considered changes in the nodal distance since in reality this parameter is very accurately determined. However, almost all evolutionary effects can cause rapid changes in this parameter (see for example Yeomans *et al* (1996) for an illustration of the changes in comet 55P/Tempel-Tuttle over very short time intervals). Consequently we do not regard this as a reliable method of determining the ejection velocity.

The fourth method considered changes in the longitude of the ascending node,  $\Omega$ . It is well known that perturbations cause changes in this parameter and so may be regarded

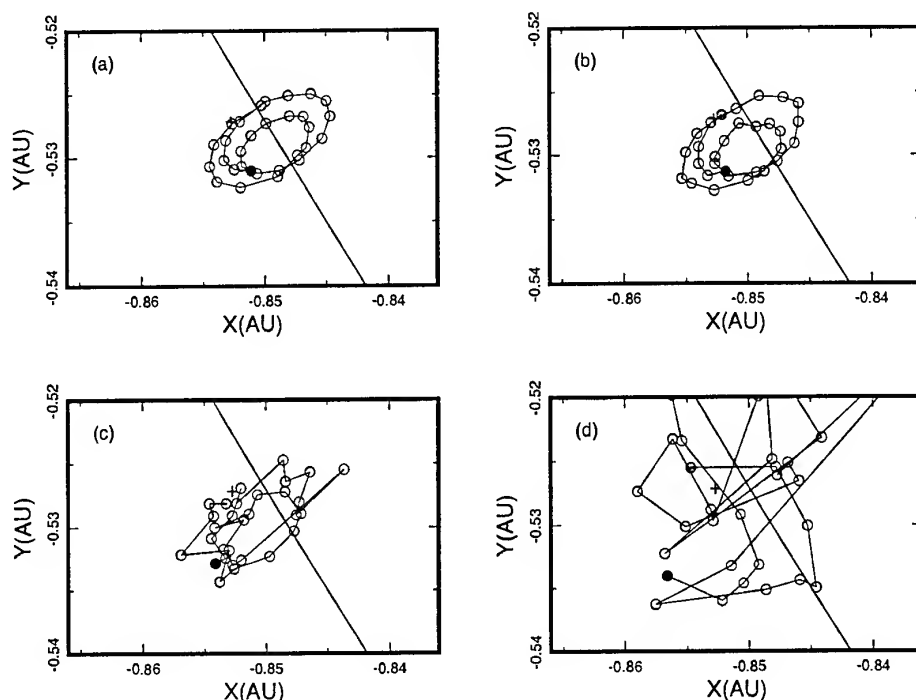


Figure 1. The median position of all the meteoroids that crossed the ecliptic in a given single year for thirty such years between 1800 and 1830. The first figure in the top left is for the first model and the last at bottom right is for the fourth model. Figures for the last two models investigated are not shown. The X-axis is towards the first point of Aries. The units are in AU's and the straight line represents Earth's orbits at the present time.

as a reliable method only for very young meteors. Consequently this method was applied only to the new peak in the Perseid activity profile and to the Leonid storms. The average value for the ejection velocity determined by this method was  $60 \text{ m s}^{-1}$ .

Finally, peculiarities such as resonance in the Leonids and a 12 year periodicity in the April Lyrids were discussed yielding a value of  $10 \text{ m s}^{-1}$  for the Leonid ejection velocity and a value in the range of  $25\text{--}150 \text{ m s}^{-1}$  for the April Lyrids.

Of course the ejection velocity for all streams should not be the same and we have calculated average values in the above discussion only as a means of establishing the likely ball-park value. The average value over all the methods (excluding the method involving considerations of  $r_A$ ) for the streams are as follows. the Geminids  $480 \text{ m s}^{-1}$ ; the Perseids  $75 \text{ m s}^{-1}$ ; the  $\eta$  Aquarids  $265 \text{ m s}^{-1}$ , the Orionids  $220 \text{ m s}^{-1}$ , the Leonids  $45 \text{ m s}^{-1}$  and the April Lyrids  $25\text{--}150 \text{ m s}^{-1}$ .

In reality one might also expect some dependence on the heliocentric distance of the ejection point. The Geminid parent gets much nearer the Sun than any of the other parents and it is interesting that higher velocities emerge for this stream. All the values found are of the general order of  $100 \text{ m s}^{-1}$ , rather than ten or several hundred. For the two streams, the Perseids and Leonids, where young meteors can be observed, the nine determined values range from  $10\text{--}120 \text{ m s}^{-1}$  with a mean of  $58 \text{ m s}^{-1}$ , almost identical to the obtained range for the Lyrids. It is in-

teresting to note that these values are very much in line with those given by the original Whipple (1951) formula.

We repeat again that the two major problems with all of these methods are taking account of planetary perturbations and the errors in determining the parameters of the mean orbit for the meteoroid stream. The first is a problem that is easiest to overcome by considering very young meteor outbursts. The second can be overcome only with more observations. Since determining orbits requires simultaneous observations from two sites, this tends not to be a popular observing method. Thus, though a huge amount of observations of the Leonids has taken place over the last few years, very few meteoroid orbits were obtained. There is a big need for more well determined orbits.

## REFERENCES

- Arlt R., Rubio L.B., Brown P. & Gyssens M., 1999, WGN, The Journal of the IMO, 27, 286
- Arter T. R. & Williams I. P., 1995, MNRAS, 277, 1087
- Arter T. R. & Williams I. P., 1997, MNRAS, 286, 163
- Arter T. R. & Williams I. P., 2001, MNRAS, (in Press)
- Asher D.J., Bailey M.E. & Emel'Yanenko V.V., 1999, MNRAS, 304, L53
- Betlem H., ter Kuile C.R., de Lignie M., van't Leven J., Jobse K., Miskotte K. & Jenniskens P., 1997, A&A Suppl. Ser., 128, 179

- Brown P. & Jones J., 1998, *Icarus*, 133, 36
- Brown P. & Jones J., 1999, in *Meteoroids 1998*, Eds Baggaley W.J. & Porubčan V., Slovak Academy of Sciences, Bratislava, 159
- Crifo J.F., 1995, *ApJ*, 445, 470
- Drummond J.D., 1981, *Icarus*, 45, 5453
- Gustafson B.A.S., 1989, *AJ*, 337, 945
- Hajduk A., 1986, 20th ESLAB Symposium on the exploration of Halley's Comet, ESA SP-250, Noordwijk, The Netherlands
- Harris N.W. & Hughes D.W., 1995, *MNRAS*, 273, 992
- Hughes D.W., 2000, *PSS*, 48, 1
- Jones J., 1985, *MNRAS*, 217, 523
- Jones J., 1995, *MNRAS*, 275, 773
- Lindblad B.A., 1990, in *Asteroids, Comets, Meteors III*, Eds Lagerkvist C.-I. Rickmann H. Lindblad B.A. & Lindgren M., Uppsala Universitet Reprocentralen, 551
- Lindblad B.A. & Porubčan V., 1991, *Bull.Astron Inst. Czech.*, 42, 354
- Lindblad B.A. & Porubčan V., 1999, in *Meteoroids 1998*, Eds Baggaley W.J. & Porubčan V., Slovak Academy of Sciences, Bratislava, 231,
- Lindblad B.A., Porubčan V. & Stohl J., 1993, in *Meteoroids and their Parent Bodies*, Eds Stohl J. & Williams I.P., Slovak Academy of Sciences, Bratislava, 177
- Ma Y. & Williams I.P., 2001, *MNRAS*, 325, 379
- Marsden B.G. & Williams G.V., 1996, *Catalogue of Cometary Orbits 1996*, International Astronomical Union
- Neslušan L. & Welch P.G., 2002, This Volume
- O'Ceallaigh D.P., Fitzsimmons A. & Williams I.P., 1995, *A&A*, 297, L17
- Probstein R.F., 1968, in *Problems of Hydrodynamics and Continuum Mechanics*, Ed Lavrent'ev M.A., Society of Industrial Applications Mathematics, p568
- Rendtel J. & Brown P., 1997, *Planet. Space Sci.*, 45 585
- Schiaparelli G.V., 1867, *Astronomische Nachrichten*, 68, 331
- Southworth R.B. & Hawkins G.S., 1963, *Smith Cont. Aph.*, 7, 261
- Steel D.I., 1994, in *Asteroids, Comets, Meteors 1993*, Eds Milano A. Di Martino M. Cellino A., IAU Symposium 160, Kluwer, Dordrecht, 111
- Voloshchuk Yu., 1999, in *Meteoroids 1998*, Eds Baggaley W.J. & Porubčan V., Slovak Academy of Sciences, Bratislava, 231
- West R.M. & Jorgensen H.E., 1989, *A&A*, 218, 307
- Whipple F.L., 1950, *ApJ*, 111, 375
- Whipple F.L., 1951, *ApJ*, 113, 464
- Williams I.P., 1996, *Earth Moon & Planets*, 72, 231
- Williams, I.P., 2001, *Celestial Mechanics and Dynamical Astronomy*, (in Press)
- Williams I.P., Hughes D.W., McBride N. & Wu Z., 1993, *MNRAS*, 259, 617
- Williams I.P. & Wu Z., 1993, *MNRAS*, 262, 231
- Williams I.P. & Wu Z., 1994, *MNRAS*, 269, 524
- Yeomans D.K., Yau K.K. & Weissman P.R., 1996, *Icarus*, 124, 407

## RESONANCE STRUCTURE OF METEOROID STREAMS

V.V.Emel'yanenko

Department of Theoretical Mechanics, South Ural University, Lenina 76, Chelyabinsk 454080, Russia,  
Email: emel@termeh.susu.ac.ru

### ABSTRACT

The dynamical behaviour of meteoroid streams is studied on the basis of the resonance theory of perturbations. Parameters of principal resonance zones near orbits of the main meteoroid streams are given. It is shown that resonant particles may produce very concentrated meteoroid streams. The Leonid, Lyrid, Ursid and Bootid outbursts as indicators of the resonant motion are discussed. Recommendations are proposed for observations of resonant structures.

### 1. INTRODUCTION

The motion of small bodies on high-eccentricity orbits in the near-Earth space is strongly perturbed by planets. The planetary perturbations lead to the gradual dispersion of meteoroid streams. The largest perturbations take place near encounters of meteoroids with planets. But there are limited intervals of time when a meteoroid stream orbit is far from the planetary ones. In this case the dynamical behaviour of meteoroids is similar to that for a typical resonant system [1]. The most important is the existence of librations near mean-motion commensurabilities with Jupiter. A rate of dispersion for librating meteoroid streams is substantially less than that for chaotic systems. Despite their age, such streams can be as compact as young ones.

### 2. LIBRATIONS OF METEOROID STREAMS

The main features of the resonant motion near the commensurability  $n/n_J = j'/j$ , where  $j$  and  $j'$  are

integers and  $n$  is the mean motion (the suffix  $J$  denotes Jupiter), can be described by the following equations [2]:

$$\frac{dx}{dt} = c \sin(\sigma - \bar{\sigma}), \quad \frac{d\sigma}{dt} = b - d(x - \bar{x}), \quad (1)$$

where  $x = \mu\sqrt{a}/j$ ,  $\sigma = jM - j'(M_J + \omega_J + \Omega_J - \omega - \Omega)$ ,  $a$  is the semi-major axis,  $M$  is the mean anomaly,  $\omega$  is the argument of perihelion,  $\Omega$  is the ascending node,  $\bar{x}$  is the value of  $x$  at the exact commensurability,  $\bar{\sigma} = \sigma_0 + ht$ , and  $\sigma_0, h, b, c, d$  are constants. The phase space is divided by separatrix into the libration and circulation zones. There are  $j$  libration zones on the orbit for the resonance  $j'/j$ .

The real motion is, of course, more complicated than that described by Equation 1. First of all, the action of periodic perturbations creates a chaotic layer near the separatrix of the system (1) and the action of secular perturbations leads to the gradual changes of the Equation (1) parameters.

But the most important is the existence of a region where meteoroids can librate for many revolutions. First, the density of librating particles changes almost periodically and sometimes can reach a value, which is even larger than that after ejection from a comet [3]. This contrasts with a typical chaotic motion of other particles. Secondly, the mean value of semi-major axis at librations is close to the resonant one, and consequently the secular changes for these particles are different from those for other parts of a meteoroid stream. Therefore, librating meteoroids produce long-lived high-density substreams separated from chaotically distributed nonlibrating meteoroids.

Parameters of resonance zones near orbits of the

Table 1. Parameters of principal resonance zones near orbits of the annual meteor showers.

Stream	$j'/j$	$\bar{a}$ , AU	$\bar{\sigma}$ , deg	$\Delta a$ , AU
Lyrids	1/12	27.30	13	1.8
	1/11	25.76	13	1.8
	1/10	24.17	13	1.7
Perseids	1/12	27.29	329	1.5
	1/11	25.76	329	1.4
	1/10	24.17	329	1.4
Orionids	1/6	17.19	172	1.0
	1/5	15.22	172	0.9
	1/4	13.12	173	0.8
$\eta$ -Aquarids	1/5	15.22	198	0.9
	1/4	13.12	198	0.8
	1/3	10.83	198	0.7
Leonids	5/14	10.35	231	0.13
	4/11	10.22	74	0.17
Ursids	6/7	5.768	269	0.09
	7/8	5.690	158	0.08
Quadrantids	2/1	3.278	4	0.17
	7/3	2.957	163	0.06
Geminids	5/2	2.824	333	0.07
	7/1	1.421	196	0.006
	8/1	1.300	19	0.002

main meteoroid streams are presented in Table 1. Here  $\bar{a}$  and  $\bar{\sigma}$  are the values of  $a$  and  $\sigma$  at the centre of the  $j'/j$  resonance near the present epoch,  $\Delta a$  is the width of the resonance zone over semi-major axis. This Table is useful to identify librating meteoroid streams among observed ones because comets eject particles to various resonances during their evolution.

### 3. STABILITY OF THE $1/J$ RESONANCES

Table 1 shows that many meteoroid streams move in high-eccentricity orbits near the  $1/j$  resonances where  $j > 1$ . They are usually connected with Halley-type comets. The features of the  $1/j$  resonances allow to estimate the boundary of their stability.

At  $e \rightarrow 1$ , the perturbed motion of a small body in a long-period orbit can approximately be described by the following mapping [4]:

$$w^{(m+1)} = w^{(m)} - \frac{4\pi c j}{\mu^2} \sin(\sigma^{(m)} - \bar{\sigma}), \quad (2)$$

$$\sigma^{(m+1)} = \sigma^{(m)} - \frac{2\pi n_J}{\mu \sqrt{w^{(m+1)}}^3}, \quad (3)$$

where  $w = 1/a$ , and  $\bar{\sigma}$  is a constant. A linear approximation of the mapping (2), (3) near the centres of the  $1/j$  resonances ( $w = (n_J/(\mu j))^{2/3}$ ,  $\sigma = \bar{\sigma}$ ) leads to the criteria of stability for the centres of the  $1/j$  resonances:

$$\frac{3\pi^2 n_J^2 c}{\mu^4 w^4} < 1. \quad (4)$$

For the present orbits of the Perseids,  $\eta$ -Aquarids, Orionids, Lyrids and Leonids, the criteria (4) is satisfied for  $w > 0.03$ . Usually meteoroids of these streams have values of  $w$  within this limit. Therefore their librations near the centres of the  $1:j$  resonances are possible.

### 4. EXAMPLES OF METEOR SHOWERS CONNECTED WITH RESONANCES

At present we have a few examples of meteor showers produced by the concentration of resonant particles. Usually they look like unexpected outbursts in activity of the annual meteor showers.

The Leonid outburst in 1998 was observed about  $16^h$  before the predicted maximum of the main shower. This phenomenon is explained by ejection of dust grains into the 5/14 resonance with Jupiter, during the perihelion passage of comet 55 P/Tempel-Tuttle in 1333 [5].

The Lyrid meteor shower has usually a low hourly rate. But in 1803, 1922, and 1982 unexpected outbursts in activity of this meteor shower were observed. Although the orbit of the Lyrids is rather uncertain, the main resonances near the Lyrids correspond to the commensurability  $1/j$  with Jupiter. In the epochs of outbursts, the critical arguments  $\sigma$  were very close to the centres of these resonances [6]. This is consistent with the suggestion that librating meteoroids caused those enhancements of meteor activity. If all abovementioned showers are connected with the same resonance, then  $j = 5$  [6].

The Ursid outburst occurred in 1945 when the parent comet 8P/Tuttle was near perihelion. This must have been connected with resonances because critical arguments for both main resonances in the vicinity of the Ursids (7/8 and 6/7) are very close to their centres [2]. Jenniskens et al. [7] pointed out that the 6/7 resonance may be a natural explanation of both

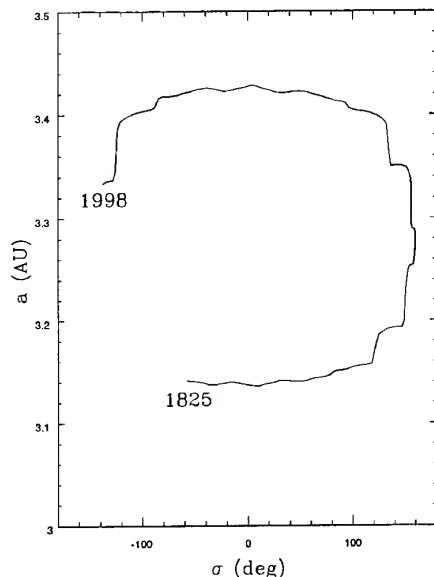


Figure 1. The 2/1 libration of the Bootid meteoroid from 1825 to 1998.

the 1945 outburst and the other Ursid outburst in 1986.

Recently, the outburst of the June Bootid meteor shower in 1998 was explained by meteoroids released from the parent comet 7 P/Pons-Winnecke in 1825 [8]. Figure 1 shows the changes of the semi-major axis and critical argument for particles which hit the Earth atmosphere in 1998. The perturbations are very strong in this case. But the librations near the 2/1 resonance inhibits chaotic motion for this part of the meteoroid stream, allowing structures in the stream to remain compact enough over centuries.

## 5. CONCLUSIONS

Compact resonant structures can survive for long timescales. As a rule, they are separated from centres of dispersed meteoroid streams. The resonant substreams may lead to meteor storms similar to those associated with recently ejected meteoroids. Unexpected meteor outbursts which cannot be predicted by ejections from parent comets during recent perihelion passages are almost certainly caused by librating particles.

Resonant streams are important objects for ground

observations. These structures have well determined parameters (pre-atmospheric velocities) if the mean-motion commensurability is known. This can be used to improve physical models of meteor phenomenon. On the other hand, the determination of more precise velocities for some resonant substreams would be useful in order to solve the problem of their origin (for instance, the Lyrids).

The investigation of resonant trails from space stations is attractive as well. They are compact structures, and the positions of resonant substreams originated from known comets can be predicted with high accuracy owing to their relatively stable dynamical behaviour.

## ACKNOWLEDGMENTS

This work was supported in part by RFBR Grant 01-02-16006. The author thanks the organizers of the Meteoroids 2001 conference for their support.

## REFERENCES

1. Lichtenberg A. and Liberman M., *Regular and Stochastic Motion*, Springer, Berlin, Heidelberg, New York, 1983.
2. Emel'yanenko V.V. Meteor-Stream Motion Near Commensurabilities with Jupiter, *SOV. ASTRON. LETT.*, Vol. 14, 278-281, 1988.
3. Emel'yanenko V.V. Meteor-Stream Density Evolution by Planetary Perturbations, *SOV. ASTRON. LETT.*, Vol. 10, 131-132, 1984.
4. Emel'yanenko V.V. Dynamics of Periodic Comets and Meteor Streams, *CEL. MECH. DYN. ASTRON.*, Vol. 54, 91-110, 1992.
5. Asher D.J., et al. Resonant Meteoroids from Comet Tempel-Tuttle in 1333: the Cause of the Unexpected Leonid Outburst in 1998, *MON. NOT. R. ASTRON. SOC.*, Vol. 304, L53-L56, 1999.
6. Emel'yanenko V.V. Dynamics of the Lyrid meteor stream, *SOL. SYST. RES.*, Vol. 24, 199-202, 1991.
7. Jenniskens P., et al. Dust Trails of 8P/Tuttle and the Unusual Outbursts of the Ursid Shower, *ICARUS*, 2001, in press.
8. Asher D.J. and Emel'yanenko V.V. The June Bootid Outburst in 1998 and Determination of Cometary Ejection Velocities, *MON. NOT. R. ASTRON. SOC.*, 2001, in press.

# CONSTRAINING COMETARY EJECTION MODELS FROM METEOR STORM OBSERVATIONS

Michael Müller, Simon F. Green, Neil McBride

*Planetary and Space Science Research Institute, The Open University, Milton Keynes, MK7 6AA, UK.  
e-mail: m.mueller@open.ac.uk, s.f.green@open.ac.uk, n.m.mcbride@open.ac.uk.*

## ABSTRACT

Modelling and observations of the Leonids have shown that maxima in the meteor storm activity can be identified as due to particles released from the comet during certain perihelion passages. If the particles originating from a certain perihelion passage can be identified, the next obvious question to ask is what information can be gained about the ejection process of particles from a cometary nucleus. We have developed a method to calculate the set of all possible dust trajectories that reach the Earth at some given time. The method involves numerical integration of a few dust particles only and is applied to the Leonid activity in the year 2000. We show that particles of different sizes entering the Earth's atmosphere at the same time were released from the comet at different heliocentric distances. Therefore one has to make assumptions about the activity of the comet with heliocentric distance in order to derive the cometary mass distribution from an observed meteor mass distribution. However, we outline how lower limits on the ejection velocity of the observed particles can be derived.

## 1. INTRODUCTION

Cometary dust trails consist of large dust particles which travel on trajectories similar to that of the comet. Modelling has shown that particles in the trail which were ejected during different comet apparitions can lie separated in space such that they can be identified in the meteor flux rates [1]. To give an example, the ecliptic intersection of dust trails was calculated and is shown in Fig. 1. Section 3 describes in detail how Fig. 1 was produced. Fig. 2 shows the meteor flux during the Leonids in the year 2000 [1]. By comparing Fig. 1 with Fig. 2 it can nicely be seen that maxima in the meteor flux are due to close approaches of the Earth with trails of particles ejected during different comet apparitions.

Theoretical models were developed which are able to predict time and intensity of meteor flux maxima [6,8]. The model in [8] focuses on the prediction of meteor flux rates. Therefore it is justified to make certain simplifications. For example, only dust particles which were ejected at perihelion need to be considered to find

the place of the ecliptic intersection of dust particles ejected during a certain apparition. Furthermore, the model was calibrated empirically in order to predict the absolute meteor flux rates of the Leonids and no

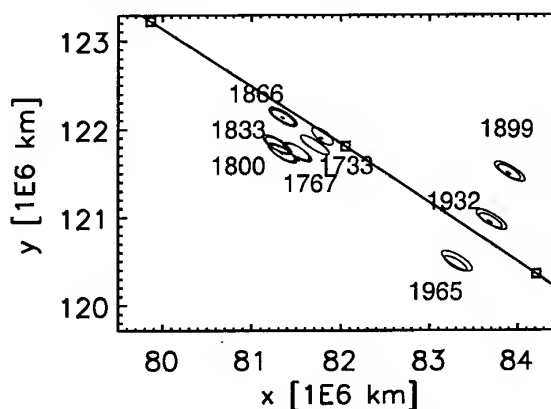


Fig. 1. The ecliptic intersections of different dust trails are shown on the 18<sup>th</sup> of November 2000. Dust trails of different comet apparitions are labeled with the year in which the comet passed its perihelion. The straight line shows the Earth orbit. The squares mark the Earth position at 0h UTC on the 17<sup>th</sup>, 18<sup>th</sup> and 19<sup>th</sup> of November 2000.

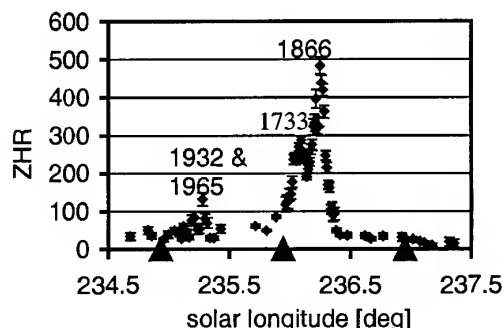


Fig. 2. The meteor activity during the time of the Leonids in the year 2000 are shown [1]. The triangles mark 0h UTC of the 17<sup>th</sup>, 18<sup>th</sup> and 19<sup>th</sup> of November 2000. By comparison with Fig. 1 maxima in the meteor flux can be identified to be due to dust particles ejected during different apparitions.

attempt was made to constrain the ejection process around the source comet 55P/Temple-Tuttle.

An attempt to constrain cometary ejection models from Leonid observations was made in [6]. This was done by calculating the Leonid flux consistent with a dust ejection model, varying some of the model parameters and comparing the results with observations. Reference [6] reports that the best agreement of the model with the observations was found for high particle densities of  $4 \text{ g cm}^{-3}$ . As [6] used a Monte Carlo model, there is very little insight in how the results depend on the model parameters, which were not varied in the calculation. These parameters are, for example, the activity distribution for different ejection directions and the dependence of the comet activity on the heliocentric distance. It cannot be said, without re-running the model how the results in [6] are affected by the assumptions about these parameters.

In this work we try to overcome the shortcomings of the use of Monte Carlo models by defining a procedure which allows, independent of an ejection model, the calculation of the set of all dust particles which can reach the Earth at a given time. To do this we introduce a model which allows calculation of the intersection point of particle trajectories with the ecliptic in a semi-analytical way. We show that for particles of given radiation pressure coefficient, which are ejected at the same time, there is only one unique ejection velocity vector such that the Earth is reached at a given time. On the basis of this, velocity constraints on the ejection velocity can be found without invoking any ejection model.

Meteor observers not only measure the meteor rates but also measure a magnitude distribution index [5]. The magnitude distribution index is a measure for the mass distribution of the dust particles in the meteor stream [10]. It is an obvious question to ask how the mass distribution of meteoroids entering the Earth's atmosphere is related to the mass distribution of particles ejected from the comet. We show that particles which enter the Earth's atmosphere at the same time might have been ejected at different heliocentric distances. Therefore the relationship between the mass distribution of ejected particles from the comet and the meteor mass distribution must be expected to be complex.

## 2. EVOLUTION OF A DUST SHELL

The term "dust shell" was introduced in [2] and denotes the set of all places which is inhabited by dust particles which have the same radiation pressure coefficient  $\beta$  and were released from a comet at the same time  $t_0$  with the same velocity  $V$ . A dust shell

initially expands spherically around a comet. Due to radiation pressure, the centre of the dust shell becomes offset from the comet position and the position of a dust particle on the dust shell at time  $t$  can be approximated by (see Fig. 3 A)

$$\mathbf{r} = \mathbf{r}_c(t_0, \beta) + \mathbf{V}(t - t_0), \quad (1)$$

where  $\mathbf{r}_c$  is the position of the centre of the shell (bold variables represent vectors). This approximation was used in [2] to model dust tails formed by small particles which only spend a small time in the tail. For long times of flight the dust shell gets distorted to an ellipsoid by tidal forces of the Sun (see Fig. 3 A). In this regime Eq. 1 can be generalised [3]

$$\mathbf{r} = \mathbf{r}_c(t_0, \beta) + \phi(t, t_0)\mathbf{V}, \quad (2)$$

where  $\phi$  is a  $3 \times 3$ -matrix. This approximation was first used in [4] to predict the position of large dust particles around 1P/Halley during the encounter of the Giotto spacecraft. Analytical equations for the matrix elements of  $\phi$  can be found in [3], where Eq. 2 was used to efficiently produce artificial images of dust comae.

One can ask whether these kinds of model are still applicable to dust trails. However, due to different orbital periods of the particles in the shell, the shell stretches out and bends around the comet orbit (Fig. 3 B). Therefore a linear approximation as in Eq. 2 is no longer valid for describing the entire dust shell. However with regard to analysing meteor fluxes on Earth, one is not interested in the shape of the entire dust shell but only in its intersection with the ecliptic plane. In the following section we show how these intersections look like and it is shown that the position of the intersection of a dust particle can be approximated by an equation analogous to Eq. 2. This is because the ejection velocity of dust particles is small compared with the orbital velocity of the comet. Therefore the dust particles move on trajectories which are very similar to the comet orbit. Assuming Keplerian trajectories, for both comet and dust particle, the dust particle reaches a maximum distance from the comet orbit during its first revolution. Still assuming purely Keplerian trajectories, this maximum distance will not increase in following revolutions around the Sun. However, if the comet and the dust particle have different orbital periods, the distance between the comet and particle along the orbit increases with every revolution. Therefore dust shells can have a typical width in the order of 100000 km, but can stretch several astronomical units in length around the comet orbit.

To understand some of the results later in this work, another property of dust shells is worth mentioning. Assuming again that the dust travels on Keplerian trajectories, all dust particles have to come back to the point of ejection. Hence, when a dust shell crosses its point of ejection, the particles with the same orbital period, which usually form a ring on the dust shell, are collapsed to a point (see Fig.3 C). Furthermore, a ring on a shell collapses to a one dimensional line, when it crosses its node with respect to the comet orbit plane ( $180^\circ$  true anomaly away from the point of ejection; see Fig. 3 C).

### 3. ECLITIC INTERSECTION OF A SHELL

In this section we describe how the set of all dust particles which intersect the ecliptic at the same time can be calculated and how the position of the ecliptic intersection depends on the initial particle velocity.

The position of a dust particle along a dust shell, which can have a length of several astronomical units, is controlled by the orbital period of the particle. Because the width of the shell is tiny compared with its length the intersection of the shell with any plane (which has at least a moderate inclination with respect to the comet orbit plane) only contains particles which have almost the same orbital periods. For a Keplerian trajectory the orbital period  $T$  is related to the orbital energy by

$$-\frac{1}{2}\left(\frac{2\pi\mu}{T}\right)^{3/2} = \frac{1}{2}(\mathbf{V}_{\text{comet}} + \mathbf{V})^2 - \frac{\mu(1-\beta)}{r}, \quad (3)$$

where  $\mu$  is the gravitational constant multiplied with the solar mass,  $\mathbf{V}$  is the ejection velocity of the particle.  $\mathbf{V}_{\text{comet}}$  and  $r$  are the comet velocity and heliocentric distance at the ejection time, respectively.

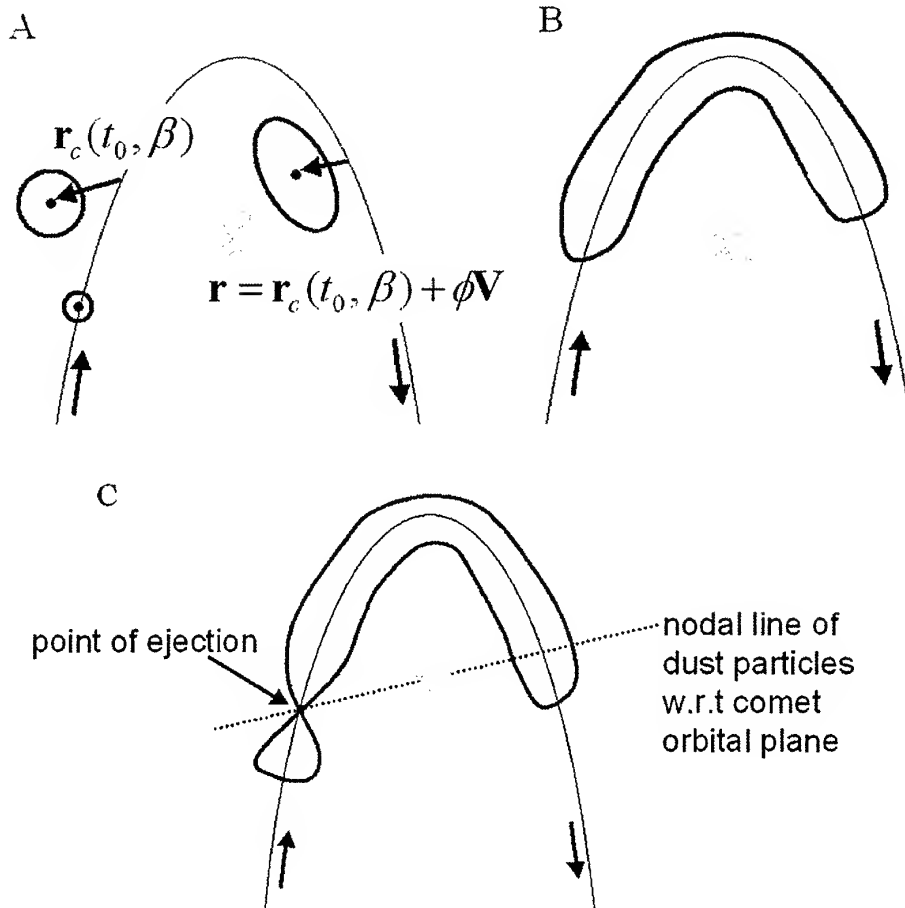


Fig. 3. Evolution of a dust shell. A: dust shell during revolution of ejection. B: dust shell after one or more revolutions. C: collapsed dust shell.

By expressing the ejection velocity  $\mathbf{V}$  by its component  $V_3$  in the direction of the comet orbital velocity vector,  $\mathbf{V}_{\text{comet}}$ , and a component perpendicular to this direction,  $\mathbf{V}_\perp$ , the orbital energy can be written

$$E = V_{\text{comet}} \cdot V_3 + \frac{1}{2}(V_3^2 + V_\perp^2) + \frac{\beta\mu}{r} + E_{\text{comet}}, \quad (4)$$

where  $E_{\text{comet}}$  is the orbital energy of the comet. From Eq. 4 it can be seen that the orbital energy, and with this the orbital period, depends to first order only on the component of the ejection velocity in the direction of the orbital velocity of the comet. With this knowledge it is easy to write a numerical procedure which searches  $V_3$  such that the dust particle which started at the given time with a given  $\mathbf{V}_\perp$  and  $\beta$  intersects the ecliptic at a given time. Even though the motivation for the procedure is based on Keplerian dynamics, our numerical procedure, which takes the perturbations of all planets and Poynting Robertson drag into account, robustly provides the required solution. The ecliptic intersection point of a particle with radiation pressure coefficient  $\beta$ , which started with an initial velocity  $\mathbf{V}_\perp$ , is denoted  $\mathbf{r}(\nu, \beta, \mathbf{V}_\perp)$ , where we refer to the ejection time by the true anomaly  $\nu$  in the following. Tab. 1 lists, for some true anomalies, the corresponding heliocentric distances.

Tab. 1. Heliocentric distances for different true anomalies of 55P/Tempel-Tuttle during the 1866 apparition.

true anomaly [deg]	heliocentric distance [AU]
0	0.977
10	0.984
20	1.006
30	1.043
40	1.099
50	1.177
60	1.282
70	1.422
80	1.609
90	1.862
100	2.210
110	2.698
120	3.404

In this work we only consider dust particles which were ejected during the perihelion passage of comet 55P/Tempel-Tuttle in 1866 and which passed through the ecliptic on the 18<sup>th</sup> November 2000 (from North to South). In Fig. 4 the ecliptic intersections of dust particles with  $\beta=0$  are shown, which were released

during perihelion passage ( $\nu=0$ ). The relative position of particles with different  $\beta$  or different ejection times look qualitatively the same. The ecliptic intersections are shown for trajectories which started with different directions of  $\mathbf{V}_\perp$ . For each direction four values for  $V_\perp$  are shown (25, 50, 75 and 100 m s<sup>-1</sup>). It can be seen that ecliptic intersections of particles, which started with a  $\mathbf{V}_\perp$  in the same direction, lie on a straight line (dotted in Fig. 4) and that the distances between two points on this line is proportional to the velocity difference. Therefore the position of the ecliptic intersection can well be approximated [9] by

$$\mathbf{r}(\nu, \beta, \mathbf{V}_\perp) = \mathbf{r}_c(\nu, \beta) + A(\nu, \beta)\mathbf{V}_\perp, \quad (5)$$

where  $\mathbf{r}_c(\nu, \beta) = \mathbf{r}(\nu, \beta, 0)$  and  $A(\nu, \beta)$  is a 2x2 matrix (note that all vectors lie in a plane; the spatial vectors in the ecliptic and the velocity vector in the plane perpendicular to the orbital velocity vector of the comet at the time of ejection). Since the elements of the matrix can be calculated on the basis of a few trajectories only, the intersection point for any initial velocity  $\mathbf{V}_\perp$  can be calculated efficiently on the basis of the numerical integration of a few trajectories only. The intersection of a dust shell with the ecliptic has elliptical shape (shown solid in Fig. 4). Such ellipses are shown in Fig. 4 and Fig. 1. The parameters which were used to produce Fig. 1 are radiation pressure coefficient  $\beta=0$ , ejection true anomaly  $\nu=0, \pm 40^\circ$  and  $V_\perp=20 \text{ m s}^{-1}$ .

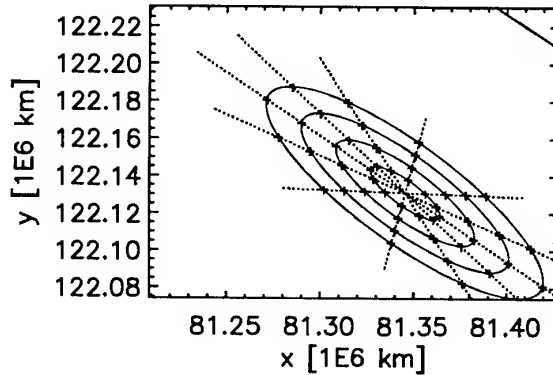


Fig. 4. Ecliptic intersections of trajectories of particles released from 55P/Tempel-Tuttle in 1866, when the comet was at perihelion. For explanation see text.

Apart from the intersection point with the ecliptic the numerical procedure also provides the ejection velocity  $V_3(\nu, \beta, \mathbf{V}_\perp)$  which is required to intersect the ecliptic at the specified time. Because the particles intersecting the ecliptic at the same time have almost the same orbital periods the required velocity in the direction of

the orbital motion of the comet is almost independent of  $V_{\perp}$ . Fig. 5 shows  $V_3$  for three different values of  $\beta$ .

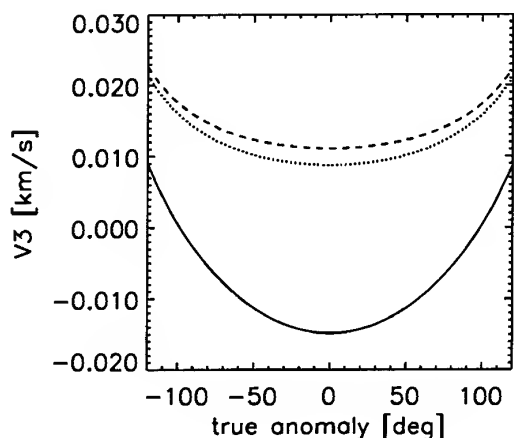


Fig. 5. Particle velocity in direction of comet orbital motion,  $V_3$ , which led to ecliptic crossings on November 18<sup>th</sup> 2000.

The different lines correspond to different  $\beta$ -values (solid:  $10^{-3}$ ; dotted:  $10^{-4}$  and dashed:  $10^{-5}$ ).

#### 4. VELOCITY REQUIRED TO REACH EARTH

Using Eq. 5 it is easy to find the trajectories which intersect the Earth. If we assume the Earth to be a point at position  $\mathbf{r}_e$ , then the ejection velocity  $V_{\perp}$  required to reach Earth can be found by

$$V_{\perp}(\nu, \beta) = A^{-1}(\nu, \beta) \{ \mathbf{r}_e - \mathbf{r}_c(\nu, \beta) \}. \quad (6)$$

Eq. 6 only gives the ejection direction in the direction perpendicular to the orbital motion of the comet. As the velocity in the direction of the orbital motion hardly changes for different  $V_{\perp}$ , we can define the velocity vector required to reach the Earth at the specified time by

$$\mathbf{V}_{\text{req}}(\nu, \beta) = \mathbf{V}_{\perp}(\nu, \beta) + V_3(\nu, \beta, 0) \frac{\mathbf{V}_{\text{comet}}}{V_{\text{comet}}}. \quad (7)$$

The absolute value of the ejection velocity required to reach the Earth position on 18<sup>th</sup> November 7am UT is shown in Fig. 6 for the  $\beta$ -values  $10^{-3}$ ,  $10^{-4}$  and  $10^{-5}$ . For all  $\beta$ -values a maximum in the required velocity can be seen for the particles which were released from the comet shortly after perihelion. This is due to the mentioned collapse of the dust shells. Comet 55P/Tempel-Tuttle crosses the ecliptic shortly after perihelion. The dust shell which was ejected during the

ecliptic crossing is therefore collapsed when it passes through the ecliptic. Similarly, the width of the ecliptic intersections of dust shells which were emitted shortly before and after the ecliptic crossing are small and high ejection velocities are required in order to reach the position of the Earth. The required velocity reaches a minimum for true anomalies  $\pm 100^\circ$ . The minimum is much lower for particles with  $\beta$ -value of  $10^{-3}$  than for the other shown  $\beta$ -values. This is because the centre of the dust shell (position of the particle with  $V_{\perp}$  and  $V_3=0$ ) with a  $\beta$ -value of  $10^{-3}$  is just crossing the ecliptic and only small values of  $V_3$  are required to make a dust particle intersect the ecliptic at the right time. The centres of the dust shells with lower  $\beta$  have already passed the ecliptic a long time ago and a  $V_3$  of  $14 \text{ m s}^{-1}$  is required such that there are still particles which intersect the ecliptic at the given time. From this, a constraint on the ejection velocity can be derived. The length of the dust shells is controlled by the absolute value of the ejection velocity. If the centre of all dust shells for some given  $\beta$ -value has long passed the ecliptic then a minimum ejection velocity is required such that there are still particles which lag behind far enough such that they still intersect the ecliptic at the given time. In the chosen example this means that if there was an 1866-Leonid observed on 18<sup>th</sup> November 2000, for which there is reason to assume that its  $\beta$ -value is not larger than  $10^{-4}$ , then it must have been ejected with an velocity of at least  $14 \text{ m s}^{-1}$ .

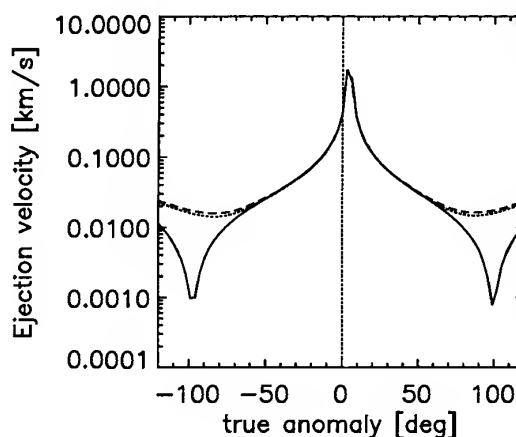


Fig. 6. Velocity required by particles released in the 1866 apparition to reach Earth on 18<sup>th</sup> November 2000 7h UT for different values of  $\beta$  (solid:  $10^{-3}$ ; dotted:  $10^{-4}$  and dashed:  $10^{-5}$ ).

#### 5. EJECTION DIRECTION

As the comet activity is driven by the Sun, the sunlit side of the comet is much more active than the night

side and most dust particles are ejected towards the Sun. Therefore it is interesting to derive the angle between the required ejection velocity vector and the Sun direction. This angle is shown in Fig. 7 for three different values of  $\beta$ . For all  $\beta$ -values there is a rapid change of this angle shortly after perihelion. This is again because of the collapse of the dust shell. Because ecliptic intersections of dust shells shortly before the collapse appear point-mirrored with respect to the ecliptic intersection of dust shells after collapse, a rapid change in the required ejection direction occurs around this point. At true anomalies of about  $\pm 100^\circ$  another rapid change in the angle can be seen for the  $\beta$ -value  $10^{-3}$ . This is because of the change of the sign of  $V_\lambda$  for these particles (see Fig. 5). As  $V_\lambda$  does not change sign for particles with  $\beta$  not larger than  $10^{-4}$ , this rapid change is only seen for the highest  $\beta$ -value.

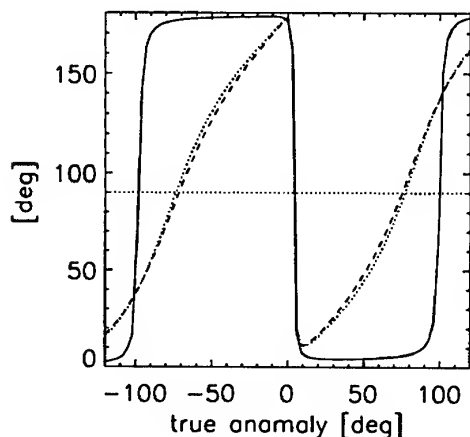


Fig. 7. For particles which were released from 55P/Tempel-Tuttle in the 1866 apparition and reach the Earth on 18<sup>th</sup> November 2000 7am UT, the angle between the required ejection velocity and the Sun direction is shown versus ejection true anomaly for three different  $\beta$ -values (solid:  $10^{-3}$ ; dotted:  $10^{-4}$  and dashed:  $10^{-5}$ ).

As the comet activity increases with decreasing heliocentric distance it seems valid to assume that most of the observed meteors were released from the comet near perihelion. From Fig. 7 it can be seen that shortly before perihelion particles need to be ejected towards the anti-solar direction in order to reach the Earth at the specified time. As comets eject most particles towards the Sun direction, Fig. 7 suggests that most of the observed meteors were ejected after perihelion. However, from Fig. 6 it can be seen that the particles which were ejected close to perihelion require high ejection velocities in order to reach the Earth. Therefore particles ejected close to perihelion might not have reached the Earth and most of the meteors are

particles which were ejected at large heliocentric distances. The fact that particles ejected at large heliocentric distance can dominate a meteor storm was shown in [7]. However, even if particles ejected at large heliocentric distances dominate the flux, then there is still information which can be gained from Fig. 7. For example, it can be seen from Fig. 7 that particles with  $\beta$  not larger than  $10^{-4}$  are more likely to have been released at true anomalies  $\nu < -70^\circ$  than at true anomalies  $\nu > +70^\circ$ .

## 6. MASS DISTRIBUTION

Due to the different dynamical behaviour of particles of different masses, one might already expect that the mass distribution of particles which enter the Earth's atmosphere is different from the mass distribution of particles ejected from the comet per unit time. In this section we want to give an example for which this expectation is confirmed. For this we assume a very simple model for the ejection velocity of particles. We assume that the comet emits dust particles radial symmetrically. We assume the ejection velocity is independent of the heliocentric distance and only dependent on the  $\beta$ -value of the particle

$$V_{ej}(\beta) = 160 \frac{m}{s} \sqrt{\frac{\beta}{10^{-3}}} \quad (8)$$

For a dust particle to reach the Earth's atmosphere the ejection velocity must equal the required velocity

$$V_{ej}(\beta) - V_{req}(\nu, \beta) = 0 \quad (9)$$

Fig. 8 shows the difference of the ejection velocity and the required velocity for the three  $\beta$ -values  $10^{-3}$ ,  $10^{-4}$  and  $10^{-5}$ . Eq. 9 is fulfilled when one of the lines intersects the horizontal axis. It can be seen in Fig. 8 that for different  $\beta$ -values, Eq. 9 is fulfilled for different true anomalies. Hence this simple example shows that particles with different  $\beta$  i.e. different masses, which reach the Earth's atmosphere at the same time originate from different heliocentric distances. Therefore one could not derive a mass distribution of ejected particles from the mass distribution of observed meteors without making assumptions about the comet activity in dependence on heliocentric distance.

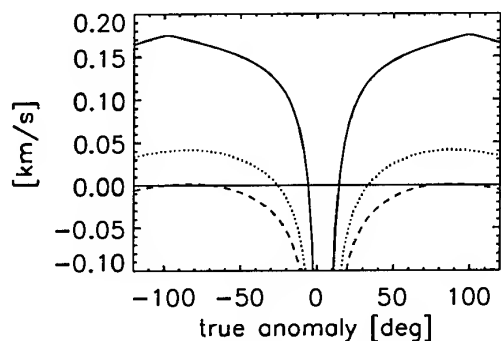


Fig. 8. Difference between ejection velocity and required velocity for different  $\beta$ -values (solid:  $10^{-3}$ ; dotted:  $10^{-4}$  and dashed:  $10^{-5}$ ).

## 7. DISCUSSION

The result of the previous section does not necessarily mean that the mass distribution of observed meteors can never be used to constrain the mass distribution of ejected particles of a comet. The magnitude distribution indices in [5] show significant variations if different meteor streams are compared. However, the magnitude distribution indices given for each meteor stream observed in different years are comparable. Therefore, there must be some information in the observed mass distribution otherwise the scatter of the magnitude distribution index for the meteor outbursts of a single meteor stream could be expected to be larger. From the example in the previous section one could expect that the heliocentric distances which contribute to the observed magnitude distribution index, change for observation of the same trail in different years. However, the fact that a typical range of magnitude distribution indices for each meteor stream seems to exist, suggests that there is some repeating pattern in how the mass distributions of observed meteors is related to the mass distribution of particles ejected from the comet. From the fact that different magnitude distribution indices are observed for meteor outbursts of different streams, it cannot necessarily be concluded that this difference is due to different mass distribution of the source comets. Effects due to different orbital configurations need to be ruled out before this conclusion can be drawn.

In section 4 it was shown that a lower limit on the ejection velocity of the dust particles can be derived, if the corresponding trail can be identified in the observed meteor rates. If the comet orbit was perfectly known, the value of the minimum velocity could be estimated with great accuracy, because of the high accuracy with which celestial mechanics can be modelled. However due to non-gravitational forces

exerted on comets, the initial conditions of the released dust particles always remain uncertain to some extent. To understand how the uncertainty of the comet orbit affects the result, one has to recall that the required velocity of particles to reach Earth can be dominated by two different components of the ejection velocity: (1) The ejection velocity perpendicular to the comet's orbital velocity at the time of ejection. In the example in section 4, this is the case for true anomalies, for which the width of the dust shell ecliptic intersection is small. Therefore large ejection velocities are required to reach the Earth. (2) The component in the direction of the orbital velocity. In the example, this is the case for particles with  $\beta$ -values not larger than  $10^{-4}$  at true anomalies  $\pm 100^\circ$ . Here the required velocity is dominated by  $V_3$ , because the centres of the corresponding dust shells have long passed through the ecliptic and a minimum ejection velocity is required such that the dust shell is long enough that there are still particles intersecting the ecliptic. In the latter case, the required velocity is hardly influenced by the uncertainty of the comet orbit. However, in the previous case small uncertainties in the position where the dust particles intersect the ecliptic can significantly change the results.

## 8. CONCLUSION

We have defined a procedure that allows the calculation of the set of all possible particle trajectories that can reach the Earth at the same time. On the basis of this it is possible to place constraints on the ejection velocity without invoking any ejection model of the dust particles from the comet nucleus. An example was given on how a lower bound of the ejection velocity can be found. The accuracy of the estimate is only dependent on the accuracy of the comet orbit during the time of ejection. For a very simple ejection model it was shown that dust particles of different sizes, which reach the Earth at the same time, originate from different heliocentric distances. Therefore, assumptions about the dependence of the comet activity on heliocentric distance have to be made in order to constrain the mass distribution of ejected particles from the mass distribution of observed meteors. Since the magnitude distribution indices vary only slightly for a given meteor stream [5], it is suggested that there might be a repeating pattern on how different heliocentric distances contribute to a meteor mass distribution. However, as there are bigger variations of the magnitude distribution indices for different meteor streams, the different mass distributions of meteors of different streams is not necessarily due to different mass distributions of the source comets, but could also be due to different orbital configurations.

## ACKNOWLEDGEMENT

The encouraging discussions with David Asher and Rüdiger Jehn which led to the present work are gratefully acknowledged. This work was funded by the UK Particle Physics and Astronomy Research Council.

## REFERENCES

1. Arlt R., Gyssens M., Results of the 2000 Leonid Shower, *WGN*, Vol. 28, 191-204, 2000.
2. Finson M. L. and Probst R. F. A Theory of Dust Comets. I. Model and Equations, *AJ*, Vol. 154, 327-352, 1968.
3. Massonne L. Modellierung einer kometaren Staubkoma, *PhD thesis*, Ruprecht-Karls-Universität, Heidelberg, Germany, in German, 1987.
4. Fertig J. and Schwehm G. Dust environment models for comet P/Halley: Support for targeting of the Giotto S/C. *Adv. Space Res.*, Vol. 4, No. 9, 213-216, 1984.
5. Jenniskens, P. Meteor stream activity II. Meteor Outbursts, *A&A*, Vol. 295, 206-235, 1995.
6. Göckel C. and Jehn R. Testing cometary ejection models to fit the 1999 Leonids, *Mon. Not. R. Astron. Soc.*, Vol. 317, L1-L5, 2000.
7. Ma Y. and Williams I. P. The ejection velocity of meteoroids from cometary nuclei deduced from observations of meteor shower outbursts, *Mon. Not. R. Astron. Soc.*, Vol. 325, 379-384, 2001.
8. McNaught R. H. and Asher D. J. Leonid Dust Trails and Meteor Storms, *WGN*, 27:2, 85-102, 1999.
9. Kondrat'eva E. D., Reznikov E. A. Comet Tempel-Tuttle and the Leonid Meteor Swarm, *Sol. Syst. Res.*, Vol. 19, 96-101, 1985.
10. McDonnell J. A. M. et al. Near Earth Environment. in *Interplanetary Dust*. Grün E. et al. (ed.), 163-192, 2001.

# PARENT OBJECTS OF $\alpha$ CAPRICORNID METEOR STREAM

## ICHIRO HASEGAWA

*Faculty of Socio-Culture, Otemae University,  
Inano, Itami 664-08612, Japan, Email: hasegawa@otemae.ac.jp*

### ABSTRACT

Complex structures of the meteor streams of photographic  $\alpha$  Capricornids observed during July and August are studied, and it is confirmed that the main parent comet is 45P/Honda-Mrkos-Pajdusakova. The motions of Comet 45P and the  $\alpha$  Capricornid meteors are under large effects of perturbations of Jupiter. 72P/Denning-Fujikawa, 141P/Machholz 2, Comet 1457 L1, an unknown comet, minor planets (2101) Adonis and (9162) 1987 OA are also suggested as parent objects.

### 1. INTRODUCTION

$\alpha$  Capricornid meteors have been observed since the end of the 19th century[1], and Wright et al. [2] studied photographic meteors found on Harvard plates and suggested that the possible parent object is Comet 45P/Honda-Mrkos-Pajdusakova. Kronk[1] discussed on three streams of the  $\alpha$  Capricornids and described the other possible parent objects suggested by some authors.

In the present study, we confirmed that those suggested candidates are possible parent objects and found new parents such as an unknown comet and minor planet (9162) 1987 OA.

### 2. METEORS of the $\alpha$ CAPRICORNIDS

Observed radiant points of the  $\alpha$  Capricornids and predicted paths of them are shown in Fig. 1. The observed meteor data are taken from the IAU Meteor Data files[3], and predictions are calculated from the orbital elements of the parent objects given in Table 1

and the q-adjusted method given by Hasegawa[4] is used.

In Table 1, orbital elements of the possible parent objects are given. In the first column of Table 1, the year of the epoch for orbital elements are given in parentheses, and the perturbed cometary orbits are computed by Nakano[5].

For the individual observed meteor, the radiant point and orbital elements are given in Table 2 in the Gothic type and the prediction is given below. According to the orbital elements, they are classified in the stream and listed in the order of the solar longitude at the meteor observation. The coordinate system used in this study is referred to the 2000.0 equinox.

Observed velocities of meteors in the Stream 5 are greater than those predicted from the orbit of (9162)1987OA, therefore, the relations between Stream 5 and the minor planet (9162) is questionable.

Stream 6 consists of thirteen meteors clearly, but, the parent object(comet?) is not known yet.

All meteors of the  $\alpha$  Capricornids probably has their twin meteors[6], however, because their radiant points are very close to the sun, the optical observations of those twin meteors likely to be impossible.

### 3. Conclusion

We have found the complex structure in the  $\alpha$  Capricornids and suggested six known and one unknown parent objects of them.

Table 1 Parent Objects of the  $\alpha$  Capricornids

Object	q	e	$\omega$	$\Omega$	i	P	L	B	Q
45P/Honda-Mrkos-Pajdusakova									
(1785)	0.7245	0.7759	323.67	92.70	3.92	5.81	56°	-2°	5.74
(1797)	0.8489	0.7483	343.92	74.42	5.57	6.19	58	-1	5.90
(1878)	0.6323	0.7971	356.08	67.71	2.00	5.50	64	0	5.60
(1938)	0.5760	0.8098	183.96	233.75	12.98	5.27	58	-1	5.48
(1985)	0.5423	0.8216	325.71	89.37	4.21	5.30	55	-2	5.54
72P/Denning-Fujikawa									
(1916)	0.7413	0.8255	330.80	48.38	8.25	8.76	19	-4	7.75
(1951)	0.7360	0.8262	335.60	41.77	9.06	9.72	18	-4	7.73
141P/Machholz 2									
(1952)	0.7395	0.7547	141.77	253.21	11.04	5.23	35	+7	5.29
(2101) Adonis									
	0.4411	0.7646	42.41	350.62	1.35	2.57	33	+1	3.31
(9162) 1987 OA									
	0.6052	0.5956	235.45	180.31	9.02	1.83	55	-7	2.39
C/Capricornids									
(1952)	0.572	0.754	271.0	123.3	7.1	3.55	34	-7	4.08
C/1457 L1									
(1457)	0.7699	1.0	183.28	187.55	7.34	—	11	0	—

Notes to the Tables: L in Table 2 is the solar longitude at meteor observation. q, e,  $\omega$ ,  $\Omega$ , and i are the usual orbital elements and P is the orbital period in years; L and B are the ecliptic coordinates of the perihelion point; Q is the aphelion distance in AU. V is the geocentric velocity of meteor in km/s and  $\Delta$  is the separation between the orbit of the parent object and the earth in AU.

Table 2-1 Individual Meteor of  $\alpha$  Capricornids Stream(Observation and Prediction)

Meteor	Date	L	$\alpha$	$\delta$	V	q	e	$\omega$	$\Omega$	i	$\Delta$	Q
Stream 1-1												
HC 8110	1953 July 21.4	118.9	311.1	-13.5	29.2	0.358	0.860	293.8	118.9	5.4		4.76
	45P(1785)		313.2	-14.2	25.9	0.367	0.776	297.5	118.9	3.5	0.367	
H 2818	1951 Aug. 10.4	137.3	323.2	-13.7	26.3	0.484	0.851	278.2	137.3	0.8		6.01
	45P(1785)		322.7	-11.3	24.0	0.500	0.776	279.1	137.3	2.8	0.458	
HA8881a	1956 Aug. 12.3	140.0	326.2	-10.2	25.1	0.479	0.805	280.5	140.0	2.9		4.43
	45P(1785)		324.1	-10.9	23.6	0.521	0.776	276.4	140.0	2.7	0.401	
HC 3567	1952 Aug. 15.3	143.1	325.8	-13.2	24.5	0.538	0.827	272.6	143.1	0.4		5.68
	45P(1785)		325.6	-10.4	23.2	0.544	0.776	273.3	143.1	2.5	0.341	
Stream 1-2												
K 176 *	1971 Aug. 19.0	145.7	329.6	-10.1	27.2	0.489	0.891	275.7	145.7	2.1		8.48
	45P(1878)		331.2	-11.3	24.5	0.500	0.797	278.1	145.7	0.4	0.271	
HC 3643	1952 Aug. 21.2	148.7	331.0	-6.5	24.4	0.525	0.808	274.4	148.7	4.3		4.94
	45P(1878)		332.8	-10.8	24.0	0.523	0.797	275.1	148.7	0.3	0.215	
O 157	1959 Aug. 26.8	153.6	333.7	-12.0	22.9	0.586	0.804	86.5	233.6	0.8		5.39
	45P(1878)		335.2	-10.1	23.4	0.561	0.797	270.2	153.6	0.1	0.134	
Stream 1-3												
MORP 1	1970 July 31.3	128.3	318.2	-17.7	29.2	0.405	0.892	285.8	128.3	1.7		7.10
	45P(1938)		320.9	-18.7	26.6	0.407	0.810	109.8	308.3	3.4	0.496	
HC 3636	1952 Aug. 20.2	147.8	324.9	-13.8	20.5	0.645	0.753	261.2	147.8	0.1		4.58
	45P(1938)		329.1	-11.4	23.6	0.561	0.810	269.8	147.8	0.9	0.235	
HC 3651	1952 Aug. 21.3	148.8	328.8	-11.0	22.5	0.586	0.787	267.6	148.8	1.2		4.92
	45P(1938)		329.4	-11.0	23.4	0.567	0.810	268.9	148.8	1.1	0.232	
PN40091B	1968 Aug. 23.4	150.8	331.7	-13.5	20.0	0.617	0.703	266.9	150.8	1.1		3.54
	45P(1938)		330.2	-10.0	23.1	0.585	0.810	266.7	150.8	1.6	0.228	
MORP 883	1983 Aug. 27.2	153.6	328.6	-3.2	23.4	0.610	0.841	262.3	153.6	6.7		7.06
	45P(1938)		331.1	-8.6	22.6	0.607	0.810	263.9	153.6	2.2	0.225	
D62 0962	1962 Aug. 28.7	155.5	336.4	-4.9	25.4	0.528	0.855	271.7	155.5	4.1		6.75
	45P(1938)		331.7	-7.7	22.2	0.622	0.810	261.9	155.5	2.6	0.229	
PN 39731C	1967 Aug. 29.1	155.5	335.5	-2.7	23.2	0.557	0.785	271.2	155.5	5.5		4.62
	45P(1938)		331.7	-7.7	22.2	0.622	0.810	261.9	155.5	2.6	0.227	
EN 290875	1975 Aug. 29.9	156.3	333.8	-7.1	25.4	0.576	0.910	264.0	156.3	2.9		12.22
	45P(1938)		331.9	-7.3	22.1	0.628	0.810	261.1	156.3	2.8	0.231	
HA 8983a	1956 Sept. 1.4	159.4	334.0	-6.5	21.4	0.646	0.799	259.1	159.4	2.7		5.78
	45P(1938)		332.8	-5.7	21.5	0.652	0.810	257.9	159.4	3.5	0.239	

Table 2-2 Individual Meteor of  $\alpha$  Capricornid Stream

Meteor	Date	L	$\alpha$	$\delta$	V	q	e	$\omega$	$\Omega$	i	$\Delta$	Q
Stream 2 - 1												
PN39707A	1967 Aug. 5.2	132.3	303°	-18°	18.8	0.727	0.753	250.0	132.3	1.1		5.16
	72P(1916)		300	-19	19.8	0.736	0.825	246.9	132.3	0.9	0.146	
Stream 2 - 2												
O286	1962 July 7.9	105.7	284.2	-14.8	23.0	0.594	0.790	266.7	105.7	6.1		5.06
	72P(1951)		287.0	-17.8	24.8	0.541	0.826	272.0	105.7	4.0	0.403	
KPM 7509	1975 Aug. 13.6	140.6	309.0	-25.3	17.5	0.779	0.734	63.0	320.6	3.3		5.08
	72P(1951)		302.8	-22.9	17.8	0.807	0.826	56.7	320.6	1.4	0.175	
HC8546	1953 Aug. 14.3	141.8	304.5	-28.2	15.3	0.834	0.701	55.0	321.9	3.6		4.74
	72P(1951)		303.2	-23.3	17.5	0.815	0.826	55.4	321.9	1.6	0.175	
O83	1958 Sept. 9.8	167.2	308.8	-32.5	12.8	0.943	0.786	31.3	347.2	4.4		7.87
	72P(1951)		307.7	-35.0	13.2	0.947	0.826	29.8	347.2	5.2	0.251	
Stream 3												
WN810730	1981 July 30.6	127.6	306.6	-29.1	20.5	0.661	0.746	79.4	307.6	6.3		4.54
	141P(1952)		311.3	-27.1	22.0	0.595	0.755	87.9	307.6	6.4	0.303	
MORP 384	1978 Aug. 14.4	141.6	318.6	-23.3	18.1	0.699	0.677	76.5	321.6	4.0		3.63
	141P(1952)		317.0	-23.5	19.5	0.699	0.755	73.7	321.6	4.0	0.195	
Stream 4												
H 4186	1952 June 28.3	96.8	289.6	-24.9	29.5	0.36	0.87	112.9	276.8	3.0		5.18
	(2101) Adonis		290.3	-22.5	25.4	0.382	0.765	116.1	276.8	0.4	0.162	
H 7947	1953 July 6.4	105	293	-22	29	0.42	0.89	105	285	0		7.22
	(2101) Adonis		295	-22	24.8	0.441	0.765	107.9	285.0	0.6	0.023	
HA 8756a	1956 Aug. 7.4	134.2	309.8	-18.0	19.8	0.684	0.752	76.1	314.2	0.2		4.83
	(2101) Adonis		310.6	-20.0	20.5	0.660	0.765	78.8	314.2	1.1	0.337	
KPM 8003	1980 Aug. 11.6	139.4	310.7	-23.5	17.5	0.753	0.695	68.1	319.4	2.7		4.18
	(2101) Adonis		312.9	-19.6	19.6	0.699	0.765	73.5	319.4	1.2	0.372	
C 15761	1958 Aug. 13.9	142.2	315.7	-17.2	19.1	0.691	0.725	75.0	322.2	0.2		4.33
	(2101) Adonis		314.1	-19.4	19.1	0.719	0.765	70.7	322.2	1.2	0.389	
KPM 7602	1976 Aug. 17.5	144.8	315.9	-16.3	18.8	0.729	0.746	70.6	324.8	0.3		5.01
	(2101) Adonis		315.2	-19.3	18.7	0.736	0.765	68.2	324.8	1.2	0.407	

Table 2-3 Individual Meteor of  $\alpha$  Capricornid Stream

Meteor	Date	L	$\alpha$	$\delta$	V	q	e	$\omega$	$\Omega$	i	$\Delta$	Q
Stream 5												
H1695	1949 Aug. 1.3	129.4	313.2	-11.5	23.5	0.525	0.767	276.5	129.4	4.8		3.98
	(9162) 1987 OA		317.0	-7.9	18.6	0.532	0.596	286.0	129.4	5.7	0.192	
HC 8147	1953 Aug. 4.2	132.2	316.6	-8.9	25.0	0.495	0.801	278.7	132.2	6.7		4.48
	(9162) 1987 OA		318.2	-6.8	18.5	0.549	0.596	283.2	132.2	6.0	0.161	
HC 8368	1953 Aug. 9.2	137.0	320.3	-2.0	25.5	0.496	0.804	278.5	137.0	11.8		4.57
	(9162) 1987 OA		320.3	-4.8	18.3	0.580	0.596	278.4	137.0	6.5	0.119	
HA 8840a	1956 Aug. 10.4	138.2	325.4	-5.4	25.8	0.446	0.798	285.1	138.2	7.8		3.97
	(9162) 1987 OA		320.8	-4.3	18.2	0.588	0.596	277.2	138.2	6.7	0.112	
DMS 97202	1997 Aug. 12.3	139.6	323.1	-5.3	26.6	0.485	0.850	277.8	139.6	8.4		5.98
	(9162) 1987 OA		321.4	-3.7	18.1	0.597	0.596	275.8	139.6	6.8	0.105	
D 641952	1964 Aug. 13.9	141.6	322.9	-5.6	23.5	0.542	0.778	273.5	141.6	7.0		4.34
	(9162) 1987 OA		322.2	-2.9	18.0	0.610	0.596	273.8	141.6	7.0	0.099	
Stream 6												
H 8026	1953 July 15.3	113.1	293	-14	19.8	0.62	0.68	268	114	6		2.56
	C/Capricornids		298.9	-12.6	23.9	0.495	0.754	281	113	7.0	0.159	
HC 3379	1952 July 24.4	122.0	300.9	-9.9	22.4	0.594	0.765	267.6	122.0	7.7		4.46
	C/		303.3	-10.6	22.7	0.562	0.754	272.3	122.0	7.1	0.019	
DMS 85004	1985 July 26	122	302.4	-10.5	25.4	0.549	0.856	270.1	122	8.1		7.08
	C/		303.4	-10.5	22.7	0.564	0.754	272.0	122	7.1	0.015	
HC 3386	1952 July 25.3	122.9	303.9	-9.5	22.0	0.573	0.732	271.9	122.9	7.6		3.70
	C/		303.7	-10.4	22.6	0.568	0.754	271.4	122.9	7.1	0.006	
HC 3405	1952 July 26.2	123.8	305.3	-9.8	23.4	0.551	0.775	272.8	123.8	7.6		4.35
	C/		304.1	-10.2	22.5	0.575	0.754	270.5	123.8	7.1	0.006	
H 3408	1952 July 26.8	123.9	302	-13	19.9	0.64	0.70	265	124	5		3.63
	C/		304.2	-10.1	22.4	0.576	0.754	270.4	123.9	7.1	0.007	
HC 3411	1952 July 26.3	123.9	305.6	-12.2	21.7	0.568	0.725	272.8	123.8	5.3		3.56
	C/		304.2	-10.1	22.4	0.576	0.754	270.4	123.9	7.1	0.007	
HC 3416	1952 July 26.4	123.9	304.1	-10.2	23.0	0.574	0.774	269.9	124.0	7.2		4.51
	C/		304.2	-10.1	22.4	0.576	0.754	270.4	123.9	7.1	0.007	
DMS 81002	1981 Aug. 1	128.6	307.3	-9.6	23.3	0.585	0.801	267.3	128.6	7.1		5.29
	C/		306.3	-9.1	21.7	0.611	0.754	265.7	128.6	7.1	0.066	
DMS 81003	1981 Aug. 2	128.8	307.0	-8.8	22.0	0.692	0.758	266.8	128.8	7.3		3.55
	C/		306.4	-9.0	21.7	0.613	0.754	265.5	128.8	7.1	0.068	
HC 8149	1953 Aug. 4.3	132.2	310.3	-8.4	22.2	0.601	0.768	266.5	132.2	7.0		4.58
	C/		307.9	-8.2	21.2	0.638	0.754	262.2	132.2	7.0	0.106	
HC 8668	1953 Aug. 10.5	138.1	311.1	-6.3	20.3	0.673	0.748	257.6	138.1	7.2		4.67
	C/		310.3	-6.9	20.2	0.681	0.754	256.3	138.1	6.9	0.165	
HC 3655	1952 Aug. 21.3	148.8	322.4	-3.8	24.4	0.621	0.902	259.3	148.8	8.0		12.05
	C/		314.1	-4.9	18.3	0.756	0.754	245.7	148.8	6.4	0.250	

Table 2-4 Individual Meteor of  $\alpha$  Capricornid Stream

Meteor	Date	L	$\alpha$	$\delta$	V	q	e	$\omega$	$\Omega$	i	$\Delta$	Q
Stream 7												
KPM 7956	1979 July 30.7	127.2	291.4	-14.4	16.3	0.800	0.704	239.0	127.2	3.6		4.61
	C/1457 L1 = 1457 II		292.2	-16.2	22.7	0.735	1.0	243.4	127.2	3.6	0.049	
DMS 94002	1994 Aug. 4.0	131.5	288.1	-15.8	16.9	0.839	0.816	232.0	131.5	3.0		8.28
	C/1457 L1		293.3	-14.8	21.7	0.765	1.0	239.1	131.5	4.1	0.003	
DMS 92012	1992 Aug. 4.0	131.9	289.3	-20.3	15.5	0.847	0.744	232.2	131.9	0.9		5.77
	C/1457 L1		293.4	-14.6	21.6	0.771	1.0	238.7	131.9	4.1	0.001	
NMS 381	1983 Aug. 12.6	139.6	294.0	-19.0	15.8	0.860	0.793	228.8	139.6	1.1		7.45
	C/1457 L1		294.8	-12.0	19.8	0.826	1.0	231.0	139.6	4.9	0.008	
NMS 382	1983 Aug. 12.6	139.6	300.2	-9.3	15.6	0.820	0.689	237.9	139.6	4.9		4.45
	C/1457 L1		294.8	-12.0	19.8	0.826	1.0	231.0	139.6	4.9	0.008	

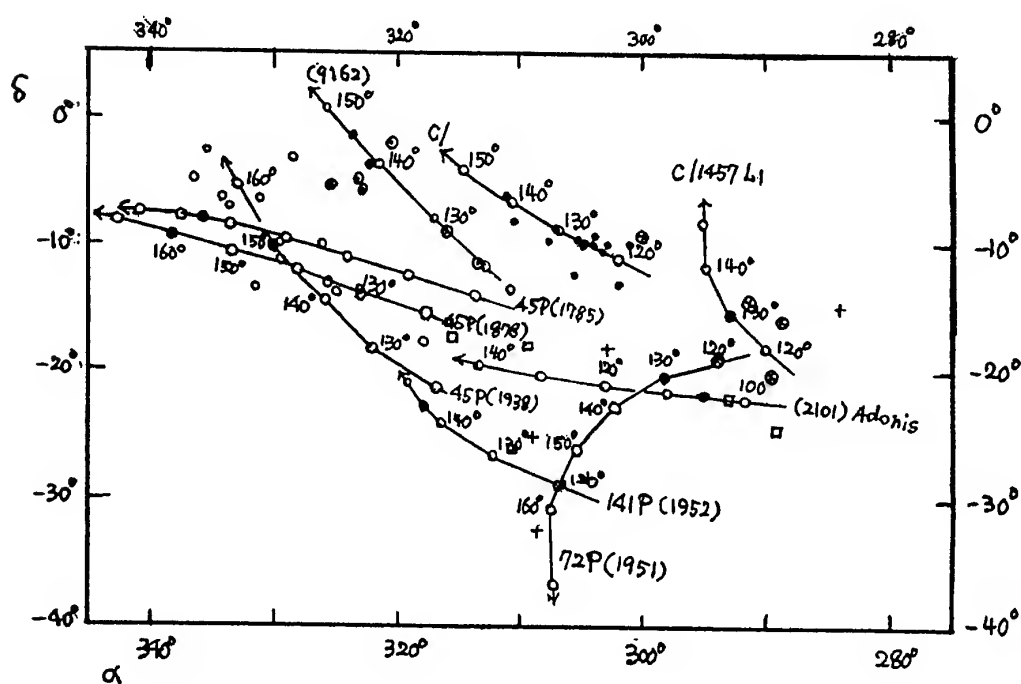


Fig. 1. Observed positions and predicted paths of radiant points of the  $\alpha$  Capricornid meteors (Numbers indicated with paths are the solar longitude referred to the equinox 2000.0).

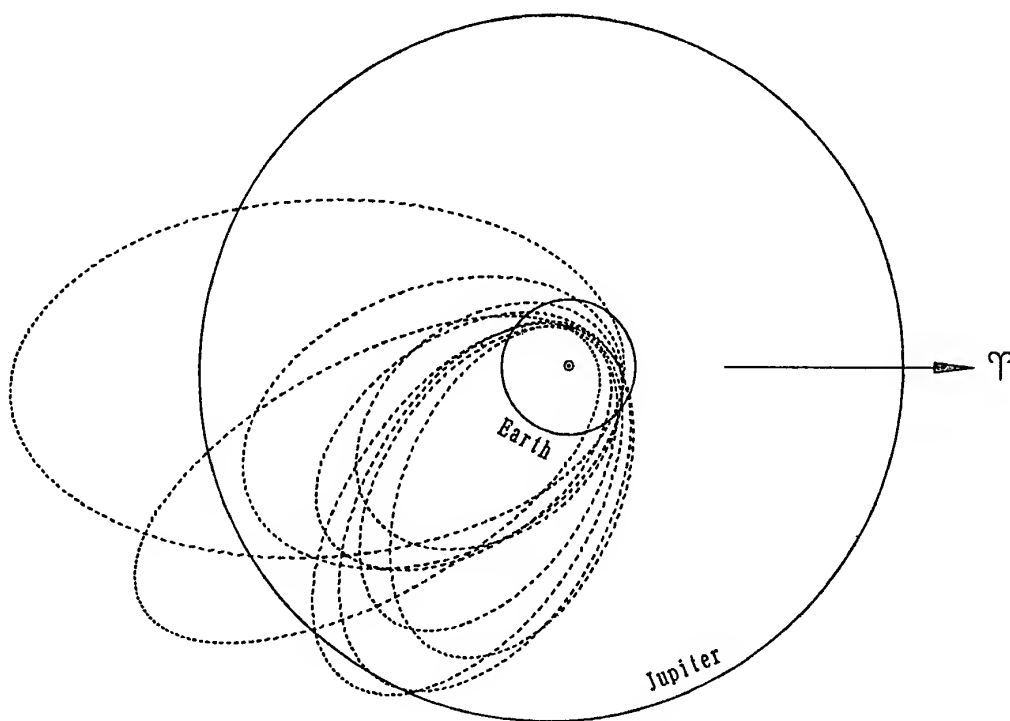


Fig. 2 Some orbits of the  $\alpha$  Capricornid meteors..

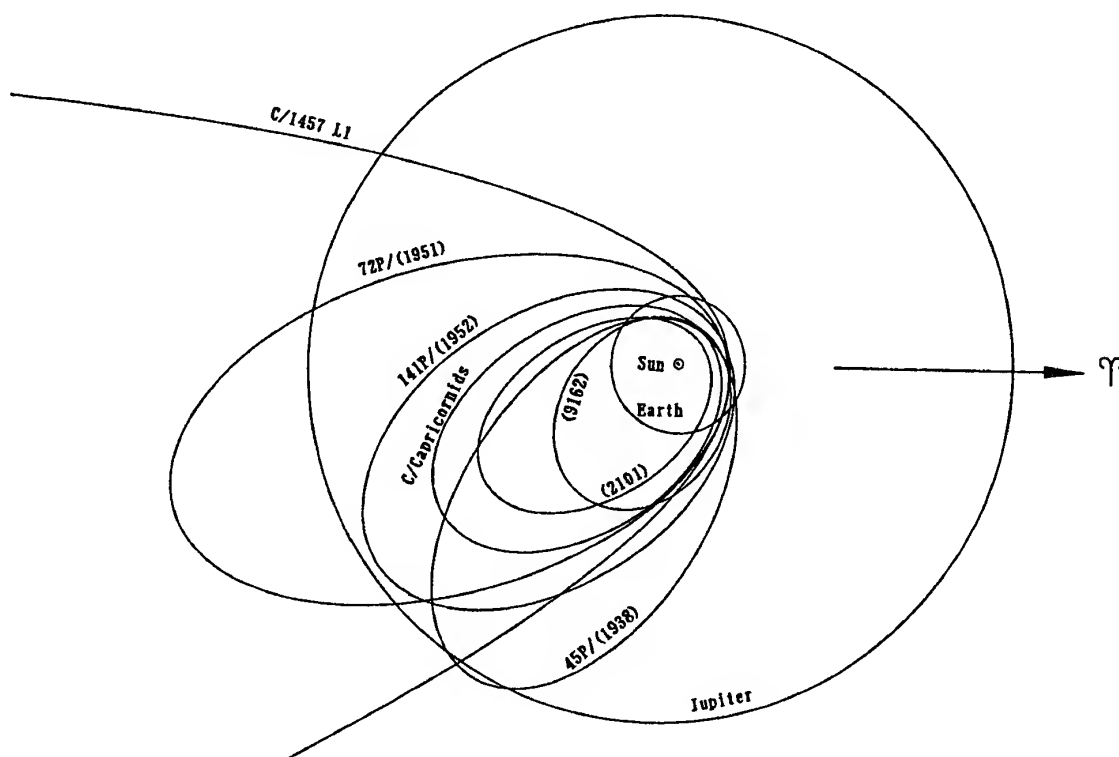


Fig. 3. Orbits of parent objects of the  $\alpha$  Capricornid meteors.

# ACKNOWLEDGEMENT

Many thanks are due to Mr. K. Ohtsuka for his search for  $\alpha$  Capricornid meteor data.

# REFERENCES

1. Kronk W., *Meteor Showers A Descriptive Catalog*, Enslow Publishers Inc., Hillside, N.J., 1988.
2. Wright, F. W., Jacchia, L. G. and Whipple, F. L., Potographic  $\alpha$  Capricornid

Meteors, *AJ*, vol. 61, 61 – 69, 1956.

3. Lindblad B. A., *Documentation of Meteor data available at the IAU meteor data center*, Lund, 1990.

4. Hasegawa I., Predictions of the Meteor Radiant Point Associated with a Comet, *PASJ*, vol. 42, 175 – 186, 1990.

- 5 Nakano S., Private communications, 2001.

6. Babadzhanov, P. B., Formation of Twin Meteor Showers, *Asteroids Comets MetIII*, 497 – 503, 1990.

# ASTEROID (1620) GEOGRAPHOS AS A POSSIBLE PARENT BODY FOR A METEOR STREAM

G.O. Ryabova

*Research Institute of Applied Mathematics and Mechanics, Tomsk, 634050, Russia,  
Email: astrodep@niipmm.tsu.ru*

## ABSTRACT

Numerous model streams having different schemes and times of ejection were considered. It was obtained that model meteoroid streams ejected with high velocities (up to 1 km/s) can approach the Earth's orbit twice, once before (February-March) and once after (August) perihelion. There were found 44 correlated meteor orbits (in databases IAU MDC and MSSWG) from the both showers and a taxon structure was derived for them. The distribution of ejection velocity vectors looks like originated at impact of a catching up small body, but the time of the collision remains unknown. So, with the high probability Geographos is the parent body for a meteor stream, generating twin meteor showers observable at the Earth: Spring and Summer Geographides.

## 1. INTRODUCTION

The asteroid (1620) Geographos is a very interesting object from the different viewpoints. In 1994 during a close (to 0.0333 AU) approach with the Earth extensive photometric [1] and radar [2] observations allowed to improve our knowledge about the asteroid's shape, rotation, orbit and physical characteristics. In particular the peculiar morphology of the Geographos' ends were revealed [2]. Protuberances at the asteroid's ends may be related, in the authors opinion, to the pattern of ejecta removal and deposition caused by the asteroids gravity field. There are strong grounds to believe that the asteroid has a small satellite [3,4]. Both Geographos orbital nodes with the ecliptic plane are located near the Earth orbit: the ascending node has minimal distance 0.03 AU and the descending node 0.08 AU. So in physical and dynamical properties Geographos may well be the parent body for a meteor stream. Reasonable assumptions as to the existence of meteoroid streams associated with Geographos have been already made [5-8]. But in all cases investigations were reduced to search for asteroid-related meteoroids in one or another catalogue of meteor orbits. The present study was undertaken to answer the following questions: when and how could particles escape from the asteroid, could they reach the Earth and can we detect some of them in available meteoroid orbit databases.

## 2. SOME DATA FOR GEOGRAPHOS

### 2.1 Shape and rotation

On the base of radar observations [2] and optical lightcurves [1] Hudson and Ostro [9] undertook an attempt to reconstruct a physical model of Geographos, including shape, photometric properties and spin state. The shape has been defined as a distorted ellipsoid, whose surface consists of 1020 triangle facets. The model has maximum dimensions along the axes of inertia of  $5.0 \times 2.0 \times 2.1$  km with accuracy of 0.15 km. Its volume is  $8.8 \pm 1.6$  km<sup>3</sup>. An equivalent homogeneous ellipsoid has the dimensions  $4.7 \times 1.9 \times 1.9$  km. Authors pointed out some limitations of the model determined mainly by unfavourable geometry of observations. The symmetrization of the model leads to overestimation of the extents along the spin vector direction and consequently the volume. It is necessary to add that dimensions of the *silhouette*, obtained by Ostro et al. [2], are  $(5.11 \times 1.85) \pm 0.11$  km. The second dimension has been taken across the envelope because one side has S-shape. And according to photometric observations [1] the following axis ratios were obtained:  $a/b = 2.58 \pm 0.16$ ,  $b/c = 1.0 \pm 0.15$ .

In the above mentioned paper [3] the ellipsoid was assumed to be rotating about the axis of maximum momentum of inertia. Authors tested the possibility of non-principle axis rotation and "observed no significant change in the fit and hence find no evidence for non-principal-axis rotation". They found sidereal spin period  $P_s = 5.2233270 \pm 0.00000072$  hours and pole direction  $\lambda = 55^\circ \pm 6^\circ$ ,  $\beta = -46^\circ \pm 4^\circ$ . These results differ little from those of Magnusson et al. [1]:  $\lambda = 56^\circ \pm 6^\circ$ ,  $\beta = -47^\circ \pm 4^\circ$ ,  $P_s = 0.21763860 \pm 0.00000003$  days.

Nevertheless it is quite possible that the asteroid has oscillations of its spin axis. In [3,4] a frequency analysis of fine photometric effects in the light variations was made and besides the well-known period  $P_s$ , periods of  $0.8^d$ ,  $2.8^d$  and  $0.224^d$  were detected. Authors associate the first period with free precession of the spin axis, the second one with forced precession caused by a small satellite and the last one

with the motion of this near-synchronous satellite. On the whole the frequency pattern is complicated and calls for further investigation.

## 2.2 Asteroid surface and density

Radar observations [2] have shown the lack of sharp angularity in the silhouette. The sharp variations in brightness are also rare in occurrence. So the asteroid was hardly subjected to a recent near catastrophic collision. At the same time several probable craters were noticed. Bottke et al. [10] pointed out that existence of large craters on a relatively small asteroid imply that its internal structure is sufficiently broken up. We know nothing about the thickness of the regolith, but from estimation of radar albedo Ostro et al. [2] calculated a bulk density about  $2.4 \text{ g cm}^{-3}$ .

## 2.3 Effects of planetary tides

Numerical simulation of tidal forces influence on the Earth-crossing objects yielded fascinating results as to Geographos. Bottke et al. [10] used a N-body code to follow the evolution of model asteroids constructed of 247-491 spherical components during encounters with the Earth. As it turned out, some of the simulated asteroids develop the same rotation rate (angular momentum increases) and specific shape as Geographos. Moreover, the final shape of one of the model presented at [10, Fig.4] surprisingly reproduces all the Geographos features: high elongation, a single convex side, tapered ends, and small protuberances swept back against the rotation direction.

## 2.4 Conclusions

The main conclusion is that not only collisions, but also tidal forces are very important factor influencing the shape and spin rate of asteroids. Specific inferences about Geographos are the following: 1) it may well be "rubble pile" and 2) separation of its fragments during an encounter with the Earth is quite possible. Also taking into account all expounded above the following two models have been used for estimations.

1) Biaxial ellipsoid  $4.7 \times 1.9 \times 1.9 \text{ km}$ .

2) Triaxial ellipsoid  $5.2 \times 2.0 \times 1.8 \text{ km}$ .

The homogeneous ellipsoids have a density at  $2.4 \text{ g cm}^{-3}$ . The pole coordinates and  $P_s$  taken according to [9].

## 3. ROTATION

If the proper rotational motion of an asteroid is little affected by outside torques, then on the small time interval it is close to the Euler-Poinsot motion. On the large time interval an asteroid rotational motion can be considered as slow evolution of Euler-Poinsot motion.

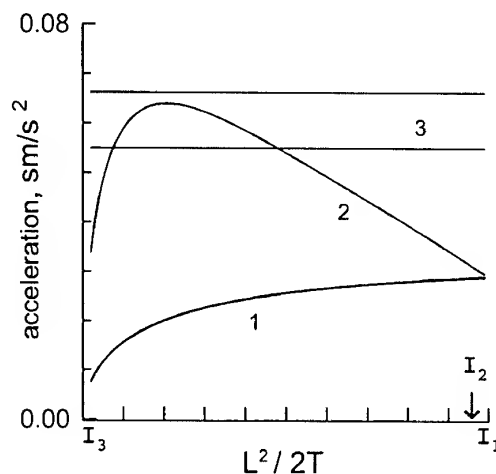


Fig. 1. Accelerations for a point on the end of the long axis of the triaxial ellipsoid. (1)  $W$ ; (2) centrifugal acceleration; (3) gravitational accelerations for the different bulk densities of the asteroid:  $2.0 \text{ g cm}^{-3}$  (the lower line) and  $2.4 \text{ g cm}^{-3}$  (the upper line).

Such is indeed the case of Geographos. The detailed analysis of its rotation is beyond the scope of the present paper. Here I only give a short presentation of some results.

Geographos has very a small ( $\approx 0.3^\circ$ ) nutation of the spin axis and an oscillatory roll about the long axis with amplitude about  $3^\circ$ . The solution was obtained leaning upon the period  $P_s$  and another period  $19.2^h$  [3] and on the pole dispersion. In terms of Euler's angles the former may be identified as period of precession  $P_\psi$  and the last as period of rotation  $P_\phi$ . It was found also that the effect of light pressure on the asteroid is negligibly small. A free particle on the asteroid surface experiences gravitational force and forces resulting from rotation. The possibility of escape depends on relation of these forces. The surface relief has also some importance, but in the first approximation we can ignore this factor. Burns [11] found for all asteroids with known dimensions and spin rates that the centrifugal force is always less than the rotational one. He suggested that in the past, when the asteroids were in other spin states, the opposite situation could take place. For any point of the asteroid we can write (in a body-framed coordinate system) the following equation for the vector  $W$  of the total rotational acceleration [12]

$$W = \dot{\omega} \times r + \omega \times (r \times \omega),$$

where  $\omega$  is the angular velocity vector,  $r$  is the vector of position for the point. The first term on the right side of the equation is acceleration caused by nonuniformity

of rotation, the second term is centrifugal acceleration. Fig.1 shows these accelerations averaged on rotational period and calculated for all the possible spin states (i.e. from rotation around long axis to rotation around short axis). The quantity  $L^2/2T$  ( $I_3 < L^2/2T < I_1$ ) characterizes a spin state with  $L$  and  $T$  being the total rotational angular momentum and total rotational kinetic energy,  $I_i$  are the principal moments of inertia. We notice that the centrifugal acceleration can exceed the gravitational one, but the total rotational acceleration never exceeds it. In the consequence the disposal of material from the surface of Geographos as a result of rotation (at invariable angular momentum) is impossible. So the two possibilities remain: escape of particles in the result of collision and in result of action of tidal forces at a close encounter with the Earth.

#### 4. REFERENCE ORBIT AND ACCURACY OF INTEGRATION

Geographos orbit OSOD-34 [2] was accepted as the reference orbit. It was obtained from fit to optical and radar observations over the interval from 1951 to 1994. For the numerical integration the Everhart procedure 19th order with variable step size has been used (program package by A.Baturin). Perturbations by all planets and the Moon were taken into account. Planetary coordinates were taken from the JPL planetary Development Ephemeris – DE406. In Tab.1 accuracy of numerical integration obtained by comparison of backward and forward integration is presented. Here  $a$ ,  $e$ ,  $i$ ,  $\Omega$ ,  $\omega$  and  $M$  are standard designations of Keplerian orbital elements ( $M$  is the mean anomaly). We see that within 1300 years (and even within 1500 years with some assumptions) accuracy can be considered as acceptable.

Tab.1. Accuracy of numerical integration

Time span	$da$ AU	$de$	$di^\circ$	$d\Omega^\circ$	$d\omega^\circ$	$dM^\circ$
-100	$1.4 \cdot 10^{-9}$	$6.0 \cdot 10^{-10}$	$2.9 \cdot 10^{-8}$	$2.1 \cdot 10^{-8}$	$6.6 \cdot 10^{-8}$	$2.1 \cdot 10^{-6}$
-300	$1.4 \cdot 10^{-7}$	$6.1 \cdot 10^{-8}$	$2.8 \cdot 10^{-6}$	$2.1 \cdot 10^{-6}$	$6.1 \cdot 10^{-6}$	$2.0 \cdot 10^{-4}$
-500	$2.5 \cdot 10^{-7}$	$1.1 \cdot 10^{-7}$	$5.0 \cdot 10^{-6}$	$3.8 \cdot 10^{-6}$	$1.1 \cdot 10^{-5}$	$3.6 \cdot 10^{-4}$
-700	$4.8 \cdot 10^{-6}$	$2.1 \cdot 10^{-6}$	$9.7 \cdot 10^{-5}$	$7.3 \cdot 10^{-5}$	$2.1 \cdot 10^{-4}$	$7.0 \cdot 10^{-3}$
-900	$7.2 \cdot 10^{-5}$	$3.4 \cdot 10^{-5}$	$1.6 \cdot 10^{-3}$	$1.2 \cdot 10^{-3}$	$2.6 \cdot 10^{-3}$	$1.2 \cdot 10^{-1}$
-1100	$1.5 \cdot 10^{-4}$	$6.1 \cdot 10^{-5}$	$2.6 \cdot 10^{-3}$	$1.9 \cdot 10^{-3}$	$8.3 \cdot 10^{-3}$	$1.9 \cdot 10^{-1}$
-1300	$2.9 \cdot 10^{-5}$	$1.2 \cdot 10^{-5}$	$5.7 \cdot 10^{-4}$	$4.2 \cdot 10^{-4}$	$1.4 \cdot 10^{-3}$	$4.1 \cdot 10^{-2}$
-1500	$2.5 \cdot 10^{-4}$	$1.8 \cdot 10^{-4}$	$1.6 \cdot 10^{-2}$	$1.8 \cdot 10^{-2}$	$3.8 \cdot 10^{-2}$	$6.8 \cdot 10^0$
-1500	$2.4 \cdot 10^{-3}$	$7.8 \cdot 10^{-4}$	$3.1 \cdot 10^{-3}$	$2.1 \cdot 10^{-2}$	$3.0 \cdot 10^{-1}$	$2.0 \cdot 10^{+1}$

Geographos has many encounters with the Earth: on the average 4-6 per a hundred years on the distance less than 0.1 AU. Because of this it is impossible to make a reliable conclusion based on the evolution of a single orbit. We consider evolution of an ensemble of so called clones, i.e. orbits defined by changing their orbital parameters within the observational errors. To

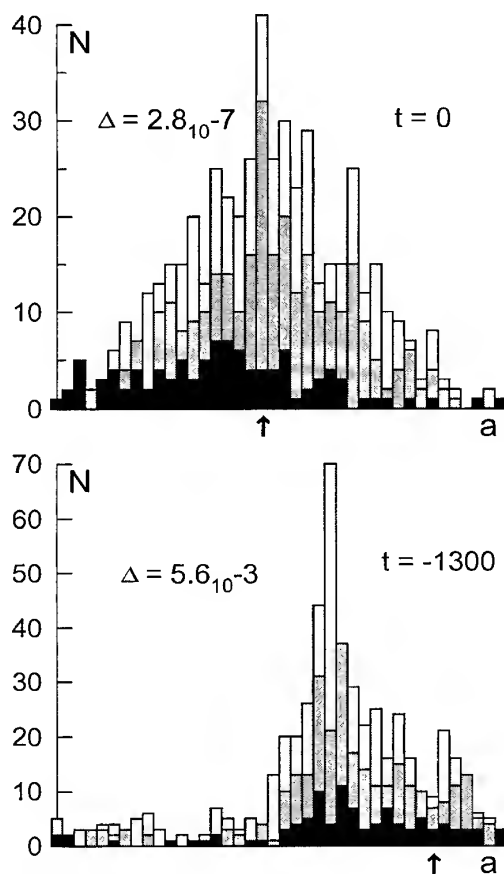


Fig. 2. Distribution in semimajor axes

generate these clones an algorithm for generation of normally distributed vectors described in [13] has been used. In this case observational errors in the orbital elements were used as dispersions.

Five hundred orbits were integrated backward and Fig.2 shows the initial ( $t=0$ ) and the final ( $t=-1300$  years) distributions in semimajor axes for 100, 300 and 500 clones. Here  $\Delta = a_{max} - a_{min}$  in AU. The arrow shows the position of the reference orbit. We can see a rise of the statistical stability of the final distribution. For ensemble of 100 orbits it is completely deficient, for 300 orbits it is still remains doubtful and the distribution for 500 orbits appears to be stable. The reference orbit goes from the center to a remote area. For other orbital elements the picture is similar. Because of this the second reference orbit was taken from the densest part of the bunch (see Tab.2).

However one should bear in mind that distributions of the observational errors not necessarily obey the normal law. Hence the new reference orbit is only one among the possible ones.

Tab.2. New reference orbit

Year	1994	694
$a, AU$	1.245527	1.244047
$E$	0.335548	0.335971
$i^\circ$	13.342143	13.399325
$\Omega^\circ$	337.370846	347.075736
$\omega^\circ$	276.721863	264.677874
$M^p$	49.744280	51.503325
Epoch, JD	2449600.5	1974775.5

## 5. PHYSICAL CHARACTERISTICS OF GEOGRAPHOS METEORIODS

To calculate orbital evolution of meteoroids we should know the range of change for the ratio of radiation repulsion to gravitational attraction [14]:

$$\beta = 7.7 \times 10^{-5} Q_{pr} \frac{A}{m},$$

where  $Q_{pr}$  is Mie scattering coefficient (here  $Q_{pr} = 1$ ),  $A$  and  $m$  are geometrical cross-section and mass of a meteoroid. The numerical coefficient was calculated with use of constants recommended by [15]. Thus to calculate  $\beta$  we should know mass, density and shape of meteoroids. About the shape we know nothing, the density is determined by material of the parent body and mass is determined by observational technique.

1620 Geographos is an S-type asteroid [16,17]. This suggests that olivin is dominated in material of the asteroid. There are also the significant (up to 20%) pyroxen component and small metallic component. But is it to be supposed that particles separated from the asteroid have densities of order  $3.6 \text{ g cm}^{-3}$ , characteristic for chondritic stone meteorites, and greater? Recent experimental studies of Durda and Flynn [18] answer this question in part. Impact disruption of porphyritic olivin basalt targets, consisting of millimeter-size olivine phenocrysts in a fine-grained matrix (simulating a stone meteorite) showed that fragments  $< 100 \mu\text{m}$  in size were low density matrix while the majority of the largest fragments ( $> 200 \mu\text{m}$  in size) were olivine. Meteoroids of Geographos probably have a collisional origin, so we can suggest that their densities vary from  $\approx 3.6 \text{ g cm}^{-3}$  for large particles till, say,  $1 \text{ g cm}^{-3}$  for small ones.

As to mass range, taking into account lower limits and the main values of magnitudes for observed magnitudes, difference in photometric standards, the uncertainty in mass scales for visual, photographic and radar observations [19-22], the upper limit for  $\beta$  was taken to be 0.0015. That corresponds to  $m = 2.4 \times 10^{-4} \text{ g}$  for a spherical uniform particle with density  $1.0 \text{ g cm}^{-3}$ .

## 6. METHOD OF MODELING

On the reference orbit a point of ejection  $r$  is chosen and a vector of ejection velocity  $c$  is generated according to one of the two schemes described below. The orbit of each ejected particle is calculated taking into account the effect of radiation pressure and the orbital motion is integrated by the same way as that of reference orbit (see above) from the moment of its separation forward till 2000 January 1<sup>st</sup>. In doing so the encounters with the Earth (after 1900) are kept under steady control. Further we shall use the following designations. *Orbit/encounter of type E*: A particle has approached the Earth on the distance less than 0.03 AU. *Orbit/encounter of type N*: Minimal distance between the orbit of the Earth and orbit of a particle is less than 0.03 AU. For the points of the minimal distance the vector of geocentric velocity  $V_G$  and coordinates  $\alpha, \delta$  of radiant are calculated.

The number of  $N$ -encounters turned out to be very copious and the following additional limitation was imposed: the distance between a particle and the Earth should be not greater than 0.04 AU. Certainly  $E$ -type is a subset of  $N$ -type. The last was introduced to take into account possible errors in position of particles. For all orbits of  $E$ - and  $N$ -types similar orbits were searched in databases (see part 7).

### 6.1 "Tidal" scheme of ejection

Release of particles takes place at relatively close encounters with the Earth in the result of combined action of tidal and centrifugal forces. Ejection is isotropic and velocities of dust particles are distributed uniformly from 1 to 2 m/s (escape velocity from the end of the long axis  $\approx 1.3 \text{ m/s}$ ). Ejections were modelled in 1901, 1876, 1794, 1726, 1511, 606 and 524, because in these years the asteroid had approaches with the Earth on the distance less than 0.5 AU. In 524 and 606 the encounters took place at the descending node and later at the ascending node.

### 6.2 "Collisional" scheme of ejection

Neither place nor time of collision are known. But it is reasonably safe to suggest that the probability of collision increases in the vicinity of ecliptics, therefore it is assumed that a collision occurs in one of the nodes. Moments of model collisions were chosen arbitrarily the same that in the above scheme.

Collisional disintegration of strength dominated asteroids differs from that of gravity dominated asteroids [23]. And although the mean ejection velocities in the first case are lower than in the second, velocities up to kilometres per second in

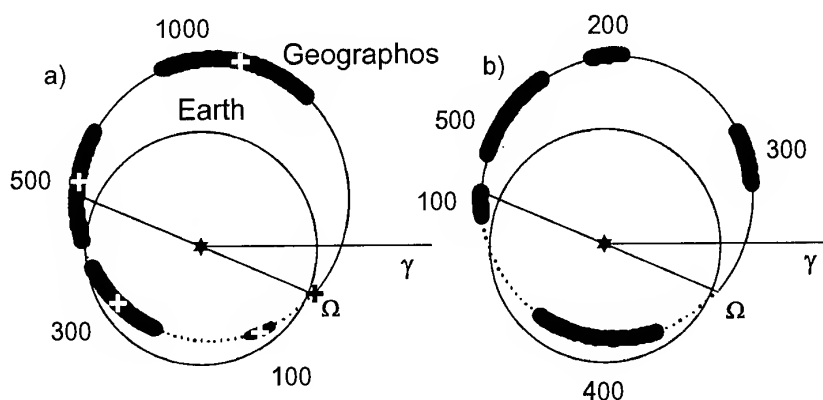


Fig. 3. Spread of particles around the reference orbit with time (in projection to ecliptic). 100 particles were ejected at the ascending node at a velocity of 1.3 m/s. Ages in years of each arc-swarm are indicated on the plot. Crosses indicate position of Geographos. a)  $\beta = 0$ , b)  $\beta = 0.0015$ .

it is important that particles with sizes  $\leq 1$  mm can gain both cases [23,24]. That is why in this scheme m/s to 1 km/s and ejection is isotropic (because the direction of impact is unknown).

Now about time of collision. It is known that an asteroid that does not undergo collisions eventually comes to the state of pure rotation about the principal axis of maximum inertia, because this is the minimum energy state for rotation with conservation of angular momentum [25]. Now Geographos is close to the state of relaxation because its precession and nutation are very small. Burns and Safronov [26] estimated characteristic time that it takes to align the rotation axis of the asteroid with the major principal axis as  $5 \times 10^6$  years. A recent work by Efoimsky and Lazarian [27] introduces a significant correction in this estimation. At the first approximation the above mentioned value should be decreased on 2-3 orders. Now it is not possible to present a more precise estimation, because study of inelastic relaxation for prolate bodies is not finished yet. But if the time of complete relaxation for Geographos is about several thousand years it is not incredible that during the last 1.5 thousand years the asteroid experienced an impact of a small body and after that has managed to reach the current spin state.

## 6.2 Loop formation

Before proceeding to integration of large amounts of particles on large time spans it is reasonable to do a reconnaissance using simpler models, namely in the framework of two-body problem. Let us consider spreading of released particles with time.

For  $c = 1.3$  m/s loop formation time is about 4000 years (independently of  $\beta$ ). But this value cannot serve as an estimation of the stream age. In order for the stream observable on Earth it is enough that a small arc of the stream met the Earth. From Fig.3 we see that location of a swarm strongly depends on  $\beta$ . In practice this may lead us to the necessity of modelling for many values of  $\beta$ . A different situation arises for high-velocity ejections. For  $c = 100$  m/s the loop formation time is about 55 years and for  $c = 1$  km/s it is only 7 years for ejection at nodes. So for any  $\beta$  particles will be extended around all the orbit.

At low-velocity ejections the stream's width is too small for registration of meteoroids on the Earth. The registrations begins from  $c \approx 500$  m/s. Perturbations, certainly, can introduce their own correction

## 7. METEOR ORBITS DATABASES AND CRITERIA OF SIMILARITY

One of the most rich from the available databases is held in the International Astronomical Union Meteor Data Center (IAU MDC) in Lund, Sweden [28]. All details and references related to this database could be found also in review [29]. I also used the catalogue MSSWG (Meteor Science Seminar Working Group). Orbits held in the catalogue were obtained from photographic (till May 1992) and TV observations in Japan [30,31]. Its last version can be found on the Internet: [http://www2.justnet.ne.jp/msswg/~index\\_e.htm](http://www2.justnet.ne.jp/msswg/~index_e.htm) or <ftp://ftp.imo.net/pub/data/msswg>. Unfortunately because of velocity-dependent selection effects only 2.5% orbits from total amount 70651 could be used for search (Geographos geocentric velocity  $\approx 12$  km/s and velocity of meteors in the atmosphere  $V_\infty \approx 16$  km/s).

There are many criteria of orbital similarity and approaches to stream identification, but for none of them any pronounced advantages over others were not revealed to date. Here well-known D-criterion of Southworth and Hawkins [32] is used. The main thing here is the threshold value  $D_t$ , which depends on the sample size  $N$ , on real scatter in the orbital elements for a given stream and on measurement errors. Southworth and Hawkins proposed the following formula  $D_t = 0.2(360/N)^{1/4}$ , which later has been modified by Lindblad [33]:  $D_t = 0.8(N)^{-1/4}$ . However these formulas were elaborated for application to precise photographic meteor orbits, and radar meteor orbits are much less precise. According to [7] scatter in the elements due to measurement uncertainties could give  $D > 0.1$ . So  $D_t = 0.2$  were taken for search.

Another problem is the probability of chance associations. Here this probability had not been estimated. Moreover, I am not sure that it is possible to do at all (at present time). To guarantee at some reliability level that a correlated meteoroid is not sporadic or belonging to another stream, we should know orbital distributions of sporadic and stream meteoroids *in the given sample*. This problem is yet awaiting its solution. Methods of evaluation of chance association probability are another topic for discussion.

## 8. DISCUSSION OF RESULTS

Ejections of 300 test particles were modelled according to above described schemes at two values of  $\beta$ : 0.0005 and 0.0015. OSOD-34 was used as the reference orbit. It turned out that the difference between streams of different  $\beta$  is modest: only phase distances  $D$  between model and real meteoroids are less in the mean for  $\beta = 0.0005$ . Then the whole modelling cycle was repeated for another reference orbit (Tab.2) only for  $\beta = 0.0005$  and beginning from 1511 (this orbit has encounters with the Earth at the same years, but in other moments). These model streams occupied an intermediate place between those ejected from OSOD-34.

### 8.1 General observations

Modelling according to "Tidal" scheme did not provide any E-type orbit, but about one third of model orbits had N-type encounters in the ascending node. Search in databases turned out to be unrewarded. Nevertheless this scheme of the stream formation cannot be rejected yet, because, firstly, model meteoroids approaches the Earth rather close ( $\leq 0.04$  AU) and, secondly, the results of search can be explained by strong observational selection (see below) in the northern hemisphere.

At modelling according to "Collisional" scheme about two-thirds orbits from every bunch had N-type encounters and from 1 to 25 orbits had E-type encounters. The minimal distance between a model meteoroid and the Earth was 0.0046 AU. As for meteoroids generated at the ascending node, their lesser part had encounters at the descending node (February 26 – March 7) and their greater part approaches the Earth at the ascending node (August 20-27). There were also meteoroids having encounters at different nodes in different years. Thus there exist twin meteor showers, which are the pre- and post-perihelion branches of the same stream. For brevity the showers of descending and ascending nodes will be referred to as "spring" and "summer" showers. Model meteoroids generated at the descending node had encounters in the ascending node.

The most part of meteoroids having E-type encounters was generated in 524 or 606. Equatorial coordinates of the model meteor radiants are in the ranges:  $\alpha = 178^\circ + 184^\circ$ ,  $\delta = 33^\circ + 41^\circ$  for one node and  $\alpha = 140^\circ + 152^\circ$ ,  $\delta = -17^\circ + -29^\circ$  for another. The distribution of ejection velocity vectors is also of interest for E-type orbits. It looks like originated at the impact of a catching up small body. For spring showers the values of ejection velocity are in the range 700–1000 m/s with mode about 900 m/s, for summer showers the range is 100–1000 m/s and mode is about 700 m/s.

### 8.2 Results of search

In Tab.3 all 44 found meteoroids are presented. Notice that most part of model meteoroids approached the Earth at the ascending node, but the overwhelming majority of correlated meteoroids from Tab.3 belongs to another node. Only four of them (NN33-36) (three of them are extremely dubious) belong to the summer shower. The lack of meteors from summer stream in catalogues could be explained by observational selection. Radiant having negative values of  $\delta$  rises low above horizon in the northern latitudes. And in Adelaide observations there is a lacuna in this time. Observations in Mogadisho practically are free from low-velocity meteors.

The orbital sample of Tab.3 was structured using a taxonomic algorithm [34]. Fig.4 shows the resulting covering tree. The length of each edge is proportional to the phase distance  $D$  between the connected orbits. Seven orbits with  $D < 0.12$  are marked. Five of them are gathered in two neighbouring ( $D(N43, N23) = 0.13$ ) clusters. Also there were found 8 model orbits (7 of spring shower) having encounters at the same years as associated real orbits. It is interesting that all the five orbits with  $D_{min} \leq 0.1$  are in their number.

Part of selected meteoroids, certainly, does not belong to Geographos' streams. Nevertheless with high probability Geographos is the parent body for a meteor stream generating twin meteor showers observable at the Earth – Spring and Summer Geographides.

## 9. REFERENCES

1. Magnusson P. et al. Photometric observations and modeling of asteroid 1620 Geographos, *Icarus*, Vol.123, 227-244, 1996.
2. Ostro S.J., et al. Radar observations of asteroid 1620 Geographos, *Icarus*, Vol.121, 46-66, 1996.
3. Prokof'eva V.V. et al. Investigations of oscillation in the brightness of asteroid 1620 Geographos during its approach to the Earth in 1994, *Astronomy Letters*, Vol.23, 758-766, 1997.
4. Karachkina L.G. et al. Modulation of brightness of asteroid 1620 Geographos, *Solar System Research*, Vol.32, 287-299, 1998.
5. Sekanina Z. Statistical model of meteor streams. IV. A study of radio streams from the synoptic year, *Icarus*, Vol.27, 265-321, 1976.
6. Ryabova G.O. On possible associations among unusual asteroids and meteor streams, *Astronomiya i Geodesiya*, Tomsk: Tomsk. Gos. Univ., N14, 59-66, 1989. (in Rus.)
7. Olsson-Steel D. Identification of meteoroid streams from Apollo asteroids in the Adelaide radar orbit surveys, *Icarus*, Vol.75, 64-96, 1988.
8. Hasegawa I. Possible associations of daytime fireballs and minor planets, *Earth, Moon and Planets*, Vol. 72, 311-316, 1996.
9. Hudson R.S. and Ostro S.J. Physical model of asteroid 1620 Geographos from radar and optical data, *Icarus*, 369-378, 1999.
10. Bottke (Jr) W.F. et al. 1620 Geographos and 433 Eros: shaped by planetary tides? *Astron. J.*, Vol.117, 1921-1928, 1999.
11. Burns J.A.. The angular momenta of solar system bodies: Implications for asteroid strength, *Icarus*, Vol.25, 545-554, 1975.
12. Landau L.D. and Lifshitz E.M. *Mechanics*, Pergamon Press, Oxford, England, 1976.
13. Pollyak Yu.G. *Probabilistic modeling on computers*, Sovetskoe Radio, Moscow, 1971. (in Rus.)
14. Burns T.A. et al. Radiation forces on small particles in the Solar System, *Icarus*, Vol. 40, 1-48, 1979.
15. IERS Standards 1992, *IERS Technical Note N13*, Central Bureau of IERS, Paris, 1992.
16. Clark B.E. et al. Results of the seven-color asteroid survey: infrared spectral observations of 50-km size S-, K- and M-type asteroids, *Icarus*, Vol.113, 387-402, 1995.
17. Hicks M. et al. Rotationally resolved spectra of 1620 Geographos, *Icarus*, Vol.113, 456-459, 1995.
18. Durda D.D. and Flynn G.J. Experimental study of the impact disruption of a porous, inhomogeneous target, *Icarus*, Vol.142, 46-55, 1999.
19. Astapovich I.S. *Meteor phenomena in the Earth atmosphere*, Fizmatgiz, Moscow, 1958. (in Rus.)
20. Bel'kovich et al. The Geminid shower from radar, photographic and visual observations, In: *Meteor matter in the interplanetary space*, Moscow-Kazan, 88-101, 1982. (in Rus.)
21. Katasev L.A. *Investigations of meteors in the Earth atmosphere by photographic method*, Gidrometeoizdat, Leningrad, 1966. (in Rus.)
22. Hughes D.W. Meteors, In: *Cosmic dust*. Wiley, Chichester, 123-185, 1978.
23. Love S.G. and Ahrens T.J. Catastrophic impacts on gravity dominated asteroids, *Icarus*, Vol.124, 141-155, 1996.
24. Martelli G. et al. Catastrophic disruption experiments: recent results, *Planet. Space Sci.*, Vol.42, 1013-1026, 1994.
25. Lamy P.L. and Burns J.A. Geometrical approach to torque free motion of a rigid body having internal energy dissipation, *Am. J. Phys.*, Vol.40, 441-445, 1972.
26. Burns J.A. and Safronov V.S. Asteroid nutation angles, *Mon. Notic. Roy. Astron. Soc.*, Vol. 165, 403-411, 1973.
27. Efroimsky M. and Lazarian A. Inelastic dissipation in wobbling asteroids and comets, *Mon. Notic. Roy. Astron. Soc.*, Vol. 311, 269-278, 2000.

28. Lindblad B.A. The IAU meteor data center in Lund, *Publ. Astron. Inst. Czechosl. Acad. Sci.*, N67, 201-204, 1987.

29. Steel D. Meteoroid orbits, *Space Science Reviews*, Vol.78, 507-553, 1996.

30. Shigeno Y. and Shioi H., Double-station TV meteor observations, *WGN*, Vol.24, 37-42, 1996.

31. Shigeno Y. et al., Double-station TV meteor observations. II, *WGN*, Vol.24, 37-42, 1996.

32. Southworth R.B., Hawkins G.S. Statistics of meteor streams, *Smithson. Contrib. Astrophys*, Vol.7, 327-335, 1963

33. Lindblad B.A. A computerised stream search among 2401 photographic meteor orbits, *Smithson. Contrib. Astrophys*, Vol.12, 14-24, 1971.

34. *Algorithms and programs for restoration of dependences*, Eds. Vapnik E.N., Nauka, Moscow, 1984. (in Rus.)

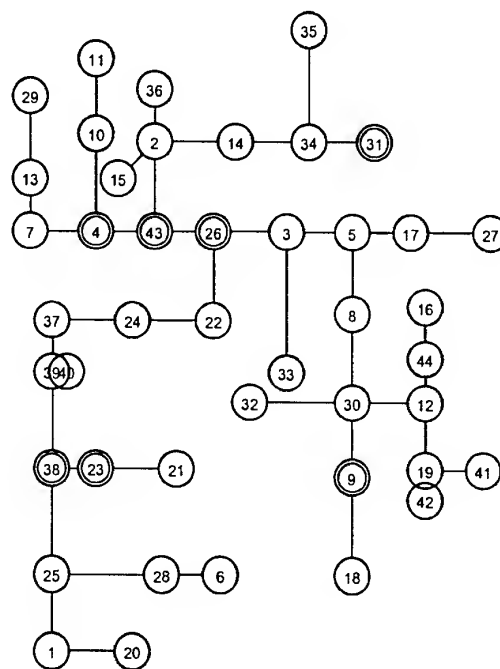


Fig.4. The covering tree

Table 2. Observed meteoroids probably associated with asteroid Geographos

N	N <sub>orig</sub>	Dmin	Year	Ref	N	N <sub>orig</sub>	Dmin	Year	Ref	N	N <sub>orig</sub>	Dmin	Year	Ref
1	1044	0.186	1957	1	16	1443	0.143	1962	4	31	3300	0.118	1969	5
2	1015	0.149	1953	2	17	1731	0.164	1962	4	32	3309	0.198	1969	5
3	1077	0.152	1953	2	18	1951	0.150	1962	4	33	11925	0.172	1969	5
4	1078	0.120	1953	2	19	14583	0.184	1965	4	34	11957	0.198	1969	5
5	1096	0.132	1953	2	20	1969	0.181	1969	5	35	12072	0.186	1969	5
6	1097	0.186	1953	2	21	2010	0.169	1969	5	36	12959	0.169	1969	5
7	1099	0.185	1953	2	22	2546	0.159	1969	5	37	5540	0.182	1968	6
8	1107	0.163	1953	2	23	2873	0.099	1969	5	38	5724	0.104	1968	6
9	1123	0.101	1953	2	24	2904	0.169	1969	5	39	5758	0.176	1968	6
10	1184	0.172	1953	2	25	2934	0.140	1969	5	40	5763	0.186	1968	6
11	1229	0.197	1953	2	26	2951	0.087	1969	5	41	5922	0.189	1968	6
12	2155	0.167	1954	2	27	2968	0.148	1969	5	42	1037	0.196	1975	7
13	2161	0.187	1954	2	28	3127	0.143	1969	5	43	434	0.078	1996	8
14	2162	0.198	1954	2	28	3151	0.188	1969	5	44	1282	0.189	1999	8
15	427	0.159	1969	3	30	3186	0.170	1969	5					

Comments: N<sub>orig</sub> is serial number of the meteor in the original publication; Dmin is minimal phase distance between this meteoroid and all model orbits; Year is year of observation; Ref.: 1 – Harvard precise photographic, 2 – Harvard graphical reduction, 3 – Adelaide, radar 1968-69, 4 – Harvard, radar 1961-65, 5 – Harvard, radar 1968-69, 6 – Obninsk, radar, 7 – Kharkov, radar, 8 – MSSWG. Meteoroids for which association with a single model meteoroid is detected are italicized (seven in all).

## IAU METEOR DATA CENTER

B.A. Lindblad

*Lund Observatory, Box 43, S-221 00 Lund, Sweden*

*e-mail: linasu@gemini ldc.lu.se*

### ABSTRACT

The purpose of the IAU Meteor Data Center is to archive, document and disseminate information on meteoroid orbits. At present 4581 precisely reduced photographic recordings, 1425 video recordings and 63330 radar determined orbits are archived at the center.

### 1. INTRODUCTION

Information on meteoroid orbits is widely scattered in the scientific literature and is often available only in publications with limited circulation. Information about individual radio meteor orbits has mainly been available as internal observatory computer lists or tapes. In the absence of key scientific personal much of this information was in the 1970's difficult to locate or even lost. At the 1976 IAU General Assembly the present author proposed to Comm. 22 that a meteor data center be established at the Lund Observatory for the collection of meteor orbits recorded by radio and photographic techniques. The decision was confirmed by the 1982 IAU General Assembly and a small amount of funding was allocated for the support of the data center.

The purpose of the IAU MDC in Lund was to acquire, format, check and disseminate information on meteoroid heliocentric orbits obtained by two-station photographic and by multi-station radar techniques. If available information related to the trajectory in the Earth's atmosphere was also archived. For previous reports on the activity of the MDC see Lindblad (1987, 1995 and 1999). See also Lindblad and Steel (1993) and Steel (1996). To date 4581 precisely reduced two-station photographic recordings and 63.330 radar determined orbits have been stored at the data center. The collection of photographic and radar data are presently distributed on seven 1.44 Mb diskettes. Recently 1425 video-recordings have been added to the data base (Lindblad 1999).

### 2. PHOTOGRAPHIC OBSERVATIONS

In the past the main effort has been to locate and collect photographic meteor orbits from as many different sources as possible. In the 1990 version of the IAU MDC photographic data a total of 3518 meteors with precisely reduced orbits were available, but only 2955 of these orbits also included complete geophysical data. In numerous cases the orbital and geophysical data were not published at the same time - the geophysical data sets as a rule being published several years later and sometimes also in a different order than in the orbital data set.

The present orbital data sample originates from 17 different stations or investigators (Table 1). This data sample is believed to contain some 95 % of all precisely reduced photographic orbits, which have been observed to date.

**Table 1.** IAU MDC catalogue of photographic orbits (version 2001). C - investigator code letter, N - the number of precisely reduced orbits per station or investigator.

C	N	Investigator/station
W	166	Whipple (small camera)
J	413	Jacchia (Super-Schmidt)
H	313	Hawkins and Southworth (Super-Schmidt)
P	353	Posen and McCrosky (Super-Schmidt)
S	314	McCrosky and Shao (Super-Schmidt)
G	25	Gale Harvey, New Mexico State Univ.
K	206	Kiev (small camera)
O	459	Shestaka et al., Odessa (small camera)
D	636	Babadzhanov et al., Dushanbe (small camera)
C	103	Ceplecha (small camera)
E	237	Ceplecha and Spurný, European Network
F	334	McCrosky, Prairie Network
I	259	Halliday, MORP Network
N	259	Koseki, Nippon Meteor Soc.
T	79	Ohtsuka, Tokyo Meteor Network
U	66	Ochai et al., Nippon Meteor soc.
B	359	Betlem, Dutch Meteor Soc.
	4581	Total number of objects

The photographic orbits have been obtained in the period 1935-99 in systematic observing programs in

USA, Canada, Holland, the former member states of the USSR and in Japan. One should note that some of the early meteor orbits were computed using electric or hand calculators. Hence this data is more affected by computing and reading errors of various kinds than recent data. In particular trigonometrical errors, such as choosing the wrong quadrant in the computation of the angular orbital elements are not uncommon in the early data. Several errors of this type have been detected at the data center or by various correspondents (Porubčan et al. 1995). An independent study of the errors in the photographic orbital data was made by Koseki (1986). However, no systematic checking involving a recomputation of *all* the precisely reduced photographic orbits has been made until recently (Lindblad et al. 2001). In these studies all orbits have been recomputed from published values of the corrected radiant and velocity at infinity.

### 3. VIDEO OBSERVATIONS

Precise meteoroid orbits have in the past mainly been obtained by two-station photographic techniques. The recent availability of inexpensive, low-light level video recording systems implies that precise orbits now can be recorded at low cost and in large numbers using video techniques. The theoretical observation limit of stars for a fast video camera system is  $11^m$  to  $12^m$ . However, owing to sky glow and diffuse star background the actual detection limit for meteors is about  $8^m$  (absolute magnitude). The majority of recent video data are in the magnitude range  $3^m$  to  $7^m$ . Recognising that the previous limit for meteor observations using Super Schmidt cameras was about  $+2.5^m$ , it is obvious that the video techniques will extend the range of luminous meteor observations by about 5 magnitudes. High-power radars cover the magnitude range  $5^m$  -  $12^m$ . It follows that the video data in a few years time will very nicely fill in the mass gap between photographic and radar data.

At present more than 2,500 video-determined meteoroid orbits from six different groups have been acquired at the meteor data center. The reformatting and checking of this large data sample started in 1997. For an analysis of 1425 video orbits observed in 1971-1996 see Lindblad (1998). Unfortunately the seasonal coverage of the video data in these surveys is very limited, with nearly all data being observed in the period July to December. It is essential for future research that the video observations be extended to include the spring and summer periods as well.

### 4. RADIO OBSERVATIONS

During the last two decades very few new radar orbits have been acquired at the data center. The interest in the radar data has also diminished somewhat. Bearing in mind that the radar-derived orbits stored at the meteor data center are very many (presently 63,330) but of lower accuracy than their photographic counterparts, the radar orbits have in recent years mainly been used in various statistical studies (see for example Steel 1996).

### 5. ACKNOWLEDGEMENTS

The author is grateful for financial support from the IAU for the operation of the meteor data center. Numerous travel grants to Bratislava from Kgl. Vetenskapsakademien, Stockholm are also gratefully acknowledged. The author further acknowledges valuable scientific support from numerous colleagues, in particular from Dr. D. Steel and Dr. V. Porubčan, who both have in many ways participated in the planning and checking of the data base. It is with confidence that I now can transfer the future responsibility for the operations of the IAU MDC to the Bratislava group.

### 6. REFERENCES

- Koski, M., *J. Brit. Astron. Assoc.*, Vol. 96, 232, 1986.
- Lindblad, B.A., The IAU Meteor Data Center in Lund, in *Interplanetary Matter, Proc. 10<sup>th</sup> European Reg. Meeting of the IAU*, Prague, 201, 1987.
- Lindblad, B.A., The IAU Meteor Data Center in Lund, *Earth, Moon and Planets*, Vol. 68, 405, 1995.
- Lindblad, B.A., in W.J. Baggaley and V. Porubčan, *Meteoroid*, Bratislava, 274, 1999.
- Lindblad, B.A. and Steel, D.I., in Milani et al. (eds.), *Asteroids, Comets, Meteors*, 497, 1993.
- Lindblad, B.A., Neslušan, L., Porubčan, V. and Svoreň, J., 2001, in prep.
- Porubčan, V., Svoreň, J. and Neslušan, L., On Separation of Major Meteoroid Streams from the Sporadic Background, *Earth, Moon and Planets*, Vol. 68, 471, 1995.
- Steel, D., *Space Sci. Rev.*, Vol 78, 507, 1996.

## THE UPDATED VERSION OF THE IAU MDC DATABASE OF PHOTOGRAPHIC METEOR ORBITS

B.A. Lindblad<sup>(1)</sup>, L. Neslušan<sup>(2)</sup>, J. Svoreň<sup>(3)</sup>, V. Porubčan<sup>(4)</sup>

<sup>(1)</sup> *Lund Observatory, S-211 00 Lund, Sweden*

*Email: [linasu@gemini ldc.lu.se](mailto:linasu@gemini ldc.lu.se)*

<sup>(2)</sup> *Queen Mary & Westfield College, Mile End Rd., London E1 4NS, United Kingdom. On leave from: Astronomical Institute of the Slovak Academy of Sciences, SK-059 60 Tatranská Lomnica, The Slovak Republic,*

*Email: [ne@ta3.sk](mailto:ne@ta3.sk)*

<sup>(3)</sup> *Astronomical Institute of the Slovak Academy of Sciences, SK-059 60 Tatranská Lomnica, The Slovak Republic,*

*Email: [astrsven@ta3.sk](mailto:astrsven@ta3.sk)*

<sup>(4)</sup> *Astronomical Institute of the Slovak Academy of Sciences, Dúbravská 9, SK-842 28 Bratislava, The Slovak Republic,*

*Email: [astropor@savba.sk](mailto:astropor@savba.sk)*

### ABSTRACT

The database of photographic meteor orbits of the IAU Meteor Data Center in Lund has gradually been updated. The version 2001, which has been prepared for distribution and which will be released soon, contains complete orbital and geophysical data on 4581 meteors (equinox J2000.0).

A new meteor identification code consisting of the publication serial number, the author or station code and number of the catalogue is introduced. The verification of mutually dependent parameters has been performed.

All the files with the pertinent documentation will be placed on a www-site to enable their free, public downloading.

### 1. INTRODUCTION

The database of precisely reduced photographic meteor orbits available at the IAU Meteor Data Center in Lund [4, 5, 7, 12] has become frequently used by meteor researchers in particular for various studies of meteor streams. Recently, the database has been updated and here we present a brief outline of the new version.

An additional 48 meteor orbits published by Spurný [10, 11], 154 meteor orbits published by Babadzhanov et al. [2] and 259 final MORP orbits published by Halliday et al. [3] have been added to the new version of the database. At present the number of complete records is 4581.

### 2. CHECKS OF INTERNAL CONSISTENCY

At the IAU MDC in Lund one of the authors has developed several check programs to test the internal consistency of the data [6]. A typical check procedure is to see if the published date and time agree with the appropriate solar longitude of the node of the orbit. Another check is to investigate if the published semi-major axis is consistent with the published heliocentric velocity of the meteor. In particular the first mentioned test revealed numerous inconsistencies in the older data. Several cases where there was a discrepancy of 1 day (sometimes 30 days) between the date and the appropriate nodal value were found. In order to resolve discrepancies repeated correspondence with the original investigators has often been necessary. The authors acknowledge lists of corrections from several authors. Babadzhanov [1] sent to the MDC a list of 109 corrected orbits from Dushanbe, etc.

In the present study we have applied also an alternative checking procedure to detect and resolve inconsistencies in the published data, namely the recalculation of all meteor orbits based on the position of the corrected radiant and the geocentric velocity at the time of meteor detection and vice versa.

Basically, two recalculations were made:

(1) Starting from the published radiant coordinates and geocentric velocity of the meteor at the time of detection, we recalculated its orbital elements  $q$ ,  $e$ ,  $\omega$ ,  $\Omega$ ,  $i$  as well as various derived quantities: elongation of radiant  $\lambda$ , (i.e. its angular distance from the apex of the Earth's motion), semi-major axis  $a$ , aphelion distance

$Q$ , longitude of perihelion  $\pi$ , heliocentric velocity  $V_h$ , and encounter velocity  $V_{inf}$ .

(2) Assuming the five published orbital elements as the input, we calculated the radiant coordinates  $\alpha$ ,  $\delta$  and geocentric velocity  $V_g$  of the meteor. An optimal method of theoretical radiant prediction [8] was utilized in this computation.

The recalculation of all the orbits and the geophysical (trajectory) parameters shows that 4.3% of the original data set of meteors are mutually inconsistent, i.e. there are typing, printing and/or computation errors not only in date and orbital elements, but also in radiant and velocities. A large fraction of these errors were easily identified and could be corrected. We found 186 such cases. 173 meteors had to be corrected in one parameter (one of  $q$ ,  $e$ ,  $\omega$ ,  $\Omega$ ,  $i$ ,  $\alpha$ ,  $\delta$ ,  $V_g$ , or date). These meteors are designated by a code "c" in columns 75 and 22 in the orbital and geophysical files, respectively.

13 meteors of the complete sample of 4581 meteors had obvious errors in two different parameters, which we could reliably correct. We distinguish these cases from one-error corrected meteors by supplying a symbol "m", instead of "c", to the appropriate comment.

Inconsistencies between geophysical and orbital data, in two or more parameters, were found in only about 0.2% of the whole data set of meteors. A probable cause of at least one error was difficult to identify in this group. For these meteors, we assumed that the geophysical data were correct and we corrected the erroneous orbital parameters. However one cannot be sure that such a procedure provides a reliable correction. Therefore we recommend to omit these meteors from the database. The orbits proposed to be rejected are marked with a code "r".

Taking into account the distribution of the heliocentric velocity based on all meteors of the database, a lower limit for extremely hyperbolic meteors could be set. A value of the heliocentric velocity exceeding  $48 \text{ km s}^{-1}$  [9] or semi-major axis at about  $-0.6 \text{ AU}^{-1}$  may be regarded as the reasonable borders and meteors fulfilling these limits are marked with code "h" in the geophysical file. All extremely hyperbolic meteors are recommended to be omitted in the statistical studies of meteor streams.

In a few cases (15 meteors) complete consistency between the orbital and geophysical parameters was achieved by correcting the date and time of meteor appearance and comparing these parameters with the

published node of the orbit. These meteors are marked with code "x" in both geophysical and orbital files.

### 3. STRUCTURE OF THE NEW DATA SETS

The updated database is similar to the former one i.e. divided into two sets containing separately the orbital and geophysical data of photographic meteors. The parameters of a meteor are listed in one record of 80 characters (in ASCII format).

The first file contains the **geophysical data**:

original meteor number; date of detection; CW; geocentric, heliocentric, and encounter (extra-atmospheric) velocities; absolute photographic magnitude;  $\cos z_R$ ; heights of the beginning, maximum brightness and end its trail; quality; geocentric position of radiant; identification code; stream number; mass (in logarithmic form).

The second file contains the **orbital data**:

original meteor number; date of detection; aphelion distance; K; stream number; perihelion distance; semi-major axis; eccentricity; inclination; argument of perihelion; longitude of ascending node; quality; longitude of perihelion; elongation of radiant; identification code; association and shower number.

The photographic database will be available also as a one file containing both orbital and geophysical parameters merged into one record. The file was prepared in such a way that in order to homogenize both the geophysical and the orbital parameters of meteors, the orbital data were calculated from the published geophysical data by a standard procedure (see section 2). In the cases where some geophysical parameter had to be corrected, the corrected value was used as the input value for the recalculation.

Since identification problems in locating the corresponding geophysical and orbital records have occurred in the past the method adopted now is to introduce a new meteor identification code consisting of the publication serial number plus the author or station code and the number of the catalogue by the given author (this number did not exist in the former version). The new identification code now enables an unambiguous identification of each meteor.

All the files of the photographic database, i.e. the three above mentioned main files and files with meteors of which parameters were corrected or commented (c, m, r, h, x) as well as the complete documentation will be available electronically on the IAU Meteor Data Center. A full description of the updated photographic meteor database (version 2001) together with a

description of its use and analysis will be submitted for publication to *Astronomy and Astrophysics*.

**Acknowledgements.** The authors are indebted to several of the original investigators for recomputing numerous orbits at the request of the IAU MDC. In particular P.B. Babadzhanov, S. Shestaka, and V.G. Kruchinenko have been very helpful. Lists of corrections have also been supplied by M. Koseki, K. Ohtsuka, and T. Jopek. One of us (B.A.L.) is indebted to the IAU for a grant in support of the activities of the Meteor Data Center and to the Royal Swed. and Slovak Acad. Sci. for several exchange visits. This research was also supported by VEGA - the Slovak Grant Agency for Science (grants No. 1023 and 1026) and by Craafordska Stiftelson, Lund, Sweden.

#### 4. REFERENCES

1. Babadzhanov P.B., *private communication*, 1998.
2. Babadzhanov P.B., et al. Elementy orbit 154 jarkich meteorov po fotograficheskim nabljudenijam 1975-1983 gg., *BULL. INST. ASTROPHYS. ACAD. SCI. TADJIK*, Vol. 82, 16-41, 1998, (in Russian)
3. Halliday I., et al. Detailed data for 259 fireballs from the Canadian camera network and inferences concerning the influx of large meteoroids, *METEORITICS PLANET. SCI.*, Vol. 31, 185-217, 1996,
4. Lindblad B.A. The IAU Meteor Data Center in Lund, *INTERPLANETARY MATTER*, PROC. 10<sup>TH</sup> ERAM, Astron. Inst. Czechosl. Acad. Sci., Prague, 201-204, 1987.
5. Lindblad B.A. The IAU Meteor Data Center in Lund, *ORIGIN AND EVOLUTION OF INTERPLANETARY DUST*, Kluwer, Dordrecht, 311-314, 1991.
6. Lindblad B.A. The IAU Meteor Data Center in Lund, *EARTH, MOON, PLANETS*, Vol. 68, 405-408, 1995.
7. Lindblad B.A. and Steel D.I. Meteoroid Orbits Available from the IAU Meteor Data Center, *ASTEROIDS, COMETS, METEORS 1993*, Kluwer, Dordrecht, 497-501, 1994.
8. Neslušan L., et al. A computer program for calculation of a theoretical meteor-stream radiant, *ASTRON. ASTROPHYS.*, Vol. 331, 411-413, 1998.
9. Porubčan V., et al. On Separation of Major Meteoroid Streams from the Sporadic Background, *EARTH, MOON, PLANETS*, Vol. 68, 471-478, 1995.
10. Spurný P., Recent fireballs photographed in central Europe, *PLANET. SPACE SCI.*, Vol. 42, 157-162, 1994.
11. Spurný P., Exceptional fireballs photographed in central Europe during the period 1993-1996, *PLANET. SPACE SCI.*, Vol. 45, 541-555, 1997.
12. Steel D., Meteoroid Orbits, *SPACE SCI. REV.*, Vol. 78, 507-553, 1996.

# MATHEMATICAL MODEL OF THE GEMINID METEOR STREAM FORMATION

G.O. Ryabova

*Research Institute of Applied Mathematics and Mechanics, Tomsk, 634050, Russia,  
Email: astrodep@niipmm.tsu.ru*

## ABSTRACT

The Geminid meteoroid stream formation and evolution was studied by the method of nested polynomials. Besides other results the present work puts forward a new theory to explain the secondary maximum of the Geminid rate profile: branches of the stream have been formed due to differences in orbital parameters of particles ejected from the cometary nucleus before and after perihelion. A comparison of the model and observed rate profiles allowed to propose a hypothetical scenario of the comet disintegration: greater intensity of dust production before perihelion, significant change of the cometary orbit due to reactive forces and ejection of dust in the wide cone toward the Sun.

## 1. INTRODUCTION

A number of the Geminids peculiarities has motivated the extensive study of the stream. Its structure is known better than that of any other stream. That is why it has been chosen for an attempt of construction of a mathematical model about fifteen years ago. The model conforms with the experimental results and explains some of the shower's features [1]. When studying the formation and the evolution of the Geminid stream there was established the following interesting fact: the bimodal activity profile of the model stream occurs only if a cometary-type model of the stream formation is used; i.e., meteoroids ejected from a nucleus during its motion along a long arc of the parent body orbit, including the perihelion. The rate profile of the stream shows single well-defined maximum, if an eruptive-type model is used; i.e., the ejection is assumed to occur at one point of the cometary orbit and ejection velocities are distributed according to the normal law. A collision-type of the stream formation [2] does not agree with observations at all. Observations of the Geminid meteor stream revealed that its activity profile is bimodal (see [3] for the details). So the stream was most probably formed by the comet Phaethon. Going to the heart of the matter the author realized the necessity of considering different factors that may influence the shape of the activity profile. In the result a rough scheme of the Geminid's formation has been elaborated.

## 2. METHOD

The asteroid (3200) Phaethon — the Geminid's parent body — has no close encounters with the major planets during the last 10 thousand years at least. Changes in its orbital elements are smooth and the semi-major axis is practically constant. So the equations of motion can be integrated by Gauss-Halphen-Goryachev method with taking into account only secular perturbations of the first order, radiation pressure and the Poynting-Robertson effect. This method is very fast and integration of one orbit on the time span of 2 thousand years takes seconds at the Pentium II/350. But to obtain a statistically reliable profile of activity (see below) we need about 10 mln orbits. Because of this the far more fast following method has been used to calculate orbital evolution of particles.

Changes in the orbital elements are approximated by a set of nested polynomials of the form

$$b = \sum_{j=1}^n \sum_{k=0}^3 b_{jk} a_0^k t^j,$$

where  $b$  is one of the Keplerian elements  $a, e, i, \pi, \Omega$ ;  $t$  is the time in hundreds or thousands years, reckoned from the initial moment  $t_0$ ;  $n$  is determined individually for each element. To obtain the coefficients the changes in the orbital elements for a sample of particles are approximated by polynomials using the least square method. Coefficients of the polynomials for the Geminids age of 2000 years see in [1], coefficients for the age of 10 thousand years see in [4]. The validity of the approximations has been monitored using several independent samples of orbits. For the time span of 2 thousand years maximal absolute deviations for 95% of the orbits comprise:  $\Delta a = 0.0001$  AU,  $\Delta e = 0.001$ ,  $\Delta i = 0.6^\circ$ ,  $\Delta \pi = 0.1^\circ$ ,  $\Delta \Omega = 2.4^\circ$ . For 5% of the orbits the approximation errors were significant. From a statistical viewpoint such a percentage of deviations is admissible. For the time span of 10 thousand years maximal absolute errors are growing twice.

We shall consider a model of Geminid formation based on the age of 2000 years, because the stream age

are most probably near to this value [4]. The details of the simulation technique have been described earlier [1]. Briefly, the stream is simulated in the following way. A point where particle(s) is/are ejected is chosen at the orbit of the parent body. Based on certain assumptions on the ejection scheme (for example, a collisional model, a cometary or an eruptive model), the velocity vectors of ejected particles are obtained using a generator of pseudorandom numbers, and the particles' orbital elements are calculated. Then evolution of these elements in the given time interval is calculated with the aid of the above-mentioned polynomials.

To obtain a qualitative picture of density distribution over a model stream cross-section 5000 orbits is enough as a rule. But to calculate the stream rate profile only those orbits, which intersect the ecliptic in the vicinity of the Earth's orbit, should be selected. Because of this we have to model 3 - 10 mln of particles.

### 3. MODEL

Here we consider only the cometary model of the stream formation. The orbit of asteroid (3200) Phaethon has been used as the reference orbit. The ejection points at the reference orbit were uniformly distributed along the true anomaly. The ejection velocities have been determined by using Whipple's formula [5] and their directions were distributed uniformly in the hemisphere faced the Sun. The ratios of the particles cross-section to its mass,  $A/m$ , were taken to be 9.375 and 20.198. For spherical uniform particles with a density of  $1 \text{ g/cm}^3$ , these values correspond to the masses  $m_1 = 2.14 \times 10^{-3} \text{ g}$  and  $m_2 = 2.14 \times 10^{-4} \text{ g}$ .

The dispersion in space of the model stream is extremely unisotropical, as was first noted in [6] and [7]. The stream expands significantly, but mainly not because of change in width (see Fig. 1). So the Geminids is probably observed on Mars and twice during one period, but only as unfrequent meteors. On Venus the Geminids probably are more abundant than on the Earth. Calculations have shown that the Geminids met the Earth at least in the IV-V centuries of the modern era.

The width of the model stream is at least twice smaller than the width of the observed stream. This fact was discussed earlier [1,3,4]; the most probable explanation is the change of the parent comet orbit under the action of reactive forces. It is most likely that this process proceeded rapidly, probably in half of the comet's revolution, when the comet moved from the aphelion to the perihelion [8].

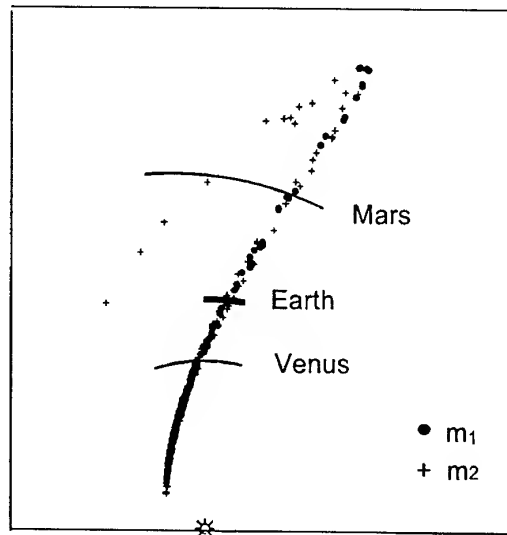


Fig. 1. The model Geminid section in the ecliptic plane at the descending node

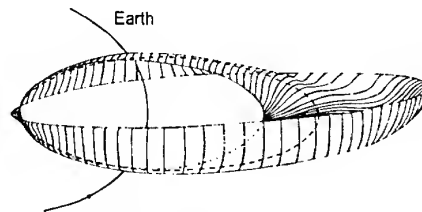


Fig. 2. Geminid meteoroid stream 2000 years after formation. Heavy dashed line indicates the reference orbit coinciding with densest part of the stream

And 3D-shape of the stream after 2000 years of evolution is also of interest. It is shown in Fig.2. Some exoticness of the outer form, which resembles a sea-shell, owes its existence to only 10-15% of the stream particles (see rarefied part of the section remote from the Earth's orbit in Fig.1). Can the entire set of particles be considered as a single stream? From the viewpoint of the common origin, the answer is yes. From the viewpoint of spatial localisation, the matter is more complicated. For 9% of the model stream particles the phase distance from the reference orbit  $D$  [9] is greater than 0.2. And maybe we should consider these particles as escaped from the stream.

### 4. BIMODALITY OF THE RATE CURVE

The distributions of the density of orbits over the cross-section of the stream at the initial and final stages of its evolution are shown in Fig.3. A certain cross-like

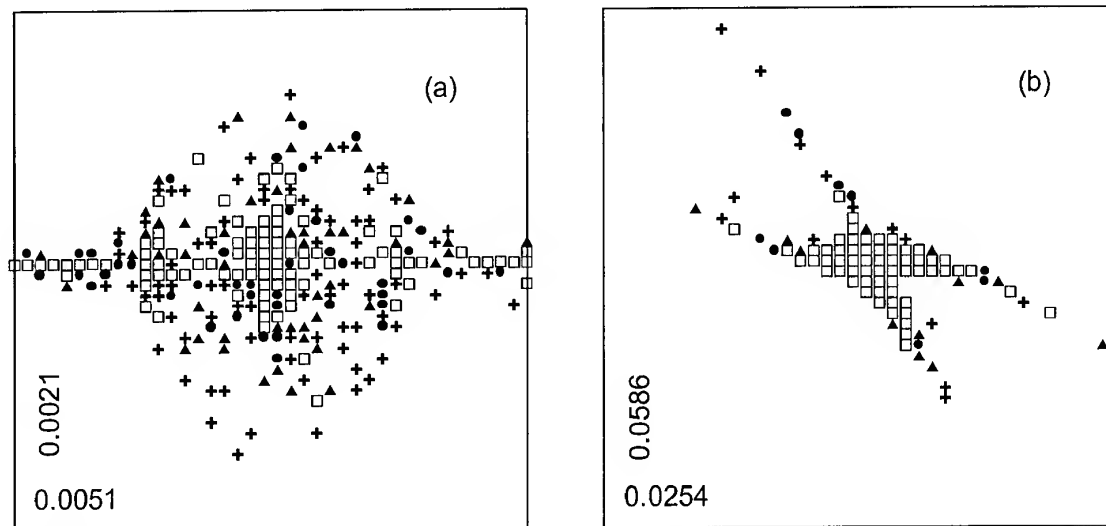


Fig. 3. Cross-sections of the model Geminid stream at the descend node. Three equidensites and the densest part (squares) are shown. The numbers along the axes are the length (in AU) of the sides of the corresponding rectangle enclosing the cross-section. (a) Just after formation. (b) The stream age is 2000 years.

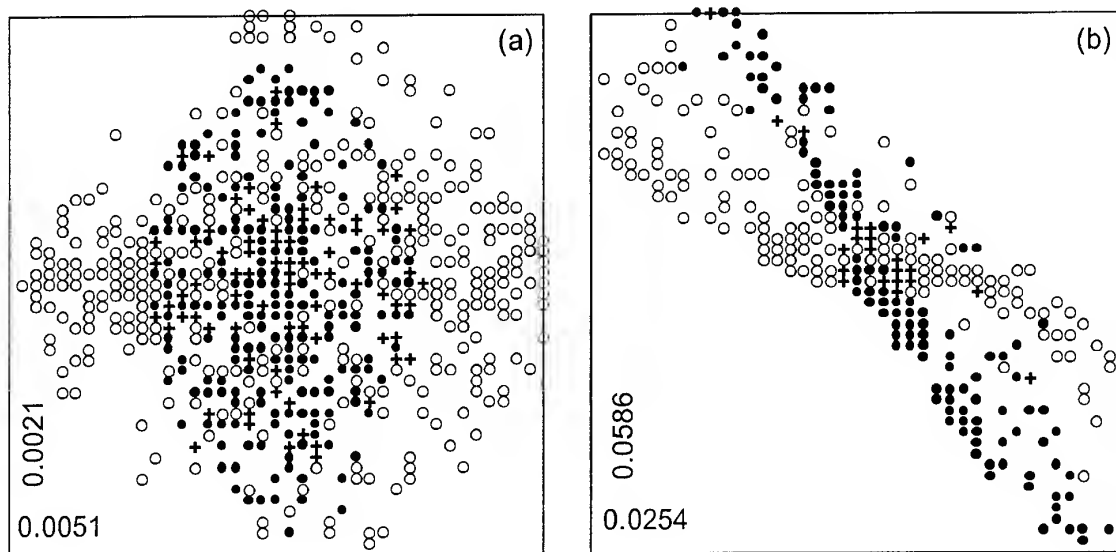


Fig. 4. Same as in Fig. 3. Different symbols show the cells (rectangular elements) of the cross-section through which the orbits of particles pass: particles ejected ( $\bullet$ ) before the perihelion passage, ( $\circ$ ) after the perihelion passage, and ( $+$ ) both before and after the perihelion passage.

structure is distinguishable in the cross-section even at  $T=0$  (age of the model stream). At  $T=2000$  years this "cross" is clearly seen. Now it is rather not "cross", but "scissors". Thus the stream separates into two branches. The reason of the separation is that the orbital characteristics of the particles ejected from the parent comet when it approaches perihelion differs

from those of the particles ejected when the comet moves away from perihelion. This difference enhances in time, resulting in the formation of different branches of the stream, which is illustrated in Fig. 4. The Earth in its motion crosses these branches sequentially, which gives rise to bimodal rate profile. Note that the cross is weakly pronounced in the case of isotropic

dust ejection, whereas it is clearly defined in the case of sunward ejection.

The distance between the first and second maxima depends of the mass of meteoroids. This is due to the fact that ejection velocity of meteoroids and, consequently, "the opening of the scissors" increase as the meteoroids mass decreases. Strictly speaking the stream branches are not parallel, but that is too fine effect to try detect it from observations. In the considered model, the distance  $\Delta L$  is  $1.3^\circ$  and  $1.8^\circ$  for  $m_1$  and  $m_2$  respectively. The distance determined from observations see in the Fig.5. It is obvious, that the  $\Delta L$  determined in the framework of the mathematical model is somewhat underestimated. The model value can be increased by increasing the ejection velocity of the meteoroids; however, these velocities already approach the limiting ones. Another and probably the only way is above mentioned change in the cometary orbit under the action of nongravitational force.

The relative positions of the maxima for different masses are determined by the age of the stream. For the young stream, where there is no considerable Poynting-Robertson shift, as the mass of meteoroids increases, every successive pair of the maxima proves to be "enclosed" into the preceding one (like a Russian doll Matrioshka). The real Geminid stream possess these properties. So it is reasonable to suggest that it was being formed in a long orbital arc including the perihelion.

## 5. THE SHAPE OF THE RATE PROFILE

The orbit of the model particle is completely determined by the set of parameters  $S = \{v_{ej}, c\}$ , where  $v_{ej}$  is the true anomaly of the ejection point at the reference orbit,  $c$  is the vector of ejection velocity. If we designate the entire set of all possible  $S$  as  $P$ , a certain subset  $P' \subset P$  will correspond to every point  $L$  at the Earth's orbit (certainly on the interval inside the stream). Every orbit  $S \subset P'$  passes through  $L$  and, vice versa, every orbit of the model stream passing through  $L$  belongs to  $P'$ . Thus, to alter the number of orbits passing through  $L$ , we should alter either the domain  $P'$  or the distribution of the parameters within this domain. Comparing the model and observed profiles and knowing the model distributions of parameters, we can deduce the following scheme for disintegration of the parent comet. The dust ejection starts before the perihelion ( $v_{ej} \approx 90^\circ$ ), and the rate of dust production is higher (probably much higher) than that after the perihelion. This process is likely accompanied by a change in the orbit of the parent

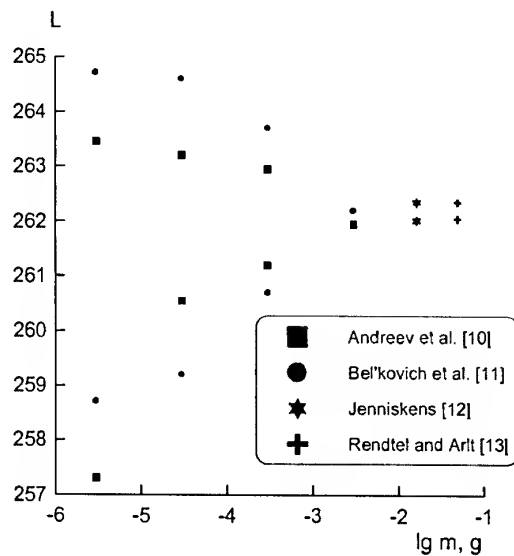


Fig. 5. Position of the activity maximum for meteoroids of various masses determined from the radar and visual observations. The solar longitude  $L$  is reduced to the epoch J2000.

comet due to action of reactive forces (which supports the hypothesis by Lebedinets [8]). Only a part of the nucleus surface is active, since the dip between the double peak is smoothed in the case of isotropic ejection. The ejection cone cannot be very narrow too, since the secondary maximum also disappears in this case. Unfortunately, there are insufficient data to develop this scenario in greater detail.

## 6. ORBITS

The following question arises: Do meteoroids ejected before and after perihelion differ in their orbital characteristics? Fig.6 shows that the answer is positive. The points on the plots form configurations of a very specific shape. Moreover, these configurations are rather stable to the small variations of the dust production rate along the cometary orbit. However, the use of, say, the eruption model of ejection gives rise to quite different configuration. The scale in Fig.6 does not shown since a quantitative comparison of the model and observational data is unjustifiable in this case. Unfortunately, a comparison with observations was impossible for the following reasons. As can be seen from Fig.6, the configuration is distinct only for discrete or narrow mass ranges. If the mass range is wide the configuration will become noisy or completely blurred. So the observational data should meet the following requirements:

1. The mass of meteoroids should be less than  $10^{-3}$  g

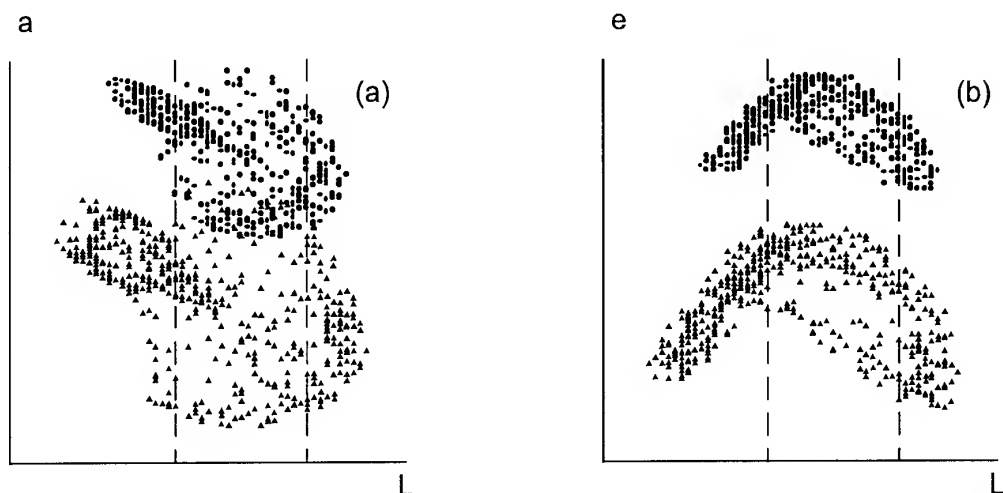


Fig. 6. Orbital elements of the model particles forming the rate profile of the stream versus the solar longitude. The vertical lines indicate the positions of the two maxima of the activity curve. Circles show the meteoroids of mass  $m_1$ ; triangles of mass  $m_2$

or, better still,  $10^{-4}$  g. Of course, the observations of meteoroids with a fixed mass cannot be ensured; however, the mass range should be as narrow as possible, at least within one order of magnitude.

2. The accuracy of determination of orbital elements should be sufficiently high.

3. The number of orbits should be sufficient for regression analysis.

Since video observations of meteors have been conducted successfully in recent years, the accumulation of the observational material is only matter of time.

## 7. REFERENCES

1. Ryabova G.O., Effect of Secular Perturbations and the Poynting-Robertson Effect on Structure of the Geminid Meteor Stream, *Solar System Research*, Vol.23, 158-165, 1989.
2. Ryabova G.O., On the Possible Formation of the Geminid Meteor Stream in Crater-forming Collisions between Asteroids, *Astronomiya i Geodesiya*, Tomsk: Tomsk. Gos. Univ., N15, 182-189, 1989.
3. Ryabova G.O., The Geminid Meteor Stream Activity Profile, *Solar System Research*, Vol.35, 151-157, 2001.
4. Ryabova G.O., Age of the Geminid Meteor Stream, *Solar System Research*, Vol.33, 258-273, 1999.
5. Whipple F.L., A Comet Model II: Physical Relations for Comets and Meteors, *Astrophys. J.*, Vol. 113, 464-474, 1951.
6. Babadzhanov P.B. and Obrubov Yu.V., Spatial Form of the Geminid and Quadrantid Meteor Streams, *Dokl. Akad. Nauk SSSR*, Vol. 290, 54-57, 1986.
7. Jones J. and Hawkes R.L., Planetary Perturbations of the Geminid Meteor Stream, *Mon. Not. R. astr. Soc.*, Vol.223, 479-486, 1986.
8. Lebedinets V.N., Origin of Meteor Streams of the Arietid and Geminid Types, *Astron. Vestn.*, Vol.19, 152-157, 1985.
9. Southworth R.B. and Hawkins G.S., Statistics of Meteor Streams, *Smiths. Contrib. Astrophys.*, Vol.7, 261-285, 1963.
10. Andreev G.V. et al. On the Structure of the Geminid Meteor Shower from Long-standing Radar Observations in Dushanbe, *Astronomiya i Geodesiya*, Tomsk: Tomsk. Gos. Univ., N13, 37-49, 1985.
11. Bel'kovich O.I. et al. The Geminid Shower from Radar, Photographic and Visual Observations, In *Meteornoe Veshchestvo v Mezplanetnom Prostranstve* (Meteor Matter in the Interplanetary Space), Moscow-Kazan, 88-101, 1982.
12. Jenniskens P., De Structuur van het Geminiden Maximum, *Radiant*, Vol.8, 58-59, 1986.
13. Rendtel J. and Arlt R., Activity Analysis of the 1996 Geminids, *WGN*, Vol.25, 75-78, 1997.

## Forecast for the remainder of the Leonid storm season. (ESA SP-495)

P. Jenniskens

*SETI Institute, NASA Ames Research Center, Mail Stop 239-4, Moffett Field, CA 94035-1000, USA*

### ABSTRACT

The dust trails of comet 55P/Tempel-Tuttle lead to Leonid storms on Earth, threatening satellites in orbit. Here we derive a model that accounts in detail for the observed properties of the dust trails evolved by the comet at previous oppositions. The model is interpreted as a projection of the comet light curve and the effects of a precessing comet nucleus. We find that the directional ejection of dust by a northerly jet causes the 1767-dust trail to be closer to Earth's orbit in 2001 than originally thought; increasing expected peak Leonid rates to a significant storm for North American observers. Predictions for the 2002 storms are less affected.

### 1. INTRODUCTION

The debris of comets that is too large to be swept into the comet tail by radiation pressure does not scatter sunlight efficiently. The dust grains end up spread along the comet orbit in the form of a trail (Davies et al. 1997, Reach et al. 2000, Fulle 2000, Epifani et al. 2001) and are a potential impact hazard to satellites (Beech et al. 1995, McBride and McDonnell 1998).

Dust trails are a natural consequence of the dispersion in the semi-major axis ( $\Delta a$ ) of the orbits after ejection, causing some grains to make a wider orbit than others and return later. Recent Leonid storms are the result of Earth's crossing of the dust trails of parent comet 55P/Tempel-Tuttle. The dust trails from many past oppositions are recognized as individual meteor showers. The trails are narrow and often separated, because the orbit of the comet nucleus changes with each return to the Sun. This important insight was gained only recently, when McNaught and Asher (1999) and Lyytinen (1999), independently following similar work by Kondrat'eva and Reznikov (1985), estimated the relative location of individual dust trails by calculating for each opposition the planetary perturbations on a single test particle that is ejected at perihelion with just the right difference in orbital period to end up near Earth at the time of a given shower. From year to year, the pattern of trails moves in and out of Earth's orbit, because planetary perturbations differ for particles that are at different

positions along the comet orbit. From this, they identified the oppositions of 55P/Tempel-Tuttle that were responsible for the recent Leonid outbursts (Table I).

Now, for the first time, meteor observations can provide insight about the comet mass loss and the dust dynamics that goes beyond information obtained from traditional mid-infrared observations of dust trails in the orbit of short period comets. The showers sample the particle size distribution, measure cross sections for a narrow range in mass, and are very sensitive to the effects of planetary perturbations. Based on recent Leonid outburst observations, we present a model of the dust distribution in a one-revolution trail that helps predict future storms and offers insight into how comets loose the bulk of their mass. A version of this forecast was published prior to the 2001 Leonid storms in *WGN, the Journal of the International Meteor Organization* (Jenniskens 2001).

### 2. DUST DISPERSION ALONG EARTH'S PATH

The relevant parameters of the model are explained in Figure 1. Each of nine equations describes various aspects of the dust distribution. The profile of the cross section in Earth's path was measured accurately during the 1999 Leonid storm caused by an 1899-dust trail crossing. An airborne perspective (Jenniskens et al. 2000, Vizard 1998) enabled us to measure simultaneously intrinsically faint meteors near the zenith and intrinsically bright meteors near the horizon.

We find that the smaller grains peak earlier in time and have a wider profile (Figure 2). The full-width-at-half-max is  $W = 0.037 \pm 0.001^\circ$  for the  $2 \times 10^{-3}$  g meteoroids seen near the horizon ( $\lambda_o = 235.284 \pm 0.001^\circ$ ),  $W = 0.046 \pm 0.004^\circ$  for the  $6 \times 10^{-4}$  g meteoroids seen higher up in the sky with similar instruments ( $\lambda_o = 235.274 \pm 0.002^\circ$ ), and  $W = 0.056 \pm 0.003^\circ$  for the  $5 \times 10^{-4}$  g particles measured in the zenith with High Definition TV cameras ( $\lambda_o = 235.275 \pm 0.001^\circ$ ) (Yano et al. 2001). Incidentally, this trend is consistent with the displaced profile of the 0.2-2.5 kHz ELF/VLF detection of meteors reported by Price and Blum (2000). We derive a width  $0.080 \pm 0.008^\circ$  and  $\lambda_o = 235.269 \pm 0.005$ ,

suggesting meteoroids of mass  $\sim 3 \times 10^{-5}$  g (200  $\mu$ m).

These cross sections are well represented by a Lorentzian shape (Eq. 1) (Jenniskens et al. 2000a). The number density is expressed in terms of Zenith Hourly Rate (ZHR), which is a commonly used measure of number influx and is proportional to the rate of meteors observed by a visual observer under clear sky conditions with the radiant overhead (Jenniskens 1995, Jenniskens and Betlem 2001).  $W$  is the full-width at half maximum of the ZHR profile, while  $\lambda_o^{\max}$  is the time of the peak in terms of solar longitude  $\lambda_o$ , which is a measure of the Earth's position in its orbit. Throughout the paper,

this angle will be in Equinox J2000.0. At the peak of the storm, the measured  $ZHR^{\max} = 4,600 \pm 700$   $\text{hr}^{-1}$  ( $\gamma=1.0$ , Jenniskens 1995) or influx =  $2.8 \pm 0.4$   $\text{km}^{-2}$   $\text{hr}^{-1}$  (Holman and Jenniskens 2001) for meteoroids with mass  $< 2 \times 10^{-5}$  g (+6.5 visual magnitude). This corresponds to an impact probability of 50% for the current satellite park as a whole (2670 sats, 50  $\text{m}^2$  each). Throughout the paper, we will use the empirical mass-luminosity relationship (Brown et al. 2000):  $\log M(\text{g}) = -1.98(\pm 0.02) - 0.43(\pm 0.01)m_v - 0.07(\pm 0.26)\log(\cos z)$  with  $m_v$  the peak visual magnitude for a distance of 100 km, and  $z$  the zenith angle of impact ( $47^\circ$  at the time of the peak).

Leonid shower prediction model:

$$ZHR = ZHR^{\max} \frac{(W/2)^2}{(\lambda_o - \lambda_o^{\max})^2 + (W/2)^2} \quad (1)$$

$$ZHR^{\max} = ZHR_o * f_m * f(\Delta a) * f(\Delta r) \quad (2)$$

$$W_E = 2 r \tan (W/2) \sin(\epsilon_h) \quad (3)$$

$$f(\Delta r) = 10^{-1450 * |\Delta r + \delta r|} \quad (4)$$

$$\delta r = \Delta r^{\text{obs}} - \Delta r^{\text{cal}} = +0.00025 + 0.00020 * \sin(2\pi (T-1910)/270) \text{ AU} \quad (5)$$

$$W_E(\Delta r) = 1.2 \times 10^{-4} 10^{-600 * |\Delta r + \delta r|} \quad (6)$$

$$f(\Delta a) = (W_a/2)^2 / ((\Delta a - 0.12 \pm 0.01)^2 + (W_a/2)^2) \quad (7)$$

$$s = 2.21 + 0.41 * \log(\Delta a) \quad (8)$$

$$\delta \lambda_o = \lambda_o^{\text{obs}} - \lambda_o^{\text{cal}} = -0.00010 + 0.00020 * \sin(2\pi (T-1910)/180) \text{ AU} \quad (9)$$

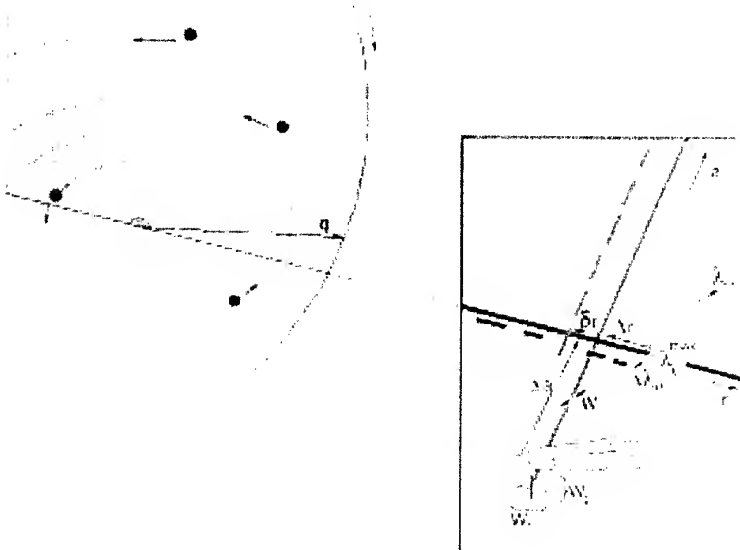


Figure 1: Diagram shows the orbit of 55P/Tempel-Tuttle and the definition of parameters used to describe the location and size of the dust trail in the prediction model (Eq. 1-9).

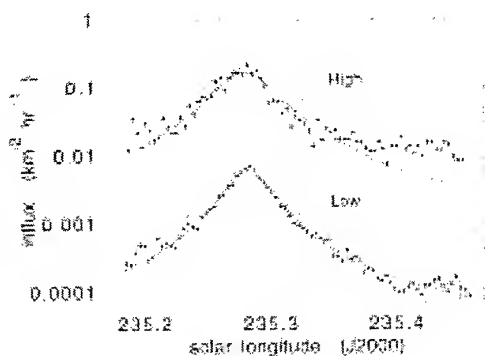


Figure 2: 1999 Leonid storm influx profiles measured by cameras pointed at 37° (high) and 21° (low) elevation from the aircraft window. They represent masses of  $5 \times 10^{-4}$  g and  $2 \times 10^{-3}$  g, respectively. Data from the intensified High Definition TV camera at 90° elevation (Yano et al. 2001) are shown as crosses. To facilitate comparison, the dashed line copies the Lorentz curve fit for the high cameras to match the peak of the low cameras. No smoothing applied. Error bars represent the statistical error from the number of meteors in each interval. The activity curves are scaled to match the cumulative influx up to the given mass that was representative of each set of observations.

Smaller particles must have impacted in larger numbers, but did not result in satellite operation anomalies (Treu et al. 2000). There is not a single power law over the whole mass range, as normally assumed in dust trail models (Davies et al. 1997, Reach et al. 2000). The mass power index  $s = 1.97 \pm 0.05$  for +6 magnitude meteors of mass  $5 \times 10^{-4}$  g (Brown et al. 2000, Arlt et al. 1999), but decreases to  $s = 1.64 \pm 0.05$  for meteoroids of mass less than  $2 \times 10^{-3}$  g (+0 magnitude). Most of the mass is in these larger meteoroids. The distribution of Moon impact flashes with  $s = 1.6 \pm 0.1$  (Bellot-Rubio et al. 2000) suggests that this size distribution is representative for masses up to 5 kg, for a total peak mass influx of  $0.070 \text{ g km}^{-2} \text{ hr}^{-1}$ . Lorentz-shaped profiles are known too from the mid-infrared brightness intensity across comet 22P/Kopff's dust trail (Davies et al. 1997). The wings of the distribution have been interpreted as due to a separate dust component from grains of different size or morphology. However, the meteor shower shows no apparent change of the power law size distribution index across the profile.

We conclude that the tail of the distribution appears to be dynamically related to the peak and is not due to a separate dust component.

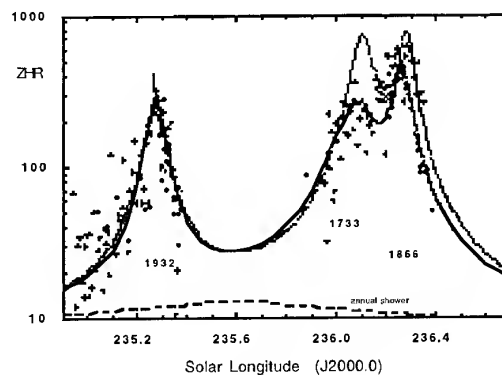


Figure 3: Zenith Hourly Rate curves for the 2000 encounters with the 1932-, 1733-, and 1866-dust trails. Black dots are results from intensified video cameras (Jenniskens and Gustafson 2000), while crosses are radio-MS data. Open circles are visual observations reported in Arlt and Gyssens (2000). The solid line is a fit of Lorentzian profiles. The broad dashed line is the level of annual shower activity in non-outburst years. The narrow dashed line shows the predicted rate by Lyytinen and Van Flandern (2000).

Rather, the shower profile can be understood as a projection of the comet's light curve (Yoshida 2001) or water production rate  $Q(r)$ , which are related (Jorda et al. 1992). Most of the dust ejected at heliocentric distance  $r$  will end up near perihelion (where Earth encounters the stream) having dispersed away from the comet orbit to a distance  $\Delta x$  perpendicular to the comet orbital plane. The ejection velocity can be measured from the width of the curve near the peak, while the tail of the Lorentz profile is sensitive to the adopted power law for the dependence with heliocentric distance. In order to get particles far from the stream center, it is necessary to invoke an increase of the ejection velocity with heliocentric distance:  $\text{Log } V_{ej} \text{ (m/s)} \sim -0.19 \pm 0.03 \text{ log } M \text{ (g)} + 1.27 \pm 0.05 \text{ log } r \text{ (AU)}$ , and low ejection speeds of  $V_{ej} = 3.0 \pm 0.3 \text{ m/s}$  at perihelion for  $3 \times 10^{-4} \text{ g}$  particles (+3.5 magn.). This is inconsistent with the Whipple model of dust ejection by water vapor drag, which has  $\text{Log } V_{ej} \text{ (m/s)} \sim -0.167 \text{ log } M \text{ (g)} - 0.60 \text{ log } r \text{ (AU)}$  and  $V_{ej} = 44 \text{ m/s}$  (within a factor of 2) (Crifo 1997, Crifo and Rodionov 1997, Crifo et al. 2000, Hainaut et al. 1998).

Because they carry the bulk of mass, it is possible that larger grains fall apart in the comet coma and are the main source of the smaller grains, more so near perihelion. In that case, the ejection velocities of

smaller grains reflect mostly those of the larger meteoroids, because gas drag is not efficient far from

the comet nucleus surface. Perihelion would see increased thermal stresses on the grains.

Table 1: Dust trail parameters from past Leonid outbursts.

Year	N*	Trail*	$r_m$	$\Delta a$	$\Delta r$	$\delta r_{obs}$	$W_{obs}$	$W_{cal}$	ZHR <sub>obs</sub>	ZHR <sub>cal</sub>	$S_{obs}$
1999	3	1899	0.38	0.138	-0.00066	+0.00020	0.00063±3	0.00073	4,600±700	4,593	1.89
1998	3	1899	0.40	0.050	+0.00440	-0.0031	0.0024±7	0.22	70±20	0	1.64
1999	4	1866	0.50	0.118	+0.00160	+0.00003	0.0049±15	0.0039	30±15	109	1.83
2000	4	1866	0.13	0.114	+0.00077	-0.00013	0.0014±2	0.0012	390±20	459	1.76
2000	2	1932	0.55	0.300	-0.00120	+0.00028	0.0014±2	0.0013	255±20	312	1.99
2000	8	1733	0.27	0.064	+0.00076	+0.00039	0.0025±6	0.0020	230±20	216	1.77
1969	1	1932	0.95	0.934	-0.00004	+0.00037	0.00052±9	0.00059	180±20	192	2.19
1966	2	1899	0.52	0.168	-0.00013	+0.00028	0.00049±5	0.00043	14,000±3,000	17,926	1.99
1867	1	1833	1.00	0.373	-0.00014	+0.00006	0.00042±7	0.00043	4,300±900	4,105	..
1866	4	1733	0.37	0.059	-0.00029	+0.00051	0.00058±11	0.00046	6,800±1,100	9,145	..
1833	1	1799	0.95	0.174	-0.00021	+0.00021	..	0.00042	~50,000	31,416	..

\*) calculations from McNaught and Asher (1999) and Lyytinen and Van Flandern (2000).

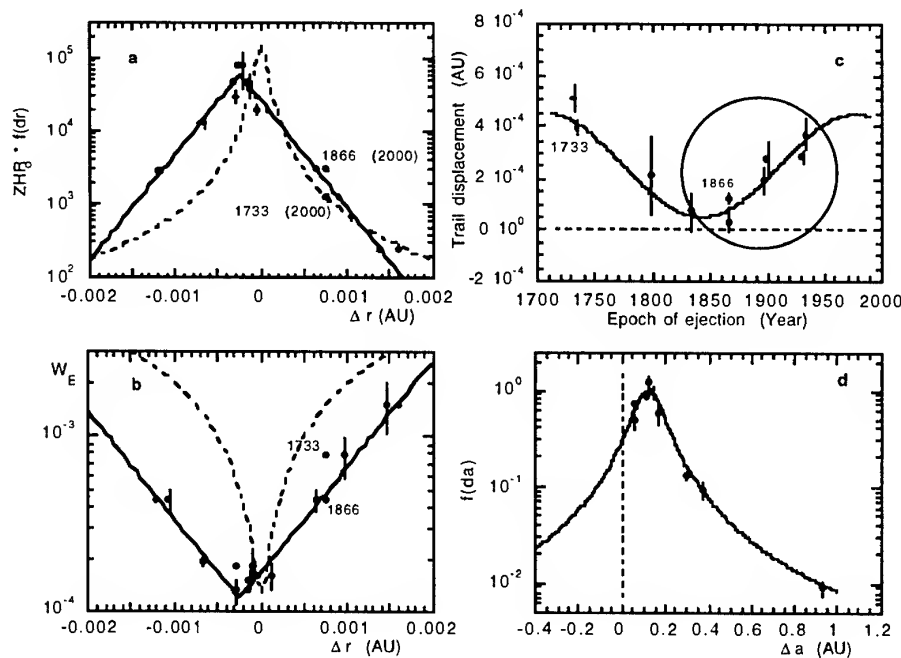


Figure 4: **4a:** Trail cross section along a radial direction to the Sun. Open symbols are observed values, dark symbols show values after correcting for trail shifts of Fig. 4c. **4b:** As Fig. 4a, for the variation of shower width with heliocentric distance. **4c:** Trail shifts that would fit the observed flux to a smooth exponential behavior (dark symbols in fig. 4a). The open circle shows one trail equivalent width. **4d:** Variation of trail dust density with intrinsic semi-major axis dispersion (variation along the comet orbit) after correction for trail shifts in Fig. 4c.

Indeed, the large grain mass distribution agrees with the value of  $s = 1.53 \pm 0.1$  (reportedly valid over a wide  $10^{-12}$  to  $10^{-3}$  kg mass range) near the nucleus of comet 1P/Halley and expected to reflect the dust distribution shortly after ejection (Fulle et al. 2000). The mass distribution for small grains is consistent with that expected for catastrophic fragmentation, where  $\Delta N(M) * M \sim M^{k/3} \Delta(\log M)$ , with  $k=0.6$  for diameters smaller than one-tenth the diameter of the original mass (Fujiwara et al. 1989). Dust fragmentation in the comet coma is frequently implied to account for dust distributions and comet dust tail striae. Our meteor observations, too, show spatial and temporal correlations that suggest breakup more than one return before Earth's encounter (Gural and Jenniskens 2000).

### 3. DUST DISPERSION IN OTHER DIMENSIONS

Three further dust trail cross sections were obtained in November 2000. The 1932-dust and 1866-dust trail were observed using the same intensified video cameras from a small Cessna aircraft over Florida, facilitated by Bo Gustafson of the University of Florida at Gainesville (Jenniskens and Gustafson 2000). The 1733-dust trail peaked over Europe and was observed by Ilkka Yrjölä in Finland using radio forward meteor scatter to measure the meteor rate. In Figure 3, these results are compared to visual observations collected by the International Meteor Organization (Arlt and Gyssens 2000). These cross sections are at appropriate distances from the calculated trail centers to measure the dispersion of dust in the comet orbital plane perpendicular to Earth's orbit. Results of Lorentz profile fits are summarized in Table I, which includes data from historic Leonid showers that originated from known trails (Jenniskens 1995). All prior results were normalised to Zenith Hourly Rates for a geometric radiant dilution factor of  $\gamma = 1.0$ .

Each shower represents a cross section at different  $\Delta a$  and  $\Delta r$ , and after a certain number of revolutions  $N$  since the opposition at time  $T$ . The observed Zenith Hourly Rate is a product of these three factors (Eq. 2): a function  $f(\Delta a)$  that describes the initial dispersion along the orbit in terms of semi-major axis, a function  $f_m \sim 1/N$  that describes the subsequent dispersion due to planetary perturbations and the number of revolutions (calculated from the relative distance between two nearby test particles), and a function  $f(\Delta r)$  that describes the dispersion in the plane of the comet orbit in terms of radial heliocentric distance (McNaught and Asher 1999).  $ZHR_0$  is the peak dust density in a one-revolution trail. The last two functions are derived iteratively by plotting the observed width and peak intensity ( $ZHR_0 * f(\Delta r)$  and  $f(\Delta a)$ , respectively) as a function of  $\Delta r$  and  $\Delta a$ . Figure 4 shows the result. The measured

width  $W$  needs to be corrected for the angle  $\epsilon_h = 18.1^\circ$  at which Earth crosses the trail (Eq. 3). The result,  $W_E$ , varies with  $\Delta r$  and is expected to be smallest at the trail center. The narrowest observed historic Leonid storms imply an intrinsic width of  $W_E^0 = 0.00013 \pm 0.00001$  AU, or  $1.9 \pm 0.2 \times 10^4$  km.

The variation with  $\Delta r$  of peak intensity (Fig. 4a) and stream width (Fig. 4b) is skewed towards negative values of  $\Delta r$  for both peak intensity and width, with comparatively narrower width and larger peak activity on the sunward side of the trail. The narrowest and strongest showers are detected when the trail position is calculated to be just outside of Earth's orbit. The observed trends do not comply with a cylindrical-symmetric Lorentz-profile dust distribution (dashed lines in Fig. 4a and 4b) and is not Gaussian, as assumed in earlier models (McNaught and Asher 1999).

For any given functional form, there are significant discrepancies. The large deviation for the 1998 encounter with the 1899-dust trail is understood from a perturbation by Earth in the previous return of 1965 (McNaught and Asher 1999). We now measure a trail displacement of  $\Delta r = \Delta r^{obs} - \Delta r^{cal} = 0.0031$  AU from the calculated position. Other discrepancies are more puzzling. Especially, the 1733- and 1866-dust trail encounters in 2000, which occurred at the same calculated  $\Delta r$ , but resulted in significantly different peak intensity and width. The agreement is not improved by assuming that the dust density falls off (and width increases) with the number of revolutions  $N^2$  (or  $N$ ) as assumed by Lyytinen and van Flandern (2000), nor with initial  $\Delta a$  as assumed by Brown (2000). The latter may sound surprising, because comet dust trails do show such a behavior (Davies et al. 1997). However, unlike mid-infrared images of comet dust trails, the Leonid showers are always measured near perihelion. The lack of dependence on  $N$  can be understood because each particle, to first order, will return to its point of ejection after one return. Thus, the width measured near perihelion reflects the heliocentric dependence on ejection velocities and does not necessarily increase with orbital period.

We postulate that the discrepancies are due to trail shifts  $\Delta r$  (and  $\delta \lambda_0$ ) possibly because of the particularities of comet dust grain ejection. One important clue is that the discrepancies in peak intensity and width deviate in sync. When the trails are too dense, they also tend to be too narrow. This argues against residual effects from significant variations in the comet activity along the orbit, or from one return to the next.

McNaught and Asher (1999) assume simply ejection at perihelion in the direction of comet motion, while

Lyytinen and van Flandern (2000) assume no ejection but high radiation pressure forces to arrive at the same initial  $\Delta a$ . However, note that the agreement in peak time and  $\Delta r$  calculated may be fortuitous because these assumptions lead to the same meteoroid orbit for given  $\Delta a$ .

We find a smooth variation of shifts with epoch of ejection after matching a symmetric profile through the variation of peak intensity and width with  $\Delta r$ . The functional form that best describes the dispersion of dust in the heliocentric direction  $f(\Delta r)$  is an exponential equation 4 (solid line in Fig. 4a), with  $\Delta r$  about  $+0.00025$  AU. The equivalent width of this distribution (defined as integrated profile = width\*peak rate) is  $W_r = 0.00060 \pm 6$  AU, or  $8.9 \pm 0.9 \times 10^4$  km, a factor of three larger than the equivalent width of  $1.57 \times W_E = 0.00020 \pm 2$  AU in the perpendicular direction.

Directional ejection can account for the lack of a Lorentz wing in  $f(\Delta r)$ . This is because the ejection vector in the comet orbital plane will be mostly in the direction of comet motion at large heliocentric distances, while nearly perpendicular to the comet motion vector at perihelion. The effect is to suppress the Lorentz wings. The 3 times higher dispersion implies that the ejection velocity at perihelion is  $V_{ej} = 9.1 \pm 1.8$  m/s, still short of the Whipple speed.

The discrepancies from the solid line in Fig. 4a are of similar magnitude and sign for ejections dating from the same epoch. There is a sinusoidal variation (Eq. 5) as a function of the year of epoch from  $T = 1733$  until 1932 (solid line Figure 4c). The 1733 and 1866 trails represent the maximum and minimum of the functional trend, thus explaining the relatively large differences in shower width and intensity, despite similar  $\Delta r^{cal}$ . After correcting with Eq. 5, we find that the variation of width is also described well by an exponential curve (Eq. 6), but with about half the scale length. The distribution is that of a ribbon in the comet plane, widening gradually away from the comet orbit.

With this definition of  $f(\Delta r)$  (Eq. 4+5), we can plot the corrected peak rate as a function of the initial dispersion in semi-major axis to find a Lorentzian shaped  $f(\Delta a)$  as expressed in Eq. 7, with  $W_a = 0.16 \pm 0.02$  AU and  $ZHR_0 = 0.6 \pm 0.1 \times 10^5$  hr<sup>-1</sup>. This function represents the dispersion of dust along a one-revolution dust trail of comet 55P/Tempel-Tuttle. Note that  $W_a$  does not measure a physical distance, but rather a dispersion in semi-major axis. The shape of the curve is not easily understood as a consequence of ejection velocities alone. However, a good fit to the data is (solid line Fig. 4d) obtained when including the effect of velocity vectors on the

dispersion in perihelion distance, which has a strong effect on the distribution in semi-major axis.

The offset in the peak of the curve is an expected result from radiation pressure effects on the grains, and should be larger for smaller meteoroids. Indeed, we observe a logarithmic increase (Eq. 8) of the mass power index ( $s$ ) with  $\Delta a$  away from the comet position (centered on magnitude +3.5 meteors). From the peak of in the distribution, we derive an average meteoroid density of  $\rho = 0.97 \pm 0.13$  g/cm<sup>3</sup>, if the radiation pressure coefficient  $\langle Q_p \rangle = 1$  and the grains are spherical in shape (Grün et al. 2001). This compares well to  $\rho \sim 0.7$  g/cm<sup>3</sup> derived from the deceleration of a Leonid fireball (Spurny et al. 2000).

Trail shifts are also expected to affect the time of the peak. The peak times calculated (McNaught and Asher, 1999; Lyytinen and Van Flandern 2000) differ from the observed peak times by up to  $\pm 16$ -minutes, which translated to astronomical units is the same as the range in Eq. 5. Six of eight data points are fitted by a sinusoidal Eq. 9, but with a different periodicity than Eq. 5.

The torque exerted by a jet will cause a precession of the comet nucleus spin axis that can qualitatively account for the observed radial displacement  $\Delta r$  with a semi-period of  $270 \pm 80$  years (Eq. 5), and in  $\delta \lambda_0$  with a semi-period of  $180 \pm 20$  years (Eq. 9), by changing the mean direction of ejection at perihelion in each return. Indeed, a dust jet was observed 1 month prior to the 1998 perihelion passage of comet 55P/Tempel-Tuttle, with an amplitude of  $25^\circ$  centered on a north-north-eastern direction (Jorda et al. 1998). The amplitude of the jet motion suggests a hot spot at  $+65^\circ$  N, and a rotation period of  $15.33 \pm 0.02$  hr. With a nuclear axis ratio larger than 1.5 (Hainaut et al. 1998), this motion is not necessary a simple sine law, hence the different semi-periodicities.

For the observed dust trail dimensions, we calculate a total dust mass loss for each return of comet 55P/Tempel-Tuttle of  $2.6 \pm 0.7 \times 10^{10}$  kg. From the observed visible magnitude light curve of comet 55P/Tempel-Tuttle we derive a total water production loss of  $1.1 \pm 0.7 \times 10^{10}$  kg. Hence the ratio  $M_{dust}/M_{gas} = 2.4 \pm 1.7$ , in agreement with estimates from the infrared signatures of comet dust trails of short period comets (Davies et al. 1997).

#### 4. IMPLICATIONS

This completes the formalism for predicting future Leonid returns (Eq. 1-9). Results are in Table II. Several dust trails are near Earth's orbit in November of 2001 and 2002 (Table II). Our results disagree

Table 2: Forecast for the 2001+2002 encounters.

N	Year	$\bar{J}_{2000}^{\max}$	Time (UT)	W (AU)	FWHM (hr)	ZHR $^{\max}$ (hr $^{-1}$ )	s	Lyytinen	Asher	Brown	Time
<i>Nov. 17, 2001 (UT)</i>											
1	(1965)	235.24	13:14	0.017	--	0	2.16		--	--	0
2	(1932)	235.37	16:20	0.030	--	0	2.04		--	--	0
3	(1899)	235.54	20:22	--	--	0	1.97		--	--	0
<i>Nov. 18, 2001 (UT)</i>											
8	(1733)	236.12	10:10	--	--	0	1.71		--	--	0
7	(1767)	236.119	<b>10:09</b>	0.00047	0.66	<b>4,200</b>	1.76		<b>2,000</b>	<b>2,500?</b>	390
6	(1800)	236.202	12:07	0.0030	4.25	40	1.76		110	--	<b>600</b>
5	(1833)	236.279	13:57	0.0049	6.80	14	1.79		60	--	390
10	(1667)	236.408	17:01	0.00147	2.05	170	1.59		600	--	170
11	(1633)	236.422	17:21	0.00091	1.26	510	1.56		260	--	150
9	(1699)	236.413	<b>17:08</b>	0.00088	1.23	<b>1,800</b>	1.64		<b>2,000</b>	<b>9,000</b>	210
4	(1866)	236.446	<b>17:55</b>	0.00058	0.81	<b>2,700</b>	1.86		<b>6,100</b>	<b>15,000</b>	190
<i>Nov. 17, 2002 (UT)</i>											
1	(1965)	235.29	20:35	0.0060	--	0	2.19		--	--	--
<i>Nov. 18, 2002 (UT)</i>											
2	(1932)	--	--	--	--	0	2.07		--	--	--
3	(1899)	235.75	07:31	--	--	0	2.00		--	--	--
<i>Nov. 19, 2002 (UT)</i>											
7	(1767)	236.615	<b>04:07</b>	0.00047	0.65	<b>4,900</b>	1.82		<b>4,500</b>	<b>15,000</b>	--
6	(1800)	236.710	06:23	0.0028	3.96	58	1.83		--	--	06:23
5	(1833)	236.709	06:22	0.0032	4.49	41	1.83		160	--	06:45
4	(1866)	236.871	<b>10:13</b>	0.00040	0.56	<b>5,700</b>	1.90		<b>7,400</b>	<b>30,000</b>	--
<i>Nov. 19, 2006 (UT)</i>											
2	(1932)	236.620	04:53	0.00055	0.77	120	2.20		50	100	04:48
<i>Nov. 18, 2007 (UT)</i>											
2	(1932)	236.109	22:51	0.00042	0.58	200	2.22		30	--	22:55

with the large dispersion and trail shifts that follow from numerical models by Brown (2000) and Cook (2000), and by Göckel and Jehn (2001).

Compared to models by McNaught and Asher (1999) and Lyytinen and Van Flandern (2000), our predictions increase the importance of the 1767 dust trail encounter relative to that of 1699/1866 and predict the latter trails half an hour earlier in time. The 1767-dust trail is now expected to give the highest peak rate for Earth-based observers, an estimated  $ZHR^{\max} = 4,200 \text{ hr}^{-1}$ . Different solutions for  $\delta r$  introduce an uncertainty over the range 3,000–6,900  $\text{hr}^{-1}$ . The 1866-dust trail will contribute only  $ZHR = 2,000\text{--}3,500$  and the 1699-dust trail 1,300–2,500  $\text{hr}^{-1}$ . However, the latter storms are slightly wider and both will merge into a single profile with a total fluence 1.6 times higher. Earlier estimates (McNaught and Asher 1999, Lyytinen and Van Flandern 2000) had this peak 4–10 times more intense. The meteors will be somewhat brighter on average than during the storm of 1999.

The observed trail shifts ( $\sim 0.00025 \text{ AU}$ ) are of the same order as the geostationary distance ( $0.00028 \text{ AU}$ ). In the anti-Sun direction, for example, the 1767-dust trail passage in 2001 causes an equivalent  $ZHR = 11,000 \text{ hr}^{-1}$ , or about 7 particles  $\text{km}^{-2} \text{ hr}^{-1}$  with mass  $> 2 \times 10^{-5} \text{ g}$  at the peak. At the sunward position of geostationary orbit, the 1866-dust and 1699-dust trails peak at 6,800 and 4,500  $\text{hr}^{-1}$ , respectively. Along similar lines, the Moon is positioned at a relatively large distance of  $0.00258 \text{ AU}$ . In 2001, the most significant impacts will occur

when passing the 1833- ( $ZHR = 2,800 \text{ hr}^{-1}$ ) and 1800-dust trails ( $ZHR = 900 \text{ hr}^{-1}$ ), 2 hours after the Earth's passage by those trails at around 14 h and 16 h UT. This compares to a peak influx of about  $ZHR = 1,100 \text{ hr}^{-1}$  in 1999. Other strong showers are predicted for 2002, but a full Moon will illuminate this next encounter and the meteors will be fainter on average. No further Leonid storms are expected until the return of 2099.

*This work benefited greatly from discussions with Dr. Didier Despois and Esko Lyytinen and a review by Kevin Zahnle. Part of this work was done while on a work visit at Bordeaux University, France. The deployment of the 1999 Leonid MAC mission was made possible by grants from the NASA Exobiology, Planetary Astronomy, Suborbital MITM, and Astrobiology Advanced Missions and Technologies programs, and by grants from NASA Ames Research Center and from the U.S. Air Force. The 2000 Leonid deployment was made possible by a grant from Data Grid Corporation. PJ is supported by the Exobiology program.*

## 5. REFERENCES

- Arlt R., Bellot Rubio L., Brown P., Gyssens M., 1999. *WGN, Journal of the IMO* 27, 286–295.
- Arlt R., Gyssens M., 2000. *WGN, the Journal of the IMO* 28, 195–208.
- Beech M., Brown P., Jones J., 1995. *Q.J.R. Astr. Soc.* 36, 127–152.

- Bellot-Rubio L.R., Ortiz J.L., Sada P.V., 2000. *Earth, Moon and Planets* **82-83**, 575-598.
- Brown P.G., 2000. Evolution of Two Periodic Meteoroid Streams: the Perseids and Leonids, Thesis (PHD). THE UNIVERSITY OF WESTERN ONTARIO (London, CANADA), 286 pp.
- Brown P., Campbell M.D., Ellis K.J., Hawkes R.L., et al., 2000. *Earth, Moon and Planets* **82-83**, 167-190.
- Cooke B., 2001. "The April (T-7) Leonid forecast for 2001", Updated in "The July Leonid forecast for 2001 (Applicable to Earth and Spacecraft in LEO)", Marshall Space Flight Center internal document, distributed electronically (2001);
- Crifo J.F., 1997. *Icarus* **130**, 549-551.
- Crifo J.F., Rodionov A.V., 1997. *Icarus* **129**, 72-93.
- Crifo J.F., Rodionov A.V., Bockelee-Morvan D., 2000. *Icarus* **138**, 85-106.
- Davies J.K., Sykes M.V., Reach W.T., Boulanger F., Sibille F., Cesarsky C.J., 1997. *Icarus* **127**, 251-254.
- Epifani E., Colangeli L., Fulle M., Brucato J.R., Bussoletti E., de Sanctis M.C., Mennella V., Palumba E., Palumbo P., Rotundi A., 2001. *Icarus* **149**, 339-350.
- Fulle M., Levasseur-Regourd A.B., McBride N., Hadamcik E., 2000. *Astrophys. J.*, **119**, 1968-1977.
- Fulle M., 2000. *Icarus* **145**, 239-251.
- Fujiwara A., Cerroni P., Davis D., Ryan E., Di Martino M., Holsapple K., Housen K., 1989. In: *Asteroids II* (eds. R. P. Binzel, T. Gehrels, and M.S. Matthews), Univ. Arizona Press, Tucson, Az., pp. 240-265.
- Göckel C., Jehn R., 2000. *MNRAS* **317**, L1-L5.
- Grün E., Baguhl M., Svedhem H., Zook H.A., 2001. In: *Interplanetary Dust*. E. Grün, B.Å.S. Gustafson, S.F. Dermott, H. Fechtig (eds.), Springer Verlag, Berlin. P. 295-346.
- Gural P., Jenniskens P., 2000. *Earth, Moon and Planets* **82-83**, 221-247.
- Hainaut O.R., Meech K.J., Boehnhardt H., West R.M., 1998. *Astron. Astrophys.* **333**, 746-752.
- Holman D., Jenniskens P., 2001. *WGN, the Journal of IMO* **29**, 77-84.
- Jenniskens P. 1995. *Astron. Astrophys.* **295**, 206-235.
- Jenniskens P., 2001. *WGN, the Journal of the IMO* **29** (in press).
- Jenniskens P., Betlem H., 2000. *Astrophys. J.* **531**, 1161-1167.
- Jenniskens P., Gustafson B. Å. S., 2000. *WGN, Journal of the IMO* **28**, 209-211.
- Jenniskens P., Butow S.J., and Fonda M., 2000. *Earth, Moon and Planets*, **82-83**, 1-26.
- Jenniskens P., Crawford C., Butow S., Nugent D., Koop M., Holman D., Houston J., Kronk G., Beatty K., 2000a. *Earth, Moon and Planets* **82-83**, 191-208.
- Jorda L., Lecacheux J., Colas F., Frappa E., and Laques P., 1998. *IAU Circular 6816* (January 30th), D.W.E. Green (ed.).
- Jorda L., Crovisier J., Green D.W.E., 1992. In: *Asteroids, Comets, Meteors 1991*, Lunar and Planetary Inst., Houston, p 285-288.
- Kondrat'eva E.D., Reznikov E.A., 1985. *Sol. Syst. Res.* **19**, 96-101.
- Lyytinen E., 1999. *Meta Research Bulletin* **8**, 33-40.
- Lyytinen E., Van Flandern T., 2000. *Earth, Moon and Planets* **82-83**, 149-166.
- McBride N., McDonnell J.A.M. 1998. *Plan. Space Sci.*, **47**, 1005-1013.
- McNaught R.H., Asher D.J., 1999. *WGN, Journal of the IMO* **27**, 85-102; See also update on website <http://www.arm.ac.uk/leonid/encounters.html>
- Price C., Blum M., 2000. *Earth, Moon and Planets*, **82-83**, 545-554.
- Reach W.T., Sykes M.V., Lien D., Davies J.K., 2000. *Icarus* **148**, 80-94.
- Spurny P., Betlem H., Van 't Leven J., Jenniskens P., 2000. *Meteoritics & Plan. Sci.* **35**, 243-249.
- Treu M.H., Worden S.P., Bedard M.G., Bartlett R.K., 2000. *Earth Moon and Planets* **82-83**, 27-38.
- Yano H., Abe S., Ebizuka N., Watanabe J.-I., 2001. Presented at: Meteoroids 2001 Conference, Kiruna, Sweden (August 6-10, 2001), ESA SP-495.
- Vizard F., 1998. *Popular Science* (Nov. issue), p. 68; See also: <http://leonid.arc.nasa.gov>.
- Yoshida S., 2001. Published on the website <http://www.aerith.net/comet/catalog/0055P/1998.html>

## COMPARATIVE ANALYSIS OF METEOR SHOWER OBSERVATIONS PROCESSED BY THREE DIFFERENT METHODS

O.I. Belkovich<sup>(1)</sup>, M.G. Ishmukhametova<sup>(2)</sup>, N.I. Suleymanov<sup>(3)</sup>

<sup>(1)</sup> Branch of Kazan State University in Zelenodolsk, Saidashego st., 4, Zelenodolsk, Tatarstan, Russia, E-mail: oleg@green.kcn.ru

<sup>(2)</sup> Kazan State University, Russia

<sup>(3)</sup> Engelhardt Astronomical Observatory, Russia

### ABSTRACT

Comparison of results of meteor shower observations obtained and processed by different methods is the best way to check reliability the methods themselves. The main condition for comparisons is the reduction of flux densities to one minimal mass and then the profiles of shower flux densities and mass exponent  $S$  as functions of solar longitudes can be obtained. Two meteor showers - Quadrantids and Geminids were chosen to check accuracy's of one methods of processing of visual and two ones of radar observations worked out at the Engelhardt Astronomical Observatory [1-4].

### 1. OBSERVATIONS AND REDUCTIONS.

Radar observations of Geminids and Quadrantids made in 1964 - 1971 at the Engelhardt observatory has been used for the comparison. Sensitivities of radar observations (minimal detectable electron linear densities  $\alpha_0$ ) have been obtained from meteor echo amplitude distributions for every day of observations. Sporadic background has been observed for 5 - 7 days before and after a shower action and then has been deducted from observed meteor hourly rates taking into account a trend. Meteoroid flux densities have been reduced to the minimal meteoroid mass  $m_0 = 10^{-3}$  g and represented as functions of the solar longitude. Flux densities  $Q_u$  and  $Q_T$  have been found from hour rates  $N_u$  and  $N_T$  of radar echoes with amplitudes greater than a threshold level  $U$  and with durations greater than  $T \approx 1$  s correspondingly.  $N_u$  corresponds to underdense and  $N_T$  corresponds to overdense meteor trails. The formulae of flux calculations are different for  $Q_u$  and  $Q_T$  so we can consider that we have two different methods of determination of meteoroid flux density from radar observations. The first approximations of the mass exponent  $S$  as functions of the solar longitude has been made for every hour of observations by selections of the  $S$  value that gives  $Q_u = Q_T = Q_0$  for the minimal meteoroid mass  $m_0 = 10^{-3}$  g. Then values of  $S$  has been averaged over some intervals of solar longitudes and after that values of  $Q_u$

and  $Q_T$  were calculated again with  $S$  values of the second approximation and then  $Q_u$  and  $Q_T$  were averaged in intervals of the solar longitude. No one observation was excluded from reduced data. Individual values of  $Q_u$  reduced to  $m_0$  and  $Q_T$  reduced to the linear electron density of a vertical meteor trail producing at the characteristic height the echo duration of 1 s are shown for Geminids in Fig. 1.

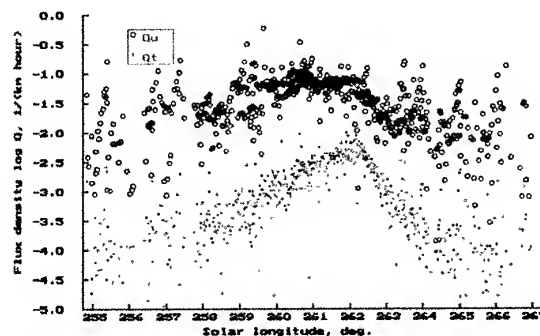


Fig. 1. Geminids. Flux density us solar longitude.

Visual observations of the Geminid meteor shower were made in Crimea in 1971 - 1994. Quadrantid observations 1991 - 1997 were taken from the IMO database. All observations has been reduced to ZHR with meteor magnitude brighter than  $+3^m$ . Values of  $S$  were found from magnitude distributions for every night. All the data were averaged in the solar longitude intervals, equinox 2000.0.

### 2. DETERMINATION OF THE VISUAL COLLECTING AREA.

The slope of the erasing branch of a shower profile depends on a minimal mass of meteoroids in a flux. That fact has been used to find the effective collecting area  $\Sigma$  of meteor visual observations. The mass corresponding to the echo duration 1 s is closer to the

mass corresponding to meteors  $+3^m$  so to find the  $\Sigma$  value we have reduced  $Q_T$  to the mass when the profile of  $Q$  coincides with the profile of ZHR. The problem was solved by the minimization of the difference between two curves - ZHR and the reduced  $Q$  - by the least square method. The comparisons are shown in Fig. 2 and Fig. 3.

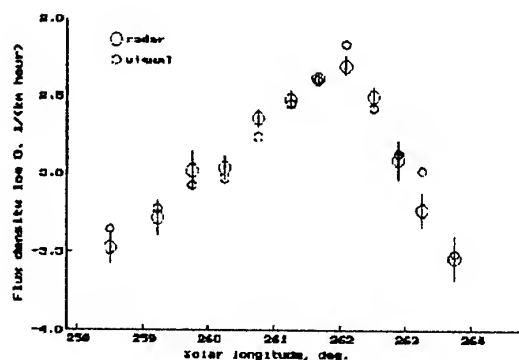


Fig. 2. Geminids. Comparison of radar and visual flux densities.

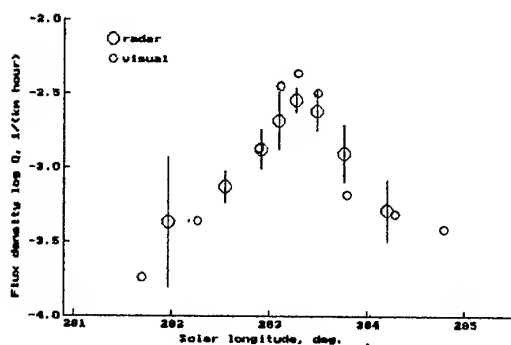


Fig. 3. Quadrantids. Comparison of radar and visual flux densities.

The minimal masses corresponding meteor echo duration  $T=1$  second were found taking into account meteor characteristic heights equal to 93.5 km for Geminids and 95 km for Quadrantids. The minimal meteoroid masses corresponding visual meteors  $+3^m$  have been found for the both of showers as 0.084 g for Geminids and 0.055 g for Quadrantids. Corresponding values of  $\Sigma$  are  $12560 \text{ km}^2$  and  $13236 \text{ km}^2$  were found as the ration

$$\Sigma = ZHR Q$$

### 3. COMPARISON OF REDUCED DATA.

The next stage of the analysis is the reduction of the data obtained by the three methods of observations to the one minimal meteoroid mass  $m_0 = 10^{-3} \text{ g}$ . To do a flux reduction in the mass range of two orders one has to know the mass exponent  $S$  with the accuracy not less than 0.01. The iteration method was used to find the  $S$  profile for the both showers (Figs. 4 - 5).

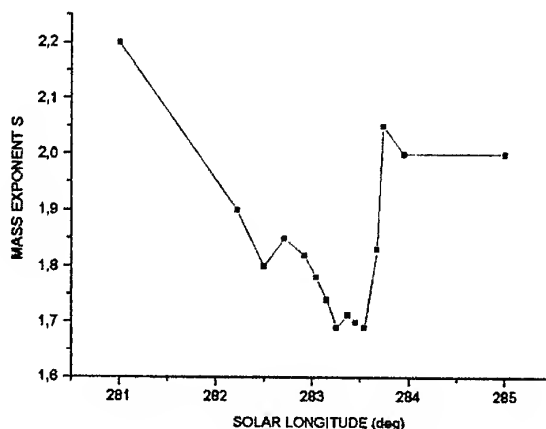


Fig. 4. Quadrantids.  $S$  as a function of Solar longitudes

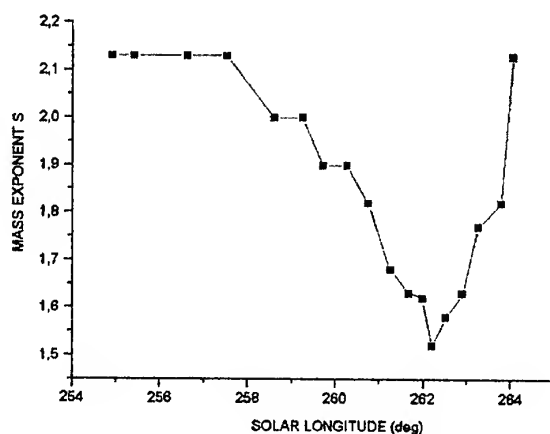


Fig. 5. Geminids.  $S$  as a function of Solar longitudes

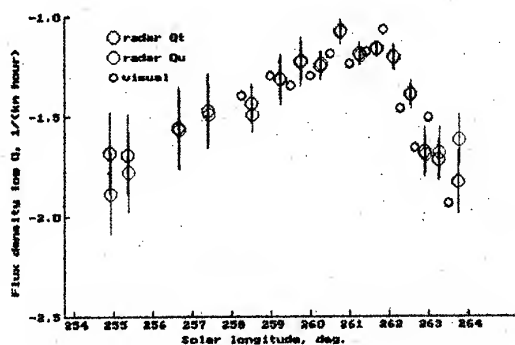


Fig. 6. Geminids. Radar and visual flux densities reduced to  $10^{-3}$  g.

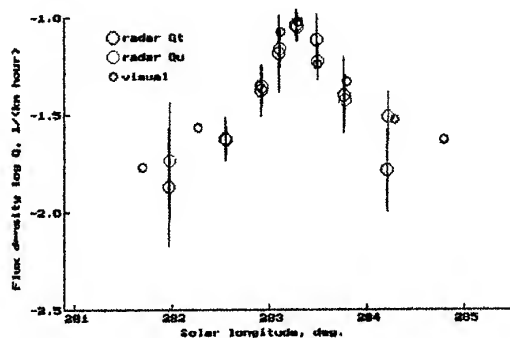


Fig. 7. Quadrantids. Radar and visual flux densities reduced to  $10^{-3}$  g.

The reduced to the mass  $m_0 = 10^{-3}$  g profiles of fluxes for the showers are shown in Fig. 6 and in Fig. 7. The coincidences of the results confirm the reliability and the accuracy of our methods of observational data reduction.

#### 4. REFERENCES

1. Belkovich O.I., *Statistical theory of radar meteors*, Kazan, 102, 1971.
2. Belkovich O.I., Tokhtashev V.S., *Determination of the Quadrantid incident flux density, Part 1*. Bull. Astron. Inst. Czechosl., Vol. 25, No. 2, 112, 115, 1974.
3. Belkovich O.I., Suleymanov N.I., Tokhtashev V.S., *The Geminid from the results of radar, photographic and visual observations*, Meteor matter in the interplanetary space. Moscow, 88-101, 1982.
4. Belkovich O.I., Suleymanov N.I., Ishmukhametova M.G., *Modern methods of meteor visual observation reduction*, Solar System Res, (in publication), 2001.

# TEMPORAL STRUCTURE OF METEOROID STREAM AND LUNAR SEISMICITY ACCORDING TO NAKAMURA'S CATALOGUE

Oleg B. Khavroshkin , Vladislav V. Tsyplakov,  
Schmidt United Institute of Physics of the Earth,  
RAS Moscow, Russia, e-mail: [khavole@uipe-ras.scgis.ru](mailto:khavole@uipe-ras.scgis.ru)

Nakamura and Oberst pioneered in receiving data on the problem of meteoroid clustering streams which require analysing of wide range their temporal time structure. As a continuation of their research we have derived some types of temporal series. . All series were studied by spectral analysis and as a result, common periodicity for all series and supplementary picks in only two series were obtained. Spectrum of the series (1969-1977) disclosed time picks on Mercury, Venus and Earth orbital periodicity (88; 115; 225; 365, 27.3 days). Comparative analysis of spectra for other series disclosed following periodicity picks: 44; 27; 5,5; 3,7 and others.. The 10 and 5-days picks are exceptionally interesting, because magnetic solar storms have the same periodicity. The dust component of meteoroid streams similar to dust plasma probably is modulated by variation of solar magnetic fields. Thin temporal structure of temporal variation of meteoroid streams has the picks which coincide with half-periods of neighbourhood binary star systems ( 2.2 day - UWCma; 3.6 days - hAql).

Nakamura and Oberst pioneered in receiving data of clustering of meteoroid streams from impact seismograms [1]. Definite tendencies are self-displayed at the conference «Meteoroids-2001». Searches of some ob-served meteoroid trails contain experimental data of record short variations of their activity (Rentel) [2]; nature of day and year changes were analyzed (K.Ohnishi, S.Hattori, O.Nishinura at all) [3], and experiments of dust streams detecting in the neighbourhood of Jupiter by cosmic crafts have displayed «existing» of Io (A.Graps,

E.Gruen, H.Krueger et all) [4].As a continuation of their research we have derived some types of temporal series. Two series 1 and 7 years in persistence (1974 and 1969-1977) are the temporal sequences of sum numbers of impacts per time unit (one day, three days). The third series one year in persistence (1974) is the temporal sequence of impact events and time intervals between them according to Catalogue. We adopted that event amplitudes are equal to one unit. The duration of these events was obtained from impact

seismograms. The forth series with the same persistence (1974) is the temporal sequence of values equal to duration of impacts averaged through day. The scheme of 3<sup>rd</sup>

and 4<sup>th</sup> series making up is explained on Fig.1.

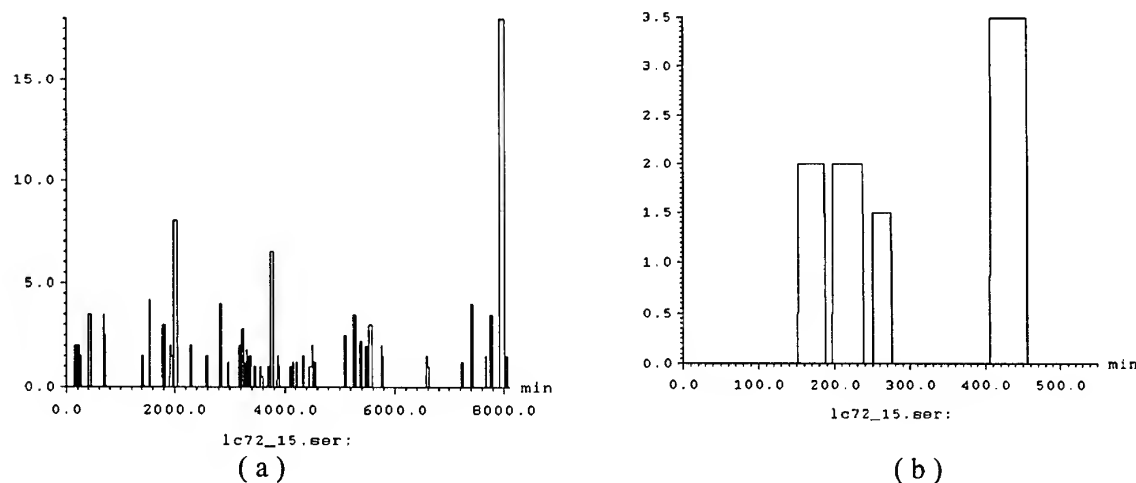


Fig.1(a,b) Exemple of presentation of Catalogue of lunar seismicity as a temporal series for constructing histogram and for further analyzing: (a) the general view of temporal series; (b) part 1 of this series (a) on an enlarged scale; t-current time in minutes, A- amplitude of seismic signal in relative unites.

All series were studied by spectral analysis. Appreciation of reliability, time resolution of spectra picks, smoothing and other procedures of spectra data processing of all series are carried out in accordance with Bendat and Pirsol [5]. Results of analysed series are represented in Fig.2 and 3.

Spectra A, B, C (Fig.2) have been averaged and smoothen over the ensemble and frequency throw 24 degrees of freedom (n) for  $\overline{\chi_u}$  - square distribution according to normalized standard deviation

$$\sigma = \sqrt{\frac{2}{n}} \cong 0.29.$$

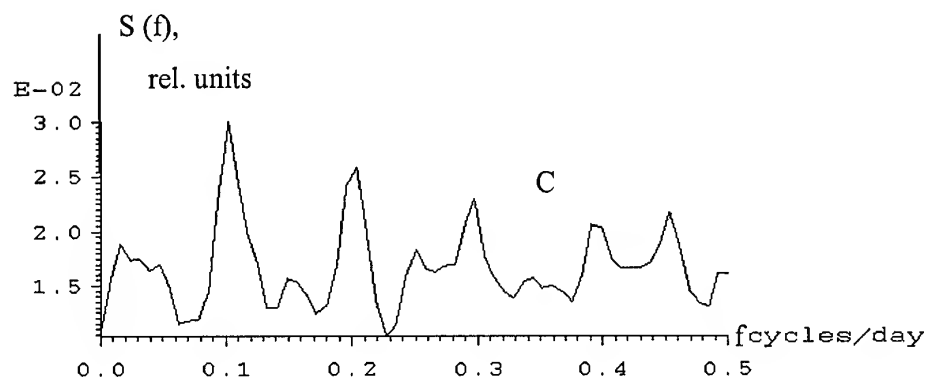
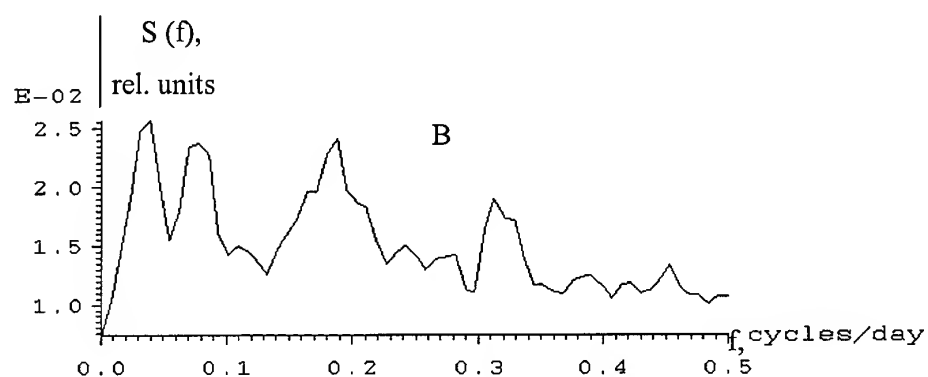
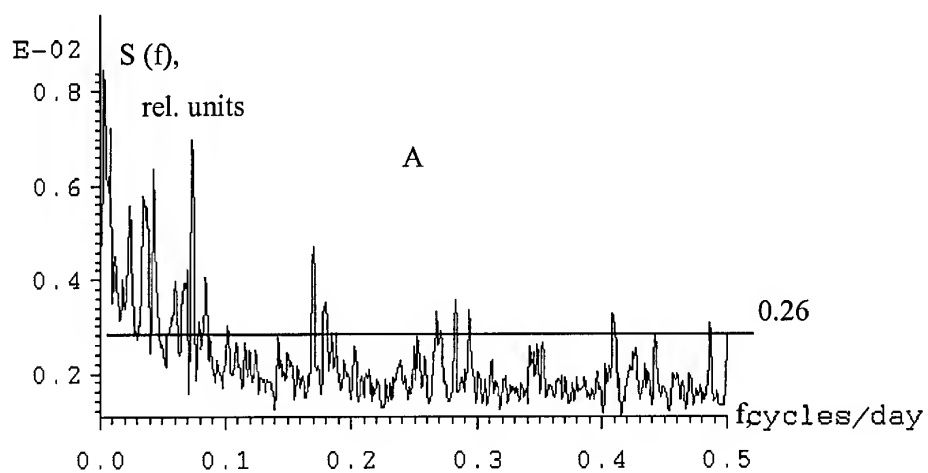
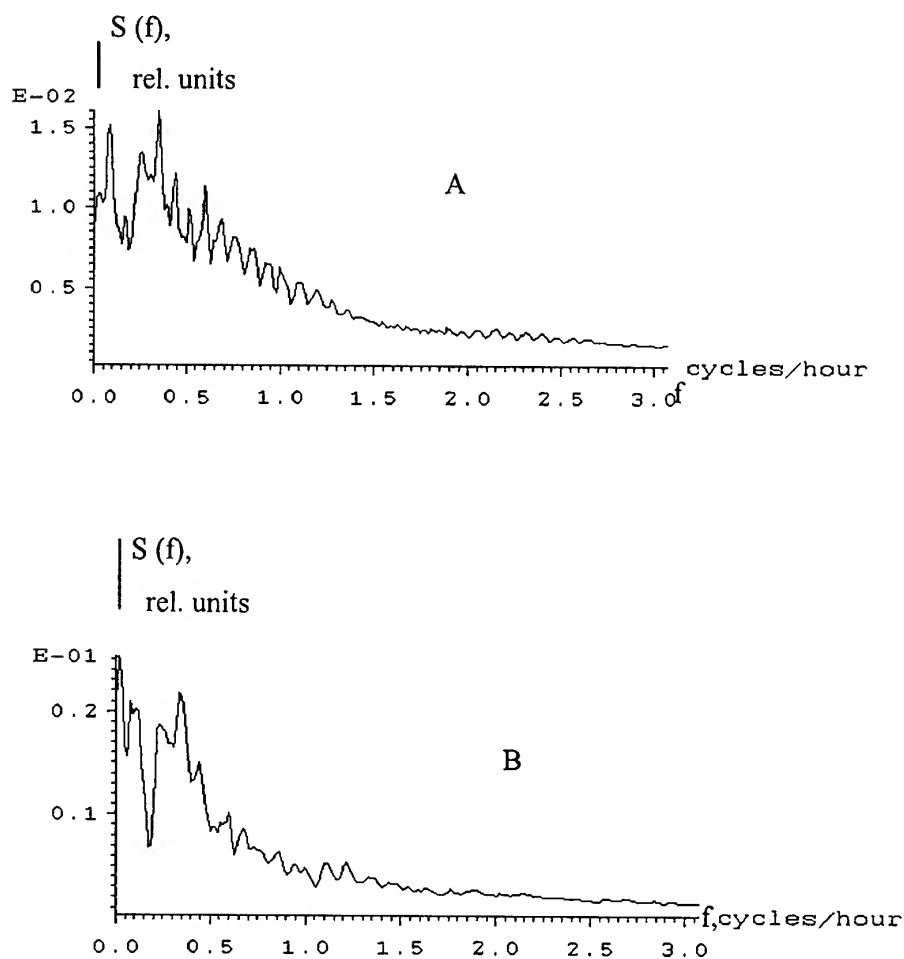


Fig.2 Power spectra of temporal series.

A - spectrum of series, which was built using number (n) meteoroid impacts per day as amplitudes for elements of series (1969-1977). B - similar to A, but only for 1974.

C - spectrum of series, which was built using average duration of impacts seismograms per day (1974).

Spectra A and B (Fig. 3) have been made for  $n = 12$  and thus  $\sigma \cong 0.4$ .



*Power spectra of temporal series of lunar meteoroids seismicity at a period of meteoroids stream "Quadrantides" (1974,01-16 January).*

A - spectrum of series, which was made using amplitudes of the impacts seismogram as amplitudes of elements of the temporal series.

B - spectrum of series, which was made using durations of seismograms as amplitudes for elements (parts) of temporal series.

Joint comparative analysis of spectra (A, B) reveals common periodicities (T in hours): 27; 8,3; 7.0; 6,35; 5,7; 3,3.

Spectrum of the series (1969-1977) disclosed time picks on Mercury, Venus and Earth orbital periodicity (88; 115; 225; 365, 27.3 days). Comparative analysis of spectra for other series disclosed following periodicity picks: 44; 27; 5,5; 3,7 (for first series 1974 in persistence); 10; 5; 3; 2.5; 2.23 days (for third series); 10; 5; 3,3; 2.5; 2,23 days (for forth series). The 10 and 5-days picks are exceptionally interesting, because magnetic solar storms have the same periodicity. The

dust component of meteoroid streams similar to dust plasma probably is modulated by variation of solar magnetic fields. Thin temporal structure of temporal variation of meteoroid streams has the picks which coincide with half-periods of neighbourhood binary star systems ( 2.2 day - UWCma; 3.6 days - hAql). Picks of the spectra in excess of 0.26 relative units of the amplitude level (Fig.2A) are used for making up and analyzing Table I.

**Table 1**

A comparison between observed periods  $T$  of the peaks of spectrum of variations of the number of meteoroid impacts on the Moon (1970 - 1977) and orbital periods of some planets and their satellites

N	A	$T$ , days	$\Delta$ Resolution days	The name of the planet or satellite	Orbital period, days	Resonance relations
1	84	350	90	Earth	365,256	$f_E$
2		230	42	Venus	224,695	$f_V$
3	72	128	13	VI; Jup	250,6	$2f_V, 3f_E, 2f_{VI}$
4	44	85	5,6	Mercury	87,969	$f_M$
5	39	57	2,6			$4f_V$
6	54	42,6	1,4	Giperion	21,28	$2f_M, 0.5f_{Gp}$
7	55	27,5	0,6	Moon	27,32	$f_L$
8	63	23,3	0,4			$10f_V, 0.25f_{Tr}$
9	40	16,69	0,3	Kallisto	16,689	$f_K$
10	42	14.4	0,3			
11	70	13,6	0,15	Moon	13,6	$2f_L$

12	40	11,9	0,12			$20f_V$
13	30	9,8	0,1			$9f_M$
14	27	9,3	0,1			
15	27	8,6	0,1			
16	28	7,1	0,05	Ganimed	7,154	$f_G$
17	47	5,9	0,03	Triton	5,87	$f_T$ ,
18	35	5,6	0,03			
19	26	4,95	0,03			
20	28	4	0,02			$60f_V, 4f_K$
21	33	3,75	0,02	Tetis	1,888	$24f_M, 0,5f_T$
22	36	3,55	0,01	Europe	3,551	$f_{Eu}$
23	34	3,41	0,01			
24	26	2,87	0,01			
25	33	2,45	0,005	Ariel	2,520	$32f_M, f_{Ar}$
26	28	2,26	0,005	Reia	4,518	$12f_L, 2f_{Re}$
27	31	2,05	0,005			

All picks of the spectra B and C (Fig.2) are used for making up Table II and III.

Table 2

A comparison between  $T_n$  - values of the periods for peaks of spectrum of variations of the number of meteoroids per day ( $n$ ) and the orbital periods of some planets and their satellites.

N	$T_n$ (days)		The orbital periods (days)	Expected frequencies which exhibit resonance
1	85	Mercury	87,969	$f_M$
2	42,7	Mercury	$T/2 = 44$	$\sim 2f_M$

3	19,7	Mercury		$\sim 4f_M$
4	13,8	Moon	$T/2 = 13,8$	$0.5 f_L$
5	11,3	Triton	5.87	$0.5 f_{tr}$
6	9,0	Reia	4.518	$0.5 f_{rei}$
7	8,1	Titania	8.706	$f_{tit}$
8	6,6	Ganimed	7,154	$(f_G + f_T)/2$
9	5,9	Triton	5,87	$f_T$
10	3,5	Europe	3,551	$f_{Eu}$
11	2,7	Diona	2.737	$f_D$
12	2,5	Ariel	2.52	$f_A$
13	2,4	Ganimed	7.154	$3f_{gn}$

Table 3

A comparison between  $T \tau_{ms}$  - values of the periods for peaks of spectrum of variations of average duration of meteoroid seismogram ( $\overline{\tau_{MS}}$ ) per day which is induced by the same meteoroids on the Moon at 1974 and the orbital periods of some planets and their satellites.

N	$T \tau_{ms}$ (days)	The name of the planet	The orbital periods (days)	Expected frequencies which exhibit resonance
1	85,3	Mercury	87,969	$f_M$
2	36,6	Earth	365,256	$\sim 10f_E$
3	18,9	Earth	-	$20f_E$
4	9,70	Reia	4.518	$0.5 f_{rei}$
5	8,4	Kallisto	16.69	$0.5 f_{tk}$
6	6,5	Ganimed	7.154	$f$
7	4.9	Reia	4.518	$f_r$
8	4.0	Titan	15.95	$4 f_{tn}$
9	3.4	Io	1.769	$0.5 f_{io}$
10	2,5	Ariel	2.52	$f_A$
11	2,2	Reia	4.518	$2f_R$

$$\overline{\tau_{MS}} = \frac{\sum_{i=1}^n \tau_{iS}}{n}, \quad \tau_{iS} \text{ — the duration of seismogram of } i\text{-impact,}$$

$$\sum_{i=1}^n \tau_{iS} \text{ — sum of meteoroid of impact seismograms per day,}$$

$$n \text{ — the number of impacts per day}$$

Spectra of meteoroid trails «Quadrantides» (Fig.3) were compared. Joint comparative analysis of spectra A and B reveals common periodicities (T in hours): 27; 8.3; 7.0; 6.35; 5.7; 3.3. Furthermore, from the common analysis of the reference book (K.Loders, B.Fegley) [6] it is followed: spectra picks with periodicities of the Earth and the Moon rotation have, of course, maxima amplitudes. It is determined by the physical mechanism of modulation effect of meteoroids streams and seismic, geophysic peculiarities of the recording system of «Apollo» network. The pronounced pick with the period  $Prot = 24.0$  days reflects the important role of the Sun. Amplitude picks which are set by Mercury moving are juxtaposed. The main pick connects with the sinodic period and may be probably classified as effect of modulation of the streams which move from the Sun side. Amplitudes of the picks with Mercury sideric and own rotational periods decreasing smaller compared with the above mentioned. The first pick is determined possibly by effect of modulation of the stream of interstellar dust and sporadic background with smaller power.

The second pick is set by slight magnetic field of the planet. The group of the next picks is determined by periods of Jupiter satellites. A few picks coincides with orbital Kalisto, Ganimed, Europe and Dion periods. Other picks are multiple of period Europe, Io, Amalten. Some spectra picks we can attribute to the satellites of Saturn (Dion, Giperion, Reia, Titan, Tatis) and Uranium (Titania, Ariel, Umbriel) and Neptun. One pick only coincides appoximately with Dion orbital period. The Saturn satellites group of other picks are multiple of fractional periodes Giperion, Reia, Titan and Tatis. Two picks correspond to orbital periods of Titania and Ariel and one pick to the first harmonic of Umbriel. The Triton is the only satellite of Neptun which is represented by the orbital period pick and his subharmonic. Thus, the picture of received data confirms the important role of giant planets systems as capacital dust stream sources, which head for internal planets and the Sun, and the existence of dust stream from periphery (Belt of Kuiper). We suppose that the pick corresponding to the Hiperion subharmonic

may also be related to the second Mercury harmonic. The picks with the period of 11.9 and 23.3 days and high amplitude are not identified, but we consider that both of picks may be corresponded to the hypothetic interior planet between Mercury and the Sun or an unknown satellite of a giant planet et cetera. High frequency pulsation which is due to the isolated meteoroid stream («Quadrantids», Fig.3) manifested in lunar seismicity and may be recorded as ground-based observation for shorter periods only [2]. Information received about time structure of meteoroid stream bases on seismograms. These seismograms reflect action of the dust-gas plasma component of the stream incident on lunar day surface. Therefore, it is necessary to analyze the particular increase of seismic efficiency of interaction between dust-gas plasma of meteoroid stream and lunar surface. It is known that the efficiency of transformation of original energy of different seismic sources into energy of wave field is normally about 1-3%. According to common views, the efficiency of shock interaction between dust-gas part of meteoroid stream and lunar surface may be below this level. But the next peculiarities of this interaction can increase the efficiency of this transformation: 1. The dust-gas component of meteoroid stream can be considered as dust-gas plasma (concept of Alfén [7]). 2. The cathode luminiscency of regolith and variant of it, for example one which have solar

origin, allow to consider lunar surface as changed one under interaction with dust-gas plasma of meteoroid stream [8]. 3. The duration of the seismic signal under this interaction (2) is deduced from processes which modulate both regolith structure (deformation waves) and cosmic factors which operate on regolith. 4. Particularities of (1) and (2) are increased by exoelectron emission of regolith [9,10] and metal particles of it [11]. 5. Detectable local magnetic fields which were recorded by «Lunar Prospector» and their interaction with exoelectron-emission effects [12,13]. 6. The potentialities of existence and occurrence of dust-gas acoustic shock waves [14].

## REFERENCES

1. Oberst J. and Nakamura Y. A Search for Clustering among the Meteoroid Impacts Detected by the Apollo Lunar Seismic Network, ICARUS, Vol. 91, 315-325, 1991.
2. Rendtel J., On Periodic Activity Variations the 1999 Leonid Meteor Storm in Various Data Sets, Abstracts of the Conference METEORIDS 2001, Swedish Institute of Space Physics, Kiruna, Sweden, 6-10 August 2001, p.13.
3. Ohnishi K., et al., PSB-6 the Earth Rotation and Resonance Effect of the Daily and Annual Variation of Sporadic Meteor Echo by HRO, *ibid*, p.81.

4. Graps A., et al, Io Revealed in the Jovian Dust Streams, *ibid*, p.96.
5. Bendat J.S. and Pierson A.G., Random Data: Analysis and Measurement Procedures, Wiley-Interscience, A division of Y.Wiley and Sons, Inc. New York-London- Sydney-Toronto, 1975.
6. Ladders K. and Fegley B., The Planetary Scientist's Companion, N.Y., Oxford, Oxford University Press, P. 371, 1998.
7. Alfen H. and Arrhenius G., Evolution of the Solar System, NASA, Washington, D.C., 1976.
8. Spivak G.V. et al, The Cathodoluminescence of Lunar Regolith Returned by the Automatic Station Luna 16. Lunar Soil from Sea of Fertility, Academy of Science of the USSR, Publishing House «Nauka», Moscow, P.624, 1974.
9. Mintz R.I. et al, Temperature Spectrum of Exoelectron Emission of the Lunar Regolith, *ibid*.
10. Mintz R.I. et al, Exoelectrons Emission of the Particles of the Lunar Regolith. Lunar Soil from Sea of Fertility, *ibid*.
11. Balazin M. and Zetzsche A., PHYS.STAT.SOL., Vol.2, 1670-1674, 1962.
12. Mintz R.I. et al, Exoemission Activity of Highland Regolith. Regolith from the Highland Region of the Moon, Academy of Science of the USSR, Publishing House «Nauka», Moscow, P.708, 1979.
13. Mintz R.I. et al, Exoemission Activity of Fragment from Luna 20 Soil, *ibid*.
14. Melands F. and Shukla P.K., Theory of Dust-Acoustic Shocks, PLANET.SPACE SCI., Pergamon, Vol.43, 635-648, 1995.

## ON A FINE STRUCTURE OF THE PERSEID METEOROID STREAM. METHOD OF INDICES

J. Svoreň<sup>(1)</sup>, V. Porubčan<sup>(2)</sup>, L. Neslušan<sup>(1)</sup>

<sup>(1)</sup>*Astronomical Institute of the Slovak Academy of Sciences, SK-059 60 Tatranská Lomnica, The Slovak Republic,  
Email: [astrsven@ta3.sk](mailto:astrsven@ta3.sk), [ne@ta3.sk](mailto:ne@ta3.sk)*

<sup>(2)</sup>*Astronomical Institute of the Slovak Academy of Sciences, Dúbravská 9, SK-842 28 Bratislava, The Slovak Republic,  
Email: [astropor@savba.sk](mailto:astropor@savba.sk)*

### ABSTRACT

A fine structure of the Perseids is studied using a method of indices.

The procedure, based only on mathematical statistics, is now used to study of a fine structure of the Perseid stream and its filaments which cannot be separated reliably by iteration methods. Besides the five orbital elements incorporated in the Southworth-Hawkins *D*-criterion, we have also included in the procedure the coordinates of the radiant which are one of the most accurately known parameters and the geocentric velocity as a significant parameter characteristic for physically related orbits.

351 (approx. 67%) of 522 Perseids taken into account were assigned to one of 11 chosen filaments of orbits.

### 1. INTRODUCTION

A method of indices was firstly used to identify the major meteor streams from the IAU Meteor Data Center Lund catalogue of precise photographic orbits [5] (hereinafter referred as Paper 1). In that test run, all the major streams (except of the northern branch of  $\delta$ -Aquarids) were identified, confirming the efficiency of the procedure. Besides the identification of the streams and associations, the method also enables a study of a fine structure of streams and their filaments which cannot be reliably separated by an iteration method. In this paper, we use the method of indices to study a fine structure of the Perseid meteoroid stream.

A detail description of the method was published in Paper 1. That is why we here inform about it only briefly to remind basic ideas of the method. The first step of the procedure is a division of the observed ranges of parameters into the appropriate successive equidistant intervals and assignment of indices to a meteor according to the interval pertinent to its parameters. Besides the five orbital elements

incorporated in the Southworth-Hawkins *D*-criterion, we have also included in the procedure the coordinates of the radiant which belong to the most accurately known parameters and the geocentric velocity as a significant parameter characteristic for physically related orbits. The relative ratios, approximated by small integers, corresponding to the reciprocal values of the relative errors of the parameters have been applied as the basic numbers for the division of the parameters. A group of meteors with the same indices reflects a similarity among the orbits. It is clear that the chosen number of intervals influences the number of groups. In the case of sufficiently detail division, meteors assigned to a given stream or a filament of the stream can fall into a few related groups.

### 2. MATERIAL USED

The IAU Meteor Data Center Lund catalogue of precise photographic orbits [2] is used. The meteors with heliocentric velocities higher than 48 km/s are rejected from the analysis and thus the final set consists of 3411 orbits [4].

Table 1. Ranges of the parameters in the selected Perseids

parameter	range
q	0.743 – 1.014 AU
e	0.535 – 1.554
$\omega$	114.9 – 182.9°
$\Omega$	109.9 – 169.8°
i	93.5 – 124.0°
$\alpha$	2.1 – 73.6°
$\delta$	49.1 – 68.5°
$v_g$	52.40 – 66.91 km/s

To acquire a basic data set for the Perseids, the method of indices is also used and a total 522 orbits of Perseids are selected (Paper 1). In the next step of the procedure the ranges of the parameters of real values in the selected set mentioned above were obtained (Table 1).

On the basis of the results presented in Paper 1, we use individual numbers of intervals in the division of each parameter reciprocally proportional to the relative errors of parameters. In this procedure an infiltration of each group into neighbouring intervals is almost equilibrated. The errors of parameters for the Perseid stream are taken from our paper concerning the determination of the mean orbits of meteoroid streams [3]. Table 2 lists the parameters, the errors for the Perseid stream parameters, the ranges - differences between the uppermost and lowest values from Table 1, the ratios of the range to the mean errors, the ratios of the range to the mean errors divided formally by an empirical value (2.52 in our case) fulfilling a condition to obtain values not too different from the closest integer, and the last column of Table 2 lists the corresponding nearest integer of the division.

By the way, a comparison of this basic set with the whole database shows that relative precision of parameters is considerably higher. If we set the precision of determination of  $e$  and  $q$  on the same level for both the Perseids and whole database, the precision of  $V_g$  for Perseids is 1.5-times higher. For  $\omega$ ,  $\Omega$  and  $i$  it is 2-times higher, and for  $\alpha$  and  $\delta$  3-times higher, so far. Of course, these results are not surprising, because a convergence of values to the characteristic value of a stream is expected.

The results of a search for compact groups (the meteors of a given group are characterized with the exactly equal set of indices) within the Perseid stream are in Table 3. We introduce the term "association" in the Table 3 for a group of meteors which contains minimally 3 similar orbits.

Table 2. The mean errors  $E$  and the numbers of intervals of basic division of parameters

	error $E$	range	range/ $E$	range/ $E$ / 2.52	numb. of intervals $M$
$q$	0.018	0.271	15.06	5.97	6
$e$	0.101	1.019	10.09	4.00	4
$\omega$	4.5	68.0	15.11	5.99	6
$\Omega$	3.4	59.9	17.62	6.99	7
$i$	2.5	30.5	12.20	4.84	5
$\alpha$	5.4	71.5	13.24	5.25	5
$\delta$	1.6	19.4	12.12	4.81	5
$V_g$	1.4	14.51	10.36	4.11	4

One can see (Table 3) that the basic numbers of division of parameters (last column of Table 2) and their 2-multiples give very similar numbers of associations. We prefer the results obtained with using of 2-multiple of the basic numbers with a lower number of members (293 from the whole set of 522) giving more concentrated, less dispersed associations. So we work with 36 associations numbered 1-36 where

counts of orbits in these associations differ from 3 (several cases) to 23 (ass. No. 15).

Table 3. The numbers of groups of related orbits

multiple of basic set of numbers $M$	number of meteors	number of associations
1	444	40
2	293	36
3	180	23
4	85	9
5	51	4
6	17	1
7	16	0
8	12	0
9	8	0
10	2	0
11	2	0
12	6	0
13	0	0

### 3. FILAMENTS IN THE PERSEID STREAM

A filament of the Perseid stream can be characterized with a mean parameter being very close to the border between two intervals of our division. In such a case, the appropriate index corresponds with both the neighbouring intervals, i.e. it is not unique and the filament is split into two associations. Or, it can be split into several associations, if more mean parameters of the filament are close to the appropriate borders of their divisions. In the following, we look for the clusters and associations, which can be identified with the filaments of the stream.

A clustering of orbits in space means a clustering of their orbital parameters. If we deal with the associations of orbits, this is true for their mean parameters. So, let us consider the associations and construct the plots showing the meaningful dependences of their mean parameters on each other. The result is a finding that the dependences  $q = q(e)$ ,  $q = q(\omega)$ , and  $\omega = \omega(\Omega)$  (Figs. 1-3) are sufficient to decide if particular associations are the components of a given clustering. The mentioned dependences are not affected by the variation of elements due to the seasonal change of  $\Omega$ . Kresák and Porubčan [1] show that  $e$  and  $q$  do not vary with the change of  $\Omega$  and the variation of  $\omega$  is minimum. We find an apparent linear dependence  $q = q(\omega)$ , whereby  $dq/d\omega = +0.0041$ .

A clustering of associations in a single parameter can occur coincidentally. If a given set of associations actually create a given filament, then the clustering has to be observed in each parameter. Actually, the plots show that the associations have a tendency to create relatively isolated areas in the graphs - 8 areas for the

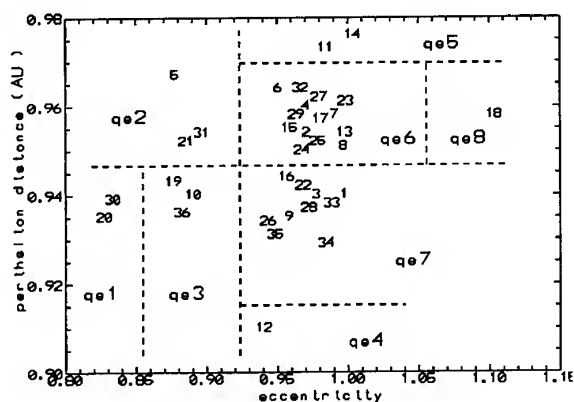


Fig. 1 Perihelion distance and eccentricity for 36 associations

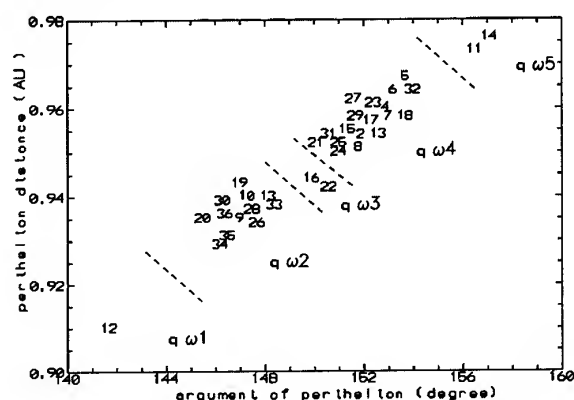


Fig. 2 Perihelion distance and argument of perihelion for 36 associations

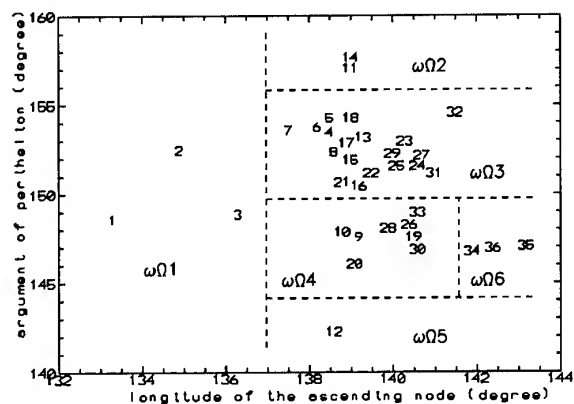


Fig. 3 Argument of perihelion and longitude of the ascending node for 36 associations.

dependence  $q = q(e)$ , 6 areas for  $\omega = \omega(\Omega)$ , and 5 areas for  $q = q(\omega)$ . Almost all the associations detected within an area on one graph are also detected within one area on the other two graphs. For example,

associations 11 and 14 are into the areas of  $q\omega 5$ ,  $qe5$ , and  $\omega\Omega 2$ . It means that there is a large mutual coherence among parameters, e.g. all the orbits of assoc. 11 and 14 have only the largest values of  $\omega$  (above 156.0), the largest values of  $q$  (above 0.967) and also the largest values of  $e$  (above 0.924). In total  $8 \times 6 \times 5 = 240$  combinations are possible, but only 11 are actually present in the data (here designed as filaments A – K, Table 5).

Table 4: Limits of parameters

parameter	range	designation
$\Omega$	below 137.0	$\Omega 1$
	137.0 – 141.7	$\Omega 2$
	above 141.7	$\Omega 3$
$\omega$	below 143.5	$\omega 1$
	143.5 – 149.4	$\omega 2$
	149.5 – 156.0	$\omega 3$
	above 156.0	$\omega 4$
$q$	below 0.915	$q 1$
	0.915 – 0.937	$q 2$
	0.938 – 0.946	$q 3$
	0.947 – 0.967	$q 4$
	above 0.967	$q 5$
$e$	below 0.855	$e 1$
	0.855 – 0.924	$e 2$
	above 0.924	$e 3$

Table 5: Filaments in the Perseid stream

interval used	attached associations	design. of filaments	numbers of orbits	% in the $\Omega$ -interval
$\Omega 1, \omega 2, q 2, e 3$	1, 3	A	11	10
$\Omega 1, \omega 3, q 4, e 3$	2	B	43	37
$\Omega 2, \omega 1, q 1, e 3$	12	C	8	2
$\Omega 2, \omega 2, q 2, e 1$	20, 30	D	6	2
$\Omega 2, \omega 2, q 2, e 2$	10, 19	E	16	4
$\Omega 2, \omega 2, q 2, e 3$	9, 26, 28, 33,	F	28	7
$\Omega 2, \omega 3, q 3, e 3$	16, 22	G	22	6
$\Omega 2, \omega 3, q 4, e 2$	21, 31, 5	H	24	6
$\Omega 2, \omega 3, q 4, e 3$	4, 6, 7, 8, 13, 15, 17, 23, 24, 25, 27, 29, 32	I	152	41
$\Omega 2, \omega 4, q 5, e 3$	11, 14	J	35	9
$\Omega 3, \omega 2, q 2, e 3$	34, 35	K	6	19

The empirical limits among the filaments were obtained from the graphs and they are listed in Table 4. The limits of some parameters can be influenced by our preceding division of ranges into intervals (e.g. partially by the eccentricity limits in the  $\Omega 2$  interval) but the limits in Table 4 are mostly caused by the natural distribution of orbits. One can notice that at the adjacent region of the stream maximum we use the limits 135.57, 139.85 and 144.13 in the procedure of

division of parameter  $\Omega$ , but the natural limits obtained from the graph are very different (137.0 and 141.7).

The derived limits are in the next step used to search in a whole datafile of 522 Perseids, not only among 293 orbits assigned to one of detected associations. 67% of the Perseid orbits are selected to 11 filaments, which are listed in Table 5. The mean orbital elements, the coordinates of geocentric radiant and geocentric velocity of the 11 filaments found are given in Table 6. The mean eccentricity (3-rd column) of five filaments (A, B, G, I, and J) exceeds unity. This is obviously an effect of a large uncertainty of this element caused by a high geocentric velocity of the stream and following errors of measurements, resulting in a higher dispersion of the measured orbits. The high determined values indicate the high real values, but the corresponding real orbits are obviously elliptic. In the given context, we note that the uncertainty of the mean eccentricity of the Perseids, as determined from the selected set of orbits [3] can vary from 0.852 to 1.054, and that of low numerous associations is even larger.

Table 6: Mean orbits of Perseid filaments

	q	e	$\omega$	$\Omega$	i	$\alpha$	$\delta$	$V_g$
A	0.931	1.010	147.0	134.3	110.9	42.9	58.2	58.95
B	0.955	1.008	152.1	132.2	112.3	37.1	56.4	59.42
C	0.902	0.988	141.2	139.5	111.7	53.6	59.0	59.05
D	0.931	0.811	145.0	139.5	112.1	48.6	57.8	57.47
E	0.930	0.896	146.1	139.6	112.7	49.6	58.0	58.49
F	0.929	0.986	146.8	139.5	113.2	50.1	58.2	59.56
G	0.944	1.011	150.2	139.3	112.8	47.6	58.2	59.70
H	0.955	0.902	151.5	139.4	113.5	45.8	57.4	59.02
I	0.956	1.014	152.6	139.2	113.5	46.1	57.9	60.05
J	0.981	1.108	160.6	139.1	113.6	40.9	57.7	61.00
K	0.933	0.975	147.2	144.1	113.3	56.4	59.2	59.45

The selected filaments are with a high probability real filaments of orbits in the space (however, many of them are so small numerous that they fade in the field of all orbits). To support their real existence we note that each of the derived filaments consists of meteors observed in different years. It also means that the filaments do not represent any clustering of meteoroids in some positions on the orbit but long-time structures of the stream. The obtained result documents the applicability of the method of indices for an efficient analysis of a fine structure of major meteor streams.

**Acknowledgements.** This research was supported by VEGA - the Slovak Grant Agency for Science (grants No. 1023 and 1026).

#### 4. REFERENCES

1. Kresák L. and Porubčan V. The Dispersion of Meteors in Meteor Streams, *BULL. ASTRON. INST. CZECHOSL.*, Vol. 21, 153-170, 1970.

2. Lindblad B.A. and Steel D.I. Meteoroid Orbits Available from the IAU Meteor Data Center, *ASTEROIDS, COMETS, METEORS 1993*, Kluwer, Dordrecht, 497-501, 1994.

3. Neslušan L., et al. A Procedure of Selection of Meteors from Major Streams for Determination of Mean Orbits, *EARTH, MOON, PLANETS*, Vol. 68, 427-433, 1995.

4. Porubčan V., et al. On Separation of Major Meteoroid Streams from the Sporadic Background, *EARTH, MOON, PLANETS*, Vol. 68, 471-478, 1995.

5. Svoreň J., et al. A Search for Streams and Associations in Meteor Databases, Method of Indices, *PLANET. SPACE SCI.*, Vol. 48, 933-937, 2000.

## THE NEW METEOR SHOWER $\eta$ ERIDANIDS

K. Ohtsuka<sup>(1)</sup>, T. Tanigawa<sup>(2)</sup>, H. Murayama<sup>(1)</sup>, I. Hasegawa<sup>(3)</sup>

<sup>(1)</sup> Tokyo Meteor Network, 1-27-5 Daisawa, Setagaya-Ku, Tokyo 155-0032, JAPAN

Email: ohtsuka@jb3.so-net.ne.jp

<sup>(2)</sup> Arima High School, 2-1-50 Tenjin, Sanda C., Hyogo 669-1531, JAPAN

<sup>(3)</sup> Ottemae University, Faculty of Socio-Culture, Inano, Itami 664-0861, JAPAN

### ABSTRACT

We discovered the new meteor shower,  $\eta$  Eridanids, active in late July to mid-August by analyzing the optical meteor data besides the visual and radar ones obtained so far. We also found two comets as parent candidates of the  $\eta$  Eridanids, Periodic Comet Pons-Gambart D/1827M1 and Comet Chacornac C/1852K1; and further, Comet Chacornac, rather than Comet Pons-Gambart, seems to be possibly associated with the  $\eta$  Eridanids.

### 1. INTRODUCTION

The Tokyo Meteor Network photographic meteor program [1] is still operating, using 35 mm-size cameras equipped with  $f/1.85 \sim 135$  mm objective lenses. Approximately 200 double-station meteors have been obtained so far,  $\sim 10\%$  meteors being the sporadics or the minor shower members. One of such non-major shower meteors was observed on August 12.74 UT, 1994, as a by-product during the 1994 Perseids observation program: a  $-1$  mag. meteor, T9408-05, radiated from near  $\eta$  Eridanus. The orbital parameters were precisely reduced since the error estimates were  $0.05^\circ$  arc and  $< 1\%$  in the radiant and velocity determinations, respectively. We found subsequently T9408-05 to be a member of the newly discovered meteor shower.

### 2. DISCOVERY OF THE NEW METEOR SHOWER: $\eta$ ERIDANIDS

#### 2.1 Optical (Photographic and TV) observations

We often use the D-criteria in investigating the orbital similarity between meteors, or a comet and meteors: e.g., DSH by Southworth and Hawkins [2]; recently proposed  $D_N$  and  $D_R$  by Valsecchi et al. [3]; etc. We applied here conventional DSH in order to survey whether the same meteor shower members as T9408-05 exist or not, discriminating by  $DSH(M, N) \leq 0.15$ , where  $DSH(M, N)$  represents DSH between a mean orbit  $M$  of the meteor stream and an individual meteor  $N$ ,

including T9408-05. As a result, interestingly, there were no associated meteors among  $\sim 6000$  orbits in the IAU photographic meteor orbit data obtained up to 1980's [4], while three associated meteors could be selected out from among  $\sim 2000$  more orbits recorded in the optical (photographic and TV) meteor catalogues published later: 2 photographic meteors, EN030895 [5] and DMS93168 [6]; 1 TV meteor, MSSIQN [7].  $DSH(M, N) \leq 0.15$  means that each individual meteor probably belongs to the same meteor shower. Furthermore, the higher  $DSH(M, N)$  threshold picked up one possible member, s8504 = NMS432, from among the IAU photographic meteor orbit data, of which linear elements indicate strong hyperbola, probably due to overestimating the atmospheric deceleration. The orbital, radiant and geocentric velocity data of these meteors along with the mean ones based on the four probable members above are given in Table 1: where EN030895, a  $-8$  mag. fireball, was the largest of all, with a photometric mass estimated to be  $\sim 30$  g as against those of the other TV and photographic meteoroids ranging in the order of  $10^{-3} \sim 1$  g. The orbital spread of the central part based on S. D. is almost comparable to those of the other annual meteor showers: e.g.,  $\eta$  Aquarids [8]; Perseids [9]; etc.

These optical observations ascertain the existence of a certain meteor shower, and then, we may designate this meteor shower as " $\eta$  Eridanids" after their radiant locations.

#### 2.2 Visual and Radar observations

Considering the radiant's daily motion, we could find some  $\eta$  Eridanid activities among visual meteor data: Hoffmeister's [10] no. 276, maximum at solar long. =  $140^\circ$ , radiant  $\alpha = 42^\circ$ ,  $\delta = -17^\circ$  (equinox 1925.0); McIntosh's [11] no. 23, active July 29–Aug. 4, radiant  $\alpha = 39^\circ$ ,  $\delta = -16^\circ$  (equinox 1900.0); Sakaguchi's [12] observation, on Aug. 5.76 UT, 1998, radiant  $\alpha = 44^\circ$ ,  $\delta = -11^\circ$  (equinox J2000), zenithal hourly rate  $\sim 6$ , comparable angular velocities with the Perseids; etc.

**Table 1.** Orbital data of the  $\eta$  Eridanids and the parent candidates (equinox J2000)

Object name	Yr	Day UT Aug.	a AU	e	q AU	$\omega$	$\Omega$	i	Radiant $\alpha$ $\delta$		V <sub>G</sub> km s <sup>-1</sup>
EN030895	95	3.05950	14.	0.932	0.956	28.4	310.339	130.9	38.4	-14.8	63.8
DMS93168	93	12.06070	-49.17	1.02	0.958	26.9	319.452	137.2	45.5	-8.7	66.3
T9408-05	94	12.74340	174.85	0.995	0.964	25.5	319.867	127.5	47.6	-14.1	63.7
MSSIQN	96	12.72543	7.11	0.864	0.968	25.4	320.3	126.1	48.7	-14.1	62.1
s8504	85	13.71257	-2.8	1.33	0.945	28.4	321.09	136.7	45.2	-9.7	69.1
mean		10.14726	20.26	0.953	0.961	26.6	317.490	130.4	45.0	-12.9	64.0
S. D.		4.10136		0.060	0.005	1.2	4.139	4.3	4.0	2.4	1.5
Ob355	68	Jul28-Aug3	3.85	0.75	0.96	28.7	307.4	133.4	36.6	-13.4	62.6
D/1827M1	13		16.26	0.950	0.807	19.311	320.061	136.452	48.8	-8.2	65.5
C/1852K1	13		$\infty$	1	0.905	37.206	319.271	131.124	43.2	-12.5	64.3

note. angular data of s8504 and Ob355 were converted from B1950 to J2000. The perihelion times of D/1827M1 and C/1852K1 are 1827 June 7.703 TT (epoch June 13.0 TT) and 1852 Apr. 20.09 UT, respectively.

On the other hand, we could notice an only record of the radar  $\eta$  Eridanids. This is Ob355 recorded by the Obninsk radar orbit survey [13]: mean data based on 6 radar meteors as shown in Table 1, where it can be seen that the orbital data of Ob355 are very similar to those of our  $\eta$  Eridanids, especially EN030895, except for the linear elements. It should also be noted that  $1/a = 0.26 \pm 0.06 \text{ AU}^{-1}$  of Ob355 is significantly larger than  $1/a = 0.0494 \pm 0.0624 \text{ AU}^{-1}$  of the optical data. This may be caused by a possible mass sorting effect inside the  $\eta$  Eridanid stream.

Therefore, these visual and radar observations sufficiently reinforce the existence of the  $\eta$  Eridanids. Nevertheless, descriptions of the  $\eta$  Eridanids have never been given in any well-known meteor shower catalogues yet. Hence, we can regard the  $\eta$  Eridanids to be a newly discovered meteor shower in the present study.

### 3. PARENT CANDIDATES: PERIODIC COMET PONS-GAMBART AND COMET CHACORNAC

We surveyed whether a parent comet of the  $\eta$  Eridanids exists or not from the "Catalogue of Cometary Orbits" [14]; consequently, we could find Periodic Comet Pons-Gambart D/1827M1 and Comet Chacornac C/1852K1 as parent candidates.

D/1827M1 was independently discovered in Hercules by J. L. Pons at Florence and J. F. A. Gambart at Marseilles during their telescopic-aided visual comet searches on June 20, 1827, when the magnitude was as

bright as 5 ~ 6. Since the absolute magnitude  $H_{10}$  was estimated at  $\sim 7$  [15], we may suppose Comet Pons-Gambart to be of an ordinary size as a comet nucleus. The periodic orbits of 46.0 and 63.8 years were computed by Ogura [16]; the latter orbital period should be more reliable. The 1827 return has only been observed and recorded so far; hence, Comet Pons-Gambart is regarded as a lost comet. However, Hasegawa [17] first pointed out a possible identification of Comet 1110K1 with D/1827M1, comparing their orbital similarity. Furthermore, Hasegawa and Nakano [18] successfully linked both orbits, integrating the comet's motion, and they also derived the improved periodic orbit of 65.6 years for D/1827M1 from 50 best positions. This orbital period is nearly equal to that of Ogura's 63.8 years. If the comet had returned 12 times between 1110-1827, the positional O-C residuals for the naked-eye observations in 1110 return should be  $0.7^\circ$  arc: it is smaller than those of  $1^\circ$  arc for Kegl's naked-eye observations in the 1737 return of Periodic Comet Swift-Tuttle 109P/1862O1 = 1992S2 [19]. There is another similar example; Carusi et al. [20] could link Comet La Hire 1678R1 (O-C residuals  $\sim 0.2^\circ$  arc in spite of naked-eye observations) with Periodic Comet d'Arrest 6P/1851M1, which should return 25 unobserved times between 1678-1851. Therefore, the linkage of C/1110K1 with D/1827M1 seems very likely if the nongravitational parameters, acting effectively on the Cometary motion, were very small during that interval. According to Hasegawa and Nakano [18], the next return of Comet Pons-Gambart is expected to be in late January, 2022; however, the conditions for observation will be not so good as those in 1110 and

1827 then.

On the other hand, C/1852K1 was discovered in Cepheus by Chacornac at Marseilles during his telescopic-aided visual comet search on May 16, 1852; then the magnitude was  $9 \sim 10$ . Its  $H_{10}$  was estimated at  $\sim 10$  [15], which may imply a smaller nucleus than Comet Pons-Gambart. Afterwards, Asten [21] determined the parabolic orbit of C/1852K1.

#### 4. COMET-METEOR ASSOCIATION

DSH between D/1827M1-mean  $\eta$  Eridanids being 0.24 as against that between C/1852K1-mean  $\eta$  Eridanids being 0.18: both are within a possible range of association. Especially, DSH between C/1852K1-EN030895 is smallest, 0.15, among all the comet-meteor pairs presented here, hence presumably associated with each other. Both comets closely approach the Earth's orbit at their ascending nodes, where the distances of the orbits between each comet and Earth, based on Hasegawa's [22]  $\omega$ - and  $q$ -adjustment methods, are 0.39 AU and 0.19 AU respectively for D/1827M1, while smaller again 0.012 AU and 0.007 AU respectively for C/1852K1, making the meteor apparitions associated with C/1852K1 more favorable. The orbital data of Comet Pons-Gambart D/1827M1 [18] and Comet Chacornac C/1852K1 [21] along with their  $q$ -adjustment meteor predictions are also given in Table 1.

Kronk [23] also pointed out an orbital similarity between Comet Pons-Gambart D/1827M1 and his discovered August Eridanids. However, the orbital elements of this meteor shower are somewhat different from those of our  $\eta$  Eridanids, and then, DSH between D/1827M1-August Eridanids reaches  $\sim 0.4$ , evidently being out of the association range.

Since Comet Pons-Gambart is one of the short-period comets with an orbital period  $\sim 65$  yr, we next investigated whether the meteoroids ejected from Comet Pons-Gambart in the past encountered the Earth's orbit or not, using the ejection velocity  $V_E$  formula (Eq. 1) of Brown and Jones [24]:

$$V_E = 10.2 r^{-1.038} \rho^{-1/3} R^{1/2} m^{-1/6} \quad (1)$$

where  $r$  is the heliocentric distance,  $\rho$  is the bulk density of the meteoroid,  $R$  is the radius of the cometary nucleus and  $m$  is the mass of the meteoroid. The adopted values here are  $r = 0.838$  AU,  $\rho \sim 800$  kg m $^{-3}$ ,  $R \sim 1$  km (assumed) and  $m \sim 0.1$  g (typical photographic  $\eta$  Eridanid), respectively, which result in

$V_E \sim 10$  m s $^{-1}$ . We performed the forward numerical integrations of motions of such isotropically-ejected meteoroids from 195 BC to AD 3000. The initial orbital data of the comet were taken from Hasegawa and Nakano [18]. As an integrator, Schubart-Stumpff's [25] method in double precision was applied, along with a time step of 0.5 day. All the nine major planets were included as perturbing bodies, of which initial coordinates were taken from the JPL Planetary and Lunar Ephemeris DE406. As a result in our model, no meteoroids encountered the Earth's orbit within 0.1 AU in this term; that is to say, meteor appearances associated with Comet Pons-Gambart would be unrealistic, judging from our 3000-y trace, while such larger meteoroids ejected from other short-period comets, e.g., 109P and 55P, can evolve into the Earth-crossing dust swarm within their several orbital revolutions, consequently being observable as the Perseids and the Leonids, respectively [24][26].

We conclude on the basis of the investigations above that Comet Chacornac, rather than Comet Pons-Gambart, seems to be possibly associated with the  $\eta$  Eridanids. It is no wonder that such a long-period comet as Comet Chacornac accompanies an associated meteor stream since several cases were confirmed [27]. However, DSH between Comet Chacornac- $\eta$  Eridanids is still somewhat larger than those of the other confirmed comet-meteor associations. Therefore, obtaining and analyzing more orbital data of the  $\eta$  Eridanids should clarify this problem.

#### ACKNOWLEDGEMENTS

We are grateful to Mr. E. Hidaka for helping the TMN observations.

#### REFERENCES

1. Ohtsuka K., Tomioka H., Murayama H. and Hidaka E., *Tokyo Meteor Network Rep.*, **12**, 69, 1992.
2. Southworth R. B. and Hawkins G. S., *Smithson. Contr. Astrophys.*, **7**, 261, 1963.
3. Valsecchi G. B., Jopek T. J. and Froeschle Cl., *Mon. Not. R. Astron. Soc.*, **304**, 743, 1999.
4. Lindblad B. A., *Earth, Moon and Planets*, **68**, 405, 1995.
5. Spurny P., *Planet. Space Sci.*, **45**, 541, 1997.
6. Betlem H., <http://home.wanadoo.nl/dms/photo/photo.html>, 2000.
7. Shigeno Y., [http://www2.justnet.ne.jp/-msswg/Ob\\_all.prn](http://www2.justnet.ne.jp/-msswg/Ob_all.prn), 2000.
8. Lindblad B. A., Ohtsuka K. and Shirakawa K., *Planet. Space Sci.*, **42**, 113, 1994.
9. Lindblad B. A. and Porubcan V., *Planet. Space Sci.*, **42**, 117, 1994.

10. Hoffmeister C., *Meteorstrome*, Verlag Johann Ambrosius Barth, Leipzig, 1948.
11. McIntosh R. A., *Mon. Not. R. Astron. Soc.*, **95**, 709, 1935.
12. Sakaguchi M., *NMS Astron. Circ.*, no. 676, 1998.
13. Lebedinets V. N., Korpusov V. N. and Sosnova A. K., *Trudy In-t ehksperium. meteorol. Gl. upr. gidrometeorol. aluzhby pri Sov. Min. SSSR*, **1(34)**, 88, 1972.
14. Marsden B. G. and Williams G. V., *Catalogue of Cometary Orbits*, 13th ed., SAO, MA, 1999.
15. Vsekhsvyatskii S. K., *Physical Characteristics of Comets*, Israel Program for Scientific Translation, Jerusalem, 1964.
16. Ogura S., *Ann. Obs. Astron. Tokyo*, **5**, 3, 1917.
17. Hasegawa I., *Publ. Astron. Soc. Japan*, **31**, 257, 1979.
18. Hasegawa I. and Nakano S., *Publ. Astron. Soc. Japan*, **47**, 669, 1995.
19. Marsden B. G., Williams G. V., Kronk G.W. and Waddington W. G., *Icarus*, **105**, 420, 1993.
20. Carusi A., Kresak L., Kresakova M. and Valsecchi G. B., *Astron. Astrophys.*, **252**, 377, 1991.
21. Asten E., *Astron. Nach.*, **81**, 35, 1873.
22. Hasegawa I., *Publ. Astron. Soc. Japan*, **42**, 175, 1990.
23. Kronk G. W., *Meteor Showers*, Enslow, Hillside, 1988.
24. Brown P. and Jones J., *Icarus*, **133**, 36, 1998.
25. Schubart J. and Stumpff P., *Veroffentlichungen Astron. Rechen-Inst. Heidelberg*, Nr. 18, 1966.
26. Asher D. J., *Mon. Not. R. Astron. Soc.*, **307**, 919, 1999.
27. Ohtsuka K., in *Origin and Evolution of Interplanetary Dust*, eds. A. C. Levasseur-Regourd and H. Hasegawa, Kluwer, Tokyo, 315, 1991.

## COMPARISON AMONG THE KEPLERIAN-ORBIT-DIVERSITY CRITERIA IN MAJOR-METEOR-SHOWER SEPARATION

L. Neslušan<sup>1,2</sup> and P. G. Welch<sup>1</sup>

(1) Queen Mary & Westfield College, University of London, Mile End Road, London E1 4NS, United Kingdom

(2) Astronomical Institute, Slovak Academy of Sciences, 05960 Tatranská Lomnica, Slovakia

### ABSTRACT

Recently, two new criteria of diversity of Keplerian orbits have been suggested, that by Valsecchi, Jopek, and Froeschlé (VJF) in 1999, and orbital-momentum-based (OMB) criterion by Neslušan in 2001. In the presented paper, there is a comparison of how the classic, Southworth-Hawkins (SH) criterion from 1963, and both new criteria behave, when these are used in the separation of several major meteor showers from the photographic IAU MDC database. The cumulative-number-on-threshold-D-dependence method, based on work by Sekanina from the beginning of 1970s, is utilized to perform an optimal separation. The quality of separation is evaluated with the help of "background-number-density test" (described here in more detail). No essential difference among the particular criteria was found. A relatively worse result is obtained using SH criterion for Perseids. The separation method does not work with the VJF and OMB criteria for the  $\alpha$ -Capricornids, and with OMB criterion for the Northern as well as Southern  $\delta$ -Aquirids. No criterion is sufficient for the optimal separation of Geminids. If the best criterion has to be chosen, the VJF one seems to be a little more appropriate than the others.

Key words: meteor shower; orbital-diversity criterion.

### 1. INTRODUCTION

To study a meteor stream, we need to separate the meteors of the particular stream from those of the background. This appears to be a non-trivial task, however.

In the separation, the orbit of an individual meteor is usually compared to the mean orbit of the separated meteor shower. To evaluate the measure of diversity of these orbits, a one-parameter criterion (let us denote it as  $D$ ) is used. If  $D$  is less than threshold  $D_t$ , a given meteor is assigned to the shower.

The actual mean shower orbit must be guessed at the first step (usually taking that of the parent body if known). After the first separation, a new mean orbit is calculated and the process repeated. The actual mean orbit is found after several such repetitions, when the difference between the final mean orbit and that obtained in the previous step is negligible.

The major problem in the separation procedure is finding the appropriate threshold value,  $D_t$ . Two basic approaches exist:

1. the statistical approach suggested by Southworth and Hawkins (1963), modified by Lindblad (1971), and by Jopek and Froeschlé (1997);
2. the approach suggested by Neslušan et al. (1995) based on the *break point* in the dependence of cumulative number of separated meteors on  $D_t$ . This dependence was described by Sekanina in 1970.

In addition to the original Southworth-Hawkins' (1963) criterion of orbit diversity, two new criteria have recently been suggested: by Valsecchi et al. (1999) and by Neslušan (2001).

In this paper, we perform a comparison of all three criteria in the separation of five major meteor showers from the photographic IAU MDC database (Lindblad, 1987, 1991; Lindblad and Steel, 1994) using the cumulative-number-on-threshold-D-dependence or "break point" (BP) method of determination of threshold discriminant,  $D_b$ . The quality of separation of shower meteors using the given value of  $D_b$  is evaluated with help of background-number-density (BND) test.

### 2. THE "BREAK POINT" METHOD OF SEPARATION

The first determination of threshold value,  $D_t$  was based on a statistical approach where  $D_t = 0.2(360/N_{data})^{1/4}$  for the sample size consisting of

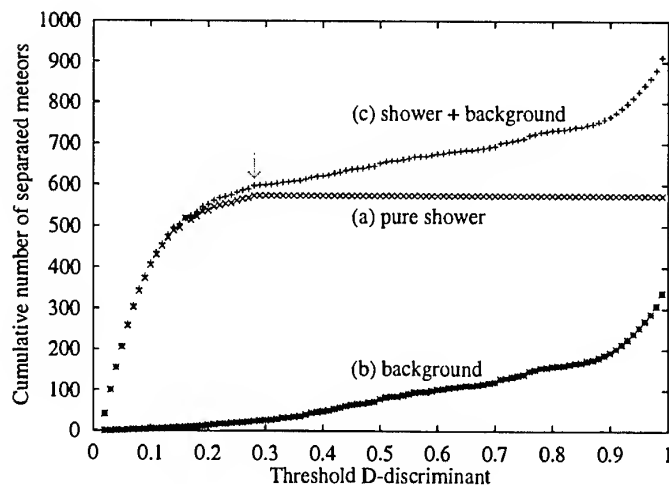


Figure 1. The cumulative number of separated meteors vs. threshold value of  $D$ -discriminant,  $D_t$ . If a given database contained only shower meteors, their number would increase with increasing  $D_t$  up to the value, for which all the meteors are separated (the appropriate point, called as "break point", of dependence is marked with an arrow). Behind the break point, the number of meteors would remain constant (curve (a)), because all the database would be separated. Since, some sporadic-background meteors (curve (b)) are also added to shower in the separation from a real database, the uppermost curve (c) is obtained as the proper result of the separation.

$N_{data}$  meteors (Southworth and Hawkins, 1963). For the relatively precise photographic orbits, the dispersion of shower orbits appears to come from the daily motion of the Earth rather than from statistical distribution of determination errors. Therefore, the sample does not represent good statistical material as a whole and the usage of Southworth-Hawkins' relation for  $D_t$  is problematic. (It is worthy to note that this relation was derived for a radar orbit database, where the orbit dispersion due to their determination errors dominates.)

In the following, we use a method developed by Neslušan et al. in 1995, based on the construction of the dependence of the number of separated meteors,  $N$ , of a given shower, on varying threshold  $D_t$ . The principle of the method is following.

If we had a database which contains only meteors from a single shower, if  $D_t$  increased,  $N$  would increase until  $D_t = D_b$  (the break point). At  $D_t = D_b$  all shower meteors would be included and  $N$  would remain constant with increasing  $D_t$  after this (Fig.1, curve (a)).

If we had a database with sporadic meteors only, for increasing  $D_t$ ,  $N$  would increase gradually with wrongly included sporadic meteors, (Fig.1, curve (b)).

For a real database, we see a composition of this behaviour (Fig.1, curve (c)). If the ratio of sporadic meteors is small in comparison with the shower meteors, the break point  $D_b$  (marked with an arrow in Fig.1) can still be seen. The corresponding  $D$ -discriminant,  $D_t = D_b$ , is the natural value for the optimal separation of a particular shower.

### 3. THE BACKGROUND-NUMBER-DENSITY TEST

If all meteor orbits that are members of a given stream are subtracted from the dataset, the number density of radiants in the stream radiant area should be approximately equal to that in the surrounding area. This can serve as a test of quality of the given separation procedure. Such the test was used by Porubčan et al. (1995; Sect. 5, item 3). Since no detail description of the test was presented there, let us describe it.

We define a stream radiant "box" given by the maxima and minima of angular position of the stream radiants, taking care to eliminate any radiants which seem clearly detached from the rest of stream. Thus the *radiant area* of the given stream is embedded into a rectangular-like *radiant box*. The eliminated radiants are then reintroduced into the reduced background dataset. Between 1 and 4 radiants were removed for each stream.

The quality of separation can be evaluated in the following way. For the reduced dataset, we compare number density in the radiant box with that of 4 neighbouring boxes of equal area (Fig.2). The size of each neighbouring box is set equal to that of the radiant box. The separation is not optimal, if the number of radiants in the original stream radiant box is significantly different from the typical number of radiants in the four neighbouring boxes. The level of statistical fluctuations can be expected to be comparable with the differences among individual numbers of radiants in the neighbouring boxes.

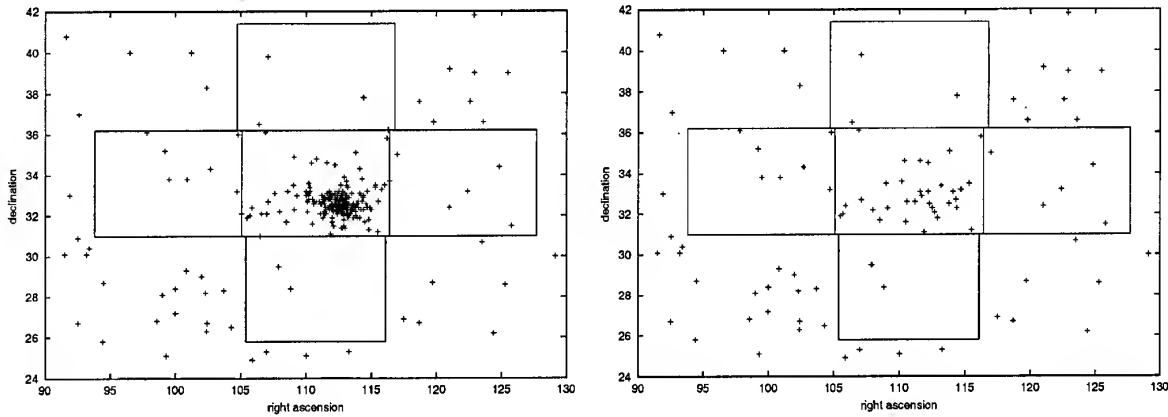


Figure 2. Unseparated Geminids and background meteor radiants (left plot) and background meteor radiants with Geminids separated and removed (right plot). We can still see a larger number of radiants in the middle (shower radiant) box than in the neighbouring boxes after the separation, therefore the separation is not optimal in this case.

Table 1. The threshold discriminant corresponding to the "break point",  $D_b$ , and the numbers of separated meteors,  $N$ , of 10 showers from the IAU MDC database. Each shower was separated, using BP method, for three orbital-diversity criteria, SH, VJF, and OMB. The iteration procedure failed in the case of VJF and OMB criteria for Orionids and  $\eta$ -Aquadrids, when started from the orbit of their parent, 1P/Halley. The presented  $D_b$  values (marked with an asterix) and corresponding numbers  $N$  were obtained starting the iteration from the mean orbit previously found with help of SH criterion. Values  $D_b$  marked with the question-sign were difficult to account from the constructed graphs and are uncertain.

shower	SH criterion		VJF criterion		OMB criterion	
	$D_b$	$N$	$D_b$	$N$	$D_b$	$N$
Perseids	0.32	539	0.28	597	0.0046	586
Geminids	0.10	192	0.15	203	0.0009	190
Orionids	0.20	55	0.13*	52	0.0013*	48
Quadrantids	0.18	39	0.12	39	0.0021	41
$\delta$ -Aquadrids S	0.18	31	0.23	31	0.0014	31
Leonids	0.17 <sup>?</sup>	28	0.08	29	0.0015	29
$\alpha$ -Capricornids	0.12 <sup>?</sup>	25	method failed		method failed	
$\delta$ -Aquadrids N	0.18	16	0.22 <sup>?</sup>	15	method failed	
$\eta$ -Aquadrids	0.08	13	0.07*	15	0.0015*	15
Lyrids	0.07	10	0.08	12	0.0014	12

#### 4. SEPARATION USING THE BREAK-POINT METHOD

Using BP method, the meteors of 10 showers are separated from the photographic IAU MDC database (Lindblad, 1987, 1991; Lindblad and Steel, 1994) containing the data on 3411 meteors (Porubčan et al., 1995). The separation is independently performed three times: using the Southworth-Hawkins' (SH), Valsecchi-Jopek-Froeschlé's (VJF), and orbital-momentum-based (OMB) criterion.

The threshold values corresponding with the appropriate break points,  $D_b$ , together with the numbers of separated stream members for individual criteria and showers are given in Table 1. The VJF criterion could not separate the complicated, multi-parent-body shower (Neslušan, 1999)  $\alpha$ -Capricornids. The OMB criterion could not separate this and the Northern  $\delta$ -Aquadrids. Also for the VJF and OMB criteria to be able to separate the Halley's comet streams, the Orionids and  $\eta$ -Aquadrids, the orbit of the parent was not sufficient at iteration startpoint and an initial orbit closer to the known mean of streams had to be taken.

Five of eight showers, separated with OMB criterion, have almost the same threshold value  $D_b$  ranging from 0.0013 to 0.0015. For this criterion a significant difference in  $D_b$  can be seen only for the numerous Perseids, extraordinary concentrated Geminids, and the Quadrantids (these being in special, Jupiter-controlled orbits). This suggests that the OMB criterion has a possible universal threshold for normal showers, at  $D_t \approx 0.0014$  in the case of used IAU MDC database.

#### 5. EVALUATION OF RESULTS WITH THE BACKGROUND-NUMBER-DENSITY TEST

In the separation, the Perseids, Geminids, Orionids, Quadrantids and  $\delta$ -Aquadrids all produced enough meteors to perform a meaningful background-number-density test. The results of this are shown in Table 2.

The separation is clearly imperfect with SH criterion for the Perseids, where the number of "background" meteors, 65, is far higher than the numbers of these meteors in the neighbourhood, ranging from 25 to 32. VJF and OMB criteria work for this most numerous shower.

No criterion works perfectly for the Geminids. The numbers of meteors after the separations are considerably higher in the original radiant box than in each neighbouring one. In five dimensional orbital element space the shower seems to have an exceptionally dense central concentration with shallow wings surrounding the peak. These wings are not obviously distinguished by the separation method used.

For the other major showers, approximatively the same numbers of shower meteors are separated for each criteria. The claim of optimal separation is here supported with the fact that the number of background-meteor radiants in both radiant and neighbouring boxes are similar in the BND test. This conclusion seems to be applicable, on the basis of Table 1, also to smaller showers (if the method of separation gives a result with all criteria).

Since some authors (e.g. Jopek et al., 1999) have suggested to use only the most precise data in the given context, we repeated all our work utilizing also the smaller database of 1075 meteors obtained only with the Super-Schmidt cameras. No qualitative difference in both results was found, however.

Finally, there is the question of whether the separation with different orbital-diversity criteria results in different mean characteristics of a given shower. In Table 3, we present the mean orbital elements of five separated and tested major showers. The difference in each element of each shower among the corresponding values, obtained by using various criteria, is much smaller than the corresponding mean deviation.

The only exception is argument of perihelion,  $\omega$ , for the Southern  $\delta$ -Aquadrids using the OMB criterion. Two near-ecliptic meteors (142P and 057D) far from the common period of activity of the shower are chosen in this separation. Both have  $q$ ,  $e$ , and  $i$  similar to that of the shower, therefore the differences between their own and the shower orbital momenta are small and eventual transit of some Southern  $\delta$ -Aquadrids to orbits of 142P and 057D is not as unlikely as initially seems. However, unless the possibility of a considerable shift of activity is reliably proved for a near-ecliptic shower, we must conclude that OMB criterion fails in this particular case.

#### 6. CONCLUSIONS

The background-number-density test is useful in assessing the quality of shower separation from a photographic database. A separation satisfying the test cannot be regarded as perfect but an insufficient separation can be revealed by it.

Examining Table 4 we can see that no criterion seems obviously to be superior and criteria do not exhibit any essential difference in their application to the separation of major meteor showers within the BP method. The corresponding mean elements of the five most numerous separated showers differ to a far lesser extent, using various criteria, than the mean deviation characterizing the intrinsic dispersion of the given element. Despite the general uniformity of the examined criteria, some particular differences of their usage can be stated.

The separation is far from the optimal for all the criteria in the case of the Geminids, most probably

Table 2. The numbers of meteor radiants  $n_b$  in the radiant box (RB) and neighbouring boxes: top ( $\uparrow$ ), below ( $\downarrow$ ), left ( $\leftarrow$ ), and right ( $\rightarrow$ ). These numbers are counted after the independent separations of appropriate shower with SH, VJF, and OMB criteria. In the case of optimal separation,  $n_b$  should be the number of radiants of background meteors, which is expected to be approximately the same in all boxes. To enable a comparison of "separated vs. background" meteor numbers, number  $N_c$  of common (extracted in all three separations) meteors is given in the second column.

shower	$N_c$	SH criterion		VJF criterion		OMB criterion	
		RB	$n_b$ ( $\uparrow/\downarrow/\leftarrow/\rightarrow$ )	RB	$n_b$ ( $\uparrow/\downarrow/\leftarrow/\rightarrow$ )	RB	$n_b$ ( $\uparrow/\downarrow/\leftarrow/\rightarrow$ )
Perseids	531	65	(32/25/27/30)	50	(52/60/50/48)	38	(46/46/30/40)
Geminids	186	28	(5/2/8/4)	22	(6/2/4/4)	34	(6/2/4/4)
Orionids	45	16	(5/7/15/7)	8	(1/3/9/6)	9	(1/3/9/6)
Quadrantids	38	3	(1/1/2/1)	4	(0/2/3/2)	5	(0/3/2/2)
$\delta$ -Aquarids S	27	5	(4/4/9/6)	3	(3/2/10/6)	8	(5/5/11/8)

Table 3. The mean elements,  $q$ ,  $e$ ,  $\omega$ ,  $\Omega$ , and  $i$ , of five separated major showers with three various orbital-diversity criteria, SH, VJF, and OMB (see text).

criterion	$q$ [AU]	$e$ [1]	$\omega$ [deg.]	$\Omega$ [deg.]	$i$ [deg.]
Perseids					
SH	0.948 $\pm$ 0.018	0.953 $\pm$ 0.101	150.3 $\pm$ 4.5	138.3 $\pm$ 3.4	113.1 $\pm$ 2.5
VJF	0.947 $\pm$ 0.024	0.957 $\pm$ 0.147	150.2 $\pm$ 6.1	138.2 $\pm$ 3.5	113.1 $\pm$ 3.5
OMB	0.948 $\pm$ 0.025	0.957 $\pm$ 0.146	150.9 $\pm$ 8.7	138.4 $\pm$ 3.1	112.9 $\pm$ 2.7
Geminids					
SH	0.141 $\pm$ 0.010	0.894 $\pm$ 0.016	324.7 $\pm$ 1.4	261.0 $\pm$ 1.3	23.7 $\pm$ 1.9
VJF	0.141 $\pm$ 0.013	0.895 $\pm$ 0.017	324.7 $\pm$ 1.8	261.0 $\pm$ 1.4	23.8 $\pm$ 2.3
OMB	0.142 $\pm$ 0.009	0.893 $\pm$ 0.016	324.6 $\pm$ 1.3	261.0 $\pm$ 1.5	23.6 $\pm$ 1.8
Orionids					
SH	0.578 $\pm$ 0.050	0.967 $\pm$ 0.056	81.4 $\pm$ 6.3	27.6 $\pm$ 4.9	164.0 $\pm$ 2.0
VJF	0.569 $\pm$ 0.037	0.962 $\pm$ 0.071	82.8 $\pm$ 5.5	28.6 $\pm$ 2.4	164.0 $\pm$ 1.9
OMB	0.570 $\pm$ 0.035	0.965 $\pm$ 0.059	82.5 $\pm$ 4.8	28.6 $\pm$ 2.4	164.3 $\pm$ 1.4
Quadrantids					
SH	0.981 $\pm$ 0.008	0.663 $\pm$ 0.066	169.9 $\pm$ 3.4	282.7 $\pm$ 0.9	71.7 $\pm$ 1.7
VJF	0.981 $\pm$ 0.008	0.668 $\pm$ 0.075	169.8 $\pm$ 3.2	282.7 $\pm$ 0.9	71.8 $\pm$ 1.8
OMB	0.981 $\pm$ 0.008	0.674 $\pm$ 0.080	169.8 $\pm$ 3.7	282.7 $\pm$ 0.9	71.9 $\pm$ 1.9
$\delta$ -Aquarids S					
SH	0.089 $\pm$ 0.023	0.967 $\pm$ 0.015	149.0 $\pm$ 4.1	310.5 $\pm$ 6.1	26.0 $\pm$ 3.5
VJF	0.087 $\pm$ 0.022	0.969 $\pm$ 0.014	149.3 $\pm$ 4.0	311.0 $\pm$ 5.6	25.7 $\pm$ 3.6
OMB	0.085 $\pm$ 0.017	0.969 $\pm$ 0.013	161 $\pm$ 45	310.8 $\pm$ 6.5	25.3 $\pm$ 3.6

Table 4. Combined results from attempted shower separation and from the background number density test, for the three criteria.

criterion	showers successfully separated	separations which passed BND test
SH	10/10	3/5
VJF	9/10	4/5
OMB	8/10	4/5

due to the specific structure of this stream. With VJF criterion, about 5% more Geminids are separated than with the other two criteria (but the number is still insufficient).

Although the SH criterion is the only one to separate all ten showers, it does not pass the background number density test for the most numerous and, thus, representative shower, the Perseids. This is a serious disadvantage in comparison with VJF and OMB criteria.

Unless a relation between a given shower and some orbits of meteors, detected apparently out of the shower-activity period, is proved, the OMB criterion is ruled out: with it, BP method separated two Southern  $\delta$ -Aquirids about 5 months out of the usually accepted period of activity. If however, such a relation were proved, then the OMB criterion would become the most appropriate.

The VJF (and OMB as well) criterion fails to separate a shower if the iteration procedure is started with an initial orbit relatively very different from the actual mean orbit. However this also means that the criterion is probably better at distinguishing whether a given group of meteors is or is not an actual meteor shower in contrast to the SH criterion. Possibly it would be more appropriate to utilize the SH to find out an initial orbit for the iteration in problematic cases and then to subsequently apply the VJF criterion.

The VJF criterion appears to be more sensitive than SH and more reliable than OMB. Its sensitivity causes it to fail in the case of the  $\alpha$ -Capricornids. As this is a multiparent shower, the criterion's oversensitivity in not separating this as a single shower could actually be desirable. Also as this criterion passes the BND test once more than the SH, it could be recommended as slightly more preferable.

The corresponding mean elements of the five most numerous separated showers differ to a far lesser extent, using various criteria, than the mean deviation characterizing the intrinsic dispersion of the given element. This fact indicates that the limits of possible most precise determination of the universal mean characteristics of a given major shower have already been reached. From the separated samples of shower meteors, one can easily find that the observed dispersion of photographic meteor orbits is larger due to the motion of the Earth than due to the error of their determination. A further improvement will be obviously possible only within the approach, where the mean parameters are treated as the time-dependent functions.

#### ACKNOWLEDGEMENTS

The work was supported by grant "Research in Theoretical Astronomy", PPARC GR/L39094 and, in

part, by grant No. 1023 of VEGA – Slovak Grant Agency for Science.

#### REFERENCES

- Jopek T.J., Froeschlé Cl., 1997, A&A 320, 631
- Jopek T.J., Valsecchi G.B., Froeschlé Cl., 1999, MNRAS 304, 751
- Lindblad B.A., 1971, *Smithson. Contr. Astrophys.* 12, 14
- Lindblad B.A., 1987, in: *Interplanetary Matter, Proc. 10th ERAM*, eds. Z. Ceplecha and P. Pecina, Astron. Inst. Czechosl. Acad. Sci., Prague, p. 201
- Lindblad B.A., 1991, in: *Origin and Evolution of Interplanetary Dust*, eds. A. C. Levasseur-Regourd and H. Hasegawa, Kluwer, Dordrecht, p. 311
- Lindblad B.A., Steel D.I., 1994, in: *Proc. Asteroids, Comets, Meteors 1993*, eds. A. Milani, M. Di Martino, and A. Cellino, Kluwer, Dordrecht, p. 497
- Neslušan L., 1999, A&A 351, 752
- Neslušan L., 2001, in: *Proc. US-European Celestial Mechanics Workshop* held in Poznań, Poland, July 3-7, 2000, Adam Mickiewicz Univ., Poznań, in press
- Neslušan L., Svoreň J., Porubčan V., 1995, *Earth, Moon, Planets* 68, 427
- Sekanina Z., 1970, *Icarus*, 13, 459
- Southworth R.B., Hawkins G.S., 1963, *Smithson. Contr. Astrophys.* 7, 261
- Valsecchi G.B., Jopek T.J., Froeschlé Cl., 1999, MNRAS 304, 743

## EXTREME BEGINNING HEIGHTS FOR NON-LEONID METEORS

Pavel Koten<sup>(1)</sup>, Pavel Spurný, Jiří Borovička and Rostislav Štork

*Astronomical Institute, Ondřejov Observatory, 251 65 Ondřejov, Czech Republic*

<sup>(1)</sup> Correspondence author's email: [koten@asu.cas.cz](mailto:koten@asu.cas.cz)

### ABSTRACT

Extreme beginning heights up to 200 km were recently discovered for bright Leonid meteors. Here we report results of the search among our double-station video data of other meteor showers. We found two  $\eta$ -Aquarid and one Perseid meteors with beginning heights up to 150 km and one Lyrid meteor with beginning height above 130 km. Surprisingly, the  $\eta$ -Aquarids and the Lyrid were not bright enough to be recorded by all-sky photographic cameras.

### 1. INTRODUCTION

Double-station observations of meteors by means of video cameras connected to the image intensifiers started at the Ondřejov Observatory in 1998 and data of several hundreds of meteors have been collected up to now. Among them we found other meteors than Leonids with beginning heights above 130 km.

Fujiwara et al. [1] found from video observations two bright Leonid meteors with beginning height about 160 km. Recently, Spurný et al. [2] reported extreme beginning heights for bright Leonids up to 200 km. Video records of seven very bright Leonid meteors show unusual meteor appearance in the heights above 130 km [3]. Comet-like diffuse structures were observed.

Now we report other four meteors that started to radiate above 130 km. These meteors do not belong to the Leonid shower. Just one of them produced a fireball recorded by all-sky photographic cameras with limiting magnitude of -3. Other meteors were recorded only by the low light level television (LLTV) technique. It is somewhat surprising because all previously detected meteors were fireballs brighter than -3 magnitude.

### 2. OBSERVATIONS AND INSTRUMENTS

All reported meteors were recorded within the double-station observation program at the Ondřejov Observatory. These observations are carried out on the base Ondřejov – Kunžak. Stations distance is 92.5 km azimuth of the second station is 340°.

Both stations operated commercial S-VHS video camcorders Panasonic connected to second-generation Russian Dedal 41 image intensifiers and equipped with an Arsat lens 1.4/50. These lenses provide field of view of about 25° in diameter. The spectral sensitivity of the system extends from 390 to 900 nm.

The Perseid meteor was recorded at Ondřejov as a zero order during the spectral observation with the same type of camera moreover equipped with a spectral grating Milton Roy with 600 grooves per mm blazed to 470 nm. The spectrum itself was out of the field of view and was not recorded.

This meteor was bright enough to be recorded by two all-sky photographic cameras in the Czech part of the European Fireball Network. Czech stations are equipped with fish-eye cameras ( $f/3.5$ ,  $f = 30$  mm).

### 3. METEOR DATA

All meteors were recorded during routine meteor shower observations. First of them belongs to the Lyrid meteor shower, second and third to the  $\eta$ -Aquarid meteor shower and fourth is the Perseid meteor. Basic data of their observations are shown in Tab. 1.

*Tab. 1. Basic data of meteor observations*

Meteor number	Date	Time [UT]
99420024	April 20, 1999	23:27:29
00502065	May 3, 2000	1:54:23
00504008	May 5, 2000	1:19:02
EN110800	August 11, 2000	22:11:53

The records were digitalized and processed by means of our standard procedures. Atmospheric and orbital trajectories were computed as well as light curves were constructed. Recently an analysis of about 250 shower and sporadic meteor light curves and height data was done [4]. A comparison revealed that luminous trajectories of the shower meteors usually begin much lower than in the case of these four meteors. The comparison is shown in Tab. 2. Note that the average beginning height is valid only for faint meteors (mass up to  $10^{-2}$  g), not for fireballs.

The beginning heights of Lyrid and  $\eta$ -Aquadrid meteor showers in comparison with three exceptional meteors are plotted in Fig. 1.

Tab. 2. Beginning heights of the exceptional meteors and their showers.  $H_B$  is the meteor beginning height and  $H_{SB}$  is the average beginning height of the shower. These values are taken for each shower from [4].

Meteor	Shower	$H_B$ [km]	$H_{SB}$ [km]
99420024	Lyrids	136.8	109.7 $\pm$ 5.3
00502065	$\eta$ -Aquadrids	150.2	113.3 $\pm$ 6.0
00504008	$\eta$ -Aquadrids	133.8	113.3 $\pm$ 6.0
EN110800	Perseids	149.0	115.2 $\pm$ 4.3

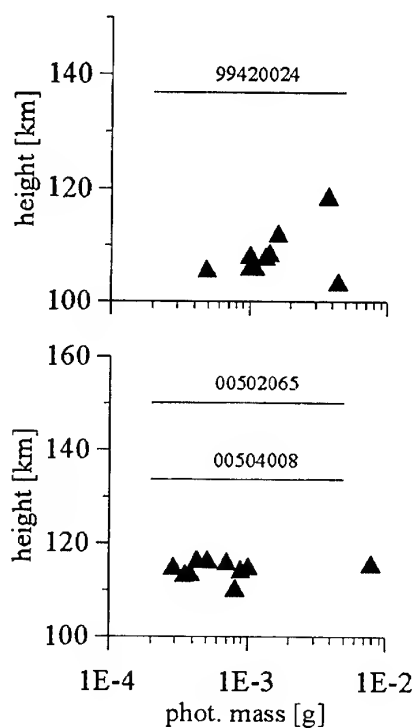


Fig. 1. Beginning heights of Lyrid (top) and  $\eta$ -Aquadrid meteor (bottom image) showers (data based on [4]). The horizontal lines mark the beginning levels of three exceptional meteors.

All meteors leave the camera field of view before they reach the maximum light and the terminal point. Only for the Perseid meteor we know the lower part of the atmospheric trajectory from all-sky cameras records. This meteor was photographed on two stations of the Czech Fireball Network – Telč and Přimda. Unfortunately, the geometry of the meteor trajectory calculated from these records was unfavourable. Thus we were lucky for video record taken at Ondřejov observatory. However, the spectral record by LLLTV

camera in Ondřejov provides only few stars for image reduction. Nevertheless, we were able to compute reliable trajectory.

Tab. 3 provides basic atmospheric trajectory data for all four meteors.

Tab. 3. The atmospheric trajectories of the meteors.  $H_B$  is beginning height of meteor,  $H_E$  end height,  $R_B$  distance of the beginning point from the station,  $Z_r$  zenith distance of radiant and  $V_\infty$  initial velocity.

Meteor	$H_B$ [km]	$H_E$ [km]	$R_B$ [km]	$Z_r$ [°]	$V_\infty$ [km/s]
99420024	136.8	116.4*	181.7	40.2	45.3
00502065	150.2	132.3*	207.5	79.2	67.5
00504008	133.8	123.4*	191.0	83.0	66.8
EN110800	149.0	87.6**	184.5	52.2	60.1

\*Not real end, meteor leaves field of view.

\*\* The photographic end.

#### 4. LIGHT CURVES

Light curves of all meteors show similar appearance as Leonid meteors mentioned above. They start around apparent magnitude +6, which is a limiting magnitude of our LLLTV system for moving objects, with exception of the Perseid meteor because the spectral grating. This meteor starts at magnitude about +4.

When we adopt the terminology of the meteor shape used in [3], we are able to detect so called *diffuse*, *intermediate* and *sharp* phases for these meteors.

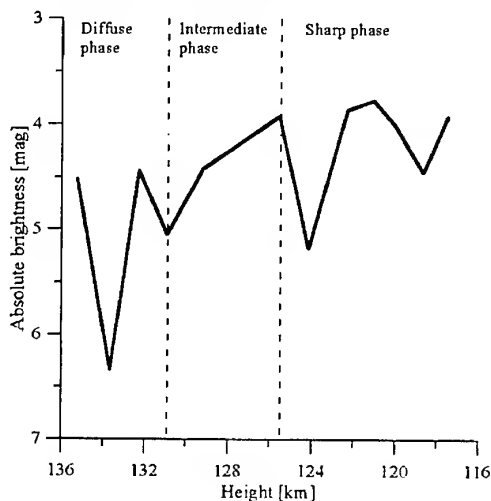


Fig. 2. Light curve of the meteor 994200024 as seen from the Ondřejov station.

#### 4.1 Meteor 99420024

This meteor starts to produce light at 136.8 km. The diffuse phase is short, recognizable only on few images. The intermediate phase, which covers two or three images, follows. At the height about 125 km sharp phase begins. Meteor leaves field of view at the altitude 117 km. The light curve is given in Fig. 2.

Only 25 km long trajectory is observed and meteor leaves field of view on the records from both stations. It still becomes brighter at this moment and we are not able to determine its maximum brightness. We can only say that it does not reach the magnitude  $-3$  what is the limiting magnitude for all-sky cameras.

#### 4.2 Meteor 00502065

Meteor with the highest beginning point of this sample begins to produce light at 150.2 km above surface. The diffuse phase is relatively long and covers about 15 km of the trajectory. During this phase the meteor appearance is typically fuzzy as was described for Leonid meteors [3]. Fig. 3 shows that light curve of this meteor is very variable what is typical for high altitude meteors. The intermediate phase is visible only on the Kunžak station record because meteor leaves Ondřejov camera field of view at the altitude 138.2 km.

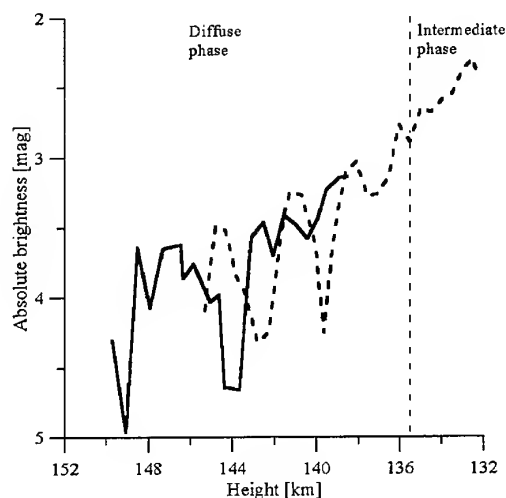


Fig. 3. Light curve of the meteor 00502065 as seen from the Ondřejov (solid) and Kunžak (dashed line) stations. The real beginning of the meteor at the Kunžak station record was out of the field of view.

Despite the highest beginning point of all meteors this one was not big enough to reach the lower limit to be recorded by all-sky cameras.

#### 4.3 Meteor 00504008

The second  $\eta$ -Aquarid meteor numbered 00504008 starts to produce light at 133.8 km. The lower beginning height causes that the diffuse phase is almost invisible. Meteor appears as diffuse object only on two or three images. The intermediate phase follows and is very short, too. Following sharp phase begin around 128 km (see Fig. 4).

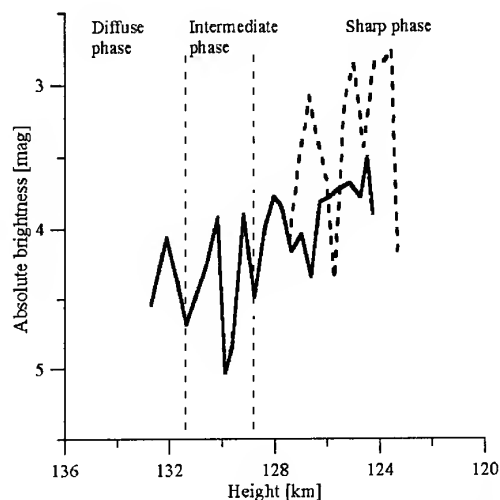


Fig. 4. Light curve of meteor 00504008. Solid line is valid for Ondřejov station, dashed line for Kunžak station.

The light curve of this meteor gradually became brighter with rapid and distinctive changes of the brightness.

#### 4.4 Meteor EN110800

As it was mentioned above, the Perseid meteor is the only one detected on the all-sky photographs. It means that the meteoroid was big enough to produce a fireball. Therefore it is different from the other meteors described here and similar to Leonids recorded in the year 1998 [3].

Fig. 5 shows that the beginning point of this meteor is at the altitude 149 km. Because the spectral grating significantly decreases sensitivity of the camera, we can assume that this meteor began to produce light even higher.

The diffuse phase is clearly visible in this case. Almost 15 km of this phase is recorded. The intermediate phase, where the appearance of the meteor changes from the diffuse to the classical drop-like shape, occurred between 135 and 125 km. Normal sharp phase follows. This meteor leaves the field of view of

the video camera at the altitude 91 km. The photographic beginning lies at 103 km. The meteor brightness was about  $-3^m$  at this moment. The discrepancy between the photographic camera sensitivity limit and the brightness determined from the video record is caused by the saturation of the video record signal at this part of the luminous trajectory (dashed line in Fig. 5). From the all-sky cameras we know that the meteor terminated at 87.6 km.

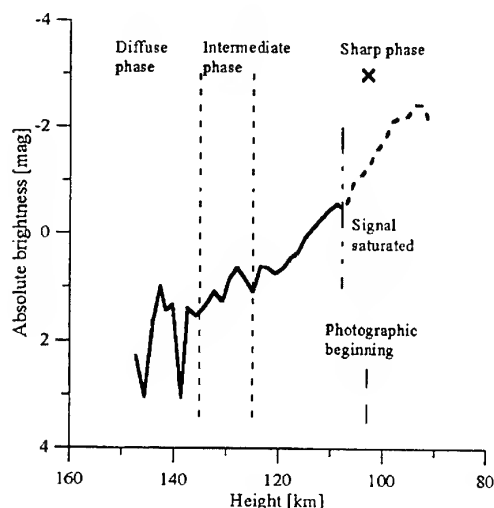


Fig. 5. The light curve of the Perseid meteor 110800 taken at the Ondřejov station. The cross marks expected brightness of the photographic beginning. The video record signal is saturated at this part of the luminous trajectory (dashed line).

## 5. CONCLUSIONS

Four non-Leonid meteors with the beginning height above 130 km were recorded. Two of them begin at about 150 km above the surface. Similar cases have been reported for Leonid shower only until now. It seems that this behaviour is probably usual not only for Leonid shower, but also for other showers.

Three of these meteors did not produce fireballs. It means that their meteoroids were smaller than meteoroids of reported Leonid meteors [3] and of our Perseid one. This fact is somewhat surprising. Unfortunately we know nothing about their luminosity after they left camera field of view except the fact that they did not reach the sensitivity limit of our all-sky photographic cameras.

The presence of the high beginning and the diffuse phase in a Lyrid meteor shows that these effects are not caused by high velocity of Leonids but rather by properties of the meteoroids.

## ACKNOWLEDGEMENT

This work was supported by grant no. 205/00/1727 from the Grant Agency of the Czech Republic.

## 6. REFERENCES

1. Fujiwara Y., et al. Meteor luminosity at 160 km altitude from TV observations for bright Leonid meteors, *Geophys. Res. Lett.*, Vol. 25, 285 – 288, 1998.
2. Spurný P., et al. Atmospheric behaviour and extreme beginning heights of the thirteen brightest photographic Leonid meteors from the ground-based expedition to China, *Meteorit. Planet. Sci.*, Vol. 35, 243 – 249, 2000.
3. Spurný P., et al. New type of radiation of bright Leonid meteors above 130 km, *Meteorit. Planet. Sci.*, Vol. 35, 1109 – 1115, 2000.
4. Koteš P., An analysis of light curves of faint meteors, *PhD thesis (in Czech)*, 2001.

## TV OBSERVATIONS OF THE 1998 GIACOBINID METEOR SHOWER IN JAPAN

Yasunori Fujiwara<sup>(1)</sup>, Masayoshi Ueda<sup>(1)</sup>, Masatoshi Sugimoto<sup>(1)</sup>, Tohru Sagayama<sup>(1)</sup>  
Masaaki Satake<sup>(2)</sup>, and Akira Furoue<sup>(2)</sup>

<sup>(1)</sup> *Nippon Meteor Society, 2-16-8 Mikunihonmachi Yodogawa-ku, Osaka 532-0005 Japan*  
*Email: DHB15312@biglobe.ne.jp*

<sup>(2)</sup> *The Kansai Astronomical Society, Marutamidourinisiiru Nakagyou-ku, Kyoto 604-0801*  
*Email: kanten@msc.biglobe.ne.jp*

### ABSTRACT

Activity of the Giacobinid (Draconid) meteor shower was recognized on October 8th, 1998, in Japan, with multi-station TV observations. 94 Giacobinid meteors have been recorded, and among which precise orbits could be determined for 48 meteors. It was found that the radiant points were concentrated compactly. Furthermore, the beginning heights of Giacobinid meteors were significantly higher than the typical TV meteors with similar velocities.

### 1. INTRODUCTION

The Giacobinid meteor shower associated with Comet 21P/Giacobini-Zinner is one of the greatest showers. High meteor activity occurred in 1933, 1946 and 1985 and many visual and photographic observations were carried out [1] [2] [3] [4] [5]. However, only a few orbits of the Giacobinids have been obtained [2] [6]. In the IAU meteor data center, there are only five orbits of the Giacobinids [7]. So, we planned to carry out multi-station simultaneous TV observations in order to determine the orbits of the Giacobinids.

### 2. OBSERVATIONS

Multi-station TV observations were carried out on 8 October 1998. The observational sites and equipments are listed in Table 1. The TV observation systems utilized image intensifiers (I.I.) and video cameras (8mm or digital). In order to determine the precise orbit, the objective lenses of f 85 mm F1.2 (Canon) and f 85 mm F1.8 (Nikon) were utilized. The objective lens of f 85 mm projects a fairly small field of view, such as 17 degrees in diameter. Because of this small field, bright meteors or fireballs are rarely recorded by such observations. So, we used the objective lenses with a focal length of 24-28 mm, in order to observe bright Giacobinid meteors with high probability. The limiting magnitude of meteors was +7 in case of f 85 mm lenses and +5 in case of f 24-28 mm lenses. The images recorded with the TV systems were digitalized with PC

(Personal Computer) with an image processing board. The positions of the meteor and of a number of surrounding reference stars were measured on the 512 x 512 pixel, the magnitudes were estimated by measuring the image density (256 gray level scale). The standard deviations of the measured positions were approximately 3' in case of f 85 mm lenses. The meteor trajectories in the atmosphere and the heliocentric orbits were calculated by a standard method [8].

### 3. RESULTS

Meteors totalling 116 were observed by multi-station TV observations, and their radiant points and orbits were determined. Among them, radiant points and orbits of the Giacobinid meteors which were observed with the objective lenses of f 85mm are listed in Tables 2 and 3. Table 2 gives the trajectories of 48 Giacobinid meteors. The columns list geocentric radiant coordinates,  $\alpha$ : Right Ascension,  $\delta$ : Declination, in degrees; Vobs., observed velocity; Vg, geocentric velocity; Vh, heliocentric velocity; Q, convergence angle; obs. Mag., observed (apparent) magnitude; abso Mag., absolute magnitude; Hb, beginning height; Hm, height of maximum brightness; He, end height; ( \* means the beginning or the end height are out of camera field) and log. Mass, logarithm of the photometric mass. Table 3 gives the corresponding orbital elements of these 48 Giacobinid meteors: semi-major axis (a), eccentricity (e), perihelion distance (q), longitude of the ascending node ( $\Omega$ ), inclination (i), argument of perihelion ( $\omega$ ) and period (P).

### 4. DISCUSSION

Figure 1 shows the distribution of the radiant points of 64 TV meteors that were observed with f 85 mm lenses. The radiant points of the Giacobinid meteors are concentrated in a small area. The distribution of the radiant points of 52 TV meteors that were observed with f 24-28mm lenses are shown in Figure 2. Table 4 gives the mean orbits of 48 Giacobinid meteors and

Table 1 Location and observational equipment

Observer	Fujiwara	Sugimoto	Ueda	Sagayama	Satake & Furoue
Location	136:00:51 E 34:34:13 N	136:00:51 E 34:34:13 N	135:38:11 E 34:32:04 N	135:42:55 E 34:45:32 N	135:40:24 E 35:07:46 N
Lens	85 mm F1.2	24 mm F1.4	85 mm F1.8 28 mm F2.8	28 mm F1.8	85 mm F1.2
Field of view	$\phi$ 17°	$\phi$ 48°	$\phi$ 17° $\phi$ 45°	$\phi$ 45°	$\phi$ 17°

Table 2. The radiant points, velocities, magnitude and heights of the Giacobinid meteors in 1998

No.	DATE YYYYMMDD	UT hhmmss	RADIANT(2000.0)				Vobs. Km/s	Vg Km/s	Vh km/s	Q deg	obs. Mag	abs. Mag	Hb Km	Hm Km	He Km	log mass g
			$\alpha$	$\pm \alpha$	$\delta$	$\pm \delta$										
UF98066	19981008	112833	259.9	3.08	54.4	0.99	22.1	19.3	38.1	18.9	4.7	4.5	102.4	97.9	95.4	-2.05
UF98067	19981008	113522	266.7	1.48	56.3	0.37	25.3	23.0	40.5	22.7	3.8	3.6	105.6	97.6	89.6	-1.64
UF98068	19981008	115106	265.6	2.86	56.8	0.95	24.0	21.5	39.3	16.1	3.8	3.6	100.5	94.2	84.3	-1.54
UF98070	19981008	115660	266.9	2.82	56.5	0.57	25.4	23.0	40.4	28.1	4.4	4.1	105.6	98.7	91.5	-1.79
UF98071	19981008	120016	263.1	1.99	55.6	0.40	24.1	21.6	39.5	32.2	6.1	5.7	103.8	101.0	96.2	-2.56
UF98072	19981008	120326	262.9	1.04	55.9	0.09	24.8	22.4	40.0	37.7	3.9	3.7	115.2	92.2	84.7	-1.24
UF98075	19981008	121647	266.6	3.15	56.5	0.49	24.9	22.5	40.1	40.8	5.6	5.3	102.3	98.4	96.5	-2.69
UF98076	19981008	122447	259.0	3.83	54.1	2.06	22.8	20.1	38.6	16.0	6.4	6.2	102.9	97.9	95.1	-2.58
UF98077	19981008	122704	262.8	1.69	55.8	0.51	24.6	22.2	39.8	43.4	3.9	3.9	101.5	98.4	91.6	-2.15
UF98079	19981008	122827	263.7	1.42	56.4	0.35	23.5	20.9	38.9	37.7	5.3	5.2	108.6	98.6	96.7	-2.04
UF98080	19981008	123044	260.8	2.20	54.7	0.65	22.2	19.4	38.2	38.4	5.0	5.0	104.7	99.0	94.7	-2.24
UF98081	19981008	123358	264.8	4.76	56.2	1.62	23.7	21.1	39.2	19.8	4.5	4.2	103.0	100.2	93.0	-2.13
UF98082	19981008	123714	262.5	3.54	55.9	0.63	23.1	20.5	38.7	36.3	5.4	5.2	100.2	97.7	95.2	-2.36
UF98083	19981008	123838	257.9	4.54	53.9	1.69	21.6	18.7	37.7	20.9	4.6	4.5	102.9	98.5	95.3	-2.11
UF98084	19981008	123934	260.9	2.56	55.5	0.87	21.9	19.1	37.8	28.7	5.0	4.7	98.7	97.2	92.2	-2.07
UF98085	19981008	124238	265.1	2.81	56.4	0.74	23.6	21.1	39.1	35.5	5.4	5.2	100.6	95.8	94.5	-2.28
UF98086	19981008	124333	263.8	1.60	55.9	0.28	22.9	20.2	38.6	36.4	3.7	3.5	100.1	95.8	90.0	-1.63
UF98087	19981008	124615	262.8	1.51	55.6	0.43	23.0	20.4	38.7	37.9	4.5	4.6	103.3	97.7	91.8	-2.25
UF98088	19981008	125003	263.4	1.79	56.0	0.48	22.5	19.8	38.2	36.6	4.0	3.8	103.3	100.0	94.7	-1.69
UF98089	19981008	130216	261.6	2.21	55.1	0.73	23.0	20.3	38.7	27.7	5.4	5.0	102.0	99.7	93.3	-2.07
UF98090	19981008	130257	264.2	4.43	56.3	1.78	22.9	20.2	38.5	31.8	5.2	4.9	100.6	95.9	94.5	-2.13
UF98093	19981008	130810	264.4	0.84	55.9	0.20	24.7	22.3	40.0	30.7	3.0	2.7	104.9	97.3	83.3	-1.11
UF98094	19981008	130854	265.0	6.13	56.6	1.25	24.4	21.9	39.6	27.3	4.6	4.4	101.8	97.4	96.8	-2.24
UF98095	19981008	130914	263.5	3.41	56.3	0.79	22.8	20.1	38.4	34.1	5.3	5.1	99.0	96.9	94.2	-2.31
UF98096	19981008	131029	264.0	2.28	56.0	0.58	24.5	22.1	39.8	28.4	4.3	4.1	103.0	96.2	93.1	-1.90
UF98097	19981008	131224	262.9	2.29	55.9	0.76	23.2	20.6	38.7	24.1	3.5	3.2	103.1	99.3	91.6	-1.58
UF98099	19981008	131602	264.2	10.79	55.5	2.59	23.5	20.9	39.2	27.1	4.5	4.3	101.6	98.6	98.6	-2.40
UF98100	19981008	131937	259.9	4.55	54.2	2.26	22.5	19.8	38.5	19.5	4.5	4.3	101.7	98.3	93.5	-1.98
UF98101	19981008	132240	255.3	6.97	52.5	3.33	22.4	19.7	38.5	20.3	3.2	3.0	102.4	99.0	97.8	-1.53
UF98102	19981008	132303	261.2	2.03	55.5	0.94	24.5	22.1	39.8	24.4	5.1	4.7	100.3	97.2	91.6	-2.17
UF98103	19981008	132440	266.6	2.41	57.0	0.70	25.5	23.1	40.4	27.0	4.4	4.1	105.0	99.3	95.5	-1.99
UF98104	19981008	132611	263.1	2.02	55.8	0.50	22.1	19.3	38.0	33.2	3.6	3.4	95.6	95.2	88.3	-1.73
UF98105	19981008	132729	264.0	2.80	56.3	0.68	22.6	19.9	38.3	28.1	3.8	3.6	101.3	98.0	93.0	-1.81
UF98106	19981008	133253	263.1	1.18	55.6	0.33	23.4	20.8	39.0	28.6	2.7	2.5	102.2	95.1	87.9	-1.20
UF98107	19981008	133512	263.3	1.69	55.4	0.51	23.5	20.9	39.1	29.2	4.7	4.5	101.4	95.8	92.0	-1.92
UF98108	19981008	133536	261.0	1.41	54.7	0.59	23.4	20.8	39.1	21.6	2.2	2.0	110.5	99.1	95.1	-0.92
UF98109	19981008	133640	260.2	3.32	55.4	1.12	23.6	21.0	39.0	22.7	3.9	3.6	108.5	102.1	97.7	-1.55
UF98110	19981008	133708	265.1	1.11	56.7	0.39	24.8	22.4	39.9	25.2	2.0	1.8	105.8	92.2	84.1	-0.81
UF98111	19981008	133803	262.1	3.05	55.6	1.09	23.1	20.4	38.7	25.8	4.7	4.3	102.6	98.8	95.3	-1.95
UF98113	19981008	135952	264.6	1.14	56.1	0.36	24.4	21.9	39.7	27.6	3.4	3.2	104.1	97.3	90.2	-1.43
UF98114	19981008	140113	262.2	2.02	55.0	0.94	24.4	22.0	39.9	21.8	2.8	2.5	104.6	100.6	92.3	-1.29
UF98116	19981008	140141	262.0	2.25	55.6	0.90	23.5	20.9	39.0	23.5	4.5	4.3	102.3	98.2	94.4	-1.85
UF98118	19981008	140755	262.1	2.59	56.0	0.93	23.5	20.9	38.9	24.6	4.0	3.8	102.7	98.3	95.0	-1.81
UF98120	19981008	141435	262.4	3.28	54.8	1.60	23.9	21.3	39.5	21.6	4.4	4.1	102.2	99.9	94.9	-1.91
UF98121	19981008	141439	263.7	2.30	56.2	0.96	23.1	20.4	38.6	23.5	4.4	4.3	102.7	97.2	94.3	-1.82
UF98122	19981008	141701	261.7	1.13	55.1	0.54	22.8	20.1	38.6	23.3	2.5	2.3	103.5	95.8	90.5	-1.04
UF98123	19981008	142200	259.5	2.93	53.3	1.56	23.7	21.2	39.6	20.8	2.6	2.4	104.6	97.6	97.2	-1.42
UF98124	19981008	142718	264.5	1.26	56.3	0.66	23.9	21.3	39.3	22.7	3.9	3.7	102.9	96.0	89.9	-1.57

Table 3. The orbital elements of the Giacobid meteor in 1998  
(eq. J2000.0)

N0.	DATE	UT	a	e	q	$\Omega$	i	$\omega$	P
	YYYYMMDD	hhmmss	AU		AU	deg	deg	deg	yr
UF98066	19981008	112833	2.741	0.6374	0.9940	195.007	29.590	170.659	4.6
UF98067	19981008	113522	6.425	0.8447	0.9981	195.011	33.925	176.091	16.3
UF98068	19981008	115106	3.844	0.7404	0.9978	195.022	32.617	175.464	7.5
UF98070	19981008	115660	6.323	0.8422	0.9981	195.026	34.024	176.273	15.9
UF98071	19981008	120016	4.165	0.7608	0.9962	195.028	32.438	173.370	8.5
UF98072	19981008	120326	5.004	0.8009	0.9961	195.031	33.360	173.325	11.2
UF98075	19981008	121647	5.241	0.8096	0.9980	195.040	33.506	176.046	12.0
UF98076	19981008	122447	3.128	0.6826	0.9928	195.045	30.419	169.902	5.5
UF98077	19981008	122704	4.696	0.7879	0.9961	195.047	33.114	173.271	10.2
UF98079	19981008	122827	3.363	0.7036	0.9969	195.048	31.860	174.050	6.2
UF98080	19981008	123044	2.799	0.6447	0.9947	195.049	29.796	171.392	4.7
UF98081	19981008	123358	3.655	0.7271	0.9973	195.052	32.027	174.761	7.0
UF98082	19981008	123714	3.180	0.6867	0.9961	195.054	31.335	172.985	5.7
UF98083	19981008	123838	2.523	0.6068	0.9921	195.055	28.818	168.925	4.0
UF98084	19981008	123934	2.564	0.6119	0.9951	195.055	29.667	171.674	4.1
UF98085	19981008	124238	3.565	0.7202	0.9975	195.057	31.998	175.029	6.7
UF98086	19981008	124333	3.094	0.6778	0.9968	195.058	31.000	173.919	5.4
UF98087	19981008	124615	3.174	0.6861	0.9962	195.060	31.070	173.170	5.7
UF98088	19981008	125003	2.832	0.6480	0.9967	195.063	30.498	173.671	4.8
UF98089	19981008	130216	3.218	0.6908	0.9952	195.071	30.932	172.105	5.8
UF98090	19981008	130257	3.018	0.6696	0.9971	195.071	31.059	174.341	5.2
UF98093	19981008	130810	4.999	0.8006	0.9970	195.075	33.148	174.364	11.2
UF98094	19981008	130854	4.229	0.7641	0.9975	195.075	32.991	175.010	8.7
UF98095	19981008	130914	2.952	0.6623	0.9968	195.076	30.972	173.814	5.1
UF98096	19981008	131029	4.599	0.7832	0.9968	195.077	33.022	174.135	9.9
UF98097	19981008	131224	3.203	0.6916	0.9963	195.078	31.368	173.332	5.8
UF98099	19981008	131602	3.654	0.7272	0.9969	195.080	31.533	174.097	7.0
UF98100	19981008	131937	3.033	0.6724	0.9937	195.083	30.123	170.576	5.3
UF98101	19981008	132240	3.001	0.6707	0.9882	195.085	29.574	166.644	5.2
UF98102	19981008	132303	4.590	0.7833	0.9949	195.085	32.994	172.047	9.9
UF98103	19981008	132440	6.087	0.8360	0.9981	195.086	34.342	176.170	15.0
UF98104	19981008	132611	2.665	0.6261	0.9965	195.087	29.933	173.353	4.6
UF98105	19981008	132729	2.853	0.6505	0.9971	195.088	30.696	174.221	4.8
UF98106	19981008	133253	3.472	0.7130	0.9963	195.092	31.556	173.356	6.5
UF98107	19981008	133512	3.588	0.7223	0.9964	195.093	31.565	173.448	6.8
UF98108	19981008	133536	3.609	0.7244	0.9946	195.094	31.359	171.608	6.9
UF98109	19981008	133640	3.492	0.7153	0.9942	195.094	31.835	171.233	6.5
UF98110	19981008	133708	4.857	0.7946	0.9974	195.095	33.575	175.051	10.7
UF98111	19981008	133803	3.170	0.6859	0.9958	195.095	31.180	172.655	5.6
UF98113	19981008	135952	4.443	0.7756	0.9971	195.110	32.872	174.552	9.4
UF98114	19981008	140113	4.761	0.7909	0.9954	195.111	32.605	172.557	10.4
UF98116	19981008	140141	3.459	0.7121	0.9956	195.112	31.661	172.564	6.4
UF98118	19981008	140755	3.345	0.7023	0.9958	195.116	31.811	172.769	6.1
UF98120	19981008	141435	4.148	0.7600	0.9955	195.120	31.878	172.659	8.4
UF98121	19981008	141439	3.140	0.6825	0.9968	195.121	31.295	173.955	5.6
UF98122	19981008	141701	3.104	0.6793	0.9953	195.122	30.668	172.135	5.5
UF98123	19981008	142200	4.274	0.7678	0.9926	195.126	31.343	170.103	8.8
UF98124	19981008	142718	3.786	0.7366	0.9972	195.129	32.296	174.547	7.4

orbits given in previous works. It is clearly shown in Table 4 that those orbits are in strong agreement to each other. There is no difference due to magnitude (mass). This compact radiant area without the dependence on mass means that the Giacobinids in 1998 situate in the early evolutionary stage.

Figure 3 shows a histogram of the absolute magnitude of TV meteors observed with f 24-28 mm lenses. The distribution of the absolute magnitude of TV meteors observed with f 85 mm lenses is shown in Figure 4. It must be noted that the bright Moon wiped out faint meteors.

Table 4 Orbits of the Giacobinid meteors with standard deviations (equinox 2000.0)

Date (8 Nov.1998)		Radiant point		Vg	a	e	q	$\Omega$	i	$\omega$	
UT		$\alpha$	$\delta$	km/s	Mag	AU					
Mean orbit (1)		263.20	+55.75	20.4	4.0	3.18	0.687	0.996	195.07	31.15	173.48
S.D.		$\pm 2.23$	$\pm 0.91$	$\pm 1.1$		$\pm 0.73$	$\pm 0.068$	$\pm 0.0005$		$\pm 1.35$	$\pm 0.025$
98G1 (2)	11h42m00s	263.40	+55.76	21.0	o	3.572	0.721	0.9966	195.0188	31.8	173.6
S.D.			$\pm 0.4$				$\pm 0.025$	$\pm 0.0001$		$\pm 0.5$	
98G2 (2)	13h11m54s	263.16	+55.75	20.9	-1	3.512	0.716	0.9964	195.0806	31.18	173.4
S.D.			$\pm 0.3$				$\pm 0.018$	$\pm 0.0001$		$\pm 0.4$	
Mean orbit (3)		263.2	+55.4	20.5	5.2	3.33	0.698	0.9963	195.08	31.09	173.36
S.D.		$\pm 1.4$	$\pm 0.7$	$\pm 0.5$		$\pm 0.32$	$\pm 0.028$	$\pm 0.0007$		$\pm 0.70$	$\pm 0.83$

(1) this work (48 TV meteors), (2) Photographic meteors (Tomita et al 1999 [9]), (3) 20 TV meteors (Suzuki et al 1999[10])

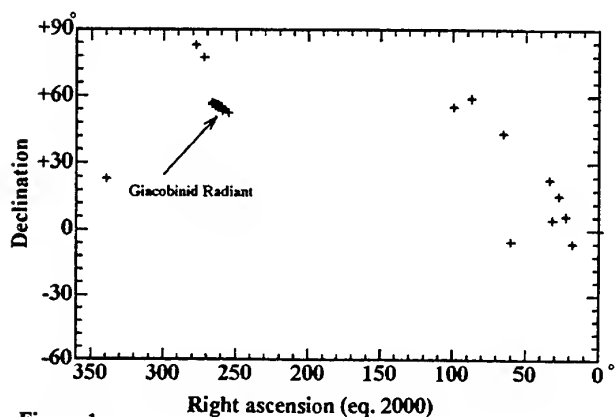


Figure 1  
The TV Meteor Radiant Mapping (Oct. 8, 1998) (85mm)

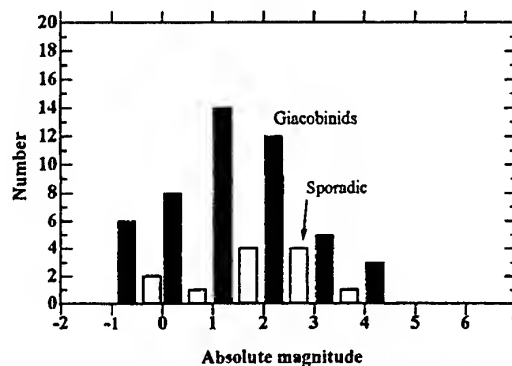


Figure 3 Absolute magnitude distribution of TV Giacobinid meteors in 1998. (f24-28mm)

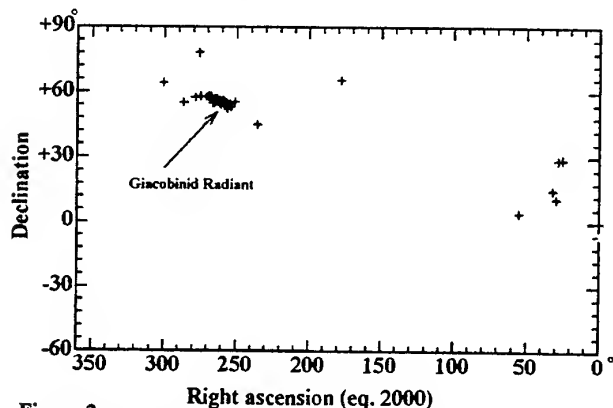


Figure 2  
The TV Meteor Radiant Mapping (Oct. 8, 1998) (f24-28mm)

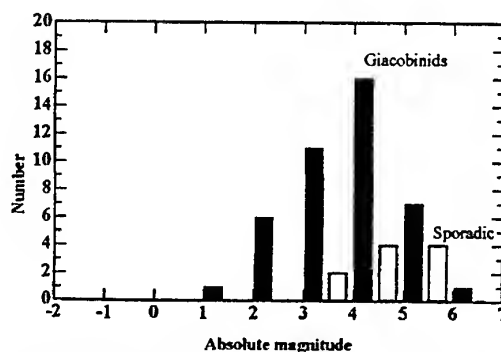


Figure 4 Absolute magnitude distribution of TV Giacobinid meteors in 1998. (f85mm)

We have plotted the beginning height ( $H_b$ ), the height of maximum brightness ( $H_m$ ) and the end height ( $H_e$ ) of the Giacobinid meteors against the absolute magnitude in Figure 5. Three lines in Figure 5 are the least-squares fits through the data. The height range of meteor luminosity is related to the physical characteristics of a meteoroid as well as the impinging velocity to the earth.

The following relationship between the beginning height ( $H_b$ ) and the geocentric velocity ( $V_g$ ) was obtained for 181 sporadic meteors observed with similar TV systems to this work. The magnitude range is from 0 to +7 (average 4.7) [11].

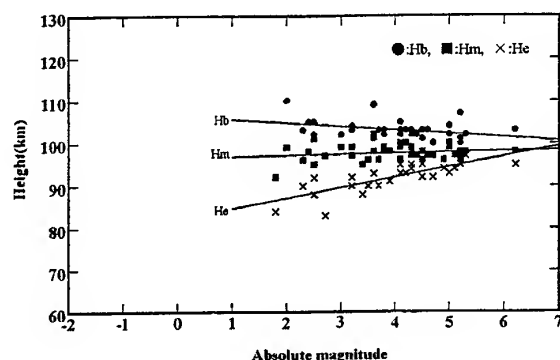


Figure 5

$$H_b \text{ (km)} = 0.361V_g \text{ (km/s)} + 87.4$$

According to this relation, the beginning height of the sporadic meteor is 94.8 km when  $V_g = 20.4$  km/s, however, the beginning height of 39 Giacobinid meteors observed with f 85 mm lenses (average magnitude 4.1) was 103.5 km. It is obvious that the beginning height of the Giacobinid meteors is higher than that of sporadic meteor with the same velocity. This result is in good agreement with the photographic data [6] [9]. The explanation of these results is a high degree of fragmentation of the original meteor body [1] [6] [9].

## 5. SUMMARY

We carried out multi-station TV observations on 8 October 1998 and 48 precious orbits of faint Giacobinid meteors were determined. The compact radiant area and the fragility of the Giacobinid meteors were quite identical to the results of previous works.

## 6. REFERENCES

1. Jacchia, L. G., Kopal, Z. and Millman, P. M., *Astrophys. J.*, 111, 104, 1950
2. Nagasawa, K. and Kawagoe, A., *Icarus*, 70, 138, 1987
3. Koseki, M., *Icarus*, 88, 122, 1990
4. Lindblad, B. A., *Astron. Astrophys.*, 187, 928, 1987
5. Simek, M. and Pecina, P., *Astron. Astrophys.*, 343, L94, 1999
6. Jacchia, L. G. *Astron. J.* 61, 6, 1956
7. Ohtsuka, K., *Astron. Circular (Nippon Meteor Society)*, 674, 16, 1998
8. Hasegawa, I., *Determination of Orbits*, Koseisha, Tokyo (in Japanese), 1983
9. Tomita, M., Murasawa, A., Shimoda, C., Muroishi, H., Okumura, S. Ohtsuka, K., *WGN the Journal of the IMO*, 27, 118, 1999
10. Suzuki, S. Akebo, T., Yoshida, T. and Suzuki, K., *WGN the Journal of the IMO*, 27, 214, 1999
11. Ueda, M. and Fujiwara, Y., *Stella (OAA)*, 6, 1, 1998

## **The Leonids Meteor Shower**

## ORBITAL PERTURBATIONS ON DUST TRAILS: PREDICTING METEOR STORMS

D.J. Asher

*Armagh Observatory, College Hill, Armagh, BT61 9DG, UK, Email: dja@star.arm.ac.uk*

### ABSTRACT

The 'dust trail technique' for calculating the occurrence of meteor storms is reviewed. It depends on the realisation (1) that the most highly structured, densest and youngest components of meteor streams are long, narrow trails, successive trails being created each time the active parent comet returns to perihelion; and (2) that gravitational perturbations, which are the dominant force in bringing meteoroids to intersect the Earth's orbit, are a function only of position along a trail, being the same for all particles within the trail cross section at a given position along the trail. The technique has been proved by the Kazan research group and others to work successfully for meteor outbursts in many different streams.

### 1 FORMATION OF COMETARY DUST TRAILS

Meteoroid streams can be highly structured, allowing the possibility of sharp meteor outbursts when the Earth encounters a region within a stream where there is a high spatial density of particles. Such high density regions have been observed: narrow trails of meteoroids and dust lying near the orbits of periodic comets were seen by the Infra-Red Astronomical Satellite IRAS [1, 2], the comets with which associated trails were detected generally being those that were reasonably near to the inner solar system at the time of the IRAS mission.

It is a consequence of orbital dynamics that several narrow, dense trails can exist simultaneously in a single stream. Thus a trail exists because of a dispersion in orbital period  $P$  among the meteoroids released over a particular perihelion return of a given comet, particles with shorter or longer  $P$  gradually getting respectively ahead or behind in the trail as time passes [3]. A meteoroid's period depends on its ejection velocity from the comet, the point on the comet's orbit where it was released, and the amount of solar radiation pressure it experiences [4, 5, 6]. A

comet's orbit is perturbed between successive perihelion passages, and therefore the trails successively created have a simultaneous but separate existence within the stream.

Streams containing trails with nodal distances near 1 AU may produce meteor outbursts. A trail's width, or cross section, relates to the outburst duration. The cross section is conveniently measured at the node and in the ecliptic, in terms of the particle distribution as a function of longitude of ascending node  $\Omega$  and heliocentric nodal distance  $r_N$  ( $r_A$  or  $r_D$  depending on whether the ascending or descending node is being considered — generally the one nearer 1 AU). For some time, e.g. of the order of a few centuries in the case of the Leonids [7, 8], the extent of the dispersion in  $r_N$  and  $\Omega$  does not change, in a model including planetary perturbations and solar radiation pressure. Perturbations do not increase the width because any given point along a trail, where the cross section is being measured, consists of particles that have been essentially comoving in space — otherwise they would not be at the same point along the trail. Unless there has been a close planetary approach, the particles have therefore been continuously at nearly the same position relative to each perturbing planet, and there is no differential force to disperse their orbits. So to a good approximation, trails remain narrow for some time, although other radiative forces may have a gradual dispersive effect [9]. Trails progressively become longer owing to the range of  $P$ , but because the cross sections remain narrow, there can continue to exist regions with high spatial densities of particles.

During close planetary approaches, particles in trails can be dispersed into the stream background, with trail survival times as narrow, coherent entities being a few centuries, depending on the stream. Beyond this timescale, the main mechanism to inhibit chaotic gravitational scattering is mean motion resonances with planets, typically Jupiter [10, 11, 12]. Streams typically contain both resonant and non-resonant meteoroids.

Since gravitational perturbations do not widen trails,

the widths are the result of orbital differences imposed by velocities of ejection from the parent comet. For trails with  $r_N \approx 1$ , widths can be constrained observationally by the frequency with which meteor outbursts do and do not occur, i.e., by seeing at what distance the Earth has to approach a trail for a noticeable outburst. It is highly encouraging that observed widths are essentially in accord with the cross sections that result from ejection speeds expected by standard cometary ejection models [13, 14, 15], for the sizes of particles capable of producing visual meteors.

## 2 PLANETARY PERTURBATIONS, EARTH INTERSECTIONS AND METEOR STORMS

Although there are essentially no differential perturbations at a single point along a given trail, gravitational forces can alter  $r_N$  and  $\Omega$  of all the particles in the cross section at that point, by a substantial amount (the same amount for all the particles). The nodal crossing point can be shifted by many times the trail width. When such shifts bring  $r_N$  especially close to the heliocentric distance  $r_E$  that the Earth has at a similar longitude, meteor outbursts become possible.

As  $r_N$  and  $\Omega$  are functions of position along a trail, numerical integration programs that evaluate planetary perturbations in order to calculate  $r_N$  and  $\Omega$  at relevant points along trails can be used to predict meteor storms. The relevant points are those where particles reach their node when the Earth is at a similar longitude. For example, the descending nodes of Leonid meteoroids with  $r_D \approx 1$  are at longitudes where the Earth is in November. Leonid meteors can therefore only come from particles whose time of nodal passage is in November of some year, i.e., the relevant points along each trail are those where particles reach the ecliptic in November of successive years (a trail may have a significant particle density for some years along its length).

In the absence of perturbations,  $P$  is invariant and the nodal crossing time  $t_N$  (equivalent to position along a trail) is a smoothly increasing function of  $P$ . In reality  $P$  is continuously perturbed and after some revolutions particles that had different values of  $P$  at ejection time might, after different orbital evolution histories, have the same  $t_N$ . This would mean that the trail in some places looped back on itself in space. When perturbation histories are different,  $r_N$  and  $\Omega$  may differ even if  $t_N$  is the same.

Owing to the continuous perturbations, it is easiest not to consider  $t_N$ ,  $r_N$  and  $\Omega$  as functions of the osculating period  $P$  (because differing perturbation histories can cause them not in fact to be single valued functions of the osculating  $P$ ), but instead as functions of the value of  $P$  at ejection time. Most authors adopt the semi-major axis, being more commonly used than  $P$  in celestial mechanics, as the independent variable. We write  $\Delta a_0$  for the difference in semi-major axis from the cometary value immediately after ejection.

Meteoroids are ejected over a range of true anomaly of the comet and with a range of speeds and directions from the comet nucleus. Different combinations of these parameters can give the same  $\Delta a_0$ . However, for the purpose of the calculations it is easier to vary only one parameter in order to cover the required range in  $\Delta a_0$ , for example to have tangential ejection at perihelion and vary only the ejection speed. Such a technique is not only simple, but turns out to be very successful in matching meteor outburst observations.

The numerical integrator therefore only needs to follow the evolution of one particle for each value of  $\Delta a_0$ . An iterative procedure is used to determine the value or values of  $\Delta a_0$  that lead to desired values of  $t_N$ , i.e., causing particles to reach their node when the Earth is at the same longitude. If  $r_E - r_N$  is near zero, then the Earth has a close encounter with the trail. If it has a close encounter, then  $\Omega$  determines the time of closest approach. Whether the time of closest approach actually equals the time at which the Earth's longitude is  $\Omega$  (or  $\Omega + 180^\circ$  as appropriate), or whether there is a small offset, depends on how skewed the trail particle orbits are relative to the Earth's path and also on the shape of the trail cross section [16]. Some encounters with Leonid trails are listed in Table 1.

To generate different values of  $\Delta a_0$  easily, an alternative to varying the tangential ejection speed at perihelion is to assume very low ejection speed and vary the radiation pressure [17]. This gives very similar results for  $r_N$  and  $\Omega$ . In the case of the Leonids, meteoroids of a size that would produce visual meteors and having zero tangential component of ejection velocity (i.e.,  $\Delta a_0 = 0$ ) would be expected to have the same  $P$  as meteoroids not subject to radiation pressure having  $\Delta a_0 \approx +0.2 \text{ AU}$  [7, 18]. Values of  $\Delta a_0$  derived for different trail encounters under a purely gravitational model may be expected to relate to typical brightnesses of observed meteors. Larger (respectively smaller)  $\Delta a_0$  corresponds to larger  $P$  which in turn will tend to be associated

Table 1: Leonid trail encounters during years around present return of 55P/Tempel-Tuttle. Listed are age of trail in revolutions, difference in semi-major axis from comet (highest densities of visual meteor sized particles expected around  $\Delta a_0 \approx +0.2$  AU), difference in heliocentric distance (AU) between Earth and descending node of trail, and estimated time of closest approach to trail.

Trail	$\Delta a_0$	$r_E - r_D$	Date (UT)
3-rev	+0.14	-0.0007	1999 11 18.09
8-rev	+0.06	+0.0008	2000 11 18.16
4-rev	+0.11	+0.0008	2000 11 18.33
7-rev	+0.08	-0.0004	2001 11 18.42
4-rev	+0.14	+0.0002	2001 11 18.76
9-rev	+0.04	+0.0002	2001 11 18.73
7-rev	+0.11	-0.0001	2002 11 19.17
4-rev	+0.17	0.0000	2002 11 19.44
2-rev	+0.96	-0.0001	2006 11 19.20

with a higher proportion of faint (respectively bright) meteors, since smaller particles are more sensitive to radiation pressure.

The success of this idealised technique — calculating  $r_N$  and  $\Omega$  for particles with appropriate  $t_N$  by integrating only one particle for any one value of  $\Delta a_0$  — cannot be confirmed by theory alone. This is because the density profile of a trail cross section depends on ejection away from perihelion and over a range of directions from the nucleus. These aspects of cometary physics are not understood quantitatively to the extent that gravitational perturbations are. The validity of the dust trail technique is confirmed by the excellent fit to observations in every case to which it has been applied, in many streams, e.g. [4, 5, 6, 8, 17, 19, 20]. Occurrences and non-occurrences of outbursts are successfully explained in terms of nodal distances: for any given stream, the encounters calculated to have the smallest values of  $|r_E - r_N|$  consistently match the observed outbursts. For the Leonids, the sharpest outbursts of the 19th and 20th centuries, for which peak times can be determined to within a few minutes [21] essentially fit the calculated peaks to that temporal accuracy [22]. And for the Draconids for example, a prediction to the nearest 0.01 days of the 1998 outburst, occurring on the Earth's encounter with the trail generated at the 1926 return of 21P/Giacobini-Zinner [6] was borne out exactly by observations [23].

Evidently, higher spatial densities of meteoroids are expected to be encountered at smaller  $|r_E - r_N|$ . Various models have been developed that link observed meteor rates with  $r_E - r_N$  and other parameters,

while the possibilities of the true maximum density being marginally shifted from the value of  $r_N$  derived from the dust trail technique, and of the density profile being asymmetrical in  $r_E - r_N$  have also been explored, e.g., [8, 24, 25, 26]. A somewhat different but still physically valid method to model spatial densities is to consider a fuller ejection model [15, 27, 28]. The idealised and simple dust trail technique has nevertheless proved to have great predictive power.

## ACKNOWLEDGEMENTS

I thank the Swedish Research Council for support towards my attendance at *Meteoroids 2001*.

## REFERENCES

- [1] Kresák Ľ., Meteor storms. *Meteoroids and their Parent Bodies*, eds Štohl J. and Williams I.P., Slovak Acad. Sci., Bratislava, 147–156, 1993.
- [2] Sykes M.V. and Walker R.G., Cometary dust trails. I. Survey. *Icarus*, Vol. 95, 180–210, 1992.
- [3] Plavec M., On the origin and early stages of the meteor streams. *Publ. Astron. Inst. Czechosl. Acad. Sci.*, Vol. 30, 1–94, 1957.
- [4] Reznikov E.A., The origin of the Bootid meteor stream. *Trudy Kazan. Gor. Astron. Obs.*, Vol. 47, 131–136, 1983. (In Russian.)
- [5] Kondrat'eva E.D. and Reznikov E.A., Comet Tempel-Tuttle and the Leonid meteor swarm. *Sol. Syst. Res.*, Vol. 19, 96–101, 1985.
- [6] Reznikov E.A., The Giacobini-Zinner comet and Giacobinid meteor stream. *Trudy Kazan. Gor. Astron. Obs.*, Vol. 53, 80–101, 1993. (In Russian.)
- [7] Asher D.J., The Leonid meteor storms of 1833 and 1966. *Mon. Not. R. Astron. Soc.*, Vol. 307, 919–924, 1999.
- [8] McNaught R.H. and Asher D.J., Leonid dust trails and meteor storms. *WGN*, Vol. 27, 85–102, 1999.
- [9] Lyytinen E.J. and van Flandern T., Leonid predictions based on the satellite model of comets. *Earth, Moon & Planets*, Vol. 82, 149–166, 2000.
- [10] Emel'yanenko V.V. and Bailey M.E., Regular and stochastic motion of meteoroid streams in Halley-type orbits. *ASP Conf. Ser. Vol. 104*,

- Physics, Chemistry and Dynamics of Interplanetary Dust*, eds Gustafson B.Å.S. and Hanner M.S., Astron. Soc. Pacif., San Francisco, 121–124, 1996.
- [11] Asher D.J. and Emel'yanenko V.V., The origin of the June Bootid outburst in 1998 and determination of cometary ejection velocities. *Mon. Not. R. Astron. Soc.*, 2001, submitted.
  - [12] Asher D.J., Predictability in meteoroid stream evolution. *Proc. IAU Colloq. No. 181 (Canterbury)*, 2002, submitted.
  - [13] Whipple F.L., A comet model. II. Physical relations for comets and meteors. *Astrophys. J.*, Vol. 113, 464–474, 1951.
  - [14] Jones J., The ejection of meteoroids from comets. *Mon. Not. R. Astron. Soc.*, Vol. 275, 773–780, 1995.
  - [15] Brown P. and Jones J., Simulation of the formation and evolution of the Perseid meteoroid stream. *Icarus*, Vol. 133, 36–68, 1998.
  - [16] McNaught R.H. and Asher D.J., Variation of Leonid maximum times with location of observer. *Meteorit. Planet. Sci.*, Vol. 34, 975–978, 1999.
  - [17] Lyytinen E., Leonid predictions for the years 1999–2007 with the satellite model of comets. *Meta Res. Bull.*, Vol. 8, 33–40, 1999.
  - [18] Williams I.P., The Leonid meteor shower: why are there storms but no regular annual activity? *Mon. Not. R. Astron. Soc.*, Vol. 292, L37–L40, 1997.
  - [19] Kondrat'eva E.D., Murav'eva I.N. and Reznikov E.A., On the forthcoming return of the Leonid meteoric swarm. *Sol. Syst. Res.*, Vol. 31, 489–492, 1997.
  - [20] Jenniskens P. and Lyytinen E., 2000 Ursid outburst confirmed. *WGN*, Vol. 29, 41–45, 2001.
  - [21] Brown P., The Leonid meteor shower: historical visual observations. *Icarus*, Vol. 138, 287–308, 1999.
  - [22] McNaught R.H., On predicting the time of Leonid storms. *The Astronomer*, Vol. 35, 279–283, 1999.
  - [23] Arlt R., Summary of 1998 Draconid outburst observations. *WGN*, Vol. 26, 256–259, 1998.
  - [24] McNaught R.H. and Asher D.J., The 2001 Leonids and dust trail radiants. *WGN*, Vol. 29, 156–164, 2001.
  - [25] Lyytinen E., Nissinen M. and van Flandern T., Improved 2001 Leonid storm predictions from a refined model. *WGN*, Vol. 29, 110–118, 2001.
  - [26] Jenniskens P., Model of a one-revolution comet dust trail from Leonid outburst observations. *WGN*, Vol. 29, 165–175, 2001.
  - [27] Brown P. and Jones J., Dynamics of the Leonid meteoroid stream: a numerical approach. *ASP Conf. Ser. Vol. 104, Physics, Chemistry and Dynamics of Interplanetary Dust*, eds Gustafson B.Å.S. and Hanner M.S., Astron. Soc. Pacif., San Francisco, 113–116, 1996.
  - [28] Brown P. and Cooke B., Model predictions for the 2001 Leonids and implications for Earth-orbiting satellites. *Mon. Not. R. Astron. Soc.*, Vol. 326, L19–L22, 2001.

# COMMON GROUND-BASED OPTICAL AND RADIOMETRIC DETECTIONS WITHIN CZECH FIREBALL NETWORK.

Pavel Spurný<sup>(1)</sup>, Richard E. Spalding<sup>(2)</sup>, Cliff Jacobs<sup>(2)</sup>

<sup>(1)</sup> *Astronomical Institute, Ondřejov Observatory, 251 65 Ondřejov, Czech Republic,*

<sup>(2)</sup> *Sandia National Laboratories, Post Office Box 5800, Albuquerque, New Mexico 87185-0978, USA*

*Email: spurny@asu.cas.cz*

## ABSTRACT

This paper describes first results of common detections of fireballs by photographic cameras in Czech Fireball Network (CFN) and the new radiometric systems equipped with sensors with very high time and intensity resolutions placed at two stations of this network, Ondřejov Observatory and Kunžak. Since August 1999, when we started regular operation of two radiometric systems, we have detected 17 different fireballs. Eleven of them were recorded simultaneously by photographic cameras, another six were only single radiometric detections as radiometers can detect meteoric events also under cloudy conditions. From two most suitable common events we performed calibration of radiometers and we determined their sensitivity. We found significant differences between lightcurves of slow and fast meteors recorded by these techniques, and finally, we found substantial differences in shapes of lightcurves for fireballs belonging to the same meteor stream observed in only 2.5 hours time interval.

**Key words:** meteors; fireballs; photometry; meteor photography; Leonids.

## 1. INTRODUCTION

This work is mainly based on comparison of lightcurves obtained from our standard optical experiment – the Czech Fireball Network, and from the new radiometric systems, which continually monitor the whole visible hemisphere and record the light and its change with a very high time resolution.

The Czech Fireball Network consists of 10 stations covering quite uniformly whole territory of the Czech Republic (Fig.1). One fixed camera is located at each station and equipped with very precise Zeiss Distagon fish-eye objective ( $f/3.5$ ,  $f = 30$  mm). More details about location and equipment of the stations are in [1].

The radiometer is a Personal Computer (PC) based hardware and software system that is used to monitor the sky for nighttime optical events with a very high time resolution of 1200 samples/sec. The radiometer

consist of the visible wavelength sensors unit, a 30m cable that transfers data from the sensor assembly to the interface box, 68 pin interface cable that transfers data from an interface box to the acquisition board inside the PC and a PC for the actual data acquisition, archiving, viewing data files and searching for events. This



Fig.1. Schematic display of stations of the Czech Fireball Network on the territory of the Czech Republic.

instrument has been developed and constructed at Sandia National Laboratories. The main advantage of the radiometer consists in its very high sample rate which enables us to record the most detailed lightcurves of fireballs ever obtained and also study very fast changes in brightness.

## 2. OBSERVATIONAL DATA

Between August 1999 and July 2001, the radiometric systems placed at Ondřejov Observatory and Kunžak station (see Fig.1) have recorded 17 individual meteoric events. Eleven of them were recorded simultaneously by photographic cameras of the CFN, another six events were only single radiometric detections, because radiometers can detect bright meteors also under cloudy conditions. Only three of these 11 common cases were bright and long enough to be used for calibration and more detailed study of lightcurves of fireballs recorded by both techniques. Other radiometric detections were used for the determination of exact timing of these

fireballs as the radiometric record is continuously corrected by the DCF time signal and for the estimate of the maximum brightness of these events.

This paper mainly deals with two above-mentioned cases, which were well detected by both experiments, the third one was published separately in [7]. Complete atmospheric trajectories data, photometry as well as orbital data were computed for all of these fireballs from multistation photographic records by means of our standard procedures [2,3].

The radiometers record total brightness of the sky with sample rate  $1200\text{s}^{-1}$  and when we plot these intensities as depend on time we obtain lightcurve of the studied event. Such lightcurves for fireballs described below are shown in Figs. 4, 6, 8 and 11. The y-axis is linear in

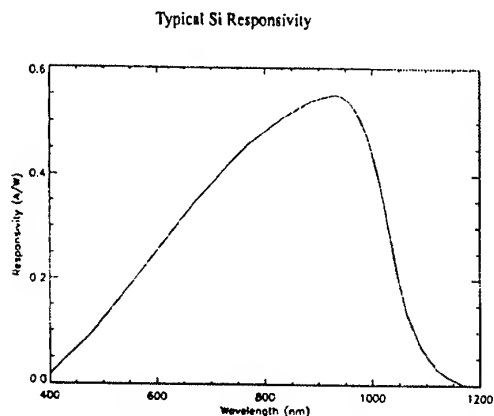


Fig. 2. Typical silicon detector responsivity (A/W) as a function of wavelength [5].

irradiance (in arbitrary units) and the x-axis represents the relative time in seconds. The responsivity function of optical sensors used in the radiometer units is presented in Fig.2 [4]. It is evident that the maximum sensitivity of these sensors is between 800 to 1000 nm in the near infrared region.

As we obtain intensities in arbitrary units, we have to find relation between these units and real brightness of meteoric event expressed in magnitudes. Such calibration of radiometric records was possible to determine from two fireballs well detected by both techniques.

## 2.1. EN270200 Fireball

This bright fireball represents the group of slow fireballs with the entry velocity below 30 km/s. All important data describing atmospheric trajectory and heliocentric orbit of this fireball along with data for the second studied fireball EN130800 are collected in Tables 1 and 2. The individual entries accompanied with their standard deviations have the following meaning:  $M_p$  is

Fireball No.	EN270200	EN130800
Date	2000 Feb 27	2000 Aug 13
Time (UT)	$19^{\text{h}}22^{\text{m}}57.0^{\text{s}} \pm 0.3^{\text{s}}$	$0^{\text{h}}33^{\text{m}}27.1^{\text{s}} \pm 0.3^{\text{s}}$
$M_p$	-10.2	-9.3
$m_{\infty}$ (kg)	10.	0.024
$h_B$ (km)	$84.938 \pm 0.005$	$102.61 \pm 0.02$
$\lambda_B$ (deg E)	$14.6604 \pm 0.0002$	$16.6314 \pm 0.0005$
$\varphi_B$ (deg N)	$49.8839 \pm 0.0001$	$51.7666 \pm 0.0003$
$h_E$ (km)	$31.505 \pm 0.005$	$76.19 \pm 0.02$
$\lambda_E$ (deg E)	$14.4956 \pm 0.0001$	$16.4267 \pm 0.0004$
$\varphi_E$ (deg N)	$49.6653 \pm 0.0001$	$51.6772 \pm 0.0003$
$l$ (km)	60.03	31.71
$t$ (s)	3.35	0.53
Slope (deg)	$62.94 \pm 0.02$	$56.42 \pm 0.08$
PE / Type	-4.57 / I	-5.27 / IIIA

Table 1. Atmospheric trajectory data of the EN270200 and EN130800 fireballs.

Fireball No.	EN270200	EN130800
$\alpha_R$ (deg)	$139.46 \pm 0.02$	$46.17 \pm 0.15$
$\delta_R$ (deg)	$70.721 \pm 0.012$	$58.33 \pm 0.08$
$v_{\infty}$ (km/s)	$18.827 \pm 0.005$	$60.37 \pm 0.12$
$\alpha_G$ (deg)	$145.33 \pm 0.03$	$46.45 \pm 0.15$
$\delta_G$ (deg)	$72.786 \pm 0.013$	$58.46 \pm 0.08$
$v_G$ (km/s)	$15.102 \pm 0.006$	$59.20 \pm 0.13$
$v_H$ (km/s)	$38.702 \pm 0.005$	$41.47 \pm 0.12$
$a$ (AU)	$3.021 \pm 0.004$	$28. \pm 9.$
$e$	$0.6818 \pm 0.0004$	$0.966 \pm 0.011$
$q$ (AU)	$0.96141 \pm 0.00003$	$0.9642 \pm 0.0009$
$Q$ (AU)	$5.080 \pm 0.007$	$56. \pm 19.$
$\omega$ (deg)	$201.896 \pm 0.011$	$154.4 \pm 0.3$
$\Omega$ (deg)	$338.51329 \pm 0.00001$	$140.5757 \pm 0.0001$
$i$ (deg)	$18.641 \pm 0.006$	$112.64 \pm 0.13$

Table 2. Radiants and orbital elements (J2000.0) of the EN270200 and EN130800 fireballs.

the maximum absolute magnitude,  $m_{\infty}$  is the initial photometric mass,  $h_B$  and  $h_E$  are the beginning and terminal heights of the luminous trajectory,  $\lambda_B$ ,  $\varphi_B$ ,  $\lambda_E$ ,  $\varphi_E$  are the geographic coordinates of the vertical projection of the beginning and terminal points onto the surface of geoid,  $l$  is the total length of the luminous trajectory of the fireball,  $t$  is its duration,  $PE$  is the empirical end height criterion for fireballs and  $Type$  is

the classification of fireballs. In Table 2  $\alpha_R$ ,  $\delta_R$  are the right ascension and declination of the observed radiant,  $v_\infty$  is the initial velocity,  $\alpha_G$ ,  $\delta_G$  are the right ascension and declination of the geocentric radiant (corrected for the Earth's rotation and for zenith attraction),  $v_G$  is the geocentric velocity,  $v_H$  is the heliocentric velocity, and  $a$ ,  $e$ ,  $q$ ,  $Q$ ,  $\omega$ ,  $\Omega$ ,  $i$  are the orbital elements using the normalized symbols. The angular orbital elements as well as all the right ascensions and declinations are given in the J2000.0 coordinate system.

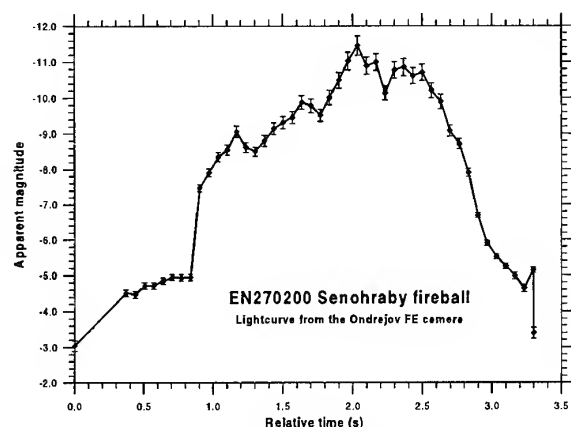


Fig. 3. Lightcurve of the EN270200 fireball from Ondřejov FE camera in apparent magnitudes as a function of time.

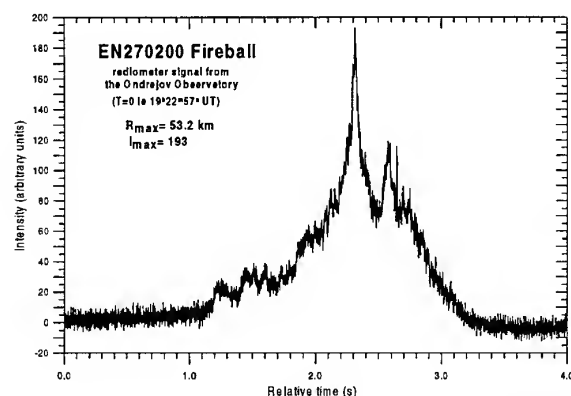


Fig. 4. Radiometer record of the EN270200 fireball from the Ondřejov Observatory. The y-axis is linear in irradiance, the x-axis is a relative time.  $T=0$  corresponds to  $19^h22^m57.0^s$  UT.

The EN270200 fireball was recorded on 4 stations of the CFN and belongs to the most precisely described fireballs ever photographed in the CFN. Along with the direct FE images we have also two very detailed photographic spectral records of this fireball containing several hundreds of emission lines taken at the Ondřejov

Observatory. Fortunately, the atmospheric trajectory was very favorable for the precise photographic photometry because the fireball was very close to the Ondřejov station. Whole luminous trail recorded on Ondřejov FE camera was between 81 to 43 degrees above horizon. The photographic lightcurve is presented in Fig. 3. Simultaneously this fireball was detected on both radiometers, at Ondřejov and Kunžak stations. The radiometric record from Ondřejov is shown in Fig. 4. The distance of the maximum intensity  $R_{\max}$  was only 53.2 km from the radiometer. The record from Kunžak station has exactly the same shape, but it is much noisy and also the maximum is not so high because distance of the fireball was significantly higher from Kunžak than from Ondřejov. The noise of this record was higher due to street lamps interference.

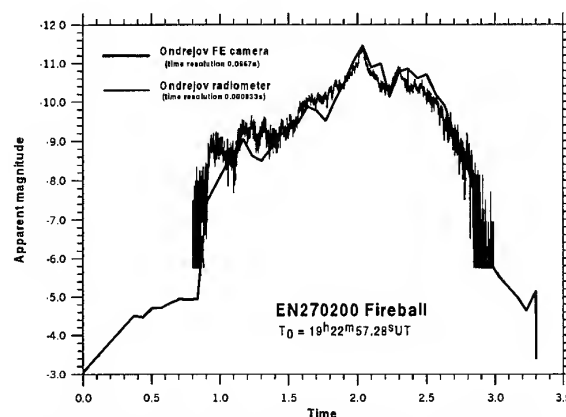


Fig. 5. Comparison of the lightcurves obtained from photographic FE camera and radiometer.

Now we can compare both lightcurves. When the y-axis of the radiometer record is in logarithm of intensities we can plot both lightcurves into one graph as it is shown in Fig. 5. It is evident that the correlation between both plots is very good. To obtain such a good agreement we have to shift radiometer data towards the photographic lightcurve. We found the following relation between intensity  $I$  of the radiometer signal and apparent magnitude  $m$ :

$$m = -2.5 \log I - 5.75 \quad (1)$$

The shift of  $-5.75$  mag with the average noise of 15 units represents the limiting magnitude of the radiometer for slow meteors, which is according to (2)  $-8.7$  mag. The relation (2) is valid for both radiometers as they have exactly the same sensors and circuits.

The shape of the lightcurve taken by radiometer or FE photographic camera at Ondřejov is quite typical for this type I fireballs. For these fireballs we can observe gradual increase and decrease phase with not so

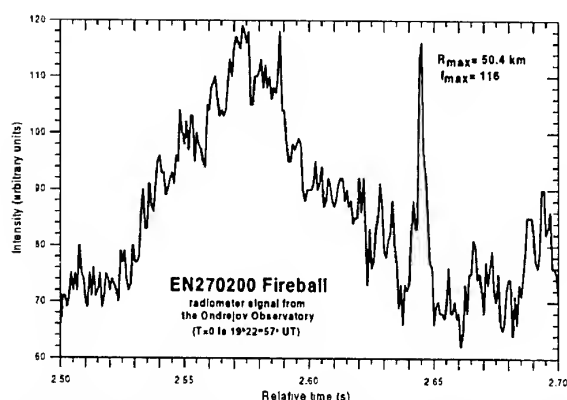


Fig. 6. Detail of the lightcurve of the EN270200 fireball with very short flare.

significant flares in the central part. It well corresponds with observed lightcurve. However, there is one very interesting feature, observed only on radiometer record because of its very high sample rate. It is a very short, only 5 ms long and 0.5 magnitude high flare at 2.65s. This part of lightcurve is shown in more detail in Fig. 6. The flare was observed at a height of 41 km and distance of 50.4 km. This very interesting feature is nicely visible also in the very detailed spectral record, which was taken by long-focal camera ( $f = 360\text{mm}$ ,  $f/3.5$ ) equipped with the transparent objective grating (600 grooves/mm). Detailed study of emission conditions in this part of spectral record could reveal processes, which can cause such an extremely short flare. The spectrum was not evaluated yet.

## 2.2. EN130800 Perseid Fireball

The EN130800 fireball was another very suitable case for comparison of photometric data of a bright meteor

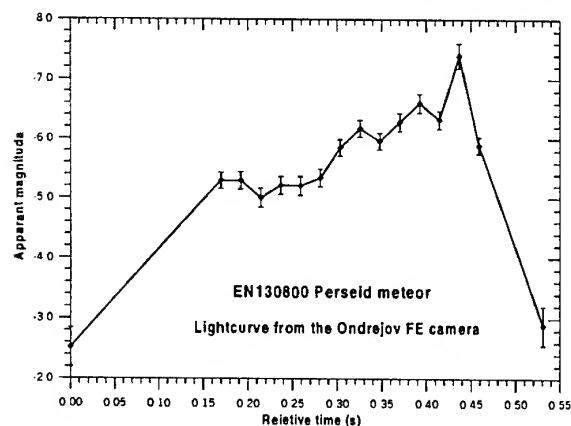


Fig. 7. Lightcurve of the EN130800 fireball from the Ondřejov FE camera in apparent magnitudes as a function of time.

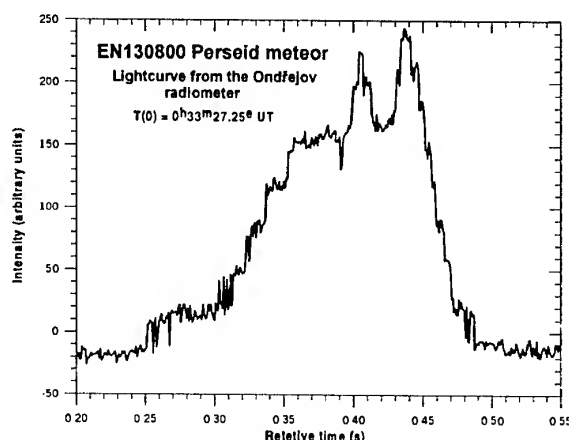


Fig. 8. Radiometer record of the EN130800 fireball from the Ondřejov Observatory. The y-axis is linear in irradiance, the x-axis is a relative time.  $T=0$  corresponds to  $0^h33^m27.25^s$  UT.

taken by photographic cameras and radiometers. All basic data describing this fireball are presented along with the previous case in Tables 1 and 2. From orbital elements it is evident that it was a member of the Perseid meteor stream. It means that in contrast to the previous fireball, it was a high velocity meteor with the cometary origin. In Figs. 7 and 8, there are presented lightcurves derived from photographic and radiometric records, respectively. Both lightcurves were taken at the Ondřejov Observatory. The photographic lightcurve is not so detailed because the meteor was very fast and it means also much shorter in duration. When we plotted both lightcurves to one graph (Fig. 9) similarly like for the EN270200 fireball in Fig. 5, we found that the agreement is evidently not so good and both lightcurves

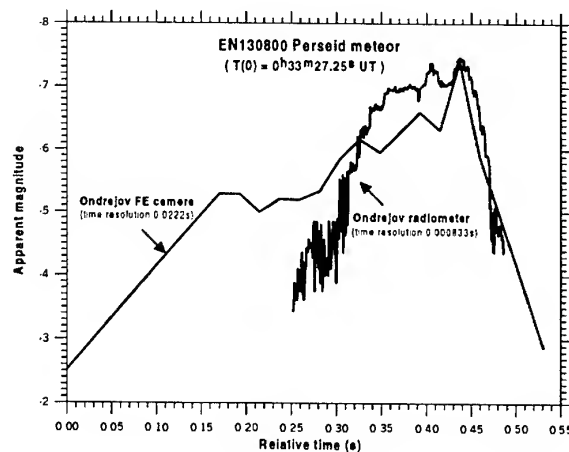


Fig. 9. Comparison of the lightcurves obtained from photographic FE camera and radiometer for the EN130800 fireball.

differ significantly. For the best correlation of both lightcurves we have to modify the relation (1) to:

$$m = -2.5 \log I - 1.5 \quad (2)$$

The shift is only  $-1.5$  magnitude and with the average noise of 15 units it means that the limiting magnitude of the radiometer is around  $-4.4$  for fast meteors. There is the evident question: why the lightcurves taken by radiometer and photographic cameras substantially differ for this case and why the radiometer is significantly more sensitive for the fast Perseid meteor than for the slow EN270200 fireball?

We found the following explanation of this observational fact. The spectral sensitivity of the silicon sensors is shown in Fig. 2. These sensors are the most sensitive between 800 to 1000 nm. On the other hand, panchromatic films used in our cameras are sensitive to radiation in the wavelength range from 360 to 675 nm. Borovicka et al. in [5] found that fast meteors radiate mainly in the near infrared spectral region. It is shown for one Leonid meteor in Fig. 10. The brightest lines belong to atomic oxygen and nitrogen. This is not observed for slow meteors with velocities below 30 km/s [6]. Therefore, when we take into account the significant difference in spectral sensitivity between photographic emulsion and silicon sensors and significant difference in spectral radiation between fast and slow meteors we can explain the observed discrepancy, which is expressed in relations 1 and 2. It means that the radiometer is significantly more sensitive (of about 4.25 magnitude) for faster meteors mostly belonging to the main meteor streams as Perseids, Leonids, Orionids, etc., than for slow, mostly sporadic meteors, which radiate dominantly in the visible region.

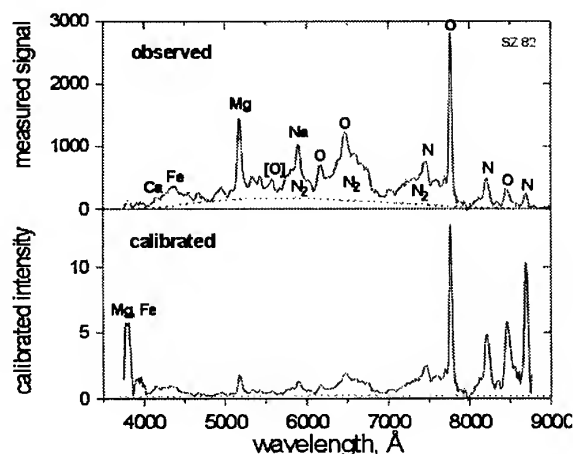


Fig. 10. The TV spectrum of the Leonid meteor with the identification of the main features [5]. The upper panel shows the spectrum as it was observed. The lower panel shows the spectrum after calibration for spectral sensitivity of the image intensified TV camera.

### 2.3. EN310800 Vimperk Fireball

This extraordinary and very bright fireball was observed photographically at two stations of the CFN and also by the Kunžak radiometer. All important data concerning the atmospheric trajectory, heliocentric orbit as well as the precise photometry from the radiometric record including the study of periodic variations in the first half part of lightcurve was published in a separate paper [7].

### 2.4. Leonids 1999

Four bright Leonid meteors were recorded by the Ondřejov radiometer during the very high activity of the Leonid meteor stream on November 18, 1999. Unfortunately we have no simultaneous photographic observations because the weather was bad over whole Czech Fireball Network. Only at Ondřejov we took one FE picture through some clear spots. All four Leonid meteors were observed in a short, only  $2^h34^m$  long interval, and probably belong to the narrow peak of activity of one filament. Lightcurves of these meteors are presented in Fig. 11 a-d. According to the relation (2), the maximum apparent brightness for meteor A was  $-6.7$ , for meteor B  $-7.5$ , for meteor C  $-5.9$  and for meteor D  $-5.6$  magnitude. Significant differences among these lightcurves are evident. While EN181199A has a symmetric lightcurve with the big and very short terminal flare, thus the EN181199C has no flare at all and the lightcurve is skewed to the beginning. The EN181199B has terminal flare but it is much broader than for EN181199A and finally, the EN181199D is skewed to the end with only small terminal flare. The shape of lightcurve can tell us something about ablation processes and structure of the radiating body. Therefore we can conclude that even all these meteors belonged to the same meteor stream and probably also to the same filament, they had to have significantly different inner structure.

## 3. DISCUSSION

We compared the photographic and radiometric detections of two fireballs. From the photometry of photographic records we derived the calibration relations for radiometric records. We found significant difference in radiometer sensitivity for slow and fast meteors of about 4.3 mag. When the slow meteors have very similar lightcurves from both experiments, the lightcurves for fast meteors differ substantially as the radiation of these meteors is mainly in the near infrared region where the radiometer sensors are the most sensitive. In one very bright case, the periodic variations were found in the first half part of the lightcurve [7]. Such variations were observed only for this fireball. Finally, the lightcurves of Leonid meteors observed in a short interval exhibit significant differences even though

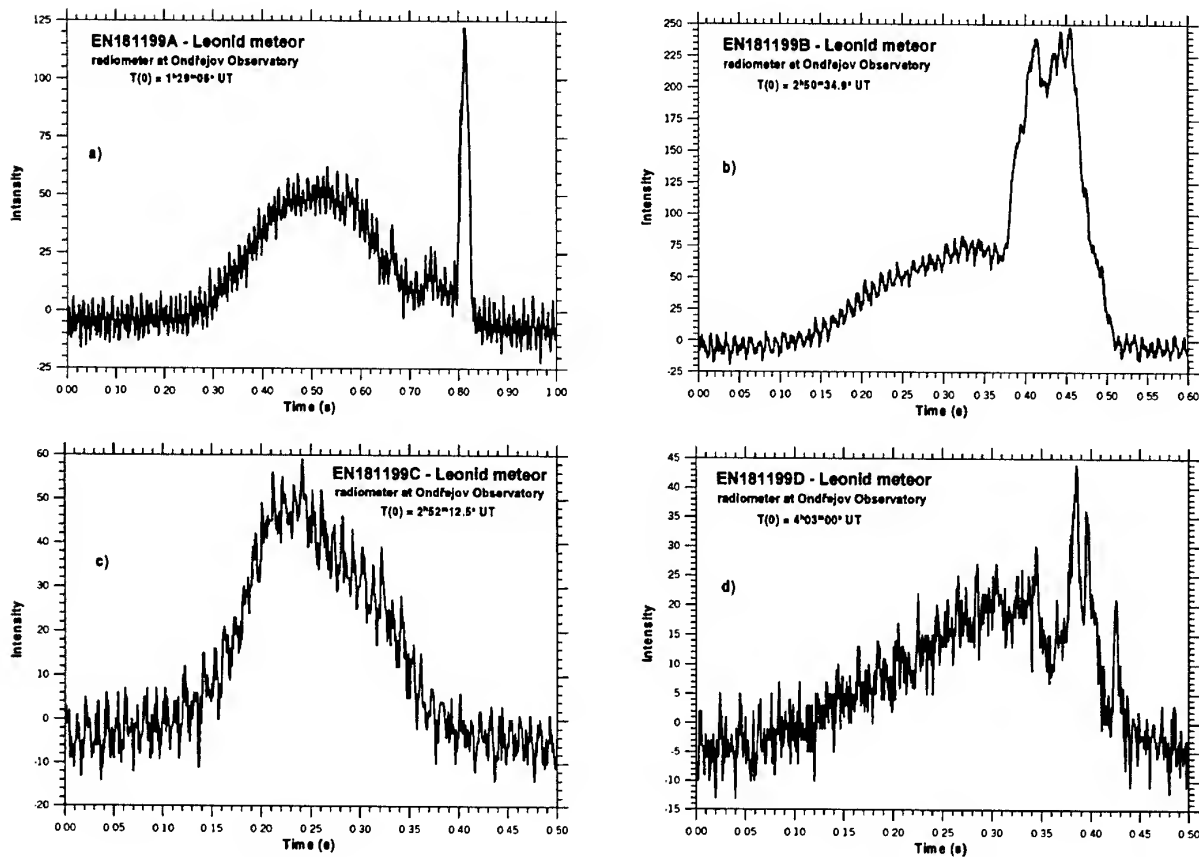


Fig.11 a-d. Radiometer lightcurves of the Leonid meteors recorded at the Ondřejov Observatory in the night of November 18, 1999. The y-axis is linear in irradiance, the x-axis is a relative time.

all these meteors belong to the same meteor stream and probably also to the same filament. It shows the structure inhomogeneity within these Leonid meteoroids.

Another important product of radiometric records is the exact timing for all observed events.

#### Acknowledgements

We are very much indebted to all observers at the stations of the Czech Fireball Network for their devoted service leading to data on fireballs published in this paper. Our special thanks are due to J. Keclíková, who measured all photographic records and to J. Boček who is systematically taking care of the Czech fireball stations. We also very much appreciate the important contribution of T. Gibson and J. Daniels from Sandia National Laboratories for their work on sensor units and radiometer software.

This work has been partly supported by project No. K1-003-601 of the Czech Academy of Sciences and by grants of the Grant Agency of the Czech Republic Nos. 205-00-1727 and 205-99-0146.

#### 4. REFERENCES

1. Spurný P. Photographic Monitoring of Fireballs in Central Europe. *SPIE Vol. 3116*, 144-155, 1997.
2. Ceplecha Z., Geometric, Dynamic, Orbital and Photometric Data on Meteoroids from Photographic Fireball Networks. *Bull. Astron. Inst. Czechosl.*, Vol. 38, 222 – 234, 1987.
3. Borovička J., et al. A New Positional Astrometric Method for All-sky Cameras. *Astronomy & Astrophys. Suppl. Ser.*, Vol. 112, 173 – 178, 1995.
4. Tagliaferri E., et al. Detection of Meteoroid Impacts by Optical Sensors in Earth Orbit. In: *Hazards due to Comets & Asteroids*, ed. T. Gehrels, 199-220, 1994.
5. Borovička J., et al. First Results from Video Spectroscopy of 1998 Leonid meteors. *Meteoritics & Planetary Science*, Vol. 34, 987 – 994, 1999.
6. Borovička J., Video Spectra of Leonids and Other Meteors. *This volume*. In print.
7. Spurný P. and Borovička J., EN310800 Vimperk Fireball: Probable Meteorite Fall of an Aten Type Meteoroid. *This volume*. In print.

# PREDICTION AND OBSERVATIONS OF LEONID METEOR SHOWER IN CHINA

Guang-jie Wu<sup>(1,3)</sup>, Guang-yu Li<sup>(2,3)</sup>, and Yue-hua Ma<sup>(2,3)</sup>

<sup>(1)</sup> Yunnan Observatory, Chinese Academy of Sciences, Kunming 650011, P. R. China,  
Email: ynaowugj@public.km.yn.cn

<sup>(2)</sup> Purple Mountain Observatory, Chinese Academy of Sciences, Nanjing 210008, P. R. China

<sup>(3)</sup> National Astronomical Observatories, Chinese Academy of Sciences, Beijing 100012, P. R. China

## ABSTRACT

Recent years, observations by both visible and radio have been performed under the organizing of Chinese Leonid Watch. We have observed some interesting phenomena, like the filamentary structure of the shower, the variations of the size distribution of meteoroids and the mass density. In addition, we made progress in their data processing. We observed the expected main shower in 1998 with radio. An abnormal peak in the ionosphere characteristic value was also detected about 18 hours after the main shower. From the fundamentals of celestial mechanics, we find the differences between the longitude of the ascending node of meteoroids and that of their parent comet depends on the ejection position as well as the ejection velocity. We successfully predicted the Leonids in 1999 and 2000.

Key words: Meteoroids; Leonids; Comet; China.

## 1. INTRODUCTION

China has long history in culture, in astronomy, including in its special field—meteor astronomy. Early in BC 1575, “stars fell like rain” was recorded. The earliest record about the Leonids in China has been found in AD 931 [1]. Leonid meteoroid stream is one of the most famous meteoroid streams. It displayed the most strong meteor storm in 1966. Recent years, this return of its parent comet Tempel-Tuttle in 1998 has brought a new research age of meteors to China and the whole world. One kind of predictions said people may observe a fairly strong but far from record-breaking outburst in 1998-2000. In 1998 the best prospects seemed to be for the longitudes of eastern Asia. It may have another

Leonid meteor storm in 1998 in China [2-4]. All of these have aroused Chinese astronomers' enthusiasm. They have paid much more attention to meteor astronomy than ever.

## 2. OBSERVATIONS IN RECENT YEARS

Observations by both visible and radio have been performed under the organizing of Chinese Leonid Watch (CLW). Since 1998, CLW has obtained financial support by the National Natural Science Foundation of China. In addition, foreign astronomers came to China for Leonids observations in 1998 from Netherlands, USA, France, and Czechoslovakia. They performed their cooperation in Qinghai and Beijing with Chinese astronomers [5-6]. Most years the Leonid shower is very weak, its  $ZHR_{max}$  being only about  $23 \pm 6$  [2], but it has already been picking up strength and becoming more active in the last few years with ZHR up to 80 and rich in bright meteors [3]. In 1998, substantial Leonid activity occurred earlier than expected. Chinese and Dutch astronomers in Qinghai firstly observed an activity of very bright fireballs [6].

We have observed Leonids continuously from 1998 to 2000 at Gaomeigu station of Yunnan Observatory. The elevation of this highland station is about 3200 meters. This place was found by the “Site Survey” team in recent years. Here the stellar image has a FWHM of only 0.7 arcseconds. In our 5 days observations in 1998, the activity of the Leonids showed an asymmetric feature for the peak maximum. The ZHR increased steadily in the early morning of November 17th in Beijing time (it is UT+8h). However, it deceased slowly in the following two days. This situation is significant and remained in 1999. On the other hand, before the peak maximum

in our observations in 1998, the population index  $r$  had been increasing [7-8]. The observations in 1998-2000 discovered interesting phenomena like filamentary structure in both number flow and mass flow, but they went to their maximum at different time. The variation of  $r$  may be more violent and frequent in 1998 than that in 1999. Whereas, in most case, it was about 2.0. It is very hard to distinguish which dust trail the Earth encountered is old or new. The dust trails of 4-revolution and 5-revolution seem to leave nothing on our records as predicted [8-9].

In data processing, the ZHR (Zenith Hourly Rates) is commonly used to express a shower's activity:

$$ZHR = \frac{N}{T_{eff}} \times r^{6.5-L_m} \times \sin(h_r)^{-\gamma} \times c_p^{-1}, \quad (1)$$

where  $N$  is the number of meteors recorded,  $T_{eff}$  is the effective observing time in hours, and  $L_m$  the limiting stellar magnitude. ( $h_r$ ) is the elevation of the radiant at the observation time, and usually we can take the parameter  $\gamma=1.0$ . ( $c_p$ ) is a correction factor, including the effects of field of view and cloudy cover, which varies between 0.4 and 2.5 and has a median value close to 1.0 [2,7]. The goal of all reductions is to correct an imperfect observation to a standard, which an ideal observer would see per hour in perfectly clear sky and the shower's radiant overhead. Obviously, in meteor observations the population index  $r$  is often used, which denotes the number distribution of meteors in their magnitude classes. In calculation of  $r$ , we need know about the probability of perception for the visual observer. We found a function

$$P(\Delta m) = \frac{1}{2} + \frac{1}{2} \sin\left\{\frac{\pi}{2}\left[\left(\frac{\Delta m}{c} + q\right)^p - \left(\frac{3.93}{c} + q\right)^p\right]\right\} \quad (2)$$

when  $\Delta m \leq 3.93$  with

$$p = 2.7, \quad q = 0.38, \quad c = 6.33,$$

and while  $\Delta m > 3.93$ , with

$$p = 0.78, \quad q = -0.80, \quad c = 4.90,$$

can fit well the data of probability of perception given by Koschack and Rendtel (see Fig. 1) [10-11].

Using this function is much convenient for calculation and analysis. It is easy to see that in any case in the distribution of visual observed number of meteors, the integrate number in subsection of  $\Delta m \geq \Delta m_{peak}$  is much great than that in subsection of  $\Delta m < \Delta m_{peak}$ , where

$$\Delta m = L_m - m \quad (3)$$

is the difference between observed magnitude  $m$  and the limiting magnitude. In virtue of the advantage of Eq.2, several methods of estimating and calculating the popular index  $r$  have been put forward. The

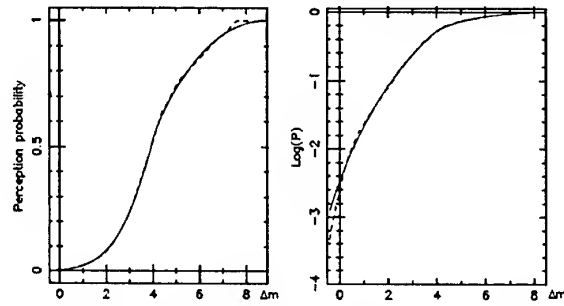


Figure 1. An analytic fitting to a set of data of perception probabilities listed by Koschack and Rendtel (1990, indicated by dash-line): (a) in digital scale, and (b) in logarithm scale.

methods of peak-magnitude-difference, Full Width at Half Maximum et al. are easy and convenient to use, could quickly estimate a rather good value of  $r$ . For observations with enough meteors and enough magnitude subsections, the Least Square Fitting would give a good result of the  $r$  conveniently. However, its improper use in some imperfect data set will give an incorrect result. This situation may be improved by the iterative method, which is suitable for two or more magnitude subsections. Crossing use of several methods could eliminate the effect of the random error in observations largely.

We have not only used the ZHR as a number counting of meteors, but also suggest a Zenithal Hourly Mass Rates (ZHMR)

$$ZHMR = \frac{\sum N_m M_m}{T_{eff} \cdot A_{red}(r)} r^{6.5-L_m} \times \sin(h_r)^{-1} \times c_p^{-1} \quad (4)$$

as a measurement of mass flow. Where its difference from ZHR is  $M_m$  and  $A_{red}(r)$ .  $M_m$  represents the mass of a meteor with magnitude  $m$ , which can be got by

$$\log M_m = 6.06 - 0.62m - 3.89 \log V_\infty - 0.67 \log(\sin(h_r)). \quad (5)$$

where  $V_\infty$  is the incoming geocentric velocity of the meteor.  $A_{red}(r)$  is the reduced area of a field of view with a radius of  $R = 52.95$  [11]. In general, the ZHMR and ZHR would have different tendency and go to their maximum at different time (see Fig. 2). In fact, the radio, telescope, visual/video and photographic meteor maximum may occur at different times from one another [6]. So that, different techniques of observations may detect meteors produced by particles whose masses differ no more than several orders of magnitude. It may make certain difficulties in the interpretation of the observations. If we use ZHMR instead of ZHR, we may not need the knowledge

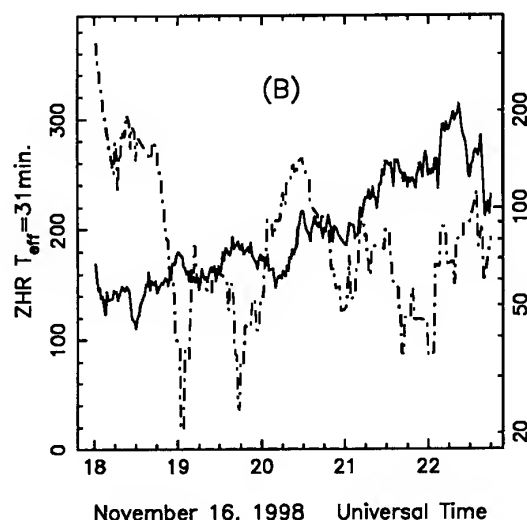


Figure 2. Leonid meteor shower on 16 November 1998: The variations of ZHR and ZHMR, both using  $T_{eff} = 31$  minutes. ZHR is indicated with left scale, and ZHMR by dash-dot curve with right scale.

of split but only the spatial density of mass. We consider using a ZHMR instead of ZHR might be more suitable for prediction [8].

Besides visual observations, though the photographic observations of two meteors with photographic magnitude of  $-10.3 \pm 0.2$  and  $-4.8 \pm 0.2$ , respectively, we found the settle time of a meteor in the sky has about  $0.6$  s [12], it means the meteors traveled about 40–50 km in the earth's atmosphere.

As for radio meteors, our radar located in Radio Wave Propagation Institute of China is a high frequency skywave radar with a frequency and a pulse power of 20.028 MHz and 15 kw, respectively. It can record all of the meteors brighter than about 8.2 mag and there is no problem about probability of discovery. During the period of 14–20 November 1998, it was found that the echo signals were few, short in time, and weak on November 15 and 16, but it displayed two peaks on 17 November and as high as about  $2500 \text{ hr}^{-1}$ . One of them occurred at 19:00–19:51 UT, and another at 20:15–21:30 [13]. This is almost the expected time for maximum of the main shower. Arlt deduced the first maximum in this year occurred at  $1\text{h}55\text{m} \pm 9\text{m}$  UT on November 17, 1998 with  $\text{ZHR} = 357 \pm 11$ . And the second maximum, which was composed chiefly of faint meteors and was comparatively transient, took place at  $20\text{h}33\text{m} \pm 10\text{m}$  UT on November 17 with  $\text{ZHR} = 136 \pm 5$ . It means that the intensity of the first maximum is twice higher than that of the second maximum [14–15, 2–4]. Moreover, the both radio peaks coincided the visual peaks at 19:20 and 20:40 observed

by Sino-Dutch expedition in Qinghai and Hebei [6, 16] (see Fig. 3). This implies that the meteoric showers observed by visual and radio methods have identical structures on November 17.

It seems that bright meteors and fireballs occupied a significant percentage on 16 November. These particles were explained to be ejected from the comet in 1333 [17]. But faint and radio meteors were more active on the next day [6]. While the first maximum the intensity of radio meteors does not exceed 200, i.e. it is less than one tenth of its burst value. We think that we should consider the complexities of the small-scale structure and composition of Leonids in this return. During the two days it must be two different particle streams [16]. See the population index  $r$ , on 16 November  $r$  is less than 2.0, in general [16, 8]. Whereas, on 17 November it exhibits a property of non-uniformity violently. At some places of China  $r$  was still less than 2.0, but in Xinjiang and Changchun  $r$  was detected to be larger than 3.0. The non-uniformity of  $r$  was not caused by the error of observer himself but by the proper characteristic of Leonid meteor stream. This discrepancy may be interpreted that during the first peak the meteor shower was a particle stream of unitary composition, but during the second peak it was formed by the combination of two different constituents. Among them, the constituent, which consisted of large particles, was similar to that of the first peak, or they were just identical. The other constituent, which was chiefly composed of small particles, joined the stream only afterwards. Because these two constituents mixed not uniformly and the peak lasted rather shortly, so on the cross section where the Earth intercepted the meteoric stream the former constituent prevailed in some places, and the latter constituent prevailed in other places. Therefore, the compositions of the meteoric shower observed at various sites were different, and the measured values of  $r$  showed also a relationship of location-dependent. In 1998, using the observations in the whole world, Arlt got  $r = 2.00$  [4]. Obviously this is a result for the mixed two particle streams. In fact, for the mixed stream,  $r$  should have a smaller value in subsection of bright meteors, and tend to a larger value in faint meteors. We can get the accumulated number of meteors up to 6.5 mag without any omission to be multiplying the observed ZHR by a factor as

$$c(r) = 0.987 - 5.918 \times r + 6.637 \times r^2 - 0.7540 \times r^3 \quad (6)$$

which is perfectly valid between  $r = 1.1$  and  $4.4$  [4]. For  $r = 1.4$  the  $c(r) = 3.64$ . If we suppose  $r = 3.4$  represents the stream containing only the abundant smaller particles, the  $c(r) = 27.95$ , which is about 7.7 times larger than that of  $r = 1.4$ . For the radar, it can record all the meteors brighter than its limiting magnitude of 8.2 and there is no any omission, it should observe 61.5 times more meteors than limiting magnitude of 6.5 mag for  $r = 3.4$ . Fig. 4

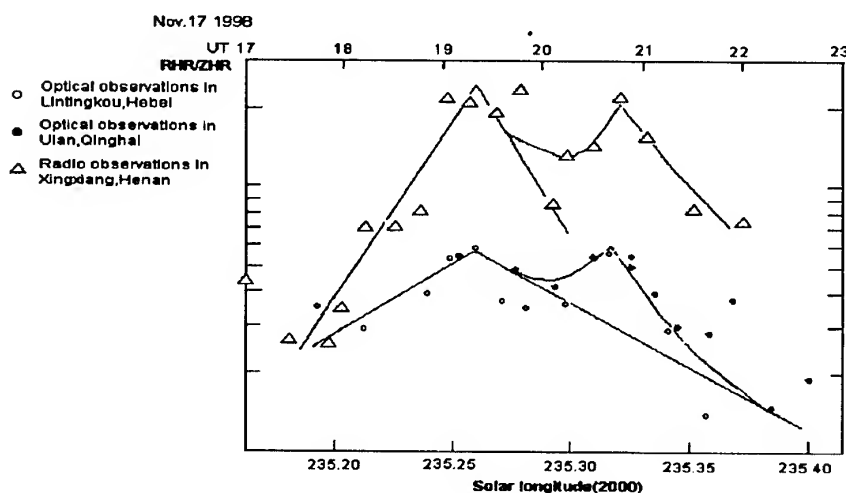


Figure 3. Comparison of optical ZHR and radio RHR during the second peak time

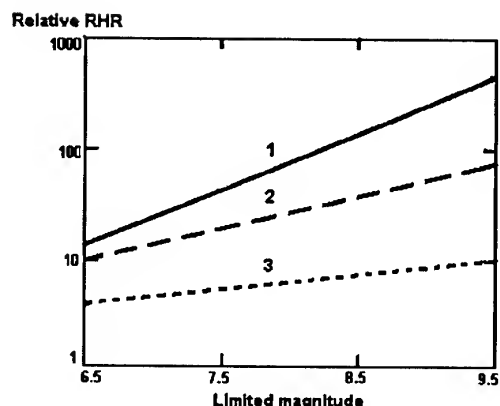


Figure 4. Relative number of meteors that can be recorded by radar per hour

provides the curves showing the general relations between the limiting stellar magnitude and the relative number of meteors that can be recorded by radar per hour. Curves 1 and 2 represent the case during the second peak, while curve 3 represents the case during the earlier period of the first peak. Curve 2 is derived as a unitary particle stream with  $r=2.0$ , and curve 1 is derived as a mixed particle stream. We think the mixed particle stream model with two-component magnitude distributions can explain well why the radio meteors was much more active on 17 November than that in previous days [16].

Another research is to set up a relationship of the orbital changes with ejection. Since meteoroids are ejected from the comet with a much smaller speed relative to its parent comet, they can only move on almost the same orbit. Gravitational perturbations

from the giant planets can change all of the orbital parameters, but its effect is mass independent. The Poynting-Roberson effect can change the orbital period according to size, but can be excluded here because it is a very long term effect. The effect of interplanetary electric magnetic field can be also neglected [18]. Hence any difference between the orbits of the parent comet and the ejected meteoroids must be predominantly due to the ejection process. From the fundamentals of celestial mechanics, the difference between the longitude of the ascending node of meteoroids and that of their parent comet

$$\Delta\Omega = \frac{r \sin(\omega + f)}{h \sin i} v \sin \phi, \quad (7)$$

where  $r$  is the heliocentric distance when the ejection occurred,  $h$  is the angular momentum per unit mass,  $\omega$  is the argument of the perihelion,  $f$  is the true anomaly,  $i$  is the inclination of the orbit,  $v$  is ejection velocity,  $\phi$  is the angle between the direction of ejection and the orbital plane. From Eq. 7, we can see that if the direction of ejection was in orbital plane of the comet or the ejection occurred at the node, there would be no change in the longitude of the ascending node  $\Omega$ .

The node change,  $\Delta\Omega$ , can be obtained from the observations of meteor showers. Suppose  $v \sin \phi$  is a constant,  $\Delta\Omega$  depends only on the position of the ejection. Therefore we can estimate the possible ejection position and the value of  $v \sin \phi$  for a special meteoroid stream from the observation of meteor outbursts. For example, in the most spectacular Leonid storms of 1833, 1866, 1966 and 1999, the value of  $\Delta\Omega$  is always very small. It means the meteoroids must have been ejected very close to the node, which is very close to perihelion for the Leonids. And the value of  $|v \sin \phi|$  for the Leonids deduced from the

observations of meteor outbursts is about  $70 \text{ ms}^{-1}$ , which towards the lower end of the literature suggested [19]. In addition, the generation of very small values for  $\Delta\Omega$  is more dependent on how close to a node the ejection occurred, rather than on the ejection velocity.

According to Eq. 7, Ma et al. studied the phenomenon of the abnormal ionosphere effect occurred on 18 November 1998 [18]. In general, abnormal ionosphere effect was thought to be caused by a large amount of micrometeors [20–21], which can disturb Earth's ionosphere, especially the  $E_s$  layer.  $E_s$  layer is a high level ionized thin sheet with an area being bigger than  $100 \text{ km}^2$  and thickness being only about  $1\text{--}2 \text{ km}$ . The lifetime of  $E_s$  layer is usually less than 15 minutes. In 1998 the abnormal ionosphere effect occurred about 18 hours after the expected visible peak. It means the longitude of the ascending node of the micrometeors was  $0.74^\circ$  different from that of the visible peak. From Eq. 7, we have

$$\frac{r_1 \sin(\omega + f_1)}{h \sin i} v_1 \sin \phi_1 - \frac{r_0 \sin(\omega + f_0)}{h \sin i} v_0 \sin \phi_0 = 0.013, \quad (8)$$

where the subscript '1' and '0' denote the respective quantities for micrometeors and visible [18]. Simplify suppose  $\sin \phi_1 = 1$  and  $\sin \phi_0 = 0$ , it is proved that the detected small meteoroids must be ejected farther from the perihelion. Assuming the ejection of both small and visible meteoroids occurred at the same position  $r$ , and assuming for visible meteors  $v=25 \text{ ms}^{-1}$  at  $r=1 \text{ au}$  and  $\beta_0 = 10^{-3}$  [22], the most probable ejection positions are around 1.44, 2.12 and  $2.78 \text{ au}$ , respectively, corresponding to the visible meteors, which completed 4, 5 and 6 orbits [9]. We suggest  $1.44 \text{ au}$  is more likely than others, and for the sharp peak, 1933 is more likely to be the ejection time than earlier years [18]. If we assume the ejection occurred at last return, the component of ejection velocity perpendicular to the orbit plane will be several  $\text{km s}^{-1}$  [23].

We would like also to mention the work of H. Meng, who is a student of Beijing 80th middle school. While made the Leonids observations in 1998–1999, with plotting maps of 37 visual sporadic meteors in total about 50, he and his amateur group confirmed the new radiant between the constellations Auriga and Perseus, at about  $\alpha = 76^\circ$  and  $\delta = +36^\circ$ . It is agreed well with the result of Koschny and Zender in 1998's video observations with 9 sporadic meteors [24]. In addition, they suggested the maximum of the stream should be on 17/18 November while its active period of 16–20 November, with incoming geocentric velocity  $V_\infty=60 \text{ km s}^{-1}$  and  $\text{ZHR} \approx 10$ .

### 3. PREDICTIONS ABOUT METEOR SHOWER AND STORM

The Leonid stream does not always produce a spectacular display in every 33 years. We put all of the observed Leonid showers and storms in a diagram of  $T_{E-C}$  versus CEOS. Where, CEOS means Comet-Earth Orbits Separation, that is the distance in  $\text{au}$  between the descending node of the comet and the point where the Earth passes the comet's orbit plane.  $T_{E-C}$  means the time gap in days that the Earth follows (+) or leads (-) the comet at their respective passages through the two points defining CEOS. This diagram looks very much like the diagrams given by Yeomans, Brown and Ferrin [25–27]. But if you analyze the diagram more deeply, it could be more distinct that the showers do not just concentrate in quadrant II, but also more concentrate in an inclined square, except few events (see Fig. 5). The width of this square tells us that the Leonid shower could be never seen on more than four consecutive years [28], but we think it is too complex to draw intensity contour lines in this diagram. However, this square could be more divided into  $3 \times 3$  pieces denoted by 'A' to 'I', and they have almost the same size. Instead of years, values of ZHR were marked at the points as possible. Certainly we can analyze the relation of one point with its neighbors. It is found in the middle strip, say accurately, in the DHF curved strip, there is more large possibility to have much stronger storms than in both sides. Moreover, showers in the up-right strip ABC may have more large percentage of bright meteors. We note that the boundaries of the up-right and the lower-left both have a slope in unit of speed with a value about  $14.7 \text{ ms}^{-1}$ . It suggests the meteoroids have a limited velocity. Although in AD 934, 1238, 1566 and 1833, the CEOS indeed had very small minus values and with greatest storms, the intensity of a shower can't be decided only by the value of the CEOS. If CEOS had a larger value, we may need to waiting for more time since the meteoroids have a limited velocity, but it doesn't mean the shower being strong or weak. If we suppose particles traveled  $0.008 \text{ au}$  in 257.0 d for the 1998 shower, a velocity of  $54 \text{ ms}^{-1}$  could be obtained. Of course, if the particles were ejected in older cometary return, the off-orbit velocity will be much smaller than  $54 \text{ ms}^{-1}$ . This is consistent with the ejected velocity of the particles  $v=36 \text{ ms}^{-1}$  [29], or  $v=25 \text{ ms}^{-1}$  [22]. Since the position of AD 1998 is inside the Block 'B', the truth of only having a shower with more bright meteors can be explained. In virtue of the position of AD 1999 (falling in Block 'F'), we predicted that Leonids in 1999 would be at least 3 to 5 times stronger than that in 1998, with a  $\text{ZHR}=2,000\text{--}5,000$ . For AD 2000, it is at the outer part of the Block 'I', we estimate there will be a moderate shower a little stronger than that in 1998 (less than double) [28,30]. Observations confirm that our

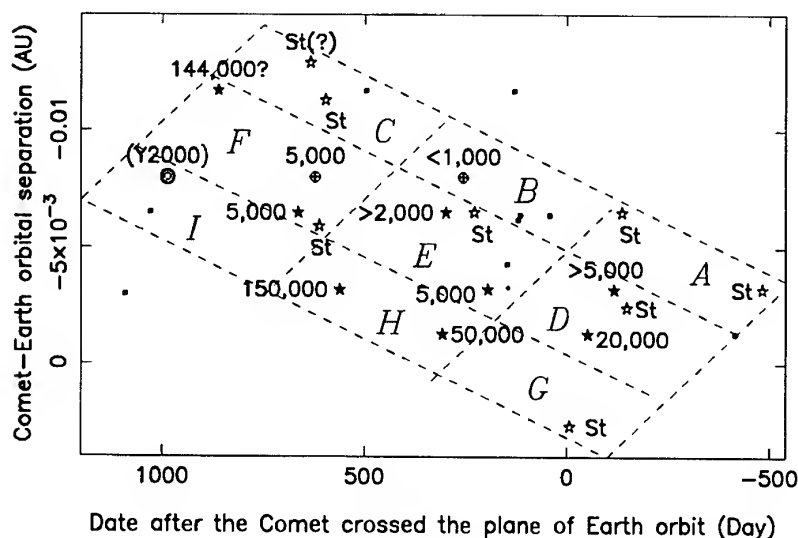


Figure 5. Distribution of Leonid showers and storms on the  $T_{E-C}$  versus CEOS diagram

prediction being great success [31–34]. Experienced visual observers in Spain and France witnessed a distinctive peak with a ZHR of around 5,000 [35–36]. Or according to Arlt, the maximum ZHR value reached 340, 3700, and 480 in 1998, 1999 and 2000, respectively [4,31–32].

Recently, we are working on the research of the orbital evolution of the meteoroid stream using calculation of celestial mechanics. We discussed the dynamic environment of Leonid meteor stream. At first, the orbit of comet Tempel-Tuttle has been re-determined for the 1997–1998 observed interval. Then the ejection model of particles from comet is set up and the orbital elements of several hundreds of test particles are also obtained. Finally, on the basis of the ejection of particles being isotropic, the dynamical origin of Leonids 1998 is analyzed. Several conclusions can be drawn as following: (1) The position of the ejection region determines whether the particles can reach Earth greatly. Those particles, which can reach Earth in the same day, must come from a narrow region of the cometary surface being about  $0.3 \times 28 m^2$ . (2) The direction of ejection should be almost in the ecliptic plane. If Tempel-Tuttle rotates in clockwise, the ejection time of those particles should be about half hour after noon. (3) The authors suggest that the ejection velocity of  $50 m s^{-1}$  is more reasonable for the visual Leonids. (4) The 2-revolutions particles with a velocity of  $50 m s^{-1}$  can reach Earth at 20h37m UT on 17 November 1998, making the main part of the second peak of Leonids 1998 [37].

#### 4. FUTURE

According to our prediction, as for AD 2001 and after, the points are far away from the inclined square of Fig. 5. Moreover, the CEOS in this cometary return of 1998 is rather large than that in other returns. So that, the Leonid storm may have gone in this return, impossible to have other great events. After AD 2000 it will be another century before significant displays are once again likely, the Leonid shower may have gone forever after AD 2500 [30,15].

Other people may give much different predictions. McNaught and Asher said that the Leonids will be very strong in 2001 and 2002 with a ZHR up to ten thousands [9]. Especially, it will be suitable for observing in China in this year. So we welcome you, all of the participants in this meeting, going to our country. And, we will do our best.

#### ACKNOWLEDGMENTS

The author acknowledge the support of this work by the National Natural Science Foundation of China through Grant numbers of 19873020 and 19653001.

#### REFERENCES

1. Zhuang T.S., Ancient Chinese records of meteor showers, *Chinese Astronomy*, Vol. 1, 197–220, 1977.

2. Jenniskens P., Meteor stream activity, I. The annual streams, *A&A*, Vol. 287, 990-1013, 1994.
3. Rao J., The return of the Leonid meteors, *Sky & Telescope*, Nov., 38-44, 1998.
4. Arlt R., The 1998 Leonid meteor shower, Bulletin 13 of the International Leonid Watch, *WGN*, the Journal of the *IMO*, Vol. 26, 239-248, 1998.
5. Zhao H.B., Li G.Y., Xu P.X., et al., Leonid 1998 visual observation in Delingha and the preliminary analysis, *Chinese Science Bulletin*, Vol. 45, 484-489, 2000.
6. Langbroek M., Zhao H.B., et al., Leonid meteors 1998, *IAU Circular*, 7052, November 17, 1998.
7. Wu G.J., Zhang Z.S., Visual observations of the Leonid meteors 1998 in Yunnan, *Earth, Moon and Planets*, Vol. 81, 193, 1998, published in 2000.
8. Wu G.J., Zhang Z.S., Comparison between the observations during 1998 - 2000 for Leonid meteor shower, submitted to *Planetary and Space Science*, 2001.
9. McNaught R.H., Asher D.J., Leonid dust trails and meteor storms, *WGN*, the Journal of the *IMO*, Vol. 27, 85-102, 1999.
10. Wu G.J., Li G.Y., Probabilities of Perception and Population Index in Visual Observations of Meteor Showers, submitted to *MNRAS*, 2001.
11. Koschack R., Rendtel J., Determination of spatial number density and mass index from visual meteor observations (II), *WGN*, the Journal of the *IMO*, Vol. 18, 119-140, 1990.
12. Zhang Z.S., Wu G.J., Analysis about photographic observations of Leonid meteor shower in 1999, *Acta Astronomica Sinica*, accepted, 2001.
13. He Y.W., The radio observation of the 1998 strong Leonid meteor shower, *Electric Wave Science Acta*, Vol. 14(supplement), 8-11, 1999.
14. Wu Z., Williams I.P., Leonid meteor storms, *MNRAS*, Vol. 280, 1210-1218, 1996.
15. Yeomans D.K., Yau K.K., Weissman P.R., The impending appearance of comet Tempel-Tuttle and the Leonid meteors, *Icarus*, Vol. 124, 407-413, 1996.
16. Li G.Y., Xu P.X., Zhao H.B., et al., Mixed particle stream model of the main peak of 1998 Leonids, *Earth, Moon and Planets*, accepted, 2001.
17. Asher D.J., Bailey M.E., Emel'yanenko V.V., Resonant meteoroids from Comet Tempel-Tuttle in 1333: the cause of the unexpected Leonid outburst in 1998, *MNRAS*, Vol. 304, L53-L56, 1999.
18. Ma Y.H., He Y.W., Williams I.P., A micrometeor shower component of the Leonids 1998, *MNRAS*, Vol. 325, 457-462, 2001.
19. Ma Y.H., Williams I.P., The ejection velocity of meteoroids from cometary nuclei deduced from the observations of meteor showers outbursts, *MNRAS*, Vol. 325, 379-384, 2001.
20. He Y.W., Xu P.X., The Es layer during the burst of the strong Leonid meteor shower in the sixties, *Electric Wave Science Acta*, Vol. 12, 65-71, 1997.
21. He Y.W., The observation and research of the strong meteor shower and ionization effects, *Annual of Chinese Geophysics Society*, 241, 1998.
22. Asher D.J., The Leonid meteor storms of 1833 and 1966, *MNRAS*, Vol. 307, 919-924, 1999.
23. Ma Y.H., He Y.W., Williams I.P., A dust swarm detected after the main Leonid meteor shower in 1998, in Green S.F., Hughes D.W., McDonnell J.A.M., Williams I.P. eds, *Dust in the Solar system and other planetary systems*, Elsevier Pub. Co. Canterbury, 2000.
24. Koschny D., Zender J., Possible new radiant in Auriga on November 17, 1998, *WGN*, the Journal of the *IMO*, Vol. 27, 51-52, 1999.
25. Yeomans D.K., Comet Tempel-Tuttle and the Leonid meteors, *Icarus*, Vol. 47, 492-499, 1981.
26. Brown P., The Leonid meteor shower: historical visual observations, *Icarus*, Vol. 138, 287-308, 1999.
27. Ferrin I., Meteor storm forecasting: Leonids 1999-2001, *A&A*, Vol. 348, 295-299, 1999.
28. Wu G.J., Prediction of the Leonid meteor storm in 1999, *CA&A (Letters)*, Vol. 23, 268-272, 1999.
29. Brown P., Jones J., Simulation of the formation and evolution of the Perseid meteoroid stream, *Icarus*, Vol. 133, 36-68, 1998.
30. Wu G.J., Comet Tempel-Tuttle and recent Leonid meteor shower, *Acta Astronomica Sinica*, Vol. 42, 125-133, 2001.
31. Arlt R., Rubio L.B., Brown P., Gyssens M., Bulletin 15 of the International Leonid Watch: First Global Analysis of the 1999 Leonid Storm, *WGN*, the Journal of *IMO*, Vol. 27, 286-295, 1999.
32. Arlt R., Gyssens M., Bulletin 16 of the International Leonid Watch: Results of the 2000 Leonid meteor shower, *WGN*, the Journal of the *IMO*, Vol. 28, 195-208, 2000.
33. Rao J., The Leonid meteor storm is this the year? *Sky & Telescope*, Nov., 28-35, 1999.
34. Rao J., Will the Leonid storms continue? *Sky & Telescope*, Jun., 30-37, 2000.
35. Gyssens M., IMO Shower Circular, leo99index.htm in <http://www.imo.net/leo99>, November 20, 1999.
36. Phillips T., Leonids rain in Spain, [ast18nov99.1.htm](http://science.nasa.gov/newhome/headlines/ast18nov99.1.htm) in <http://science.nasa.gov/newhome/headlines/ast18nov99.1.htm>, 1999.
37. Zhao H.B., Li G.Y., The dynamical evolution of Leonids 1998, private communication, 2001.

# THEORETICAL LEONID ENTRY MODELING

D. O. ReVelle

*Los Alamos National Laboratory, P.O. Box 1663, MS J577, Earth and Environmental Sciences Division,  
EES-8, Atmospheric and Climate Sciences Group, Los Alamos, New Mexico 87545 USA  
Email: dor@vega.lanl.gov*

## ABSTRACT

In this work we present a model originally developed by ReVelle (1979, 1993) that has been applied to model large Leonid bolides with a few relatively minor modifications and one major modification which allows for catastrophic "pancake: fragmentation processes as described below. The minor modifications include allowing the energy of ablation per unit mass for vaporization,  $Q_{vap}$ , to be a free variable that is adjusted until agreement is obtained between the theoretical model and the statistically expected ablation coefficient for the Leonids (Group IIIB type bolide). It was found that the  $Q_{vap}$  had to be reduced by a factor of about five times compared to the accepted value of  $Q_{vap}$  for cometary materials. Alternative ways of achieving this degree of agreement between theory and observations are also suggested as well. In a separate paper we apply this model to a specific Leonid bolide during the 1998 storm period.

$H_f$  = Fragmentation scale height  
 $H_p$  = Pressure scale height

This limit includes a self-similar ablation solution with no shape change for  $\mu \equiv 2/3$ .

For  $0 \leq \mu < 2/3$ , the solution includes ablation and deceleration, as well as shape change with the frontal cross-sectional area,  $A(z)$ , decreasing with decreasing height

ii)  $H_p / H_f \gg 1$ :  
Catastrophic fragmentation limit

With  $\mu < 0$ , this solution allows for ablation and deceleration as well as shape change, but  $A(z)$  increases with decreasing height.

## 1. INTRODUCTION AND OVERVIEW

### 1.1 Key assumptions- following Levin (1961), Bronshten (1993) and ReVelle (1999):

We start from the numerical solution proposed by ReVelle (1979, 1993, 2000) which comes from an analytic solution for hypersonic meteoroid entry, assuming a hydrostatic, isothermal, atmosphere with the ablation coefficient,  $\sigma$ , a constant and a height variable velocity. This solution simultaneously includes ablation, deceleration, shape change and fragmentation while neglecting lift, coriolis effects and gravity gradients, etc.

### 1.2 Fundamental regimes:

i)  $|H_p / H_f| \ll 1$ : Single-body model

where

## 2. ENTRY MODELING APPROACH: OVERALL SUMMARY

### 2.1 Key assumptions

An entry modeling summary can be found in ReVelle (1979, 1985, 1993, 1999). In order to model the very high speed Leonids, we will regard all variables as known as in ReVelle (1979), except for the energy of ablation/mass,  $Q_i$ , for the Leonid's as a function of  $k = V_\infty^2 / (2 \cdot Q_{vap})$ , the ablation interaction number. For  $Q_{vap} \approx 3.8$  MJ/kg,  $V_\infty = 70.7$  km/s,  $k \approx 657.7$ . From previous arcjet wind tunnel data for chondritic meteorites, vaporization occurs at the stagnation point if  $k > \sim 25$  so there seems to be little doubt that the Leonid's will vaporize profusely.

For large bodies (radius  $> \sim 1$  cm), we will neglect the gas cap absorption of the radiative energy emission from the high temperature leading shock wave. If this effect had been included, this may allow substantial agreement to be obtained between modeling and observations, without systematically decreasing  $Q_{vap}$ . We will also neglect precursor ionization

(which is also called free stream absorption by hypersonic aerodynamicists) ahead of the body, i.e., we will assume no preheating of the local air by the strong ultraviolet radiation from the shock wave. At the end height of the interaction for a typical Leonid bolide, the neutral air density is quite low while the mean free path is somewhat less than the body radius so that the near-continuum flow regime has been reached. Thus this preheating is unlikely to be very significant for the Leonids. We will also assume that single-body theory ( $|H_r| \gg H_p$ ) with a height variable ablation coefficient and velocity, etc. is adequate until the stagnation pressure exceeds the tensile/compressive strength of an "average" Leonid. If this occurs, we computed the fragmentation scale height (ReVelle, 2001) as a function of the  $\mu$  parameter (Bronshten, 1983) to evaluate the entry behavior at still lower altitudes.

## 2.2 Single-body approximation approach:

In this work we have adopted the formal approach developed in ReVelle (1979, 1993, 1999) where the generalized form of the analytic solution of the equations for the dynamics and energetics of large meteor entry for the limiting case of constant coefficients was solved numerically. Within each small numerical time (or altitude) interval, the relevant coefficients at each height were assumed constant and explicitly calculated using analytic expressions that had been derived for each of the relevant heat transfer terms. In this paper we have also added the effects of shape change on the solution as well using the  $\mu$  parameter. Next, starting at sufficiently high altitude, we have computed the Knudsen number,  $Kn$ , (local neutral gas mean free path divided by the body radius) over a sufficiently small height interval such that the computed ablation coefficient was slowly varying over all heights:

$$(1/\sigma_0) \cdot \partial\sigma/\partial z \cdot \delta z \ll 1$$

This limiting condition formally results from an explicit power series expansion of  $\sigma$  which can be expressed to first order in the form:

$$\sigma(z) = \sigma_0 + \{\partial\sigma/\partial z\} \cdot \delta z + \dots \text{ (higher order terms)}$$

LTE (local thermodynamic equilibrium) was assumed throughout all of these calculations.

The calculations were further also evaluated within each height interval according to the magnitude of the Knudsen number since this completely controls the relevant aerodynamical possibilities for hypersonic flows:

- i) **If  $Kn > 10$ :**  
**Free molecule flow relations from laboratory experiments were utilized**
- ii) **If  $10 > Kn > 0.1$ :**  
**Analytic flow bridging expressions between the limiting regimes were utilized (based on kinetic theory expansions in  $Kn$ )**
- iii) **If  $Kn < 0.1$ :**  
**Continuum flow regime**

In the latter case, we computed gas cap (boundary layer) state and decided if it was either turbulent or laminar. We then computed either the laminar or turbulent convective heat transfer and the corresponding radiative heat transfer coefficients. These coefficients were normalized and summed in order to get the total equilibrium heat transfer coefficient. During all of these calculations, we computed the variable ablation coefficient as height changes (over small altitude intervals). We also computed the percentage ablation and the corresponding instantaneous mass, size, shape factor, stagnation pressure and velocity as well as the next value of  $Kn$  in order to evaluate the flow regime during the next height step, etc. In addition, we computed the relevant line source blast wave relaxation radius and relevant infrasound properties since these large bodies can generate infrasonic signals that can be detected at the ground (ReVelle, 1976, ReVelle, 1997, ReVelle and Whitaker, 1999)

## 3. APPLICATION TO LARGE LEONID BOLIDES

### 3.1 Leonid material properties:

In order to complete the entry model for application to the Leonids, we first require their material properties. We expect that the large Leonids to be of type IIIB meteor-fireballs (weak cometary materials). The statistically expected bulk density is  $270 \text{ kg/m}^3$ . If these are porous,

chondritic bodies, their degree of porosity is ~91 % (ReVelle, 1983, 2001). The expected ablation coefficient is 0.21 kg/MJ (1 MJ =  $10^6$  J) and their energy of ablation/mass is 3.8 MJ/kg (Jessberger et. al., 1988). We initially assumed a spherical shape with a corresponding shape factor: 1.208. Next we consider the shape change parameter,  $\mu$ , and its implications for the possible solutions. In general as  $\mu$  decreases the corresponding bolide end height increases. If for example,  $\mu = 2/3$ , a self-similar solution with no shape change is predicted. Until recently (although see ReVelle, 1980) this was the standard solution type assumed since there are so many free variables in the entry problem even without considering the luminosity part of the prediction problem. For  $0 \leq \mu < 2/3$ , solutions with shape change and simultaneous ablation and deceleration are allowed. For  $\mu < 0$ , a catastrophic break-up, subject to a stagnation pressure onset criterion is predicted (for details see ReVelle, 2001). In addition we also need values of the drag coefficients. These values are of the drag coefficient for free-molecular hypersonic flow,  $C_{D0} = 2.00$  and for continuum hypersonic flow (for a sphere),  $C_{D00} = 0.92$ . Values of the dimensionless heat transfer coefficient,  $C_h$ , were taken from arcjet wind tunnel experiments in the free molecule flow regime as quoted in ReVelle (1979).

### 3.2 Bolide dynamics and energetics :

Following ReVelle (1993) we have used an energetics approach that follows from the standard dynamical equations given in Cepelcha (1998). This approach relies on the D parameter (from  $E_k = E_{k\infty} \cdot \exp[-D]$ ) which specifies the kinetic energy that will remain at the end height. For example, for  $D = 2.303$ , 10 % of the initial kinetic energy has been removed at the end height whereas for  $D = 4.603$ , 99 % of the initial kinetic energy has been removed (or 1 % remaining). We expect on the basis of the observed end height velocities that the smaller D values correspond to weaker bodies of cometary origin (smaller decelerations) and vice versa.

In this approach, we first solve iteratively for the end height velocity,  $V_{end}$  (when  $V(z) = V_{end}$ ):

$$V(z) = V_{\infty} \cdot \exp[(\sigma/4) \cdot \{V_{\infty}^2 - V^2(z)\}] \cdot \exp[-D/2]$$

This equation predicts the end height velocity as a function of D and  $\sigma$ .

The resulting end height equation for a constant ablation coefficient is given by:

$$z_{KE}(V) = -H_p \cdot \{\ln(p_{\infty}^*/p_0) \cdot \exp[-(\sigma \cdot A) \cdot V_{\infty}^2] \cdot \{D - D'\} + \exp[-z'/H_p]\}$$

$$z' = -H_p \cdot \{\ln(p_{\infty}^*/p_0) \cdot (2gH_p/V_{\infty}^2)\}$$

where

$z'$  is the altitude where  $dV/dt = 0$  initially

$$D' = -\{Ei[(\sigma \cdot A) \cdot V_{\infty}^2] - Ei[(\sigma \cdot A) \cdot V^2(z)] - \ln(V_{\infty}/V(z))^2 - [(\sigma/2)(V_{\infty}^2 - V^2(z))]\}$$

$Ei(\sigma \cdot A)$  = the exponential integral function

$A = (1 - \mu)/2$

$p_0$  = surface pressure

$p_{\infty}^* = mg \cdot \sin\theta / (C_D A)$

" = Modified ballistic entry parameter

$p_{\infty}^* = 4 \cdot \rho_m \cdot r \cdot g \cdot \sin\theta / (3C_D)$  for a sphere

### 3.3 Ablation model assumptions:

We have assumed that when the instantaneous bolide velocity  $\leq 3$  km/s, all ablation will cease (before the aerodynamic cold wall approximation breaks down since the shock temperature lowers significantly as the bolide velocity decreases). This assumption is in agreement with wind tunnel experiments with meteorite samples. Also, when the entry velocity is sufficiently small (large), stagnation point ablation proceeds directly by melting (vaporization). This is numerically evaluated by calculating the ablation interaction number,  $k$ , as mentioned earlier. The specific velocity limits between melting and vaporization were chosen purely empirically based on arc-jet wind tunnel ablative observations (from NASA-Langley's former PERF-Planetary Entry Radiation Facility). Finally, when the entry velocity is intermediate in its magnitude, a mix of ablative processes is assumed to occur near the stagnation point whose energy of ablation/mass is also intermediate to that of either pure melting or pure vaporization.

### 3.4 More calculation details

The laminar heat transfer through this plasma can be decomposed into at least three identifiable

parts, of which the first two are the most significant:

- i) Heat transfer by conduction through the plasma
- ii) Heat transfer due to mass diffusion caused by concentration gradients
- iii) Heat transfer due to mass diffusion caused by thermal gradients.

There are also additional heat transfer mechanisms including those in transitional and in free molecular flow. For example, we expect a shielded impact of the oncoming flow with the meteoroid ( $Kn > \sim O(1)$ ). There is also a turbulent plasma conductive/convective heat transfer depending on the flow conditions and on the Stanton number as well as a radiative heat transfer during continuum flow (ReVelle, 1979). There are also non-equilibrium turbulent and radiative heat transfer coefficients that have not been included in this analysis, since such effects are generally only important at sufficiently high altitudes where the ablation itself is also very small regardless of the magnitude of the ablation coefficient. Since we have not discussed the equilibrium radiative heat transfer in great detail before we will focus on that subject directly below.

### 3.5 Radiation transfer predictions:

Here we can divide the problem up into unshielded versus shielded (radiation blockage) flows. The key dimensionless parameters for a one-dimensional model are the Re (Reynolds number), Bu (Bouguer number), Bo (Gould number). Alternatively, we can also use:  $\Gamma$  (Radiation-convection parameter) instead of Bo. The specific gas opacity limits are respectively an optically thin gas cap specified by  $Bu \ll 1$  and an optically thick gas cap specified by  $Bu \gg 1$ . The radiation transfer calculations have been carried out assuming that the flow is axisymmetric flow over a blunt body at its stagnation point. The shock wave radiation flux and turbulent heat flux are assumed to be uncoupled and thus can be calculated separately. This is in agreement with the well known and reliable reference enthalpy approach. This approximation is most reliable however for  $Bu \gg 1$ . The front face of the bolide has been assumed to be a cold, non-reflecting black wall (assumed: "cold" with respect to the plasma gas cap and the leading shock front). The air in the

high temperature plasma of the gas cap is assumed to be  $> 10,000$  K. Also, both local thermodynamic equilibrium (LTE) and chemical equilibrium have been assumed in the inviscid, non-heat conducting plasma. As mentioned above non-equilibrium processes have not been incorporated. The solution available to solve the equations of *Radiation Gas Dynamics* called the Method of Integral Relations, which is acceptable for all subsonic flow regions with respect to the body. These equations are a system of integro-differential equations with flow-coupled radiative transfer and simultaneous solution of the mass, momentum and energy conservation equations. The 1-D (one-dimensional) radiation transfer model (RATRAP) utilizes the tangent slab approximation and is due originally to Wilson (1972). Both atomic line radiation and continuum radiation in a non-gray gas are included in the numerical computations as well as self absorption in the plasma.

ReVelle (1976, 1979) predicted a limiting value of the radiative heating coefficient at speeds  $> 20$  km/s because of the presence of strong radiative cooling by the initially very high temperature of the gas cap plasma. This limiting behavior is directly observable in the numerical simulations at progressively larger velocities. Ablation products absorption in the gas cap plasma has not been not incorporated (unshielded flows) as will be discussed later. Also as mentioned earlier precursor ionization (free stream absorption) ahead of the body is not calculated. This also applies to wavelength-dependent radiative coupling in the gas cap's turbulent boundary layer, which also has not been considered. The equations used for this calculation are given in ReVelle (1979).

The radiation transfer for shielded flows (blockage) by ablated vapors has been calculated by a number of different authors. In some cases the radiative heating coefficient was reduced by up to  $\sim 90\%$ , but in other cases, it was much smaller. Unfortunately if this blockage effect is significant for the Leonids, we are faced with reducing  $Q_{vap}$  even further than has already been suggested in this paper compared to the currently quoted values in the literature.

Although this topic is extremely complicated, one obvious question is whether this energy is simply convected into the wake or whether it is reradiated in different spectral regions downstream of the stagnation point? Part of the answer to these questions depends on the composition of the inhomogeneous body. Some

of the numerous elements that have been identified in the spectra of bolides are included in the following list: Fe, Ni, Na, Li, C, Ca, Cr, Mn, Mg, Al, Si, K, Co, etc. The degree to which this absorption of the radiative emission from the leading shock front is also dependent upon the ablated vapor properties in a very high temperature, low density plasma (with very large gradients). ReVelle (2000) addressed this issue using scaling arguments for translational motion and decided that it should not be very important for the Leonids because of their very high entry velocity, but for slower bolides it could play a more significant role. Furthermore this also depends on position of the flow relative to the stagnation point: In two-dimensional (2-D) flows, a nearly Gaussian heating profile prevails (ReVelle, 1980), but it also depends on the rotation rate and on the axis of the rotational relative to the flow. Clearly there will be less reduction of the radiative emission by ablative vapors near the body if ablation occurs with a mixture of melting and vaporization and none at all if only melting is occurring.

In this work we have not modeled either the normalized or un-normalized light from bolides, but it will be a topic of a forthcoming publication. It is also briefly discussed in ReVelle (2001a). Line source blast wave interactions and shock wave development and subsequent propagation of infrasound are also not considered here, but are covered in other references of the author ReVelle (1997, 2001b)

#### 4. SUMMARY AND CONCLUSIONS

The Leonids experience probably the most severe atmospheric entry conditions. We have tested sizes from  $10^{-3}$  to 10 m. Extensive ablation is predicted, generally exceeding  $\sim 90\%$ . Using a  $Q_1$  value for vaporization which is approximately five times smaller than the proposed value for cometary materials, we obtained a height averaged ablation coefficient of  $\sim 0.20$  kg/MJ in agreement with Ceplecha et al. (1998). The fundamental flow regime conditions can cover the entire range from free molecular to continuum flow over the mass range from  $1.31 \cdot 10^{-6}$  to  $1.31 \cdot 10^6$  kg. The ablation coefficient can be nearly constant or be distinctly height variable, depending on the initial body size. The shock wave radiation is a dominant heat transfer contributor for the larger bodies tested with plasma convective (or laminar conductive) heat transfer dominated for the

smaller bodies. At certain altitudes turbulent for the largest bodies above about 1 m in radius, convective heat transfer can also be very important. Can this laminar/turbulent boundary layer transition affect the predicted and observed light curve? Preliminary results soon to be published suggest that its effect is significant for a certain size range of bodies. In addition, for large Leonids, strong shock, blast wave generation and consequently infrasound propagation with subsequent ground-based detection is readily possible. This was recently demonstrated for the Leonids by ReVelle and Whitaker (1999).

#### 5. REFERENCES:

- Bronshten, V.A., Physics of Meteoric Phenomena, D. Reidel Pub. Co., Dordrecht, 356 pp., 1983.
- Ceplecha, Z., J. Borovicka, W. G. Elford, D.O. ReVelle, R.L. Hawkes, V. Porubcan and M. Simek, Meteor Phenomena and Bodies, Space Science Reviews, **84**, 327-471, 1998.
- Jessberger, E.K., A. Christoforids and J. Kissel, Aspects of the major elemental composition of Halley's dust, Nature, **332**, 691-695, 1988.
- Levin, B., Fragmentation of Meteor Bodies, Nature, **196**, 527-529, 1962.
- ReVelle, D.O., On Meteor-Generated Infrasound, J. Geophys. Res., **81**, 1217-1230, 1976.
- ReVelle, D.O., A Quasi-simple Ablation Model for Large Meteorite Entry: Theory versus Observations, J. Atmos. Terr. Physics, **41**, 453-473, 1979.
- ReVelle, D.O., Interactions of Large Bodies in the Earth's Atmosphere, IAU Symposium Number 90, Solid Bodies in the Solar System, eds. I. Halliday and B.A. McIntosh, D. Reidel Pub. Co., Dordrecht, 185-198, 1980.
- ReVelle, D.O., The Meteoroid/Atmosphere Interaction Spectrum, Meteoroids and Their Parent Bodies, eds. J. Stohl and I. P. Williams, Slovak Academy of Sciences, Bratislava, Slovakia, 343-346, 1993.
- ReVelle, D.O., Historical Detection of Atmospheric Impacts by Large Bolides Using Acoustic-Gravity Waves, Near-Earth Objects, The United Nations International Conference, Annals of the New York Academy of Sciences, eds J. Remo, Vol. 822, 284-302, New York, New York, 1997.
- ReVelle, D.O. and R.W. Whitaker, Infrasonic Detection of a Leonid Bolide 1998 November 17, Meteoritics and Planetary Science, **34**, 995-

1005, 1999.

ReVelle, D.O., Bolide Fragmentation Processes: Modeling the Break-up of Very Large Meteors, Presented at the Cornell ACM Conference, Ithaca, New York, July, 1999.

ReVelle, D.O., Bolide Dynamics and Luminosity Modeling: Comparisons between Uniform Bulk Density and Porous Meteoroid Models, Conference Proceedings, Meteoroids2001, Kiruna, Sweden, August 6-10, 2001, 2001a.

ReVelle, D.O., Large Leonid Entry Modeling: Application to the Bolide of 11/17/1998, Conference Proceedings, Meteoroids2001, Kiruna, Sweden, August 6-10, 2001, 2001b.

ReVelle, D.O., Plasma Heat Conduction and Radiative Transfer During Atmospheric Interactions with Large Leonids, AIAA Paper 2000-0585, Presented at American Institute of Aeronautics and Astronautics, 38<sup>th</sup> Aerospace Sciences Meeting, Reno, Nevada, Special Session 83-PDL-5, Aerothermochemistry in Meteoric Plasmas, 11 pp., 2000.

ReVelle, D.O., Bolide Fragmentation Processes: Single-body Modeling versus the Catastrophic Fragmentation Limit, Conference Proceedings, Meteoroids2001, Kiruna, Sweden August 6-10, 2001, 2001d.

# PERIODIC ACTIVITY VARIATIONS DURING THE 1999 LEONID METEOR STORM IN VARIOUS DATA SETS

J. Rendtel

International Meteor Organization, PF 600118, 14401 Potsdam, Germany, e-mail: president@imo.net

## ABSTRACT

Observational data obtained during the 1999 Leonid meteor storm using intensified video meteor cameras as well as meteor radar systems at different locations distributed over distances of about 6000 km show significant rate fluctuations. Applying a wavelet analysis to the data it is shown that we see quasi-periodic variations with a typical period of 7–8 minutes. Given the geocentric velocity of the Leonid meteoroids, this hints at structures within the stream at a scale of about 30 000 km along the Earth's passage, or about 9 000 km vertical to the stream's plane. Collection of sufficient data samples within about 2 minutes to detect small-scale structures are only possible during meteor storms.

Key words: Leonids; meteors; meteor storms.

## 1. INTRODUCTION

Different model calculations of the Leonid meteoroid stream indicated a sharp and dense peak on November 18, 1999, at 02<sup>h</sup>08<sup>m</sup> UT (cf. McNaught and Asher, 1999a and references therein). Observations applying different techniques were prepared on a worldwide scale because only a meteor storm allows to collect a substantial sample of meteor data within reasonably short time intervals. Here we analyse recordings obtained by intensified video meteor cameras at three locations and radar data from two sites. Observing locations are shown in Fig. 1 and listed in Tab. 1. Details of the observations carried out with intensified video cameras can be found in Rendtel et al. (2000); the measuring regimes of the two SkyMet radars are described by Singer et al. (2000).

All observing systems were unguided. In the case of the ground-based systems, the atmospheric volume remained constant during the entire observation. The peak activity analysis concerns the 2-hour interval between 01<sup>h</sup>00<sup>m</sup> and 03<sup>h</sup>00<sup>m</sup> UT. Within this interval, the corrections for altitude and extinction etc. did not change significantly at the observing sites. This is also valid for the one airborne observation, although the field center drifted slightly depending on the aircraft's direction.

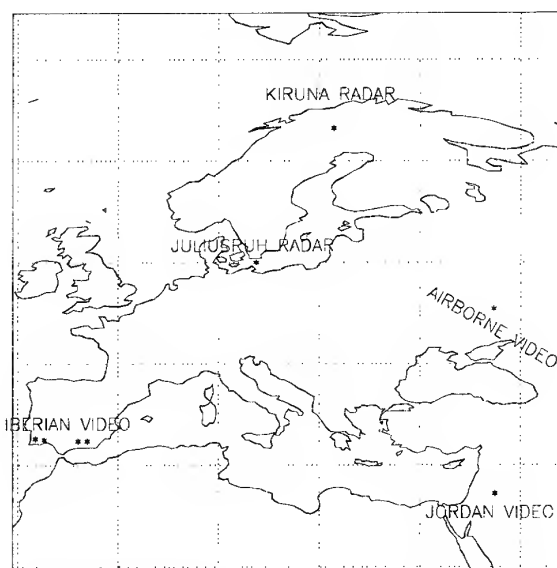


Figure 1. Locations of the meteor video cameras included in this analysis, represented by stars. One camera was operated aboard an aircraft over Eastern Europe. The star refers to the position at 02<sup>h</sup>08<sup>m</sup> UT.

Table 1. Observing locations during the 1999 Leonid meteor storm included in this analysis. The position of Okamura's airborne camera refers to 02<sup>h</sup>08<sup>m</sup> UT; in the 2-hour interval 01<sup>h</sup>00<sup>m</sup>–03<sup>h</sup>00<sup>m</sup> UT the position changed from 47° 5' E, 46° 2' N to 27° 7' E, 51° 2' N.

	Observer	Region	Longitude	Latitude
1	Okamura	Eastern Eur.	37° 11'E	50° 18'N
2	Dittie	Jordan	37° 7'E	31° 45'N
3	Koschny	Iberia	3° 23'W	37° 4'N
4	Molau	Iberia	4° 20'W	36° 57'N
5	Rendtel	Iberia	4° 20'W	36° 57'N
6	Evans	Iberia	7° 43'W	37° 9'N
7	Elliott	Iberia	8° 36'W	37° 11'N
8	Nitschke	Tenerife	16° 40'W	28° 12'N
9	Bellot	Tenerife	16° 40'W	28° 12'N
10	Singer	Germany	13° 24'E	54° 38'N
11	Mitchell	Sweden	21° 6'E	67° 53'N

All times were corrected for the topocentric time of the Leonid stream encounter as described by McNaught and Asher (1999b). The counts in 1-minute intervals, centered to the full minute, were multiplied with the sine of the radiant altitude  $\sin^{\gamma} h_R$  (with  $\gamma = 1.0$ ) to account for the radiant elevation. Then, the number of Leonids was binned in 2 min intervals, shifted by half of the bin length. There was no further smoothing for the analysis.

The complete data sets are shown in Fig. 8 of Rendtel et al. (2000) for the video cameras and in Fig. 1 of Singer et al. (2000) for the radar data.

The "Iberia" data set is a combination of data from five cameras operated from the Iberian peninsula within about 500 km maximum distance, observing different (non-overlapping) atmospheric volumes and thus giving independent data series (Molau et al., 2001; Rendtel, 2000). The obvious fluctuations in the data hint at real structures as the modulation depth is larger than the error bars. As an example for this we show the Iberian data binned in 2 minute intervals (Fig. 2).

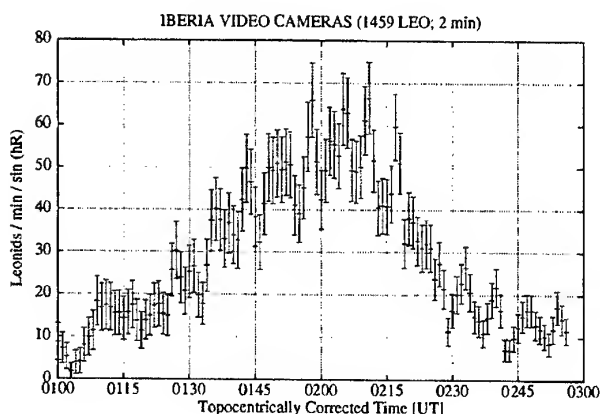


Figure 2. Leonid counts from the "Iberian" cameras, binned in 2-minute intervals. Variations found in the rate curve are larger than the statistical scatter and should thus represent real structures in the stream.

## 2. DATA ANALYSIS

Generally, the corrected rate profile of all data sets is skew. This becomes obvious from Fig. 3 which shows the "Iberia" profile after extracting all high frequency portions from the raw data applying a discrete wavelet analysis as introduced by Mallat (1989). The descending branch is 1.6 times steeper than the ascent: the time from 0.5 of the peak rate is 30 minutes while the descent to 0.5 of the peak is only 19 minutes. A secondary maximum or activity plateau in the period 01<sup>h</sup>39<sup>m</sup>–01<sup>h</sup>53<sup>m</sup> UT occurs especially in the East European and Jordanian data. This was tentatively associated with the passage of the 1932 dust trail in Singer et al. (2000). This feature also occurs in the visual Leonid data (Arlt &

Bellot, 1999). More interestingly, we find further indications of small scale structures within the meteoroid stream.

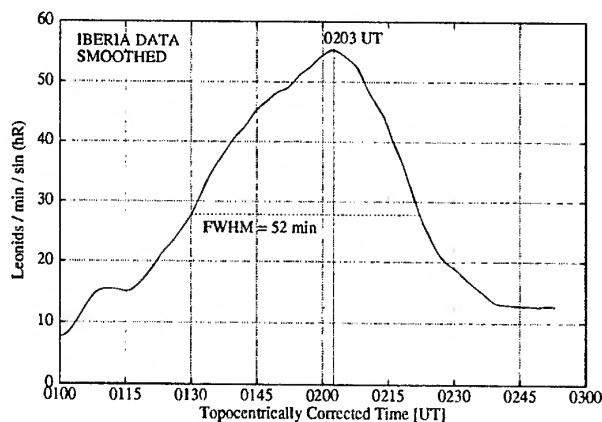


Figure 3. The "Iberia" profile after extracting all high frequency portions from the raw data applying a discrete wavelet analysis. Here we clearly see the shape of the general rate profile and its skewness.

If we look carefully at the rate curves (e.g. Fig. 2), we will find rate fluctuations which seem to occur periodically, especially around the rate maximum. Such fluctuations with virtually identical peak periods were also found from radar data obtained at sites further north in Germany and Sweden (Singer et al., 2000).

To analyse such periodic variations occurring in a part of a time series we applied a wavelet analysis. Wavelet analyses have been applied to various data sets in astronomy and geophysics (see, for example Ireland et al., 1999; Rendtel, 2001; Torrence & Compo, 1998). This method allows to localize frequencies as well as periods with periodic signals. For each data series, the temporal and frequency resolution have to be optimized to find out which frequencies exist within the time series.

From such analyses we obtain the graphs shown in Figures 4–8. The large panel shows the signal power over frequency and time, with the highest value of power set to 100. The right panel gives the integral of the power over the frequency range (ordinate). In the case of no time resolution, this is equivalent to a Fourier spectrum of the signal. The most prominent frequency is marked with a solid line, another obvious frequency is marked with a dash-dot line. The lower panel shows the variation of the power of the selected frequencies with time. A higher value of power means that the given frequency is more prominent.

For comparison and tests we generated a number of test profiles with noise and artificial signals. A detailed description of the procedures and examples are shown in Rendtel et al. (2000) and Rendtel (2001).

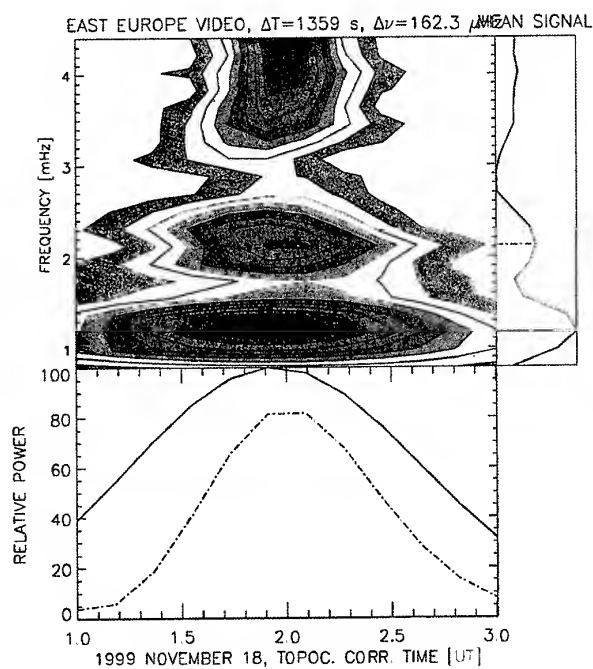


Figure 4. Result of a wavelet analysis of the East European data series (airborne video camera). Most prominent frequencies are 1.2 mHz (14 min period) and 2.2 mHz (8 min).

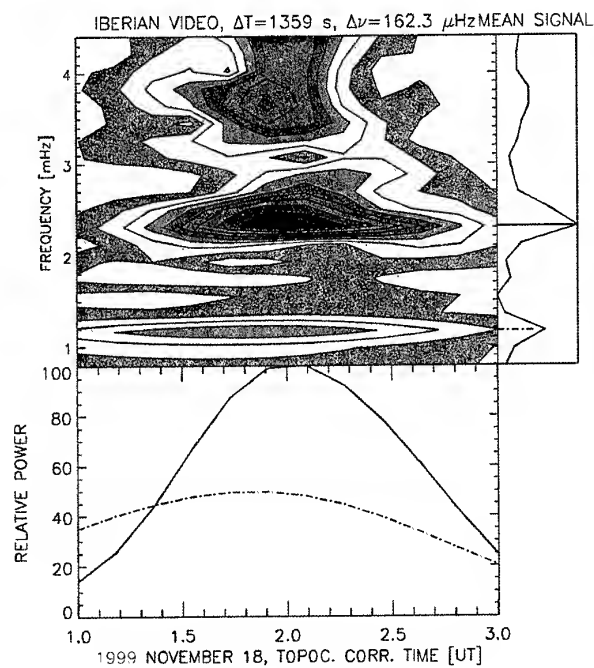


Figure 6. Result of a wavelet analysis of the data from the ground-based "Iberian" video cameras. Most prominent frequencies at 1.2 mHz (14 min period) and 2.3 mHz (7.2 min).

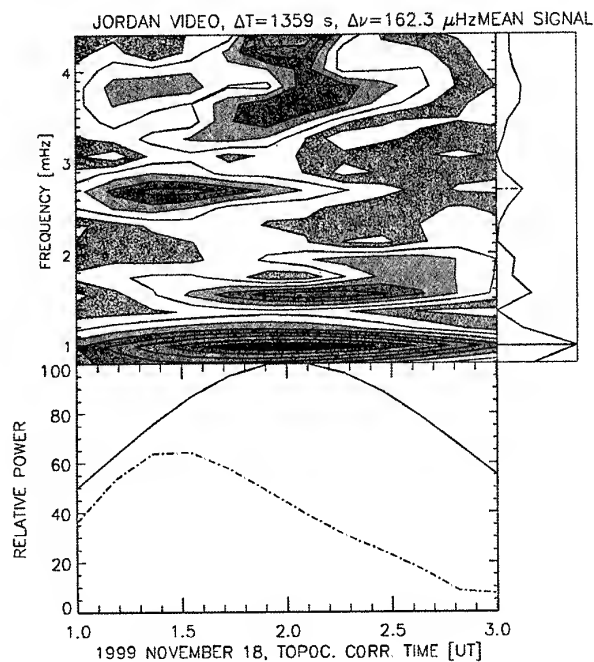


Figure 5. Result of a wavelet analysis of the ground-based video data series obtained from Jordan. Significant power at 1.0 mHz (17 min period), 1.6 mHz (10 min) and 2.7 mHz (6 min).

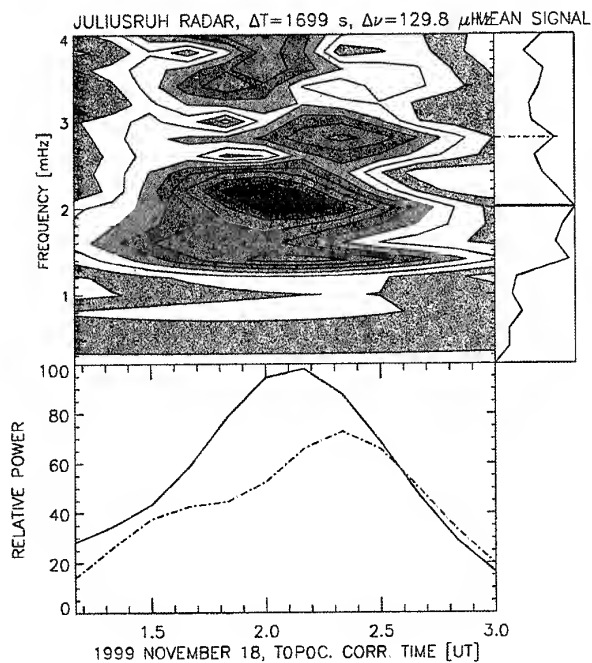


Figure 7. Result of a wavelet analysis of the data from the Juliusruh meteor radar. Most prominent frequencies at 2.0 mHz (8 min period) around the main rate peak and 2.8 mHz (6 min).

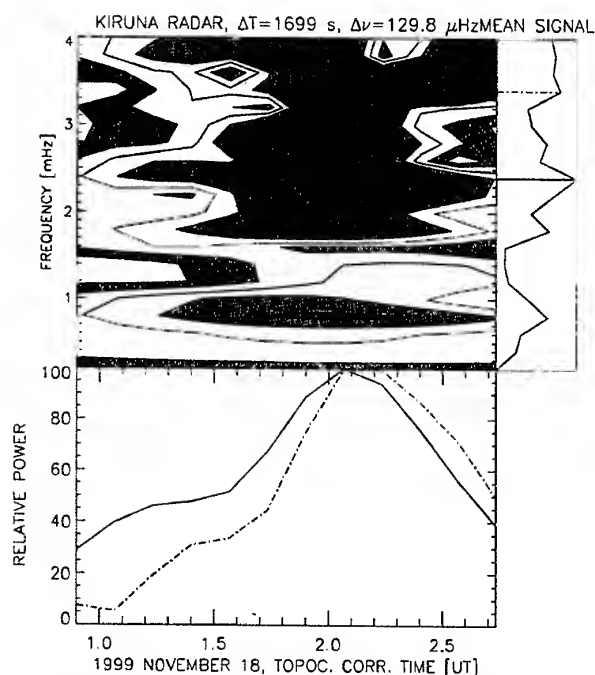


Figure 8. Result of a wavelet analysis of the data from the Kiruna meteor radar. Most prominent frequencies occur at 2.4 mHz (7 min period) and 3.4 mHz (5 min) centered at the main activity peak.

### 3. DISCUSSION

Here we have a close look at the results obtained from the Leonid data series from the different geographical regions. Unfortunately, the Tenerife data do not allow to check whether these periodic rate variations also occur at this further western location. The statistics is comparatively poor because the radiant was much lower in the sky at the peak time and both cameras had a rather small field of view.

Table 2. Periods found in the three data series applying a wavelet analysis, sorted by the period length. The most prominent period is printed in *italics*.

Region	Observation	Detected periods
East Europe	airborne video	<i>14 min</i> , 8 min
Jordan	ground based vid.	<i>17 min</i> , 10 min, 6 min
Iberia	ground based vid.	14 min, <i>7 min</i>
Juliusruh	meteor radar	<i>8 min</i> , 6 min
Kiruna	meteor radar	<i>7 min</i> , 5 min

At the eastern longitudes (cameras 1 and 2 listed in Tab. 1) the largest variation occurs near 1 to 1.2 mHz (close to 15 minutes period). This period is most prominent centered at the activity peak. Further periodic variations are found at 2.2 mHz (8 min) in the airborne data (Fig. 4) and at 1.6 mHz and 2.7 mHz (10 and 6 minutes, respectively) ground based Jordanian data (Fig. 5). Such a long period can also be found in the Iberian data (Fig. 6), but with less power. Instead we find a more intense fluctuation at 2.3 mHz (7 min) which also occurs in the analysis of

the two radar data series from Juliusruh (2.0 mHz or 8 minutes period; Fig. 7) and Kiruna (2.4 mHz or 7 minutes period; Fig. 8).

A summary of periods detected in our data is given in Table 2. The quasi-periodic variations are most pronounced close to the peak period. This may indicate that we see a characteristic of the stream's center itself or the sign of a structure in the immediate vicinity of the 1899 (or 3-revolution) dust trail. Investigations have shown that structures of a scale of a few hundred kilometers may survive in the Leonid meteoroid stream from 1899 to 1999 (Singer et al., 2000) and may be the reason for the observed quasi-periodic variations. If structures of smaller extension than the distance between the observing locations exist in the stream, the individual periodic patterns may be different. Even if the structures are crossed by several observing sites, they do not necessarily have to be in phase. The applied geocentric correction assumes a certain geometric situation, and the detected smaller features can be aligned in a different direction as compared to the main (1899) dust trail. Given the geocentric velocity of Leonid meteoroids of 71 km/s, periodic fluctuations of about 7–10 minutes would hint at structures within the stream at a scale of about 35,000 km along the Earth's passage, or 10,000 km vertical to the stream's plane.

When comparing these findings with other data series, it is important to consider the geometry between the observer and the recorded atmospheric volume. This is of particular importance if we deal with small scales. For example, one should bear in mind that the distance of a meteor from the observer varies between around 120 and 180 km for an elevation of the field of view of 40°, versus 290 to 420 km at 15° and even larger distances closer to the horizon. Of course, the sampled volume at 15° is increased by about a factor 10 as compared to the 40° elevation field center. Any local spatial "clumping" of material in the meteoroid cloud entering the atmosphere on small scales would thus be more pronounced in the observations at higher elevations. In the case of camera data obtained close to the horizon or through extreme wide angle lenses, the appearance time of each individual meteor needs to be corrected according to its topocentric position. Otherwise short time variations may be smeared out.

The described observations regard the 3-revolution dust trail observed in 1999. It will be interesting to see whether small-scale structures are detectable in the 4-, 7- and 9-revolution dust trails to be crossed in November 2001. If a similar pattern occurs, the reason for it should have acted in the immediate cometary environment (e.g. the rotation of the cometary nucleus). The strength of such density variations in the trails of different age may also provide information about the stability of small scale structures. However, this is only possible if the samples for each of the trails are sufficiently large. Assumed that the cometary surface is not completely different at subsequent perihelion passages, the density and velocity of the solar wind makes the major difference in the meteoroid ejection rate and velocity. If rate fluctuations at comparable scales do not occur in the 2001 data, the 1999 observation may reflect either a singular effect which produced a "wavy structure" in the interplanetary space during the dust trail's evo-

lution (solar wind?) or just an accidental feature, or such density fluctuations do not survive significantly more than a century.

#### 4. CONCLUSION

We analysed video meteor data as well as meteor radar data of the 1999 Leonid meteor storm obtained over a large east-west range (Eastern Europe, 37° E, to Tenerife, 17° W) and a large north-south range (Northern Sweden, 68° N, to North Africa, 28° N). The data of the more easterly sites show a significant sub-peak or activity plateau between 01<sup>h</sup>39<sup>m</sup> and 01<sup>h</sup>53<sup>m</sup> UT which may be associated with the passage of the 1932 dust trail. This feature is much less pronounced in the data sets obtained at more westerly locations. Obviously we also find periodic rate variations of about 7 to 10 minutes period, corresponding to structures within the stream of the order of 10,000 to 35,000 kilometers. The described results regard the 3-revolution dust trail observed in 1999. Only high rates allow to collect sufficient samples within short intervals to look for such structures. Observations of the 2001 return when parts of the 4-, 7- and 9-revolution dust trails are expected to produce significant activity may yield important information about the existence, size and stability of the suspected small scale structures in the Leonid meteoroid stream.

#### 5. Acknowledgements

We gratefully acknowledge the support from Andrew Elliott (BAA, UK), Luis Bellot Rubio (IAC, Spain), Georg Dittie (Germany), Detlef Koschny (ESA), Osamu Okamura (Japan) and Sirko Molau and Mirko Nitschke (AKM, Germany) who provided their video meteor recordings or raw data for this analysis. The raw video data was handed by Sirko Molau. The Juliusruh radar is operated by the Leibniz Institut für Atmosphärenphysik (IAP) Kühlungsborn (Germany); the Kiruna radar is operated by the University of Aberystwyth (Wales, UK). Data was kindly provided by Ulf von Zahn of the IAP.

#### 6. References

- Arlt R., Bellot Rubio L., Brown P., Gyssens M., Bulletin 15 of the International Leonid Watch: First global analysis of the 1999 Leonid storm, 1999, *WGN, Journal of the IMO*, Vol. 27, 286–295.
- Ireland J., Walsh R.W., Harrison R.A., Priest E.R., 1999, A wavelet analysis of active region oscillations, *Astronomy & Astrophysics*, Vol. 347, 355–365.
- Mallat S., 1989, A theory for multi-resolution signal decomposition: the wavelet representation *IEEE Trans. on Pattern Anal. and Machine Intell.*, Vol. 11, 674–693.
- McNaught R., Asher D., 1999a, Leonid dust trails and meteor storms *WGN, Journal of the IMO*, Vol. 27, 85–102.
- McNaught R., Asher D., 1999b, Variation of Leonid maximum times with location of observer *Meteoritics and Plan. Sci.*, Vol. 34, 975–978.
- Molau S., Rendtel J., Bellot-Rubio L.R., 2001, Video observations of Leonids 1999 *Earth, Moon, and Planets*, Vol. 87, 1–10.
- Rendtel J., 2001, *PhD thesis*, Univ. Potsdam.
- Rendtel J., Molau S., Koschny D., Evans S., Okamura O., Nitschke M., 2000, Video observations of the 1999 Leonid meteor storm recorded at different locations, *WGN, Journal of the IMO*, Vol. 28, 150–165.
- Singer W., Molau S., Rendtel J., Asher D.J., Mitchell N.J., von Zahn U., 2000, The Leonid 1999 meteor storm: verification of rapid activity variations by observations at three sites, *MNRAS* Vol. 318, L25–L29.
- Torrence C., Compo G.P., 1998, A practical guide to wavelet analysis, *Bull. Amer. Meteorol. Society*, Vol. 79, 61–78.

## FIVE-YEAR COOPERATIVE OBSERVATIONS OF THE LEONID SHOWER BY THE BLM FORWARD SCATTER RADIO SYSTEM

V. Porubčan<sup>(1)</sup>, A. Hajduk<sup>(2)</sup>, G. Cevolani<sup>(3)</sup>, G. Pupillo<sup>(3)</sup>,

<sup>(1)</sup>*Astronomical Institute FMFI, Comenius University, Mlynská dolina 1, 845 00 Bratislava, Slovakia*  
On leave from: *Astronomical Institute of the Slovak Academy of Sciences, 842 28 Bratislava, Slovakia*  
Email: [porubcan@fmph.uniba.sk](mailto:porubcan@fmph.uniba.sk)

<sup>(2)</sup>*Astronomical Institute of the Slovak Academy of Sciences, Dúbravská 9, SK-842 28 Bratislava, Slovakia*  
Email: [astrohaj@savba.sk](mailto:astrohaj@savba.sk)

<sup>(3)</sup>*Institute ISAO, CNR, Via Gobetti 101, 40129 Bologna, Italy*  
Email: [cevolani@isao.bo.cnr.it](mailto:cevolani@isao.bo.cnr.it)

### ABSTRACT

A survey of results from joint campaigns of the Leonids observed in 1996-2000 by the BLM (Bologna-Lecce-Modra) forward scatter system is presented. Leonid radio observations were carried out about November 10-24 each year, along two baselines: Bologna-Lecce (Italy) and Bologna-Modra (Slovakia).

Trends of long-duration echoes and their variations indicate a multiple peak activity which may be associated with a filamentary structure of the stream. The mass distribution exponent of the Leonid meteoroids in the period of the shower maximum shows significant changes throughout the 5-year observational period, with a higher representation of larger particles mainly in 1998. The observed results are consistent with those obtained by other techniques.

### 1. FORWARD-SCATTER RADIO SYSTEM BOLOGNA-LECCE-MODRA (BLM)

Since September 1996, there has been operating a new forward-scatter system for meteor observations, where a radio signal is transmitted simultaneously along two mutually almost rectangular baselines. The system consists of a transmitter located at Budrio near Bologna (44.6°N; 11.5°E, Italy) and two receivers at Lecce (40.3°N; 18.2°E, Italy) and Modra (48.4°N; 17.3°E, Slovakia). The system was built up for monitoring meteor activity, to study meteor flux from different baselines directions. It is operating regularly each month for about 10-14 days, 24 hours per day. It is expected that the system may also assist in detecting short-term meteor activity enhancements and identify spurious bursts of non-meteor origin. The equipment utilizes a continuous wave transmitting frequency at 42.7 MHz, a fixed modulating tone at 1

kHz and 0.25 kW mean power transmitted in the direction of both receiving stations. The transmitting and receiving antennas (Yagi) are horizontally polarized with an elevation angle of 15°. The baseline distances between the transmitter and receivers are: Bologna-Lecce of 700 km (azimuth 307°) and Bologna-Modra of 590 km (azimuth 224°).

### 2. ACTIVITY OF LEONIDS IN 1996-2000

The Leonid activity was monitored by the new forward-scatter system already in 1995 (Nov. 14-21), however, along the baseline Bologna-Lecce only. Since 1996, the observations are regularly carried out in both directions, so the data are recorded by both receivers.

From the studies of echo counts obtained by the BLM forward scatter system it is apparent that a shower activity can be clearly recognized only for echoes of longer duration. In the counts of all echoes, shower echoes are almost completely covered by sporadic background echoes. This trend is observed also in the data from all years of the observation of the Leonids. Therefore, in the present study, the Leonid activity curves were derived only for long-duration echoes (duration  $\geq 8$ s).

Shower activity was obtained by subtracting sporadic background counts from all echo counts (shower and sporadic) in corresponding hours. Due to technical problems causing various interruptions or interferences at receiving stations, it was not possible to use the same periods (days) for sporadic background in each year. The Leonid activity curves (echoes  $\geq 8$ s) corrected for the radiant elevation were obtained by combining data from both stations.

There should exist some differences in the counts of echoes in corresponding intervals between both receiving stations as a result of the fact that the stations are located about 900 km apart, with the midpoints of the baselines about 500 km apart. Thus each station is recording different meteoroids (groups) from a stream population. Further it is due to a rather small statistics and selection of the sporadic background for each station independently.

In 1996 the observations were carried out on Nov. 12-26 and the data show that the Leonid activity curve exhibits a rather flat maximum on Nov. 17 lasting for about 10-11 hrs (solar longitude  $235.0^\circ$ - $235.4^\circ$ , equinox 2000.0), with at least two peaks ( $235.23^\circ$  and  $235.29^\circ$ ). Though the peaks are not so pronounced, they are well consistent with the observations by the Ondrejov backscatter radar ( $235.20^\circ$  and  $235.32^\circ$ , [1]). The backscatter data indicate a peak rate near  $235.2^\circ$  characterized by a significant number of bright Leonids demonstrated by a lowering of the mass exponent  $s$  near the peak. Visual observations yield a peak at  $235.17^\circ$  (short-lived and richer in fainter meteors).

The 1997 Leonid activity curve shows an apparent increase in the activity until 09:00-09:30 UT, Nov. 17 (solar longitude  $235.1^\circ$ ), with some indication of smaller enhancements in between. The observations were carried out on Nov. 10-25. Actually, the 1997 Leonid maximum could not be observed by the BLM system due to the shower radiant being just on the horizon at the time of the peak itself. According to visual observations maximum appeared on Nov. 17, 12:15 UT (solar longitude  $235.22^\circ$ ) and an increased Leonid activity was observed in the interval  $235.0^\circ$ - $236.0^\circ$  [2].

In 1998 the BLM system operated on Nov. 10-24 and the 1998 Leonids with a large number of bright bolides observed on Nov. 16/17 ranked for meteor observers among the most impressive observational events. The counts of echoes observed by the BLM system show a very broad maximum, however, due to overlapping long-duration echoes the peak itself could not be recorded. At least two secondary peaks at  $234.48^\circ$  and  $234.84^\circ$  are apparent. These peaks were recorded also by the backscatter radar at Ondrejov for echoes  $>10s$ , showing a broad maximum ( $234.6^\circ$ - $234.7^\circ$ ) with at least three secondary peaks [3]. The event was recorded also by the photographic all-sky cameras at Modra Observatory (receiving station of the BLM system) [4]. The maximum derived from photographic observations (between 01:30 - 02:00 UT) appeared at  $234.52^\circ$  and is also apparent on the Modra FS record. At Modra, there are operating two all-sky cameras. One is in a fixed mode (equipped with a rotating

shutter) and the other is in a guided mode, so by their combination the time of appearance of photographed meteors can be calculated. Visual observations confirmed a very broad component of the 1998 Leonid fireballs with a peak between  $234.4^\circ$ - $225.0^\circ$  [5].

In 1999 the observations were carried out on Nov. 10-24 and the BLM data show a pronounced maximum at  $235.28^\circ$  which is consistent with other radar and visual observations. According to the Ondrejov backscatter radar data the 1999 Leonid activity culminated at  $235.285^\circ$  with prevailing fainter echoes yielding a mean value of  $s = 1.58$  [3]. The Leonid activity showed only one distinct peak and this was the main outburst of the Leonids in this return of the parent comet to the Sun. An overall activity profile based on the observations of more than 400 visual observers shows a storm activity of the 1999 Leonids with the ZHR = 3 700 on Nov. 18, 02:02 UT (solar longitude  $235.285^\circ$ ) [6]. The TV observations [7] exhibit the most prominent peaks on Nov. 18 at 01:58 and 02:11 UT.

The observations in 2000 were carried out in the period Nov. 13 - 24 and the shower echoes of duration  $\geq 8s$  obtained from the BLM data shows multiple peak activity ( $236.10^\circ$ ,  $236.19^\circ$  and  $236.25^\circ$ ). The peaks at  $236.1^\circ$  and  $236.25^\circ$  are consistent with visual data [8] and are close to the predicted time of the dust trail of the 1733 and 1866 perihelion passages of the Leonid parent comet, respectively [9].

### 3. MASS DISTRIBUTION

The FS data from Modra and Lecce provided a possibility to derive the mass distribution exponent from the observed echo durations of the shower and sporadic meteor echoes. The mass distribution exponent  $s$  was derived from the cumulative numbers of echo duration considering diffusion for dominant process of an echo decay and was found from the conventional formula [10] in the form:

$$\log N = -3/4 (s-1) \log T + \text{const.},$$

where  $T$  is the observed duration and  $N$  is the cumulative number of echoes with the duration  $T$  or greater.

The values of  $s$  in individual years were obtained as the mean values from the period of the shower maximum (approx. 12 hrs) and the sporadic background (Tab. 1). The mass exponent values derived for each station separately are listed in Table 1 (M - Modra, L - Lecce) and are compared with

the values obtained from other radar (O - Ondrejov) and visual observations.

**Table 1:** The mass exponent  $s$  derived for shower (sh) and sporadic (sp) meteors (M - Modra, L - Lecce).

	sp-M	sp-L	sh-M	sh-L	sh-O	$s_{vis}$
1995	-	2.34	-	1.69	-	1.6 [11]
1996	2.22	2.32	1.63	1.50	-	1.65 [1]
1997	2.38	2.71	1.64	1.61	-	1.7 [2]
1998	2.32	2.67	1.20	1.15	1.23 [3]	1.3 [5]
1999	2.23	2.25	1.56	1.52	1.58 [3]	1.8 [6]
2000	2.44	2.28	1.84	1.56	-	1.8 [8]

#### 4. CONCLUSIONS

The observations of the Leonids by the Bologna-Lecce-Modra forward scatter system in 1996-2000 were analysed and the activity curves of long-duration echoes ( $\geq 8s$ ) were derived. The activity curves indicate a multiple peak structure especially in 1996, 1998 and 2000, which may be attributed to a filamentary structure of the stream. The analysis of the mass distribution of meteoroids within the stream shows an apparent decrease of the mass distribution exponent  $s$  with the approaching parent comet of the stream to perihelion and an increase after its passage in 1998. The lowest value of  $s$  was observed in 1998 and the derived results are consistent with the results obtained by other techniques.

**Acknowledgements.** The authors are indebted for the support of the research to the Institute ISAO CNR, Bologna and to VEGA, the Slovak Grant Agency for Science, grant No. 1026.

#### 5. REFERENCES

1. Brown P., Šimek M., Jones J., Arlt R., Hocking W., Beach M., Observations of the 1996 Leonid meteor shower by radar, visual and video techniques, *MON. NOT. R. ASTRON. SOC.* Vol. 300, 244-250, 1998
2. Arlt R., Brown P., Bulletin 12 of the International Leonid Watch: Final results of the 1997 Leonids and prospects for 1998, *WGN, the J. of the IMO*, Vol. 26/4, 161-165, 1998
3. Šimek M., Pecina P., Radar observation of the Leonids in 1998 and 1999, *ASTRON. ASTROPHYS.*, Vol. 365, 622-626, 2001
4. Tóth J., Kornoš L., Porubčan V., Photographic Leonids 1998 observed at Modra Observatory, *EARTH, MOON AND PLANETS*, Vol. 82-83, 285-294, 2000
5. Brown P., Arlt R., Detailed visual observations and modelling of the 1998 Leonid shower, *MON. NOT. R. ASTRON. SOC.*, Vol. 319, 419-428, 2000
6. Arlt R., Rubio L.B., Brown P., Gyssens M., Bulletin 15 of the International Leonid Watch: First global analysis of the 1999 Leonid storm, *WGN, J. of the IMO*, Vol. 27/6, 286-295, 1999
7. Molau S., Rendtel J., Nitschke M., First results of video observations during the 1999 Leonid storm, *WGN, J. of the IMO*, Vol. 27/6, 296-300, 1999
8. Arlt R., Gyssens M., Bulletin 16 of the International Leonid Watch: Results of the 2000 Leonid meteor shower, *WGN J. of the IMO*, Vol. 28/6, 195-208, 2000
9. Asher D., Leonid dust trail theories, in *Proc. Inter. Met. Conf. 1999*, ed. R. Arlt, IMO, 5-21, 2000
10. Kaiser T.R., *Meteors*, Pergamon Press, London, 1955
11. Brown P., The Leonids. Bulletin 8 of the International Leonid Watch, *WGN, J. of the IMO*, Vol. 24/5, 139-147, 1996

# METEOR OBSERVATIONS FROM ISRAEL

Noah Brosch<sup>1</sup>, L.S. Schijvarg<sup>2</sup>, M. Podolak<sup>2</sup>, and M. R. Rosenkrantz<sup>3</sup>

<sup>1</sup>School of Physics and Astronomy, Beverly & Raymond Sackler Faculty of Exact Sciences, Tel Aviv University, Tel Aviv 69978, Israel

<sup>2</sup>Dept. of Geophysics and Planetary Sciences, Beverly & Raymond Sackler Faculty of Exact Sciences, Tel Aviv University, Tel Aviv 69978, Israel

<sup>3</sup>Radar Division, ELTA, Ltd., 100 Yitzhak Hanassi Blvd., P.O. Box 330, Ashdod 77102, Israel

## ABSTRACT

We observed the 1998 and 1999 Leonid meteor shower with phased-array radar systems operating in the L-band from Israel. We discovered that the radar meteors exhibit a two-peaked height distribution. One population corresponds to that of the regular optical meteors and peaks at  $\sim 120$  km. The newly discovered population forms a wide distribution centered at  $\sim 240$  km with a long tail to high altitudes. We propose that this population consists essentially of H<sub>2</sub>O-ice bodies ejected from the nucleus of P55/Tempel-Tuttle comet along with the "regular" meteoroids. The high-velocity interaction between the fluffy-ice cometary chunks and the thermosphere ions causes sputtering and the subsequent disruption of the ice chunk, while producing the detected radar return. Supporting evidence for our finding is the newly-identified long tail of the meteor distribution at high altitudes, identified in intensified-video observations of the Leonids. The analogy with the water-ice mini-comets proposed by Frank and collaborators is emphasized and observational tests of the suggestion of H<sub>2</sub>O-ice meteoroids are proposed.

Key words: Meteors; Radar; Leonids.

## 1. INTRODUCTION

Meteors bombarding our planet represent one of the few sources of interplanetary material, and the single one of interstellar matter, that we can study directly. The ablation of small meteoroids, typically the size of tenths of millimeters captured by the Earth's gravitation field, releases metallic atoms and ions in the atmosphere. The meteoroids produce the well-known visible signature of a meteor, and the plasma produced by their passage can be detected by the forward or back-scattering of electromagnetic waves and by the VLF waves they produce by their passage (Price & Blum 2000). A valid model to predict the radar signature of a meteoroid must

be capable of treating a wide variety of low and high altitude radar reflection phenomena. While significant advances have been made in the models related to the meteoroid radar reflection below  $\sim 150$  km, a prediction method has not yet been developed to adequately treat meteoroid radar reflections originating above 200 km.

Here we present novel radar observations of meteors performed in 1998 and 1999 that show, for the first time, the existence of a population of radar meteors at altitudes above  $\sim 200$  km, reaching as high as 400+ km. We also present a tentative explanation for these high-altitude radar meteors. Classical meteor radars that work at MHz and tens of MHz bands have been used for studying the shower and sporadic populations. At the Arecibo Observatory, a narrow-beam radar operating at 430 MHz has been used successfully to study sporadic (Mathews *et al.* 1997) and Leonid meteors (Janches *et al.* 2000). At the EISCAT facility, Pellinen-Wannberg & Wannberg (1994) used a narrow-beam 930 MHz radar to study head and trail meteor echoes. Such narrow-beam radar systems can detect meteors only when they cross the beam, but cannot follow its flight because they use mechanical tracking. Here we present observations with phased-array installations operating in the L-band (frequency  $\simeq$  one GHz  $\rightarrow$  30 cm wavelength). Phased-array radar systems have been used to study orbital debris, *e.g.*, some of the US military installations listed by Jackson (1992), such as the AN/FPS 115 PAVE PAWS system operating in the UHF regime (420–450 MHz). The advantage of such systems in the study of meteors, as will be seen below, is the much larger atmospheric volume explored quasi-simultaneously by the scanning, electronically-steered radar beam. This has already been pointed out by Pellinen-Wannberg *et al.* (1998).

The most relevant result we report here from the radar observations is, as mentioned above, the detection of a high-altitude meteor population. Classical meteors are observed by optical and radar means at altitudes within the 80–120 km stratum (*e.g.*, Porubčan & Getman 1992) yet there are tantalizing new indications of much higher altitude me-

tears. Meteor trails were observed with the EISCAT narrow-beam radar facility up to  $\sim 165$  km (Pellinen-Wannberg & Wannberg 1994) and even higher (Pellinen-Wannberg 2001). The height distribution of radar meteors reported in Brown *et al.* (2000) and observed at 38 MHz shows, in addition to a  $\sim$ Gaussian distribution centered at  $\sim 110$  km, a long tail to higher altitudes. However, as the Skyinet radar system they used gives no indication on the exact trajectories of the objects it observes, there is no confidence that these high-altitude echoes belong to the Leonid shower population. Also, it is possible that many radar observations of meteors are initially biased against high-altitude meteors (*e.g.*, the ALTAIR observations reported by Close *et al.* 2000, limited to echoes below 140 km). Recent optical (intensified TV) observations revealed meteors at even higher altitudes (153.6 km for the highest altitude beginning-of-trail recorded by de Ligne *et al.* 2000; close to 200 km: Spurny *et al.* 2000) and even higher than 200 km (*e.g.*, Brown *et al.* 2000 *cf.* Fig. 14).

Our observations reveal that, at least for the 1998 and 1999 Leonid storms, two populations of bodies must have been responsible for the behavior at different altitudes. We propose that the high-altitude radar meteors are produced by bodies of mainly water-ice, and that these bodies are destroyed at high altitudes by sputtering following high-velocity collisions with ions in the thermosphere.

## 2. RADAR OBSERVATIONS

In November 1998 and November 1999 the Leonid shower was observed in Israel with a large phased-array radar operating in the L-band. The physical size of the active phased-array used is of order  $40 \text{ m}^2$ . In 1998 only one phased-array radar was used, and in 1999 two phased-array radar systems were used with the second being smaller, of order  $12 \text{ m}^2$ . Both devices operated at an intermediate pulse repetition frequency with extremely short-duration pulses.

For the 1998 observations, the array's boresight was pointed in the general direction of the shower radiant and was scanned continuously in azimuth tens of degrees to either side of the boresight. The scanning with phased-arrays is done by electronically steering the synthesized beam at extremely fast rates (scan times much shorter than one second). A similar coverage was achieved in the vertical direction. For observations of the 1999 shower, the smaller phased-array system was pointed in the general direction of the radiant and the larger one was set to scan a portion of the western sky. In both cases, the sky area surveyed by the radar beam was of order a sizable fraction of a steradian. The information collected during the observation, for each set of echoes identified as belonging to the same meteoroid, consisted of its topocentric location, its Doppler velocity, and its radar cross-section (RCS) derived from the strength of the echo and its distance. The topocentric velocity was derived from the line-of-sight velocity and from

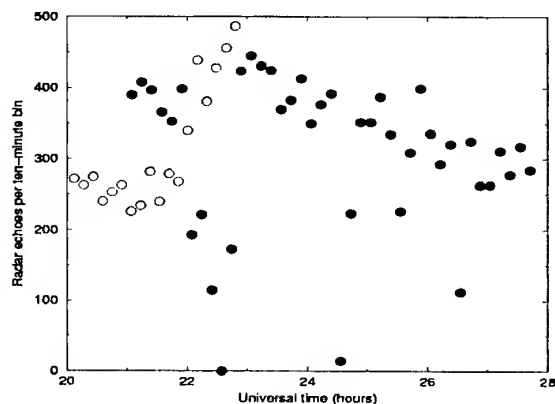


Figure 1. Distribution of radar meteors with time measured by the large radar system (filled circles from 17-18 November 1999 and open circles from the previous night). The vertical axis represents the raw counts of echoes in 10-minute bins and the horizontal axis is Universal Time in hours of the relevant day of observation.

the distance to the echo coupled with its transversal angular-motion rate.

During the course of a few hours observation, thousands of short-duration (2-3 seconds) meteoroid trails were recorded. Long-duration ( $\sim 20$  sec) meteoroidic trails were also observed, with ranges and altitudes of a few hundred kilometers and spatial velocities of  $\sim 3-5$  km/s. Figure 1 shows the number of radar echoes detected in ten-minute bins by our large radar system during the two nights of Nov. 16-17 and 17-18. Figure 2 shows a similar plot derived from the measurements with the small radar system, with an overplot of the zenithal hourly rate (ZHR) of the optically-detected meteors. In both cases, only radar echoes with altitudes above 70 km were considered and are plotted. Note that the intervals with low echo rates are those for which no data, or only partial data, were available. The ZHR plot is a smoothed version of the official records of the International Meteor Organization (IMO: Arlt *et al.* 1999) and for the purpose of plotting here it was scaled to one percent of its 'true' value. The shapes of the two distributions (ZHR and radar echoes counted in a direction  $\sim$ perpendicular to the Leonid radiant) are not identical. While the optical observations, representing meteors that were visually observed (*i.e.*, optically-brighter than 6.5 mag), are strongly peaked near the time of the meteor storm ( $\sim 2^{\text{h}}5^{\text{m}}\text{UT}$ ), the radar echoes show an  $\sim$ flat distribution with time. Measurements from the night before the Leonid storm show a  $\sim$ flat distribution of echoes before  $22^{\text{h}}\text{UT}$  and a steeply rising rate after this time; this may represent a component not specifically linked to the Leonid storm contributing a rate of  $\sim 1,500 \text{ h}^{-1}$  before the Leonid radiant rises and an additional component that becomes visible as the radiant rises and whose rate increases with time. Note that the expectation for the behavior of sporadic meteors is that

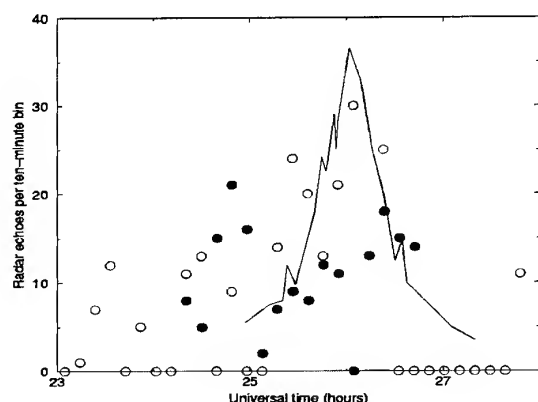


Figure 2. Distribution of radar Leonid meteors with time measured by the small radar system (date coding as in Figure 1) superposed on a smoothed version of Fig. 3 of Arit et al. (1999) of the ZHR of the optically-detected meteors represented by the solid line.

their number will increase with time after midnight and into the morning; this is opposite to the trend we observed with the large radar system indicating that most objects we observed do not belong to the sporadic population.

The general trend of increasing radar echo rates with increasing radiant altitudes supports our interpretation that most radar echoes detected by us belong to the Leonid population. Note that the large radar system was looking in a direction opposite to that of the radiant during the 1999 storm, while the small system was observing in a southerly direction. The issue of the proper altitude of the radar echoes is crucial to the subject of this paper and has been objected to by persons who saw our first-cut results. It has been suggested that the high-altitude echoes could be the result of range-doubling, i.e., that the echo of one pulse is recorded during the second interpulse interval; we point out this is not possible with the system we used. We can also rule out artifacts that could have been caused by sidelobe reception or by sideband transmission; these are strongly suppressed with our radar systems. Unfortunately, we cannot elaborate on sensitive technical details due to security limitations.

### 2.1. Impact to Meteoroid Investigation

Our radar measurements of the Leonid shower, and the finding of high-altitude meteor radar returns, raise a number of new questions regarding meteoroid theory. This theory, established by Öpik (1958), Bronshten (1983), and others, does not predict ionization processes at altitudes where the atmospheric particle density is 2-4 orders of magnitude lower than where classical meteors are observed (80-120 km). Yet, in order to explain our observations, we require a process connected with the passage of the meteoroid

that can produce plasma at high altitudes, which could produce the observed radar echoes.

In this paper we suggest a new model for radar meteors based on the existing meteoroid-atmosphere interaction theory, but including a new interaction ingredient. This will provide a consistent explanation for ionization processes giving rise to meteoroid radar reflections both for the expected low ( $\sim 120$  km) and unexpected high ( $\geq 200$  km) altitudes.

For consistency further along in this paper, we define, at this point, two classes of radar meteors: the **First Class (FC)** consists of the classical low altitude meteors, those observed below  $\sim 120$  km. The **Second Class (SC)** consists of the high-altitude meteors measured above a somewhat arbitrary threshold set at  $\sim 160$  km.

### 2.2. Results

Figures 1 and 2 showed the distribution of radar echoes with time during the peak of the Leonid meteor shower, on the night November 17-18 1999. Figure 2 also displayed the ZHR during the peak of activity. The results from the large radar system imply that (a) there is a steady population of bodies producing radar returns on both observation nights, that is of order 1,500 echoes per hour in a sky area of about one steradian, and (b) there is a population of bodies producing radar returns that is probably linked to the Leonid meteors. However, the finding that the radar returns do not peak near the optical ZHR peak indicates that not all the meteoroids producing radar echoes have optical counterparts, at least as described by the IMO ZHR plot.

Figure 3 is a plot of the radar echo altitude distribution showing the two peaks in altitudes for all the radar events collected during this night. There was evidence for detection of high-altitude meteor echoes also in our first set of radar measurements of the Leonid shower collected in November 1998. Unfortunately, not enough measurements were obtained during this observing run to show the distinct features evident in Figure 3 for the 1999 shower. We believe that these measurements, by our radar systems, are among the first showing evidence for meteoroid trails at much higher than expected altitude.

The altitude plot can tentatively be decomposed as two different distributions. One appears as an approximately-symmetric Gaussian with a peak at  $\sim 120$  km. The other peak, at  $\sim 240$  km, is wider and could possibly have a long tail to very high altitudes. We do not observe a continuous distribution with altitude, but instead we detect a significant drop in the fraction of radar meteors at  $\sim 170$  km. This indicates that we detect two different populations of radar meteors, or two distinct mechanisms for the production of radar meteors, that do not overlap significantly. The population of high-altitude meteors appears to be similar in number to that of the FC radar echoes.

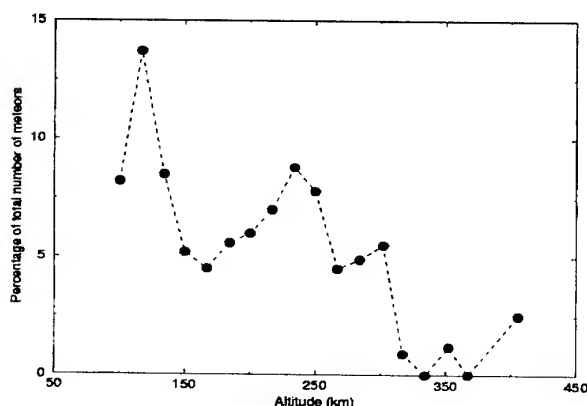


Figure 3. Distribution with altitude of radar Leonid meteors.

However, we cannot rule out the possibility of a much larger SC population, because it is probable that the meteoroids with a small RCS are missed out at large distances by the limited system sensitivity. A possible explanation for the two-peaked behavior in the altitude distribution of the detections will be discussed below.

One of the more important parameters relevant to radar meteors is their radar cross-section. The RCS is approximately the radar equivalent of the intrinsic brightness of an object; the larger the RCS the easier is its detection. This was measured for all the detections of Leonid meteors and a histogram of the RCS as function of the altitude is shown in Schjvarg *et al.* (2001). Our measured RCS values show a slight trend for larger RCS values at higher altitudes. This is at least partly a selection effect: the detection of a distant target requires a larger RCS than for nearby targets. Considering also that lower altitude radar returns come, on average, from meteor tracks that are closer than those from high-altitude meteors, therefore they sample a smaller volume than the high-altitude tracks, we conclude that there seems to be no significant difference in RCS between FC and SC populations.

### 3. HIGH-ALTITUDE METEORS

For the purpose of theoretical classification the radar measurements were divided above into two main classes: FC tracks that occur at the classical meteor altitudes and SC tracks that occur at much greater altitudes than normally expected. The spatial velocity magnitude and the RCS distribution of the two classes are almost identical.

The following questions can be posed at this stage:

1. How are SC events produced?
2. Why is the spatial velocity of the two classes of order  $3\text{--}5 \text{ km sec}^{-1}$ ?

### 3. Why is the RCS behavior of the two classes almost identical?

After listing the problems posed by the radar measurements of the Leonid shower we now examine more closely some problems directly connected with the SC ionization mechanism. We concentrate here mostly on a possible answer to the first question, and leave the other two questions to further papers. This is done here by simulating the phenomena expected following the entrance into the atmosphere of a Leonid meteoroid.

The simulation code used for computing the trajectory of a meteoroid as it passes through the atmosphere (using the 1976 U.S Standard Atmosphere model) is based on a protoplanet ablation model developed by Podolak *et al.* (1988). The model computes the trajectory of a meteoric body composed of silicates, water ice, or a mixture of the two. The model includes techniques for treating gas drag, heating, ablation, and the computation of the resultant surface temperature of the body. Also, thermal conduction, as well as heat transfer by advecting gases, is taken into account. Melting and sublimation of the meteoroid material, via the classical meteor mechanism, are also included in the calculations.

In addition to ablation, which is considered a classical erosion mechanism for meteoroids, a new process was added to the program in order to simulate Leonid meteors: erosion due to physical sputtering. The impact of high-speed particles (for example: atmospheric particles hitting meteoroid particles) may promptly eject atoms or molecules from a solid or liquid surface causing physical sputtering. Physical sputtering is an atomic-scale process that can occur if the incident particle (ion) can transfer sufficient energy to a surface or bulk atom in the target to overcome its bulk displacement energy and/or its surface binding energy. Note that in most cases these two energies, as well as the ionization and molecular dissociation energies, are commensurate (a few eV or tens of eV). Therefore, from a statistical mechanics point of view we should expect  $\sim$ equal fractions of the kinetic energy of the incident ion to be deposited in each such process. Unlike vaporization, the sputtering mechanism does not depend significantly upon the body temperature and the ejected meteoroid atoms are not necessarily at  $\sim$ rest, hinting that further interactions, either among the ejecta or between them and the ambient medium, are possible.

Sputtering is not a classical mechanism considered in meteor theory, although it is the basic mechanism invoked for the demise of interstellar dust particles. However, it was included in planetary science research as a mechanism to explain the interaction of Saturn satellite surfaces with the planet's magnetosphere (*e.g.*, Jurac *et al.* 2001), or the sputtering of the Martian atmosphere by ions picked up by the Solar wind (*e.g.*, Leblanc & Johnson 2001). Its inclusion within the theory for the erosion of high-velocity

Table 1. Standard atmospheric abundances by height

Species	120 km	250 km	340 km
O	$9.7 \cdot 10^{10}$	$2.5 \cdot 10^9$	$5.4 \cdot 10^8$
O <sub>2</sub>	$3.9 \cdot 10^{10}$	$3.5 \cdot 10^7$	$1.6 \cdot 10^6$
N <sub>2</sub>	$3.0 \cdot 10^{11}$	$6.9 \cdot 10^8$	$4.5 \cdot 10^7$

meteoroids, such as the Leonids, is justified by the relative collision energy. A Leonid meteoroid sees the ions in the upper atmosphere as particles bombarding it at  $\sim 71$  km/sec. A typical oxygen ion with this relative velocity carries, therefore, a kinetic energy of 440 eV while a bi-atomic nitrogen molecule carries 750 eV. The abundance of the various species per cm<sup>3</sup> at different altitudes, relevant for our radar meteor observations, are listed in Table 1. It is clear that at high altitudes atomic oxygen dominates the other species in its efficiency to induce sputtering. At the altitude of FC meteors, the dominating contribution is from molecular nitrogen, with a much higher energy deposition per impact.

The erosion by this latter mechanism is given by the sputtering yield  $\gamma$ , a statistical variable defined as the mean number of atoms removed from a solid target per incident ion (Öpik 1958). Johnson (1998) presented a compilation of laboratory data for low-temperature water-ice sputtering. Sputtering yields were reported for the release of Mg, Fe, Si and O under impact of He, C, O, Si and Fe on grain material composed of Mg and Fe bearing silicates by May *et al.* (2000). These were used successfully in our model for the meteoroid interaction with the atmosphere. When meteoroids encounter the Earth's atmosphere, two different physical processes arise in the removal of meteoroid mass. The mass-removal mechanism for the FC tracks is ablation, which causes ionization to occur between altitudes of 80 to 150 km (E-region of the ionosphere), and below the lower height the meteoroid is usually destroyed. Above the E-region, in the F-region of the ionosphere, the particle density is too low for the ablation-ionization processes to operate efficiently. We therefore assume that the mass-removal and ionization mechanisms for the SC tracks should be connected with the high-velocity impact between the meteoroid and atmospheric particles, mainly O<sup>+</sup> ions, causing physical sputtering. During its atmospheric passage, a Leonid meteoroid can therefore be disrupted either by ablation or through physical sputtering.

The  $\gamma$  parameter can be measured in sputtering experiments and can also be calculated theoretically (e.g., Jurac *et al.* 1998). The sputtering mass-loss equation follows from the assumption that for velocities characteristic of Leonid meteors ( $v \sim 71$  km sec<sup>-1</sup>) the upper layers of the meteoroid would essentially be completely sputtered ( $\gamma=2$ ), due to multiple collisions with atmospheric particles, yielding a mass-loss rate of  $dM$  in the time interval  $dt$ :

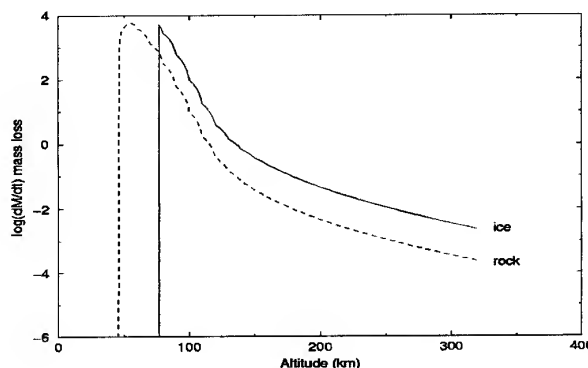


Figure 4. Evolution of the mass-loss rate with altitude when passing through the atmosphere for two theoretical meteoroid models; a stony one (dashed line labeled 'rock') and an icy one (solid).

$$\frac{dM}{dt} = \gamma \rho v \pi r^2 \quad (1)$$

Here  $\rho$  is the ambient atmospheric number density,  $v$  is the meteoroid speed, and  $r$  is the meteoroid radius (for simplicity, we assume spherical bodies with a radius of 20 cm). The value adopted here for  $\gamma$  is a severe underestimate for the following reason. It is likely that water ice forms at least part of the composition of meteoroids originating from a comet. The sputtering yield of water ice at normal incidence and at  $\sim 440$  eV kinetic energy for the ion is  $\gamma \sim 10$  (cf. Jurac *et al.* 2001, Fig. 1). As some of the ions will not bombard the meteoroid at normal incidence, it is necessary to adopt an angle-averaged yield which is  $\sim 2.2$  times larger (cf. Jurac *et al.* 2001, Fig. 2), raising the yield to  $\gamma \simeq 22$ . Adopting  $\gamma=2$  in our calculations, a good choice for silicate meteoroids, is probably a severe underestimation of the sputtering effect on Leonid meteoroids, perhaps by as much as an order of magnitude. Note, in addition, that the  $\gamma$  values quoted by Jurac *et al.* are for sputtering of water ice at 80-100K; above this temperature they mention that  $\gamma$  shows a temperature dependence. This is not accounted for in the present model.

Since the mass-loss behavior of the meteoroid will depend on the details of its path through the atmosphere, it is necessary to follow the trajectory in detail by solving the equation of motion:

$$m \frac{d\vec{v}}{dt} = \frac{GmM_{\oplus}}{r^3} \vec{r} - \vec{F}_{drag} \quad (2)$$

Here  $m$  is the meteoroid mass,  $v$  is its velocity with respect to the ambient atmosphere, and  $r$  is its geocentric distance. The solution was calculated using a fourth-order Runge-Kutta integration scheme and allowed us to follow meteors that enter the atmosphere at all angles of incidence.

Once the meteoroid collides with the atmospheric particles and ionizes neutral air molecules and atoms, it generates local plasma regions and causes the formation of an ionized meteoroid trail. Although different, the two mechanisms (ablation and sputtering) lead to similar radar reflection patterns, since both eject meteoroid particles and trigger ionization. The main difference is that ejecta produced by sputtering probably have considerable kinetic energy, can ionize neutral atmospheric species (although not many of these can be expected at high altitudes), and may consist of fragments of molecules, ions, or radicals.

The parameters that determine the characteristics of a meteor when it traverses the atmosphere are its size, entry velocity, angle of entry, and its composition. For the Leonids, the entry velocity is roughly  $71 \text{ km s}^{-1}$ . In the following we describe two runs of the model, one for the case of Leonid meteoroids composed of pure silicates (rocky, or stony) and the other for Leonids composed of pure water-ice (icy). Two different trajectory orientations are considered: one vertically incident onto the atmosphere (radiant at zenith) and the other with the meteoroid track parallel to the plane tangent to the Earth's surface and passing "overhead" the location of the radar site (horizontal track).

As might be expected, the body penetrates into the atmosphere before being vaporized. The temperature at the surface of the meteoroid is mainly determined by the rate of vaporization of the surface material, as well as by the atmospheric heating. In general, the latter quantity depends on the history of the meteoroid trajectory, but for the cases considered here the surface temperature is almost entirely a function of the composition. Thus, meteoroids of the same composition but of different sizes will reach the same temperature at a given level in the atmosphere, but larger bodies will be able to penetrate to deeper levels in the atmosphere before being completely dissipated and will, therefore, reach higher temperatures. Our model allows for the change in radius of the body due to ablation and sputtering, permitting the evaluation of both First and Second Class events. The mass loss from the meteoroid, in  $\text{g s}^{-1}$ , for the cases of a silicate body and for one composed of water ice, are shown in Figure 4 as functions of the altitude.

The electron line densities calculated by the model for the two types of meteoroids are shown in Figure 5 together with an indication of the location of the underdense/overdense boundary. The simulation demonstrates that a  $\text{H}_2\text{O}$ -ice meteoroid produces an overdense radar track even at very high altitudes, whereas a stony meteoroid will produce a track that becomes overdense only at  $\sim 250 \text{ km}$ . Figure 6 shows the behavior of the radar cross-section for the four cases described above (rocky or icy meteoroid, viewed horizontally or vertically). For most of its trajectory through the atmosphere, simulated Leonid meteors produce significant RCS values. For equal-sized bodies, the water-ice meteoroid produces a higher RCS than a rocky meteoroid at high alti-

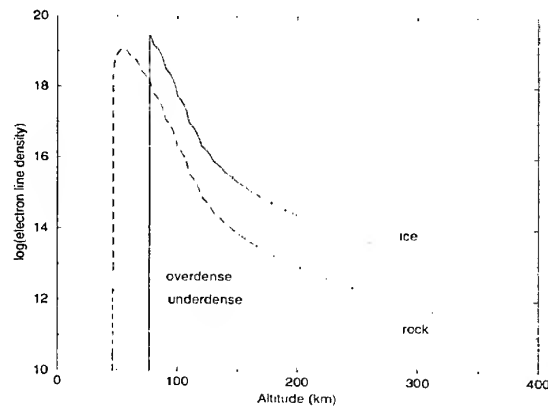


Figure 5. Electron line density as function of altitude for a stony meteoroid and for one composed of water ice. The boundary between underdense and overdense trails, where reflection of radio waves occurs, is shown by a dashed horizontal line.

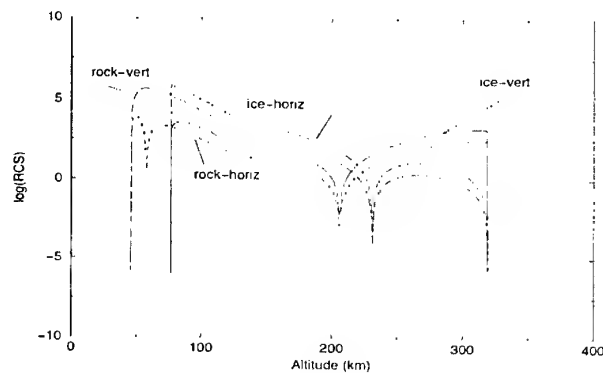


Figure 6. The radar cross-section of a stony meteoroid and an equally-sized icy meteoroid viewed vertically or horizontally.

tudes when viewed vertically (high radiant altitude). This situation is reversed at low altitudes (higher RCS for a rocky meteoroid).

We have performed only preliminary simulations of the high-altitude water-ice meteoroid penetration in the atmosphere, which we present here. In particular, the choice of a 20 cm radius is only indicative; similar results (after properly scaling) are expected for sizes from mm to a few meters. This is relevant to the Leonid meteoroids, because Beech & Nikolova (2001) showed that cometary ejecta made of water ice can survive a number of perihelion passages, thus forming a population of water-ice candidate meteoroids. In particular, their Figure 2 shows that bodies of four-meter diameter ejected from P/55 Tempel-Tuttle will survive for three perihelion passages, whereas ten-meter bodies will survive ten passages. It is clear that comets shed material not always at perihelion: Comet C/1999 S4 LINEAR broke up into remnants with most of its mass distributed in

bodies between 1 millimeter and 50 meters in diameter (Farnham *et al.* 2001). The "normal" cometary material contains probably significant quantities of water ice (~39% by mass: Greenberg & Li 1999; ~31% by mass: Greenberg 2000), somewhat larger than the fraction of silicates, or of organic refractory matter that are each ~25% by mass. As the P/55 Tempel-Tuttle comet does not show silicate signatures in emission (Lynch *et al.* 2000), it is possible that its water content is even higher than that of the canonical cometary material. Moreover, as the 1999 storm was caused probably by ejecta produced during the 1899 perihelion passage, this implies that the cometary chunks had been in space for only three orbits before encountering the Earth, thus could have retained significant amounts of water ice. Therefore, one cannot reject immediately the possibility of a significant population of water-ice Leonids among the radar meteors. Obviously, a realistic composition of such a cometary chunk would consist of water-ice mixed with silicate and organic refractory compounds; such a complicated composition has not yet been calculated by us.

#### 4. WATER-ICE MINI-COMETES?

If we accept the possibility that some Leonid meteoroids may consist of water-ice, we should consider an observational analog reported in the literature. Louis Frank and collaborators (cf. Frank & Sigwarth 1999a) reported FUV observations of the dayglow obtained with imaging cameras on the *Dynamics Explorer* and *Polar* satellites. The observations, with different cameras and on different platforms, show ubiquitous transient dark spots over the illuminated side of the Earth. Frank *et al.* identified these dark spots as the signatures of mini-comets (~50-m diameter bodies) disrupted at high altitudes, which produce clouds of water and products of the photodissociation of water molecules (atomic oxygen absorbing at 130.4 nm: Frank & Sigwarth 1997a, and OH radicals emitting at 308.5 nm: Frank & Sigwarth 1997b). Recently, Frank & Sigwarth (2001) claimed direct optical imaging evidence for the existence of the mini-comets. The physical properties of the mini-comets, as compiled from the various Frank *et al.* papers, indicate that these should contain  $10^7$ – $10^8$  gr of water and should arrive at Earth at a rate of a few to a few tens per minute. Their interaction with the terrestrial neighborhood causes them to evaporate into large, 50 km water clouds above 600 km. These clouds should then obscure the oxygen airglow signal.

Knowles *et al.* (1999) used the Naval Space Surveillance Radar (NAVSPASUR) to attempt direct detection of the mini-comet phenomenon proposed by Frank *et al.* Knowles *et al.* reported negative results from their observations, although according to theoretical calculations their system should have been able to detect the mini-comets. Frank & Sigwarth (1999b) contested this non-detection and claimed

that the theoretical detection limits have been set by assuming similar amounts of dust in the mini-comets as measured for large comets.

In general, most Frank *et al.* papers on the subject of the mini-comets have been followed by various refutation comments from the scientific community, and by counter-arguments from the original authors. Dressler (1991) published a summary and discussion of the mini-comet proposition. He pointed out the many difficulties to accept this hypothesis and expressed his opinion that the apparent detections by the *Dynamics Explorer* satellite were essentially instrumental artifacts. Note also that Dressler's paper was published before the claims of Frank & Sigwarth (1999a) of similar detections by the *Polar* satellite.

Irrespective of whether 100-ton water-ice mini-comets bombard the Earth at a rate of a few every minute, the arguments presented here in favor of ice chunks from P55/Temple-Tuttle being part of the Leonid meteoroid stream should still be valid. The various constraints developed during the "Great Mini-Comet Debate" may be useful in characterizing the H<sub>2</sub>O-ice Leonid meteoroids.

##### 4.1. Observational tests

If there are indeed water-ice meteoroids, and if these are specifically ejected from comet P55/Temple-Tuttle, then observations during the coming showers in 2001 and 2002, when high ZHR values are predicted, could concentrate on the detection of water and of water dissociation products at high altitudes. It may be possible to specifically target the *Polar* spacecraft to observe the dayglow immediately after the peak activity of the Leonids. The observations should be similar to those performed by Frank & Sigwarth (1997a, b), *i.e.*, searches for suitable signatures of atomic oxygen and OH radical. Note that ground-based attempts to measure the 308.5 nm OH emission from meteors have, at best, been ambiguous (e.g., Harvey 1977). Yet, the only ground-based ultraviolet observation of a Leonid meteor (Almozno & Topaz 2000) was performed in a spectral region where emission from the resonance transition of OH is expected. Also, the near-infrared observations performed from the FISTA aircraft by Kristl *et al.* (2000) detected "a small but significant enhancement in the OH airglow emission during the peak of the [Leonid] storm". These findings support the possibility of water-ice Leonid meteoroids and argue for targeted observations during the 2001 and 2002 Leonid showers.

A prediction from this scenario is that Leonid storms produced by ejecta from earlier perihelion passages, such as the predicted peak of 18 Nov. 2001 at 10:07UT (seven revolutions), will be poorer in high-altitude meteors relative to the peak of 18 Nov. 2001 at 18:19UT (four revolutions), because of the depletion of water-ice meteoroids from the Leonid stream (cf. the calculations of Beech & Nikolova 2001).

Also, dust-poor comets with high velocities relative to Earth (in retrograde orbits) are predicted to produce high-altitude meteors by sputtering their H<sub>2</sub>O-ice meteoroids. The release of H<sub>2</sub>O molecules in the F-region of the ionosphere, as this scenario predicts, could cause plasma depletion at the deposition sites. This phenomenon was demonstrated experimentally by Mendillo *et al.* (1990) but was not specifically sought in conjunction with the Leonid storms. One possible way to test this would be to search for short-duration changes in the signal strength from the GPS satellites, which should be correlated with the local ZHR of the icy meteoroids.

## 5. CONCLUSIONS

We presented here results of meteor observations by phased-array L-band (~1 GHz) radar systems during the Leonid showers of 1998 and 1999. Our observations show the existence of two populations of radar meteors. One population, labeled here First Class, produces radar echoes at altitudes below ~200 km (mainly at 120 km). The second population appears above this altitude, peaks at ~240 km, and is labeled Second Class. This second population may be similar to that detected among TV meteors by Spurny *et al.* (2000a); there the high-altitude meteors were found to be the most fragile and weak, from a density-derivation point of view. Spurny *et al.* (2000b) also identified a different optical behavior of the high-altitude meteors with respect to those at classical altitudes: the high-altitude ones produced diffuse halos and jets above ~130 km but behaved "normally" below this altitude.

We developed a code to compute the heating, ablation and sputtering of a meteoric body as it passes through the atmosphere. The code uses simple but realistic approximations to calculate the drag forces acting on the body and the subsequent trajectory of the meteoroid. The code has the important advantage that it requires only a short computation time on widely available PC platforms, thus it can be easily used to explore a broad parameter space. By comparing the results computed for different initial conditions of composition, size, structure, and angle of incidence, with radar observations of meteoroids presented here, we were able to identify sets of parameters that best fit the observational data. These will provide important clues to the structure and composition of meteoroidic bodies.

Comparison of the theoretical results with radar data collected on Leonid meteors shows that significant sputtering takes place at high altitudes (>250 km). The sputtering is the result of high-velocity collisions of the meteoroid surface with ions in the upper atmosphere, and is facilitated by the high entry velocity of the Leonid meteoroids and by the relatively high sputtering yield of water ice. The disintegration of meteoroids at high altitudes should deposit there significant quantities of meteoric material; satellites in very low Earth orbit, such as CHAMP, may be

able to detect these enhancements. It is likely that most meteor showers, which have a much lower entry velocity, will not show a major high-altitude component of meteoroids. Particles sputtered off the meteoroid thermalize to a velocity of ~5 km/sec through multiple collisions with the ionospheric plasma.

We do not yet have direct evidence for the composition of the high-altitude radar meteors. However, we point out the related long survival of water-bearing cometary chunks calculated by Beech & Nikolova (2001). The accepted explanation for the Leonid storms is that the meteoroids are ejected from the comet during brief intervals at perihelion passage. It is logical to assume that water-ice meteoroids form part of the shower material.

As the yield of sputtered molecules from water ice is high for the case of Leonids, because of the high relative velocity, it is likely that the phenomenon observed by us for the case of radar meteors, and by Spurny *et al.* (2000a, b) in the optical, is due to the disruption of water-ice meteoroids. This should produce some observable signatures, searched for and found in the case of the mini-comets of Frank and collaborators in the form of atomic oxygen and OH radicals. Further observations along these lines are, therefore, in order. A few predictions originating from this scenario have also been presented.

## ACKNOWLEDGMENTS

We are grateful for the financial support of the Israel Science Foundation to study meteors from Israel, and for the support of ELTA, Ltd., to use their radar systems and analyze the results. The help of the Israel Space Agency in organizing the 1999 Leonid campaign together with NASA and the US Air Force is appreciated.

## REFERENCES

- Almoznino, E. & Topaz, J.M. 2000, *Leonid Storm Research* (P. Jenniskens, F. Rietmeijer, N. Brosch & M. Fonda, eds.), Dordrecht: Kluwer Academic Publishers, p.391
- Arlt, R., Rubio, L.B., Brown, P. & Gyssens, M. 1999, WGN (Journal of IMO), 27:6, 286
- Beech, M. & Nikolova, S. 2001, P&SS, 49, 23
- Boyd, I.D. 2000, *Leonid Storm Research* op. cit., p.93
- Bronshten, V.A. 1983, *Physics of Meteoric Phenomena*. Dordrecht: Reidel
- Brown, P., Campbell, M.D., et al., 2000, *Leonid Storm Research* op. cit., p.167
- Close, S., Hunt, S.M., Minardi, M.J. & McKeen, F.M., 2000, Lincoln Lab. J., 12, 33
- de Ligne, M.C., Langbroek, M., Betlem, H. & Spurny, P. 2000, *Leonid Storm Research*, op. cit., p.295
- Dressler, A.J. 1991, RevGeo, 29, 355

- Farnham, T.L., Schleicher, D. G., Woodney, L.M., Birch, P.V., Eberhardy, C.A. & Levy, L. 2001, *Science*, 292, 1348
- Frank, L.A. & Sigwarth, J.B., 1997a, *GRL*, 24, 2431
- Frank, L.A. & Sigwarth, J.B., 1997b, *GRL*, 24, 2435
- Frank, L.A. & Sigwarth, J.B., 1999a, *JGR* 104, 115
- Frank, L.A. & Sigwarth, J.B., 1999b, *JGR* 104, 22605
- Frank, L.A. & Sigwarth, J.B., 2001, *JGR* 106, 3665
- Greenberg, J. Mayo 2000, *Leonid Storm Research* op. cit., p.313
- Greenberg, J. Mayo & Li, A. 1999, *Sp.Sci.Rev.*, 90, 149
- Harvey, G.A. 1977, *ApJ*, 217, 688
- Jackson, P.A. 1992, in *Orbital debris: Technical issues and future directions* (A. Potter, ed.), NASA Conference Publication 10077, p. 218
- Janches, D., Mathews, J.D., Meisel, D.D. & Zhou, Q.-H., 2000, *Icarus*, 145, 53
- Johnson, R.E. 1998, in *Solar System Ices*, (B. Schmitt and C. deBergh, eds.), Dordrecht: Kuwer, p.303
- Jones, W. 1995, *MNRAS*, 275, 812
- Jurac, S., Johnson, R.E. & Donn, B. 1998, *ApJ*, 503, 247
- Jurac, S., Johnson, R.E., Richardson, J.D. & Paranicas, C. 2001, *Planetary and Space Sciences* 49, 319
- Knowles, S., Meier, R.R., Gustafson, B.A.S. & Giovane, F.J., 1999, *JGR* 104, 12637
- Kristl, J., Esplin, M., Hudson, T. & Taylor, M. 2000, *Leonid Storm Research* op. cit., p.525
- Leblanc, F. & Johnson, R. E. 2001, *Planetary and Space Sciences* 49, 645
- Lynch, D.K., Russell, R.W. & Sitko, M.L. 2000, *Icarus*, 144, 187
- May, P.W., Pineau des Forets, G., Flower, D.R., Field, D., Allan, N.L. & Purton, J.A. 2000, *Mon. Not. R. Astron. Soc.* 318, 809
- Mathews, J.D., Meisel, D.D., Hunter, K.P., Getman, V.S. & Zhou, Q. 1997 *Icarus*, 126, 157
- Mendillo, M., Sigwarth, J.B., Craven, J.D., Frank, L.A., Holt, J. & Tetenbaum, D. 1990, *AdSpRes*, 10, 83
- Öpik, E.J. 1958, *Physics of meteor flight in the atmosphere*, New York: Interscience
- Pellinen-Wannberg, A. 2001, private communication to NB
- Pellinen-Wannberg, A., Westnam, A., Wannberg, G. & Kaila, K. 1998, *Ann. Geophys.*, 116, 1475
- Pellinen-Wannberg, A. & Wannberg, G. 1994, *JGR*, 99, 11,379-11,390, 1994
- Podolak, M., Pollack, J.B. & Reynolds, R.H. 1988, *Icarus*, 73, 163
- Porubčan, V. & Getman, V.S. 1992, *Contrib. Astron. Obs. Skalnaté Pleso*, 22, 33-39, 1992.
- Price, C. & Blum, M. 2000, *Leonid Storm Research* op. cit., p.545
- Schijvarg, S., Podolak, M., Rosenkrantz, M.R. & Brosch, N. 2001, in preparation
- Smith A. & Jones B., 1996, *A&A* 555, 999
- Spurny, P., Betlem, H., van't Leven, J. & Jenniskens, P. 2000a, *M&PS*, 35, 243
- Spurny, P., Betlem, H., Jobse, K., Kolen, P. & van't Leven, J. 2000b, *M&PS*, 35, 1109

# THE ACTIVITY PROFILE OF COMET 55P/TEMPEL-TUTTLE IN 1998 RETURN: METEOROID RELEASE CONCENTRATION ON THE PERIHELION

Jun-ichi Watanabe<sup>1</sup>, Hideo Fukushima<sup>1</sup>, and Takashi Nakamura<sup>2</sup>

<sup>1</sup>National Astronomical Observatory of Japan, Mitaka, TOKYO 181-8588

<sup>2</sup>The University of Electro-Communications, Chofu, TOKYO 182-8585

## ABSTRACT

It is important to know the activity profile of the parent comets of meteor showers. The activity of the parent comet of the Leonids, 55P/Tempel-Tuttle had never been followed until the recent return in 1998 mainly due to the poor observational condition of the comet relative to the Earth. We carried out a CCD imaging monitor of this comet from January through February in 1998 by using 50-cm telescope of National Astronomical Observatory, Japan. The circular shape of the coma was not changed during this period for the pre-perihelion phase. This indicated that the dust production rate was not so high, which was also confirmed as a high value of the gas to dust ratio obtained by spectroscopic observations. The photometric measurements of the coma indicated high dependency of the activity on the heliocentric distance, of which the photometric index  $n$  is derived as about 10. These facts suggest that the ejection of the Leonids' meteoroids strongly concentrated at around the perihelion passage.

Key words: Comets; Comet: Individual-55P/Tempel-Tuttle; Solar System.

## 1. INTRODUCTION

Comet 55P/Tempel-Tuttle is the famous as the parent of the Leonid meteor storm. This comet was discovered by Tempel in 1865, and independently by Tuttle in 1866. The initial orbit of this comet was determined by Oppolzer(1867) as that the orbital period is about 33 years along with the retrograde orbit of the inclination of about 162 deg. By considering the similarity of this orbit, he suggested the strong relationship to the Leonid meteor shower. This was also indicated independently by Schiaparelli(1867) and by Peters(1867). After this discovery, this comet could not be recovered for about hundred years, although the Leonids displayed some activity either the large or small scale. In 1965, Schubart et al.(1965) came to success in recovering this comet,

based on their original estimates of the position calculated by Schubart, at the Boyden Observatory, South Africa. However, due to the poor observational condition, they could take only several photographs of this comet. In the return of this comet in 1965, there was no other successful observation in the world. Therefore, there has been no idea on the physical characteristics of Comet 55P/Tempel-Tuttle, in spite of its importance as the parent of the Leonids.

The next return, in 1998, was actually the first chance for us to explore the physical properties of this comet by using modern observational method. We carried out sequential monitor of this comet by using a CCD camera attached to the 50-cm telescope. The main purpose of this observation is to derive the heliocentric dependence of the brightness variation, which is one of the basic parameters indicating activity of comets. Especially in case of Comet 55P/Tempel-Tuttle, this parameter is important when we consider the formation and evolution of the Leonid meteor stream, because the evolution of the flux tube of the meteor stream strongly depends on how the parent comet ejects meteoroids in the orbit.

## 2. OBSERVATIONS

The imaging monitor was carried out from January 13 through February 23, 1998. A CCD camera (CV-16, MUTOH Co.) was attached to the cassegrain focus of the 50-cm telescope (f/12) at Mitaka campus of National Astronomical Observatory of Japan, located near Tokyo, Japan (35.66°N, 139.55°E, H=59m). In order to keep wide field of view for expected large coma due to the small geocentric distance, we used a focal reducer, which made it to 3.65m(f/7.3). The CCD is 1536 x 1024(Kodak type KAF-1600), which was binned to 768 x 512 size data. Each pixel is  $9\mu\text{m} \times 9\mu\text{m}$ , which corresponds to  $1.017 \times 1.017 \text{ arcsec}^2$ . This system gives a field of view of  $13.0 \times 8.7 \text{ arcmin}^2$ . In order to reduce the background sky level from the severe light pollution, and to study dust activity of the coma, a R-

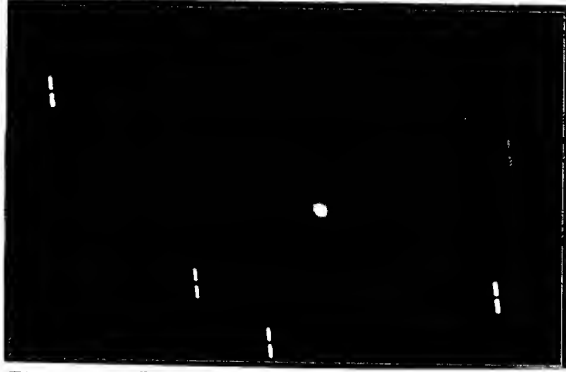


Figure 1. R-band image of Comet 55P/Tempel-Tuttle taken on February 17. The field of view is  $12.9 \times 8.0$  arcmin<sup>2</sup>. The north is top, and west is right.

band filter (R-60, Hoya Co.) was applied along with the infrared cut filter (HA-30 Hoya) for realizing the R-band. The telescope was tracked automatically by following the apparent motion of the comet. Although the image of the comet is mostly stationary, the several stars passed closely to the cometary coma in certain images. We performed the imaging observation on 22 nights from January 13 through February 23, before the perihelion passage. The reduction was made by using the NOAO IRAF. The standard bias subtraction and flat-field correction were applied by using appropriate data for calibration. Figure 1 shows an example of the image of Comet 55P/Tempel-Tuttle taken on February 17.

### 3. HELIOCENTRIC DEPENDENCE OF THE ACTIVITY

Although we performed the imaging observation on 22 nights, only data of 8 nights could be used for this analysis mainly due to the favorite condition without cloud, and to the high-quality data of the standard star. Table 1 shows the journal of the observations in this study. For photometric purpose, we tried to take several images of the same standard star (BSC146) except February 23 when we applied the standard star (BSC351).

The measurement of the brightness of comets is generally difficult due to the diffuseness of the coma, especially when the comet is close to the Earth. In order to compare the brightness precisely, the aperture applied for the photometry should be the same linear size around the nucleus. We applied three different aperture sizes as 8600km, 12900km, and 17200km. The largest diameter was chosen so that there was no severe contamination of the field stars into the aperture. However, the image taken on January 20, one bright star was located within the largest aperture. We removed the signal of this star by replacing the average signal value around it. The smallest aperture was selected at the half of the largest one, and we confirmed that it exceeds enough effective

Table 1. Journal of our imaging observation of Comet 55P/Tempel-Tuttle

Date (1998)	Time* (UT)	Heliocentric distance (A.U.)	Geocentric distance (A.U.)
Jan. 20	10 h 02 m	1.165433	0.369087
Jan. 25	10 h 33 m	1.124216	0.455999
Jan. 29	9 h 39 m	1.093978	0.560723
Jan. 31	10 h 27 m	1.079879	0.619105
Feb. 6	9 h 57 m	1.042148	0.805089
Feb. 9	10 h 36 m	1.026103	0.900344
Feb. 17	9 h 26 m	0.993695	1.150966
Feb. 23	9 h 51 m	0.980234	1.329687

Note \*:Time is the central time of the exposure frames composited.

Table 2. Result of our measurements

Date (1998)	Measured	Brightness (R-Mag.)	
Aperture	8600 km	12900 km	17200 km
Jan. 20	14.72	14.29	14.00
Jan. 25	14.63	14.18	13.87
Jan. 29	14.40	13.92	13.61
Jan. 31	14.33	13.79	13.48
Feb. 6	13.99	13.50	13.17
Feb. 9	13.82	13.31	12.96
Feb. 17	13.29	12.73	12.39
Feb. 23	13.14	12.56	12.21

seeing size of the stellar image when the comet was located at the farthest geocentric distance. The actual pixel size  $A$  of the aperture in each image is proportional to the inverse of the geocentric distance  $\Delta$  as  $A = 0.00425 \times a / (\pi \Delta)$ , where  $a$  is the corresponding linear size of the aperture in km. Comparing the signal integrated within the aperture to those of the standard star, we derived the R-band magnitude as shown in table 2.

The measured brightness for all the cases of three apertures increases with time, namely with approaching to the perihelion passage on February 28. Figure 2 shows the relation between the heliocentric distance and the measured brightness corrected by the geocentric distance. Error bar is the one-sigma derived from the statistical fluctuation of the measured signal, along with the consideration of the atmospheric absorption. The resultant error is 0.1 magnitude at most.

Generally the cometary brightness  $m$  is represented by

$$m = m_0 + 5(\log(\Delta)) + 2.5n(\log r), \quad (1)$$

where  $r$  is the heliocentric distance,  $m_0$  is the abso-

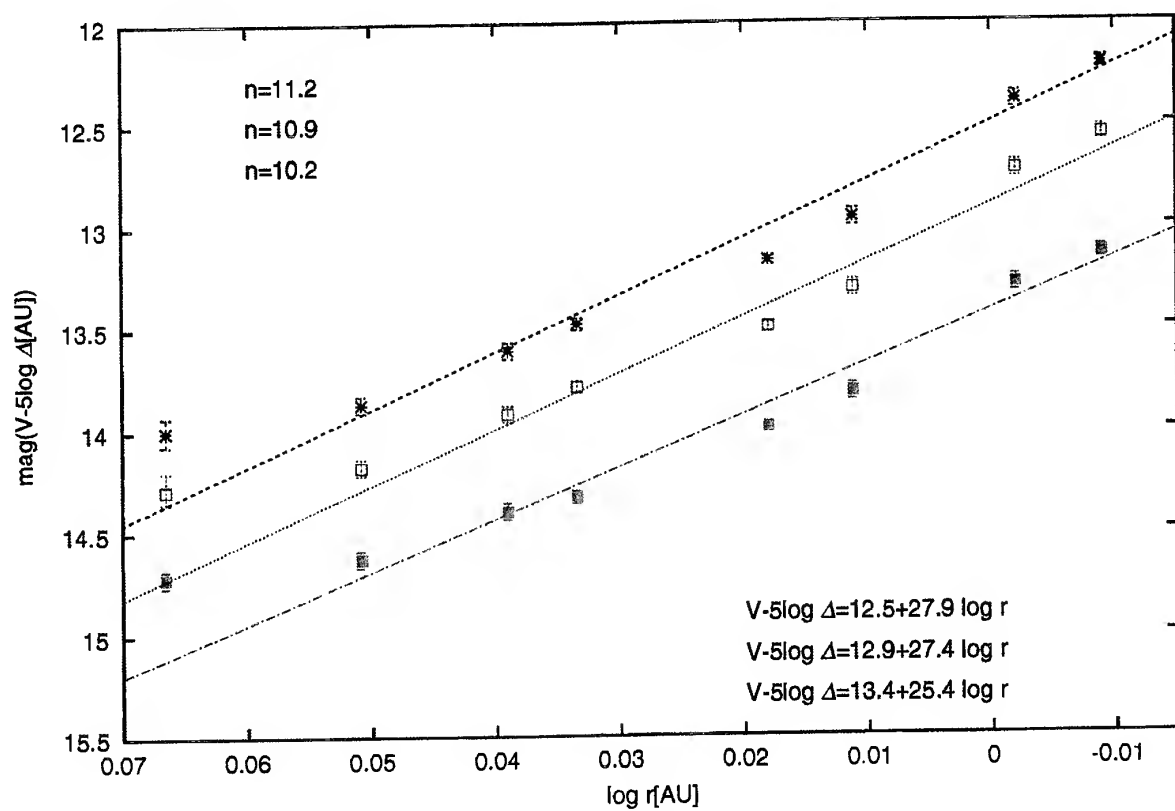


Figure 2. Time variation of the measured brightness, geocentric distance corrected, of comet 55P/Tempel-Tuttle for three different aperture sizes. The broken, dotted, and dashed lines correspond to regression lines of each aperture to the equation 1 (see text).

lute magnitude which the comet should be if it is located at  $r = \Delta = 1AU$ , and  $n$  is so-called photometric index which we are mainly focusing on. We fitted the obtained data for this equation, and derived the parameter  $n$  as 10.2, 10.9, and 11.2, respectively for corresponding three apertures. In order to compare our result to the other observations, we examined the total brightness of visual observations reported by amateur astronomers to the ICQ. Although the error bar is large, the regression of the averaged brightness is fitted to the equation having the index  $n$  of 10.6, which is consistent with our value.

#### 4. DISCUSSION

The derived parameter  $n$  of comet 55P/Tempel-Tuttle is larger than average value, which is believed to be about 4 in general. Kámel(1996) examined the photometric index of available short period comets, and obtained the mean value as 7.4. Moreover, it became 6.3 if the periodic comets of which period is between 20 and 200 years before the perihelion passage. It is true that this index tends to be larger with the shorter periods of comets. However, even among the comets having similar period the obtained index is definitely large, which suggests the rapid increase of the activity with approaching to the perihelion. Actually, Hainaut et al(1998) observed this comet at large heliocentric distance, and indicated that no cometary activity until June 1997, when the heliocentric distance was 3.5 A.U. The representative parent comet of Perseids, Comet 109P/Swift-Tuttle has smaller value as about 7.5(A. Nakamura priv. comm.). It should also be also noted that the observed period is confined as about one month. There may be a possibility of the outburst or extraordinary situation during this period for realizing large value of  $n$ , while no evidence was reported so far. The large  $n$  also means that the ejection rate of the meteoroids grow rapidly as the comet comes close to the Sun. This suggests that the meteoroids of the Leonids are mainly ejected from the parent comet at around the perihelion. At least for the pre-perihelion phase, the production of the meteoroids is thought to be concentrated around the perihelion. Basically the no regular activity of the Leonids is thought to be due to the younger generation as a meteor shower together with the perturbation of the Uranus(Williams 1997). However, the concentration of the meteoroids release at around the perihelion may be another one of the reasons for the short, narrow spatial distribution of the strong display of the Leonids meteor shower. Other observations, especially after the perihelion passage, should be important for future discussion.

Another important physical property is the gas to dust ratio. The spectroscopic observation, performed simultaneously by using 188-cm telescope at the Okayama Astrophysical Observatory, indicated the high ratio of the gas to dust. The obtained gas to dust ratio, defined as the water molecule produc-

tion to the continuum by  $\log[Q(H_2O)/Afr(625nm)]$ , was 26.8(T. Hamane priv. comm.). The dust-rich comets such as Comet P/Halley, it was 26.0–25.7, while 26.9 was obtained for a dust-poor comet, Comet Okazaki-Levy-Rudenko (Brooke et al. 1991). It is safely said that Comet 55P/Tempel-Tuttle belonged to the dust-poor comets. This result is qualitatively consistent with that of Hasegawa et al.(2000), who also found out no evidence of the dust rich properties from the millimeter continuum observations.

In order to clarify the formation and evolution of meteor streams, it should be important to study physical characteristics of parent comets such as heliocentric variation of the activity.

#### ACKNOWLEDGMENTS

We thank all the staff of the Public Information Office, National Astronomical Observatory of Japan, for their kind support of our observations. We also thank to Mrs. T. Nakamura, T. Sekiguchi, D. Kinoshita, and N. Yamamoto for their various support in the data analysis.

#### REFERENCES

- Brooke, T. Y., Tokunaga, A. T., Knacke, R. F., 1991, *Astron. J.*, **101**, 268.
- Hainaut, O. R., Meech, K. J., Boehnhardt, H., West, R. M., 1998, *Astron. Astrophys.*, **333**, 746.
- Hasegawa, H., Ukita, N., Matsuo, H., Kuno, N., Saitoh, T., Sekiguchi, T., Fuse, T., Nakamura, R., Yokogawa, S., 1999, *Astron. J.*, **119**, 417.
- Kámel, L., 1996, *Icarus*, **122**, 428.
- Kosugi, G., Ohtani, H., Sasaki, T., Koyano, H., Shimizu, Y., Yoshida, M., Sasaki, M., Aoki, K., Baba, A., 1995, *Pub. Astron. Soc. Pacific*, **107**, 474.
- von Oppolzer, T. 1867, *Astron. Nachr.*, **68**, 333
- Peters, C.F.W., 1867, *Astron. Nachr.*, **68**, 287
- Schiaparelli, G.V., 1867, *Astron. Nachr.*, **68**, 331
- Schubart, J., Bester, M. J., and Geyer, E., 1965, *IAU Circ. No.* 1926
- Williams, I.P. 1997, *Mon. Not. R. Astron. Soc.*, **292**, L37

# LARGE LEONID ENTRY MODELING: APPLICATION TO THE BOLIDE OF 11/17/1998

D. O. ReVelle

*Los Alamos National Laboratory, P.O. Box 1663, MS J577, Earth and Environmental Sciences Division,  
Atmospheric and Climate Sciences Group, Los Alamos, New Mexico 87545 USA  
Email: dor@vega.lanl.gov*

## ABSTRACT

In this paper we apply the theoretical entry model of ReVelle (2001c) to the large Leonid bolide of November 17, 1998. We modeled the entry both using hypersonic aerodynamics and compared the results to the infrasonic detection and interpretation of the event by ReVelle and Whitaker (1999).

## 1. INTRODUCTION AND OVERVIEW:

### 1.1 Low frequency acoustics and infrasonics and bolides as an infrasonic source

This section is a very brief overview of the field and characteristics of low frequency, sub-audible acoustics ( $\sim 0.01$  to  $10.0$  Hz), i.e., the field of infrasonics, in analogy to the infrared light regime for electromagnetic wave propagation. Further references and details are provided in ReVelle (1997). It is well known that explosive sources with progressively larger energies produce correspondingly lower frequency (longer period) signals at maximum amplitude. Such long-distance propagation can occur with very small dissipation effects: The propagation for larger sources or during inversion type conditions in the planetary boundary layer can also be influenced by the fundamental mode, i.e., the Lamb wave which propagates along the Earth's surface as an evanescent wave. Atmospheric propagation is also characterized by various forms of ducting including a tropospheric duct (Polar jet stream-associated and due to wind perturbations), a stratospheric duct (with-wind and against-wind along with effects due to wind perturbations) and finally a thermospheric duct. The refractive propagation is controlled by changes with height and range of the local adiabatic, thermodynamic sound speed

(due to the combined effects of air temperature and mean molecular weight) and of the horizontal winds. It is also due to the perturbations from ambient turbulence and from naturally occurring acoustic-gravity waves from a multitude of sources. The analyses of the wave propagation in the near-field can be done using ray theory type approaches, but for sufficiently great ranges, a normal mode (full-wave) type synthesis is needed, i.e. for  $R > 2H^2/\lambda$  ( $H$  = duct height,  $\lambda$  = wavelength). For example, at a frequency of  $0.1$  Hz signal for the stratospheric duct,  $R > \sim 1430$  km, which is the range beyond which geometrical acoustics ray tracing should be abandoned in favor of a full-wave approach.

Finally, waves are detected using multi-element arrays (using standard cross-correlation beam-forming) in order to determine the back-azimuth and elevation arrival angle (trace velocity of arrivals) of the assumed planar wavefronts.

### 1.2 Bolide aerodynamic characteristics

The entry of a sufficiently large Leonid bolide can be categorized as having a large Reynolds number (turbulent flow interaction), a large Mach number (hypersonic, compressible flow and strong shock waves and atmospheric as well as ablative products radiation) as well as a small Knudsen number,  $Kn$  (continuum flow regime). Thus, such meteoroids are expected to experience severe ablation and fragmentation effects (depending on their tensile and compressive strength) since the ablation interaction number is also large (ReVelle, 1979). For more details see Ceplecha et al. (1998) and ReVelle (2001c).

### 1.3 Line sources and modified line sources:

For small,  $Kn$ , the line source blast wave relaxation radius,  $R_0$ ,  $\sim$  Mach number  $\cdot$  diameter  $\geq 10$  m for ground based detection (ReVelle, 1976). Thus, the wavelength,  $\lambda \sim 2 \cdot 81 \cdot R_0$  and the frequency,  $f$ , of the wave sources at  $10 \cdot R_0$ , is  $= c_s / \lambda$ , where  $c_s$  is the local adiabatic thermodynamic sound speed. As the downward heading wave normals propagate a transition from weak shock propagation to linear acoustic propagation generally occurs at sufficient range (ReVelle, 1976, 1997). The wave normal paths are subject to refractive effects from the changes in the vertical and horizontal profiles of the time variable atmospheric temperature and winds (Snell's law of acoustics)

The waves are also subject to scattering and diffraction effects due to the presence of acoustic-gravity waves and turbulence aloft.

## 2. OBSERVATIONS OF THE NOVEMBER 17, 1998 LEONID BOLIDE:

### 2.1 Basic Infrasonic observations

$\Delta t = \{z_{\text{end}} / \cos(90-A)\} / \langle V_{\text{ph}} \rangle$  for a straight, unrefracted path

The time delay,  $\Delta t$ , is between the visual sighting or instrumental recording of the bolide and the arrival of the infrasonic signal. This was assumed to be a direct, non-ducted path from the source to the observer. In the above  $z_{\text{end}}$  is the end height and  $\langle V_{\text{ph}} \rangle$  is the height averaged phase speed, which includes the height averaged effects of sound speed and of the horizontal winds in the direction of travel of the wave. The angle  $A$  is the elevation arrival angle of the infrasound at the ground array. We now analyze the possibilities for  $\langle V_{\text{ph}} \rangle = 0.309$  km/s ( $\langle T \rangle = 238.5$  K) and  $A = 68.3^\circ$ . If signals were propagating against a uniform 30 m/s wind at all heights for this source height, we find that  $\Delta t = 347.2$  s = 5.78 minutes for  $z_{\text{end}} = 90$  km (with a  $\langle V_{\text{ph}} \rangle = 0.279$  km/s). The observed time delay:  $\sim 5$  minutes, 49 seconds (= 5.82 minutes) indicates a discrepancy of  $\sim -0.58\%$  (theory earlier than observed) If we assume instead that  $z_{\text{end}} = 85$  km,  $\Delta t = 327.9$  s = 5.46 minutes, which is about  $-6.1\%$  early. Both of these are clearly very acceptable time delays. The total distance to the bolide can range from 89.0-102.2 km for infrasonic source heights from 85-95 km.

### 2.2 Additional Infrasonic Observations

A brief summary of additional relevant infrasound parameters for this bolide is given in Table 1. below.

**Table 1. Infrasonic from the 11/17/1998 Leonid bolide (ReVelle and Whitaker, 1999)**

Deduced Parameters	IMS Prototype Array in Los Alamos, New Mexico
Arrival time of infrasonic signals	10:10:49 UTC
Total signal duration	$\sim 4$ seconds (for the strongest signals)
Bolide source azimuth	$353.6 \pm 0.4$ deg
Bolide source altitude	93.5 km
Total range to the bolide	97.9 km
Slant range signal velocity	0.27 km/s
Signal trace velocity	920 m/s
Signal elevation arrival angle	68.3 deg
Signal type	Direct path: Source to observer
Dominant frequency content at maximum signal amplitude	0.71 Hz: (1.4 seconds)
Maximum, cross-correlation coefficient (squared value)	0.92
Maximum signal/noise ratio	4
Maximum signal amplitude	2.1 microbars (0.21 Pa)

### 2.3 Ancillary observations

Ancillary observations have come from at least two ground-based video patrol camera detection's near Albuquerque as well as radiometer data at SNL (R.E. Spalding, Sandia National Laboratory, personal communication, 1998). Their corrected estimate of the bolides apparent stellar magnitude from radiometers is -14 (normalized to 100 km and corrected for range. The original uncorrected magnitude estimate is -12). In addition there were numerous visual reports and photographic records from this event as well. In Los Alamos there were sightings by Dr. T. Kunkle, EES-5 and Dr. S. Becker, X-TA, both of Los Alamos National Laboratory. They both independently witnessed the bolide and its persistent train, which could be visually followed for many minutes after the event. Their estimates of the bolide observations produced an estimate of -10 stellar magnitudes. Their independent time for the sighting was at 10:05 UTC at an estimated source location of 106.40 W, 36.05 N.

There was also ground-based, intensified all-sky camera coverage from Placitas, NM, 65 km to the south of Los Alamos by Dr. W.T. Armstrong, EES-8 of the Los Alamos National Laboratory. Using the data at Placitas and from the visual observations in Los Alamos an estimated height of the bolide from the two intersecting bearings yielded  $91 \pm 7$  km ( $\sim 84 - 98$  km). There were also independent observations taken at the USAF Starfire Optical Range. These yielded a horizontal entry angle of 42 degrees, a bolide heading of 302 degrees (from SE-NW) and an end height of 85 km. With the latitude and longitude of our IMS (International Monitoring System) infrasound array, Drummond independently calculated the azimuth and elevation angle of the arrival of the infrasound in Los Alamos from the Starfire data (personal communication, 2001). The results are virtually identical for each of these infrasonic parameters, which leaves absolutely no doubt about the reality of this infrasound detection even though it is from a type IIIA. or IIIB. body at an altitude of the mesopause. As shown below, the main reasons for our success infrasonically was the low wind-noise at the time of the event in combination with the very large and unusual initial size of this Leonid.

### 3. ENTRY MODELING OF LARGE LEONID BOLIDES

In a companion paper (ReVelle, 2001c), we have used simple ablation theory for either the case of constant  $\sigma$  or of a height variable  $\sigma$  over small altitude intervals to model this Leonid bolide. The constant  $\sigma$  solutions were done assuming source properties for bolide group IIIA. or for meteor group B. The height variable  $\sigma$  values were determined directly from theory allowing for both convective and radiative heat transfer, etc. For either constant shape or allowing for shape change, we used the  $\mu$  parameter over the respective ranges:  $\mu = 2/3$ ,  $0 \leq \mu < 2/3$  and  $\mu < 0$ . We also assumed either a uniform or a porous meteoroid model. This approach allowed us to calculate the expected entry dynamics and luminosity for the 11/17/1998 Leonid bolide over Los Alamos. We have also compared these entry modeling estimates against the observations from SNLA radiometers and from the USAF Starfire Optical Range as well as from observations from the Los Alamos infrasound array as discussed below.

### 4. MODELING APPLICATION: 11/17/1998 LEONID

The relevant combination of source parameters includes a bolide of either type B or IIIA/IIIB. as listed in Ceplecha et al. (1998) at a known Leonid entry velocity (geocentric) of 70.7 km/s. Recent data taken from the same Leonid storm, but in Mongolia by Spurny produced ablation coefficients intermediate between the statistical values for type IIIA and IIB bolides (Spurny, personal communication, 1999). We initially computed an end height for vertical entry (90 degrees) for a steady state, isothermal or non-isothermal, hydrostatic atmosphere model. Later the elevation of the radiant above the horizon for this Leonid was determined to be 42 degrees as noted above. For this change in entry angle all of the computed end heights move up uniformly about 2.8 km. This change brings the predicted entry dynamics results into even better agreement with the observations. As noted earlier, we tried to model this Leonid using a number of different approximations of the simple ablation theory, using either a single-body model approach or using the catastrophic fragmentation approach in ReVelle (2001d). We initially assumed a spherical shape in all cases. Shape change was initially not considered for a case with constant drag coefficient and ablation coefficient, etc. and  $\mu$  was set to  $2/3$  (self-similar ablation and deceleration solution in the single body approximation). We computed the Knudsen number at the end height (= local neutral gas mean free path divided by the radius of the body) We searched for cases with  $Kn < 0.10$  (continuum flow). We also computed the maximum stellar magnitude from Naumann and Clifton (1973) for a  $\tau_L \sim 0.10\%$  (differential luminous efficiency) which is valid for small bodies of chondritic origin while assuming a color index of 0. This should underestimate the brightness of large chondritic (uniform) bodies.

For the hydrostatic, steady state, isothermal atmosphere model, we used a height averaged temperature=238.5 K, pressure scale height = 7.006 km and height averaged sound speed = 0.3096 km/sec, surface pressure= $1.01325 \cdot 10^5$  Pa, surface, neutral gas mean free path =  $5.49 \cdot 10^{-8}$  m.

For the bolide, the key parameters assumed were the continuum flow drag coefficient = 0.92, an initial spherical shape factor = 1.208 (ReVelle, 1979). For the extremes of meteor group B to type IIIA or IIIB bolides, we used the following material parameter values.

**Meteor Group B:**

Bulk density =  $1000 \text{ kg/m}^3$ ,  $\sigma = 0.08 \text{ sec}^2/\text{km}^2$

**Bolide Type IIIA:**

Bulk density =  $750 \text{ kg/m}^3$ ,  $\sigma = 0.10 \text{ sec}^2/\text{km}^2$

For comparison, for type IIIB bolides, the bulk density =  $270 \text{ kg/m}^3$ ,  $\sigma = 0.21 \text{ sec}^2/\text{km}^2$ . Had these values been used in the entry dynamics calculations, we would have had even better agreement than is now predicted regardless of the specific method used. The results of our entry dynamics calculations are as follows (where all magnitude values have standardized to 100 km in the zenith):

**Meteor Group B Results:**

$R_\infty = 0.05 \text{ m}$  ( $M_\infty = 0.524 \text{ kg}$ )  
 $E_k = 0.313 \text{ t}$  (TNT equivalent) = source energy  
 Predicted end heights: 64.1–68.6 km  
 Knudsen number:  $2.1 \cdot 10^{-2}$  to  $3.0 \cdot 10^{-2}$   
 Maximum stellar magnitude: -11.8

$R_\infty = 0.1 \text{ m}$  ( $M_\infty = 4.19 \text{ kg}$ )  
 $E_k = 2.5 \text{ t}$  (TNT equivalent)  
 Predicted end heights: 59.2–63.7 km  
 Knudsen number:  $5.2 \cdot 10^{-3}$  to  $7.6 \cdot 10^{-3}$   
 Maximum stellar magnitude: -14.1

$R_\infty = 0.2 \text{ m}$  ( $M_\infty = 33.5 \text{ kg}$ )  
 $E_k = 20.0 \text{ t}$  (TNT equivalent)  
 Predicted end heights: 54.4–58.9 km  
 Knudsen number:  $1.3 \cdot 10^{-3}$  to  $1.9 \cdot 10^{-3}$   
 Maximum stellar magnitude: -16.4

**Bolide Type IIIA. Results:**

$R_\infty = 0.055 \text{ m}$  ( $M_\infty = 0.523 \text{ kg}$ )  
 $E_k = 0.312 \text{ t}$  (TNT equivalent)  
 Predicted end heights: 67.0–71.4 km  
 Knudsen number:  $2.9 \cdot 10^{-2}$  to  $4.2 \cdot 10^{-2}$   
 Maximum stellar magnitude: -11.8:

$R_\infty = 0.11 \text{ m}$  ( $M_\infty = 4.18 \text{ kg}$ )  
 $E_k = 2.5 \text{ t}$  (TNT equivalent)  
 Predicted end heights: 62.2–66.5 km  
 Knudsen number:  $7.2 \cdot 10^{-3}$  to  $1.05 \cdot 10^{-2}$   
 Maximum stellar magnitude: -14.1:

$R_\infty = 0.22 \text{ m}$  ( $M_\infty = 33.5 \text{ kg}$ )  
 $E_k = 19.98 \text{ t}$  (TNT equivalent)  
 Predicted end heights: 57.3–61.7 km  
 Knudsen number:  $1.8 \cdot 10^{-3}$  to  $2.6 \cdot 10^{-3}$   
 Maximum stellar magnitude: -16.4

A series of representative graphs of the results of these calculations are given below in Figures 1. to 4. for the velocity, Knudsen no., ablation coefficient and predicted mass loss, respectively for an initial sphere of radius = 0.10 m.

From our infrasonic analyses (ReVelle and Whitaker, 1999), we have also been able to deduce the source energy of this bolide using our observed infrasonic data totally independently of the entry dynamics modeling effort discussed above. This estimate was made using a line source model of the blast wave generated during entry and the subsequent production of infrasound that was detected at ground level by our prototype array. The model could be used to interpret the energy of this bolide using only the observed wave period at maximum amplitude of the infrasonic signal or in conjunction with the observed wave amplitude. Both approaches give different results, but both are fully consistent with the entry dynamics modeling done here.

Since the entry trajectory of this body is now known quite precisely (personal communication with R.E. Spalding, Sandia National Laboratory), our future plans include a line source ray tracing through an MSIS atmospheric temperature and wind profiles to determine the refractive paths for these unique signals.

**5. SUMMARY AND CONCLUSIONS**

The first infrasonic detection of a Leonid was made at Los Alamos on 11/18/1998 at ~10:10:49 UT during the Leonid meteor storm. Estimates of source energy are available from hypersonic aerodynamics (ReVelle, 1979, 1993, 1999) with stellar magnitudes having been estimated using a 0.1 % differential luminous efficiency, from SNL ground-based radiometers (R.E. Spalding), from a Los Alamos all-sky CCD camera system (W.T. Armstrong) and from visual observer estimates (T. Kunkle, S. Becker). Finally, we can also estimate the hydrodynamic source energy from independent infrasonic source estimates summarized in Ceplecha et al. (1998). All of the above methods are in reasonably good agreement with a predicted source energy of ~0.31–1.2 t (TNT equivalent). Finally, a cometary origin was definitely confirmed from our analyses of this Leonid, i.e., a very weak fragile material of low density and large ablation coefficient. Regarding the height regimes of the bolide interaction with the atmosphere, we find that the single-body estimates of end height are likely to be too low since fragmentation effects were initially

ignored. Using ReVelle's (1999-2001d) new theoretical approach we have also estimated fragmentation effects as a function of  $\mu$  for this bolide, which we will report on separately.

## 6. REFERENCES

- Ceplecha, Z., J. Borovicka, W. G. Elford, D.O. ReVelle, R.L. Hawkes, V. Porubcan and M. Simek, Meteor Phenomena and Bodies, Space Science Reviews, 84, 327-471, 1998.
- Naumann, R.J., and K.S. Clifton, Section 5., Mass Influx Obtained from Low-Light-Level Television and Observations of Faint Meteors, Evolutionary and Physical Properties of Meteoroids, NASA SP-319, eds. C.L. Hemenway, P.M. Millman and A.F. Cook, 45-52, 1973.
- ReVelle, D.O., On Meteor-Generated Infrasound, J. Geophysical Res., 81, 1217-1230, (1976)
- ReVelle, D.O., Historical Detection of Atmospheric Impacts by Large Bolides Using Acoustic-Gravity Waves, Near-Earth Objects, The United Nations International Conference eds. J. Remo, Annals of the New York Academy of Sciences, New York, New York, 822, 284-302, 1997.
- ReVelle, D.O. and R.W. Whitaker, Infrasonic Detection of a Leonid Bolide: 1998 November 17, Meteoritics and Planetary Science, 34, 995-1005, 1999.
- ReVelle, D.O., Theoretical Leonid Entry Modeling, Conference Proceedings, Meteoroids2001, Kiruna, Sweden, August 6-10, 2001, 2001c.
- ReVelle, D.O., Bolide Fragmentation Processes: Single-body Modeling versus the Catastrophic Fragmentation Limit, Conference Proceedings, Meteoroids2001, Kiruna, Sweden, August 6-10, 2001, 2001d.

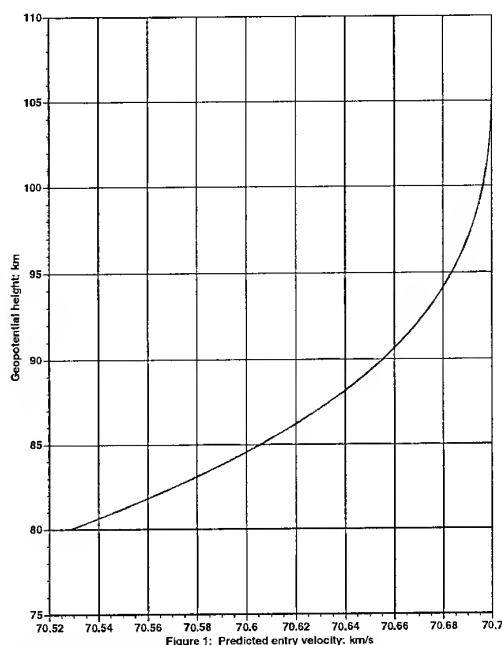


Figure 1. Velocity versus altitude.

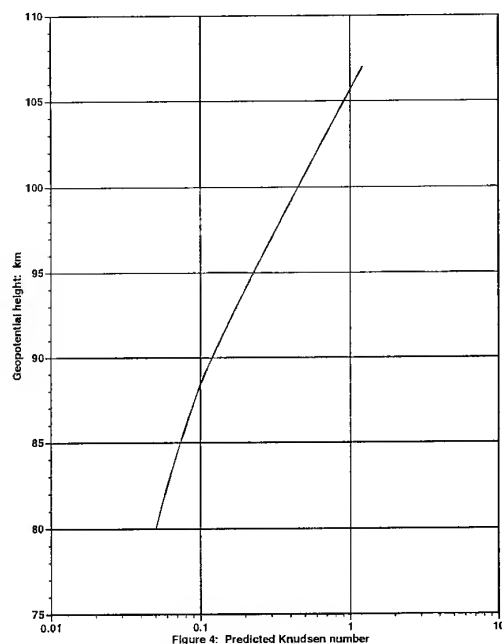


Figure 2. Knudsen number versus altitude.

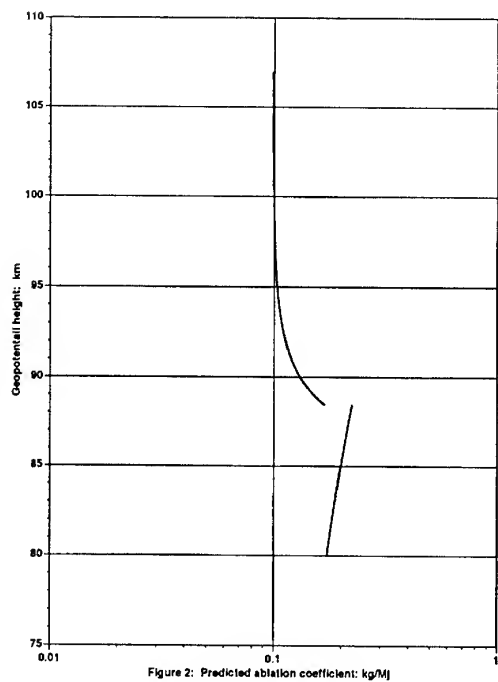


Figure 3. Ablation coefficient versus altitude.

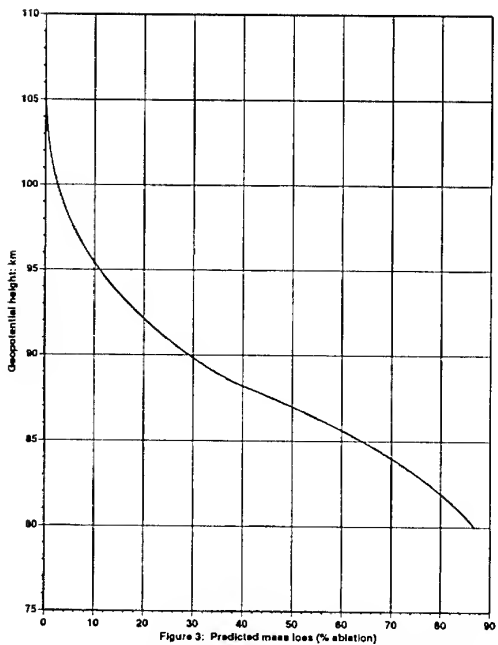


Figure 4. Predicted mass loss versus altitude.

## RADIOSEISMOLOGY AS A NEW METHOD OF INVESTIGATIONS OF METEOR STREAMS ON THE MOON AND PLANETS

Berezhnoi A.A.<sup>(1)</sup>, Bervalds E.<sup>(2)</sup>, Khavroshkin O.B.<sup>(3)</sup>, Ozolins G.<sup>(2)</sup>

(1) Sternberg Astronomical Institute, Universitetskij pr. 13, 119899 Moscow, Russia, Email: [ber@sai.msu.ru](mailto:ber@sai.msu.ru)

(2) Ventspils International Radio Astronomy Center, Akademijas laukums 1, LV-1050 Riga, Latvia,  
Email: [berv@latnet.lv](mailto:berv@latnet.lv)

(2) Ventspils International Radio Astronomy Center, Akademijas laukums 1, LV-1050 Riga, Latvia,  
Email: [ozo@acad.latnet.lv](mailto:ozo@acad.latnet.lv)

(3) Institute of Earth Physics, B. Gruzinskaya 10, 123810 Moscow, Russia, Email: [khavole@uipe-ras.scgis.ru](mailto:khavole@uipe-ras.scgis.ru)

### 1. ABSTRACT

Radioseismology is based on registration and interpretation of radio emission of seismic origin. Such radioseismic processes occur on the Moon, planets, and asteroids. Non-thermal radio emission of the Moon caused by rock fracturing, seismic activity, and thermal cracking of the regolith was detected during observations of the Moon at the 64 m Kaliazin radio telescope at 13 and 21 cm on July 30 – August 2, 1999. We observed the Moon with the 32 m Ventspils antenna at 25 mm on November 16 - 18, 2000. During the morning of November 17 we registered significant quasiperiodic oscillations of the lunar radio emission starting near 1:44 UT and continuing until the end of observations at 7:17 UT. Oscillations were also registered on November 18 starting near 2:28 UT. Intensive oscillations were registered until about 7:00 UT with bottom to peak heights of 5-10 K. The time of maxima of oscillations does not contradict theoretical predictions about the existence of three maxima of the Leonid meteor shower on the Moon. Amplitudes of oscillations were equal to 1-2 K before and after the time of Leonid's maxima. These results can be explained as the detection of lunar radio emission of seismic origin caused by meteoroid impacts. The implications of the radioseismic method for determination of the intensity of meteor showers on the Moon and planets and the internal structure of the Moon are described.

### 2. INTRODUCTION

There are some sources of radio emission on the Moon: the thermal radiation, reflected from the Moon solar radiation and radiation of our Galaxy, and the radio emission of seismic origin. The main component of the lunar radio emission is the thermal radiation. Investigations of the lunar thermal radio emission can estimate density and electric properties of the lunar regolith, temperature regime and thermal gradient of surface layers (see for example [1]). Reflected solar and

galactic radiation are essential only for observations of the Moon at  $\lambda > 50$  cm. However during intensive solar flares it is possible to detect additional lunar radio emission caused by such flares at  $\lambda > 5$  cm.

Radioseismology is based on registration and interpretation of electromagnetic radiation of seismic origin. The frequency of such radiation before earthquakes [2] and during the rock fracture experiments [3] lies in the range from the frequency of kHz radio to the frequency of optical and soft X-ray radiation. There are not articles about the detection of radio emission during rock fracture at 100 MHz -  $10^{14}$  Hz. The probable three models of transformation of mechanical stress into electromagnetic radiation are: 1) the formation of new microcracks; 2) charges arising at the peaks of existing cracks forming under the action of increasing load; 3) the piezoeffect. Radio emission associated with quartz-bearing rock fracture was detected at 1-2 MHz [4]. The nature of such electromagnetic emission has not been investigated very well. Such radioseismic processes occur on the Moon and airless planets and asteroids. Non-thermal radio emission of the Moon ( $\nu = 1 - 5$  kHz) caused by rock fracturing, seismic activity, and thermal cracking during lunar transient phenomena is discussed in [5]. The possibility of the detection of collisions of cosmic rays with energies from  $10^{20}$  to  $10^{23}$  eV with the Moon during lunar radio observations at  $\lambda = 1 - 100$  m was discussed in [6].

### 3. LUNAR OBSERVATIONS AFTER THE LUNAR PROSPECTOR IMPACT AT 13 AND 21 CM

The collision between the American spacecraft Lunar Prospector and the Moon was at 9:52 UT on July 31, 1999. Due to singularities of the lunar lithosphere the duration of seismic effect accompanied this collision may be equal to some hours. Lunar non-thermal radio emission was detected during observations of the Moon at the 64-m Kaliazin radio telescope at 13 and 21 cm on July 30 - August 2, 1999 [7].

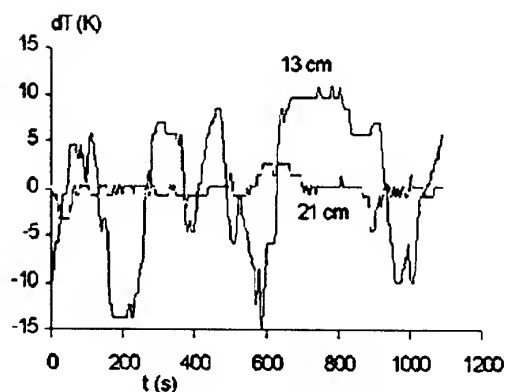


Fig. 1. Variations of the radio flux (in K) of a seismically active region of the Moon (30W, 5S) at 13 and 21 cm versus time. Starting point is July 31, 1999; 22:38 UT.

The mean amplitude of variations of the lunar radio flux at 13 cm was 4, 8, 10, 3 K (and at 13 cm - 2, 2, 4, 3 K) on July 29/30, July 30/31, July 31/August 1, August 1/2 respectively. The correlation between variations of the total lunar radio flux at 13 and 21 cm was detected also [8]. The correlation coefficient was equal to 0.5. This fact can be explained as a similar nature of the non-thermal radio emission at both frequencies. Oscillations with periods of about 20 s and 1 - 11 minutes were registered during observations of the Moon at 13 and 21 cm (see fig. 1).

Short periods (60 s or less) can be caused by the atmospheric turbulence. Namely periods at 13 cm were equal to 1.5, 1.5, 1.7, 2.8, 3.1, 3.5, 4.2, 6.7, 8.5, and 11.7 minutes. Periods at 21 cm were equal to 1.5, 2.8, and 6.8 minutes. Such periods are close to theoretical predictions of periods of free oscillations of the Moon [9]. Meteorite bombardment and moonquakes excite oscillations of the Moon, which lead to generation of radioseismic emission. Accurate determination of periods of free oscillations of the Moon can increase our knowledge about the internal structure of the Moon.

Let us compare the kinetic energy of the Lunar Prospector impact ( $M \sim 200$  kg,  $V \sim 1.7$  km/s,  $E \sim 3 \cdot 10^8$  J) and meteorite bombardment. The current estimation of the micrometeorite flux into Earth and the Moon is  $10^{-7}$  kg/year $\cdot$ m $^2$  [10]. So the micrometeorite flux into the Moon is about  $5 \cdot 10^3$  kg per day. At the mean speed of micrometeorites of about 20 km/s the power of micrometeorite bombardment of the Moon is about  $10^7$  Wt. Comparing the kinetic energy of the Lunar Prospector impact with the intensity of micrometeorite bombardment of the Moon we can conclude that the Lunar Prospector impact can not explain increasing of the non-thermal lunar radio emission at 13 cm on July 31, 1999.

#### 4. THE MOON AT 25 MM DURING THE LEONID 2000 METEOR SHOWER

For determination of dependence of the intensity of the non-thermal lunar radio emission from micrometeorite bombardment we conducted observations of the Moon during the Leonid 2000 meteor shower. The Leonid meteor stream was the strongest meteor stream crossing the Earth orbit in 1999 and 2000. Optical flashes on the dark side of the Moon caused by Leonid meteoroid impacts were detected on November 1999 [11]. We observed the Moon on November 16 - 18 with the 32 m antenna of the Ventspils International Radio Astronomy Center at  $\lambda = 25$  mm [12]. The half-power beam width was 3.5 arcminutes. The bandwidth was 44 MHz, and the output time constant was 1 s. We could not exactly track the antenna with the velocity of the Moon, and the observable region lagged behind and during 30 minutes of observation cycle the beam draw a 15 arcminutes long trip on the lunar surface in direction to Mare Serenitatis. Then the next half - hour scanning repeated starting from a seismic active lunar region (30W, 5S).

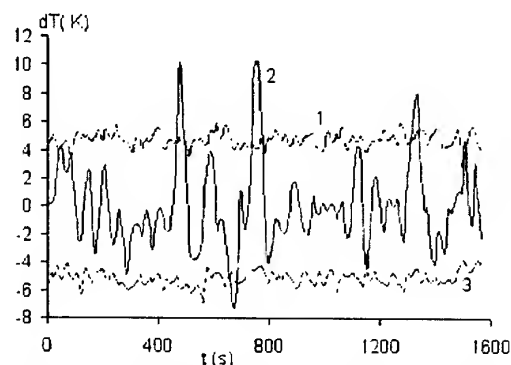


Fig. 2. Variations of the lunar radio flux (in K) at 25 mm during the Leonid 2000 meteor shower versus time. Starting points are Nov. 17, 22:17 UT (curve 1), Nov. 18, 4:31 UT (curve 2), Nov. 18, 7:32 UT (curve 3).

During the morning of November 17 we registered significant quasiperiodic oscillations of the lunar radio emission starting near 1:44 UT and continuing until the end of observations at 7:17 UT. There were at least two isolated events with amplitudes exceeding 10 K at 3:12 UT and 4:33 UT. The maximal amplitudes of observed variations were registered on November 18, 4-5 UT also (see fig. 2). Intensive oscillations were registered until about 7 UT with bottom to peak heights of some K, sometimes up to 10 K. The periods were equal to 1.8, 2.2, 3.0, 3.6, 4.4 minutes. Disagreement between values of periods at 25 mm and 13, 21 cm can be explained by different observational method of lunar radio observations (Kaliazin radio telescope can follow to the Moon, Ventspils radio telescope can not follow to the Moon). The time of maxima of oscillations does not

contradict to theoretical results about the existence at least first and third maxima from three predicted maxima of the Leonid shower on the Moon [13] (November 17, 4:58 UT (the predicted zenith rate ZHR is about 1000 per hour); November 18, 0:52 (ZHR ~ 10) and 5:01 UT (ZHR ~ 50)). Amplitudes of oscillations were equal to 1-2 K before and after the time of maxima of the Leonid meteor shower. The correlation between variations of the lunar radio flux from same lunar regions at different moments of observations is absent. It is an evidence of weak dependence of the intensity of non-thermal radio emission from the mineral composition of the lunar regolith.

We hope that our future observations of the Moon can solve the following unresolved problems: determination of the spectral index and the total power of the non-thermal radio emission, estimation of intensity of such emission as a function of mass and speed of impactors. What source (micrometeorite bombardment, moonquakes or thermal cracking) is the main source of the non-thermal emission at different wavelengths? For solving of these problems the organisation of continuum radio observations of the Moon at  $\lambda = 1 \text{ mm} - 1 \text{ m}$  is desirable.

## 5. CONCLUSIONS

Our results of observations of the Moon at 25 mm during the Leonid meteor shower can be explained as the detection of lunar radio emission of seismic origin caused by meteoroid impacts.

Oscillations of the lunar radio flux can be explained as a result of excitation of free oscillations of the Moon and the transformation of seismic energy to electromagnetic radiation.

Radio observations of the Moon can help us to determine the intensity of meteor showers on the Moon and the structure of meteoroid streams.

In the future the detection of radio emission of seismic origin from Earth-type planets is possible.

## 6. REFERENCES

1. Keihm S.J. Interpretation of the lunar microwave brightness temperature spectrum - Feasibility of orbital heat flow mapping, *Icarus*, V. 60, p. 568-589, 1984.
2. Gokhberg M.B., Morgunov V.A., Pokhotelov V.A. *Earthquake prediction. Seismoelectromagnetic phenomena*, Gordon and Breach Publishers, Amsterdam, 193 p., 1995.
3. Surkov V.V. *Electromagnetic phenomena during earthquakes and explosions*, MIPI Publishers, Moscow, 448 p., 2000 (in Russian).
4. Warwick J.W., Stoker C., Meyer T.R. Radio emission associated with rock fracture: possible application to the great Chilean earthquake on May 22, 1960, *J. Geophys. Res.*, V. 87, p. 2851-2859, 1982.
5. Zito R.R. A new mechanism for lunar transient phenomena, *Icarus*, V. 82, p. 419-422, 1989.
6. Golubnichij P.I., Filonenko A.D. Detection of super high energy cosmic rays using a lunar satellite, *Kosmichna nauka i tekhnologija*, V. 5, No. 4, p. 87-92, 1999 (in Russian).
7. Khavroshkin O. B., Tsyplakov V. V., Poperechenko B. A. et al. Modification of the Moon's Microwave Radiation by the Fall of Lunar Prospector, *Doklady Earth Sciences*, V. 376, No. 1, p. 90-92, 2001.
8. Berezhnoi A.A., Gusev S.G., Khavroshkin O.B. et al. Radio Emission of the Moon before and after the Lunar Prospector impact, *Proceedings of the Fourth International Conference on Exploration and Utilisation of the Moon*, p. 179-181, ESTEC, Noordwijk, The Netherlands, 10-14 July 2000.
9. Gudkova T.V., Zharkov V.N. The spectrum of torsional oscillations of the Moon, *Solar System Research*, V. 34, Is. 6, p. 460-468, 2000.
10. Love S.G., Brownlee D.E., A direct measurement of the terrestrial mass accretion rate of cosmic dust, *Science*, V. 262, No. 5113, p. 550-553, 1993.
11. Ortiz J.L., Sada P.V., Bellot Rubio L.R. et al., Optical detection of meteoroidal impacts on the Moon, *Nature*, V. 405, Is. 6789, p. 921-923, 2000.
12. Bervalds E., Ozolins G., Paupere M. et al. Observations of the lunar radio emission during the year 2000 Leonid meteor shower maximum, *VIRAC Scientific Preprint*, No. 1, 5 p., 2001.
13. McNaught R. H. Lunar Leonids: Encounters of the Moon with Leonid dust trails, October 2000 <http://www.spaceweather.com/meteoroutlook/lunarleonids.html>

## THE GLOBAL MONITOR OF METEOR STREAMS BY RADIO METEOR OBSERVATION ALL OVER THE WORLD

Hiroshi Ogawa<sup>(1)</sup>, Shinji Toyomasu<sup>(2)</sup>, Kouji Ohnishi<sup>(3)</sup>, Kimio Maegawa<sup>(4)</sup>

<sup>(1)</sup> University of Tsukuba, D-201 2-11-4 Amakubo, Tsukuba, Ibaraki, 305-0005, Japan, E-mail: HZH02257@nifty.ne.jp

<sup>(2)</sup> Misato Observatory, 180 Matsugamine, Misato, Kaiso, Wakayama 640-1366, Japan, E-mail:  
Toyomasu@obs.misato.wakayama.jp

<sup>(3)</sup> Nagano National College of Technology, 716 Tokuma, Nagano, Nagano, 381-8550, Japan, E-mail:  
ohnishi@ge.nagano-nct.ac.jp

<sup>(4)</sup> Fukui National College of Technology, Geshi, Sabae, Fukui, 916-8507, Japan, E-mail: kmaegawa@fukui-nct.ac.jp

### ABSTRACT

In recently, Radio Meteor Observation (RMO) has spread in Japan. Then, to grasp the whole aspect of meteor stream activity accurately, the necessity of unifying the observational data all over the world came out. Then, we tried to collect and integrate them. There are many observational sites in the world. The difference in geographical factor or the observational equipment has to be considered. However, information of them is not enough. Therefore, in this time, data were estimated by relative value. Data were divided by average counts previous two weeks. The Leonids 2000 RMO result at eight sites of the world was unified by this method, and three peaks appeared. This was similar to the result of Visual Observation. Also, the daily meteor activity was caught. Therefore, this meteor monitor was useful for all meteor activity. In this time, however, it was considered without using the radar equation etc. we could get similar result to Visual Observation. Therefore, the more exact result could be obtained if we consider of them.

### 1. INTRODUCTION

When the meteor appears, the density of electrons in atmosphere increase. Then, the radio wave of high frequency reflects. This observational method is Radio Meteor Observation. Radio Meteor Observation has an advantage in its stable data. In this method, however, only one observational site may lose the maximum by radiant elevation. For this reason, all activity of meteor stream may not be caught at only one site. In addition, observational configuration is different. Therefore, observed data all over the world need to be unified to catch all activity of meteor stream, to research the characteristics of outburst and the history of meteoroids and meteor streams.

Important problems of this observation are next two points. One is "Geographical condition". The relation of the transmitting and the receiving station is different for each pair. Another is "Observational equipments". This problem caused by performances of transmitter,

receiver, antenna, etc. To solve these problems, all observational data were unified under the same standard. Then the calculated result each site must be compared. In addition, we defined the background level and removed it from observational data, meteor stream activities finally appeared. Properly speaking, to consider characteristics of each site is the best way. Actually, however, information of observational site is not enough. Therefore, the radar equation cannot be applied. Then, in this time, meteor activities were estimated by relative value.

### 2. METHODS

The method of unification of the world data is not established now. Therefore, the unification plan was to unify under the same standard. This method was adapted the idea which was shown in the annual meeting of ASJ (Astronomical Society of Japan) in 2001 spring (H.Ogawa etc, 2001).

$$\frac{H - H_0}{D} \quad (2 \cdot 1)$$

"H" means the number of echoes for a certain 1 hour "H". "H<sub>0</sub>" is the average of "H" during 2 weeks before the day. "D" is the average of echoes for 1 day during 2 weeks before the day. The result of calculation means that how many times echoes are observed than average echoes during two weeks. Also, the sampling period for "D" is 2weeks. If it is 1 week, the average is influenced by daily radio condition. And if it is more than 3weeks, the average is influenced by long-term trend. Therefore, the sampling period is defined 2weeks.

In addition, by using histograms each observational site, define the background level. This time, the background level was assumed  $\pm 2\sigma$ . From this background level, detect unusual values and reduce unusual variations from sampling data. By removing unusual data, the overlook toward minus is reduced.

### 3. OBSERVATIONAL SITES

Stable sites that report observational data every day are needed because unstable sites cannot be defined the background level. In this time, five data in five countries were used. The figure 3.1 is the map of using data. And table 3.2 is the detail of observational system.



Figure 3.1 the map of using observational data

Country	Frequency	Latitude	Longitude	Observer
USA	88.7 MHz	33.43	-104.5	S. Nelson
UK	55.25MHz	50.47	-1.44	D. Swan
France	96.8 MHz	43.68	3.60	P. Terrier
Australia	88.3 MHz	-27.50	153.70	B. Young
Japan	53.75MHz	34.14	135.41	H. Ogawa

Table 3.2 the detail of using observational data  
( $\phi < 0$ : south latitude,  $\lambda < 0$ : west longitude)

### 4. RESULTS

The following figure 4.1 is the result of the calculation in January 2001. Around 3<sup>rd</sup> January, calculated results in USA, UK, France and Japan recorded unusual value.

This unusual result was the activity of Quadrantids. On the other hand, in Australia, this unusual value was not observed because Australia is located in the South Hemisphere. Therefore, the activity of Quadrantids was not seen. Also, unusual value was sometimes observed. However, most of these results are observed by only one site. Therefore, these result could not be decided whether these activities were the error of observation or something meteor streams. Following figures 4.2 and 4.3 are some histograms of each observational site.

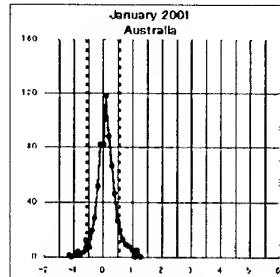


Figure 4.2 (Australia)

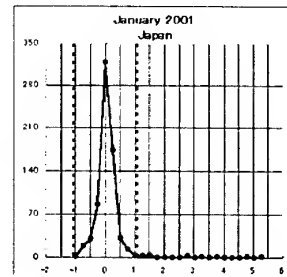


Figure 4.3 (Japan)

The horizontal axis is the calculated result. Dotted lines are  $\pm 2\sigma$  line. Beyond the limits of these lines are unusual values. Then, these data was reduced from the original sampling data. And within the limits of these lines are background levels. Sigma of each observational site was USA:0.50, UK:0.39, Australia:0.32, France:0.36 and Japan:0.51. In this time, the background level was defined  $\pm 2\sigma$ .

Also, especially, the figure 4.4 is the calculated result of one active period of meteor stream. This meteor streams is Leonids in 2000. Observational data are 10 in eight countries (UK, France, Spain, Belgium,

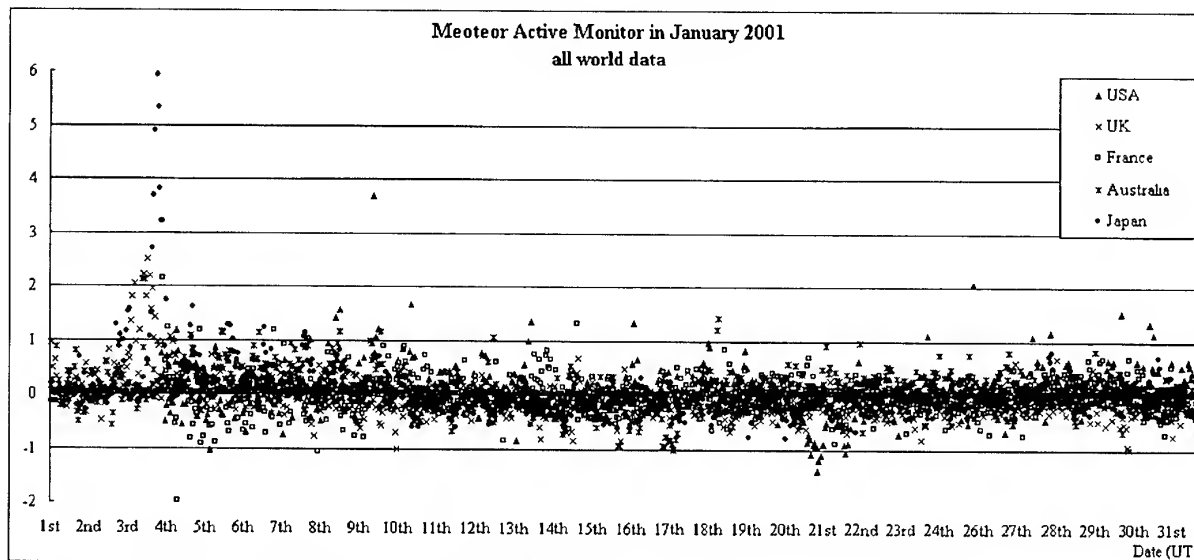


Figure 4.1 the result of calculation in January 2001

Australia, Taiwan, Netherlands and Japan). Three vertical lines are dust trails that were calculated by D. Asher. This result was similar to the result of Visual Observation and the forecast by D. Asher. But Leonids has the fastest incident speed in all meteor streams. In order to investigate the slower speed stream, the same analyses for Gemnids, 2000 was carried out. The activity caught by Radio Meteor Observation method indicates the similar curve of visual observation. Therefore, this method is useful for the activity monitor of all meteor streams.

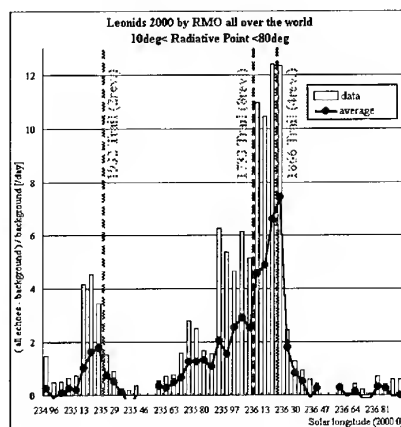


Figure 4.4 the results of Leonids 2000

## 5. CONCLUSIONS

By unifying all observational data all over the world, the active monitor of meteor streams were made. And to unify data all over the world has some clues to know whether the local appearance or the possibility of something as meteor stream. In addition, this monitor has the possibility of the discovery of new meteor streams. Especially, this monitor is useful for daylight meteor streams (for example, Arieids, omicron-Perseids, etc.). Also, Radio Meteor Observation is more stable than Visual Observation. Therefore, this monitor is the best method for catching all activity of meteor streams.

In this time, this result indicated similar to the result of Visual Observation without consideration of the radiant elevation, radar equation, etc. From this result, however, this monitor worked as "the daily meteor active monitor" enough.

## 6. FUTURE WORKS

In this time, calculated value under the same standard solved some problems of difference of observational site's condition. Therefore, the research of the better unifying method with the consideration of Geographical conditions and Observational equipments

is needed. In addition, the consideration of the radiant elevation, and the characteristic of meteor stream (for example, velocity, size, etc) are needed.

Also, to observe the long-term variation that is larger than a few hours or a few days, we have to extend the period of sampling time up to one year by stable observation.

Finally, to obtain the fine density distribution map of meteoroids, we need the fine observational network of this kind of activity monitor in the world.

## 7. REFERENCES

- [1] R.Arlt, M.Gyssens, "Result of the 2000 Leonids Meteor Shower", *WGN28:6*, 2000, pp195-208
- [2] Christian Steyaert, "Radio Meteor Observation Bulletin", No.88-94, 2000-2001
- [3] David J Asher, "Dust trail theory", 2000

## 8. ACKNOWLEDGEMENT

- [1] Kazuhiro Suzuki (Japan)
- [2] David J Asher (Armagh Observatory)
- [3] Peter Jenniskens (NASA)
- [4] Stan Nelson (USA, report on RMOB)
- [5] Dave Swan (UK, report on RMOB)
- [6] Pierre Terrier (France, report on RMOB)
- [7] Bruce Young (Australia, report on RMOB)
- [8] Sadao Okamoto (Japan, report on RMOB)
- [9] Christian Steyaert (RMOB)
- [10] Takuji Nakamura (Japan)

# Results of 1999 Leonids Daytime Observation in Japan

Hiroataka Serizawa (1), Masayuki Toda (1)

(1): Nippon Meteor Society

## ABSTRACT

The large appearance of Leonids was observed in Europe on November 18 in 1999 at the 2:00UT (11:00JST). Then, daytime-meteor was detected some observers in each place, and the number of 40 meteors were detected in 4 hours in Japan. Since globally daytime-meteor observation is rare most people would have doubt about the objectivity of data.

Therefore, I tried to identify with each Radio Meteor Observation, in order to acquire the objectivity of data. Consequently, four shooting stars were in accorded with the result of Radio Meteor Observation. Besides, two synchronous meteors were observed by two observers. Therefore, these meteors could be reliable.

However, there were few bright (shooting stars  $> -5$  magnitude) which could be observed in Europe in daytime at the same time. For that reason, the question arose in the luminous intensity of the meteor that we observed. As one of this cause, it can be considered that the meteor luminescence mechanisms differ daytime from night.

I would like to call more observers all over the world to carry on meteor observation from now on to collect the data about a daytime-meteor.

## Introduction

In 1999, Leonids showed big meteor shower in Europe. About 2hUT (11hJST) on 18<sup>th</sup> November, some daylight meteors observed by 8 meteor observers. It seems these meteors are Leonids.

Observer	Location	UT	18d00h	01h	02h	03h
		JST	18d09h	10h	11h	12h
Kazuhiro O	138d57'38.5"E .35d19'57.2"N		1			
Takashi S.	139d27'44"E .35d51'21"N		2			
Koi M.	131d23'41"E .31d50'58"N			5	9	
Rvosuke M.	138d26'24"E .35d54'56"N			1	2	
Masavuki O.	138d58'76"E .35d22'00"N			1	10	
Takema H.	138d58'76"E .35d22'00"N				9	1
Masayuki T.	138d58'76"E .35d22'00"N				3	2
Hiroataka S.	138d58'76"E .35d22'00"N				1	
Radiative Point Height(+138d58'76"E .+35d22'00"N) (deg)			45	32	20	8

## Details

The following table is the list of meteors in the same time of Radio Meteor Observation

JST	Visual	Radio Obs. Station	Details (S:second)
10h46m30s	Mivazaki	Komae, Tovokawa	Komae:10dB.1S. T:10dB.2.5S
10h56m25s	Ovama	Chigusa, Damine, Habikino	C:20dB.5S. D:20dB.2.5S. H:20dB.2.5S
10h58m12s	Mivazaki	Komae, Damine, Tovokawa, Habikino	K:20dB.1S. D:20dB.2.5S. T:10dB.2.5S. H:20dB.5S
11h02m16s	Miyazaki	Misato, Damine, Habikino	M:10dB.1S. D:20dB.2.5S. H:10dB.7.5S
11h08m21s	Ovama	Komae, Damine, Tovokawa, Habikino	K:20dB.1S. D:10dB.2.5S. T:20dB.2.5S. H:10dB.2.5
11h10m56s	Ovama	Damine, Tovokawa	Damine:20dB.2.5S. Tovokawa:10dB.2.5S
11h15m01s	Mivazaki	Habikino	Habikino:10dB.2.5S
11h20m10s	Ovama	Damine	Damine:10dB.2.5S
11h31m01s	Ovama	Damine	Damine:10dB.2.5S
11h34m30s	Ovama	Chigusa, Komae, Misato	C:20dB.2.5S K:10dB.4S M:10dB.1S
11h39m40s	Ovama	Komae, Misato	K:20dB.1S. M:10dB.4S
11h41m25s	Ovama	Damine	Damine:10dB.2.5S
11h44m30s	Ovama	Damine, Habikino	Damine:10dB.2.5S Habikino:10dB.5S
11h51m30s	Ovama	Chigusa	Chigusa:20dB.7.5S

## Results

20meteors (these meteors have high quality of time) were conformed Radio Meteor Observation, too. 15meteors were satisfied next conditions in 20 daylight meteors. One, the period of duration was more than 1sec. Another, the power level was more than 10dB

As the results, Objects we saw in daytime were "meteor"

Then, we tried to calculate ZHR(Zenithal Hourly Rate) of daylight meteor by HR(Hourly Rate) data.

$$\text{ZHR} = \text{CHR} * 1/\sin(h) \quad h: \text{radiant elevation}$$

HR(Hourly Rate) is the number of meteors by Masayuki Oka. Limiting magnitude is -4mag.(the magnitude of Venus).

Cloudness is the data of each observational site. The population index is 1.6(by AMOTA, Japan).

As the result, calculated ZHR is 3,700 .

At the same time, in Europe, Leonids activity was ZHR5,400 (Gyssens. 1999 ). This is the similar result of daylight observation in Japan. But, in Europe, bright meteors were few. (Arlt. et.al. 1999). Therefore, we tried to analyze the radiate mechanism.

## Problems

In this time, we try to analyze the radiate mechanism of daylight meteor by considering the diffraction, scattering and chemical methods. But we can not make clear it.

This causes are few objective data and no correct magnitude and specter. Because we can see the few daylight meteors.

### Future work

- The improvement of observational quality
- The establishment of observational method
- The detection of radiate model
- To make clear the radiate mechanism

We do not have the enough knowledge about daylight meteor. Therefore, the correction of data is needed in the future.

### References

Arlt, R., Rubio, L.B., Brown, P., Gyssens, M. 1999, WGN 27, 286-295.

Gyssens M. 1999, LEONID Activity 1999/UPDATE(2) IMO Shower Circular

McNaught, R.H., Asher, D.J. 1999, WGN, 27, 85-102

Toda M., Oka M., Hashimoto T., Serizawa H., Osada K., Maeda K., Sekiguchi T., Morita M.,

Takanashi M., and Shigeno Y., 2000, WGN, 28, 77

The Association of Meteor Observers in and around Tokyo Area 1996, Encyclopedia of Leonids

Specially, We'll dedicated to my astronomical father. : Masaaki Takanashi

## GROUND-BASED OBSERVATIONS OF THE LEONIDS 1999-2000

M. Campbell<sup>1</sup>, C. Theijsmeijer<sup>1</sup>, J. Jones<sup>1</sup>, R.L. Hawkes<sup>2</sup>, and P. Brown<sup>3</sup>

<sup>1</sup>University of Western Ontario, London, ON, N6A 3K7 Canada

<sup>2</sup>Mount Allison University, Sackville, NB, E4L 1E6 Canada

<sup>3</sup>Los Alamos National Laboratories Los Alamos, NM 87545 USA

### ABSTRACT

We present ground-based observations of the 1999 and 2000 Leonid showers. The 1999 shower was observed with image intensified video cameras at various sites around the world. Two station data were obtained in Israel, and heights were obtained for 233 double-station Leonids. The peak flux was also found from Israel data. The 2000 shower was observed with video and radar; both show an early peak much stronger than reported in visual observations. Video data from three sites, (Spain, New Mexico and Alabama) and radar data on two frequencies were used to define the two observed peaks.

### 1. INTRODUCTION

The purpose of the 1999 and 2000 Leonid observation campaigns was primarily to record the fluxes for the shower. The timing of the peaks is important in determining whether model predictions are correct, and the flux intensities can be used to calibrate models.

Double station video heights are very accurate, and of great use in determining the true height distribution of meteor populations. Video heights do not suffer from the biases that radar heights do, so give a better picture of the actual heights of ablation. In particular, it is interesting to look for bright Leonids with very high beginning heights like those recorded during the 1998 shower (Fujiwara et al, 1998). These extreme beginning heights cannot be explained by standard models of ablation and are therefore of great interest.

Observations for both years were carried out with image-intensified video cameras. To ensure that most of the shower would be observed, optical stations were placed at different longitudes. In 1999, the time of interest was just after 2UT on the night of 18 November, so the data from one site is of greatest interest. In 2000, there were several predicted maxima, namely near 8 UT on 17 November, 2000 and near

3 UT and 7 UT 18 November, 2000. The cameras were placed mainly to cover the predicted maxima, but cameras (the data from which is not presented here) were deployed to other longitudes to minimize the risk of missing any unpredicted activity.

### 2. EQUIPMENT AND DATA COLLECTION

#### 2.1. 1999 Campaign

There were seven optical sites in the 1999 campaign, of which we present results only from one in this report. The main optical location was in Israel, which was well located to observe the peak of the shower around 2UT. Two stations were set up 48.5 km apart. The main site was located at the Wise Observatory near Mitzpe Ramon, Israel (34.76°E, 30.60°N) and consisted of four MCP (microchannel plate) image intensified CCD cameras, two with Generation III intensifiers and two Generation II intensifiers. One of the Generation IIIs was equipped with a diffraction grating for spectral observations: the results from that camera will not be treated here. The remote site was located near Mitzpe Revivim (34.72°E, 31.04°N) also consisted of four cameras, which were pointed so that they overlapped the fields of view of the cameras at the main site. The cameras had C-mount video lenses as objectives with focal lengths between 25mm and 75mm, producing fields of view between 35° and 9°, and the maximum limiting stellar magnitude on the most sensitive systems of nearly +9<sup>M</sup>. Each camera pair was biased to a different height, to ensure that high-altitude Leonids would not be discriminated against in the study. The two pairs of cameras used in the analysis were cameras K and F, which overlapped at 160 km, and E and J, which overlapped at 110 km. While the cameras are biased toward a particular height, they are still capable of detecting simultaneous meteors over a wide range of heights.

The video signal for all cameras was recorded on VHS video tape, at NTSC video rates (30 frames per second, two interlaced video fields per frame). The dig-

itization was done directly from these tapes.

## 2.2. 2000 Campaign

Data from three optical sites from the 2000 shower will be presented in this paper. The sites were located in Spain, near Huntsville, Alabama and Socorro, New Mexico. The site in Spain had clear skies on the peak night, while New Mexico had some cloud problems and Alabama recorded during a few intervals of clear sky. The site in Spain consisted of four cameras, the New Mexico site three cameras and two cameras were deployed in Alabama. Cameras at all three sites were equipped with Generation III intensifiers, and lenses similar to those in the 1999 campaign were used, giving again a limiting magnitude for the most sensitive cameras of  $+9^M$ . No two-station work was done in 2000. The Leonids were also observed with a three frequency (17.45 MHz, 29.85 MHz and 38.15 MHz) radar, which was located near London, Ontario, Canada. Two of the frequencies (29 and 38 MHz) were operating at the time. Each radar has a seven-element interferometer which permits the altitude and azimuth of each echo to be measured with great precision.

## 3. ANALYSIS PROCEDURES

Meteors were detected by eye on several playbacks of the video tapes. The meteors were then digitized using a SCION LG-3 card to  $640 \times 480 \times 8$ -bit resolution. Custom macros written for NIH Image 1.62 were used for the photometric and positional analysis. For each two hour tape, a calibration for both positional and photometric measurements was performed on a large number of stars. The positional calibrations used the 'plate constants' approach (Wray, 1967; Marsden, 1982; Hawkes et al, 1993). This essentially deals with any distortion in the field of view and can accurately place the elevation and azimuth of any meteor using background stars for calibration. The same stars are used in the photometric calibration: their apparent brightness on the video is compared to the actual visual magnitude of the star and the resulting curve can be used to find the apparent magnitude of any meteor. For details of the photometric calibration (used for calculating masses) see Hawkes et al (1993). The photometric analysis was complicated a little by the fact that the Generation III intensifiers are more sensitive in the infrared: class M stars in particular gave on average higher pixel intensities for similar magnitudes. This was corrected for in the calibration. The double station analysis procedures are described in detail in Hawkes et al (1993). The analysis involves finding the vector which matches the projection of the trail seen by both stations, and fitting a line to the observed points.

Echoes on the radar were found with Skymet real-time detection software, and the time, amplitude,

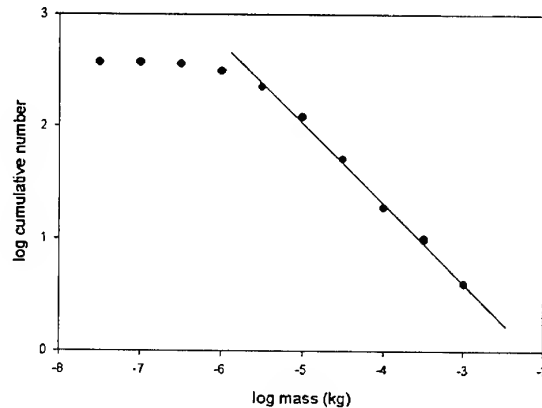


Figure 1. Mass distribution index for Camera F (1999 campaign)

altitude and azimuth, range and height are recorded for each. While it is not possible to identify a single echo as a Leonid or non-Leonid, it is possible to get a statistical measure of the activity of a particular radiant. Since all echoes are specular (at right angles to the line of sight), the radiant of any echo must lie somewhere on a great circle  $90^\circ$  from the echo point. By counting the number of echoes at right angles to a particular radiant, one can get a measure of the number of meteors associated with that radiant.

## 4. RESULTS

### 4.1. 1999 Fluxes

In general, the mass distribution of shower meteors is of the form:

$$N_C = \frac{C}{1-s} m^{1-s} \quad (1)$$

where  $N_C$  is the cumulative number of meteors larger than mass  $m$ ,  $C$  is some constant and  $s$  is the mass distribution index. A larger value of  $s$  means a larger proportion of faint meteors, while a smaller value indicates that the number of meteors does not increase significantly at smaller magnitudes.

To calculate the mass distribution index, the mass of each meteor that was entirely captured by the camera was calculated by summing the intensities on each frame. Meteors which had only been partially observed, which either began or ended out of the field of view were rejected for this analysis. The log of the cumulative number of meteors was plotted against the log of the photometric mass, and the slope of the graph gives  $1-s$ . Figure 1 shows the results for camera F. The data from fainter meteors are neglected because of incomplete coverage at higher magnitudes.

The mass distribution index was found to be 1.75 at the time of the Leonid maximum. The index was calculated at intervals, each containing 50-80 Leonids, in an attempt to determine if the mass distribution changed around the time of the peak. No significant variation was observed, either due to intrinsic lack of variation or because of the small numbers available.

The calculation of fluxes requires a limiting magnitude for Leonids for each camera, and the area of observation. Meteor limiting magnitudes are much lower than stellar limiting magnitudes since meteors are not point sources of light. The limiting magnitude for a particular shower can be calculated by (Hawkes et al, 1998):

$$\Delta_M = 2.5 \log \left( \frac{180 r_l V \tau \sin \xi}{\pi F_{ov} R} \right) \quad (2)$$

where  $\Delta_M$  is the difference in magnitude between the stellar limiting magnitude and the meteor limiting magnitude,  $r_l$  is the resolution of the detector in number of video lines (which for our systems is 300),  $V$  is the geocentric velocity in km/s (71 km/s for the Leonids),  $\tau$  is the effective CCD integration time (0.033s at NTSC frame rates),  $\xi$  is the solid angle between the radiant and the pointing direction of the camera,  $F_{ov}$  is the field of view (taken as the average of vertical and horizontal fields of view) and  $R$  is the range to meteors in the center of the field (taken to be at altitudes of 100 km). This gives a limiting magnitude around  $+2^M$  for the systems.

The collecting area of each system was calculated using basic geometry. It is essentially the area of the field of view when projected on a surface at an altitude of 110km. The simple calculation used neglects the curvature of the Earth, but is still accurate to better than 5% at elevations greater than  $30^\circ$ .

The fluxes were calculated in 15 and 3 minute bins. The 15 minute binning shows the peak clearly (Figure 2). The profile is asymmetric, the ascending branch being longer than the descending. The peak flux is  $0.81 \pm 0.06$  meteoroids  $\text{km}^{-2} \text{hr}^{-1}$  to  $+6.5^M$ . With the mass distribution index of 1.75, this corresponds to a visual ZHR of  $4000 \pm 300$ . The full width at half max of the curve is 54 minutes.

The higher time resolution gives higher fluxes and higher errors. For the three minute binning, the maximum flux was found to be  $0.99 \pm 0.11$  meteoroids  $\text{km}^{-2} \text{hr}^{-1}$  to  $+6.5^M$ , which is equivalent to a ZHR of  $4900 \pm 600$  (Figure 3).

The peak time estimated from the lower temporal resolution data is  $235.285 \pm 0.005^\circ$ . The high resolution peak is less well defined, since the maximum is really a plateau lasting from  $325.276^\circ$  to  $235.285^\circ$ .

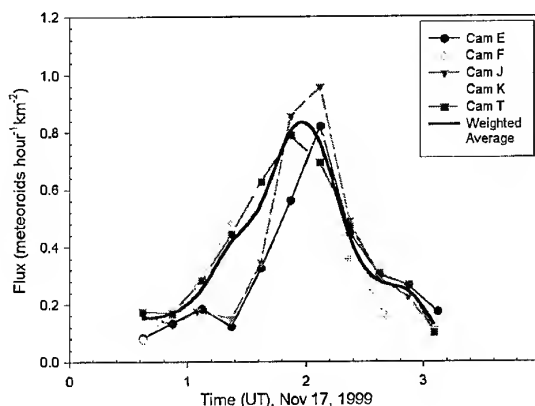


Figure 2. Individual camera and weighted average fluxes in 15 minute bins (1999 campaign)

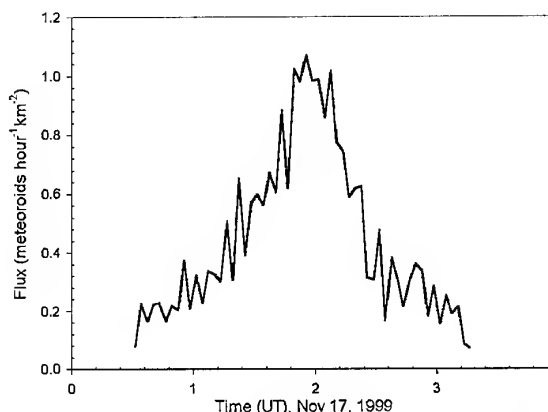


Figure 3. Weighted average of fluxes in 3 minute bins (1999 campaign)

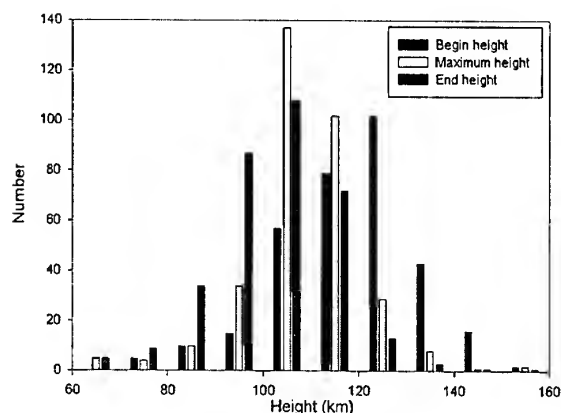


Figure 4. Two-station begin, maximum and end heights for Leonids (1999 campaign)

#### 4.2. 1999 Heights

Double station meteors were found by comparing the times of appearance on both systems. False associations are readily identifiable from the unphysical trajectory solutions (heights over 250 km or under 40 km for example). Once the false associations were removed, the Leonids were isolated by comparing the radiant computed for each meteor to the Leonid radiant: anything less than  $10^\circ$  from the radiant was accepted. A total of 114 double station Leonids were obtained from the E-J camera pair and 118 from the F-K pairing. For each of these pairings, one camera was a Generation II and the other a Generation III. The average mean mass is that calculated from cameras E and F, the generation II cameras, since these cameras have the more visual response.

We calculated the number of meteor with beginning, maximum or end heights in 5 km bins. Neither camera pair showed any significant number of meteors beginning at unusual heights ( $>160$  km). We do not expect any significant biases against high meteors, even on the pair with the lower intersection height, until 190 km. The meteors in this sample are smaller by several orders of magnitude from those in Fujiwara et al (1998); all high-altitude meteors recorded are very large meteors. The results for both camera pairs are shown in Figure 4.

#### 4.3. 2000 Fluxes

The mass distribution index was calculated from the 2000 data in the same way as the 1999 data. Since the cameras in Spain yielded the most meteors, those give the most meaningful estimate of mass distribution index from the optical data: only one measurement, a total from all the meteors detected on the peak night, was possible. Since the radars collect much more data, it was possible to calculate the mass distribution index at several time intervals (Figure 5). The 29 MHz system collected more

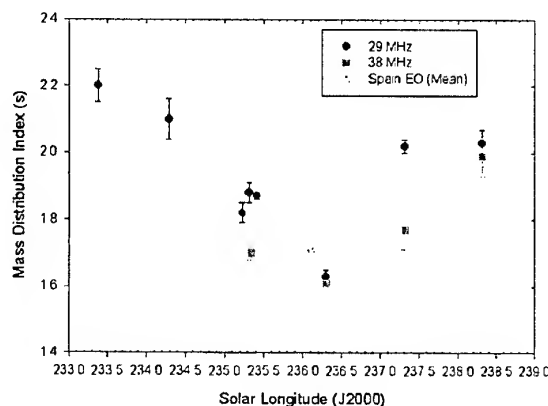


Figure 5. Mass distribution indices from radar and video observations (2000 campaign)

echoes, since it suffers less bias against high meteors than 38 MHz. The mass distribution index will be slightly contaminated with sporadic meteors.

The average sporadic mass distribution index is between 2.2 and 2.3. The general trend of the radar data is a mass distribution index which goes down from an initial value of 2.2 to 1.6 at the time of the predicted peak at  $236.25^\circ$ . This indicates that in the binning intervals shown, Leonids dominated the numbers at this time. At other times, sporadics were significant. The values of  $s$  at the November 18 peak agree well with the one calculated from the video data from Spain.

The collecting area for the radar is calculated as a combination of the physical area of sky where echoes from a given radiant can be detected, and the response function of the radar in that direction. It also takes into account the length of the ionized trails (as calculated from optical data) and the range of heights at which each system detects meteors.

The fluxes obtained with this method are then corrected for the initial radius effect. This frequency dependent effect occurs because of the finite radius of the ionized trails, which results in destructive interference at large heights. We have used the corrections derived from Greenhow & Hall (1960). It should be noted that this effect is poorly understood and this could be a significant source of error for the radar fluxes.

The radar and video fluxes are shown in Figure 6. The video data is from New Mexico and Alabama for the earlier peak, and Spain for the second peak. They are in good agreement, particularly the 38 MHz with the video data. Significantly, all three methods show a larger first peak at a solar longitude of  $235.29 \pm 0.02$ . The flux at this earlier peak is  $0.15$  meteoroids  $\text{km}^{-2} \text{hour}^{-1}$  brighter than  $+6.5^M$ , corresponding to a visual ZHR of roughly 800. The second peak agrees with the one shown in visual observations, at  $236.25 \pm 0.02$ , which had a calculated flux of only  $0.07$  meteoroids  $\text{km}^{-2} \text{hour}^{-1}$  brighter

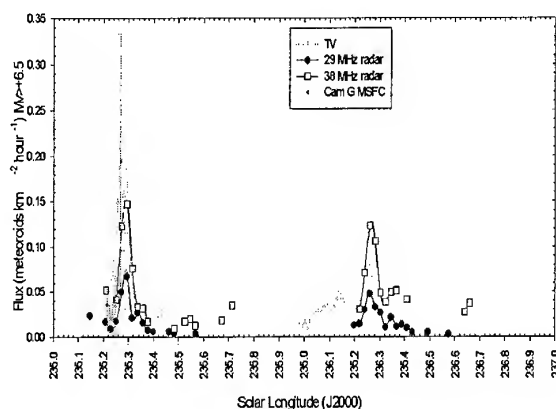


Figure 6. Radar and video fluxes (2000 campaign)

than  $+6.5^M$  (ZHR of roughly 450). The second peak is broader than the first.

## 5. CONCLUSIONS

The heights in the 1999 campaign showed no evidence of the very high altitude meteors detected by other studies. This was in spite of the care that was taken to avoid biasing the results against high-altitude meteors. This is probably because of the relative faintness of the majority of the meteors detected during this campaign, compared to the previous year, when very bright Leonids were much more numerous. Very large Leonids may begin to emit radiation at very high altitudes due to interactions of volatile components (Hawkes & Jones, 1975) with the atmosphere. In faint meteors there may not be enough of this radiation released for the meteor to be visible.

The 2000 observations showed two peaks, with the first being greater than the second. This is not in agreement with visual observations (Arlt & Gyssens, 2000): the International Meteor Organization calculated ZHRs of 130 and 450 for the two peaks, in contrast with 800 and 450 for our results (Figure 7).

There are several possible reasons for this discrepancy. The mass distribution index was probably higher on the night of November 17, meaning more faint meteors: since visual observations were hampered by moonlight this would tend to decrease the number seen. There may also have been the psychological effect of the expectation (from model predictions) that the first peak would be weaker than the second.

There was no evidence of a significant decrease in mass distribution index for the first peak: this is probably due to an intrinsic property of the stream, but could also be partially due to the narrowness of the peak, meaning a greater number of sporadics were counted in the measurement.

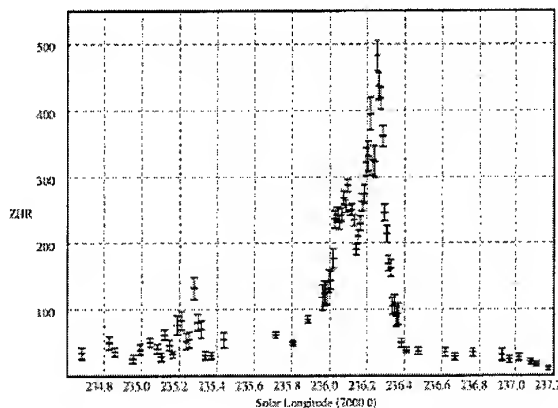


Figure 7. Visual Zenithal Hourly Rate (2000)(Arlt & Gyssens, 2000)

This campaign shows the importance of careful observations off the times when the models show major peaks, since the strength of peaks is not well calibrated in the models.

## REFERENCES

- Arlt R., Gyssens M., 2000, WGN 28,6, 191-204.
- Fujiwara V., Ueda M., Shiba Y., Sugimoto M., Kinoshita M., Shimoda C., Nakamura, T., 1998, Geophys. Res. Lett. 25, 285-288.
- Greenhow J. S., Hall J. E., 1960, MNRAS 121, 183-196.
- Hawkes R. L., Babcock D. D., Campbell M. D., 1998, CRESTech Contract report, 58pp.
- Hawkes R.L., Mason K. I., Fleming D. E. B. and Stultz C.T. 1993, International Meteor Conference 1992, 28-43.
- Hawkes R. L., J. Jones., 1975, MNRAS 173, 339-356.
- Marsden B. G., 1982, Sky & Telescope 64, 284.
- Wray J. D., 1967, The computation of Orbits of Doubly Photographed Meteors, Univ. New Mexico Press, Albuquerque, NM, USA.

# VIDEO SPECTRA OF LEONIDS AND OTHER METEORS

Jiří Borovička

Astronomical Institute, Academy of Sciences, 251 65 Ondřejov, Czech Republic

## ABSTRACT

Video spectra of 33 meteors of medium brightness (+1 to -1 mag) were compared. The intensity of the main meteoric emissions of Mg, Na, Fe, and atmospheric emissions of N<sub>2</sub>, O, N were studied. The Na/Mg ratio is different in different meteors, showing variations in Na abundance. Moreover, much earlier ablation of Na during the atmospheric entry than of other elements observed in some Leonids and one Orionid, Quadrantid and Leo Minorid evidences fragile structure of those meteoroids. One sporadic meteor was completely deficient in sodium. The strength of atmospheric emissions increases with increasing meteor velocity. Taurids are notable by the near-absence of O and N emissions.

Key words: meteors; meteor showers; spectra; sodium.

## 1. INTRODUCTION

Meteor spectroscopy is a tool for studying composition of meteoroids and their interaction with the atmosphere. Video techniques have been used since the work of Millman et al. (1971), but relatively few conclusions about meteors of different origin have been obtained so far. This short paper is a progress report of a spectroscopic project which uses image intensified video camera and started at the Ondřejov Observatory in October 1998. Data were taken also during the 1998 and 1999 Leonid Multi-Instrument Aircraft Campaigns (Jenniskens & Butow, 1999, Jenniskens et al., 2000) and the Dutch-Czech Leonid expedition to Spain in 2000. This work extends the report of Štork et al. (1999), which was based on data taken by another video system.

Our spectrograph consists of a generation II image intensifier Dedal 41 with 25 mm micro-channel plate, 1.4/50 mm photographic lens and 600 grooves/mm spectral grating. The data were taken by video camera Panasonic NV-S88E in the S-VHS PAL format and later digitized on PC (768×576 pixels, 8 bits per frame). The resulting field of view is 25° and dispersion is 11 Å/pixel. Meteor limiting magnitude for

spectra is about +3. The spectral range is 3800–9000 Å with maximum near 5500 Å and sensitivity higher than 20% of maximum between 4350–7900 Å.

In general, meteor spectrum will depend on meteor velocity, brightness (which depends primarily on meteoroid mass and, again, velocity), and the composition of the meteoroid. The spectrum can also depend on the meteor height in the atmosphere. In a previous paper (Borovička et al., 1999, hereafter referred to as Paper I), we studied Leonids 1998 and compared them with several other meteors, most of them observed by another spectrograph. It was found that the intensity of the Mg<sup>+</sup> line increases with meteor brightness and that faint meteors are somewhat poorer in Na. Moreover, for Leonids fainter than about magnitude -2, preferential ablation of sodium in the upper part of trajectory was discovered. This effect was not seen in the majority of other meteors, in particular it was not seen in Perseids. The intensity of atmospheric emissions in meteor spectra was found to depend on meteor velocity.

## 2. PROCEDURES

Up to now, more than 1300 meteor spectra were obtained with the above described spectrograph. We are interested mostly in the composition and structure of meteoroids. In this paper, 17 selected excellent Leonid spectra from 1998–2000 will be compared

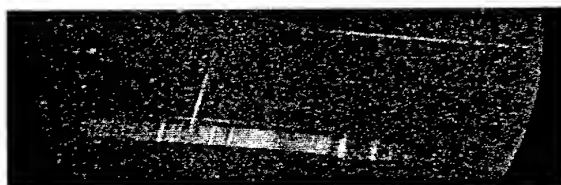


Figure 1. Part of a single frame containing Leonid meteor spectrum SZ1237. Wavelengths increase from left to right. The meteor flew from above down. The vertical extend of the spectrum represents the path traveled by the meteor during the 0.04 sec exposure time. The single line delayed behind the meteor is the green oxygen line, 5577 Å.

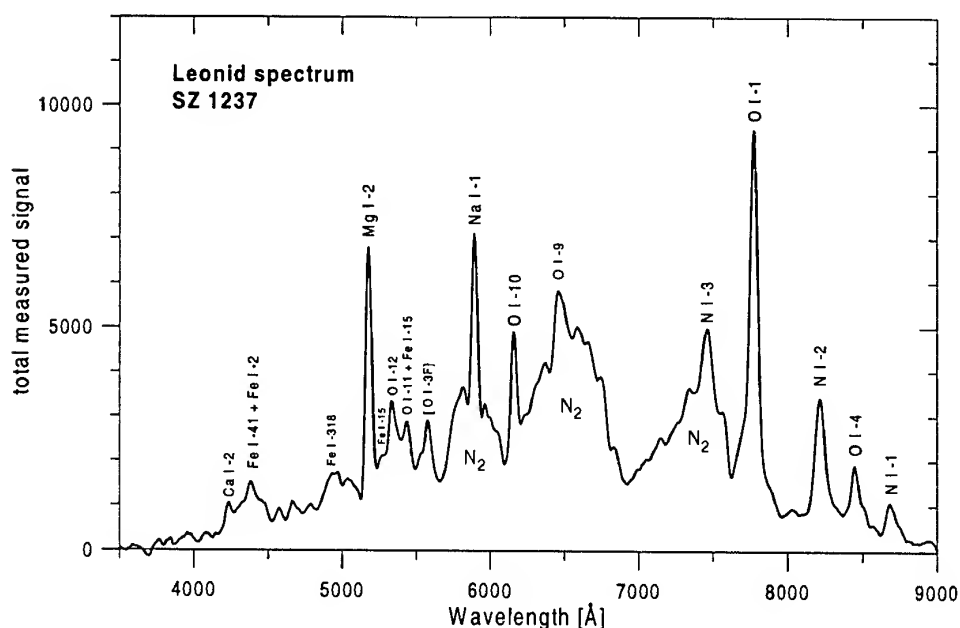


Figure 2. Example of a Leonid spectrum. The signal was summed from all frames and was not corrected for spectral sensitivity of the instrument. Significant emissions are identified with atom and multiplet number (Moore 1945).

with 16 meteors from other showers or sporadic. The list of the spectra is given in Table 1. Velocities  $v$  [in km/s] given in bold were computed from double station observation of the meteor; other velocities were taken from the shower assignment. The brightness of all meteors was between magnitudes +1 and -1. This is optimal range for the instrument since the spectra have good signal-to-noise ratio and are not saturated. This relatively narrow magnitude range also allows us to ignore the dependence of spectra on meteor brightness.

An example of a single video frame showing meteor spectrum is given in Fig. 1. The spectrum was extracted from each such frame by a scanning procedure. The spectra were then studied in two ways. First, all spectra were summed to obtain integrated intensities of the emissions along the whole meteor path. For meteoric emissions, the integrated intensity is, in the first approximation, proportional to the total content of the element in the meteoroid. Second, the development of the spectrum along the meteor path was studied. This can be well done only for bright emissions. The monochromatic light curves in the lines of Mg, Na, and O were therefore constructed and used to study the early ablation of sodium.

### 3. INTEGRATED INTENSITIES

Figure 2 shows the integrated spectrum of one Leonid meteor with all important emissions identified. The spectrum contains Planck continuum, strong emissions of Mg, Na, O, N, and  $N_2$  molecule and minor emissions including Fe and Ca. The calibration to

Table 1. List of studied meteors

number	date	time UT	shower	$v$
SZ 028	98-11-17	16:46:15	Tau	32
SZ 066	98-11-17	18:54:18	Leo	71
SZ 082	98-11-17	19:29:14	Leo	71
SZ 116	98-11-17	20:31:39	Leo	71
SZ 147	98-11-19	15:17:40	Leo	71
SZ 155	98-12-11	23:41:37	Gem	36
SZ 164	98-10-20	01:37:39	Ori	<b>67</b>
SZ 171	98-10-20	02:40:23	spor	<b>69</b>
SZ 218	99-11-18	00:26:04	Leo	71
SZ 263	99-11-18	01:04:55	Leo	71
SZ 464	99-11-18	01:43:16	Leo	71
SZ 481	99-11-18	01:45:07	Leo	71
SZ 492	99-11-18	01:45:52	Leo	71
SZ 543	99-11-18	01:49:30	Leo	71
SZ 987	99-12-13	22:33:14	Gem	36
SZ 1008	99-12-15	00:51:47	Gem	36
SZ 1060	00-08-11	22:03:00	Per	61
SZ 1077	00-08-13	00:04:39	Per	61
SZ 1098	00-10-21	21:39:02	Tau	<b>30</b>
SZ 1101	00-10-21	23:44:00	LMi	<b>63</b>
SZ 1110	00-10-22	04:12:07	spor	<b>66</b>
SZ 1173	00-11-18	03:03:22	Leo	<b>72</b>
SZ 1193	00-11-18	03:25:39	Leo	71
SZ 1214	00-11-18	03:55:08	Leo	<b>71</b>
SZ 1237	00-11-18	04:39:23	Leo	<b>73</b>
SZ 1245	00-11-18	04:49:18	Leo	<b>71</b>
SZ 1284	00-11-18	05:29:03	Leo	71
SZ 1291	00-11-18	05:35:18	Leo	71
SZ 1308	00-11-19	00:17:55	spor	<b>69</b>
SZ 1309	00-11-19	00:35:09	spor	<b>44</b>
SZ 1334	00-12-22	05:17:05	UMi	35
SZ 1337	01-01-03	21:39:02	Qua	42
SZ 1338	01-01-03	23:11:12	Qua	42

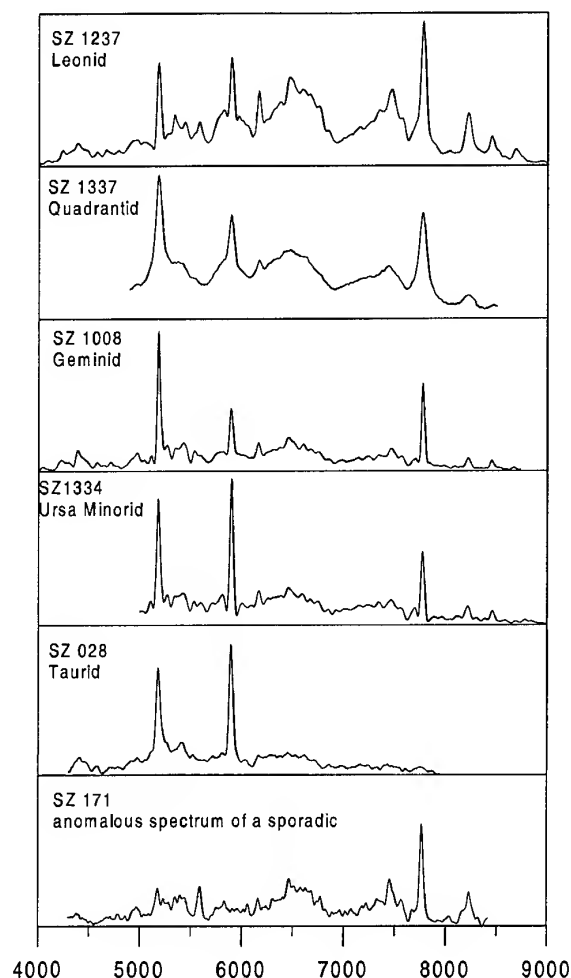


Figure 3. Comparison of integrated spectra of meteors of different showers. The Quadrantid spectrum has poorer resolution because the meteor was observed through clouds.

the spectral sensitivity of the instrument would show that the O and N lines above 7500 Å are by far the brightest lines in the spectrum (see Paper I).

In Fig. 3 the integrated spectra of six meteors of different origin are compared. It can be seen that the same emissions as in Leonids are present in the other spectra, but in different proportions. This is quantified in Fig. 4 for all studied meteors. The relative integrated intensities of selected emissions of Mg, Na, Fe, O, and N<sub>2</sub> are shown in form of two ternary diagrams. Only emissions from the central part of the spectra, 5000–6500 Å, were used because the sensitivity of the instrument is good here and all studied spectra had this region in the field of view. Intensities have been corrected to the spectral sensitivity of the instrument.

Leonids occupy certain space in the Mg-Na-Fe diagram with some real spread in the Na/Mg ratio. The 2000 Leonids tend to have more Na on average. A number of other meteors fall in the same

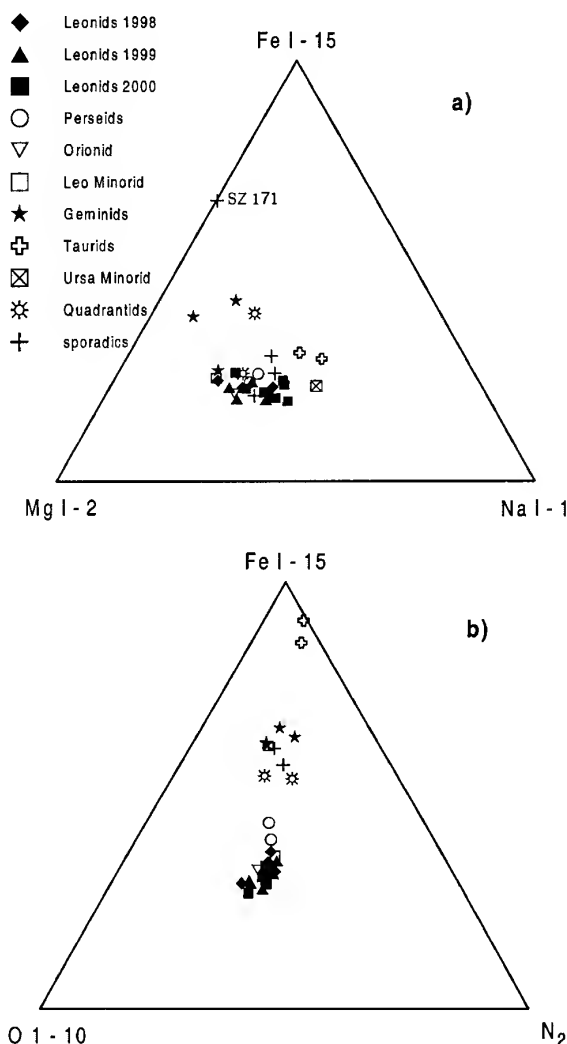


Figure 4. Diagrams comparing relative intensities of three emissions in the integrated spectra. Each point represents one meteor. Meteor showers are distinguished by different symbols. The closer lies the point to a vertex of the triangle, the stronger was the corresponding emission relative to the other two. For atomic lines, the emission means the sum of all lines of the given multiplet. For N<sub>2</sub> a single representative band near 6300 Å was considered.

region as Leonids. Geminids, however, are generally poorer in Na and richer in Fe. Taurids and the Ursa Minorid are richer in Na, and Taurids are also somewhat richer in Fe. Quadrantids also tend to be richer in Fe. The Leo Minorid is relatively sodium poor. These differences probably reflect real differences in chemical composition, at least for the Na/Mg ratio. For Fe we must be more careful since the other multiplets than multiplet 15 do not show the differences so clearly.

Really anomalous was the Na-free and Mg-poor sporadic meteor SZ 171. This meteor of short duration (0.2 s) appeared at relatively low altitude for its high velocity (beginning at 98 km for  $v = 69$  km/s). The

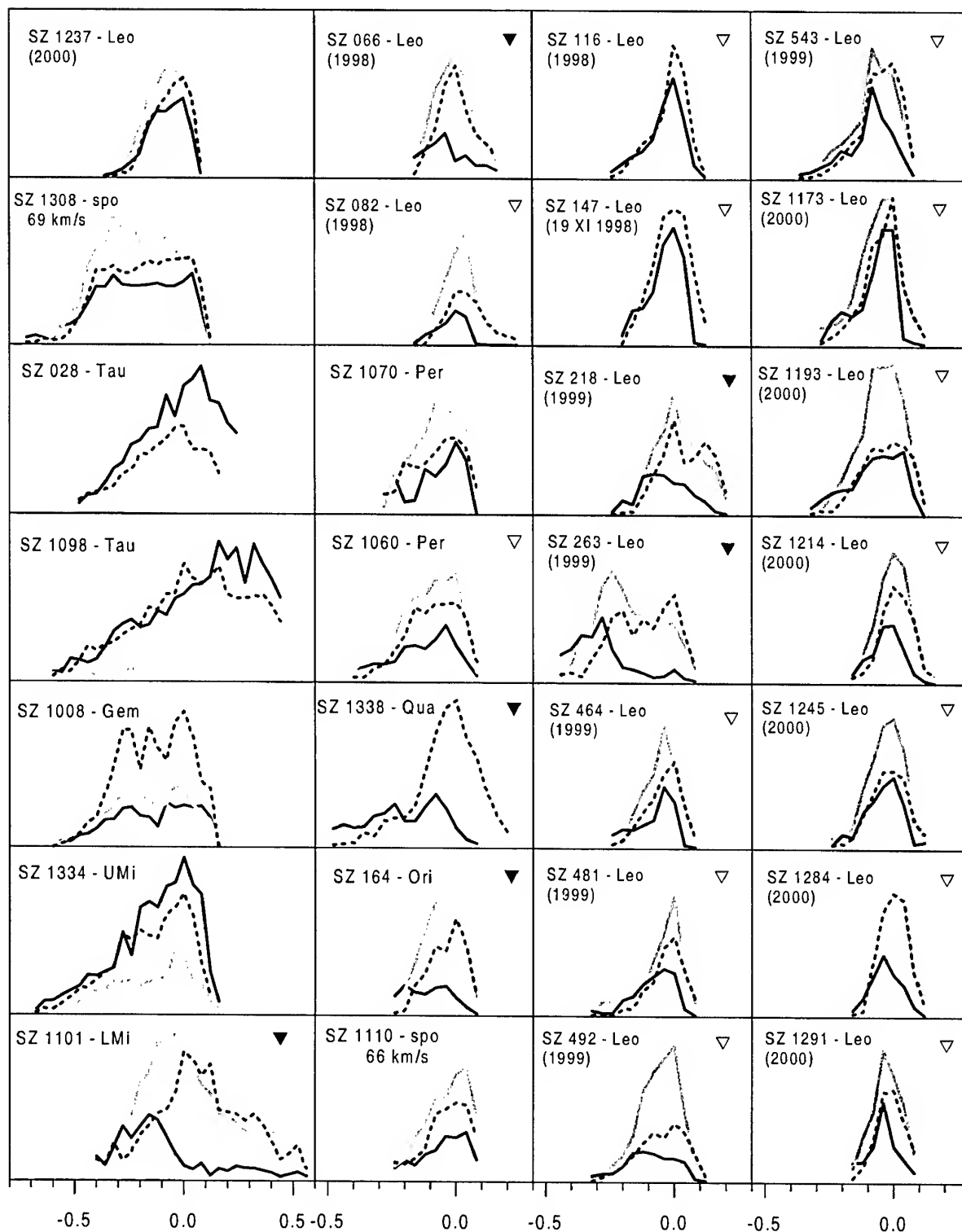


Figure 5. Monochromatic light curves in Mg I-2 (dashed line), Na I-1 (full line), and O I-1 (thick grey line) for 28 meteors. Time in seconds is on the horizontal axis. Zero time was set to the time of maximum of the Mg line for each spectrum. The relative intensity in arbitrary linear scale (different in each spectrum) is on vertical axis. The calibrated intensity of the O line was divided by five in order to set it to the same range as other two lines in most spectra. Triangles designate spectra with the effect of early release of sodium. Where the triangles are full, the effect is particularly strong.

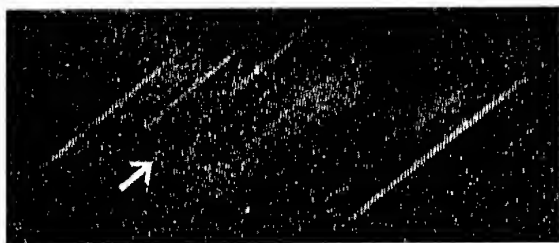


Figure 6. Co-added image of a Leonid spectrum SZ 263. Wavelengths increase from left to right, the meteor moved from upper right to lower left. The sodium line is marked by an arrow.

orbit was retrograde ( $i = 174^\circ$ ) with perihelion near 1 AU. This meteor seems to represent the same type of material and orbit as the anomalous Karlštejn fireball (Spurný & Borovička, 1999).

Figure 4b shows that the ratio of atmospheric emissions  $O/N_2$  is nearly the same in all meteors. This is also true for the  $O/N$  ratio. The intensity of atmospheric emissions relative to meteoritic emissions primarily depends on meteor velocity. Faster meteors produce more atmospheric emissions. Only Taurids are peculiar by a surprisingly low intensity of O and N lines. Their velocity is not too much lower than those of Geminids and Ursids but the O and N lines are almost absent.

#### 4. MONOCHROMATIC LIGHT CURVES

Following its discovery in 1998 Leonids in Paper I, the effect of early release of sodium was confirmed in Leonids by Abe et al. (2000), Tsukamoto et al. (2001), and, to some extent, by Murray et al. (2000). Murray et al. pointed out that the sodium light curves start later than light curves taken in white light. The white light in Leonids, however, contains also Planck continuum and atmospheric emissions. That observation therefore does not exclude the possibility that Na ablation started earlier than the ablation of other elements. In the following, we compare the Na, Mg, and O light curves directly. The question is how Leonids from different years differ and whether the effect is present also in other meteors.

The monochromatic light curves of most of the studied meteors are plotted in Fig. 5. If some curve is missing in the plot it is because the line was outside of the field of view. In meteors designed by empty triangle, the effect of sodium early release is present, i.e. sodium line begins earlier than magnesium and fades more quickly toward the end of the meteor. In meteors designed by full triangle, the effect is very strong, the Na and Mg curves are quite different with Na maximum occurring much earlier. A direct image of one such a spectrum is shown in Fig. 6. In unmarked meteors the effect is absent or only marginally present.

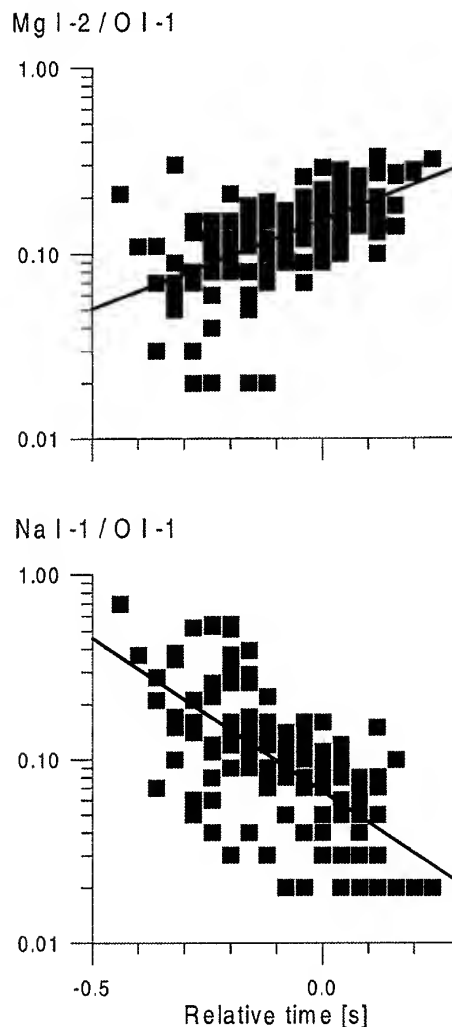


Figure 7. The dependence of the ratios of intensities of main emissions in Leonid spectra. Each point in this plot represents a single frame of one spectrum. All Leonids were combined together in the way that time zero was set to the time of the maximum of the Mg line.

The early release of sodium is present in almost all Leonids (except SZ 1237) but it seems to be less pronounced on average in 2000 than in 1998 and 1999. In 2000, we observed on November 18 between 0-6 UT and meteors from the 8 revolution old trail were captured, while younger meteoroids were observed in 1998 and 1999 (McNaught & Asher, 1999). However, significant differences were observed also within the same year, e.g. during the 1999 storm. Meteoroids of the same origin and age have therefore different properties. Nevertheless, general trends of the Na/O ratio decreasing and Mg/O increasing along the trajectory can be seen in all Leonids. This is demonstrated in Fig. 7, where all Leonids were combined together.

The overall shape of Leonid light curves (e.g. the Mg curves) are more or less classical. We do not see the

flat topped curves which Murray et al. (2000) observed in 1999 Leonids. This is certainly due to the fact, that their sample contains much fainter meteors. We observe larger meteoroids which behave more classically. Despite this, the early sodium release, i.e. differential ablation, is present in our sample.

From the other meteors studied, the effect of sodium early release is strong in the Orionid, Quadrantid, and Leo Minorid. It is much weaker in Perseids. No sodium preferential ablation was observed in Geminids, Taurids and the Ursa Minorid. Considering the variability within Leonids, however, these results cannot be taken as representative to all meteors of the respective showers. Indeed, Tsukamoto et al. (2001) did not observe the sodium effect in one Quadrantid spectrum, and Jenniskens & Lyytinen (2001), on the contrary, saw the effect in one Ursa Minorid. More spectra are needed to obtain firmer conclusions.

## 5. CONCLUDING REMARKS

We compared spectra of meteors of about zero visual magnitude of various meteor showers. The spectra have similar character and contain meteoritic emissions of Mg, Na, Fe and atmospheric emissions of O, N, and N<sub>2</sub>. The intensity of atmospheric emissions increases with meteor velocity. Varying intensities of meteoric emissions show variations in chemical composition of meteoroids, in particular of the abundance of Na. Some meteors show the Na line only in the early part of their trajectories, which suggests their fragile structure and early evaporation of volatile material. There are differences in both the Na content and the degree of Na early evaporation among meteors of the same shower. The differences between different showers are, however, larger. Geminids have lower content of Na than Leonids and do not show Na early evaporation. In Perseids, the Na early evaporation is much less pronounced than in Leonids, while the total Na content is similar. Taurids show more Na and the early evaporation is not present. The early evaporation of Na was strong, in addition to some Leonids, in one Orionid, Quadrantid and Leo Minorid.

The most peculiar spectrum observed belongs to a sporadic meteor on retrograde orbit. It was Na-free and Mg-poor. The appearance of this meteor at relatively low height evidences its compact structure. It is somewhat surprising to find compact non-chondritic material on a cometary-like orbit.

The work reported in this paper is continuing. A deeper analysis and interpretation will be made after more spectra are observed and reduced. In addition, future combination of spectral data with meteor height and light curve classification schemes may provide more insight in the structure and composition of meteoroids.

## ACKNOWLEDGEMENTS

The 1998 and 1999 Leonid Multi-Instrument Aircraft Campaigns were supported by NASA and U.S. Air Force. The 2000 Leonid expedition was supported by the Dutch Meteor Society. I specially thank P. Jenniskens from NASA/Ames and H. Betlem from DMS for their support. Further thanks go to R. Štok, P. Koteň, P. Špurný, J. Boček, and J. Palek who participated in the observations and/or data preparation. This project was supported by the grant no. 205/99/0146 from GAČR.

## REFERENCES

- Abe S., Yano H., Ebizuka N., Watanabe J., 2000, EMP 82-83, 369
- Borovička J., Štok R., Boček J., 1999, MAPS 34, 987 (Paper I)
- Jenniskens P., Butow S.J., 1999, MAPS 34, 933
- Jenniskens P., Butow S.J., Fonda M., 2000, EMP 82-83, 1
- Jenniskens P., Lyytinen E., 2001, poster at this conference
- McNaught R.H., Asher D.J., 1999, WGN 27, 85
- Millman P.M., Cook A.F., Hemenway C.L., 1971, Canad. J. Phys. 49, 1365
- Moore R.E., 1945, Contr. Princeton Univ. Obs. 20
- Murray I.S., Beech M., Taylor M.J., Jenniskens P., Hawkes R., 2000, EMP 82-83, 351
- Špurný P., Borovička J., 1999, in Meteoroids 1998 (Ed. W.J. Baggaley, V. Porubčan), Slovak Acad. Sci. Bratislava, p. 143
- Štok R., Borovička J., Boček J., Šolc M., 1999, in Meteoroids 1998 (Ed. W.J. Baggaley, V. Porubčan), Slovak Acad. Sci. Bratislava, p. 371
- Tsukamoto T., Abe S., Ebizuka N. et al., 2001, poster at this conference

# LEONID METEORS FOUND IN CHINESE HISTORICAL RECORDS

Yasunori Fujiwara<sup>(1)</sup> and Ichiro Hasegawa<sup>(2)</sup>

<sup>(1)</sup> *Nippon Meteor Society, 2-16-8 Mikunihonmachi Yodogawa-ku Osaka, 532-0005, Japan,  
Email: DHB15312@biglobe.ne.jp*

<sup>(2)</sup> *Otemae University, Inano Itami, 884-0861, Japan, Email: hasegawa@otemae.ac.jp*

## ABSTRACT

Many records of individual meteors in Chinese historical records were collected and published by Beijing Observatory [1]. In those records, Hasegawa [2] found fifteen historical records of the Leonid meteors during BC651 and the end of the 19<sup>th</sup> century. In the present study, we reexamined those records and found additional five possible Leonid meteors, and we summarize the individual record of twenty Leonid meteors and discuss some problems of the ancient Leonid meteor.

## 1. INTRODUCTION

The Leonids is one of most famous meteor showers that have occurred during several centuries, and the historical records of the storms are already researched [3] [4]. In Chinese historical records, there are also many records of individual meteors in addition to meteor showers (storms). Some studies of those data were undertaken already. Using Chinese records translated by Biot [5], Astapovich and Terenteva identified seven major showers including Leonids [6]. Hasegawa found Geminids and December Monocerotids [7] and Leonids [2] in the Chinese chronicles. In the present study, we have enlarged and revised Hasegawa's work [2].

## 2. METHOD OF IDENTIFICATION

Beijing Observatory published the complete historical records, the General Compilation of Chinese Ancient Astronomical Records (1988), in which there are three sections of the meteorite falls, the meteor showers and the individual meteors. More than 5000 individual meteor records during BC 651 and AD 1900 are presented. Most of the records of the fireballs indicate the meteor path with Chinese constellations or bright fixed stars and the directions of the path, so we can identify with the permanent shower meteor not only the aid of the solar longitude at the meteor apparition but also its path [6] [7].

The parent comet of the Leonids, 55P/Tempel-Tuttle, was discovered again in 1997, and its improved orbit between 1366 and 1997 together with predictions before 1366 were calculated by Nakano [8]. The

predicted longitude of the descending node of the cometary orbit can be compared with the solar longitude at the meteor apparition.

The first criterion of identification of a meteor record is the solar longitude (Long.) at the time of meteor apparition. Using the calculated longitude of the descending node (Node) of parent comet, with the possible range of ten degrees, we have found suitable meteor records and have drawn their path in the star chart to make identifications with the belonged meteor shower.

## 3. HISTORICAL RECORDS OF THE INDIVIDUAL LEONID METEOR

We researched the records of the individual meteor during BC651 to AD1800 and found a number of Chinese records of bright Leonid meteors as shown in Table 1. First 15 records (Nos.1 - 15) in this table were found by Hasegawa [2] and five (Nos.16 - 20) are added in this study. Those paths of meteor are shown in Figures 1a, 1b and 1c. The predicted position (X) of the radiant point of Leonids are given in these Figures. The numbers attached to the path are the record numbers given in Table 1.

## 4. DISCUSSION

Variations of the ascending node ( $\Omega$ ) of parent comet and the longitude of the sun at the storm and individual meteor appearance are shown in Figure 2. It is obvious that both variations are in good agreement. Variations of the longitude of the sun and that of individual Leonid meteors are also shown in Figure 2. It is likely that those variations have same tendency in increase. Astapovich and Terenteva found that the longitude of 220° (B1950.0) corresponds to the date of maximum in the 11<sup>th</sup> century [6]. This value is in good agreement with our result. 85 percent of individual Leonid meteors were observed near the longitude of ascending node ( $\Omega$ ) of parent comet in the range of  $\pm 2.5^\circ$  (Table 2).

It is well known that Leonid storms have occurred around the year when the parent comet passed its

Table 1. Chinese Historical Records of Bright Leonid Meteors

No.	Year	Date	Meteors – Comet			Meteor Path			Characters of Meteor						
			Sol. Long.	Eq. 2000	Long. - Node	t - T	App.	Dir.	End	Brightness	Speed	Color	Trail	Size	
1	81	Sep. 17	199.7	-6.4°		+0.4 yrs	軒轅		文昌						like a clench
2	1010	Oct. 14	220.4	+0.1°		+9.4 yrs	軒轅		太微垣						
3	1024	Oct. 11	217.8	-2.5°		-10.2 yrs	太微垣		右執法						
4	1034	Oct. 13	219.3	-1.1°		-0.2 yrs	北斗	NW	紫微東南垣		fast				
5	1034	Oct. 13	219.3	-1.1°		-0.2 yrs	文昌	NW	鉤陳	○	fast		○		
6	1037	Oct. 12	218.5	-2.0°		+2.8 yrs	南河	SE	狼星	○	fast	B/W	○	like Venus	
7	1055	Oct. 17	222.9	+1.8°		-14.4 yrs	軒轅	N	中台		fast				
8	1077	Oct. 14	220.2	-1.8°		+8.6 yrs	少尉	N		○	fast	B/W	○	like a cup	
9	1096	Oct. 16	222.4	+0.5°		-5.7 yrs	文昌		鉤陳	○	fast	R/Y	○	like a cup	
10	1403	Oct. 23	226.7	-0.1°		+3.4 yrs	太微西垣	E	五帝座			B/W		like an egg	
11	1420	Oct. 27	231.3	+4.4°		-12.8 yrs	內階	W	閣道			R	○		
12	1427	Oct. 23	226.5	-0.4°		-5.8 yrs	軒轅	SW	星	○		B/R	○	like a cup	
13	1430	Oct. 21	224.7	-2.2°		-2.8 yrs	中台	NE	北斗	○		B/R	○	like a cup	
14	1433	Oct. 24	228.0	+1.0°		+0.2 yrs	北斗	NW	紫微垣	○		R		like a cup	
15	1461	Oct. 24	227.8	+0.8°		4.8 yrs	文昌	NW	鉤陳	○		B/W		like a cup	
16	1066	Oct. 17	223.1	+1.3°		-2.4 yrs	參		天倉						
17	1096	Oct. 16	222.4	+0.5°		-5.7 yrs	柳		屏	○	fast	R/Y	○	like Venus	
18	1098	Oct. 18	223.9	+1.3°		-3.7 yrs	井		室	○	fast	R/Y	○	like Venus	
19	1408	Oct. 17	221.4	-5.4°		+8.4 yrs	太微西垣	E	太微	○		B/W		like a wineglass	
20	1519	Oct. 24	226.9	-0.6°		-13.3 yrs	下台	NE	招搖	○		R	○	like a wineglass	

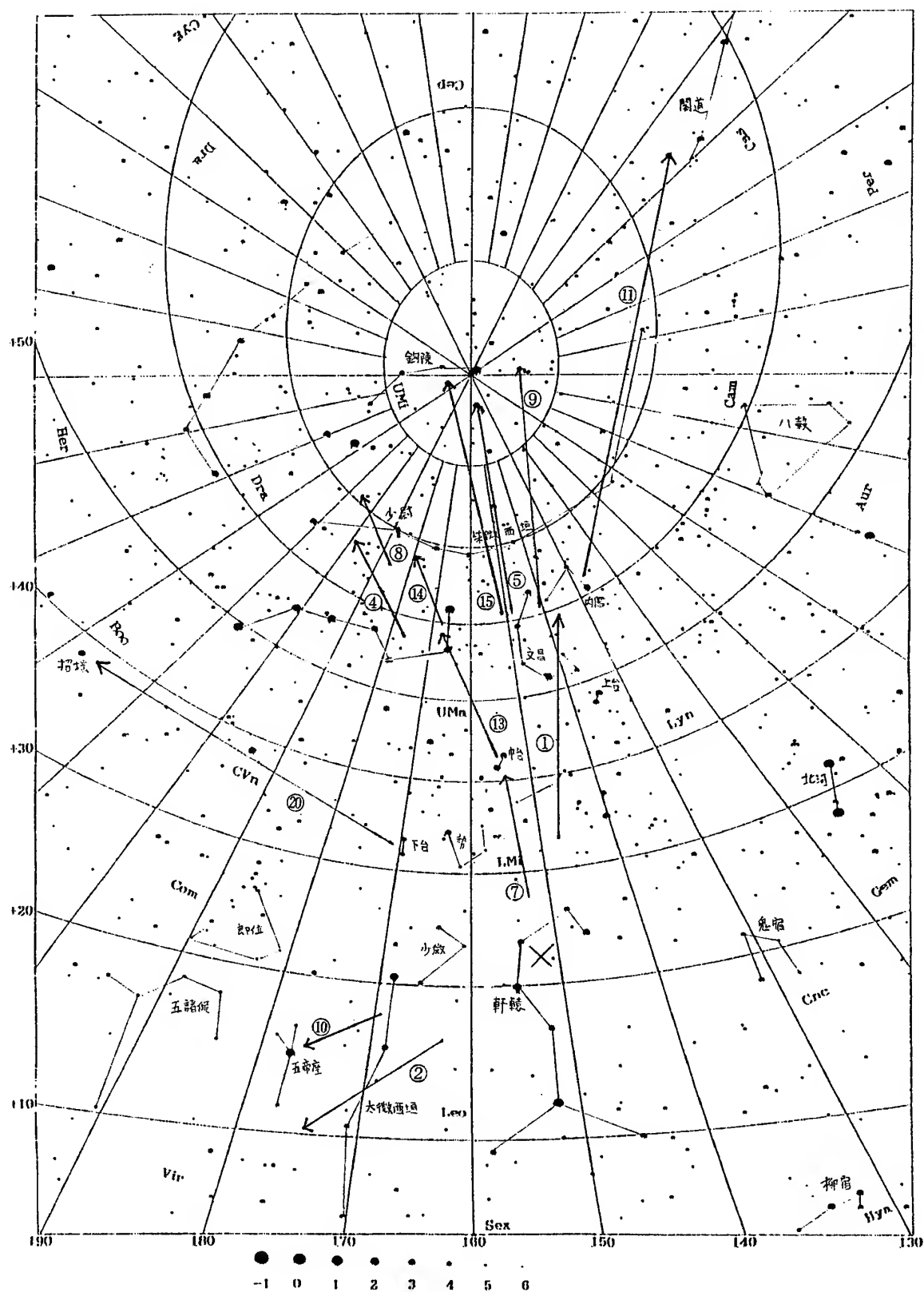


Figure 1a Paths of Leonid meteors

**Figure 1b** Paths of Leonid meteors

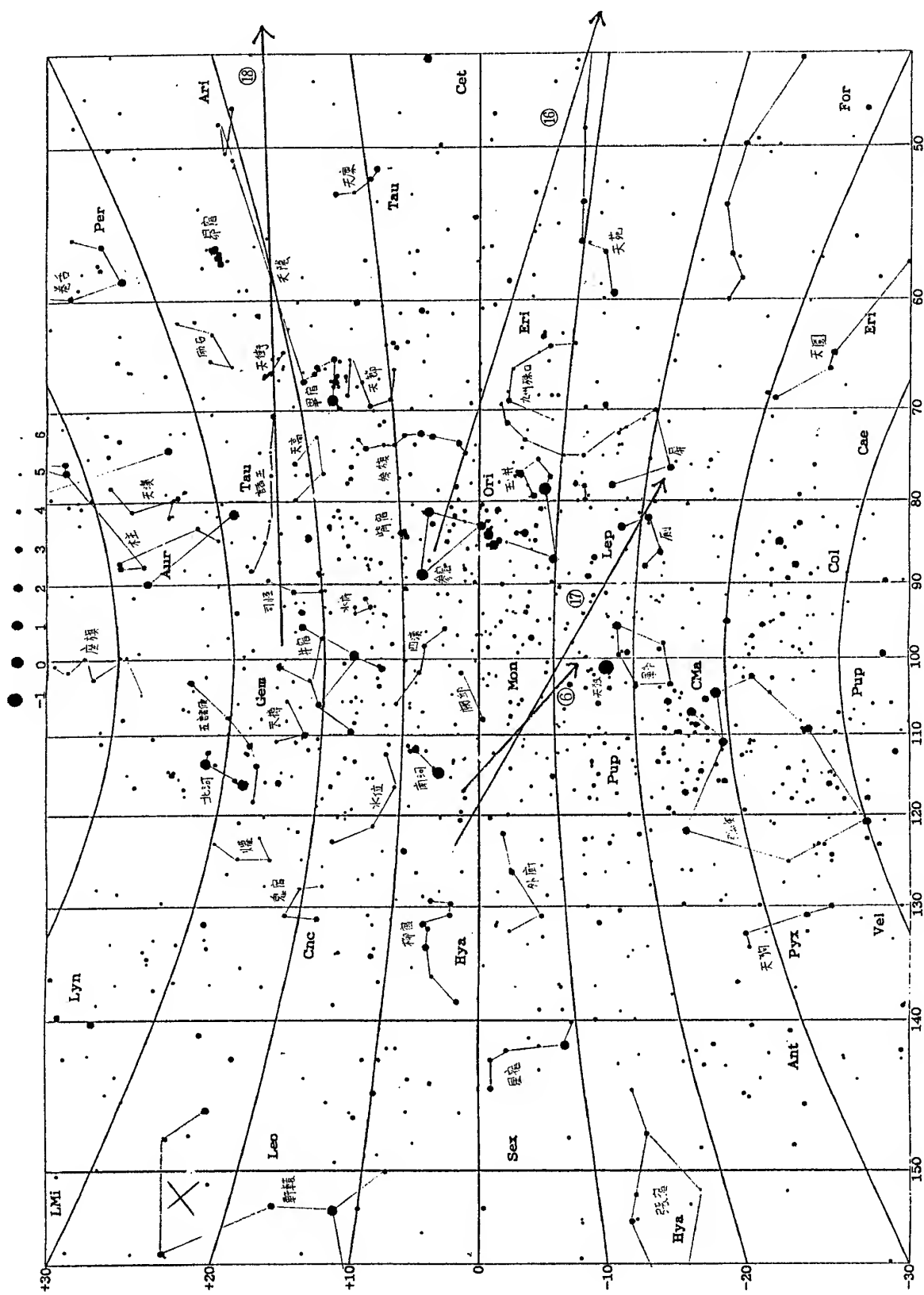


Figure 1c Paths of Leonid meteors

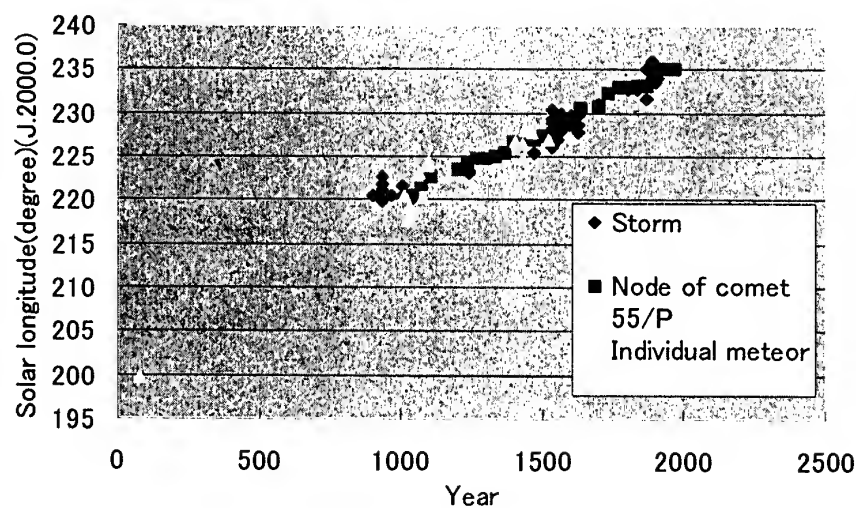


Figure 2

Table 2. Difference in longitude between node of the parent comet and meteor apparition

L-N (° )	<0.5	0.5~1.0	1.1~1.5	1.6~2.0	2.1~2.5	>2.5	Total
Number	6	1	5	3	2	3	20

perihelion. On the contrary, the relation between the activity of individual Leonid meteors and the perihelion passages of the parent comet can not be seen (Table 3).

Table 3. Difference in year between meteor apparition and perihelion passage of the parent comet

t - T(years)	<1	1~5	6~10	>10	Total
Number	5	6	5	4	20

Regarding to characters of individual Leonid meteors, a number of meteors were recorded as high speed (fast) and with a trail (or short train). It is well known that the velocities of the Leonid meteor are nearly 70km/s. More than half of meteors are extremely bright, and in the column of brightness in Table 1, ○ means that the record is remarked as “the ground has been lighted up”.

REFERENCES

1. Beijing Observatory, *General Compilation of Chinese Ancient Astronomical Records*, 1988

2. Hasegawa, I., *Highlight of Astronomy*, Vol.118, 1005, 1998

3. Imoto, S. and Hasegawa, I., *Smithon. Contr. Astrophys.* 2, 131, 1958

4. Hasegawa, I., *Meteoroids and their Parent Bodies*, ed. J. Stohl and I.P. Williams, Astron. Inst. Slovak Acad. Sci., 209, 1993

5. Biot, E., *Mem. de l'Acad. Sci. de l'Inst. Nat. de France* 10, 129, 1848

6. Astapovich, I.S. and Terenteva, A.K., *Physics and Dynamics of Meteors*, ed.: L. Kresak and P.M. Millman, Reidel, Dordrecht, 308, 1968

7. Hasegawa, I., *Meteoroids II* 1998, ed W.J. Baggaley and V. Porubcan, Astron. Inst. Slovak Acad. Sci., 153, 1999

8. Nakano, S., Private communication, 1997

## PERSISTENT LEONID METEOR TRAILS: TYPES I AND II

Jack D. Drummond<sup>1</sup>, Scott Milster<sup>1</sup>, Brent W. Grime<sup>1</sup>, David Barnaby<sup>1</sup>,  
 Chester S. Gardner<sup>2</sup>, Alan Z. Liu<sup>2</sup>, Xinzhaoh Chu<sup>2</sup>,  
 Michael C. Kelley<sup>3</sup>, Craig Kruschwitz<sup>3</sup>, and Timothy J. Kane<sup>4</sup>

<sup>1</sup>Directed Energy Directorate, Air Force Research Laboratory, Kirtland AFB, New Mexico

<sup>2</sup>Department of Electrical and Computer Engineering, University of Illinois, Urbana, Illinois

<sup>3</sup>Department of Electrical Engineering, Cornell University, Ithaca, New York

<sup>4</sup>Department of Electrical Engineering, The Pennsylvania State University, University Park, Pennsylvania

### ABSTRACT

A campaign to study the trails left behind by bright Leonid meteors was conducted in November 1998 and 1999. These mysterious lingering trails have been observed for up to an hour. Such persistence allowed a visual observer at the Starfire Optical Range on Kirtland Air Force Base, near Albuquerque, New Mexico, USA, to direct a sodium resonance laser, a CCD camera, and an intensified video camera to the trail within two minutes of the meteor's appearance. Subsequent study of this data has identified two kinds of trails, Type I and II, although both may be found in a single trail. Type I trails appear turbid, wider (1 km), and optically thicker than Type II trails, and show very high diffusion rates of  $800 \text{ m}^2 \text{ s}^{-1}$ . Type II trails are thin (100-200 m), smooth in appearance, and exhibit low diffusion rates of  $25 \text{ m}^2 \text{ s}^{-1}$ . Type I trails also have higher line emission rates, and Type II trails often appear parallel. This latter phenomenon is still unexplained.

Key words: Leonids; Meteors; Meteor Trails.

### 1. INTRODUCTION

Although known since the Leonids of 1866 [1], persistent meteor trains, or lingering trails, have remained a mystery because they are relatively rare and difficult to study in a planned and systematic way. They are characteristic of, but not unique to, the Leonid meteor shower. In 1998 and 1999, scientists gathered to mount a study specifically aimed at this elusive meteor phenomenon at the Air Force Research Laboratory's Starfire Optical Range, which is part of its Directed Energy Directorate on Kirtland Air Force Base outside of Albuquerque, New Mexico. As a result of this campaign we are now beginning to quantitatively understand the mechanism of light production, which involves the sodium airglow cat-

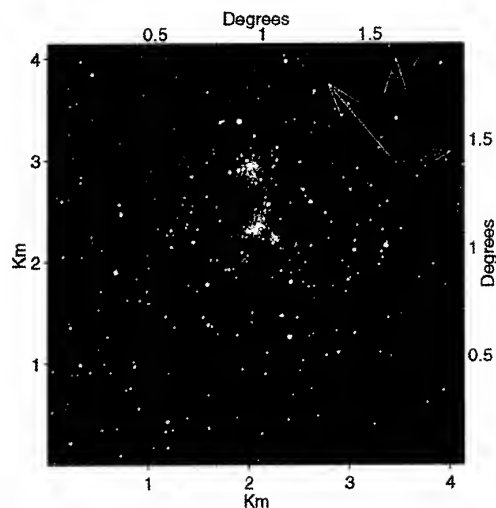


Figure 1. The Diamond Ring. A one second exposure of the lingering trail from a Leonid was taken 82 seconds after the appearance of a  $-1.5$  meteor over Albuquerque, N.M., at 2:28 MST on November 17, 1998. Marked arrows in all of the figures indicate the direction to North and to the zenith, and the unmarked arrow shows the length and direction of 1 km of the original trail. The laser from the sodium lidar can be seen coming in from the right, along the trail.

alytic cycle first proposed by [2]. However, while we have shown that the parallel Type II trails are not due to the long accepted explanation [3] of light production from the shell of a cylinder, at this point we still cannot explain this peculiar appearance.

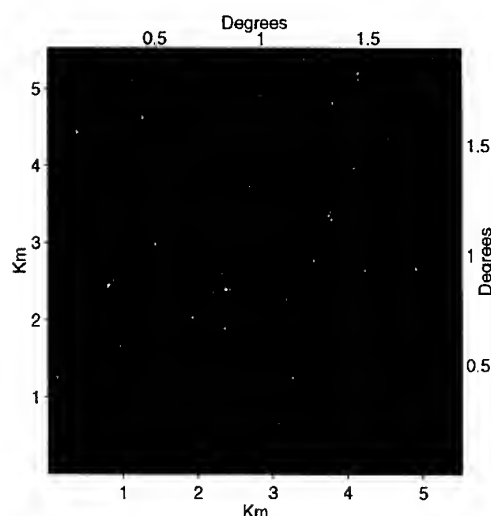


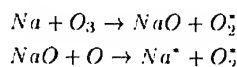
Figure 2. The Glowworm. Ninety four seconds after the appearance of a -14 magnitude fireball at 3:06 MST, Nov 17, 1998, the first one second exposure of its lingering trail was made. Subsequent images led to a determination of its diffusion coefficient of  $800 \text{ m}^2 \text{ s}^{-1}$ . The sodium lidar can be seen coming in from the left.

## 2. CAMPAIGN RESULTS

Initial results of the campaign [4,5,6,7], as well as in depth studies of individual trails [8,9,10,11], have been reported elsewhere. The trails have been given fanciful names to facilitate discussions about them. The Diamond Ring (Fig. 1), for example, looks exactly like a double ring with a diamond on top. Its double ring structure is a prime example of a Type II trail while its diamond is a Type I trail, although it is not as well developed as the Glowworm (below).

### 2.1. Photometry

Sodium airglow is produced by naturally occurring neutral sodium at  $\sim 95 \text{ km}$ , which catalyzes ozone into diatomic oxygen.



The reaction is exothermic, resulting in excited sodium (starred species above) that quickly decays to its ground state by emitting the familiar  $D$  line. When a meteor brings in a great amount of sodium, an enhancement of the  $D$  line in the ensuing trail persists because the sodium is not destroyed in the cycle. It is this mechanism which is responsible for the long lasting light visible to the naked eye. However, numerical models [9,12] show that the calculated flux from sodium is insufficient to explain the

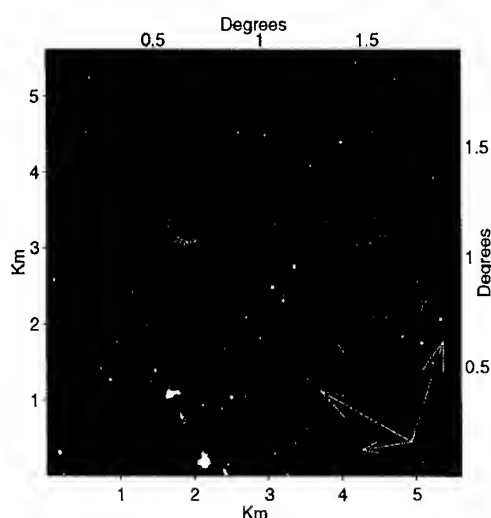


Figure 3. The Puff Daddy. Ninety eight seconds after a -2 magnitude Leonid meteor appeared at 3:05 MST on November 19, 1999, a lingering trail was first captured in a one second CCD exposure. Its 'puffs' are probably due to explosive events.

calibrated images of the trails in Figs. 1-4. Apparently enough excess energy is produced in the sodium catalytic cycle that not only is sodium excited but so is diatomic oxygen [13]. Both electronic and vibrational transitions occur in the infrared and contribute heavily to the appearance of the trails through our CCD cameras with sensitivities between  $0.5\text{-}1 \mu\text{m}$ . Although those transitions which terminate on the ground state should be absorbed by intervening oxygen, apparently there are still enough photons from oxygen to produce strong CCD images.

### 2.2. Morphology

Fig. 1 shows an image of the Diamond Ring, exhibiting both types of trails. Thirty three minutes after the Diamond Ring, a very bright fireball appeared, resulting in a lingering trail dubbed the Glowworm, shown in Fig. 2. It received its name because it appears as a snake or worm, and because the chemiluminescence that produces its light is similar to the 'cold light' of bioluminescence produced by organisms such as fireflies, or their larvae called glowworms. The Glowworm was well seen across northern New Mexico. A group at Los Alamos detected infrasound from the bolide and determined its mass to be  $550 \text{ gm}$  [12,14]. The Glowworm was exclusively a Type I trail.

Another Leonid meteor, this time from 1999, resulted in a lingering trail (Fig. 3) named Puff Daddy. Two images were obtained 98 and 118 seconds after its appearance, and led to a determination of the wind field at  $90\text{-}103 \text{ km}$  altitude. The residuals from the mean wind strongly imply that the appearance of the

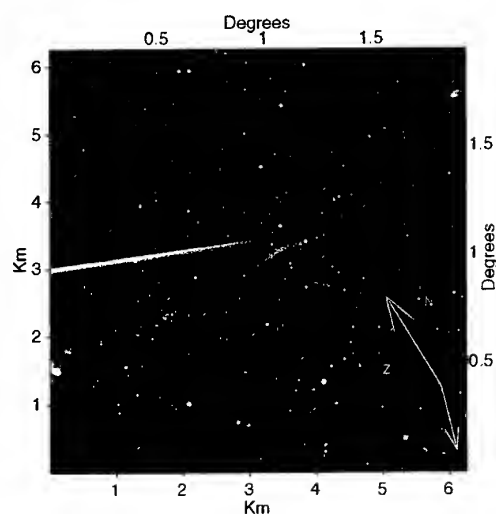


Figure 4. The French Curve. Eighty one seconds after the appearance of -1.5 meteor at 5:25 MST, Nov 19, 1999, its lingering trail became distorted into the shape of a draftsman's tool. The laser of the sodium lidar is the bright beam coming in from the left. The direction to North and to the zenith are the same.

trail is due to explosive events, helping to name the trail. Notice the peculiar Type II trail feature near the bottom of the image.

Later on the same night, a long, thin, exclusively Type II trail (Fig. 4) appeared after a -1.5 magnitude meteor. It only lingered to the naked eye for about five minutes, but lasted for twenty minutes in the intensified video camera. During this time, a portion of the trail formed a perfect French Curve, hence its name. This trail has yet to be studied in detail.

### 3. TYPE I AND TYPE II TRAILS

The parallel trail appearance of Type II trails cannot be the result of chemiluminescence in the outer shell of a cylinder, as proposed by [3]. In such a case, although the path through the shell at the edges of the cylinder is longer, and should produce limb brightening, because there is still light being emitted from the front and back of the cylinder the middle should not be completely dark. Fig. 5 illustrates the case for a cylinder with several different shell radii. The wider the shell, the brighter the middle should become.

For comparison, in Fig. 6 we show a close up of the Type II portions of the Diamond Ring and the Puff Daddy at the same scale. The scale in all of the images is determined from the sodium lidar, since it measures the distance to the trail in the same fashion as a radar. Inspection and measurements of Fig 6. reveal that the middle of the parallel trails is completely dark, despite the substantial widths of the visible trails. Thus, the trails are independent and

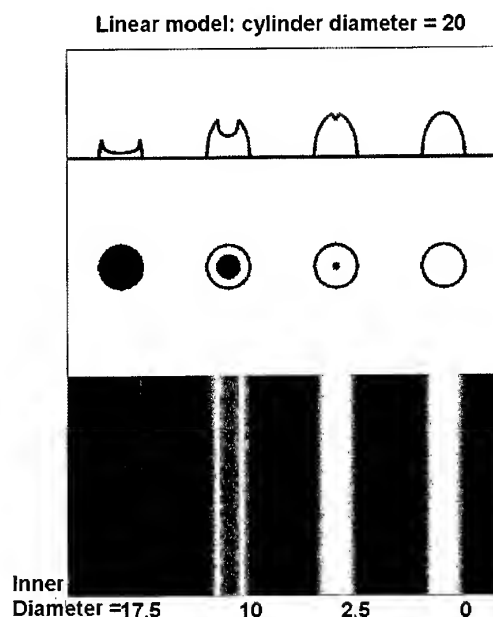


Figure 5. Shell burning in cylinder. At top are the intensity profiles of the cylinders below with light emitted from progressively larger (left to right) shells. The dimensions of the shell can be seen in white in the middle panel.

not the edge of a single cylinder, a conclusion also reached by [15].

For pictures and a video of a persistent trail made during the German expedition to Mongolia in 1998, go to the International Meteor Organization's video web site: <http://www.imo.net/video/vdemo5.html>. A video shows the development of an apparently Type II trail, although at its resolution it is not clear if the trail is beginning to split, or if it exhibits the expected limb brightening of a shell burning cylinder.

Qualitatively, Type I trails (the Glowworm, parts of the Diamond ring and parts of the Puff Daddy) are wide, bright, and show high diffusion rates compared to Type II trails (the French Curve, parts of the Diamond Ring, and parts of the Puff Daddy). Quantitatively, we have determined the diffusion rates at various portions of all of the trails, except the French Curve. We have also measured the total line emission rates ( $Le_t$ ) at the same places. Assuming cylindrical geometry, the line emission rate is the number of photons emitted in all directions per length of trail per second. As the trails diffuse, the line emission rate decays, but we can still determine  $Le_t$  at 90 seconds after ablation through interpolation or a small extrapolation in time.

Plotting  $Le_t$  at 90 s against the diffusion coefficient  $D$  in Fig. 7 shows that there is indeed a locus of points, and not a scatter between the two parameters. Trails with low diffusion rates have smaller total

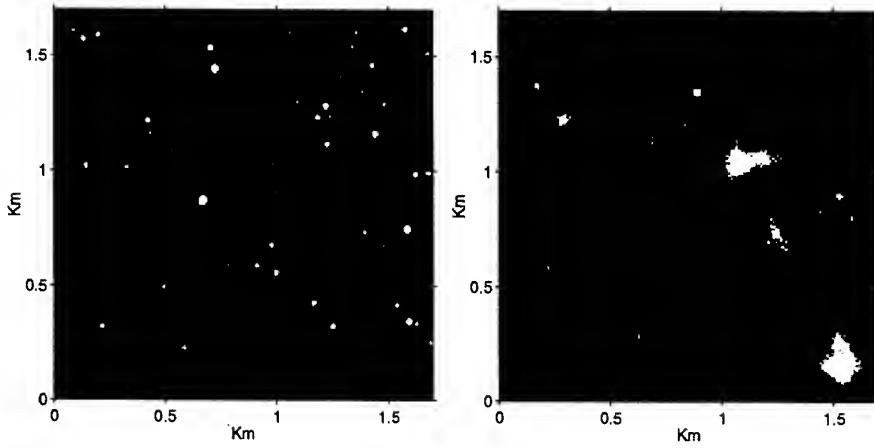


Figure 6. Close up of the Type II trail portions of the Diamond Ring (left) and the Puff Daddy (right), both to the same scale. Notice the complete darkness between the parallel trails.

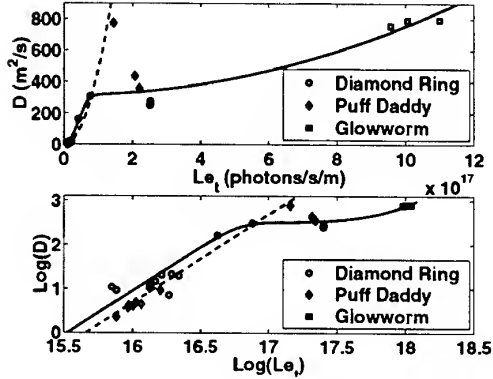


Figure 7. Diffusion as a function of total emission rate 90 seconds after ablation. In order to spread the data for better visibility, the bottom panel is a log-log plot of the top panel. The dashed line shows the trend for a linear fit of  $Le_t^2$  to the 16 lowest  $D$ 's. The highest Puff Daddy  $D$  is not included in the fits.

emission rates and  $D$  follows a linear trend with  $Le_t^2$ . However, for the parts of all three trails with higher diffusion rates and higher total emission, the relation changes, with the diffusion appearing to level off.

We can describe the relation between  $D$  and  $Le_t^2$  with a combination of a linear and a  $\tanh$  function

$$ALe_t^2 + B \tanh\left(\frac{Le_t^2}{C}\right) = D \quad 1$$

where the coefficients are given in Table 1.

#### 4. SUMMARY

Table II summarizes the distinction between Type I and Type II trails. The transition between the two,

Table 1. Eq 1 Coefficients

A	$4.4 \pm 0.3$	$(\times 10^{-34} \text{m}^4 \text{s photon}^{-2})$
B	$314 \pm 19$	$(\text{m}^2 \text{s}^{-1})$
C	$0.36 \pm 0.09$	$(\times 10^{34} \text{photon}^2 \text{m}^{-2} \text{s}^{-2})$

where both occur, is very sudden [10,11], less than a few km in altitude. While the parallel structure of some Type II trails is not due to shell burning in a cylinder, why the trail is split is still not known.

Table 2. Type I and II Trails

Type	I	II
Appearance	turbid, puffy	smooth, clean, often parallel
Width	wide, $\sim 1$ km	narrow, $< 200$ m
Optical thickness	thicker	thinner
Diffusion	up to $800 \text{ m}^2 \text{ s}^{-1}$	$< 25 \text{ m}^2 \text{ s}^{-1}$
Line emission @90s	$> 2.5 \times 10^{16} \text{ photons s}^{-1}$	$< 2.5 \times 10^{16} \text{ photons s}^{-1}$
Altitude	higher than II ?	lower than I ?

## 5. REFERENCES

- Lockyer, N., Editorial note, *Nature*, **1**, 58, 1869.
- Chapman, S., Notes on atmospheric sodium. *Astrophys. Journ.*, **90**, 309-316, 1939.
- Trowbridge, C.C., Physical nature of meteor trains. *Astrophys. Journ.*, **26**, 95-116, 1907.
- Chu, X., A. Z. Liu, G. Papen, C. S. Gardner, M. C. Kelley, J. Drummond, and R. Fugate, Lidar observations of elevated temperatures in bright chemiluminescent meteor trails during the 1998 Leonid shower, *Geophys. Res. Lett.*, **27**, 1815-1818, 2000.
- Grime, B. W., T. J. Kane, A. Liu, G. Papen, C. S. Gardner, M. C. Kelley, C. Kruschwitz, and J. D. Drummond, Meteor trail advection observed during the 1998 Leonid shower, *Geophys. Res. Lett.*, **27**, 1819-1822, 2000.
- Kelley, M.C., C. Gardner, J. Drummond, T. Armstrong, A. Liu, X. Chu, G. Papen, C. Kruschwitz, P. Loughmiller, B. Grime, and J. Engleman, First observations of long-lived meteor trains with resonance lidar and other optical instruments, *Geophys. Res. Lett.*, **27**, 1811-1814, 2000.
- Drummond, J., C. S. Gardner, and M. C. Kelley, Catching a falling star, *Sky Tel.*, **99**, 46-49, 2000.
- Drummond, J.D., B.W. Grime, C.S. Gardner, A.Z. Liu, X. Chu, and T.J. Kane, Observations of persistent Leonid meteor trails, 1. Advection of the 'Diamond Ring', *Journ. Geo. Res.*, in press, 2001.
- Kruschwitz, C. A., M.C. Kelley, C.S. Gardner, G. Swenson, A.Z. Liu, X. Chu, J.D. Drummond, B.W. Grime, W. T. Armstrong, J.M.C. Plane, and P. Jenniskens, Observations of persistent meteor trails, 2. Photometry and numerical modeling, *J. Geophys. Res.*, in press, 2001.
- Drummond, J.D., B.W. Grime, C.S. Gardner, A.Z. Liu, X. Chu, M.C. Kelley, Kruschwitz, C. A., and T.J. Kane, Observations of persistent meteor trails, 3. The 'Glowworm'. *J. Geophys. Res.*, submitted.
- Drummond, J.D., S. Milster, B.W. Grime, D. Barnaby, C.S. Gardner, A.Z. Liu, X. Chu, M.C. Kelley, Kruschwitz, C. A., and T.J. Kane, Observations of persistent meteor trails, 4. The 'Puff Daddy'. *J. Geophys. Res.*, in preparation.
- Zinn, J., J. Wren, R. Whitaker, J. Szymanski, D.O. ReVelle, W. Friedhorsky, J. Hills, G. Gisler, S. Fletcher, D. Casperson, J. Bloch, R. Balsano, W.T. Armstrong, C. Akerlof, R. Kehoe, T. McKay, B. Lee, M.C. Kelley, R.E. Spalding, and S. Marshall, Co-ordinated observations of two large Leonid meteor fireballs over northern New Mexico, and computer model comparisons. *Meteor. and Plan. Sci.*, **34**, 1007-1015, 1999.
- Hapgood, M.A., IR observation of a persistent meteor train. *Nature*, **286**, 582-583, 1980.
- ReVelle, D.O and R.W. Whitaker, Infrasonic detection of a Leonid bolide: 1998 November 17. *Meteor. and Plan. Sci.*, **34**, 995-1005, 1999.
- Jenniskens, P., D. Nugent, and J.M.C. Plane, The dynamical evolution of a tubular leonid persistent train. *Earth, Moon, and Planets*, **82-83**, 471-488, 2000.

# RADAR OBSERVATIONS OF THE 1999 AND 2000 LEONID METEOR STORMS AT MIDDLE EUROPE AND NORTHERN SCANDINAVIA

W. Singer (1), N. J. Mitchell (2), and J. Weiß (1)

(1) *Leibniz-Institut für Atmosphärenphysik an der Universität Rostock, D-18225 Kühlungsborn, Germany*

(2) *Department of Physics, University of Wales, Ceredigion SY23 3BZ, Wales, UK*

Email: [singer@iap-kborn.de](mailto:singer@iap-kborn.de), [njm@aber.ac.uk](mailto:njm@aber.ac.uk), [weiss@iap-kborn.de](mailto:weiss@iap-kborn.de)

## ABSTRACT

Observations of the 1999 and 2000 Leonid meteor storms made with all-sky meteor radars in Middle Europe (54°N) and northern Scandinavia (68°N) were analysed in terms of height-dependent meteor rates and entrance velocities. The 1999 Leonid meteor storm is characterised by a major activity peak on November 18 at 02h05m UT with a peak rate of about 1400 meteors/h. In contrast to the 1999 observations, we found three activity maxima for the 2000 Leonid storm. The first peak (160 meteors/h) was observed on November 17, 2000, at 08h15m UT related with the 1932 Leonid dust trail. The second well pronounced maximum (145 meteors/h) was detected on November 18 at 07h25m UT associated with the 1866 Leonid dust trail. The third broad activity event (about 100 meteors/h on average) was found on November 18 between 01h UT and 05h UT related with the 1733 Leonid dust trail. During both years the Leonid storm activity was dominant at altitudes above 100 km.

## 1. INTRODUCTION

Meteoroid streams with high dust flux rates generate meteor storms with spectacular displays of numerous persistent trails as seen with the Leonid storm of 1966 and the 1998 Leonids but the fireball activity in 1998 occurred 24 hours before the predicted storm peak. The improved model calculations in [1, 2] provided an optimistic forecast of the activity peak for the 1999 Leonids at about 02:08 ± 15 minutes UT on November 18. The improved peak forecast stimulated the observations of a meteor storm with modern radar experiments.

## 2. OBSERVATIONS AND TECHNIQUES

We report observations of height-dependent meteor rates and entrance velocities obtained during the 1999 and 2000 Leonid meteor storms. The observations were

made with all-sky meteor radars, SKiYMET systems [3], in Middle Europe at Juliusruh (54°38'N, 13°24'E) and in northern Scandinavia at Esrange (67°53'N, 21°06'E) near Kiruna. The distance between Juliusruh and Kiruna is about 1600 km. The radars apply crossed antenna elements to ensure a near uniform azimuthal sensitivity to meteor echoes. Both systems are all-sky meteor radars using a 5-antenna interferometer with circular polarized antennas on reception. The radar parameters are summarised in Tab. 1. We note that the system only detects meteor trails oriented perpendicularly to the radial direction from the radar to the meteor trail. A range accuracy of 2 km and angular accuracy of 1 to 2 degrees in meteor location were possible.

Tab. 1. Radar parameters for Leonid observations

Parameter	Juliusruh	Esrange
Frequency	32.55 MHz	32.5 MHz
Peak power	12 kW	6 kW
Coherent integrations	2	4
Pulse width	13 µs	13 µs
PRF	2144 Hz	2144 Hz
sample resolution	0.94 ms	1.88 ms
Height range	70 – 120 km	70 – 110 km

In the Leonids experiment at Juliusruh the objective was to locate as many meteors as possible as well as to determine entrance velocities. A two-point coherent integration was used in order to optimize the time resolution for entrance speed estimation, resulting in a sample resolution of 0.94 ms at a pulse repetition frequency of 2144 Hz. The radar was configured for a cut-off altitude of 120 km. About 200 Gbyte raw data were stored for a post-analysis of persistent trails.

The University of Wales Aberystwyth radar at Esrange was operating in a mode optimised for meteor drift measurements of mesospheric winds and so it did not reliably record meteors at heights greater than 110 km.

### 3. RESULTS

#### 3.1 1999 Leonid Meteor Storm

An overview of the 1999 Leonid storm at the radar sites Kiruna and Juliusruh is presented in Fig. 1 for the period from November 15, 22:00 UT to November 19, 10:00 UT. The peak of the storm is well expressed by the total meteor rates from the altitude range 70 to 120 km (bottom panel of Fig. 1) as well as by the meteor rates from altitudes above 100 km and by the time evolution of the measured entrance velocities above the level of sporadic meteors (top panel of Fig. 1).

The 1999 Leonid storm is characterised by one large activity peak at 02:05  $\pm$  5 minutes UT on November 18 estimated from 10-min means. The peak of the radar observations is in good agreement with the peak occurrence at 02:02  $\pm$  2 minutes UT obtained by a global analysis of visual observations [4]. The time evolution of the zenithal hourly rates is depicted in Fig. 1 (second panel from bottom). The radar peak as well as

the visual peak estimates are in excellent agreement with the model calculations [1] which relate the activity peak to the 1899 Leonid dust trail.

The storm phase lasts for about two hours from 01:00 to 03:00 UT. Only during that period meteors are detected above 100 km altitude and a peak altitude close to 110 km as shown by the height-resolved meteor rates in Fig. 2. Meteors with high entrance velocities (larger than the entrance velocities of sporadic meteors) are also confined to this time period. The second activity peak around 91 to 94 km in Fig. 2 is more related to the enhanced occurrence of sporadic meteors. At mid-latitudes south-eastward directed winds are observed above 95 km during the storm phase and north-westward directed winds are dominant below [5].

Radar observations at Kiruna and Juliusruh in combination with video observations in southern Spain clearly show quasi periodic variations of the meteor rate with temporal variations in the 6- to 9-min range [6]. Fig. 3 shows the in the activity profile observed at Juliusruh.

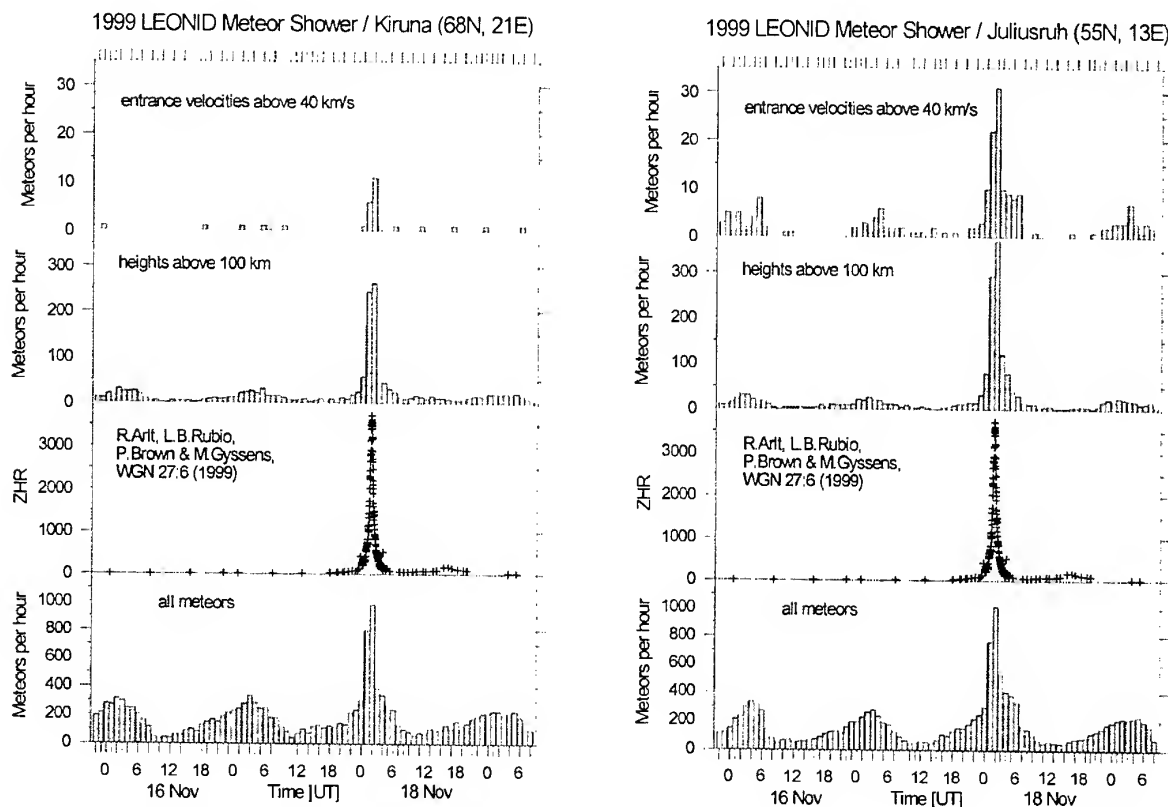


Fig. 1. Characteristics of the 1999 Leonid storm observed at the locations Kiruna and Juliusruh for the period November 15, 22:00 UT to November 19, 10:00 UT. The panels show from bottom to top: hourly means of the total meteor rate, the zenithal hourly meteor rates after global visual observations, hourly rates of meteors detected above 100 km, hourly rates of meteor with entrance velocities greater than 40 km/s.

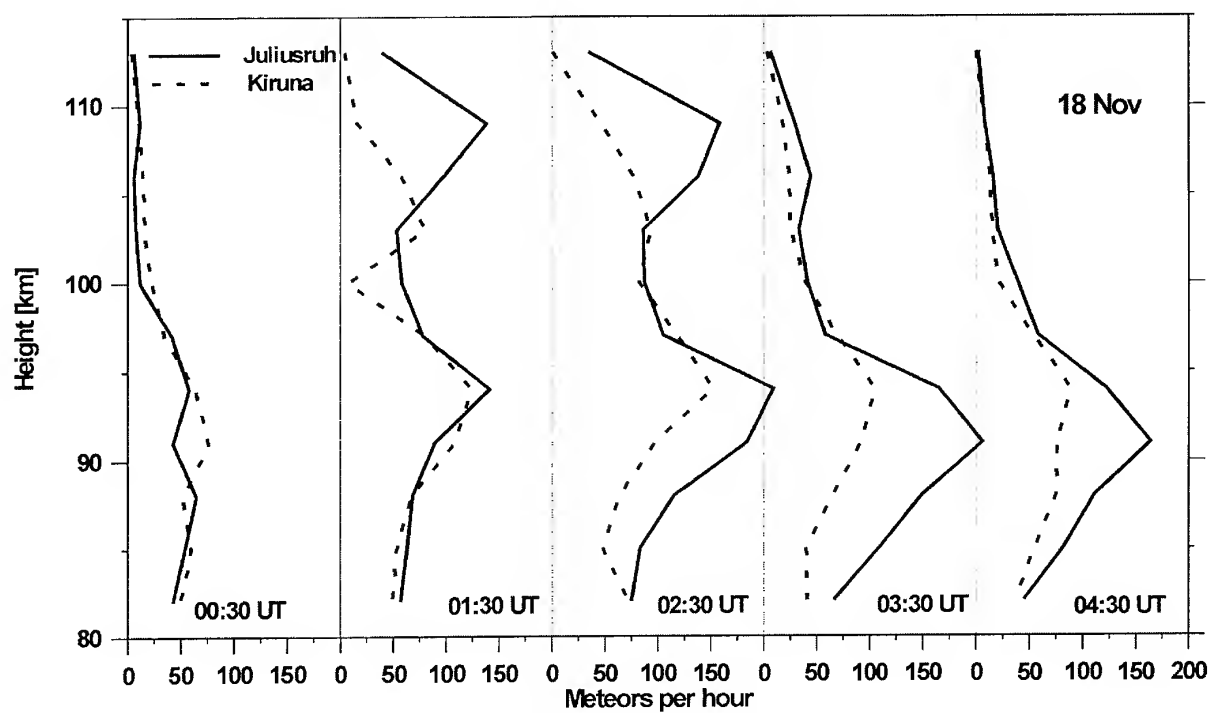


Fig. 2. Hourly meteor rates during the 1999 Leonid storm observed at Juliusruh and Kiruna on November 18.

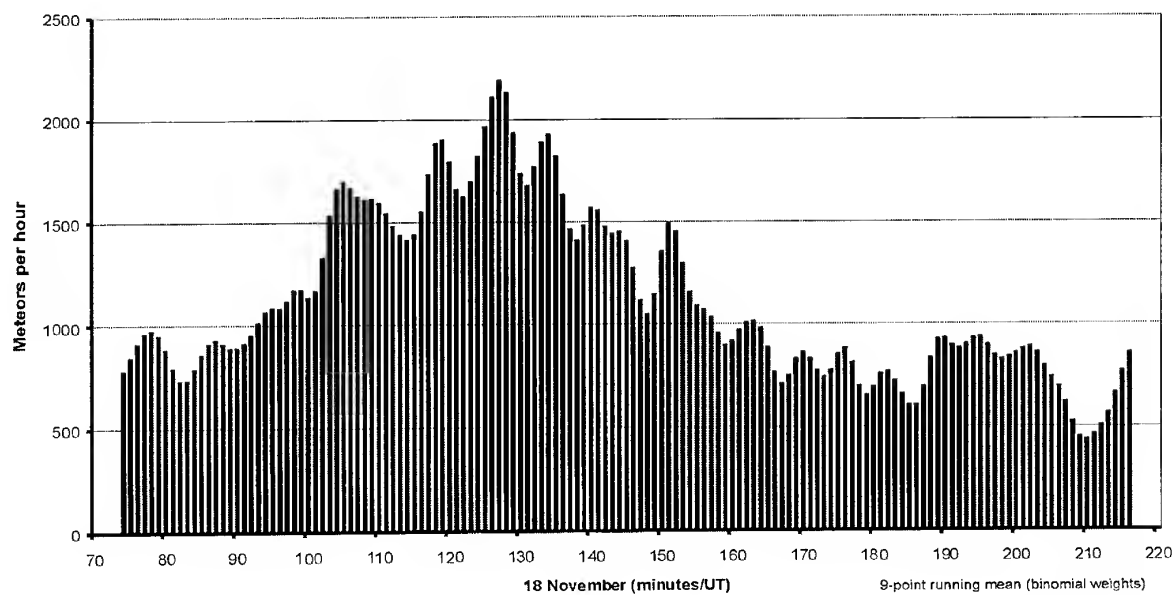


Fig. 3. High-resolved meteor rates versus UT time (minutes past 00:00 UT) at Juliusruh on November 18, 1999.

### 3.2 2000 Leonid Meteor Storm

In contrast to the 1999 storm the 2000 Leonid storm is characterised by three activity peaks which can be clearly identified only by the meteor fluxes at altitudes above 100 km and by the entrance velocities as shown in the 3<sup>rd</sup> and 4<sup>th</sup> panels of Fig. 4 by the measurements at both radar sites. The temporal variation of the total meteor rates is dominated by the daily variation of the meteor flux.

Along the meteor rates derived from the meteors detected at heights above about 100 km are in a clear relation with the predicted storm activities at 07:53 UT on November 17 after [7] and at 03:44 UT on November 18 after [8]. Three well pronounced activity peaks are observed by the Juliusruh meteor radar between November 17, 00:00 UT and November 18, 12:00 UT (Fig. 5). The meteor fluxes are estimated with 10-min resolution and are shown together with the zenithal hourly rate profile obtained from global visual observations [8]. The peak estimates after radar and visual observations are summarised in Tab. 2.

The first activity peak related with the 1932 Leonid dust trail was found on November 17 at 08:15 UT with a meteor rate of about 160 meteors per hour. The other

Tab. 2. Activity peaks of the 2000 Leonid storm

	Radar	Visual [9]
Nov. 17	08:15 UT $\pm$ 5 min	08:07 UT $\pm$ 15 min
Nov. 18	03:35 UT $\pm$ 5 min	03:24 UT $\pm$ 15 min
Nov. 18	07:25 UT $\pm$ 5 min	07:12 UT $\pm$ 15 min

two activity events were observed on November 18. A broad activity peak with about 100 meteors per hour occurred between 01:00 and 04:00 UT (1733 meteor dust trail) and a well pronounced activity peak of about 145 meteors per hour was detected at 07:25 UT associated with the 1866 Leonid dust trail. The activity peaks by the radars are in good agreement with the visual observations [9].

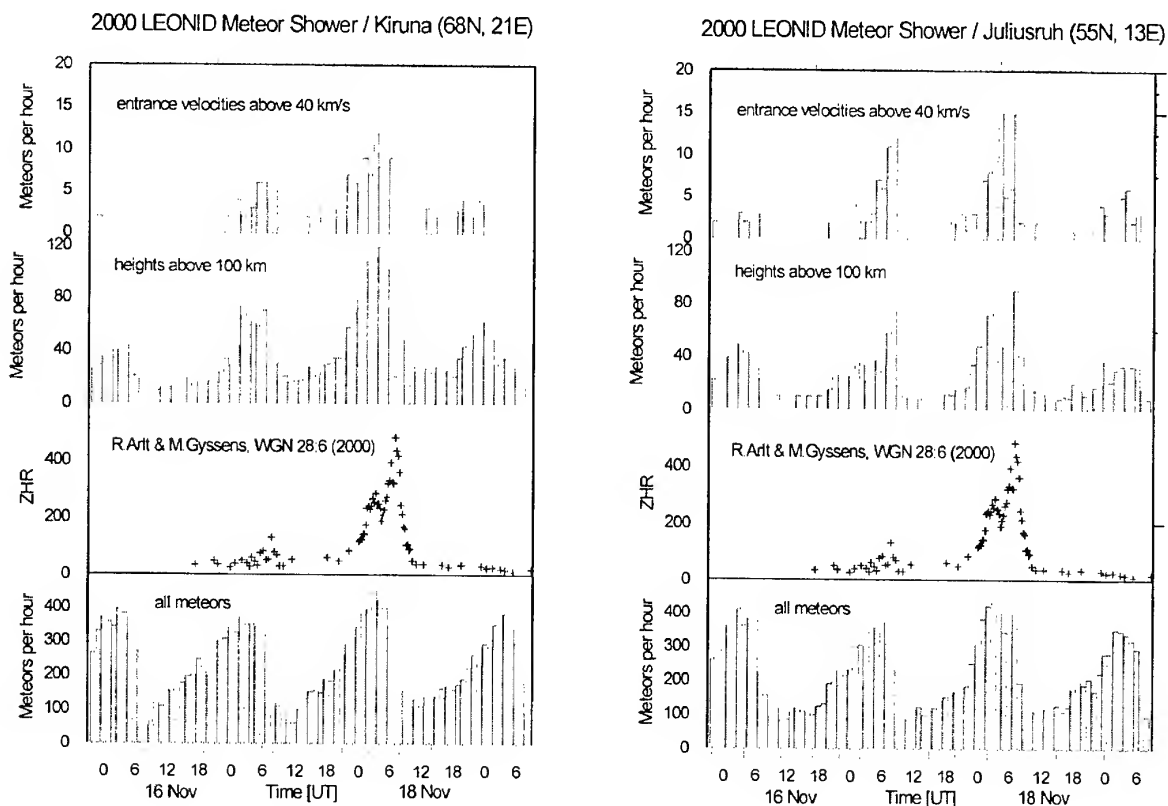


Fig. 4. Characteristics of the 2000 Leonid storm observed at the locations Kiruna and Juliusruh for the period November 15, 22:00 UT to November 19, 10:00 UT. The panels show from bottom to top: hourly means of the total meteor rate, the zenithal hourly meteor rates after global visual observations, hourly rates of meteors detected above 100 km, hourly rates of meteor with entrance velocities greater than 40 km/s.

## 2000 LEONID Meteor Shower / Juliusruh (55N, 13E)

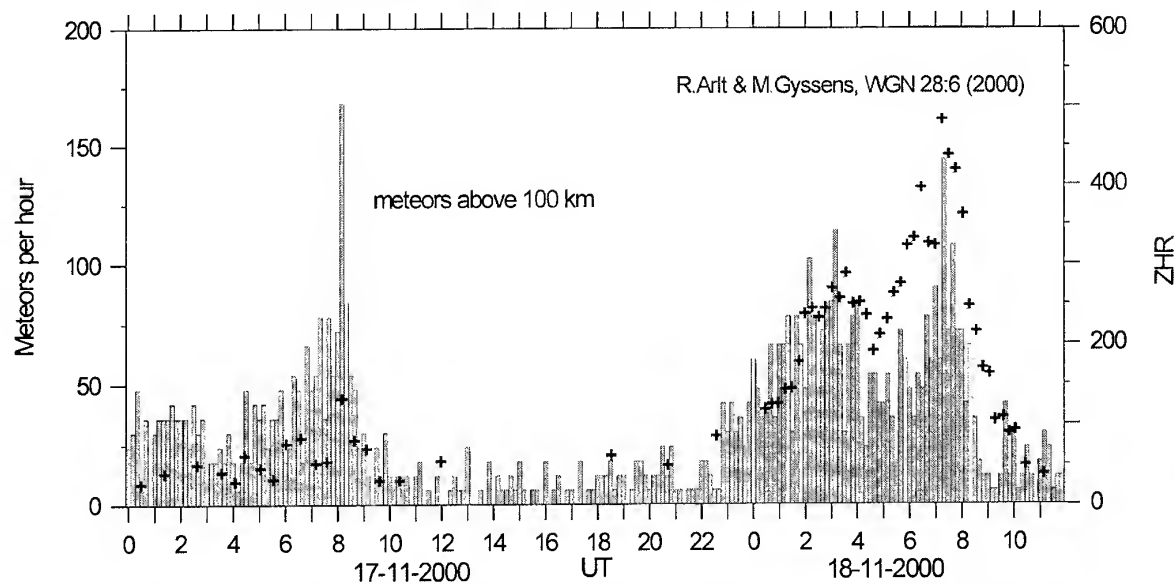


Fig. 5. High-resolution meteor fluxes (10-min means) observed with the Juliusruh meteor radar together with the evolution of the zenithal hourly rate (ZHR) obtained from global visual observations (crosses).

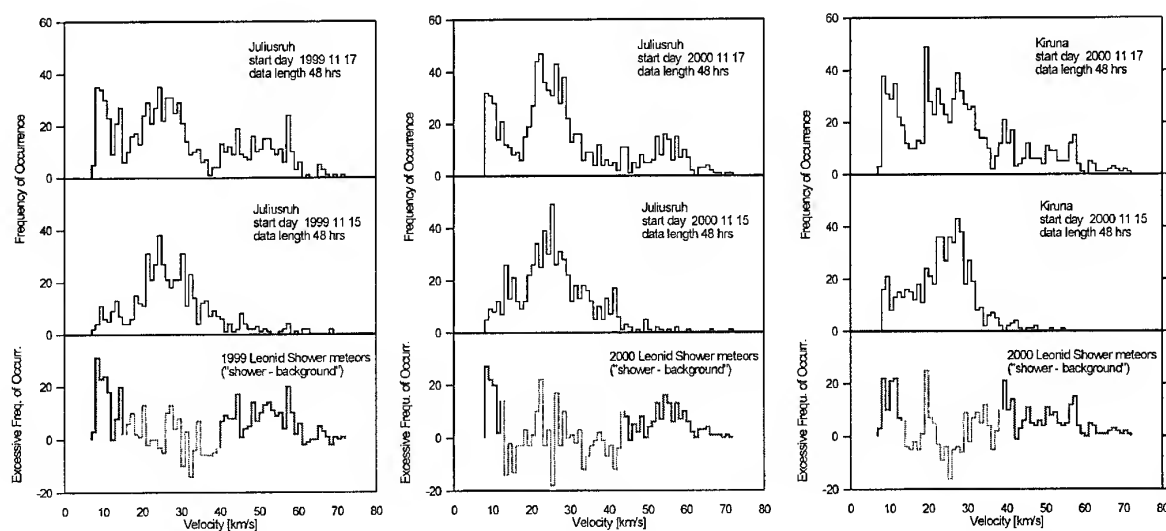


Fig. 6. Distributions of the meteor entrance velocities observed at Juliusruh and Kiruna during the 1999 and 2000 Leonid storms (for details see text).

## **Physics and Chemistry of Meteors**

# PHYSICS AND CHEMISTRY OF METEOROIDS IN THE UPPER ATMOSPHERE

Edmond Murad\*

Air Force Research Laboratory, Space Vehicles Directorate, Hanscom AFB, MA 01731-3010, U. S.A.

## ABSTRACT

Meteoroids entering the Earth's atmosphere are heated by collisions with the atmospheric gases, and at  $\sim 120$  km reach temperatures at which evaporation can begin. For meteoroids  $< 1000 \mu\text{m}$  in diameter heating is uniform and evaporation proceeds according to thermodynamic equilibrium. A summary is presented of the uncertainties that hinder accurate modeling efforts, namely meteoroid composition, velocities, and size distribution.

Key words: meteoroids; upper atmosphere; meteors.

Table 1. Regular meteor showers - data taken from the International Meteor Organization website ([www.imo.org](http://www.imo.org))

Shower	v(km/s)	r	ZHR	Dates
Quadrantids	41	2.1	120	01-05 Jan
$\eta$ -Aquarids	66	2.7	60	19 Apr-28 May
Perseids	59	2.6	200	17 Jul-24 Aug
Orionids	66	2.9	20	2 Oct-27 Nov
Leonids	71	2.5	40+	14-21 Nov
Geminids	35	2.6	110	7-17 Dec
Ursids	33	3.0	10	17-26 Dec

## 1. INTRODUCTION

Of the approximately  $40 \times 10^6$  kg/year of extraterrestrial matter that is captured by Earth the great majority consists of particles having a size distribution with a maximum at diameter  $\sim 200 \mu\text{m}$ . This size distribution is based on analysis of the *Long Duration Exposure Facility* (LDEF) results carried out by Love & Brownlee (1993). This topic, the flux of extraterrestrial dust, will be discussed further in a later section. Suffice it to say at this point that this extraterrestrial dust enters the Earth's atmosphere at velocities that vary between  $\sim 12$  and  $\sim 72$  km/s, depending on whether it is cosmic dust background or meteoric dust. Some of this dust evaporates as its temperature rises due to momentum transfer by collisions with atmospheric gases. The amount of evaporated material, the altitude at which evaporation occurs, and the reactions that it undergoes depends critically on the entry velocity, on the density of the material, composition, and entry angle. These points will be discussed in this article. By way of introduction, Table 1 shows an abbreviated list of the most intense meteor showers and their parameters. In this table  $v$  is the velocity,  $r$  a constant that essentially measures the quality of the visually-observed meteor, and  $ZHR$  the zenithal hourly rate.

## 2. PHYSICAL PROPERTIES

### 2.1. Flux

Hughes (1978) analyzed data from visual and radar observations and derived a value for the total flux of meteoric matter to Earth to be  $16 \times 10^6$  kg/year. Later, Love & Brownlee (1993) studied LDEF exposure plates for particle impact and measured the depths and sizes of pits formed by impact and some chemical analysis. This data was then integrated into a framework that assumed a distribution of particle velocities, densities, and direction of impact. When all of this was done Love & Brownlee (1993) derived a mass distribution of extraterrestrial matter that has a peak at  $1.5 \times 10^{-5}$  gm (assuming a density of  $\sim 3 \text{ gm/cm}^3$  this corresponds to a particle having a diameter of  $\sim 200 \mu\text{m}$ ). The total flux to Earth surface was derived to be  $(40 \pm 20) \times 10^6$  kg/year. In comparison, lidar data [Kane & Gardner (1993)] were used to derive a value of  $(2 \pm 0.6) \times 10^6$  kg/year. Later analysis of visual, radar, and collections [Ceplecha et al. (1998)] concluded that the total influx to Earth is  $(40 \pm 0.6) \times 10^6$  kg/year. Recently, however, Janches et al. (2000) and Mathews et al. (2001) have reexamined the question of influx in light of the sporadic meteor observations at the Arecibo Observatory using the 430 MHz radar. The dataset examined by Mathews et al. (2001) consisted of 8034 radar echoes recorded during 1997 and 1998. Under the influence of this dataset and

\*Email: ed.murad@hanscom.af.mil

of the analysis by Ceplecha et al. (1998), Mathews et al. (2001) re-analyzed the LDEF data used by Love & Brownlee (1993) using more realistic velocities (50 km/s instead of 16.9 km/s) and came to the conclusion that the total influx based on the LDEF data is  $1.8 \times 10^6$  kg/year. The Arecibo Observatory data yield  $(1.6 - 2.7) \times 10^6$  kg/year.

## 2.2. Velocities

Modern radars, such as the Arecibo Observatory [Janches et al. (2001)], EISCAT [Pellinen-Wannberg et al. (1998)], MU-radar [Nishimura et al. (In Press)], and AMOR [Baggaley et al. (1997)] have such high sensitivities that, in principle, the velocity should be accurately determinable. The majority of incoming extraterrestrial matter arises from the dust background, which represents the slowest component of extraterrestrial matter. None the less, an accurate determination of meteoroid velocity distribution is needed in order to develop realistic models of the phenomenology of meteoroids entering the Earth's atmosphere. The measurements reported by Janches et al. (2001), mentioned above, are averaged over the period 1997/1998. The 1997 measurements seem to show a trimodal distribution with the largest peak at  $v \sim 50$  km/s and two smaller peaks at  $\sim 15$  km/s and  $\sim 35$  km/s. The 1998 measurements seem to show a bimodal distribution with the main peak at  $\sim 60$  km/s and a smaller one at  $\sim 15$  km/s. It remains to be seen whether there is a selection process in the technique that influences the observations. Suffice it to say that these measurements, if substantiated, would imply that heating and subsequent evaporation occur at higher altitudes (close to 140 km).

## 2.3. Composition

It is common to use the CI-chondrite composition as a basis for modeling meteor ablation. However, it bears repeated stress that meteorites are associated with asteroidal fragmentation for the most part while the meteoric phenomena are associated with comets. Table 2 below, presents an average of the CI-chondrite composition as given in three standard references. Also given are the elemental composition obtained from the Giotto mission to Comet P/Halley. We see that there are significant differences. A recent study of the spectra of Leonid meteors [Borovička et al. (1999)] suggests that the composition of the Leonids is close to that of CI-chondrites. Thus, there is an uncertainty associated with the appropriate composition that is needed for modeling. It is to be hoped that a ground-based spectral study of the Orionids (associated with Halley's comet) will reveal whether there are differences that arise from the observation vehicle. Also very useful, would be a ground-based spectral study of the Geminids, which are attributed to the asteroid Phaeton. Data from the future *Rosetta* mission that will rendezvous with

Table 2. Comparison of elemental abundances of CI-Chondrites and Comet P/Halley. Si is arbitrarily taken to be  $10^6$ .

Element	Abundances	
	Avg. CI-Chondrite <sup>a</sup>	Halley Dust <sup>b</sup>
Na	$5.9 \times 10^4$	$5.4 \times 10^4$
Mg	$1.06 \times 10^6$	$5.4 \times 10^5$
Al	$8.5 \times 10^4$	$3.6 \times 10^4$
Si	$10^6$	$10^6$
S	$4.8 \times 10^5$	$3.9 \times 10^5$
K	3750	1080
Ca	$5.9 \times 10^4$	$3.4 \times 10^4$
Fe	$8.8 \times 10^5$	$2.8 \times 10^5$

<sup>a</sup>Values given represent average of those given in 3 standard references Mason (1971); Sears & Dodd (1988); Lodders & Fegley (1998)

<sup>b</sup>Grün & Jessberger (1990)

Comet P/Wirtanen [Verdant & Schwehm (1998), the current *Near Earth Asteroid Rendezvous - NEAR* mission and the *STARDUST* mission [Brownlee et al. (2000)], and the dust instrument, SPADUST, on the *ARGOS* satellite [see preliminary results in Tuzzolino et al. (2001a) and Tuzzolino et al. (2001b)] will be very helpful in resolving some of these questions.

## 2.4. Size Distribution

This topic has already been alluded to in the discussion of the flux. The most reliable study has, until recently, been based on analysis of the LDEF data [Love & Brownlee (1993)], where the peak distribution occurs for particles having a diameter  $\sim 200$   $\mu$ m (based on assuming a density of 3 g/cm<sup>3</sup>). The analysis presented by Ceplecha et al. (1998) suggests that the maximum diameter is  $\sim 80$   $\mu$ m. The observations made by Mathews et al. (2001) are for the most part made on much smaller particles.

## 2.5. Density

The consensus of the nature of the cometary fragments that produce meteoric phenomena is that they are "dustballs" consisting of small meteoroids held together by a matrix of relatively volatile materials, such as ice and frozen organic matter [Whipple (1943), Öpik (1958)]. When these "dustballs" enter the Earth's atmosphere, the initial heating melts the ice and the organic matter releasing the meteoroids [for a full discussion see textbooks by Öpik (1958) and Bronshten (1983)]. There is agreement that the density of the small meteoroids that are released by the melting of the matrix is  $\sim 3$  g/cm<sup>3</sup>. That is the figure that is used in almost all the modeling efforts.

### 3. DISCUSSION

#### 3.1. Heating

Öpik [Öpik (1936a), Öpik (1936b), Öpik (1936b)] seems to have made the first attempt at developing a theory for the heating of meteoroids by collision with atmospheric species. His work preceded slightly a similar study by Whipple [Whipple (1943)]. A number of studies, in addition to those cited, have been undertaken with the idea of conducting *ab initio* analysis of the heating and evaporation of meteoroids in the upper atmosphere [Jones & Kaiser (1966), Lebedinets (1973), Hawkes & Jones (1975), Nicol et al. (1985), Fyfe & Hawkes (1986), Flynn (1989), Love & Brownlee (1991), and McNeil et al. (1998)]. More recently *monte carlo* techniques have been applied to the problem [Popova et al. (2000); Boyd (2000)]. However, these treatments are limited to the larger sizes where the mean free path (accounting for the pressure buildup due to ablation) is  $<$  the radius of the meteoroid (depending on the velocity and meteoroid composition, this radius may be 0.01-1 cm). In this case a vapor screen is established and helps the meteoroid to keep its physical integrity if the meteoroid is a homogeneous solid, such as one of the rare Fe-Ni meteorites [Cf. Mittlefehldt et al. (1998)]; for the majority of the larger meteoroids, however, this scenario is not true as they are composed of "dustballs" held by a volatile binder, as discussed by Öpik (1958). For the purpose of this review, we will follow the analysis given by Jones & Kaiser (1966) and Love & Brownlee (1991).

Collisions with atmospheric molecules cause meteoroids to be heated by momentum transfer. As the meteoroids are heated they begin to radiate heat, first in the infrared and as the temperature continues to increase, in the visible region of the spectrum. By the time the latter even occurs, a variety of thermodynamic processes will have taken place:

- Solid state reactions, including transition from silicate phases to oxide phases;
- Evaporation of the more volatile products of the phase transitions, e.g.  $O_2$  and  $CO_2$ , especially if carbonates are present;
- Continued heating leads to further phase changes from solid oxides to gas-liquid equilibria, with consequent evaporation of low-boiling point metals, such as sodium and potassium;
- Continued heating leads to decomposition of the refractory metals oxides, such as  $CaO$  and  $MgO$ , followed by partial evaporation of the metals, e.g.  $Ca$  and  $Mg$ ;
- Cooling due to ablation of material (loss of heat of vaporization); and
- Radiative cooling.

Assuming that the meteoroid is spherical in shape and that it is not rotating, the energy balance *per unit surface area* for these processes is given by Equation 1 [The reader is referred to the original work of Jones & Kaiser (1966) and to the excellent presentation by Bronshten (1983) for details]

$$\frac{1}{2}\Lambda\rho_a v^3 = 4\sigma\epsilon(T_s^4 - T_a^4) + \frac{4}{3}R\rho_m C \frac{dT_m}{dt} \quad (1)$$

The left side of equation 1 represents the heating due to momentum transfer; the right side represents the cooling term, which itself consists of two terms: the first representing energy loss by radiation, and the second representing energy lost due to internal heat changes (phase transitions, evaporation, and heat capacity).  $\Lambda$  is the fraction of the total kinetic energy of the air molecules that is transferred to the meteoroid,  $\rho_a$  the atmospheric density,  $v$  the meteoroid velocity,  $\sigma$  Stefan's constant,  $\epsilon$  the emissivity of the meteoroid at temperature  $T$ ,  $T_s$  the surface temperature of the meteoroid,  $T_a$  the temperature of the ambient atmosphere,  $R$  the initial meteoroid radius,  $\rho_m$  the meteoroid density,  $C$  the meteoroid specific heat,  $T_m$  the mean temperature, and  $t$  the time. There are two limiting cases for Equation (1):

- The radius of the meteoroid is so large that the radiative losses are negligible. In this case phase transitions and evaporation occurs. Jones & Kaiser (1966) calculated this to be for  $R \geq 1 \mu m$  radius.
- The radius of the meteoroid is very small and the radiative losses are much more important than the thermochemical effects. In this case the meteoroid stays cold and does not evaporate. Jones & Kaiser (1966) calculated this to be for  $R \leq 0.1 \mu m$  radius.

Figure 1 shows a plot of the calculated temperature for a 10 mg particle entering the atmosphere at a velocity of 15 km/s. The density is assumed to be  $3 g/cm^3$ . This figure is similar in nature to the family of curves that are given by Bronshten (1983)[p. 58] for different particle sizes and speeds. The loss of

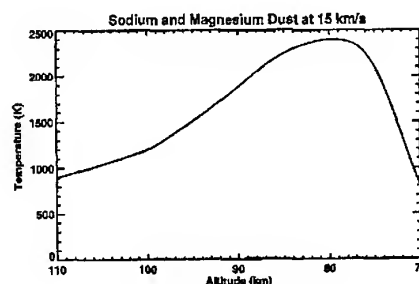


Figure 1. Calculated temperature profile for a 10 mg meteoroid, assuming a density of  $3 g/cm^3$  and an incoming velocity of 15 km/s.

mass as a function of time is given by Equation 2

$$\frac{dm}{dt} = 4\pi r^2 C p_v \sqrt{\frac{M}{T}} \quad (2)$$

where  $m$  is the meteoroid mass,  $t$  time,  $r$  the radius,  $C$  a proportionality constant,  $p_v$  the vapor pressure,  $M$  the average molecular weight, and  $T$  the temperature. Figure 2 shows a plot of the calculated mass loss for a hypothetical 10 mg particle consisting of sodium and magnesium and entering the atmosphere at 15 km/s. The important points to notice are that

- For the velocity, mass, and density in question, the meteoroid does not slow down appreciably until 85 km altitude.
- Sodium disappears almost completely by the time the meteoroid descends to 80 km.

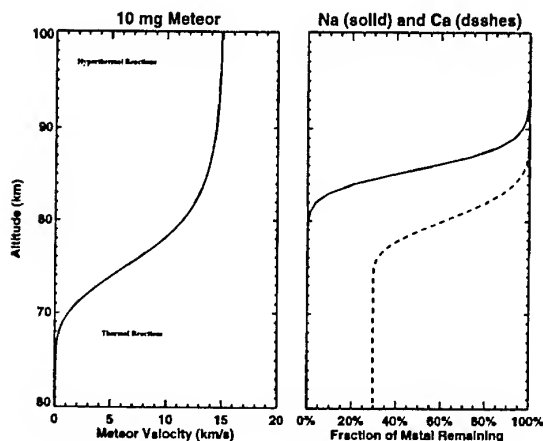


Figure 2. The left figure shows the calculated velocity profile for a 10 mg meteoroid entering the atmosphere at 15 km/s and assuming a density of 3 g/cm<sup>3</sup>. The right figure shows the loss of sodium and calcium as a function of altitude, using the vapor pressures given by Fegley & Cameron (1987)

At higher incoming velocities, the heating of the meteoroids begins at higher altitudes, with consequent deposition of the vapor and deceleration beginning earlier. Figure 3 shows the same calculation for a meteoroid entering the Earth's atmosphere at 30 km/s. It is clear that now the meteoroid will not have slowed appreciably until it is below 80 km; in the meantime it will have lost all of the sodium and a substantial part of the calcium.

Of course an important assumption in all this discussion is that the meteoroid had reached thermal equilibrium (i.e. *uniform temperature*) by the time the temperature is high enough for evaporation to occur. The problem is actually quite complex, and several attempts have been made to evaluate the limitation that thermal conductivity imposes on the uniformity of temperature in a meteoroid entering the

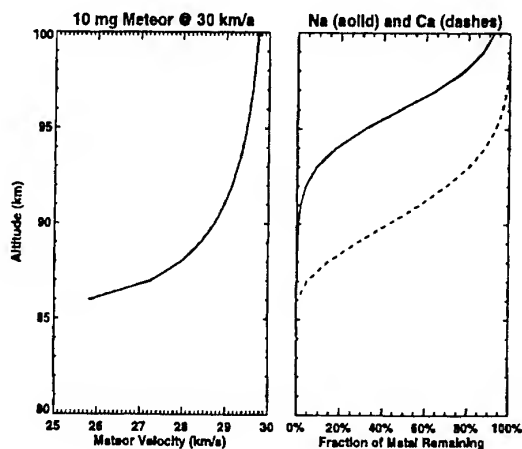


Figure 3. The same conditions specified in Figure 2, except that the meteoroid velocity is 30 km/s.

Earth's atmosphere. The problems arise from having to make assumptions about the shape of the meteoroid (spherical or fractal), its composition (stony or iron), its entry velocity (speed and direction), and whether it is rotating or not. A spherical particle is more likely to reach a high temperature and be thermally-equilibrated than a fractal particle whose surface area-to-volume ratio is much larger. Similarly, a stony meteoroid (with poor thermal conductivity) is not likely to be at thermal equilibrium as a iron meteoroid of the same size. And, finally, a rotating meteoroid is more likely to be at thermal equilibrium than a non-rotating meteoroid. Öpik (1937) was the first to attempt a theoretical treatment of these questions. Later studies [Whipple (1950); Whipple (1951); Öpik (1958); Jones & Kaiser (1966); Flynn (1989); and Love & Brownlee (1991)] have consistently shown that for certain sizes of meteoroids, thermal equilibration occurs rather quickly. For example, Jones & Kaiser (1966) calculated a limiting radius of 100  $\mu$ m for meteoroids with uniform temperatures; in other words, if  $R \geq 100 \mu$ m, there is a temperature gradient across the meteoroid, while if  $R \leq 100 \mu$ m the temperature of the meteoroid is uniform.

### 3.2. Evaporation

As the meteoroid heats and the silicate phases are reduced to oxide phases and the latter begin to melt, the low-boiling elements begin to ablate. One can calculate the vapor pressures of these elements from well known thermodynamic data, such as the NIST-JANAF Tables [Chase, Jr. (1998)]. An example is shown in Table 3 in which the equilibrium vapor pressures of Na, Mg, and Ca are presented at several temperatures. It is probably worth dwelling on this subject because it is important to the proper calculation of vapor pressures for modeling purposes. There

Table 3. Calculated equilibrium vapor pressures of Na, Mg, and Ca. Pressures are given in atmospheres.

T (K)	$P_{Na}$	$P_{Mg}$	$P_{Ca}$
1000	$5.8 \times 10^{-12}$	$4.1 \times 10^{-19}$	$1.3 \times 10^{-21}$
1200	$5.1 \times 10^{-9}$	$8.1 \times 10^{-15}$	$6.0 \times 10^{-17}$
1400	$8.8 \times 10^{-7}$	$9.2 \times 10^{-12}$	$1.2 \times 10^{-13}$
1600	$1.6 \times 10^{-5}$	$2.4 \times 10^{-9}$	$3.7 \times 10^{-11}$
1800	$2.1 \times 10^{-4}$	$1.3 \times 10^{-7}$	$3.0 \times 10^{-9}$

are two different definitions of vapor pressure:

- Knudsen (or equilibrium) vapor pressure
- Langmuir (or free) vapor pressure

In the case of Knudsen, or equilibrium, evaporation, it is implicitly assumed that evaporating molecules undergo collisions amongst themselves as well as with walls and surfaces so that the molecular species in the vapor are full equilibrated in all degrees of freedom [see discussion in Carlson (1967)]. In contrast, Langmuir, or free, evaporation refers to the case where a species leave a hot surface exposed to vacuum, i.e. without undergoing collisions with the surroundings [see discussion in Paule & Margrave (1967)]. The two vapor pressures are related by the accommodation coefficient,  $\alpha$ , as in Equation 3:

$$P_{Langmuir} = \alpha \times P_{eq} \quad (3)$$

where  $P_{Langmuir}$  is the free vapor pressure, and  $P_{eq}$  the equilibrium vapor pressure, which is obtained from Equation 4.

$$P_{eq} = \frac{1}{A_0} \sqrt{\frac{2\pi kT}{m}} \frac{dw}{dt} \quad (4)$$

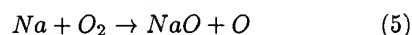
where  $A_0$  is the area of the orifice from which the flux of equilibrium vapor is measured,  $T$  the temperature,  $m$  the average molecular weight, and  $\frac{dw}{dt}$  the rate of mass loss from the reservoir. For the case of ablation of the metals from a hot meteoroid surface, the situation is neither pure Knudsen nor pure Langmuir evaporation. This arises from the fact that there is a pile-up of gas in front of the meteoroid, and that may lead to some collisions between the evaporating species and other gaseous species. How to take this into account is not clear at this time, as the amount of pile-up is very size dependent. Even if we assume, for lack of better information, that the evaporation is pure Langmuir evaporation, we still have to correct the vapor pressures given in Table 3 by the accommodation coefficient,  $\alpha$ . This is characteristic of the surface, the temperature, and species in question (e.g. Na). Unfortunately such data is not available for the cases under discussion: metal atoms evaporating from molten silicate or oxide surfaces. Generally,  $\alpha$  has a value that lies in the range 0.5–0.01, a very wide range, indeed. Of course, to

calculate relative abundances, only the ratios of the different  $\alpha$ 's are needed, and that may reduce the error.

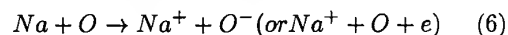
The only purpose in raising this question is to point out that there is an uncertainty associated with *ab initio* modeling the metal release from meteoroids entering the Earth's atmosphere.

### 3.3. Hyperthermal Collisions

As shown in Figures 2 and 3, the velocity of the meteoroid continues to be large even after it had begun to lose mass. The meaning of this observation is that the first few collisions between an ablating atom and atmospheric gases occur at the velocity of the meteoroid,  $\sim 15$  km/s in the case of the meteoroid considered in Figure 2. For example, Na colliding with atmospheric  $O_2$  at 15 km/s has an energy of 26.8 eV in the laboratory frame of reference ( $E_{Lab}$ ), or  $\sim 10.5$  eV in the center-of-mass frame of reference ( $E_{CM}$ ). For collisions with O atoms, ( $E_{CM}$ ) is  $\sim 16$  eV. Thus in the collision between Na and either O or  $O_2$  there is enough energy to overcome a number of potential barriers to reaction to form molecular species, e.g. NaO. However, such reactions depend a great deal on the details of the molecular states that are available for the transition from the atomic collision partners through a molecular complex to the product species [see a full discussion of this question in Dressler & Murad (2001)]. In the case of Na there are no stable molecular species that are available, since potentially reaction 5:



leads to the formation of a molecule, NaO, whose dissociation energy,  $D_0^0(NaO)$ , is  $\sim 2.7$  eV [Hildenbrand & Murad (1970); O'Hare & Wahl (1972); Langhoff et al. (1986); and Hildenbrand & Lau (1993)], which is much less than the dissociation energy of  $O_2$ ,  $D_0^0(O_2)$ , which is 5.12 eV [Huber & Herzberg (1979)]. Thus, even if NaO is formed, it will be only transitory and revert back to Na via the reverse reaction. It is worth noting, in passing, that the temporary formation of NaO might lead to its being formed in an excited state, such as the  $A^2\sigma^+$  [Joo et al. (1999)], in which case it would affect the optical emissions observed in the nightglow and in twilight. However, this will not affect the dynamics of meteoroid ablation and subsequent reactions. The only remaining endoergic reaction that can be reached because of the high collision energy is the collisional ionization reaction 6



The cross section for this reaction has not been measured, but an estimate was made [Dressler & Murad (2001)] as shown in Figure 4. It is clear from this figure that the cross section at velocities  $< 20$  km/s is so small as to be unimportant. However as the velocity reaches  $\geq 40$  km/s the collisional ionization reaction begins to become important. At 60

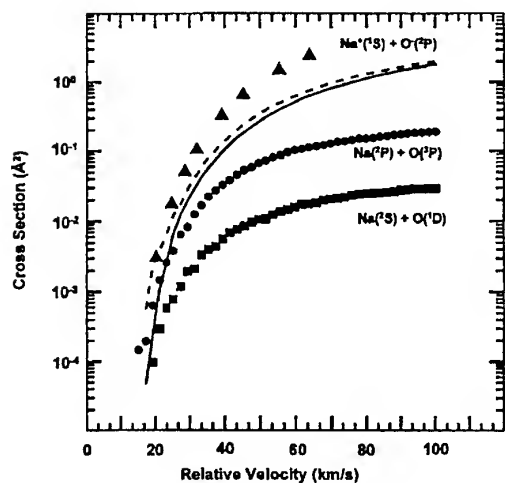


Figure 4. Calculated cross section for the collisional ionization reaction of Na with O as a function of energy. Details of the calculation will be found in Dressler & Murad (2001).

or 70 km/s the cross section,  $\sigma$ , reaches a plateau at  $2 \times 10^{-16} \text{ cm}^2$ , equivalent to a rate coefficient ( $k = \sigma \times v$ , where  $v$  is the meteoroid velocity),  $k$ , of  $\sim 10^{-9} \text{ cm}^3/\text{molecule/s}$ . This is close to gas kinetic, and suggests that at an altitude of  $\sim 120 \text{ km}$  the time constant for this reaction is  $\sim 10 \text{ ms}$  (based on  $[\text{O}] \sim 10^{11}/\text{cm}^3$ ). Similar reactions are likely to occur in collisions with  $\text{O}_2$  as well as between the other metals and O and  $\text{O}_2$ . However, the molecular states are not known well enough to calculate cross sections such as the ones shown in Figure 4.

Support for the suggestion that hyperthermal collisions play an important part in the phenomenology of meteoroid-atmosphere interactions is shown by the spectral studies reported by Millman & McKinley (1963) who observed strong metal ion signals from a Perseid shower ( $v \sim 60 \text{ km/s}$ ) but not from a Giacobinid shower ( $v \sim 23 \text{ km/s}$ ); these spectra were obtained for meteoroids at altitude interval 78–97 km. A recent observations of the spectra of Leonid meteoroids [Borovička et al. (1999); Abe et al. (2000)] have shown the presence of spectral lines attributed to  $\text{Ca}^+$  and  $\text{Mg}^+$ . However, these studies did not compare the Leonid spectra with low-velocity meteoroids, such as the Giacobinids.

### 3.4. Leonid Storm

The Leonid meteor shower, which arises from Comet P/Temple-Tuttle has been of interest recently because of the  $\sim 33$  year period of the comet. The most recent storm, 1966, was quite intense and ZHR's of  $\sim 150,000$  were reported. The expectation of a storm of similar intensity in 1999 did not materialize. Accurate orbital calculations [Asher (1999)] have provided explanation for the much weaker storm in 1999

[Singer et al. (2000)]. Nonetheless, there is still some interest in the Leonids, particularly as pertains to the occurrence of a storm of historic intensity, such as that of 1966. The effect of such a storm might be felt by direct satellite impact, as has been discussed by Beech & Brown (1994), Brown et al. (1996), & Foschini & Cevolani (1997). In addition to satellite impact, however, there is an equally important effect on the ionosphere. In a recent study [McNeil et al. (2001)] the effect of such a storm on the ionosphere was calculated using a simple dynamic ionosphere that included solar radiation and photoionization. The model was then adapted to include the ablation of meteoroids as described earlier using thermal equilibrium assumptions (in other words fractionation of the elements, or, *differential ablation* [McNeil et al. (1998)]). In addition, collisional ionization processes, such as reaction 6, were included in the initial collisions. Because of the velocity of the Leonid meteoroids,  $\sim 70 \text{ km/s}$ , ablation begins at higher altitudes,  $\sim 130 \text{ km}$ , and at these altitudes the atomic metal ions have a long lifetime due to the low probability of electron-ion recombination. As the ions descend, they undergo complex chemical reactions with minor species present at altitudes below 100 km. For the latter set of reactions, rate coefficients measured by Plane and his colleagues [Plane & Helmer (1995); Plane et al. (1999)] were used in this model. Figure 5 shows the results of these calcu-

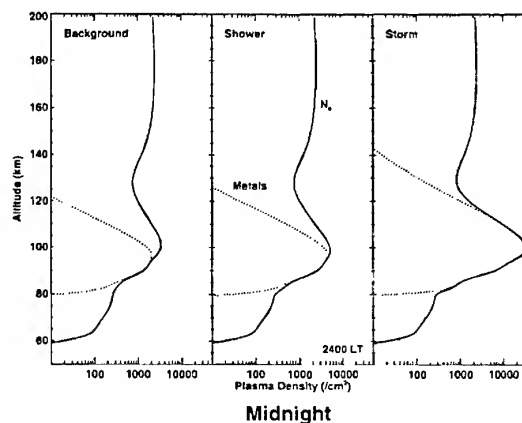


Figure 5. Calculated cross section for the collisional ionization reaction of Na with O as a function of energy. Details of the calculation will be found in McNeil et al. (2001).

lations. It is clear that a Leonid storm of historic proportion would overwhelm the ionosphere and would increase the total electron content by, perhaps two orders of magnitude. Moreover, because the ionization occurs at much higher altitudes, where atomic ion-electron recombination is unlikely, this enhanced ionization level may last several hours - until transport by winds or gravity waves moves the atomic ions to lower altitudes.

#### 4. SUMMARY AND CONCLUSIONS

What has been presented in this paper shows that understanding the nature of the meteoroids-atmosphere interaction is at a fairly advanced state although a number of factors need to be studied or confirmed in order to achieve a truly useful model that can predict the effects from first principles. These factors are:

- *Flux*: The recent analysis given by Mathews et al. (2001) needs to be confirmed so as to achieve an accurate representation of the sporadic metal content of the ionosphere.
- *Composition*: An accurate measure of differences in the composition of comets and asteroids needs to be established in order to relate the composition of meteorites (asteroids) to those of meteors (comets).
- *Langmuir pressures*: Langmuir vapor pressures of the metals over silicates and oxides need to be measured in order to correct the equilibrium vapor pressures that are currently used in models.
- *Cross Sections*: Cross sections for hyperthermal reactions, such as that of reaction 6, need to be measured in order to have a realistic calculation of the initial ionization levels.

Once these additional data are available, it becomes feasible them to include the meteor models that have been developed so far [Cox & Plane (1998); McNeil et al. (1998); Carter & Forbes (1999)] into global circulation models [Roble (1995); Roble (2000)] to obtain a global picture of the metal layers and the effect of showers and storms.

*Acknowledgements*: I wish to thank W. J. McNeil for helpful discussions and for calculating the data shown in Figures 1-3, C. P. Pike and A. Pellinen-Wannberg for helpful comments, and Professors B. Fegley, Jr. and A. W. Cameron for providing a copy of the MAGMA model that is used for the calculations shown in Figures 2 and 3.

#### REFERENCES

- Abe S., Yano H., Ebizuka N. & Watanabe J.-I., 2000, *Earth Moon Planets*, 82-83, 369.
- Asher D. J., 1999, *Mon. Not. R. Astron. Soc.*, 307, 919
- Baggaley W.J., Bennett R. G. T. & Taylor A. D., 1997, *Planet. Space Sci.* 45, 577
- Beech M. & Brown P., 1994, *ESA Journal*, 18, 63
- Borovička J., Stork R. & Boček J., 1999, *Meteorit. Planet. Sci.*, 34, 987
- Boyd I. D., 2000, *Earth Moon Planets*, 82-83, 93
- Bronshten V.A., 1983, *Physics of Meteoric Phenomena*, Kluwer, Dordrecht, Holland, 356 pp.
- Brown P., Jones J. & Beech M., 1996, in *Fifth International Conference on Space '96*, edited by S.W. Johnson., Am. Soc. Civil Eng., 13
- Brownlee D. E., Tsou P., Clark B., Hanner M. S., Hörz F., Kissel J., McDonnell J. A. M., Newburn R. L., Sandford S., Sekanina Z., Tuzzolinoo A. J. & Zolensky M., 2000, *Meteorit. Planet. Sci.*, 35, A35
- Carlson K. D., 1967, in *The Characterization of High Temperature Vapors*, edited by J. L. Margrave, Wiley, 115
- Carter L. N. & Forbes J. M., 1999, *Ann. Geophysicae*, 17, 190
- Cepelcha Z., Borovička J., Elford W. G., Revelle D. O., Hawkes R. L., Porubčan V. & Šimek M., 1998, *Space Sci. Rev.*, 84, 327
- Chase, Jr. M. W., 1998, *NIST-JANAF Thermochemical Tables, 4th Edition*, American Institute of Physics, 1946 pp.
- Cox R. M. & Plane J. M. C., 1998, *J. Geophys. Res.*, 103, 6349
- Dressler R. A. & Murad E., 2001, in *Chemistry Under Extreme Conditions*, World Scientific, 268
- Fegley, Jr. B. & Cameron A. G. W., 1987, *Earth Planet. Sci. Lett.*, 82, 207
- Flynn G.J., 1989, in *19th Lunar and Planetary Science Conference, Houston, TX*, 673
- Foschini L. & Cevolani G., 1997, *Il Nuvo Cimento*, 20 C, 211
- Fyfe J. D. D. & Hawkes R. L., 1986, *Planet. Space Sci.*, 34, 1201
- Grün E. & Jessberger E. K., 1990, in *Physics and Chemistry of Comets*, edited by W. F. Huebner, Springer-Verlag
- Hawkes R. L. & Jones J., 1975, *Mon. Not. R. Astr. Soc.*, 173, 339
- Hildebrand D. L. & Murad E., 1970, *J. Chem. Phys.*, 53, 3403
- Hildenbrand D. L. & Lau K. H., 1993, *J. Chem. Phys.*, 98, 4076
- Huber K. P. & Herzberg G., 1979, *Molecular Spectra and Molecular Structure: IV. Constants of Diatomic Molecules*, Van Nostrand, 716 pp.
- Hughes D. W., 1978, in *Cosmic Dust*, edited by J. A. M. McDonnell, Wiley, 123
- Janches D., Mathews J. D., Meisel D. D. & Zhou Q.-H., 2000, *Icarus*, 145, 53
- Janches D., Meisel D. D. & Mathews J. D., 2001, *Icarus*, 150, 206
- Jones J. & Kaiser T. R., 1966, *Mon. Not. R. Astr. Soc.*, 133, 411
- Joo S., Worsnop D. R., Kolb C. E., Kim S. K. & Herschbach D. R., 1999, *J. Phys. Chem. A*, 103, 3193
- Kane T. J. & Gardner C. S., 1993, *Science* 259, 1297.

- Langhoff S. R., Bauschlicher Jr. C. W. & Partridge H., 1986, *J. Chem. Phys.*, 84, 4474
- Lebedinets V. N. 1973, in *Evolutionary and Physical Properties of Meteoroids*, Edited by C. L. Hemenway, P. M. Millman & A. F. Cook, NASA, Washington DC. 259
- Lodders K. & Fegley, Jr. B., 1998, *The Planetary Scientist's Companion*, Oxford University Press
- Love S. G., & Brownlee D. E., 1991, *Icarus* 89, 26
- Love S.G. & Brownlee D.E., 1993, *Science* 262, 550
- Mason B. (Editor), 1971, *Handbook of Elemental Abundances of the Elements in Meteorites*, Gordon and Breach
- Mathews J. D., Janches D., Meisel D. D. & Zhou Q.-H., 2001, *Geophys. Res. Lett.* 28, 1929
- McNeil W. J., Lai S. T. & Murad E., 1998, *J. Geophys. Res.*, 103, 10899
- McNeil W.J., Dressler R. & Murad E., 2001, *J. Geophys. Res.*, 106, 10447
- Miao J. & Stark J. P. W., 2001, *Planet. Space Sci.*, 49, 927
- Millman P.M. & McKinley D. W. R., 1963, in *The Moon, Meteorites, Comets*, edited by B. M. Middlehurst & G. P. Kuiper, University of Chicago, 674
- Mittlefehldt D. W., McCoy T. J., Goodrich C. A. & Kracher A., 1998, in *Planetary Materials*, Reviews in Mineralogy - Volume 36, Edited by J. J. Papike, Mineralogical Society, Washington DC, 4-01
- Nicol E. J., Macfarlane J. & Hawkes R. L., 1985, *Planet. Space Sci.*, 33, 315
- Nishimura K., Sato T., Nakamura T. & Masayoshi U., 2001, *IEICE Trans. Commun. (Japan)*, 84-C, *In Press*
- O'Hare P. A. G. & Wahl A. C., 1972, *J. Chem. Phys.*, 56, 4516
- Öpik E. J., 1936a, *Publ. de l'Observatoire astronomique de l'Université de Tartu*, 28, 1
- Öpik E. J., 1936b, *Publ. de l'Observatoire astronomique de l'Université de Tartu*, 28, 13
- Öpik E. J., 1937, *Publ. de l'Observatoire astronomique de l'Université de Tartu*, 33, 1
- Öpik E. J., 1958, *Physics of Meteor Flight in the Atmosphere*, Interscience Publishers New York, 174 pp.
- Paule R. C. & Margrave J. L., 1967, in *The Characterization of High Temperature Vapors*, edited by J. L. Margrave, Wiley, 130
- Pellinen-Wannberg A., Westman A., Wannberg G. & Kaila K., 1998, *Ann. Geophysicae* 16, 1475
- Plane J. M. C. & Helmer M., 1995, *Faraday Discuss.*, 100, 411
- Plane J. M. C., Cox R. M. & Rollason R. J., 1999, *Adv. Space Res.*, 24, 1559
- Popova O., Sidneva S. N., Shuvalov V. V. & Strelkov A. S., 2000, *Earth Moon Planets*, 82-83, 109
- Roble R. G., 1995, in *The Upper Mesosphere and Lower Thermosphere: A review of experiment and theory*, edited by R. M. Johnson & T. L. Killeen, Amer. Geophys. Union Washington DC, 1
- Roble R. G., 2000, in *Atmospheric Science Across the Stratopause*, edited by D. E. Siskind, S. D. Eckermann & M. E. Summers, Amer. Geophys. Union, 53
- Sears D. W. & Dodd R. T., 1988, in *Meteorites and the Early Solar System*, J. F. Kerridge & M. S. Matthews (Editors), University of Arizona Press
- Singer W., Molau S., Rendtel J., Asher D. J., Mitchell N. J. & von Zahn U., 2000, *Earth, Moon, and Planets*, 318, L25
- Tuzzolino A. J., McKibben R. B., Simpson J. A., BenZvi S., Voss H. D. & Gursky H., 2001, *Planet. Space Sci.* 49, 689
- Tuzzolino A. J., McKibben R. B., Simpson J. A., BenZvi S., Voss H. D. & Gursky H., 2001, *Planet. Space Sci.* 49, 705
- Verdant, M. & Schwehm G. H., 1998, *ESA Bull.* 93, 39
- Whipple F. L., 1943, *Rev. Mod. Phys.*, 15, 246
- Whipple F.L., 1950, *Proc. Nat'l. Acad. Sci. (USA)*, 36, 687
- Whipple F.L., 1951, *Proc. Nat'l. Acad. Sci. (USA)*, 37, 19

# FORMATION OF DISTURBED AREA AROUND FAST METEOR BODY

Popova O.P., Sidneva S.N., Strelkov A.S., Shuvalov V.V.

*Institute for Dynamics of Geospheres Russian Academy of Sciences  
Leninsky pr.38, bld.6, Moscow, 117979, Russia, Email: olga@idg.chph.ras.ru*

## ABSTRACT

The ablation of meteoroids essentially influences on all processes connected with or initiated by meteoroid entry. Evaporated meteor substance interacts with incoming air flow and forms disturbed area both around and behind the meteor body. Air-meteoroid interaction may be described in the frame of particle-beam model which permits to estimate parameters of formed vapor. The solution of Boltzman equation by the Monte Carlo method allows us to consider air particles interactions with meteor body and vapor cloud formed around it, permits to determine the energy, momentum and mass transfer and to consider not only primary particle interaction but also the fate of secondary formed particles. The gasdynamical description is used for vapor cloud formed as the result of ablation, nearby wake evolution, radiation field.

## 1. INTRODUCTION

The entry of meteoroids into the Earth's upper atmosphere provides a very important tool for the investigation of interplanetary matter composition and high-velocity reactions between the meteoroid and the ambient atmosphere both of which are consequential for extending our understanding of the evolution of the solar system. Interplanetary particles enter continuously into the Earth's atmosphere as sporadic meteors or during meteor showers providing up to  $4 \times 10^4$  tons/year [1]. About 30% of the meteors are due to shower activity with high initial velocities [2]. Meteor showers are particularly interesting as they provide a direct source of information about the composition and morphology of relatively large cometary grains.

Once released into the atmosphere the meteoroid atoms and molecules have a significant influence on the aerothermochemical processes that can take place in the upper mesosphere and lower thermosphere [3, 4]. For example, meteor particles are now known to be responsible for the atmospheric neutral atom metal layers observed around 90 km altitude [5, 6]. Meteors may also provide an alternative source for high altitude atmospheric water or other compounds (HCN, CN).

There are even some data that connect meteors with electrical processes taking place in the lower and upper atmosphere [7].

Meteors are considered to have been a major source of carbon, organic matter and metallic compounds around the time of the origin of life on Earth [8, 9]. Surprisingly, however, very little is known about the physical conditions that take place during normal meteor ablation or the fate of the ablated materials in the Earth's atmosphere. High velocity meteor interactions with atmosphere differ substantially from entries of artificial bodies due to the ~10-fold excess in entry velocity and the body's properties (i.e. its composition and strength).

Despite many attempts, the details of the interaction between the entering particles and the atmosphere are still poorly understood. Additionally, there are now new evidence detailing several intriguing features that have, as yet, no theoretical explanation. The grain model of [10] is often applied for meteors [11-13]. This model predicts no dependence of beginning altitude on meteoroid mass, whereas a strong increase in beginning heights was recently observed by [14]. The spectra recorded for about 1-cm sized meteoroid at altitude 90-100 km were analyzed in [3] and show that a large luminous volume may be formed during meteor passage, much larger than that predicted by the initial train theory [15]. Extreme beginning heights of bright Leonids up to altitudes of ~200 km have also been observed. Classical ablation theory, which assumes evaporation following a temperature rise of up to about 2000 K, does not explain luminosity at these heights. Detailed images have also shown diffuse comet-like structures above 130 km altitude [16].

Most recently a number of unusual meteors exhibiting nebulosity caused by radiation of meteoric atoms (the spreading of meteor luminous area up to 1-2 km) and jet-like features were imaged during the 1998 and 1999 Leonid meteor shower/storm. It was speculated in [17] that this unexpected structuring, which appears to be present in a significant fraction (up to 8%) of Leonid meteors may in part be due to explosive ejection of

meteoroid fragments. However, the nature of such an explosive reaction is not yet known. Another possible explanation may be connected with evaporation from irregularly shaped bodies that could result in vapor-like jets.

To better understand this growing body of "unusual" observational data on fast meteoroids one needs to have clear description of the meteoroid-air-vapor interaction. No such picture of this interaction currently exists.

## 2. ABLATION MODEL

All processes connected with or initiated by meteoroid entry are essentially affected by fragmentation and ablation. That results in formation of large disturbed area around meteor body.

Although ablation can involve fragmentation and the generation of debris, here we will assume that the majority of the ablated material is released in vapor form [2]. We consider meteoroid ablation as a process of evaporation [18]. We do not consider the differential ablation of individual mineral compounds [19]. Instead, the simultaneous evaporation of the mixture as a whole at the given temperature is assumed. Our approach is to calculate the thermodynamic properties of the ablated material for a single solid body at different points along its trajectory. A whole model can then be constructed by combining the effect on individual meteoroid fragments.

At given altitude, the behavior of entering meteoroids in atmosphere is conditioned by their size and velocity. Standard heat balance equation implies that the heat flux received from the impinging air molecules is treated to evaporation, heat conduction and radiation cooling. Broadly speaking, the smallest bodies ( $< 10^{-4}$  cm) decelerate before essential heating. The heating of bodies with  $R < 0.01$  cm is stopped by thermal radiation. Bigger bodies enter more deep atmosphere layers without deceleration and the received heat flux increases.

An altitude where the incoming air energy flux becomes larger than energy losses due to meteoroid heating and thermal radiative cooling may be called the height of intensive evaporation. For porous bodies with  $R \sim 0.01$ -10 cm this altitude is about 90 - 130 km (for  $V \sim 70$  km/s). It is estimated following [2] and is shown on Fig.1

We will consider here 0.01-10 cm meteoroids with altitude of intensive evaporation higher 100 km, i.e. with velocities bigger about 30-40 km/s. A lot of observational data were collected during Leonids

observational campaigns and MAC missions so the most part of our modelling were performed with entry velocities as high as 71 km/s. These bodies correspond to about  $+3^{\text{mag}} - 10^{\text{mag}}$  meteors.

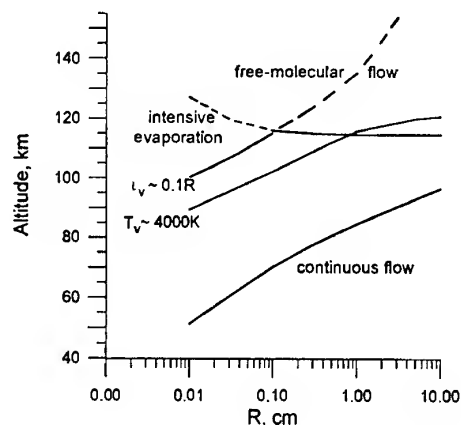


Fig.1 Boundaries of different flow regimes in the presence of a dense ablation vapor cloud in front of a Leonid meteor.

The high velocity of fast meteors results in high-altitude beginning of intensive evaporation and also provides high evaporation rate. Simple estimates show that pressure of formed vapor is higher than aerodynamical loading [20]. That results in formation of vapor cloud around the body and vapor cloud screening. As a result the boundary of pure free-molecular regime is shifted to higher altitudes. Roughly, presence of vapor is essential if the free path length in it is smaller than body size  $l_v \sim 0.1R$  (Fig.1). Below this line vapor is enough dense to be described hydrodynamically. Our further consideration also allows us to estimate altitude where the temperature of vapor is higher 4000-5000K, and probably the radiation should be taken into account (Fig.1).

The energy transfer during the penetration of air into the layer of evaporated molecules may be described similar to radiation transfer assuming some effective mass absorption coefficient:

$$\kappa = (n l_a \rho_v)^{-1} \quad (1)$$

where  $\rho_v$  is the vapor density and  $l_a$  is an average free path of air molecules in the vapor layer. Impinging air molecules may be considered as particle beam with energy flux

$$q_0 = \rho_a V^3 / 2 \quad (2)$$

We assume that the energy transfer takes place in about  $n \sim 10$  collisions (see below). Treating of air-meteoroid interaction in a frame of air beam model allows taking into account evaporation, heating of forming vapor, screening of meteoroid surface and radiation of heated vapor.

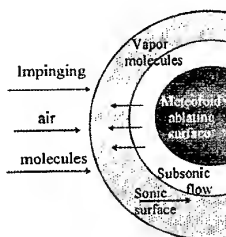


Fig.2 Schematic picture of flow.

When the formed vapor pressure exceeds the air one vapor expands in gasdynamic regime as into vacuum (Fig.2). Due to intensive evaporation formed vapor have relatively high density and may be described in the frame of hydrodynamics. The outer layers of vapor attain the supersonic velocity. The outer layers of vapor cloud become transparent for impinging air molecules. Absorption occurs mainly in the subsonic part of the flow. The self-regulating regime is realised [21, 22]. For smaller vapor densities screening decreases and ablation rate and vapor density increase. For larger vapor densities screening increases and vapor production and density decrease.

Vapor parameters in the total flow area can be derived directly from 1D hydrodynamic numerical simulations or by solving the ordinary differential equations that describe the 1D flow [21, 20]. The results confirm formation of vapor cloud with pressure exceeding aerodynamical loading for meteoroid sizes under consideration [20]. The unclear question is the energy deposition length.

### 3. INTERACTION OF AIR PARTICLES WITH VAPOR

Collisions of air particles with evaporated ones and particle dynamics were considered by number of authors. They studied screening of meteoroid surface by evaporated substance ([23], [24], see also [18] for review), initial train radius [25, 15] and head echo formation [26], ionization and excitation coefficients of meteors [27, 28]. The main used approximation was the meteoroid flight in almost free-molecular regime, that allowed one to take into account only first collisions of vapor particle with air molecule. This approximation holds for relatively small meteoroids. When the vapor density around body becomes essential the secondary collisions should be taken into account.

Recently, the Monte Carlo (MC) approach was used to describe the rarefied flow around a Leonid meteoroid with a simplified ablation model [29] and has demonstrated the critical influence of ablation on formation of long hot meteor wake. The size of hot meteor wake essentially increases if the ablation is taken into account.

We simulated the energy transfer from air flow to meteor body, concentrating on the ablation process itself and the vapor cloud surrounding the meteoroid. Our model is a 2D MC calculation of the action of impinging air molecules from one direction on a spherical vapor cloud with densities from  $10^{-11}$  to  $10^{-5}$  g/cm<sup>3</sup>.

The initial kinetic energy of high velocity air molecules is much larger than the thermal energy of the vapor. The simulation process involves the construction of a trajectory for the impacting air particle and several generations of fast vapor particles (Fig.3). Trajectory finishes (and particle is considered as captured) when kinetic energy or velocity reaches background values. This approach allows studying different types of problems – air particles interaction with quasistationary object (cloud around meteor body) or with object with changing parameters (for example high-velocity jet of explosive generator).

Impinging air molecule has energy about 600-700 eV when it collides with vapor atoms. This energy is sufficient for inelastic processes (ionization, excitation, various chemical reactions). Unfortunately, integral and differential cross sections data for atom and ion collisions with atmosphere species in this energy range ( $\sim 1$ -1000 eV, corresponding to relative velocities 1-100 km/s) are very scarce. Detail review of chemical dynamics in meteor phenomenon and available data is provided by [4]. We intend to incorporate the most important nonelastic phenomena in our simulations on the next step. As the first approximation the interaction of the impacting air particles with the meteoroid and vapor cloud is assumed to be paired elastic collisions.

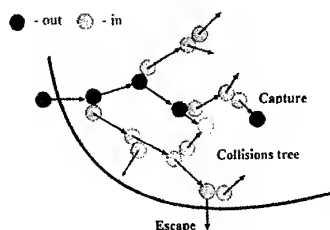


Fig. 3 Schematic picture of particles trajectories

We consider the flow of air particles impacting the cross section area of a meteoroid with radius 1 cm, surrounded by ablation vapor at the altitude of 100 km. It is supposed for simplicity that the meteoroid is Silicon gas with high density ( $2.3 \text{ g/cm}^3$ ). The density distribution in the vapor cloud is assumed to be almost uniform with constant density value  $\rho_c$ , in order to understand better the collision processes. Only at the boundaries the density changes rapidly, from  $2.3 \text{ g/cm}^3$  at the inner boundary down to surrounding air one at the outer boundary. The value of cloud density  $\rho_c$  is a variable in a wide range ( $\rho_c = 0.001\text{--}1\rho_{c0}$ , where  $\rho_{c0} = 10^{-5} \text{ g/cm}^3$ ,  $\rho_c \sim 10^{-9}\text{--}10^{-5} \text{ g/cm}^3$ ). Our simulations were performed both for a constant interaction cross-section and for a cross-section decreasing with impacting-particle velocity. We consider impacts of air particles through small area equal to body size or large area corresponding to developed spherical vapor cloud. The size of the cloud is not critical when considering the air particle interactions with a constant density vapor cloud.

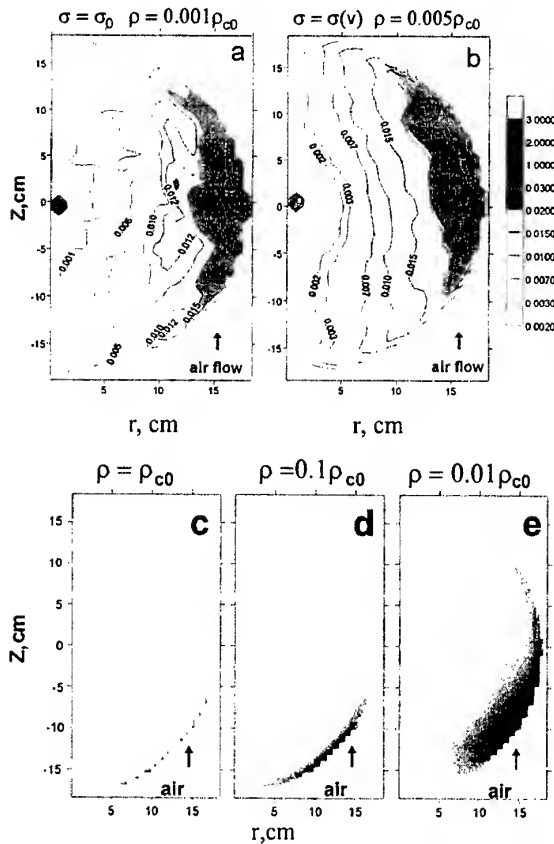


Fig.4 Absorbed energy spatial distribution in vapor cloud

The mechanism of energy transfer from impinging air molecules to vapor and meteoroid itself is more demonstrative on the pictures corresponding to irradiation of well developed vapor cloud and large area of irradiation (Fig.4). The energy distribution in vapor-body system with change of vapor density  $\rho_{c0}$  is presented. Density contours show the transferred energy. At low cloud densities the energy absorption takes place in the whole volume of the vapor cloud and body itself. The captured air particles, stopped after all energy has been transferred, are distributed in the cloud. As the vapor cloud density increases, the region of highest energy absorption shifts to the volume outer boundary and becomes a thin layer located on the frontal surface of the cloud. At high vapor densities, all energy absorption occurs in the thin layer of the cloud.

A part  $\delta$  of air flow energy  $E_{flow}$  incoming through the effective meteoroid cross-section is absorbed by vapor-body system ( $\delta = E_{abs}/E_{flow}$ ). This energy  $E_{abs}$  is distributed between meteoroid ( $E_{body}$ ) and vapor ( $E_{vap}$ ). Dimensionless values  $\delta_{body} = E_{body}/E_{abs}$ ,  $\delta_{vap} = E_{vap}/E_{abs}$  show its distribution in the system. These characteristics describe the energy transfer from air particles to the meteoroid and vapor cloud.

If the vapor cloud is transparent for impacting air particles, then about half of the incoming energy is absorbed by the system (Fig.5a). This value is two times lower than usually used in free molecule conditions. The decrease is caused by fast particles reemitted by the body.

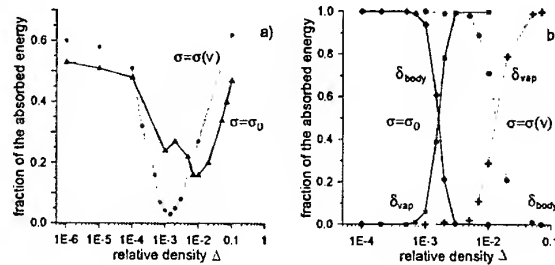


Fig.5 (a)- the absorbed energy fraction  $\delta$  versus vapors relative density  $\Delta = \rho_c/\rho_{c0}$ ; (b) - the energy fractions absorbed by meteoroid  $\delta_{body}$  and by vapor cloud  $\delta_{vap}$ . The air flow radius  $R = 1 \text{ cm}$ .

The fraction of absorbed energy  $\delta$  decreases due to decrease of body absorption with cloud density increase ( $\rho_c = 0.001\rho_{c0}$ ,  $\rho_c \sim 10^{-8} \text{ g/cm}^3$ ). Then the fraction of energy increases due to increase of vapor

cloud absorption. If we consider larger radius of incoming air flow, the character of dependence is the same. The dependence of particle interaction cross-section on velocity leads to the beginning of screening under higher vapor density.

We don't include ablation itself into MC simulations. Vapor parameters are found in the course of GD modeling. Based on estimates of vapor cloud optical depth it is possible to predict that relative density of about 0.001-0.01 ( $\rho_c \sim 10^{-9}-10^{-7}$  g/cm<sup>3</sup>) should be established in the real vapor cloud around body.

What is the fate of impinging air particles? The fractions of air atoms escaping from the head cloud into wake and remaining in the head with thermal energy are shown on Fig.6a. The fraction of remaining particles increases with relative density from few % to about 70%. At relative densities 0.001-0.01  $\rho_{c0}$  about 70-90% of air particles with nonthermal energy penetrates further in meteor wake forming extended area of vapor-air mixing. This area probably is the source of radiation registered in observations [3].

The number of meteor particles escaped from meteor head per one air molecule is given on Fig.6b. In relatively dense cloud one air molecule causes about 20-70 meteor particles to be thrown into meteor wake. It should be noted here, that one initial air molecule could cause appearance of hundreds vapor particles and some stationar picture is established.

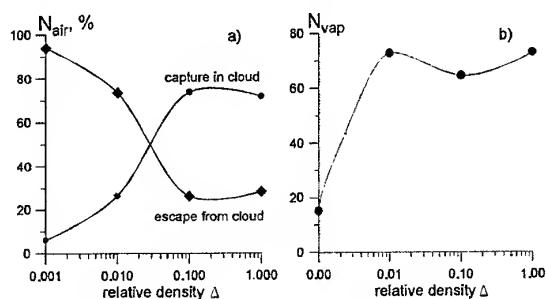


Fig.6 (a)-the fraction of air atoms captured by vapor cloud and escaped from it; (b)-the number of vapor particles escaped from meteor head per one air molecule.

It was speculated by [3] that organic carbon may survive in meteor, if it is only momentarily heated and subsequently quickly cooled by collisions with other molecules. We found that evaporated particles are effectively shifted into the wake, but the possibility of organic compounds survival should be studied additionally.

Our simulations show that air particles initiate collisions, which redistribute energy and momentum. The main air-cloud interaction is determined both by air-vapor and fast vapor-vapor particles collisions. The size of initial particle's influence area is larger than the initial particle free path length  $l_a$  by an order of magnitude. In dense vapor cloud further energy and momentum transfer is determined by several ( $\sim 8$ ) generations of vapor particles. So, it may be assumed that energy deposition length is equal to  $10 l_a$ .

In further modelling we are going to include non-elastic collisions and more realistic composition of meteor body itself. The equilibrium part of non-elastic processes is taken into account during the gasdynamical description of the vapor (we used real equation of state). The nonequilibrium part (ionization, excitation by hard particles) may be included in MC simulations. Some preliminary estimates made for integral ionization cross sections for meteor constitutions show that the main addition into equilibrium ionization will be formed by ionization of Fe, Mg, Si.

It should be mentioned that in the case of relatively big and fast meteor bodies coefficients of ionization and excitation should be calculated taking into account both collisions with air particles and with fast vapor particles. There is enough large number of collisions in the meteor head, and the vapor-vapor collisions should be taken into account. The observations show that LTE may be used as adaptable approximation to meteor radiation and this also proves the necessity of total collisions consideration.

#### 4. VAPOR PARAMETERS

Preliminary estimates and modelling of vapor parameters were done in one-dimensional approximation [20]. Cylindrical geometry may be assumed and a good approximation to 3D reality may be obtained from 2D approach. According to beam model it is assumed that the energy release due to deceleration of incoming air molecules is determined from the equations:

$$\frac{\partial q}{\partial x} = -\rho_v \kappa q \quad (3)$$

$$\frac{\partial e}{\partial t} = -\frac{1}{\rho_v} \frac{\partial q}{\partial x} \quad (4)$$

where  $\rho_v$  and  $e$  are the vapor density and thermal energy,  $q$  is energy flux, which equals  $q_0$  at the outer boundary. Beam energy is absorbed both by the dense vapor causing its heating and expansion and by the

meteoroid surface causing its evaporation. Numerical simulations were performed with the use of SOVA hydrodynamic code [30]. Extended description is given in [20], here we will mention the main results.

Density and energy distributions around 1 cm body at the altitude of 100 km are shown on Fig.7(a,b). Our simulations confirm that vapor cloud is formed around the body. Its size is several times larger than body size. The white lines (Fig.7) show the boundary where free path length are substantially smaller than body size. Gasdynamic description cannot be used for nonablating meteoroid, whereas it can be applied to ablating one. The sound surface is formed (black lines on Fig.7). The parameters in subsonic part are not influenced by the outer part of flow, they depend only on  $\kappa$  and energy flux in the sonic cross section.

The beam causes also momentum and mass transfer. Fig.7(c,d) demonstrates vapor parameters under assumption that momentum and mass are absorbed in the same way as energy. Momentum absorption acts as a counter pressure, at low altitudes it causes flow to be subsonic. Model of momentum transfer should be yet verified by MC simulations.

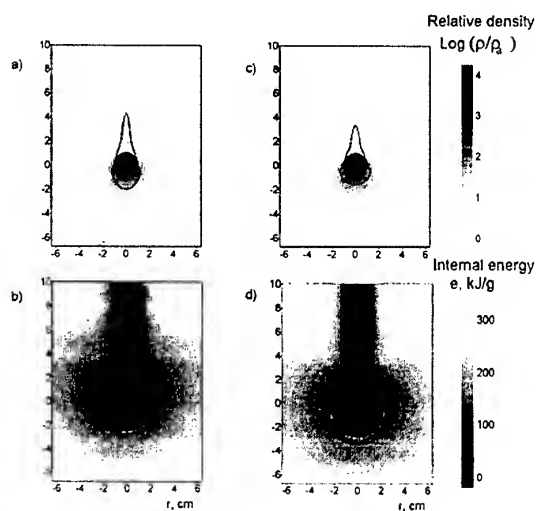


Fig.7 Distribution of relative density (upper panels) and dimensionless internal energy (lower panels) around 1 cm body at 100 km altitude. Left – only energy absorption is considered, right – momentum and mass absorption are also taken into account

The result of 2D calculations are rather close to those obtained from 1D spherical problem. The 2D modelling was used as a foundation to introduce any modifications in 1D simulations, in details of energy, momentum and mass transfer processes. 1D modelling may be supplemented with more complete physical

model more easily. 2D modelling assumes ideal gas equation of state. Real equation of state of cometary substance (similar to Halley comet, with water ice) [31] was introduced into 1D consideration.

In both cases the vapor density rapidly decreases with the distance from the surface and is about  $\rho_v \sim 10^{-6} - 10^{-9} \text{ g/cm}^3$ . Near the meteoroid surface vapor has the lowest temperature, close to the evaporation temperature. Vapor temperature reaches several eV and increases with altitude decrease (Fig.8a). Size of cloud decreases with altitude decrease, it exceeds body size in about 5-10 times. The use of either H-chondrite or comet substance properties leads to similar dependencies of parameters on the size and altitude.

The high temperatures of vapor need vapor thermal radiation to be included into the model. According to both observational data [32, 3] and modeling [29] LTE may be adaptable assumption. We estimated the radiation influence [20] without considering possible effects of deviation from LTE. At high altitude ablation is caused by particle beam, at low altitude meteoroid surface is screened by vapor. Heating of meteoroid may be dominated by radiation. At all altitudes the radiation decreases maximal temperature, at low altitudes it also results in density increase and cloud size increase (Fig.8b). So, reradiation of vapor may be essential in formation of vapor cloud.

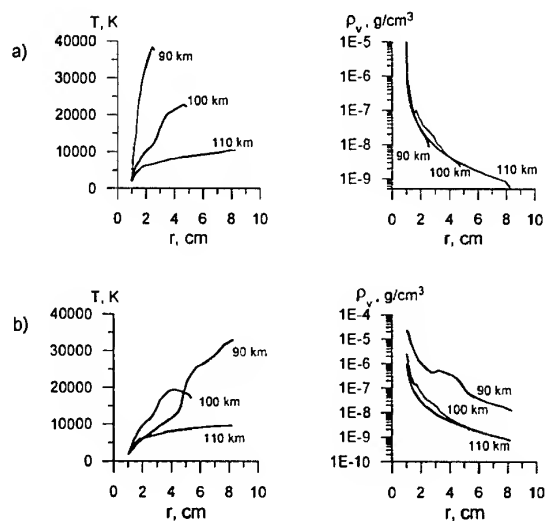


Fig.8 Vapor parameters for 1 cm meteoroid at 100 km altitude found - (a) without radiation, (b)-including radiative transfer

Precise values of vapor parameters depend on model of momentum transfer and mass stripping, on parameters of substance. And we have some uncertainties here. Nevertheless, the main features are evident. The

meteoroid-air interaction depends on altitude of flight and meteoroid size and velocity. We should take into account the momentum transfer and vapor radiation below some size-dependent altitude. Vapor cloud is formed around body; ablation may be caused both by air and vapor particles and hot vapor radiation.

## 5. METEOR WAKE AND SPECTRA ESTIMATES

Total meteor luminous area includes both head and wake. The precise boundary between the head and the wake, as well as a shape of the luminous volume, is not well known. On instantaneous meteor photographs ( $6 \cdot 10^{-4}$  s exposure) the average image length of fast meteors is of about 50 - 150 m [33].

The wake itself is described in [29]. However, estimate of the wake parameters near the meteoroid itself can be made using the air beam model. A cylindrical layer of vapor is stripped by the incoming air and is thrown into the nearby wake. The initial state of this vapor layer corresponds to the conditions formed in the vapor cloud around the body. Its further evolution is determined by expansion into the undisturbed air and radiative cooling.

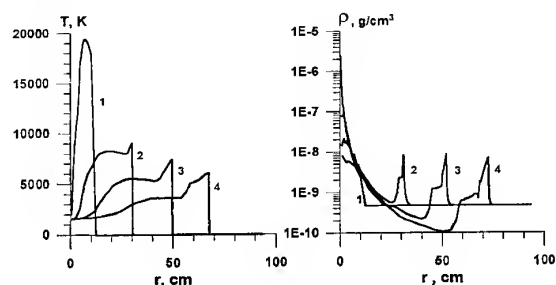


Fig.9 Evolution of stripped vapor. Temperature and density radial distribution in the head and at the distances 2, 5, and 10 m behind the meteor head ( $R=1$  cm,  $H=100$  km).

Simulations show that at the distance of about 5 meters, the vapor temperature is still about  $\sim 5,000$ - $6,000$ K. The extended hot area far exceeds the meteoroid size itself (Fig.9). Our estimate agrees with result of MC simulations [29], where the formation of a large (10 - 40 m in length) wake with temperature of about  $5,000$ - $10,000$ K is calculated. And this identifies the wake as the source of the temperature measured from atmospheric line and band emission of Leonid meteors in the 1998 Leonid MAC [3].

Meteor spectra can be calculated from thermodynamical parameters in the luminous volume and opacities for radiation. The optical properties of

comet material and H-chondrite vapor are those calculated in [31]. Spectra from the vapor layers at different distances from the meteor head are shown on Fig.10. It should be noted here that registered meteor spectra consist of the radiation of both vapor layers and air. Model spectra are approximate, because we only have information on the assumed properties of the wake near the meteor head and only vapor radiation is taken into account.

The spectra change with the distance from the meteoroid. Lines with high excitation energy (Sill, H, MgII, some O lines) originate mainly from the meteor head and warmer portions of the wake. The lower excitation lines of MgI and NaI are emitted from a more extended area in the wake.

The evidence of high temperature in the vapor are both predicted and observed in the Leonid spectra. Many Leonid spectra were recorded during the Leonid MAC missions. Video spectra in the range 380-880 nm from millimeter - centimeter sized Leonids ( $+2 \dots -6^{mag}$ ) were analysed in [32] assuming presence of two spectral components [34].

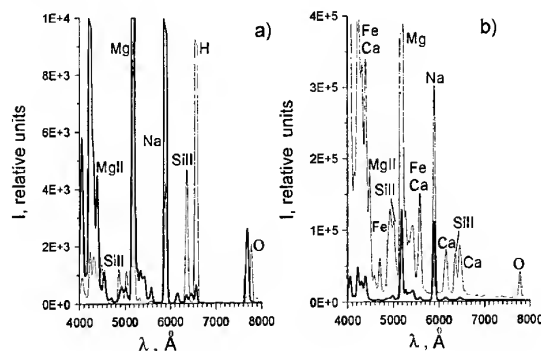


Fig.10 Example of spectra emitted by vapor layers of equal thickness for 1 cm body at 100 km altitude: a) for cometary composition (at distances of 2 m (thin) and 4 m (thick) behind the meteor head); b) H-chondrite composition (at distances of 0.2 m (thin) and 2.5 m (thick)).

The altitudes of the observed spectra are not given. It was found that about  $2/3$  of radiated energy in the given wavelength range is due to atmospheric air emissions,  $1/6$  is due to the line emissions of the meteoric vapor and another  $1/6$  is radiated as thermal continuum. The spectra were found to have two components of quite different temperature. The temperature of main component is estimated of about  $4500$  K while the second component was about  $10,000$  K [32].

If we compare observations and theory, we find that the diameter of the vapor volume derived from the observations [32, 3] appears to be one to two orders of magnitude greater than the meteoroid size (of about 1–10 cm for a 0<sup>mag</sup> Leonid), which may confirm the effect of vapor accumulation around the body. The estimate of vapor density in [32], proves to be similar to our ( $10^{-5}$  to  $10^{-10}$  g/cm<sup>3</sup>), whereas we predict higher temperatures in the area of air-vapor interaction.

Theoretical spectra depend on altitude and body size. The high resolution spectra recorded during Leonid MAC 1999 also demonstrate that spectra change with altitude [35]. The influence of altitude, size and composition on meteor spectra should be considered in details in future.

## 6. CONCLUSIONS

Preliminary comparison between theoretical predictions and observations shows both agreements and disagreements. Nevertheless the main features of ablation are evident.

For fast meteor bodies (0.01 – 10 cm sized) presence of evaporated material is essential in their interaction with atmosphere. Dense vapor cloud is formed around the body. Vapor may be described hydrodynamically. For bodies of equal velocities we should take into account the momentum transfer and vapor radiation below some size-dependent altitude. The direct MC simulations estimate the mass, momentum and energy transfer and will allow us to include non-equilibrium processes into consideration. Calculated vapor spectra show general agreement with observations. Particle beam model including both gasdynamical and MC simulations allows us to describe the air–meteoroid–vapor interaction well.

The present model is only a first step. It yet can't explain new observations mentioned in introduction. Nevertheless, our consideration revealed the questions which should be cleared up, allow to obtain qualitative picture and to estimate main flow characteristics. Non-elastic processes should be included in MC simulations, mass and momentum absorption should be studied more carefully. Further analysis of observational data and elaboration of theoretical model are needed to understand the physical processes that determine interaction of small meteoroids with atmosphere.

## References

1. Love S.G. and Brownlee D.E., A direct measurement of the terrestrial mass accretion rate of cosmic dust. *Science*, Vol. 262, 550–553, 1993.
2. Ceplecha Z., et al. Meteor phenomena and bodies, *Space Sci. Rev.*, Vol. 84, 327 – 471, 1998.
3. Jenniskens P., et al. Meteors: a delivery mechanism of organic matter to the early Earth, *Earth, Moon and Planets*, Vol. 82–83, 57 – 70, 2000.
4. Dressler R.A. and Murad E., The gas-phase chemical dynamics associated with meteors, In *Chemical Dynamics in Extreme Environments*, World Science, Singapore, 268 – 345, 2001.
5. Höffner J., et al. The 1996 Leonid shower as studied with a potassium lidar: Observations and inferred meteoroid sizes, *J. Geophys. Res.*, Vol. 104, 2633–2643, 1999.
6. Chu X., et al. Characteristics of Fe Ablation Trails Observed During the 1998 Leonid Meteor Shower, *Geophys. Res. Lett.*, Vol. 27, 1807 – 1810, 2000.
7. Symbalisty E.M.D., et al. Meteor Trails and Columniform Sprites, *Icarus*, Vol. 148, 65 – 79, 2000.
8. Chyba C.F., and Sagan C., *Comets and the origin and evolution of life*, New York: Springer-Verlag, 147 – 173, 1997.
9. Jenniskens P. and Butow S.J., The 1998 Leonid multi-instrument aircraft campaign—an early review, *Meteorit. Planet. Sci.*, Vol. 34, 933 – 943, 1999.
10. Hawkes R.L. and Jones J., A quantitative model for the ablation of dustball meteors, *Mon. Not. R. Ast. Soc.*, Vol. 173, 339 – 356, 1975.
11. Campbell M.D., Hawkes R.L., and Babcock D.D., Light curves of shower meteors: implications for physical structure, In *Meteoroids 1998*, Slovak. Acad. Sci, Bratislava, Slovakia, 363 – 366, 1999.
12. Murray I.S., R.L. Hawkes, P. Jenniskens, Airborne intensified charge-coupled device observations of the 1998 Leonid shower, *Meteoritics & Planetary Science*, Vol. 34, 949 – 958, 1999.
13. Murray I.S., et al. Comparison of 1998 and 1999 Leonid light curve morphology and meteoroid structure, *Earth, Moon and Planets*, Vol. 82–83, 351 – 368, 2000.
14. Brown P., et al. Global ground-based electro-optical and radar observations of the 1999 Leonid shower: first results, *Earth, Moon and Planets* 82–83, 167–190, 2000.

15. Jones W., Theory of the initial radius of meteor trains, *Mon. Not. R. Astr. Soc.*, Vol. 275, 812 – 818, 1995.
16. Spurny P., et al. Atmospheric behavior and extreme beginning heights of the 13 brightest photographic Leonids from the ground-based expedition to China, *Meteoritics Planet. Sci.*, Vol. 35, 243 – 249, 2000.
17. Taylor M.J., et al. Jet like structure and wake in Mgl (518 nm) images of Leonid storm meteors, *Earth, Moon and Planets*, Vol. 82-83, 379-389, 2000.
18. Bronshten V.A., *Physics of Meteoric Phenomena*, D. Reidel. Publ. Co. Dordrecht, 356p., 1983.
19. McNeil W.J., Lai S.T. and Murad E., Differential ablation of cosmic dust and implications for the relative abundances of atmospheric metals, *J. Geophys. Res.* Vol. 103, 10899-10911, 1998.
20. Popova O.P., et al. Screening of Meteoroids by Ablation Vapor in High-Velocity Meteors, *Earth, Moon and Planets*, Vol. 82-83, 109 – 128, 2000.
21. Nemtchinov, I.V., Stationary regime of motion of substance vapor heated by radiation under the conditions of lateral spreading, *Prikl. Matem. i Mech.*, Vol. 31 (2), 300-319 (in Russian), 1967.
22. Maljavina, T.B. and Nemtchinov, I.V., Parameters of stationar vapor jet with radial symmetry, heated by laser radiation, *Prikl. Mech. i Techn. Fizika*, Vol. 5, 59-75 (in Russian), 1972.
23. Levin B.Yu., *Physical theory of meteors and meteor substance in the solar system*. USSR Academy of Sciences Publ.Co, (in Russian), 294p, 1956.
24. Lebedinets V.N., Portnyagin Yu.I., Sosnova A.K., *Astronom. vestnik*, Vol. 3, 223-229, (in Russian), 1969.
25. Manning L.A., *J. Geophys. Res.*, Vol. 63, 181 – 196, 1958.
26. Jones J., Jones W., Halliday I., The head echo problem - a solution at last? In *Meteoroids 1998*, Astron.Inst., Slovak Acad. Sci., Bratislava, 29 - 36, 1999.
27. Jones W. Theoretical and observational determinations of the ionization coefficient of meteors, *Monthly Notices of the Royal Astronomical Society*, Vol. 288, 995 - 1003, 1997.
28. Jones W., Halliday I., Effects of excitation and ionization in meteor trains, *Monthly Notices of the Royal Astronomical Society*, Vol. 320, 417 – 423, 2001.
29. Boyd I.D., Computation of atmospheric entry flow about a Leonid meteoroid, *Earth, Moon and Planets*, Vol. 82-83, 93-108, 2000.
30. Shuvalov V.V., Multi-dimensional hydrodynamic code SOVA for interfacial flows: application to the thermal layer effect, *Shock Waves*, Vol. 9, 381 – 390, 1999.
31. Kosarev I.B., Loseva T.V., Nemtchinov I.V., Vapor optical properties and ablation of large chondrite and ice bodies in the Earth's atmosphere, *Solar System Research*, Vol. 30, 265 – 278, 1996.
32. Borovička J., Stork R. and Boček J., First results from video spectroscopy of 1998 Leonid meteors, *Meteorit. Planet. Sci.*, Vol. 34, 987 – 994, 1999.
33. Babadžanov, P.B., and Kramer E.N., Some results of investigations of instantaneous meteor photographs, In *Physics and Dynamics of Meteors*, Dordrech, D.Reidel, 128 – 142, 1968.
34. Borovička J., Two components in meteor spectra, *Planet Space Sci.*, Vol. 42, 145 – 150, 1994.
35. Abe Sh., et al. Chemical evolution of Meteoroid through Meteor and persistent train, *Meteoritics Plan. Sci.*, in press, 2000

## Meteors as a Delivery Vehicle for Organic Matter to the Early Earth (ESA SP-495)

P. Jenniskens

*SETI Institute, NASA Ames Research Center, Mail Stop 239-4, Moffett Field, CA 94035-1000, USA*

### ABSTRACT

Only in recent years has a concerted effort been made to study the circumstances under which extraterrestrial organic matter is accreted on Earth by way of meteors. Meteors are the luminous phenomena associated with the (partial) ablation of meteoric matter and represent the dominant pathway from space to Earth, with the possible exception of rare giant impacts of asteroids and comets. Meteors dominated the supply of organics to the early Earth if organic matter survived this pathway efficiently. Moreover, meteors are a source of kinetic energy that can convert inert atmospheric gasses such as CO<sub>2</sub>, N<sub>2</sub> and H<sub>2</sub>O into useful compounds, such as HCN and NO. Understanding these processes relies heavily on empirical evidence that is still very limited. Here I report on the observations in hand and discuss their relevance in the context of the origin of life.

### 1. INTRODUCTION

The origin of life on Earth is a difficult chemical problem involving organic chemistry of compounds more primitive than those dominating life today and in an environment that is quite alien to us. A key question has always been what chemistry predated the origin of life. Earth was formed in the hot inner parts of the solar system over a period of about 0.10 GYr at a time -4.55 GYr since the present. At the end of that period an impact with a Mars-sized protoplanet created the Moon. Earth was a hot, dry, and sterile place. In the next 0.1 GYr, the cratering rate was a factor of 10<sup>6</sup> higher than today and decreased exponentially with a half life of 0.1 GYr. Between about -4.2 and -3.9 GYr (the accretion period called the "late veneer"), the cratering rate of large impactors gradually decreased so that water could condense into liquid water and organic matter could accumulate over periods of time. This impact rate leveled off around -3.6 GYr. Early signs of life date from as early as -3.8 GYr, suggesting that life formed as soon as conditions were favorable and that early life survived many giant impacts (see Thomas et al. 1997, and recent reviews by Mordibelli et al. 2000, Maurette et al. 2000, Robert et al. 2000).

The source of the water and organic matter on Earth can be traced through isotopes and dynamical models of planetesimal evolution. The water in our oceans has a D/H isotope ratio similar to that found in meteoritic matter. Because of that, it has been argued that most of Earth's water is from asteroidal origin. However, asteroid bombardment declined rapidly after the formation of Jupiter and was most significant when Earth was less than 60% of its final mass. Mordibelli et al. (2000) argued that the only sufficient source of water was a large planetary embryo originating in the outer asteroid belt that may have become part of Earth late in the accretion process (Wetherill 1992). I assume that this must have happened shortly before the Moon forming event at -4.50 GYr, which occurred when Earth already had >90% of its present mass. Much of the volatiles may have been lost in the collision and it is not clear how much and in what form organic matter would have been available at the surface. Since shortly after core formation, Earth had an oxydizing (water rich) mantle, I assume that much of the carbon would have oxydized and vented only as CO<sub>2</sub>. Also, Mordibelli et al. point out that the neon content of Earth's atmosphere is a factor of 8-10 too high with respect to what would be expected in a scenario where all the rare gases and the water have been delivered by carbonaceous chondritic material.

More significant for the origin of life is what complex organic matter may have been available at the Earth's surface in the period of the late veneer. The long half-life of Moon impacts argues for comets being the dominant source for the late veneer. Delsemme (1997) and others have argued that comets in the Jupiter-Saturn region were the dominant source, based on dynamical time scales of planetesimal loss, but that is now disputed by Mordibelli et al. (2000). They rather suggest that comets in the Uranus-Neptune region and Kuiper Belt had the correct loss rate to account for the exponential decay of the Moon impact crater rate. The D/H ratio of these comets, however, is known from Oort-cloud comet observations and measured to be a factor of two higher than observed in Earth's oceans. The D/H ratio of the present day Earth argues for a cometary contribution not exceeding 12% of total and also the anticipated mass influx would have been less

than 10% of all available water (Mordibelli et al. 2000, Robert et al. 2000). D/H of the bulk of the organic matter tends to be slightly higher than for water in comets Halley and Hale-Bopp (Robert et al. 2000), so proton exchange with organics can not solve the D/H issue with oceanic water. The D/H of Jupiter-Saturn comets is not known, but is expected to be less because of more hydrogen exchange of the ice with the D/H poor protosolar nebula during grain accretion (Robert et al. 2000). It is possible, however, that much of the water predated the delivery of the complex organic matter that was needed for the origin of life at the time of the late veneer.

With the water, a lot of extraterrestrial organic matter was accumulated as well. Comets contain nearly as much mass in complex refractory organic matter (23 wt %) than water ice (31 wt %) (Greenberg 2000). Outer belt asteroids can contain up to 10 wt % of organic matter, and ~5 wt % water. The present day water content of Earth is  $\sim 1.4 \times 10^{24}$  g (Delsemme 1992), while the amount of organic refractory matter in the total biomass is only about  $6 \times 10^{17}$  g (Chyba and Sagan 1997). Over time, most of the organic matter must have been oxidized into  $\text{CO}_2$  and deposited in the form of carbonates. The carbon locked up in Earth's carbonate deposits is  $\sim 8 \times 10^{23}$  g, and may be a relict of an early  $\text{CO}_2$ -rich atmosphere, up to 60 bars. It is not clear what was responsible for this oxidation. However, it is thought that the Earth had an oxidizing (water rich) mantle and most likely also an oxidizing ( $\text{CO}_2$ -rich) atmosphere very early on in its history. The production of reduced organic molecules in these conditions is difficult and that makes an exogenous source of the organic molecules more likely.

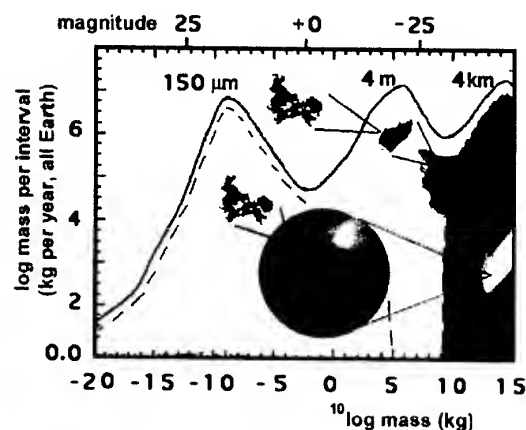


Fig. 1. Yearly influx of extraterrestrial matter (from: Jenniskens et al. 2000)

## 2. METEOROIDS AS A SOURCE OF ORGANICS

Of all exogenous sources of organic matter, dust particles can be the most important (Anders 1989, Chyba and Sagan 1992). Until recently, only "interplanetary dust particles" (IDP's) were considered, which represent grains small enough and slow enough to survive the accretion in Earth's atmosphere without melting or evaporating. IDP's are collected in Earth's atmosphere and can be studied in the laboratory (e.g. Rietmeijer and Nuth 2000).

Much more mass, however, is ablated in the Earth's atmosphere in a luminous phase called a "meteor". Figure 1 shows the present day influx rate of exogenous matter (Jenniskens et al. 2000, and references therein). The graph spans 35 orders of mass, from micron sized dust particles to tens of kilometer-sized asteroids and comets. The mass influx is dominated by three components: a) 100-200 micron sized meteoroids, b) asteroid fragments of ~ 4 meter (the magnitude of this peak is debated), and c) ~ 4 km sized asteroids and comets.

Figure 2 shows what happens to the infalling mass. Of all extraterrestrial matter small enough to not impact as a giant explosion, the bulk is deposited in the atmosphere rather than deposited as unmolten IDP's or meteorite fragments. Only 0.04 percent of asteroidal matter is found as meteorites and less than 8% of all particles smaller than 50 micron will end up as mostly unheated IDP's that can be collected in the stratosphere. Particles less than about 10 micron in size are evaporated as well, because they are thought to be so small that they do not efficiently radiate heat.

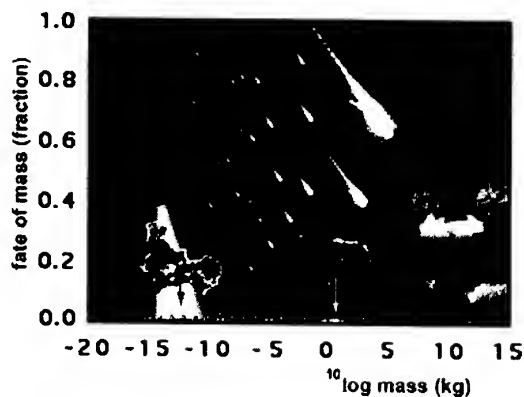


Fig. 2 - The end product of impacts of various sizes (from: Jenniskens et al. 2000).

Meteoric ablation is the dominant fate of most infalling matter. Many of large 100-200 micron micrometeorites collected on the Greenland and Antarctic ice sheets (Maurette et al. 2000) show signs of melting and may well be a product of the meteor pathway. Solid debris, however, is only one form in which this matter is deposited in Earth's environment. In particular, much of the volatile organic matter and water are lost from the meteoroids during this phase and will undergo their own characteristic chemistry before settling to Earth's surface. Much of this paper is about those processes.

It is not clear if Figure 1 is representative for the mass influx at the time of the origin of life. The relative contribution of comets and asteroids may have been different, however. Surprisingly enough, there is much debate over the origin of the various dust components in the present day mass influx. About half of dust and half of large impactors appear to originate from the asteroid belt, but arguments are made that favor the dominance of either origin. The dynamics of comet dust loss is expected to be very similar now than it was at -4 GYr. The orbital dynamics may have been different however, which determines how much dust is lost before a typical impact occurs. More comets may have ended up in short-period orbits, loosing a larger amount of dust to Earth impacts, or less if dynamical conditions led predominantly to hyperbolic impacts. The cratering rate suggests that comet impacts dominated the Moon cratering and thus meteoroids may well have been correspondingly more abundant. The Moon impact record shows that the impact rate was a factor of 100 higher at -4 GYr and a factor of 500 higher in the 0.1 GYr following the formation of the Moon.

If the meteoroid influx was so much higher at the time of the origin of life, then meteoroids represent sufficient organic carbon to account for all carbon in Earth's carbonate deposits and sufficient solar wind implanted Neon to account for the Neon in Earth's atmosphere, but possibly too little water to account for Earth's oceans (Maurette et al. 2000). In light of the efficient loss of organics from the Earth environment, meteoroids are important by providing a continuous source of complex organic molecules to such environments as the ocean surface.

### 3 THE DEPOSITION OF ORGANIC MATTER BY METEORS

The organic carbon in cometary and asteroidal dust has its origins in accretion processes in the interstellar medium (Jenniskens *et al.*, 1993), while a small fraction originates in the atmospheres of late-type stars. The Giotto and Vega spacecraft probes measured the elemental composition of dust grains in the coma of

comet 1P/Halley and found many to be rich in the elements C, H, O and N (Kissel and Krueger, 1987; Jessberger and Kissel, 1991). This organic carbon was mixed intimately with the silicate component and has high molecular mass. Most of it is expected to survive exposure to the vacuum of space and will only be gently warmed when grains come as close to the Sun as Earth's orbit ( $T_{\max} \sim 300$  K). Organic matter in Interplanetary Dust Particles is typically lost only after heating to 600-800 K.

TABLE I

source:	amount (kg/yr)	ref.
Exogenous:		
IDP	$2 \times 10^8$	[1]
<b>Meteors (if 100 % C survives)</b>	<b><math>1 \times 10^9</math></b>	<b>[2]</b>
(Micrometeorites)	$2 \times 10^8$	[3]
Meteorites*	$1 \times 10^6$	[1]
Comets/Asteroid impacts	$10^8$	[1]
Atmospheric:		
<b>Meteors (if LTE, <math>V \sim [OI]</math>)</b>	<b><math>&lt; 1 \times 10^9</math></b>	<b>[2]</b>
Comet/asteroid impacts	$2 \times 10^8$	[1]
Electric discharge	$3 \times 10^7$	[1]
UV photolysis	$3 \times 10^8$	[1]
(mild reducing atmosphere)		
Volcanic:		
Hot or cold springs	(CH <sub>4</sub> only)	[4]

[1] Chyba and Sagan (1997); [2] Jenniskens et al. (2000); [3] Maurette et al. (2000); [4] Mojzsis et al. (1999).

Whether the meteor pathway is important for the delivery of organic matter to the early Earth depends on how efficiently the organic matter survives the ablation process in some useful form. In Table I, my own estimates for the delivery of organic matter from meteors (Jenniskens et al. 2000) are compared to estimates from Chyba and Sagan (1997), Mojzsis et al. (1999) and Maurette et al. (2000), without an effort to re-evaluate the latter. Until now, meteors were not considered in such evaluations, because it was generally assumed that the material that is ablated is destroyed (read: converted to CO<sub>2</sub>). However, if organic matter survives ablation efficiently (Table I), meteors may have contributed more than 2/3 of all infalling organic matter.

Meteors are also potentially efficient sources of energy for atmospheric chemistry, with estimated production rates in Table I if the plasma is in chemical equilibrium and the volume is represented by the measured OI line intensity (Jenniskens et al. 2000, see below).

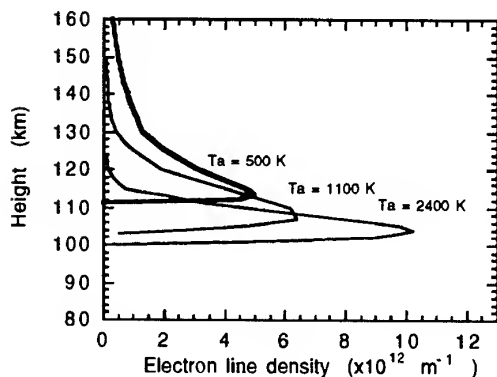


Figure 3 - Ionization profiles for meteoroids with contrasting critical temperatures of ablation ( $T_a$ ), for entry speed of 71 km/s (From: Elford et al. 1997).

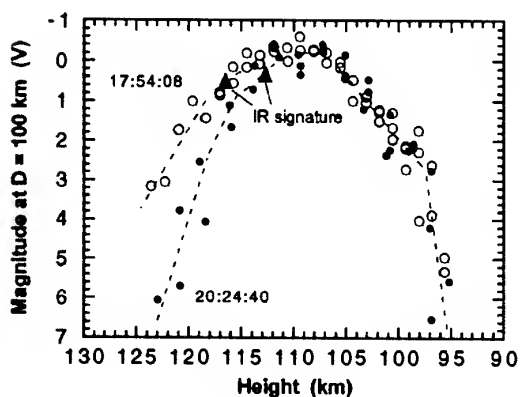


Figure 4 - Position of Mid-IR flares in two Leonid meteor lightcurves (From: Rossano et al. 2000).

The Leonid Multi-Instrument Aircraft Campaign (Jenniskens et al. 2000a) was NASA's first Astrobiology mission to study organic matter accretion in meteors. The Leonid meteor storms have provided an opportunity to deploy instruments that normally would have little chance to detect a meteor. Ground-based observations, too, have provided clues as to where the organic matter may be lost in Earth's atmosphere.

### 3.1 Ablation at high altitude

Classic models of meteor physics assume that the meteoroid is gradually heated by collisions with air molecules until the particle melts and starts to

evaporate individual compounds in order of sublimation temperature. This model is called differential ablation. Because it takes some time for the more volatile compounds to diffuse outwards, each compound is lost over a range of altitude. Figure 3 shows calculations by Elford et al. (1997). The volatile organic material would be lost predominantly at about 117 km in the case of Leonid meteors. More volatile components would come out even higher.

Unusual ablation at a record height was discovered by Spurny et al. (2000), who reported the discovery of high altitude emissions in bright Leonid fireballs. Above 136 km, the meteor looks like a V and must emit very efficiently to explain the observed luminosity. This high-altitude luminosity is probably associated with plasma interaction of electrons emitted in the collisions with air molecules. Only compounds near the surface can be lost as a result of the violent collisions of air molecules with the meteoroid.

Evidence for the differential loss of organic matter was reported by Rossano et al. (2000), who detected a bright infrared flare in the mid-IR images of two meteors. Those flares occurred at 115 and 117 km altitude, respectively, which would be consistent with the release of organic material. The mid-IR intensity was ten times the brightness of the meteor in the optical. However, no spectrum has been recorded yet and it is not certain that this unusual emission was due to the organic matter in the meteoroid.

### 3.2 Ablation at moderate altitudes

Borovicka et al. (1999) did report the early release of a sodium-containing mineral in Leonid meteoroids that were ejected only 100 years ago, consistent with differential ablation. Similar behavior is now known from Draconid and Ursid meteoroids, all from relatively recent ejecta. This phenomenon was linked to the fragile nature of the Leonids meteors that may expose the volatile minerals more efficiently. In fact, most meteors show a simultaneous release of all mineral components, suggesting that also the organic matter is mostly deposited at moderate elevations of 70-110 km altitude, and mostly around 85-90 km where ~150 micron meteoroids with typical 25 km/s entry velocities tend to ablate. There, the organics are shielded from the most ionizing UV radiation and will ultimately settle to the ground.

Three stages need to be considered for the survival of organic matter during deposition at these moderate altitudes. First of all, the impact of air molecules can potentially strongly heat the molecules near the head of the meteor and destroy the compounds. Secondly, the molecules reside for a short period of time in a hot

meteor plasma. A plasma temperature of 4,300 K was measured from the  $N_2/N$  ratio in high resolution Leonid spectra during the 1998 Leonid MAC mission (Jenniskens *et al.* 2000). That temperature was similar to the ~4500 K temperature measured for the metal atom ablation lines of Fe and Mg (Abe *et al.* 2000). Third, once the molecules have cooled they are affected by the ambient chemistry in the upper atmosphere, before sooner or later coming down to the surface.

We used Direct Simulation Monte Carlo techniques to study the rarefied flow field about a meteoroid and the physical conditions in an effort to understand the relatively moderate temperature of 4300 K (Jenniskens *et al.* 2000, Boyd 2000). We also studied the conditions near the head of the meteoroid, where densities are high, using classical hydrodynamic codes to understand the ablation process (Popova *et al.* 2000).

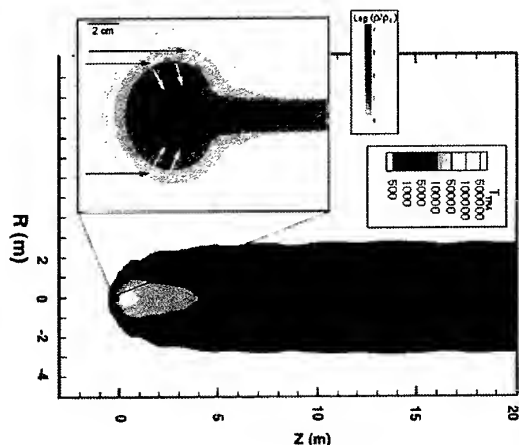


Figure 5 - Meteor model (Compilation from: Jenniskens *et al.* 2000, Boyd 2000, and Popova *et al.* 2000).

The following picture of a meteor has emerged (Figure 5). Initially, the meteoroid is hit by impacting air molecules. But each molecule sputters off 40-80 atoms and molecules of the meteoroid which will thermally expand from the meteoroid. This process rapidly builds a spherical vapor cloud that travels along with the meteoroid. The cloud is ten times bigger than the meteoroid itself. Most air collisions subsequently occur with the cloud, rather than with the meteoroid. Especially with the outer edges of the cloud, where the surface area is highest. The violent collisions with those outer edge vapor cloud compounds leads to momentum transfer to the inside of the vapor cloud, resulting in a leaking out of the densest vapor near the

head as a tail behind the meteoroid. That relatively cold tail subsequently mixes with the hot air molecules to form 4300 K plasma in the wake of the meteor.

It is from this plasma that most meteor emissions are observed. Emissions from the head are observed only in very large meteoroids, where the vapor cloud is large enough to produce a significant number of excitations. Radar head-echoes are now also understood as a result of the vapor cloud, and demonstrate that the cloud is mostly spherical. The size of the vapor cloud increases with speed and with meteoroid mass. Only then can we understand why the plasma temperature in the wake of the meteor is more or less independent from speed and meteoroid mass.

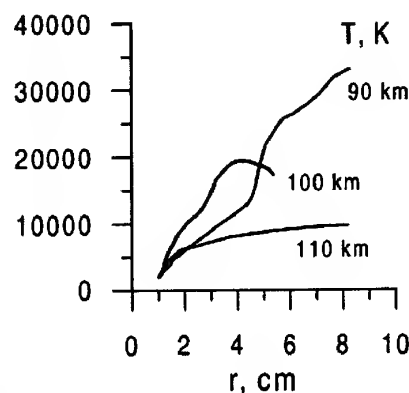


Figure 6 - Temperature of matter leaving head of meteoroid along the center line in the direction of the meteor wake (From: Popova *et al.* 2000).

What happens when a complex organic molecule is sputtered off the surface of a meteoroid? Initially, chances are that it will be close to the meteoroid surface where it can undergo a number of collisions at a relatively low temperature, less than the evaporation temperature, about 1,400 K. More than half of the matter are reducing compounds from the meteoroid.

When organic carbon, containing some fraction of nitrogen and oxygen, is heated to high temperatures, or sputtered by fast ions or energetic photons, small fragments are lost such as H, O,  $H_2$ ,  $O_2$ , OH,  $H_2O$ , CO,  $CO_2$  and  $CH_4$  in a process called carbonization (Jenniskens *et al.*, 1993; Fristrom, 1995, p. 318). Further heating (up to 700 K) leads to further loss of H and  $H_2$  in a process of polymerization, with growth of aromatic ring structures, and some graphitization by stacking of those rings (e.g. Koidl *et al.*, 1990). Ultimately, temperature increase leads to decomposition by loss of  $H_2$ , CN, CH,  $C_2$ , and  $C_3H$ . Hydrocarbon radicals higher than  $C_2$  are so excited by

their formation that they rapidly fission into lower products, leaving only the thermally stable single and double carbon radicals, unless prevented by rapid radiative cooling. Carbon atoms are present too, but at lower abundance because of thermodynamic considerations (Rairden et al. 2000).

It is not clear, how much decomposition of organic molecules will occur in the head of the meteor. After being accelerated by even a single collision, the molecule will stream along the wake line, mix with heated air molecules and expand in volume, during which the average temperature will gradually increase to the plasma temperature of 4,300 K (Figure 6). The temperature increase is more rapid at lower altitudes. The meteoric material represents about 1% of the material in that meteor wake. At the collision frequencies occurring in the wake ( $\sim 25,000$ – $50,000 \text{ sec}^{-1}$ ) a compound will generally undergo 25–50 collisions before quickly (time scales of  $\sim 1 \text{ msec}$ ) cooling down to modest temperatures (Boyd 2000). Each collision (which has to be with the right species in the right orientation) will generally remove only one atom from an organic compound under the type of radical chemistry that will be occurring. This can be particularly important for larger organic compounds such as PAHs (polycyclic aromatic hydrocarbons) that will need more than a few collisions to be destroyed.

The products of this chemistry are different from the original organic compounds in the meteoroid. Notably, they will contain more entrained oxygen, potentially leading to useful compounds for prebiotic chemistry. However, their chemical evolution has not stopped. Once the plasma has cooled, the meteoric matter will reside in the upper atmosphere for long periods of time. These compounds can then become mixed with the atmosphere, engaging in photochemistry, before finally settling to the ground.

In an effort to understand the fate of organic matter in this process, one could search for mid-IR emissions from complex organic matter in the meteoroid or for the molecular breakup products that cause emissions at optical wavelengths. Of all breakup products, the CN radical is the most easily detected because of a strong  $B \rightarrow X$  transition of low energy potential. This electronic transition has a band head at 388.3 nm in the near ultraviolet, but also many nearby iron atom emissions. An upper limit of  $[\text{CN}]/[\text{Fe}] < 0.32$  at 4,300 K was derived from the best observations –2 magnitude Leonid meteor observations to date (Rairden et al. 2000), which translates to less than 1 CN molecule is present per three Fe atoms in the meteor plasma. Comet Halley's dust has a nitrogen abundance of  $[\text{N}]/[\text{Fe}] = 0.79 \pm 0.02$  (Delsemme, 1991). All of that nitrogen is part of the organic carbon. Our upper limit

suggests that half of the nitrogen survives the ablation process. However, nitrogen and iron may also be released in other form than studied here. Clearly, this upper limit has to be improved upon. No infrared spectrum of a meteor has been obtained so far.

### 3.3 Deposition as debris

Organic debris is found in many large micrometeorites that are collected at the Earth's surface (Maurette et al. 2000). If the particle is not completely melted, or the organic matter has not sufficient time to diffuse out of the melt, then some of it can survive the accretion process as a solid particle.

Until recently, this process was not observed in-situ at altitude. Now, Borovicka and Jenniskens (2000) reported that a 1-kg Leonid fireball, with sufficient kinetic energy to break every single bond in the meteoroid a thousand times, was found to leave debris in its path. An afterglow emission was observed that consisted of metal atom emissions but not the usual atomic lines of oxygen and nitrogen of the air plasma. A continuum emission was observed as well, with a blackbody temperature of 1,400 K, the melting temperature of chondritic material.

From persistent emissions in the path of the same fireball at 84-km altitude several minutes later, Russell et al. (2000) reported a continuum emission and the possible detection of a C-H stretch vibration band. This important result awaits further study, but would be consistent with the intimately mixed organic matter surviving the breakup process.

## 4. AEROTHERMOCHEMISTRY

Meteors are also a potential source of energy for interesting aerothermochemistry in an  $\text{N}_2/\text{CO}_2$  rich early-Earth atmosphere (Table I). The violent collisions and high plasma temperatures break molecular bonds and rapid cooling can result in a significant yield of small molecules such as NO, CN and  $\text{C}_2$ . In fact, Local Thermodynamic Equilibrium (LTE) abundances of such compounds peak at the observed plasma temperature of 4,300 K (Figure 7). We discovered that the meteor wake temperature is just high enough to break  $\text{CO}_2$  into its atomic constituents, without ionizing the atoms (Jenniskens et al. 2000).

To estimate the yield of this process is not easy. Non-equilibrium conditions may affect the outcome of the process. The meteoritic material entrained is fairly reducing and can lower the net redox level of the meteor's train, which alters the chemistry during cooling. Also, many processes affect the total volume of air that is affected.

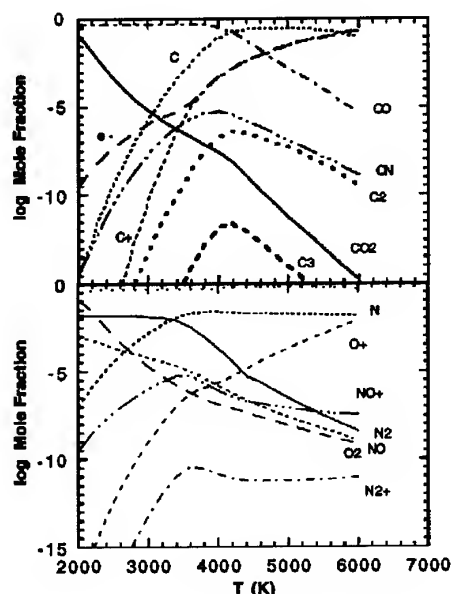


Figure 7 - Molecular abundances for equilibrium air plasma at 95 km altitude in a range of LTE temperatures for an assumed early-Earth atmosphere of particle number composition  $\text{CO}_2/\text{O}_2/\text{N}_2/\text{Ar}/\text{CO} = 95.32/0.13/2.7/1.6/0.08\%$  (From: Jenniskens *et al.* 2000).

The plasma volume has to be derived from measurements. Jenniskens *et al.* (2000) measured from the intensity of OI line emission an effective volume  $10^6$  times larger than expected for a spherical cloud with the classical initial-radius. Part of that is understood from the formation of a warm wake behind the meteor, part may also be simply a result of non-LTE conditions in the air plasma. To complicate matters, the meteoroids were found to eject small bits and pieces to distances up to 2 km away from the cm-sized meteoroid (Taylor *et al.* 2000).

The non-detection of the 389 nm CN emission band sets an upper limit to the volume of the airplasma for -2 magnitude Leonid meteors. The calculated CN abundance for a 4,300 K air plasma in LTE at 95 km altitude equals  $1.0 \times 10^5$  molecules of CN per cubic centimeter for a -2 magnitude Leonid, or an expected  $[\text{CN}]/[\text{Fe}]$  of about  $5 \times 10^{-5}$ . However, if the plasma volume is as large as inferred from the OI emission intensity, this would increase the  $[\text{CN}]/[\text{Fe}]$  to 50 atoms /  $\text{cm}^3$ , a factor of 150 above our detection limit. If LTE applies, the observations suggest that the expected yield for atmospheric processing to CN by meteors in Table I is only  $7 \times 10^6$  g/yr, much less than other estimates. However, unlike other such estimates in

Table I, we assumed an oxidizing  $\text{CO}_2$  rich atmosphere, with little nitrogen, and the yield of CN would be significantly higher in a mildly reducing atmosphere.

Moreover, the chemistry in the wake is significantly affected by the entrained meteoric matter. This material is generally made up of reducing species (metallic/ferrous iron, reduced organics, sulfur/sulfides, etc.) and it will lower the redox level of the meteor's train, reducing the number of oxidizing reactants. For most of these species, the stoichiometry of oxidation is greater than 1:1 and each molecule of meteoritic material can consume more than one oxygen atom. Organic molecules can consume dozens or more. This has the potential to shift the products of such processing away from the usual NO and CO that one typically sees from a non-reducing atmosphere to those one might see for a more reduced atmosphere. Probably the two most important sources of oxygen during such heating are carbon dioxide (which gives up an oxygen to form carbon monoxide) and molecular oxygen itself. In an early Earth's atmosphere, there should be enough meteoritic material entrained to compensate for an atmosphere containing up to several percent of such species depending on stoichiometry and composition of the meteoroid.

## 5. ORGANIC MATTER IN INTERPLANETARY MEDIUM.

No discussion of the fate of organics is complete without considering the chemical evolution from organic matter in comets to organic matter in the meteoroids just before accretion. Of interest are chemical changes that may occur by exposure to sunlight and solar wind during the period from comet ejection to Earth impact. Of interest is our recent find that freshly ejected meteoroids tend to break apart more easily than meteoroids that spend thousands of years in the interplanetary medium (Murray *et al.* 1999, Borovicka *et al.* 1999), but their density is much the same. Jenniskens (2001) derived  $0.97 \pm 0.13$  g/ $\text{cm}^3$  from the effects of solar radiation pressure, in good agreement with the density of about 0.7 g/ $\text{cm}^3$  derived by Spurny *et al.* (2000a) from the deceleration of a Leonid in the Earth's atmosphere. It appears that exposure to the interplanetary medium does not affect the surface-to-mass ratio of the particles as much as the adhesiveness of the rocky subunits in the meteoroid. It is possible that the organic matter becomes more sticky over time, sintering occurs, or the grains otherwise subtly increase their VanderWaals contact areas.

Clearly, much has been learned in recent years about the evolution from organic matter in small solar system bodies to organic compounds in the early Earth environment, but much is still to be learned. Future

Leonid MAC missions and ground-based observations may shed further light on this matter.

*This work was supported by a grant from NASA's Exobiology Program.*

## 9. REFERENCES

- Anders E., 1989, Pre-biotic organic matter from comets and asteroids. *Nature* 342, 255-257.
- Borovicka J., Stork R., Bocek J., 1999. Meteoritics Planet. Sci. 34, 987-994.
- Borovicka J., Jenniskens P., 2000. Time resolved spectroscopy of a Leonid fireball afterglow. *Earth, Moon and Planets* 82-83, 399-428.
- Boyd I.D., 2000. Computation of Atmospheric Entry Flow About a Leonid Meteoroid. *Earth, Moon and Planets* 82-83, 93-108.
- Chyba C.F., Sagan C., 1992. *Nature* 335, 125-132.
- Chyba C.F., Sagan C., 1998. Comets as a source of prebiotic organic molecules for the early Earth. In: *Comets and the Origin and Evolution of Life*. P.J. Thomas, C.F. Chyba and C.P. McKay (eds.), Springer Verlag, p. 147-173.
- Delsemme A.H., 1992. Cometary origin of carbon, nitrogen, and water on the Earth. *Origins of Life* 21, 279-298.
- Delsemme A., 1997. The origin of the atmosphere and of the oceans. In: *Comets and the Origin of Life*, P.J. Thomas, C.F. Chyba, C.P. McKay (eds). Springer Verlag, NY, p. 29-67.
- Despois D., Ricaud P., Lautié N., Schneider N., Jacq T., Biver N., Lis D.C., Chamberlin R.A., Phillips T.G., Miller M., Jenniskens P., 2000. Search for extraterrestrial origin of atmospheric trace molecules - radio sub-mm observations during the Leonids. *Earth, Moon and Planets* 82-83, 129-140.
- Elford W.G., Steel D.L., Taylor A.D., 1997. Implications for meteoroid chemistry from the height distribution of radar meteors. *Adv. Space Res.* Vol. 20, 1501-1504.
- Fristrom R.M., 1995. *Flame Structure and Processes*. Oxford University Press, NY, 510 pp.
- Greenberg J.M., 2000. From comets to meteors. *Earth, Moon and Planets* 82-83, 313-324.
- Jenniskens P., 1993. Carbon dust formation on interstellar grains. *Astron. Astrophys.* 273, 583-600.
- Jenniskens P., 2001. Model of a 1-revolution comet dust trail from Leonid outburst observations. *WGN, the Journal of IMO* 29.
- Jenniskens P., Wilson M. A., Packan D., Lanx C.O., Krueger C.H., Boyd I.D., Popova O.P., Fonda M., 2000. Meteors: A delivery mechanism of organic matter to the early Earth. *Earth, Moon and Planets* 82-83, 57-70.
- Jenniskens P., Butow S.J., Fonda M., 2000a. The 1999 Leonid Multi-Instrument Aircraft Campaign - An early Review. *Earth, Moon and Planets* 82-83, 1-26.
- Jessberger E.K., Kissel J., 1991. Chemical properties of cometary dust and a note on carbon isotopes. In: R. Newburn, M. Neugebauer, J. Rahe (eds.), *Comets in the Post-Halley Era*, Kluwer, Dordrecht, Vol. 2, 1075-1092.
- Kissel J., Krueger F.R., 1987, the organic component in dust from comet Halley as measured by the PUMA mass spectrometer onboard Vega 1, *Nature* 326, 755-760.
- Koidl P., Wild Ch., Dischler B., Wagner J., Ramsteiner M., 1990. *Materials Science Forum* 52-53, 41-70.
- Maugette M., Duprat J., Ingrand C., Gounelle M., Kurat G., Matrajt G., Toppani A., 2000. Accretion of neon, organics, CO<sub>2</sub>, nitrogen and water from large interplanetary dust particles on the early Earth. *Planetary and Space Science* 48, 1117-1137.
- Mojzsis S.J., Krishnamurthy R., Arrhenius G., 1999. In: R.F. Gesteland, T.R. Cech, J.F. Atkins (eds.), *The RNA World*, Second edition. Cold Spring Harbor Laboratory Press, Cold Spring Harbor, NY, 709 pp, p. 1-47.
- Morbidelli A., Chambers J., Lunine J.I., Petit J.M., Robert F., Valsecchi G.B., Cyr K.E., 2000. Source regions and timescales for the delivery of water to the Earth. *Meteoritics and Planetary Science* 35, 1309-1320.
- Murray I.S., Beech M., Taylor M.J., Jenniskens P., Hawkes R.L., 2000. Comparison of 1998 and 1999 Leonid light curve morphology and meteoroid structure. *Earth, Moon and Planets* 82-83, 351-367.
- Pavlov A.A., Pavlov A.K., Kasting J.K., 1999. Irradiated interplanetary dust particles as a possible solution for the deuterium/hydrogen paradox of Earth's oceans. *J. Geophys. Res.* 104, 30725-30728.
- Popova O.P., Sidneva S.N., Shuvalov V.V., Strelkov A.S., 2000. Screening of meteoroids by ablation vapor in high-velocity meteors. *Earth, Moon and Planets* 82-83, 109-128.
- Rietmeijer F.J.M., Nuth J.A., 2000. Collected Extraterrestrial materials: constraints on meteor and fireball compositions. *Earth, Moon and Planets* 82-83, 325-350.
- Robert F., Gautier D., Duhruille B., 2000. The solar system D/H ratio: observations and theories. *Space Science Reviews* 92, 201-224.
- Rossano G.S., Russell R.W., Lynch D.K., Tessensohn T.K., Warren D., 2000. Observations of Leonid Meteors Using a Mid-Wave Infrared Imaging Spectrograph. *Earth, Moon and Planets* 82-83, 81-92.
- Russell R.W., Rossano G.S., Chatelain M.A., Lynch D.K., Tessensohn T.K., Abendroth E., Kim D., 2000. Mid-Infrared Spectroscopy of Persistent Leonid Trains. *Earth, Moon and Planets* 82-83, 439-456.
- Spurny P., Betlem H., Van 't Leven J., Jenniskens P., 2000. Atmospheric behavior and extreme beginning heights of the thirteen brightest photographic Leonid meteors from the ground-based expedition to China. *Meteoritics and Plan. Science* 35, 243-249.
- Spurny P., Betlem H., Jobse K., Koten P., Van 't Leven J., 2000a. New type of radiation of bright Leonid meteors above 130 km. *Meteoritics & Plan. Science* 35, 1109-1115.
- Taylor M.J., Gardner I.C., Murray I.S., Jenniskens P., 2000. Jet-like structures and wake in MgI (518 nm) images of 1999 Leonid storm meteors. *Earth, Moon and Planets* 82-83, 379-389.
- Thomas P.J., Chyba C.F., McKay C.P. (editors), 1997, *Comets and the Origin and Evolution of Life*. Springer Verlag, New York, Inc., 296 pp.
- Wetherill G.W., 1992. An alternative model for the formation of the asteroids. *Icarus* 100, 307-325.

# THE MODEL OF THE QUASI-CONTINUOUS FRAGMENTATION

V. L. Kuznetsov and G. G. Novikov

Novgorod State University, Department of Theoretical and Mathematical Physics,  
St.-Petersburgskaya st., 41, 173003 Novgorod the Great, RUSSIA,  
Email: kvl@nrofsirf.natm.ru; ngg@info.novsu.ac.ru

## 2. THEORY

### ABSTRACT

The amount of data evidencing fragmentation led Levin (1963) to the conclusion that, if fragmentation was not taken into consideration in processing the observations, erroneous result would results. Knowledge of sizes and masses of particles, which separate from a meteor body or on which it is fragmented during moving in atmosphere of the Earth, is of interest for understanding of processes of its interaction with air, and for improvement of our notion idea of a structure of meteor bodies. The new formula, describing an appearance of fragmentation is obtained on the basis of a new mathematical model approach to solution of the task about fragmentation of a meteoric body of quasi-continuous type. The new approach has allowed describing two kind of quasi-continuous fragmentation (QCF) of uniform mathematical formula. The limiting case slow QCF is the pure evaporation and the limiting case fast QCF is the flares of meteors in its classical definition are exhibited.

### 1. INTRODUCTION

The basic theory of light curves of meteoroids ablating via quasi-continuous fragmentation (QCF) has been put forward by Simonenko (1973). Further development has been carried out by Lebedinets (1980), Kalenichenko (1980) and Novikov et al. (1984 – 1998). Novikov et al. have used the theory of QCF of parent meteor body (PMB) to infer the bulk densities of meteoroids and to describe quantitatively the evolution and the structure of meteor coma observed photographically by the method of instantaneous exposure. However present theory has a series of mistakes. We derive the formulas describing the light curves of meteor ablating by QCF of PMB; we also rectify some mistakes present in the theory of Novikov et al. and present the above formulas in compact form.

Novikov et al. have made the following assumptions when constructing the theory QCF (e.g. Novikov et al. (1998)):

1. the only mechanism of ablation of PMB is QCF;
2. the only mechanism of ablation of fragments is evaporation;
3. initial masses of all fragments are the same;
4. deceleration of both PMB and fragments is negligibly small;
5. the basic formulae of the physics theory of meteors are valid for both PMB and fragments.

We shall accept these assumptions, too.

We will neglect the deceleration when deriving formulae for light intensity. The formula for light intensity  $I$  according to the present theory (e.g. Bronshten (1983))

$$I = -\frac{\tau_v v^2}{2} \frac{dM_e}{dt}, \quad (1)$$

where  $dM_e/dt$  — stands for the rate of evaporation of meteoroid mass,  $\tau_v$  represents the luminous efficiency (considered as a function of velocity,  $v$ ). We have adopted also the assumption of the dependence of atmospheric density on the height within the meteor zone in the form  $\rho = 3 \times 10^{-9} \exp[(90 - h)/6]$ , where  $h$  is expressed in km (e.g. Poole & Nicholson (1975)).

Let

$$J_e(t, t') = -\frac{\tau_v v^2}{2} \frac{dm_e(t, t')}{dt} \quad (2)$$

represent the luminosity produced at time  $t$  by an individual fragments detached from PMB at the instant  $t'$ . The function  $m_e(t, t')$  is the mass of the

fragment. The number of fragments detached from PMB per unit time can be expressed as

$$N(t') = -\frac{1}{m_0} \frac{dM}{dt'}, \quad (3)$$

where  $M(t')$  denotes the mass of PMB at time  $t'$ ,  $m_0$  the initial mass of fragment.

Taking into consideration the lifetime of fragments and of PMB, and summing up the contribution of all fragments we get the following formula for the meteor luminosity

$$I = \int_0^t J(t, t') N(t') \Theta(t' + \tau_b - t) \Theta(\tau_0 - t') dt', \quad (4)$$

with  $\Theta(t)$  representing Heaviside's unit step function,  $\tau_0$  denoting the lifetime of PMB to complete fragmentation,  $\tau_b$  being the lifetime of the fragment having been released at the instant of beginning of fragmentation.

Thus, the expression for rate of evaporation of meteoroid mass  $dM_e/dt$  can be written as

$$\frac{dM_e}{dt} = \frac{\rho}{m_0 T} \int_{\rho_b}^{\rho} \frac{dm_e(\rho, \rho')}{d\rho} \frac{dM(\rho')}{d\rho'} \times \quad (5)$$

$$\times \Theta(\rho' + \rho_{frg} - \rho) \Theta(\rho_{rmt} - \rho') d\rho',$$

where  $\rho_{frg}$  represents atmospheric density at the height of disappearance of fragments which were detached at the height of beginning of QCF,  $\rho_{rmt}$  represents the atmospheric density at the height of termination of fragmentation of PMB,  $\rho_b$  being the corresponding atmospheric density,  $\rho'$  designates the atmospheric density at any height  $h'$  and  $T = H/(v \cos z_R)$  ( $z_R$  being zenith distance of the radiant).

Let's place an origin in a point of the beginning QCF.

The equation for  $dM/d\rho'$  and  $dm_e/d\rho$  has been derived by Lebedinets (1980). They are

$$\frac{dM}{d\rho'} = -\frac{\Lambda A H v^2 M^{2/3}}{2 Q_f \delta_0^{2/3} \cos z_R}, \quad (6)$$

$$\frac{dm_e}{d\rho} = -\frac{\Lambda' A' H v^2 m_e^{2/3}}{2(Q - Q_f) \delta^{2/3} \cos z_R},$$

where  $H$  is the constant scale height,  $\Lambda$ ,  $A$ ,  $\delta_0$  stand for the heat transfer coefficient, the shape-density coefficient and the bulk density of PMB respectively, and  $\Lambda'$ ,  $A'$ ,  $\delta$  are analogous quantities valid for fragments,  $Q$  denotes the energy of evaporation, while  $Q_f$  is the energy of fragmentation.

With assumption of constant meteoroid velocity the solution of (6) are

$$M(\rho') = M_0 \left(1 - \frac{\Lambda}{R_0} \rho'\right)^3, \quad (7)$$

$$m_e(\rho, \rho') = m_0 \left(1 - \frac{\Lambda'}{R_1} (\rho - \rho')\right)^3,$$

where we have introduced the auxiliary quantities

$$R_0 = \frac{6 Q_f (M_0 \delta_0^2)^{1/3}}{A T v^3}, \quad (8)$$

$$R_1 = \frac{6(Q - Q_f)(m_0 \delta^2)^{1/3}}{A' T v^3}.$$

$R_0$  and  $R_1$  characterizing PMB and debris of its desintegration.

By substituting (7) and (5) into (1) we can see that the expression for light intensity  $I$  attains form

$$I = \frac{9}{2} \frac{\tau_b v^2 M_0}{T} \left(\frac{\Lambda \Lambda'}{R_0 R_1}\right)^3 \int_0^{\rho} \left(\frac{R_1}{\Lambda'} - (\rho - \rho')\right)^3 \times \quad (9)$$

$$\times \left(\frac{R_0}{\Lambda} - \rho'\right)^3 \Theta\left(\frac{R_1}{\Lambda'} - (\rho - \rho')\right) \Theta\left(\frac{R_0}{\Lambda} - \rho'\right) d\rho'.$$

On carrying out the integration we arrive at

$$I = I_0 \left[ I_1(\rho) + I_2(\rho) \Theta\left(\frac{R_1}{\Lambda'} - \rho\right) + I_3(\rho) \Theta\left(\rho - \frac{R_0}{\Lambda}\right) \right], \quad (10)$$

where

$$I_0 = \frac{9}{2} \frac{\tau_b v^2 M_0}{T} \left(\frac{\Lambda \Lambda'}{R_0 R_1}\right)^3, \quad (11)$$

$$I_1(\rho) = \left(\frac{R_1}{\Lambda'}\right)^3 \rho \left\{ \frac{(\rho_e - \rho)^2}{3} - \frac{(\rho_e - \rho)}{2} \frac{R_1}{\Lambda'} + \frac{1}{5} \left(\frac{R_1}{\Lambda'}\right)^2 \right\}, \quad (12)$$

$$I_2(\rho) = -\left(\frac{R_1}{\Lambda'} - \rho\right)^3 \rho \left\{ \frac{(\rho_e - \rho)^2}{3} - \frac{(\rho_e - \rho)}{2} \left(\frac{R_1}{\Lambda'} - \rho\right) + \frac{1}{5} \left(\frac{R_1}{\Lambda'} - \rho\right)^2 \right\}, \quad (13)$$

$$I_3(\rho) = -\left(\rho - \frac{R_0}{\Lambda}\right)^3 \rho \left\{ \frac{(\rho_e - \rho)^2}{3} + \frac{(\rho_e - \rho)}{2} \left(\rho - \frac{R_0}{\Lambda}\right) + \frac{1}{5} \left(\rho - \frac{R_0}{\Lambda}\right)^2 \right\}. \quad (14)$$

and  $\rho_e = \frac{R_1}{\Lambda'} + \frac{R_0}{\Lambda}$  stands for the atmospheric density at the height of termination of the whole meteor event,  $R_1/\Lambda'$  — represents atmospheric density at the height of disappearance of fragments which were detached at the height of beginning of QCF,  $R_0/\Lambda$  — represents the atmospheric density at the height of termination of fragmentation of PMB.

It can be seen easily that the brightness of a meteor can be implemented by two kinds of fragmentation: fast ( $R_0 < R_1$ ) — parent meteor body is completely fragmented before the fragments release at the height of beginning of QCF can evaporate, and

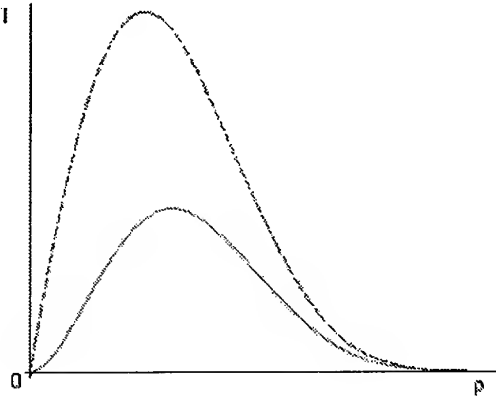


Figure 1. The dependence of intensity of brightness from height (the atmospheric density).

slow ( $R_1 < R_0$ ) — concerns those fragments that have detached at the height of the beginning of fragmentation and disappeared due to evaporation before the PMB completely fragmented. The observed light curve can result from both kinds of fragmentation, which corresponds to two different types of meteoroid material. These kinds are differed by bulk densities of PMB  $\delta_0$  and fragments  $\delta$ , by their initial masses fragments  $m_0$ , and also by their energies of fragmentation,  $Q_f$  ( $Q_f = 10^{10} \times (0.1 + 0.18 \delta_0)$ ).

Novikov et al. (1998) have introduced the intervals taking into account the physical theory QCF and have received two formulae QCF: first — characterizing fast quasi-continuous fragmentation and second — characterizing slow QCF. The exchange of kind of QCF from fast to slow can be simply performed by substituting  $R_1 \leftrightarrow R_0$ , which present the possible ambiguity in the determination of physical parameters of PMB and fragmentation.

The new obtained formula QCF is more compact and is unified for both types of fragmentation that it's being more convenient for meteor physics.

It can be seen easily that the exchange of the former coordinate system into coordinate system in which place an origin not equal beginning of QCF can simply be performed by substituting  $\rho \rightarrow (\rho - \rho_0)$ .

Carrying out the procedure we get

$$I = I_0 \left[ I_1(\rho) + I_2(\rho) \Theta \left( \rho_0 + \frac{R_1}{\Lambda'} - \rho \right) + I_3(\rho) \Theta \left( \rho - \rho_0 - \frac{R_0}{\Lambda} \right) \right], \quad (15)$$

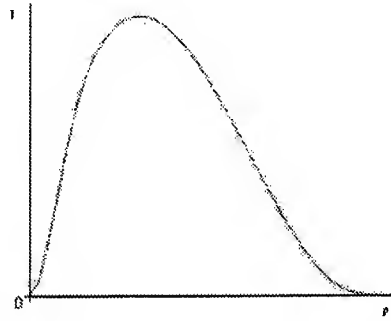


Figure 2. The light curve of meteoroid ablating via fast QCF ( $R_0 < R_1$ ).

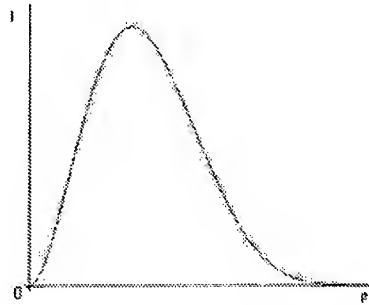


Figure 3. The light curve of meteoroid ablating via slow QCF ( $R_0 > R_1$ ).

where now

$$I_0 = \frac{9 \tau_v v^2 M_0}{2 T} \left( \frac{\Lambda \Lambda'}{R_0 R_1} \right)^3, \quad (16)$$

$$I_1(\rho) = \left( \frac{R_1}{\Lambda'} \right)^3 (\rho - \rho_0) \left\{ \frac{(\rho_e - \rho)^2}{3} - \frac{(\rho_e - \rho) R_1}{2 \Lambda'} + \frac{1}{5} \left( \frac{R_1}{\Lambda'} \right)^2 \right\}, \quad (17)$$

$$I_2(\rho) = - \left( \rho_0 + \frac{R_1}{\Lambda'} - \rho \right)^3 (\rho - \rho_0) \left\{ \frac{(\rho_e - \rho)^2}{3} - \frac{(\rho_e - \rho)}{2} \left( \rho_0 + \frac{R_1}{\Lambda'} - \rho \right) + \frac{1}{5} \left( \rho_0 + \frac{R_1}{\Lambda'} - \rho \right)^2 \right\}, \quad (18)$$

$$I_3(\rho) = - \left( \rho - \rho_0 - \frac{R_0}{\Lambda} \right)^3 (\rho - \rho_0) \left\{ \frac{(\rho_e - \rho)^2}{3} + \frac{(\rho_e - \rho)}{2} \left( \rho - \rho_0 - \frac{R_0}{\Lambda} \right) + \frac{1}{5} \left( \rho - \rho_0 - \frac{R_0}{\Lambda} \right)^2 \right\}. \quad (19)$$

and

$$\rho_e = \rho_0 + \frac{R_1}{\Lambda'} + \frac{R_0}{\Lambda}.$$

In Fig. 1 it is possible to see differences between the light curves constructed under the formula obtained

above (full line) and a light curve, constructed under the formulas given in article Novikov et al. (dashed line). It is possible to see that differences in quantity of a maximum of brightness are observed. For build-ups of both light curves were used identical parameters PMB and fragments.

The limiting case of slow fragmentation is the pure evaporation, and the limiting case of fast fragmentation — flare in its classic definition. Let initial masses fragments be negligibly small ( $m_0 \rightarrow 0$ ), i.e. we will consider that  $R_1 \rightarrow 0$ . It is sufficient to analyse only first addend, which is the pure evaporation.

$$I = -\frac{\tau_v v^2 \rho}{2 T} \left[ -\frac{3M_0 \Lambda}{R_0} \left( 1 - \frac{\Lambda \rho}{R_0} \right)^2 \right] =$$

$$= -\frac{\tau_v v^2 \rho}{2 T} \frac{dM}{d\rho} = -\frac{\tau_v v^2}{2} \frac{dM}{dt}. \quad (20)$$

Let's bulk density PMB negligibly small ( $\delta_0 \rightarrow 0$ ), i. e. we will consider that  $R_0 \rightarrow 0$ .

$$I = -\frac{\tau_v v^2 M_0 \rho}{2 m_0 T} \left[ -\frac{3m_0 \Lambda'}{R_1} \left( 1 - \frac{\Lambda' \rho}{R_1} \right)^2 \right] =$$

$$= -\frac{\tau_v v^2 M_0 \rho}{2 m_0 T} \frac{dm_e(\rho, \rho')}{d\rho} = \quad (21)$$

$$= -\frac{\tau_v v^2 M_0}{2 m_0} \frac{dm_e(t, t')}{dt},$$

that corresponds to a flare in its classic definition.

Figs. 2-3 show the theoretical light curves  $I(\rho)$  of meteoroid ablating via QCF.

Thus, the expression (10) contents to all indispensable requirement.

## REFERENCES

- Bronshten V. A., 1983, *The Physics of Meteoric Phenomena*, Nauka, Moscow
- Kalenichenko V. V., 1980, *Astron. Vestnik*, No. 14, 35
- Levin (Lewin) B. Yu., 1963, *AZh*, No. 40, 304
- Lebedinets V. N., 1980, *Pyl' v Vercnej Atmosfere i Kosmicheskom Prostranstve*. Meteory., Gidrometeoizdat, Moscow
- Novikov G. G., Lebedinets V. N., Blokhin A. V., 1984, *Pis'ma v AZh*, No. 10, 71
- Novikov G. G., Lebedinets V. N., Blokhin A. V., 1984, *Pis'ma v AZh*, No. 10, 785
- Novikov G. G., Konovalova N. A., 1995, *Astron. Vestnik*, No. 29, 547
- Novikov G. G., Konovalova N. A., 1996, *Astron. Vestnik*, No. 30, 454
- Novikov G. G., Pecina P., Konovalova N. A., 1998, *A&A*, No. 329, 769-775
- Poole L.M. G., Nicholson T. F., 1975, *Planet Space Sci.* No. 23, 1261
- Simonenko A. N., 1973, *Meteoritika*, No. 32, 50

# LIGHT CURVES OF FAINT METEORS

Pavel Koten and Jiří Borovička

Astronomical Institute, Ondřejov Observatory, 251 65 Ondřejov, Czech Republic

## ABSTRACT

The results of the light curves analysis of 234 meteors observed and recorded within the double-station image intensifier observations at the Ondřejov observatory are presented. Double-station observations allow to compute the meteor trajectory in the Solar system and in the atmosphere as well as to determine the absolute magnitude of meteor and its mass. Light curves and heights data of all major meteor showers – Lyrids,  $\eta$ -Aquarids, Perseids, Orionids, Leonids, Geminids as well as many sporadic meteors – were analysed. The differences between individual showers were found, e.g. Perseids appear to be more compact than Leonids. There is also difference between 1998 and 1999 Leonids. This suggests different composition or structure of parent bodies. Our data show that the beginning heights of Perseids, Orionids and Leonids are weakly dependent on meteor mass, although the dust-ball theory assumes they should be mass independent.

**Key words:** light curve; meteor shower.

## 1. INTRODUCTION

Double station observations of meteors by a videotechnique started at the Ondřejov observatory in 1998 and data on several hundreds of meteors have been collected during the first three years.

The present work had two main goals. Firstly to develop methods and software for processing of the video records and measuring the position and brightness of meteors, secondly to analyse light curves of these meteors and search for relations between their shapes and other parameters.

The light curve of a meteor, i.e. the dependence of its brightness on time or height, is a clue for studying of the meteor structure. Because there is not significant deceleration in case of faint meteors, the produced light is directly proportional to the rate of ablation. The light curves of the most important meteor showers as are Lyrid,  $\eta$ -Aquadrid, Perseid, Orionid, Leonid and Geminid meteor showers, as well

*Table 1. The coordinates of Ondřejov and Kunžak stations.*

	Ondřejov	Kunžak
eastern longitude	14°46'48.75"	15°12'2.75"
northern latitude	49°54'36.8"	49°06'27.2"
altitude [m]	524	652
distance of stations	92.5 km	
azimuth of stations	340°	

as many sporadic meteors were analyzed and their properties were compared.

## 2. OBSERVATIONS AND INSTRUMENTATION

The double station observation programme at the Ondřejov observatory started in 1998. The commercial videocameras Panasonic S-VHS equipped with a Russian made, second generation Dedal 41 image intensifiers and Arsat lenses 1.4/50 mm are used. The diameter of the field of view depends on the zoom of the camera. Typically it is about 25°. The observations are made on the baseline Ondřejov – Kunžak, the coordinates of both stations are shown in Table 1.

The limiting magnitude of our instrumentation is about +6 for moving objects as meteors are. The corresponding mass for this brightness is approximately  $10^{-5}$  to  $10^{-6}$  g and our sample extends to meteors of about  $10^{-2}$  g.

The video signal is recorded using the S-VHS PAL system, giving time resolution 0.04 second. Time authority is provided by DCF77 signal receiver and time is directly included into the video record.

The records are searched either by using automatic software Metrec (Molau, 1999) or by human inspection and the recorded data are digitalized with a Miro DC-30 framegrabber on a PC computer. Each frame is transformed into 768 x 576 pixel, 8-bit monochrome image and stored as a sequence in the non-compressed AVI format.

Table 2. Overview of processed and used meteors.

shower	processed	used
Lyrids	11	11
$\eta$ Aquarids	10	10
Perseids	45	43
Orionids	16	12
Leonids '98	34	20
Leonids '99	76	46
Geminids	15	12
sporadic	80	80
other showers	74	–

Almost 400 records of double station meteors have been processed up to now and 234 of them were used for the analysis within this work. Table 2 provides an overview. The Leonid records were taken during the joint Dutch-Czech expeditions to China in 1998 (Betlem et al., 1999) and to Spain in 1999.

### 3. DATA PROCESSING

A software PHOTOMET was developed to measure the digitalized records. The processing of the records can be divided into two important steps. The identification of the stars and the calibration of the image is the first step and the measurement of the position and brightness of the meteor is the second one. More details of the photometric procedure are given in Koten (1999).

#### 3.1. Photometric procedure

First step includes flat-fielding, dark image subtraction and reduction. The identification of the stars follows. It is useful for a calibration curve construction and for an image coordinate system determination. The signal of the star is computed as the sum of pixel intensities in the area of interest. The calibration curve is computed as a plot of the stars catalogue brightness against their signal intensities logarithm. Linear response of the image intensifier is assumed, which proved to be true. An example of the calibration curve of the meteor number 98811089 is shown in Figure 1.

Similarly the signal of the meteor is measured as the sum of pixel intensities in the area of interest on each frame of the record. The background value is subtracted and the apparent magnitude of the meteor is determined using the calibration curve. The light curves of several Perseid meteors are shown in Figure 2. Position of the meteor on each frame is measured simultaneously.

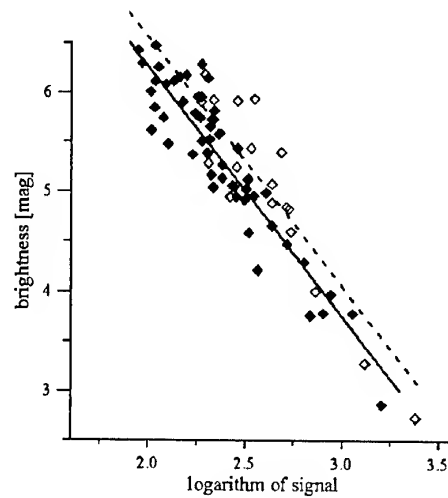


Figure 1. The calibration curve of the meteor 98811089 recorded at the Ondřejov (full symbols) and Kunžak (empty symbols) stations.

#### 3.2. Trajectory computation

Atmospheric and orbital trajectories were computed by means of our standard procedures as well as absolute magnitudes (apparent ones converted to the distance of 100 km) and masses of meteoroids. The errors of all parameters of the meteor trajectory were computed, too.

The majority of the meteor parameters were studied in dependence on the mass of the meteors. The initial photometric mass  $m_\infty$  was computed by integration of the light curve using equation:

$$m_\infty = 2 \int_{t_B}^{t_E} \frac{I dt}{\tau v^2} + m_E \quad (1)$$

(Ceplecha et al., 1998), where  $t_B$  is time of the beginning and  $t_E$  time of the end of the meteor luminous trajectory,  $I$  is the luminosity of the meteor,  $v$  is its velocity,  $m_E$  is the terminal mass (in case of faint meteors it is always zero) and  $\tau$  is the luminous efficiency which is a function of the velocity itself (Ceplecha, 1988).

For each meteor the *Southworth-Hawkins D-criterion* was used to determine the shower membership (Southworth and Hawkins, 1963).

### 4. LIGHT CURVE ANALYSIS

The light curve analysis was done in two ways. Firstly, we investigated the shape of the light curves, secondly, the meteor height data.

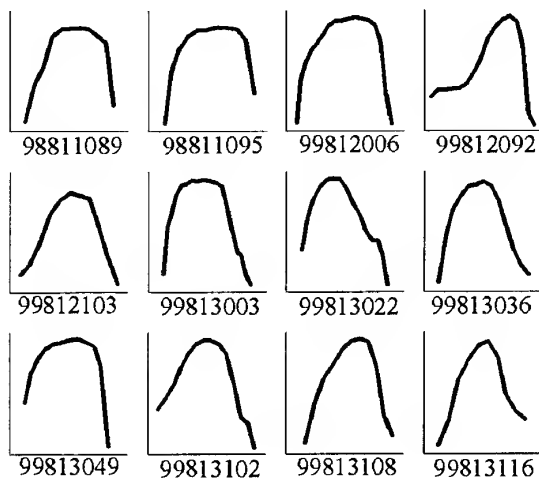


Figure 2. The light curves of several Perseid meteors. Both axes are a relative scale, because the plot only purpose is to demonstrate a variability of the light curves shapes. The x-axis is the height, the y-axis is the absolute magnitude.

#### 4.1. Light curves

The shape of the meteor light curve is described by the set of *F*-parameters as suggested Fleming et al. (1993). For each meteor this set is given by following equations:

$$F_{\Delta M} = \frac{H_{B\Delta M} - H_M}{H_{B\Delta M} - H_{E\Delta M}} \quad (2)$$

where  $\Delta M = 0.25, 0.5, 0.75, 1.00, \dots, 2.5, 2.75, 3.0$ . For these  $\Delta M$  values  $H_{B\Delta M}$  and  $H_{E\Delta M}$  were computed as the heights, where the meteor brightness is by  $\Delta M$  weaker than the maximum brightness  $M_{max}$ .

A meteor with symmetrical light curve, i.e. the light curve with the maximum brightness point exactly at the half of the luminous trajectory, has  $F = 0.5$ . For meteors whose light curves are skewed to the end of the trajectory is  $F > 0.5$  and for meteors with light curve skewed to the beginning of trajectory is  $F < 0.5$ .

We also defined so called *leading* and *trailing slope* of the light curve as the connection lines between the maximum brightness point and the beginning resp. terminal point of the trajectory.

#### 4.2. Dust-ball theory

A quantitative model for the ablation of a dust-ball meteor was suggested by Hawkes and Jones (1975). The dust-ball model assumes a meteoroid as a conglomerate of stone or metal grains with typical mass of  $10^{-6}$  g, which is held together by a lower melting point 'glue'. According to this theory the first

Table 3. The light curves shapes for Leonid '98 and '99 meteor showers.

year	1998	1999
number of meteors	20	46
range $F_{\Delta M=1}$	0.20 – 0.72	0.17 – 0.79
average $F_{\Delta M=1}$	$0.39 \pm 0.14$	$0.47 \pm 0.14$
range $F$	0.10 – 0.81	0.16 – 0.89
average $F$	$0.42 \pm 0.15$	$0.48 \pm 0.16$

stage of ablation involves melting of the glue without light emission and the next stage is the release of the grains and their ablation. Two important predictions resulted from this theory:

- The beginning heights of all meteors with the same velocity should be mass independent
- There should be difference in the behaviour of small and large meteoroids. The heights of the maximum light and the terminal heights should be also mass independent for small meteoroids and should decrease with increasing mass for large meteoroids, which behave more classically.

## 5. RESULTS

The light curves of the most active meteor showers as are the Lyrid,  $\eta$ -Aquadrid, Perseid, Orionid, Leonid and Geminid meteor shower, as well as many of sporadic meteors were analysed. Table 2 shows their overview. The samples of the Lyrid and  $\eta$ -Aquadrid meteor showers are too small mainly because an unfavourable weather conditions in the central Europe. Thus the Perseid, Orionid and Leonid meteor showers were the most important ones for this study.

#### 5.1. Meteor light curve shape

We found that the range of *F*-values is very broad for each shower. For example the parameter *F* varies between 0.17 and 0.79 for Leonid '99 meteor shower. Nevertheless we computed a typical value for each shower. A distribution of *F*-values for the Leonid '99 shower is shown in Figure 3.

We calculated the average value of *F* for each meteor. For many meteors this value is close to  $F = 0.5$ . It means that their light curves are nearly symmetrical. Because some meteors are too weak to cover the whole range of magnitudes in Equation 2 we calculated also *F* for  $\Delta M = 1$ . The results for Leonid '98 and '99 meteor showers are shown in Table 3.

The difference between both years is obvious. The light curves of Leonid '98 meteors reach the maximum brightness point earlier than the light curves

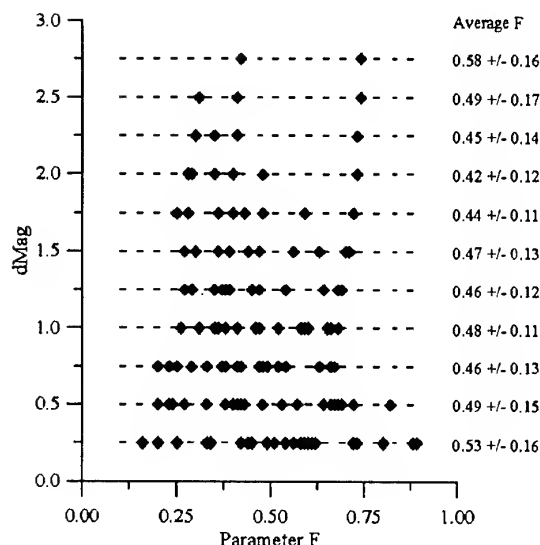


Figure 3. The  $F$ -values distribution for the Leonid '99 meteor shower. The  $x$ -axis is the  $F$ -parameter, the  $y$ -axis is  $\Delta M$ . For each  $\Delta M$  one point represents one meteor. One meteor, however, contributes points to several  $\Delta M$ 's. The average value  $F$  was calculated for each value  $\Delta M$  and is given on the right.

of Leonids '99. We suppose that it is caused probably due different time of the meteoroid exposure to the space environment. The meteoroids of 1998 were ejected from the parent comet earlier than particles of 1999 and they are more porous.

Murray et al. (2000) reported values  $F_1 = 0.47 \pm 0.14$  (for 1998) and  $F_1 = 0.63 \pm 0.15$  (for 1999). The difference between both years is similar but our values are somewhat lower. It could be caused by different instrumentation. Remarkable is fact, that their value  $F_1 = 0.63$  is even greater than the value we found for the Geminid meteors!

Results for other showers in comparison with Leonids are shown in Table 4. The showers were arranged in the order of increasing value of  $F$ . One can easily recognize that the Leonid meteor shower is the most weakest of the studied ones. On the other hand the position of the Geminid meteor shower as the strongest one is not surprising. Remarkable is also very good correspondence of the Orionid and  $\eta$ -Aquarid showers, i.e. the showers with the same parent comet.

Calculation of the light curve slopes gave comparable results. It also revealed that the light curves of Leonid '99 meteors were flatter than Leonid '98 ones. This is confirmed by the height data investigation and explained in Section 5.2.

When we plot the average  $F$ -value against the initial mass we can see that bigger meteors tend to produce light curves that are skewed to the end of the luminous trajectory. This is valid for all showers as is shown in Figure 4. The lack of meteors in the lower

Table 4. The light curve shapes analysis results for shower and sporadic meteors.

shower	parameter $F$	parameter $F_1$
Leonid '98	$0.42 \pm 0.15$	$0.39 \pm 0.14$
Leonid '99	$0.48 \pm 0.16$	$0.47 \pm 0.14$
Lyrid	$0.49 \pm 0.11$	$0.48 \pm 0.10$
Orionid	$0.49 \pm 0.12$	$0.48 \pm 0.13$
eta-Aquarid	$0.50 \pm 0.12$	—
sporadic	$0.53 \pm 0.16$	$0.52 \pm 0.17$
Perseid	$0.54 \pm 0.13$	$0.54 \pm 0.12$
Geminid	$0.57 \pm 0.15$	$0.60 \pm 0.14$

right part of this plot is evident for each shower. This finding is also confirmed by the height data analysis as shown in Section 5.2.

At the end of this section we can conclude that the light curves of the majority of the shower and sporadic meteors are nearly symmetrical. This finding is in good agreement with the dust-ball theory predictions. The classical theory of the meteor ablation results in the light curves which are skewed toward the end of the luminous trajectory. This begins to be valid only for the brightest meteors in our sample.

## 5.2. Height data

Another criterion used for the meteor analysis were height data, i. e. beginning height  $H_B$ , height of the maximum brightness  $H_M$  and terminal height  $H_E$ .

Figure 5 shows that simple plot of these heights against the photometric mass of the Leonid '98 and '99 meteors is not too much illustrative. There is a noticeable weak increase of the beginning height with increasing photometric mass. For the height of the maximum light we are not able to recognize any dependence. Finally the terminal height clearly decrease with increasing mass.

To show the dependences more clearly we adopted a method used by Hapgood et al. (1982). It means that we arranged the meteors in order of increasing mass and divided them into several groups each containing the same number of meteors. For each group we calculated the mean values of  $H_B$ ,  $H_M$ ,  $H_E$  and photometric mass  $m_\infty$ . These values are plotted in Figure 6.

The increase of the beginning height is evident also in this representation. For other heights we can now recognize the behaviour predicted by the dust-ball theory, i. e. the maximum and end heights are constant up to a critical mass and then decrease. The critical mass lies about  $2 \cdot 10^{-3}$  g for Perseids and  $1 \cdot 10^{-3}$  g for other meteor showers.

We should note that the absolute differences in be-

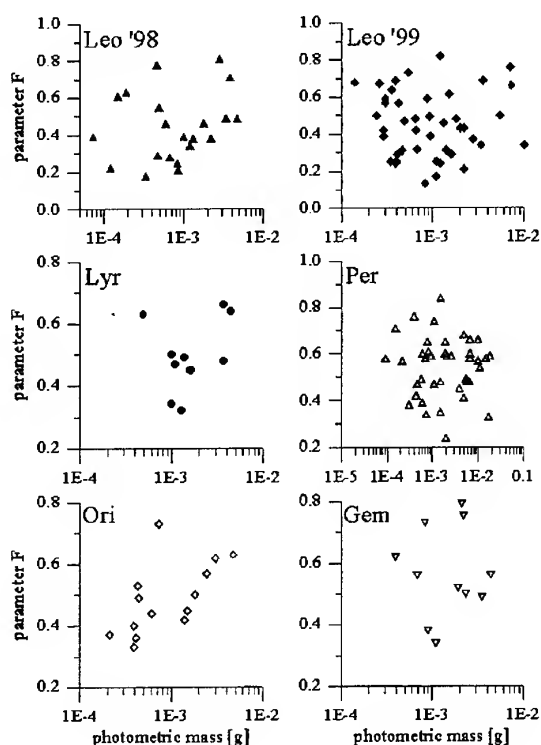


Figure 4. The plot of the  $F$ -values against the meteors photometric mass. The lack of meteors in the lower right part is evident for each shower.

gining and end heights between both Leonid samples were caused by the different geometry of the observation. The 1999 Leonids were observed very close to 101 km and they are mass independent. This is a big distinction in comparison with the Perseid, Orionid and Leonid meteors. The heights of maximum brightness and terminal heights of the Geminid meteors decrease with increasing mass. Unfortunately, the small sample of the meteors does not allow us to determinate if this is valid also for smaller masses.

Although we analyzed only 12 light curves of the Geminid meteors, we found that it is very compact sample. The beginning heights are generally very close to 101 km and they are mass independent. This is a big distinction in comparison with the Perseid, Orionid and Leonid meteors. The heights of maximum brightness and terminal heights of the Geminid meteors decrease with increasing mass. Unfortunately, the small sample of the meteors does not allow us to determinate if this is valid also for smaller masses.

### 5.3. Comparison with sporadic meteors

For each shower we selected a sample of sporadic meteors with similar geocentric velocities and compared their properties with the shower meteors. We found that sporadic meteors do not show the same behaviour as shower meteors. Sporadic meteors usually begin lower than shower meteors, but the difference is not very significant because it is still within the standard deviation of the average value.

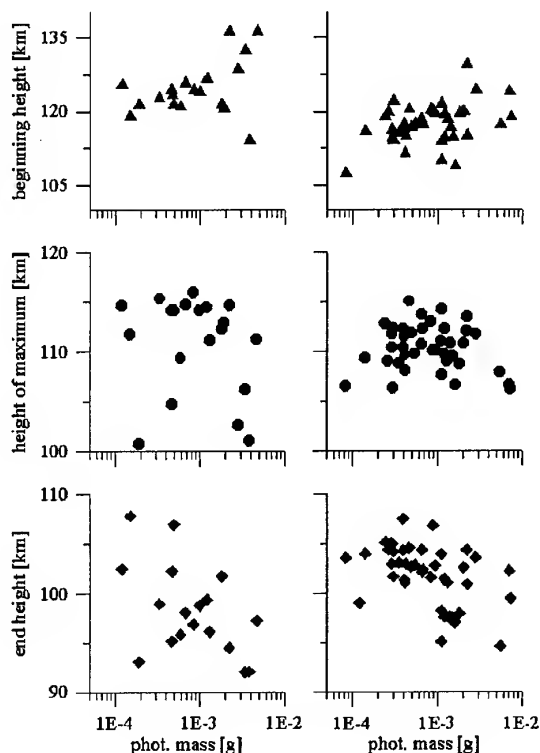


Figure 5. Beginning heights (top), heights of the maximum brightness (middle) and terminal heights (bottom) as a function of the photometric mass of the Leonid '98 (left column) and '99 meteors (right column).

We demonstrate this fact on the Perseid meteors. 14 sporadic meteors with geocentric velocities between 57.2 and 61.2 km/s were selected. The heights of both groups are plotted in Figure 7.

Naturally, sporadic meteors do not form homogeneous sample. Meteors of various origin are contained among them. Some are similar to Perseids, some other are more compact with beginning, maximum and end heights lower than any Perseid of similar mass. No sporadic meteor begins above 120 km, while there are five Perseids with beginning height above 120 km. This suggests that there are quite fragile specimens among Perseids. Similar results were obtained also for the Orionid shower.

### 5.4. Extreme beginning heights of meteors

As a by-product of this work we found several other interesting meteors with the beginning height above 130 km. It was interesting that three of them do not belong to the Leonid meteor shower. The meteors with beginning heights up to 200 km were discovered recently but only for Leonid meteor shower (Spurný et al., 2000). We found one Lyrid meteor with beginning height at 136.8 km and two  $\eta$ -Aquadrid meteors with beginning height at 133.8 km and 150.2 km. Moreover these meteors were not big enough to pro-

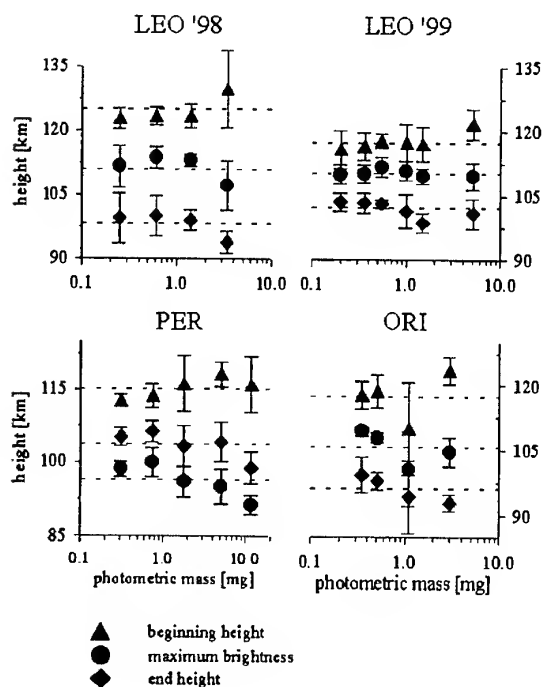


Figure 6. Meteor showers height distribution. Dashed lines show the average values for beginning height, height of maximum brightness and terminal height. Symbols mark average values for each group of meteors as it is explained in the text.

duce fireballs, which is surprising. Details are given in Koten et al. (2001).

We also found another Leonid meteor no. 99173 with  $H_B = 161.2$  km. It is a beginning of fireball. The diffuse, intermediate and sharp ablation phases were detected.

## 6. CONCLUSION

The light curves and the atmospheric trajectories of 234 meteors were analysed. The shapes of the light curves vary very much from meteor to meteor, but generally the light curves are symmetric with maximum point located near the middle of the luminous trajectory. Because the wide range of values of parameter  $F$ , we would like to look for another description of the light curve shape in the future, more physical than the  $F$  parameter.

We found that Leonids are the weakest particles and Geminids the strongest and that there is difference between individual filaments of the single shower.

The beginning heights are weakly dependent on the photometric mass for Perseid, Orionid and Leonid meteor showers but are mass independent for the Geminid meteor shower. For other showers we have not enough data to assess the situation. The heights of the maximum light and the end of the trajectory

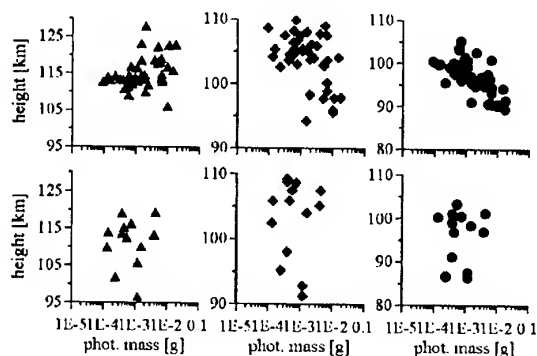


Figure 7. The beginning heights (left column), the heights of the maximum brightness (middle column) and the terminal heights (right column) for the Perseid (top row) and sporadic (bottom row) meteors.

behave in agreement with the dust-ball theory for all showers.

## ACKNOWLEDGMENTS

This work was supported by the Grant Agency of the Czech Republic, grants No. 205/00/1728 and 205/99/0146.

## REFERENCES

- Betlem H., Jenniskens P., van't Leven J., Ter Kuile C., Johannink C., Zhao H., Lei Chenming L., Guanyou Zhu J.; Evans S. and Spurný P., 1999, *Meteorit. Planet. Sci.* 34, 979-986.
- Cepelch Z., 1998, *Bull. Astron. Inst. Czech.* 39, 4, 221-235.
- Cepelch Z., Borovička J., Elford G.W., ReVelle D.O., Hawkes R.L. Porubčan V. and Šimek M., 1998, *Space Sci. Rev.* 84, 327-471.
- Fleming D.E.B., Hawkes R.L. and Jones J., 1993, *Meteoroids and their parent bodies*, Bratislava, 261-264.
- Hapgood M., Rothwell P. and Royrvik O., 1982, *Mon. Not. R. Astron. Soc.* 210, 569-577.
- Hawkes R.L. and Jones J., 1975, *Mon. Not. R. Astron. Soc.* 173, 339-356.
- Koten P., 1999, *Proceedings of the Meteoroids 1998 conference*, Bratislava, 274-282.
- Koten P., Spurný P., Borovička J. and Štork R., 2001, *this proceedings*.
- Molau S., 1999, *Proceedings of the Meteoroids 1998 conference*, Bratislava, 131-134.
- Murray I.S., Hawkes R.L. and Jenniskens P., 2000, *Meteorit. Planet. Sci.* 34, 949-958.
- Southworth R.B. and Hawkins G.S., 1997, *Smithson. Contr. Astrophys.* 7, 261-285.
- Spurný P., Betlem H., Jobse K., Koten P. a Leven van't J., 2000, *Meteorit. Planet. Sci.* 35, 243-249.

## FRAGMENTATION AND INITIAL RADIUS

M. Campbell and J. Jones

University of Western Ontario, London, ON, N6A 3K7 Canada

### ABSTRACT

The initial radius effect is one of the major obstacles to well-calibrated fluxes from meteor radars. This effect is dependent on the wavelength of the radar used, and will be affected by the dependence of initial radius on height and the density profile of electrons in the ionized trail. Most previous studies have assumed a Gaussian profile of electrons in the trail, and have found from multifrequency studies that the initial radius varies more slowly than the mean free path with height. Studies of meteors in the size range similar to that detected by most radars show that they are not single bodies, but fragment prior to luminous ablation; fragmentation is potentially a very significant effect in the initial radius correction. We present a study of the effects of fragmentation on initial radius using a combination of numerical simulation and data from a multifrequency radar.

### 1. INTRODUCTION

Determining the flux of sporadic meteors on the Earth is an important problem, both in terms of defining the sporadic complex and for practical reasons. Meteoroids pose a hazard to spacecraft, both in orbit around the Earth and on interplanetary flights. To be useful, a model must have an accurate measure of the flux in any size range.

Radar is well-suited to studying objects in the millimeter size range. Optical observations can only be used for radiants in the night sky, and are limited to times when the sky is clear; space-based observations are very expensive. Radar observations can be made day and night, in any weather, and so offer relatively inexpensive and complete coverage of the portion of the sporadic complex which is visible from a single hemisphere. Like any observing system, however, meteor radars are subject to biases which must be understood and corrected for in order to get meaningful results.

One of the most significant and least well understood biases is the initial radius effect. Meteor trails typically reach an initial size much greater than the size

of the meteoroids which created them in a very short period of time. Since the meteoroid has an initial velocity between 11 and 72 km/s, atoms ablated from the surface will initially have very high kinetic energies, and will take 15 to 20 collisions (Jones, 1995) to slow to thermal velocities. Meteor trails therefore undergo extremely rapid expansion to an initial dimension, at least a meter at 100 km, then diffuse outward.

Typical radar observations are made of specular reflections from underdense trails. For an overdense trail, created by large meteoroids, the trail is optically thick and scattering occurs mainly from the near side of the trail: in this case the ionization column acts like a metallic cylinder in reflecting the radar beam. Smaller meteoroids, in the size range of interest, produce optically thin underdense trails. In an underdense trail, scattering occurs from electrons throughout the trail, and if the meteor trail has an initial radius of order  $\lambda/2\pi$  (where  $\lambda$  is the wavelength of the system), there will be destructive interference between radiation scattered from the front and back of the trail and the echo will be severely attenuated.

The attenuation due to initial radius is responsible for the well-known echo height ceiling effect. Since atmospheric density decreases with height, the initial radius is expected to increase, and for a radar at any given wavelength there is a height beyond which no underdense echoes can be seen. Models of trail formation (Manning, 1958; Jones, 1995) predict that the initial radius should be directly proportional to the mean free path (inversely proportional to the atmospheric density). However, observational studies have found a smaller dependence of initial radius on mean free path. We have

$$r_i \propto \ell^n \quad (1)$$

where  $\ell$  is the mean free path, or equivalently

$$r_i \propto \rho^{-n} \quad (2)$$

where  $\rho$  is the atmospheric density.

Table 1. Initial radius dependence with height

Study	n
Greenhow and Hall (1960)	0.35
Bayrachenko (1965)	0.82
Baggaley (1970)	$0.45 \pm 0.03$
Baggaley (1980)	$0.42 \pm 0.07$
Baggaley and Fisher (1980)	$0.63 \pm 10\%$
Baggaley (1981)	0.26
Manning (1958) (model)	1
Jones (1995) (model)	1

The exponent  $n$  is 1 if the initial radius is directly proportional to mean free path, and less than 1 if the initial radius increases more slowly than the mean free path.

There is evidently a lot of scatter in the values of  $n$ . Hawkes & Jones (1978) attributed the low values of  $n$  to fragmentation of meteoroids. This is consistent with the dustball model of meteors, which has been so successful in explaining the characteristics of optical meteors (Hawkes & Jones, 1975). According to the dustball hypothesis, a meteoroid is composed of grains of solid material embedded in a low boiling point matrix. The matrix melts prior to the onset of intensive ablation, and the light and ionization observed is therefore due to the collection of small grains. If these grains develop lateral separation, they will add to the initial radius problem. Since the interference due to fragmentation may not be the same for all heights, the exponent  $n$  would be measured to be different from 1 even if each individual fragment were producing ionization consistent with the trail formation models.

The main variables in the calculation of initial radius are the dependence of initial radius on height and the shape of the electron density function across the trail. All experimental studies assume a Gaussian distribution of electrons through the trail, which is a reasonable assumption for a random process and computationally easy to work with, but Jones (1995) found a non-Gaussian distribution from his model. The shape of the density function will affect the dependence of attenuation on wavelength. Performing a Fourier-Bessel transform of the electron density function gives the function relating the attenuation to the radar wavenumber and the initial radius; this can be directly derived from the cylindrical integral of the radiation scattered from each electron in the trail. A Gaussian density profile transforms to a Gaussian dependence of attenuation on initial radius.

## 2. OBSERVATIONS

### 2.1. Equipment

In order to investigate the initial radius effect, a three-frequency meteor radar has been constructed.

It consists of three identical coupled radars running at 17.45MHz, 29.85MHz and 38.15MHz (wavelengths of 17.19m, 10.05m and 7.86m). The transmitters have a peak power of 6kW, and the limiting magnitude of the systems is roughly  $+8.0^M$ . The transmit antennas are three-element Yagis. Each radar has a seven-element interferometer consisting of two-element Yagis, permitting the determination of elevation and azimuth angles to better than 2 degrees. The combination of the transmitting and receiving antenna gain patterns produces a nearly all-sky system. The radar is located near London, Ontario (43°N, 81°W). It uses a commercial software package from Skymet to detect meteor echoes automatically, and filters out noise and overdense echoes. The amplitudes, range and directional information is recorded with the time as read from GPS.

### 2.2. Method

There are two ways to look at the ratio of attenuation on radar systems with different wavelengths. One can compare amplitudes of the same echo seen simultaneously on the two systems, or compare the total numbers seen on each frequency. If amplitudes are compared, the transmit powers of the radars must be well known and the gain patterns of the antennas on each system must be identical. If numbers are compared, the limiting magnitudes for each system must be known accurately. In addition, the selection effects must be the same, or at least well known, on all systems. The mass distribution index must also be well known in order to compare echo numbers.

The method of amplitude comparison is the better method for our radar. Because of lower ionospheric effects, 17.45MHz is subject to interference which decreases the rates at certain times of day; in addition, because echoes have much longer diffusion times on 17MHz some of the echoes may be rejected by the detection software. Amplitude comparison is not without problems: the main difficulty is that the radar produces shaped pulses which are 2km long in the standard operating mode. The pulses are sampled on return at 2km intervals. The amplitude recorded may not be the true amplitude of the signal, if the measurement occurred to one side of the peak of the pulse. To correct for this, we ran the radars in a special mode with 4 km pulses which were sampled every 1.5km. The shape of the pulse was calculated using the return from a large number of echoes. This provided many returns from a single pulse in adjacent range bins, from which we could calculate the maximum amplitude with high accuracy by fitting the points to the known shape of the pulse. Increasing the pulses to 8 km gave no significant improvement.

Speed potentially has an important effect on initial radius, so for this study we used only Geminid meteors from the 2000 shower. The Geminids were identified by taking only those echoes which occurred at 90 degrees from the Geminid radiant; while some sporadics may contaminate the data the vast majority

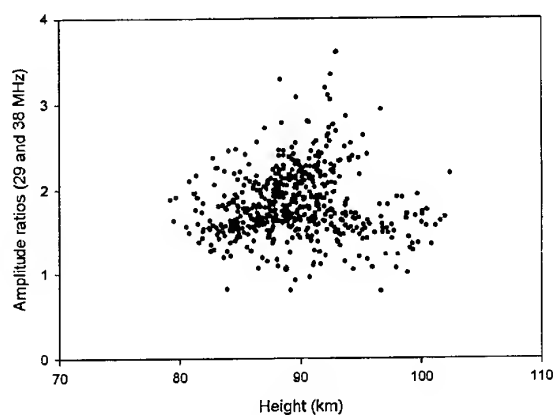


Figure 1. Amplitude ratios for the 2000 Geminids

of these meteors will be shower meteors. Using only Geminids also controls for the possibility of different compositions of meteors from different sources: some meteors may be more fragile than others and therefore show more fragmentation effects.

### 2.3. Results of observations

Data from only 29 and 38 MHz were used for the 2000 Geminids, due to very high levels of interference on 17 MHz which resulted in virtually no usable echoes on that system. The results (Figure 1) showed a large scatter, but there are two general trends: the majority of the echoes follow a trend which seems to turn up around 95 km, while a smaller population has a fairly constant amplitude ratio. The amplitude ratio is expected (in the absence of initial radius effects) to have a value greater than one, since the effective reflecting length of the trail (the first Fresnel zone) is longer at 29 MHz than at 38 MHz. Power differences between the two radars cannot be responsible for the scatter, unless the power of each system underwent large fluctuations in the course of a day (the power has been monitored and stays fairly constant over the course of a day). A miscalibration in the power will otherwise only raise or lower all the points by the same amount. The scatter must be due to frequency or system dependent effect, otherwise it would not affect the amplitude ratios.

## 3. COMPUTER SIMULATIONS

### 3.1. Basic simulation

To investigate initial radius as well as other possible sources of scatter, a computer model was developed to simulate the observations. The model started with meteors with heights generated with a typical height distribution, electron line densities generated according to a mass distribution index, and random azimuthal angles. The returned power was then calcu-

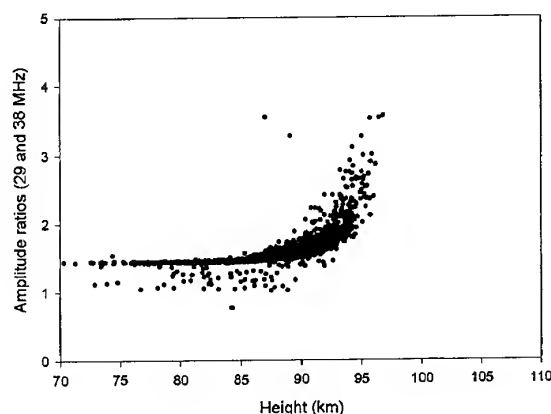


Figure 2. Theoretical amplitude ratios: no fragmentation; includes measurement error and Faraday rotation

lated for each radar, taking into account the gain of transmitting and receiving antennas in the appropriate direction, the transmitting power, and the generated electron line density. Faraday rotation is a potential cause of scatter, since it is greater for systems with longer wavelengths. The radars all had plane polarized radiation. As the beam passes through a region of ionization, the polarization vector is rotated if a magnetic field is present along the direction of the radar beam. If this rotation approaches  $90^\circ$ , the receiving antenna will be unable to detect the return. Using a standard ionospheric model, we calculated the theoretical Faraday rotation for echoes on the two systems. On the 29 MHz system, the Faraday rotation could be more than  $90^\circ$  in the middle of the afternoon for low elevation echoes: it is therefore important to include in the model. Faraday rotation was calculated for each echo based on the time of day and the orientation of the radar beam relative to the magnetic field. An initial radius attenuation factor was then applied at each wavelength.

The initial radius was initially set proportional to the mean free path ( $n=1$ ) and a Gaussian distribution of electrons was used in the trail. This produced a distribution (Figure 2) which turns up at 95 km, like the observational data, but has much less scatter. To increase the scatter, fragmentation was added to the model. In the most basic treatment, there are three variables which can be adjusted to fit the model to the data. The fragments will have some mass distribution index,  $s$ . They will have some radial distribution about the meteor trail axis, and they may have some dependence with height. To limit the number of parameters which must be guessed, optical data was used to derive a reasonable value of  $s$ .

### 3.2. Optical determination of mass distribution of fragments

In order to obtain a large number of light curves, single station observations of sporadic meteors from the 1999 Leonid campaign in Israel were used. Since heights could not be calculated from these observations, the light curves were plotted as luminosity against time. The classical equations of meteor ablation (McKinley, 1961; Campbell et al, 1998) can be used to generate light curves. For some angle of entry, particle velocity and reasonable physical parameters, the light produced as a function of time or of height can be generated. It has been shown (Campbell et al, 1998) that a good fit to most video light curves is only possible if the meteor is assumed to be a collection of fragments ablating individually.

The unmodified classical equations may not be the best way to simulate meteor ablation. They assume that the kinetic energy received by the meteoroid from collisions with air molecules initially go into heating the body, until the object reaches its boiling point. The energy is then used to ablate the meteor surface. While it is true that meteoroids in the size range of interest will heat essentially uniformly, they should begin to produce light before they reach the boiling point. For this reason the equations were modified slightly from the classical formulation. The Clausius-Clapeyron equation was used to calculate the vapor pressure of the substance based on its temperature, and this was used to derive the rate of mass loss, as in Bronshten (1983).

$$\frac{dm}{dt} = \left(\frac{m}{\rho_m}\right)^{2/3} A \psi \exp(K) P_a \frac{\exp\left(\frac{-L\mu}{k_B T}\right)}{\left(\frac{2\pi k_B T}{\mu}\right)^{1/2}} \quad (3)$$

where

$$K = \frac{L\mu}{k_B T_b} \quad (4)$$

Here  $\rho_m$  is the meteor density,  $A$  is the shape factor (1.2 for a sphere),  $\psi$  is the condensation coefficient (1 for metals, 0.5 for other substances (Bronshten, 1983)),  $P_a$  is the atmospheric pressure,  $L$  the heat of ablation,  $k_B$  the Boltzmann constant,  $T$  the meteor temperature, and  $\mu$  the atomic mass of the substance.

The temperature equation is therefore used throughout the meteor's flight, and is modified to include the effect of energy lost with ablating meteor atoms.

$$\frac{dT}{dt} = \frac{A}{cm^{1/3}\rho_m^{2/3}} \left( \frac{\Lambda\rho_a V^3}{2} - \frac{dm}{dt} L - 4\sigma\epsilon (T^4 - T_a^4) \right) \quad (5)$$

Where  $c$  is specific heat,  $\rho_a$  the atmospheric density,  $\Lambda$  the heat transfer coefficient (usually taken as 0.5),

$\sigma$  is the emissivity, and  $T_a$  the atmospheric temperature.

The standard luminosity equation is then used to find the luminous intensity, which is proportional to the mass lost:

$$I = -\frac{1}{2}\tau_I \frac{dm}{dt} V^2 \quad (6)$$

One significant parameter describing a light curve is the  $F$  value, which measures the skew of the curve. It is defined as:

$$F = \frac{t_B - t_M}{t_B - t_F} \quad (7)$$

Where  $t_B$  is the begin time,  $t_F$  is the end time and  $t_M$  is the time of maximum luminosity. The begin and end times are obviously dependent on the limiting magnitude:  $F$  values are usually calculated a certain number of magnitudes below the maximum. Since most useful light curves are 3 magnitudes above noise,  $F$  values were calculated at every half magnitude down from the maximum up to three below maximum. The average of these was used as the final value.  $F$  values can range between 0 and 1. A value less than 0.5 indicates that a light curve peaks in the first half of its trajectory; greater than 0.5 indicates a curve skewed toward the later part of the trajectory. An  $F$  of 0.5 describes a curve which is perfectly symmetric.

The sporadic light curves were found to have  $F$  values which varied depending on magnitude. The brightest meteors had  $F$  values greater than 0.5, and usually close to 1. Fainter meteors had a much wider range of  $F$  values, which averaged roughly 0.5. This is consistent with previous light curve studies (e.g. Murray et al (2000)) which found that faint meteors have symmetric light curves on average.

Light curves were generated using individual fragments with a range of mass distributions, and the intensities were added to produce a cumulative light curve. Mass distribution indices between 1.5 and 2.5 were used for particle masses of  $10^{-6}$ ,  $10^{-7}$  and  $10^{-8}$  kg. For each mass distribution and mass, a large number of light curves were produced and an average  $F$  value calculated. The mass distribution index which best fit the three masses was roughly 1.65 (Figure 3).

### 3.3. Fragmentation simulation

Once the mass distribution index has been specified, the radial distribution of fragments and the height dependence of the fragmentation radius must be calculated. The radial distribution of fragments controls how concentrated the echoes are towards the

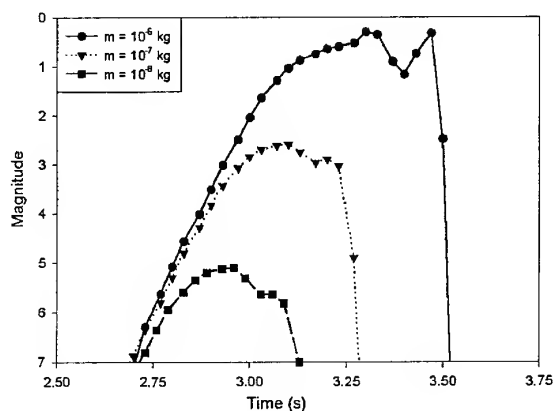


Figure 3. Average simulated light curves with  $s=1.65$

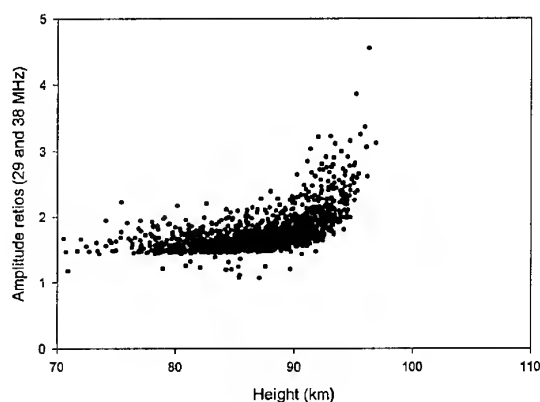


Figure 4. Theoretical amplitude ratios:  $r_f=2m$

basic curve, while the radius of fragmentation will specify the scatter.

The first model to be simulated used a flat distribution of fragments and a fragmentation radius of 2m. The flat distribution indicates that there is no concentration of fragments toward the meteor axis: the particles are randomly distributed in a cylinder of radius  $r_f$ . This produces (Figure 4) more scatter than the single particle model, but the scatter is uniform with respect to height. In the experimental data the scatter increases at higher altitudes.

The next simulation attempted to fit the change in scatter with height. Using  $r_f \propto h$  produced a distribution very like the one we actually observed. The majority of the observations can be explained with this model of fragmentation, but there remains the other segment of the observed echoes, which does not appear to depend on height at all. A reasonable explanation might be that the detection software is not perfectly efficient at removing overdense echoes; when the simulation allowed a few overdense echoes to be measured the results matched the observed results quite well (Figure 5).

To check this explanation, the echoes in the second

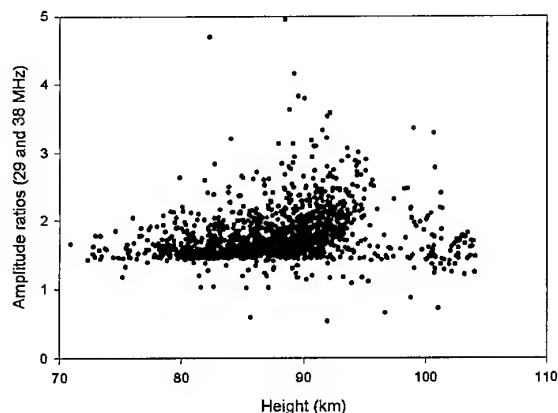


Figure 5. Theoretical amplitude ratios:  $r_f=0.06h-2.3$  with overdense echoes

population were examined individually. In 75% of the data, the echoes were clearly overdense, having a quick rise followed by a constant amplitude. In every case the echo ended suddenly, rather than the usual exponential decay. Apparently these trails had been twisted out of specular alignment by winds shortly after formation and the software was unable to distinguish them from underdense echoes.

#### 4. CONCLUSIONS

Fragmentation is a likely explanation of the scatter in the experimental values of amplitude ratios. It also explains why previous studies have found such a variety of values of the  $n$ , and from this such different functions of initial radius with height. There is no exact value of attenuation due to initial radius effects at any height and wavelength, since the distribution of fragments is random, so no data sets will be exactly the same. The scatter in the values will also cause errors in fitting a profile of initial radius with height: in general the value of  $n$  will be decreased because the attenuations will be larger than predicted at medium heights. At large heights, the initial radius of individual fragments will become so large it will swamp fragmentation.

A good fit to the data was obtained with a large number of fragments, each of which produces its own column of ionization with a Gaussian profile, and a direct dependence on the mean free path. The fragments had a mass distribution index of 1.6 and a uniform radial distribution which increased in radius with height.

While the fact that the radius of the fragments decreases with height may seem counterintuitive, it can be explained. Each meteor starts out as a collection of grains of many sizes: most of these are quite small with a few large particles. At the start of the meteor's ablation, all of the particles ablate at the same time, but at the end of its trajectory, only the largest

fragments remain. This is equivalent to having a smaller fragmentation radius.

The initial radii found in this study are much larger than those found in previous studies. However, recent high-resolution optical images seem to indicate that meteor trails do have significant width.

This study has not dealt with the problem of the dependence of initial radius on speed. Previous studies have found everything from initial radius constant with speed to initial radius directly proportional to speed. This effect will be studied using other show-ers, and for sporadics when the three frequency radar has been equipped to measure speed accurately.

While the model proposed here fits the data, it is not necessarily unique. When data can be obtained from the third frequency, more constraints can be put on the model. In addition, height distributions from other radars operating at a range of frequencies will be used to check the accuracy of the model.

#### REFERENCES

- Bayrachenko I. V., 1963, *Geomag. & Aer.* 5, 353-356.
- Baggaley W. J., 1970, *MNRAS* 147, 231-243.
- Baggaley W. J., 1980, *Bull. Astron. Inst. Czechosl.* 31, 308-311.
- Baggaley W. J., 1981, *Bull. Astron. Inst. Czechosl.* 32, 345-349.
- Baggaley W. J., Fisher G. W., 1980, *Planct. Space Sci.* 28, 575-580.
- Bronshten V. A., 1983, *The Physics of Meteoritic Phenomena*. Reidel, Dordrecht.
- Campbell M. D., Hawkes R. L., Babcock D. D., 1998, *Meteoroids 1998* 363-366.
- Greenhow J. S., Hall J. E., 1960, *MNRAS* 121, 183-196.
- Hawkes R. L., J. Jones., 1975, *MNRAS* 173, 339-356.
- Hawkes R. L., J. Jones., 1978, *MNRAS* 185, 727-734.
- Jones W., 1995, *MNRAS* 275, 812-818.
- Manning L. A., 1958, *J. Geophys. Res.* 63, 181.
- McKinley D. W. R., 1961, *Meteor Science and Engineering*. McGraw-Hill.
- Murray I. S., Beech M., Taylor M. J., Jenniskens P., Hawkes R. L., 2000, *Earth, Moon and Planets* 82-83, 351-367.

## ON THE VARIABLE METEOR PARAMETERS

P. Pecina

Astronomical Institute of the Academy of Sciences of Czech Republic, 251 65 Ondřejov, Czech Republic

### ABSTRACT

Problem of variable shape-density coefficient and ablation parameter is treated. Two new alternatives to approaches published so far are proposed. These alternatives make use of observed distances flown by meteoroid considered as a function of time and observed light curve also as a function of time. The first alternative deals with the case of quasi-isotropic ablation of a body while the second one considers its cross-sectional area to be general function of time. As a result, the time dependence of both parameters inferred from the observational data of 5 fireballs, is presented. As a byproduct, there is also determined the exponent,  $n$ , in the light efficiency dependence on meteoroid velocity,  $\tau \sim v^n$ , for each fireball.

### 1. INTRODUCTION

Photographic or TV observations of meteors provide us with data such as lengths (or equivalently heights) flown by a meteoroid during its atmospheric flight as a function of time. When analyzing such function we can get some parameters of meteoroid, namely its velocity at some chosen height, ablation parameter, and shape-density coefficient divided by the third root of meteoroid mass at the same height (e. g. [8]). In fifties and sixties it was already recognized that observed meteors had not followed simple physical theory of meteors based on the assumption of constant shape-density coefficient and ablation parameter. Therefore, the necessity arose to generalize the theory. The first step was probably performed by Levin [7] who supposed that the cross-sectional area of meteoroid could depend on its mass as  $S \sim m^\mu$  with  $\mu$  being almost arbitrary constant, contrary to previous setting  $S \sim m^{2/3}$  valid strictly only for a sphere. Later Bronshten [1] assumed the parameters depending on velocity of a meteoroid. It was also recognized that the differences between the theory and observations could be attributed to meteoroid fragmentation which was not considered by the old version of the theory. One of latest versions of theory with fragmentation taken into consideration was put forward in [3]. In fact, this is theory published in [8] applied separately on particular parts of mete-

oroid trajectory divided by the fragmentation point. The recent generalization was carried by Ceplecha in [2] who considered the parameters as functions of time even though he has derived only one relation containing two unknown functions and, therefore, he had to suppose some behaviour of one function to be able to get the remaining one. Our approach in this work is based on the derivation of another expression based on observed light curve which contains both functions in question. We consider two cases of the dependence of  $S$  on the quantities involved in ablation process. The first one is embodied by the assumption  $S \sim m^{2/3}f(t)$  where the function  $f(t)$  must follow from the process of solution of the motion and ablation of meteoroid in the atmosphere. It is quite natural generalization of the above relation where  $f(t) \equiv 1$  was put. We will designate this case as quasi-isotropic. The second case arises when putting  $S \sim c(t)$  with  $c(t)$  being a general function of time which must again be inferred from the solution of the meteoroid motion and ablation. We will designate this case as anisotropic. This seems to be the most general setting possible.

The article is divided into several parts. The following brings the mathematical background necessary for the determination of the parameters and functions we want. It is divided into two subsections the former one dealing with the quasi-isotropic case while the latter one with anisotropic case. The section following the mathematical background presents results of application of the theory to 5 fireballs with observed light curves. This article is intended as an description of the method and presentation of the results of its application to selected fireballs. The method will also be applied to other cases including the case of meteors observed simultaneously by TV and radar whenever it is possible. This will be a subject of some future work.

### 2. MATHEMATICAL BACKGROUND

Some parameters of meteoroids can be inferred from the comparison of the observed lengths (or equivalently the heights) flown by a body in the atmosphere as a function of time with the corresponding computed (or theoretical) quantities depending on these

parameters when using the least squares method

$$\sum_i^N (h_i^{obs} - h_i^{com})^2 = \min, \quad (1)$$

where  $N$  stands for the number of lengths (or heights) available. Function  $h_i^{com}(t; p_j)$  depending on time and the meteoroid parameters,  $p_j$ , must follow from the solution of the drag and ablation equations of the meteoroid motion. The parameters  $p_j$  of particular meteoroid, considered as constants, can then be found from (1).

The drag and ablation equation can be written in the form (e. g. [1])

$$m dv/dt = -\Gamma S \rho v^2, \quad Q dm/dt = -\frac{1}{2} \Lambda S \rho v^3, \quad (2)$$

where  $m$  and  $v$  represent the instantaneous meteoroid mass and velocity, respectively,  $\Gamma$  stands for the drag coefficient while  $\Lambda$  for the heat transfer one,  $S$  denotes the cross-sectional area of the body,  $Q$  is the specific heat of the ablation and  $\rho$  the atmospheric density. When introducing the ablation parameter,  $\sigma = \Lambda/2Q\Gamma$ , the set of Eqs. (2) can be replaced by

$$m dv/dt = -\Gamma S \rho v^2, \quad dm/dt = -\sigma \Gamma S \rho v^3. \quad (3)$$

Dividing the 2nd of Eqs. (3) by the 1st one we get

$$dm/dv = \sigma m v, \quad (4)$$

the relation which is widely used for the derivation of the first integral of Eqs. (3). It relies on the functional dependence of  $\sigma$ . It is clear from (4) that this differential equation can be solved under these assumptions:

- $\sigma$  is constant at least on particular subintervals of the whole time interval. The case of the only one constant has been treated by the classical theory (e. g. [8]) while the case of two different constants has been studied in [3];
- $\sigma = \sigma(m)$  or  $\sigma = \sigma(v)$  so that variables in (4) separate. The latter case has been applied in somewhat different form in [1];
- $\sigma = \sigma(m, v)$  for the function  $\sigma$  enabling the Eq. (4) to be solved.

We have still discussed only the mathematical view of the problem. The physical one can discard even the case soluble from previous stand points. One can easily imagine meteoroid having inhomogeneous structure so that its ablation ability changes during the ablation itself. This process need not be a function of the body mass or its velocity. The functional dependence of  $\sigma$  can then manifest as a general function of time or height (which is equivalent). However, such possibility does not fall into the above categories and no first integral exists in this case. In this respect, a general variability of  $\sigma$  of Příbram and Lost City fireballs has been published in [9].

We did not use any other assumption on the ablation process so far. But to proceed further so that we would be able to solve Eqs. (3) and to get the functional dependence  $h = h(t; p)$  where  $p$  represents all the parameters which can enter this function (e. g. the velocity at chosen time instant, the shape-density coefficient,  $K$ ,  $\sigma$ , and so on) we must adopt some assumption about the dependence of  $S$  on quantities involved in the ablation process. The most frequent approach is based on the assumption that body ablates so that it remains a sphere during the whole process (self similar ablation). Even though it is probably not the case in practice it can be considered a good first approximation. It will be treated in the next subsection. The more general case of anisotropic ablation will be a subject of the second subsection.

## 2.1. Quasi-isotropic ablation

Meteoroids are usually modelled as a sphere in this case. Since

$$S = A(m/\delta)^{2/3} \quad (5)$$

is valid for a sphere with  $A = \pi(3/4\pi)^{2/3} \simeq 1.21$ , this relation is frequently used in Eqs. (3). It is sometimes convenient to consider height,  $h$ , as an independent variable instead of time via

$$d/dt = -v \cos z_R d/dh$$

with  $z_R$  representing zenith angle of the meteoroid radiant. Considering meteor as an event starting at the beginning height,  $h_B$ , defined as closely to the beginning of its light curve as possible, the Eqs. (3) further simplify when we define the new independent variable

$$\xi = - \int_{h_B}^h \rho(\bar{h}) d\bar{h}, \quad (6)$$

and introduce another quantity

$$K = A \Gamma / \delta^{2/3}, \quad (7)$$

designated as shape-density coefficient. With  $K$  kept constant but  $\sigma = \sigma(\xi)$  inserted into the Eqs. (3) we obtain the following separate second order nonlinear equations for  $v$  and  $m$  (since no first integral exists in this case):

$$v \frac{d^2 v}{d\xi^2} - \left(1 - \frac{\sigma(\xi)v^2}{3}\right) \left(\frac{dv}{d\xi}\right)^2 = 0 \quad (8)$$

and

$$\frac{d^2 m}{d\xi^2} - \frac{\sigma_\xi}{\sigma(\xi)} \frac{dm}{d\xi} - \frac{2}{3m} \left(\frac{dm}{d\xi}\right)^2 - \frac{2K}{\cos z_R m^{1/3}} \frac{dm}{d\xi} = 0, \quad (9)$$

where  $\sigma_\xi = d\sigma(\xi)/d\xi$ . Unfortunately, these equations are probably not integrable in analytical functions in case of general  $\sigma(\xi)$  since we were not able to find any integration procedure suitable for performing the integration (e. g. [6]). Thus, we cannot get

an analytical formula for  $h = h(\xi)$  from (8). The integration can easily be carried out in case of constant  $\sigma$ . The solution (i. e.  $h = h(t)$ ) then reads

$$t = t_B + \int_{h(t)}^{h_B} \frac{d\bar{h}}{\cos z_R v(\bar{h})}, \quad (10)$$

where  $v(h)$  must be computed from

$$Ei(\sigma v_B^2/6) - Ei(\sigma v^2/6) = \frac{2K e^{\sigma v_B^2/6}}{m_B^{1/3}} \int_h^{h_B} \frac{\rho(\bar{h}) d\bar{h}}{\cos z_R}, \quad (11)$$

with  $Ei(\cdot)$  denoting the integral exponential function. In (11)  $v_B$  and  $m_B$  are meteoroid velocity and mass at the height of  $h_B$ . The mass  $m_B$  cannot be determined without knowledge of  $K$ . Thus, having the observed heights,  $h^{obs}$ , as a function of time we can get  $t_B$ ,  $v_B$ ,  $K m_B^{-1/3}$ , and  $\sigma$  as a result of employing (1). This approach was used as a first approximation for all subsequent computations. The derivatives  $\partial h^{com}(t; p_j) / \partial p_k$  needed for the iterative evaluation of (1) can be computed from analytical formulae in this case.

Quite natural extension of preceding method is to consider also  $K$  to be variable. Since we do not have any evidence of the possible functional dependence of these parameters on any quantities we will simply assume that  $K = K(t)$  and  $\sigma = \sigma(t)$ . This approach was adopted also by Cepelch in [2] where he integrated the drag and ablation equation to obtain one relation between  $K(t)$  and  $\sigma(t)$ . This result was later applied in [4] to selected fireballs with very precise dynamical data. Since the authors had only one relation connecting two quantities they had to adopt some assumption of the behaviour of  $\sigma$  on the beginning part of meteoroid trajectory. They used its value inferred from their previous works. Our approach will be different. We will also integrate the system of basic equations but we will derive and then use another relation connecting  $K(t)$  and  $\sigma(t)$ . Since it is clear from Eq. (4) that no first integral exists in this case the system of equations can be integrated only numerically. The quantities entering the system can be quite different as for their magnitudes. To avoid this difficulty we define the relative quantities as follows:

$$h = h_B x(t), \quad v = v_B y(t), \quad m = m_B z^3(t),$$

$$K(t) = K_B f(t), \quad \sigma(t) = \sigma_B g(t) \quad (12)$$

for which the following initial conditions must be satisfied

$$x(t_B) = y(t_B) = z(t_B) = f(t_B) = g(t_B) = 1. \quad (13)$$

The system of equations governing behaviour of the above quantities reads

$$\dot{x}(t) = -(\cos z_R v_B / h_B) y(t), \quad (14)$$

$$\dot{y}(t) = -K_B m_B^{-1/3} v_B f(t) \rho(x) y^2(t) z^{-1}(t), \quad (15)$$

$$\dot{z}(t) = -\frac{\sigma_B v_B^3}{3} K_B m_B^{-1/3} f(t) g(t) \rho(x) y^3(t). \quad (16)$$

The dot above functions on left hand sides of previous equations represents derivative with respect to time. We will need also function  $\dot{y}(t)$  in the course of further computations. The governing equation can easily be derived when taking the derivative of Eq. (15) with respect to time:

$$\ddot{y}(t) = [\dot{f}/f + h_B(\rho'/\rho)\dot{x} + (2/y)\dot{y} - (1/z)\dot{z}] \dot{y}, \quad (17)$$

where  $\rho' = d\rho(x)/dx$  and  $\dot{f}$  must be computed numerically. The Eq. (15) yields readily the initial condition

$$\dot{y}_B \equiv \dot{y}(t_B) = -K_B m_B^{-1/3} v_B \rho_B, \quad (18)$$

where  $\rho_B = \rho(h_B)$ .

As already stated, dynamical data (i. e.  $x(t)$  in our case) depend both on  $\sigma$  (or  $g(t)$ ) and  $K(t)$  (or  $f(t)$ ). Since  $y(t)$  is related to  $x(t)$  and  $z(t)$  is not directly observable we need another relation connecting these functions. Another observable quantity depending on the functions in question is the light. Its production is connected with the meteoroid mass loss via (e. g. [1])

$$I = -(\tau(v)/2) v^2 \dot{m}, \quad (19)$$

where  $\tau(v) = \tau_0 v^n$  is the light efficiency and  $\tau_0$  together with  $n$  are constants. Inserting into Eq. (19) for  $\dot{m}$  from the second Eq. (3) and bearing in mind the definitions (12) we get

$$I(t) = \frac{\tau_0}{2} v_B^{n+5} \sigma_B K_B m_B^{2/3} f(t) g(t) \rho(x) y^{n+5} z^2. \quad (20)$$

This expression holds also for  $t = t_B$ . Designating  $I(t_B) = I_B$  we get from (20)

$$I_B = \frac{\tau_0}{2} v_B^{n+5} \sigma_B K_B m_B^{2/3} \rho_B.$$

Defining the relative light intensity,  $I_r(t) = I(t)/I_B$ , we have the following expression for this new quantity

$$I_r(t) = f(t) g(t) [\rho(x)/\rho_B] y^{n+5}(t) z^2(t) \quad (21)$$

connecting functions  $f(t)$  and  $g(t)$ . Extracting  $f(t)$  from Eq. (15) and bearing in mind the initial condition (18) we get the following relation

$$f(t) = [\rho_B / \rho(x)] [z(t)/y^2(t)] [\dot{y}(t)/\dot{y}_B]. \quad (22)$$

Using (22) to eliminate  $f(t)$  from (21) we obtain the functional relation for  $g(t)$

$$g(t) = [I_r(t)/y^{n+3}(t) z^3(t)] [\dot{y}_B / \dot{y}(t)]. \quad (23)$$

Since both functions are expressed as functions of  $y(t)$  and  $z(t)$  which must be found from the integration procedure involving also these functions it seems that we did not make any step forward. But we will use (22) and (23) in an iteration procedure with  $y(t)$  and  $z(t)$  derived in previous step. Hence, we can consider the right hand sides of (22) and (23) to be known. This method allows also parameter  $n$

to be determined in each iteration step when comparing "observed"  $\ln I_r^{obs}$  with corresponding theoretical quantity derived from (21). The least squares sum condition requiring the following sum to be minimized with respect to  $n$

$$\sum_i \{(\ln I_r^{obs})_i - \ln[f(t_i)g(t_i)(\rho(x_i)/\rho_B)y_i^5 z_i^2] - n \ln y_i\}^2$$

leads to the formula

$$n = \frac{\sum_i \{(\ln I_r^{obs})_i - \ln[f(t_i)g(t_i)(\rho(x_i)/\rho_B)y_i^5 z_i^2]\} \ln y_i}{\sum_i \ln^2 y_i}, \quad (24)$$

used for the computation of  $n$ . Since the least squares fit of  $x^{obs}(t)$  vs  $x^{com}(t)$  is nonlinear in  $p_j$  (for the designation see Table 1) we must use some iteration method for finding of these parameters. We employ the Gauss-Newton method (e. g. [5]) requiring the derivatives  $\partial x^{com}(t)/\partial p_j$  to be evaluated. These can be computed from an analytical formulae in case of (10) and (11). But this is not possible in case of (14) - (17). Thus, they must be computed numerically together with  $x(t)$ ,  $y(t)$ ,  $z(t)$ , and  $\dot{y}(t)$ . Corresponding equations can be obtained when taking derivatives of (14) - (17) with respect to  $p_j$ . Resulting equations have the general form

$$\frac{d}{dt} \left( \frac{\partial F}{\partial p_j} \right) = G \left( x, y, z, \dot{y}, \frac{\partial x}{\partial p_j}, \frac{\partial y}{\partial p_j}, \frac{\partial z}{\partial p_j}, \frac{\partial \dot{y}}{\partial p_j} \right), \quad (25)$$

where  $F = x, y, z, \dot{y}$  and  $G$  is function resulting from taking the derivatives of right hand sides of (14) - (17) with respect to  $p_j$ . We need also the initial conditions for  $\partial F/\partial p_j$  to be able to integrate the whole system. These are

$$\frac{\partial x}{\partial p_1}(t_B) = \frac{p_2 \cos z_R}{h_B}, \quad \frac{\partial x}{\partial p_k}(t_B) = 0, \quad \text{for } k = 2, 3, 4, \quad (26)$$

$$\frac{\partial y}{\partial p_k}(t_B) = 0, \quad \frac{\partial z}{\partial p_k}(t_B) = 0, \quad \text{for } k = 1, 2, 3, 4, \quad (27)$$

$$\frac{\partial \dot{y}}{\partial p_1}(t_B) = -p_3 p_2' \rho_B' \cos z_R, \quad \frac{\partial \dot{y}}{\partial p_2}(t_B) = -p_3 \rho_B,$$

$$\frac{\partial \dot{y}}{\partial p_3}(t_B) = -p_2 \rho_B, \quad \frac{\partial \dot{y}}{\partial p_4}(t_B) = 0. \quad (28)$$

The first condition in (26) follows from (10) since meteoroid must always move in accord with this relation. The expressions (28) follow from Eq. (15) when evaluating derivatives of its right hand side with respect to  $p_j$  at  $t = t_B$  and employing (26). The remaining zero expressions in (26) - (28) follow from the fact that functions in question do not depend on particular parameter at  $t_B$ .

The numerical integration was performed by using the 4th order Runge-Kutta integrator with constant time step. The comparison of results following from the application of the analytical method (10) and (11) and the numerical one embodied by (14) - (17) and (13), (26) - (28) for  $f(t) \equiv 1$  and  $g(t) \equiv 1$  revealed that the integration time step should be inversely proportional to meteoroid velocity to obtain

Table 1. The parameters entering the description of meteoroid atmospheric motion and ablation.

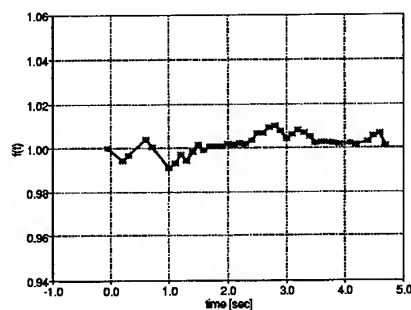
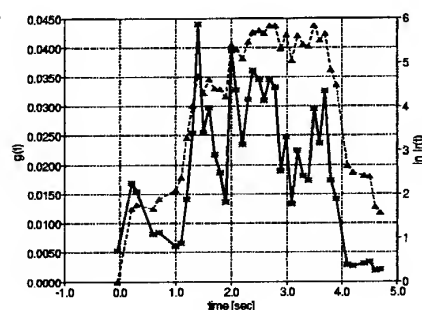
j	1	2	3	4
$p_j$	$t_B$	$v_B$	$K_B m_B^{-1/3}$	$\sigma_B$

comparable results. This time step was found to be equivalent to the step of about  $10^{-3}$  m when expressed in lengths. This comparison was used as a test of the proper function of the numerical approach (14) - (17).

The process of determination of  $f(t)$  and  $g(t)$  can now be described as follows. The description of meteoroid atmospheric motion and ablation depends on the parameters listed in Table 1. The solution begins with finding the first approximation values of  $p_j$  when  $f(t) = g(t) \equiv 1$ . This is performed by the least squares fit of observed  $x^{obs}(t)$  vs computed  $x^{com}(t)$  using Eqs. (10) and (11) as described in [8]. We then get also functions  $x(t)$ ,  $y(t)$ ,  $z(t)$ , and  $\dot{y}(t)$  as an output. Inserting these functions into Eqs. (22), (23) and (24) we receive the first approximation of functions  $f(t)$ ,  $g(t)$ , and the exponent  $n$ . Using the method of numerical derivative on  $f(t)$  provides us with the function  $\dot{f}(t)$ . All these functions and  $n$  are then used in Eqs. (14) - (17) to obtain further approximation of the desired quantities. The procedure of getting these approximations consists of two iteration cycles. The first, we designate as external one, begins with finding the functions  $f(t)$ ,  $g(t)$ , and  $\dot{f}(t)$  as well as  $n$  from (10) and (11) when inserting its results into (22), (23), and (24). Then the second iteration cycle (called the internal one) begins. It consists of least squares fit of  $x^{obs}(t)$  vs  $x^{com}(t)$  where  $x^{com}(t)$  depending on  $p_j$  stems from the numerical integration of (14) - (17) yielding new values of parameters  $p_j$ . Functions  $f(t)$  and  $g(t)$  as well as  $n$  are kept unchanged during this cycle. The internal procedure is terminated when  $|p_j^{new} - p_j^{old}| < 10^{-3} |p_j^{old}|$  is satisfied. After the termination of the internal procedure the new functions  $f(t)$ ,  $g(t)$ , and  $\dot{f}(t)$  together with  $n$  are computed. These quantities enter the new round of the internal procedure, and so on. The external procedure is terminated when  $|n^{new} - n^{old}| < 10^{-4} |n^{new} + n^{old}|$  holds true. The end of the external procedure represents also the end of the whole process of computing the desired quantities. Inserting them into (21) we can get also the theoretical light curve. The result of application of the above described method to some observed fireballs will be presented in the next section.

## 2.2. Anisotropic ablation

We will now pay attention to the more general case than is that in the previous subsection. The assumption that  $S \sim m^{2/3}$  was kept in all works dealing with the variability of meteor parameters (e. g. [1], [2]) with the exception of [7] where Levin supposed

Figure 1. Function  $f(t)$  of Kremnica fireball.Figure 2. Function  $g(t)$  (full line) and observed  $\ln I_r(t)$  (dashed line) of Kremnica fireball, quasi-isotropic case.

that  $S \sim m^\mu$  with general constant  $\mu \geq 0$ . However, we can imagine the ablation of a nonrotating sphere ablating only from the hemisphere faced to the incoming atmospheric flow so that its cross-sectional area does not change at least during some limited time span. It would look as if  $S$  were independent of  $m$  in this case. This forces us to consider the most general functional dependence of  $S$  on quantities involved in the ablation process as possible. We think that it can be achieved when putting

$$S = S_B c(t) \quad (29)$$

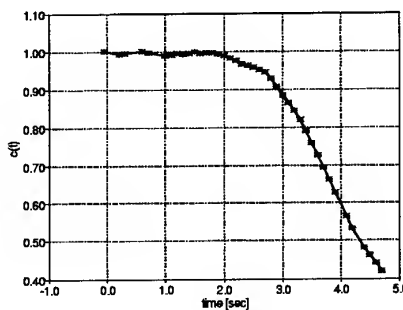
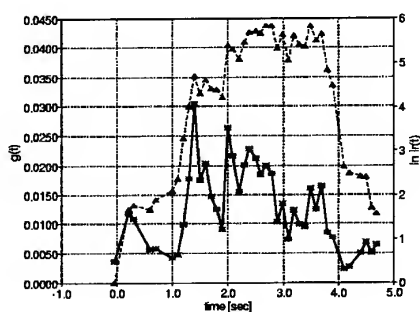
Putting  $S_B = A_B(m_B/\delta)^{2/3}$  we can again define  $K_B$  as in the previous subsection. The first approximation corresponding to constant  $S = S_B$  and  $\sigma$  inserted into (3) is embodied by (10) now with

$$Ei(\sigma v_B^2/2) - Ei(\sigma v^2/2) = \frac{2Ke^{\sigma v_B^2/2}}{m_B^{1/3}} \int_h^{h_B} \frac{\rho(\bar{h}) d\bar{h}}{\cos z_R} \quad (30)$$

instead of (11). It is clear from the setting (29) that  $c(t_B) = 1$ . The definitions of  $x(t)$ ,  $y(t)$ ,  $z(t)$ , and  $g(t)$  from (12) preserves also in this case. However, due to our new relation (29) the set of Eqs. (14) - (17) must be replaced by

$$\dot{x}(t) = -(\cos z_R v_B / h_B) y(t), \quad (31)$$

$$\dot{y}(t) = -K_B m_B^{-1/3} v_B c(t) \rho(x) y^2(t) z^{-3}(t), \quad (32)$$

Figure 3. Function  $c(t)$  of Kremnica fireball.Figure 4. Function  $g(t)$  (full line) and observed  $\ln I_r(t)$  (dashed line) of Kremnica fireball, anisotropic case.

$$\dot{z}(t) = -\frac{\sigma_B v_B^3}{3} K_B m_B^{-1/3} c(t) g(t) \rho(x) y^3(t) z^{-2}(t), \quad (33)$$

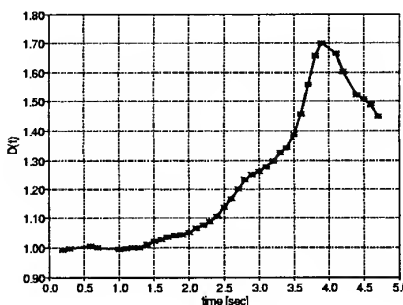
$$\ddot{y}(t) = [(\dot{c}/c) + h_B(\rho'/\rho)\dot{x} + (2/y)\dot{y} - (3/z)\dot{z}] \dot{y}. \quad (34)$$

The initial conditions (13), (18) and (26) - (28) remain valid. The expression for  $I_r(t)$  (i. e. (21)) changes now into

$$I_r(t) = c(t) g(t) [\rho(x)/\rho_B] y^{n+5}(t). \quad (35)$$

Also the expression of  $c(t)$  will differ from (22), namely

$$c(t) = [\rho_B/\rho(x)] [z^3(t)/y^2(t)] [\dot{y}(t)/\dot{y}_B], \quad (36)$$

Figure 5. Function  $D(t)$  of Kremnica fireball.

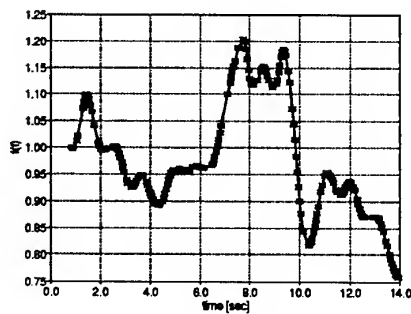


Figure 6. Function  $f(t)$  of PN39499 fireball.

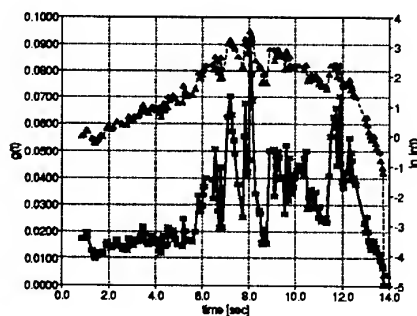


Figure 7. Function  $g(t)$  (full line) and observed  $\ln I_r(t)$  (dashed line) of PN39499 fireball, quasi-isotropic case.

while the relation (23) will be kept unchanged. The last change concerns the relation for  $n$  which should now read

$$n = \frac{\sum_i \{(\ln I_r^{obs})_i - \ln[c(t_i)g(t_i)(\rho(x_i)/\rho_B)y_i^5]\} \ln y_i}{\sum_i \ln^2 y_i} \quad (37)$$

We have now all necessary equations at our disposal and can apply the newly defined procedure to observations. We used the same two-stages iteration process as described at the end of previous subsection. In order to be able to describe how the actual ablation differs from the quasi-isotropic one we are forced to define another function. Indeed, we have

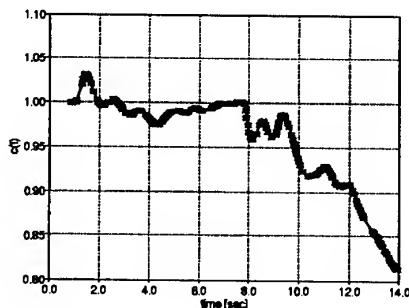


Figure 8. Function  $c(t)$  of PN39499 fireball.

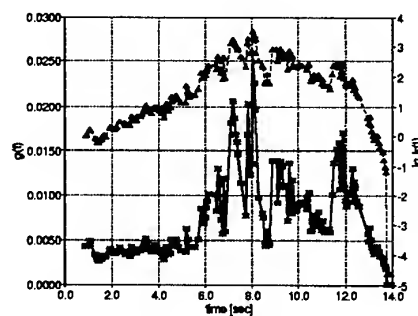


Figure 9. Function  $g(t)$  (full line) and observed  $\ln I_r(t)$  (dashed line) of PN39499 fireball, anisotropic case.

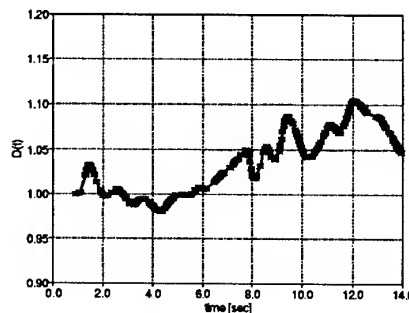


Figure 10. Function  $D(t)$  of PN39499 fireball.

the new relation (29) on the one hand. On the other hand, the relation used in the previous subsection can now be reformulated to read:

$$S_{q-iso} = S_B(m/m_B)^{2/3} = S_B z^2(t).$$

We will characterize the deviation of  $S$  from  $S_{q-iso}$  by its ratio so that

$$D(t) = S/S_{q-iso} = c(t)/z^2(t). \quad (38)$$

This is the function we will use as a measure of anisotropic ablation.

### 3. RESULTS

Results of the application of the methods to 5 meteors described in the previous two subsections are collected in Table 2. These results indicate that each meteor behaves quite independently from any other one as for the found course of their functions  $f(t)$ . The values of  $\sigma_B$  following from the second method are generally lower than those following from the first one. The parameter  $n$  resulting from the former method attains also negative values while the latter approach yields only positive values. The behaviour of functions  $g(t)$  is similar in both results and copies the course of the particular light curve with the exception of Kremnica (see Fig. 4) reaching its maximum value between 1.0 and 1.5 seconds while the

Table 2. Results of application of the methods from two preceding subsections to 5 selected meteors. The quantity  $\sigma_l = \sqrt{\sum_i (l_i^{obs} - l_i^{com})^2 / (N - 4)}$  where  $l_i^{obs}$  are observed distances along the meteoroid atmospheric trajectory while  $l_i^{com}$  are corresponding computed quantities ( $l_i^{com} = h_i^{com} / \cos z_R$ ), serves as an measure of the quality of fit. It is expressed in meters.  $N$  is the number of heights used in computation. The last but one column of each block contains the resulting exponent  $n$  from  $\tau(v)$  (see (19)) while the number of iterations needed in the external iteration cycle,  $ni$ , is presented in the last column of each block.

functions	$f + g$						$c + g$					
meteor	$v_B$	$Km_B^{-1/3}$	$\sigma_B$	$\sigma_l$	$n$	$ni$	$v_B$	$Km_B^{-1/3}$	$\sigma_B$	$\sigma_l$	$n$	$ni$
Kremnica	21.915	2.870	0.005228	20.6	-2.436	7	21.892	2.607	0.003646	26.4	0.868	11
	$\pm 0.007$	$\pm 0.025$	$\pm 0.000092$				$\pm 0.008$	$\pm 0.027$	$\pm 0.000051$			
PN 39499	12.292	1.798	0.0172	97.4	2.412	151	12.321	1.976	0.00425	85.4	5.026	16
	$\pm 0.007$	$\pm 0.026$	$\pm 0.0013$				$\pm 0.007$	$\pm 0.026$	$\pm 0.00037$			
PN 39828	13.365	5.14	0.0115	39.6	3.481	123	13.386	5.57	0.0086	35.5	4.436	4
	$\pm 0.012$	$\pm 0.13$	$\pm 0.0048$				$\pm 0.011$	$\pm 0.12$	$\pm 0.0011$			
PN 39122	22.291	9.74	0.000288	19.9	0.370	8	22.282	9.51	0.000245	21.5	0.910	30
	$\pm 0.011$	$\pm 0.13$	$\pm 0.000048$				$\pm 0.011$	$\pm 0.13$	$\pm 0.000017$			
PN 39608	19.695	10.60	0.0022	23.2	-0.333	79	19.687	10.18	0.00231	22.9	0.551	3
	$\pm 0.013$	$\pm 0.26$	$\pm 0.0012$				$\pm 0.012$	$\pm 0.22$	$\pm 0.00037$			

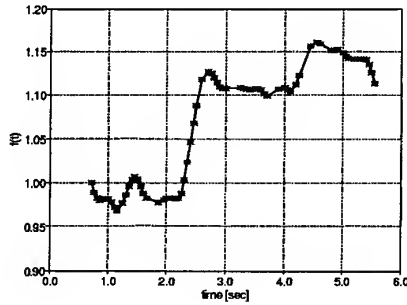


Figure 11. Function  $f(t)$  of PN39828 fireball.

maximum of light was reached between 2.2 – 3.5 sec. Some of meteors display their maximum ablation near the beginning (Kremnica, PN39828) while the others in the middle (PN39499, PN39122, PN39608) or even at the end (PN39828). Most of meteors possess more than one peak. Interesting is the behaviour of functions  $c(t)$  describing the way by which particular body changes its cross-sectional area during ablation. While Kremnica (Fig. 3) and PN39122 (Fig. 18) show the behaviour we considered when the introduction of the function  $c(t)$  (Eq. (29)) was motivated, the remaining meteors (Figs. 8, 13, and 23) show the variability close to the quasi-isotropic case. As to the function  $D(t)$ , it deviates from 1 for all meteors, at least on the second parts of their trajectories. As the most pronounced example can serve Kremnica (see Fig. 5). Other meteors have less pronounced behaviour. Even though not presented here in graphical form the theoretical light curves (embodied either by relation (21) or (35)) are very close to those observed so that they would coalesce into one curve when having been drawn into one graph.

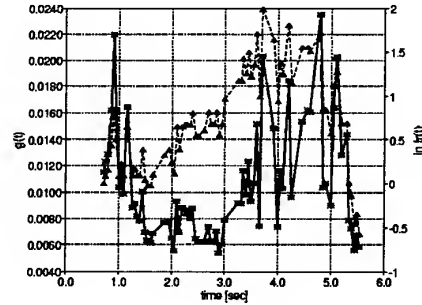


Figure 12. Function  $g(t)$  (full line) and observed  $\ln I_r(t)$  (dashed line) of PN39828 fireball, quasi-isotropic case.

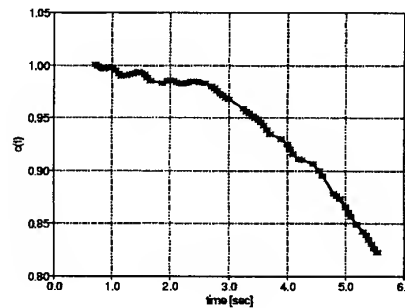


Figure 13. Function  $c(t)$  of PN39828 fireball.

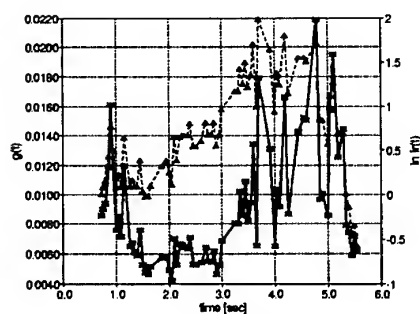


Figure 14. Function  $g(t)$  (full line) and observed  $\ln I_r(t)$  (dashed line) of PN39828 fireball, anisotropic case.

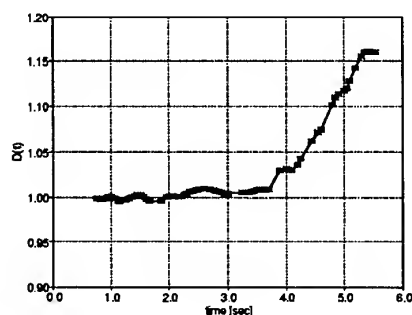


Figure 15. Function  $D(t)$  of PN39828 fireball.

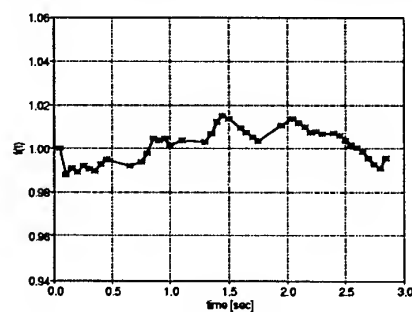


Figure 16. Function  $f(t)$  of PN39122 fireball.

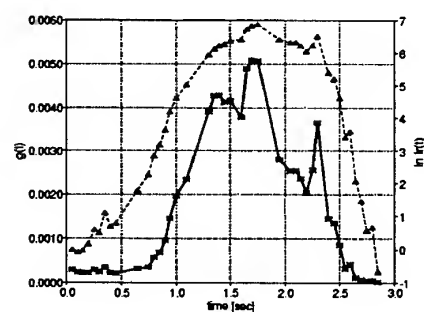


Figure 17. Function  $g(t)$  (full line) and observed  $\ln I_r(t)$  (dashed line) of PN39122 fireball, quasi-isotropic case.

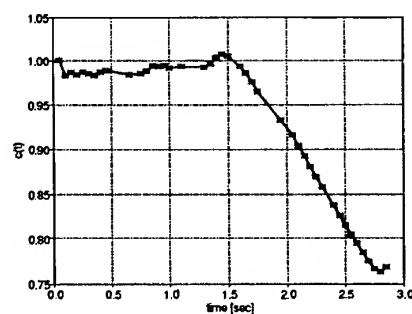


Figure 18. Function  $c(t)$  of PN39122 fireball.

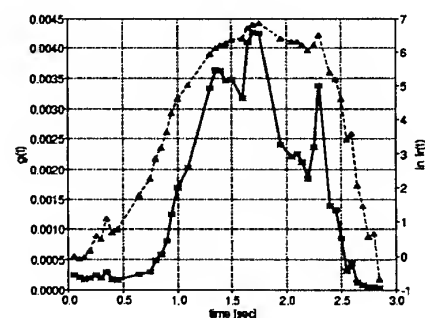


Figure 19. Function  $g(t)$  (full line) and observed  $\ln I_r(t)$  (dashed line) of PN39122 fireball, anisotropic case.

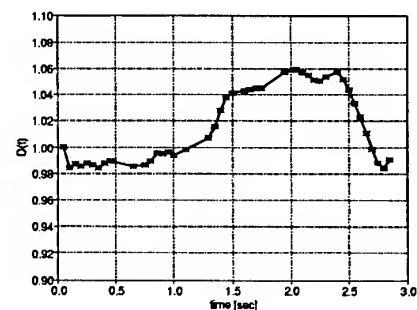


Figure 20. Function  $D(t)$  of PN39122 fireball.

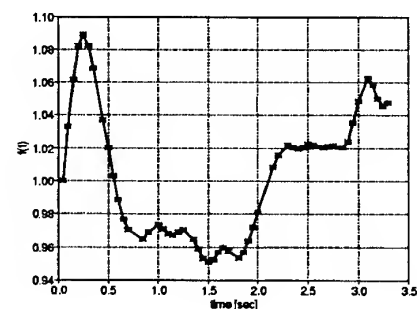


Figure 21. Function  $f(t)$  of PN39608 fireball.

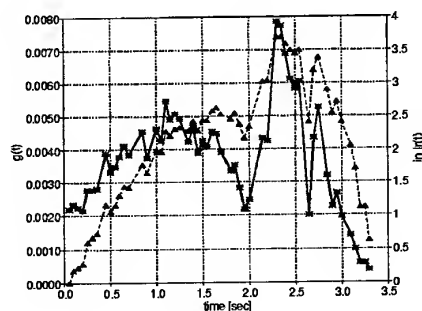


Figure 22. Function  $g(t)$  (full line) and observed  $\ln I_r(t)$  (dashed line) of PN39608 fireball, quasi-isotropic case.

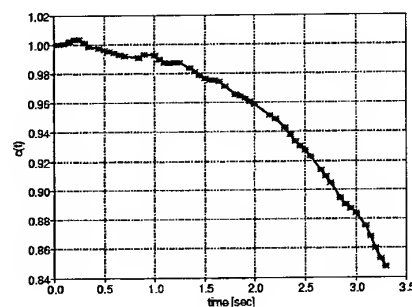


Figure 23. Function  $c(t)$  of PN39608 fireball.

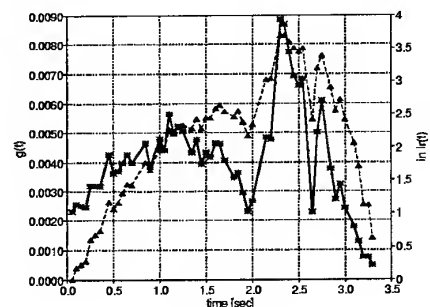


Figure 24. Function  $g(t)$  (full line) and observed  $\ln I_r(t)$  (dashed line) of PN39608 fireball, anisotropic case.

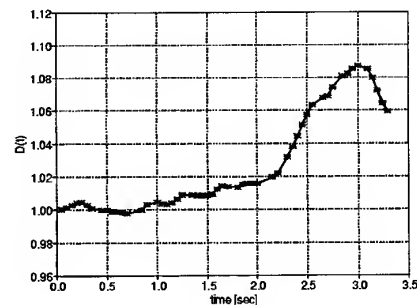


Figure 25. Function  $D(t)$  of PN39608 fireball.

#### 4. CONCLUSION

We have presented two approaches to the problem of finding the variable meteor parameters from the observational data and have applied them to 5 observed meteors with light curves. The most general conclusion we can draw is that each of these meteors behaved quite differently as compared with any other one remaining. The methods can be applied to all meteors providing sufficiently precise data, i. e. lengths (or heights) as a function of time. To be able to infer the general features of meteor behaviour it is necessary to study much more cases than in this work which was intended only as a presentation of new possible approaches.

Since we did not assume anything about the behaviour of  $f(t)$  or  $g(t)$  and these functions had to be reconstructed only from observational data of each particular meteor our approach could not be designated as mathematical modelling of meteor event.

#### ACKNOWLEDGMENTS

This work was supported by the scientific key project K3012103 and the grant No 205/00/1728 of the Grant Agency of Czech Republic.

#### REFERENCES

1. Bronshten V. A., 1983, *Physics of Meteor Phenomena*. Kluwer acad. publ., Dordrecht, Boston, Lancaster
2. Ceplecha Z., 1999, in *Meteoroids 1998*, eds. W. J. Baggaley and V. Porubčan, Exact dynamical behavior of meteoroids in the atmosphere. pp. 55 – 58, Bratislava
3. Ceplecha Z., Spurný P., Borovička J., Keckliková J., 1993, *A&A*, 279, 615
4. Ceplecha Z., Borovička J., Spurný P., 2000, *A&A*, 357, 1115
5. Demidenko E. Z., 1989, *Optimizacija i regressija*. Nauka, Moscow
6. Kamke E., 1959, *Differential Gleichungen, Lösungsmethoden und Lösungen. I: gewöhnliche Differentialgleichungen*. Leipzig
7. Levin (Lewin) B. Yu., 1961, *Theorie der Meteore und die meteoritische Substanz im Sonnensystem*. Scientia Astronomica 4, Akademie Verlag, Berlin
8. Pecina P. and Ceplecha Z., 1983, *Bull. Astron. Inst. Czechosl.*, 34, 102
9. ReVelle D. O., 1976, Dynamics and thermodynamics of large meteor entry: A quasi-simple ablation model. Herzberg Institute of Astrophysics, Planetary Sciences, SR-76-1

## TECHNIQUES FOR HIGH RESOLUTION METEOR LIGHT CURVE INVESTIGATIONS

R.L. Hawkes<sup>(1)</sup>, J.E. Bussey<sup>(2)</sup>, S.L. MacPhee<sup>(3)</sup>, C.S. Pollock<sup>(4)</sup>, L.W. Taggart<sup>(5)</sup>

<sup>(1)</sup>Physics Dept., Mt. Allison Univ., Sackville, NB Canada E4L 1E6 Email: rhawkes@mta.ca

<sup>(2)</sup>Physics Dept., Mt. Allison Univ., Sackville, NB Canada E4L 1E6 Email: jebssy@mta.ca @mta.ca

<sup>(3)</sup>Physics Dept., Mt. Allison Univ., Sackville, NB Canada E4L 1E6 Email: slmcp@mta.ca

<sup>(4)</sup>Physics Dept., Mt. Allison Univ., Sackville, NB Canada E4L 1E6 Email: cpllck@mta.ca

<sup>(5)</sup>Physics Dept., Mt. Allison Univ., Sackville, NB Canada E4L 1E6 Email: lwtggrt@mta.ca

### ABSTRACT

The dustball model of meteoroid structure would be expected to lead to short duration fluctuations on light curves, anomalous decelerations, and instantaneous light production over a significant spatial region. Detection of these features with conventional image intensified CCD approaches has proved elusive. We provide an overview of six improvements to traditional meteor light curve analysis in order to provide higher resolution: use of generation III image intensifier technology; digital recording techniques; digital image processing algorithms which separate the even and odd video fields; whole image background subtraction; analysis of pixel by pixel high resolution meteor light curves and utilization of coincidence and correlation techniques. Large aperture, long focal length systems are ideally suited to the studies mentioned here, and will be briefly mentioned.

### 1. INTRODUCTION

There is considerable evidence that most cometary meteors have a dustball structure [1–5]. This model of silicate and metallic grains embedded in a matrix of CHON or other volatile elements is consistent with current views of cometary dust and also with some models of interstellar grains. The overall light curves of shower meteors can be successfully modeled based upon the assumption of such a model [6–8] and the atmospheric ablation trajectories of faint meteors are consistent with the dustball model [9]. However efforts to directly measure wake produced by differential aerodynamic drag on grains of different masses have met with only limited success [10, 11, 5]. Surprising recent evidence of significant transverse spread in grain ablation from Leonid meteors [12–14] is not yet adequately explained theoretically. In this paper we overview some new techniques in image intensified CCD analysis of faint meteors which may permit more direct measurement of dustball meteor disintegration.

### 2. SIX ADVANCES IN IMAGE INTENSIFIED CCD METEOR TECHNOLOGY

Traditional video based meteor astronomy [15–18] has utilized moderate focal lengths (25 to 75 mm objective lenses) and equipment which had only limited resolution ( $\approx 250$  lines true resolution). With such systems it is difficult to resolve spatial elements less than about 100  $\mu$ m. In addition blooming, persistence and other instrumental artifacts serve to mask fine scale meteor ablation profile features. In particular, it has been very difficult to discriminate between small amounts of spatial spread in the instantaneous light production region and instrumentally introduced image degradation. While the high definition prototype systems which have been pioneered by Japanese scientists [19] offer incredible promise, the steep current cost of such systems keep them from widespread use at this time. In addition, most work so far has used short to medium focal lengths so that the spatial resolution has not been improved to the degree possible with the technology. In this article we will describe how generation III image intensifier technology combined with digital video recording can be used to extract additional information about the meteor ablation.

Starting in January 1999 we have implemented six improvements over conventional image intensified CCD meteor astronomy. First, we have utilized high quality generation III image intensifiers. The research reported here was accomplished using Litton NiteMate and ITT Model generation III devices. While these differ slightly in precise performance specifications and physical details, they are essentially comparable systems. Each utilizes an 18 mm diameter microchannel plate (MCP) image intensifier which is lens coupled with a micro macro coupling lens to a CCD camera. The CCD camera is provided by the user, and the module can be attached to any C mount CCD camera. We have utilized the Cohu 4910 series video rate CCD camera, which is high performance, relatively low light level, monochrome CCD. With a 50 mm f/0.95 lens these systems can detect stars down

to about +9 magnitude under dark sky conditions. This appears at first glance to be only a marginal improvement over the better generation II systems currently in use. However, the true improvement over generation II technology is a very crisp video frames with almost no persistence from one video frame to the next.

directly to computers, as well as an analog video out terminal. A typical single frame digitally recorded generation III image intensified CCD image is shown in Fig. 1.

Most video rate CCD cameras used an interlaced image. A third improvement is the separation of the

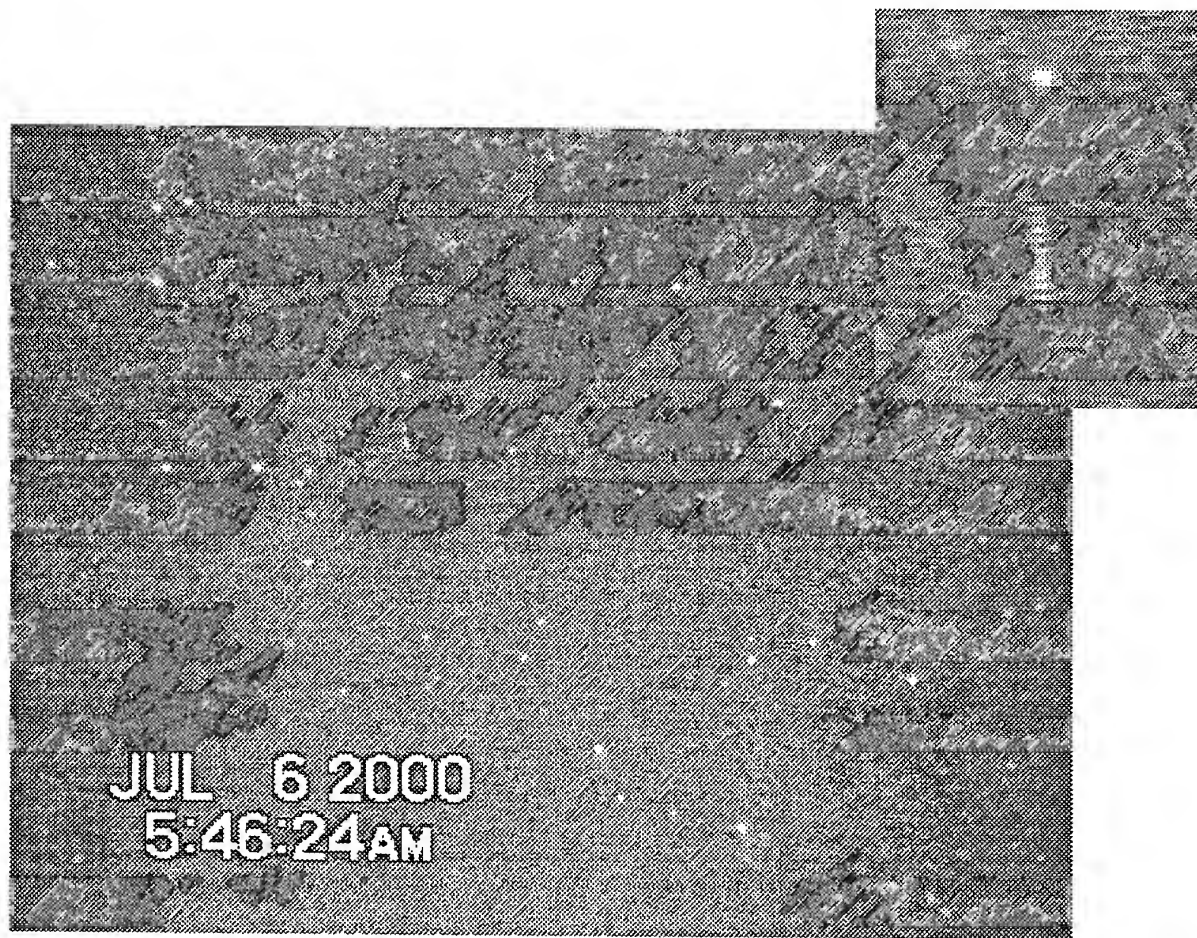


Fig. 1 A generation III microchannel plate image intensified meteor image digitally recorded. The even and odd video field lines are obvious in the inset image.

The second improvement which we have instituted is use of digital video recorders. We have adopted Sony Digital 8 technology which employs digital recording onto Digital Hi-8 format tape. Digital recording represents about a 60% improvement in resolution over VHS tape standards. Also, there is perfectly stable playback so no additional jitter is added (this is an important additional advantage for use with MeteorScan automated detection software which we use). These recorders offer IEEE 1394 digital output

even and odd video fields in the NTSC video. When these are combined in a single frame the scan lines interfere with recognition of short term fluctuations on the light curve. We have modified macros in the digital image processing software NIH Image (developed by Wayne Rasband of the U.S. National Institutes of Health) to handle the task of separation of even and odd video fields.

As well as separating the even and odd video fields, it is important to subtract the background from the frame containing the meteor, to obtain an image which is simply the meteor with all background stars removed. Stellar images which are near the limit of detection may produce light curve artifacts if this is not done carefully. We show in Fig. 2 a composite of a series of

even meteor video fields after background subtraction. Note the absence of light in the "off" segments, indicating that the size of the instantaneous light production region is very limited for this meteor. There is some hint of filling in the later portions of the trail (upper left).

In traditional [20,6,7,8] image intensified CCD meteor light curve analysis one uses the integrated light over each video frame (after appropriate correction for the background intensity – see [18]) to determine typically six to eight light curve points per meteor. This does not provide adequate spatial resolution for study of fine-scale fragmentation. Particularly for meteors with high angular speeds one has additional information if the meteor passes through many pixels per video frame time. Therefore one can in principle study 200 or more points along a meteor light curve, rather than 6 to 8. We show in Figure 3 a high resolution meteor light curve obtained by this method.

Despite the improvements in signal quality represented by these four changes, nevertheless the signal from very faint meteors will always be inherently noisy. This is partially due to the fact that one is not very far removed from the quantum limit [15, 16] - there simply are not very many photons per pixel per video frame. Therefore, one must have some method to separate small scale fluctuations on the actual ablation profile from noise. The technique which we have used is to coaxially align two identical cameras, and then to use coincidence methods to separate true meteor light curve fluctuations from noise. Studies of stellar scintillations [21] show that as long as the cameras are separated by 0.5 m or more the stellar scintillation noise will essentially be uncorrelated on the two cameras. One would expect electronic noise to be uncorrelated (as long as noise from power lines or other local sources is eliminated).

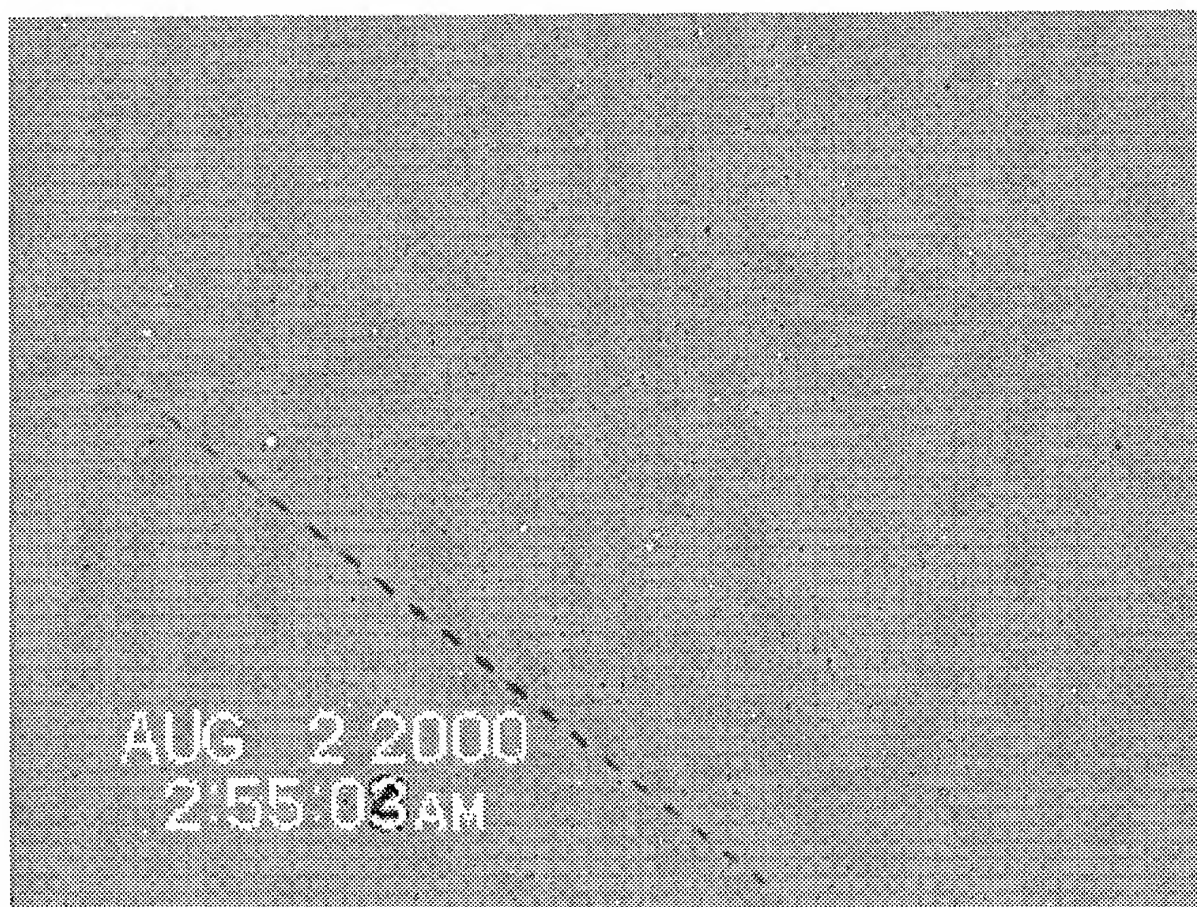


Fig. 2 Composite of even video fields obtained after background subtraction for a digitally recorded Northern  $\delta$ -Aquad meteor. The meteor moves from bottom to top in the image.

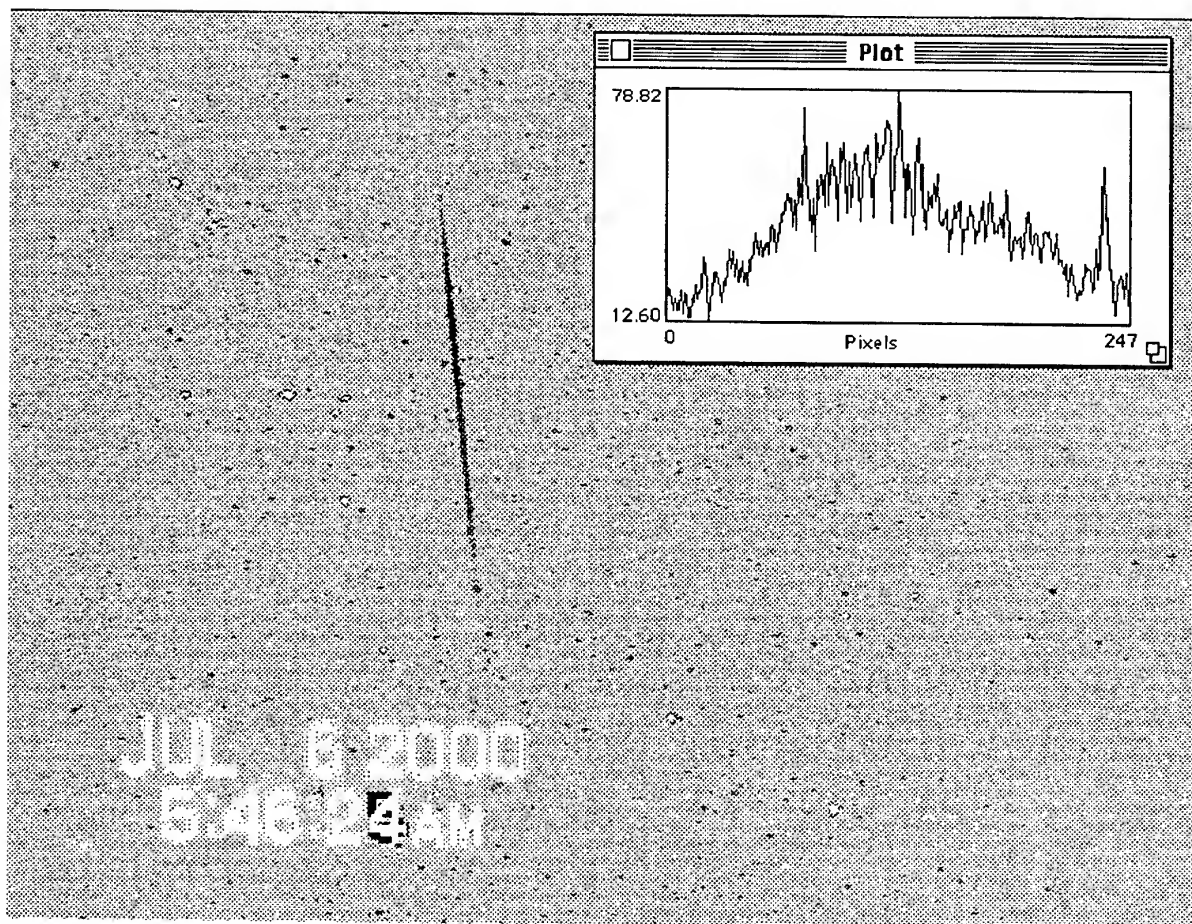


Fig. 3 Composite of even and odd video fields superimposed on one image with a fine scale meteor light curve determined.

### 3. RESULTS AND DISCUSSION

This paper represents an overview of techniques as the analysis is still in the preliminary stage. We obtained data using two coaxial Litton Nitemate gen III MCP systems with 50 mm/f0.95 objective lenses during observations in January to March 2000 from dark sky, dry atmosphere locations in dark-sky desert regions in eastern California, Arizona and western Texas. During June and July 2000 we used coincident ITT gen III MCP systems with 50 mm/f0.95 objective lenses from a dark sky location near Alma, NB, Canada. During June 2001 we obtained additional information using several gen II and gen III systems divided between two sites (Alma, NB and Economy, NS, Canada) to permit triangulation using overlapping systems. The majority of meteors are sporadic, with some  $\delta$ -Aquadrid meteors in the July 2000 observations.

While it is still in the preliminary stages of the analysis, early results indicate that there is little evidence for

significant fine scale light curve irregularities on most meteors when the coincidence test is applied. This would seem to suggest that in-flight fragmentation is either into such small grains that release of new grains cannot be observed, or that additional in-flight fragmentation is not taking place. It should be pointed out that some indication of dustball fragmentation and short duration light curve irregularity has been found on a very small sample of bright Leonid meteors [22].

A close examination of Fig. 1, and similar results for other meteors, indicates that in some cases there seems to be an overlap between the even and odd video lines which would not be expected in if the meteor was a point light source. In order to study this effect we measured the apparent overlap and subtracted a correction for the blooming of the image. We found that some meteors have zero overlap (indicating the correction of the analysis procedures), but others have a positive overlap of up to 700 m or more on certain meteor frames. This provides a new way to search for meteor wake which can complement the earlier work [5,10,11]. A typical result applying this technique for one meteor is indicated in Fig. 4. Each pixel corresponds to approximately 38 m for this meteor. We will report more complete results at a later time.

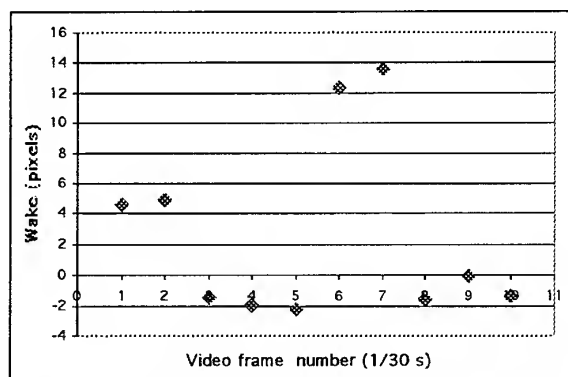


Fig. 4 Wake as a function of position along the meteor trail. Each pixel corresponds to 38 m.

There is also some hint of terminal blending in the later stages of several of the meteors (including that pictured in Fig. 2, indicating that differential aerodynamic lag between fragments of dustball meteors will be most important in the later stages of flight, as the simulations of [5] suggest.

Our ultimate goal is to apply the techniques of this paper to meteors of asteroidal, cometary and interstellar origin, to search for indicators of physical structure.

Large aperture and long focal length systems offer the promise to extend these techniques to very small aerodynamic lag. The largest aperture system ever used for meteor studies is the NASA 3 m liquid mirror telescope [24].

## ACKNOWLEDGEMENTS

This research program is supported by a Research Grant from the Natural Sciences and Engineering Research Council (NSERC) of Canada. Two of the authors (JB,CP) were supported by NSERC Undergraduate Research Awards. An internal research grant to RH by Mount Allison University supported this work. The M.Y. Bell Faculty Fund provided travel support for some of the preliminary work during 1999-2000. Some of the equipment used in this study was provided from the Leonid International Research Campaigns (see [23] for a detailed acknowledgement of funding agencies), which were directed by Jim Jones and Peter Brown of the University of Western Ontario. Laura Parker assisted with data recording.

## REFERENCES:

1. Jacchia, L.G. The physical theory of meteors VIII: Fragmentation as cause of the faint meteor anomaly, *Astrophys. J.*, Vol. 121, 521-527, 1955
2. Verniani, F. Structure and fragmentation of meteoroids, *Space Sci. Rev.*, Vol.10, 230-261, 196
3. Hawkes, R.L. and Jones, J. A quantitative model for the ablation of dustball meteors, *MNRAS*, Vol. 173, 339-356, 1975
4. Beech, M. The structure of meteoroids, *MNRAS*, Vol. 211, 617-620, 1984
5. Fisher, A.A. et al. Are meteoroids really dustballs?, *Planet. Space Sci.*, Vol. 48, 911-920, 2000
6. Campbell, M.D., Hawkes, R.L. and Babcock, D.D. Light curves of faint shower meteors: implications for physical structure, in *Meteoroids 1998*, Ed. By W.J. Baggaley and V. Porubcan, Astron. Inst. Slovak Acad. Sci., Bratislava, Slovak Republic, 363-366, 1999.
7. Murray, I.S., Hawkes, R.L. and Jenniskens, P. Airborne intensified CCD observations of the 1998 Leonid shower, *Meteoritics Planet. Sci.*, Vol. 34, 949-958, 1999
8. Murray, I.S. et al. Comparison of 1998 and 1999 Leonid light curve morphology and meteoroid structure, *Earth Moon Planets*, Vol. 82-83, 351-367, 2000.
9. Campbell, M.D. et al. Electro-Optical Results from the 1998 Leonid Shower: I. Atmospheric Trajectories and Physical Structure, *Meteoritics Planet. Sci.*, Vol. 35, 1259-1268, 2000
10. Robertson, M.C. and Hawkes, R.L., Wake in faint television meteors, in *Asteroids, Comets, Meteors 1991*, Ed. by A. Harris and E. Bowell, Lunar & Planetary Institute, Houston, 517-520, 1992
11. Shadbolt, L. and Hawkes, R.L., Absence of wake in faint television meteors, *Earth, Moon & Planets*, Vol. 68, 493-502, 1995
12. LeBlanc, A.G. et al., Evidence for transverse spread in Leonid meteors, *MNRAS*, Vol. 313, L9-L13, 2000.
13. Spurny, P. et al., New type of radiation of bright Leonid meteors above 130 km, *Meteoritics Planet. Sci.*, Vol. 35, 1109-1115, 2000

13. Spurný, P. et al., New type of radiation of bright Leonid meteors above 130 km, *Meteoritics Planet. Sci.*, Vol. 35, 1109–1115, 2000
14. Taylor, M. et al., Jet-Like Structures and Wake in Mg I (518 nm) Images of 1999 Leonid Storm Meteors, *Earth Moon Planets*, Vol. 82–83, 379–389, 2000.
15. Hawkes, R.L. and Jones, J., Electro-optical meteor observation techniques and results, *Quart. J. R. astr. Soc.*, Vol. 27, 569–589, 1986
16. Hawkes, R.L., Television meteors, in *Meteoroids and Their Parent Bodies*, Ed. by J. Stohl and I.P.W. Williams, Slovak Academy of Sciences, Bratislava, 227–234, 1993
17. Molau, S. et al., Video observation of meteors: History, current status and future prospects, *WGN: J. Inter. Meteor. Org.*, Vol. 25, 15–20, 1997
18. Hawkes, R.L., Detection and analysis procedures for visual, photographic and image intensified CCD meteor observations, in *Monograph on Meteors*, Ed. by E. Murad and I.P. Williams, Cambridge University Press, Cambridge (in press), 2001
19. Abe, S. et al., First Results of High-Definition TV Spectroscopic Observations of the 1999 Leonid Meteor Shower, *Earth Moon Planets*, Vol. 82–83, 369–377, 2000
20. Fleming, D.E.B., Hawkes, R.L. and Jones, J., Light curves of faint television meteors, proceedings in *Meteoroids and Their Parent Bodies*, Ed. by J. Stohl and I.P.W. Williams, Slovak Academy of Sciences, Bratislava, 261–265, 1993
21. Jakeman, E. et al., The twinkling of stars, *Contemporary Physics*, Vol. 19, 127–145, 1978
22. Jiang, X. and Hu, J., High resolution Leonid meteor light curves: Implications for meteoroid structure, *Planet. Space Sci.*, Vol. 49, 1281–1283, 2001
23. Brown, P. et al., Global Ground-Based Electro-Optical and Radar Observations of the 1999 Leonid Shower: First Results, *Earth Moon Planets*, Vol. 82–83, 167–190, 2000
24. Pawlowski, J. et al., Flux of very faint Leonid meteors observed with a 3m liquid mirror telescope intensified CCD system, 2001, *Meteoritics Planet. Sci.* (in press), 2001

# ABOUT PULSATION BRIGHTNESS OF THE BRIGHT METEORS

G. G. Novikov and O. V. Sokolov

*Novgorod State University, Department of the Theoretical and Mathematical Physics,  
Bolshaya Sankt-Peterburgskaya 41, 173000 Novgorod the Great, Russia*  
e-mail: ngg@novsu.ac.ru / o-v-sokolov@mail.ru

## ABSTRACT

On the example of the solution of the model problem it is shown that one of the possible reasons of pulsation of the brightness of the bright meteors is rotation. Theoretically counted curves of the brightness of the meteoroids, having the cubic and ellipsoid forms, qualitatively agree with the observations.

## 1. INTRODUCTION

One of the main sources of information about meteors is the data of spectrophotometric observations, allowing to get alterations of the brightness of a meteor along the trajectory of the flight. Among the great variety of the types of the curves of brightness of the meteors it is possible to state the ones where at the very beginning or at a certain section the cyclic changes of the brightness are observed – these are so – called pulsing meteors. The purpose of this paper work is to show that rotation of the meteoroids is one of the most possible reasons of the pulsation of the brightness of the bright meteors.

## 2. THE SOLUTION OF THE MODEL TASK

In the paper work [1] it is stated that the cyclic changes of the brightness of the meteors is a rather frequent phenomenon; besides this fact, these changes take place in the bright slow meteors. As for the fast meteors, they don't give any pulsation of the brightness, even the brightest ones among Perseid. It turns out that the cyclic changes of brightness appear when the big meteors move in the Earth atmosphere [1,2]. In the paper work [1], as an example, there are data about the meteor during the flight of which the pulsations of the brightness were observed.

For the explanation of the observed brightness in the bright meteors the following mechanisms were offered [1]: rotation or vibration, the split of the meteoric bodies, periodic break of the melted layer and self-sustained oscillation process of evaporation. Among the stated mechanisms the analytic description was given and made only for self-sustained oscillation process [1,2].

However, as the equation of the heat – conductivity has no periodic solutions, that's why it can be used in a certain diapason of the temperature, supposing that the break of the melted layer take place at a critical temperature. Further the temperature becomes lower because of the rapid evaporation of the meteoric

substance and then it becomes higher in accordance with the equation of the heat – conductivity. In our opinion, this is a rather artificial mechanism. As the rotation is the distinctive feature of an celestial bodies, then it's natural to use this mechanism for the explanation of the observed cyclic changes of the brightness of the bright meteors.

It's complicated to solve such a task for the meteoric body of an arbitrary form, the moment of impulse of which is oriented arbitrary with respect to vector of the speed of the meteor. That's why we'll consider a meteoroid of the various forms: cubic, triaxial ellipsoid, supposing that the meteoroid doesn't change its form during the flight, besides we certain, that rotation of meteoroids is freely. While rotation its cross-sectional area will be changing, it will lead to the change of speed of evaporation of neutral fractions from the meteoroid surface while its move along the flight trajectory, that is, it will lead to the change of brightness of the meteor.

According to [3,4], the equations of the evaporation and luminosity have the following form:

$$\frac{dM}{dt} = \frac{-\Lambda \cdot S(t) \cdot \rho(t) \cdot V^3}{2 \cdot Q} \quad (1)$$

$$I(t) = \frac{-\tau_v \cdot V^2}{2} \cdot \frac{dM}{dt} \quad (2)$$

where  $M$  – stands for the instantaneous meteoroid mass at time  $t$ ,  $V$  for its velocity,  $\Lambda$  is the heat transfer coefficient,  $S$  designates the cross-section area of the meteoroid,  $Q$  denotes the energy need for a mass unit to ablate, and  $\rho$  is the air density. We will assume that at the meteor heights

$$\rho = \rho_b \cdot \exp\left(\frac{t}{T}\right), \quad (3)$$

where

$$T = \frac{H}{V \cdot \cos Z_R} \quad (4)$$

with  $H$  being the scale height,  $\rho_b$  the atmospheric density at the height at which the meteors originates, and  $Z_R$  is the zenith angle of meteoroid radiant.  $\tau_v$  is the light efficiency.

Further we'll consider that the braking of the meteoroid is very little and  $\Lambda$ ,  $H$ ,  $\tau$ , don't change along the flight trajectory. Thus, to answer the raised question, it's necessary to know the expression of the cross-sectional of meteoroid. As it was stated above, we'll illustrate the effect of the meteoroid rotation on the meteoric bodies of a cubic and triaxial ellipsoid form.

### 3. CUBIC FORM

The classic theory of meteors goes that under the cross-sectional area it's necessary to understand the area of projection of cube on surface, which is perpendicular to its velocity  $\vec{V}$ . Let this surface be set by unit normal  $\vec{n} = (n_1, n_2, n_3)$  in the coordinate system, the axes of which are parallel to the ribs of the cube. Then the area of the cross-sectional

$$S_M = S'_1 + S'_2 + S'_3, \quad (5)$$

where  $S'_1, S'_2, S'_3$  are the areas of the projection of the cube edges on the surface (see fig. 1).

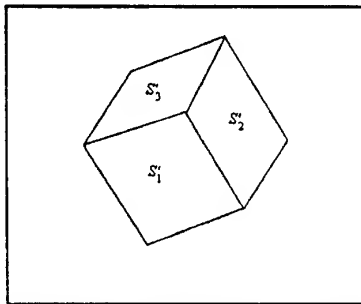


Fig. 1. The projection of the cubic form meteoroid on the cross-section plane

The areas of the cube edges

$$S_1 = S_2 = S_3 = a^2, \quad (6)$$

where  $a$  – length of the cube rib.

$$S'_1 = S_1 \cdot |\cos(\alpha_1)|, \quad (7)$$

where  $\alpha_1$  – angle between the edge and surface or (it is just the same), the angle between their normals.

$\vec{k}_1(1,0,0)$  – normal to the edge.

$$\cos(\alpha_1) = \frac{\vec{k}_1 \cdot \vec{n}}{|\vec{k}_1| \cdot |\vec{n}|} = 1 \cdot n_1 + 0 \cdot n_2 + 0 \cdot n_3 = n_1; \quad (8)$$

thus, we can get:

$$\left. \begin{aligned} S'_1 &= a^2 \cdot |n_1| \\ S'_2 &= a^2 \cdot |n_2| \\ S'_3 &= a^2 \cdot |n_3| \end{aligned} \right\}. \quad (9)$$

Finally, we have:

$$S_M = a^2 \cdot (|n_1| + |n_2| + |n_3|). \quad (10)$$

We'll consider the cube rotation to be free, disregard to friction. It is a spherical top, that is the moments of inertia

$$I_1 = I_2 = I_3 = \frac{M \cdot a^2}{6}. \quad (11)$$

It means, that the formula

$$\vec{L} = I \cdot \vec{\Omega} \quad (12)$$

is fair, where  $\vec{L}$  – moment of impulse of the cube, and  $\vec{\Omega}$  – its angle velocity. At free rotation the moment of impulse is kept, hence the angle velocity is permanent.

Let's introduce inertia system of count  $Oxyz$ , which is connected with the center of the cube inertia. The axis  $Oz$  we'll direct at the vector of moment of impulse, and the axis  $Ox$  in the surface of vectors of moment of impulse and velocity of the inertia center, we'll direct so that the projection  $V_x$  to be positive. Also we'll use the count system  $Ox_1x_2x_3$ , which is strictly connected with the cube, the axes of which are parallel to its ribs. The position of the system  $Ox_1x_2x_3$  relatively to  $Oxyz$  is set by the angles of Euler  $\theta, \psi, \varphi$ .

The orts of the system  $Oxyz$  are expressed through the orts of the system  $Ox_1x_2x_3$  with the following formulae:

$$\left. \begin{aligned} \vec{e}_x &= \vec{e}_1(\cos \varphi \cos \psi - \sin \varphi \cos \theta \sin \psi) + \\ &+ \vec{e}_2(-\cos \varphi \sin \psi - \sin \varphi \cos \theta \cos \psi) + \\ &+ \vec{e}_3 \sin \varphi \sin \theta, \\ \vec{e}_y &= \vec{e}_1(\sin \varphi \cos \psi + \cos \varphi \cos \theta \sin \psi) + \\ &+ \vec{e}_2(-\sin \varphi \sin \psi + \cos \varphi \cos \theta \cos \psi) - \\ &- \vec{e}_3 \cos \varphi \sin \theta, \\ \vec{e}_z &= \vec{e}_1 \sin \theta \sin \psi + \vec{e}_2 \sin \theta \cos \psi + \\ &+ \vec{e}_3 \cos \theta. \end{aligned} \right\} \quad (13)$$

As the cube rotates with the permanent angle velocity around the axis  $Oz$ , it means that the angles of nutation and wobbling are permanent, and

$$\varphi(t) = \varphi_0 + \Omega \cdot t. \quad (14)$$

The components of the vector of velocity of the inertia center in the system  $Oxyz$  are expressed through its quantity  $V$  and the angle between it and vector of the moment of impulse  $\alpha$ , thus

$$\left. \begin{aligned} V_x &= V \cdot \sin \alpha; \\ V_y &= 0; \\ V_z &= V \cdot \cos \alpha \end{aligned} \right\}. \quad (15)$$

The earlier introduced vector of normal is:

$$\vec{n} = \frac{\vec{V}}{V}, \quad (16)$$

and its components, accordingly, are:

$$\left. \begin{aligned} n_1 &= \sin \alpha (\cos \varphi \cos \psi - \sin \varphi \cos \theta \sin \psi) + \\ &+ \cos \alpha \sin \theta \sin \psi, \\ n_2 &= -\sin \alpha (\cos \varphi \sin \psi + \sin \varphi \cos \theta \cos \psi) + \\ &+ \cos \alpha \sin \theta \cos \psi, \\ n_3 &= \sin \alpha \sin \varphi \sin \theta + \cos \alpha \cos \theta. \end{aligned} \right\} \quad (17)$$

The cross-sectional area can be expressed in the following form:

$$S_M = a^2 \cdot f(t), \quad (18)$$

where

$$f(t) = |n_1| + |n_2| + |n_3| \quad (19)$$

is already found function of time.

Now, let's take into account, that the length of the cube rib is also the function from time. Let's write down the mass of the meteor as

$$M(t) = \delta \cdot (a(t))^3 \quad (20)$$

( $\delta$  – density of the meteoroid) and put it into the formula (1). After the simple transformation we'll get:

$$\frac{da}{dt} = -\frac{\Lambda \cdot V^3 \cdot \rho_b}{6 \cdot Q \cdot \delta} \cdot \exp\left(\frac{t}{T}\right) \cdot f(t). \quad (21)$$

After integration by time, we have:

$$a(t) = a(0) - \frac{\Lambda \cdot V^3 \cdot \rho_b}{6Q \cdot \delta} \int_0^t \exp\left(\frac{\tau}{T}\right) \cdot f(\tau) d\tau, \quad (22)$$

where

$$a(0) = \sqrt[3]{\frac{M(0)}{\delta}} \quad (23)$$

is initial length of the rib.

Now we can get the formula of the brightness:

$$I(t) = \frac{\Lambda \tau_v \rho_b V^5}{4Q} [a(t)]^2 f(t) \cdot \exp\left(\frac{t}{T}\right). \quad (24)$$

In the paper [4] there are the data about three pulsing meteors of the stream Gemenid, for which it is known: out-atmospheric velocity  $V$ , height of the beginning  $h_b$ , zenith angle  $Z_R$  and the initial masses  $M_0$ . The average values of these parameters are accordingly equal to:  $V_{av} = 36$  km/s,  $h_{b\ av} = 92$  km,  $Z_{R\ av} = 38^\circ$ ,  $M_{0\ av} = 14$  g.

For the construction of diagrams the following values of parameters were chosen and used:  $\Lambda = 1$ ,  $Q = 8 \cdot 10^{10}$  erg/g,  $H = 6$  km. The coefficient of the efficiency was chosen according to the model of "B" Opik [3].

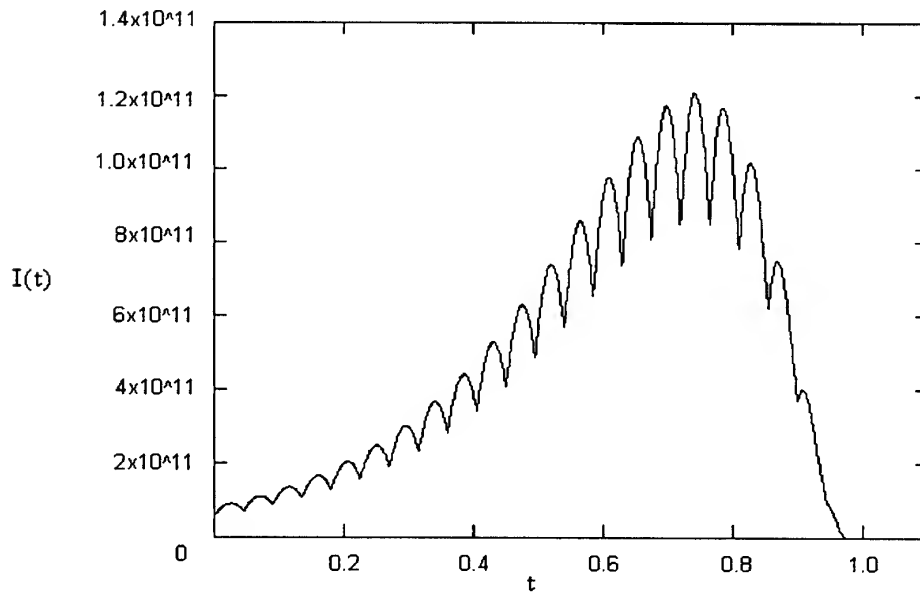


Fig. 2. The diagram  $I(t)$  for  $\Omega = 35$  rad/s,  $\alpha = 90^\circ$ ,  $\theta = 0^\circ$ ,  $\varphi_0 = 0^\circ$ ,  $\psi = 0^\circ$ . The time expressed in seconds is on the axis of abscissae, and the brightness of the meteor expressed in erg/s is on the axis of ordinates.

#### 4. TRIAXIAL ELLIPSOID

The meteoroid is considered to have the form of a triaxial ellipsoid. It's necessary to find the cross-sectional area as it was done with the cube.

The ellipsoid is projected on the surface by the tangents, directed along the vector of the normal  $\vec{n}$ . The parametric equation of the tangent, going through the point  $(x_0, y_0, z_0)$  of the surface of the ellipsoid, has the following form:

$$\begin{cases} x = x_0 + n_1 \cdot \chi, \\ y = y_0 + n_2 \cdot \chi, \\ z = z_0 + n_3 \cdot \chi. \end{cases} \quad (25)$$

Here  $\chi$  is a parameter. Having put  $x, y, z$  into the equation of the ellipsoid surface

$$\frac{x^2}{l_1^2} + \frac{y^2}{l_2^2} + \frac{z^2}{l_3^2} = 1 \quad (26)$$

(where  $l_1, l_2, l_3$  - semi axes of the ellipsoid), we'll get the equation for  $\chi$ :

$$\begin{aligned} & \left( \frac{x_0^2}{l_1^2} + \frac{y_0^2}{l_2^2} + \frac{z_0^2}{l_3^2} \right) + \\ & + 2 \cdot \left( \frac{n_1}{l_1^2} \cdot x_0 + \frac{n_2}{l_2^2} \cdot y_0 + \frac{n_3}{l_3^2} \cdot z_0 \right) \cdot \chi + \\ & + \left( \frac{n_1^2}{l_1^2} + \frac{n_2^2}{l_2^2} + \frac{n_3^2}{l_3^2} \right) \cdot \chi^2 = 1. \end{aligned} \quad (27)$$

Taking into account that the point  $(x_0, y_0, z_0)$  belongs to the ellipsoid surface, it's clear that the sum in the brackets is equal to one. As we deal with the tangent, it means that the equation must have the only one root  $\chi = 0$ . That's why it must be this way:

$$\frac{n_1}{l_1^2} \cdot x_0 + \frac{n_2}{l_2^2} \cdot y_0 + \frac{n_3}{l_3^2} \cdot z_0 = 0. \quad (28)$$

That is all the points of contact belong the surface, the vector of normal of which has the following components:

$$\left. \begin{aligned} k_1 &= \frac{n_1}{l_1^2}, \\ k_2 &= \frac{n_2}{l_2^2}, \\ k_3 &= \frac{n_3}{l_3^2}. \end{aligned} \right\} \quad (29)$$

The section of the ellipsoid by this surface is an ellipsis. It's obvious that the cross-sectional area will be equal to the area of the projection of this ellipsis on the surface with the normal  $\vec{n}$ .

It's necessary to solve such a task: to find the area of the ellipsoid section by the surface, the single vector of the normal has the components  $m_1, m_2, m_3$ ;

$$m_1 \cdot x + m_2 \cdot y + m_3 \cdot z = 0 \quad (30)$$

is an equation of the surface.

Let's express  $z$  from the equation (30) and put it into the equation (26). The equations (31) and (32) set the section border

$$z = -\frac{m_1 \cdot x + m_2 \cdot y}{m_3} \quad (31)$$

$$\frac{x^2}{l_1^2} + \frac{y^2}{l_2^2} + \frac{1}{l_3^2} \cdot \left( \frac{m_1 \cdot x + m_2 \cdot y}{m_3} \right)^2 = 1 \quad (32)$$

The equation (32) together with the condition  $z = 0$  set the section border on the surface  $xOy$ . Opening the brackets and set the following items, we'll get:

$$\begin{aligned} &\left( \frac{1}{l_1^2} + \frac{m_1^2}{l_3^2 m_3^2} \right) x^2 + 2 \frac{m_1 m_2}{l_3^2 m_3^2} xy + \\ &+ \left( \frac{1}{l_2^2} + \frac{m_2^2}{l_3^2 m_3^2} \right) y^2 = 1. \end{aligned} \quad (33)$$

The symmetrical matrix is conformed to equation (33) of the second order:

$$\begin{pmatrix} c_{11} & c_{12} \\ c_{21} & c_{22} \end{pmatrix}. \quad (34)$$

It's possible to reduce it to the diagonal form

$$\begin{pmatrix} q_1 & 0 \\ 0 & q_2 \end{pmatrix}, \quad (35)$$

where  $q_1, q_2$  are found from the equation

$$q^2 - I_1 q + I_2 = 0, \quad (36)$$

where  $I_1, I_2$  - are invariants of the matrix:

$$I_1 = c_{11} + c_{22} \quad (37)$$

$$I_2 = \begin{vmatrix} c_{11} & c_{12} \\ c_{21} & c_{22} \end{vmatrix} = \frac{m_1^2 \cdot l_1^2 + m_2^2 \cdot l_2^2 + m_3^2 \cdot l_3^2}{l_1^2 \cdot l_2^2 \cdot l_3^2 \cdot m_3^2}. \quad (38)$$

After diagonalization of matrix, the equation (33) gets the following form:

$$q_1 \cdot x^2 + q_2 \cdot y^2 = 1. \quad (39)$$

This is an equation of ellipsis with the semi-axes

$$\frac{1}{\sqrt{q_1}}, \quad \frac{1}{\sqrt{q_2}}.$$

It's known that

$$\left. \begin{aligned} q_1 q_2 &= I_2, \\ q_1 + q_2 &= I_1. \end{aligned} \right\} \quad (40)$$

Because of equation (40) the area of the ellipsis is:

$$\begin{aligned} S &= \pi \frac{1}{\sqrt{q_1}} \cdot \frac{1}{\sqrt{q_2}} = \frac{\pi}{\sqrt{q_1 q_2}} = \frac{\pi}{\sqrt{I_2}} = \\ &= \frac{\pi \cdot l_1 l_2 l_3 |m_3|}{\sqrt{m_1^2 l_1^2 + m_2^2 l_2^2 + m_3^2 l_3^2}}, \end{aligned} \quad (41)$$

$$S_s = \frac{S}{|m_3|} = \frac{\pi \cdot l_1 l_2 l_3}{\sqrt{m_1^2 l_1^2 + m_2^2 l_2^2 + m_3^2 l_3^2}}. \quad (42)$$

Let

$$\vec{m} = \frac{\vec{k}}{k}, \quad (43)$$

then

$$S_s = \frac{\pi \cdot l_1 \cdot l_2 \cdot l_3 \cdot k}{\sqrt{k_1^2 \cdot l_1^2 + k_2^2 \cdot l_2^2 + k_3^2 \cdot l_3^2}} \quad (44)$$

$$S_M = S_s \cdot \cos \beta, \quad (45)$$

$$\cos \beta = \frac{\vec{k} \cdot \vec{n}}{k}, \quad (46)$$

where  $\beta$  is an angle between the cross-sectional area and the surface with the normal  $\vec{k}$ . Finally we get

$$S_M = \pi \cdot \sqrt{l_2^2 \cdot l_3^2 \cdot n_1^2 + l_1^2 \cdot l_3^2 \cdot n_2^2 + l_1^2 \cdot l_2^2 \cdot n_3^2} \quad (47)$$

Considering that at evaporation ellipsoid keeps its form, let's write down

$$\left. \begin{aligned} l_1(t) &= p_1 \cdot a(t) \\ l_2(t) &= p_2 \cdot a(t) \\ l_3(t) &= p_3 \cdot a(t) \end{aligned} \right\}, \quad (48)$$

where  $p_1, p_2, p_3$  set the permanent ratio of the ellipsoid's semi axes. Therefore, the cross-sectional area can be

presented in a way, which is analogous to the formula (6), where

$$f(t) = \pi \sqrt{p_2^2 p_3^2 n_1^2 + p_1^2 p_3^2 n_2^2 + p_1^2 p_2^2 n_3^2} \quad (49)$$

The formulae for  $n_1, n_2, n_3$  are the same as in the case with the cube, but it's necessary to find Euler's angles from the notion about the ellipsoid as an asymmetrical top. This task is solved in [5].

The mass of meteoroid

$$M(t) = \frac{4 \cdot \pi}{3} \cdot l_1 \cdot l_2 \cdot l_3 \cdot \delta = \delta' \cdot (a(t))^3, \quad (50)$$

where

$$\delta' = \frac{4 \cdot \pi \cdot \delta \cdot p_1 \cdot p_2 \cdot p_3}{3}. \quad (51)$$

The formulas (22) and (24) are fair and correct for the ellipsoid, if in them  $\delta$  is substituted for  $\delta'$  and if under  $f(t)$  we'll understand the comfortable function for the ellipsoid. From the fig.2 - 3 it is showed, that the theoretically counted light curves for the meteoroids, having the cubic and ellipsoid forms qualitatively agree with the observations.

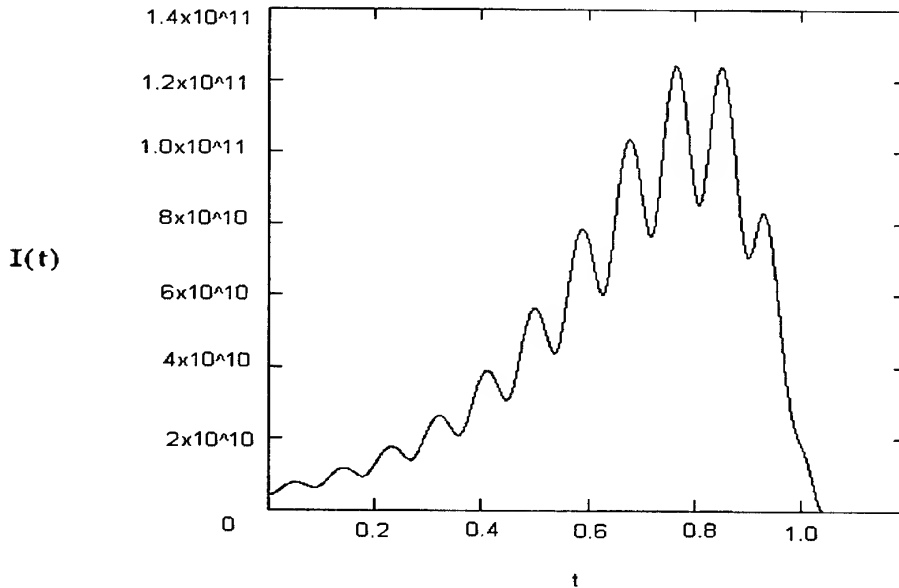


Fig. 3. The diagram  $I(t)$  for  $\Omega = 35 \text{ rad/s}$ ,  $\alpha = 90^\circ$ ,  $\theta_0 = 0^\circ$ ,  $\varphi_0 = 0^\circ$ ,  $\psi_0 = 0^\circ$ . Parameters are:  $p_1 = 3$ ,  $p_2 = 2$ ,  $p_3 = 1$

## REFERENCES

1. Kramer E. N. and Shestaka I. S., *Meteornaya materiya v atmosfere Zemli i okolosolnechnom kosmicheskom prostranstve*, Nauka, Moskva, 1983.
2. Babadzhanov P. B. and Konovalova N. A., On the light pulsation of bright gemenids according to photographic data, *Publication of astronomical institute of Czechoslovak Academy of Sciences. Publication No.67.10 - th European regional astronomy meeting of the IAM, Praga, Czechoslovakia, august 24 -29, 1987. Interplanetary matter, edited by Zdenek Ceplecha, Petr Pecina. Proceedings*, vol. 2, p.189 - 193, 1987.
3. Lebedinets V. N., *Pyl v verkhney atmosfere i kosmicheskom prostranstve. Meteory*, Gidrometeoizdat, Leningrad, 1980.
4. Bronshten V. A., *Fizika meteornih yavleniy*, Nauka, Moskva, 1981.
5. Landau L. D. and Livshic E. M., *Mehanika*, Nauka, Moskva, 1973.

# KINETIC SIMULATION OF MAGNETIC FIELD EFFECTS ON WAKES OF METEOROIDS IMAGINARY EMISSION METHOD

Maxim Ponomarjov

*University Libre de Bruxelles, Physique Statistique et Plasmas  
C.P. 231 boulevard du Triomphe, B-1050 Brussels, Belgium  
Email: ponomarjov maxim@mail.ru*

## ABSTRACT/RESUME

Simulations of time-dependent stratifications, multiplicity, flute structure, loops of plasma flows and wakes of meteoroids are proposed in external magnetic fields based on the kinetic approach. The Imaginary Emission Method is applied for modeling wakes of meteoroids. The model Boltzmann equation is solved taking into account collisions between the plasma ions, their interactions with ambient neutral particles and effects of external magnetic fields. Using this solution the analytical and numerical results are obtained, which describe developing magnetic field aligned stratifications of the flows and wakes. For magnetic field aligned drifting velocity of the plasma flows, formation of flute structures along the edges of the flows and wakes is obtained analytically and numerically.

The simulations allow describing multiple and stratified meteor and bolid trains, loops under effects of geomagnetic field.

## 1. INTRODUCTION

Multiple observations of Leonid trains reported and discussed by Jenniskens et al. [7], [8], [9], [10], Taylor et al. [18] show a number of fine structures such as multiple and stratified meteor and bolid trains, loops. On the basis of experimental data Boyd [4] simulated the two dimensional flow field about a typical Leonid meteoroid entering the Earth's atmosphere. It was supposed that the flow conditions provide very rarefied, hypersonic flow and the direct simulation Monte Carlo technique is used.

The present paper considers kinetic simulation of ionized flows due to moving bodies through the upper atmosphere (at altitudes above 150 km) on the basis of the model Boltzmann equation. However, the results can be used for only qualitative simulations of the flows at altitudes 100-150 km too.

Earlier author's results, which are outlined in [13-15],

are related to kinetic simulations of collisionless plasma flows behind of small objects with taking into account effects of external magnetic field. These results are described persistent flute structures in the wakes of bodies moving along magnetic field lines. The stratifications of iso-density contours are described analytically in the wakes of moving bodies and sources at different angles to the magnetic field lines. These stratifications can be observed as multiplications of meteor and bolid trains. The present paper develops previous author's results by including effects of ion-ion and ion-neutrals collisions into the simulations.

For more than 50 years, plasma disturbances and wakes due to moving bodies have been intensively studied. For wide reviews you can see Alpert et al. [1-3]; Gurevich et al. [6]; Samir et al. [16], Senbetu and Henley [17]. Because of the high complexity of the many correlated effects, which take place as results of relative motion between an object in space and its ambient medium, all existing theoretical models involved considerable simplifications.

The following basic simplifications have been made in the definition of the existing theoretical models for bodies moving through a rarefied plasma:

- (1) In the case of the very small size of the Debye length compared to the body radius, the quasi-neutral condition of equal local density for ions and electrons in the plasma is assumed to be valid;
- (2) If the object velocity is much greater than the average thermal velocity of the ions, a common practice is to neglect ion thermal motion and to replace the unknown ion distribution function in front of the object by a beam moving in a straight line with the constant object velocity

Different kinds of interactions of the ambient particles with meteoroid surfaces can be described by the

$$w_k^\alpha(\vec{u}, \vec{u}_1, \vec{r}, t) - \text{the probability that the } k\text{-}$$

particle, impinging on the object surface S at the point

$\vec{r}$  with the velocity  $\vec{u}_1$ , will produce the  $\alpha$ -particle emitting from the S at the  $\vec{r}$  with the velocity  $\vec{u}$  at time  $t$ . This probability is defined by the boundary condition at the body surface:

$$(\vec{n} \cdot \vec{u}) F_{\alpha}(\vec{r}, \vec{u}, t) = - \int_{\vec{n} \cdot \vec{u} < 0} \sum_k u_k^p(\vec{u}, \vec{u}_1, \vec{r}, t) (\vec{n} \cdot \vec{u}_1) F_k^f(\vec{r}, \vec{u}_1, t) d^3 u_1 \quad (1)$$

For the absorption, direct and diffuse reflection the probability is introduced firstly by Alpert et al. [1-3] and then the cases of direct and diffuse reflection are considered in detail by Ponomarev [13-15]. Usually, at distances far from the body the plasma is considered undisturbed and in a state of thermodynamic equilibrium:

$$F_{\alpha} |_{|\vec{r}| \rightarrow +\infty} \rightarrow N \left( \frac{\beta_{\alpha}}{\pi} \right)^{3/2} \exp(-\beta_{\alpha} (\vec{v})^2) \quad (2)$$

where  $\beta_{\alpha} = m_{\alpha} / 2kT_{\alpha}$

Alpert et al. [2-3] introduced the 'special term', that allowed to consider effects of ambient particle interactions with the body surface. This term was placed in the right hand of the stationary Boltzmann equation. The basic aim was to avoid consideration of the boundary conditions Eqs.(1), (2) on the body surfaces. This term contains the implicit function that describes the body surface entirely and the gradient of this function. This pioneering approach covers a lot of interesting problems, which have not been considered in detail so far. This present paper briefly describes the imaginary emission method, which allows avoiding the treatment of the implicit function and its gradient. These circumstances allow considering surfaces with undefined normals and gradients, such as sharp antennas, point-like objects, small two-sided plates. It should be noted that for smooth bodies the imaginary emission method gives results, which are in good agreement with results presented by Alpert et al. [1-3]; Gurevich et al. [6]. Besides, the proposed imaginary emission method allows time-dependent simulations.

## 2. BASIC METHOD

According to the imaginary emission method [13-15], the disturbances of a-spice of plasma by point-like object or small two-sided plate are simulated on the basis of the Boltzmann equation with imaginary and additional sources

$$\begin{aligned} \frac{\partial F_{\alpha}^{imw}}{\partial t} + \vec{v} \frac{\partial F_{\alpha}^{imw}}{\partial \vec{r}} + \frac{e_{\alpha}}{m_{\alpha}} \left( \frac{1}{c} [\vec{v}, \vec{B}] + \vec{E} \right) \frac{\partial F_{\alpha}^{imw}}{\partial \vec{v}} \\ = Q_{\alpha}^{im} + Q_{\alpha}^w + \sum_{\beta} C_{\alpha\beta}(F_{\alpha}, F_{\beta}) \end{aligned} \quad (3)$$

where  $q_{\alpha}$  is the electric charge of the  $\alpha$ -particles,  $m_{\alpha}$  the  $\alpha$ -particle mass,  $\vec{B}$  the magnetic field induction and  $\vec{E}$  the electric field strength. In general,  $\vec{B}$ ,  $\vec{E}$  and  $F_{\alpha}(\vec{r}, \vec{v}, t)$  are related by the Maxwell's equations with appropriate boundary conditions.

The boundary conditions both near the small body surface and far from the small body Eqs.(1) and (2) are transformed into the image and additional sources:

$$Q_{\alpha}^{im} + Q_{\alpha}^w = Q_{\alpha}^{im+} + Q_{\alpha}^{im-} + Q_{\alpha}^{w+} + Q_{\alpha}^{w-} \quad (4)$$

$$\begin{aligned} Q_{\alpha}^{im+} + Q_{\alpha}^{w+} = \delta(\vec{r} - \vec{r}_s) \times \\ \left[ \begin{aligned} & \int_{\vec{n} \cdot \vec{u} < 0} \sum_k u_k^p(\vec{u}, \vec{u}_1, \vec{r}, t) (\vec{n} \cdot \vec{u}_1) F_k^f(\vec{r}, \vec{u}_1, t) d^3 u_1 & \text{if } (\vec{n} \cdot \vec{u}) > 0 \\ & - (\vec{n} \cdot \vec{u}) F_{\alpha}^f(\vec{r}, \vec{u}, t) & \text{if } (\vec{n} \cdot \vec{u}) < 0 \end{aligned} \right] \end{aligned} \quad (5)$$

$$\begin{aligned} Q_{\alpha}^{im-} + Q_{\alpha}^{w-} = \delta(\vec{r} - \vec{r}_s) \times \\ \left[ \begin{aligned} & - \int_{\vec{n} \cdot \vec{u} < 0} \sum_k u_k^p(\vec{u}, \vec{u}_1, \vec{r}, t) (\vec{n} \cdot \vec{u}_1) F_k^f(\vec{r}, \vec{u}_1, t) d^3 u_1 & \text{if } (\vec{n} \cdot \vec{u}) > 0 \\ & (\vec{n} \cdot \vec{u}) F_{\alpha}^f(\vec{r}, \vec{u}, t) & \text{if } (\vec{n} \cdot \vec{u}) < 0 \end{aligned} \right] \end{aligned} \quad (6)$$

The imaginary point-like source

$$Q_{\alpha}^{im} = Q_{\alpha}^{im+} + Q_{\alpha}^{im-} \quad (7)$$

is the source of negative intensity, so that it simulates losses of  $\alpha$ -spice particles at the small surface.

$Q_{\alpha}^{im+}$  and  $Q_{\alpha}^{im-}$  are intensities of the losses by

frontal and reverse sides of the small surface (respectively). The small surface sides should be selected according to fixed outside normal  $\vec{n}$ . The additional point-like source

$$Q_\alpha^w = Q_\alpha^{w+} + Q_\alpha^{w-} \quad (8)$$

simulates reflections and emissions of the  $\alpha$ -spice particles by small surface.  $Q_\alpha^{w+}$  and  $Q_\alpha^{w-}$  are intensities of the reflections and emissions by frontal and reverse sides of the small surface (respectively). For 'non small' 2D and 3D bodies or initial clouds with a boundary surface S we introduce the following imaginary and additional sources:

$$Q_\alpha^{imS} + Q_\alpha^{wS} = \oint_S (Q_\alpha^{im+} + Q_\alpha^{w+}) dS \quad (9)$$

where the integration should be made over entire surface S, so that we obtain the distributed (on the surface S) imaginary and additional sources.

The Boltzmann collision integral has the following general form:

$$C_{\alpha\beta} = \int W(\vec{v}_\alpha, \vec{v}_\beta; \vec{v}_{1\alpha}, \vec{v}_{1\beta}) [F(\vec{v}_\alpha) f(\vec{v}_\beta) - F(\vec{v}_{1\alpha}) f(\vec{v}_{1\beta})] d^3v_{1\alpha} d^3v_\beta d^3v_{1\beta} \quad (10)$$

where  $\vec{v}_\alpha$  is the velocity of particle from the distribution  $F(\vec{v}_\alpha)$  (i.e.  $F(\vec{v}_\alpha) = F_\alpha$ ), and

$\vec{v}_\beta$  - from the distribution  $f(\vec{v}_\beta)$ ;

$W(\vec{v}_\alpha, \vec{v}_\beta; \vec{v}_{1\alpha}, \vec{v}_{1\beta})$  is the probability of collision

between the particle of sort  $\alpha$  and the particle of sort  $\beta$  when their velocities  $\vec{v}_{1\alpha}, \vec{v}_{1\beta}$  changes to  $\vec{v}_\alpha, \vec{v}_\beta$  (respectively).

Because of the very complicated form, the collision integral in Eq.10 is introduced usually in simplified forms (Cercignani, [5], Kogan, [11]). For Coulomb interactions (ion-ion, ion-electron, and electron-electron interactions) the collision term take the form (Landau, [12])

$$C_{\alpha\beta} = \sum_{k=1}^3 \frac{\partial j_k}{\partial v_k} \quad (11)$$

where

$$j_k = \frac{\pi e_\alpha^2 e_\beta^2 \Lambda}{m_\alpha} \sum_{l=1}^3 \int \left[ \frac{F(\vec{v}_\alpha)}{m_\beta} \frac{\partial f(\vec{v}_\beta)}{\partial v_{\beta,l}} - \frac{f(\vec{v}_\beta)}{m_\alpha} \frac{\partial F(\vec{v}_\alpha)}{\partial v_{\alpha,l}} \right] \frac{|\vec{w}| \delta_{lk} - w_l w_k}{|\vec{w}|^3} d^3v_\beta \quad (12)$$

$$\vec{w} = \vec{v}_\alpha - \vec{v}_\beta$$

$$\Lambda = \frac{3}{2} \ln \left( \frac{\kappa T}{e^2 N_0^{-1/3}} \right) - \text{the Coulomb logarithm}$$

### 3. ION DISTURBANCES UNDER THE MAGNETIC FIELD EFFECT

As a first approximation, for simulation of ion collisions with neutral particles and other ions we will use the BGK model in the form introduced by Gurevich [6] and Al'pert et al.[1-3]. So we will consider ion flow with distribution

$F_\alpha(\vec{r}, \vec{v}, t) = F_{0\alpha} + F'_\alpha$  and the collision integral in Eq.3, which according to Eq.10, takes the following form:

$$C = -\nu \left( F_\alpha - \frac{F_{0\alpha}}{N_0} \int F_\alpha d^3v \right) = -\nu \left( F'_\alpha - \frac{F_{0\alpha}}{N_0} \int F'_\alpha d^3v \right) \quad (13)$$

where effective collision frequency is equal to the sum of the ion-neutral collision frequency and the ion-ion frequency:

$$\nu = 2.2 n_0 \sigma_{\alpha n} \sqrt{\frac{\kappa T}{m_\alpha}} + \frac{5e^4 N_0 \Lambda}{(\kappa T)^{3/2} \sqrt{m_\alpha}} \quad (14)$$

$n_0$  is the concentration of ambient neutral particles, and  $\sigma_{\alpha n}$  - effective cross-section of ion-neutral collisions. Further, we make the Fourier transform for the Eq.3 with collisional term Eq.13

$$\begin{aligned} i\vec{q} \cdot \vec{v} F_q + i\vec{q} \cdot \vec{v} \phi_q \frac{e F_{\alpha 0}}{\kappa T N_0} + \frac{e}{m_\alpha c} \vec{v} \times \vec{B} \cdot \frac{\partial F_q}{\partial \vec{v}} \\ = -S V F_{\alpha 0} - \nu \left( F_q - \frac{F_{\alpha 0}}{N_0} \int F_q d^3 v \right) \end{aligned} \quad (15)$$

where

$$F_q = \int F'_\alpha(\vec{r}, \vec{v}, t) \exp\{-i\vec{q} \cdot \vec{r}\} d^3 r \quad (16)$$

S, V are the cross section of initial cloud and its velocity (respectively) and  $F_{\alpha 0}$  is the undisturbed distribution of ambient ions. After using an analytic solution of Eq.15, we obtain

$$n_{\alpha q} = \int F_q d^3 v = - \frac{\frac{S n_{\alpha 0} V}{\omega} J}{2 + \frac{i q V - 2\nu}{\omega} J} \quad (17)$$

where

$$\begin{aligned} J = \int_0^\infty \exp\left\{\frac{i q V - \nu}{\omega} x\right. \\ \left. - \frac{\kappa T}{2 m_\alpha \omega^2} \left(q_\parallel^2 x^2 + 4 q_\perp^2 \sin^2\left(\frac{x}{2}\right)\right)\right\} dx \\ q_\parallel = \frac{\vec{q} \cdot \vec{B}}{|\vec{B}|}; \quad q_\perp = \sqrt{q^2 - q_\parallel^2}; \\ \omega = \frac{e_\alpha |\vec{B}|}{m_\alpha c} \end{aligned} \quad (18)$$

The concentration of ions can be calculated from Eq.17 using the reverse Fourier transform:

$$n'_\alpha = \frac{1}{(2\pi)^3} \int n_{\alpha q} \exp\{i\vec{q} \cdot \vec{r}\} d^3 q \quad (19)$$

Due to significant complexity of obtained results from Eqs.17-19 and very limited computing resources, there is no possibility for the visualization of these results in general form. Below, however, the asymptotical expressions are derived for the special case when  $\vec{V} \parallel \vec{B}$ , which allow illustration of the effect of the external magnetic field on the ion disturbances.

#### 4. DISTURBANCES OF ION CONCENTRATION BY DIFFUSE EMITTING CLOUD

Let us consider disturbances of ions by rapidly moving cloud, which emits ions with initial diffuse maxwellian distribution. The cloud moves with the velocity  $\vec{V}$  along the magnetic field  $\vec{B}$ . We use a Cartesian coordinate system OXYZ with the OX axis directed parallel to  $\vec{B}$ . The cloud moves along the OX axis during time from 0 to t. At initial time - zero the cloud center is the origin of the coordinate system - point O. Then, because of the symmetry of particle distribution with respect to the OX axis, the disturbance of ion concentration depends on the D - distance from the OX axis, x coordinate and time t:

$$\begin{aligned} \delta n(x, D, t) = N_p \int_0^R \frac{\exp\left\{\frac{m \omega^2 (D^2 + r^2)}{4 \kappa T \sin^2\left\{\frac{\omega(t-x/V)}{2}\right\}}\right\}}{2 \sin^2\left\{\frac{\omega(t-x/V)}{2}\right\}} \\ \times I_0\left\{\frac{m \omega^2 D r}{2 \kappa T \sin^2\left\{\frac{\omega(t-x/V)}{2}\right\}}\right\} r dr \end{aligned} \quad (20)$$

where  $I_0(\zeta) = \pi^{-1} \int_0^\pi \exp\{\zeta \cos \tau\} d\tau$  - the zero-order modified Bessel function

$$N_p = NV \quad \text{if } x < Vt$$

$$N_p = \frac{N \exp\{-\beta V^2\}}{2\sqrt{\beta\pi}} \quad \text{if } x > Vt \quad (21)$$

$N$  - initial concentration of ions (in initial cloud),  $R$  - the radius of in initial cloud.

The Eq.20 is the asymptotic approximation for the case of rapid motion (the velocity  $V$  is well above the ion

mean thermal velocity:  $\beta V^2 = \frac{mV^2}{\kappa T} \gg 1$ ) and

slow collision limit:  $\nu/\omega \rightarrow 0$ . For the great distances from the cloud (as compared to its radius  $R$ ), we obtain further simple asymptotic expression of the disturbance of ion concentration

$$\delta n(x, y, z, t) = N_p S \frac{m\omega^2}{2\pi\kappa T} \times \frac{\exp\left\{-\frac{m\omega^2(y^2 + z^2)}{4\kappa T \sin^2\left\{\frac{\omega(t - x/V)}{2}\right\}}\right\}}{\sin^2\left\{\frac{\omega(t - x/V)}{2}\right\}} \quad (22)$$

It should be noted, that Eq.22 is quite correct for arbitrary small cloud with appropriate  $N_p$ . And we introduced that any cloud is small if its size is significantly smaller than the distance from the cloud where the concentration is calculated.

Cross-sections of isodensity contours (at the plane  $Z=0$ ) are plotted at Fig.1 by direct computations from

to Eq.20 (for  $\vec{V} \parallel \vec{B}$ ). One can see the long unstable quasi-periodical flute structures of the ion disturbances behind the cloud. The space quasi-period of these structures (the longitude along the OX-axis) is the path length of the cloud during the time of the gyro-period of ions in the magnetic field.

## 5. CONCLUSIONS

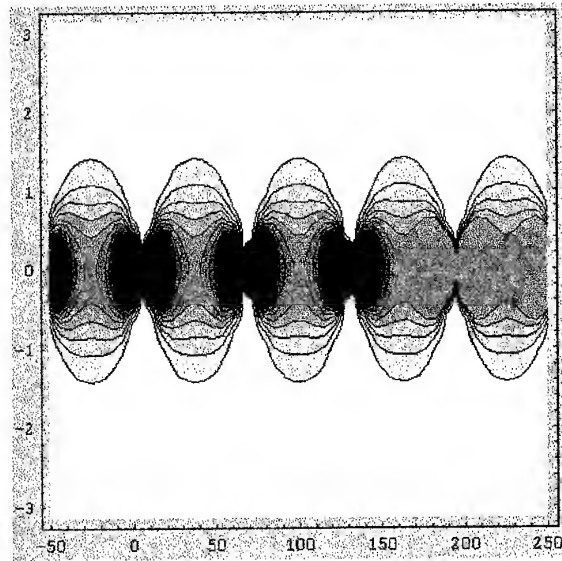
The imaginary emission method is discussed here for plasma with many species and different types of their interactions with body surfaces. In the meteoroid wakes the particle distributions are simulated using imaginary and additional sources with different initial particle distributions. The model Boltzmann equation with image and additional sources is solved analytically and 3D distributions of plasma

disturbances are obtained in the geomagnetic field in quadratures with asymptotic approximations. The effects of ion collisions with neutral particles and other ions are considered in this paper

The presented research can be developed to further simulations of particular meteor trails under effects of geomagnetic field. In addition it can be proposed to simulate the wakes in transitional regimes (from collisionless to MHD) and to generalize the imaginary emission method for these regimes.

The basic goal of this paper is to attract the organizations and specialists in related fields to the method and the possibility of its adaptation and development for widely related topics. So, proposals for collaborations are welcomed.

x10 (meters)



(meters)

Fig. 1. Cross-sections of isodensity contours (at the plane  $Z=0$ ) for the ion concentration disturbances by the cloud (cf. Eq.20 for  $\vec{V} \parallel \vec{B}$ ). The cloud moves with the velocity  $\vec{V}$  along the magnetic field  $\vec{B}$ , and the OX-axis (horizontal direction from right to left). The cloud trajectory (and the OX-axis) is the unique symmetry axis of the all cross-sections here. The cloud is located around point 0 at the left side of the Fig. The more dark contours correspond to the higher concentrations. The more bright contours show the lower particle concentrations. The radius of the initial cloud is 5 meters, its velocity  $V=70$  km/s.

## 6. REFERENCES

1. Alpert Ya.L., A.V.Gurevich, L.P.Pitaevskii, *Space Science Review*, Vol.2, 680, 1963
2. Alpert Ya.L., A.V.Gurevich, L.P.Pitaevskii, *Space Physics with Artificial Satellites*, Consultant Bureau, N.-Y., 1965
3. Alpert Ya.L., A.V.Gurevich, L.P.Pitaevskii, *Space Science Review*, Vol.6, 419, 1965
4. Boyd,I.D., *Earth, Moon, and Planets*, Vol.82-83, 93, 2000
5. Cercignani,C., *Mathematical methods in kinetic theory*, MACMILLAN, 1969.
6. Gurevich A.V., L.P.Pitaevskii, *Nonlinear Dynamics of Rarefied Plasmas and Ionospheric Aerodynamics*, in "Voprosy Teorii Plasmy", ed. by M.A.Leontovich, Vol.10, Atomizdat, 1980 (in Russian)
7. Jenniskens,P and Butov,S.J., *Meteoritics Planet. Sci.*, Vol.34, 933, 1999.
8. Jenniskens,P. and Rairden,R.L., *Earth, Moon, and Planets*, Vol.82-83, 457, 2000
9. Jenniskens,P., Nugent,D., and Plane,J.M.C., *Earth, Moon, and Planets*, Vol.82-83, 471, 2000
10. Jenniskens,P., Packan,D., Laux,C., Wilson,M., Boyd,I.D., Popova,O., Krueger,C.H., and Fonda,M., *Earth, Moon, and Planets*, Vol.82-83, 93, 2000
11. Kogan,M.N., *Rarefied gas dynamics*, Moscow, Nauka, 1967 (in Russian).
12. Landau,L.D., *JETP* 7, 203, 1937 (in Russian).
13. Ponomarjov,M.G., *Planet. Space Sci.*, Vol.43, No 10/11, 1419-1427, 1995.
14. Ponomarjov,M.G., *Physical Review E*, Vol.54, No 1, 5591-5598, 1996.
15. Ponomarjov,M.G., *Astrophys. Space Sci.*, Vol.274, 423-429, 2000
16. Samir U., Comfort R.H., Singh N., Hwang K.S., Stone N.H., *Planet. Space Sci.*, Vol.37, 873, 1989
17. Senbetu L. and Henley J.R., *J. geophys. Res. (A)*, Vol.94, 5441, 1989
18. Taylor,M.J., Gardner,L.C., Murray,I.S., and Jenniskens,P., *Earth, Moon, and Planets*, Vol.82-83, 379, 2000.

## **Optical Observations of Meteors**

# LIDAR OBSERVATIONS OF METEOR TRAILS: EVIDENCE FOR FRAGMENTATION OF METEOROIDS AND THEIR SUBSEQUENT DIFFERENTIAL ABLATION

U. von Zahn

Leibniz-Institute of Atmospheric Physics, Schloss-Str. 6, 18225 Kühlungsborn, Germany  
vonzahn@iap-kborn.de

## ABSTRACT

We report on new observations of meteor trails by ground-based lidars. The observations are performed with metal resonance lidars which sound simultaneously the densities of Na, K, Fe, and Ca atoms and  $\text{Ca}^+$  ions in the altitude range from 80 to 105 km. So far, we have measured more than 1200 trails. We estimate that these trails were produced by meteoroids in the 10  $\mu\text{g}$  to gram range. A comparison of the occurrence rates of single-element and two-element trails and measurements of the ratios of metal atom abundances in the trails indicate that the lidar-observed meteoroids ablate almost exclusively differentially. The preponderance of differential ablation processes throughout this mass range of meteoroids suggests that during their atmospheric entry a large percentage of all meteoroids fragments into tiny particles which are small enough to ablate differentially.

## 1. INTRODUCTION

When meteoroids hit the Earth's upper atmosphere, they do so with entry speeds between 11 and 72 km/s. Due to these high entry speeds, most of the meteoroids with sizes below a few centimeter experience, through aerodynamic friction, strong enough heating to entirely ablate and/or vaporize in the upper atmosphere at altitudes between 140 and 70 km. Two important questions about these entry processes are: (1) To what extent do meteoroids suffer mechanical or thermal fragmentation before they start to ablate? (2) Do meteoroids and their fragments undergo dominantly chemically homogeneous or differential ablation? *Homogeneous* ablation of a meteoroid as it passes through the atmosphere is a process in which at any part of the meteor trail the composition of the ablated material is close to the bulk composition of the ablating meteoroid. *Differential* ablation is a process by which different elements are released from the meteoroid at different points along the meteor's trajectory (McNeil et al., 1998). It is suggested that the point at which any given element is released is related to its volatility relative to the remainder of the meteoric material at the time of release. The more volatile elements, such as Na, are hypothesized to be released early in meteor flight while the less volatile elements, such as Fe and Ca, are released later or perhaps retained to some extent in the meteor, never being released at all, especially in slow meteors. This report is to show that observations by groundbased lidars can provide quantitative answers to

question (2) which in turn shed some new light on question (1).

Ablating meteoroids produce spatially well-defined trails of meteoroid debris in the atmosphere, called meteor trails, which last from seconds to tens of minutes before they are dissipated into the ambient atmosphere by diffusive and chemical processes. The composition and abundances of metal atoms set free in the debris trail depend in yet to be explored ways on the initial composition of the meteoroid and on the heating and ablation processes which act on the meteoroid during its atmospheric flight. It is at this point that ground-based lidars come into play because they give us the capability to quantify the abundances of a number of elements in these meteor trails and to allow a characterization of the ablation processes. Lidars have demonstrated the capability of measuring quantitatively the absolute number densities of metal atoms in volumes that are separated from the lidar by 100 km. The suite of metals which can be investigated by this technique extends from the moderately volatile Na and K to the refractory Ca. In the trails left behind by ablating meteoroids, all these elements can be present in amounts substantially higher than the detection thresholds of these lidars. To study them by lidar "only" requires sampling such trails by the lidar right after their formation and before they are dissipated.

The initial masses of meteoroids, of which the trails can be observed by lidar, are estimated by us to range from about 10 micrograms to several grams (see section 3.3). Meteoroids of the latter mass fall in the centimeter size range and, if assumed to be rock-like, are commonly assumed to undergo homogeneous ablation, not differential ablation. One way to explain the preponderance of differential ablation even for reasonably "massive" meteoroids is to postulate that they undergo an efficient fragmentation process early during their atmospheric entry. Here "efficient" fragmentation is to denote a fragmentation down to particle sizes of below 0.1 mm. These secondary particles would be predicted to undergo differential ablation for almost any realistic combination of entry velocity and entry angle.

In the following, we will use the nomenclature as given in Kerridge and Matthews (1988): A meteoroid is "a natural small (sub-km) object in an independent orbit in the solar system", a meteor is "the light phenomenon produced by a meteoroid experiencing frictional heating when entering a

planetary atmosphere". We will compare the lidar-measured ratios of metal abundances with those in CI carbonaceous chondrites. As justification for this comparison, we note that more than 70% of all meteorite falls are either CI, H, or L chondrites. Fortunately, the differences in composition between CI, H, and L chondrites do not matter for our deliberations because we are dealing with only four selected metals (Na, K, Fe, Ca). In CI, H, and L chondrites, their abundances and abundance ratios vary little (see Table 1). The differences between the three classes are small (less than a factor 1.4) in comparison to the variations found in meteor trails and the metal layers. Therefore, we take the liberty to use for comparison purposes the CI chondritic composition (as done very often in the literature), still recognizing the fact that the majority of the incoming meteoroids may not have CI chondritic composition.

Table 1. Ratios of number densities in selected classes of chondrites (after Kerridge and Matthews, 1988)

chondrite class	K/Ca	K/Fe	Fe/Ca
CI	0.058	0.0042	13.9
H	0.066	0.0042	15.8
L	0.063	0.0053	11.8

## 2. THE OBSERVATION TECHNIQUE

Light radars, or in short "lidars", use pulsed laser beams to illuminate intermittently columns of air in our atmosphere (Fig. 1). Atoms, molecules, and particles contained in this column scatter part of the photons of the laser beam, some of which are directly backscattered towards a receiving telescope at the site of the lidar. The photons collected by this telescope are then analyzed for their time-of-flight between their emission from the lidar and reception at the telescope (yielding the altitude of the scattering volume), for the rate at which they are received (yielding information on the density of the scatterers) and for their exact wavelengths (yielding information on motions, temperature, and composition of the scattering particle).

Lidars can be classified according to the scattering process which they use for detection of the scatterer: Meteor lidars use the process of resonant scatter. Here the laser photon excites a resonant, hence allowed transition of an atom. The excited atom falls back to its ground state with a time constant on the order of 10 ns (the equivalent light path being a few meters) and by re-emitting the absorbed photon. In first approximation, the photon is emitted isotropically from the atom and thus has a finite chance of being backscattered into the lidar telescope. A great advantage of these lidars is that resonant scatter involves huge backscatter cross sections which are typically in the order of

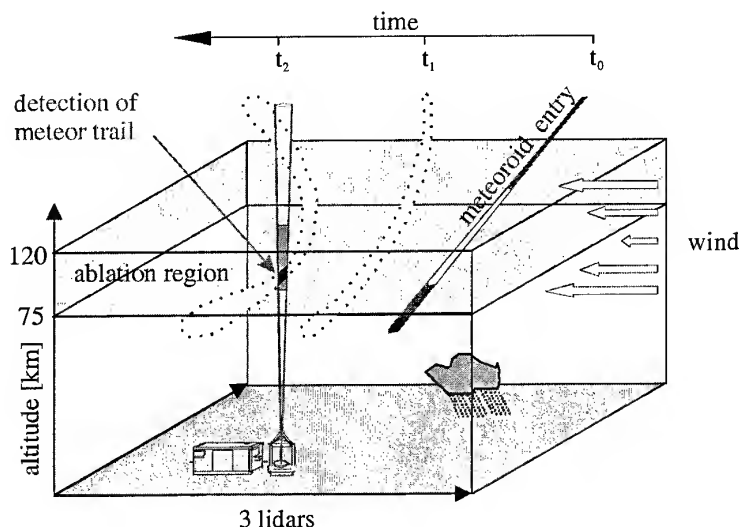
$1 \cdot 10^{-16} \text{ m}^2 \text{ sr}^{-1}$ . They are thus more than 15 orders of magnitude larger than the Rayleigh backscatter cross section of a  $\text{N}_2$  molecule. Lidars using resonant backscatter achieve impressively low detection thresholds. For integration periods of, say, 5 min and altitude intervals of 200 m, the ground-based metal resonance lidars sound the metal layers at 80 to 100 km altitude at nighttime with detection thresholds between 0.1 and 1 atom  $\text{cm}^{-3}$ .

To make meteor trails detectable for a ground-based lidar, the debris of ablated meteoroids must be illuminated at least for a few seconds by the laser beam of the lidar. In reality, however, meteoroids pass very, very rarely right through the very narrow laser beam of the lidar. An overwhelming percentage of all lidar-observed trails are caused by meteoroids entering the upper atmosphere well to the side of the laser beam (Fig. 1). The lifetime of the metal atoms in the trail and the trails's coherence are long enough, however, that the upper atmosphere winds can blow the trail through the laser beam tens of minutes after the meteoroid entry and while the trail is still recognizable by the lidar. Thus, there is no strict temporal correlation between an entering meteoroid ("shooting star") and the lidar-observed passage of the meteor trail through the laser beam.

Lidar studies have shown that meteor trails may have diameters from a few meters to many 100 meters, depending on their age and altitude. At meteor heights, the laser beams have diameters of typically 50 m. In addition, wind velocities at meteor heights are typically of the order 20 m/s (Fleming et al., 1990). These conditions, considered together, support our experience which shows that most of the meteor trails pass through the laser beams in between 2 and 10 seconds (a few can be monitored by the lidar for up to minutes). The latter statement explains in part why "normal" lidars have not noticed meteor trails for decades: They employed integration times that were much too long thereby swamping the normally feeble signals of the meteors by those from the metal layers and by background.

A lidar, dedicated to meteor work, therefore has to have a data acquisition system that allows it to collect altitude profiles of the backscattered photons with an integration period as short as possible. An ideal system stores the data of each individual laser pulse. After data acquisition, post-integration of these data with a running mean can always be used to reduce the time resolution to the desired value. Use of such short integration periods drives the currently used lidars close (or below, depending on altitude) their useful limits of photon count statistics. In the individual profiles obtained from one laser pulse, most of the altitude channels contain either none or one count. Only strong meteors produce a few counts per altitude channel and laser pulse, and can be recognized readily in the raw data stream. The average meteor can be recognized only after integrating the data over periods of a few seconds.

Fig. 1. Schematic of the instrument set-up for observing meteor trails with lidar(s). Meteoroids enter the upper atmosphere well to the side of the laser beam. Shortly thereafter, the debris produced by ablation of the meteoroid (= meteor trail) is blown through the laser beam by the upper atmosphere winds (obviously depending on their direction).



The IAP lidars store the count profiles from each laser pulse resulting typically in 2 million profiles for an observation time of 10 hours and using three simultaneously operating lidars. It is obvious that this amount of data can not be processed visually. An automated computer code is absolutely required to search and identify meteor trails versus background counts in each of the sampled altitude profiles. For this search we use running means of typically 4 s. Höffner et al. (1999) describe their automatic computer code which takes into account, among other peculiarities, Poisson statistics of received counts.

At this point, a figure should illustrate the type of data which our meteor lidars acquire. Fig. 2 shows the simultaneous observation of a Leonid meteor trail (on Nov 17, 1998) by three different lidars, one each for the elements K, Ca, and Fe. The altitude of the trail was  $103.5 \pm 0.2$  km, the altitude resolution 200 m. The integration time for the count profiles was 4 s and the trail passed through the laser beams in about 80 s. The count profiles were sampled during the period of maximum metal atom densities (= „core“ of the trail). The regular metal layers are visible below 100 km (their data being taken also with only 4 s integration time). The absolute atom number densities are derived by comparing the signal from resonant scatter by metal atoms with that of Rayleigh scatter by air molecules at lower altitudes.

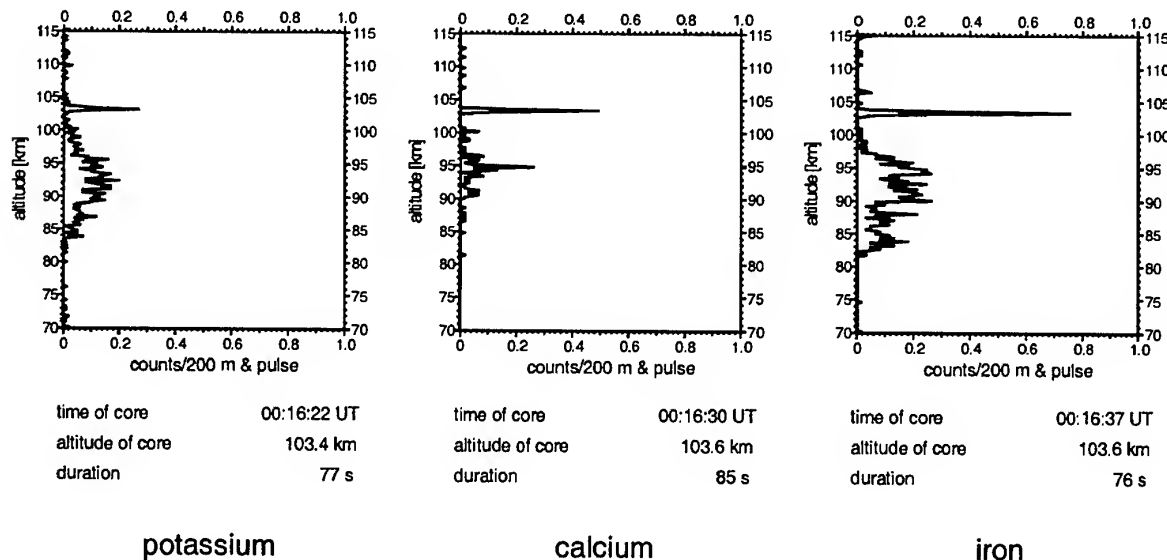
### 3. SINGLE-ELEMENT TRAILS

#### 3.1. Rate of trail detections

In October 1996, our IAP lidar group started its studies of meteor trails at Kühlungsborn with a K lidar, the laser of which is tuned to the  $K(D_1)$  resonance line (von Zahn and Höffner, 1996). In January 1997, an additional twin lidar system for studies of the mesospheric Na, Fe, Ca, and  $Ca^+$  layers (Alpers et al., 1996) became operational at the Kühlungsborn site. Since that time, we have operated these three lidars during more than 450 instrument-nights (if during 1 night we operated 3 lidars, we will call this 3 “instrument-nights”). As of today, this effort has given us a data base of more than 1200 meteor trail observations.

In table 2 we have listed for each of the elements under study the total number of trails that we have detected and analyzed since October 1996, the number of nights and hours that our lidars have observed the specific metal layer, and the rates per night and per hour of lidar sounding. The average “night of lidar observation” lasted 4.4 h, being limited mostly by variable cloudiness and rather short summer nights (at  $54^\circ N$  latitude). We recognize that (a) the mean rate of detection (= trails  $h^{-1}$ ) is similar for each of the four metals and that (b) the overall mean rate of trail detections has been 0.8 trails  $h^{-1}$ . At first sight, one may have expected to see that rate to scale somehow with the absolute densities of metals in the trails. This is clearly not the case. For the abundant Fe, one of the reasons for this is the small oscillator strength of the Fe line that is used by the lidar.

Fig. 2. Profiles of a Leonid meteor trail at 103.5 km altitude, taken simultaneously on November 17, 1998 by our lidars, one each for K, Ca, and Fe. The absolute metal densities have been 84 K atoms/ccm, 872 Ca atoms /ccm, and 208,000 Fe atoms/ccm. The regular metal layers are located below 100 km. The integration time for these profiles was 4 s. For additional details, see text.



The rate at which our lidars detect meteor trails is clearly variable from night to night. Somewhat, but not dramatically higher rates were reached during the Leonid showers (see below). Yet, significantly higher rates have been observed in sporadic enhancements of meteor activity. Gerding et al. (1999) have described one case in which over a period of slightly more than 5 h our Ca lidar detected (at least) 19 meteor trails. Thus the rate on this night approached  $4 \text{ h}^{-1}$ .

Table 2. Statistics of meteor trail observations by IAP lidars (Kühlungsborn and Tenerife; Oct 1996 - Dec 2000)

element	number of trails	number of nights	number of hours	trails/night	trails/hour	mean altitude [km]
Na	83	30	111	2.8	0.75	92.4
K	519	199	1060	2.6	0.49	88
Fe	107	28	122	3.8	0.88	89.3
Ca	570	137	530	4.2	1.08	89.9
sum or mean	1279	394	1823	3.3	0.8	89.9

### 3.2. Altitude distributions

Fig. 3 shows the altitude distributions of Na, K, Fe, and Ca meteor trails. In the four panels of Fig. 3 each of the lidar-observed trails is shown as one dot according to its altitude

and its maximum absolute atom density. We notice the following:

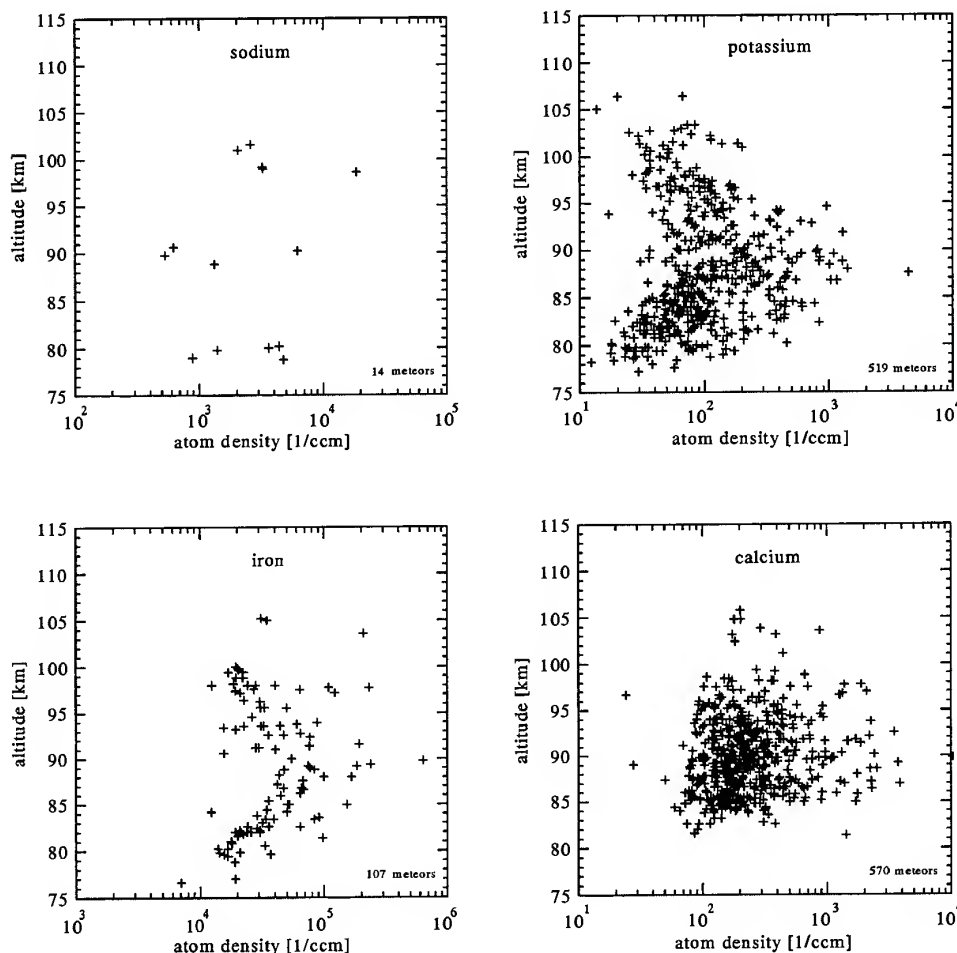
(a) For at least K and Fe, the detection thresholds of the lidars are low enough, even at the very short integration times used here, to show the "shadow" of the regular metal layers, in which altitude range thin meteor trails can not be detected. In the case of the Ca lidar, our detection threshold of about  $80 \text{ cm}^{-3}$  is higher than the peak density of the regular Ca layer, which is only  $22 \text{ cm}^{-3}$  (Gerding et al., 2000). Therefore, the "shadow" of the regular Ca layer does not show up in our altitude distribution.

(b) The trails of K, Fe, and Ca appear to be most abundant near the 90 km level. This initial impression need be corrected, though, for K. The altitude of the maximum rate of K trails is much effected by a cluster of trails at altitudes below 87 km, and densities below  $100 \text{ cm}^{-3}$  (see Fig. 3). It is in fact 83.5 km and falls 6 km lower than that for Ca trails.

(c) The panels show well the maximum altitude at which meteors were observed for each of the four elements. All four lidars lose their detection sensitivity for meteor trails above 105 km. This is an important detail for lidar-studies of meteor trails and was first recognized by Höffner et al. (1999).

(d) Finally, we draw attention to the unexpected result that for each of the four different metals, the lidar-observed trail parameters are very similar with respect to the mean occurrence rate of trails and the maximum trail altitudes.

Fig. 3. The altitude and maximum atom density of meteor trails observed by the Na, K, Fe, and Ca lidars of the IAP during the period October 1996 through 2000.



We take these data as strong evidence for the fact that the altitude distributions shown in Fig. 3 have little to do with the intrinsic altitude distribution of meteor trails. The measured altitude distributions resemble basically profiles of the “instrument functions” of the different lidars. This fact can best be demonstrated for Leonid trails. Due to their extremely high velocity of 72 km/s, the Leonids ablate at particularly high altitudes. de Lignie et al. (2000) published a list of 55 Leonid orbits, all obtained through double-station video camera observations during the 1998 Leonid shower (visual magnitudes from +6 to -1). The height of maximum brightness for the complete sample was 110 km. Our lidar group at the IAP at Kühlungsborn observed the Leonids in 1996 with their K lidar at Kühlungsborn (Höffner et al., 1999), the 1998 Leonids with three lidars (for K, Fe, and Ca) at Kühlungsborn (von Zahn et al., 1999), and both the 1999 and 2000 Leonids with a K lidar at Tenerife (Höffner

et al., 2000) and with Ca and Na lidars at Kühlungsborn (von Zahn et al., 2001). The highest of all our lidar-observed meteor trails had, however, “only” an altitude of 107.8 km. This result means that even the highest of the lidar-observed trails are definitely below the mean altitude of maximum brightness of Leonids as measured by video cameras (de Lignie et al., 2000; Campbell et al., 2000). This allows two conclusions: (1) The lidar-observed Leonid trails provide us information exclusively on a late phase of ablation of the trail-producing Leonid meteoroids; (2) More generally speaking: Lidar-derived altitude distributions of meteor trails cannot be taken to represent truthfully the intrinsic meteor altitude distributions.

### 3.3. Estimation of the mass of meteoroids which produce lidar-observable trails

von Zahn et al. (2001) derived an estimate for the mass of the lightest meteoroids, the trails of which can still be observed by lidars. They asked for the *order of magnitude* of a limiting meteoroid mass (not anything like 10% accuracy). To this end, they compared the rates at which meteors are detected by two independent methods: (a) visual observations of meteors and by video cameras and (b) through detection of their trails by lidars. Methods (a) not only provide total meteor rates (such as the zenithal hourly rate: ZHR), but additional information such as the luminosity of the meteors and derived photographic masses for each individual meteor. Availability of the latter parameters allowed them to assign a minimum mass to those meteors, the trails of which are just barely observable by lidars. von Zahn et al. (2001) concluded, that lidars can detect Leonid meteors down to a limiting brightness of about +7 m, which are slightly dimmer than those detected by methods (a).

Campbell et al. (2000) and Brown et al. (2000) give conversions of maximum luminosity of Leonid meteors into photometric mass. For a Leonid of +7 m, both Fig.12 of Campbell et al. (2000) and equation (4) of Brown et al. (2000) yield about 10  $\mu\text{g}$  for its photometric mass. We consider this value a reasonable estimate for the limiting mass of lidar-observed *Leonids*. Furthermore, we obtain for lidar observations the limiting mass of typical *sporadics* to be 0.7 mg if we apply the Jenniskens et al. (1999)-dependence of limiting mass on meteoroid velocity. We believe that this estimation yields the limiting mass with an uncertainty of about one order of magnitude. This we consider a "small" uncertainty if compared with the total mass range of objects impacting the Earth's atmosphere which is be more than 25 orders of magnitude (see Flynn, 2001).

The mass of one of the brightest Leonids observed by the IAP lidars was modeled by von Zahn et al. (1999) who arrive at an approximate mass of 10 g for this Leonid. It is for these reasons that we give the mass range of meteoroids, of which the lidars can observe the meteor trails, to fall between 10  $\mu\text{g}$  and a few grams. The upper "limit" is a practical limit and given by the rapidly diminishing probability for the occurrence of ever brighter fireballs.

## 4. TWO- AND THREE-ELEMENT TRAILS

By observing simultaneously and in the same volume different metals with two or more lidars, the *abundance ratios of different metals* in meteor trails can be measured. This type of information produces new knowledge (e.g. about the complex ablation processes of the meteoroids) that is independent from other methods.

### 4.1. Two-element trails: Frequency of occurrence and mean altitudes

Since Oct 1996, we have operated two metal lidars (with various combinations of metals) during 273 nights. This number includes the nights that we measured with three lidars. Table 3 gives in the first column the element combinations which were measured simultaneously and in the fourth column the rate of detection of two-element trails. The average rate is 0.15 trails per night. Here we remind the reader of our rate of trail detections by single lidars which is 3.3 trails per night (see table 2). If the same detection rate would apply for two-element trails, the 273 nights of two-lidar measurements should have given us about 900 trails with two observed elements. In reality, however, we observed during these nights only 42 meteor trails in which both species of metals could be detected and be quantitatively evaluated. This rate is merely 4% of the single-element trail detection rate and indicates that it takes about 6 nights of operations with two lidars to record one two-element trail.

Table 3. Trail statistics for nights with two simultaneously observing metal lidars of the IAP.

element combination	number of 2-elem. trails	number of nights	2-elem. trails per night	mean altitude [km]
Fe and K	7	18	0.39	93.4
Fe and Ca	9	27	0.33	93.2
Ca and Ca <sup>+</sup>	11	74	0.15	93.2
Ca and K	9	75	0.12	92.9
Ca and Na	4	27	0.15	91.3
K and Na	1	11	0.09	88.9
K and Ca <sup>+</sup>	1	41	0.02	94.5
sum or mean	42	273	0.15	92.9

It is of interest that the trails involving Fe (combinations #1 and #2) have about three times the occurrence rate of combinations involving Ca (#3 - #5).

What part of this substantial difference in detection rates for single- and two-element trails might be due to a limited dynamic range of the observable atom densities in the meteor trails for either element involved? This question is difficult to answer quantitatively as this would require performing many hundred case studies of the actual detection threshold of the "missing" element and relating them to a somehow predicted atom density for this element. von Zahn et al. (1999) performed such an analysis for 5 strong K-trails observed in 2 nights of November 1998 which all were missing entirely a Ca signature. They

calculated a predicted Ca density in the K-trails for the assumption that the two elements would be present in a CI chondritic abundance ratio  $\text{Ca/K} = 17.1$ . They showed that the Ca detection threshold of the lidar for Ca was between 8 and 71 times lower than the predicted Ca trail density. Thus, the observation of the "K-only" trails implied highly significant deviations of the Ca/K ratio in the trails from CI composition. It is undeniable that the detection thresholds may play a role in these arguments. But examination of the data strongly suggests that another process is also shaping the results of the two-lidar observations; this, we suggest, is the differential ablation of the meteoroids.

The mean altitudes of the families of two-element trails scatter surprisingly little about the weighted mean of 92.9 km. One can not overlook, though, the small statistics for some of the trail families which certainly allows for some chance results. Nevertheless, even the strongest statistical sample, the  $\{\text{Ca} + \text{Ca}^+\}$  trails, have a mean altitude which is only 3.3 km higher than that of single Ca trails. We expect that strong  $\text{Ca}^+$  trails are formed preferentially by fast meteoroids which in turn ablate at higher altitudes than slow meteoroids. Therefore we anticipated the  $\{\text{Ca} + \text{Ca}^+\}$  trails to occur on average considerably higher than the single Ca trails. The fact that our observations show this difference to be only rather moderate may again indicate that the observed altitude distributions are strongly driven by the common instrument function of the lidars as discussed previously.

#### 4.2. Three-element trails

We have had 78 nights with three metal lidars observing simultaneously a common zenith-directed column of the upper atmosphere. In table 4 we have listed the various element combinations which we studied during these nights. We recorded only six three-element trails or, in other words, 0.08 three-element-trails per night. The drop in detection rate is certainly less dramatic in going from two- to three-element trails than going from single- to two-element trails.

Table 4. Trail statistics for nights with three simultaneously observing metal lidars of the IAP.

element combination	number of nights	number of 3-element trails
K and Ca and Fe	17	5
K and Ca and $\text{Ca}^+$	50	1
K and Ca and Na	10	-
K and Fe and $\text{Ca}^+$	1	-
sum	78	6

As there are comparatively few three-element trails, it is possible to list in table 5 the dates, altitudes, and possible

origins of these trails. These trails are formed almost solely by fast meteoroids such as the Leonids and Perseids. Independent from the dates of the 6 three-element trails, the average altitudes point towards a higher entry speed of those meteoroids producing three-element trails than of those producing only single-element trails. The average altitude of the three-element trails is 94.4 km, whereas that of all the single-element trails is 89.9 km.

Table 5. Dates and altitudes of the three-element trails.

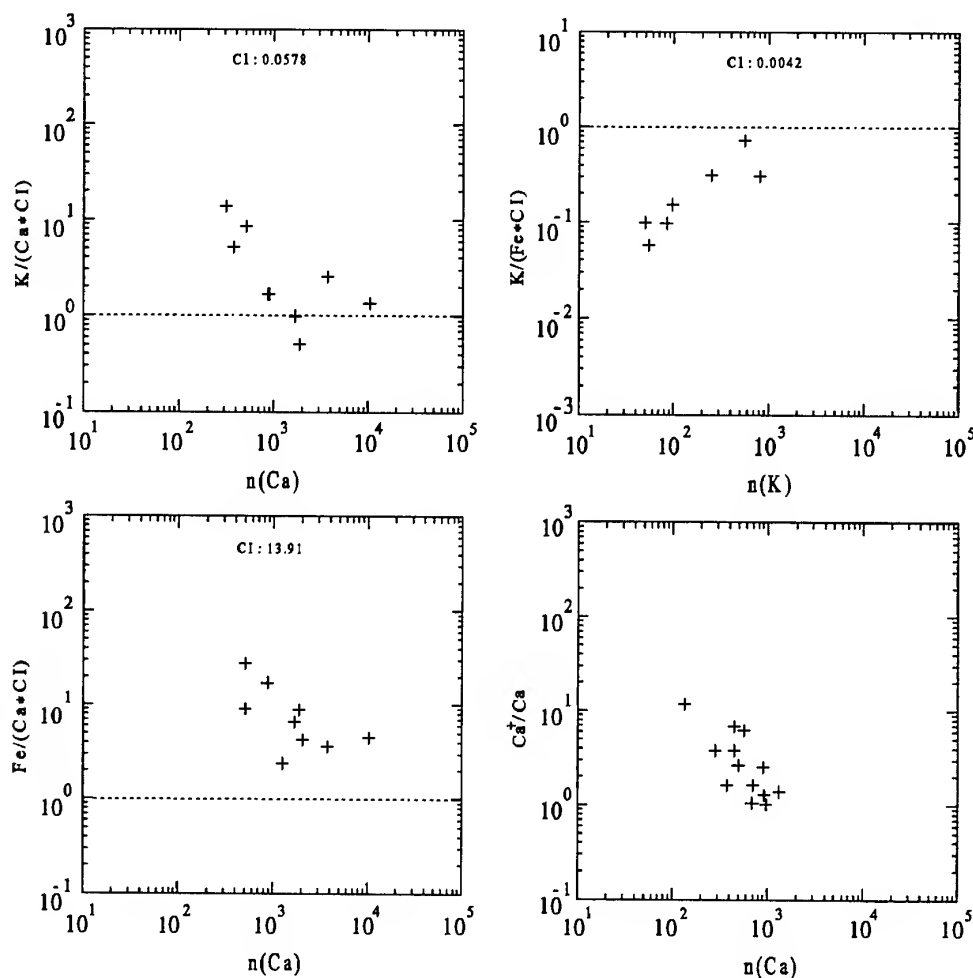
element combination	date	altitude [km]	suggested origin
K and Ca and Fe	May 13, 1997	89.2	sporadic
"	Aug 05, 1997	91.5	Perseid
"	Oct 27, 1997	89.8	Orionid
"	Nov 16, 1998	97.8	Leonid
"	Nov 17, 1998	103.5	Leonid
K and Ca and $\text{Ca}^+$	Nov 03, 1997	94.5	Leonid

There is also a tendency for the two-element trails to occur during showers of fast meteoroids. One is attempted to speculate, therefore, that slow meteoroids preferentially produce single-element trails. We have no means to prove this point on a case-by-case basis (lacking camera information to quantify the speed of the meteoroids for many events). We suggest, though, that a clustering of single-element K trails at altitudes below 88 km is a result of this property of meteoroid ablation. This low-altitude cluster of trails, having densities  $< 150 \text{ cm}^{-3}$ , can be recognized in Fig. 3. We add that a K meteor trail with a density of  $100 \text{ cm}^{-3}$  is a very prominent feature and much stronger than the regular K layer.

#### 4.3. Ratios of metal abundances

In this section we present and discuss the ratios of the number densities  $n(X)$ , where X can stand for K, Fe, Ca, and  $\text{Ca}^+$ , and where densities were simultaneously measured in two-element trails by our lidars. These ratios spread out over many orders of magnitude and are thus difficult to comprehend and compare. This wide "dynamic range" can be restricted considerably by normalizing all the ratios to that in CI carbonaceous chondrites (see our remark in section 1). In Fig. 4, the center piece of this paper, we present measured abundance ratios from our observed two- and three-element trails for K/Ca, K/Fe, Fe/Ca and  $\text{Ca}^+/\text{Ca}$ . The former three are normalized by dividing the measured ratios by those in CI chondrites (table 1). The normalized ratios are plotted against the number density of one of the constituents where we take the latter as a proxy for the size of the entering meteoroid.

Fig. 4. Ratios of the number densities of two elements (or ion over atom) measured in two-constituent trails versus density of one of the constituents. The ratios are normalized to the ratios in CI chondritic meteorites. At the dashed lines, the measured abundance ratios would equal the CI ratios. The lower right panel shows the ratio of ionized over neutral Ca as measured in  $\{\text{Ca}^+ \text{ plus Ca}\}$  trails.



Two features are immediately apparent in Fig. 4: (a) The means of the 3 normalized elemental ratios are significantly different from 1 (= the CI composition); (b) All four scatter plots show a distinct trend of the data coming closer to unity the higher the absolute density is. We elaborate on these features as follows:

(a) The fact that our observed ratios all come out differently from CI composition can be interpreted in two different ways: Either we suggest that our lidar-measured trail composition reflects indeed that of the meteoroids. Then the composition of the meteoroids must be quite dissimilar to that of CI chondrites. Or we suggest that the meteoroids have a composition like or at least close to that of CI meteorites. Then the differences of composition between meteoroids and trails would be caused by specific processes

acting during the trail formation. We prefer to follow the second argument guided by two considerations. Firstly and as pointed out in section 1, chondrites contribute by far the largest share to the total influx of meteorites. We consider it unlikely that the population of meteoroids, which are sampled by our lidars, has a mean composition *drastically* different from the population of meteorites. Secondly, as pointed out above, two- and three-element trails are formed preferentially by fast meteoroids. Those are more likely to be of cometary (and not of asteroidal) origin and hence their composition closer to CI chondrites than to any other.

Table 6. Means of metal abundance ratios in meteor trails as measured by IAP ground-based lidars

element ratio	number of trails	mean of lidar ratios	ratio in CI meteorites	ratio of lidar over CI
K/Ca	9	0.23	0.057 8	4
K/Fe	7	0.001 1	0.004 2	0.25
Fe/Ca	9	129	13.9	9.3

If we average the density ratios obtained in the different types of multi-element trails, we derive the mean ratios (and their full range of measured values) as given in table 6. An immediate conclusion drawn from the numbers in table 6 is that in the meteor trails Ca is much underabundant with respect to Fe and K. In addition, K is underabundant with respect to Fe. Note that the three ratios of the three constituents are derived from independent sets of trail observations and do not constitute an overdetermined set of values. Causes contributing to the underabundance of Ca could be a lack of complete vaporization and a vaporization at too low altitudes of Ca during the ablation process. The lidar-observed underabundance of Ca in meteor trails goes a long way towards explaining the weakness of the upper atmosphere regular Ca layer in comparison to the regular Fe layer.

(b) The strong trends exhibited by all four scatter plots of Fig. 4 need consideration too. We take them as an indication of differential ablation of the meteoroids. Differential ablation is the process by which the elements are vaporized from the meteoroid sequentially with increasing temperature of the meteoroid body. The process can be important only over volumes in which the time constants of thermal heat conduction and material diffusion are small in comparison to that of the temperature increase at the volume's surface. This allows differential ablation to be important only for small sized meteoroids. But what is "small" in this connection? We interpret the trends in the scatter plots as indicating that differential ablation becomes stronger and stronger the smaller the meteoroid is. As mentioned before, we take here the measured density as proxy for the size of the meteoroid. In all three cases of ratios of neutrals, the deviations from the CI composition (that we would interpret as representing homogeneous ablation) become stronger the smaller the size of the meteoroid is. Another clue for the prevalence of differential ablation of lidar-observed meteoroids is the fact that we observe hardly any meteoroid with CI composition.

One more gross feature of the scatter plots in Fig. 4 is noteworthy. The trends in the K/Ca and Fe/Ca ratios could mean that for the smaller meteoroids the ablation temperature does not become high enough to fully vaporize

Ca. This effect works, at least qualitatively, in the expected direction (producing an underabundance of Ca). If we carry this argument over to the measured K/Fe ratios, it would imply that K is the element of the two which ablates (unexpectedly) at the *higher* temperature or for any other reason less completely than Fe.

At the end of this section we reiterate that we observed many Ca trails without any detectable concurrent  $\text{Ca}^+$  trail. Therefore, the mean ratio  $\text{Ca}^+/\text{Ca} = 4$  as derived from  $\{\text{Ca}^+ \text{ plus Ca}\}$ -trails, must not be implied for all Ca trails which we have observed.

#### 4.4. Comparison with literature

A comparison of our lidar-measured metal abundance ratios with other lidar results is not possible as we do not know of any other lidar results. We can only mention the report of Kane and Gardner (1993) on the observation of a single  $\{\text{Na plus Fe}\}$ -trail. The absolute atom densities in this trail remain, however, quite uncertain due to rather long and different integration times applied in the two lidars. On the topic of two-element trails, the authors comment: "Fe meteor trails have been observed at several occasions at Urbana when Na meteor trails were not". While interesting within the context of the previous discussion, the statement does not lend itself to a quantitative comparison with our data.

The optical phenomenon of meteors has been studied in sophisticated spectroscopic experiments, which subject is treated at some length in the review on meteor phenomena by Ceplecha et al. (1998). In these experiments one investigates, however, the hot plasma conditions very close to the ablating meteoroid. In addition, the sensitivity of the spectrographic instruments generally limits the observations to fireball-type meteors at altitudes below 70 km.

For purposes of comparison with our lidar observations better suited are the more recent results obtained by video spectroscopy of Leonid meteors because they cover a mass range of meteoroids similar to that of our lidar observations. Borovička et al. (1999) selected for their study 20 Leonids which they observed November 17, 1998 and having apparent maximum visual magnitudes between +2.4 and -3.6. Borovička et al. (1999) observe Na to evaporate earlier than other metals. The early release of Na was detected by video spectroscopy also from 1999 and 2000 Leonids by Murray et al. (2000), Abe et al. (2000) and Borovička (2001). We use this opportunity to point out that the entire light curves of these Leonids last typically only 0.4 to 0.5 s. This short time scale sets stringent limitations for the maximum size of particles which can experience *differential* ablation. Nevertheless, the observed early release of Na is a sign of at least a limited amount of differential ablation in general agreement with our lidar observations.

Concerning the behavior of other metals, a direct comparison of the results from optical spectroscopy and our lidar observations becomes hard. Borovička et al. (1999) state that the relative bulk abundances of Mg, Fe, and Ca in Leonid meteors are nearly CI-chondritic. Yet, they give the derived ratios of metal abundances only after having the line intensities integrated along the entire meteor trajectory. By this analysis method, they undoubtedly smooth over the potentially present effects of differential ablation which makes a quantitative comparison with our lidar results impractical. At the same time, we want to point out that the few Leonid trails, which our lidars could observe, form a very distinct group within our ensemble of over 1200 meteor trails. For example, among the group of our 3-element trails, the Leonids contribute 3 to the total of 6 observed trails (see table 5). These numbers imply a strong over-representation of Leonid trails in this group if we compare them with the occurrence rates of 3- and 1-element lidar trails in general, which are 0.03 and 3.3 trails per night, respectively, of lidar observations. For reasons of limited dynamic range of our detection scheme, 3-element trails could not be observed if strong deviations from CI composition would be present in these trails. We therefore take the prevalence of Leonid trails in our family of 3-element trails as indicating that their metal composition is closer to chondritic than for the (overwhelming) rest of our meteor trails.

## 5. DIFFERENTIAL ABLATION: REVIEW AND CONSEQUENCES

Lidar observations of the number densities of Na, K, Fe, and Ca in more than 1200 meteor trails have by now clearly shown that

- (a) at anyone part of the trails, the metal abundances inside the meteor trails are strongly dominated by a single metal in almost all observed cases
- (b) in the few cases, in which the abundances of two or three metals allowed their simultaneous measurement, the means of the abundance ratios deviate significantly from CI meteoric composition
- (c) the observed metal abundance ratios deviate from CI meteoric composition the stronger the smaller the meteoroid mass is.

Lidar observations have shown these features to be common to almost the entire ensemble of observed meteor trails.

The metal abundance ratios observed in meteor trails by lidar may deviate from the meteoroid bulk composition not only because of differences in volatility of the various (pure) metals. Deviations of the metal atom ratios (as determined by the lidars) may occur through different thermal stabilities of the metal oxides which may cause one of the metals, such as Ca, to stay more in a molecular form than the other. Another scenario could be that in the case of slow sporadics the entire ablation process starts at so low an altitude that only the volatile metals Na and K are released above, say, 80

km altitude. All metals released from the meteoroid below 80 km are essentially undetectable for lidars due to their extremely short chemical lifetime in the atomic state. Lidar observations of this kind (strong, low altitude, single-element K trails) have been reported by von Zahn et al. (1999). Yet, the "opposite" scenario can also become true: A group of single-element Ca trails and entirely missing K trails was observed by Gerding et al. (1999). These authors explained them by the existence of a rather sharp drop-off of the capabilities of lidars for trail detections (see Fig. 3) at altitudes above 100 km. For a specific meteor shower, this can place the Ca atoms in the well-observed altitude region near 90 km, but the volatile elements above 105 km where they are invisible for the lidars.

We emphasize that the existence of altitude limits for lidar detection of meteor trails will not make a homogeneously ablating meteoroid to look like a differentially ablating meteoroid for the lidar. If two or even three simultaneously observing lidars can detect only one metal in a specific portion of the meteor trail then there must be differential ablation ongoing (up to the point that the detection thresholds of the lidars allow the detection of the various metals). The finding, that more than 95% of the detected trails contain only one element, is therefore strong evidence that differential ablation is taking place in these meteors.

Differential ablation has been observed and is expected on theoretical grounds for micrometeorites with masses of, say, below 1  $\mu\text{g}$  (or sizes smaller than 0.1 mm). We argued above, however, that the meteor trails recorded and studied by our lidars were produced by meteoroids with masses in the milligram-to-gram range. Former expectations that lidar-observed meteoroids undergo homogeneous ablation processes were based on earlier modeling results which assumed, among other constraints, the meteoroid to consist of a solid grain or piece of rock. The preponderance of differential ablation processes for meteoroids with masses in the gram range indicate that during the atmospheric entry a much larger percentage than expected of all meteoroids fragment into many tiny particles. The average size of these secondary particles would be so small that they independently ablate differentially. Still, the secondary particles would all travel closely together and thus create a single meteor trail (at least as looked at with our current spatial resolution of a few meters).

We recognize the possibility that this fragmentation process leads to the formation of secondary particles with distinctly different composition and hence ablation processes (see e.g. Flynn, 2001). Due to extreme g-loads during their deceleration, millimeter-size debris particles might experience mineralogical segregation during the fragmentation process. Thus, the fragmentation of material from a single source could produce secondary particles with a diverse range of chemical composition (chondrules, matrix and/or other sub-units). Our current lidar observations of

meteor trails neither specifically support nor refute the existence of this process leading to a chemical differentiation of the secondary particles.

The concept of abundant meteoroid fragmentation has been developed on theoretical grounds and from studies of the initial radius of trails observed by meteor radars, of the lack of Fresnel oscillations in radar echoes, of light curves of meteors, of high-resolution imaging of meteors and high-resolution radar observations, of non-linear trajectories of bolides, of meteorite strewn field from major break-ups and other observations. We see our lidar-observations as contributing another interesting stone to the mosaic of information on the fragmentation processes of meteoroids.

## 6. CONCLUSIONS

Groundbased lidars are shown to give us a capability to study the abundances of specific metals in meteor trails with hitherto unavailable accuracy. An ensemble of over 1200 meteor trails studied by lidar provide us with strong evidence that meteoroids ablate differentially and not homogeneously. Only with the latter condition fulfilled could we expect to relate in a straightforward way the composition recorded in a meteor trail with that of the meteoroid. The primary result of our study is to learn that meteoroids with masses up to the gram range ablate almost exclusively differentially and not homogeneously. Differential ablation shows up in (a) the number of single-element trails being very large in comparison to that of two- and three-element trails and (b) the lidar-measured ratios of metal abundances in meteor trails. We interpret our observations as indicating that during atmospheric entry most meteoroids in the 10  $\mu$ g to gram range fragment into many smaller, secondary particles which are small enough to undergo independently differential ablation.

## 7. ACKNOWLEDGMENTS

U.v.Z. acknowledges the highly spirited assistance in collecting and analyzing the IAP lidar data by M. Alpers, V. Eška, C. Fricke-Begemann, M. Gerding, J. Höffner, T. Köpnick, and J. Oldag. Also, U.v.Z. wishes to thank EOARD for a Window-on-Science visit to AFRL.

## 8. REFERENCES

- Abe, S., H. Yano, N. Ebizuka, and J.-I. Watanabe, First results of high-definition TV spectroscopic observations of the 1999 Leonid meteor shower, *Earth, Moon and Planets*, 82-83, 369-377, 2000.
- Alpers, M., J. Höffner, and U. von Zahn, Upper atmosphere Ca and Ca<sup>+</sup> at mid-latitudes: First simultaneous and common-volume lidar observations, *Geophys. Res. Lett.*, 23, 567-570, 1996.
- Borovička, J., R., Video spectra of Leonids and other meteors, poster presented at the *Meteoroids 2001 Conference*, Kiruna, Sweden, 6-10 August 2001.
- Borovička, J., R. Stork, and J. Boček, First results from video spectroscopy of 1998 Leonid meteors, *Meteorit. Planet. Sci.*, 34, 987-994, 1999.
- Brown, P., et al., Global ground-based electro-optical and radar observations of the 1999 Leonid shower: First results, *Earth, Moon and Planets*, 82-83, 167-190, 2000.
- Campbell, M.D., P.G. Brown, A.G. LeBlanc, R.L. Hawkes, J. Jones, S.P. Worden, and R.R. Correll, Image-intensified video results from the 1998 Leonid shower: I. Atmospheric trajectories and physical structure, *Meteorit. Planet. Sci.*, 35, 1259-1267, 2000.
- Cepelcha, Z., J. Borovička, W.G. Elford, D.O. ReVelle, R.L. Hawkes, V. Porubčan, and M. Simek, Meteor phenomena and bodies, *Space Sci. Rev.* 84, 327-471, 1998.
- de Lignie, M., M. Langbroek, H. Betlem, and P. Spurný, Temporal variation in the orbital element distribution of the 1998 Leonid outburst, *Earth, Moon and Planets*, 82-82, 295-304, 2000.
- Fleming, E.L., S. Chandra, J.J. Barnett, and M. Corney, Zonal mean temperature, pressure zonal wind and geopotential height as functions of latitude, *Adv. Space Res.*, Vol. 10, No. 12, 11-59, 1990.
- Flynn, G.J., Extraterrestrial dust in the near-Earth environment, in *Meteors in the Earth's Atmosphere*, edited by I.P. Williams and E. Murad, Cambridge University Press, in press, 2001.
- Gerding, M., M. Alpers, J. Höffner, and U. von Zahn, Simultaneous K and Ca lidar observations during a meteor shower on March 6-7, 1997, at Kühlungsborn, Germany, *J. Geophys. Res.*, 104, 24689-24698, 1999.
- Gerding, M., M. Alpers, U. von Zahn, R.J. Rollason, and J.M.C. Plane, The atmospheric Ca and Ca<sup>+</sup> layers: Midlatitude observations and modeling, *J. Geophys. Res.*, 105, 27131-27146, 2000.
- Höffner, J., C. Fricke-Begemann, and U. von Zahn, Note on the reaction of the upper atmosphere potassium layer to the 1999 Leonid meteor storm, *Earth, Moon and Planets*, 82-82, 555-564, 2000.
- Höffner, J., U. von Zahn, W.J. McNeil, and E. Murad, The 1996 Leonid shower as studied with a potassium lidar: Observations and inferred meteoroid sizes, *J. Geophys. Res.*, 104, 2633, 1999.
- Jenniskens, P., M. De Lignie, H. Betlem, J. Borovička, C.O. Laux, D. Packan, and C.H. Kruger, Preparing for the 1998/99 Leonid Storms, in *Laboratory Astrophysics and Space Research*, edited by P. Ehrenfreund, pp. 425-455, Kluwer Acad. Publ., 1999.
- Kane, T. J., and C. S. Gardner, Lidar observations of the meteoric deposition of mesospheric metals, *Science*, 259, 1297-1300, 1993.
- Kerridge, J.F., and M.S. Matthews (editors), *Meteorites and the Early Solar System*, The University of Arizona Press, Tucson, AZ, 1988.
- McNeil, W.J., S.T. Lai and E. Murad, Differential ablation

of cosmic dust and implications for the relative abundances of atmospheric metals, *J. Geophys. Res.*, **103**, 10899–10911, 1998.

Murray, I.S., M. Beech, M.J. Taylor, P. Jenniskens, and R.L. Hawkes, Comparison of 1998 and 1999 Leonid light curve morphology and meteoroid structure, *Earth, Moon and Planets*, **82-83**, 351-367, 2000.

von Zahn, U., and J. Höffner, Mesopause temperature profiling by potassium lidar, *Geophys. Res. Lett.*, **23**, 141-144, 1996.

von Zahn, U., J. Höffner, and W.J. McNeil, Meteor trails as observed by lidar, in *Meteors in the Earth's Atmosphere*, edited by I.P. Williams and E. Murad, Cambridge University Press, in press, 2001.

von Zahn, U., M. Gerding, J. Höffner, W.J. McNeil, and E. Murad, Fe, Ca, and K atom densities in the trails of Leonids and other meteors: Strong evidence for differential ablation, *Meteorit. Planet. Sci.*, **34**, 1017-1027, 1999.

## THE AKM VIDEO METEOR NETWORK

Sirko Molau

*International Meteor Organization, PF 600118, D-14401 Potsdam, Germany, E-Mail: video@imo.net*

### ABSTRACT

The German "Arbeitskreis Meteore" (AKM) group has been installing and operating a network of automated image-intensified video cameras since March 1999. It is based on the MetRec meteor detection and analysis software, which allows for efficient video observations with only a minimum of human interaction. It is the first network of video cameras ever that operates on a regular basis and collects large amounts of meteor data in the optical domain throughout the full year. As of June 2001, the network consists of ten stations. Further observers in Germany and abroad are preparing to join the effort, expanding the AKM network into a global one. All data are compiled into an archive that is freely accessible through the Internet. The video meteor database contains currently more than 32.000 single-station meteor records from over 500 observing nights.

Key words: video observation; automatic meteor detection; meteor network.

### 1. INTRODUCTION

Video observation of meteors has a long history. Professionals have been operating image-intensified camera since the sixties and seventies [1], and amateurs have been applying this meteor observing technique since 1987/88 [2,3]. However, video systems were only operated during selected showers, as data analysis was very time consuming and expensive. Only recently video meteor data are collected on a regular basis. A network of cameras was installed in Germany in 1999 and is growing ever since. It is the first network of video systems ever that operates on a regular basis and collects large amounts of meteor data in the optical domain throughout the full year. Camera stations in other countries have joined the network recently or prepare to do so in the coming months and years.

This paper describes the "Arbeitskreis Meteore" (AKM) video meteor network, the software it relies on, and the database that is created. It is organized as follows: The next section describes the MetRec

(Meteor Recognizer) software package, which is the basis for the network. It gives a brief account on the history of the program, the hard- and software requirements, and how an observations with MetRec is carried out. The following chapter describes the video network, its history, objectives, and the current status. The video meteor database that results from network operation is described in the fourth section. The contents of the database and means of access to the data are introduced in detail. In the outlook future extensions of the software and network as well as Internet resources are discussed.

### 2. THE METREC METEOR DETECTION SOFTWARE

#### 2.1. History

Whereas computers have been supporting the position measurement of video meteors since the late eighties, there were no attempts for computer-based meteor detection before 1993 [4]. In 1996 a system capable of searching for meteors in real-time was developed by Gural [5]. The first version of MetRec was presented in 1998 [6]. At that time it was a pure detection software which could do little more than detecting meteors and saving their appearance times. There have been numerous extensions and improvements since then. The software got the functionality to compute equatorial meteor positions, the meteor brightness and velocity, and the corresponding meteor shower. From each detected meteor a sum image and a short movie showing its temporal development can be saved. The positional data is stored in a dBase file in IMO's PosDat format. Supplementary tools were provided that allow for efficient preparation and post-processing of observations. In spring 1999 the software was ready for automated video meteor observations doing both meteor detection and analysis in real-time.

#### 2.2. Hard- and software requirements

To run an automated video meteor system you need a (preferably image-intensified) PAL or NTSC video

camera. The software should run on a PC with at least 400 MHz clock rate and 32 MB of main memory. MetRec supports the frame grabber family of the Canadian company Matrox, preferably a "Meteor II" grabber. The software runs under the operating systems DOS and Win95/98.

The MetRec software package can be downloaded from the Internet and the source code is available on request from the author. MetRec is shareware. Amateur astronomers may use it at no cost, professional or commercial users are required to pay a registration fee first.

### 2.3. Software operation

An automated video observation with MetRec is typically carried out in three steps.

1. preparation: First a reference image of the camera's field of view must be grabbed. With the help of the RefStars tool you then supply data about the observing site and date, and measure the position and brightness of a set of reference stars. These are required for astrometry and photometry of meteors during observation. Depending on whether the orientation of the camera has changed, the preparation takes about one to ten minutes.
2. observation: The main program MetRec allows to analyse a video data stream both off-line (from a video tape) and on-line (directly from the meteor camera). MetRec can be adapted to specific camera systems and tasks by a number of parameters which are set in a configuration file. It carries out meteor detection and analysis on the fly without human interaction. Live images and detected meteors are displayed during observation and results are written to disc.
3. post-processing: There is typically a number of false detections during observation caused by birds, insects, airplanes, or strong camera noise. The PostProc tool enables you to inspect the recorded events and delete false detections efficiently from all databases. For a typical night this requires again in the order of ten minutes of manual work.

In summary there is only little human interaction involved which allows to operate video systems round the clock and throughout the year at very little costs.

## 3. THE AKM VIDEO METEOR NETWORK

### 3.1. History

A first automated video meteor camera was installed in Aachen (Germany) in March 1999 after the meteor detection and analysis software was ready. Since

then it has been operated by the author in almost every clear night. Four months later a second video observer joined the effort and by the end of 1999 there were two systems in regular and three other in "sporadic" operation in Germany. A first observer outside Germany joined the network in September 2000, and in the following year a number of new observers in Germany, Australia, U.K., and Spain could be welcomed. By June 2001 the network consisted of seven regular and five "sporadic" observers in six countries. Almost all of them are amateur astronomers who operate their private video systems and computer hardware at home.

### 3.2. Objectives

The AKM video meteor network has two main objectives: On the one hand it aims at monitoring meteor shower activity in the optical domain throughout the full year and on a global scale. Data collected by the network allow to detect and confirm unusual shower activity, to revise the list of meteor showers, and to study special meteor shower properties (e.g. radiant structures and light curves). On the other hand all observations are collected at a central site, where a high quality database of consistent video meteor records is created and maintained. The data is easily accessible and usable for everybody via a free download from the Internet.

### 3.3. Network status

Fig. 1 to 4 reflect the development of the video network and its current state. Fig. 1 shows the number of participating observers in Germany and other countries in 1999, 2000, and in the first half of 2001. It has grown steadily and we expect further network expansion in the coming months and years.

Fig. 2 depicts in how many nights video cameras were operated. Recently the coverage has improved drastically. In the first six months of 2001 there was in 84% of all nights at least one camera in operation for some time.

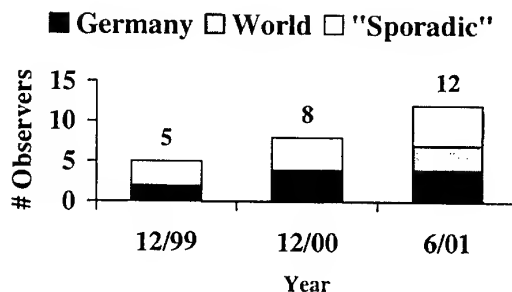


Figure 1. Number of video meteor observers participating in the AKM video network.

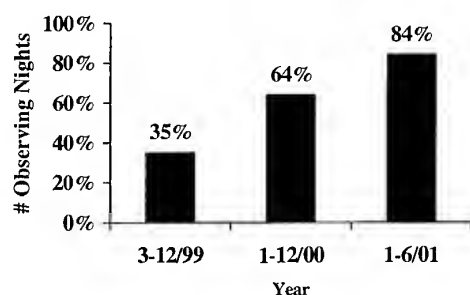


Figure 2. Percentage of nights in which at least one camera of the AKM video network was in operation.

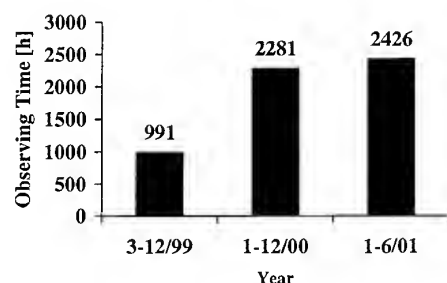


Figure 3. Effective observing time of the AKM video network.

The effective observing time and the number of meteors recorded by the network are shown in Fig. 3 and 4. Especially thanks to observations from Australia both values for the first half of 2001 have already passed the results of 2000.

Fig. 5 finally shows the geographic distribution of the cameras in central Europe as of June 2001. Not shown are the video systems operated in Finland, Spain, and Australia.

#### 4. THE VIDEO METEOR DATABASE

The video meteor database is created from the data of all cameras that participate in the AKM network. There are a number of resources available from each observation:

- a log file that lists all observational circumstances and results (software configuration, operation times, detected meteors and their parameters, observation statistics) in a plain text format
- sum images created from all video frames of a meteor (see Fig. 6)
- "meteor bands" that capture the temporal meteor development (see Fig. 7)

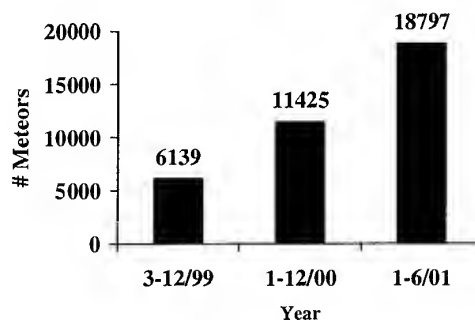


Figure 4. Number of meteors recorded by the AKM video network.

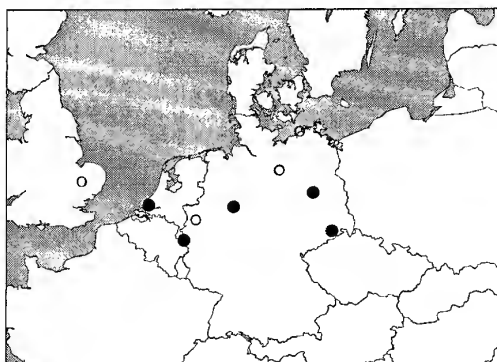


Figure 5. Locations of the AKM video network cameras as of June 2001. Full dots mark cameras that are operated regularly, open dots cameras which are active at selected times only. Not shown are the Finnish, Spanish, and the Australian camera.

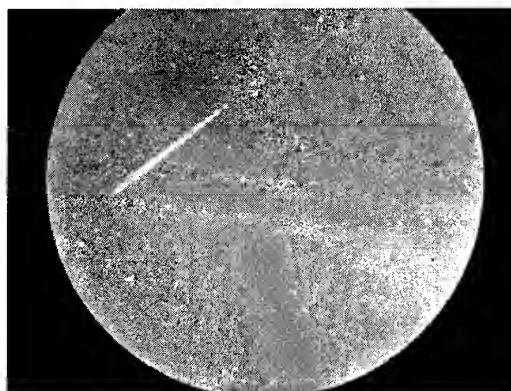


Figure 6. Typical sum image of a bright meteor. The breaks in the meteor trail are not caused by a rotating shutter but by the motion of the meteor from one video frame to the next.



Figure 7. This sequence shows the temporal development of the meteor in Fig. 6 as stored in the "mteor band".

- text files with detailed astrometric and photometric data for each meteor
- dBase files in IMO's PosDat format with the position data. These files can be read by other software like Radiant [7] for detailed meteor shower analyses.

After the end of a month the new observations are appended to the database, and observation statistics are published in the Internet. Old video tapes from meteor observing campaigns of selected showers between 1993 and 1998 were re-analysed in parallel. As of June 2001 the database contains 32,414 single station meteor records from 514 observing nights.

All PosDat files can be downloaded from the Internet. Meteor position data can be selected for a particular month, a particular year, or a combination of both. An extra table allows to check beforehand if and how many camera systems were active at any given date. All other data (log files, images, movies) are made available on CD-Rom.

## 5. OUTLOOK AND INTERNET RESOURCES

Beside normal software maintenance and implementation of additional functionality by the author a number of further software developments are currently under way or in preparation. Tom Kreyche is porting the software to the Windows ME/2000/NT operating systems. Luis Bellot et al. are working on improved photometry of video meteors. Rob McNaught and the author are working on a supplementary tool for the efficient semi-automatic meteoroid orbit determination from double-station video observations.

We hope that in a few years the database has grown such that a detailed revision of northern and southern meteor shower activity becomes feasible. The video network is expected to expand further in the coming months and years. Currently new stations are setup in Germany, the Netherlands, Austria, Australia, U.S.A., the Czech Republic, and Japan. We would like to strongly encourage other video observers to contact us and join the network.

The MetRec software and a description of the AKM video network can be found in the Internet at <http://www.metrec.org>. The meteor database is accessible at <http://www.metrec.org/database.html>.

A mailing list [metrec@yahoogroups.com](mailto:metrec@yahoogroups.com) was created for questions, discussions, and announcements regarding automated meteor observations and MetRec. You can subscribe to that list at <http://groups.yahoo.com/group/metrec>.

## ACKNOWLEDGMENTS

I would like to thank Janko Richter and Marc deLignie, who provided subroutines for the MetRec software. A number of discussions with Pete Gural and suggestions by the camera operators helped to improve the quality of the software significantly. I'm grateful to all members of the AKM video network, which are as of June 2001: Michael Gerding, André Knöfel, Sirko Molau, Mirko Nitschke, Jürgen Rendtel, Ulrich Sperberg, Jörg Strunk (all Germany), Detlef Koschny (the Netherlands), Ilkka Yrjölä (Finland), Rob McNaught (Australia), Orlando Benitez Sanchez (Spain), and Stephen Evans (U.K.)

## REFERENCES

1. Hawkes R. L., *Television Meteors*, In: Štohl J. and Williams I. P. (eds.), Proc. Meteoroids 1992, Smolenice, Slovakia, 227, 1993.
2. de Lignie M. and Jobse K., *Accurate Radiant Determination from TV Meteors*, In: Lanzig J. (ed), Proc. Int. Meteor Conf. 1989, Hengelo, the Netherlands, 41, 1988.
3. Fujiwara Y., *Television Observations of Meteors in Japan*, In: Štohl J. and Williams I. P. (eds.), Proc. Meteoroids 1992, Smolenice, Slovakia, 265, 1993.
4. Molau S., *MOVIE - Meteor Observation with Video Equipment*, In: Roggemans P. and Verbeeck C. (eds.), Proc. Int. Meteor Conf. 1993, Puimichel, France, 71, 1994.
5. Gural P. S., *An Operational Autonomous Meteor Detector: Development Issues and Early Results*, WGN, IMO J., Vol. 25, 136, 1997.
6. Molau S., *The Meteor Detection Software MetRec*, In: Baggaley W. J. and Porubčan V. (eds.), Proc. Meteoroids 1998, Tatranská Lomnica, Slovakia, 131, 1999.
7. Arlt R., *The Software 'Radiant'*, WGN, IMO J., Vol. 20, 62, 1992.

# DOUBLE STATION TV METEORS AND ANALYSIS OF THEIR TRAJECTORIES

R. Štork

*Astronomical Institute, Academy of Sciences of the Czech Republic, CZ-25165 Ondřejov, Czech Republic  
Email: stork@asu.cas.cz*

## ABSTRACT

The TV observation of meteors is performed in Ondřejov since 1990. Together with taking meteor spectra we started also double station observations in the integral light in 1998. The stations are located in Ondřejov and Kunžak; it gives the base distance of 92.5 kilometers. We use camcorders with image intensifier; the diameter of the field of view is about 20 degrees, limiting magnitude about 8 for stars and 6–7 for moving object (meteor). Hundreds of shower and sporadic meteors were recorded; about half of them are double station ones. The selected meteors were measured on digitized records from both stations and their trajectories in the atmosphere and heliocentric orbits were computed. Also  $K_B$  parameter [1] was computed for meteors and the distribution of shower and non-shower meteors into classes using that criterion will be presented.

## 1. PROGRAM AND INSTRUMENTATION

TV observation of meteors in Ondřejov started since 1990. The high sensitive SIT-vidicon tube has been using for taking spectra of faint meteors (details in [2]).

In 1998 we started also double station observation in the integral light using the commercial camcorders equipped with second-generation image intensifiers Dedal.

Observations are performed in Ondřejov and Kunžak stations. It gives a base distance of 92.5 km, which is very good for meteor geometry and computing trajectory. The orientation is almost north south; azimuth of Kunžak station is 340 degrees (south = 0). It may complicate observation of circumpolar showers with radiant in the line Ondřejov – Kunžak but it is good for the most of our observation.

Experiments consist of objectives Arsat 1.4/50, second generation image intensifiers Dedal and S-VHS-C camcorders Panasonic. The observation is usually recorded on external S-VHS video recorders JVC.

Our technique gives the diameter of the field of view about 22 degrees and limiting magnitude about 8 for stars and 6–7 for moving object – meteor.



Fig. 1. Position of our stations

## 2. RECORDED METEORS 1998-1999

This paper is based on meteor observed in 1998-1999. Two years represent 57 hours of observation, during which 472 double station meteors were recorded. 207 of them were digitised and measured.

We observe main meteor showers, but also many sporadic meteors were detected at the time of showers activity, of course.

We would like to thank Pavel Spurný who operated Kunžak station and Jaroslav Boček who digitised our meteor records using Miro DC30 card.

We use Sirko Molau's MetRec ([www.metrec.org](http://www.metrec.org)) for searching meteors on videotapes. But the shower membership and meteor brightness computed by MetRec is just brief information for us; we determine it by analysing meteor trajectory and photometry.

Pavel Koten created and used software for measuring meteor positions and photometry [6]. The software created by Jiří Borovička, Zdeněk Cepelcha and Pavel Spurný was used for computing trajectory. The straight least-squared method [5] was used for determining trajectory in the atmosphere.

106 meteors with certain membership of any major shower and sporadic ones were used for the following analysis (11 Geminids, 8 Lyrids, 14 Orionids, 32 Perseids, 41 sporadic).

### 3. METEOR DATA

Our meteor data are stored in database created in Microsoft Excel, what allows studying physical parameters and dependences as displayed in the following graphs.

The shower and sporadic meteors are marked uniformly in all graphs using following symbols:  $\eta$  Aquarids – diamond, Geminids – triangle, Lyrids – square, Orionids – circle, Perseids – cross, sporadic – point.

#### 3.1 Beginning height – absolute brightness

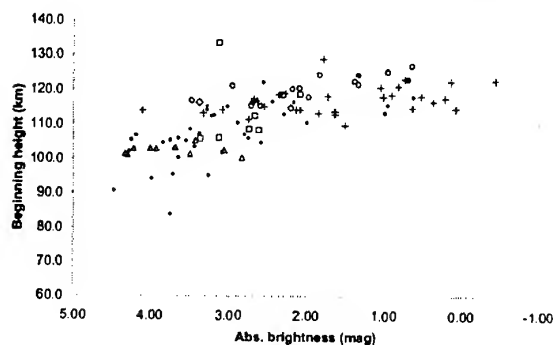


Fig. 2. Beg. height – abs. brightness

Fig. 2 shows the dependence of beginning height on absolute brightness of meteor. Two trends are visible here:

- Beginning height of brighter meteors is higher. Strictly speaking the fainter ones cannot be observed in those distances.
- The group (line) of faster meteor shower is higher.

The unusually high Lyrid is one of non-Leonid meteor with extreme beginning height observed in Ondřejov. This paper covers data 1998-1999 only; but we observed another extremely high meteors in 2000; see [3].

#### 3.2 End height – abs. brightness

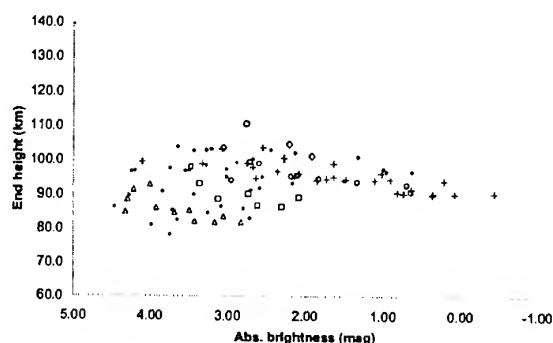


Fig. 3. End height – abs. brightness

It is and expected that the brighter meteors penetrate deeper than the fainter meteors of the same velocity as is visible in Fig. 3. And slower meteors penetrate deeper; it is also evident and expected.

The zenith distance of the radiant affects the graph. It is important for  $\eta$  Aquarids, which may be observed from Central Europe in high zenith distance of radiant only. See subsection 3.5.

#### 3.3 Beginning height – geocentric velocity

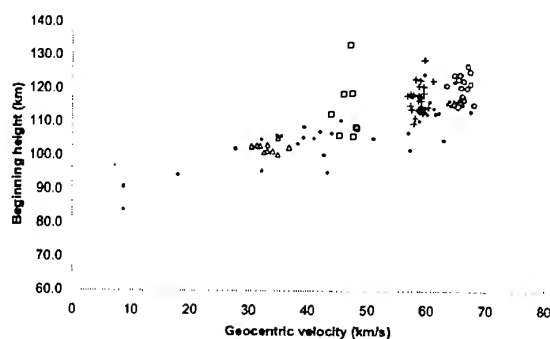


Fig. 4. Beg. height – geocentric velocity

As expected the faster meteors have higher beginning heights. But what is not expected; Perseids and Orionids start luminous part of their trajectories higher than sporadic meteors of the same velocity.

Data of slower meteors are more inaccurate. It may be said generally; TV observation gives better results for faster meteor due to finite number of image elements.

### 3.4 End height – geocentric velocity

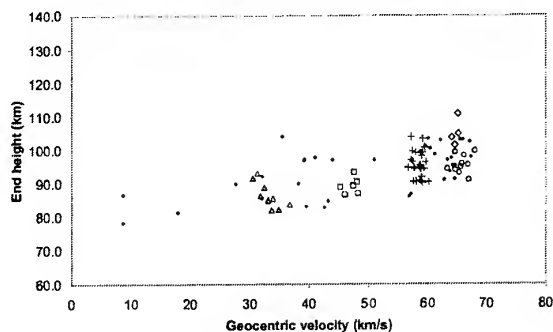


Fig. 5. End height – geocentric velocity

As above mentioned data of slower meteors are more inaccurate. The higher dispersion of Geminids may be seen in Fig. 5. This graph is also affected by effect of zenith distance; the end heights for  $\eta$  Aquarids are too high.

### 3.5 Effect of zenith distance

The effect of zenith distance of radiant may be explained by plotting dependence of beginning and end heights on radiant zenith distance.

If a radiant is near to the horizon, the meteor trajectory in the atmosphere is more horizontal and it causes high end height.

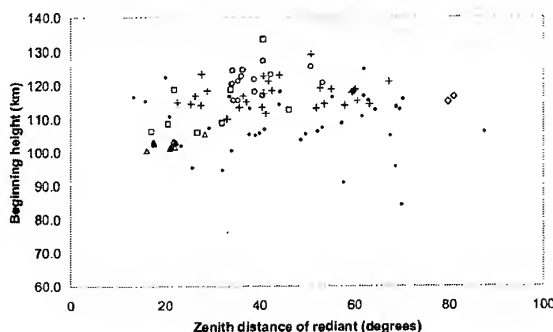


Fig. 6. Beg. height – zenith distance of radiant

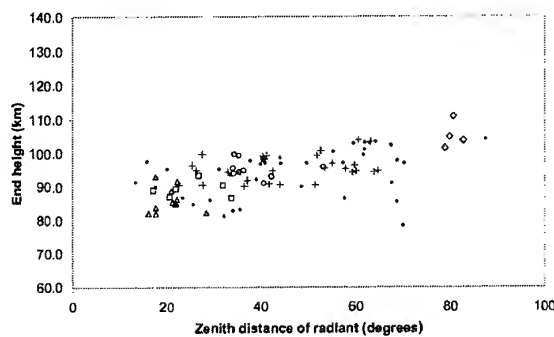


Fig. 7. End height – zenith distance of radiant

### 3.6 Beginning height – photometric mass

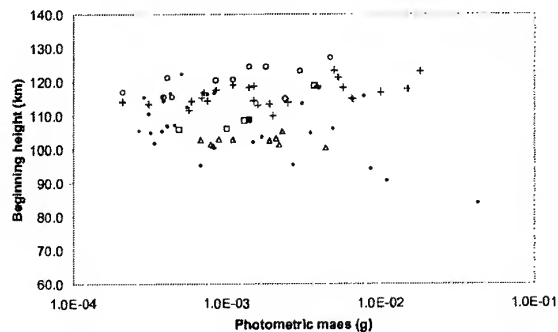


Fig. 8. Beg. height – photometric mass

The Fig. 8 shows that the dependence of beginning height on photometric mass of the particle. The bigger particles start the luminous part of trajectory higher. It is clearly visible for Orionids and Perseids. Analogous to Fig. 2 strictly speaking the fainter meteors (smaller particles) cannot be observed in those distances. Of course, the meteors of fast meteor shower have higher beginning height than the slower ones.

### 3.7 End height – photometric mass

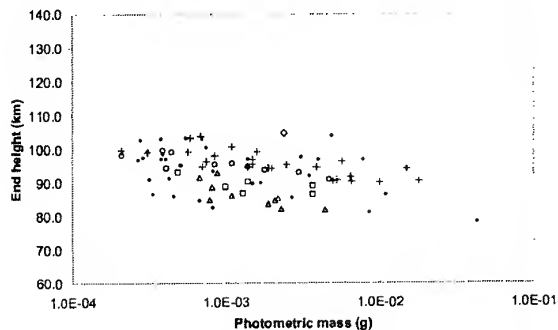


Fig. 9. End height – photometric mass

Our results confirmed expected feature that the bigger particles penetrate deeper into atmosphere. It is evident for individual showers and also for sporadic meteors although the dispersion is greater for them.

Another expected feature visible in Fig. 9 is finding that slow meteors penetrate deeper. Points of Lyrids and Geminids lie significantly lower than Perseids' and Orionids' ones. In case of Geminids it is probably caused also by the compactness of their particles but Fig. 9 cannot confirm it due to lack of comparison with another comparable slow shower.

### 3.8 Abs. brightness – photometric mass

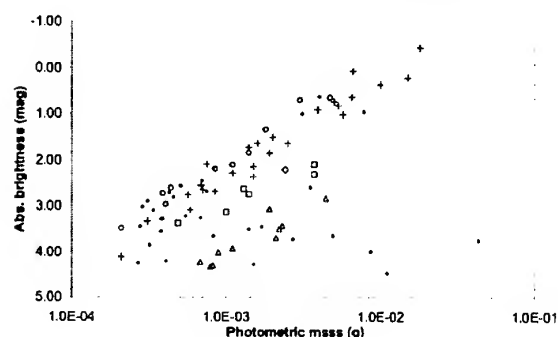


Fig. 10. Abs. brightness – photometric mass

The graph shape is given by the definition. The shower meteors lie in the lines sequenced by the shower velocity. Of course the faster meteors are brighter than the slower ones of the same particle mass.

The detailed photometric study based on our TV meteors including their light curves may be found in [4].

## 4. $K_B$ PARAMETER

For further analysis we use the  $K_B$  parameter defined by Ceplecha [1]:

$$K_B = \log \rho_B + 2.5 \log v_\infty - 0.5 \log \cos z_R \quad (1)$$

where  $\rho_B$  is the air density at the beginning of the luminous trajectory (in  $\text{g cm}^{-3}$ ),  $v_\infty$  is the initial velocity (in  $\text{cm s}^{-1}$ ) and  $z_R$  is zenith distance of radiant.

The  $K_B$  parameter was initially defined for meteors photographed by Super Schmidt cameras. For TV meteors  $K_B$  value should be increased of 0.15.

Using this criterion we may divide meteors into groups by  $K_B$  and the orbital elements:

"asteroidal meteors":  $8.00 \leq K_B$

group A:  $7.30 \leq K_B < 8.00$

group B:  $7.10 \leq K_B < 7.30$ ;  $q \leq 0.30 \text{ AU}$

group C1:  $6.60 \leq K_B < 7.10$ ;  $a < 5 \text{ AU}$ ;  $i \leq 35^\circ$

group C2:  $6.60 \leq K_B < 7.10$ ;  $a \geq 5 \text{ AU}$

group C3:  $6.60 \leq K_B < 7.10$ ;  $a < 5 \text{ AU}$ ;  $i > 35^\circ$

group D:  $K_B < 6.60$

If the meteor does not fit any of these groups, this scheme cannot be used to classify it uniquely.

### 4.1 Beginning height – $K_B$

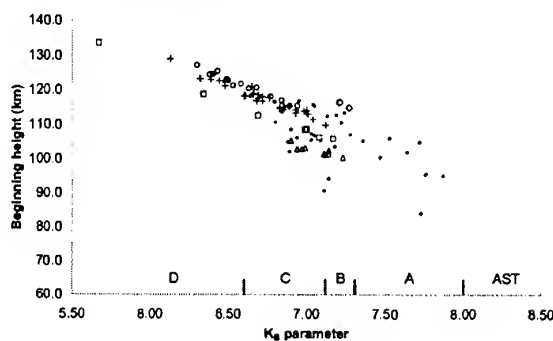


Fig. 11. Beginning height –  $K_B$

The  $K_B$  parameter depends on beginning height (strictly speaking on the air density at the beginning height) so the graph shape is given by the definition of  $K_B$ .

The  $\eta$  Aquarid points are significantly shifted to the right. It is a question if it is a real feature or an effect of inexact correction of radiant zenith distance in  $K_B$  definition (Eq. 1).

### 4.2 End height – $K_B$

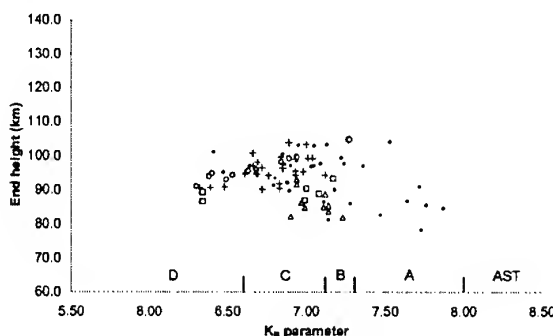


Fig. 12. End height –  $K_B$

The Fig. 12 shows that we find the expected result for sporadic meteors; compact (higher value of  $K_B$  parameter) particles penetrate deeper into the atmosphere than the fragile ones.

In the graph we may distinguish the group of cometary showers (Perseids and Orionids) and the group of Geminids.

#### 4.3 Perihelion distance – $K_B$

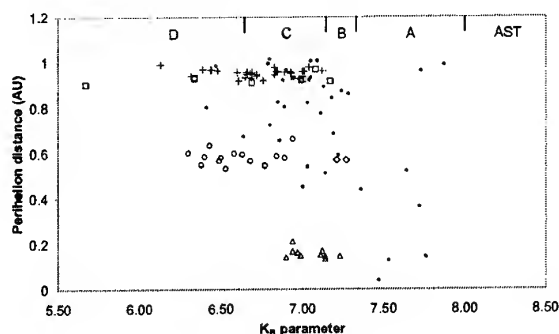


Fig. 12. Perihelion distance –  $K_B$

This graph for sporadic meteors shows that no fragile particles (low  $K_B$  parameter) exist in small perihelion distances.

#### 4.4 Relative percent of meteoroids in individual groups

[1] shows the relative distribution of meteoroids into individual groups through the mass intervals. For comparison with our results we averaged the populations in mass intervals of our meteors. The average was weighted by the real number of our meteors in the intervals.

AST	A	B	C1	C2	C3	D
0.5	23.4	3.3	30.9	14.6	23.0	4.3
weighted average of table in [1]						
0.0	30.0	0.0	0.0	26.7	36.7	6.7
from our set of 30 high quality sporadic meteors						

The distribution of our meteors into classes AST, A, B, C, D is in agreement with [1]. But the population of subclasses C1, C2, C3 disagrees. The reason of this disagreement is unclear so far.

## 5. CONCLUSIONS

- Beginning heights of Orionids and Perseids are higher then beginning heights of sporadic meteors with the same velocity.
- No cometary (fragile) particles with low perihelion distance exist in our set of sporadic meteors.
- The effect of zenith distance of radiant ( $\eta$  Aquarids) appeared also in  $K_B$  graphs, where it would be corrected in definition of  $K_B$ .
- Although the distribution of our meteors to the classes AST, A, B, C, D agree with [1], the population of subclasses C1, C2, C3 disagree.

The graphs in full resolution may be downloaded from <http://www.asu.cas.cz/~stork/talks/kiruna/>

## ACKNOWLEDGMENTS

This work was supported by the Grant Agency of the Czech Republic (GACR), grant No. 205/99/D097 and the scientific key project K3012103.

## REFERENCES

1. Ceplecha Z., Earth's influx of different populations of sporadic meteoroids from photographic and television data, *Bull. Astron. Inst. Czechosl.* 39, 221–236, 1988
2. Borovička J. and Boček J., Television spectra of meteors, *Earth, Moon, and Planets* 71, 237–244, 1995
3. Koteň P., Špurný P., Borovička J. and Štork R., Extreme beginning heights for non-Leonid meteors, *this volume*, 2001
4. Koteň P. and Borovička J., Light curves of faint meteors, *this volume*, 2001
5. Borovička J., The comparison of two methods of determining meteor trajectories from photographs, *Bull. Astron. Inst. Czechosl.* 41, 391–396, 1990
6. Koteň P., Ph.D. thesis, 2001

## Results of Double-station TV Observations in 1998 and 1999

Masayoshi Ueda<sup>(1)</sup>, Yasunori Fujiwara, Masatoshi Sugimoto, Masao Kinoshita, (Nippon Meteor Society)

<sup>(1)</sup> 43-2 Asuka, Habikino-shi, Osaka 583-0842, Japan  
E-mail: m-ueda@mua.biglobe.ne.jp

### Abstract

We have carried out double-station TV observations in 1998 and 1999. Numbers of meteors of which the orbits could be determined were 77 and 186 in 1998 and 1999, respectively. Among them, stream meteors are 263 in total: 22 of Leonids, 13 of Northern Taurids, two of Perseids, one of Arietids (Daytime shower), and one of  $\zeta$  Perseids (Daytime shower). The number of sporadic meteors was 224.

From this database, distributions of radiant points, velocities and magnitudes are investigated for Leonids and Northern Taurids. There was a lack of Leonid meteors with magnitude not brighter than +6.

After November 13, Northern Taurids became active and doubly meteors were recorded, whereas the Southern Taurids were not observed. Doubly TV observation was successful for meteors of daytime shower just before dawn in June 1999.

### 1. Observation

Our TV observations utilizes an image intensifier, a 35mm photographic lens and an 8 mm video camera or digital video camera.

Double-station TV observations

Date	Lenses (Field of view)
Nov. 17, 18, 1998	f85mm (17°)
Jun. 11, 1999	f50mm (25°)
Aug. 13, 1999	f200mm (7°)
Nov. 13, 16, 18, 1999	f85mm (17°)

### 2. Results

Figure 1 shows distribution of 263 radiant points observed in 1998 and 1999. Radiant points of Leonids, Northern Taurids and  $\gamma$  Perseids are clearly found.

#### 22 Leonid meteors

R.A.:  $154.0^\circ \pm 1.1^\circ$  Dec.:  $+21.8^\circ \pm 0.5^\circ$   
geocentric velocity :  $71.1\text{km/s} \pm 3.5\text{km/s}$   
Solar longitude :  $\lambda_\odot = 235.482^\circ$  (J2000.0)

#### 13 Northern Taurid meteors

R.A.:  $62.0^\circ \pm 2.0^\circ$  Dec.:  $+23.2^\circ \pm 0.7^\circ$   
geocentric velocity :  $27.1\text{km/s} \pm 2.1\text{km/s}$   
Solar longitude :  $\lambda_\odot = 234.673^\circ$  (J2000.0)

#### 2 Perseid meteors

R.A.:  $43.8^\circ \pm 0.8^\circ$  Dec.:  $+56.4^\circ \pm 0.4^\circ$   
geocentric velocity :  $61.3\text{km/s} \pm 5.3\text{km/s}$   
Solar longitude :  $\lambda_\odot = 140.516^\circ$  (J2000.0)

#### 1 Arietid meteor (Daytime shower)

R.A.:  $44.9^\circ \pm 1.8^\circ$  Dec.:  $+25.7^\circ \pm 0.6^\circ$   
geocentric velocity :  $42.1\text{km/s} \pm 11.2\text{km/s}$   
Solar longitude :  $\lambda_\odot = 80.411^\circ$  (J2000.0)

#### 1 $\zeta$ Perseid meteor (Daytime shower)

R.A.:  $58.3^\circ \pm 1.7^\circ$  Dec.:  $+24.7^\circ \pm 0.7^\circ$   
geocentric velocity :  $26.2\text{km/s} \pm 8.9\text{km/s}$   
Solar longitude :  $\lambda_\odot = 80.414^\circ$  (J2000.0)

Figure 2 shows the distribution of absolute magnitude of 60 doubly observed sporadic meteors on November 18, 1999, and it is very clear that the number of Leonid meteors fainter than the 6th magnitude are fewer than that of the sporadic meteors.

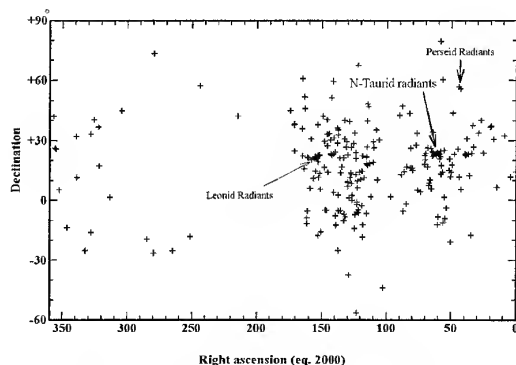


Figure 1 Distribution of 263 radiant points observed in Nov. 17-18, 1998, Jun. 11, Aug. 13, Nov. 13, 16, 18, 1999. The TV Meteor Radiant Mapping

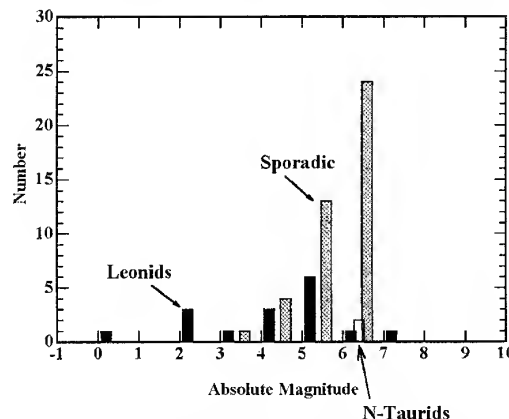


Figure 2 Absolute magnitude distribution of 60 TV meteors (Nov. 18, 1999).

TABLE-1. The radiant positions, velocities and heights of TV meteors.

No.	DATE YYYYMMDD	UT hhmmss	RADIANT(2000.0) $\alpha$	$d\alpha$	$\delta$	$d\delta$	Vobs. Km/s	V error %	Vg Km/s	Vh km/s	Q deg	obs. Mag.	abso. Mag.	Hb Km *	Hm Km	He Km *	dH Km	log (mass)
UF96125	19961117	160110	66.3	0.96	10.2	0.61	33.3	17.7	31.5	39.5	40.8	5.5	5.7	87.1	85.6	79.2	0.4	-3.38
UF96126	19961117	160531	127.5	0.91	26.5	0.15	84.3	18.6	63.1	37.5	20.3	6.3	6.1	109.2	103.9	94.7 *	0.2	-4.27
UF96127	19961117	161351	81.5	0.35	16.2	0.15	44.4	27.2	42.9	40.3	52.7	5.5	5.6	100	92.7	83.4	0.6	-3.45
UF96128	19961117	162211	50.4	1.31	11.8	0.62	21.4	32.5	16.5	36.6	25.2	6.6	6.7	95	90.7	86.6	0.2	-2.96
UF96129	19961117	162319	123.1	4.24	-56.5	3.19	12.9	41.3	6.3	26.9	16	6.7	7	84.7	82	80.5	0.3	-2.05
UF96130	19961117	162339	322	7.66	36.7	5.46	12	29.9	5.1	33.7	20.2	8.8	7.1	82.7	82	80.3	0.2	-2.28
UF96131	19961117	162346	163.2	10.53	51.9	0.36	61.1	13.1	59.9	42	6.8	7	6.7	112.4	108.3	106.5 *	0.6	-4.47
UF96132	19961117	162436	71	0.26	18	0.1	35.6	23.9	34.1	38.7	59.1	5.5	5.3	110.8	102	87.4	0.2	-2.89
UF96133	19961117	162451	48.9	3.34	43.7	0.74	21.7	24	25.5	36.6	25.4	4.6	4.8	100.6	94.8	87.6	0.5	-2.6
UF96134	19961117	164800	27.3	5.71	40.2	1.06	23	36	20.4	40.2	21.4	6	8	96.5	94.2	93.2 *	0.2	-3.77
UF96135	19961117	164901	58.8	32.72	79.5	4.41	17.3	28.2	13.2	30.1	12	5.6	5.9	65.7	85.7	82.1	0.3	-2.58
UF96136	19961117	165535	115.6	0.4	21.8	0.25	55.9	18.2	54.6	33.2	59.4	5.9	5.8	101.2	99.8	88.6	0.2	-4.07
UF96137	19961117	170537	133.2	1.51	-10.3	1.23	59.2	21.2	57.9	34.1	21.5	8.6	6.3	113.1 *	108.2	105.3	0.4	-4.36
UF96138	19961117	174632	61.6	1.47	22.6	0.21	28.3	14.7	26.2	37.1	25.4	4.9	4.8	105.6	96	95 *	0.2	-2.6
UF96139	19961117	181155	152.7	0.34	22.3	0.06	72.6	23.3	71.5	42.2	31.6	2.7	2.4	118.7	111.1	102.5	0.2	-3.07
UF96140	19961118	151223	155.8	1.17	20.5	0.46	73.9	13.7	72.7	43.3	11.4	5.5	5.0	132.7 *	128.5	128.4 *	0.3	-4.00
UF96141	19961118	151423	51.4	0.62	20.8	0.19	24.8	18.5	22.2	38.2	48.2	4.1	4.1	100.4	97.0	89.7	0.2	-2.20
UF96142	19961118	151428	56.8	1.13	14.1	0.36	23.7	38.2	20.9	36.4	56.7	7.1	7.4	91.0	87.6	86.1	0.1	-3.38
UF96143	19961118	151632	59.3	0.81	23.3	0.29	27.2	25.2	24.8	37.2	51.2	6.2	6.2	96.7	93.6	89.9	0.2	-3.07
UF96144	19961118	151850	124.7	0.93	-13.9	0.66	58.2	20.9	58.8	36.9	18.1	8.8	6.4	115.8 *	112.7	110.3	0.3	-4.08
UF96145	19961118	152256	102.4	1.49	-43.9	2.01	36.6	17.0	34.7	37.7	11.9	6.5	6.3	107.9	107.3	106.7 *	0.3	-3.35
UF96146	19961118	152831	54.1	3.31	-3.8	3.16	18.4	49.5	14.8	34.8	18.8	6.4	6.5	89.8	87.8	84.2	0.3	-2.79
UF96147	19961118	153044	81.5	0.17	26.0	0.23	28.0	23.4	25.6	29.9	65.6	2.8	2.9	104.2	91.6	84.9	0.2	-1.72
UF96148	19961118	153736	60.7	0.55	24.0	0.16	25.8	24.7	24.4	36.5	66.2	3.0	3.0	101.0 *	93.1	86.7	0.3	-1.87
UF96149	19961118	154349	58.0	0.58	12.9	0.15	24.3	22.6	21.7	36.6	41.8	3.3	3.3	98.5	89.3	85.3	0.2	-1.82
UF96150	19961118	154350	107.0	0.78	10.2	1.07	49.8	27.4	48.3	32.4	38.3	6.2	5.9	114.2	110.1	105.5	0.2	-3.94
UF96151	19961118	154536	60.0	1.89	-8.2	2.37	26.5	33.5	24.1	38.9	10.7	6.5	6.5	101.4	93.8	91.6	0.3	-2.99
UF96152	19961118	155106	62.0	1.63	23.3	0.55	28.7	33.6	26.6	37.4	49.0	6.2	6.1	97.4	96.2	93.7	0.2	-3.43
UF96153	19961118	155124	76.0	0.98	33.6	0.44	46.7	84.6	45.3	44.5	83.4	6.3	6.3	100.7	99.2	90.9	0.3	-3.85
UF96154	19961118	155211	142.5	3.70	51.4	0.58	81.0	27.6	59.8	41.1	8.8	7.1	6.9	111.6	102.6	94.1	0.6	-4.26
UF96155	19961118	155921	33.9	2.71	37.6	0.45	18.6	26.5	15.1	36.2	27.7	8.1	8.2	88.1	86.6	82.7	0.1	-2.58
UF96156	19961118	160110	63.8	1.58	22.7	0.56	28.6	31.1	26.4	36.8	52.0	6.3	6.3	97.4	96.6	93.8	0.2	-3.46
UF96157	19961118	160125	153.0	2.41	19.3	1.09	60.9	10.4	59.6	30.0	15.7	6.9	6.5	117.8	116.3	115.1 *	0.3	-4.49
UF96158	19961118	160300	160.2	2.55	21.2	0.40	66.0	10.7	64.7	35.2	13.0	5.5	5.2	105.9 *	105.3	104.5 *	0.3	-4.06
UF96159	19961118	160300	58.2	1.05	13.3	0.37	26.2	30.0	23.9	37.7	25.7	2.0	2.1	102.1	89.8	89.8 *	0.3	-1.58
UF96160	19961118	160704	141.1	1.54	4.0	0.84	68.8	31.5	67.6	36.6	18.6	6.3	6.0	116.1	114.9	112.0	0.3	-4.46
UF96161	19961118	160925	49.6	1.79	17.8	0.43	23.1	38.9	20.4	37.8	34.8	4.7	4.7	97.2	95.2	91.8	0.2	-2.51
UF96162	19961118	161442	67.1	1.03	8.7	0.64	23.5	34.4	20.7	33.6	31.6	5.5	5.4	99.0	94.3	90.3	0.3	-2.58
UF96163	19961118	161548	145.2	1.17	14.0	0.43	70.4	21.6	69.2	39.2	18.9	6.2	5.8	116.5	112.9	111.1	0.2	-4.39
UF96164	19961118	161704	158.4	3.40	30.7	0.88	67.2	16.1	65.9	39.0	14.5	6.5	6.1	113.5 *	113.5	110.9	0.2	-4.58
UF96165	19961118	162513	355.9	4.96	26.2	2.28	16.3	17.3	12.4	39.7	19.1	5.6	5.6	94.8	91.1	90.8 *	0.3	-2.18
UF96166	19961118	162705	61.7	1.01	23.0	0.15	29.4	26.6	27.3	38.0	31.8	3.8	3.7	102.0	94.8	87.2	0.2	-2.26
UF96167	19961118	163206	127.9	2.25	13.9	0.94	50.0	25.0	48.5	22.9	24.8	5.4	5.0	114.8	113.5	112.1 *	0.2	-4.01
UF96168	19961118	163357	154.8	1.20	21.8	0.12	73.8	8.6	72.6	43.4	12.5	2.8	2.1	140.4 *	125.0	123.5 *	0.4	-2.98
UF96169	19961118	163623	39.6	1.76	23.3	0.49	16.4	31.8	12.3	34.9	33.0	3.7	4.0	84.6	84.1	79.3	0.1	-1.82
UF96170	19961118	165132	130.1	0.95	9.0	0.50	69.4	16.5	88.2	40.9	24.8	4.9	4.5	125.3	114.3	114.3 *	0.2	-4.04
UF96171	19961118	171120	130.6	1.07	29.3	0.24	63.0	18.0	61.8	36.4	29.5	6.3	5.9	110.7	110.7	103.2	0.2	-4.32
UF96172	19961118	171551	147.9	1.30	29.6	0.22	63.8	13.3	82.5	34.8	22.6	8.3	6.0	115.4 *	111.1	106.6	0.2	-4.27
UF96173	19961118	171608	39.0	1.34	22.6	0.39	20.4	21.0	17.4	38.1	24.5	5.3	5.4	94.9	91.3	88.0	0.1	-2.28
UF96174	19961118	171716	50.5	5.63	-20.8	4.18	19.4	20.3	18.2	37.1	11.8	6.2	6.4	89.7	89.8	85.9	0.3	-2.56
UF96175	19961118	171712	96.8	0.87	1.7	1.07	50.2	38.8	49.0	39.0	16.6	5.5	5.3	107.0	104.0	90.9	1.0	-3.54
UF96176	19961118	173242	84.8	1.46	-1.5	1.81	29.5	29.5	38.0	27.3	15.8	8.8	8.7	106.7	100.3	97.3	0.2	-3.83
UF96177	19961118	173751	82.3	1.32	43.5	0.27	44.0	26.5	42.6	40.3	33.4	6.5	6.4	108.8	101.5	95.3	0.2	-3.87
UF96178	19961118	173821	38.2	1.87	23.2	0.56	15.5	24.1	11.2	34.5	22.5	6.1	8.3	92.2	88.5	81.0 *	0.2	-2.08
UF96179	19961118	174015	161.2	0.78	-11.7	0.72	67.4	14.0	66.2	41.7	18.6	6.5	6.2	113.3	110.6	107.9	0.2	-4.31
UF96180	19961118	174245	160.9	1.36	-5.4	0.52	88.6	7.1	67.3	40.8	18.7	3.9	3.5	113.3 *	109.0	107.6 *	0.2	-3.41
UF96181	19961118	174353	114.9	0.39	48.2	1.34	19.5	45.1	15.9	22.1	24.1	5.8	6.0	93.9	89.1	85.1	0.4	-2.47
UF96182	19961118	174638	118.2	0.37	-12.3	1.67	56.0	9.5	54.8	36.9	18.0	7.0	7.0	110.5	98.9	96.9	0.4	-4.23
UF96183	19961118	175144	64.9	2.56	24.3	0.78	29.6	14.6	27.7	37.1	27.6	6.8	6.8	95.8	95.1	92.6	0.2	-3.69
UF96184	19961118	175557	70.0	1.69	20.4	0.56	39.4	21.6	38.0	42.2	22.4	7.3	7.1	107.7	104.0	102.2	0.2	-4.05
UF96185	19961118	180021	19.9	2.28	36.9	0.82	19.6	13.1	16.4	39.2	20.4	5.1	5.2	93.2 *	91.7	89.0	0.1	-2.21
UF96186	19961118	180352	62.1	1.21	23.6	0.28	26.9	17.8	24.8	36.3	28.9	6.3	6.5	89.5	86.7	82.7	0.1	-3.15
UF96187	19961118	180554	135.4	1.33	-5.3	1.66	57.1	12.0	55.8	30.2	22.6	5.2	4.9	118.8	110.2	110.2 *	0.3	-3.97
UF96188	19961118	181341	45.0	3.67	1.5	1.67	18.2	17.0	14.7	34.4	20.9	7.0	7.2	88.5	86.1	85.6	0.2	-2.94
UF96189	19961118	181557	119.0	0.30	-23.8	1.21	65.6	14.1	68.8	42.9	19.1	4.3	4.1	119.4	109.4	105.8 *	0.4	-3.65
UF96190	19961118	181612	132.2	0.77	40.1	0.46	55.6	10.5	54.4	32.6	31.0	2.9	2.7	117.1	105.1	99.6	0.2	-3.15
UF96191	19961118	181941	159.2	0.98	6.0	0.56</												

	No.	DATE YYYYMMDD	UT hhmmss	RADIANT(2000.0)				Vobs. Km/s	V error %	Vg Km/s	Vh km/s	Q deg	obs. Mag	absc. Mag	Hb Km *	Hm Km	He Km *	dH Km	log (mass)
				$\alpha$	$d\alpha$	$\delta$	$d\delta$												
UF99031	19991113	144206	50.1	1.35	14.0	0.99	24.1	32.5	21.3	36.9	18.1	4.8	4.9	96.4	90.7	62.3	1.3	-2.35	
UF99032	19991113	150703	146.1	0.74	40.6	0.09	66.2	4.7	65.0	40.3	17.4	5.4	5.0	118.1 *	112.2	107.0 *	0.1	-3.76	
UF99033	19991113	150936	55.5	1.51	25.0	0.40	22.4	36.5	19.4	33.6	23.4	4.2	4.1	106.1	97.5	90.7	0.5	-2.03	
UF99034	19991113	152328	65.9	0.80	26.0	0.56	19.4	24.6	15.9	29.7	71.3	4.5	4.1	94.0	89.5	83.2	0.2	-1.77	
UF99035	19991113	152938	121.8	0.80	-4.8	0.52	66.1	12.8	64.8	41.2	13.4	4.3	3.6	119.3	114.6	107.1	0.5	-3.20	
UF99036	19991113	153301	122.7	0.52	-5.9	0.34	64.8	9.8	63.5	40.0	14.8	5.9	5.4	120.3	115.5	108.6 *	0.3	-3.90	
UF99037	19991113	154442	8.4	5.51	32.6	0.78	20.4	26.5	17.3	40.8	13.9	6.0	5.9	97.7	93.0	89.3	0.3	-2.57	
UF99038	19991113	154442	165.2	1.05	35.9	0.10	64.2	16.2	62.9	39.3	16.0	7.3	7.1	107.2 *	103.7	101.4 *	0.1	-4.40	
UF99039	19991113	154846	113.1	2.77	18.6	0.71	62.6	13.3	61.3	36.2	17.5	4.4	4.0	101.5	98.2	92.6	1.1	-3.64	
UF99040	19991113	155123	126.6	1.82	2.5	0.49	73.1	26.6	71.1	45.0	6.3	7.2	6.7	116.8	111.3	104.7 *	0.7	-4.44	
UF99041	19991113	155141	132.5	1.10	30.8	0.22	65.5	19.8	64.3	37.3	21.4	7.1	6.9	101.6	99.5	93.0	0.1	-4.58	
UF99042	19991113	155559	136.7	1.98	-5.5	1.07	62.3	28.1	60.9	34.6	9.6	5.6	4.8	117.1	116.4	112.3	0.8	-3.59	
UF99043	19991113	162549	70.3	0.90	22.5	0.52	27.8	34.0	25.5	32.0	33.9	5.1	5.1	105.4	89.5	85.1 *	0.3	-2.40	
UF99044	19991113	163314	32.9	1.85	26.9	0.17	20.7	18.8	17.7	37.8	13.9	5.0	5.2	94.3 *	85.7	82.5	0.3	-2.13	
UF99045	19991113	163521	107.9	0.74	35.2	1.32	61.4	22.2	60.2	41.2	60.9	5.8	5.0	110.5	107.0	104.9	0.2	-4.01	
UF99046	19991113	163528	44.0	4.54	11.7	0.53	27.6	49.9	25.5	41.6	4.6	4.7	4.6	103.5	98.1	92.4	0.9	-2.33	
UF99047	19991113	164627	163.8	1.98	15.8	0.45	70.1	17.6	68.8	41.6	5.3	4.5	3.9	114.1 *	109.3	103.2 *	0.9	-3.21	
UF99048	19991113	165207	105.7	0.51	30.3	0.46	60.2	16.1	59.0	40.1	71.2	6.4	6.1	109.9	109.9	102.0	0.2	-4.49	
UF99049	19991113	165417	137.1	0.86	-5.2	0.79	68.2	12.8	66.9	40.2	18.3	5.2	4.5	122.8	117.6	111.4 *	0.5	-3.57	
UF99050	19991113	165439	51.7	5.84	15.1	0.35	28.3	32.1	26.2	39.4	5.8	3.5	3.2	110.1	104.0	94.7 *	1.0	-1.72	
UF99051	19991113	165855	164.8	1.45	60.8	0.24	55.6	8.9	54.3	41.3	26.1	4.7	4.5	112.3	106.1	101.0	0.1	-3.44	
UF99052	19991113	170647	122.9	4.08	-2.0	4.73	71.3	14.2	70.2	45.3	49.8	4.5	4.0	105.0	99.3	99.3 *	0.2	-3.87	
UF99053	19991113	170853	25.5	3.84	23.9	0.32	19.3	25.1	16.1	38.4	13.4	6.4	6.4	94.7 *	92.4	86.7	0.4	-2.43	
UF99054	19991113	171324	69.6	2.57	23.5	0.23	40.0	31.4	38.5	40.1	11.5	6.1	5.9	109.8	101.3	94.8	0.5	-3.43	
UF99055	19991113	171501	110.3	0.59	19.0	0.66	66.7	18.2	65.6	43.4	82.3	5.9	5.7	102.0	96.0	92.0 *	0.3	-4.30	
UF99056	19991113	171942	153.1	0.42	-17.6	0.30	65.0	10.8	63.7	41.9	19.5	5.0	4.2	103.1 *	103.1	96.8	0.2	-3.29	
UF99057	19991113	172144	147.9	1.21	16.6	0.09	66.6	36.2	65.4	35.5	9.9	5.6	5.5	104.8 *	98.0	92.9	0.3	-3.95	
UF99058	19991113	172159	138.0	1.22	28.9	0.77	67.8	22.1	86.6	38.5	28.9	6.5	6.1	112.4	108.9	105.8 *	0.2	-4.50	
UF99059	19991113	172647	137.1	0.94	2.8	0.90	59.5	24.0	58.1	29.7	31.0	6.4	6.1	111.5	106.0	107.2	0.2	-4.35	
UF99060	19991113	172930	152.9	1.39	22.7	0.11	69.3	24.7	68.1	39.1	11.5	6.2	4.6	110.5	106.5	99.1	0.5	-3.67	
UF99061	19991113	173507	135.5	0.43	-5.3	0.45	81.7	23.5	60.4	34.2	35.6	5.8	5.4	114.6	113.0	105.2	0.2	-3.94	
UF99062	19991113	173556	109.9	0.39	26.4	0.46	58.7	18.9	57.8	36.7	80.2	5.7	5.4	113.4	109.2	102.2	0.2	-4.04	
UF99063	19991113	173703	73.8	1.96	4.2	0.92	35.4	24.4	33.8	36.6	12.2	5.9	5.7	105.2	103.6	96.1	0.4	-3.37	
UF99064	19991113	173952	115.5	0.33	21.5	0.43	64.0	23.9	62.9	39.0	87.2	8.4	8.0	108.3	104.3	98.3	0.2	-4.40	
UF99065	19991113	174039	133.2	0.28	21.4	0.22	63.3	31.0	62.0	33.3	67.1	5.7	5.6	105.1	97.8	93.9	0.1	-4.15	
UF99066	19991113	174239	142.7	1.26	22.7	0.23	58.8	33.2	57.5	28.0	19.7	6.4	6.3	108.0	100.4	100.4 *	0.1	-4.35	
UF99067	19991113	174528	118.4	0.58	22.3	0.45	87.2	17.6	86.4	60.6	72.2	5.8	5.0	112.7	107.4	104.7	0.2	-4.43	
UF99068	19991113	175122	130.1	0.24	22.9	0.35	64.0	16.9	62.8	34.8	74.7	4.9	4.5	112.5	108.6	101.8	0.1	-3.90	
UF99069	19991113	175156	128.8	0.10	39.5	0.17	66.5	8.9	65.4	41.5	36.6	3.5	3.5	119.8	109.4	98.3	0.1	-3.47	
UF99070	19991113	175337	128.9	0.19	1.4	0.28	69.8	11.1	68.7	41.6	52.9	3.9	3.3	118.3	108.2	94.9	0.5	-3.12	
UF99071	19991113	175403	42.3	1.55	22.6	0.58	72.9	28.9	71.8	42.3	23.4	5.7	5.0	117.3	112.9	108.0	0.3	-4.09	
UF99072	19991113	175443	60.1	4.86	23.1	0.30	32.2	17.9	30.4	38.4	9.6	5.6	5.4	104.4	100.3	93.3	0.6	-2.93	
UF99073	19991113	175544	146.5	0.37	-4.9	0.30	72.0	18.2	70.8	43.6	28.6	6.4	6.2	111.7	102.0	99.2	0.2	-4.25	
UF99074	19991113	175741	160.9	4.46	21.5	0.38	51.0	19.1	49.4	22.6	11.3	5.6	4.9	111.3	109.5	106.3	0.3	-3.58	
UF99075	19991113	180142	125.3	0.19	28.6	0.32	66.3	12.4	65.2	39.1	70.4	5.1	4.7	124.1	108.9	101.9	0.2	-3.87	
UF99076	19991113	181029	138.5	0.76	-7.8	1.29	63.9	15.3	62.7	36.8	38.6	5.1	4.6	105.7	105.7	99.7	0.4	-3.87	
UF99077	19991113	181531	114.7	0.42	17.5	0.49	66.2	18.8	65.2	41.3	67.8	6.3	5.9	116.1	108.3	101.6	0.4	-4.28	
UF99078	19991113	182413	153.5	0.77	38.0	0.57	67.5	8.7	66.3	41.1	30.8	6.4	5.9	117.7	113.5	102.9	0.2	-4.25	
UF99079	19991113	182605	130.2	0.58	9.2	0.19	68.2	28.5	65.1	38.7	46.0	6.5	6.4	108.1	101.0	92.4	0.3	-4.38	
UF99080	19991113	182816	139.0	0.24	-12.7	0.52	63.5	13.8	62.3	38.2	50.1	5.5	5.1	113.9 *	109.0	104.4	0.2	-3.96	
UF99081	19991113	182914	147.1	0.76	-5.0	0.61	72.2	19.9	71.1	43.9	27.6	6.3	5.8	121.4	114.4	114.4 *	0.2	-4.47	
UF99082	19991113	183015	115.4	4.70	18.2	0.94	67.1	38.9	66.1	41.9	43.9	5.6	4.9	112.9	108.0	106.2	0.4	-4.00	
UF99083	19991113	183246	122.5	0.27	9.7	0.19	66.3	11.9	69.5	38.9	89.9	5.6	5.1	104.4	94.3	94.3 *	0.1	-3.97	
UF99084	19991113	183425	143.1	0.64	23.4	0.49	70.7	7.7	69.5	40.2	42.9	5.8	5.4	123.4	110.1	110.1 *	0.2	-4.26	
UF99085	19991113	191227	131.2	0.41	26.6	0.33	60.5	11.3	59.4	31.9	78.8	5.5	5.1	117.0	115.3	105.4	0.3	-3.97	
UF99086	19991113	191245	37.2	3.20	33.1	1.36	18.8	9.1	15.6	36.1	11.7	5.6	5.3	96.8	94.1	90.9 *	0.2	-1.93	
UF99087	19991113																		

No.	DATE YYYYMMDD	UT hhmmss	RADIANT(2000.0)				Vobs. Km/s	V error %	Vg Km/s	Vh km/s	Q deg	obs. Mag.	atso. Mag.	Hb Km *	Hm Km	He Km *	dH Km	log (mass)
			$\alpha$	$d\alpha$	$\delta$	$d\delta$												
UF99142	19991118	161756	118.2	0.59	-18.5	0.80	55.8	11.7	54.4	38.5	18.5	6.4	6.2	107.3	104.3	99.4 *	0.2	-4.10
UF99143	19991116	162251	67.2	0.34	7.6	0.23	26.4	22.8	24.1	35.2	52.6	3.9	3.9	91.6 *	90.1	80.8	0.2	-2.19
UF99144	19991118	163331	29.0	1.04	33.7	0.15	20.3	17.6	17.3	38.7	22.5	4.0	4.0	100.7	87.0	86.4 *	0.1	-1.80
UF99145	19991118	163528	174.4	3.63	44.8	0.33	61.7	22.4	60.4	41.5	7.4	6.8	6.4	112.6	109.5	105.6 *	0.4	-4.27
UF99146	19991118	164147	155.3	1.81	22.1	0.49	63.4	10.9	62.1	33.1	19.3	5.7	5.5	103.7 *	103.7	98.9	0.1	-4.29
UF99147	19991118	164342	131.8	0.71	-8.2	0.59	62.3	15.4	61.1	36.8	22.1	6.7	6.6	105.8	102.7	98.2	0.2	-4.34
UF99148	19991118	164858	90.0	0.73	42.5	0.97	56.3	37.6	55.1	47.1	38.6	6.5	6.4	103.5	100.9	96.1	0.2	-4.30
UF99149	19991118	164935	155.4	1.09	21.6	0.10	72.3	21.2	71.1	41.9	13.6	5.8	5.2	129.4 *	120.0	111.7 *	0.2	-3.90
UF99150	19991118	165522	151.7	1.59	22.5	0.21	78.8	16.1	77.7	48.4	13.9	5.1	4.5	126.6	117.7	117.7 *	0.2	-4.15
UF99151	19991118	165816	116.7	0.62	-6.4	1.21	63.4	11.0	62.2	42.7	21.2	6.1	5.8	111.8	110.8	103.5 *	0.3	-4.27
UF99152	19991118	165956	68.3	0.81	16.9	0.18	31.6	12.6	29.7	37.4	33.5	4.6	4.6	103.0	91.2	86.7 *	0.2	-2.55
UF99153	19991118	170316	154.0	0.58	21.7	0.22	74.5	6.8	73.3	44.0	17.8	5.3	5.1	125.7 *	112.0	108.1 *	0.2	-3.95
UF99154	19991118	170343	123.5	0.83	24.0	0.15	69.2	16.8	68.1	43.2	28.3	6.7	6.4	107.7	102.3	96.8	0.2	-4.45
UF99155	19991118	170448	121.8	0.58	-6.1	0.76	58.8	17.5	57.6	36.1	25.7	6.9	6.7	115.8	109.0	104.1	0.3	-4.22
UF99156	19991118	170533	154.0	0.48	21.6	0.11	73.4	6.5	72.2	42.9	18.9	2.5	2.2	116.3 *	108.3	97.2	0.1	-2.75
UF99157	19991116	170701	54.9	2.44	-9.1	1.77	26.1	20.8	23.8	40.2	15.1	5.9	5.9	100.9	97.2	97.0	0.2	-3.17
UF99158	19991118	171238	128.2	0.86	11.4	0.37	76.6	16.2	75.6	48.4	26.1	6.3	6.0	118.1	111.9	108.1 *	0.2	-4.58
UF99159	19991116	171552	152.0	1.60	22.4	0.27	78.2	24.3	77.1	47.7	15.5	5.8	5.5	125.1	116.0	116.0 *	0.2	-4.51
UF99160	19991118	172718	84.6	0.44	16.9	0.17	43.7	16.0	42.3	38.8	55.3	5.8	5.8	97.0	95.5	84.5	0.2	-3.75
UF99161	19991118	173019	135.3	0.69	13.9	0.33	61.1	8.8	66.0	37.3	34.4	5.8	5.7	103.2	99.5	91.8	0.2	-4.23
UF99162	19991118	173416	141.5	6.20	59.6	2.82	63.1	37.9	62.0	47.1	2.6	6.5	6.5	111.2	98.3	87.3	2.0	-4.08
UF99163	19991118	174828	64.8	0.75	22.1	0.22	28.8	16.8	26.8	36.6	27.9	6.2	6.2	102.6	92.3	89.9	0.2	-3.03
UF99164	19991118	174733	151.8	1.08	22.9	0.43	74.0	21.9	72.9	43.6	21.6	5.1	4.9	119.3	112.2	109.1 *	0.3	-4.16
UF99165	19991118	175224	139.7	0.56	24.3	0.28	72.2	24.7	71.1	42.6	32.3	6.0	5.8	117.7	107.4	104.2 *	0.2	-4.48
UF99166	19991118	180040	154.7	0.70	21.3	0.18	71.0	15.4	69.8	40.5	23.9	6.4	6.1	114.3	109.2	103.8	0.2	-4.49
UF99167	19991118	180048	153.9	0.73	21.3	0.14	70.8	5.6	69.7	40.3	23.3	3.3	2.9	115.5	108.5	96.1	0.2	-3.20
UF99168	19991118	180235	132.7	0.81	-6.9	1.86	58.8	23.6	57.5	32.9	20.2	6.3	6.1	113.9	108.5	108.5 *	0.2	-4.43
UF99169	19991118	180652	119.1	0.19	14.5	0.13	62.8	21.7	61.7	38.2	67.8	6.6	6.4	117.7	108.3	100.9	0.2	-4.26
UF99170	19991118	181038	154.2	0.40	21.4	0.17	72.3	14.4	71.2	41.9	22.6	1.0	0.7	139.3	112.1	112.1 *	0.3	-2.81
UF99171	19991118	181115	153.1	0.41	21.6	0.16	70.7	13.2	69.5	40.3	26.8	7.2	7.1	117.0	105.0	101.8	0.2	-4.55
UF99172	19991118	181307	123.7	0.20	12.8	0.42	67.2	22.8	66.2	40.7	48.8	5.5	5.1	118.6	112.2	102.7	0.5	-4.15
UF99173	19991118	182520	136.2	0.48	21.2	0.20	71.6	25.9	70.6	42.2	44.4	6.7	6.3	108.8	106.8	98.3	0.2	-4.62
UF99174	19991118	182732	127.4	0.21	13.1	0.16	62.6	20.4	61.5	35.1	70.9	5.0	4.8	106.2	98.6	89.9	0.2	-3.94
UF99175	19991118	182905	115.2	0.33	26.8	0.20	21.6	28.7	18.5	18.2	81.5	5.3	5.3	88.1	87.5	79.5 *	0.1	-2.76
UF99176	19991118	183912	126.7	0.68	0.0	2.29	64.0	24.7	62.9	37.9	19.5	5.9	5.6	119.0	109.0	103.3	0.4	-4.15
UF99177	19991118	183953	154.2	0.47	21.2	0.14	72.1	6.1	71.0	41.7	38.8	6.3	6.1	118.5	112.6	92.3	0.2	-2.84
UF99178	19991118	184957	56.2	2.05	-11.2	1.23	16.1	25.5	12.0	33.4	18.1	6.3	6.5	87.0	86.2	82.6	0.2	-2.34
UF99179	19991118	185121	122.2	0.15	6.3	0.28	59.3	26.6	58.2	34.2	71.2	6.4	6.4	103.3	91.1	90.1	0.2	-3.49
UF99180	19991118	185617	88.7	0.71	12.7	0.34	38.8	21.5	37.3	33.6	25.7	5.8	5.7	105.4	100.9	92.0	0.2	-4.61
UF99181	19991118	185710	152.6	1.00	11.5	0.57	63.1	18.7	61.9	31.9	30.3	6.9	6.7	113.2	113.2	106.6	0.2	-3.60
UF99182	19991118	185747	124.3	0.55	-7.2	3.21	40.8	38.2	39.2	20.7	22.7	4.9	4.7	102.4 *	102.4	99.4	0.4	-3.60
UF99183	19991118	185827	154.1	0.15	21.4	0.05	72.7	13.9	71.6	42.3	31.4	3.9	3.8	139.7	113.1	95.3	0.2	-3.25
UF99184	19991118	190929	138.7	0.26	-12.1	0.68	64.6	13.9	63.5	39.0	18.3	5.6	5.4	119.4	107.7	101.1	0.3	-3.89
UF99185	19991118	191558	153.5	0.48	21.8	0.14	72.0	17.8	71.0	41.6	31.8	6.3	5.9	117.4	110.7	100.8	0.2	-4.30
UF99186	19991118	191623	140.9	0.83	31.3	0.32	89.1	21.1	88.1	41.2	39.7	6.3	6.0	112.3	107.5	102.5	0.2	-4.60

TABLE-2. The orbital elements of TV meteors.

(eq.J2000.0)

No.	DATE	UT	a	e	q	$\Omega$	i	$\omega$	P	Observers	Solar deg.	Shower
	YYMMDD	hhmmss	AU		AU	deg	deg	deg	yr			
UF98125	19981117	160110	3.787	0.9048	0.3605	55.121	14.348	109.731	7.369	U-F	235.121	
UF98126	19981117	160531	2.268	0.7669	0.5287	235.124	163.983	274.13	3.415	U-F	235.124	
UF98127	19981117	161351	5.155	0.984	0.0825	55.13	25.503	147.99	11.705	U-F	235.13	
UF98128	19981117	162211	1.951	0.6633	0.6569	55.134	3.809	80.885	2.725	U-F	235.138	
UF98129	19981117	162319	0.923	0.0723	0.8559	55.136	12.032	186.567	0.886	U-F	235.137	
UF98130	19981117	162339	1.342	0.2659	0.9851	235.138	6.525	190.603	1.555	U-F	235.137	
UF98131	19981117	162346	28.559	0.963	0.9815	235.137	111.29	189.857	136.875	U-F	235.137	
UF98132	19981117	162438	3.023	0.9206	0.2399	55.137	7.193	125.446	5.256	U-F	235.138	
UF98133	19981117	162451	2.926	0.8034	0.5752	235.138	20.235	266.485	5.005	U-F	235.138	
UF98134	19981117	164800	4.911	0.8426	0.7729	235.154	14.867	238.484	10.883	U-F	235.154	
UF98135	19981117	164901	0.999	0.2283	0.7706	235.155	22.282	280.748	0.998	U-F	235.155	
UF98136	19981117	165535	1.285	0.8766	0.1586	235.154	178.503	322.887	1.456	U-F	235.159	
UF98137	19981117	170537	1.407	0.3413	0.927	55.166	129.24	40.978	1.87	U-F	235.166	
UF98138	19981117	174632	2.104	0.8009	0.419	235.199	1.689	287.2	3.052	U-F	235.195	N-Taurids
UF98139	19981117	181155	62.119	0.9841	0.9875	235.212	162.26	176.034	489.592	U-F	235.213	Leonids
UF98140	19981118	151223	-10.555	1.0926	0.9779	236.095	183.508	168.371		U-F	236.096	Leonids
UF98141	19981118	151423	2.635	0.7761	0.5888	236.102	1.468	265.577	4.277	U-F	236.097	
UF98142	19981118	151428	1.883	0.6979	0.5689	56.095	4.072	91.875	2.565	U-F	236.097	
UF98143	19981118	151632	2.174	0.7837	0.4702	236.102	2.521	281.153	3.205	U-F	236.099	
UF98144	19981118	151850	2.039	0.595	0.8257	56.1	117.748	56.055	2.911	U-F	236.100	
UF98145	19981118	152256	2.359	0.6063	0.9288	56.103	59.787	32.843	3.623	U-F	236.103	
UF98146	19981118	152831	1.526	0.514	0.7417	56.106	10.19	74.663	1.885	U-F	236.107	
UF98147	19981118	153044	0.987	0.7753	0.2208	236.111	3.685	320.989	0.981	U-F	236.109	
UF98148	19981118	153738	1.919	0.7615	0.4578	236.116	2.896	283.998	2.659	U-F	236.113	N-Taurids
UF98149	19981118	154349	1.946	0.7163	0.5519	56.1	5.262	93.336	2.714	U-F	236.118	
UF98150	19981118	154350	1.19	0.9293	0.0841	56.116	122.808	154.08	1.298	U-F	236.118	
UF98151	19981118	154536	3.142	0.7963	0.6402	56.119	20.638	78.166	5.57	U-F	236.119	
UF98152	19981118	155106	2.244	0.8126	0.2407	236.126	2.348	286.337	3.362	U-F	236.123	N-Taurids
UF98153	19981118	155124	-4.756	1.0285	0.1358	236.123	32.097	314.534		U-F	236.123	
UF98154	19981118	155211	8.103	0.899	0.8182	236.124	115.903	230.491	23.065	U-F	236.124	
UF98155	19981118	155221	1.844	0.5758	0.7809	236.129	9.988	244.831	2.498	U-F	236.129	
UF98156	19981118	160110	2.013	0.8	0.4025	236.135	1.49	289.495	2.886	U-F	236.130	N-Taurids
UF98157	19981118	160525	0.989	0.8529	0.8366	236.13	164.755	87.52	0.984	U-F	236.130	
UF98158	19981118	160300	1.817	0.4961	0.9157	236.131	157.18	141.082	2.45	U-F	236.131	
UF98159	19981118	160300	2.392	0.7808	0.5243	56.13	5.541	94.066	3.7	U-F	236.131	
UF98160	19981118	160704	2.675	0.6631	0.9685	56.134	160.892	18.305	4.875	U-F	236.134	
UF98161	19981118	160925	2.431	0.7383	0.8337	56.114	0.343	81.051	3.789	U-F	236.136	
UF98162	19981118	161442	1.327	0.6354	0.4838	58.139	9.947	108.306	1.528	U-F	236.139	
UF98163	19981118	161548	3.445	0.7173	0.9738	238.092	79.845	195.337	6.393	U-F	236.140	
UF98164	19981118	161704	3.224	0.6944	0.9853	236.141	144.671	172.773	5.788	U-F	236.141	
UF98165	19981118	162513	3.999	0.7636	0.9452	236.148	7.869	205.977	7.997	U-F	236.147	
UF98166	19981118	162705	2.541	0.8356	0.4177	236.152	2.121	285.659	4.05	U-F	236.148	N-Taurids
UF98167	19981118	163206	0.699	0.7726	0.1589	56.152	165.019	157.742	0.584	U-F	236.152	
UF98168	19981118	163357	-10.163	1.0869	0.9845	236.152	162.066	172.909		U-F	236.153	Leonids
UF98169	19981118	163623	1.536	0.4855	0.7901	236.157	2.78	247.292	1.903	U-F	236.155	
UF98170	19981118	165132	7.333	0.8959	0.7631	56.166	162.724	58.828	19.858	U-F	236.165	
UF98171	19981118	171120	1.881	0.7129	0.5401	236.179	156.617	275.159	2.58	U-F	236.179	
UF98172	19981118	171551	1.525	0.3981	0.9177	236.182	150.43	221.443	1.883	U-F	236.182	
UF98173	19981118	171608	2.559	0.71	0.7421	236.185	3.546	264.54	4.084	U-F	236.182	
UF98174	19981118	171716	2.13	0.6083	0.8333	56.183	16.528	54.193	3.109	U-F	236.183	
UF98175	19981118	173112	3.2	0.8437	0.184	58.198	89.398	132.556	5.913	U-F	236.193	
UF98176	19981118	173242	2.217	0.8811	0.2635	56.194	48.073	124.455	3.301	U-F	236.194	
UF98177	19981118	173751	5.175	0.9623	0.1952	238.198	52.184	308.51	11.771	U-F	236.198	
UF98178	19981118	173821	1.147	0.4476	0.8118	236.201	2.641	245.038		U-F	236.198	
UF98179	19981118	174015	14.752	0.9527	0.6976	56.2	44.187	293.388	56.682	U-F	236.198	
UF98180	19981118	174245	6.768	0.892	0.7307	56.201	155.736	296.548	17.608	U-F	236.199	
UF98181	19981118	174353	0.679	0.5851	0.2818	238.202	20.505	338.489	0.56	U-F	236.202	
UF98182	19981118	174638	2.054	0.6709	0.6757	56.204	112.725	77.756	2.943	U-F	236.204	
UF98183	19981118	175144	2.105	0.8224	0.374	236.21	3.119	292.187	3.055	U-F	236.207	N-Taurids
UF98184	19981118	175557	65.392	0.9965	0.2272	56.208	3.243	122.886	528.789	U-F	236.210	
UF98185	19981118	180021	3.458	0.756	0.8438	236.214	11.435	228.7	6.431	U-F	236.213	
UF98186	19981118	180352	1.867	0.7645	0.4396	236.219	2.413	286.353	2.551	U-F	236.216	N-Taurids

	DATE	UT	a	e	q	$\Omega$	i	$\omega$	P	Observers	Solar deg.	Shower
	No. YYYYMMDD	hhmmss	AU		AU	deg	deg	deg	yr			
UF98187	19981118	180954	1.008	0.2114	0.7936	58.22	136.73	97.463	1.009	U-F	236.220	
UF98188	19981118	181341	1.447	0.5072	0.713	58.222	8.212	80.101	1.74	U-F	236.223	
UF98189	19981118	181557	-19.818	1.0333	0.6597	56.224	133.326	89.792		U-F	236.224	
UF98190	19981118	181612	1.216	0.628	0.4522	236.224	129.73	293.985	1.34	U-F	236.225	
UF98191	19981118	181941	1.398	0.4683	0.7423	58.228	174.838	282.851	1.849	U-F	236.227	
UF98192	19981118	182204	1.278	0.2414	0.9692	236.228	160.214	154.182	1.444	U-F	236.229	Leonids
UF98193	19981118	184103	1.044	0.5165	0.5047	236.242	139.462	295.915	1.066	U-F	236.242	
UF98194	19981118	184236	2.512	0.6549	0.867	236.243	151.931	226.401	3.982	U-F	236.243	
UF98195	19981118	184546	-5.051	1.1938	0.9788	236.245	48.633	190.86		U-F	236.245	
UF98196	19981118	184620	6.033	0.9486	0.3101	236.246	129.081	294.183	14.818	U-F	236.246	
UF98197	19981118	184704	5.928	0.8423	0.9345	236.242	178.255	151.722	14.432	U-F	236.246	
UF98198	19981118	190402	1.895	0.8318	0.6979	58.258	19.1	78.072	2.609	U-F	236.258	
UF98199	19981118	190420	1.127	0.7619	0.2882	236.258	142.14	313.235	1.196	U-F	236.258	
UF98200	19981118	190427	1.431	0.5121	0.6983	236.258	80.844	97.658	1.712	U-F	236.258	
UF98201	19981118	190716	2.602	0.8176	0.4747	236.288	0.268	278.949	4.198	U-F	236.280	
UF99001	19990611	171924	2.061	0.5382	0.7458	80.365	154.410	108.574	2.959	U-SU	80.365	
UF99002	19990611	172029	2.615	0.7203	0.7316	80.366	100.468	109.412	4.229	U-SU	80.366	
UF99003	19990611	172854	1.665	0.8516	0.2471	280.372	5.041	130.176	2.149	U-SU	80.371	
UF99004	19990611	173509	4.076	0.9744	0.1044	80.375	9.881	324.881	8.230	U-SU	80.375	
UF99005	19990611	173547	1.373	0.5108	0.6720	80.376	116.499	270.028	1.809	U-SU	80.376	
UF99006	19990611	173623	3.835	0.8250	0.8712	80.375	2.862	255.515	7.510	U-SU	80.376	
UF99007	19990611	174605	4.285	0.8970	0.4414	280.385	2.156	101.278	8.869	U-SU	80.383	
UF99008	19990611	175320	-3.116	1.1510	0.4705	80.388	136.594	270.160		U-SU	80.388	
UF99009	19990611	180051	6.882	0.8944	0.7270	80.393	162.242	113.475	18.053	U-SU	80.393	
UF99010	19990611	182306	5.537	0.8993	0.5576	280.407	152.182	87.256	13.029	U-SU	80.407	
UF99011	19990611	182353	2.066	0.5095	1.0134	80.408	91.653	188.193	2.969	U-SU	80.408	
UF99012	19990611	182826	2.581	0.9766	0.0604	80.411	36.963	25.376	4.148	U-SU	80.411	Arietids
UF99013	19990611	183320	1.283	0.7771	0.2860	80.413	5.506	60.012	1.454	U-SU	80.414	$\zeta$ Perseids
UF99014	19990611	183834	30.092	0.9670	0.9938	80.418	147.606	198.933	185.073	U-SU	80.418	
UF99015	19990611	184727	2.078	0.5387	0.9633	80.423	69.021	211.442	2.898	U-SU	80.423	
UF99016	19990813	182833	38.279	0.9745	0.6773	140.507	115.122	158.152	236.828	K-SU	140.507	Perseids
UF99017	19990813	185517	6.159	0.9766	0.1444	320.518	18.379	137.349	15.286	K-SU	140.518	
UF99018	19990813	170530	-7.810	1.1266	0.9889	140.525	117.370	162.686		K-SU	140.525	Perseids
UF99019	19990813	171924	2.757	0.7177	0.7783	140.534	128.362	243.566	4.578	K-SU	140.534	
UF99020	19990813	173035	4.483	0.8520	0.6634	140.542	136.576	255.545	9.492	U-K	140.542	
UF99021	19990813	173402	3.289	0.8597	0.4588	140.544	67.178	280.587	5.911	U-SU	140.544	
UF99022	19990813	174241	2.448	0.9203	0.1950	140.553	179.481	313.235	3.829	U-SU	140.550	
UF99023	19990813	181852	-1.998	1.4594	0.9169	140.574	113.358	147.127		K-SU	140.574	
UF99024	19990813	182356	3.169	0.7076	0.9269	320.577	161.356	37.401	5.642	K-SU	140.578	
UF99025	19990813	182448	2.415	0.7938	0.4979	320.579	2.677	98.584	3.753	K-SU	140.578	
UF99026	19990813	185428	3.637	0.7541	0.8944	140.598	163.058	223.338	6.935	K-SU	140.598	
UF99027	19990813	190000	4.342	0.8848	0.5873	140.602	53.575	254.628	9.049	U-K	140.602	
UF99028	19990813	190236	3.629	0.8425	0.5715	320.603	141.552	272.670	6.914	K-SU	140.603	
UF99029	19990813	191856	1.831	0.5928	0.7863	320.614	175.977	86.531	2.883	U-K	140.614	
UF99030	19990813	192057	1.504	0.9699	0.0453	140.616	38.243	340.101	1.845	U-K	140.616	
UF99031	19991113	144206	2.064	0.7223	0.5733	50.781	3.070	90.175	2.966	U-SU	230.781	
UF99032	19991113	150703	5.293	0.8195	0.9552	230.799	135.372	202.643	12.176	U-SU	230.799	
UF99033	19991113	150936	1.342	0.8179	0.5125	230.801	3.842	285.199	1.554	U-SU	230.800	
UF99034	19991113	152328	0.972	0.5208	0.4659	230.810	2.693	303.043	0.959	U-SU	230.810	
UF99035	19991113	152938	9.319	0.9112	0.8275	50.814	134.945	48.986	28.447	U-SU	230.814	
UF99036	19991113	153301	4.520	0.8137	0.8423	50.817	133.265	48.071	9.611	U-SU	230.817	
UF99037	19991113	154442	6.558	0.8759	0.8639	230.825	11.467	223.288	18.355	U-SU	230.825	
UF99038	19991113	154442	3.533	0.7418	0.9124	230.825	130.982	144.761	6.642	U-SU	230.825	
UF99039	19991113	154846	2.688	0.8777	0.3288	50.828	171.976	115.374	4.408	U-SU	230.828	
UF99040	19991113	155123	-3.791	1.2337	0.8859	50.830	151.724	35.874		U-SU	230.830	
UF99041	19991113	155141	2.204	0.6565	0.7589	230.830	155.469	245.994	3.271	U-SU	230.830	
UF99042	19991113	155558	1.482	0.3324	0.9894	50.833	140.671	1.924	1.804	U-SU	230.833	
UF99043	19991113	162549	1.158	0.7622	0.2753	230.858	0.345	311.975	1.246	U-SU	230.854	
UF99044	19991113	163214	2.456	0.7006	0.7345	230.859	6.684	248.013	3.849	U-SU	230.859	
UF99045	19991113	183521	9.046	0.9704	0.2680	230.860	142.941	298.726	27.205	U-SU	230.860	
UF99046	19991113	183528	14.273	0.9576	0.5048	50.860	3.798	78.164	53.922	U-SU	230.860	
UF99047	19991113	184827	14.573	0.9496	0.7342	230.868	184.150	118.045	55.632	U-SU	230.868	
UF99048	19991113	185207	4.888	0.9819	0.1863	230.872	154.713	310.971	10.806	U-SU	230.872	
UF99049	19991113	185417	5.024	0.8030	0.9696	50.874	144.035	359.904	11.261	U-SU	230.874	
UF99050	19991113	185439	3.876	0.8635	0.5019	50.874	3.198	93.645	7.049	U-SU	230.874	
UF99051	19991113	185855	10.076	0.9027	0.9807	230.877	97.890	191.151	31.983	U-SU	230.877	
UF99052	19991113	170647	-3.420	1.2506	0.8572	50.882	142.012	40.593		U-SU	230.882	
UF99053	19991113	170853	2.788	0.7128	0.8006	230.884	5.604	237.233	4.654	U-SU	230.884	
UF99054	19991113	171324	4.710	0.9688	0.1583	230.887	3.042	315.481	10.221	U-SU	230.887	
UF99055	19991113	171501	-10.159	1.0358	0.3618	50.888	172.122	140.302		U-SU	230.888	
UF99056	19991113	171942	23.897	0.9684	0.7580	50.891	128.708	301.353	116.821	U-SU	230.891	
UF99057	19991113	172144	1.855	0.4130	0.9713	230.893	173.681	159.535	2.128	U-SU	230.893	
UF99058	19991113	172159	2.861	0.6873	0.8647	230.893	157.855	220.116	4.839	U-SU	230.893	
UF99059	19991113	172647	0.972	0.0665	0.8880	50.896	163.577	106.713	0.959	U-SU	230.896	
UF99060	19991113	172930	3.376	0.7164	0.9580	230.898	160.813	157.463	8.208	U-SU	230.898	Leonids
UF99061	19991113	173507	1.421	0.3069	0.9847	50.902	140.109	11.692	1.693	U-SU	230.902	
UF99062	19991113	173558	1.987	0.9001	0.1984	230.903	187.046	313.454	2.800	U-SU	230.903	
UF99063	19991113	173703	1.972	0.8688	0.2587	50.903	30.395	126.068	2.788	U-SU	230.903	
UF99064	19991113	173952	3.286	0.8810	0.3812	230.903	179.617	286.927	5.857	U-SU	230.905	
UF99065	19991113	174039	1.295	0.4318	0.7358	230.906	172.445	261.398	1.473	U-SU	230.906	
UF99066	19991113	174239	0.881	0.1755	0.7264	230.907	164.190	321.367	0.827	U-SU	230.907	
UF99067	19991113	174528	-0.472	2.5436	0.7281	230.909	177.533	230.808		U-SU	230.909	
UF99068	19991113	175122	1.523	0.5533	0.6804	230.913	171.113	262.942	1.880	U-SU	230.914	
UF99069	19991113	175156	12.944	0.9442	0.7221	230.914	140.923	243.879	46.571	U-SU	230.914	
UF99070	19991113	175337	14.275	0.9364	0.9082	50.915	150.378	33.894	53.933	U-SU	230.915	
UF99071	19991113	175403	200.833	0.9951	0.9774	230.915	167.420	192.761	2846.125	U-SU	230.915	
UF99072	19991113	175443	2.819	0.8808	0.3360	230.916	3.095					

	DATE No. YYYYMMDD	UT hhmmss	a AU	e	q AU	$\Omega$ deg	i deg	$\omega$ deg	P yr	Observers	Solar deg.	Shower
UF99086	19991113	193318	1.139	0.3735	0.7133	230.985	140.836	271.528	1.215	U-SU	230.985	
UF99087	19991113	193844	1.084	0.3154	0.7283	50.988	179.295	85.790	1.097	U-SU	230.987	
UF99088	19991113	193848	3.792	0.7643	0.8940	50.987	189.082	320.999	7.385	U-SU	230.987	
UF99089	19991113	193921	81.189	0.6842	0.9884	230.989	186.750	197.881	478.402	U-SU	230.989	
UF99100	19991113	193951	0.994	0.7059	0.2922	50.989	138.962	225.328	0.990	U-SU	230.989	
UF99101	19991113	194306	2.718	0.8478	0.9579	230.992	44.881	156.714	4.482	U-SU	230.992	
UF99102	19991113	194518	0.853	0.8337	0.0585	230.993	145.124	342.306	0.787	U-SU	230.993	
UF99103	19991113	194755	-11.348	1.0794	0.9005	230.995	124.958	145.754		U-SU	230.995	
UF99104	19991113	194831	1.049	0.1004	0.8434	230.995	154.700	240.731	1.074	U-SU	230.995	
UF99105	19991113	195144	1.276	0.7157	0.3828	50.988	158.089	121.228	1.441	U-SU	230.998	
UF99108	19991113	195333	1.881	0.4158	0.9820	230.999	114.945	168.930	2.179	U-SU	230.999	
UF99107	19991113	195649	1.298	0.5938	0.5268	231.001	137.807	75.199	1.476	U-SU	231.001	
UF99108	19991113	200339	2.149	0.6498	0.7524	51.008	129.242	293.057	3.150	U-SU	231.006	
UF99109	19991113	200658	3.067	0.7837	0.7247	231.008	84.731	247.552	5.370	U-SU	231.008	
UF99110	19991113	200751	8.050	0.8804	0.9830	231.009	148.095	199.508	22.841	U-SU	231.009	
UF99111	19991113	201042	-4.730	1.2021	0.9581	231.011	184.246	159.733		U-SU	231.011	
UF99112	19991113	201238	3.289	0.7178	0.9280	231.012	178.887	148.338	5.985	U-SU	231.012	
UF99113	19991113	201317	2.841	0.7890	0.5996	231.012	177.421	263.888	4.790	U-SU	231.013	
UF99114	19991113	201531	2.221	0.6888	0.7358	231.014	151.437	111.112	3.311	U-SU	231.014	
UF99115	19991113	201759	0.985	0.3469	0.8432	231.018	171.817	88.981	0.977	U-SU	231.016	
UF99116	19991113	201801	1.019	0.3285	0.8845	51.015	0.888	104.292	1.029	U-SU	231.016	
UF99117	19991113	202115	3.241	0.7329	0.8656	231.018	122.748	134.744	5.834	U-SU	231.018	
UF99118	19991116	170031	2.421	0.8353	0.3987	53.899	130.548	108.141	3.787	U-SU	233.899	
UF99119	19991116	171242	3.280	0.9020	0.3194	233.908	3.414	295.308	5.886	U-SU	233.908	N-Taurids
UF99120	19991116	172210	3.805	0.8658	0.5106	53.915	168.387	82.427	7.421	U-SU	233.915	
UF99121	19991116	172844	1.264	0.5559	0.5813	53.919	135.443	102.125	1.421	U-SU	233.919	
UF99122	19991116	173206	37.921	0.9798	0.7645	53.922	160.484	57.207	233.518	U-SU	233.921	
UF99123	19991116	174337	2.198	0.5874	0.9507	233.930	8.484	208.708	3.258	U-SU	233.930	
UF99124	19991116	174504	-22.673	1.0028	0.0642	53.931	30.395	150.181		U-SU	233.931	
UF99125	19991116	175124	4.885	0.8083	0.9423	233.935	130.788	208.585	10.730	U-SU	233.935	
UF99126	19991116	181805	1.191	0.7912	0.2487	233.952	102.525	313.990	1.300	U-SU	233.952	
UF99127	19991118	144357	4.888	0.9750	0.1186	55.820	23.380	141.889	10.088	U-F	235.820	
UF99128	19991118	145118	5.077	0.8270	0.8788	55.825	12.205	41.021	11.441	U-F	235.825	
UF99129	19991118	150838	2.265	0.5820	0.9487	235.837	161.585	152.259	3.408	U-F	235.837	
UF99130	19991118	151244	1.810	0.9478	0.0844	55.840	29.970	151.628	2.044	U-F	235.840	
UF99131	19991118	151537	-18.870	1.0207	0.3903	55.842	20.415	101.427		U-F	235.842	
UF99132	19991118	152217	1.238	0.3878	0.7581	235.847	1.740	260.482	1.377	U-F	235.847	
UF99133	19991118	152354	3.284	0.8940	0.3480	235.848	18.851	291.888	5.951	U-F	235.848	
UF99134	19991118	152427	1.145	0.2418	0.8887	235.848	3.042	247.806	1.228	U-F	235.848	
UF99135	19991118	152435	3.108	0.7091	0.9042	235.848	148.522	217.390	5.480	U-F	235.848	
UF99136	19991118	152548	7.391	0.9844	0.1151	235.849	28.537	320.529	20.095	U-F	235.849	
UF99137	19991118	153153	0.863	0.6655	0.2886	235.853	13.082	321.359	0.801	U-F	235.853	
UF99138	19991118	154352	1.904	0.8323	0.3193	235.882	5.551	299.383	2.827	U-F	235.882	
UF99139	19991118	160523	-12.632	1.0776	0.8798	235.877	182.665	189.475		U-F	235.877	Leonids
UF99140	19991118	161019	-24.597	1.0399	0.9822	235.880	182.488	170.959		U-F	235.880	Leonids
UF99141	19991118	161648	2.140	0.7888	0.4945	235.888	1.284	278.590	3.130	U-F	235.885	N-Taurids
UF99142	19991118	161756	2.849	0.7212	0.7944	55.886	105.814	57.902	4.809	U-F	235.886	
UF99143	19991118	162251	1.599	0.7205	0.4488	55.889	12.780	107.971	2.021	U-F	235.889	
UF99144	19991118	183331	3.011	0.7371	0.7919	235.897	9.819	237.908	5.228	U-F	235.897	
UF99145	19991118	183528	11.583	0.9168	0.9638	235.898	114.239	181.416	39.420	U-F	235.898	
UF99146	19991118	184147	1.285	0.2359	0.9888	235.902	158.813	152.310	1.423	U-F	235.902	Leonids
UF99147	19991118	184342	2.002	0.5498	0.9018	55.904	133.401	41.219	2.832	U-F	235.904	
UF99148	19991118	184558	-0.998	1.0819	0.1718	235.907	88.949	308.139		U-F	235.907	
UF99149	19991118	184935	25.818	0.9590	0.9803	235.908	161.765	169.449	118.972	U-F	235.908	Leonids
UF99150	19991118	185522	-1.832	1.8057	0.9683	235.912	163.443	181.085		U-F	235.912	Leonids
UF99151	19991118	185818	-31.432	1.0205	0.6438	55.914	123.958	71.991		U-F	235.914	
UF99152	19991118	185956	2.245	0.8543	0.3271	55.915	8.280	116.883	3.384	U-F	235.915	
UF99153	19991118	170318	-6.351	1.1552	0.9858	235.917	182.889	174.298		U-F	235.917	Leonids
UF99154	19991118	170343	-11.827	1.0451	0.5336	235.918	171.331	284.293		U-F	235.918	
UF99155	19991118	170448	1.810	0.8425	0.6471	55.918	126.575	83.265	2.435	U-F	235.918	
UF99156	19991118	170533	-18.904	1.0521	0.9858	235.919	182.788	173.928		U-F	235.919	Leonids
UF99157	19991118	170701	5.031	0.8630	0.8893	55.920	18.997	89.710	11.284	U-F	235.920	
UF99158	19991118	171238	-1.807	1.4892	0.7860	55.924	186.964	48.878		U-F	235.924	
UF99159	19991118	171552	-1.851	1.5340	0.9884	235.928	183.429	180.274		U-F	235.926	Leonids
UF99160	19991118	172718	3.048	0.9781	0.0668	55.934	25.864	152.347	5.320	U-F	235.934	
UF99161	19991118	173019	2.185	0.8355	0.7965	55.938	174.384	59.991	3.230	U-F	235.936	
UF99162	19991118	173418	-2.112	1.4019	0.8488	235.939	106.440	220.718		U-F	235.939	
UF99163	19991118	174628	1.957	0.8030	0.3858	235.949	0.723	291.879	2.738	U-F	235.948	N-Taurids
UF99164	19991118	174753	-9.203	1.1205	0.9882	235.952	162.055	181.845		U-F	235.948	Leonids
UF99165	19991118	175224	-46.293	1.0190	0.8002	235.956	162.460	170.160	13.787	U-F	235.958	Leonids
UF99166	19991118	180040	5.744	0.8291	0.9918	235.958	162.904	172.881	12.057	U-F	235.958	Leonids
UF99167	19991118	180048	5.258	0.8127	0.9850	235.958	162.904	172.881	1.399	U-F	235.959	
UF99168	19991118	180235	1.245	0.3225	0.8433	55.959	133.667	86.560		U-F	235.962	
UF99169	19991118	180852	2.639	0.8591	0.3719	55.962	164.749	110.478	4.287	U-F	235.965	Leonids
UF99170	19991118	181038	20.836	0.9527	0.9847	235.965	182.788	172.884	95.109	U-F	235.965	Leonids
UF99171	19991118	181115	5.228	0.8124	0.9809	235.965	181.580	189.395	11.953	U-F	235.985	Leonids
UF99172	19991118	181307	8.571	0.9137	0.5871	55.966	165.488	83.848	18.845	U-F	235.968	
UF99173	19991118	182520	59.283	0.9860	0.8296	235.975	172.198	227.440	458.452	U-F	235.975	
UF99174	19991118	182732	1.568	0.6631	0.5283	55.976	187.320	99.638	1.964	U-F	235.976	
UF99175	19991118	182905	0.607	0.7725	0.1380	235.978	8.505	346.937	0.473	U-F	235.977	
UF99176	19991118	183912	2.496	0.7089	0.7267	55.985	143.303	88.802	3.944	U-F	235.985	
UF99177	19991118	183953	15.713	0.9373	0.9845	235.985	163.065	172.618	82.287	U-F	235.985	Leonids
UF99178	19991118	184957	1.308	0.3948	0.7905	55.992	11.045	72.986	1.493	U-F	235.992	
UF99179	19991118	185121	1.423	0.6953	0.4335	55.993	148.083	111.640	1.697	U-F	235.993	
UF99180	19991118	185617	1.334	0.9339	0.0881	55.997	33.901	152.387	1.540	U-F	235.997	
UF99181	19991118	185710	1.139	0.1909	0.9216	235.995	178.594	125.308	1.216	U-F	235.997	
UF99182	19991118	185747	0.650	0.6874	0.2031	55.998	101.074	181.871	0.524	U-F	235.998	

## ALIS (AURORAL LARGE IMAGING SYSTEM) USED FOR OPTICAL OBSERVATIONS OF THE METEOR IMPACT PROCESS

U. Brändström<sup>1</sup>, B. Gustavsson<sup>2</sup>, A. Steen<sup>3</sup>, and Asta Pellinen-Wannberg<sup>1</sup>

<sup>1</sup>Swedish Institute of Space Physics (IRF-K), SE-981 28 Kiruna, Sweden,  
email: urban.brandstrom@irf.se, asta.pellinen-wannberg@irf.se

<sup>2</sup>National Institute of Polar Research, Tokyo, Japan. email: bjorn@uap.nipr.ac.jp

<sup>3</sup>RemSpace group, Linköping, Sweden. email: ake.steen@remspace.com

### ABSTRACT

This paper outlines a possibly new use of the Auroral Large Imaging System (ALIS) for studies of differential ablation phenomena in meteor trails. By simultaneous imaging from up to six stations, the altitude distribution of the meteor trails could be triangulated, while some stations simultaneously image the trails in for example the sodium (5893 Å) and calcium (4227 Å) lines.

ALIS was primarily designed for auroral studies, but has also been used for studies of heater-induced airglow, polar stratospheric clouds as well as other phenomena. The system consists of six unmanned remote-controlled observation stations located in northern Sweden.

Key words: ALIS; meteoroids; differential ablation; spectroscopic; multi-station; triangulation; meteor trails; imaging.

### 1. INTRODUCTION

Meteor showers are one of few processes taking place above the troposphere that are observable by the naked eye. This influx of extraterrestrial matter to the Earth, on the order of 100 tons per day (Love & Brownlee 1993) gives rise to the permanent layer of metal atoms in the 80–110 km altitude region (Höffner & von Zahn 1999). The study of these phenomena has important implications with respect to irregularities in long range radio communications, sporadic E-layers, as well as the survivability of artificial satellites, etc.

Modelling studies (McNeil et al. 1995, 2001) combined with LIDAR observations (Höffner & von Zahn 1999; von Zahn et al. 1999) as well as observations by the GLO-1 instrument on the space-shuttle (Gardner et al. 1999) has yielded significantly new information on the mechanisms involved in the formation of meteor-trails and their properties.

### 1.1. Differential ablation

*As cosmic dust travels through the atmosphere, heating and ablation of the material causes deposition of the metals at altitudes between 80 and 110 km. The exponential increase in atmospheric density along the cosmic dust particle's path leads to increasing ablation with decreasing altitude. However, frictional deceleration of the particle causes it to reach a terminal velocity which corresponds to a temperature below that at which ablation takes place. Therefore, ablation from a single particle is deposited in a narrow layer, the altitude of which depends on particle mass and particle velocity. At high enough velocities, above about 30 km/s, cosmic dust particles ablate completely. At low velocities, a major fraction of the material falls to earth unablated. (McNeil et al. 1998). In essence this means that different elements are released from the meteor at different times, as demonstrated by (von Zahn et al. 1999) using groundbased LIDARs.*

In this paper we briefly outline a possibly new measurement method of differential ablation phenomena in meteor trails, using a set of groundbased high resolution spectroscopic imagers, thus enabling the observer to simultaneously triangulate the height of the meteor trail and measure the velocity distribution, while getting spectroscopic intensities in a few selected emission lines. These results would be highly interesting to compare with model calculations (Figure 1).

### 2. ALIS

ALIS (*Auroral Large Imaging System*) was conceived in 1989 suggesting a net in Northern Scandinavia of 28 stations, spaced 100 km, with a medium field of view of 90° (Steen 1989). The number of stations was later reduced to 14 within Sweden and possible expansions into the surrounding countries (Steen et al. 1990). Due to limited funding, the number of stations were reduced to six.

The present six stations consists of a high-performance camera, which is a thinned, backside illuminated 1024 ×

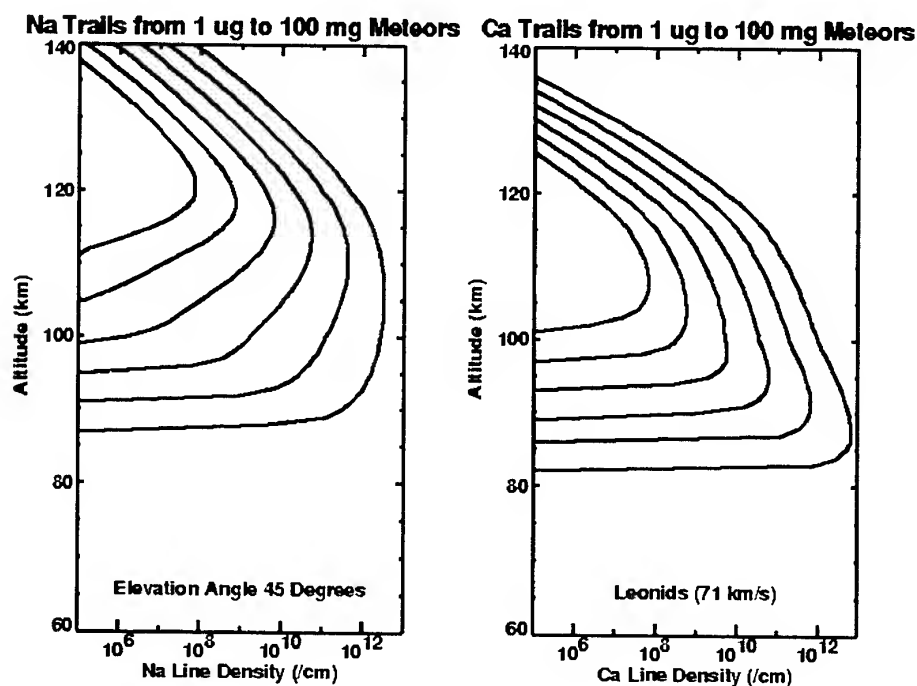


Figure 1. Model calculations (Courtesy of William McNeil, Shu Lai and Ed Murad, USAF) on sodium and calcium ion densities for Leonids at  $45^\circ$  elevation angle. The deposition rates are computed by differential ablation model for 1 mg to 100 mg. In the following simulations we use the results from the 100 mg particles.

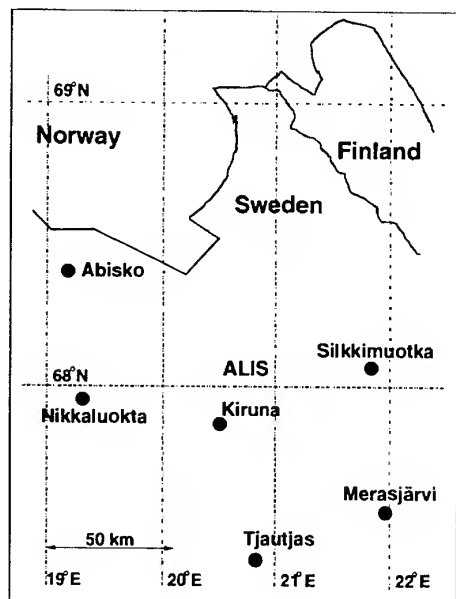


Table 1. Available filters at the various ALIS stations. The stations are numbered as follows: 1 Kiruna, 2 Merasjärvi, 3 Silkkimuotka, 4 Tjautjas, 5 Abisko, 6 Nikkaluokta (see also figure 2)

pos.	line. [ $\text{\AA}$ ]	use	stations
0	5577	$O(^1S)$	all
1	6300	$O(^1D)$	all
2	4227	Ca	1
2	5893	Na	4
2	6230	bg.	2,3,5,6
3	white		all
4	8446	$OI$	1,4,5,6
4		lidar	3
5	4278	$N_2^+$	all

Figure 2. Map displaying the layout of the ALIS system. In this paper it is suggested to use a sodium (5893  $\text{\AA}$ ) filter at station 4 (Tjautjas) and a calcium (4227  $\text{\AA}$ ) filter at station 3 (Silkkimuotka)

1024 pixels CCD (Charge Coupled Device) imager, with quad. readout channels. The detector is attached to a telecentric lens-system equipped with a six position filter-wheel intended for 3-inch narrow-band interference filters (Table 1). The front lens has a moderate field-of-view of  $54^\circ \times 54^\circ$  at four stations and  $90^\circ \times 90^\circ$  at the remaining two stations.

Each camera is mounted in a camera positioning system (CPS), making it possible to individually direct any camera to image any desired region of the sky.

The main scientific objective of ALIS was aimed at spectroscopic reconstruction of the three-dimensional auroral signal, by the use of tomographic inversion techniques (Gustavsson 1998; Gustavsson et al. 2000b; Aso et al. 1998a,b, 1999). Another important issue were to expand absolute measurements of the auroral signal, traditionally made by scanning or imaging photometers to two dimensions (Sergienko et al. 2001). It is important to stress that the ALIS detector is a *spectroscopic imager* and not a traditional camera.

Other scientific objectives expanded to studies of polar-stratospheric clouds (Steen et al. 1997; Enell et al. 1999, 2000), artificially generated aurora (Brändström et al. 1999; Gustavsson et al. 2000a; Leyser et al. 2000), day-time aurora (Rees et al. 2000) etc. This report deals with the possible application of ALIS for studying differential-ablation phenomena in meteor trails.

Key features of ALIS:

- Six imaging stations, separated  $\approx 50$  km.
- Non-intensified thinned, back-side illuminated CCD-cameras  $1024 \times 1024$  pixels, 16 bits ADC, quad. readout system.
- Telecentric lens system (FoV  $54^\circ \times 54^\circ$  or  $90^\circ \times 90^\circ$ )
- Steerable camera positioning system (CPS).
- Narrow-band (40 Å) interference filters (see table 1).
- Fully remote-controlled operation over Internet.
- More information at <http://alis.irf.se>.

### 3. SUGGESTED MODE OF OPERATION

In this simulation it is suggested that ALIS operates with all six stations. The cameras are oriented to observe a common volume, in order to enable triangulation of altitudes (Figure 3). The CCD-detector is used in full resolution mode ( $1024 \times 1024$  pixels) and with longest possible integration times (ie. the time between reading out images, typically several minutes). The dynamics is recorded by quickly opening and closing the shutter, with a period down to 50 ms. In this way the probability of observing a meteor is increased, as well as the possibility to study the velocities at different altitudes.

Station 4 (Tjautjas) uses a sodium (5893 Å) filter, and station 3 (Silkkimuotka) observes with a calcium (4227 Å)

filter. The remaining stations observe in white light (no filter). This setup enables triangulation of the meteor trail (Figure 4 E) as well as velocity fits as function of altitude (Figure 4 F).

### 4. OBSERVATION ATTEMPTS

Some preliminary studies were carried out during the Leonids 1999 and 2000. These observations yielded no usable results due to bad weather conditions, however, important knowledge about how to perform an observation of this type was gained. Technical limitations include the shutter speed, synchronisation, CCD-readout and disk-space availability. Operational constraints are mainly related to weather conditions and the presence of the full moon, or other bright objects (eg. man made light pollution).

### 5. SIMULATED OBSERVATIONS

In figure 3 the stations are observing an meteor trail passing through the common observing volume. The shutters on all stations are synchronised via GPS (Global Positioning System) timing at a period of 50 ms. The integration time is as long as possible without saturating the detectors. The resulting images from four stations are shown in figure 4 (A–D) and the triangulated 3-D meteor-trail are shown in figure 4 (E). The calculated velocities versus altitudes are displayed in figure 4 (F).

### 6. SUMMARY

- ALIS is a novel facility with a high scientific potential in many fields of optical studies of the upper atmosphere.
- Some preliminary studies carried out during the Leonids 1999 and 2000 has not yielded any results mainly due to cloudy weather conditions, yet important facts about the feasibility of the proposed experiment were learned.
- ALIS is currently put into hibernation due to management and funding difficulties. It is however our hope that the simulated measurements similar to those described in this paper could be carried out with a revived ALIS in a near future. Such measurements might shed some more light on the physical mechanisms involved.
- The model calculations show that it would be possible to determine the terminal velocity of a meteoroid with  $\pm 2 \text{ ms}^{-1}$  as well as accurately determine the altitude variation of the Na and Ca emissions in the altitude region between 80–130 km.

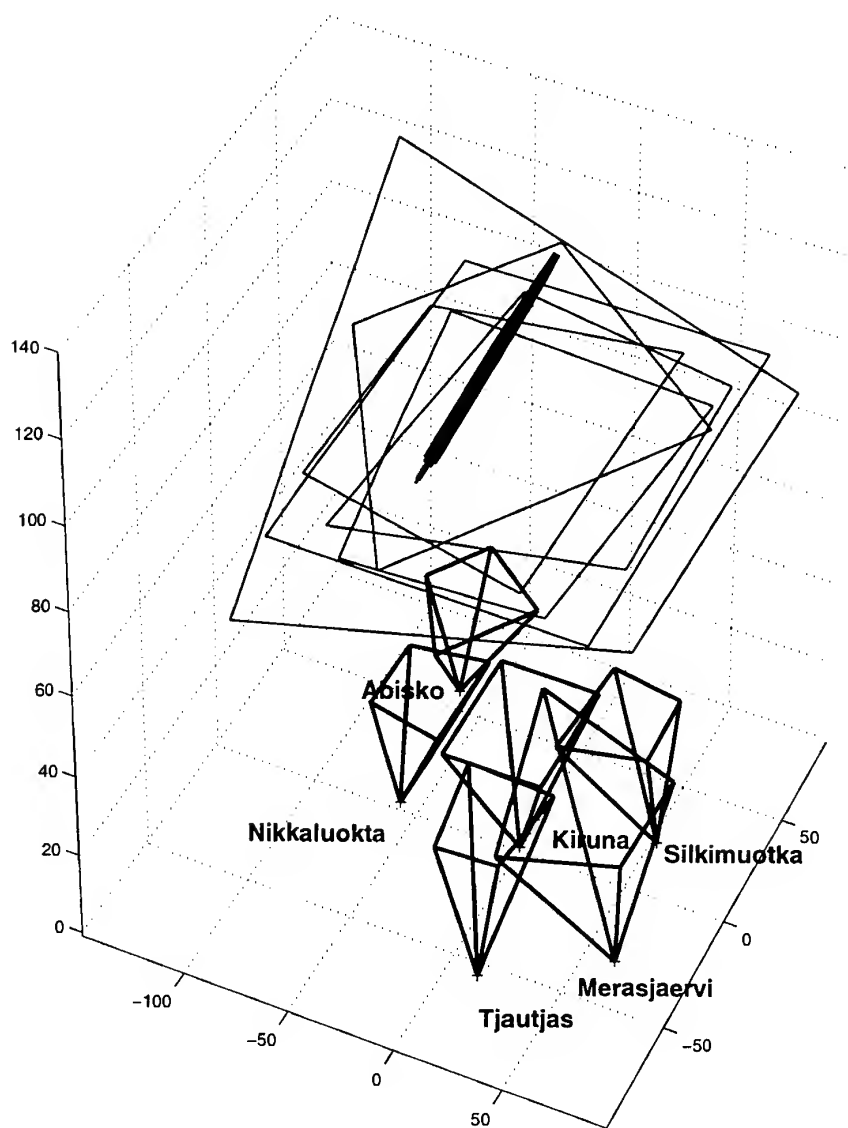


Figure 3. A 100 mg meteor observation simulated for ALIS. The figure shows six ALIS stations and their field-of-views at 100 km altitude. As observing the trail with white light at four stations and with a sodium filter ( $5893 \text{ \AA}$ ) and calcium filter ( $4227 \text{ \AA}$ ) at two stations.

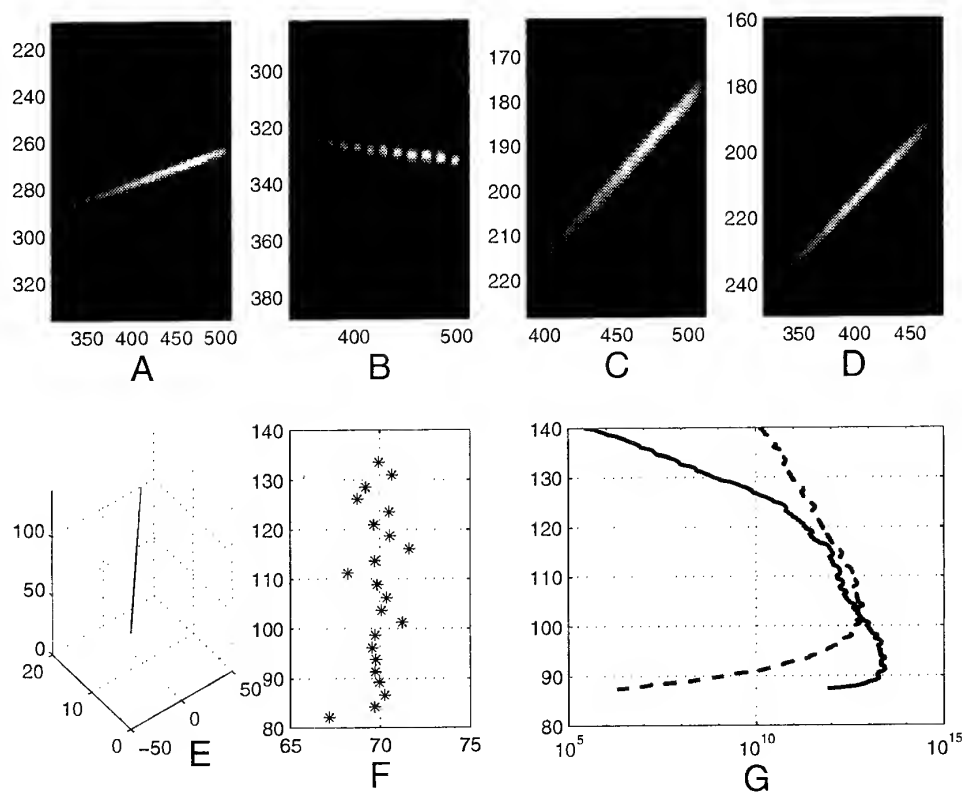


Figure 4. The simulated observations as seen from Kiruna (A), Merasjärvi (B), Silkimuotka (C) and Tjautas (D) stations. The sodium filter is at the Tjautas station and the calcium at the Silkimuotka station. (E) shows the plain meteor trail, (F) results of the velocity fits after the modelling with an initial Leonid velocity of 71 km/s and (G) the same information as Figure 1 but calculated from the images and plotted against altitude using the triangulation results. (Note. background and noise neglected in this simple simulation.). Plot coordinates: (A–D) pixels, (E) distance from Kiruna [km], (F) velocity [ $\text{km s}^{-1}$ ] versus altitude [km] (solid Ca, dashed Na), (G) line density [ $\text{cm}^{-1}$ ] versus altitude [km].

## ACKNOWLEDGMENTS

The authors are indebted to William McNeil, Shu Lai and Edmond Murad, at Space Vehicles Directorate, Air-Force Research Laboratory, Hanscom AFB, Ma. 01731 USA for kindly contributing their model calculations (Fig. 1) as well as for encouragement and inspiration. S.D.G.

Steen Å., Gustavsson B., Brändström U., 1997, In: Proceedings of the 4th European symposium of polar stratospheric ozone

von Zahn U., Gerding M., Höffner J., Neil W.J.M., Murad E., 1999, Meteorit. Planet. Sci., 34, 1017

## REFERENCES

- Aso T., Ejiri M., Urashima A., et al., 1998a, Earth Planets Space, 50, 81
- Aso T., Ejiri M., Urashima A., et al., January 1998b, In: Proceedings of the NIPR Symposium on upper atmosphere Physics, vol. 11, 1–10, National Institute of Polar Research, Tokyo
- Aso T., Ejiri M., Urashima A., et al., 1999, In: Proceedings of the 25th annual European Meeting on Atmospheric Studies by Optical Methods, IN PRESS
- Brändström B.U.E., Leyser T.B., Steen Å., et al., December 1999, Geophysical Research letters, 26, 3561
- Enell C.F., Steen Å., Gustavsson B., et al., 1999, In: XXV annual European Meeting on Atmospheric Studies by Optical Methods
- Enell C.F., Gustavsson B., Steen Å., Brändström U., Rydesäter P., 2000, Physics and Chemistry of the Earth (B), 25, 451
- Gardner J.A., Broadfoot A.L., McNeil W.J., Lai S.T., Murad E., 1999, J. Atmos. Terr. Phys., 61, 545
- Gustavsson B., November 1998, Journal of Geophysical Research, 103, 26,621
- Gustavsson B., Sergienko T., Rietveld M.T., et al., 2000a, J. Geophys. Res.
- Gustavsson B., Steen Å., Sergienko T., Brändström B.U.E., 2000b, Physics and Chemistry of the Earth (B)
- Höffner J., von Zahn U., February 1999, Journal of Geophysical Research, 104, 2633
- Leyser T.B., Gustavsson B., Brändström B.U.E., et al., 2000, Adv. Polar Upper Atmos. Res., 14, 1
- Love S.G., Brownlee D.E., 1993, Science, 262, 550
- McNeil W.J., Murad E., Lai S.T., August 1995, Journal of Geophysical Research, 100, 16847
- McNeil W.J., Lai S.T., Murad E., 1998, Adv. Space Res., 21, 863
- McNeil W.J., Dressler R.A., Murad E., June 2001, Journal of Geophysical Research, 106, 10447
- Rees D., Conde M., Steen Å., Brändström U., February 2000, Geophysical Research letters, 27, 313
- Sergienko T., Gustavsson B., Steen Å., et al., 2001, Physics and Chemistry of the Earth (B)
- Steen Å., April 1989, In: Proc. 9th Symposium on European rocket and balloon programmes and related research, Lahnstein, FRG, 299–303, ESA, eSA SP-291
- Steen Å., Brändström U., Kaila K., November 1990, In: Proc. NSSR Annual meeting Bolkesjø, Norway, 153–164, NSSR

# SOME FEATURES OF DIGITAL KINEMATIC AND PHOTOMETRICAL PROCESSING OF FAINT TV METEORS

Pavlo M. Kozak, Alexander A. Rozhilo, Yury G. Taranukha

*Astronomical Observatory of Taras Shevchenko National University, 04053, 3 Observatorna Str., Kyiv, Ukraine,  
Email: kozak@observ.univ.kiev.ua*

## ABSTRACT

Some features of digital kinematic and photometrical processing of TV faint meteors are discussed. For these purpose a computer original program has been worked out. The program uses data obtained by TV devices equipped by izokon TV tubes. The observed images are recorded on videotape and digitized with the help of a framegrabber. Precision of measurements of meteor coordinates in the frame is estimated. The kinematic processing is based on an original method using elements of vector analysis and calculating both meteor trajectory parameters in Earth's atmosphere and orbit elements. The errors of these parameters are also computed. Photometrical characteristics of TV systems were investigated. Some experiments for photometrical field correction, spectral sensitivity of TV tube cathode and correction for the motion of a meteor were carried out. The method was approbated on the results of double-station observations of meteors in Kyiv for the last years.

## 1. INTRODUCTION

Double station observations of meteors with the help of TV devices have been carried out in Kyiv for the last 20 years. There are TV systems equipped by TV transmission tubes of izokon type at two observational stations with the distance 54 km between them. Usually wide angle objective lenses "Gelios-40" ( $F = 85$  mm,  $D:F = 1:1.5$ ) and "Jupiter-3" ( $F = 50$  mm,  $D:F = 1:1.5$ ) are used. Results of observations are recorded on videotape. Then the frames with the meteor images are digitized with the help of standard frame grabber. It should be noted that both the size of the frame and its scale along the axes depend on the frame grabber type. Kinematic and photometrical processing is done according to the method worked out in the department, using software specially written by the authors for these purposes. The obtained sequence of frames is used for meteor velocity calculation and the summarized frame allows for more accurate radiant coordinates determination and for photometrical measurements. A TV meteor in its progress is demonstrated in Fig. 1. There are 7 full frames (numbers 1, 3, 5, 7, 9, 11 and 13; numbers 2, 4, 6, 8, 10 and 12 are not shown) with a moving meteor and the frame of the same meteor, summarized over 41 frames. As it can be seen, the last frame is similar to meteor images of photographic observations. The bad visual quality of the last frame is conditioned by the fact the the

numbers in a summary frame are much higher than a computer can show with 256 gray scale.

## 2. THE ASTRONOMICAL CATALOGUES USE AND THE PROBLEM OF FRAME STARS IDENTIFICATION

The most convenient variant for kinematic and photometrical meteor processing in the digital frame obtained by such a dynamical device as a TV system is the use of reference stars, which are presented in the same frame at the same time. Therefore the problem of star identification in the frame is a very important task in this situation. Many star catalogues have a digital form. But the main problem of the identification is the star map visualization connected with a catalogue near the real frame on the screen in the same scale. This task is impeded by the fact the real frame is violent due to distortions of different types. The same problem limits the wholly automation of the star identification process.

We have used the formulas of ideal projection for star map construction, which are as follows in the final view:

$$\begin{aligned} x &= x_{OC} + F_x (-\xi \cos \varphi + \eta \sin \varphi) \\ y &= y_{OC} + F_y (\xi \sin \varphi + \eta \cos \varphi), \end{aligned} \quad (1)$$

where  $x, y$  are the coordinates of the drawn star in the artificial frame-map,  $x_{OC}, y_{OC}$  are the coordinates of the optical center,  $F_x$  and  $F_y$  are the focal distances along axes, which are different because of ratio abnormality at digitizing,  $\varphi$  is an angle of axes turn,  $\xi = \xi(\alpha, \delta, \alpha_{OC}, \delta_{OC})$  and  $\eta = \eta(\alpha, \delta, \alpha_{OC}, \delta_{OC})$  are the ideal coordinates of shown stars which are determined by standard formulas and are the functions of equatorial coordinates of stars and optical center. Varying these parameters under visual control we can achieve satisfactory identity of real and artificial frames. The Fig.2 demonstrates the real frame (RF) and artificial frame-map (AF) of a sky field in Corona Borealis constellation.

Now the stars are identified by a simple click of the computer mouse consecutively in both frames. This task can be automated in part if we previously calculate the coordinates of optical center, for instance, over four stars near the center according to [1] and obtain focal distances from the image scale (angular pixel size), which can be determined over a small star group. The last unknown parameter  $\varphi$  we

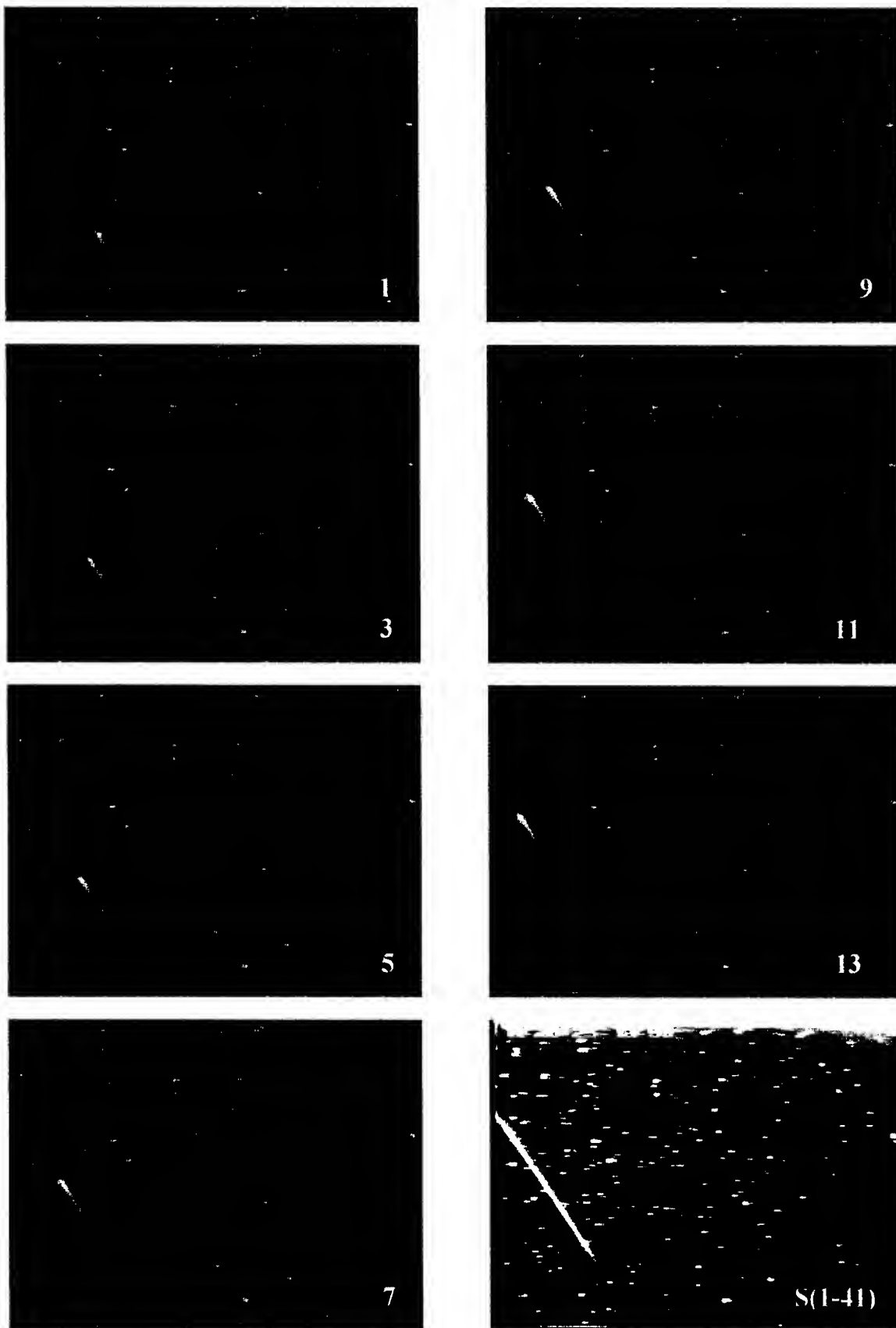


Fig. 1. Digitized TV meteor in its progress and the summed frame

also find over some stars from the Eqs. 1 using the least square method. If, after star map reconstruction with the parameters determined like it was explained above, the measured coordinates in the both frames do not differ very much, the procedure of automation based on the similarity of the above mentioned  $x$  and  $y$  coordinates can be run.

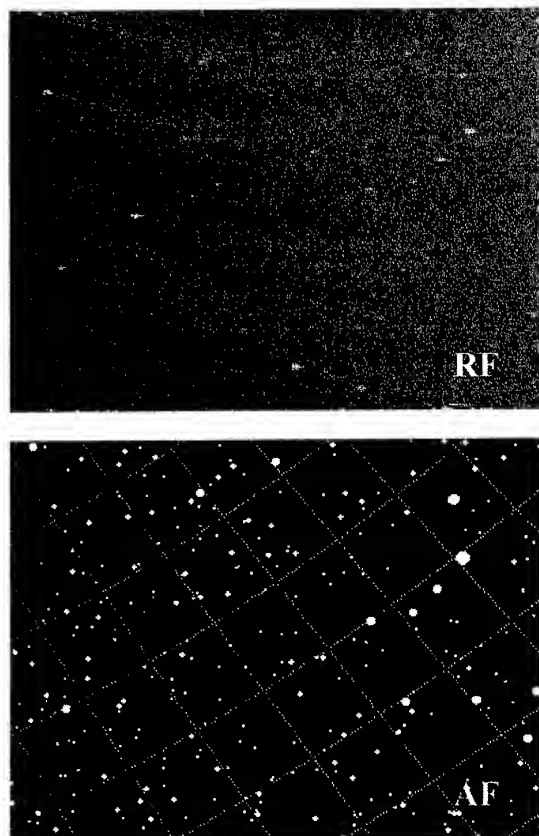


Fig. 2. Real TV frame (RF) and artificial frame-map (AF)

### 3. MEASUREMENT OF EQUATORIAL COORDINATES IN A FRAME

In order to determine ideal and then equatorial coordinates of a meteor over reference stars we should establish the criteria of a choice of both the computation model and parameters of stars themselves. As a rule, the polynomial models of connections between ideal and measured coordinates are used in astrometrical processing. The use of the regression analysis means [2], including the method of least squares, requires sufficient number of reference stars. But when observing with wide angle lenses it is often possible to increase the star number only by increasing the geometrical area of star sample at the same time. And this in turn will increase errors of calculation. We used the "sliding sample" method in meteor images processing. In this case, for each point on the meteor trail its own sample of stars is composed which are placed

roughly uniformly around the point. The number of reference stars depends on the model used.

Therefore, for every meteor point, it is proposed to carry out the measurements with a range of known methods using in each case own reference star sample. Then one needs to choose the best method according to some criteria and use the data obtained by this method in the sequel. Such procedure has to be repeated for every point on a meteor image along the trail.

In order to establish a connection between ideal and measured coordinates we used four well known in astrometry methods.

1. Fit by linear polynomial (6 constants method):

$$\begin{aligned}\xi &= a_0 + a_1x + a_2y \\ \eta &= b_0 + b_1x + b_2y\end{aligned}$$

2. Fit by truncated second-degree polynomial (10 constants method):

$$\begin{aligned}\xi &= a_0 + a_1x + a_2y + a_3xy + a_4x^2 \\ \eta &= b_0 + b_1x + b_2y + b_3xy + b_4y^2\end{aligned}$$

3. Fit by full second-degree polynomial (12 constant method):

$$\begin{aligned}\xi &= a_0 + a_1x + a_2y + a_3xy + a_4x^2 + a_5y^2 \\ \eta &= b_0 + b_1x + b_2y + b_3xy + b_4x^2 + b_5y^2\end{aligned}$$

4. Fit by Deutsch's [3] method at free selected optical center (8 constants method):

$$\xi = \frac{a_0 + a_1x + a_2y}{1 + c_1x + c_2y} \quad \eta = \frac{b_0 + b_1x + b_2y}{1 + c_1x + c_2y}$$

Solving in each case the conventional equations system we obtain the values of ideal coordinates  $\xi$ ,  $\eta$  and deviation obtained from conventional equations residuals, which can be used as characteristics of current model quality

$$\sigma^2 = \sum_{i=1}^n \delta_i^2 / (n - p), \quad (2)$$

where  $n$  is a number of stars in the sample,  $p$  is an order of fit polynomial,  $\delta_i$  is a residual of an equation. Also we obtain a deviation of prediction, determined from the following formula [2]:

$$\sigma_0^2 = \sigma^2 [\varepsilon]^T \cdot [D] \cdot [\varepsilon], \quad (3)$$

where  $[\varepsilon]$  is a matrix-column and  $[\varepsilon]^T$  is the transposed matrix  $[\varepsilon]$  (matrix-row) which consist of

regressors of the desired object,  $[D]$  is a dispersion matrix. For a more rigorous control we can also use a "sliding exam" method as an additional criterion of a model quality. In this exam each star is consecutively excluded from the star sample and processed as an object. Denoting the shift between computed coordinates of the star and its real ones as  $\Delta_i$  we will obtain the following formula for the deviation [2]

$$\Delta^2 = \sum_{i=1}^n \Delta_i^2 / (n - p). \quad (4)$$

Let us carry out an experiment where we will use a star with known coordinates as an unknown object. We shall use the result of the experiment for the model examination as follows:

- ideal coordinates determination accuracy, comparing obtained star coordinates with ones taken from a catalogue;
- prediction error adequacy given by Eq. 3 comparing it with real shift in ideal coordinates;
- minimum values correlation given by Eqs. 2 and 4 as a criterion of a model choice in every case, comparing it with the real minimum.

Carrying out a range of experiments with different positions of such an "unknown object" and different reference star samples we have obtained the results presented in Figs.3-4. The bar chart in Fig.3 shows a meeting frequency of every method as the one giving the best result. Fig.4 corresponds to the processing results obtained by models 6, 8, 10, 12 constants according to symbol denoting in the figure.

$N$  in Fig.4 is the number of experiment,  $N_*$  is amount of stars in the sample. It demonstrates the real shift of coordinates expressed in arc minutes by each model. According to Fig.4 we found the method of 8 and 6 constants to fit the data best. As regards to the prediction deviation we obtained good results in each method except the linear one. As of criteria of the model choice we found that neither Eq. 1 nor Eq. 3 gives the answer on this question. We plan to continue an examination of this problem over larger statistics.

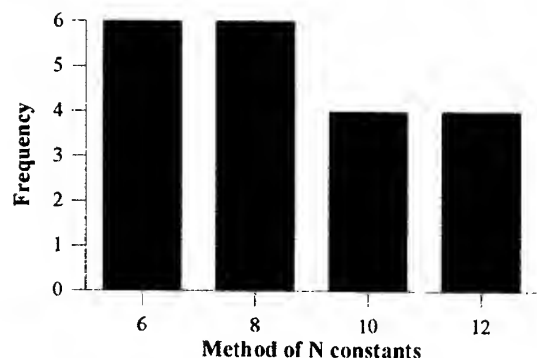


Fig. 3. Meeting frequency of each method as the one giving the best result

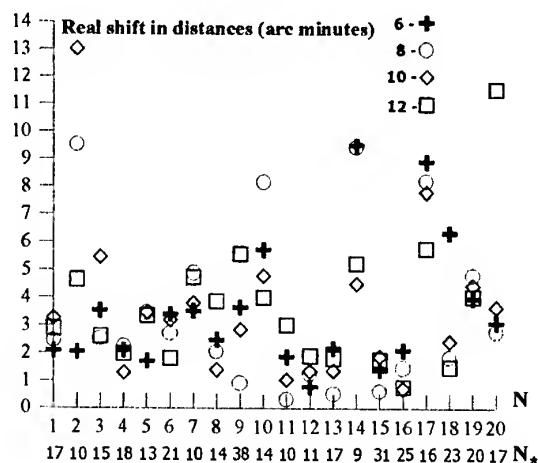


Fig. 4. Processing of a star as unknown object with different models

#### 4. KINEMATIC PROCESSING METHOD OF TV METEORS

For the sequential kinematic processing of measured coordinates of a meteor a method was used which is wholly based on the vector analysis. All computations of meteor trajectory were carried out in rectangular coordinates in geocentric geographical system and its topocentric analogs. Some of formulas are similar to ones obtained by other authors, for example [4]. For the orbit parameters calculation we used some formulas from [5] and [6]. The detailed description of the method is given elsewhere.

#### 5. PHOTOMETRICAL MEASUREMENTS

Photometrical parameters of a meteor and reference stars, which are proportional to the energy emitted by them and can be measured in a TV frame are volumes of their images  $V_*$  and  $V_m$ . For a star exposed in the same point during a whole frame time  $\tau = 0.04$  seconds we measure total volume of star image  $V_*$ . To get the best quality for a meteor we have to make as many orthogonal to the direction of the meteor motion narrow photometrical profiles as possible – Fig.5.

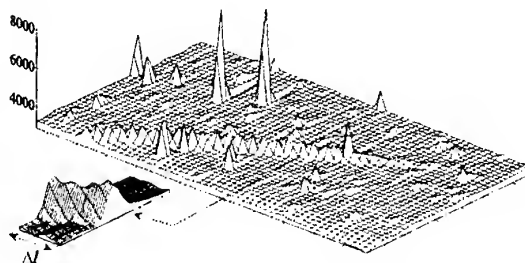


Fig. 5. Three dimensional image of a meteor and the scheme of the photometrical profiles

If we denote the length of the photometrical profile along the meteor trail as  $\Delta l$  it is obvious that the most possible narrow profile has the length of one pixel, that is  $\Delta l = 1$ . In order to compare the measurements, say volume of the meteor image  $V_m$  with the profile length  $\Delta l$  and a star image volume  $V_*$  one should know the time the meteor spent to pass the way  $\Delta l$ . For a meteor point placed at the angular distance  $\alpha$  from the optical center we can derive the following formula by means of geometrical projection method

$$\Delta l = \Delta \gamma \frac{F}{\cos \alpha} \sqrt{1 + \frac{\tan^2 \alpha \cos \alpha}{\tan \beta + \cos \alpha}}, \quad (5)$$

where  $\Delta \gamma$  is an angular shift of meteor which corresponds to desired projection shift  $\Delta l$  in the focal area,  $F$  is the lens focal distance expressed in pixels,  $\beta$  is an angle in the focal area between meteor trail direction and direction from the given meteor point to the optical center. As it can be seen the square root in the right part of Eq. 5 is equal to  $\cos^2 \alpha$  when the meteor is moving along a line directed to the optical center ( $\beta = 0^\circ$ ) and 1 when along orthogonal direction to the one mentioned above ( $\beta = 90^\circ$ ). Denoting everything in the right part in Eq. 5 except  $\Delta \gamma$  as  $P_S^{-1}$  we will obtain the following formula

$$\Delta l = \Delta \gamma / P_S. \quad (6)$$

The new variable  $P_S(F, \alpha, \beta) = \Delta \gamma / \Delta l$  introduced like that is nothing else but a scale in the focal area (angular pixel size), which is correct for the frame region at angular distance  $\alpha$  from the optical center. This value can be easily determined experimentally over reference stars around the meteor except being calculated by Eq. 5. Such approach is also more preferable, taking into account that Eq. 5 was derived for the ideal projection, whereas pixels can have different sizes along two axes as it was noted above. The average value can be determined by the following formula

$$P_S(\alpha) = \frac{2}{N(N-1)} \sum_{i=1}^{N-1} \sum_{j=i+1}^N \frac{\Delta \gamma_{*ij}}{\Delta l_{*ij}},$$

where  $\Delta \gamma_{*ij}$  and  $\Delta l_{*ij}$  are angular and linear distances between  $i$ -th and  $j$ -th stars in the star sample respectively. If we also want to take into account the dependence of this value on meteor trail direction (angle  $\beta$ ) we can plot the graph like in the Fig. 6 and select the direction we need. The circle symbols in the Fig. 6 correspond to pixel size near the optical

center, plus signs – at the peripheral region of the frame.

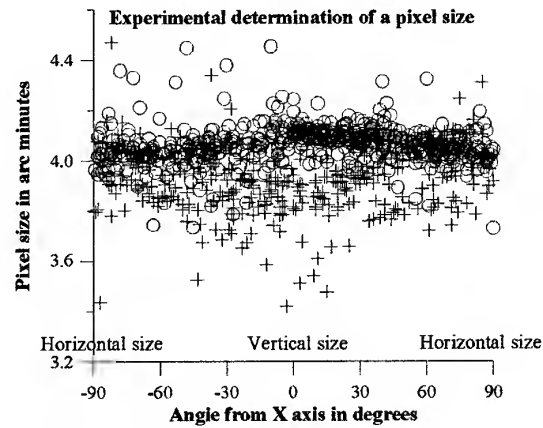


Fig. 6. Pixel size calculated over the stars

Dividing Eq. 6 by  $\Delta t$  and initiating angular velocity  $\Delta \gamma / \Delta t = \omega$  we obtain the following final expression for  $\Delta t$  interval determination:

$$\Delta t = \frac{\Delta l \cdot P_S}{\omega} \quad (7)$$

So, the measured star volume  $V_*$  refers to the exposure time  $\tau$  and the meteor profile volume  $V_m$  of the length  $\Delta l$  refers to the time interval  $\Delta t$ .

## 6. DETERMINATION OF TV METEOR STAR MAGNITUDE

As it is known, star magnitude of any point object on the celestial sphere in  $k$ -th photometrical system can be expressed by Pogson's formula:

$$m_k = -2.5 \lg \int E_\lambda S_{k\lambda} d\lambda + C_k, \quad (8)$$

where  $E_\lambda$  is the curve of luminosity of an object as a function of wave-length,  $S_{k\lambda}$  is the curve of spectral sensitivity of  $k$ -th photometrical system. The constant  $C_k$  is a logarithm of the luminosity of a star the star magnitude of which is assumed to be zero in the given photometrical system. Usually this star is one of spectral type A with a zero visual magnitude

$$C_k = 2.5 \lg \int E_{A0\lambda} S_{k\lambda} d\lambda. \quad (9)$$

Let us denote the spectral sensitivity curve of multialkali photocathode used in our TV system as  $S_{TV\lambda}$ . As far as there are no catalogues obtained with such spectral curve we have to derive a formula to establish connection between the TV system and any other photometrical system. Star magnitude in TV

system and zero point of our system can be written similarly to Eqs. 8-9 supposing  $k = TV$ . The formula of connection between two systems can be written now as

$$m_{TV} = m_k - 2.5 \lg \frac{\int E_{\lambda} S_{TV} d\lambda}{\int E_{\lambda} S_k d\lambda} + C_{TV} - C_k. \quad (10)$$

This correction can be calculated theoretically for each spectral type star and, for instance, presented as a table. For this purpose one can use relative curves  $E_{\lambda}$  normalized to a some wave-length, for example  $\lambda = 555 \text{ nm}$ .

Let's consider briefly the process of applied determination of the meteor star magnitude. First we measure  $V_*$  of reference stars with known star magnitudes in  $k$ -th photometrical system. Then we calculate the TV star magnitudes of these stars according to Eq. 10 and plot the calibration curve as a dependence of  $V_*$  (or  $\lg V_*$ ) on  $m_{TV}$ . The next step of photometrical processing is to measure the volumes  $V_m$  (profiles) of the length  $\Delta l$  (usually  $\Delta l = 1$ ) along the meteor trail and to calculate corresponding time intervals  $\Delta t$  by Eq. 7. We assume that angular velocities  $\omega$  and pixel sizes  $P_s(f, \alpha, \beta)$  are already calculated. As the calibration curve is built by stars with exposure time of one frame  $\tau$  the computed meteor volumes  $V_m(\Delta t)$  has to be brought to the same times as follow:

$$V_m(\tau) = \frac{\tau}{\Delta t} V_m(\Delta t). \quad (11)$$

If we had to deal with ideal TV system with strongly linear response we could use the value computed by the Eq. 11 and obtain the desired star magnitude of meteor from the calibration curve. As it was shown in [7], the real situation is such that we cannot be sure that the image volume  $V(\tau, \omega_i)$  of the object, which moves with angular velocity  $\omega$ , brought to time  $\tau$  is equal to its really immovable volume  $V(\tau, 0)$ . In order to compute this possible difference an experiment can be used with moving camera (a type of "artificial meteor" experiment) with the range of fixed angular velocities. In this case image volumes of the same stationary and movable stars are measured. Then the results of such experiment can be presented as a table or in functional form, for instance, as a following relation:

$$V(\tau, \omega_i) / V(\tau, 0) = f_{\exp} \{ \omega, V(\tau, 0) \}. \quad (12)$$

So, the value obtained from Eq. 11 has to be corrected to its "stationary volumes" by experimentally obtained Eq. 12 before using the calibration curve.

Also one should note such an important element of photometrical measurements as photometrical field correction. In our investigations we brought the measured volumes up to the center of the frame before using. The photometrical correction itself was carried out over stars, which had been exposed in different places of the frame. The results of such correction can be seen in Fig. 7. According to the figure, this correction does not exceed 0.4 star magnitude and is usually smaller.

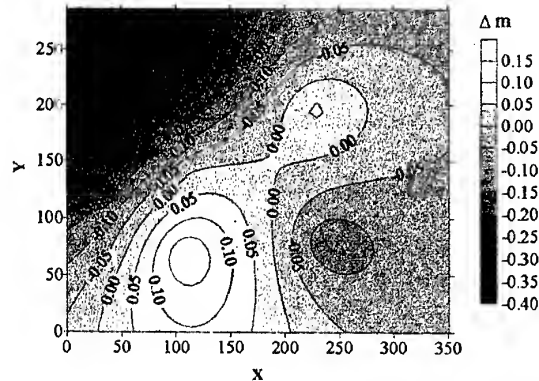


Fig. 7. Photometrical field correction determined over the stars in the frame.

## 7. CONCLUSIONS

Computer processing allows us to realize kinematic and photometrical treatment of TV meteors in a very convenient way and quickly. The precision of results obtained from such processing is conditioned mainly by the TV system parameters: one pixel is approximately 4 arc minutes, temporal resolution is 0.04 second. The altitudes determination precision of meteors trajectory is about 100-200 meters. The velocity error corresponds to 2-3 km/sec. We estimate that the star magnitude of the faintest meteor we can observe with our TV system and objective lens "Jupiter-3" is approximately 7.

## 8. REFERENCES

1. Kiselev A.A., A vector interpretation of main methods of photographic astrometry, *Astronomical Journal (Rus.)*, XLII, Vol. 2, 452-463, 1965.
2. Valeev S.G., *Regression modeling in observations treatment*, Nauka, Moscow, 1991.
3. Whipple F.L. and Jaccia L.G. Reduction methods for photographic meteor trails, *Smithsonian Contr. to Astrophys.*, I, Vol. 2, 183-206, 1957.
4. Deutsch A.N., On the reduction of photographic positions at an arbitrary optical center, *Astronomical Journal (Rus.)*, XLII, Vol. 5, 1114-1116, 1965.
5. Roy A.E. *Orbital motion*, Mir, Moscow, 1961.
6. Herrick S., *Astrodynamic*, Mir, Moscow, 1976.
7. Kozak P.M. On the internal precision of digital photometry of meteors from TV observations, *Kinematics and physics of celestial bodies (Ukr.)*, 14, Vol. 6, 1998.

## **Impacts of Meteoroids on the Atmosphere**

# THE DISPERSION OF THE SWARM OF FRAGMENTS OF LARGE METEORIDS DUE TO AERODYNAMIC FORCES

Yang Su

*Beijing Astronomical Observatory, Chinese Academy of Sciences, Beijing 100012, P.R.China*  
*National Astronomical Observatories, Chinese Academy of Sciences, Beijing 100012, P.R.China*  
*Email: ysu@bao.ac.cn*

## ABSTRACT

To gain insight into the dispersion of the swarm of fragments due to differential atmospheric pressure across it, I derive an approximate analytical solution to the simple analytic model of lateral spreading of the cylinder-like swarm of fragments in which gravitational acceleration and ablation are neglected <sup>[1]</sup>, <sup>[2]</sup>. The solution is applicable to the initial fragmentation stage of large meteoroids with  $R_0 < R_c$ ,  $\leq 0.05 R_c$ , where  $R_c$  is the critical radius for aerodynamic dispersion. For such meteoroids, fragmentation by aerodynamic forces is too small to cause catastrophic fragmentation or atmospheric explosion. The swarm of fragments never expands up to 1.3 times the initial radius of meteoroid at the end of the initial fragmentation stage. After that, further fragmentation and even atmospheric explosion is possible to occur, but the simple analytic model and its solution are no longer applicable.

**Key Words:** meteoroids, atmosphere, dynamics

## 1. INTRODUCTION

Fragmentation by aerodynamic forces is an important mechanism of disintegration of meteoroids during their flight in the atmosphere. So long as the size of meteoroid is not too small or too large, fragmentation is inevitable. If a meteoroid is too small, it would be either completely ablated or be aerobraked to a free-fall speed, so fragmentation won't occur. But if a meteoroid is too large, it can go through the atmosphere without fragmentation, because an atmospherically induced pressure has insufficient time to cross it before it strikes the Earth.

Melsosh <sup>[3]</sup>, <sup>[4]</sup> defined a critical radius  $R_c$  for the aerodynamic dispersion of meteoroids in the atmosphere as

$$R_c = \frac{H}{\sin \theta} \left( \frac{\rho_0}{\rho_m} e^{-\frac{z}{H}} \right)^{\frac{1}{2}} \quad (1)$$

where  $\theta$  and  $\rho_m$  are the entry angle (measured from the horizontal) and density of meteoroid respectively, and  $z$  denotes the altitude at which fragmentation occurs. Here an exponential atmosphere is adopted,  $\rho_0 = 0.001293 \text{ g cm}^{-3}$  is the atmospheric density at  $z = 0$ ,  $H$  is the scale height of the atmosphere. If  $R_0 > R_c$ , the atmospheric dispersion would be negligible; if  $R_0 < R_c$ , aerodynamic forces is enough to cause deceleration and fragmentation of meteoroids.

The critical value  $R_c$  is closely connected with the strength of meteoroids which depends on material, structure, composition, dimension, shape, and their evolutionary history. Thus  $R_c$  is not a universal constant, the value of  $R_c$  may be distinct for each individual meteoroid. In order to have a idea of the magnitude of  $R_c$ , assuming  $H=8.5 \text{ km}$  and the atmospheric density  $\rho_a = \rho_0 \exp(-z/H) = 0.001 \text{ g cm}^{-3}$ , and taking  $\theta$  to be the most probable entry angle of  $45^\circ$  for an incident meteoroid, we can get rough estimates of  $R_c$  for four types of meteoroids:  $R_c=135 \text{ m}$  for the iron meteoroid ( $\rho_m=7.9 \text{ g cm}^{-3}$ ),  $R_c=200 \text{ m}$  for the stony meteoroid ( $\rho_m=3.5 \text{ g cm}^{-3}$ ) and  $R_c=260 \text{ m}$  for the carbonaceous meteoroid ( $\rho_m=2.2 \text{ g cm}^{-3}$ ),  $R_c=380 \text{ m}$  for icy meteoroids ( $\rho_m=1 \text{ g cm}^{-3}$ ).

The work presented here is only concerned with the meteoroids with  $R_0 < R_c \leq 0.05 R_c$ . From the estimates of  $R_c$  above, we can see that the meteoroids with  $R_0=0.05 R_c$  would be above several meter in radius, so we may classify them as large meteoroids. In this paper the term "large meteoroid" always means the meteoroids with  $R_0 < R_c \leq 0.05 R_c$ . For meteoroids with  $R_0 < 0.05 R_c$ , ablation may not be completely neglected, and there is not enough mass to form a swarm of fragments with a somewhat aerodynamic dispersion, so they are not in our consideration. But for meteoroids with  $R_0 \geq 0.05 R_c$ , ablation is so little as to be ignored, as the first-order approximation we can only consider mechanical processes. <sup>[5]</sup>

Heavy fragmentation always takes place on the whole of large meteoroid, the heavily fragmented matter can be enclosed by a single collective bow shock and behaves as a fluid, so that the swarm of fragments

presents a united front to the atmosphere. However, the atmospheric pressure on its front doesn't match up to the atmospheric pressure on its sides, thus the swarm of fragments spread laterally, with the increases of its effective cross-section. By approximating the effective cross-section by balancing the aerodynamic forces on its front with its inertia, Chyba et al.<sup>[1]</sup> derived a simple analytic model of fragments spreading.

The simple model has been applied to assess Tunguska explosion<sup>[1]</sup> and the atmospheric explosions happened on Jupiter<sup>[2]</sup> and Venus<sup>[6]</sup>. Catastrophic fragmentation is regarded as a likely means of producing an explosion of a meteoroid<sup>[1], [6]</sup>. With the increase of effective cross-section, the swarm of fragments is possible to intercept a more and more mass of atmosphere, being seriously decelerated by aerobraking. If the swarm of fragments is abruptly decelerated to stop, surrendering its kinetic energy explosively, then catastrophic fragmentation is expected to happen.

In this paper, I will give an analytic approximation to the spreading model, and then the solution will be used to discuss the aerodynamic dispersion of the swarm of fragments of large meteoroids. My primary concern in this paper is to make clear whether aerodynamic forces is enough to cause catastrophic fragmentation or atmospheric explosion at the initial fragmentation of large meteoroids.

## 2. APPROXIMATE ANALYTIC SOLUTION OF FRAGMENTS SPREADING EQUATION

Assuming that the swarm of fragments has a cylinder-like shape, and assume that the density of heavily fragmented matter remains constant, Chyba et al.<sup>[1]</sup> have derived a fragments spreading equation. in the form

$$\frac{d^2 R}{dt^2} = \frac{C_D}{2} \frac{\rho_0}{\rho_m} e^{-\frac{z}{H}} v^2 \quad (2)$$

where  $R$  denotes the effective radius of the swarm of fragments,  $C_D$  is the drag coefficient ( $C_D \approx 0.9$  for a sphere and 1.7 for a cylinder). In terms of the altitude  $z$  and entry angle  $\theta$ , Eq.(2) can be expressed as<sup>[2]</sup>

$$\frac{d^2 R}{dz^2} + \frac{1}{v} \frac{dv}{dz} \frac{dR}{dz} = \frac{C_D}{2} \frac{1}{\sin^2 \theta} \frac{\rho_0}{\rho_m} e^{-\frac{z}{H}} \quad (3)$$

Deceleration of the swarm of fragments can be described by the equation in terms of the altitude  $z$  and entry angle  $\theta$ <sup>[2]</sup>:

$$m \frac{dv}{dz} = \frac{C_D}{2} \frac{S}{\sin \theta} \frac{\rho_0}{\rho_m} e^{-\frac{z}{H}} v \quad (4)$$

where  $S = \pi R^2$  is the geometric cross section of the swarm of fragments,  $m = \frac{3}{4} \pi R_0^3 \rho_m$ , assuming the initial meteoroid is a sphere of radius  $R_0$  and density  $\rho_m$  and no the loss of mass by ablation. Substituting Eq.(4) into Eq.(3), we can rewrite the fragments spreading equation Eq.(2) as

$$R \frac{d^2 R}{dz^2} + \frac{3C_D}{8} \frac{1}{\sin \theta} \frac{\rho_0}{R_0^3 \rho_m} e^{-\frac{z}{H}} R^3 \frac{dR}{dz} - \frac{C_D}{2} \frac{1}{\sin^2 \theta} \frac{\rho_0}{\rho_m} e^{-\frac{z}{H}} = 0 \quad (5)$$

Clearly, the dispersion of the swarm of fragments occurs after meteoroid breakup, the initial conditions

$$R(z_b) = R_0, \quad \frac{dR(z_b)}{dz} = 0 \quad (6)$$

must be satisfied, where  $z_b$  is the breakup altitude at which the meteoroid begins to break up. Then we now look for a solution of Eq.(5) in the power series form

$$R(z) = \sum_{i \geq 0} a_i(z) \left( \frac{\rho_0}{\rho_m} \right)^i \quad (7)$$

where  $a_i(z)$  is the undermined coefficient. From the initial condition (6), we obtain

$$\begin{aligned} a_0(z_b) &= R_0, \quad a_i(z_b) = 0 \quad (i \geq 1), \\ \frac{d a_i(z_b)}{dz} &= 0 \quad (i \geq 0). \end{aligned} \quad (8)$$

By substituting Eq.(7) into Eq.(5), combining coefficients of like power of  $\rho_0/\rho_m$ , we get a second

order linear differential equation of  $a_i(z)$  ( $i \geq 2$ ) in the form

$$\frac{d^2 a_i(z)}{dz^2} = f(z, a_{i-1}(z), a_{i-2}(z)) \quad (9)$$

Solving recursively Eq.(7), we can derive the solution of Eq.(5) term by term. For the first-order approximation, it is enough to carry it to the third-order term, thus the analytic approximate solution to Eq.(5) is written as

$$\begin{aligned} R(z) = R_0 & \left\{ 1 + \left( \frac{C_D}{8} \right) \left( \frac{H}{R_0 \sin \theta} \right)^2 e^{-\frac{z}{H}} \frac{\rho_0}{\rho_m} + \left( \frac{C_D}{8} \right)^2 \times \right. \\ & \left[ \frac{2}{3} \left( \frac{H}{R_0 \sin \theta} \right)^3 e^{-\frac{3z}{H}} - \frac{1}{4} \left( \frac{H}{R_0 \sin \theta} \right)^4 e^{-\frac{4z}{H}} \right] \left( \frac{\rho_0}{\rho_m} \right)^2 \\ & + \left( \frac{C_D}{8} \right)^3 \left[ \frac{13}{432} \left( \frac{H}{R_0 \sin \theta} \right)^6 e^{-\frac{6z}{H}} - \frac{3}{50} \left( \frac{H}{R_0 \sin \theta} \right)^5 e^{-\frac{5z}{H}} \right] \\ & \left. \times \left( \frac{\rho_0}{\rho_m} \right)^3 \right\} \quad (10) \end{aligned}$$

### 3. THE CONVERGENCE OF THE SOLUTION

It is important to make sure whether the solution (10) is a good approximation to Eq. (5). To this end, we need to examine the convergence of the solution (10). By substituting Eq. (1) into Eq. (10), the solution becomes

$$\begin{aligned} R(z) = R_0 & \left\{ 1 + \frac{C_D}{8} \left( \frac{R_*}{R_0} e^{-\frac{z}{2H}} \right)^2 + \left( \frac{C_D}{8} \right)^2 \times \right. \\ & \left[ \frac{2}{3} \left( \frac{R_*}{R_0} e^{-\frac{z}{2H}} \right)^3 \left( \frac{\rho_0}{\rho_m} \right)^{\frac{1}{2}} - \frac{1}{4} \left( \frac{R_*}{R_0} e^{-\frac{z}{2H}} \right)^4 \right] \\ & + \left( \frac{C_D}{8} \right)^3 \left[ \frac{13}{432} \left( \frac{R_*}{R_0} e^{-\frac{z}{2H}} \right)^6 - \frac{3}{50} \left( \frac{R_*}{R_0} e^{-\frac{z}{2H}} \right)^5 \right] \\ & \left. \times \left( \frac{\rho_0}{\rho_m} \right)^{\frac{1}{2}} \right\} \quad (11) \end{aligned}$$

Moreover, if need be, we can continue to solve recursively Eq.(9) to any order in  $\rho_0/\rho_m$ . For  $i > 3$ , the  $i$ -order term  $R_i(z)$  can be put in the form

$$\begin{aligned} R_i(z) = & \left( \frac{C_D}{8} \right)^i \left[ \frac{a_{i,2i}}{(2i)^2} \left( \frac{R_*}{R_0} e^{-\frac{z}{2H}} \right)^{2i} \right. \\ & \left. - \frac{a_{i,2i-1}}{(2i-1)^2} \left( \frac{R_*}{R_0} e^{-\frac{z}{2H}} \right)^{2i-1} \left( \frac{\rho_0}{\rho_m} \right)^{\frac{1}{2}} \right] \quad (12) \end{aligned}$$

where  $a_{i,2i}$ ,  $a_{i,2i-1}$  are the relevant coefficients, satisfying

$$\begin{aligned} a_{i,2i} & \sim 1, & a_{i,2i-1} & \sim 1, \\ a_{i+1,2(i+1)} & < a_{i,2i}, & a_{i+1,2i+1} & < a_{i,2i-1}. \end{aligned}$$

Noting that  $(\rho_0/\rho_m)^{1/2} \sim 10^{-2}$ , the last term in the brackets of Eq.(12) is an order of magnitude less than the first term, hence

$$R_i(z) < \left( \frac{C_D}{8} \right)^i = 0.2^i \quad \text{if} \quad \frac{R_*}{R_0} e^{-\frac{z}{2H}} \leq 1$$

where  $C_D \sim 1.7$ . Therefore,  $R(z) = \sum R_i(z) < \sum (C_D/8)^i$  is uniformly absolutely convergent, thus Eq.(10) is indeed an analytic approximate solution of fragments spreading equation.

We now estimate the error of the solution (10). As showed above, the convergent infinite series  $R(z) = \sum R_i(z)$  represents the exact solution to Eq.(5), the approximate solution is taken as the truncation of the infinite series, so the error of the approximate solution is given by its truncation error. Let  $R^N(z)$  indicate  $N$ -order approximate solution to Eq.(5) and  $r^N(z)$  indicate the remainder after  $N$  term, that is,  $R(z) = \sum R_i(z) = R^N(z) + r^N(z)$ , hence the truncation error of  $N$ -order approximate solution can be given by the error bound of the remainder  $r^N(z)$ :

$$\begin{aligned} r^N(z) &= R_0 \sum_{N+1}^{\infty} \left( \frac{C_D}{8} \right)^i = R_0 \left( \frac{C_D}{8} \right)^i \left( 1 - \frac{C_D}{8} \right)^{-1} \\ &< 1.3 \times 0.2^N R_0 \end{aligned}$$

Hence the error of the solution (10) is less than  $0.01R_0$ , and the error of the first-order solution, which only contains the first two terms of Eq.(10), is less than  $0.1R_0$ . Therefore, the solution given here is good approximation to the simple analytic model.

For the large meteoroid, the convergence condition can be rewritten as

$$R_* > R_0 \geq R_* e^{-\frac{z_c}{2H}} \quad (13)$$

where  $z_c$  is the critical altitude at which the collective bow shock breaks down. If  $R_0 \geq R_*$ , then aerodynamic dispersion can be neglected. Thus the convergence domain of the solution (10) depends on not only  $R_0$  but also  $z_c$ .

Fig. 1 indicates the range of large meteoroids which the solution (10) is applicable to, where  $z_c$  and  $R_0$  is normalized by dividing by  $H$  and  $R_*$  respectively. In Fig. 1, the line "Breakup" denotes the breakup altitude  $z_c$  of a meteoroid with density  $3 \text{ g cm}^{-3}$  and velocity  $v = 15 \text{ km s}^{-1}$  as a function of  $R_0$ , which is based on Svetsov et al.<sup>[5]</sup>. The region where the solution (10) is applicable to large stony meteoroids is between the two lines in Fig. 1. The region to be applicable to large icy and carbonaceous meteoroids should be above that while the region to be applicable to large iron meteoroids should be below that. If  $R_0$  is close to  $R_*$ ,  $z_c$  is close to  $6H$ , few iron meteoroids of such a size fracture above such a altitude, thus the solution (10) is not applicable to them. However, it is still applicable to large icy meteoroids, large carbonaceous meteoroids and most of large stony meteoroids, their initial fragmentation should take place above such altitudes. Therefore we can conclude that the solution (10) is applicable for the most part of large meteoroids.

#### 4. THE DISPERSION OF THE SWARM OF FRAGMENTS OF LARGE METEORIODS

Using the approximate analytical solution (10), we may go further into the aerodynamic dispersion of the swarm of fragments described by the simple analysis model (1). In the simple model (1), the aerodynamic dispersion only results from the differential atmospheric pressure across the swarm of fragments. The differential atmospheric pressure makes fragments spread laterally, with the consequence that the descent of the swarm slows down due to the increase of its effective cross-section. It is an open question that how far the swarm of fragments can spread to during the period of the simple model being effective; it is

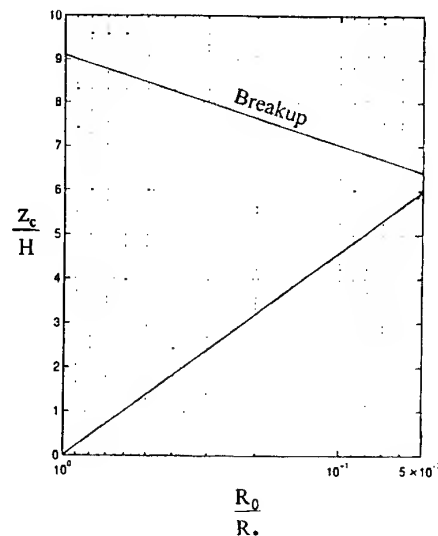


Fig. 1. The applicable range of the analytical solution. The "Breakup" line is based on Svetsov et al.<sup>[5]</sup>, an analytical estimation for large meteoroids with density  $3 \text{ g cm}^{-3}$  and velocity  $v = 15 \text{ km s}^{-1}$ .

conventionally assumed to be twice the initial radius  $R_0$ <sup>[1][2][6]</sup>

The simple model (1) has applied to assess atmospheric explosions occurred on Earth<sup>[1]</sup>, Jupiter<sup>[2]</sup> and Venus<sup>[6]</sup>. Catastrophic fragmentation was considered to be a likely means of producing an atmospheric explosion of a fragmenting meteoroid. Zahnle and MacLow<sup>[2]</sup> suppose an atmospheric explosion would happen if the swarm of fragments stops over about half a scale height, liberating most of its kinetic energy in about 1 s. The explosion altitude was define by Chyba et al.<sup>[1]</sup> as the altitude at which the swarm of fragments has spread to twice its initial radius. They hold that once  $R=2R_0$ , its further spreading happens so quickly that the explosion altitude can be defined to a few kilometers.

However, the solution (10) demonstrates a rather small lateral spreading of the swarm of fragments. From Eq.(10), it follows that

$$R(z) \approx R_0 \left[ 1 + \frac{C_D}{8} \left( \frac{R_*}{R_0} e^{-\frac{z}{2H}} \right)^2 \right] < 1.3 R_0$$

hence the effective cross-section area of the swarm is always less than twice its initial cross-section area, so its fragmentation is far from being catastrophic.

Anyway, so long as the swarm of fragments has been confined within such a small area, there have to be no catastrophic fragmentation. Therefore the aerodynamic forces described by the simple model (1) seem to be not enough to cause the atmospheric explosion of large meteoroids.

We must keep in mind that Eq.(1) is hold only if the collective bow-shock approximation is effective. It is a short time interval after fragmentation that a single bow shock encloses the swarm of fragments. After that, the initial bow shock wave would be severely distorted soon, even the single bow shock dissolves into separate bow shocks, so that Eq.(1) is no longer a good approximation. Besides aerodynamic forces, mechanical mass losses caused by hydrodynamic instabilities play an important role in the evolution of the swarm of fragments<sup>[5]</sup>, the atmospheric explosion obviously is the results of the instabilities developed after the initial bow shock wave broken down.

Actually, the swarm of fragments can be subjected to multiple-stage fragmentation. In the case of multiple-stage fragmentation, the aerodynamic dispersion of the swarm of fragments described by the simple model (1) should occur in the first-stage fragmentation, while the atmospheric explosion should happen in the final fragmentation stage. Thus the solution Eq.(10) is no longer applicable to the latter stage of evolution of the swarm, but it is still able to set the upper bounds to the atmospheric explosion., let us get some understanding of it.

Tunguska belongs to the large meteoroids studied here, its explosion altitude  $z_A \approx 1H$ ,  $H=8.4$  km,  $30^\circ \leq \theta \leq 45^\circ$ , with a preferred value of  $\theta=40^\circ$ . As stated above, the fragmentation of Tunguska should occur in several stages. For each type of meteoroid (iron, carbonaceous, stony and icy meteoroid), we suppose a lower bound of critical altitude  $z_c$  based on its strengths, and then we can set a upper bound of the initial radius  $R_0$  of Tunguska meteoroid, respectively. They are given in Table 1 where  $\theta=40^\circ$ ,  $H=8.4$  km, and the atmospheric density  $\rho_a = 0.001$  g cm<sup>-3</sup>.

Table 1 The upper bound of the initial radius  $R_0$  of Tunguska meteoroid

Type	$\rho_m$ (g cm <sup>-3</sup> )	$R_c$ (m)	$z_c$ (H)	$R_0$ (m)
Iron	7.9	148	$\geq 2$	$\leq 54$
Stony	3.5	220	$\geq 3$	$\leq 48$
Carbonaceous	2.2	280	$\geq 4$	$\leq 38$
Icy	1	415	$\geq 5$	$\leq 34$

It can be seen from Table 1 that, no matter which type of meteoroid it was, the initial radius  $R_0$  of Tunguska meteoroid should be less than a upper bound between 34 m and 54 m. The bound is consistent with the ones Chyba et al<sup>[1]</sup> gave by using the same model (1). However, with the purpose of defining an explosion altitude, Chyba et al<sup>[1]</sup> used the simple model (1) to calculate the spreading radius  $R$  up to twice or 5-10 times the initial radius  $R_0$ . As pointed out above, it is doubtful. If  $R > 1.3 R_0$ , Eq.(1) is no long a good approximation, thus the explosion altitude is not true.

## 5. CONCLUSION

In the virtue of the analytic approximate solution of fragments spreading equation<sup>[1], [2]</sup>, we have an insight into the lateral dispersion of the swarm of fragments in the initial fragmentation stage due to differential atmospheric pressure across it. For large meteoroids ( $R_c < R_0 \leq 0.05 R_c$ ), fragmentation by aerodynamic forces is far from catastrophic, the spreading radius  $R$  is always less than  $1.3R_0$ . Once  $R > 1.3R_0$ , the simple model (1) and its solution (10) is no longer applicable. During the period, no atmospheric explosion can occur.

The swarm of fragments is usually subjected to multiple-stage fragmentation. If so, the aerodynamic dispersion of the swarm of fragments described by Eq. (1) should occur in the first-stage fragmentation while atmospheric explosion should happen in the final fragmentation stage. Still we may use the simple model (1) to set upper bounds to atmospheric explosion, but it is problematic to determine an explosion altitude by applying it up to twice or 5-10 times the initial radius  $R_0$ .

## ACKNOWLEDGMENTS

The author is grateful for the financial support from the Local Organizing Committee of the Meteoroids 2001 Conference at the Swedish Institute of Space Physics, Kiruna, Sweden. The author also thanks the National Natural Science Foundation of China (NFSC) for providing travelling expenses for me to extend to the Meteoroids 2001 Conference. The work is supported by the NFSC grant 19973011.

## REFERENCES

1. Chyba, C. F., P. J. Thomas, & K.J. Zahnle., The 1908 Tunguska explosion: atmospheric disruption of a stony asteroid, *NATURE*, Vol. 361, 40-41, 1993.

2. Zahnle, K. and M.-M. MacLow., The collision of Jupiter and Comet Shoemaker-levy 9. *ICARUS*, Vol. 108, 1-17, 1994.
3. Melsosh, H. J., *Impact cratering: A geologic Process*, Oxford Univ. Press, New York /Clarendon Press, Oxford, 1989.
4. Svetsov, V. V. and Nemtchinov, I. V., Consequences of impacts of cosmic bodies on the surface of the Earth, In: *Hazards Due to Comets and Asteroids* (T. Gehrels, Ed.) pp. 721-778, Univ. Arizona Press, Tucson, 1995.
5. Svetsov, V.V. and Nemchinov, I. V., Disintegration of large meteoroids in Earth's atmosphere: Theoretical models, *ICARUS*, Vol. 116, 131-153, 1995.
6. Zahnle, K.J., Airburst origin of dark shadows on Venus, *J. Geophys. Res.*, Vol. 97, 10243-10255, 1992.
7. Hill, J.G. and Goda, M. P., The fragmentation of small asteroids in the atmosphere, *Astron. J.*, Vol. 105, 1114-1144, 1993.

# THERMAL EXPLOSIONS OF METEOROIDS IN THE EARTH ATMOSPHERE

Vitaliy G. Kruchynenko

*Astronomical Observatory of Taras Shevchenko National University,  
Observatorna Str. 3, 04053 Kyiv, Ukraine, Email: [kruch@observ.univ.kiev.ua](mailto:kruch@observ.univ.kiev.ua)*

## ABSTRACT

Based on a data analysis about bright flashes of large meteoroids in a terrestrial atmosphere we come to a conclusion, that such thermal explosions happen at the height of maximum deceleration. Such assumption confirms also explosion of Shoemaker-Levy 9 comet in atmosphere of Jove. In this area on a small interval of altitudes (significant less than altitude of a homogenous atmosphere, therefore explosion can be considered as the point one) the loss of energy by a body on deceleration surpasses energy, which is indispensable for a full evaporation of whole body. At the same time, achievement by a meteoroid of the altitude of maximum deceleration is condition indispensable, but not sufficient that there was a thermal explosion. It is known the meteoroids, which reach the altitude of maximum deceleration, but explosion does not happen.

## 1. INTRODUCTION

Today a significant number of cases of explosions of large meteoroids in the Earth atmosphere is already known. Registrations of bolids by geostationary satellites [7,11] and data of measurements of acoustic and gravity waves from explosions of the meteoroids [10] also testify to the fact.

According to the results from Prairie Network Fireball Data [5,6], approximately 30% of meteoroids with the initial masses no less than 1 kg have reached heights  $H \leq 30$  km. Only a minor part of these meteoroids (no more than 1% – 2%) can generate thermal explosions in the low layers of atmosphere.

On the basis of the data analysis concerning such terrestrial phenomena as Tunguskiy, Sikhote-Alin', Sterlitamak, Kun'-Urgench etc., we came to a conclusion that thermal explosions of similar meteoroids and, as a consequence, flashes of brightness, happen in the areas of the altitudes of maximum deceleration.

When studying destruction of pieces of the Shoemaker-Levy 9 nucleus in atmosphere of the Jupiter we confirmed idea of thermal explosion at the altitude of maximum deceleration [4]. The main argument is the good agreement of time of the Plume exit to the Jupiter's atmosphere "surface" with the data of direct observations from space vehicles.

Independent confirmation of the depth, obtained by us, of explosion of a cometary piece diameter of 1 km can be found in the work of Berezhnoi et al. [1]. In this work the depth of explosion is determined from the analysis of measurement results of radiation of molecules which are generated by explosion and are carried to the upper atmosphere of the Jupiter.

## 2. THE ALTITUDE OF MAXIMUM DECELERATION

By what is characteristic of the altitude of maximum deceleration?

Apparently, it can be determined if we assume that the second derivative from velocity is zero. Sometimes an area of maximum deceleration is incorrectly perceived as an area of delay which is determined from equality of gravity and force of aerodynamic load.

For the analysis of conditions in the field of maximum deceleration the indispensable mathematical model is developed. When calculating an altitude of maximum deceleration two versions can be considered: a cross-section of the body  $S = S_0 = \text{Const.}$  and  $S \neq \text{Const.}$ , where the cross-section depends on the time  $t$  or on the altitude  $H$ . The first case will be realized for very small-sized meteor particles, so-called Whipple's micrometeorites [14], and for very large bodies, for which the effect of Earth atmosphere is minimum. Such large bodies reach the surface of our planet practically without the loss of velocity or mass. The technique of calculation of meteoroid parameters at the altitude of maximum deceleration is simple in this case. The dependence of the deceleration on velocity has a view:

$$\frac{dV}{dt} = -\frac{\cos Z_R}{H^*} \cdot V^2 \cdot \ln \frac{V}{V_0}$$

Maximum deceleration occurs at the velocity of

$$V_* = V_0 \exp(-0,5) \quad (1)$$

and equals

$$\left(\frac{dV}{dt}\right)_* = -\frac{0.184 \cdot \cos Z_R \cdot V_0^2}{H_*} \quad (2)$$

Here  $V$  is the velocity,  $V_0$  is initial of the meteoroid velocity,  $V_*$  is the velocity at the altitude of maximum deceleration,  $Z_R$  is the zenith angle of entry,  $H_*$  is altitude of a homogeneous atmosphere (scale of altitudes).

We determine the maximum deceleration height  $H_*$  from the equation of deceleration, written for  $H_*$ .

$$\rho(H_*) = \frac{M_0^{1/3} \delta^{2/3} \cos Z_R}{2A_0 \Gamma H_*} \quad (3)$$

The mass of a body does not change in this case, i.e. mass of the body at the altitude  $H_*$  equals initial of the meteoroid mass,  $M_* = M_0$ .

Let's consider the second case when the cross-section depends on time or altitude. Thus, the condition of maximum deceleration is as follows:

$$[E_i(U_0) - E_i(U_*)] \cdot (1 - U_*) \cdot \exp(-U_*) = 1, \quad (4)$$

where

$$E_i(U) = \int_{-\infty}^U \frac{\exp t \cdot dt}{t} \quad (5)$$

is the exponential integral function. Eq. 4 determines relation of the meteoroid velocity  $V_*$  at the altitude  $H_*$  of maximum deceleration from its initial velocity, i.e.  $V_*(V_0)$ .

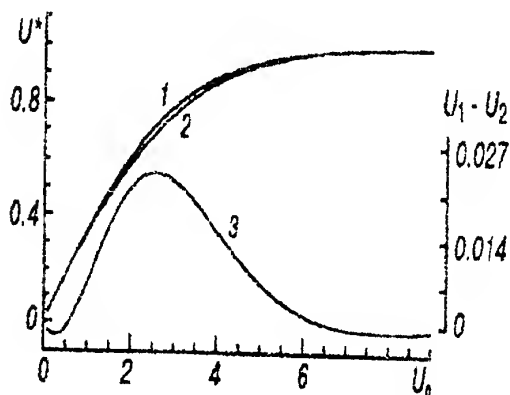


Fig. 1. Relation  $U_*(U_0)$ , obtained from Eq. 4 (curve 2) and its approximation by Eq. 6 (curve 1). Curve  $(U_* - U_p)$  is the difference between the approximating Eq. 6 and precise Eq. 4, multiplied by a factor of 20. The values of the latter are plotted on the axis on the right.

Pecina and Cepelcha [9] were probably the first to obtain it. Here

$$U_0 = \sigma(1 - \mu) \cdot V_0^2 / 2,$$

$\sigma = A / 2\Gamma Q$ , ablation coefficient;  $A$ , heat transfer coefficient;  $\Gamma$ , coefficient of deceleration;  $Q$ , specific ablation energy of a body;  $\mu$ , parameter of body's shape;

$$U_* = \sigma(1 - \mu) \cdot V_*^2 / 2.$$

All values with an lower index "\*" refer to altitude of maximum deceleration. Function  $V_*(V_0)$  is expressed by Eq. 4 implicitly and is not convenient for practical use. Therefore we found rather a precise and quite simple analytical approximation which can be applied to the whole range of the meteor velocity and values of the parameters  $\sigma$  and  $\mu$  [13]:

$$U_* = \text{th}(0.35 U_0),$$

or

$$V_* = \{2\text{th}[0.175\sigma(1-\mu)V_0^2] / \sigma(1-\mu)\}^{1/2} \quad (6)$$

The maximum difference of approximating Eq. 6 and precise Eq. 4 equals 0.0276 at  $U_0 = 2.56$ . With decrease and increase in  $U_0$  from the value of 2.56, difference of reduced functions continuously tends to zero (see the Fig. 1).

When we use Eq. 6, the maximum error in the velocity does not exceed 0.35 km/s.

Relying on Eq. 6, it is easy to receive the formula for maximum deceleration depending on initial velocity:

$$\left[\frac{dV}{dt}\right]_* = -\frac{\text{th}[0.175\sigma \cdot (1-\mu) \cdot V_0^2]}{\{1 - \text{th}[0.175\sigma \cdot (1-\mu) \cdot V_0^2]\}} \times \frac{\cos Z_R}{H_* \sigma \cdot (1-\mu)} \quad (7)$$

The altitude of maximum deceleration of the meteoroid can be determined from the joint Eq. 7 and equation of drag recorded for altitude  $H_*$ .

$$\left[\frac{dV}{dt}\right]_* = -\frac{\Gamma \cdot A_0}{M_0^{1/3} \cdot \delta^{2/3}} \cdot \exp[0.5 \cdot \sigma \cdot (1-\mu)(V_0^2 - V_*^2)] \cdot \rho(H_*) \cdot V_*^2$$

Here  $M_0$  is initial of the meteoroid mass;  $\delta$  is density of the body;  $A_0$  is coefficient of the body's shape;  $\rho$  is density of the atmosphere.

We shall obtain a relation for the density of atmosphere at the altitude of maximum deceleration in the following way:

$$\rho(H_*) = \frac{M_0^{1/3} \cdot \delta^{2/3} \cdot \cos Z_R}{2 \cdot \Gamma \cdot A_0 \cdot H_*} \times \frac{\exp\{th[0.175\sigma(1-\mu)V_0^2] - 0.5\sigma(1-\mu)V_0^2\}}{\{1 - th[0.175\sigma(1-\mu)V_0^2]\}}$$

Mass of a body  $M_*$  in the field of maximum deceleration is defined according to the classic formula suggested by Fisher [2]:

$$M_* = M_0 \cdot \exp\left[-\frac{\sigma \cdot (1-\mu)}{2} (V_0^2 - V_*^2)\right] \quad (8)$$

### 3. CAPABILITY OF THERMAL EXPLOSION

The Table 2 contains data for some known phenomena which are obtained on the basis of reduced relations.

Thermal explosion and flash of the solid brightness at the altitude of maximum deceleration are due to momentary (on a small range of altitudes) evaporation of a significant amount of dispersed meteor matter. From power considerations we assume that almost full evaporation of the remaining mass of the meteoroid in the area of the maximum deceleration may occur in the range of heights

$$\Delta H_* = \frac{2M_* \cdot Q \cdot \cos Z_R}{S_* \cdot \rho_* \cdot V_*^2} \quad (9)$$

or during the time

$$\Delta t_* = \frac{2M_* \cdot Q}{S_* \cdot \rho_* \cdot V_*^3} \quad (10)$$

The energy loss by a body on the deceleration per unit of mass for this time equals:

$$\frac{\Delta E_*}{M_*} = V_* \cdot \left[ \frac{dV}{dt} \right]_* \cdot \Delta t \quad (11)$$

As an example, the latter value (energy loss by a body) for the Tunguskiy phenomenon and for the Sterlitamak meteoroid is accordingly equal  $1.2 \cdot 10^{12}$  ergs/g and  $6 \cdot 10^{10}$  ergs/g. The loss happens within the range of the altitudes of 130 m and 900 m, accordingly. It is necessary to notice that the latter

values are essentially overstated. In both cases an effective cross-section of the evaporation was considerably higher than  $S_*$ , adopted for a monolithic body. In case of the Sterlitamak meteoroid, no more than 0.1  $M_*$  evaporated during the flash, the remaining mass fell out on the Earth. Therefore, the range of the altitudes of the flash is overstated for more than an order.

The velocity of a body at the altitude of maximum deceleration aims to limiting value at increase of extra-atmospheric velocity. This value is determined by values of parameters  $\sigma$  and  $\mu$  only. This conclusion follows from Eq. 4 - with increase  $U_0$  value  $U_*$  aims to an asymptote  $U_* = 1.0$ , i.e. velocity

$$V_* \rightarrow [2 / \sigma(1-\mu)]^{1/2} = 2 [\Gamma Q / \Lambda(1-\mu)]^{1/2}.$$

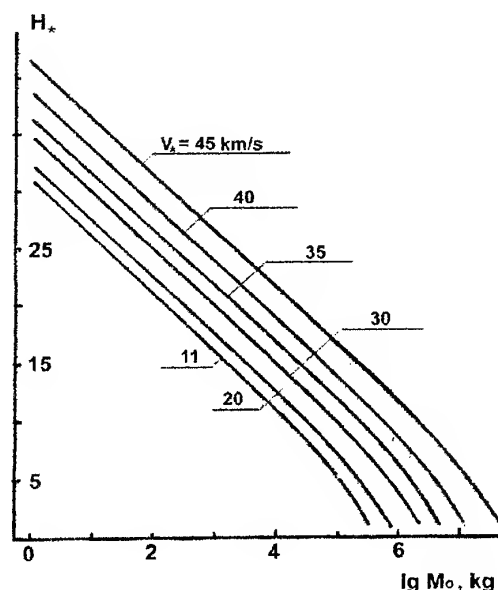


Fig. 2. Dependence of an altitude of maximum deceleration on initial values of mass and velocity.

The maximum value  $V_*$  which is determined by this formula does not depend on initial velocity and becomes close to the real one according to Eq. 6, when the multiplier

$$\{th[0.175 \sigma(1-\mu) V_0^2]\}^{1/2}$$

is near to a unity, i.e.  $V_0 \geq 50$  km/s. Thus mass  $M_*$  will have value of the order  $10^{-2} - 10^{-3}$  from the initial mass. Therefore even large meteoroids at high velocity of an entrance or the altitudes  $H_*$ , do not reach, or reach it, having small mass.

Hence, we conclude:

1. The thermal explosion of the meteoroid can be considered "a point explosion", as its expansion on an altitude is significantly less than  $H^*$ , which is altitude of a homogeneous atmosphere.

2. The energy loss on the deceleration on this range at these altitudes is equal to the value which is sufficient for full evaporation of the remaining meteoroid mass.

#### 4. THE THEORY

The theory of a "point explosion" in a heterogeneous atmosphere with exponential density distribution is well-known [3,12]. This theory can be applied to similar phenomena. The spreading velocity of an explosive wave depends on its direction in a heterogeneous atmosphere: when moving downward in the direction of the highest possible increase in density, the explosive wave is slowed down and its energy is maximally reduced; when moving vertically upwards, in the direction of maximum density decrease, the explosive wave accelerates and, within a limited time, "breaks through" the atmosphere. The explosion wave travels downwards on a distance which does not exceed 2 scale of altitudes  $H^*$ , in a perpendicular direction at the altitude of explosion – on a distance approximately equal  $3.5H^*$ . Further it turns into an elastic or sound wave.

Vertical upward explosive wave velocity can be shown as a dependence as follows:

$$V_n = \left[ \frac{(\gamma^2 - 1) \cdot \alpha}{2\pi} \right]^{1/2} \cdot \frac{E_*^{1/2}}{\rho_*^{1/2} \cdot r^{3/2}} \exp \left[ \frac{r}{2H^*} \right],$$

where  $\gamma$  is an adiabatic index (equal 1.2 or 1.4);  $\alpha$  is a constant, which in our case  $\approx 1.0$ ;  $E_* = M_* \cdot V_*^2/2$ , explosion energy;  $r$ , distance from the explosion point. It follows from the ratio that where  $r \rightarrow \infty$  velocity  $V_n$  also tends to infinity. When  $r = 3H^*$ , the spreading velocity of the explosion wave has a minimum value. Table 1 shows values of  $V_n$  depending on the distance from the explosion site.

The time of explosive wave tending to infinity is limited by

$$\tau_r = \int_0^r \frac{dr}{V_n} = 6\pi \left[ \frac{\rho_* H^{*5}}{(\gamma^2 - 1) \alpha E_*} \right]^{1/2}$$

The explosion energy for the Tunguskiy phenomenon  $E_* = 6.3 \cdot 10^{23}$  ergs. The time necessary for the explosive wave to reach infinity equals  $\tau_\infty \approx 5.5^m$ , where  $\gamma = 1.2$  and  $\tau_\infty \approx 3.7^m$ , where  $\gamma = 1.4$ .

Table 1. The velocity  $V_n$  of the explosion wave spreading in the vertical direction

$R$	$V_n$ , km/s	$R$	$V_n$ , km/s
$H^*$	0.38	$6H^*$	0.32
$2H^*$	0.22	$8H^*$	0.57
$3H^*$	0.20	$10H^*$	1.11
$4H^*$	0.22	$12H^*$	2.29

The achievement by a meteoroid of the altitude of maximum deceleration is an indispensable condition, but not sufficient for a thermal explosion to occur. It is known that some meteoroids reached the altitude  $H_*$ , but explosion did not happen (for example, Kourim, Lost-City).

We assume that when an explosion happens, the pressure behind the front of the explosion wave should exceed the pressure in front of the strong shock waves, i.e.

$$P_{*2} = \rho_{*2} \cdot R \cdot T_* > \frac{2 \cdot \rho_{*1} \cdot V_*^2}{(\gamma + 1)}, \quad (12)$$

where  $R$  is the gas constant;  $T_*$  is the temperature in an explosion wave.

The emission intensity of an explosion wave is equal:

$$I_* = S_{*w} \cdot \sigma_s \cdot T_*^4, \quad (13)$$

and also

$$I_* = -\beta_* \frac{d}{dt} \left[ \frac{M V_*^2}{2} \right] = -\beta_* M_* V_* \left[ \frac{dV}{dt} \right] \cdot (1 + 0.5 \sigma V_*^2) \quad (14)$$

In calculations the following relations are also used: the jump of density in an impact (explosive) wave is determined by the formula

$$\frac{\rho_{*2}}{\rho_{*1}} = \frac{\gamma + 1}{\gamma - 1} \quad (15)$$

The dependence of the luminosity of a meteor (bold) on its absolute stellar magnitude for a visual system according to Öpik [8], is represented in the following way:

$$\lg I_* = 9.72 - 0.4m_*, \quad (16)$$

and also correlations

$$\beta_* = \beta_0 \cdot V_*, \quad \beta_0 = 5 \cdot 10^{-10}, \quad (17)$$

where  $\beta$  is a coefficient of the luminous efficiency;  $S_{*w}$  is an area of an explosion wave;  $\sigma_s$  is Stefan-Boltzmann's constant.

## 5. RESULTS OF CALCULATIONS

The Table 2 adduces values of  $I_*$ , calculated for selected meteoroids, absolute magnitudes  $m_*$ , temperature  $T_*$  in the region of maximum deceleration and another parameters. For example, for the Kourim bolid, calculations give  $m_* = -9.7^m$  (from observations it is  $-9.5^m$ ),  $T_* = 3.8 \cdot 10^3$  K; for the Tunguskiy phenomenon  $m_* = -29.2^m$ ,  $T_* = 1.5 \cdot 10^4$  K. In Table 2 all values marked through (o) are obtained from observations, (c) - are calculated at  $S \neq \text{Const}$ , (c<sub>1</sub>) - are calculated at  $S = S_0 = \text{Const}$ ,  $M_{\text{Met}}$  - mass of the dropped out meteorite.

The data of calculations testify that our suggestion can be valid: the pressure behind the front of the explosion wave of the Kourim and Lost-City meteoroids are not sufficient to generate explosion.

## 6. CONCLUSION

1. The analysis is based on a number of the selected meteoroids, and we believe that it is necessary to further investigate the conditions under which thermal explosion is bound to occur at the altitude of maximum deceleration.

2. At thermal explosion the value of mass loss and energy depends on structure and strength of a body. If the body not strong also has cometary structure, its destruction is practically complete. If a body monolithic (stony or iron), depending on its strength the value of mass loss (and educed energy) makes from 10% up to 100%.

3. Temperature in an explosion wave of Tunguskiy phenomenon will make no more than  $10^4$  K, if one takes into account cooling its during intensive emission. The jump of atmospheric density in the explosion wave in relation to density up to an explosion wave, which one is determined by an Eq. 15, thus will be accordingly increased.

Table 2. Characteristics of the selected meteoroids

	Tungus.	Sichote - Alin	Sterlit.
$M_0, g$	$6.5 \cdot 10^{12}$	$10^8$	$5 \cdot 10^6$
$\delta, g/cm^3$	1.0	7.6	7.6
$V_0, km/s$	45	15	15
$Z_R,$	$82^o$	$45^o$	$43^o$
$H_*, km$	6.4	9.2	10.5
$V_*, km/s$	16.3	6.2	9.0
$(dV/dt)_*$ km/s <sup>2</sup>	-24.4	-5.1	-5.0
$M_*, g$	$4.7 \cdot 10^{11}$	$5.0 \cdot 10^7$	$1.2 \cdot 10^6$
$P(H_*)$ , N/m <sup>2</sup>	$6.7 \cdot 10^8$	$2.6 \cdot 10^7$	$1.4 \cdot 10^7$
Tensile Streng, N/m <sup>2</sup>	$10^5 - 10^6$	$4.4 \cdot 10^7$	$4.4 \cdot 10^7$
$\sigma_*$	$5 \cdot 10^{-13}$	$2.5 \cdot 10^{-13}$	$5 \cdot 10^{-13}$
$M_{\text{Met}}$	-	$5 \cdot 10^7$	$10^6$
$I_*, \text{ergs/s}$	$2.54 \cdot 10^{21}$	$5.1 \cdot 10^{15}$	$2.9 \cdot 10^{14}$
$M_*^{(c)}$	-29.2	-15.0	-11.9
$M_*^{(o)}$	-	-	-
$T_*^{(c)}, K$	$1.5 \cdot 10^4$	$3.5 \cdot 10^3$	$3.2 \cdot 10^3$

	Kun - Urgench	Kourim	Lost-City
$M_0, g$	$3 \cdot 10^6$	$1.09 \cdot 10^5$	$3.5 \cdot 10^7$
$\delta, g/cm^3$	3.32		3.73
$V_0, km/s$	13	27.53	14.2
$Z_R,$	$60^o - 70^o$	$57.5^o$	$52.3^o$
$H_*, km$	14.8	34.15	25.5 (o) 27.9 (c)
$V_*, km/s$	7.6	15.45 (o) 16.70 (c <sub>1</sub> ) 15.58 (c)	8.3

$(dV/dt)_*$ , km/s <sup>2</sup>	- 4.8	-17.2 (o) -11.5 (c <sub>1</sub> ) -18.8 (c)	- 4.2 (o) - 3.7 (c)
$M_*$ , g	$9.9 \cdot 10^5$	$9.0 \cdot 10^3$	$2.8 \cdot 10^5$
$P(H_*)$ , N/m <sup>2</sup>	$1.2 \cdot 10^7$	$1.14 \cdot 10^6$	$1.4 \cdot 10^7$
Tensile Streng, N/m <sup>2</sup>	$2 \cdot 10^6$	$2 \cdot 10^6$	$2 \cdot 10^6$
$\sigma_*$	$6.7 \cdot 10^{-13}$	$9.6 \cdot 10^{-13}$	$4 \cdot 10^{-13}$
$M_{Met}$	$10^6$	—	$1.7 \cdot 10^4$
$I_*$ , ergs/s	$1.6 \cdot 10^{14}$	$3.96 \cdot 10^{13}$	$5.0 \cdot 10^{13}$
$m_*^{(c)}$	- 11.2	- 9.7	- 9.9
$m_*^{(o)}$		- 9.5	- 10.0
$T_*^{(c)}$ , °K	$2.5 \cdot 10^3$	$3.8 \cdot 10^3$	$2.3 \cdot 10^3$

## 7. REFERENCES

1. Berezhnoi A.A., Shevchenko V.V., Klumov B.A., Fortov V.E., Collision of a comet with Jupiter: Determination of fragment penetration depths the molecular spectra, *Pis'ma Zh. Eksp. Teor. Fiz.*, Vol 63, 6, 387 – 391, 1996. (1996 American Institute of Physics. [S0021-3640(96)00106-5]).
2. Fisher W.I., Mass and velocity of meteorites and the air density along their luminous paths, *Harv. Circ.*, № 385, 1 – 16, 1934.
3. Kompaneets A. S., Tochechnyj vzryv v neodnorodnoj atmosfere (A point explosion in the heterogeneous atmosphere), *Dokl. Acad. Sci. USSR*, Vol. 130, 5, 1001 – 1003, 1960.
4. Kruchinenko V.G., The collision of the comet Shoemaker-Levy 9 with Jupiter, *Astron. and Astrophys. Transactions*, Vol. 13, 191 – 197, 1997.
5. McCrosky R.E., Shao C.- Y. and Posen A., Prairie network fireball data. I. Summary and orbits, *Center for Astrophysics. Prep. Ser.*, № 665, 1976.
6. McCrosky R.E., Shao C.- Y., and Posen A., Prairie network fireball data. II. Trajectories and light curves, *Center for Astrophysics. Prep. Ser.*, № 721, 1977.
7. Nemtchinov I.V., Svetsov V.V., Kosarev I.B. and al. Assessment of Kinetic Energy of Meteoroids Detected by Satellite-Based Light Sensors, *Icarus*, Vol. 130, 259 – 274, 1997.
8. Öpik E.J., Physics of Meteor Flight in the Atmosphere, *New York, Interscience Publ.*, 1958.
9. Pecina P. and Cepelcha Z., New aspects in single-body meteor physics, *Bull. Astron. Inst. Czech.*, Vol. 34, № 2, 102 – 121, 1983.
10. ReVelle D.O., Historical Detection of Atmospheric Impacts by Large Bolides Using Acoustic-Gravity Waves, *Repr. from Near-Earth Objects. Annals of the New York Academy of Sciences*, Vol. 822, 284 – 300, 1997.
11. Tagliaferri E., Satellite observations of large meteoroid impacts, *Meteoroid Impact Workshop, Sandia National Laboratories*, June 4-7, Albuquerque, NM, 1996.
12. Zel'dovich Ja. B., Rajzer Ju. P., *Fizika Udarnykh Voln i Vysokotemperaturnykh Gidrodinamicheskikh Yavlenij (Physics of Shock Waves and High-Temperature Hydrodynamic Phenomena)*, Moscow, "Nauka". 1966.
13. Voloshchuk Ju. I., Kashcheev B. L., Kruchinenko V. G., *Meteory i meteornoye Veshchestvo*, Kiev, "Naukova Dumka", 1989.
14. Whipple F. L., The theory of micro-meteorites. Part I. In an isothermal atmosphere, *Proc. Nat. Acad. Sci. Amer.*, Vol. 36, 12, 686 – 695, 1950.

## THE EFFECTIVE DIFFUSION COEFFICIENT OF METEOR TRAILS ABOVE 100 KM (ESA 5.4)

W. G. Elford<sup>(1)</sup>, M. T. Elford<sup>(2)</sup>

<sup>(1)</sup>Dept. of Physics and Mathematical Physics, Adelaide University, 5005 Australia. gelford@physics.adelaide.edu.au

<sup>(2)</sup>Atomic and Molecular Physics Labs., Res. School of Physical Sciences and Eng., Australian National University, Canberra, 0200 Australia. mte107@rsphyl.anu.edu.au

### ABSTRACT

In a recent paper R E Robson [Phys Rev E, 63 (2) 026404, 2001] has set the problem of the diffusion of meteor trails 'in the context of mainstream plasma physics'. The outcome is a new expression for the effective diffusion coefficient of a meteor trail that includes the effect of the magnetic field of the Earth and is thus applicable to meteor trails at all heights. Using laboratory based data for the values of the parallel diffusion coefficient and the collision frequencies, values of the effective diffusion coefficient have been calculated for radar observations of underdense trails as a function of beam direction for a number of meteor radars. Dramatic increases in the lifetime of radar echoes are predicted for trails above 100 km when the radar beam is directed to within 10° of the orthogonal to the magnetic field.

### 1. INTRODUCTION

The majority of meteor trails detected by radar are underdense, i.e. the electron line density is  $< 10^{14}$  electrons/metre, and each electron scatters radio waves independently of neighbouring electrons. For radar the basic backscattering features are well described in McKinley, 1961 [1], in terms of the central Fresnel zone of the highly linear trail, and radial diffusion of the ionization. The theoretical expression for the amplitude of the echo is

$$a = a_0 e^{-4k^2 D t},$$

where  $k = \frac{2\pi}{\lambda}$  and  $D$  is the ambipolar diffusion coefficient. At heights below 90 km the collision frequency of electrons with atmospheric atoms and molecules is sufficiently large that the effect of the Earth's magnetic field on the trajectory of the electrons can be ignored. Above 90 km the effect of the field must be considered, and the diffusion of the trail becomes anisotropic. The study of this latter situation now extends over more than 30 years (Jones 1991 and references therein [2]). However the analysis of this problem has only been set in the con-

text of mainstream plasma physics in very recent times with the publication of a paper by Robson (2001) [3]. In what follows we apply the expressions for the 'effective' diffusion coefficients derived by Robson to meteor trails formed above 100 km.

### 2. DIFFUSION OF METEOR TRAILS AT HEIGHTS EXCEEDING 100 KM

The presence of the Earth's magnetic field tends to increase the lifetime of meteor trails by inhibiting the diffusion of the plasma in a direction orthogonal to the field. This increased lifetime manifests itself in the increase in the duration of a meteor radar echo. An estimate of the increase in the lifetime of a radar echo from a meteor trail formed above 100 km was carried out by Elford and Elford (1999) [4], who based their calculations on values of the effective diffusion coefficient published by Jones 1991 [2]. The analysis by Robson [3] gives values for the effective diffusion coefficient that differ substantially from those of Jones. It is thus appropriate to carry out a fresh analysis of the expected lifetimes of radar echoes based on Robson's analysis.

The basic expression for the effective diffusion coefficient derived by Robson is

$$D_{eff} = D_{||} \sin^2 \mu \sin^2 \theta + D_{\perp} (1 - \sin^2 \mu \sin^2 \theta) \quad (1)$$

where  $D_{||}$  and  $D_{\perp}$  are the ambipolar diffusion coefficients parallel and perpendicular to the magnetic field,  $\theta$  is the angle the field makes with the trail, and  $\mu$  is the angle between the wave vector and the normal to the plane of the trail and the field. Values of  $D_{||}$  are those applicable when the effects of the magnetic field can be ignored. Such values are known for many positive ions from laboratory measurements (Mason and McDaniel, 1988 [5]; Elford and Elford [4]). In the case of alkali ions in nitrogen  $D_{||} \approx 1.4 \times 10^{-5} T^2 / p \text{ m}^2/\text{s}$ , where  $T$  is the ambient gas temperature and  $p$  the gas pressure.

Robson [3] has shown that values of  $D_{\perp}$ , the ambipolar

diffusion coefficient perpendicular to the field, are simply related to  $D_{||}$  through the expression,

$$D_{\perp} = \frac{D_{||}}{1 + \rho}, \quad (2)$$

where  $\rho$  is given by

$$\rho = \frac{e^2 B^2}{m_e \nu_e \mu_i \nu_i} = \frac{\omega_e \omega_i}{\nu_e \nu_i}. \quad (3)$$

In this expression  $\mu_i$  is the reduced ion mass, and  $\omega_{e,i}$  and  $\nu_{e,i}$  are the gyro and collision frequencies of the electrons and ions. Thus  $\rho$  is the product of the ratios of the gyro to collision frequencies for ions and electrons.

The basic data required to calculate  $\rho$  from Eq. 3 and hence  $D_{\perp}$  from Eq. 2 are available from published laboratory measurements. Values of  $\nu_i$  can be determined from values of ion mobilities  $K_i$  and then using the relation  $\nu_i = e/(\mu_i K_i)$ . Values of  $\nu_e$  can be calculated from published values of momentum transfer cross-sections for electron collisions with atmospheric gases at low energies. The  $N_2$  data were taken from Robertson *et al.* (1997) [6], and the  $O_2$  data from Hake and Phelps (1967) [7]. Data for atomic oxygen have been published by Williams and Allen (1989) [8], but the lowest energy listed is 0.54 eV. To estimate values of cross-sections for the energy range 0–0.4 eV two extrapolations were adopted: (a) the curves of Williams and Allen were smoothly continued to give a cross-section value of 2 square Angstroms at 0 eV, and (b) the value at 0 eV was set at 1 square Angstrom and a smooth graph joined to the listed value at 0.54 eV. The values of  $D_{\perp}$  determined using these two sets of cross-sections differed by less than 2% at 120 km and less than 1% at 110 km.

Fig.1 shows the dependence of  $D_{||}$  and  $D_{\perp}$  as a function of height for a meteor trail of line density  $10^{13}$  electrons/m. For trails of larger electron line density, collisions between ions and electrons cause a significant increase in the values of  $D_{\perp}$  over the height range 90 to 110 km. A trail of  $10^{14}$  electrons/m has a maximum increase in  $D_{\perp}$  near 95 km where the value is about 40% larger than that for trails  $\geq 10^{13}$  c/m.

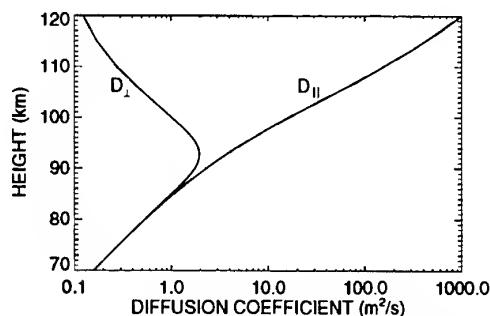


Fig. 1. Height variation of the ambipolar diffusion coefficients relevant to meteor studies:  $D_{||,\perp}$ , diffusion parallel and perpendicular to the magnetic field.

The chief feature of Fig.1 is the dramatic reduction in diffusion orthogonal to the field ( $D_{\perp}$ ) in comparison to diffusion parallel to the field ( $D_{||}$ ) at heights above 95 km. As an example, a meteor trail at 112 km has a value of  $D_{\perp}$  about 1000 times smaller than the value of  $D_{||}$ . The variation of  $\rho$  with height is shown in Table 1. Robson [3] introduced the parameter  $\Delta = (1 - \rho)/(1 + \rho)$ , which has the advantage of having extrema values of +1 and -1, and being zero when  $\rho = 1$ . A plot of  $\Delta$  against height is shown in Fig.2 where the behaviour of  $\Delta$  suggests that this parameter can be used as a measure of 'the degree of magnetisation' of a meteor trail. Below a height of 85 km the effect of the magnetic field is negligible, whereas above 105 km the motion of the plasma in the trail is dominated by the magnetic field.

Table 1. Variation of  $\rho$  and  $\Delta$  with height.

Height (km)	$\rho$	$\Delta$
80	0.002	1
95	1.2	-0.09
110	550	-1

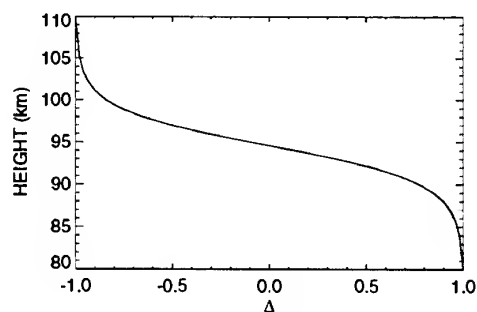


Fig. 2. Height variation of the parameter  $\Delta$  used in studies of diffusion of meteor trails.

### 3. LIFETIME OF METEOR ECHOES

To examine the effect of the magnetic field on the lifetime of radio echoes from meteor trails, the duration of meteor echoes detected by a narrow beam radar are calculated using the expressions discussed above and also when the effect of the magnetic field is ignored. In the case of a beam lying in the North-South plane through the zenith, the data can be presented as the enhancement in echo duration at a given height as a function of the elevation of the beam. The results for the MU radar at Shigaraki, Japan (geomagnetic dip,  $51^\circ$ ) are shown in Fig.3 where the plot has been centred on an elevation angle that is the complement of the magnetic dip angle. When the beam is directed orthogonal to the field the enhancement of the echo duration ranges from a factor of 2 for a trail at 95 km to 550 at 110 km. Even for elevation angles  $20^\circ$  from the position of orthogonality to the field the enhancement in duration of the echo is still a factor of 8 for a trail at 110 km.

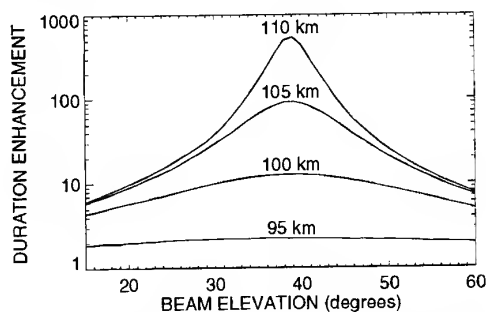


Fig. 3. Enhanced duration of meteor echoes from trails detected with the MU radar, as a function of the elevation of the beam in the NS plane, and for four heights.

It is an interesting characteristic of the expression for the effective diffusion coefficient (Eq. 1) that the enhancement in echo duration is independent of the azimuth angle of the meteor trail in the echo plane (plane orthogonal to the radar beam). For other narrow beam meteor radars, plots similar to Fig.3 are obtained with the peak values always occurring at a beam angle that is the complement of the dip angle at the radar site.

### 4. DISCUSSION

It is evident from Fig.3 that meteor trails formed above 100 km and observed by narrow beam radars directed orthogonal to the Earth's magnetic field should produce echoes that have exceptional lifetimes. While observations have been carried out to test this expectation the

results show only modest enhancements in the lifetime of meteor echoes. Thus it appears that an alternative process must be acting on trails diffusing at heights above 95 km that overrides the effect of the magnetic field. A possible explanation is the presence of gradient-drift instabilities that develop into waves in the plasma of the trail. This has been discussed by Dyrud *et al.* 2001, [9] who point out that such waves create an anomalous cross-field diffusion, that can exceed the value of the orthogonal ambipolar diffusion coefficient by as much as an order of magnitude. Actual values of the anomalous diffusion discussed in [9] are based on a trail with a line density of  $2 \times 10^{14}$  e/m. Further numerical studies are required that apply to trails of  $10^{13}$  e/m and smaller.

### 5. REFERENCES

1. McKinley, D. W. R., *Meteor Science and Engineering* McGraw Hill, New York, 1961.
2. Jones, W., Theory of diffusion of meteor trains in the geomagnetic field, *Planet. Space Sci.* Vol. 39, 1283–1288, 1991.
3. Robson, R. E., Dispersion of meteor trails in the geomagnetic field, *Phys. Rev. E* Vol. 63, 026404, 2001.
4. Elford, W. G. and Elford, M. T., The effect of the Earth's magnetic field on the lifetime of radar meteor echoes, *Proceedings of Meteoroids 1998, Astron. Inst. Slovak Acad. Sci., Bratislava* 71–74, 1999.
5. Mason, E. A. and McDaniel, E. W., *Transport Properties of Ions in Gases* Wiley, London, 1988.
6. Robertson, A. G., Elford, M. T., Crompton, R. W., Morrison, M. A., Sun, W. and Trail, W. K., Rotational and Vibrational Excitation of Nitrogen by Electron Impact, *Aust J. Phys.* Vol. 50, 441–472, 1997.
7. Hake, R. D. and Phelps, A. V., Momentum-Transfer and Inelastic-Collision Cross Sections for Electrons in  $O_2$ , CO,  $CO_2$ , *Phys. Rev.* Vol. 158, 70, 1967.
8. Williams, J. F. and Allen, L. J., Low-energy elastic scattering of electrons from atomic oxygen, *J. Phys. B: At. Mol. Opt. Phys.* Vol. 22, 3529, 1989.
9. Dyrud, L. P., Oppenheim, M. M. and vom Endt, A. F., The anomalous diffusion of meteor trails, *Geophys. Res. Lett.* Vol. 28, 2775–2778, 2001.

# THEORY AND SIMULATIONS OF FIELD-ALIGNED IRREGULARITIES IN METEOR TRAILS

Meers M. Oppenheim, Lars P. Dyrud, Sigrid Close, and Stephen Hunt

Center for Space Physics, Boston U., 725 Comm. Ave., Boston, MA 02215 U.S.A., Email meerso@bu.edu

## ABSTRACT

Meteor trails created by the ablation of micro-meteoroids between 70 and 130 km altitude in the atmosphere create columns of plasma often with densities that exceed the ambient ionospheric plasma density by orders of magnitude. Density gradients at the edges of these trails can create ambipolar electric fields with amplitudes in excess of hundreds of mV/m. These fields, in turn, drive Farley-Buneman and gradient-drift (FBGD) instabilities which create field-aligned plasma density irregularities detectable by large aperture radars. This paper presents a new theory of meteor trail instabilities and compares this theory with simulations, observations, and related theories. In particular, this paper discusses the origin of the driving electric field, the resulting electron drifts, and the mechanism and mathematics necessary to describe the linear, fluid, instabilities. Finally, this paper shows that linear theory predicts a limited range of altitudes over which one expects instabilities and, therefore, non-specular radar observations of meteor trails.

## 1. INTRODUCTION AND BACKGROUND

Radars probing the atmosphere between 75 km and 120 km frequently receive echoes from plasma trails left by passing and disintegrating meteors. These echoes have proven useful in characterizing small meteors and in estimating atmospheric temperatures and wind velocities. Two distinct types of radar echoes return from meteor trails. Strong echoes return when the radar pointing direction lies perpendicular to the meteoroid's trajectory, creating a "specular" reflection (Cepkecha et al. 1998b). Weaker echoes are frequently observed by highly sensitive, large-aperture, radars not pointing perpendicular to the trail's orientation, creating echoes labeled as "non-specular" reflections (Chapin & Kudeki 1994; Zhou et al. 2001).

Long-duration, non-specular radar echoes of meteor trails observed at the geomagnetic equator have been attributed to the Farley-Buneman/gradient-drift

(FBGD) instability mechanism (Chapin & Kudeki 1994; Chang et al. 1999). This FBGD turbulence may not be confined to equatorial latitudes, since the same type of radar signatures from meteor trails have been observed at midlatitudes (Haldoupis & Schlegel 1993; Zhou et al. 2001) as well as at low latitudes outside the electrojet (Reddi & Nair 1998). Other researchers have investigated similar electrodynamics generated by barium cloud releases (Blaunstein et al. 1993).

The fundamental behavior of meteor trails and collisionally dominated plasmas has been discussed in many books and review articles (Öpik 1958; Cepkecha et al. 1998a; Rishbeth & Garriott 1969). More specifically, a number of authors have evaluated the ambipolar diffusion of meteor trails in collisional plasmas (Pickering & Windle 1970; Jones 1991). Most of our understanding of weakly ionized meteor trails derives from radar observations and relies on detailed analyses of the precise interaction between meteor trails and radar signals (Jones & Jones 1991).

In an earlier paper, we used simulations to show that non-specular echoes can easily result from the FBGD instability which rapidly develops into plasma turbulence (Oppenheim et al. 2000). In a subsequent paper we showed that FBGD waves develop without an external electric field and also demonstrated that the waves and turbulence cause an anomalous diffusion much larger than the expected cross-field ambipolar diffusion (Dyrud et al. 2001). This paper develops the linear plasma fluid instability theory of these trails and predicts the altitude range at which one expects to find field-aligned irregularities (FAI) and therefore non-specular meteor trails.

## 2. THEORY OF METEOR TRAIL PLASMA

A small meteoroid ( $< \sim 10^{-5}$  kg) ablating in the upper atmosphere creates a narrow column of energetic neutrals and plasma. This column expands rapidly until slowed, partially ionized, and cooled by collisions. The radius of the column at the point when it transitions from a rapid kinetic expansion to a slower diffusive expansion is called the initial radius of the

trail and it appears to be somewhat smaller than the mean free path length (Baggaley 1981; Bronshten 1983). After the column reaches this initial radius, the dynamics of the expanding column of charged particles may be approximately described as a plasma fluid.

Above 75 km in altitude and perpendicular to the geomagnetic field,  $\mathbf{B}$ , electrons are highly magnetized while ions are de-magnetized by collisions. Hence, as the trail plasma expands beyond its initial radius, a strong ambipolar electric field develops as a result of the differing ion and electron mobilities. The electrons respond to this cross-field ambipolar field by  $\mathbf{E} \times \mathbf{B}$ -drifting perpendicular to both  $\mathbf{B}$  and the density gradient of the meteor trail. This drift, combined with a diamagnetic drift caused by the plasma density gradients, can generate an unstable plasma (Fejer et al. 1975). This instability leads to the formation of waves which rapidly develop into turbulence. This field aligned instability also creates plasma density perturbations visible to radars, allowing for non-specular radar reflections. Further it causes anomalous diffusion, effecting the meteor trail's expansion rate. The following sections describe how the electric fields, electron drifts, and instabilities depend upon the altitude and trail density.

### 2.1. Equilibrium Condition

In order to evaluate the stability of a meteor trail, we must first define an equilibrium state. We will use the ambipolar expansion of a diffusing plasma column perpendicular to the magnetic field. We conduct this analysis only in the plane perpendicular to  $\mathbf{B}$  and assume that in the plane parallel to  $\mathbf{B}$  the trail expands through ambipolar diffusion and is not unstable to plasma instabilities (Kudeki & Farley 1989). To define the equilibrium state we will assume the ions are an inertialess, isothermal, collisional, and unmagnetized fluid plasma where

$$\mathbf{v}_i = -\mu_i \nabla \phi - D_i \nabla s \quad (1)$$

and  $\mu_{i,e} \equiv e/(m_{i,e} \nu_{i,e})$  defines the ion and electron mobilities,  $D_{i,e} \equiv kT_{i,e}/(m_{i,e} \nu_{i,e})$  defines the ion and electron diffusion rates,  $\phi$  is the electric potential, and  $\nabla s \equiv \nabla n/n = \nabla \ln(n/n_b)$  defines the gradient of the log of the plasma density normalized to the background density,  $n_b$ . The electrons are an inertialess and magnetized fluid whose velocity perpendicular to  $\mathbf{B}$  can be expressed as

$$\mathbf{v}_{e\perp} = \mu_{e\perp} \nabla \phi - D_{e\perp} \nabla s + \frac{\mathbf{v}_{E \times B} + \mathbf{v}_D}{1 + \nu_e^2 / \Omega_e^2} \quad (2)$$

where

$$\mu_{e\perp} \equiv \frac{\mu_e}{1 + \Omega_e^2 / \nu_e^2}, \quad D_{e\perp} \equiv \frac{D_e}{1 + \Omega_e^2 / \nu_e^2},$$

$$\mathbf{v}_{E \times B} \equiv \frac{\mathbf{E} \times \mathbf{B}}{B^2}, \quad \mathbf{v}_D \equiv -\frac{kT_e}{e} \frac{\nabla s \times \mathbf{B}}{B^2},$$

$\mathbf{v}_D$  is the diamagnetic drift, and  $\Omega_e = eB/m_e$  is the electron cyclotron frequency (see Chen (1984),

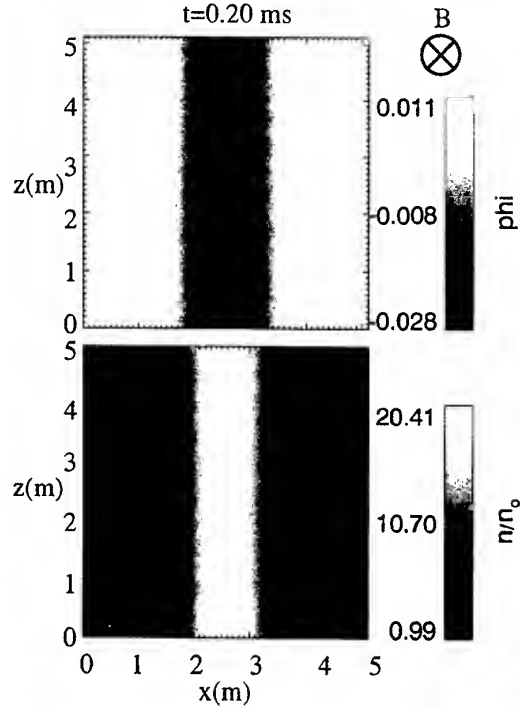


Figure 1. Electric potential,  $\phi$ , in volts (top) and plasma density enhancements,  $n_e/n_0$ , (bottom) for a slab trail perpendicular  $\mathbf{B}$ . The magnitude of each quantity is represented by the grey-scale bar to the right.

p. 171, for an explanation of these terms). For altitudes above 85 km,  $\Omega_e^2 / \nu_e^2 \gg 1$  and electrons predominantly engage in  $\mathbf{E} \times \mathbf{B}$  and diamagnetic drifts, as described by third term of eqn. (2).

The assumption of quasi-neutrality,  $\nabla \cdot \mathbf{J} = 0$ , allows us to generate an expression for the potential ( $\perp$  to  $\mathbf{B}$ ) in terms of density,

$$\mu_T \nabla \cdot (n \nabla \phi) - D_T \nabla^2 n + \frac{\nabla n \cdot \nabla \phi \times \mathbf{B}_0}{1 + \Omega_e^2 / \nu_e^2} = 0 \quad (3)$$

where  $D_T \equiv D_{e\perp} - D_i$  and  $\mu_T \equiv \mu_{e\perp} + \mu_i$ . This equation allows us to solve for the cross-field ambipolar electric potential,  $\phi$ , for a prescribed density distribution,  $n$ , and vice-versa.

In many configurations eqn. 3 becomes easy to evaluate. One simple trail geometry in Cartesian coordinates aligns the magnetic field,  $\mathbf{B}$ , along the  $\hat{y}$  direction; allows the density gradient to vary only along  $\hat{x}$ ; and assumes homogeneity along both  $\hat{y}$  and  $\hat{z}$ . Figure 1 shows a trail with this geometry. While homogeneity along  $\mathbf{B}$  is unrealistic, at high altitudes one expects trails stretched in the direction parallel to  $\mathbf{B}$ , so this assumption is not entirely unrealistic. An alternate geometry which may be evaluated in cylindrical coordinates aligns the trail parallel to  $\mathbf{B}$ , leaving a circular cross-section perpendicular to  $\mathbf{B}$ . As long as  $\nabla n$  is perpendicular to  $\mathbf{E} \times \mathbf{B}$ , eqn. (3) becomes merely,

$$\nabla \cdot (n \nabla \phi) = D_T / \mu_T \nabla^2 n \quad (4)$$

Table 1. Physical and simulation parameters for 105km equatorial simulation.

External magnetic field	$B_0$	$2.5 \times 10^{-5} \text{ T}$
Neutral gas density	$n_n$	$5.0 \times 10^{18} \text{ m}^{-3}$
Temperature	$T_{i,n}$	220 K
$e^-$ -neutral coll. freq.	$\nu_{en}$	$2.8 \times 10^4 \text{ s}^{-1}$
Ion mass	$m_i$	$5.0 \times 10^{-26} \text{ kg}$
Peak/background ratio	$n_e/n_0$	20
Trail line density	$N_{line}$	$2.0 \times 10^{14} \text{ m}^{-1}$
Trail radius	$r_t$	1.0 m
Ion-neutral coll. freq.	$\nu_{in}$	$2.0 \times 10^3 \text{ s}^{-1}$
Grid size	$n_{x,z}$	256
Grid spacing	$\Delta_{x,z}$	$2.0 \times 10^{-2} \text{ m}$
Time step	$\Delta_t$	$1.0 \times 10^{-5} \text{ s}$

and may be easily solved for either slab or cylindrical geometries.

In the case of a slab trail as shown in fig. 1,

$$E_x = -\frac{D_T}{\mu_T} \frac{\partial s}{\partial x} + \frac{C}{n} \quad (5)$$

where  $C$  is a constant of integration set by boundary conditions. If we further assume that the density of the trail is the sum of a Maxwellian plus a background density,  $n = n_0 \exp(-x^2/x_0^2) + n_b$ , then eqn. 5 gives the ambipolar field

$$E_x = -\frac{D_T}{\mu_T} \left[ \frac{n_0 \exp(-x^2/x_0^2)(-2x/x_0^2)}{n_0 \exp(-x^2/x_0^2) + n_b} \right]. \quad (6)$$

Figure 1 shows the ambipolar electric field for a trail at 105km with a Maxwellian density profile and other parameters specified in Table 2.1. Due to the limitation of grey-scale figures we have chosen to plot the electric potential,  $\phi$ . A trail, perfectly aligned along  $\mathbf{B}$ , develops the same electric field except  $x \rightarrow r$ . A trail making a 45° angle with respect to  $\mathbf{B}$  will have an oval cross-section and will develop similar fields and potentials.

For the system shown in Fig. 1, the ion cross-field mobility,  $\mu_i$  exceeds the electron one,  $\mu_{e\perp}$ . In this case, the electric field points toward the center of the trail and prevents the ions from escaping from the magnetized and less mobile electrons. At different altitudes, the changing collision rates alter the relationship between these mobilities. Below  $\sim 100$  km (near the equator), the collision rates become high enough that the electron diffusion rate exceeds the ion rate causing the ambipolar electric field to reverse directions.

The transition altitude where  $\mathbf{E}$  shifts from inward to outward pointing depends on latitude because of the changing geomagnetic field. This altitude also plays less of a role in the generation of instabilities than one might expect, because the instability driver results from the total electron drift speed, which derives from a combination of  $\mathbf{E} \times \mathbf{B}$  and diamagnetic drifts as discussed in the following section.

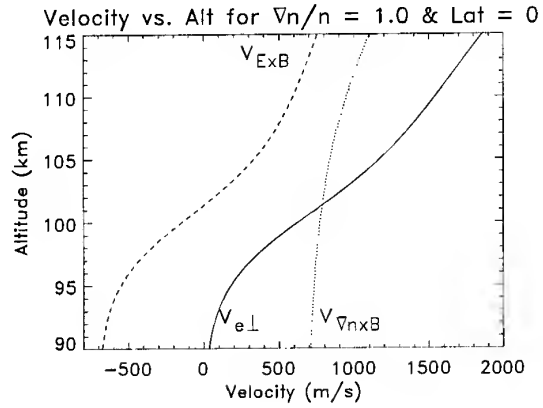


Figure 2. Velocity vs. altitude assuming parameters from the international reference ionosphere (IRI) for the equator.  $v_{\mathbf{E} \times \mathbf{B}}$  shows the  $\mathbf{E} \times \mathbf{B}$  drift velocity;  $v_{\nabla n \times \mathbf{B}}$  shows the diamagnetic drift velocity; and  $v_{e\perp}$  shows the sum of the two velocities.

### 2.1.1. Electron Drift

Electron drift motion results from the combination of  $\mathbf{E} \times \mathbf{B}$  and diamagnetic drifts where, in the absence of external electric fields or, equivalently, neutral winds,  $\mathbf{E}$  arises from the self-generated ambipolar electric fields. Combining eqns. (2) and (4) makes the electron drift velocity

$$\mathbf{v}_{e\perp} = \left( \frac{D_T}{\mu_T} + \frac{D_e}{\mu_e} \right) \frac{\nabla s \times \hat{\mathbf{B}}}{|\mathbf{B}|} - \left( \mu_{e\perp} \frac{D_T}{\mu_T} + D_{e\perp} \right) \nabla s \quad (7)$$

where  $\hat{\mathbf{B}} \equiv \mathbf{B}/|\mathbf{B}|$ . In the case where electron motion lies purely perpendicular to  $\nabla n$ , this simplifies to

$$v_{e\perp} = \frac{C_s^2}{\Omega_i(1 + \Psi_0)} \nabla s \times \hat{\mathbf{B}} \quad (8)$$

where  $C_s^2 = \sqrt{k(T_e + T_i)/m_i}$  is the ion acoustic velocity and  $\Psi_0 \equiv \frac{\nu_{en}\nu_i}{\Omega_e\Omega_i}$ , a ratio that shows up repeatedly in E-region dynamics. This equation tells us that, regardless of the direction of  $\mathbf{E}$ , the electrons always drift in the positive  $\nabla n \times \hat{\mathbf{B}}$  direction. At high altitudes  $\mathbf{E} \times \mathbf{B}$  drifting dominates, but at lower altitudes, as  $\mathbf{E}$  changes sign, the electrons continue to drift in the same direction. This occurs because the diamagnetic drift rate,  $v_D$ , becomes larger, preventing the electrons from reversing direction. Figure 2 compares drift velocities as a function of altitude for a trail with  $\nabla s = 1 \text{ m}^{-1}$ . For larger (or smaller) values of  $\nabla s$ , the velocities scale linearly with  $\nabla s$ . Figure 1 shows a trail with  $\nabla s = 4 \text{ m}^{-1}$  at 105 km altitude which results in drifts of  $\sim 5.2 \text{ km/s}$ . This rapid drift motion drives the instabilities discussed in Dyrud et al. (2001) and Oppenheim et al. (2000).

### 2.2. Stability

Linear plasma theory allows us to evaluate the stability of these meteor trails. Further, it teaches us

about the phase and group velocities and growth or damping of any wave which might develop within the trail. Since radars are extremely sensitive to plasma waves, understanding the characteristics of these waves should allow us to better understand non-specular radar echoes.

The simplest linear analysis assumes both the electrons and ions behave as plasma fluids and recreates the dispersion relation described in Fejer et al. (1984). To obtain the dispersion relation, assume inertialess electrons as in eqn. (2) and quasineutrality as before, but keep ion inertia. The linear, Fourier transformed, ion momentum equation remains the same as eqn. (1) except  $\nu_i \rightarrow \nu_i - i\omega$  where  $\omega$  is the complex wave frequency. With these assumptions the following relation may be derived:

$$\omega - \mathbf{k} \cdot \mathbf{v}_{e0} = -A [(\omega - \mathbf{k} \cdot \mathbf{v}_{i0})(\nu_i - i\omega) + ik^{\perp 2} C_s^2] \quad (9)$$

$$A \equiv \left( \frac{\Psi_0}{\nu_i} - \frac{i}{\Omega_i} \frac{\mathbf{k} \cdot \nabla s_0 \times \hat{\mathbf{B}}}{k^{\perp 2}} \right) \quad (10)$$

where  $\mathbf{v}_{i0}$  and  $\mathbf{v}_{e0}$  are the equilibrium (drift) velocities of each species;  $\nabla s_0 \equiv \nabla n_0/n_0$  is the initial density gradient scale length;  $k^{\perp 2} \equiv (\mathbf{k} - i\nabla s_0) \cdot \mathbf{k}$ .

When applying this equation to E-region gradient drift and Farley-Buneman instabilities, one typically assumes that  $\nu_i \gg \omega_r \gg \omega_i$  where  $\omega \equiv \omega_r + i\omega_i$ . These assumptions allow one to simplify eqn. (9) to

$$\begin{aligned} \omega_r &= \mathbf{k} \cdot \mathbf{v}_{e0} / (1 + \Psi_0) \quad (\text{incorrect}) \quad (11) \\ \omega_i &= \frac{\Psi_0/\nu_i}{1 + \Psi_0} \left( w_r^2 - k^2 C_s^2 + \frac{\omega_r \mathbf{k} \cdot \nabla s_0 \times \hat{\mathbf{z}}}{\Psi_0 \Omega_i k^2} \right) \end{aligned}$$

which do not apply to meteor trails. In the case of meteor trails  $\omega_r$  often has a similar magnitude as  $\nu_i$  and, therefore, one must solve eqn. (9) as a quadratic equation.

Two assumptions do apply, allowing some simplification of eqn. (9). If  $\mathbf{B} = B_0 \hat{\mathbf{z}}$ , then  $A$  simplifies to

$$A \equiv \Psi_0/\nu_i - (i/\Omega_i) \mathbf{k} \cdot \nabla s_0 \times \hat{\mathbf{z}}/k^{\perp 2}, \quad (12)$$

and if  $\mathbf{v}_{i0}$  is negligible compared to  $\mathbf{v}_{e0}$ , which it always is for E-region plasmas, the quadratic equation simplifies to

$$\omega - \mathbf{k} \cdot \mathbf{v}_{e0} = -A[(\nu_i \omega - i\omega^2) + ik^{\perp 2} C_s^2]. \quad (13)$$

One interesting point follows: In FBGD theory, the  $\mathbf{k} \cdot \mathbf{v}_{e0}$  term drives the instability. For meteor trails, with no driving external electric field, the  $Aik^2 C_s^2$  term also contains a real component which always exceeds the  $\mathbf{k} \cdot \mathbf{v}_{e0}$  term such that adding the real components of the two terms yields

$$\Re[Aik^2 C_s^2 - \mathbf{k} \cdot \mathbf{v}_{e0}] = \frac{C_s^2 \mathbf{k} \cdot \nabla s_0 \times \hat{\mathbf{B}}}{\Omega_i} \frac{\Psi_0}{1 + \Psi_0}. \quad (14)$$

This assumes that  $\nabla s_0 \cdot \mathbf{k}/k^2 \ll 1$ , which applies when  $\mathbf{k}$  represents waves aligned mostly perpendicular to the gradient,  $\nabla s$ .

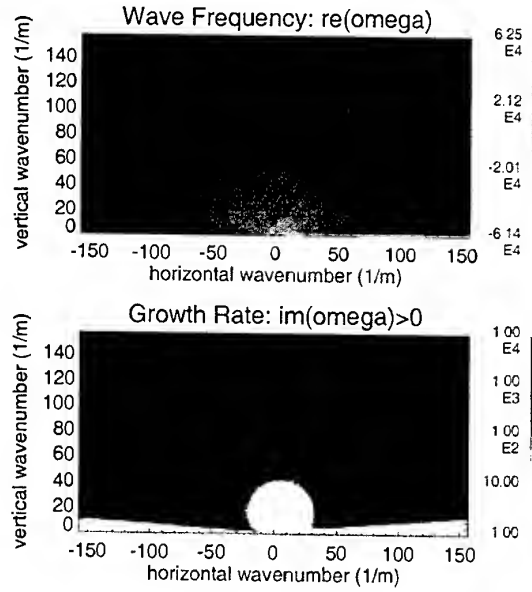


Figure 3. Shows the real (top) and imaginary (bottom) parts of  $\omega$  as a function of vertical and horizontal wavenumber,  $\mathbf{k}$ . Of the two roots the one with the larger  $\omega_i$  is shown and the bottom panel only shows values for  $\omega_i > 0$ .

Fig. 3 shows an example of a solution to eqn. (13) for the parameters shown in Table 2.1. The simulation results shown in Fig. 4 demonstrate that waves grow for a system with these parameters.

Though fig. 3 shows increasing growth rates for increasing values of  $|\mathbf{k}|$ , the simulation shows a peak wavelength at  $\sim 20$  cm. However, the fluid theory ignores kinetic plasma phenomena. In particular, at these short wavelengths, we expect ion Landau damping to reduce the growth rate short wavelength modes (Schmidt & Gary 1973; Lee et al. 1971). We have attempted to include these effects but have not yet succeeded. The fluid equations most accurately represent the physics at the longest unstable wavelengths and, in the discussion below, we will limit ourselves to that case.

### 2.2.1. Criterion for instability onset

While eqn. (13) may not be appropriate to predict the growth rate of the instability for all wavelengths, it does provide an approximation for the instability threshold. Figure 5 shows positive growth rates as a function of altitude and peak plasma density for meteor trails having a Maxwellian density profile,  $n = n_0 \exp(-r^2/r_0^2) + n_b$ . To set the crucial scale length,  $r_0$ , we used two initial radius measurements: the Bronshten (1983) prediction and the smaller Baggaley (1981) measurement. To limit the very short wavelength modes, we required that the instability develop a positive growth rate for waves longer than twice the Debye length. The results are only weakly

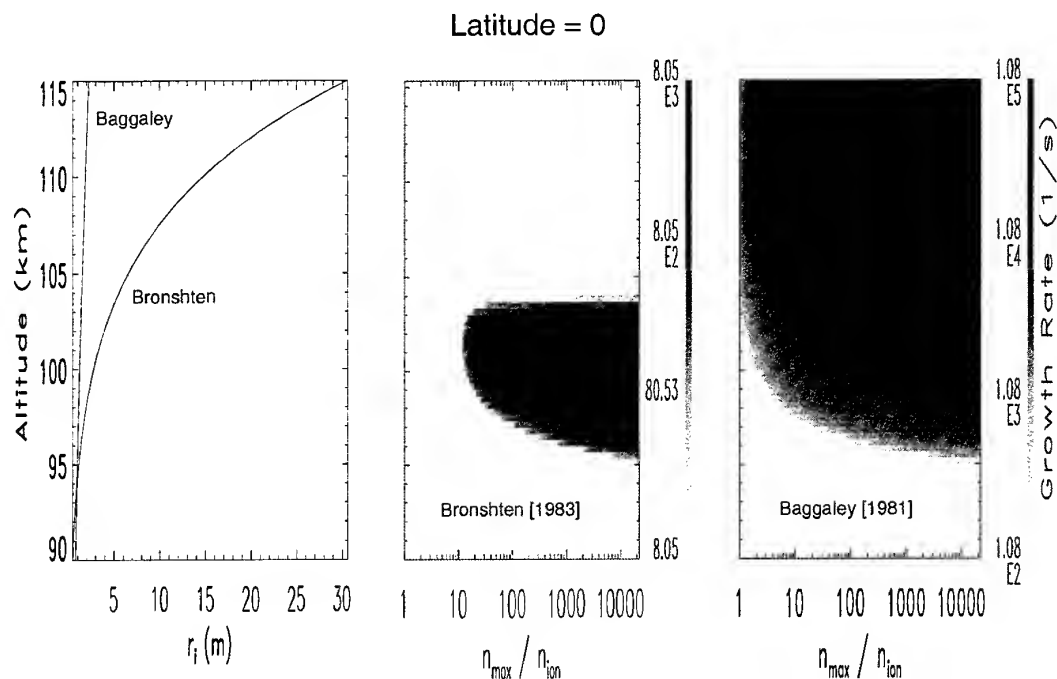


Figure 5. Left panel plots initial radius of trail versus altitude for the Baggeley and Bronshten models. The center panel shows the predicted growth rate as a function of altitude and peak plasma density,  $n_0/n_b$ , for the radius suggested by the Bronshten model. The right panel shows the same for the radius suggested by the Baggeley model.

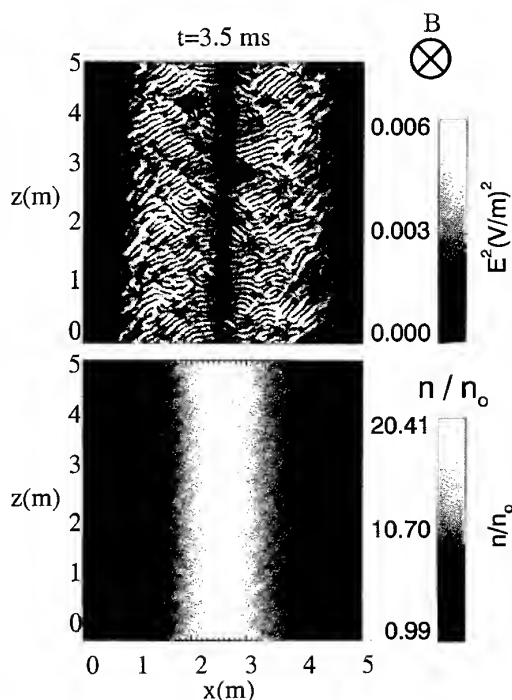


Figure 4. Electric field energy,  $E^2$ , in  $(V/m)^2$  (top) and plasma density enhancements,  $n_e/n_0$ , (bottom) from the cross-section of a slab trail in the plane perpendicular to  $\mathbf{B}$  after 3.5 ms.

sensitive to changes in this criterion. One can see that the instability growth rate depends strongly on the initial radius and only weakly on the peak plasma density. The minimum altitude is mostly determined by the high collision rates and depends only weakly on meteor parameters.

The maximum instability altitude is set principally by the initial radius of the trail which determines  $\nabla s$ . The Bronshten (1983) values allow us to predict instability over a limited altitude range. The smaller radii predicted by Baggeley (1981) lead us to predict essentially no ceiling on the instability altitude.

The observational data appears to predict a limited range of altitudes over which trails become unstable. Figure 6 shows a strong trail at high resolution. The line on the left hand side of the image results from the head echo (see, *S. Hunt, et. al.* and *J. Mathews, et. al.* this volume). The trail echo on the right spans a smaller range of altitudes than did the head echo. This difference occurs frequently and is discussed in more detail in *L. P. Dyrud, et. al* (this issue).

### 3. CONCLUSIONS

We have used a fluid description of meteor trail plasma dynamics to better understand the results from both simulations and large-aperture radar observations. We have solved for the equilibrium state of a diffusing meteor trail perpendicular to  $\mathbf{B}$  and shown that both the electron diamagnetic drift and

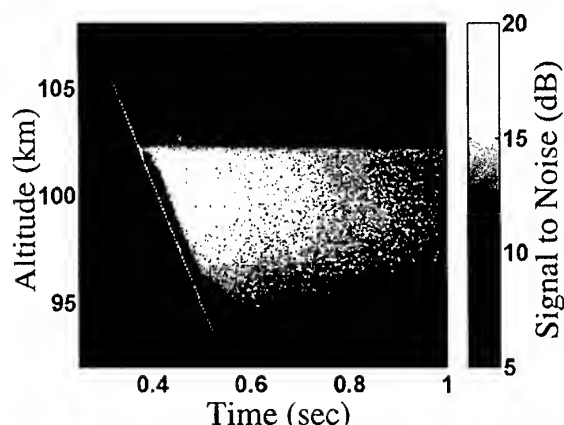


Figure 6. Example of a trail echo recorded by the VHF ALTAIR radar at the Kwajalein missile range as a function of altitude and time

$\mathbf{E} \times \mathbf{B}$  drift contribute to the total electron drift. Further, this total electron drift is always in the  $\nabla n \times \mathbf{B}$  direction, even when the  $\mathbf{E} \times \mathbf{B}$  drift drives electrons in the opposite direction.

We then solved the linear, perturbed system of equations around this equilibrium state, showing that standard FBGD assumptions do not apply to meteor trails and that it is necessary to solve the complete quadratic dispersion relation. Nevertheless, one may use this equation to calculate the range of wavelengths over which instability may occur and the characteristics of the resulting waves.

Making a number of assumptions about the state of "typical" meteor trails, we solved this dispersion relation, showing the limited range of altitudes at which one expects instability growth. The minimum altitude depends principally on the composition and latitude of the trail. The maximum altitude depends primarily on the gradient scale length of the trail which results from the initial radius of the meteor trail. We used this dependency to show that the Bronshten (1983) description of initial radius better matches observations, than the description put forth by Baggaley (1981).

**Acknowledgments:** The authors would like to thank Kelly McMillon and Licia Ray for editing and producing many of the figures. This material is based upon work partially supported by the National Science Foundation under Grant No. ATM9986976 and NASA Grant No. NGT5-50288.

## REFERENCES

- Baggaley W.J., 1981, *Bull. Astron. Inst. Czech.*, 32, 345  
 Blaunstein N.S., Milinevsky G.P., Savchenko V.A., Mishin E.V., 1993, *Planet. Space Sci.*, 41, 453  
 Bronshten V.A., 1983, *Physics of Meteoric Phenomena*, chap. 100-105, Reidel Publishing Company

- Cepkecha Z., Borovicka J., Elford W.G., et al., 1998a, *Space Science Reviews*, 84, 327  
 Cepkecha Z., Borovicka J., Elford W.G., et al., 1998b, *Space Science Reviews*, 84, 327  
 Chang J.L., Avery S.K., Vincent R.A., 1999, *Radio Sci.*, 34, 179  
 Chapin E., Kudeki E., 1994, *Geophys. Res. Lett.*, 21, 2433  
 Chen F.F., 1984, *Introduction to Plasma Physics and Controlled Fusion*, 2nd ed, Plenum, New York  
 Dyrud L.P., Oppenheim M.M., vom Endt A.F., 2001, *Geophysics Research Letters*, 28, 2775  
 Fejer B.G., Farley D.T., Balsley B.B., Woodman R.F., 1975, *J. Geophys. Res.*, 80, 1313  
 Fejer B.G., Providakes J., Farley D.T., 1984, *J. Geophys. Res.*, 89, 7487  
 Haldoupis C., Schlegel K., 1993, *Radio Sci.*, 28, 959  
 Jones J., Jones W., 1991, *Planet. Space Sci.*, 39, 1289  
 Jones W., 1991, *Planet. Space Sci.*, 39, 1283  
 Kudeki E., Farley D.T., 1989, *J. Geophys. Res.*, 94, 426  
 Lee K., Kennel C.F., Kindel J.M., 1971, *Radio sci.*, 6, 209  
 Öpik E.J., 1958, *Physics of Meteor Flight in the Atmosphere*, Interscience Publishers  
 Oppenheim M.M., vom Endt A.F., Dyrud L.P., 2000, *Geophysics Research Letters*, 27, 3173  
 Pickering W.M., Windle D.W., 1970, *Planet. Space Sci.*, 18, 1153  
 Reddi C.R., Nair S.M., 1998, *GRL*, 25, 473  
 Rishbeth H., Garriott O.D., 1969, *Introduction to Ionospheric Physics*, Academic  
 Schmidt M.J., Gary S.P., 1973, *J. Geophys. Res.*, 78, 8261  
 Zhou Q.H., Mathews J.D., Nakamura T., 2001, *Geophys. Res. Lett.*, 28, 1299

## THE COMPUTER MODEL "KAMET": THE NEW GENERATION VERSION

Arkady Karpov, Sergey Tereshin, Joury Abrosimov

Russia 420110 Kazan st. Zorge53 – 54, Email: Arkadi.Karpov@ksu.ru  
 Russia 420012 Zelenodolsk st. Ajvazovsky 14 - 26, Email: stereshi@green.kcn.ru  
 Russia 420140 Kazan st. Minska 20 – 33, Email: Jouri.Abrossimov@ksu.ru

### ABSTRACT

In this work, we present the results of the modernization of the computer model "KAMET". "KAMET" contains the following primary software modules: astronomical model of the flux of meteoric material into an atmosphere of the Earth; a block of geometrical aspect equations; the physical model; the electrodynamics model; a block of power equations. An astronomical component of model "KAMET" is based on long-term experimental radar observation which are carried out on the meteoric radar of the Kazan university. Modification of the radiotomography input data gives us the possibility of taking into account a thinner structure of meteor flux. The simulation method also allows revision of the tables of meteor flux density for new physical models that may be introduced. The experimental measurements are used to demonstrate prediction accuracy of the «KAMET» model.

### INTRODUCTION

The capacity of the statistical model is defined, to the great degree, by the correct choice of the generation area of the stochastic parameters. The optimal choice of the generation area is made through the realization of original dispersion decline procedures of modeling results. The main procedures are "generation contour" and "procedure of defining the minimal generated mass". The use of the "contours" has allowed to significantly narrow the shelling area by random trajectories of meteoric radiants. The Fig.1 shows the generation contour for radio waves of the length  $L = 500$  km (1a), 1100 km (1b), 1600 km (1c) and trajectory set  $n=0.55-0.65$ ,  $m=0.2-0.3$ ,  $l=0.69-0.81$ . Figures are executed in scale of length of radioline. Items of a radioline mark by the points. The trajectory generation is made only in the crosshatched region. When these procedures are used the modeling velocity increases by 150 times, on average. Now the calculation of a chosen point (modeling of the meteoric radio communication system for the period of 1 hour) takes several seconds when Pentium-3 is used.

The computer model "KAMET" allows to model the following: characteristics of the meteoric phenomenon (meteoroid mass and energy, height of its combustion), characteristics of the meteoric trail (linear electronic density, trail lifetime taking into account the main fac-

tors that destroy the trail), characteristics of the radio reflection from the trail (amplitude-time behaviour, peak amplitude of the reflected signal, signal/noise relation, radio reflection duration, amount of the transmitted information).

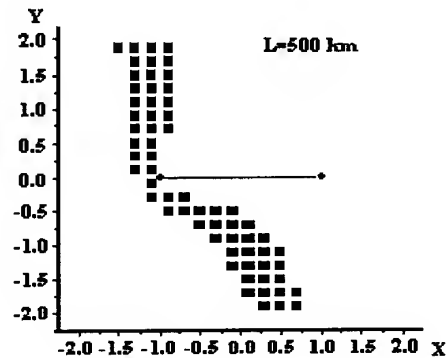


Fig.1-a Example of generation contour

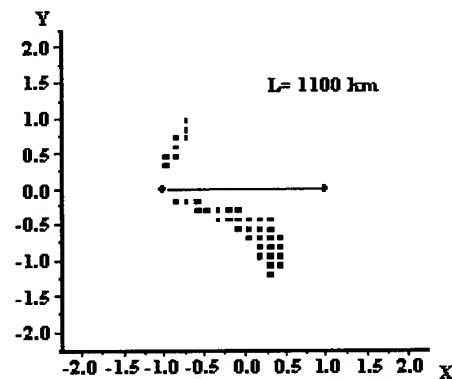


Fig.1-b Example of generation contour

Here are also the integral characteristics obtained over a certain period of time (e.g. 1 hour): the number of radio reflections (meteor rate) and mark-to-space ratio (duty cycle). The input characteristics of model are: characteristics of the radio links (transmitter power, frequency of radiation, kind of modulation, protocol of information interchange, kind and polarization of antennas etc.), geographical coordinates of items of communication and date of realization of experiment. The program complex functions on PC under the control of operational system Windows. The work with "KAMET" is conducted in the conversational mode.

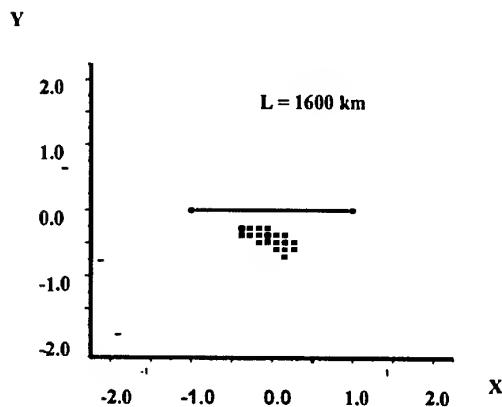


Fig. 1-c Examples of generation contour

## 1. ASTRONOMICAL MODEL

The astronomical component of the "KAMET" model is based on the long-term experimental radar observations conducted in Kazan State University. The astronomical model is the empirical chart of radiant density distribution over the coelosphere obtained for a certain date. Two astronomical models are used in the "KAMET". The first was obtained by Yu.A. Pupyshv [1] on a radar with an antenna that has a wide polar pattern and is called azimuth-statistical. At present the shift is being made for a new astronomical model the creation of which became possible as a result of the development of the new statistical method of processing radio-location observations of meteors with the measurement of the radio wave angle of arrival reflected from meteoric trails, which was proposed in the works by O.I. Belkovich, V.V. Sidorov and T.K. Filimonova [2]. This is usually called a "radio tomographic" model and this is how we will distinguish it later in this paper. The radio tomographic astronomical model allows considering a finer structure of the meteoric substance influx. Essentially, it reflects the micro-flow concept of the meteoric complex. We will compare these two astronomical models using the experimental data of 1988.

The Fig. 2 shows the radiant density distributions obtained from September 7 to September 21, 1988. The Fig. 2a shows the distribution obtained using the azimuth data while the Fig. 2b gives the "radio tomographic" distribution. Obviously, the main rules in the distributions repeat. The distribution can be presented in the form of several "ridges" with the following coordinates:  $\epsilon = 5^\circ - 125^\circ$  and  $\psi = 5^\circ - 65^\circ$ ,  $\epsilon = 5^\circ - 125^\circ$  and  $\psi = 115^\circ - 165^\circ$ ,  $\epsilon = 5^\circ - 95^\circ$  and  $\psi = 175^\circ - 245^\circ$ ,  $\epsilon = 5^\circ - 125^\circ$  and  $\psi = 305^\circ - 355^\circ$  and these "ridges" can be clearly seen in the both distributions. The "radio tomographic" distribution reveals much more details. The azimuth-statistical distribution obtained by a rougher measuring instrument (when averaging areas reach  $40^\circ$ ) becomes more leveled with some of its parts being indistinguishable and, on the whole, it is less informative.

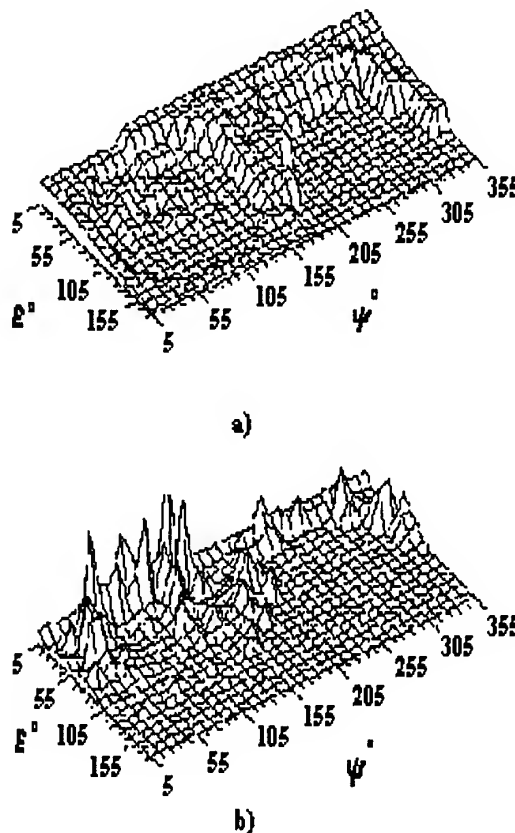


Fig. 2. The radiant density distributions

## 2. PHYSICAL MODEL

The physical characteristics of mass and geometric selection are generated in the physical model block for each trajectory that satisfies the geometric selection conditions. Then the trail characteristics (linear elec-

tronic density, etc.) and the reflected signal capacity are calculated taking into account equipment characteristics and radio line parameters. Let us consider the main elements of the physical model in the radio tomographic modification "KAMET" proposed in the works by V.S.Tokhtasiev and O.I.Belkovich [3]. One of the most important characteristics of the physical model is the dependence of pressure in the maximum point from the meteoric particle mass  $m$ , its velocity  $v$  and zenithal distance  $z_p$ . The formulas are true in the mass range  $10^{-7}$  gr.  $\div$  1 gr. Two types of particles with the following densities were introduced for the consideration [3]:

- $\delta_1 = 3 \text{ r/cm}^3 - 50\%$
- $\delta_2 = 0.3 \text{ r/cm}^3 - 50\%$ .

$$\begin{cases} P_m = 2.654 \cdot 10^2 \cdot v^{-1.8} \cdot m^{1/3} \cdot \delta^{2/5} \cdot (\cos z_p)^{0.85}, & m > m^* \\ P_m = 3.831 \cdot 10^2 \cdot v^{-2} \cdot m^{1/5} \cdot \delta^{(2/5)} \cdot (\cos z_p)^{0.65}, & m' \leq m \leq m^* \\ P_m = 4.483 \cdot 10^2 \cdot v^{-2.3} \cdot \delta^{0.54} \cdot (\cos z_p)^{0.35}, & m'' \leq m \leq m' \\ P_m = 7.728 \cdot 10^2 \cdot v^{-2} \cdot m^{1/5} \cdot (\cos z_p)^{0.65}, & 10^{-7} \leq m \leq m'' \end{cases}$$

$$\begin{aligned} m^* &= 15.7 \cdot v^{-1.5} \cdot (\cos z_p)^{-1.5} \\ m' &= 2.89 \cdot \left(\frac{3.4}{\delta}\right)^2 \cdot m'' \\ m'' &= 6.569 \cdot 10^{-2} \cdot v^{-1.5} \cdot \delta^{2.7} \cdot (\cos z_p)^{-1.5} \end{aligned} \quad (1)$$

The linear electronic density is defined according to the expression (2):

$$\alpha \approx m(v - 8.15)^3 \quad (2)$$

Normalization is implemented in compliance with the mass scale adopted for this case – stone meteoric body with the mass  $4 \cdot 10^{-4}$  gr. that vertically flies into atmosphere with the velocity  $40 \text{ km} \cdot \text{sec}^{-1}$ , and makes the trail with the linear electronic density in the ionization peak  $= 10^{14} \text{ electron} \cdot \text{m}^{-1}$ .

The initial radius is defined taking into account the dependence from the velocity according to the expression [4-6]:

$$r_0 = 10^{-2} \left(\frac{v}{36}\right)^{0.5} \exp(0.05h) \quad [4,5] \quad (3)$$

$$r_0 = 1.2 \cdot \left(\frac{v}{40}\right)^{0.6} \cdot \frac{\rho_0}{\rho} \quad [6] \quad (4)$$

, where  $\rho$  is the atmosphere density on the given height and  $\rho_0$  is the atmosphere density on the height of 95

km. The dependence of the ambipolar diffusion coefficient from the height is defined according to the expression:

$$D_a = 8.3 \cdot \exp\left(\frac{h - 95}{5.45}\right) \quad (5)$$

The parameter of meteoric bodies distribution in masses is taken as constant and equal of  $s=2.35$ .

### 3. MODELING RESULTS

The Fig.3 shows the comparison of the experimental results of the number of meteoric radio reflections registered on the radio line having the length of about 1100 km with the modeling results obtained using the "classical" dependence of the initial radius from the height (formula 3) and the dependence proposed by V.S.Tokhtasiev (formula 4). In the morning the modeling results (formula 3) significantly (by 2.2 dB) exceed the experimental results. The use of the dependence (formula 4) coordinates the results of the experiment and modeling well.

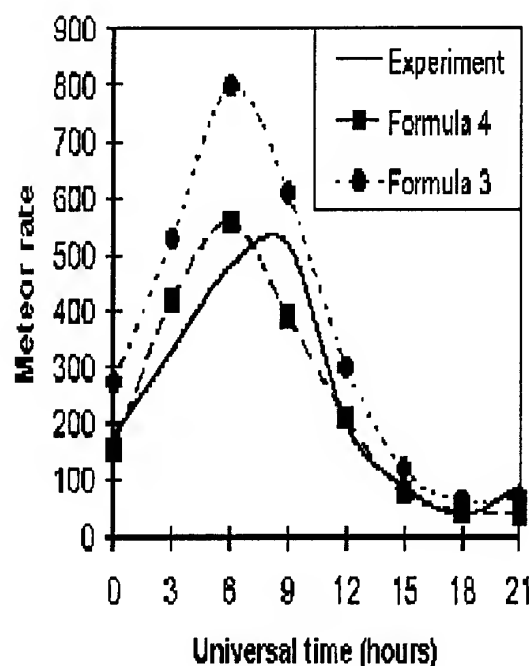


Fig.3. Forward scatter measurement – prediction

The Fig.4 shows the normalized distribution of radio echo heights when two models of the initial radius are used: the line 1 is obtained using the expression (formula) 4 and line 2 using the expression (formula) 3. In fact, the distributions are identical at heights of up to 95 km, while differences are obvious at heights of over 100 km. There is a registration in heights of over 100

km when the "classical model" is used. They contribute 30% to the general number.

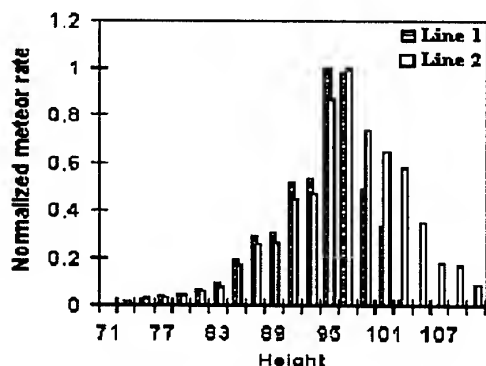


Fig.4. Model distribution of heights of reflecting points. The Fig.5 shows the comparison of the modeling results with the experimental data for the radio line of 1100 km. These experimental data are a good standard for the model test due to their sufficient statistical provision. The main parameters of the meteoric radio line and equipment are as follows: wave length 7,5 m, transmitter capacity 2 KW, registration boundary  $U = 1\text{mkV}$ , antennas – yagi with five elements. The comparison of the modeling results with the experimental data in relation to the average hourly number of meteoric radio reflections was conducted for the season of the low meteoric activity (March). The average hourly number of meteors in the experiment is 241.2 and in the projection – 253.1. The difference between the modeling results and the experimental data makes 0.2 dB. The peak deviation in the morning is 1.2 dB (9 a.m.) and 3.5 dB at 9 p.m.

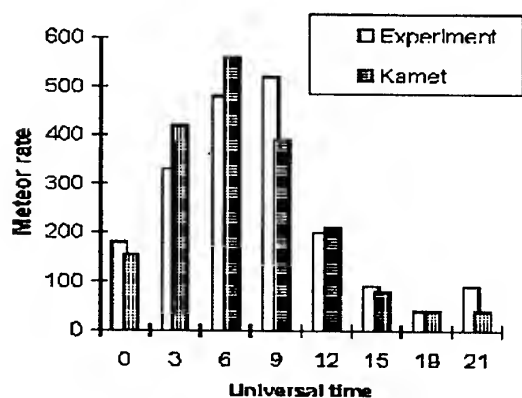


Fig.5. Data of a meteoric radiolink of length 1100 km

#### ACKNOWLEDGMENTS

1. This work was funded by the Russian Foundation for Fundamental Research (Project № 00-02-16845) the grant by the Russian Federation Ministry for Edu-

cation – T00-3.1-1168

#### 4. REFERENCES

1. Pupyshev Yu.A., et al. Maps of the distribution over the entire celestial sphere of the sporadic meteor radiant of the visible density of radiants, *Meteoritic propagation of radiowaves*, Vol.15, 21 – 41, 1980.
2. Belkovich O.I., et al. Tomographic method for meteor-flux determination from radar observations, *Solar System Research*, Vol. 31, 531 - 538, 1997.
3. Belkovich O.I., Tokhtashev V.S. Determination of the Quadrantid incident flux density. Part 2, *Bull. Astron. Inst. Czech.*, Vol. 25, 370-373, 1974.
4. Greenhow J.S., Hall J.E. The importance of initial trails radius on the apparent height and number distributions of meteor echoes, *Mon. Not. Roy. Astron.* Vol.121, 183-196, 1960.
5. Greenhow J.S., Neufeld E.L. The diffusion of ionized meteor trails in the upper atmosphere, *J.Atmos.Terr.Phys.* Vol.18, 133-140, 1960.
6. Tokhtashev V.S. Dependence of factor of ionization on speed, *Scientific News AOE*, Vol 41-42. 228-230, 1976.

# ON THE ATMOSPHERICS DYNAMICS OF THE TUNGUSKA COSMIC BODY

L. Foschini<sup>1</sup>, G. Longo<sup>2</sup>, T.J. Jopek<sup>3</sup>, Ch. Froeschlé<sup>4</sup>, R. Gonczi<sup>4</sup>, and P. Michel<sup>4</sup>

<sup>1</sup>Istituto TeSRE – CNR, Via Gobetti 101, 40129 Bologna (Italy); email: foschini@tesre.bo.cnr.it

<sup>2</sup>Dipartimento di Fisica, Università di Bologna, Via Irnerio 46, 40126 Bologna (Italy)

<sup>3</sup>INFN, Sezione di Bologna, Via Irnerio 46, 40126 Bologna (Italy)

<sup>4</sup>Observatorium Astronomiczne Uniwersytetu A. Mickiewicza, Słoneczna 36, 60286 Poznań (Poland)

<sup>4</sup>Observatoire de la Côte d'Azur, Departement Cassini, URA CNRS 1362, B.P. 229, 06304 Nice (France)

## ABSTRACT

We studied the available scientific literature on the Tunguska event of 30 June 1908 to obtain parameter sets of the Tunguska Cosmic Body atmospheric dynamics. We performed a comparative analysis by means of available theoretical models and with the help of interplanetary dynamics, and we excluded unphysical orbits. Our results indicate a very high probability that the TCB was an asteroid.

Key words: Tunguska, fragmentation, atmospheric dynamics.

## 1. INTRODUCTION

At the dawn of 30<sup>th</sup> June 1908, a powerful explosion over the basin of the Podkamennaya Tunguska river flattened  $2150 \pm 50 \text{ km}^2$  of Siberian *taiga*, releasing in the atmosphere about 10 – 15 Mton of energy. After more than ninety years of studies and researches, the origin of the cosmic body that caused the devastation is still dubious, though a cometary or asteroidal origin is more accredited. The majority of Russian scientists follows the cometary hypothesis, while many western scientists prefer an asteroidal model: a comprehensive review of theoretical and experimental works can be found in the proceedings of the international workshop *Tunguska96*, held in Bologna (Italy) on 15<sup>th</sup> – 17<sup>th</sup> July 1996 (see the special issue of *Planetary and Space Science*, vol. 46, n. 2/3, 1996, edited by M. Di Martino, P. Farinella, and G. Longo). See also Krinov (1966), Trayner (1997), Vasilyev (1998), Bronshten (2000b).

Almost each year there is some expedition to Tunguska, but so far there was no recovery of macroscopic remnants. The data and samples collected in the burned area have not permitted a certain discrimination to be made between an asteroidal or a cometary nature of the TCB. In July 1999, an Ital-



Figure 1. Boarding the helicopter MI-26 at Krasnoyarsk during the Tunguska99 Scientific Expedition.

ian Scientific Expedition (Figure 1), organized by the University of Bologna with the collaboration of researchers from the Turin Astronomical Observatory and the Institute of Marine Geology of the National Research Council (CNR), went to Siberia in order to collect more data and samples (Longo et al. 1999, Amaroli et al. 2000, Longo et al. 2001)<sup>1</sup>.

While part of the collected samples of the lake sediments (Gasperini et al. 2001) and of the aerophotosurvey (Longo et al. 2001) have been analysed, we performed theoretical studies and modelling to support the field research. We studied the available

<sup>1</sup>See also <http://www-th.bo.infn.it/tunguska/>.

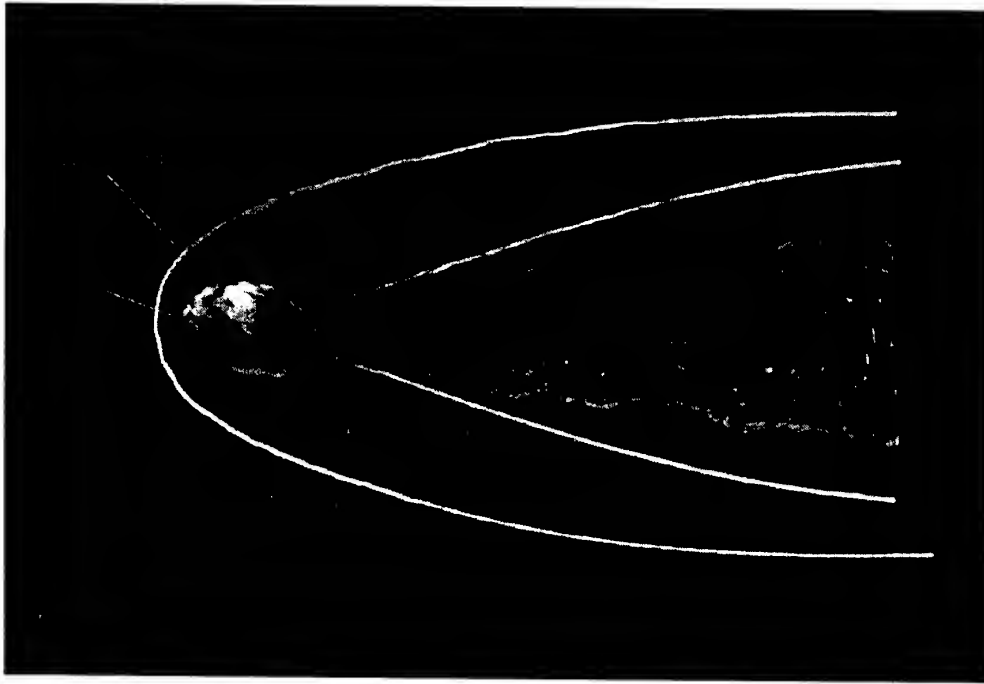


Figure 2. The hypersonic flow around a small asteroid (drawing not in scale). For a description see the text.

literature and the atmospheric dynamics of the TCB in order to extract a set of possible trajectories, from which we calculated the corresponding orbits.

In our work we prefer to assume, as one usually does, that a single explosion caused the Tunguska event, though some authors suggested the possibility of multiple explosions (cf. the discussion in Sect. 2.1 of Farinella et al. 2001). As recently newly underlined (Jull et al. 2001), most of the gas and debris would be injected in the stratosphere and, up to now, there are no proofs that distinct explosions have occurred at low altitude. We are studying this question using the aerophotosurvey's results. In the meanwhile we consider the fact that many witnesses have heard a single explosion and some of them have heard multiple explosions, that can be echoes. Anyway, if there were many bodies, like in the case of the impact of the Shoemaker-Levy 9 comet with Jupiter, all orbits would be very similar and the differences between the individual orbits would be much smaller than the differences due to the uncertainties in the parameters chosen.

Then, we studied the interplanetary dynamics and evaluated the probability that the TCB could come from one certain source in the Solar System. The complete study can be found in the paper by Farinella et al. (2001), while in the present proceedings we focus on the atmospheric dynamics calculations.

## 2. THE HYPERSONIC FLOW

The physical phenomena developing when a small asteroid (or a large meteoroid) enters the Earth atmosphere are quite different from the physics of bolides or the collision with kilometre-sized asteroids. It is very difficult to put boundaries among different regimes, but we can roughly identify that when we speak about the impact of small asteroids we are in the size range from some metres to some hundreds of metres. When such a cosmic body enters the atmosphere with velocities in the range  $12 \div 72$  km/s, it moves at hypersonic speed, i.e. with Mach number higher than 5. In addition, the size of the meteoroid is large when compared to the atmospheric mean free path already in the upper atmosphere, so that it is possible to consider the continuum approximation for the fluid flow. A schema hypersonic flow is shown in Figure 2.

A bow shock that envelops the body, develops in the front of the cosmic body. When the shock is normal to the stream – on the symmetry axis – we have the strongest point. The maximum strength is in the stagnation point, i.e. in the point of maximal thermal and mechanical stress. As the air flows toward the rear of the asteroid (or comet), it is reattracted to the axis, just like in a Prandtl-Meyer expansion. Therefore, there is a rotation of the stream in the sense opposite to that of the motion and this creates an oblique shock wave, which is called wake shock. Since the pressure rise across the bow shock is huge when compared to the pressure decrease across the Prandtl-Meyer expansion, we can adopt the reasonable approximation that there is a vacuum behind the cosmic body.

Closer to the body surface, there is a zone where the main process is the molecular dissociation and even closer to the surface, there is the boundary layer, where viscous effects are dominant. The fluid temperature increases in the boundary layer, because the speed must decrease to zero at the meteoroid surface; moreover there are heating effects due to viscous dissipation. In the flow, there are also regions (as the rear of the body) in which the presence of near-vacuum strongly reduces the heat transfer. This contributes to the increasing body temperature. If the generation of heat increases so quickly that the loss of heat may be inadequate to achieve an equilibrium state, we may have a thermal explosion. In addition, the presence of massive ablation – although tiny when compared to the whole mass of the incoming cosmic body – changes the flow properties. We expect that the layer between the shock and the surface is entirely turbulent, because of the ablation and the large Reynolds number. The turbulence can interact with shock waves, if the Mach number is not constant, while on the contrary the effect of compressibility suppress the turbulence.

Therefore, it is necessary to distinguish between two flow regimes, according to the fact that the Mach number during the atmospheric entry is constant (*steady state*) or not (*unsteady state*). In the latter case, the distortion of shock waves caused by changes in the Mach number causes the amplification of the turbulent kinetic energy. So, we expect sudden outburst of pressure that can overcome the mechanical strength of the body, starting the fragmentation process.

On the other hand, in the first case – the steady state – the effect of compressibility suppress the turbulence, and then the viscous heat transfer becomes negligible. The cosmic body is subjected to a combined thermal and mechanical stress.

For more details about these concepts refer to Farinella et al. (2001) and Foschini (1999, 2001).

### 3. THE CASE OF TUNGUSKA

The temperature as a function of height during subarctic summer is almost constant along the stratosphere down to the troposphere. Therefore, it is reasonable to assume that the Mach number of the hypersonic flow around the TCB remained almost constant during the second half of its atmospheric path. In this case, it is possible to relate the maximum speed of the flow with the temperature at the stagnation point. Changes in the stream properties are mainly due to changes in the stagnation temperature, which is a direct measure of the amount of heat transfer.

Under these conditions, it is possible to relate the *maximum* speed  $V_{\max}$  of the TCB at the fragmentation height (Foschini 1999, 2001):

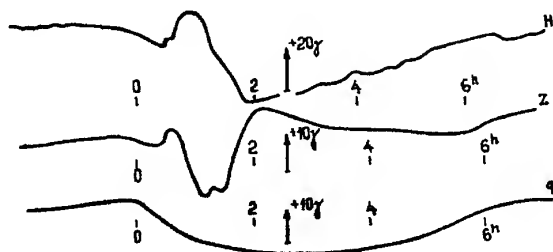


Figure 3. Local disturbances of the geomagnetic field recorded at Irkutsk Observatory 5.9–6.6 minutes after the explosion. From Ivanov (1964).

$$V_{\max} = \sqrt{\frac{2\gamma}{\gamma - 1} \frac{S}{(1 + \alpha)\rho_{fr}}} \quad (1)$$

where  $S$  is the mechanical strength of the TCB,  $\rho_{fr}$  is the undisturbed air density at the height of fragmentation,  $\alpha$  is the percentage of ionization ( $\alpha = 1$  full ionization), and  $\gamma$  is the specific heat ratio.

The selection of parameters is not straightforward: as stated above, the ablation changes the hypersonic flow, so that  $\alpha$  and  $\gamma$  changes along the atmospheric path. For sake of simplicity, it is possible to assume that these parameters remain constant: it is a commonly used assumption. But the problem is now connected to the value of  $\gamma$ , that is the most important parameter in this type of study. Foschini (1999) used a value of  $\gamma = 1.7$ , according to the experimental investigation of hypervelocity impact by Kadono & Fujiwara (1996); this is also the value commonly used for a monatomic gas or metal vapors. The gas around the TCB is composed by air compressed, dissociated, and even ionized, in addition to the metal vapors derived from the ablation: therefore,  $\gamma = 1.7$  could be reasonable.

However Bronsthen (2000a) raised a doubt about this value and he proposed  $\gamma = 1.15$ , derived from the equation (rearranged from Zel'dovich & Raizer 1966):

$$\gamma = \frac{5\epsilon_{trans} + 3Q}{3(\epsilon_{trans} + Q)} \quad (2)$$

where the sum of  $Q$  and  $\epsilon_{trans}$  gives the internal energy of the gas, i.e. the sum of translational energy  $\epsilon_{trans}$  and  $Q$ , the potential energy and the energy of the internal degree of freedom of the particles (vibrational and rotational, for molecules).

There is a third possibility: if the hypersonic flow around the TCB was in the state of plasma (i.e. a ionized gas where the charged particles density is sufficient to dominate the dynamics of particles), this means that electric and magnetic fields are present (e.g. Beech & Foschini 1999) and, therefore, they can limit the degree of freedom of particles. Indeed, the specific heat ratio can be written, according to

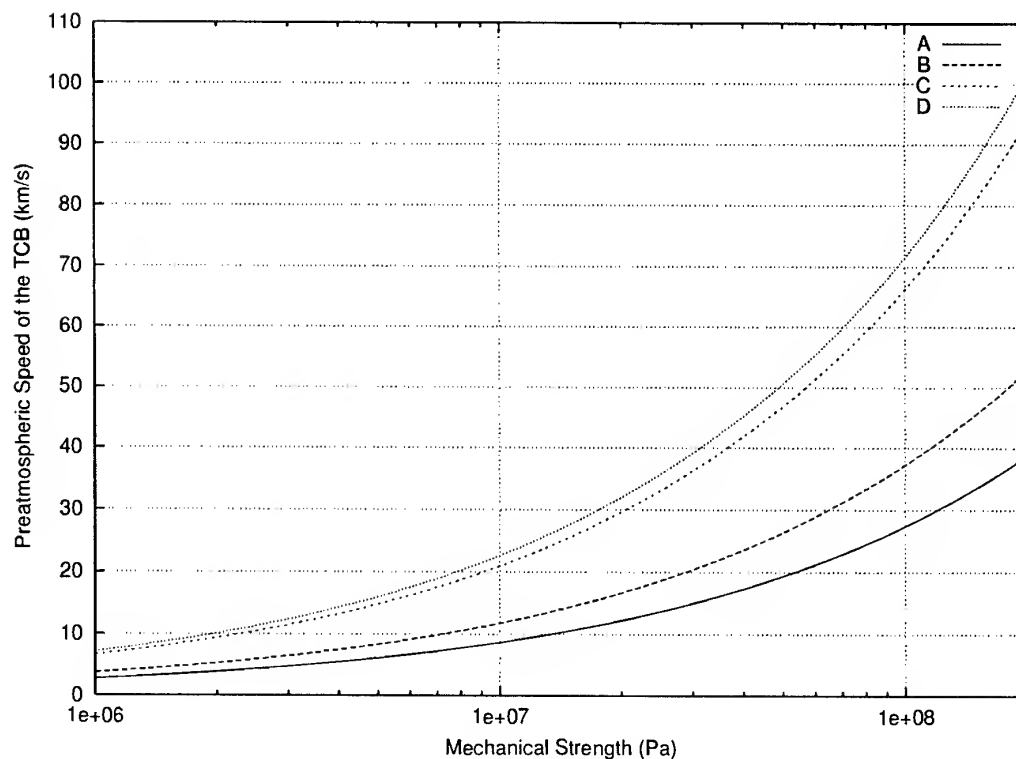


Figure 4. Evaluation of maximum speed of the TCB for four different compositions of the TCB and four different states of the shocked air: (A)  $\gamma = 3$ ,  $\alpha = 1$ , plasma; (B)  $\gamma = 1.7$ ,  $\alpha = 0.75$ , fully ionised gas; (C)  $\gamma = 1.15$ ,  $\alpha = 0.75$ , partially dissociated and ionised air at high temperature; (D)  $\gamma = 1.15$ ,  $\alpha = 0.5$ , dissociated and ionised air at high temperature.

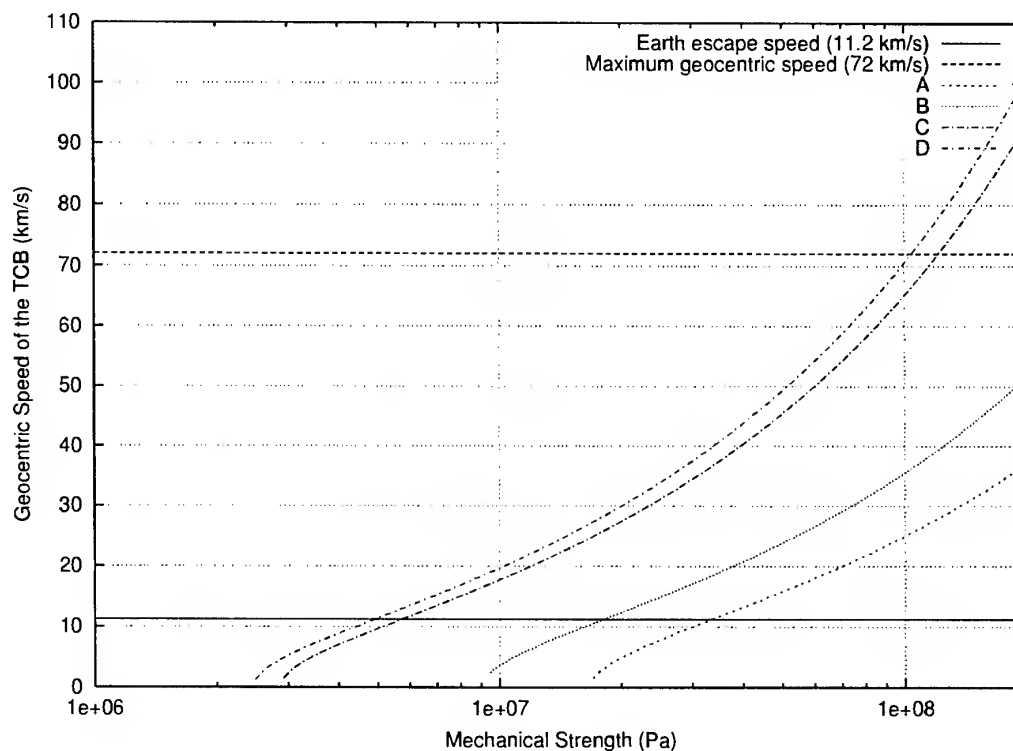


Figure 5. As in Figure 4, but with values of geocentric speed.

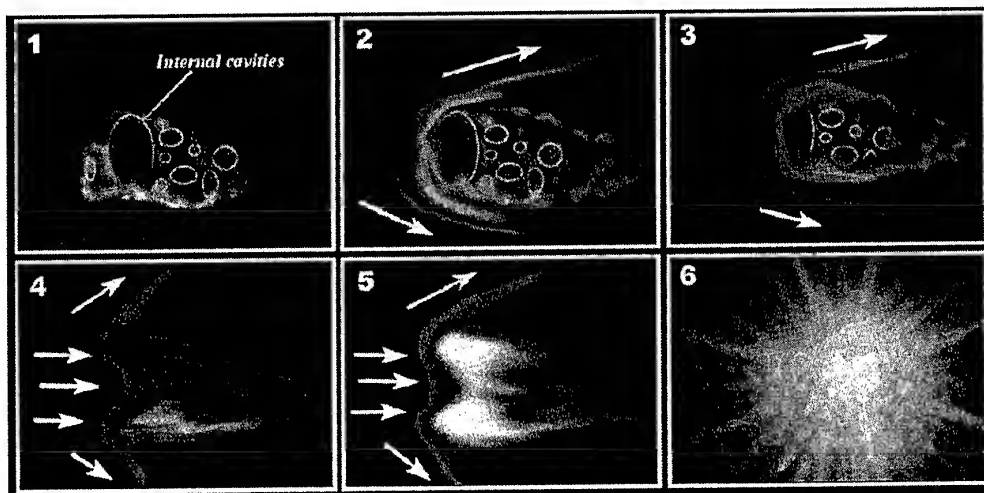


Figure 6. Schema of the possible process by means internal cavities could increase the deceleration and airburst efficiency. As the cosmic body enters the Earth atmosphere, the ablation removes the surface, discovering the internal cavities, which act as something like a parachute, increasing the deceleration.

the law of equipartition of energy (Landau & Lifshitz 1980):

$$\gamma = \frac{l+2}{l} \quad (3)$$

where  $l$  is the degree of freedom of particles. For example,  $l = 3$  for a monatomic gas or metal vapours, because the atom has three degrees of freedom (translation of atoms along  $x$ ,  $y$ ,  $z$  directions) and  $\gamma = 5/3$ . For plasma, the presence of electric fields forces the ions or even ionised molecules, if present, to move along the field lines, and therefore  $l = 1$ . This implies that  $\gamma = 3$ , close to Kadono & Fujiwara's original experimental value of 2.6 (Kadono & Fujiwara 1996). Indeed, their original experimental results gave a value of  $\gamma = 2.6$ , that the authors considered too high. They modified the calculations considering that the expansion velocity of the leading edge of the plasma was about twice that of the isothermal sound speed, obtaining a more reasonable – in their opinion –  $\gamma = 1.7$ .

Concerning the Tunguska event, it is worth noting that a *local* disturbance of the geomagnetic field had been registered 5.9 – 6.6 minutes after the beginning of seismic waves and continued for about four hours, reaching a peak of 0.056 A/m for the  $H$  component (Figure 3; see Ivanov 1964). So there were electromagnetic effects and we can expect that they derived from the plasma cloud developed during the explosion or even from the hypersonic flow before the explosion. In any case, it is reasonable to include the possibility to have  $\gamma = 3$  in the hypersonic flow during – at least – the terminal part of the atmospheric trajectory of the TCB.

In Figure 4, the maximum speed according to Eq. (1) is plotted as a function of the mechanical strength and for different values of specific heat ratio and ionisation coefficient. The undisturbed air density at

the fragmentation height is taken equal to  $\rho_{fr} \approx 0.2$  kg/m<sup>3</sup> (Allen 1976), that corresponds to a height of 15 km, just a scale height before the airburst. In Figure 5 the same as in Figure 4 is plotted, but for the geocentric speed as a function of the mechanical strength: in this case, the two reference speeds (11.2 and 72 km/s, the minimum and maximum geocentric speeds of a cosmic body at 1 AU) can give further constraints on the values of velocities.

As already noted by Ceplecha (1999, personal communication), the key point in fragmentation is how the ablation changes the hypersonic flow. If the ablation does not appreciably modify the shocked air around the TCB, the carbonaceous body hypothesis could be plausible (cases C and D). However, if the shocked air is mixed with ionised atoms from the TCB so that the gas around the body is fully ionised or even plasma, the only possible solution appears to be an asteroidal body (stony or even iron; cases A and B). The values obtained in Figure 4 show that, in any case, it is very unlikely that a cometary body could reach such a low height, because it would have an unphysical low value of speed. However, given the large uncertainties, it is not possible to exclude at all the cometary hypothesis. In addition, the existence of asteroids with an extremely low density is known, such as Mathilde ( $\approx 1300$  kg/m<sup>3</sup>), which suggest some connections with comets. Such a body could have an increased efficiency in deceleration (see Figure 6; cf. Foschini 1998).

During the *Meteoroids* 2001 conference, the results about the Tagish lake meteorite (see contribution by P. Brown and D.O. ReVelle in this issue) showed spectral characteristics close to D-class asteroids and a bulk density of 1670 kg/m<sup>3</sup>. This means that the parent body should have lower density, because the cosmic body is compacted by aerodynamic load. On the basis of these studies, D.O. ReVelle (personal communication) suggested that the Tunguska Cos-

mic Body could have a similar structure. ReVelle's studies also suggest that a porous body have an enhanced luminous and vaporization efficiency, so that it could explain why a chondritic body was completely vaporized. In addition, it can also explain the absence of smoky trails, which generally occur during the falling of chondritic bodies, bypassing the objection invoked by Rasmussen et al. (2001) as argument in favour of the cometary hypothesis, and the fact that no macroscopic remnant has been found until now.

#### 4. FINAL REMARKS

These studies on atmospheric dynamics together with a comprehensive examination of the available literature on the Tunguska event, allowed us to select a set of possible atmospheric trajectories, from which we computed the related orbits (1120). This set was later restricted, by eliminating orbits hyperbolic (30) and with semi-major axis greater than 4.2 AU (204). The remaining 886 orbits were examined by using the Bottke et al. (2000, 2001) method, based on the dynamic properties of celestial bodies, in order to find the sources. We find that 739 orbits (83%) are of bodies coming from typical asteroidal sources, while only 17% are from cometary sources. This result, combined with what we obtained from the atmospheric dynamics, suggest that the asteroidal nature is the most probable for the Tunguska Cosmic Body. Full details of the part concerning the interplanetary dynamics can be found in the paper by Farinella et al. (2001).

#### ACKNOWLEDGMENTS

This work originated from an idea of the late Paolo Farinella, deceased on March 25th, 2000: we dedicate it to him. This research has been partially supported by MURST Cofinanziamento 2000 and has made use of the *NASA's Astrophysics Data System Abstract Service*. We like to acknowledge P.A. Dybczyński for helping us with the JPL DE405 ephemeris and R. Baldini for the realization of Figures 2 and 6.

#### REFERENCES

- Allen C.W., 1976. *Astrophysical quantities*. The Athlone Press, London
- Amaroli L., Andreev G., Anfinogenov J. et al., 2000. In S. Aiello, A. Blanco (eds) IX GIFCO: What are the prospects for cosmic physics in Italy?, SIF Conference Proceedings 68, Bologna, p. 113
- Beech M., Foschini L., 1999, A&A 345, L27
- Bottke W., Jedicke R., Morbidelli A. et al., 2000, *Science* 288, 2190
- Bottke W., Morbidelli A., Jedicke R., et al., 2001, submitted to *Icarus*
- Bronshten V.A., 2000a, A&A 359, 777
- Bronshten V.A., 2000b, *Tungusskiy Meteorit: Istoria Issledovaniya*. A. D. Selyanov, Moskva
- Farinella P., Foschini L., Froeschlé Ch., et al., 2001, A&A, accepted for publication
- Foschini L., 1998, A&A 337, L5
- Foschini L., 1999, A&A 342, L1
- Foschini L., 2001, A&A 365, 612
- Gasperini L., Alvisi F., Biasini G., et al., 2001. In: M. Smelror, H. Dypvik, F. Tsikalas (eds) NGF Abstracts and Proceedings: 7th Workshop of the ESF IMPACT Programme 1, p. 29
- Ivanov K.G., 1964, *Meteoritika* 24,141
- Jull A.J.T., Burr G.S., Kring D.A., 2001, *Meteorit. Planet. Sci.* 36, 999
- Kadono T., Fujiwara A., 1996, *J. Geophys. Res.* 101, 26097
- Krinov E. L., 1966. *Giant Meteorites*. Pergamon Press, Oxford
- Landau L.D., Lifshitz E.M., 1980. *Statistical Physics Part 1 – Course of Theoretical Physics vol. 5*, 3rd edition, Butterworth-Heinemann, Oxford
- Longo G. and the Tunguska99 Expedition Team, 1999, *Bull. AAS* 31, 1591
- Longo G., Bonatti E., Di Martino M., et al., 2001. In: M. Smelror, H. Dypvik, F. Tsikalas (eds) NGF Abstracts and Proceedings: 7th Workshop of the ESF IMPACT Programme 1, p. 48
- Rasmussen K.L., Olsen H.J.F., Gwóźdz R. et al., 2001, *Meteorit. Planet. Sci.* 36, 1001
- Trayner C., 1997, *J. Br. Astron. Assoc.* 107, 3
- Vasilyev N.V., 1998, *Planet. Space Sci.* 46, 129
- Zel'dovich Ya. B., Raizer Yu. P., 1966. *Physics of Shock Waves and High-Temperature Hydrodynamic Phenomena*, Vol. 1. Academic Press, New York

# THE MEASUREMENT OF OZONE CONCENTRATION BY KAZAN RADAR OBSERVATIONS

Arkady Karpov, Andrey Konnov

Russia 420110 Kazan st. Zorge53 – 54, Email: Arkadi.Karpov@ksu.ru  
Russia 420106 Kazan st. Amirhan 26 – 156, Email: komkur@radiotelcom.ru

## ABSTRACT

In this paper the indirect method of measuring the ozone concentration based on the investigation of the radio echo duration is considered. The computer model "KAMET" was used to conduct the comparative analysis of various processes that limit the radio echo duration: radiative recombination, dissociative recombination and the recombination of triple collisions with electronic stabilization. The dissociative recombination and the recombination of triple collisions with electronic stabilization play the most important role in processes of the meteoric trail destruction. The modeling of the reflection duration was fulfilled for various mechanisms:

Without taking recombination into account;  
Taking only dissociative recombination into account;  
Taking recombination with electronic stabilization into account.

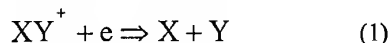
## INTRODUCTION

Most researchers believe that the main mechanism that restricts the radio echo duration is the recombination. There is no unity any more in questions of defining a specific recombination mechanism. The attention is paid to the three main reactions:

- dissociative recombination;
- recombinations with electronic stabilization;
- two-step process with participation of atmospheric ozone [1,2].

Let us consider each of the above mechanisms.

## 1. DISSOCIATIVE RECOMBINATION



The solution of the radial diffusion equation

$$\frac{\partial n}{\partial t} = \frac{D}{r} \frac{\partial}{\partial r} \left( r \frac{\partial n}{\partial r} \right) - \beta_1 n^2 \quad (2)$$

has the following form:

$$n(t) = \frac{\alpha}{4\pi D(t+t_1) + \alpha\beta_1(t+t_1) \cdot \ln\left(\frac{t+t_1}{t_1}\right)} \quad (3)$$

In the formulas (2-3)

$n(t)$  - volumetric electron density in a meteoric trail

$\alpha$  - linear electron density in a meteoric trail

$D$  - diffusion

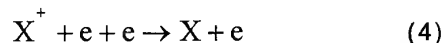
$r_0$  - initial radius

$\beta_1$  - rate constant

$$t_1 = \frac{r_0^2}{4D}$$

In the formula (3) a member is omitted that depends on  $r$  - distance from the trail axis.

## 2. RECOMBINATIONS WITH THE ELECTRONIC STABILIZATION



V.S.Tokhtasiev [3] has shown, that the solution of the radial diffusion equation

$$\frac{\partial n}{\partial t} = \frac{D}{r} \frac{\partial}{\partial r} \left( r \frac{\partial n}{\partial r} \right) - \beta_2 n^3 \quad (5)$$

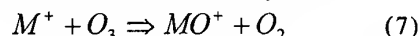
has the following form:

$$n(t) = \frac{\alpha}{\left( 16\pi^2 D^2(t+t_1) + \frac{2}{3}\beta_2 \cdot \alpha^2 \frac{t}{t_1} \right)^{\frac{1}{2}} \cdot (t+t_1)^{\frac{1}{2}}} \quad (6)$$

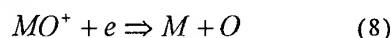
rate constant -  $\beta_2 = 4.1 \cdot 10^{-27} \text{ (M}^6/\text{cek)}$ .

## 3. TWO-STEP PROCESS WITH PARTICIPATION ATMOSPHERIC OZONE

Baggaley [1,2] has shown the loss electrons in this regime is a two-step process: first the meteoric ions are oxidized by ozone



with rate constant  $\alpha = 2 \cdot 10^{-15} \text{ M}^3 \text{ c}^{-1}$ . The oxide ions then recombine dissociatively with electrons



Last reaction proceeds very rapidly ( $\alpha = 5 \cdot 10^{-13} \text{ m}^3 \text{ c}^{-1}$ ) so that the radar of combined process is effectively by the oxidation. Decision of the equation radial diffusion has the following kind

$$n(t) = \alpha \cdot \exp(-\beta_1 \cdot n[\text{O}_3]t) \cdot \frac{1}{4\pi D(t+t_1)} \quad (9)$$

#### 4. MODELING

The real situation is complicated by the fact that the above chemical reactions occur simultaneously with the trail expansion due to the ambipolar diffusion. Besides, there is a problem of defining rate constant. According to different researchers, the rate constant differ by one or two orders (e.g. the rate constant defined in the laboratory and the one defined at the observation of meteors).

In this paper we present the results of modeling conditions for the meteor trail disintegration with the help of the computer model "KAMET".

The radioecho duration from underdense trails is calculated without taking into account the recombination since its effects become significant when the underdense trail is almost destroyed by the ambipolar diffusion. The radio echo duration from the overdense trail is calculated by the numerical method taking into account the recombination effect according to the formula (10). Let us define the radio echo duration as the time interval when radio signal amplitude

$U = \sqrt{2 \cdot P \cdot R_0}$  ( $R_0$  — internal transmitter resistance) exceeds the threshold sensitivity of the transmitter  $U_0$ .

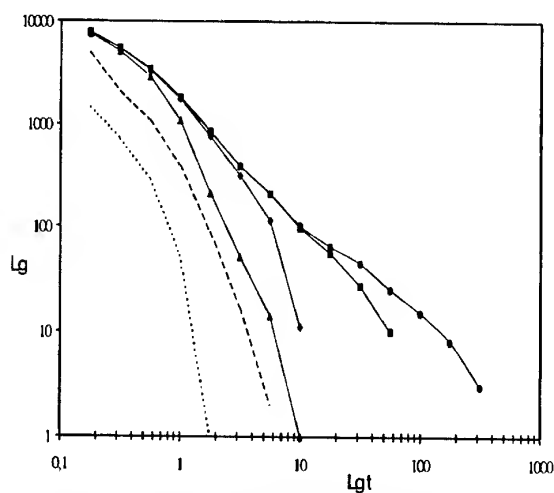


Fig. 1 The distribution of echo durations (dissociative recombination)

The figs 1 – 3 show the modeling results for the three mechanisms, that limit the duration of the radioecho. For the dissociative recombination the rate constant ranged within the bounds  $10^{12} - 10^{16} \text{ m}^3 \text{ sec}^{-1}$ . The extremely right curve was obtained without taking into account the recombination. For the recombination with the electronic stabilization the rate constant ranged within the bounds  $10^{29} - 10^{32} \text{ m}^6 \text{ sec}^{-1}$ . For the reaction with ozone the concentration ranged within the bounds  $10^{12} - 10^{15} \text{ m}$ . The Fig 4 shows the modeling results for two values of the wavelength (the two-step reaction with ozone was modeled):  $\lambda = 5 \text{ m}$  и  $\lambda = 10 \text{ m}$ .

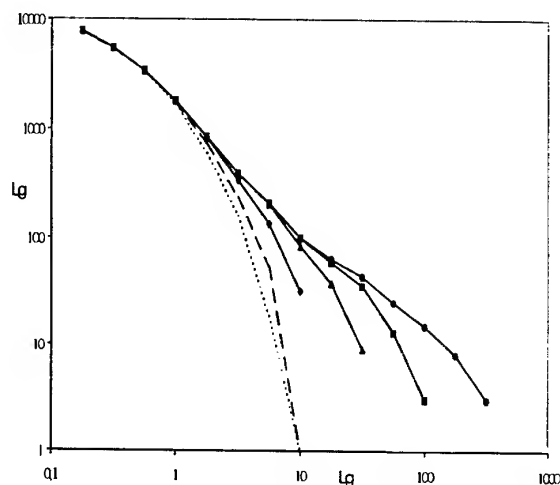


Fig. 2. The distribution of echo durations (recombinations with electronic stabilization)

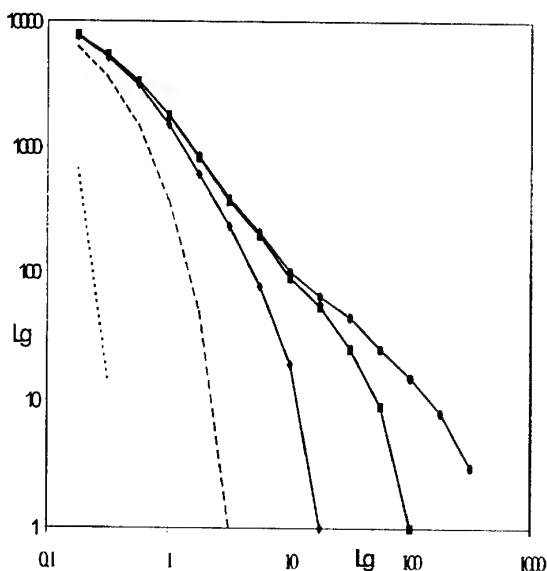


Fig.3 The distribution of echo durations (reaction with ozone)

## 5. THE DISCUSSION OF THE MODELING RESULTS

The modeling results show that all three mechanisms give approximately the same distributions of the radio echo duration. When the ozone concentration is defined by the radio meteoric method it is necessary to take into account all main mechanisms. Rate constant should be defined rather accurately using independent (non-meteoric methods). Besides, the analysis of the results given on the Fig 4 shows that the method of defining the ozone concentration by the inflection point in the distribution of the radio echo activity leads to the methodical mistake since the ozone concentration cannot depend on the radar's wavelength. One of the most important problems in the experiment is defining the duration of the continuous radio echo. In the end of the trail existence the reflection fading occurs that is stipulated by turbulent processes leading to the emergence of additional reflection centers. As a result, the continuous reflection can be accepted as several short reflections. And visa versa, several short reflections that exist together can be accepted as a single whole. In the meteor radar "KGU-M5" the problem of dividing the radio echo is solved thanks to the possibility of the accurate measurement of the distance from the radar to the trail.

## ACKNOWLEDGMENTS

This work was funded by the Russian Foundation for Fundamental Research (Project № 00-02-16845) the grant by the Russian Federation Ministry for Education -- T00-3.1-1168

## REFERENCES

1. Baggaley W.J. *Mon. Not. R. astron. Soc.*, Vol. 159, 203 – 207, 1972.
2. Baggaley W.J., Cummac C.H. *J. atmos. terr. Phys.*, Vol. 36, 1759 – 1762, 1974.
3. Tokhtasiev V.S. *Scientific News AOE*, Vol 41-42. 225-227, 1976.

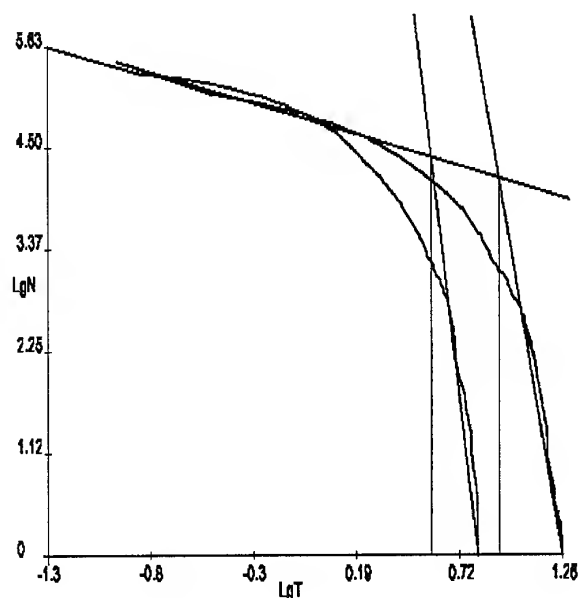


Fig. 4. Plots of number of radio-meteor echoes with duration for various meanings of frequency (30 и 60 MHz).

# METEOR TRAINS AS A PROBE FOR MEASURING THE DYNAMICS OF THE UPPER ATMOSPHERE

S. H. Marsh and W. J. Baggaley

University of Canterbury, New Zealand

## ABSTRACT

The AMOR meteor orbit radar operated near Banks Peninsula on the South Island of New Zealand (172° 39' E, 43° 34' S) has recently been extended to enable wind measurements in the upper mesosphere and lower thermosphere.

As the meteoroid encounters the increasing density of the Earth's atmosphere it ablates and leaves a train of ionisation. Radar signals reflecting from this wind-blown train are Doppler shifted and a line of sight wind measurement is made. A dual interferometer enables the height of the wind measurement to be determined to within 1 km. Hence a detailed vertical profile of motion in the meteor region is obtained.

This paper details the meteor radar method of wind measurement. The analysis presented includes a time series analysis of the AMOR winds data for the period May 1997 to June 1999. Results include a strong 12-hour semidiurnal tide as well as occasional longer period planetary waves. It is also shown that the amplitude of the supposedly significant 8 hour terdiurnal tide is exaggerated due to the combination of a large semidiurnal tide and diurnal sampling.

Key words: Meteor radar, Upper atmosphere winds.

## 1. INTRODUCTION

The Advanced Meteor Orbit Radar Facility, AMOR, (Baggaley & Bennett, 1996) has been determining meteor orbits since 1990. During 1996 the system was modified to allow simultaneous measurement of the meridional (north-south) component of the atmosphere's motion in the meteor region of 70–120 km (Marsh et al., 2000).

The system operates at a frequency of 26.2 MHz and a Pulse Repetition Frequency ( $P$ ) of 379 s<sup>-1</sup>. It utilises a 40 λ collinear broadside array to irradiate the sky with a pattern which is only 2° wide (FWHM) in azimuth and aligned along the meridian (Baggaley & Bennett, 1996). Due to the azimuthal

constraints, only the elevation angle and range of the echo are required to accurately locate the meteor detection point. Hence the region enclosing the wind measurement is easily identified.

This paper presents results of a Lomb-Scargle Fourier Transform (Scargle, 1989) time series analysis of AMOR winds data recorded between May 1997 and June 1999. Application of the Lomb-Scargle Fourier Transform (LSFT) to the AMOR data set reveals oscillations with periods less than or equal to one day, called atmospheric tides (Forbes, 1982), as well as planetary waves with periods of several days (Andrews et al., 1987).

## 2. DETERMINING A WIND SPEED MEASUREMENT

Each wind measurement requires the derivation of two parameters: the velocity and the position at which the measurement was made.

Wind speeds are obtained from the rate of change of phase of the signal returned from the meteor train. The echo's phase is measured and recorded by the system as an 8 bit integer with dynamic range,  $d$ . The magnitude of the line of sight wind velocity,  $v_l$ , is given by

$$|v_l| = \frac{\lambda P}{2d} \left| \frac{\delta\phi}{\delta t} \right|. \quad (1)$$

The analysis process needs to ensure that the wind speed is only calculated from that part of the echo which displays a constant rate of phase change. Figure 1 shows the amplitude and phase of a typical echo. Prior to the identified region of constant phase we see phase curvature. This effect is caused by the transmitted signal reflecting from the already formed ionisation train as well as the meteor itself (McKinley, 1961). As a result the meteor speed (typically 10 to 70 km s<sup>-1</sup>) aliases the wind velocity during this time. As the meteor train expands, due to diffusion processes (McKinley, 1961), the amount of received

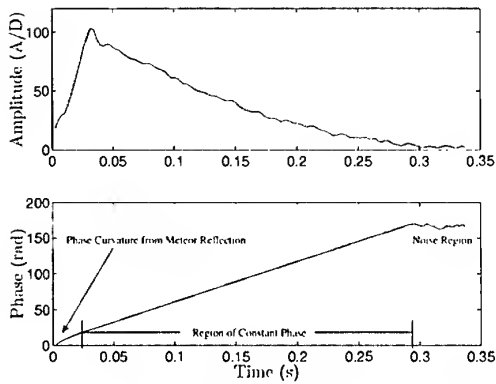


Figure 1. The amplitude (top) and phase (bottom) profiles for a typical echo.

signal decreases exponentially. Phase information is lost once the received power falls to the level of the background noise.

Absolute wind velocity uncertainties measured by the AMOR system are generally  $\ll 3 \text{ m s}^{-1}$ .

The spatial location of these measurements is achieved from the range and elevation angle of the returned echo's specular reflection point. Range is measured by sampling the signal returned from each transmitted pulse at  $40 \mu\text{s}$  intervals where each "range bin" represents an increase in range of approximately 6 km. An algorithm in the data collection software improves this range resolution to  $\sim 1 \text{ km}$  by interpolating between range bins containing the largest and second largest signal to find the signal peak.

The elevation angle,  $\phi$ , is measured unambiguously using a dual interferometer with spacings of 3.0 and 7.5  $\lambda$ . The uncertainty in this measurement is  $\sim 0.5^\circ$  (Baggaley & Bennett, 1996). The combination of low range and elevation uncertainties along with the narrow fan shaped beam means that individual wind velocity measurements are confined to a 3dB volume in space of  $\sim 8 \text{ km}^3$  (Marsh et al., 2000).

Having measured the elevation angle, the horizontal wind velocity,  $v_h$ , is determined from the line of sight wind velocity by

$$|v| = \frac{|v_l|}{\cos \phi}. \quad (2)$$

This expression makes the assumption that the vertical component of the wind field is not significant at meteoric heights (Smith, 1998).

Speeds calculated are assigned a negative value for winds headed in either a southerly or westerly direction.

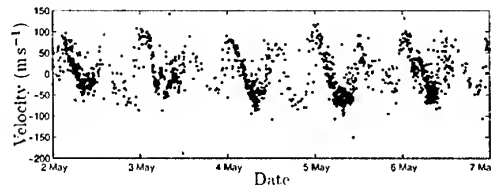


Figure 2. Wind velocities calculated from individual meteors at  $95 \pm 0.5 \text{ km}$ .

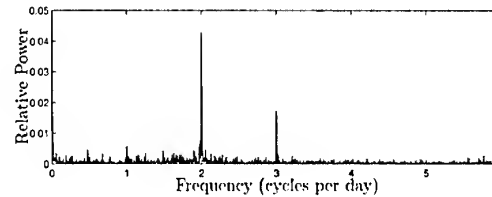


Figure 3. Power spectrum showing dominant oscillations in two years of AMOR wind measurements. The dotted line indicates the 99% confidence value for Siegel's test statistic.

### 3. RESULTS AND DISCUSSION

AMOR wind velocity measurements from altitudes at  $95 \pm 0.5 \text{ km}$  for five days in 1997 are presented in figure 2. There are some obvious features present. Firstly, the data describe a sinusoidal variation with period equal to approximately half a day. Secondly, the data rate varies from a maximum in the early morning (approx. 6 am) to a minimum in the early evening 12 hours later.

The sinusoidal variation is generated by thermal forcing of the Sun as the Earth rotates on its axis and is called the semidiurnal tide (Forbes, 1982). Generally this tide is the strongest signature observed in atmospheric winds at mid-latitude meteoric heights. The diurnal data rate is due to the amount of data being dependent on the position of the local prime meridian relative to the apex of the Earth's motion.

A search for oscillatory behaviour in the AMOR data set was performed with application of the Lomb-Scargle Algorithm. Time-series analysis of data from April 1997 to June 1999 gave the spectrum in figure 3. As expected from previous discussion the two cycle per day semidiurnal tide contained the most power and was well above the Siegel's test statistic at a 99% confidence level (dotted line) for data containing up to a maximum of three harmonics. Additionally the 1 cycle per day diurnal tide and 3 cycle per day terdiurnal tide are deemed statistically significant.

Due to the diurnal sampling of wind measurements figure 3 needs to be interpreted with care. The influence, on the spectrum, of periodically sampling data which contains oscillatory components can be

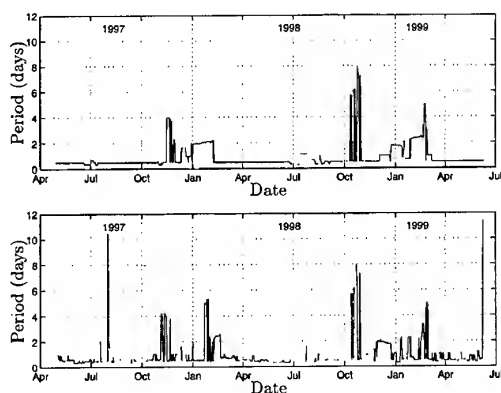


Figure 4. Occurrence of dominant (upper) and second most dominant (lower) oscillations.

represented by the expression

$$\text{Spectrum} = \sum_{m=1}^q \sum_{n=1}^p \cos \omega_m t \cos \omega_n t, \quad (3)$$

where  $p$  and  $q$  are the number of significant harmonics in the sampling function and wind data respectively. Expanding the product on the right hand side of this equation gives

$$\begin{aligned} \cos \omega_m t \cos \omega_n t &= \frac{1}{2} \cos(\omega_m + \omega_n)t \\ &+ \frac{1}{2} \cos(\omega_m - \omega_n)t. \end{aligned} \quad (4)$$

For the particular case  $\omega_m = 2\pi f_m$  and  $\omega_n = 2\pi f_n$  where  $f_m$  and  $f_n$  are the 2 cycle per day semidiurnal tide and 1 cycle per day diurnal sampling respectively, it is apparent that the spectrum obtained will contain additional power at frequencies of 1 and 3 cycles per day. The more detailed analysis performed by Marsh (2000) showed that the diurnal sampling had little effect on the value of the diurnal component however it did significantly over represent the amplitude of the terdiurnal component.

It should also be mentioned that the use of a diurnally sampling wind measuring instrument in regions where a large diurnal component exists could see contamination of the semidiurnal tide or mean wind.

The same data were also inspected for oscillations with periods of a few days known as planetary waves. The technique applies a LSFT to data within a sliding window (the window was moved in intervals of one day). Results are summarised in figure 4.

As expected this analysis finds the semidiurnal tide to be the dominant oscillation at most times. Interestingly though, this analysis does indicate the presence of several long period oscillations called planetary waves. Referring to the upper panel only we see a four-day event during November 1997 (Prata, 1984). A long-lived two-day wave (Phillips, 1989) is detected during January 1998 and again in 1999. Six

and eight-day waves (Kal'chanko & Bulgakov, 1973) are present during October 1998.

Although an inspection of the lower panel generally reveals the onset stages of behaviour observed in the top panel only, it does indicate the presence of ten-day wave activity in August 1997 and a five-day wave (Salby, 1984) in February 1998.

#### 4. CONCLUSION

The Advanced Meteor Orbit Radar (AMOR) has been measuring meridional winds in the upper mesosphere above the South Island of New Zealand since April 1997. The technique used allows meridional wind measurements to be made with small uncertainties. The measurements are also determined with excellent spatial resolution.

A time-series analysis of the data at  $95 \pm 0.5$  km heights has indicated the presence of diurnal, semidiurnal and terdiurnal tides. It has been suggested that the large terdiurnal component is over represented as a result of the combination of a larger semidiurnal tide and diurnal sampling.

The semidiurnal tide is seen to dominate the atmosphere's motion most of the year. Analysis has also revealed planetary wave activity. These oscillations, with periods of several days, are at times seen to occur with amplitudes even larger than that of the semidiurnal tide.

#### ACKNOWLEDGMENTS

The authors would like to thank the support of the Department of Physics and Astronomy at the University of Canterbury. In particular for the funding of a Ph.D. scholarship for S. H. Marsh, a time during which much of this work was achieved.

#### REFERENCES

- Andrews D., Holton J., Leovy C., 1987, Middle atmosphere dynamics, University Press
- Baggaley W., Bennett R., 1996, Astr. Soc. Pac. Conf. Series, 104, 65
- Forbes J., 1982, JATP, 36, 385
- Kal'chanko B., Gulgakov S., 1973, JGR 1973, 90a, 1735
- Marsh S., 2000, Ph.D. Thesis, University of Canterbury
- Marsh S., Bennett R., Baggaley W., Fraser G., Plank G., 2000, JASTP 62, 1129
- McKinley D., 1961, Meteor science and engineering, McGraw-Hill
- Phillips A., 1989, JATP 51, 119

Prata A., 1984, JAS, 150

Salby M., 1984, Rev. Geo. Spa. Phys. 22, 209

Scargle J., 1989, ApJ 343, 874

Smith R., 1998, JASTP 60, 1425

## **Classical Radar Observations of Meteors**

## FEATURES OF THE ENHANCED AMOR FACILITY: THE ADVANCED METEOR ORBIT RADAR

W. J. Baggaley, S. H. Marsh, R. G. T. Bennett, and D. P. Galligan

*Department of Physics and Astronomy, University of Canterbury, Christchurch, New Zealand*

### ABSTRACT

AMOR is a continuously operating radar facility for measuring the heliocentric orbits of Earth-impacting grains down to particle sizes of  $\sim 40 \mu\text{m}$ . It provides a data base containing  $\sim 10^6$  orbits. Recent extensions to AMOR including augmented directional antenna arrays and increased velocity resolution are providing an enhanced system capability.

Key words: meteor radar; interplanetary dust.

### 1. INTRODUCTION

The AMOR facility, designed to provide a continuous survey of the heliocentric orbits of interplanetary dust, has been in operation from 1990 to date. This multi-site radar measures the atmospheric trajectories of meteoroids, corrects for the motion of the observer, for the gravitational field of the Earth and for the Earth's orbital motion to provide the heliocentric velocity components of meteoroids prior to their entry into the sphere of influence of the Earth. Those components then yield the orbital elements - the geometrical elements  $i$ ,  $\omega$ ,  $\Omega$  and the size elements  $e$  and  $q$  (and hence  $a$ ). The facility employs the transverse reflection geometry mode utilizing three spaced sites to measure the east-west, north-south and vertical velocity components of the meteor's atmospheric trajectory. This geometry contrasts with that used to detect the scattering from the head plasma surrounding the ablating meteoroid - the radial geometry mode (see papers from session 7 of these conference proceedings).

### 2. THE TECHNIQUE

In the transverse radar mode, as the meteor approaches the specular condition (the  $t_0$  point) creating ionization, successive Fresnel intervals (each of length  $(R\lambda/2)^{1/2}$ ) are traversed and the phase of the

reflection coefficient increases monotonically to attain a maximum phase value at the  $t_0$  point. Post- $t_0$ , as more Fresnel lengths are added, the phase fluctuates with small ( $< \pi/9$ ) oscillations. Conversely, the real part of the reflection coefficient (and therefore recorded radar echo power) for a smooth plasma column increases to achieve a maximum value about 0.6 Fresnel intervals after the  $t_0$  point and thereafter undergoes pronounced oscillations ( $\sim 10\%$  in power). This radar behaviour has an exact analogy in the diffraction of light produced at a straight edge. Both the real and imaginary parts of the scattering cross-section time behaviour (and therefore echo power and phase signals) enable measurements of the scalar meteoroid speed. Meteoroid fragmentation and the action of wind shear may distort the ideal phase and power variations so that the post- $t_0$  power oscillations (termed the Fresnel diffraction record) are significantly damped in some cases. In contrast such distortions are absent early in the life of an echo so that the pre- $t_0$  phase function provides a good estimate of the meteoroid's atmospheric speed even for echoes having poor signal-to-noise ratios. The phase and power behaviour of an ideal echo can be analysed in terms of Fresnel functions (and depicted graphically using the Cornu spiral) and software can be developed to analyse radar signals to extract the meteoroid speed.

### 3. RADAR SYSTEM CONFIGURATION

The AMOR system uses three  $\sim 8$  km spaced stations to measure the time-of-flight north-south and east-west velocity components together with a dual-spacing interferometer at the central station to measure echo elevation. In the previous operation (years 1990-1999) echo spatial sampling was confined to the N-S meridian: a single transmitter illuminates an area of atmosphere via a narrow  $1^\circ.6$  (full-width-half power) antenna beam with received echoes detected on N-S pointing antenna arrays. In the enhanced system operative from January 2000 three upgrades to the system have been implemented.

- In order to provide a more complete coverage

of the celestial sphere the facility has been augmented by constructing additionally a pointing direction in the E-W meridian: the purpose is to produce increased sensitivity to meteors having radiants at mid-southern ecliptic latitudes. An additional orthogonal pointing antenna system is now in place consisting of: a new central site transmitter antenna array; central site triple receiving antennas forming a E-W direction elevation-finding interferometer; an orthogonal receiving antenna at each of the north and west remote sites. As for the previous N-S configuration the transmitting and receiving antennas are designed so as to reduce the antenna pattern side-lobes by non-uniform excitation combined with the use of different electrical lengths of the antenna arrays. Directional switching is provided by GPS controlled antenna switches. At the central site all interferometer antennas feed the receivers via underground ducted coaxial cables.

- Upgrades to the remote site signal transmission to the central site with new UHF link systems.
- The installation of a phase detection technique providing an individual independent phase (replacing the previous phase-difference method) signal from each of the six (three for each look-direction interferometer) central site receiving antennas. Such individual phase records are used to provide both the pre- $t_0$  and post- $t_0$  scalar speed measurements.

Three operational features are also incorporated in the enhanced recording programme: the radar system operation can be monitored by telephone; a backup transmitter has been constructed to secure near-continuous operation; recorded echo data are downloaded on a daily basis via a dedicated telephone line.

#### 4. ECHO DIRECTION FIXING

The overall radar system antenna radiation patterns provide azimuthal beams of width  $1^\circ.6$  (FWHP) directed in the geographic N-S and E-W meridians. Azimuth is not explicitly measured so that the lobe width determines the uncertainty in the horizontal plane. Echo elevation is achieved via two interferometer systems for each pointing direction consisting of three antenna arrays giving separations  $3.0\lambda$ ,  $7.5\lambda$  and  $10.5\lambda$ . Phases are measured at each individual antenna so that, for each pointing direction, three phase difference values permit the unambiguous elevation determination  $0^\circ$  to  $70^\circ$  for echo heights of 60 to 130 km. The elevation uncertainty is determined fundamentally by the angular size of the central region of the scattering plasma column – about one Fresnel interval ( $\approx 1.5$  km) – and experimentally by the phase measurement accuracy for the particular echo: the elevation uncertainty is  $\sim 0^\circ.3$  for echo

signal-to-noise ratio of  $> 8$  dB. Figure 1 shows the principal components of the enhanced AMOR system.

#### 5. METEOR VELOCITY

In the enhanced AMOR operation three independent methods are used to secure the meteor atmospheric trajectory and speed. During the echo formation phase as Fresnel intervals increasingly contribute to the scattered energy the maximum rate of increase of the echo scattering cross-section occurs at the instant when the meteoroid crosses the  $t_0$  point (refer to the behaviour of the Fresnel integrals). In the AMOR technique the derivative maximum of each of the three echo signals of the triple-site configuration is determined and it is the time differences in these values (after allowance for signal transmission through the hardware) that provides the echo time differences. The time-of-flight velocity components then follow using the echo elevation angle. Also determined are the radiant (the meteoroid trajectory upstream direction) azimuth and zenith angle.

Oscillations in the echo power as the meteoroid traverses successive Fresnel intervals after the  $t_0$  point yield the Fresnel diffraction scalar speed. For a given meteor three diffraction speeds for each site may be available depending on the signal-to-noise ratio of each. From signal analysis in terms of the Fresnel functions the enhanced AMOR system yields diffraction speeds for one or more sites for about 70% of echoes.

The pre- $t_0$  phase behaviour (as the mean range of the developing plasma decreases) shows a rapid monotonic increase – the phase changing by many cycles of  $2\pi$  to maximize at the  $t_0$  point. To extract the meteor speed two effects need consideration. During the whole echo life the phase of the recorded echo signal may change due to the transport of the meteoric plasma as a result of atmospheric winds. This bulk motion arises from solar tides, gravity wave oscillations as well as a mean flow. Since the variation of the phase after the  $t_0$  point arising from Fresnel behaviour is small and oscillatory, the wind contribution can be derived from examination of the post- $t_0$  time interval of an echo. With three echoes available a robust estimate of the line-of-sight wind can be extracted. The pre- $t_0$  true phase can then be derived. Since phase sensitive detectors cannot sense an absolute phase but yield a value in the range 0 to  $2\pi$ , the original phase has to be recovered from that measured by a process of ‘unwrapping’. Signal analysis routines are therefore used to extract the true phase. Correlating the time behaviour of the measured phase with the Fresnel functional form (from Fresnel integrals) yields the meteor speed. With three elevation-finding antennas AMOR produces an average of three such speeds: we have found that consistent phase behaviour and firm speeds are measured for all those echoes for which the maximum echo power of signal-to-noise ratio in excess of 8 dB

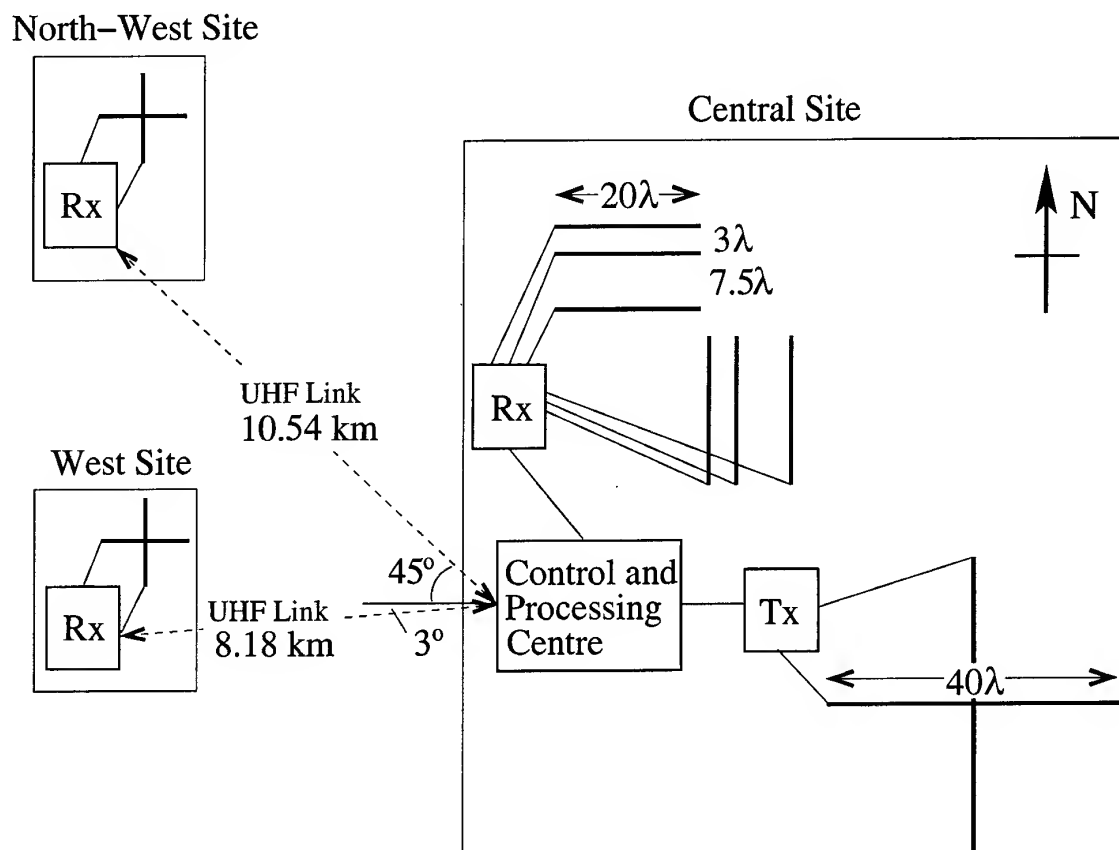


Figure 1. Schematic of the AMOR system showing the north, west and central sites. The site separation used for time-of-flight velocity measurements is  $\sim 8$  km. Echo signals from the remote sites are transmitted to the central control site via frequency modulated UHF links.

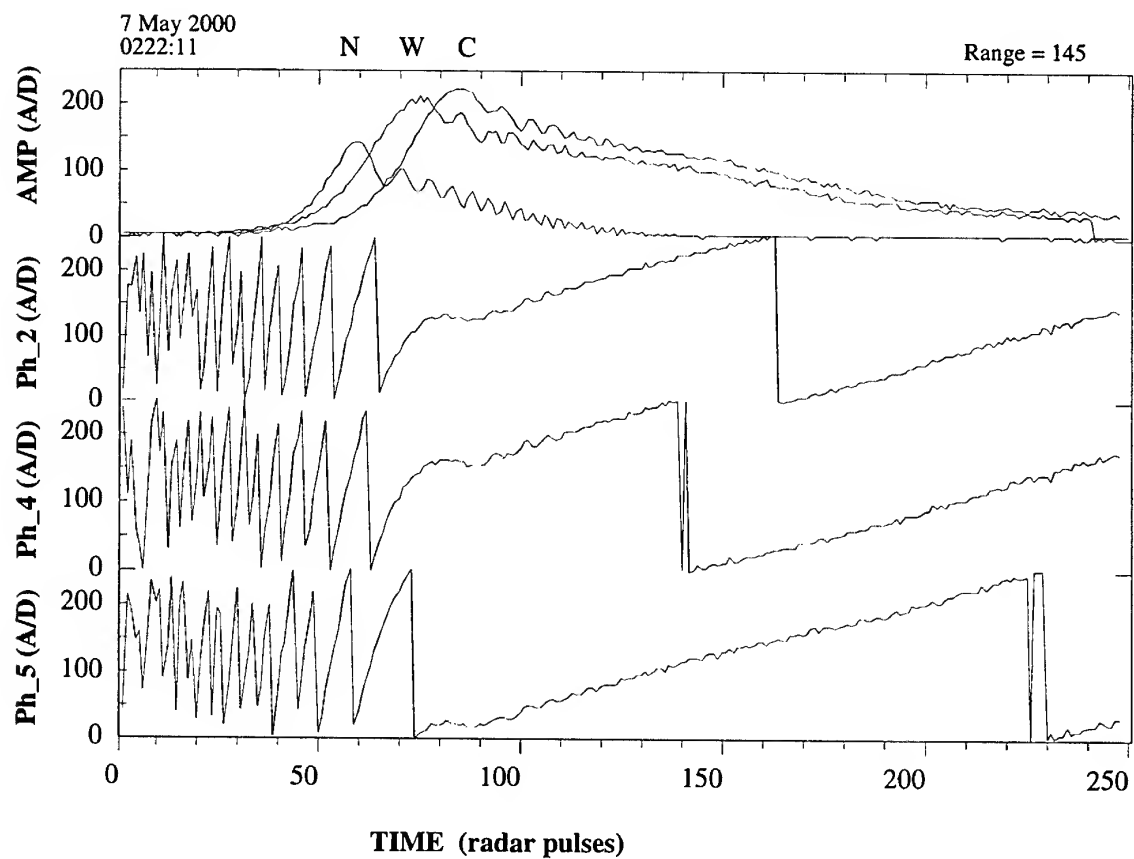


Figure 2. An example of a meteor record display. Top three traces – echo amplitudes recorded at sites N (north), W (west), and C (central). Lower traces – the three phases recorded on the three antennas of the elevation-finding interferometer.

- in practice all echoes used for orbit determination  
 - giving pre- $t_0$  speeds of uncertainty  $< 1\%$  for the bulk of measured trajectories. Figure 2 is an example of an AMOR meteor record. For many echoes the system is able to fix the meteoroid speed using three independent methods.

Because independent scalar speeds separated in time are available – diffraction speeds recorded on each spaced site and pre- $t_0$  and post- $t_0$  for the central site – decelerations can be determined for a proportion of the meteors. This is valuable because an important parameter required for accurate heliocentric orbit determination is the velocity prior to encountering the Earth's atmosphere. The atmospheric deceleration has been modeled and depends on the meteoroid mass, speed and meteoroid ablation coefficient and on the height and entry zenith angle. Direct measurements for some meteoroids are therefore available for comparison with dynamical models.

## 6. SYSTEM SENSITIVITY

The limiting plasma column electron line-density detectable by a radar using transverse geometry can be derived from the radar equation for a given received echo signal power (see e.g. [1]). There are several wavelength dependent effects: the scattering cross-section attenuation due to the plasma train radius at creation; the rapid diffusion for high altitude echoes; and magneto-ionic Faraday rotation in the lower E-region during daytime. Such altitude and time dependent effects can be factored into the system sensitivity. With the AMOR parameters – operating frequency 26.2 MHz, TX pulse power  $10^5$  W, TX antenna gain 600, RX gains 400, the limiting electron linear density is  $\sim 10^{10} \text{ m}^{-1}$ ; for the bulk of archived meteor records the limiting mass for a  $40 \text{ km s}^{-1}$  meteoroid is  $\sim 3 \times 10^{-7} \text{ gm}$  corresponding to a particle radius of  $\sim 40 \text{ }\mu\text{m}$ .

Though of greater meteoroid mass sensitivity than photographic, TV and image intensifier techniques, radars cannot achieve the same directional accuracy: the AMOR uncertainty in orbital elements is dependent on the heliocentric speed but is  $\sim 2^\circ$  in angular elements  $i$ ,  $\omega$  and  $\sim 5\%$  in size parameters  $e$ ,  $q$  and  $a$ .

## 7. CALIBRATION

Phase paths, range delays and such system parameters are electronically measured and the heliocentric orbits verified with reference to independent calibration: this was achieved by comparisons with cometary stream orbits established by photographic, TV and image-intensifier techniques. This astronomical calibration is available employing several well-recorded streams e.g.  $\chi$  Scorpiids,  $\alpha$  Scorpiids, Sextantids and  $\eta$  Aquarids.

## 8. PROGRAMME

The enhanced system has been in near continuous operation ( $< 5\%$  downtime) during years 2000–2001: the current projects include:

- the orbital distribution and mass distribution of solar system dust as observed at 1 A.U. as input to an ongoing development of an ESA model ([2], [3]). To correlate such ground based data on the dynamical characteristics of inner solar system particles with the results of other observational techniques it is necessary to de-bias the raw heliocentric orbital distributions. Such biases include: the Earth-meteoroid collision probability (dependent on orbital elements); the density of the meteoric plasma generated (a function of meteoroid mass, speed and atmospheric entry angle) and the system response function (dependent on radar antenna patterns, range and echo altitude).
- studies of dust debris produced by Near Earth Asteroids.
- mapping the sources of Interstellar dust ([4]).

## ACKNOWLEDGMENTS

This work was supported by the New Zealand Marsden Fund UoC 911-2000 and European Space Agency ESOC RFQ/3-9528/99/D/CS.

## REFERENCES

1. Baggaley W.J., Bennett R.G.T., Steel D.I. and Taylor A.D., 1994, The Advanced Meteor Orbit Radar: AMOR. *Q. J. Roy. Astr. Soc.* 35, 293-320.
2. Dikarev V., Gruen E., Landgraf M., Baggaley W.J., Galligan D.P., 2001, Components of a New Interplanetary Meteoroid Model. *Proceedings Meteoroids 2001 Conference.* (ESA SP-495)
3. Galligan D.P., Baggaley W.J., 2001, Probing the Structure of the Interplanetary Dust Cloud using the AMOR Meteoroid Orbit Radar. *Proceedings Meteoroids 2001 Conference.* (ESA SP-495)
4. Baggaley W.J., Galligan D.P., 2001, Mapping the Interstellar Dust Flow into the Solar System. *Proceedings Meteoroids 2001 Conference.* (ESA SP-495)

## Interferometric Radar Observations of Meteors at Widely Separated Locations

A.R. Webster<sup>1</sup>, J. Jones<sup>1</sup>, K.J.Ellis<sup>1</sup>, M. Campbell<sup>1</sup>,  
B. Clemesha<sup>2</sup>, P. Batista<sup>2</sup> and M.A. Abdu<sup>2</sup>.

<sup>1</sup> *Department of Physics,  
The University of Western Ontario,  
London, ON. N6A 5B9  
Canada.*

<sup>2</sup> *Instituto Nacional de Pesquisas Espaciais  
C.P. 515, S. J. dos Campos,  
12201-970, SP, Brazil.*

### ABSTRACT/RESUME

Back-scatter radars have been operated simultaneously and on a continuous basis at Tavistock, near London Canada and near Sao Paulo, Brazil. Each system consists of five separate receiving antennas arranged as two orthogonal 3-element arrays that allows the unambiguous determination of the direction in space of the meteor echo relative to the station location. The antennas used are two-element Yagi type with horizontal elements and pointed vertically upwards to give all round coverage. Aside from the operating frequency, 29.3MHz in Canada and 34.2MHz in Brazil, the systems are identical. Results from these operations during the time of the 1999 Geminids are presented illustrating the similarities and differences arising from the significantly different site coordinates.

### 1. INTRODUCTION

Radio-echo observations of meteors have been made at a site at Tavistock, near London, Ontario using a triple-frequency radar. A single-frequency sister radar has operated in a similar fashion near Sao Paulo, Brazil. Here we compare the results of these observations during the 1999 Geminid shower from the 3<sup>rd</sup> to 18<sup>th</sup> December. The operational frequencies are 29.85MHz at Tavistock and 34.2MHz in Brazil. Other than that, the systems are essentially identical. The coordinates of the sites are given in Table 1.

Table 1. Site Coordinates

Site	Latitude.	Longitude
Tavistock	43.3°N	-80.8°E
Brazil	-22.7°N	-45.0°E

Because the Geminid meteor stream is a Northern hemisphere event (nominal declination +32°, R.A. 112°), the elevation of the radiant at transit is much

higher at Tavistock than Brazil; this is illustrated in fig.1.

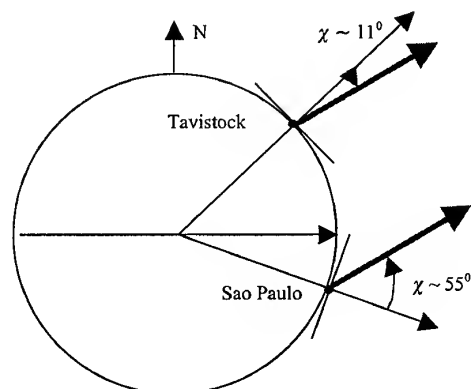


Fig.1 The radiant direction at transit.

### 2. THE EQUIPMENT

The radar is basically a pulsed back-scatter system using a single transmitting antenna and 5 carefully spaced receiving antennas. These latter antennas form the cornerstone of the angle-of-arrival measurements and the layout is illustrated in fig.2. The 3 antennas on

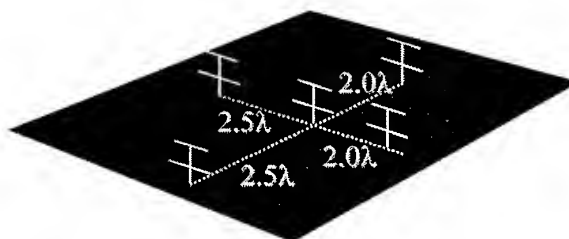


Fig.2 The 5 receiving antennas arranged as orthogonal arrays

each axis of the array provides an accurate estimate of the angle-of-arrival of the incoming signal relative to the normal to that array axis. These two angles are readily translated into the elevation and azimuth of the

signal. A key point of this arrangement is that the spacings of the two outer elements relative to the centre antenna differ by  $0.5\lambda$ . The two outer antennas on each axis provide a wider aperture, which allows a more accurate estimate of the angle-of-arrival. The principle is illustrated in fig.3. Phase measurements,  $\phi_{10}$  and  $\phi_{20}$ , at the outer elements relative to the centre element give two estimates of the angle-of-arrival  $\xi$  relative to the normal to the array axis according to:

$$\sin \xi = -\frac{\lambda}{2\pi} \frac{(\phi_{10} - \phi_{20})}{d_1 + d_2} = -\frac{\lambda}{2\pi} \frac{(\phi_{10} + \phi_{20})}{d_1 - d_2} \quad (1)$$

The first gives an accurate but ambiguous estimate, while the second resolves the ambiguity (see [1]). For values of  $\xi < 75^\circ$  and s:n ratio  $> 10\text{dB}$ , the uncertainty in  $\xi$  is typically  $< 0.2^\circ$ .

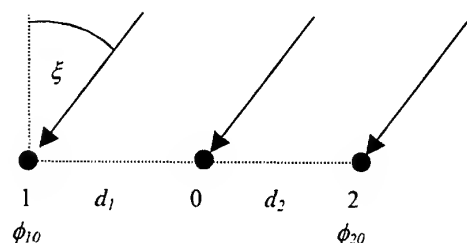


Fig.3 The 3-element antenna array.

Once the accurate estimates of the angle-of-arrival relative to these two orthogonal axes are available, translation to azimuth and elevation angles, to a similar accuracy, is straightforward.

Each of the antennas consists of a 2-element Yagi pointing vertically upwards. The gain is modest so that reasonable all-round coverage is provided down to about  $20^\circ$  in elevation angle; this corresponds to about 275km in radial distance on the echo surface at a height of 100km, the average height at which meteors occur. This is illustrated in fig.4 for Tavistock where effect of the orientation of the antennas is clearly seen, the gain being less along the axis of the dipoles (aligned  $104^\circ - 284^\circ$ ).

The "dead spots" caused by the high pulse repetition frequency ( $\sim 2000$  pps) are also clearly visible. Similar results were also obtained at the Sao Paulo site, though at a somewhat lower rate due to the higher frequency and a slightly higher threshold setting. As an example, on 12 December, 1999, a total of 4508 echoes were recorded at Tavistock and 2240 at Sao Paulo.

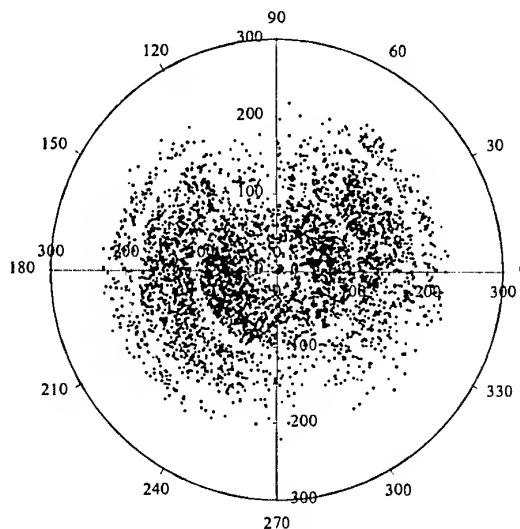


Fig.4 A total of 4508 echoes received at Tavistock on 12 December 1999, projected onto the echo-surface at a height of 100km. The radial scale is distance in km.

### 3. DATA REDUCTION.

In order to separate out the echoes from the Geminid shower, use was made of a technique based on the "echo-line" concept. This is illustrated in fig.5 where echoes are received from meteors satisfying the "specular" condition, that is, the meteor train is perpendicular to the line from the back-scatter radar. Since all meteors from the shower radiant are essentially parallel, only those on the indicated "echo-line" are observed; in fact, since meteors ablate over a height range of  $\sim 85 - 110\text{km}$ , an "echo-band" is perhaps more appropriate. Nevertheless, the line concept is useful in providing a first approximation.

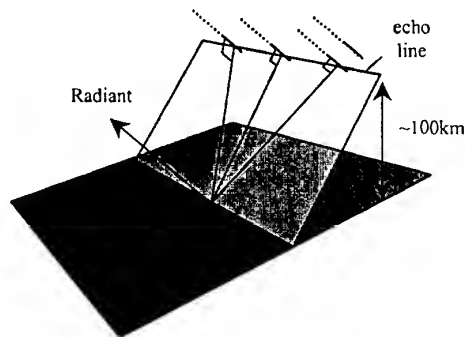


Fig.5 The echo-line relating to the back-scatter observation of shower meteors.

Since the direction of the meteor as seen from the radar is accurately known and since this direction is

necessarily perpendicular to the radiant, then the possibility that a given meteor is related to a given radiant may be tested by taking the dot product of the meteor direction and the proposed radiant [2]. To account for measuring inaccuracies and the height variation mentioned above, an allowance of a few degrees can be made in the radiant direction.

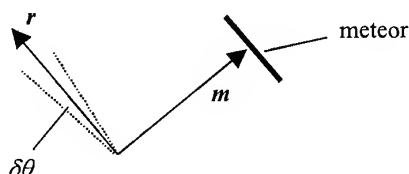


Fig.6 Illustrating the selection of shower meteors.

This is illustrated in fig.6 where unit vectors  $r$  and  $m$  give a value  $r \cdot m < \delta a$  and  $\delta a = \sin \delta \theta$ ,  $\delta \theta$  being the chosen angular tolerance. For  $\delta \theta = 5^\circ$ , for example,  $\delta a = 0.087$ . It should be noted that this approach will accept meteors with radiant in a band across the sky which is within  $\delta \theta$  of the normal to the meteor direction, so that some contamination from sporadic meteors satisfying this criterion is to be expected. Nevertheless, most of such sporadics are eliminated by applying this technique.

Returning to the echo-line concept, fig.7 shows the motion of the echo-line across the echo-surface at a height of 100km as seen looking down on the surface.

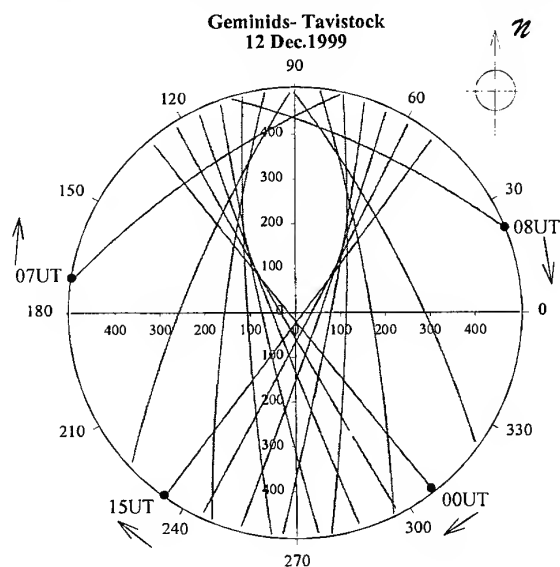


Fig.7 The motion of the echo-lines from the Geminid radiant at Tavistock.

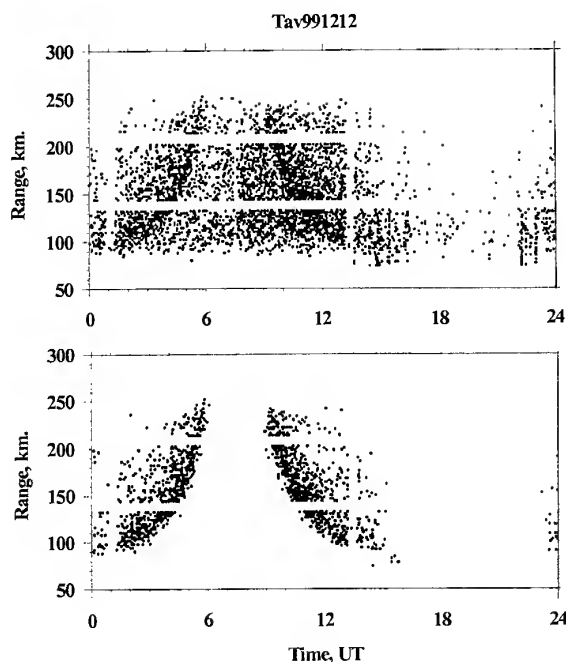


Fig.8 A range-time plot of echoes received at Tavistock on 12 December 1999. Top half, all the echoes; bottom half, most non-shower meteors eliminated.

The radiant rises in the NE at  $\sim 00.00$ UT, transits just south and high in the sky at  $\sim 07.35$ UT and sets in the NW at  $\sim 15.00$ UT. The motion of the echo-lines is such that shorter range echoes are possible early on, but the possible range moves out as transit approaches beyond the reach of the receiving antennas; it will be remembered that the antennas essentially look upwards and out to a distance  $\sim 250$ km on the echo surface (see fig.4). The motion then produces a "mirror-image" effect and the range of the echoes diminishes towards the time of the setting of the radiant. This is well illustrated in fig.8 where all echoes for 12 December are included in the top half. Application of the above described selection process, with  $\delta \theta = 5^\circ$ , does an excellent job of eliminating most of the non-shower meteors as is evidenced in the bottom half of fig.8.

In Brazil, the radiant is always relatively low in the sky and moves from NE to NW in a counterclockwise direction, transiting N of the site at  $\sim 05.05$ UT. The range-time plot for 12 December 1999 for that site is shown in fig.9, with  $\delta \theta = 5^\circ$ , and the effectiveness of the shower selection process is again demonstrated.

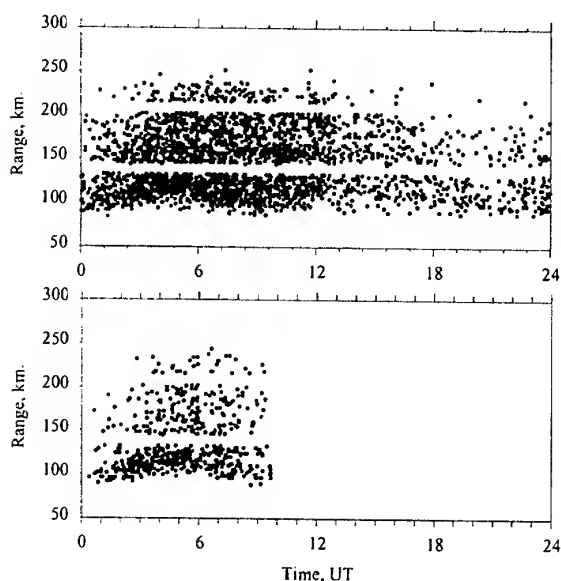


Fig.9 A range-time plot for Brazil on 12 December 1999 with all echoes (top) and with most non-Geminids removed (bottom).

#### 4. RESULTS.

The Geminid meteor shower is a well-established phenomenon lasting for about 10 days and peaking around 12-13 December. The activity in 1999 as seen from our two sites is shown in fig.10, normalized to allow for the slightly different sensitivities. The peak counts on the 13<sup>th</sup> were 1764 and 736 at Tavistock and Brazil respectively. Examination of figs. 8 and 9 shows that the Tavistock observational period covers about 11 hours which straddles that of about 8 hours at Brazil. Thus averaged, the two data sets show excellent consistency in the meteor rates.

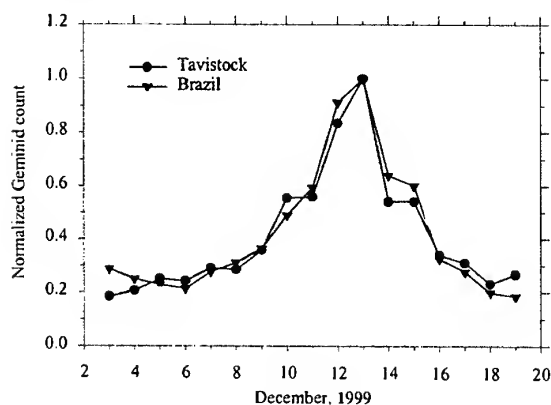


Fig.10 The normalized count of Geminid meteors at the two sites obtained by the selection process outlined in the text

By applying the radiant selection technique over an area on the celestial sphere around the expected point, and computing the numbers meeting the selection requirement, a good estimate of the actual radiant position may be obtained. Contour plots for the two sites over a  $20^\circ$  range in declination and right ascension for 13 December 1999, are shown in fig.11. While the right ascension values are in very good agreement, the declination estimates are seen to differ by almost  $3^\circ$ .

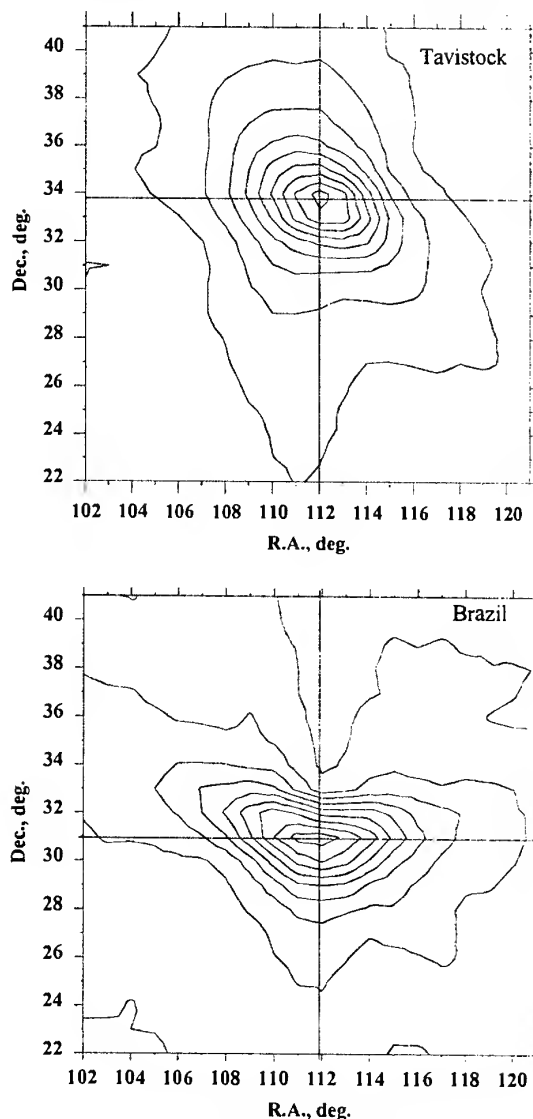


Fig.12 Geminid radiant coordinates for 13 December 1999 from the two sites, using a grid increment of  $1^\circ$  and a selection  $\delta\theta = 1^\circ$ . The contours have starting and incremental values of 100 and 50 for Tavistock and Brazil respectively.

In generating the data for fig.12, no allowance was made for the effects of "zenith attraction", where the meteor appears to radiate from a point higher in the sky due to the gravitational attraction of the Earth. When due allowance is made, the derived radiant position shifts significantly so that both sites are in very close agreement as shown in fig.13. These radiant positions, then, are those that would be observed were there no gravitational attraction due to the Earth

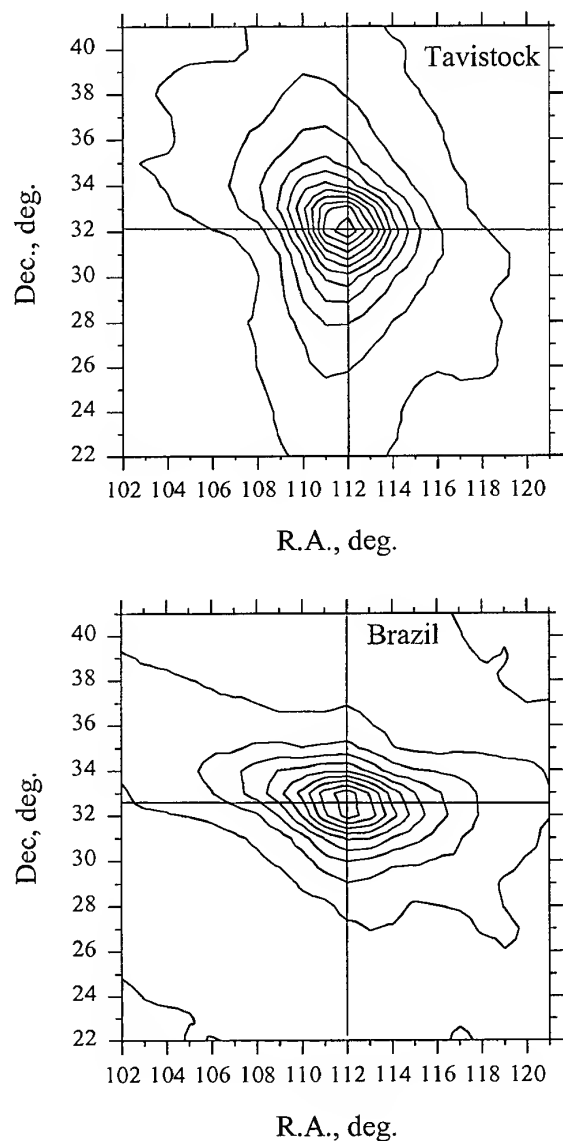


Fig.13 Contour plots of the radiant position on 13 December, 1999 after allowance has been made for zenith attraction. Derivation and contours as for fig.12.

The position of the radiant was determined in a similar fashion with zenith attraction corrected, for all the days of significant Geminid activity and the movement in declination and right ascension is shown in fig.14. and separately versus Solar longitude in fig 15.

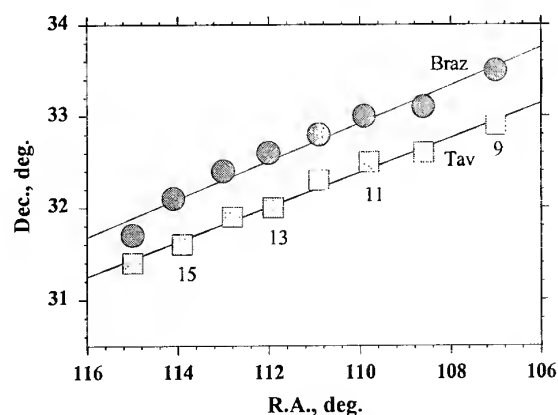


Fig.14 The variation in Declination and Right Ascension of the Geminid radiant as observed from the two sites from 9<sup>th</sup> to 16<sup>th</sup> December, 1999.

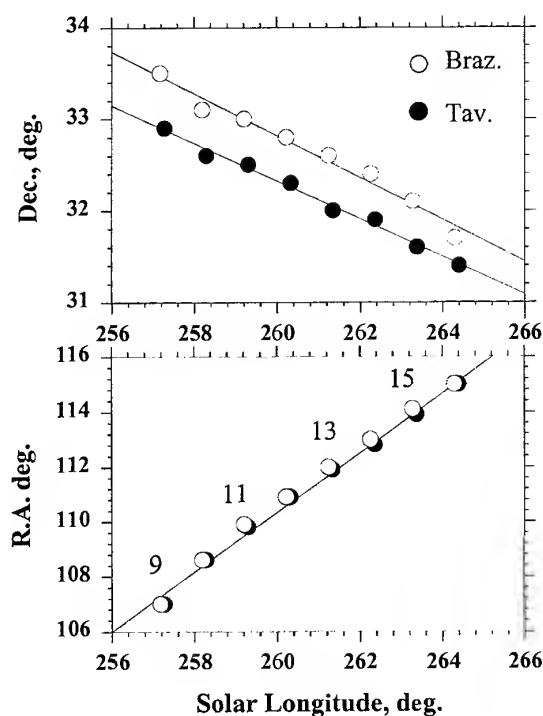


Fig.15 Declination and right Ascension versus Solar Longitude over the period 9<sup>th</sup> to 16<sup>th</sup> December, 1999.

## 5. DISCUSSION AND CONCLUSIONS.

From the results presented here it is clear that the interferometer technique used is capable of great accuracy in the determination of the direction of meteor echoes from a back-scatter radar. It is estimated that individual echoes are typically placed within  $0.5^\circ$  of their position in terms of azimuth and elevation. This translates into very accurate estimates of the radiant position in the case of shower meteors as is demonstrated here. The importance for allowing for the effects of zenith attraction in exercises of this kind has been demonstrated.

After allowance for zenith attraction, the estimates from the two sites agree to within  $0.5^\circ$  in declination and better than that in right ascension. The consistency of the results over the several days of observation, and the nature of the discrepancy in declination, suggests a systematic origin for the difference. One possibility is that the plane of the array is not quite horizontal at one site or the other, or both, resulting in systematically high or low estimates for the elevation angle. The effect is clearly small and likely to involve a height difference in the order of 0.5m between the antennas at each end of one of the array legs, separated by a distance in the order of 45m. Although care was taken in the original siting of the antennas, a more accurate survey is planned for the near future.

In the meantime, the accuracy and consistency of the results from the two sites is very encouraging. The activity of the Geminid shower as the days progressed was estimated from both sites and the results were clearly very consistent. This is in spite of the significantly different site latitudes, which resulted in quite different radiant movement in the local sky and hence the different rate characteristics with time.

All of this is taken to illustrate that the operation of these radars provides accurate information regarding the rate and direction of meteor echoes, which allows significant estimation of the direction in space and the flux associated with both shower and sporadic activity. Confidence may be placed in results generated from different locations and it is anticipated that more radars of this type will be deployed.

## 6. REFERENCES.

1. Jones, J. Webster, A.R. and Hocking, W.K., *Radio Science*, Vol. 33. 55 – 65, 1998.
2. Morton, J.D. and Jones, J., *Mon. Not. Roy. Astr. Soc.*, vol 198, 737 – 746, 1982.

## RELATION BETWEEN THE OPTICAL AND RADAR CHARACTERISTICS OF METEORS: PERSEIDS 1998 AND 1999

P. Pecina, P. Koteš, R. Štork, P. Přidal, and D. Nováková

Astronomical Institute of the Academy of Sciences of the Czech Republic, 25165 Ondřejov, Czech Republic

### ABSTRACT

Some results of simultaneous double TV and radar observations of meteors performed at the Ondřejov observatory in the Czech Republic in 1998 and 1999 during the Perseid period, are presented. The relation of the optical magnitude of each TV meteor at the height corresponding to the radar reflection point, to the radar echo amplitude or the duration, is studied.

### 1. INTRODUCTION

Relation of optical magnitude of meteors to the corresponding radar quantity (i. e. the electron line density inferred from duration of the radar echo or its amplitude) has already been studied for many years, e. g. [10] - [16]. Relation of the type

$$M = A - B \log \alpha_e,$$

with  $M$  representing the absolute optical magnitude of the optical meteor and  $\alpha_e$  the electron line density of its radar counterpart, was extracted from these studies. However, the constants  $A$  and  $B$  found by various authors differed from one author to other and also for different shower meteors used in the analysis. These observations were not mostly carried out as optical double-station so that the heights could not be determined for the observed meteors. To avoid this shortcoming an attempt was undertaken to perform the simultaneous radar and telescopic double-station observations yielding among other also heights of each meteor (see [18] and [19]). Unfortunately, the authors had to consider their attempt as unsuccessful due to very limited amount of data they collected. Simultaneous TV and radar observations have also been reported in [6]. However, the authors used only one TV camera so that the heights of optical meteors could not again be determined. As a rule, all preceding authors obtained the constants  $A$  and  $B$  differing from those of any other author. Recently the usage of radar equipped by the interferometer so that the direction of radar echo could be determined together with 3 TV camera

systems, was described in [7]. The authors published preliminary results on 20 simultaneous meteors they observed. It can be appended with respect to simultaneous TV and radar observations that they may serve also to establishing the velocity dependence of the ionization probability, as stated in [1].

This article deals with results of simultaneous TV and radar observations performed during the Perseid period in 1998 and 1999. The system consisted of two TV cameras the first of which operated at Kunžak located in southern part of the Czech Republic, and the second one together with the radar (e. g. [17]) operated at Ondřejov observatory. The distance between these two TV sites was XX km. This configuration of sites enabled the height of each point of light curves of TV meteors to be determined. Also the angular distance of the particular point from the radiant was known together with its distance from the Ondřejov site. This distance was compared with the range observed by the radar and served as the second criterion of the possible commonness of TV and radar meteor. The first one used was simply the time coincidence of both events.

### 2. RELATION BETWEEN OPTICAL AND RADAR CHARACTERISTICS OF METEOR

Relation between the optical quantity characterizing a meteor such as the intensity of its light,  $I$ , and the electron line density inherent to the radar manifestation of the same meteoroid,  $\alpha_e$ , can be derived from the luminosity equation and the ionization one (e. g. [3]):

$$I = -\tau(v) v^2 \dot{m}/2, \quad \alpha_e v \mu = -\beta(v) \dot{m}, \quad (1)$$

where  $v$  denotes meteoroid instantaneous velocity,  $\tau(v)$  stands for the luminous efficiency and  $\beta(v)$  for the ionization probability,  $\mu$  is the average mass of an ablated meteoroid atom and  $\dot{m}$  designates the meteoroid mass loss during its atmospheric flight. The quantities  $\tau(v)$  and  $\beta(v)$  are considered to be functions only of meteoroid velocity. Elimination of  $\dot{m}$  between the above two equations yields

$$I = \mu [\tau(v) v^3 / 2 \beta(v)] \alpha_e. \quad (2)$$

It is more usual to express the light intensity in absolute magnitude,  $M$ . Since the relation connecting  $I$  and  $M$  reads (e. g. [4])

$$I = 10^{-0.4 M},$$

the following expression of  $M$  as a function of  $\alpha_e$  results

$$M = -2.5 \log_{10} I = C - 2.5 \log_{10} \alpha_e, \quad (3)$$

where

$$C = -2.5 \log_{10} [\mu \tau(v) v^3 / 2 \beta(v)]. \quad (4)$$

We can see that 2.5 in Eq. (3) stems from the relation  $I = I(M)$  so that any value of this constant deviating from 2.5 should result in the magnitude scale definition different from that of commonly employed at present. The definition of  $C$  provide us with the possibility to study the ratio of luminous efficiency to the ionization probability and to contribute so to solution of the old problem which has again been posed recently in [8] and [9]. The ratio of both efficiencies can be established from (4)

$$\tau(v)/\beta(v) = (2/\mu v^3) 10^{-0.4 C}. \quad (5)$$

When having observational data on dependence of  $M$  on  $\alpha_e$  for meteors of different velocities and showers we would be able to map the above ratio. It should be stressed here that it could depend not only on velocity but also on the chemical composition of meteors via  $\mu$  which can differ from one shower to other.

Observing meteors as members of one particular shower could ensure that the velocities of all these meteors will be inside narrow velocity interval. This would be the case if meteors would not decelerate in the atmosphere and the radar reflection point would be at the same height for all meteors. However, this is not usually the case in practice. Therefore, it is necessary to determine the meteor velocity at the radar reflection point. Since double-station TV observation yielded the lengths flown by any meteor as a function of time the first attempt consisted in finding the constants  $l_0$  and  $v_0$  in the relation

$$l(t) = l_0 + v_0 t, \quad (6)$$

by means of the least squares fit. This worked for all observed meteors. However, this approximation does not consider possible meteoroid deceleration. Thus, the second attempt was carried out with

$$l(t) = l_1 + v_1 t + a_1 t^2. \quad (7)$$

Comparison of results provided by both approaches revealed that the latter function gave better results in most cases and enabled more precise velocities at the radar reflection points to be used in the analysis. Results are presented in Table 1.

In order to find the constant  $C$  from Eq. (3) we must compare absolute magnitude of optical meteor, i. e. magnitude related to the distance of 100

km, with corresponding electron line density. As is known radar echoes can be divided into two principal categories [14]. When the electron line density  $\alpha_e \ll 2.4 \times 10^{14} \text{ m}^{-1}$  the radar echo amplitude drops exponentially with time and power received by radar,  $P_R$ , is

$$P_R \sim P_T G^2 / R^3. \quad (8)$$

Here  $P_T$  stands for power transmitted by the radar,  $G$  denotes the antenna gain (common to transmission and reception), and  $R$  is the range at which particular echo was observed. The echo of this kind is designated as underdense. Since the optical absolute magnitudes are related to standard distance of 100 km we have to recompute observed radar amplitudes to the same range. Moreover, since amplitude of underdense echo depends according to (8) also on  $G$  and, therefore, on the direction in the antenna diagram within which it is observed, we decided to relate the underdense amplitudes to the direction of gain maximum. Since the amplitude expressed in  $\mu V$ ,  $a_{obs}$ , is proportional to the square root of the received power we have according to (8) the relation

$$a_c = a_{obs} [G_{max}/G_{obs}] [R_{obs}/R_{rel}]^{3/2}, \quad (9)$$

where  $R_{rel}$  is the range to which the corrected amplitudes should be related (i. e. 100 km in our case) and all quantities with the subscript *obs* relate to observation. In case that the amplitudes are expressed in dB they should be recomputed using

$$A_c = A_{obs} + 20 \log_{10} \left\{ [G_{max}/G_{obs}] [R_{obs}/R_{rel}]^{3/2} \right\}. \quad (10)$$

Physical theory of underdense echoes in [14] says that

$$\log_{10} \alpha_e \sim \log_{10} a \sim A. \quad (11)$$

When the electron line density  $\alpha_e \gg 2.4 \times 10^{14} \text{ m}^{-1}$  the corresponding echo is called overdense. Physical theory of reflection of radar waves from the meteor trails yields the relation (e. g. [3])

$$T = r_e (\lambda/2\pi)^2 \alpha_e / D - r_0^2 / 4D, \quad (12)$$

expressing the duration of overdense echo,  $T$ , as a function of  $\alpha_e$ , the ambipolar diffusion coefficient,  $D$ , and the initial radius of a trail,  $r_0$ . The wavelength of wave transmitted by radar is  $\lambda$  and  $r_e$  is the classical radius of electron. We use Eq. (12) to compute  $\alpha_e$  when  $T$  is known for particular echo. The ambipolar diffusion coefficient  $D$  will be evaluated using the formula

$$D \rho(h) = D_r \rho_r,$$

where  $D_r$  represents the ambipolar diffusion coefficient at some reference height level. We will use the value  $D_{93} = 4.2 \text{ m}^2 \text{ s}^{-1}$  during computations together with the atmospheric profile  $\rho = \rho(h)$  valid for August provided by [5]. The initial trail radius will be computed according to [2]. At the end of this section we should note that according to the physical theory duration  $T$  depends neither on the distance of the trail nor on the observational direction. Hence, the overdense echoes need not be corrected for the observational conditions.

Table 1. Meteors observed simultaneously by TV camera and Ondřejov meteor radar during Perseid period in 1998 and 1999. Quantity  $\tau_R$  is the angular distance from the radiant (in degrees) of the point on the light curve,  $h$  is the height in kilometers,  $M$  is the absolute magnitude of TV meteor in the point having  $\tau = \tau_R$ , (i. e. of the radar specular point),  $R_{TV}$  is its distance in kilometers,  $v_0$  and  $v_1$  are velocities inferred from the least squares fits, in kilometers per second,  $m_{ph}$  is photometric mass of a meteoroid in grams,  $R_r$  is radar range in kilometers,  $T$  is the duration of overdense echo, and  $A$  is the amplitude of underdense type echo corrected for the distance and the direction in the antenna diagram, in dB. The amplitude count was made starting from an arbitrarily chosen reference level. The higher the absolute value of each amplitude the fainter was the echo. The last column indicates whether particular meteor could have been considered as common to both techniques, yes (Y) or not (N).

No	Shower	Date	Time [UT]	$\tau_R$	$h$	$M$	$R_{TV}$	$v_0$	$v_1$	$m_{ph}$	$R_r$	$T$	$A$	Y/N
1	Per 1998	Aug 10	20:41:59	90.0	114.4	1.92	129.2	59.7	59.7	0.00087	130	51.5		Y
2			20:47:02	90.0	105.0	3.10	120.7	58.6	58.5	0.00700	122		-17.6	Y
3			21:48:26	89.0	94.4	5.20	116.0	55.9	57.0	0.00330	120	1.2		Y
4		Aug 11	20:04:21	89.0	94.7	5.52	102.6	55.9	60.1	0.00023	105	0.5		Y
5			21:09:33	90.0	98.8	5.97	116.6	51.4	60.7	0.00015	118		-13.6	Y
6			21:19:04	90.6	116.1	5.69	121.8	66.7	76.1	0.00018	400		-13.0	N
7			21:33:24	90.0	102.7	3.46	123.6	58.2	55.6	0.00110	125		-21.3	Y
8			21:35:53	90.0	117.4	3.61	139.8	59.5	59.6	0.00080	145		-11.1	N
9			21:56:27	89.5	90.6	5.58	111.1	57.7	55.9	0.00420	110	5.0		Y
10			22:09:56	90.0	104.9	5.55	124.9	58.4	56.6	0.00029	125		-19.0	Y
11	Per 1999	Aug 12	21:29:58	90.0	109.3	0.54	134.5	58.5	58.8	0.01400	135	3.0		Y
12			21:52:32	90.0	92.7	2.09	121.6	56.5	60.7	0.00110	125	4.3		Y
13		Aug 13	00:11:21	90.0	92.7	1.63	143.7	60.6	54.4	0.01100	145	20.0		Y
14			20:50:21	90.0	92.7	3.12	132.9	49.6	55.7	0.00180	135	2.7		Y
15			21:14:25	91.0	111.5	2.41	131.4	58.9	60.6	0.00210	135	0.8		Y
16			21:29:24	90.0	107.5	3.00	126.8	57.0	52.2	0.00042	130		-12.3	Y
17			21:50:00	90.0	110.8	4.08	132.8	59.4	59.6	0.00250	135	0.6		Y
18			21:53:36	90.0	109.8	3.15	134.8	58.5	59.3	0.00110	140		-20.1	N
19			22:19:43	90.0	97.2	0.38	126.4	55.6	56.1	0.01000	130	8.8		Y
20			22:26:08	90.0	106.1	1.64	136.7	60.6	60.8	0.00160	140		-15.2	Y
21			22:37:11	90.0	105.7	3.58	132.3	61.8	60.7	0.00049	135		-24.5	Y
22			23:40:02	90.0	110.2	1.94	134.5	65.9	62.7	0.00170	140		-23.0	N
23		Aug 14	00:44:32	90.0	105.2	3.96	138.8	65.5	68.0	0.00022	140		-30.3	Y

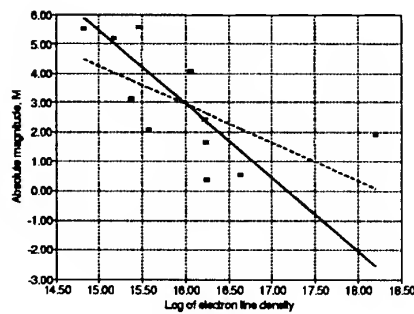


Figure 1. The fit of absolute magnitude  $M$  vs  $\log_{10} \alpha_e$  for overdense echoes. The solid line corresponds to (13) while the dashed one to (14). All echoes having duration  $T$  from the Table 1 are included. The electron line density  $\alpha_e$  was expressed in  $\text{m}^{-1}$  units.

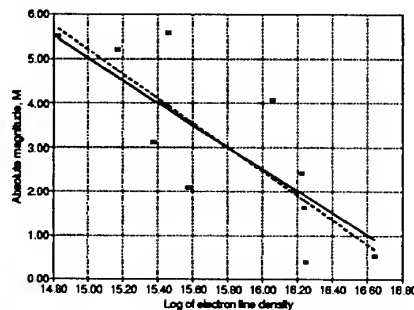


Figure 2. The same as in Figure 1 but with the duration  $T = 51.5$  s being excluded.

### 3. OBSERVATIONS AND RESULTS

Simultaneous observations were conducted during the activity of the Perseid shower in 1998 and 1999 within the days listed in Table 1. From preliminary number of 199 meteors suspected as having been common to TV and radar only 42 were observed simultaneously by two TV stations so that their heights and other parameters could have been determined. These were observed also by radar approximately at the same time instant. Whether they were also meteors common to both technique depended on their distance from the Ondřejov station as computed from TV data at the angular distance from the actual radiant,  $\tau_R \simeq 89^\circ - 91^\circ$ , and the radar range which was reduced from a film with the accuracy of about 5 km. So, when these quantities differed by more than 5 km the meteor was not considered as common observed simultaneously. All meteors having  $\tau_R$  within the above interval were included into Table 1. We can count 23 cases from which only 19 satisfied the condition of similar range.

We can see from (12) that the electron line density of overdense echo can be computed directly from its duration. Thus, using only the overdense echoes from

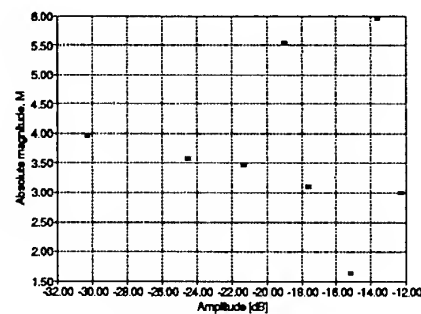


Figure 3. The fit of absolute magnitude  $M$  vs  $A_c$  for underdense echoes. The amplitudes  $A_c$  are in dB.

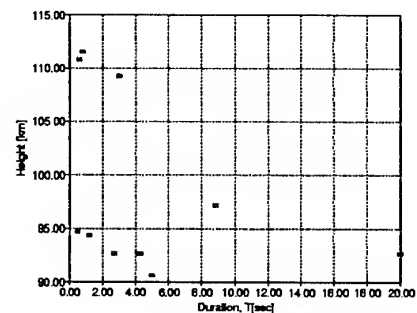


Figure 4. The fit of the height of occurrence vs duration.

Table 1 we have obtained the dependence of  $M$  on  $\log_{10} \alpha_e$  depicted in Figure 1. We have distinguished two cases. The former one corresponds to the assumption

$$M = C_1 - 2.5 \log_{10} \alpha_e, \quad (13)$$

while the latter one to

$$M = C_2 - B \log_{10} \alpha_e. \quad (14)$$

Numerical least squares fit yields  $C_1 = 42.95$  and  $C_2 = 23.7 \pm 8.7$ ,  $B = -1.3 \pm 0.5$ . We can see from the graph that lines deviate. The cause is clearly due to the presence of the last point  $T = 51.5$  s. Such duration can be influenced by the chemistry inside the trail while Eq. (12) deals only with deionization due to ambipolar diffusion. So, it can be justified leaving out of this point from our consideration. The corresponding graphs are shown in Figure 2. Numerical calculation provides us with  $C_1 = 42.51$  and  $C_2 = 46.57 \pm 11.1$ ,  $B = -2.8 \pm 0.7$ . The sum of squares of deviations is 12.1 in the case of (13) while 11.9 in case of (14). This difference is quite small. However, the line (13), even though somewhat higher than (14), is better from the point of view of physics as described in the second section. The dependence of absolute magnitude  $M$  on an amplitude of underdense echo  $A_c$  is presented in Figure 3 from which it is seen that the data suffer from large scatter so that the line analogous to lines in Figures 2 or 3 cannot be drawn. Conspicuous are also high values of

absolute magnitudes for faint echoes which are expected to be fainter than the 5th magnitude. The cause of the behaviour of our underdense echoes is still unclear and requires further investigation to be carried out. Our data enable also the dependence of the height of occurrence of overdense echoes on the duration to be found. The result is drawn in Figure 4. We can see here that one curve can hardly be employed when constructing the graph. It looks like the dependence were made from two levels the former one at left bottom corner and the latter consisting of remaining points. But we must be aware of low number of our data. Thus, we need another data to decide whether the overdense Perseids consist of two distinct populations.

#### ACKNOWLEDGMENTS

This work was supported by the scientific key project K3012103 and the grant No 205/00/1728 of the Grant Agency of Czech Republic.

#### REFERENCES

1. Babadzhanov P. B., 1970, *Bull. Astron. Inst. Czechosl.*, 21, 193
2. Baggaley W. J., 1980, *Bull. Astron. Inst. Czechosl.*, 31, 308
3. Bronshten, V. A., 1983, *Physics of Meteor Phenomena*. Kluwer acad. publ., Dordrecht, Boston, Lancaster
4. Ceplecha Z., Borovička J., Elford W. G., ReVelle D. O., Hawkes R. L., Porubčan V., Šimek M., 1998, Meteor Phenomena and Bodies. *Space Sci. Reviews*, 84, 327–471
5. CIRA, 1972, Akademie Verlag, Berlin
6. Cook A. F., Forti G., McCrosky R. E., Posen A., Southworth R. B., Williams J. T., 1973, in *Evolutionary and Physical Properties of Meteoroids*, eds. C. L. Hemmenway, P. M. Millman, and A. F. Cook, Combined Observations of Meteors by Image-Orthicon Television Camera and Multistation Radar. pp. 23 – 44, NASA, Washington D.C.
7. Fujiwara Y., Ueda M., Nakamura T., Tsutsumi M., 1995, *Earth, Moon and Planets*, 68, 277
8. Jones W., 1997, *Mon. Not. R. Astron. Soc.*, 288, 995
9. Jones W. and Halliday I., 2001, *Mon. Not. R. Astron. Soc.*, 320, 417
10. Kaiser T. R., 1955, in *Meteors*, ed. T. R. Kaiser, Pergamon Press, London, p. 55
11. Lindblad B. A., 1956, *Medd. Lunds astr. obs.* I, No. 189
12. Lindblad B. A., 1961, *Univ. Gothenburg astr. Notes*, No. 7
13. Lindblad B. A., 1963, *Smithson. Contr. Astrophys.*, 7, 27
14. McKinley D. W. R., 1961, *Meteor Science and Engineering*, McGraw-Hill, New York
15. Millman P. M., 1950, *J. Roy. Astron. Soc. Canada*, 44, 209
16. Millman P. M. and McKinley D. W. R., 1956, *Canad. J. Phys.*, 34, 50
17. Plavcová Z. and Šimek M., 1960, *Bull. Astron. Inst. Czechosl.*, 11, 228
18. Znojil V., Grygar J., Mikulášek Z., Šimek M., Šulc M., 1980, *Bull. Astron. Inst. Czechosl.*, 31, 14
19. Znojil V., Šimek M., Grygar J., Hollan J., 1981, *Bull. Astron. Inst. Czechosl.*, 32, 1

# OBSERVATIONS OF THE STRUCTURE OF METEOR TRAILS AT RADIO WAVELENGTHS USING FRESNEL HOLOGRAPHY (ESA 6-5)

W. G. Elford

*Department of Physics and Mathematical Physics, University of Adelaide, Adelaide, 5005, Australia  
gelford@physics.adelaide.edu.au*

## ABSTRACT

Radar observations of a meteor trail are the temporal variations in the amplitude and phase of the scattered radio signal usually recorded at one site. During the formation of the trail in the radar beam the recorded received signal can be considered as a one-dimensional diffraction pattern produced by a moving source. This diffraction data contains information on the structure of the trail that can be revealed by an appropriate Fresnel Transform.

An analytical technique for carrying out this transform of meteor radar data will be described and examples given of the outcomes for a range of typical diffraction data. Inherent in the outcomes are refinements in the value of the speed of the meteoroid, the presence of multiple sources (presumed due to fragmentation) and a measure of the lateral motion of the trail during formation due to wind drift.

## 1. INTRODUCTION

N. Herlofson is credited by Ellyett and Davies (1948) [1] with recognising that as a meteor trail is formed within the beam of a radar the fluctuations in the echo-amplitude are the radio analogue of the optical diffraction at a straight edge of a half-plane. Further, it was realised that a record of these fluctuations could be used to determine the speed of the meteoroid producing the trail. This technique has been used by many workers in many countries to carry out such measurements (McKinley, 1961 [2], Cepkecha et al 1998 [3]). In the early 1990's existing VHF narrow beam radars were shown to be a valuable tool for meteor studies, and in 1997 Cervera, Elford and Steel described a new technique for precise measurements of meteoroid speeds based on phase measurements of the radar echo (Elford, 2001 [4]).

VHF radars record the in-phase and quadrature components of the echo from any target at a repetition rate usually exceeding 1500 pulses per second. These are the required parameters for measuring the full characteristics of the scattering properties of a meteor

trail as it is formed in the radar beam. It is anticipated that such scattering properties could have sufficient resolution to reveal the structure of the trail and in particular any evidence of superimposed trails resulting from fragmentation of the meteoroid.

Radar echoes from meteor trails are recorded as a function of time, and are thus the radio analogue of a one-dimensional optical hologram. The process by which meteor trail characteristics are deduced from the radar record is in the nature of a Fresnel Transform and the derivation of the appropriate transform is described in what follows. The application of this transform process to a number of examples reveals some surprising features of meteor trails and their radio scattering properties.

## 2. GEOMETRY AND FRESNEL TRANSFORM

A meteor trail is formed in the atmosphere at an orthogonal distance  $R_0$  from a radar at  $T$ , as shown in Fig. 1. The radar signal received from a meteor trail is a measure of the amplitude and phase of the total scattering from the trail within the radar beam. In general the antenna beam is sufficiently wide to encompass the whole of the ionised trail, typically 10-15 km in length. However for very narrow beam radars and for very 'bright' trails some part of the trail may lie outside of the beam. These special cases need to be addressed separately.

Time is measured from the instant the meteoroid passes the orthogonal point  $O$  (commonly called the  $t_0$  point). We consider a time  $t$  when the 'head' of the trail has reached  $H$ , a distance  $x$  from  $O$ . Assuming that any deceleration can be neglected, the distance  $x$  is equal to  $vt$  where  $v$  is the speed of the meteoroid. (The assumption of negligible deceleration is justified by the observation that significant deceleration of the meteoroid only occurs close to the termination of its path).

We consider a small element  $dz$  of the trail at point  $P$ , a distance  $z$  from the ' $t_0$ -point'  $O$ , and let the radio reflection coefficient of the element be  $G(z)$ . The total

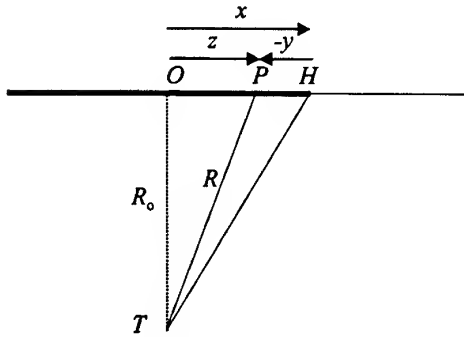


Fig.1. Geometry of trail and radar scattering

scattered signal detected at the radar site  $T$  at an instant of time  $t$ , is given by

$$E(t) \propto \int_{-\infty}^x G(z) \exp(j2kR) dz \quad (1)$$

where  $t = x/v$ ,  $v$  is the speed of the meteoroid,  $k = 2\pi/\lambda$ , and  $R$  is the range of  $P$  from the radar, which can be written as  $R \cong R_0 + z^2/(2R_0)$ , since  $R_0 > 10z$ . In (1) the optics convention for the phase has been adopted.

We seek a 'radio image' of the trail as described in the moving frame of the meteoroid. Thus we set up a co-ordinate system with the origin at the head of the trail  $H$  and with all distances  $y$  measured to the left of  $H$ . All distances are measured positively to the right, so that  $z = x + y$ . (This expression is made more obvious by considering a positive distance  $y$  to a fictitious point  $P'$  to the right of  $H$  so that all distances are then measured positively to the right.)

We now define the reflection coefficient of the element of the trail at  $P$  in terms of the position of  $P$  with respect to the head of the trail,  $H$ . Let  $A(y) = G(z)$ , noting that  $z = x + y = vt + y$ , and that at any instant  $dz = dy$ .

Whence (1) becomes

$$E(t) \propto \int_{-\infty}^0 A(y) \exp(jkx^2/R_0) \exp(jky^2/R_0) \exp(jk2xy/R_0) dy$$

Write  $E(t) = E(x/v) = E^*(X)$ , and  $A^*(Y) = A(y)$ ,

where  $X = x/\sigma$ ,  $Y = y/\sigma$ ,  $Z = z/\sigma$ ,  $\sigma = [\lambda R_0/(4\pi)]^{1/2}$ , and  $Z = X + Y$ .

Thus  $E^*(X) \propto$

$$\int_{-\infty}^0 A^*(Y) \exp(jX^2/2) \exp(jY^2/2) \exp(jXY) dY$$

As  $A^*(Y)$  is zero for all  $Y > 0$ , we can without loss of generality set the upper bound of the integral to  $\infty$ .

Also put  $f(Y) = A^*(Y) \exp(jY^2/2)$ .

$$\text{Then } E^*(X) \propto \exp(jX^2/2) \int_{-\infty}^{\infty} f(Y) \exp(jXY) dY \quad (2)$$

$$\text{Let } F(X) = \int_{-\infty}^{\infty} f(Y) \exp(jXY) dY$$

Then  $F(X)$  is in the nature of a Fourier Integral whose transform can be written as

$$f(Y) = (2\pi)^{-1} \int_{-\infty}^{\infty} F(X) \exp(-jXY) dX$$

But  $f(Y) = A^*(Y) \exp(jY^2/2)$ ,

and from (2)  $F(X) \propto E^*(X) \exp(-jX^2/2)$

Whence substituting in the transform equation we have

$$A^*(Y) \exp(jY^2/2) \propto \int_{-\infty}^{\infty} E^*(X) \exp(-jX^2/2) \exp(-jXY) dX$$

Finally, rearranging leads to

$$A^*(Y) \propto \int_{-\infty}^{\infty} E^*(X) \exp(-jX^2/2) \exp(-jY^2/2) \exp(-jXY) dX$$

$$\text{or } A^*(Y) \propto \int_{-\infty}^{\infty} E^*(X) \exp(-jZ^2/2) dX,$$

and replacing  $A^*(Y)$  with  $A(y)$ , and  $E^*(X)$  with  $E(t)$

$$\text{gives } A(y) \propto \int_{-\infty}^{\infty} E(t) \exp(-jZ^2/2) dX, \quad (3)$$

where  $Z = X + Y$ .

The left hand side of (1) is the scattering function of the trail measured with respect to the position of the head as origin, and the right hand side is the Fresnel Transform of the complex signal recorded at the radar station.

The convolution calculation implied in equation (3) is carried out in terms of real and imaginary components. The weighting function  $\exp(-jZ^2/2)$  has components  $\cos(Z^2/2)$  and  $-\sin(Z^2/2)$  which oscillate with increasing frequency as  $Z$  increases. Hence the real and imaginary parts of the radar signal described by  $E(t)$  must be sampled with sufficient frequency to avoid problems of aliasing.

The numerical integration of (1) is carried out for a range of  $X$  that includes the full extent of the time series of the radar echo given by  $E(t)$ . The relationship between  $X$  and  $t$  is given by  $X = (v/\sigma) t$ , which implies a knowledge of the meteoroid speed  $v$ . In general the meteoroid speed is measured using the phase method described by Cervera et al (1997) [5]. The interpulse period of the radar  $\Delta t$  defines the increment  $\Delta X$ .

### 3. INTEGRITY OF THE TRANSFORM PROCESS

The expression (3) was tested using known Fresnel diffraction data, such as are available for the diffraction at the straight edge of an infinite half-plane. The amplitude and phase of the diffraction aperture were recovered with excellent resolution. The straight edge Fresnel diffraction data were also used to simulate a radar echo from an underdense meteor trail subject to the effect of diffusion during and after formation. Again an excellent outcome was achieved, with the scattering function exhibiting a very sharp frontal edge ('head' of the trail) and then an exponential decay back from the head.

It needs to be emphasised that the transform process described by (3) implies that during the formation of the meteor trail in the radar beam the trail maintains the same scattering function relative to the head taken as the geometrical origin. This assumption is clearly an approximation but is justified by the fact that for VHF radars the total length of the trail contributing to the radar echo is typically 2-3 km, and the result of the transform is an average profile over this distance behind the head.

### 5. RESULTS OF THE FRESNEL TRANSFORM

The transform described above was applied to several radar echoes recorded during 2000 using the 54 MHz radar at Buckland Park, near Adelaide, South Australia. The radar has a beam width of about 3 degrees and a pulse repetition frequency of 1650 Hz.

Fig.2. shows the amplitude and phase of a radar echo from a trail formed at a height of 94 km and produced by the ablation of a meteoroid that entered the atmosphere with a speed of 45.0 km/s. The echo lasted for about 0.12 sec. The amplitude shows a few cycles of Fresnel diffraction and the accumulated phase is typical of most underdense echoes with this amplitude behaviour.

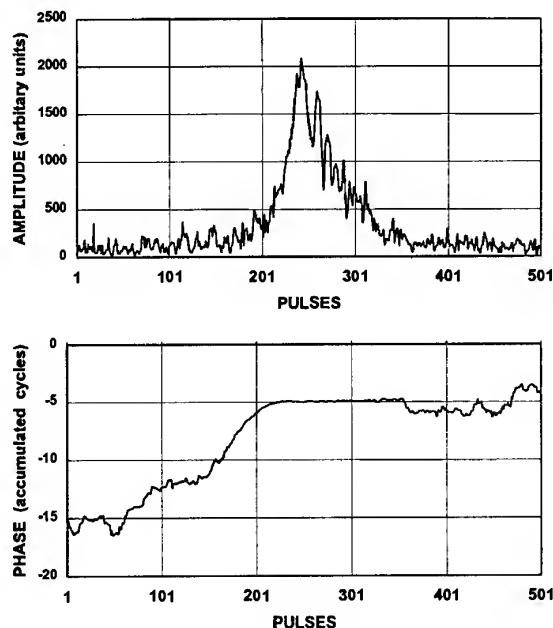


Fig. 2. Observed amplitude and phase of echo 1748; speed 45.0 km/s

The transform of this echo is shown in Fig.3. While the exponential decay of the scattering amplitude back from the head is expected, the 'spike' at the trail head is unexpected. Other examples also show this strong scattering at the head of the trail and suggest that this is

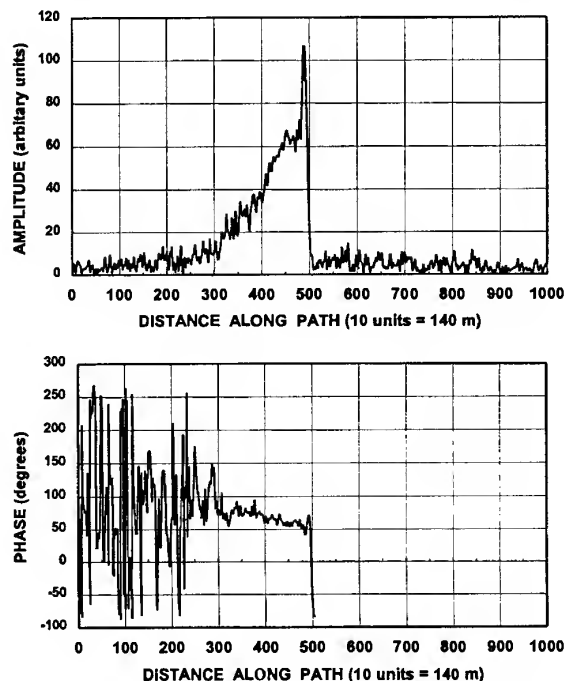


Fig. 3. Scattering function of trail 1748. Head of trail at 500 path units

a common feature of radio scattering from meteor trails. The scattering amplitude also shows a ledge about 500 m back from the head that indicates the possibility of a major fragment ablating at this position. The scattering phase is only plotted back from the head as the phase subsequent to the position of the head is random, as is to be expected. For 300 distance units ( $\sim 4$  km) the phase changes by about  $50^\circ$  due to the trail being formed in a wind driven atmosphere.

Fig. 4. shows the amplitude and phase of a radar echo from a trail formed at a height of 98 km and produced by the ablation of a meteoroid that entered the atmosphere with a speed of 61.6 km/s. This echo shows no features that are characteristic of transverse scattering from a trail; the amplitude appears to be the lobe pattern of the antenna, and the phase variation between pulses 550 and 750 is precisely parabolic with time. This is the type of radar signal expected from a 'hard target' crossing a radar beam, or in terms of meteor physics a 'head echo'

The interpretation of Fig. 4 as a head echo is confirmed by the Fresnel transform result shown in Fig. 5. The amplitude of the scattering function is relatively large, but distributed over a very short length of path, about 200m in extent. The leading edge of the 'head' has a finite slope determined by the relatively short duration of the echo  $\sim 0.1$  sec. There is some evidence of a very short trail extending 150 - 200m behind the head. The phase of the scattering function shows no distinctive trend over the very short length of the trail and is not

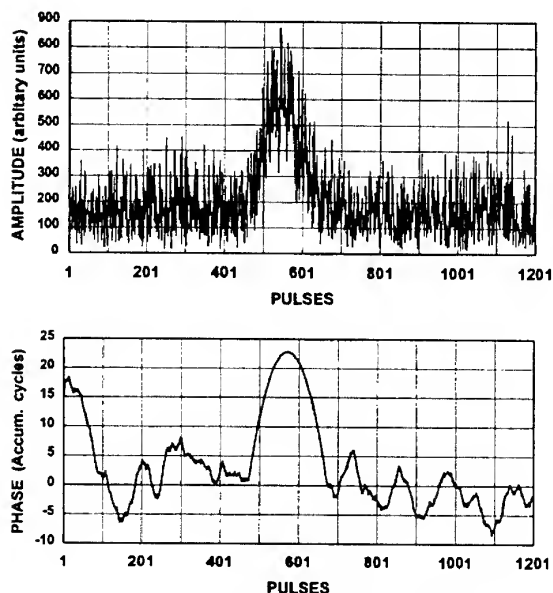


Fig. 4. Observed amplitude and phase of echo 5154; speed 61.6 km/s

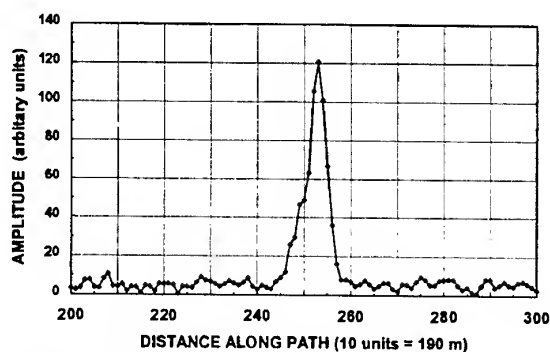


Fig. 5. Scattering function of trail 5154.  
Only amplitude component is shown.

included in the plot. Fig. 4 and Fig. 5 taken together are a very good example of how a strong but short spatial function ('narrow aperture') produces a relatively weak widely spread diffraction pattern.

Echo 3952, shown in Fig. 6, was selected as it had unusually large Fresnel oscillations which also are just discernible in the accumulated phase plot. The trail occurred at a height of 99 km and was produced by the ablation of a meteoroid entering the atmosphere with a speed of a 62.7 km/s. The phase plot showed coherence over about 0.15 sec.

The Fresnel transform of echo 3952 is shown in Fig. 7. The striking feature of the amplitude of the scattering

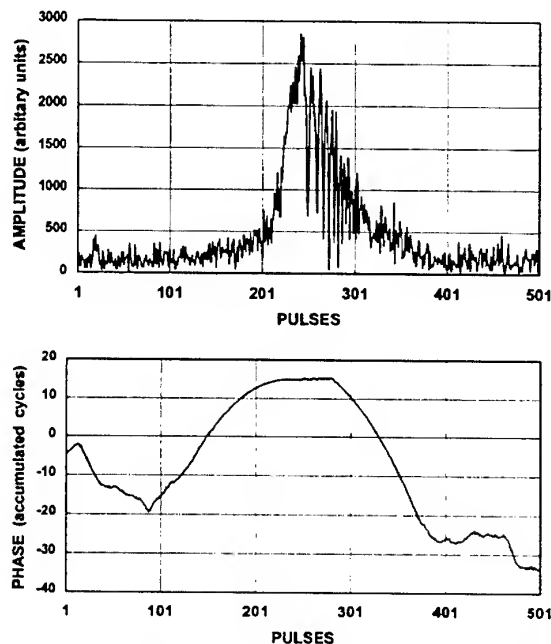


Fig. 6. Observed amplitude and phase of echo 3952; speed 62.7 km/s

function is the large value immediately behind the head, in fact the position of the maximum cannot be resolved from the position of the head of the trail. This scattering feature decays rapidly in a distance of about 600 m behind the head. At a distance  $\sim 1$  km behind the head a trail commences and extends back over a distance of about 2.5 km. It is the combination of scatter from the 'head feature' and from the trail that gives rise to the apparently strong Fresnel oscillations in the observed echo (Fig.6). The phase of the scattering function is typical of a meteor trail formed in an atmosphere moving under the action of winds, and in fact the line-of-sight component of the wind can be deduced from the slope of the phase plot. The phase behaviour close to the position of the head differs from the behaviour further back and this also supports the interpretation that the 'head feature' and the trail are independent characteristics of the ablating meteoroid.

Fig.8. shows the amplitude and phase of a relatively long duration radar echo from a trail formed at a height of 94 km and produced by the ablation of a meteoroid that entered the atmosphere with a speed of 35.3 km/s. The echo lasted for about 0.60 sec. While the amplitude behaviour is quite complex, the phase variation is smoothly changing over almost 160 cycles. The observation of such a large phase change is very unusual and was one of the reasons for the choice of this echo.

The Fresnel transform of the data plotted in Fig.8 is

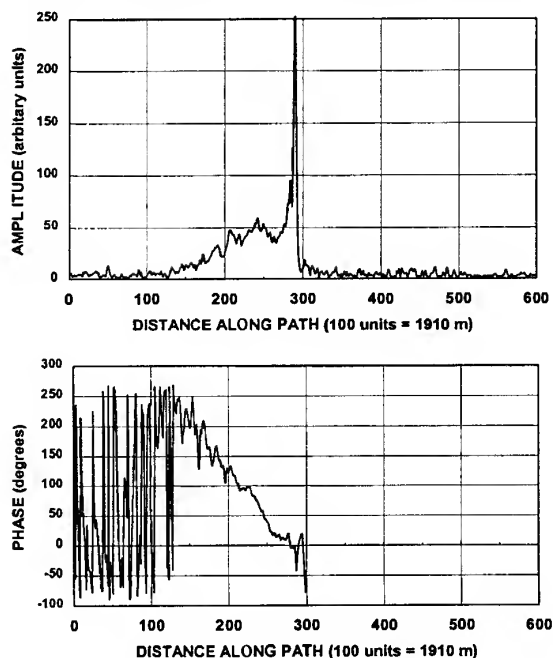


Fig.7. Scattering function of trail 3952

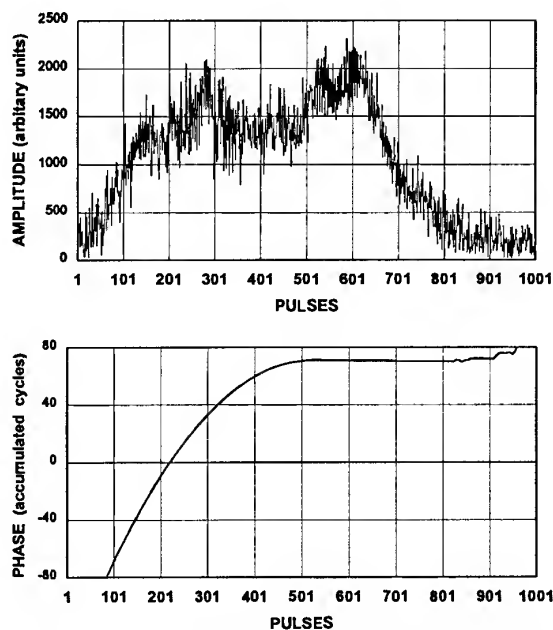


Fig. 8. Observed amplitude and phase of echo 1652: speed 35.3 km/s.

shown in Fig.9. Again the scattering function has a large amplitude at the head of the trail with much weaker scattering in the trail that stretches back about 5 km. The scattering phase has strong coherence for almost 6.7 km behind the head, and the line-of-sight wind speed can be readily measured from the slope of

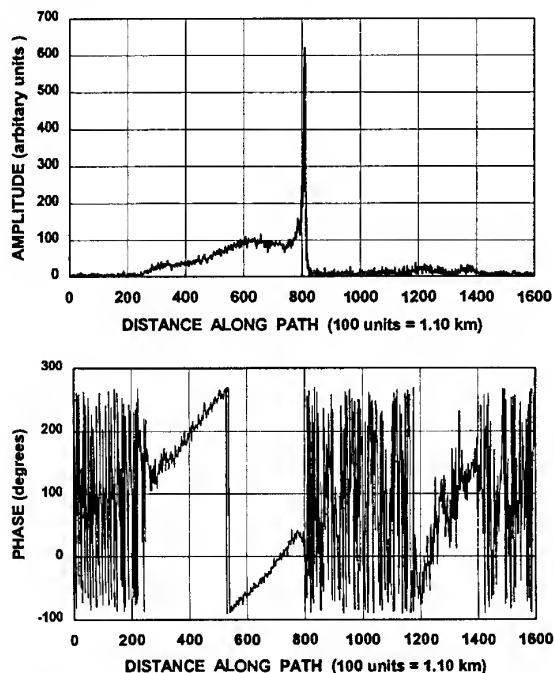


Fig. 9. Scattering function of echo 1652

the phase plot. There is also some coherence in the phase to the right of the position of the head. This is clearly related to the weak scattering shown in the amplitude plot in the region between 1200 and 1400 units of path. This is interpreted as the result of ionization deposited 4 - 6 km ahead of the main trail by the ablation of two or more small meteoroids moving on the same path and with the same speed as the meteoroid that produced the main trail. It is to be noted that the slopes of the phases of the scattering functions of the weaker trails differ somewhat from the phase slopes associated with the main trail. This suggests that the minor trails are produced at a slightly different height and thus in different wind field regions from the main trail.

The amplitude and phase plots shown in Fig.10 are typical of most echoes from underdense trails, in that the amplitude shows little or no Fresnel oscillations and the phase shows the effect of a significant drift of the trail due to winds.

The effect of applying the Fresnel transform to the data presented in Fig.10 is shown in Fig.11. In contrast to the previous results the scattering function shows no amplitude enhancement near the head of the trail. In fact the peak amplitude occurs about 500m behind the head, and the 'stepped' appearance of the scattering amplitude in the region stretching back about 1100m behind the head indicates several overlapping trails presumably due to a number of meteoroid fragments.

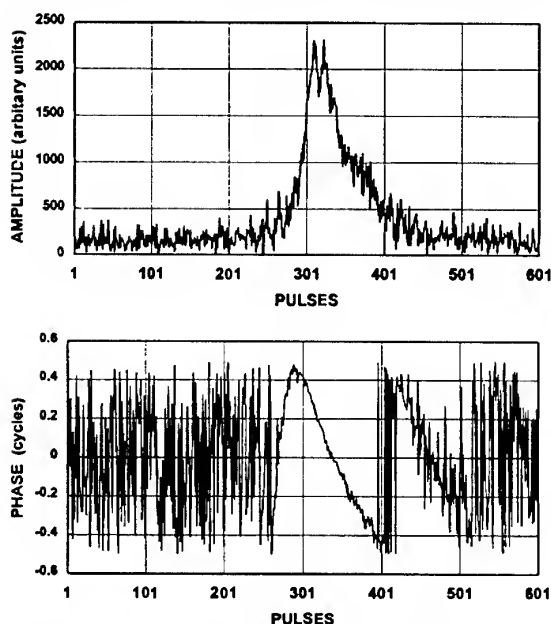


Fig.10. Observed amplitude and phase of echo 0544; speed 45.1 km/s.

The exponential fall in the amplitude back from the head is what one would expect and allows a better estimate of diffusion than that estimated from the observed echo amplitude in Fig.10. While the phase of the scattering function has a variation impressed by the motion of the trail due to winds, there are some sections that show lateral off-sets that suggest scattering from several slightly displaced trails consistent with the multiple trails observed just behind the head. Thus the absence of Fresnel oscillations in the echo amplitude record is well explained by the presence of fragmentation as shown in the scattering function of Fig.11.

## 6. DISCUSSION

The examples discussed above have indicated the efficacy of the Fresnel transform described by equation (3) in determining the scattering function of a meteor trail at radio wavelengths. While some features of the outcome were expected, such as the diffusion of the trail during formation and the effect of the background winds, others have given new insights into the properties of meteor trails. These include the effect of fragmentation in producing multiple overlapping trails that can be detected near the head of the trail. Perhaps most surprising is the strong scatter observed in a very small region at the head of several trails. These are true 'head echoes' although the total energy scattered is

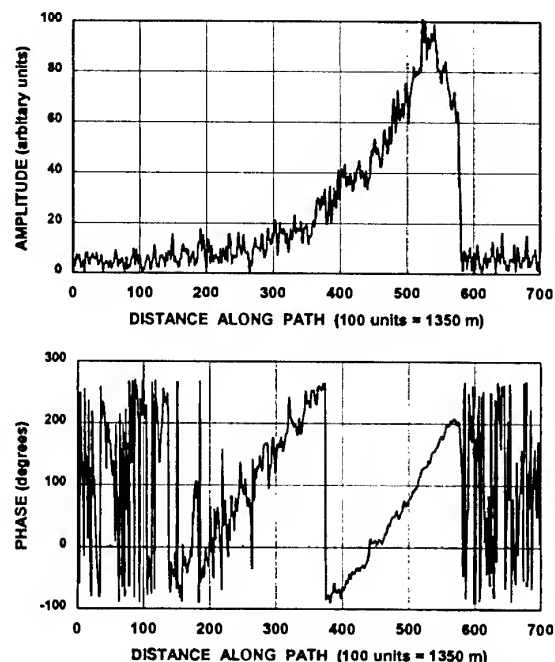


Fig.11. Scattering function of trail 0544. Head of trail is at 580 path units.

often small compared to the integrated scatter from the whole of the trail.

One feature that is inherent in this analysis is that the resolution of the derived scattering function is dependent on the correct choice of the speed of the meteoroid. In fact a preliminary investigation has shown that the 'sharpness' of the leading edge of the scattering function can be improved by incremental changes in the chosen speed. It appears that this feature can be exploited to determine the meteoroid speed with a precision of a fraction of a percent.

It is now proposed to apply this technique to a wide range of meteor echoes, particularly comparing the results of various showers and sporadic meteors. The effects of the assumptions mentioned in sections 2 and 3 will also be tested by setting up appropriate models.

## 7. REFERENCES

1. Ellyett, C. D. and Davies, J. G. Velocity of meteors measured by diffraction of radio waves from trails during formation, *Nature*, Vol. 161, 596-597, 1948.
2. McKinley, D. W. R. *Meteor Science and Engineering*. McGraw Hill, New York, 1961.
3. Ceplecha, Z., Borovicka, J., Elford, W.G., Revelle, D.O., Hawkes, R.L., Porubcan, V., and Simek, M. Meteor Phenomena and Bodies, *Space Science Reviews*, Vol. 84, 327-471, 1998.
4. Elford, W.G. Novel applications of MST radars in meteor studies. *J. Atmos. Solar-Terr. Phys.* Vol 63, 143-153, 2001.
5. Cervera, M. A., Elford, W. G. and Steel, D. I. A new method for the measurement of meteor speeds: the pre- $t_0$  phase technique. *Radio Science*, Vol 32, 805-816, 1997.

## RESULTS OF FORWARD-SCATTER RADIO ECHO OBSERVATIONS IN 2000

Masayoshi Ueda<sup>(1)</sup>, Kimio Maegawa<sup>(2)</sup>

<sup>(1)</sup> 43-2 Asuka Habikino-shi Osaka 583-0842 (Japan)

E-mail: m-ueda@mua.biglobe.ne.jp

<sup>(2)</sup> Fukui National College of Technology, Geshi Sabae-shi Fukui 916-8507 (Japan)

E-mail: kmaegawa@fukui-nct.ac.jp

(136.18°E, +35.93°N)

### ABSTRACT

We had been performing a forward scatter radio observation of meteor since 1996. The transmitting station was at Fukui (Japan), and the frequency is 53.750MHz and the power is 50W. The receiving station is Osaka (Japan) and base line has 160km distance and NE-SW direction. 504,588 meteor echoes have been observed from January to December 2000. Total of radio observation was 8,238 hours. We made the activities of these showers clear : Quadrantids(January), Daytime showers(June),  $\delta$  Aquarids(July), Perseids(August), Leonids(November), Geminids(December) and Ursids(December).

Moreover, We reported the daily variation of mean meteor rates and the annual variation of mean meteor rates.

### 1. INTRODUCTION

It is possible to continue the Ham-band Radio Observation (HRO) for one year [1]. In the result was 725 echoes per day which used HRO method in 1997. That software was used FFTDSP (M. W. Cook, MS-DOS version) in 1997. And Kazuhiko Ohkawa made new spectral display software (HROFFT) in 1999. By using this highly spectral display software (HROFFT), the number of meteor echoes increased twice. For this research, it observed using this HROFFT software. In the past, there is the mean annual variation by forward scatter radio observation. However, there are few the appearances as hourly rate(HR) 3. And there are few appearances of the mean daily variation as HR=30 [2]. We did study using observation data of mean appearance number of HR=61.

### 2. RADIO OBSERVATION SYSTEM in 2000

Forward scatter radio observation system in 2000 year  
transmitting station : JA9YDB Sabae-shi, Fukui

manager : Kimio Maegawa

transmitter : ICOM, IC-706

antenna : 2 element / crossed Yagi aim to Zenith

frequency : 53.750MHz, CW, power:50W

Receiving station : Habikino-shi, Osaka (135.64 °  
E, +34.53°N)

observer : Masayoshi Ueda

receiver : ICOM, IC-706MK II G

antenna : 2element Yagi (DIAMOND, A502HB)  
aim to Zenith

Computer : NEC, VALUESTAR-VU45L  
(Windows98)

Software : HROFFT (sound spectral display and  
storage software)

### 3. RESULTS

(1) The annual variation of mean meteor rates

Figs. 1-4 are the numbers of meteor echoes in every hour. The number of mean appearances of meteor for every month of 2000 had the most in June. This is based on prolonged activity of daytime showers. March had the least appearances. The curve of the numbers of appearances, such as a peak, is well alike in 1997 years 2000 (Fig. 5). The mean every month appearances between 4:00-9:59 LT of for every month were counted, (a). The mean every month appearances between 15:00-20:59 LT of for every month were computed, too. (b). Consequently, (a) shows the peak in June but (b) has gentle peak between August and September (Fig. 6).

The mean every month appearances between 15:00-20:59 of for every month was computed, too.

(b).

Consequently, (a) became the peak in June. But, (b) became the peaks in August and September (Fig. 6).

(2) The daily variation of mean meteor rates

In 2000 the maximum number of appearances for every hour became at 5hr and 6hr LT and the minimum number of appearances were at around 17hr, 18hr LT (Fig. 8). This phenomenon is by apex revolution of the earth.

(3) Appearance of overdense echo

Fig. 7 showed the number of long echoes (more than 20 seconds) per hour. Long echoes appeared on Quadrantids (January), Perseids (August), and Leonids (November) time.

(4) Activity of a meteor shower

Fig. 9-14 showed the activity of meteor showers.

# REFERENCES

1. Maegawa K., WGN, the Journal of the IMO, 27:1, 64-72, 1999.
2. McKinley D. W. R., Meteor Science and Engineering, McGRAW-HILL, New York, 1961, 114.

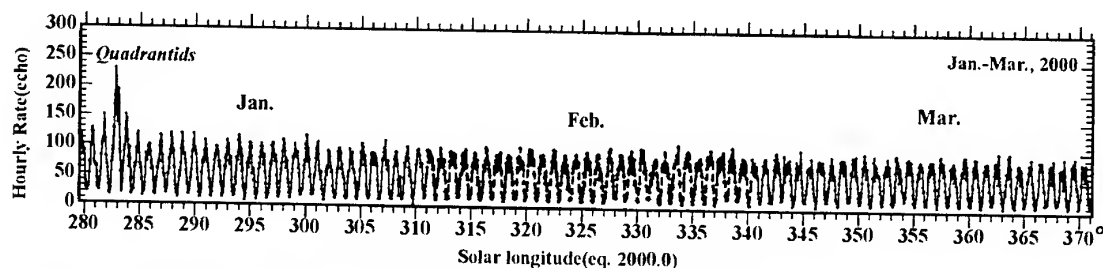


Figure 1 Raw hourly radio meteor echo counts during the period Jan. to Mar., 2000.

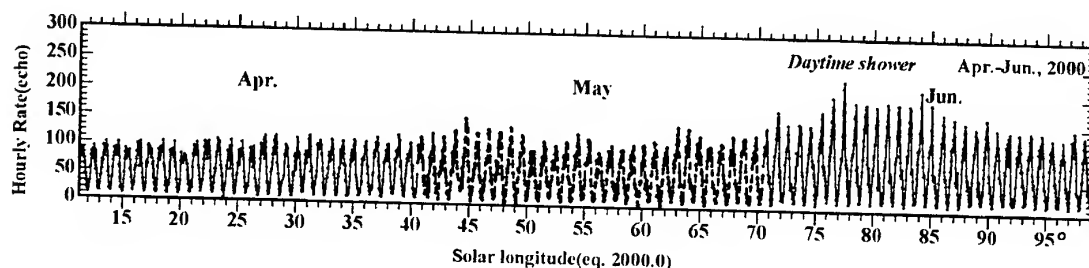


Figure 2 Raw hourly radio meteor echo counts during the period Apr. to Jun., 2000.

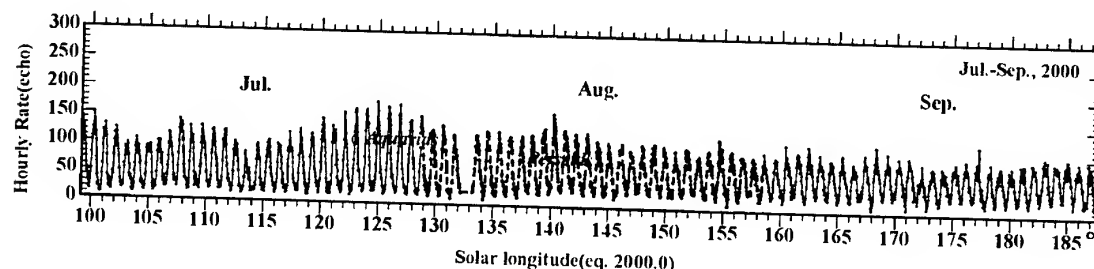


Figure 3 Raw hourly radio meteor echo counts during the period Jul. to Sep., 2000.

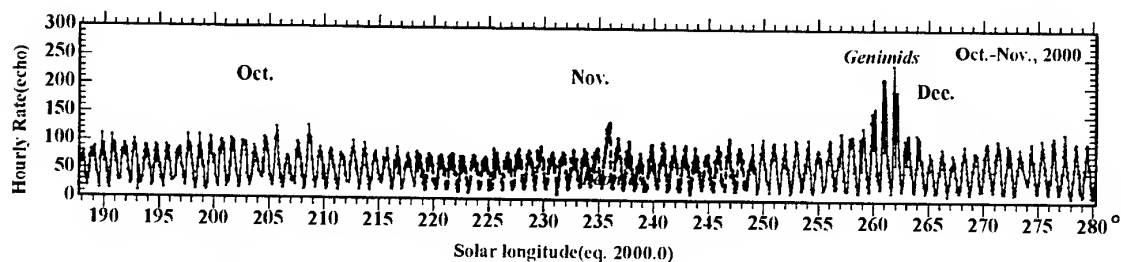


Figure 4 Raw hourly radio meteor echo counts during the period Oct. to Dec., 2000.

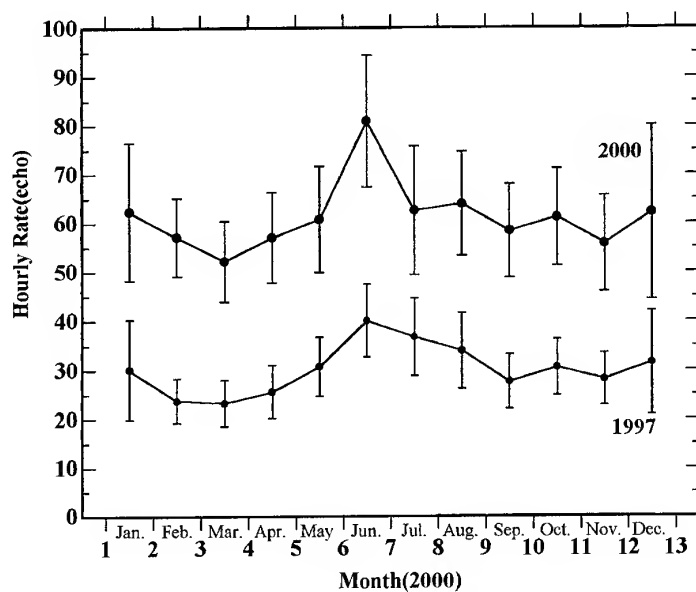


Figure 5 The annual variation of meteor rates (2000).  
Forward scatter radio-echo observations.  
Frequency : 53.750MHz, CW

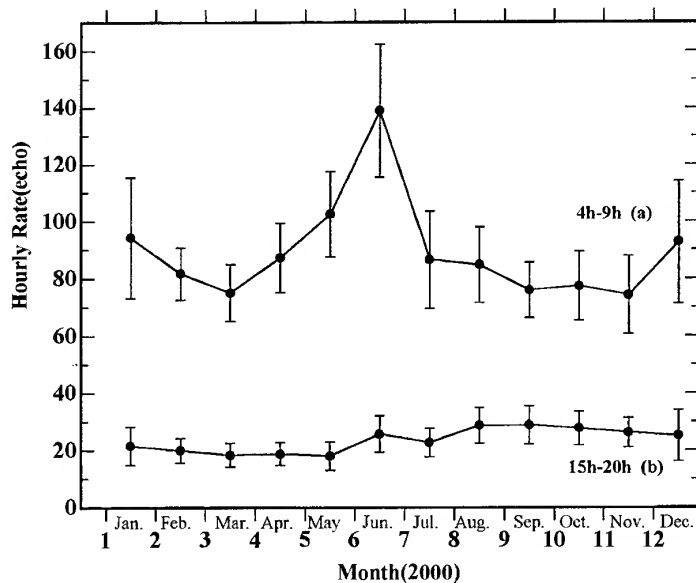


Figure 6 The annual variation of meteor rates (2000).  
Forward scatter radio-echo observations.  
The mean every month appearances between 4:00-9:59 LT of for every month were counted. (a).  
The mean every month appearances between 15:00-20:59 LT of for every month were computed. (b).

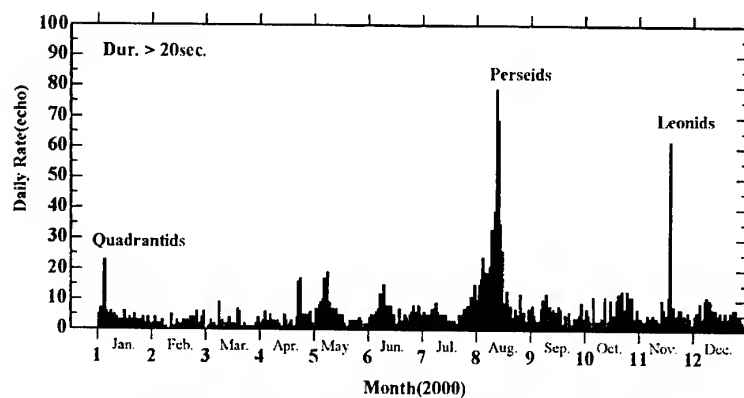


Figure 7 The annual variation of meteor daily rates. Number of meteor echoes more than 20 seconds duration. Forward scatter radio-echo observations.

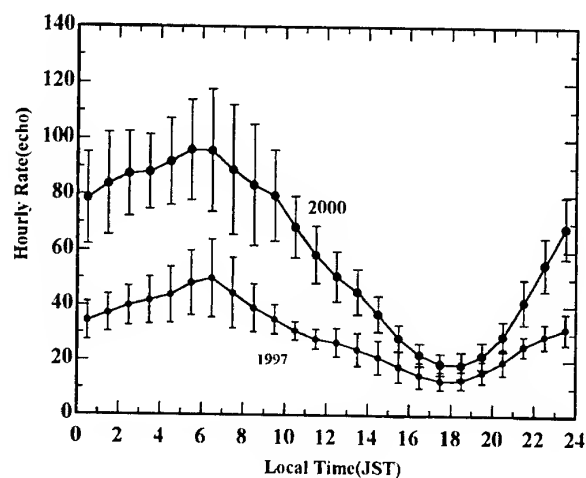


Figure 8 The mean daily variation of meteor rates (Jan.-Dec. 2000). Forward scatter radio-echo observations. Frequency : 53.750MHz, CW

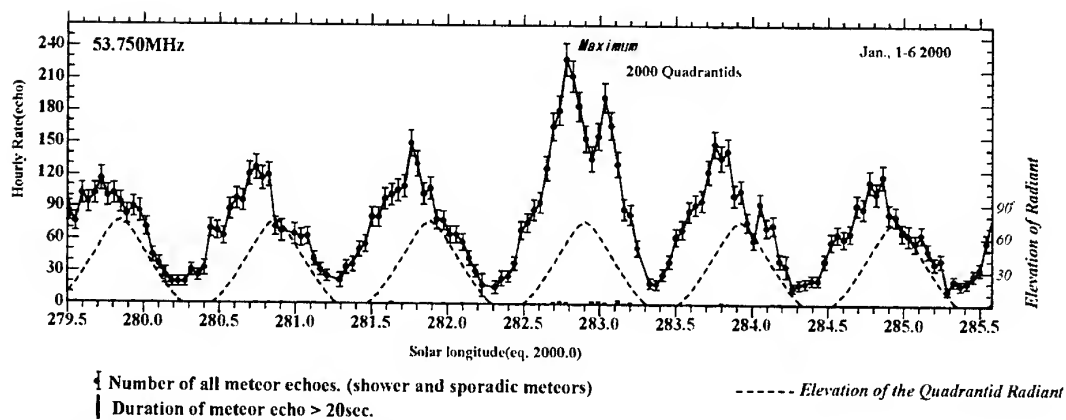


Figure 9 Raw hourly radio meteor echo counts during the period Jan. 1 to 6, 2000. Max. of 2000 Quadrantids: Jan. 3, 2000 at 20:30 UT,  $\lambda = 282.78^\circ$  (J2000.0)

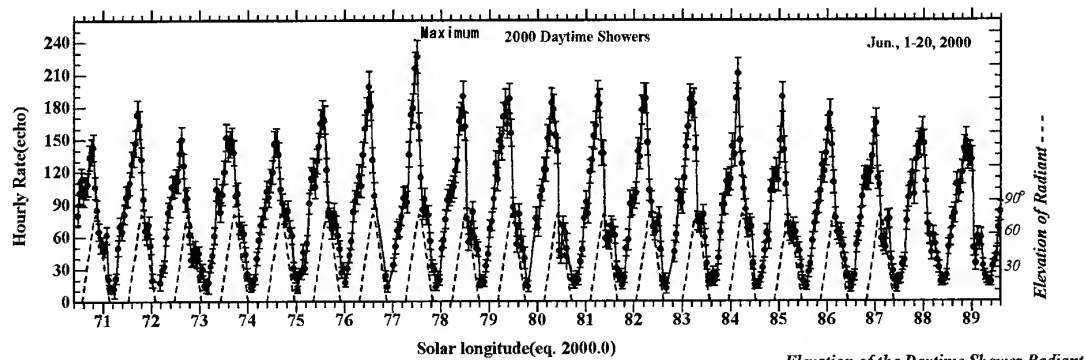


Figure 10 Raw hourly radio meteor echo counts during the period Jun. 1 to 20, 2000.

Max. of 2000 Daytime showers: Jun. 7 to 15, 2000,  $\lambda = 76^\circ - 85^\circ$  (J2000.0)

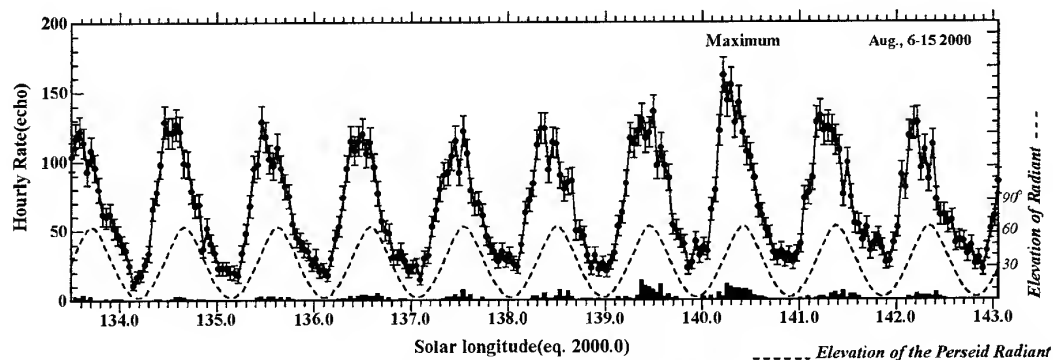


Figure 11 Raw hourly radio meteor echo counts during the period Aug. 6 to 15, 2000.

Max. of 2000 Perseids: Aug. 12, 2000, UT,  $\lambda = 140.25^\circ$  (J2000.0)

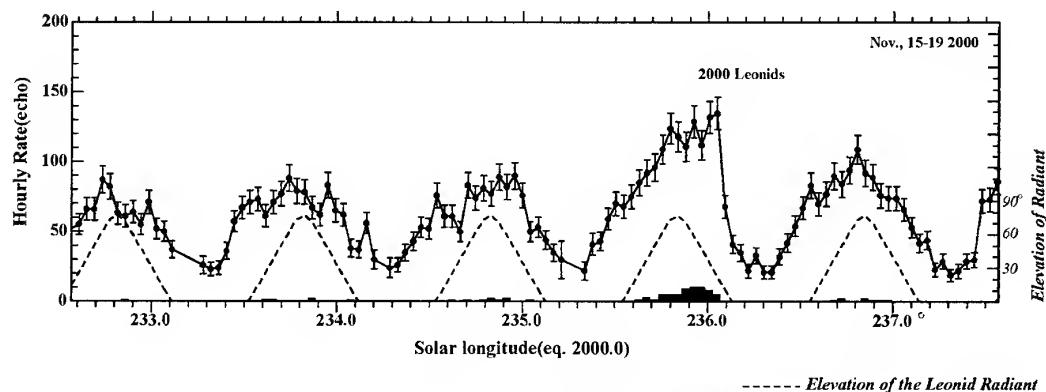


Figure 12 Raw hourly radio meteor echo counts during the period Nov. 15 to 19, 2000.

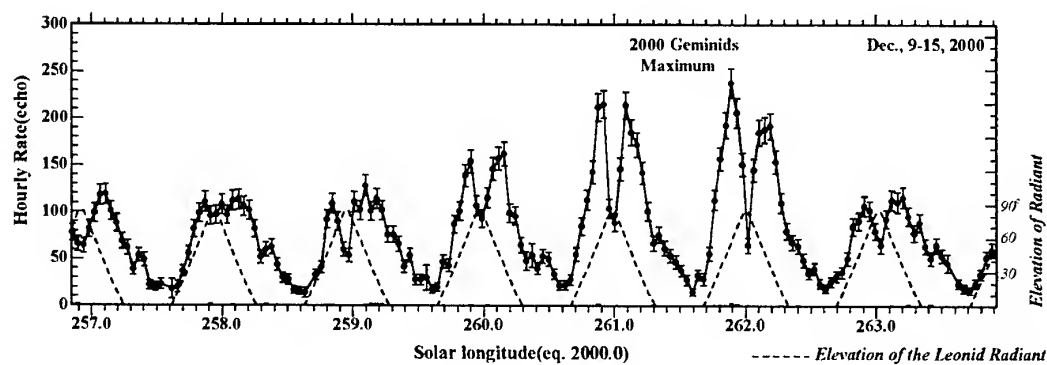


Figure 13 Raw hourly radio meteor echo counts during the period Dec. 9 to 15, 2000.

Max. of 2000 Geminids : Dec. 12-13, 2000, UT,  $\lambda = 261^\circ - 262^\circ$  (J2000.0)

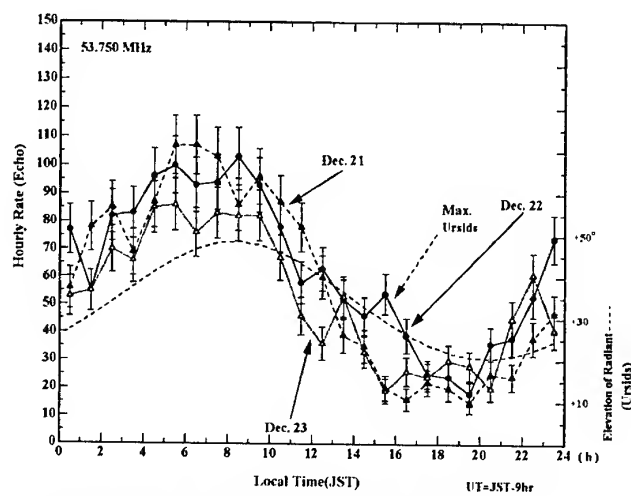


Figure 14 Ursids was observed by our forward scatter radio observations.

Max. of 2000 Ursids : Dec. 22, 2000 at 14hr, 15hr, 16hr J.T,  $\lambda = 270.7^\circ$  (J2000.0)

## EFFECTS OF METEOROID FRAGMENTATION ON RADAR OBSERVATIONS OF METEOR TRAILS (ESA PSB-2)

W. Graham Elford<sup>(1)</sup>, L Campbell<sup>(2)</sup>

<sup>(1)</sup>*Dept. of Physics and Mathematical Physics, Adelaide University, 5005 Australia. gelford@physics.adelaide.edu.au*

<sup>(2)</sup>*Dept. of Physics and Mathematical Physics, Adelaide University, 5005 Australia. lcampbel@physics.adelaide.edu.au*

### ABSTRACT

Radar reflections from meteor trails often differ from the predictions of simple models. There is general consensus that these differences are probably the result of fragmentation of the meteoroid. Several examples taken from different types of meteor radar observations are considered in order to test the validity of the fragmentation hypothesis. The absence of the expected Fresnel oscillations in many observations of transverse scatter from meteor trails is readily explained by assuming a number of ablating fragments spread out along the trails. Observations of amplitude fluctuations in head echoes from "down-the-beam" meteoroids are explained by gross fragmentation of a meteoroid into two or more pieces. Another down-the-beam event is modeled by simulation of the differential retardation of two fragments of different mass, giving reasonable agreement between the observed and predicted radar signals.

### 1. INTRODUCTION

Observations of reflections of radio waves from ionisation produced by meteoroids entering the Earth's atmosphere often differ from the predictions of simple models, all of which are based on the ablation of a single body that maintains its integrity until ablation ceases. In the 1950s the detailed study of telescopic observations of meteors led to the suggestion that many meteoroids were conglomerate dustballs that broke up early in their flight through the atmosphere into a cluster of small fragments.

On the other hand, the measurements of thousands of orbits from radio observations in England, USA, USSR and Australia in the 1960s and 1970s all depended on echoes that showed significant Fresnel oscillations whose occurrence predicates against significant fragmentation. Nevertheless, fragmentation was recognised as occurring in the majority of meteoroids that produced meteor trails observed by the Harvard Radio Meteor Project 1961-1969 [1] although a detailed statistical analysis failed to show

that the phenomenon caused any bias to the meteor orbit distributions [2]. More recently, the measurement of meteor orbits in New Zealand with a technique that is not dependent on the detection of Fresnel oscillations [3] clearly shows that the selection of meteors that show Fresnel oscillations grossly reduces the number of usable meteors.

In 1975 Sekanina and Southworth [2] stated that "we badly need a physical theory of fragmentation to interpret the observations". It is now a matter of record that in the same year Hawkes and Jones [4] published "A Quantitative Model for the Ablation of Dustball Meteors", and since then this model has stood the test of a number of radio and optical studies. In contrast, the new studies of down-the-beam meteors using narrow-beam VHF radars have shown that the meteoroids giving rise to "head echo" observations appear to be solid bodies that either do not fragment, or undergo "gross fragmentation" into two, or possibly a few particles prior to or during ablation. Gross fragmentation and its derivative, continuous fragmentation, have been put on a sound theoretical basis by Ceplecha *et al.* [5].

In this paper we examine several examples of radio observations of meteors that illustrate the types of fragmentation mentioned above and indicate how some quantitative information on the characteristics of the fragmentation can be determined from the data. The observations were recorded at Buckland Park, near Adelaide, South Australia, using a 54.1 MHz radar with a 3° steerable beam.

### 2. ABSENCE OF FRESNEL OSCILLATIONS

The record of a VHF radar observation of a meteor trail is shown in Fig.1 where the amplitude and phase of each pulse return are joined as smooth curves. The oscillations in the amplitude are due to the Fresnel diffraction associated with the ionised trail scattering almost orthogonally as it is formed within the radar beam.

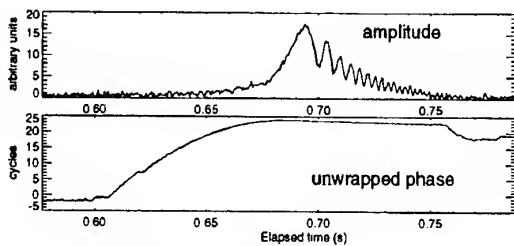


Fig. 1. Meteor reflection showing Fresnel oscillations

In fact records of this type are rare. A more common record is shown in Fig.2 where the Fresnel oscillations are hardly detectable. Many meteor radar echoes show no evidence of Fresnel oscillations.

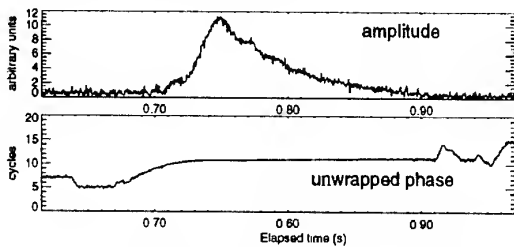


Fig. 2. Meteor reflection without Fresnel oscillations

It has long been conjectured that the **absence** of Fresnel oscillations in radar meteor records is an indication of the **presence** of fragmentation of the meteoroid. A plausible model is suggested below.

### 2.1. Modelling the echo from a fragmented meteoroid

A meteoroid is assumed to fragment into many particles that become distributed along the trajectory of the parent meteoroid. The resultant meteor trail is the superposition of many trails each due to a fragment of the parent body. The scattered radar signal from all small trails is summed to produce the total echo recorded by the radar.

In general the meteoroid fragments become separated along the trajectory due to differential retardation or small differences in speed associated with the fragmentation event. For modelling purposes it is sufficient to take a group of particles of identical mass, and allow them to be evenly distributed over a limited distance. It was found that it was sufficient to take 10 particles. For a radar operating at 54 Mhz the results are shown in Fig.3.

It can be seen that the Fresnel oscillations are substantially reduced as the separation of the particles is increased. By spreading the particles over 200 m the Fresnel oscillations are almost obliterated.

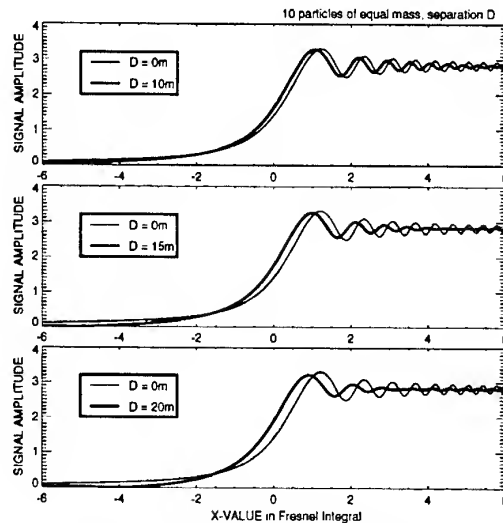


Fig. 3. Comparison of simulated reflections

## 3. FRAGMENTATION OF "DOWN-THE-BEAM" METEORIODS

The preceding examples are of meteoroids travelling transverse to the radar beam, as illustrated in Fig.4 (right panel), with the signal dominated by specular reflection from the trail of ionisation. For a "down-the-beam" meteoroid (left) the reflection from the trail is not detected by the radar, but if the ionisation around the meteoroid is sufficiently strong, a "head echo" is observed.

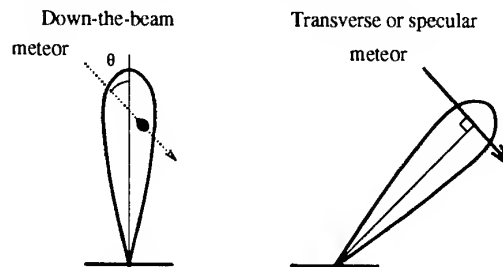


Fig. 4. The two modes of detection of meteors by radar

A rare meteor reflection is shown in Fig.5, in which the returned signal appears to be proportional to the radar beam strength as a function of angle, modulated by interference. This can be explained as a meteoroid which has split into two similar pieces before entering the beam, with each producing a head echo determined by its position in the beam. The modulation is due to the interference of the two reflections as the particles slowly separate.

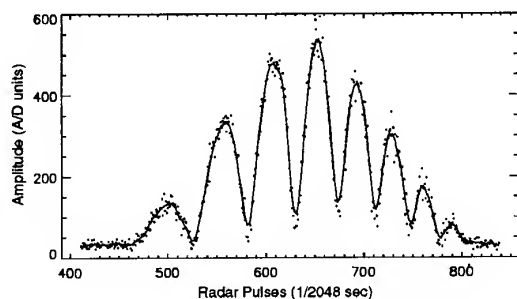


Fig. 5. Amplitude for two fragments entering beam

The change in separation between successive maxima or minima indicates a separation speed that increases from 96 to 197 m/s during the passage of both fragments through the beam. The speed of the incoming particles is 68.8 km/s and from the separation speeds it can be inferred that fragmentation occurred 11.2 km before the daughter fragments entered the beam.

The record in Fig. 6 is interpreted as a meteoroid which is observed to undergo gross fragmentation during its passage through the radar beam at heights near 100 km. At **A** there is an ejection of a short-lived fragment. At **B** the meteoroid fragments into two parts of approximately equal size that slowly separate along the trajectory and give rise to the "beat signal". The fragmentation is accompanied by severe retardation in speed, shown in the lower diagram by the deviation from the line indicating the initial speed. The overall amplitude variation is due to the approximate Gaussian form of the polar diagram of the beam.

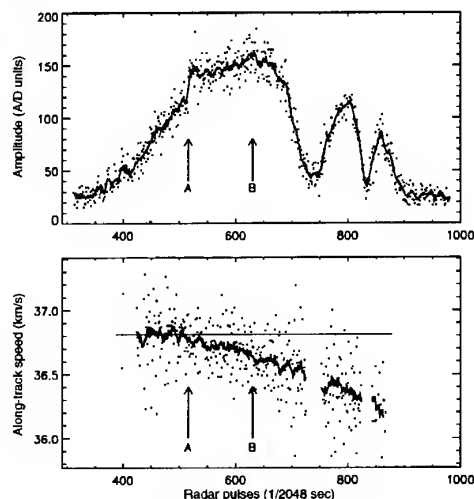


Fig. 6. Fragmentation within the beam

#### 4. FRAGMENTATION DURING ABLATION

The data shown in Fig. 7 were obtained with the beam directed vertically. The radar operated with a pulse repetition rate of 2048 per second, and the range, amplitude, and phase of each pulse echo were the basic data. The analysis is discussed by Taylor *et al.* [6].

The meteoroid entered the beam with an initial speed of 44.2 km/s and at a zenith angle of  $44^\circ$ . The deviation from the initial, constant deceleration (indicated by the straight line in Fig. 7, lower diagram), indicates that two gross fragmentation events occurred. The first event (A) occurred when the meteoroid was at a height of 95.8 km where the speed was 44.1 km/s. The second event (B) occurred at a height of 94.6 km where the speed was 43.9 km/s.

The following model accounts for the deceleration observed in the data in Fig. 7:

- (1) at 95.8 km the parent particle splits into 20 equal mass daughter particles;
- (2) at 94.6 km each daughter fragment further splits into 10 equal mass particles.

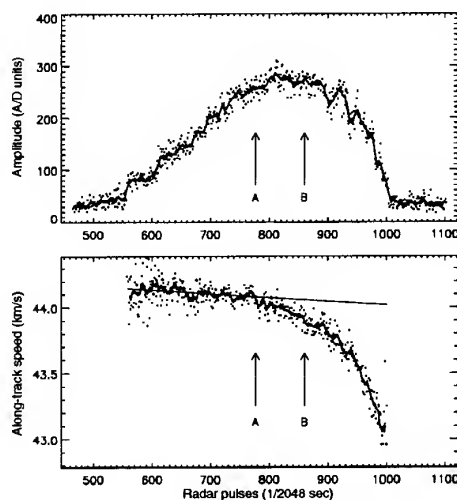


Fig. 7. Double, multiple-fragmentation event

To compare the model with the data, the "along-track speed" is re-plotted (as points) in a plot of height versus speed in the right-hand panel of Fig. 8. (The calculated ionisation profile from the ablating particles is shown in the left panel.) The curves show the model calculations for none, one or two of the fragmentations

described above. Agreement with the data is obtained for the case of two fragmentations.

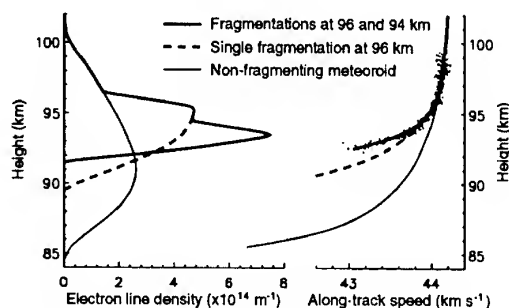


Fig. 8. Electron density and meteoroid speed

## 5. SIMULATING A FRAGMENTATION EVENT

In Fig.9 the time series of the amplitude of a meteor reflection is shown (lower trace) for five adjacent range bins at 0.5-km intervals at heights of 90–92 km. An initial short event, occurring at later times at lower heights, indicates a down-the-beam meteoroid, with the two-hump structure suggesting that there is interference between reflections from two or more fragments. The later, irregular reflection in each range bin is likely due to ionisation produced by the meteoroid which spread out to form a reflecting layer.

The complex power spectra of these signals (lower traces in Fig.10) provide an indication as to the fragmentation of the meteoroid. The down-the-beam signal transforms to a double peak at higher frequencies (with the peak around zero being produced by the remnant ionisation). The change in frequency with height indicates the deceleration of the meteoroid in the atmosphere, while the double-peak suggests that there are two fragments, travelling at different speeds, but decelerating similarly.

To confirm that this interpretation of two fragments is physically realistic, a program has been written to simulate the case of a meteoroid splitting into two unequal fragments and calculate the expected reflection. The path through the atmosphere of each fragment is calculated (taking into account the deceleration due to the atmosphere) for the parameters in Table 1.

This calculation gives the amplitude, complex power spectra and phase shown by the upper traces in Fig.9 and Fig.10 and by the shorter traces in Fig.11. (To show the phase of the down-beam signals clearly, Fig.11 corresponds to only a section of Fig.9.)

Table 1. Parameters for simulation.

Parameter	Value
Mass of meteoroid	1.1 $\mu\text{g}$
Density of meteoroid	3500 $\text{kg m}^{-3}$
Mass ratio of the two fragments	0.77
Meteoroid speed at fragmentation	23.65 $\text{km s}^{-1}$
Height of fragmentation point	110 km

The similarity of the observed and simulated series and spectra indicates that the particular observed event can be explained by a meteoroid splitting into two fragments of slightly different mass.

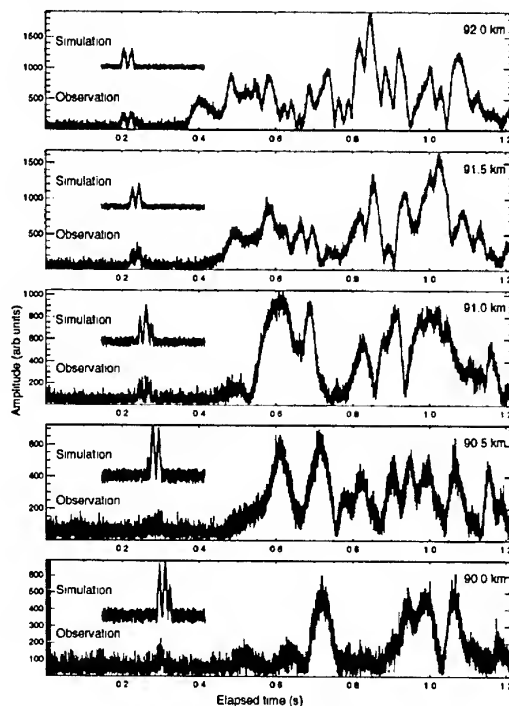


Fig. 9. Amplitude at five heights for "down-beam" event

## 6. CONCLUSION

The detailed structure of several VHF radar reflections by meteor ionisation in the atmosphere has been explained by consideration of fragmentation of the meteoroid into two or more pieces. Simulations have been used to justify plausible explanations for the absence of Fresnel oscillation in most transverse reflections from meteor trails. Structure in three "down-the-beam" events is accounted for by fragmentation of the meteoroid into two pieces in two cases and multiple fragmentation in the third.

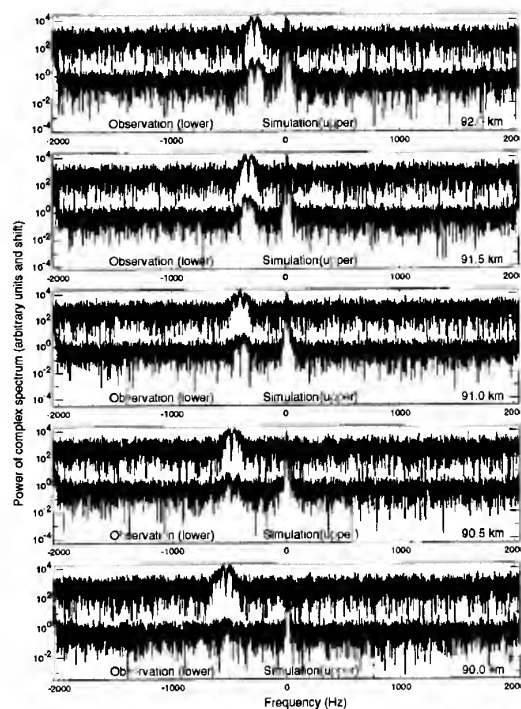


Fig. 10. Complex power spectra at five heights

A detailed simulation of the differential atmospheric retardation of two slightly different meteoroid fragments shows agreement with the amplitude, phase and power spectra of another "down-the-beam" event. Thus it is concluded that fragmentation is a common feature of meteoroids in their passage prior to or during ablation in the atmosphere.

## 7. REFERENCES

1. Southworth, R. B. and Sekanina, Z., Physical and dynamical studies of meteors, *NASA Contractor Report CR-2316*, Washington, USA, October 1973.
2. Sekanina, Z. and Southworth, R. B., Physical and dynamical studies of meteors: meteor fragmentation and stream distribution studies, *NASA Contractor Report CR-2615*, Washington, USA, November 1975.
3. Baggaley, W. J., Bennett, R. G. T., Taylor, A. D. and Steel, D. I., The Advanced Meteor Orbit Radar Facility: AMOR, *Quant. J. Roy. Astron. Soc.*, Vol. 35, 293–320, 1994.
4. Hawkes, R. L. and Jones, J., A Quantitative Model for the Ablation of Dustball Meteors, *Monthly Notices Roy. Astron. Soc.* Vol. 173, 339–356, 1975.
5. Ceplecha, Z., Spurný, P., Borovička, J., and Kečliková, J., Atmospheric Fragmentation of Meteoroids, *Astron. Astrophys.*, Vol. 279, 615–626, 1993.
6. Taylor A. D., Cervera M. A. and Elford W. G., *Astron. Soc. Pac. Conf. Series* Vol. 104, 75–78, 1996.

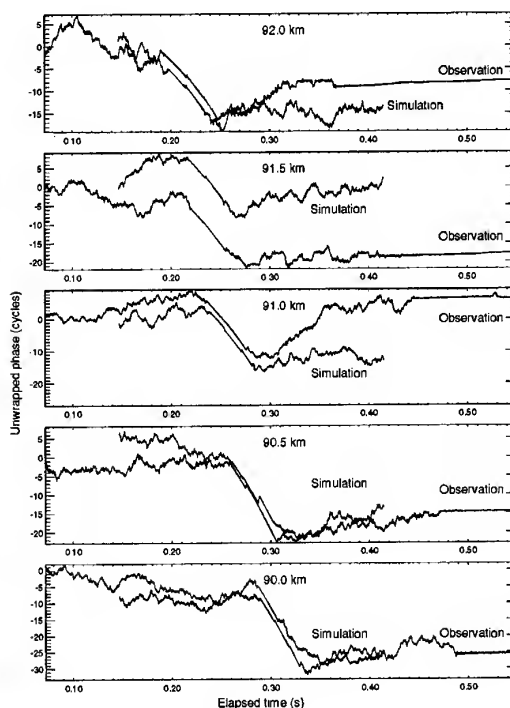


Fig. 11. Unwrapped phase at five heights

# SIMULTANEOUS OPTICAL AND RADAR OBSERVATIONS OF METEORS: ANOTHER CRITERION OF COMMONNESS

P. Pecina, P. Koteš, and R. Štokr

Astronomical Institute of the Academy of Sciences of the Czech Republic, 25165 Ondřejov, Czech Republic

## ABSTRACT

An identification of common meteors observed simultaneously optically and by radar is usually based on time coincidence of both events. Another criterion of commonness of such meteors can be based on the comparison of radar specular point range and the corresponding distance inferred from the optical data of simultaneous multistation observation. In case when only single station optical data are available together with wide beam radar data, only the height interval within which the optical train formed, can be estimated. Such estimation of possible heights of occurrence of Leonid bright meteor observed in 1999 is used to decide which recorded radar echo could be caused by a counterpart of the optical meteor. The derivation of the positional vector of the radar specular point following from the multistation optical observation, in case when the location of radar does not coincide with that of any optical station, is also carried out.

## 1. INTRODUCTION

An identification of common optical and radar meteors is usually based on the time coincidence of both events. However, this is not the only one possible criterion since also the distance to specular point of the trajectory determined from the optical station located at the radar site and corresponding radar range should coincide. Thus, both quantities can serve as an additional criterion of the commonness of both meteors.

When performing the simultaneous optical/TV and radar observations of meteors, it is desirable to have the most complex information of both events at hand as possible. The best configuration of the observational stations consists of two or multistation optical (or TV) observational sites accompanied by radar. The optical observation is then capable of yielding a directional position of the point of the trajectory having an angular distance of  $90^\circ$  from a radiant, its height above the ground, and also its distance from the chosen station (e. g. [1]) which should coin-

cide with the radar range within the precision limits in case when the radar location coincides with the location of corresponding optical station. The characteristics of radar echoes can then be corrected for different conditions under which they were observed such as the range and the direction within the antenna diagram and, consequently, the electron line density derived from echo duration or amplitude can well be compared to the corresponding optical/TV magnitude.

However, sometimes the optical/TV data from only single station are available together with the data from wide beam radar such as in Ondřejov [3] which enable neither the position nor the height of the radar specular point to be determined. If the optical data indicate the possible membership of the meteor to known shower (i. e. colour of the meteor, its flight direction at specified time), it can be shown that the height of radar specular point as well as the height of any point of the optical trajectory can be computed under these conditions. Since the interval of heights of appearance of known shower members is known then this height can serve as a criterion whether the observed meteor was common to both techniques. We will apply this criterion to bright Leonid meteor observed in 1999 which had 4 possible counterparts in radar echoes.

A more common case of simultaneous radar and optical multistation observation from sites the locations of which are mutually different, can also occur. We will derive the formula for computation of the radar specular point position vector from the optical data.

## 2. DERIVATION OF THE FORMULAE

Now we will derive the formulae enabling the computation of the positional vector of the radar specular point,  $\mathbf{r}_0$ , and consequently the height of this point together with height of any chosen point of optical trajectory of a meteor. We will begin with the case of single optical station.

## 2.1. Radar and single optical/TV station

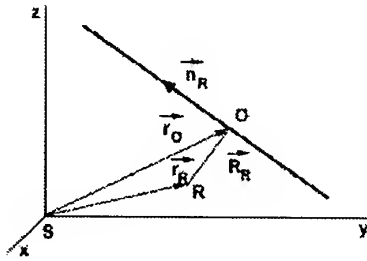


Figure 1. The coordinate system used for the computation of  $r_0$ . The optical station is located at  $S$  while the radar one at  $R$ . The radar specular point coincides with  $O$ . The vector  $R_R$  is perpendicular to  $n_R$ .

The coordinate system we use is depicted in Figure 1. Let the optical station coincide with the origin of the reference frame. The  $xy$ -plane of the system is tangent to the Earth's sphere. The  $x$ -axis points to south, the  $y$ -axis to east and the  $z$ -axis to the local zenith. The positional vector of radar in this system is  $r_R$ . The position of the specular point with respect to radar is given by the vector  $R_R$ . Optical trajectory of a meteor is considered to be linear so that it lies within a plane containing the origin and two arbitrary directions to the path characterized by unit vector,  $n$ . The normal unit vector of this plane,  $N$ , can be computed from at least two known  $n$  as

$$N = (n_i \times n_j) / \sqrt{1 - (n_i \cdot n_j)^2}, \quad (1)$$

where  $\times$  designates the vector product and the dot between vectors means their scalar product. The meteor path can in our coordinate system be described by the equation

$$r = r_0 + n_R p, \quad (2)$$

where  $r_0$  is arbitrary but fixed positional vector of some chosen point of the path,  $n_R$  stands for the unit vector pointing to meteor radiant, and  $p$  is the parameter. We choose the vector  $r_0$  so that it coincides with the positional vector of the radar specular point,  $O$ , for  $p = 0$ , and  $r_0 = r_R + R_R$ . We will now derive equations enabling computation of  $r_0$  from known quantities. Since the vectors  $n_R$  and  $r$  lie in the observational plane it should hold true that  $N \cdot n_R = 0$  and also  $N \cdot r = 0$  which implies

$$N \cdot r_0 = 0. \quad (3)$$

The physics of radar wave reflection from meteor trains requires that  $R_R \cdot n_R \equiv (r_0 - r_R) \cdot n_R = 0$  from which we get the second equation containing  $r_0$

$$n_R \cdot r_0 = n_R \cdot r_R, \quad (4)$$

with the right hand side containing only known vectors. The third equation follows from the demand

that  $O$  is the point common to both the line and a sphere drawn around the radar. This sphere has equation

$$(r - r_R)^2 = R_R^2,$$

where  $R_R = |R_R|$ . Since according to our definition  $r \equiv r_0$  for  $p = 0$  (i. e. at the common point of both the line and the sphere) this condition reads

$$(r_0 - r_R)^2 = R_R^2,$$

implying that

$$r_R \cdot r_0 = (r_0^2 + r_R^2 - R_R^2)/2, \quad (5)$$

where  $r_0 = |r_0|$  and  $r_R = |r_R|$ . The Eqs. (3) - (5) form a set of linear equations for computing the components of the vector  $r_0$ . It can easily be proved that its solution may be written in the form

$$r_0 = (n_R \cdot r_R) [r_R \times N] / [n_R \cdot (r_R \times N)] + \frac{1}{2} (r_0^2 + r_R^2 - R_R^2) [n_R \times N] / [r_R \cdot (n_R \times N)]. \quad (6)$$

However, we can see that  $r_0$  depends on its still unknown magnitude  $r_0$ . Let us define the auxiliary vectors

$$a = (n_R \cdot r_R) \frac{r_R \times N}{n_R \cdot (r_R \times N)} + \frac{1}{2} (r_R^2 - R_R^2) \frac{n_R \times N}{r_R \cdot (n_R \times N)}$$

and

$$b = \frac{1}{2} \frac{n_R \times N}{r_R \cdot (n_R \times N)},$$

which are built only from known vectors. The Eq. (6) then converts into

$$r_0 = a + r_0^2 b, \quad (7)$$

yielding the following quadratic equation for  $r_0^2$

$$|b|^2 r_0^4 - (1 - 2a \cdot b) r_0^2 + |a|^2 = 0. \quad (8)$$

Thus,  $r_0^2$  can be computed from known quantities. On substituting it into Eq. (6) or (7) we get the whole vector  $r_0$ . To be able to compute the positional vector of an arbitrary point of meteor trajectory we must know the value of parameter  $p$  from Eq. (2). Let the direction of this point be characterized by the unit vector  $n_i$  which itself has to be colinear with the positional vector of the point,  $r_i$ , i. e.

$$n_i \times r_i = 0.$$

When inserting for  $r_i$  from Eq. (2) we arrive at the equation for particular parameter,  $p_i$ :

$$n_i \times r_0 + n_i \times n_R p_i = 0,$$

yielding for the parameter  $p_i$  the following expression

$$p_i = -(n_i \times n_R) \cdot (n_i \times r_0) / |n_i \times n_R|^2. \quad (9)$$

The above formulae are not appropriate when the locations of both stations coincide i. e. when  $r_R = 0$ . In this case the system of equations for components of  $r_0$  reduces to

$$N \cdot r_0 = 0, \quad n_R \cdot r_0 = 0, \quad |r_0| = R_R. \quad (10)$$

It can easily be seen from the first two above equations that  $\mathbf{r}_0 \simeq \mathbf{n}_R \times \mathbf{N}$  or  $\mathbf{r}_0 \simeq \mathbf{N} \times \mathbf{n}_R$  satisfies these equations. Let us choose the first possibility. Then the solution to (10) reads

$$\mathbf{r}_0 = \pm R_R \mathbf{n}_R \times \mathbf{N} / |\mathbf{n}_R \times \mathbf{N}|, \quad (11)$$

where the appropriate sign must be chosen so that the  $z$ -component of  $\mathbf{r}_0$  is positive. This vector can again be inserted into (9) and the positional vector of each point of the meteor trajectory can be computed. Also the interval of observed heights of optical meteor can then be deduced. Thus, we have solved the posed task.

## 2.2. Radar location differing from that of any optical station

Now we will treat the case when the radar location differs from that of any optical station. The optical observation from at least two stations yields the parameters of the trajectory of the meteor in the atmosphere and enables the range of the radar specular point to be computed. Our aim now is to compute the vector  $\mathbf{R}_R$  (see Figure 1). The equation of the meteor path can be written as

$$\mathbf{r} = \mathbf{R}_0 + \mathbf{n}_R p, \quad (12)$$

where  $\mathbf{R}_0$  is the positional vector of the specular point with respect to selected (1st) optical station so that  $\mathbf{R}_0 \cdot \mathbf{n}_R = 0$ . Let the vector of the normal of the plane containing both the meteor and the 1st station be  $\mathbf{N}_1$ . The plane containing both the same meteor and any other optical station does not go through the origin of the coordinate system coinciding with the location of the 1st station. Let its distance from the origin be  $d$  (this quantity is known from the two station triangulation, e. g. [1]). Since the vector  $\mathbf{R}_0$  must be common to both planes the following set of linear equations for its components has to be satisfied

$$\mathbf{N}_1 \cdot \mathbf{R}_0 = 0, \quad \mathbf{N}_2 \cdot \mathbf{R}_0 = d, \quad \mathbf{n}_R \cdot \mathbf{R}_0 = 0. \quad (13)$$

One can easily verify that the solution to (13) is

$$\mathbf{R}_0 = d [\mathbf{N}_1 \times \mathbf{n}_R] / [\mathbf{N}_2 \cdot (\mathbf{N}_1 \times \mathbf{n}_R)]. \quad (14)$$

We can see from Figure 1 that

$$\mathbf{r}_0 = \mathbf{r}_R + \mathbf{R}_R = \mathbf{R}_0 + \mathbf{n}_R p_0. \quad (15)$$

Since the radar observation condition requires  $\mathbf{R}_R \cdot \mathbf{n}_R = 0$  to be valid we can get from the previous relation

$$p_0 = \mathbf{r}_R \cdot \mathbf{n}_R, \quad (16)$$

yielding for the vector  $\mathbf{R}_R$  the formula

$$\mathbf{R}_R = \mathbf{R}_0 + (\mathbf{r}_R \cdot \mathbf{n}_R) \mathbf{n}_R - \mathbf{r}_R,$$

which may finally be written as

$$\mathbf{R}_R = \mathbf{R}_0 + \mathbf{n}_R \times (\mathbf{n}_R \times \mathbf{r}_R). \quad (17)$$

The magnitude of this vector must be equal to the range observed by the radar. The expressions (15) - (17) enable also the computation of height of the radar specular point. These formulae solve our task.

*Table 1. The heights (in kilometers) following from Eq. (6) when using the station S1 or S2 data. The duration of both overdense echoes exceeded 60 seconds. The overdense echo at  $R_R = 125$  km was preceded by the head echo. The second column lists the radar range determined from the film record. The last column contains the optical beginning height common to both stations, i. e. the height at which the particular meteor was firstly observed from both stations.*

Type of radar echo	range in km	height from S1	height from S2	beginning height
underdense	265	147.0	148.1	251.6
underdense	190	107.7	108.0	179.8
overdense	125	73.8	73.6	117.3
overdense	130	77.4	77.3	124.1

## 3. APPLICATION

We will now apply the formulae from the first subsection to the bright Leonid meteor which appeared on Nov 18, 1999 2h 50m 35s UT. It was photographed simultaneously from two sites having the geographical coordinates (50°10' 10" N, 14°12' 48" E)(station S1) and (50°9' 16" N, 14°41' 16" E)(station S2). Also its possible 4 radar counterparts were recorded in Ondřejov (45°54' 38" N, 14°47' 1" E). Application of two stations geometry rules yielded the following radiant coordinates:  $\alpha = 168.4^\circ$ ,  $\delta = 18.1^\circ$  while the correct Leonid radiant is located at  $\alpha = 152.3^\circ$ ,  $\delta = 22.2^\circ$  (e. g. [2]). This discrepancy can easily be explained by the very inappropriate geometry since the planes going through sites S1 and S2 were almost parallel with the angle between their normals  $\varphi \simeq 1.5^\circ$ . Thus, we could not use formulae developed in the second subsection. However, we could estimate the height of radar reflecting point using the formulae of the first subsection. Using the formula (6) we arrive at the height of the radar reflection point and also at the height of the first point of the luminous trajectory common to both stations. The results are collected in Table 1. We can see there that the third as well as fourth radar meteor has very low height of specular point and should, therefore, be discarded from our considerations. The height of the first and second meteor is acceptable. However, the optical beginning height of the first one (i. e. 251.6 km) is unacceptable, since the beginning heights of Leonid meteors have recently been reported as high as 180 - 190 km, [4]. So, only the beginning height of the second meteor as well as its height of radar specular point can be realistic.

## 4. CONCLUSION

We have derived the formulae enabling the computation of the positional vectors and, consequently, also the heights of meteor observed simultaneously by optical technique and radar when only one optical station was under operation. We have extended

the derivation also on the case when more than one optical station operated and also a radar the location of which does not coincide with that of any of the optical station. We have applied the formulae to decision which of radar echoes recorded simultaneously with optical Leonid meteor was its possible counterpart. We arrived at the conclusion that it could be the second meteor from Table 1.

#### ACKNOWLEDGMENTS

This work was supported by the scientific key project K3012103 and the grant No 205/00/1728 of the Grant Agency of Czech Republic.

#### REFERENCES

1. Cepřecha Z., 1987, *Bull. Astron. Inst. Czechosl.*, 38, 222
2. Cook A. F., 1973, in *Evolutionary and Physical Properties of Meteoroids*, eds. C. L. Hemmenway, P. M. Millman, and A. F. Cook, A Working List of Meteor Streams, pp.183 – 208, NASA, Washington D.C.
3. Plavcová Z. and Šimek M., 1960, *Bull. Astron. Inst. Czechosl.*, 11, 228
4. Spurný P., Betlem H., Jobse K., Koten P., van't Leven J., 2000, *Meteoritics and Planetary Science*, 35, 1109

## THE MOTION OF RADIO METEOR REFLECTION POINT OF GEMINIDS

Kouji Ohnishi<sup>(1)</sup>, Toshiyuki Ishikawa<sup>(2)</sup>, Shinobu Hattori<sup>(2)</sup>, Osamu Nishimura<sup>(2)</sup>, Akiko Miyazawa<sup>(2)</sup>,  
Masatoshi Yanagisawa<sup>(2)</sup>, Makoto Endo<sup>(2)</sup>, Masaki Kawamura<sup>(2)</sup>, Toshiyuki Maruyama<sup>(2)</sup>,  
Kai Hosayama<sup>(2)</sup>, Mai Tokunaga<sup>(2)</sup>, Kimio Maegawa<sup>(3)</sup> and Shinsuke Abe<sup>(4)</sup>

<sup>(1)</sup> Nagano National College of Technology, 716, Tokuma, Nagano, Nagano 381-8550, Japan:  
ohnishi@ge.nagano-nct.ac.jp:

<sup>(2)</sup> Nagano National College of Technology, 716, Tokuma, Nagano, Nagano 381-8550, Japan:

<sup>(3)</sup> Fukui National College of Technology, Geshi, Sabae, Fukui 916-8507, Japan:  
kmaegawa@fukui-nct.ac.jp:

<sup>(4)</sup> The Institute of Space and Astronautical Science, Sagamihara, Kanagawa, 229-8510, Japan:  
avell@planeta.sci.isas.ac.jp:

**Abstract.** Ham-band Radio Observation (HRO) is one of the observational techniques for the forward scatter observation of meteors. We observe the meteor echo with two-element loop antennas (F/B ratio is 10 dB) at the Nagano National College of Technology (Nagano, JAPAN) using the continuous transmission of beacon signals for meteor observations at 53.750MHz, 50W from Fukui National College of Technology (Fukui, JAPAN). To prove that the radio echo is really the echo due to meteor, we have constructed the direction determination system using the paired antennas that can detect the direction roughly where the radio echo come from. The direction of one of this paired antennas was *West* toward Sabae and the other was *East* which has proved to be the most sensitive for this research. Using this system, we detected the change of the direction of reflection point of meteor radio signal of Geminids in 2000; from the westward to eastward before and after the culmination of the radiant which is consistent the formula of reflection point of meteors. At the same time, we detected the change of an intensity and a trend of the Doppler shift of meteor echoes. This result is consistent of the meteor wind data of MU Rader of Radio Science Center for Space & Atmosphere (RASC), Kyoto University.

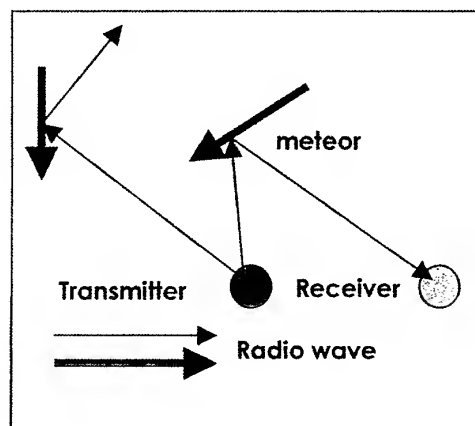


Fig. 1. Radio reflection due to meter trails

1976, Shimoda et al. 1993, Suzuki & Nakamura 1995, Maegawa et al. 1999) However, we must note that the number of detected meteor is out of proportion to the flux of the meteoroid in this observation. For example, if the meteor incident angle is nearly 90°, the reflected radio signal cannot be received any receiver station (see Fig.1).

In the visual meteor observation, the detectable region of the meteor on the sky is fixed all the time so that the number of detected meteor is proportion to the flux of the meteoroid. On the other hand, in the forward radio meteor scattering observation, the detectable region of the meteor changes in time due to the transition of the incident angle of meteor stream. For example, the region of the reflection point varies hard at when the radiant of the meteor stream is near the culmination. Therefore, to monitor the meteor stream activity by the forward radio meteor scattering observation, we must compensate the observed data for some peculiarities on the radio meteor observation (e.g. response

### 1. Introduction

The forward meteor scattering observation can be a method to monitor the activity of meteor and meteor stream by using simple and inexpensive equipment (McKinley 1961, Schilling 1993, Yrjölä & Jenniskens 1998). Using the forward meteor scattering observation, many results have been published about the monitor of meteor activity and outbursts of streams (e.g. Suzuki

function or observability function by Hines 1955, Hines & Vogan 1957, Elford et al. 1994, Yrjölä & Jenniskens 1998, Cepelcha et al. 1998).

- the location of the transmitter and receiver.
- the incident angle of the meteor ( $\theta_r, \phi_r$ ).
- the antenna pattern and the gain of the transmitter.
- the antenna pattern and the gain of the receiver.

We have made a simple formula for the compensation of above peculiarities. Using this formula, we have analyzed the data from 3 receiver sites for Leonids and Geminids 2000, and have found that this data is consistent (Ohnishi et al. 2001).

To analyze each effect of these peculiarities more deeply, we must identify each effect directly. In this research, we concentrated only on finding point the shift of radio reflection point of the ionization trail of meteor in meteor stream. For this purpose, we used the paired antenna and receivers, and the FFT spectrogram software with PC. And we have tried to show the evidence of the shift of radio reflection point by

- (1) detecting the change of the direction of meteor echo.
- (2) detecting the variation of the received power due to the shift of reflection point.
- (3) detecting the change of a trend of the Doppler shift of meteor echoes due to the shift of reflection point.

For our results, we have detected (1) and (2) clearly. Though we could not get the direct evidence in (3), our data is consistent of the meteor wind data of MU Rader of Radio Science Center for Space & Atmosphere (RASC), Kyoto University.

## 2. HRO observation

### 2.1. HRO

Radio meteor scatter is an ideal technique for observing meteors continuously. Meteor trails can reflect radio waves from distant transmitters back to earth, so when a meteor appears one can sometimes receive meteor echoes from radio source away from the observing site. For radio observation of meteors, amateur Ham-band beacon signals are useful as a stable radio source. Since 1996, K. Maegawa has been keeping up the continuous transmission of a beacon signal at 53.750MHz(50 W) from Fukui National College of Technology (136.18E, 35.95N) in Sabae, Fukui, Japan, for meteor radio observation (Maegawa 1999). We started the direction determination system of automating HRO (Ham-band Radio Observation) by monitoring the signals from the radio receiver with computers in August 2000. In this research, the receiver is located at Nagano National College of Technology (138.18E, 36.63N) in Nagano, Nagano, Japan. The distance between Sabae and Nagano is about 200km, and the direction to the Sabae from Nagano is almost due west. Fig.2 show the location of the transmitter and the receiver.

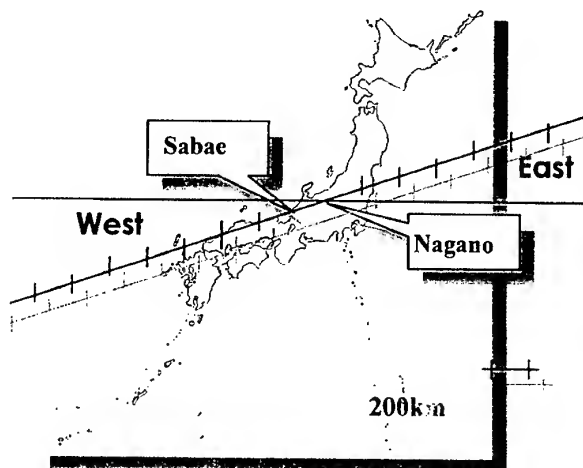


Fig. 2. Baseline of the Transmitter and Receiver: Transmitter at Fukui National College of Technology (136.18E, 35.95N) in Sabae, Fukui, Japan Receiver at Nagano National College of Technology (138.18E, 36.63N) in Nagano, Nagano, Japan.

### 2.2. Incident angle and reflection point

The relation of an incident angle of meteor and the distance of reflection point from the receiver is illustrated in Fig.3 and are shown in Fig.4. As the incident angle of meteor becomes large, the reflection point shift far away. Especially, when the incident angle is beyond  $80^\circ$ , the distance of reflection point becomes larger quickly and its distance becomes more than 1000km.

The detection efficiency of meteors depends on the position of transmitters and receivers and incident angle of meteor. The baseline from Transmitter(Sabae) to Receiver(Nagano) is almost *East* and *West* baseline. In this case, the detection efficiency of east-west directional meteor is high and that of north south is low.

## 3. Observation

### 3.1. To detect the shift of reflection point

To know the position of meteor echo is very important for investigating the meteor physics, for example, the near-Earth dust environment et al.(Yrjölä & Jenniskens 1998). The position is possible to determine by Radar and an interferometer(McKinley 1961). On the other hand, an ordinary forward scattering observation using only one antenna cannot determine the positional information of echoes at all.

Using some antennas that have an adequate directivity, we can detect the direction roughly where the radio echo comes from. In this research, we used one paired two-element Loop Antennas that are illustrated in Fig.5. This beam pattern is shown in Fig.6. This directivity is  $\pm 30^\circ$

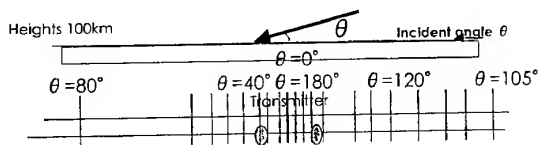


Fig. 3. The relation of the incident angle  $\theta$  and the reflection point.

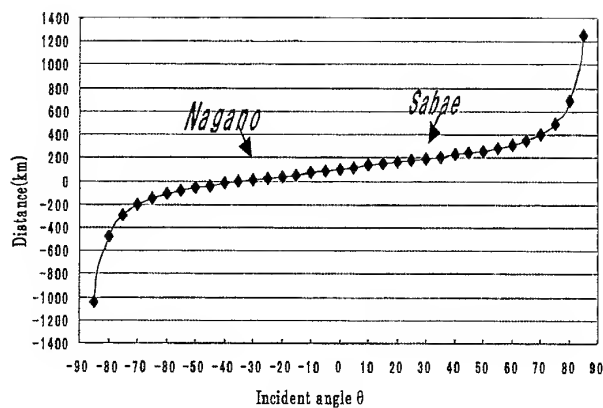


Fig. 4. The incident angle and the distance of the reflection point from Nagano.

degree and has no side lobe. Its front/back (F/B) rate is 14dB in our measurement. Using two Antennas, we have constructed a direction determination system; the direction of one of this paired antenna is toward the transmitter (hereafter, we called this *West antenna*) and the other is an opposite direction to the transmitter (*East antenna*). When the difference of received power of the same meteor echo between *East antenna* and *West antenna* was larger than 3dB, we call them either *East echoes* or *West echoes* in this experiment; that is, corresponding to the area of *E (W)* is that the reflection position of echo exits within an upward 70-degree angle and  $\pm 30$  degree horizontally in the direction of East(West).

### 3.2. Observation System

This system chart is illustrated in Fig.7. Using an SSB receiver(ICOM IC-R75), we convert radio frequency echoes into the audio spectrum. To detect the weak echo and to store the date, a spectrogram software (HROFFT) with PC (Epson Edi cube with Intel Celeron766MHz ,128MB,HD20GB) is used. This HROFFT is developing

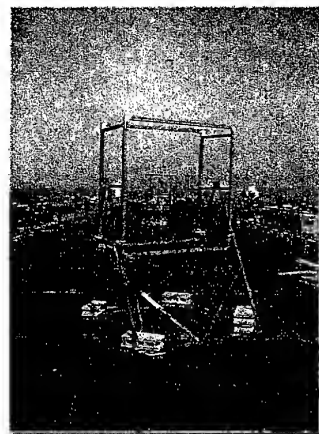


Fig. 5. Hand-made 2-element loop antenna

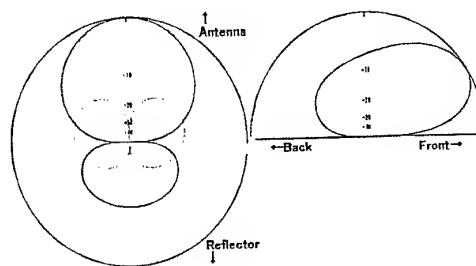


Fig. 6. Antenna beam pattern

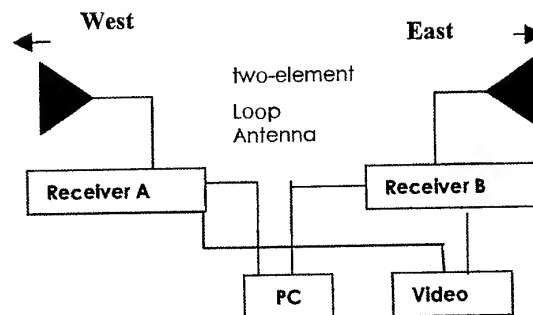


Fig. 7. System Chart

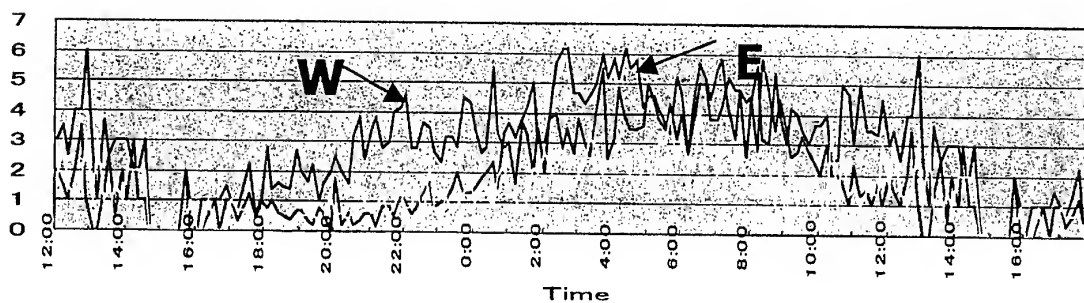


Fig. 8. Mean Sporadic meteor (2000.12.1-6) at 10-minute intervals.

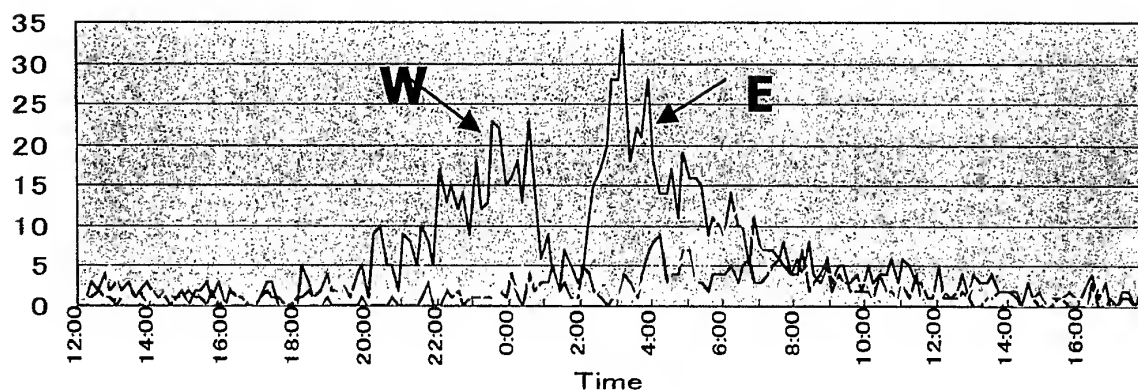


Fig. 9. Geminids (2000.12.12-13) at 10-minute intervals.

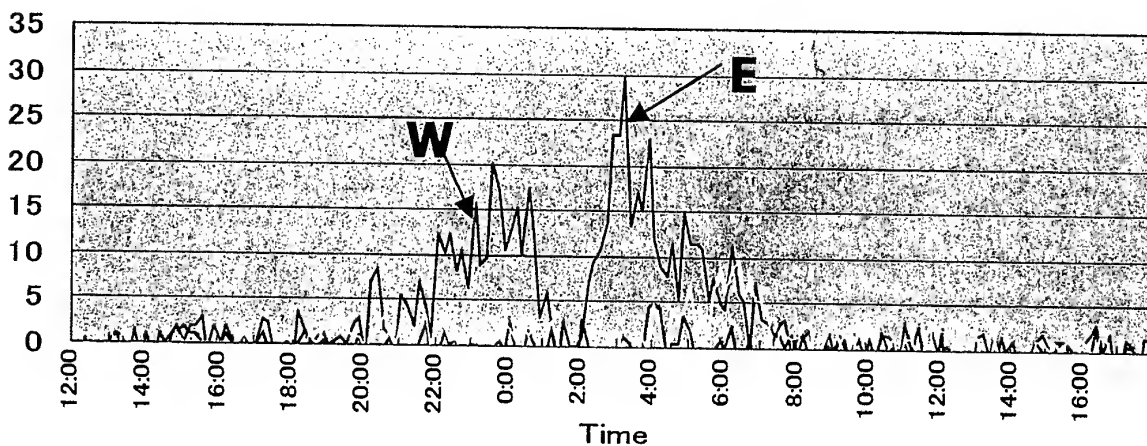


Fig. 10. Geminids minus sporadic meteor at 10-minute intervals.

by Kazuhiko Ookawa at Kasugabe High school of Technology, Saitama, Japan. In this observation, we use the 2ch-HROFFT spectrogram which could be used with the synchronous 2-channel Fourier transformations (signal from the *East antenna* and *West antenna* at the same time). The images of 2ch-HROFFT are shown in Fig.12. Upper panel in this image shows the *East echoes* and lower panel shows the *West echoes*. The received signal power are shown above baseline with S/N bar graph grid at 10,20,30dB in each panels. From this image, we can identify the *East echoes* and *West echoes*.

#### 4. The Detection of Reflection Shift in Geminids

##### 4.1. Daily variation by Sporadic Meteors

Fig.8 shows the mean daily variation of *East* and *West* echoes rates at 10 - minute intervals due to sporadic meteors. This value is the average of 6 days, 1-6 Dec.2000; that is just 2-weeks before the maximum of Geminids. The rate of *East* and *West* echoes will vary from a minimum around 18:00 hours local time to a maximum in the early morning hours. This variation is clearly explained as the effect of the Earth rotation.

Fig.9 shows the daily variation of 12-13 Dec.2000; that is the periods of Geminids. The maximum elevation of the Geminids radiant at Nagano was found to be  $85.4^\circ$  at 01:49 JST. At when the radiant was just around the culmination, the severe decrease in echo rate due to high elevation angle of radiant could be seen. This is the consistent with the formula of reflection point of meteors as shown in Fig.1.

##### 4.2. Subtract the Sporadic meteor

To get the echoes due to Geminids, we subtract the mean daily sporadic meteor echoes from the echoes at the periods of Geminids. Fig.10 shows that the number of detected echoes rates minus the number of the average sporadic meteor echoes rates.

We obtain that from Fig.10;

- 1) There are no Geminids when the radiant of Geminids is under the horizon.
- 2) the severe decrease in echo rate due to high elevation angle of radiant was detected clearly.
- 3) The change of the direction of reflection point of meteor radio signal was detected; from the *West echoes* to *East echoes* before and after the culmination of the radiant.

These results are consistent with the formula of reflection point of meteors.

##### 4.3. Received power variation due to the shift of reflection point

The received power  $P$  from the meteor trail relative to

$$P \propto \frac{1}{R_T R_R (R_T + R_R)}, \quad (1)$$

where,  $R_T$  and  $R_R$  are the distance between the transmitter and the reflection point and the distance between the receiver and the reflection point, respectively (McKinley 1961). The decrement of received power is shown as

$$G(t) = -10 \log \left( \frac{P(t)}{P(t_0)} \right) [\text{dB}], \quad (2)$$

here received power  $P(t)$  is normalized by received power  $P(t_0)$  at the time  $t_0$ . Fig.11 shows the theoretical decrement of received power  $G$  due to the shift of reflection point with time and the observed variation of the averaged received power of meteor echoes.

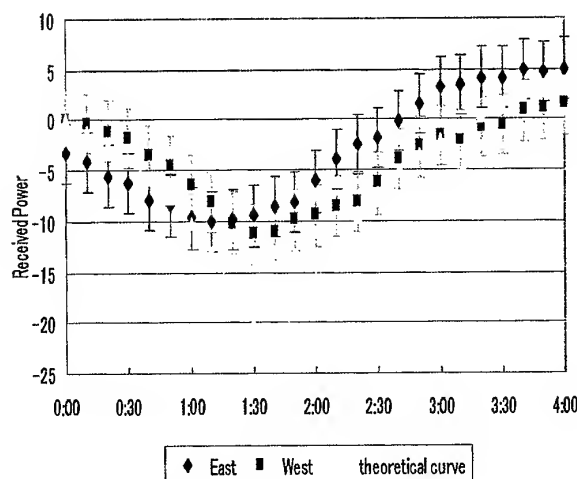


Fig. 11. The variation of received power

From this,

- 1) The observed time variation of received power coincides with the theoretical decrement curve. This is explained due to the effect of the shift of reflection point.
- 2) The difference of the received power between *West antenna* and *East antenna* is 10dB. This is consistent with the fact that F/B ratio of our antenna is 10dB.

#### 5. Concluding Remark

- (1) We detected the shift of the reflection point of meteor by the number counting of *West echoes* and *East echoes*.
- (2) We detect the decrement of received power of echoes which is consistent with theoretically. These are the direct evidence that the meteor echo really come from the meteor trails. We also detected the change of a trend of the Doppler shift of meteor echoes. At the presence, the resolution of frequency in this observation is some Hz, so that, it is insufficient to measure the meteor wind with a few m/s accuracy. However, this result is consistent of the meteor wind data of MU Rader of Radio Science Center for Space & Atmosphere (RASC), Kyoto University.

At the presence, observed baseline is only one; the East-West baseline. To get the sensitivity for North-South,

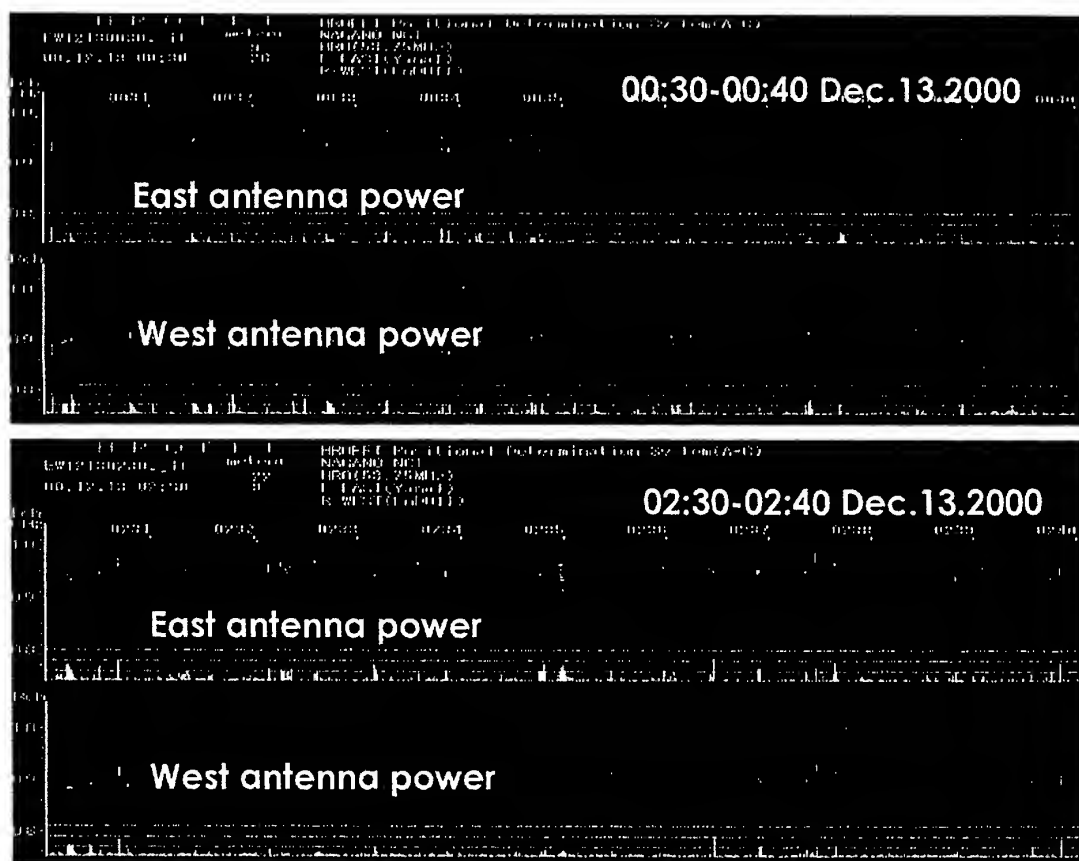


Fig. 12. Shift of reflection point from *West* to *East* before (Upper panel 00:30-00:40 Dec.13.2000 JST) and after ( Lower panel 02:30-02:40 Dec.13.2000 JST) the culmination of the radiant. The time of meridian passage of the radiant of Geminids is 01:49 JST at this day. From the upper panel, we can see that the average power of the echoes by *West antenna* is larger than that by *East antenna*. From the lower panel, we can see that the average power of the echoes by *East antenna* is larger than that by *West antenna*.

we are planning to construct the other three observational sites, Misato Astronomical Observatory at Wakayama, the Institute of Space and Astronautical Science at Sagami-hara, Kanagawa, and Nishi-Harima Astronomical Observatory at Hyogo. The former is Northwest-Southeast baseline. The latter 2 sites are West-East baseline. To combine these sites date, We can monitor the meteor wind by counting the number of meteors.

## References

- Elford, G., Cervera, A., Steel, I., 1994, Mon.Not.R.Astron.Soc, 270, 401
- Hines, C.O., 1955, Can.Journ.Phys, 33, 493
- Hines, C.O., Vogan, 1957, Can.Journ.Phys, 35, 703
- Ceplecha, Z., Borovicka, J., Elford, G., Revelle, D., Hawkes, R., Porubcan, V., Simek, M., 1998, Space Science Reviews, 84, 327
- Maegawa, K., 1999, WGN, the Journal of the IMO, 27, 64
- Maegawa, K., Ueda, M., Minagawa, Y., 1999, WGN, Journal of IMO, 27, 76
- McKinley D.W.R., 1961, "Meteor science and engineering", McGraw-Hill
- Ohnishi et al., in annual meeting of Astronomical Society of Japan 2001 spring, (2001)
- Schilling, D.L., 1993, "Meteor Burst Communications (Theory and Practice)", Wiley Series in Communication
- Suzuki, K., 1976, Sky and Telescope, 51, 359
- Suzuki, K., Nakamura, T., 1995, WGN, Journal of IMO, 23, 236
- Shimoda, C., Suzuki, K., Maeda, K., 1993, WGN, Journal of IMO, 21, 130
- Wislez J.-M., Proceedings of the International Meteor Conference, 1995, edited by Paul Roggemans and Andre Knofel, IMO, 1995, p.83-98.
- Yrjölä, I., and Jenniskens, P., 1998, A&A, 330, 739

# THE EARTH ROTATION AND REVOLUTION EFFECT ON THE DAILY AND ANNUAL VARIATION OF SPORADIC METEOR ECHO

Kouji Ohnishi<sup>(1)</sup>, Shinobu Hattori<sup>(2)</sup>, Osamu Nishimura<sup>(2)</sup>, Toshiyuki Ishikawa<sup>(2)</sup>,  
Yoshie Aoki<sup>(2)</sup>, Yukiko Iijima<sup>(2)</sup>, Aya Kobayashi<sup>(2)</sup>,  
Kimio Maegawa<sup>(3)</sup> and Shinsuke Abe<sup>(3)</sup>

<sup>(1)</sup> Nagano National College of Technology, 716, Tokuma, Nagano 381-8550, Japan,  
ohnishi@ge.nagano-nct.ac.jp:

<sup>(2)</sup> Nagano National College of Technology, 716, Tokuma, Nagano, Nagano 381-8550, Japan:

<sup>(3)</sup> Fukui National College of Technology, Geshi, Sabae, Fukui 916-8507, Japan,  
kmaegawa@fukui-nct.ac.jp:

<sup>(4)</sup> The Institute of Space and Astronautical Science, Sagamihara, Kanagawa, 229-8510, Japan,  
avell@planeta.sci.isas.ac.jp:

**Abstract.** The Earth rotation and revolution will affect the daily and annual variation of sporadic meteor echo. We try to investigate such effect using Ham-band Radio Observation(HRO). Our system is constructed with paired two-element loop antennas (F/B ratio is 10 dB) at Nagano, Japan using the beacon signals at 53.750MHz, 50W from Sabae, Fukui, Japan. The direction of one of this paired antenna was *West* toward Sabae and the other was *East*, so that this system could be roughly detected the direction of the reflected radio echoes. Using this system, (1) The total echo rose from midnight with the peak coming at about 6:00 and decreasing to the noon. This is well known daily variation due to the Earth rotation. (2) The peak echoes time by *Eastward* antenna and by *Westward* antennas was different; *Westward* was at 3:00 and *Eastward* was at 10:00. This daily variation is interpreted as the effect of the Earth rotation and revolution and the specular reflection property of forward meteor scattering observation.

For the starting of our observation, we have checked the system stability. Fig.1 and Fig.2 show the result of this test.

Using this simple and inexpensive equipment, we have confirmed the shift of reflection point of meteor echoes which is the fundamental property in the forward meteor scattering observation (Ohnishi et al. 2001, hereafter cited as Paper I). And furthermore, we can research these subjects:

- to get the spatial distribution and velocity distribution of meteoroid on the near Earth orbit by the observation of the sporadic meteors echoes rate.
- to get the fundamental data of sporadic meteor activity and anisotropy for monitoring the meteor streams and outburst.
- to investigate the correlation of the variation of counted meteor echoes with the change of the degree of ionization in the upper atmosphere (~100km) due to the solar radiation and solar activity.
- to check how the effect of the Earth rotation and revolution would be appeared in the variation of detected meteor echoes.

## 1. Introduction

Radio meteor scatter is an ideal technique for observing meteors continuously (McKinley 1961). Using this method, we can monitor the activity of meteors and meteor stream (Suzuki & Nakamura 1995, Yrjölä & Jenniskens 1998 Maegawa et al. 1999, ).

We have constructed the directional determination system using paired loop antennas, one of these directions is the *Eastward* and the other is *Westward*. These antennas are called as *East antenna* and *West antenna*, respectively. This system can detect the direction roughly where the radio echo comes from. Then we can monitor the meteor streams and outburst with the knowledge of the rough direction of the meteor echoes.

For the first step of our research, we try to get the fundamental data of the sporadic meteor activity and anisotropy. And we have found the difference in the observed diurnal variation of the *East antenna*'s echoes and *West antenna*'s echoes. This difference seems to be concerned with the radio reflection mechanism and the rotation and the revolution of the Earth. We could not find any remarkable variation of the trend of the diurnal variation of *East echoes* and *West echoes* during one year observation. These data is good demonstration of the spatial distribution of meteoroid on the near Earth orbit. And more, these becomes a good database to check the formula of the *response function* ( *observability function* ) for sporadic meteors by the forward meteor scattering observa-

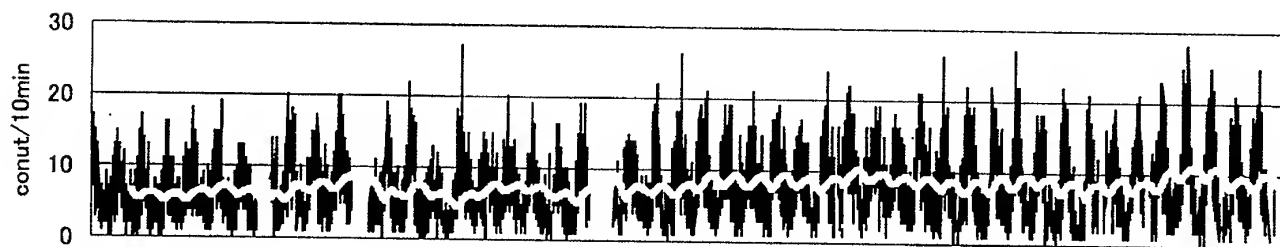


Fig. 1. The daily variation at Sep. to Oct. 2000 in the test observation period. White thick line shows the moving average during 5 days. In spite of an hourly variation of every day, we know that there is no fluctuation of the average values of one-day unit. These data indicate that this system is well stable for the observation the daily and annual variation of meteor echoes.

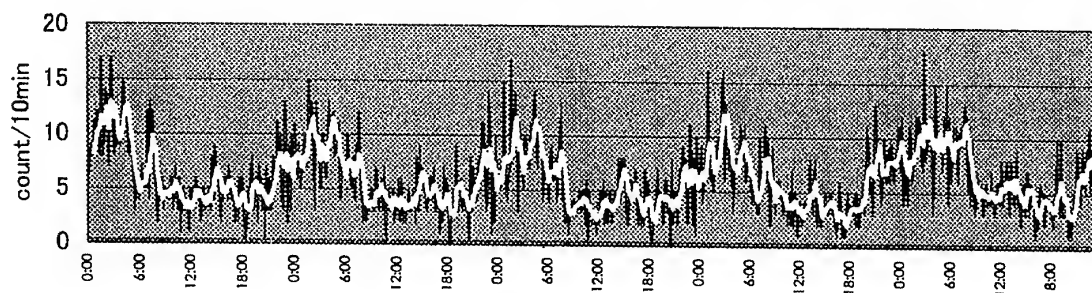


Fig. 2. The diurnal variation of Sep.2 to Sep.6, 2000 in the test observation period. White thick line shows the moving average during one hour. This diurnal variation can be explained by the distribution of meteoroid and the effect of the Earth rotation and revolution.

tion (e.g. Eshleman & Manning 1954, Hines 1955, Hines & Vogan 1957, Elford et al. 1994, Yrjölä & Jenniskens 1998, Ceplecha et al. 1998).

## 2. Observation System

We have constructed the directional determination system by using paired handmade loop antenna. The antenna beam pattern is  $\pm 30^\circ$  and has no side lobe. Its front/back (F/B) rate is 14dB (see Fig.3). The direction of one of them is toward the Transmitter (*West antenna*) and the other is an opposite direction of Transmitter (*East antenna*). The details of this system are described in Paper I.

The detection sensitivity is depend on the location of the transmitter and receiver, and also the incident angle of meteor. For example, the sensitivity is high when the meteor trail is on the same plane with the transmitter and receiver baseline. In our situation, the transmitter (Fukui National College of Technology (136.18E, 35.95N)) is the *Westward* from the receiver (Nagano National College of Technology (138.18E, 36.63N)). Then the east-west directional trail is highly sensitive. On the other hand, the north-south directional trail is less sensitive.

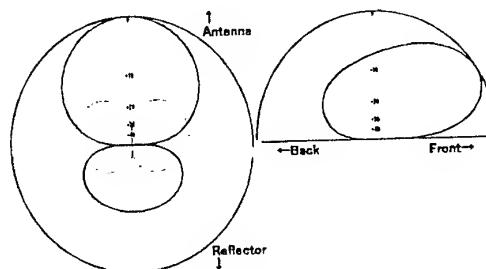


Fig. 3. Antenna beam pattern. This directivity is  $\pm 30$  degree and has no side lobe. Its front/back (F/B) rate is 14dB in our measurement.

In this experiment, we call it *East echo* or *West echo* when the difference of received power of the same meteor echo between by *East antenna* and by *West antenna* is larger than 3dB (see Fig.4); that is, corresponding to the

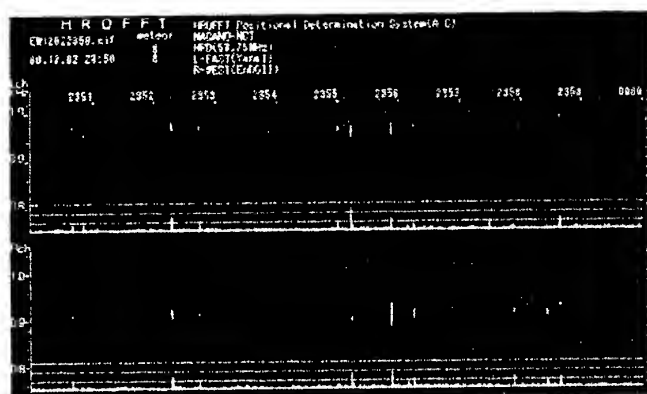


Fig. 4. The image of 2ch-HROFFT spectrogram. Upper channel in this image shows the *East echoes* and lower channel shows the *West echoes*. The received signal power are shown above baseline with S/N bar graph grid at 10,20,30dB in each channels. From this image, we can identify the *East echoes* or *West echoes*.

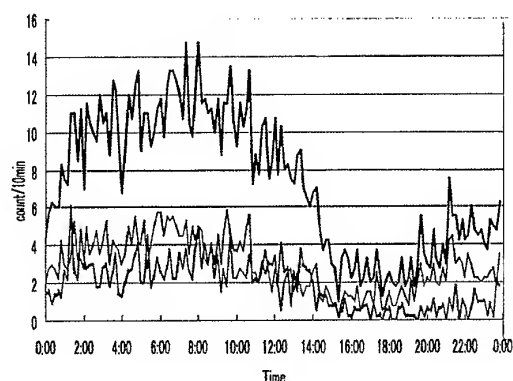


Fig. 5. The daily variation of the total echoes by the *East antenna* and *West antenna* at 10-minute intervals in January 2001. The thick line indicates the total echoes, thin line is *West echoes* and dot line is *East echoes*.

area of E (W) is that the reflection position of echo exits within an upward  $70^\circ$  angle and  $\pm 60^\circ$  horizontally in the direction of East (West). We call *Other echo* when the difference of received power by paired antenna is less than 3dB.

### 3. Diurnal variation of sporadic meteor

Fig.5 show that the daily variation of the 4 days' average of the detected echoes rate by *East antenna* and *West*

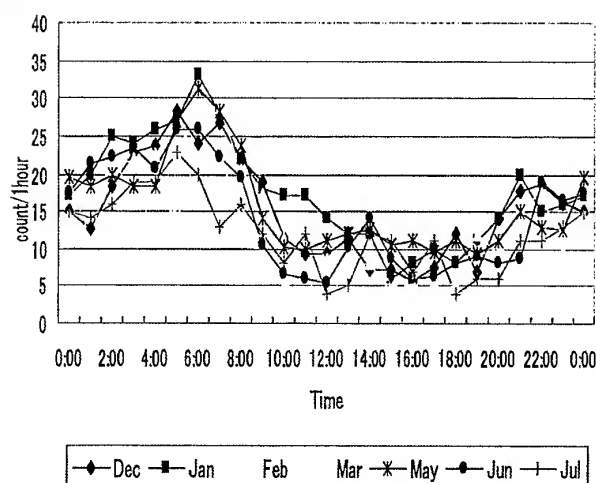
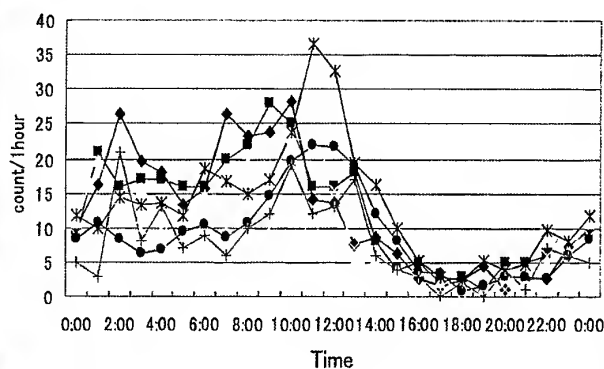


Fig. 6. Monthly average of the daily variation of sporadic meteor. Upper panel is the sporadic meteor by *East antenna* and lower panel is the sporadic meteor by *West antenna*.

*antenna* at 10-minute intervals in January 2001. The echo rate will vary from a minimum around 18:00 hours local time to a maximum in the early morning hours. Total number variation are clearly explained as the effect of the Earth rotation.

The Earth revolves around the sun with the velocity of 30km/s. In the early morning, the zenith is consistent with the direction of the Earth revolution (Apex). Then the Earth collides with many meteoroids. On the other hand, in the evening time, only a few meteoroids, which the velocity is larger than 30km/s and the direction is the same as the Earth exist to collide with the Earth (Anti-apex). Therefore, if no appreciable shower activity is present, the rate of arrival of meteors will vary from a minimum around 18:00 hours local time to a maximum

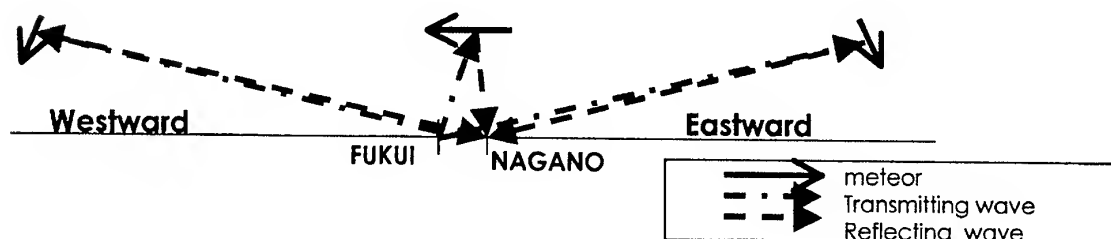


Fig. 7. The relation of the incident angle of the meteors and the reflection point of the echoes. In the case that the incident angle  $\theta$  of the meteors is nearly  $90^\circ$ , the direction of the reflection point will change the *Westward* to *Eastward* at  $\theta = 90^\circ$ .

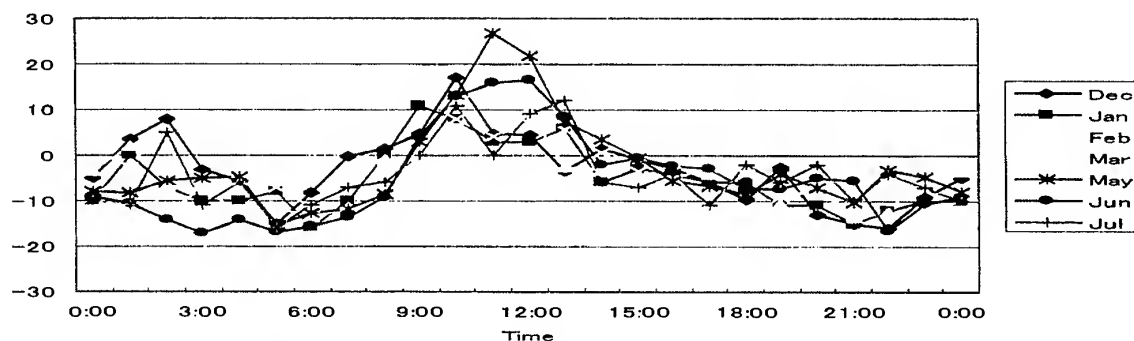


Fig. 8. The number variation of *East echoes* minus *West echoes* at one-hour interval. The *West echoes* number is larger than *East echoes* one around 3:00 and the reverse around 10:00.

in the early morning hours. However, there are some peculiarities in forward scattering radio meteor observation, e.g. specular reflection. For example, we can detect the difference of the rate of *East echoes* and *West echoes*.

#### 4. Sporadic meteor by East antenna and West antenna

Fig.6 shows the monthly average of the daily rate distribution of sporadic meteor (from Dec.2000 to Jul.2001). Each monthly data are represented to the average of several days' data, which do not affect the artificial noise, and/or the disturbance of an ionosphere all the day.

The reflection of radio wave off meteor trails is secular. Therefore the reflection point is very sensitive to the incident angle of the meteor (See Fig.7). Here note that the incident angle is defined as to measure the angle from

Eastward baseline in our notation; i.e.  $\theta \ll 90^\circ$  mean the meteor comes from *Eastward*,  $\theta \gg 90^\circ$  mean the meteor comes from *Westward*.  $\theta = 90^\circ$  is just the singular point; all the echoes goes to the upper sky so that no observer can receive this echoes. If the incident angle  $\theta$  is nearly  $90^\circ$ , the distance of the reflection point is more than 1000km (Sec Fig.4 in Paper I). And if the incident angle of meteor is  $\theta < 90^\circ$ , the reflection point of it is *Westward* sky, and, if  $\theta > 90^\circ$ , the reflection point is *Eastward* sky. Then, we can detect *West echoes* in the case of  $\theta < 90^\circ$ , and *East echoes* in the case of  $\theta > 90^\circ$ .

Fig.8 shows the diurnal variation of *East echoes* minus *West echoes*. *West echoes* is larger than *East echoes* before 6:00. On the contrary, *East echoes* is larger than *West echoes* after 6:00. We can explain this phenomenon that the average reflected region of echoes change in time;

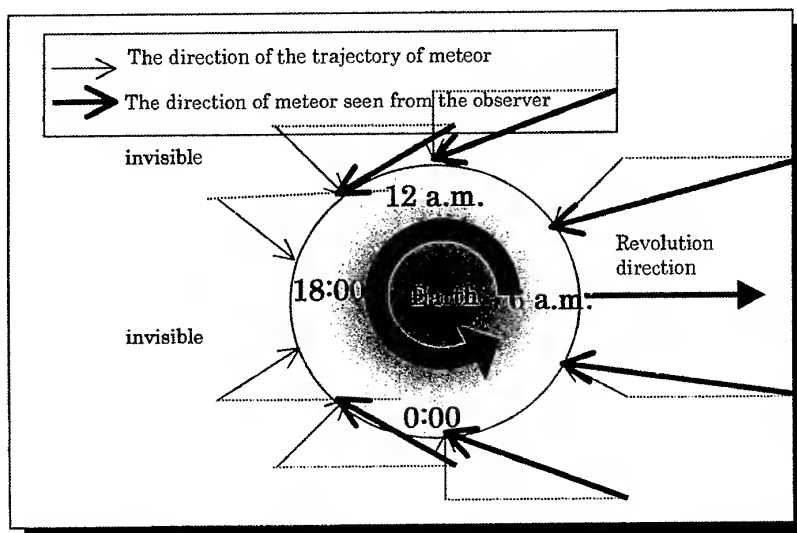


Fig. 9. The intuitive interpretation of the variation of *East-West echoes* tendency in Fig.8. The incident angle of each meteor seen from the Earth would be converged on the direction of the Earth revolution. That is that the average incident angle becomes almost  $90^\circ$ . Before 6:00A.M., the average incident angle of meteors  $\bar{\theta}$  is less than  $90^\circ$ , i.e. an average meteor incident angle shift to the *Eastward*. Then an average reflection point of the echoes is *Westward*. Thus the number of *West echoes* is larger than that of *East* one. After 6:00 a.m.,  $\bar{\theta} > 90^\circ$ , an average meteor incident angle shift to the *Westward*. Then, an average reflection point of the echoes is *Eastward*.

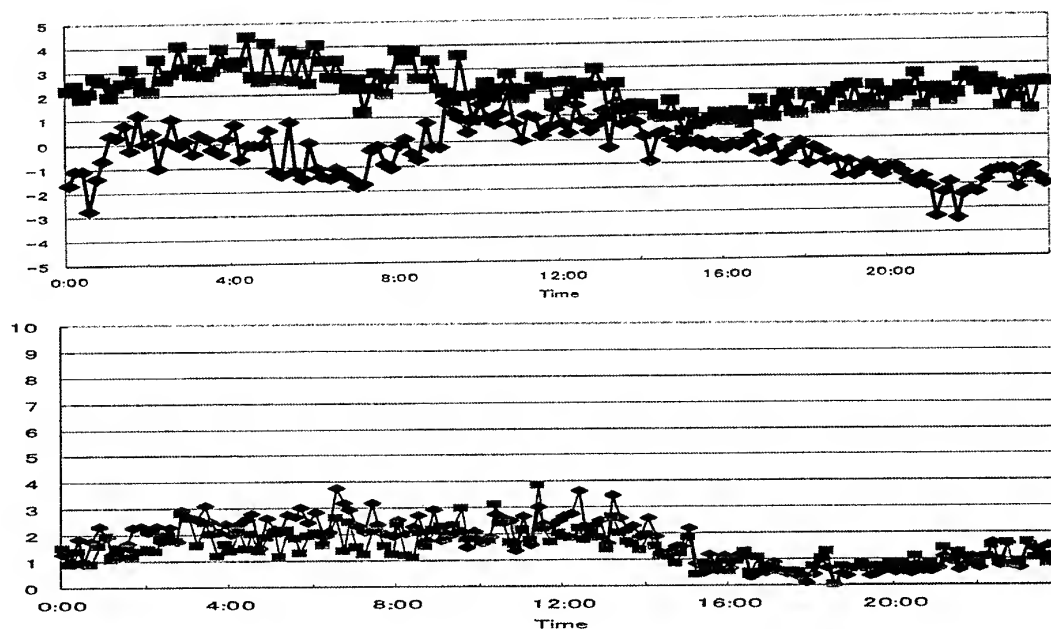


Fig. 10. The average of the standard deviation (thick line) and the average of number (thin line) of *East echoes* minus *West echoes* (upper panel) and also *Other echoes* (lower panel) at 10-minute intervals. The number fluctuation of the *East - West* is maximum at 6:00, the zenith of observer is consistent with the apex. On the other hand, the number fluctuation of *Other echoes* does not change around 6:00.

*Westward* at around 3:00 and *Eastward* at around 10:00. From 10-months observation, we find that the trend of *East-West echoes* rate is no change in time. Therefore, this phenomenon would be caused not by the external factor, e.g., anisotropy of the spatial distribution of meteoroid, but by the intrinsic factor, e.g., "response function" and/or the motion of the Earth.

For an intuitive interpretation this phenomenon, we consider the simple situation; the average angle of incidence of meteoroid trajectory to the Earth is almost vertically and its velocity is nearly 30km/s, the same as the Earth velocity. Here one-dimensional velocity toward the Earth is about 17km/s in this case. In this situation, the incident angle of each meteor seen from the Earth is converged on the direction of the Earth revolution. Then the average incident angle of the sporadic meteor seen from the observer will vary as in Fig.9, the average incident angle shift to the *Eastward* before 6:00, *Westward* after 6:00. Therefore we observed the large number of *West echoes* in the early morning and *East echoes* in the late morning. At the presence, we explain that this phenomenon is caused by

- (1) the convergence of the average of the meteor radiant due to the effect of the Earth revolution (See Fig.9), and
- (2) the specular reflection mechanism in forward scattering radio meteor observation (See Fig.7).

## 5. Fluctuation of the direction of reflection point

We show the other evidence of our interpretation. Fig.10 show the time variation of the standard deviation (thick line) and the average (thin line) of *East minus West* for 12 days within Dec.2000 and Jan.2001 and Mar. 2001. And also show the time variation of the standard deviation (thick line) and the average (thin line) of the *Other echoes*. At 6:00, the zenith of observer is consistent with the apex. Then the incident angle of each meteor seen from the Earth would be converged on the direction to the zenith. That is that the average incident angle becomes almost 90°. At this case, the reflection point of the each meteor with large incident angle will be shaken to *Eastward* or *Westward* according to its incident angle ( $\theta > 90^\circ$  or  $< 90^\circ$ ). Therefore, the fluctuation of the *East* or *West* direction of reflection point will be maximum value at this time. Then the standard deviation is larger than the other time one. On the other hand, the reflection point of the low incident angle meteor is not affected much by this convergence effect due to the Earth revolution. Note that the *Other echo* correspond to such meteor. So the number fluctuation of *Other echoes* does not change around 6:00 a.m.

## 6. Concluding Remark

Using paired loop antennas system, we can monitor the meteor streams and the outburst with the information from the rough direction of meteor. For the first step, we have tried to get the fundamental data of sporadic meteor activity and anisotropy, and have found that

- (1) Detection the *East echoes* and *West echoes* daily variation of sporadic meteor that is caused by the Earth rotation and revolution effect.
- (2) Detection of the Earth rotation and revolution effect in the *East echoes* and *West echoes* annual variation of sporadic meteor. This variation is due to the varying altitude of the ecliptic plane over the year.

We can see this from the monthly average data in Fig.5. On the northern hemisphere, echo rates are expected to the peak in the Autumnal Equinox (about September 21) and to be lowest during the Vernal Equinox (March 21).

At the presence, the observed baseline is only one; *East-West* baseline. To get the sensitivity for *North-South*, we are planning to construct two other observational sites. One is the Misato Astronomical Observatory at Wakayama. The other is the Institute of Space and Astronautical Science at Sagami-hara, Kanagawa, and Nishi-Harima Astronomical Observatory at Hyogo. The former is the Northwest-Southeast baseline. The latter is the West-East baseline. To combine the data from these sites, We can obtain the spatial distribution and velocity distribution of meteoroid on the near Earth orbit by the observation of the number of the sporadic meteors.

## References

- Elford, G., Cervera, A., Steel, I., 1994, Mon.Not.R.Astron.Soc, 270, 401
- Hines, C.O., 1955, Can.Journ.Phys, 33, 493
- Hines, C.O., Vogan, 1957, Can.Journ.Phys, 35, 703
- Cepilecha, Z., Borovicka, J., Elford, G., Revelle, D., Hawkes, R., Porubcan, V., Simek, M., 1998, Space Science Reviews, 84, 327
- Maegawa, K., 1999, WGN, the Journal of the IMO, 27, 64
- Maegawa, K., Ueda, M., Minagawa, Y., 1999, WGN, Journal of IMO, 27, 76
- McKinley D.W.R., 1961, "Meteor science and engineering", McGraw-Hill
- Ohnishi, K., Ishikawa, T., Hattori, S., Nishimura, O., Miyazawa, A., Yanagisawa, M., Endo, M., Kawamura, Maruyama, T., Hosayama, K., Tokunaga, M., Maegawa, K. and Abe, S., in this proceedings, (2001)
- Schilling, D.L., 1993, "Meteor Burst Communications (Theory and Practice)", Wiley Series in Communication
- Suzuki, K., 1976, Sky and Telescope, 51, 359
- Suzuki, K., Nakamura, T., 1995, WGN, Journal of IMO, 23, 236
- Shimoda, C., Suzuki, K., Maeda, K., 1993, WGN, Journal of IMO, 21, 130
- Yrjölä, I., and Jenniskens, P., 1998, A&A, 330, 739

**Observations of Meteors  
Using Large Aperture Radars**

# THE HIGH POWER LARGE APERTURE RADAR METHOD FOR METEOR OBSERVATIONS

Asta Pellinen-Wannberg

Swedish Institute of Space Physics, Box 812, SE-981 28 Kiruna, Sweden, Email: asta.pellinen-wannberg@irf.se

## ABSTRACT

The high power large aperture (HPLA) radar meteor method is presented. It is compared to the classical meteor radar method in terms of working frequency ranges, beam widths and power densities at meteor altitudes to show the basic differences. The classical meteor radars are sensitive to perpendicular meteor trails. The large aperture radars, with higher working frequencies and higher transmitted power, observe the meteoroid-atmosphere interaction at all look-angles. Due to the narrow beams, these radars mainly observe the population of numerous very small sporadic background particles. Almost no shower-related increase in fluxes has been observed in the EISCAT Geminid, Perseid and Leonid observations. Simultaneously with the meteor mode, the HPLA radars can operate in their usual incoherent scatter modes to observe the electron density variations in the background ionosphere. Thus evolution of sporadic E layers, their average ion composition and their relation to meteor activity can be monitored.

Key words: HPLA, large aperture radars, meteor radars, meteors.

## 1. INTRODUCTION

Radars were developed during the second world war to detect approaching aircraft. Occasionally, the radar operators were misled by false targets produced by bright meteors. However, they soon learned to recognize these harmless objects. After the war, many radars were adapted for meteor observing purposes. Using radars operating at frequencies of 100, 600, 1 200, 3 000, and 10 000  $\text{Mc s}^{-1}$ , it was found that meteor echoes were seen with the 100  $\text{Mc s}^{-1}$  equipments only [Stewart et al., 1947]. At lower frequencies, such as 3.5  $\text{Mc s}^{-1}$  [Pierce, 1947], 29  $\text{Mc s}^{-1}$  [Manning et al., 1946] and 64  $\text{Mc s}^{-1}$  [Hey and Stewart, 1947] a lot of meteors were recorded.

Meteor radar systems operate typically in the 15 to 40 MHz frequency range. The lower limit is logical

as it lies just above the usual ionospheric plasma frequencies. Below this value, ionospherically reflected signals may obscure the echo signals from meteors, while above it even a slightly enhanced ionisation can give a total reflection from a meteor trail. The reason for the upper frequency limit is the radio meteor ceiling effect that will be discussed in the next section.

In addition to ionosondes that monitor the ionospheric plasma frequency, and meteor radars at slightly higher frequencies, monitoring meteor trails, the idea of using VHF-UHF systems for studying scattering from the free electrons in the ionosphere were generated. The process is known as Thomson or incoherent scattering. According to incoherent scatter theory, a few instantaneous basic plasma parameters of the ionosphere such as electron density, temperatures and plasma drifts can be estimated. The cross-section for incoherent scatter is very small, thus powerful transmitters, large antennas and sophisticated signal processing facilities are required to exploit this process as a useful ionospheric diagnostic.

Already in the 60's some attempts were made to use HPLA radar facilities for meteor studies. Greenhow and Watkins [1964], using a 25 m radio telescope working at 300  $\text{Mc s}^{-1}$  at the Royal Radar Establishment in Malvern, and Evans [1965; 1966], using the 84 foot Millstone Hill radar working at 440  $\text{Mc s}^{-1}$ , showed that meteors could be observed at these frequencies, even if not so numerous as at lower frequencies. However, the conditions for scattering in these studies were still believed to be the same as for the ordinary meteor radars at lower frequencies - perpendicular to the trails.

In the early 90's, independently of each other, meteor studies were initiated with the EISCAT 930 MHz and the Arecibo 430 MHz incoherent scatter radars [Pellinen-Wannberg and Wannberg, 1994; Zhou et al., 1995]. Later, a lot of work has been done both at EISCAT and Arecibo. One common feature observed in studies performed at these facilities is the aspect angle insensitivity, revealing the fundamentally different scattering conditions. The studies at EISCAT and Arecibo show that conventional radio

methods combined with modern signal analysis capabilities can still contribute to new inventions in classical research fields. They can also contribute to significant applications in the increasingly interesting fields of dust distribution in the solar system and meteoroid impact effects on the ionosphere and atmosphere, as will be outlined in the next sections.

## 2. THE CLASSICAL METEOR RADAR AND HPLA RADAR METHODS

### 2.1. The Scattering Processes

As a meteoric body enters the atmosphere, its collisions with the air molecules result in the production of heat, light and ionisation distributed in the form of a long thin paraboloid with the meteoroid at the head of it. In this process the region of ionised gas formed near the meteoroid expands almost instantaneously to a dimension called "initial radius" which is about 3 cm at 85 km and about 2 m at 115 km [Manning, 1958]. Farther back, the trail continues to expand at a much slower rate due to the normal radial ambipolar diffusion process. The electron line density in the trail can be assumed to be proportional to the mass of the particle. In meteor radar studies, the geometry is an important factor [McKinley, 1961]. To be observed, a meteor trail must be oriented close to normal to the scattering bisector. For backscatter systems where the transmitter and receiver are located at the same site, the meteor trail must be normal to the radar beam. The major part of the received signal is scattered by electrons in the first Fresnel zone. The zone is centered at that point on the trail which is normal to the radar beam. Over this zone the phase of the wave front varies less than  $\pm \pi/2$ , and the partial wave contributions add constructively as in a normal diffraction process.

In classical meteor radar terminology, trails are classified as underdense or overdense depending on the electron density within the ionised column [McKinley, 1961]. An underdense trail is one in which the electron density is sufficiently low that the radar wave penetrates the trail and scattering occurs independently from free electrons within the trail. As the trail expands due to diffusion, the phase difference of the contributions from individual electrons distributed across the trail increases so that the received power decreases exponentially. In an overdense trail, the electron density is sufficiently large, at least on the trail axis, that the wave can be assumed to reflect from the overdense part of the trail as from a metallic cylinder. The ionised cylinder expands as the trail diffuses and the overdense condition suddenly collapses when the electron density on the axis falls below the critical value. Subsequently the underdense model is valid. However, by this time the trail radius is usually quite large compared to the wavelength and thus the signal contribution quite small.

The detection of meteors using conventional radars depends on the amplitude and duration of the echo. Of particular interest is the "finite initial radius effect" on the amplitude of signals scattered from underdense trails. If the exploring wavelength is comparable to, or less than, the initial diameter of the trail, the received signal is severely attenuated. As the initial radius increases with increasing altitude, this effect determines the radio meteor ceiling for a given wavelength. At VHF the radio meteor ceiling for underdense trails is about 105-110 km [McKinley, 1961]. It has been suggested that this is one of the main reasons why VHF radars only detect about 3.5 % of the meteors they should see, if the mass distribution is continuous [Olsson-Steel and Elford, 1987].

For meter wavelengths an underdense meteor trail formed below the radio meteor ceiling can be assumed to remain for a while as a cylindrical column of ionised particles with a diameter less than the exploring wavelength, and a length much longer than the width of the first Fresnel zone from which the main reflection can be assumed to occur. As the exploring wavelength is decreased to the cm range, the expanding trail remains small compared to the wavelength only for a short time [Loewenthal, 1956; Hawkins, 1956; Flood, 1957; von Eshleman, 1960]. Signals can then be assumed to be reflected only from a small portion of the trail, which can be modelled as the head (region of maximum curvature) of a paraboloid immediately behind the evaporating meteoroid. This effect, together with the initial radius effect and the equipment sensitivity limitations, define an upper maximum usable frequency.

Prior to 1958, incoherent scatter was generally taken to mean the Thomson scattering from free electrons in an electron gas. Gordon [1958] outlined the theory and Bowles [1958] performed the first experiments looking for this scattering process in the ionosphere. Bowles' observations showed that the positive ions played a very important role in the process. The correct theory for incoherent scatter was worked out by Fejer [1960], Dougherty and Farley [1960], Salpeter [1960], and Hagfors [1961]. Thus the term incoherent scatter today is understood to refer to scattering from collective density fluctuations, organized by plasma waves created near thermal equilibrium conditions in the ionosphere [Farley, 1979; Evans, 1969]. The dominant wave modes are ion-acoustic waves, corresponding to the collective motion of a cloud of electrons bound to ions, and Langmuir waves, corresponding to local longitudinal electron oscillations. By scattering from these waves, an incoherent scatter radar can monitor some instantaneous basic plasma parameters such as electron density, temperatures and plasma drifts. Other quantities, such as collision frequency, mean ionic mass, electric field vector, and some neutral atmosphere parameters, can also be estimated. As the cross-section for incoherent scatter is very small, powerful transmitters and large antennas are needed. Thus there exist only about 10 such facilities in the world.

Table 1. Technical differences between meteor and HPLA radars.

Feature	Meteor radar	HPLA radar
Frequency	15 - 40 MHz	40 MHz to GHz
Power	W - kW	MW
Antenna type	Yagis	Reflectors or phased arrays
Beam width	3.2° to tens of degrees	< 1°
Echoes	Trail echoes	Head echoes
Scattering orientation	Beam-perpendicular	Isotropic
Velocities	Fresnel diffraction patterns	Time-of-flight or Doppler shifts
Echo origin	Shower/sporadic meteors	Sporadic meteors

The scattering process by which meteor head echoes are observed with HPLA radars is not the same as for the ambient background ionosphere. Nor is it the same process as the scattering from meteor trails observed with meteor radars. The scattering target moves with meteor velocities and the scattering cross-section appears to be isotropic out to large angles from the direction of propagation. The first head echo observation on a meteor radar was reported by Hey et al., [1947]. Jones and Webster [1991] reported observations of more than 700 head echoes over a period of 25 years, but the meteor radar head echo scattering has still not got a comprehensive explanation which would explain all the features associated with the process. The meteor radar head echo and the HPLA radar head echo have similarities, but they are not necessarily the results of the same scattering process. One interpretation of the head echo process, based on dual-frequency observations at EISCAT, is discussed in Wannberg et al., 1996, while another one based on Arecibo observations is discussed by Mathews et al., 1997. For realistic modeling of head echo scattering and meteoroid impact processes it is important to relate the meteoroid sizes and velocities to the altitude ranges in which they are observable as well as to the deceleration and mass loss mechanisms. All physical and chemical processes on the meteoroid surface and within the coma developed due to the interaction process with the ambient atmosphere, including a possible net charge on the meteoroid, must be taken into account.

## 2.2. Technical differences between the two radar types

Table 1 summarises some typical technical differences between meteor and HPLA radar systems. The frequency range for meteor radars extends from slightly above the maximum ionospheric plasma frequency, where meteor trails first become observable, to the value corresponding to the situation where the wavelength is of the same order as the trail radius and the trail becomes invisible for the radar due to destructive interference. The frequency range for incoherent scatter radars is chosen so that the effect

of the ions can be seen in the scatter spectrum. This occurs when the exploring wavelength is much larger than the Debye length in the ionosphere. This parameter is less than 1 cm at 1000 km and about 6 cm at 2000 km altitude [Evans, 1969]. Thus the radars dedicated for this process operate from 40 MHz to 1 GHz. Many military radars and radar telescopes with large apertures work at these frequencies and can be classified as HPLA radars in the sense presented in this paper.

The ionisation caused by meteors exceeds the background ionospheric levels locally along the trail, and diffuses away only after a time in the order of seconds. Thus the process is observable with standard Yagi antennas with quite low power if the geometry is right. On the other hand, the cross-section for the Thomson scatter from ionospheric electrons is very small, thus very large collecting areas for the signals, combined with high transmitter power are needed. Most systems use steerable parabolic dishes (Sondrestrom, Millstone, EISCAT UHF and ESR, ALTAIR) while the huge spherical 300 meter Arecibo disk is semi-fixed and the Jicamarca and MU radars use phased arrays. Even some other forms exist, eg the 40 m x 120 m parabolic trough EISCAT VHF antenna. The antenna geometry together with the radar frequency define the beam width. For classical meteor radars, the opening angle is usually tens of degrees and can approach  $\pi$  steradians, if the intention is to study sporadic meteors. The HPLA radars have very narrow beams, usually under 1°. The extreme case, the Arecibo radar, has a beam width of about 300 m at meteor altitudes.

The velocity of the meteoroids observed with meteor radars are estimated with the Fresnel diffraction method [McKinley, 1961]. At EISCAT, velocities have been estimated both from Doppler shifts derived from the Barker-code ambiguity function distortion [Pellinen-Wannberg and Wannberg, 1994] and time-of-flight estimates [Wannberg et al., 1996]. At Arecibo, both physical principles have been used in slightly different techniques [Mathews et al., 1997; Janches et al., 2000a].

Most of the echoes observed with meteor radars are

beam-perpendicular trail echoes, but head echoes have occasionally been observed with the most powerful radars. At EISCAT UHF about 73 % of the echoes were transient highly Doppler shifted head echoes, while the rest could be classified as longer lasting trail echoes. A possible interpretation for the trail echo mechanism at UHF HPLA radars is described in Pellinen-Wannberg and Wannberg, [1996]. However, these meteor trails are important mainly as monitors of the ambient atmosphere.

Meteor radars can be optimised for shower meteor observations due to the beam perpendicularity requirement. If the radar beam is not too broad and it is oriented perpendicular to the radiant direction of the meteor shower, only meteors in the radiant plane will be observed. Most of them are then probably related to the shower. Observations at EISCAT during Geminids 1990 and 1991 and Perseids 1993 and at both Arecibo and EISCAT during the Leonids 1997 and 1998 do not show any apparent flux increases during the shower maxima [Pellinen-Wannberg and Wannberg, 1994; Pellinen-Wannberg et al., 1998; Janches et al., 2001a]. The reason for this is probably that the radar observation volumes are very small, about 300 m diameter for Arecibo, 1 km diameter for EISCAT UHF and 150-450 m high. The probability of catching a shower meteor is thus very small, while it is much larger for the numerous very small sporadic background population.

Some advantages of classical meteor radars are that they are small, simple and cheap both in construction and in use. They can be deployed in areas of interest quite quickly and they can be run for long periods. HPLA radars are multi-million dollar projects and require years of planning. Thus there are just around 10 such facilities in the world, located at strategic places adapted to their primary application, such as auroral zone research (EISCAT, ESR, Sondrestrom) or along a magnetic meridian (Sondrestrom, Millstone, Arecibo, Jicamarca). These instruments are expensive to operate and can only be run for a limited number of hours annually - for example EISCAT for 2000 hours. There is also strong competition between different user groups - astronomers, space and atmospheric scientists and possibly even the military.

### 3. WHAT DO HPLA RADARS MEASURE?

The scattering process of interest when using HPLA radars for meteor studies is the head echo process. The first definition of head echoes observed with meteor radars can be traced back to McIntosh [1962]. The head echo is described as "an instantaneous echo moving with the velocity of the meteor". This is also one of the characteristic features of the head echoes observed with HPLA radars. There are a few other features that can be measured at different radars due to the varying design solutions of these facilities.

The EISCAT UHF radar is a tristatic radar with the original aim of measuring three-dimensional plasma

drifts in the ionosphere. However, the facility can also be used for tristatic meteor observations by orienting the remote receiver antennas towards the transmitted beam at meteor altitudes [Pellinen-Wannberg et al., 1999]. When a meteor passes the common volume of about  $10 \text{ km}^3$ , all three receivers observe head echoes Doppler-shifted by different amounts proportional to the radial velocity components in the three observing directions defined by the scattering bisectors. As the common volume is quite small, tristatic meteors are rare. However, a set of 10 tristatic meteors were observed in November 1997 and 1998. In a preliminary analysis, the angles between the meteor velocity and the scattering  $\mathbf{k}$ -vectors for the three receivers were obtained [Wannberg et al., 1999]. Echoes were observed up to an angle of  $110^\circ$  from the meteor velocity vector. The signal temperatures of these echoes received at the three sites vary between 3000 and 8000 K, showing a quite uniform distribution not dependent on scattering angles. This indicates that the scattering process is quite isotropic out to  $110^\circ$ .

The above tristatic EISCAT data can also be used for vector velocity determinations. Thus the true velocities and orbital parameters of the meteoroids can be determined. The velocities for the 10 cases above varied between  $38.65 \text{ km s}^{-1}$  and  $85.7 \text{ km s}^{-1}$  while the mean value was  $64.71 \text{ km s}^{-1}$ . When considering this value, one should note that the meteoroid size range observable for EISCAT is  $100\text{--}1000 \mu\text{m}$ . This study also showed that none of the tristatic meteors was a Leonid, even though the measurements were concentrated around the expected Leonid maximum 1997 and 1998. The tristatic vector velocity study will be soon published by Janches et al. [2001b] and an analysis on the origin of these meteoroids will be done later.

Another way to study the possible appearance of shower meteors is to consider the diurnal rates. The background diurnal rate has a maximum in the local morning hours, as the observer meets all the dust in the direction of the Earth's motion (apex) while there is a minimum in the local evening hours (antapex). Both Arecibo and EISCAT observations from November 1997 and 1998 around the Leonids maximum fit only to the background curve [Mathews et al., 2001; Janches et al., 2001b]. Thus one can conclude that HPLA radars only observe the numerous population of the very small sporadic background particles. There does not seem to be any significant increase of the same-size shower particles, while the larger ones are probably too rare to hit the radar beam.

HPLA radars can conduct very high resolution measurements. Thus many instantaneous independent velocity estimates can be done on the same meteor and possible deceleration can be observed [Janches et al., 2000b]. By making some assumptions the meteoroid mass can be estimated from the deceleration, and finally a global mass flux estimate can be done from these results [Mathews et al., 2001]. At EISCAT a method for estimating the meteoroid masses

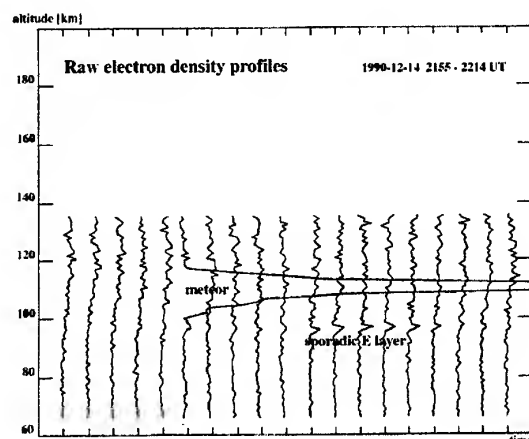


Figure 1. Raw electron density profiles measured with the EISCAT UHF radar. Each profile comprises 1 minute of integrated data. The strong meteor trail echo was registered at about 110 km altitude in three consecutive 2-second raw data dumps between 2200:24 and 2200:28 UT. Simultaneously a sporadic E layer grows up at about 96 km altitude. This layer has about 1 km half width. It grows for about 10 minutes as shown in the data, disappears for a while and appears again with a total lifetime of about 50 minutes.

from the echo signal temperature has been proposed [Westman et al., 1997]. However, no further flux estimates have been done yet based on this method. One crucial thing concerning mass flux estimates with the HPLA radars is the power density distribution of the beam, which is roughly gaussian. For meteoroids passing through the edges of the beam, the scattered signal is much weaker than for same-size meteoroids passing through the middle of the beam. This leads to a discrepancy in the flux and size estimates, which can in principle be corrected by convolving with the beam distribution form. For radars with interferometric capacity the meteor position in the beam can be defined.

Incoherent scatter radars are designed to monitor height profiles of different ionospheric parameters. The measurements extend from 70–80 km altitude up to several hundred kilometers. One of the parameters is the electron density. Thus common ionisation effects of meteor input can be studied, for example whether the ionisation level is increasing due to meteor showers as some models assume. This is a difficult topic to study at high latitudes where the auroral precipitation is continuously present, but possible at mid- and low latitudes [Zhou et al., 1999].

Figure 1 shows 1 minute integrated electron density profiles as a function of time. The data were taken on December 14, 1990, between 2155 and 2214 UT with the EISCAT UHF radar over Tromsø. At 2200:24 UT there is a meteor event at about 110 km al-

titude causing a very strong echo. Just after this event a sporadic E layer grows up at 97 km altitude and lasts for about 10 minutes. These data show how strong meteor echoes can be compared to background ionospheric echoes. The present meteor trail echo was seen for 6 seconds. This contribution is integrated together with the background contribution in one minute. Moreover, the target extension is very small compared to the observational volume. After both time- and volume averaging the echo is still so strong that it goes off the scale. This can be compared with the quite strong sporadic E layer in the data. Rough ion content estimates of sporadic E layers can be done with the incoherent scatter method [Huuskonen et al., 1988]. It is also of common space environmental interest to understand the meteoric matter input and dynamics at these altitudes.

#### 4. PROBLEMS WHICH CAN BE ADDRESSED WITH THE METHOD

The use of the HPLA radar method for meteor studies is new and still under development. Systematic studies have been done only at EISCAT and Arecibo, while the other facilities have taken up the topic just recently [Close et al., 2000; Zhou et al., 2001]. However, there are many problems to be addressed still at EISCAT and Arecibo. The HPLA radars are distributed all over the world due to their task of exploring the globally-varying ionospheric and magnetospheric conditions. This is good even for the meteor and solar system dust studies. Besides, there are individual design solutions at the different facilities, which allow them to measure different and complementary parameters.

A common feature for all incoherent scatter facilities is that they can simultaneously observe both meteors and the background ionosphere. Thus effects of increased meteor input into electron density, ion composition and sporadic E layers can be studied.

With measurements with simultaneous high temporal and spatial resolution of microseconds and a few hundred meters, features of the head echo process can be studied in detail. Tens of independent consecutive observations can be done on the same meteor. This allows us to study in detail quantities such as the variation of the signal temperature, which is proportional to the object size as well as has a relation to the atmospheric density and the velocity and deceleration. Both quantities are also dependent on the mass loss mechanisms. Many of the facilities operate on more than one frequency, which allows us to study the frequency dependence of the radio wave scattering process as well as the processes described above. The EISCAT UHF radar is tristatic, enabling us to look at the meteor process at different angles - even from the rear if the meteor comes from south-east low elevation angle. Further studies with systematic measurements with this method should establish the aspect angle scattering dependence, which is

## Fields of view

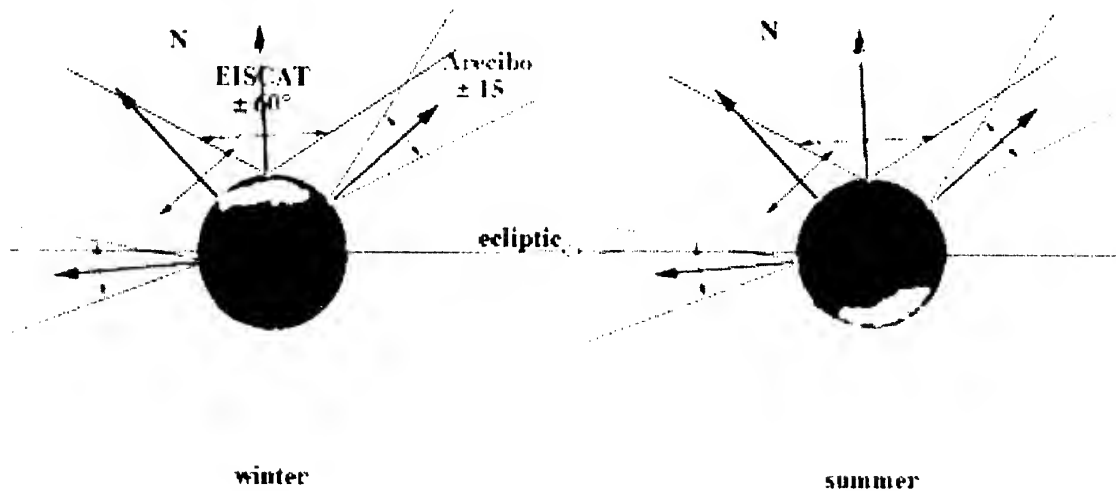


Figure 2. The fields-of-view for EISCAT and Arecibo radars in daytime towards the sun in the middle (not to scale) and during night away from the sun for northern hemisphere winter and summer.

crucially important for the interpretation of the head echo scattering process.

Different HPLA radar facilities can be used for systematic monitoring of the global interplanetary dust distribution at 1 AU. Most of the space missions with dust detectors onboard so far have been interplanetary, eg Ulysses, Galileo and Cassini. Figure 2 shows the fields-of-views for EISCAT and Arecibo for northern hemisphere summer and winter. At Arecibo, orbits for meteoroids impacting at up to  $\pm 15^\circ$  from the local vertical can be determined [Janches et al., 2001b]. With the EISCAT tristatic system, orbits up to  $\pm 60^\circ$  from the local vertical can be defined. The upper limit here is probably set by the longer path through the atmosphere rather than due to the angle at which the meteoroid can technically be observed. Arecibo looks at the ecliptical plane during the night time in winter and during the day time in summer. EISCAT has a very wide diurnal coverage of the northern hemisphere at any time. These geometrical circumstances create a lot of interesting opportunities for making systematic studies of the seasonal variations of the global solar system dust distributions at 1AU.

## ACKNOWLEDGMENTS

I wish to thank G. Wannberg for valuable comments and A. Westman and D. Janches for their contribu-

tion to results reviewed in this paper. I gratefully acknowledge the assistance of the EISCAT staff during the meteor experiments. The EISCAT Scientific Association is supported by the CNRS of France, the MPG of Germany, the PPARC of the United Kingdom, the NFR of Norway, the VR of Sweden, the SA of Finland, and the NIPR of Japan. This work is supported by the European Office of Aerospace Research and Development, Air Force Office of Scientific Research, Air Force Research Laboratory, under Contract No. F61775-01-WE084.

## REFERENCES

- Bowles, K. L., Observations of vertical incidence scatter from the ionosphere at 41 Mc/sec, *Phys. Rev. Lett.*, 1, 454, 1958.
- Close, S., S. M. Hunt, M. J. Minardi, and F. M. McKeen, Analysis of Perseid meteor head echo data collected using the Advanced Research Projects Agency Long-Range Tracking and Instrumentation Radar (ALTAIR), *Radio Sci.*, 25, 1233-1240, 2000.
- Dougherty, J. P., and D. T. Farley, A theory of incoherent scattering of radio waves by a plasma, *Proc. Roy. Soc. A*, 259, 79, 1960.
- Eshleman, V. R., Meteor Scatter, in *The radio noise spectrum*, edited by D. H. Menzel, Harvard University Press, Cambridge, Mass., 1960.

- Evans, J. V., Radio-echo studies of meteors at 68-centimeter wavelength, *J. Geophys. Res.*, 70, 5395, 1965.
- Evans, J. V., Radar observations of meteor deceleration, *J. Geophys. Res.*, 71, 171, 1966.
- Evans, J. V., Theory and practice of ionosphere study by Thomson scatter radar, *Proc. IEEE*, 57, 496, 1969.
- Farley, D. T., The ionospheric plasma, in *Solar system plasma physics*, vol. III, edited by L. J. Lanzerotti, C. F. Kennel, and E. N. Parker, North Holland, New York, 1979.
- Fejer, J., Scattering of radiowaves by an ionized gas in thermal equilibrium, *J. Geophys. Res.*, 65, 2635, 1960.
- Flood, W. A., Meteor echoes at ultra-high frequencies, *J. Geophys. Res.*, 62, 79, 1957.
- Gordon, W. E., Incoherent scattering of radio waves by free electrons with applications to space exploration by radar, *Proc. IRE*, 46, 1824-1829, 1958.
- Greenhow, J. S., and C. D. Watkins, The characteristics of meteor trails observed at a frequency of 300 Mc/s, *J. Atmos. Terr. Phys.*, 26, 539, 1964.
- Hagfors, T., Density fluctuations in a plasma in a magnetic field with applications to the ionosphere, *J. Geophys. Res.*, 66, 1699, 1961.
- Hawkins, G. S., Radar echoes from meteor trails under conditions of severe diffusion, *Proc. IRE*, 44, 1192, 1956.
- Hey, J. S., and G. S. Stewart, Radar observations of meteors, *Proc. Phys. Soc.*, 59, 858-883, 1947.
- Hey, J. S., S. J. Parsons, and G. S. Stewart, Radar Observations of the Giacobinid Meteor Shower, *Mon. Not. R. Astron. Soc.*, 107, 176, 1947.
- Huuskonen, A., T. Nygren, L. Jalonen, N. Brorna, T. L. Hansen, A. Brekke, and T. Turunen, Ion composition in sporadic E layers measured by the EISCAT UHF radar, *J. Geophys. Res.*, 93, 14603, 1988.
- Janches, D., J. D. Mathews, D. D. Meisel, V. Getman, and Q. Zhou, Doppler Studies of Near-Antapex UHF Radar Micrometeors, *Icarus*, 143, 2, 347-353, 2000a.
- Janches, D., J. D. Mathews, D. D. Meisel, and Q. Zhou, Micrometeor Observations using the Arecibo 430 MHz Radar: I. Determination of the Ballistic Parameters from Measured Doppler Velocity and Deceleration Results, *Icarus*, 145, 2, 2000b.
- Janches, D., J. D. Mathews, D. D. Meisel, and Q. Zhou, Orbital Properties of the Arecibo Micrometeors at Earth Intersection, *Icarus*, 150, 206-218, 2001a.
- Janches, D., A. Pellinen-Wannberg, D. D. Meisel, I. Haggstrom, G. Wannberg and A. Westman, Tristatic observation of meteors using the 930 MHz EISCAT radar system, in manuscript, 2001b.
- Jones, J., and A. R. Webster, Visual and radar studies of meteor head echoes, *Planet. Space Sci.*, 39, 873, 1991.
- Loewenthal, M., On meteor echoes from under dense trails at very high frequencies, Tech. Rept., 132, (DDC 137608), Lincoln Laboratory, Massachusetts Institute of Technology, Lexington, Massachusetts, 1956.
- Manning, L. A., The initial radius of meteoric ionization trails, *J. Geophys. Res.*, 63, 181-196, 1958.
- Manning, L. A., R. A. Helliwell, O. G. Villard, and W. E. Evans, On the detection of meteors by radio, *Phys. Rev.*, 70, 767-768, 1946.
- Mathews, J. D., K. P. Hunter, D. D. Meisel, V. S. Getman, and Q. Zhou, Very High Resolution Studies of Micrometeors using the Arecibo 430 MHz Radar, *Icarus*, 126, 157, 1997.
- Mathews, J. D., D. Janches, D. D. Meisel, and Q. H. Zhou, The Micrometeoroid Mass Flux into the Upper Atmosphere: Arecibo Results and a Comparison with Prior Estimates, *Geophys. Res. Lett.*, 28, 1929, 2001.
- McIntosh, B. A., The Meteoric Head Echo, *J. Atmos. Terr. Phys.*, 24, 311, 1962.
- McKinley D. W. R., *Meteor science and engineering*, McGraw-Hill, 1961.
- Meisel, D. D., D. Janches, and J. D. Mathews, Extrasolar MICROMETEORS Radiating from the Vicinity of the Local Interstellar Bubble, *ApJ*, In Press, 2001.
- Olsson-Steel, D., and W. G. Elford, The height distribution of radio meteors: observations at 2 MHz, *J. Atmos. Terr. Phys.*, 49, 243-258, 1987.
- Pellinen-Wannberg, A., and G. Wannberg, Meteor observations with the European incoherent scatter UHF radar, *J. Geophys. Res.*, 99, 11379-11390, 1994.
- Pellinen-Wannberg, A., and G. Wannberg, Enhanced ion-acoustic echoes from meteor trails, *J. Atmos. Terr. Phys.*, 58, 1-4, 495-506, 1996.
- Pellinen-Wannberg, A., A. Westman, G. Wannberg, and K. Kaila, Meteor fluxes and visual magnitudes from EISCAT radar event rates: a comparison with cross-section based magnitude estimates and optical data, *Ann. Geophysicae*, 16, 1475-1485, 1998.
- Pellinen-Wannberg, A., A. Westman, and G. Wannberg, A three-dimensional meteor head echo Doppler shift method for the EISCAT UHF radar, Meteoroids 1998 proceedings, Astron. Inst., Slovak Acad. Sci., 83-86, 1999.
- Pierce, J. A., Ionization by meteoric bombardment, *Phys. Rev.*, 71, 88-92, 1947.
- Salpeter, E. E., Scattering of radiowaves by electrons above the ionosphere, *J. Geophys. Res.*, 65, 1851, 1960.
- Stewart, J. Q., M. Ference, J. J. Slattery, and H. A. Zahl, Radar observations of the Draconids, *Sky & Telescope*, 6, 3-5, 1947.
- Wannberg, G., A. Pellinen-Wannberg, and A. Westman, Meteoric head echo observations with the EISCAT radar, *Radio Sci.*, 31, 497-518, 1996.

- Wannberg, G., A. Westman, and A. Pellinen-Wannberg, Three-dimension head echo cross-sections at 931 MHz measured by EISCAT, National Radio Science Meeting, Boulder, Colorado, U.S.A., January, 1999.
- Westman, A., A. Pellinen-Wannberg, and G. Wannberg, Meteor head echo height effect observed by the European Incoherent Scatter UHF and VHF radars, in Assar Westman's Ph.D. thesis, IRF Scientific Report 246, 1997.
- Zhou, Q., C. A. Tepley, and M. P. Sulzer, Meteor observations by the Arecibo 430 MHz incoherent scatter radar, I. Results from time-integrated observations, *J. Atmos. Terr. Phys.*, 57, 421-431, 1995.
- Zhou, Q. H., J. D. Mathews, and Q. N. Zhou, Incoherent scatter radar study of impact of meteoric influx on the nocturnal E-region ionization, *Geophys. Res. Lett.*, 1833-1836, 1999.
- Zhou, Q. H., J. D. Mathews, and T. Nakamura, Implications of meteor observations by the MU radar, *Geophys. Res. Lett.*, 28, 7, 2001.

## TWO-FREQUENCY METEOR OBSERVATIONS USING THE ADVANCED RESEARCH PROJECT AGENCY LONG RANGE TRACKING AND INSTRUMENTATION RADAR (ALTAIR)

S. Hunt<sup>(1)</sup>, S. Close<sup>(1)</sup>, M. Oppenheim<sup>(2)</sup>, L. Dyrud<sup>(2)</sup>

<sup>(1)</sup> MIT Lincoln Laboratory, 244 Wood St., Lexington, Massachusetts USA Email: [hunt@ll.mit.edu](mailto:hunt@ll.mit.edu)

<sup>(2)</sup> Boston University, Boston Massachusetts USA

### ABSTRACT

We present a sample of radar meteors observed during the November 1998 Leonid shower using the Advanced Research Project Agency (ARPA) Long Range Tracking and Instrumentation Radar (ALTAIR). Approximately 29 minutes of VHF data which produced over 900 VHF head echoes and 17 minutes of simultaneous UHF data were collected, which resulted in over 500 head echo detections.

These data were analyzed to determine frequency-dependent radar cross section (RCS) characteristics [Close]. The techniques outlined here for determining meteor velocity from ALTAIR data produced a meteor distribution with a peak number of meteors at 56 km/s, consistent with viewing the Northern Apex meteor source. The angle between the radar line of sight and geomagnetic field shows a strong correlation with the radar's ability to detect nonspecular meteor trails. In addition, the range, azimuth and elevation angle data were used to compute the 3-d velocity of the head echoes. The first head echo that was detected using three frequencies (160, 422, and 1320 MHz) is also discussed.

### 1. INTRODUCTION

The ionization that forms in the Earth's atmosphere when meteors ablate material is especially sensitive to detection at lower radio frequencies. The meteor ionization production rate is related to meteoroid velocity and mass in a manner that causes radar to preferentially detect faster-moving meteors due to the increased amount of ionization. The ionization that is immediately detected near the meteoroid during its rapid descent through the E-region atmosphere (approximately 80- to 140-km altitude) results in a volume of intense electron number density that results in a radar return or head echo. The ionization trail is left behind which is essentially at rest (m/s) when compared to head echo velocities (km/s). Based on ALTAIR measurements collected during Perseid 1998 and Leonid 1998-1999, the majority of UHF and VHF head echoes occur at an average altitude of approximately 103 km (Fig. 1).

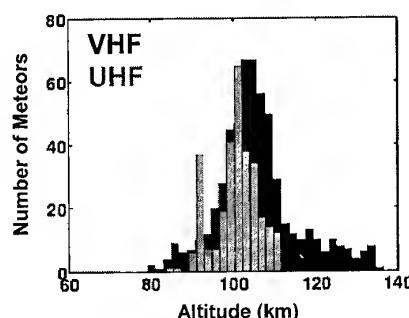


Fig. 1. Number of UHF and VHF meteors as a function of detection altitude collected during the Leonid 1998 campaign.

The ALTAIR system, a missile test radar at Kwajalein Missile Range (KMR) since the 1960s, is tailored to observe the conditions caused by a high-velocity projectile traveling through the upper atmosphere. The ALTAIR head echo data, at UHF and VHF, are similar to those obtained by other high-power radars such as the Aricebo [Mathews, Zhou, Janches], EISCAT [Pellinen-Wannberg], and MU radar systems [Watanabe].

ALTAIR is a high-power (6.0 MW peak at both frequencies), narrow-beam (2.8° at VHF/1.2° at UHF), 46 m diameter, mechanically steered parabolic dish radar. ALTAIR transmits right circular polarized energy and receives both left and right circular polarizations, as well as azimuth and elevation difference channel data. A 5-horn focal point VHF feed and single horn multimode Cassegrain UHF feed is used in conjunction with a frequency selective subreflector (5.5 m diameter) to collect monopulse angle measurement data at either frequency. Receiver electronics are located at the base of each feed to separately measure the voltage response from the left- and right-circularly polarized signal returns. The voltage response from the receive channels are added together to form the sum left circular (SLC) and sum right circular (SRC) measurements. These receive channels form a response pattern offset from the focus of the dish. Their signal energies are subtracted

from one another to produce the left-circular azimuth (ALC) and elevation (ELC) angle difference measurements. This process, known as amplitude comparison monopulse, is a form of phase interferometry that measures the angle of arrival of the radar return to a small fraction of the beamwidth. These data allow the accurate determination of a target's position, velocity, and deceleration.

When the two-way signal travel time is combined with the monopulse angle data it determines the three-dimensional topocentric position of the meteor as a function of time with a spatial detection separation that depends on the radar pulse repetition interval. These position measurements are then differenced to create the velocity as a function of time for each head echo. The receivers also measure the phase of the return signals and have been used for many years for phase-derived range for applications such as missile reentry vehicle and artificial satellite tracking. In the future, these signal processing techniques will be applied to ALTAIR data for determining precise meteor decelerations. ALTAIR's system sensitivity allow the reliable detection of a  $-80$  dBsm target in VHF and a  $-74$  dBsm target at UHF at a range of 100 km.

Highly calibrated observables are simultaneously collected at two frequencies that include (1) radar time delay (radar slant-range), (2) azimuth angle, (3) elevation angle, (4) polarization ratio, (5) radar cross section, and (6) phase shift. Mechanical and electrical system bias models are applied to remove systematic errors from radar measurements. A mean tropospheric model and real-time ionospheric model are also employed to remove atmospheric time delay and phase advance signal propagation effects [Hunt].

## 2. DATA REDUCTION

ALTAIR waveform and data recording techniques that have been employed for decades were applied to meteor data collection. While no radar modifications were made at ALTAIR, the signal processing techniques applied to reduce the ALTAIR data were specifically developed to determine the physical parameters of meteors. Each analog receive pulse for both UHF and VHF is digitally sampled at slightly greater than the Nyquist rate and then immediately recorded on a redundant array of independent disks. Starting with these digital amplitude and phase data, the meteor RCS, position, and velocity are determined using the steps outlined below.

The first step in the data reduction sequence is to apply a 10-dB signal-to-noise ratio (SNR) threshold to the SLC and SRC signal power to eliminate the majority of the noise data samples. Next, the remaining SRC, AZ,

and EL digital samples are interpolated to the range of the interpolated SLC peak to provide a consistent measurement for all four channels for each pulse (Fig. 2).

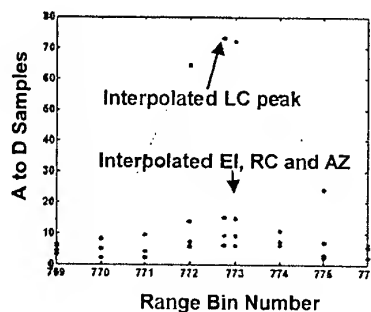


Fig. 2. Interpolation of the LC digital receiver samples to the peak of the SLC signal.

Once the interpolation is performed, only the interpolated amplitude and phase (at the SLC peak) are saved for further head echo processing. With pulse compression, the  $40\text{-}\mu\text{s}$  VHF pulse provides a 30-m range resolution and the  $150\text{-}\mu\text{s}$  UHF pulse provides a 7.5-m range resolution. We used a 333 Hz pulse-repetition frequency.

A variation of the Hough Transform is then applied to associate each series of interpolated SLC pulse detections that form straight lines in a range-time map (Fig. 3) as head echoes.

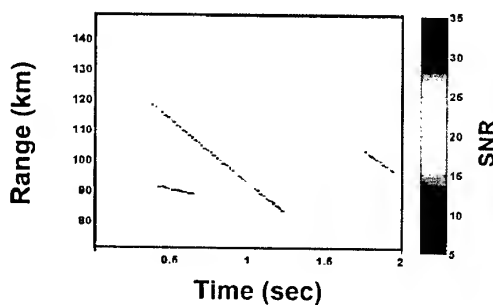


Fig. 3. Range-time map of meteor head echoes after the noise floor has been removed.

A threshold on the length of a pulse detection sequence was used to discard detections not associated with meteors. (This threshold is a function of radar pulse-repetition-frequency). These head echoes are then used to compute the range rate (Fig. 4) of each head echo and

the number distributions of the entire UHF and VHF data sets processed up to this point (Fig. 5).

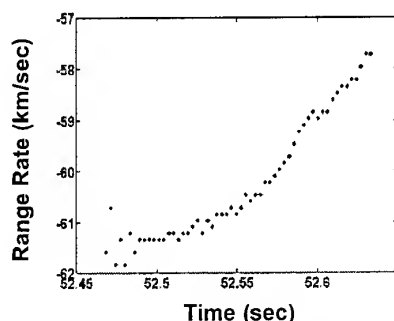


Fig. 4. Meteor range rate as a function of time.

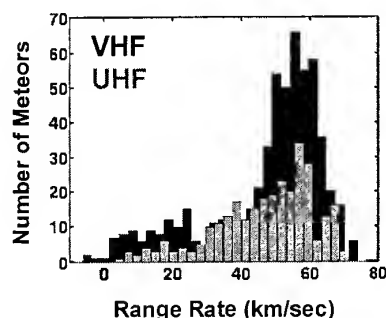


Fig. 5. Number of meteors detected at UHF and VHF as a function of range rate.

The data from the ALC and ELC angle difference channels were then used to determine the angular offset of each head-echo detection from radar line of sight. Meteors detected outside of the main radar beam were eliminated. By applying the angle measurements to the radar range data, the 3-d position of the head echo is determined and the time rate of change of position is computed to obtain the atmospheric velocity and deceleration for each meteor. Atmospheric (or 3-d) velocity refers to the speed of the meteoroid along its flight path while in the atmosphere, versus its speed just prior to atmospheric entry or at the time of capture by Earth's gravity.

Radar system calibration parameters such as time delay, RCS, monopulse angle, mechanical and electrical biases are applied during this stage of the reduction sequence. ALTAIR's UHF and VHF RCS are regularly calibrated using a 56-cm balloonborne sphere; the ALTAIR RCS measurement uncertainty is 1.0 dB.

### 3. METEOR ORIENTATION

During each data collection period of the Leonid 1998 meteor campaign the orientation of the ALTAIR beam remained fixed in space. An investigation of the radar boresight angle with the geomagnetic field line (Fig. 6) shows a strong correlation with detection of nonspecular meteor trails.

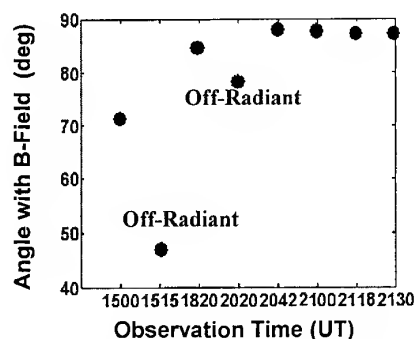


Fig. 6. Head echo angle with geomagnetic field versus observation time.

The detection of these trails is due to the formation of field-aligned irregularities (FAI) that form along the magnetic field line perpendicular to the radar line of sight [Oppenheim]. Once the radar boresight angle moves beyond 6 to 11 degrees off perpendicular, the number of nonspecular trails detected essentially drops to zero.

The orientation of the head echo with the radar line of sight (Fig. 7a) shows a strong correlation with range rate and orientation to the meteor stream radiant.

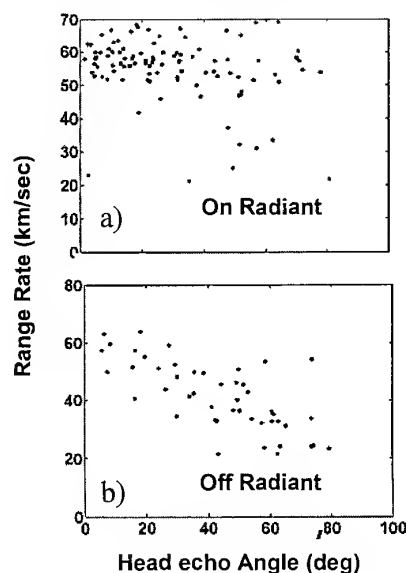


Fig. 7. Head echo angle with radar line of sight versus observation time.

While observing the radiant, the meteors tend to be grouped near a velocity of 60 km/s with head echo angles spanning 0 to 80 degrees. These observations were collected while viewing North Apex meteor source [Jones and Brown]. Observations were also collected with the radar line of sight oriented away from the radiant, which resulted in a head echo angle distribution that basically decreases linearly with range rate (Fig. 7b).

#### 4. THREE-FREQUENCY HEAD ECHO

We conclude our discussion with the presentation of the first head echo/nonspecular trail pair, simultaneously detected at VHF, UHF, and L-band on November 17, 1998. The range-time-intensity images are shown in Fig. 8. ALTAIR was pointing 1.8 degrees from  $\perp$  to the geomagnetic field. The head echo angle with  $B_0$  was also calculated and decreased from 88.8 degrees from  $\perp$  at 99 km to 87.3 degrees from  $\perp$  at 92 km. Oppenheim attributed the delay between the detection of the head echo and the detection of the trail as the time needed for plasma instabilities to grow strong enough to be visible to the radar. Oppenheim showed that for a simulated trail at 105 km, GDFB waves begin to appear after only 1 ms and at approximately 40 ms, plasma turbulence breaks the trail into multiple segments. The time delay of 25 ms is consistent with his theory that we are seeing nonspecular reflection from these segments.

The head echo traversed the main beam of the TRADEX radar system (Fig. 8a) and the ALTAIR system (Fig. 8b). TRADEX operates at both L- and S-band, however although the head echo was clearly located in the main beam of the L-/S-band system, there was no S-band detection. Our previous paper reported that the VHF RCS values were on average 20-25 dBsm higher than at UHF. The UHF cross sections ranged from  $3.2 \times 10^{-8}$  (limit of the UHF system) to  $1.0 \times 10^{-2}$ . The VHF cross sections were between  $3.2 \times 10^{-6}$  (limit of the VHF system) and  $1.6 \times 10^{-1}$ ; these values are consistent with Mathews and Zhou. We computed the RCS dependence on wavelength by comparing the LC and RC RCS values on a per-pulse basis. This technique was applied to 34 head echoes that were detected simultaneously at VHF and UHF. The maximum VHF cross sections were between 12 to 32 dBsm higher than their corresponding maximum UHF detection. By assuming that the RCS is proportional to  $\lambda^3$ , the x values varied from 2.8 to 7.6.

#### 5. SUMMARY

A total of 29 minutes of VHF data were collected near the peak of the Leonid 1998 shower, which produced over 900 VHF head echoes; 17 minutes of simultaneous UHF data were collected, which resulted in over 500

head echoes. This count produced an approximate rate of 1 VHF head echo every 2 seconds.

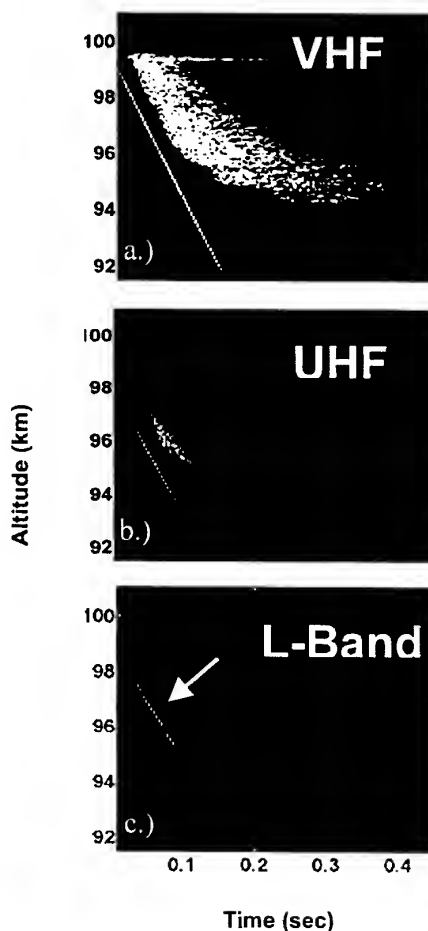


Fig. 8. Three-frequency head echo at UHF, VHF, and L-band.

These data were analyzed to determine frequency-dependent RCS characteristics, as well as altitude and aspect angle trends.

Azimuth and elevation monopulse data were used to compute the 3-d velocity and deceleration of the head echoes, indicating that a meteoroid's deceleration is not constant. The techniques outlined here for determining meteor velocity from ALTAIR data produced a meteor distribution with a peak number of meteors at 56 km/s, consistent with viewing the Northern Apex meteor source. The angle between the radar line of sight and geomagnetic field shows a strong correlation with the radar's ability to detect nonspecular meteor trails. Finally, the first head echo that was detected at VHF, UHF, and L-band frequencies was presented and used to

determine the frequency dependence on radar wavelength.

## 6. ACKNOWLEDGMENTS

The authors acknowledge the contributions of the following people: Ramaswamy Sridharan and Kurt Schwan from the Aerospace Division at MIT Lincoln Laboratory; Tom White, the ALTAIR sensor leader; Scott Coutts and Mark Corbin, for valuable input in data collection and analysis; Ken Roth and Chris Moulton from the Ballistic Missile and Defense Technology Division; and Andy Frase and Wil Pierre-Mike for software and hardware support. The Leonid 1998 data collection effort, in particular, involved many MIT Lincoln Laboratory and Raytheon Range Systems Engineering personnel from the Kwajalein sensors, including Jeff DeLong, Bob Foltz, Tim McLaughlin, Glen McClellan, Bill Riley, Dave Gibson, LeRoy Sievers, and Dave Shattuck. The Department of the Army under Air Force contract F19628-95-C-0002 sponsored this work. Opinions, interpretations, conclusions, and recommendations are those of the authors and are not necessarily endorsed by the U.S. Department of Defense. This material is based upon work partially supported by the National Science Foundation under Grant No.-ATM9986976.

## 7. REFERENCES

- Close S., Hunt S., Minardi M., and McKeen F., Analysis of Perseid Meteor Head Echo Data Collected using the Advanced Research Projects Agency Long-Range Tracking and Instrumentation Radar (ALTAIR), *Radio Science*, 35, 1233-1240, 2000.
- Close S., Hunt S., Minardi M., and McKeen F., Characterization of Leonid meteor head echo data collected using the VHF/UHF Advanced Research Projects Agency Long-Range Tracking and Instrumentation Radar (ALTAIR), *Radio Science*, in press.
- Hunt S., Close S., Coster A., Stevens E., Schuett L., Vardaro A., Equatorial Atmospheric and Ionospheric Modeling at Kwajalein Missile Range, MIT Lincoln Laboratory Journal, Vol. 12, No. 1, 2000.
- Janches D., Mathews J. D., Meisel D. D., Getman V. S., and Zhou Q., Doppler Studies of Near-Antapex UHF Radar Micrometeors, *Icarus*, 143, 347-353, 2000.
- Jones, J., and P. Brown. 1993. Sporadic meteor radiant distributions: orbital survey results. *Mon. Not. R. Astron. Soc.* 265, 524-532
- Mathews J. D., Meisel D. D., Hunter K. P., Getman V. S., and Zhou Q., Very High Resolution Studies of Micrometeors using the Arecibo 430 MHz Radar, *Icarus*, 126, 157-169, 1997.
- Oppenheim, M. M., vom Endt, A. F., Dyrud, L. P., "Electrodynamics of meteor trail evolution in the equatorial E-region ionosphere", *Geophys Res. Lett.*, 2000.
- Pellinen-Wannberg A., and Wannberg G., Meteor Observations with the European Incoherent Scatter UHF Radar, *J. Geophys. Res.*, 99, 11,379-11,390, 1994.
- Watanabe, J., T. Nakamura, M. Tsutsumi, and T. Tsuda, Radar Observation of Strong Activity of Perseid Meteor Shower in 1991, *Publ. Astron. Soc. Japan*, 44, 677-685, 1993.
- Zhou Q.-H., Perillat P., Cho J. Y. N., and Mathews J. D., Simultaneous Meteor Echo Observations by Large Aperture VHF and UHF Radars, *Radio Science*, 33, 1641-1654, 1998.

# METEOR HEAD ECHO OBSERVATIONS USING THE MILLSTONE HILL UHF INCOHERENT SCATTER RADAR SYSTEM

Phillip J. Erickson<sup>1</sup>, Frank D. Lind<sup>1</sup>, Suzanne M. Wendelken<sup>2</sup>, and Melissa A. Faubert<sup>3</sup>

<sup>1</sup>*Atmospheric Sciences Group, MIT Haystack Observatory, Westford, MA 01886, USA; pje@haystack.mit.edu*

<sup>2</sup>*Dartmouth College, Hanover, NH 03755, USA; Suzanne.M.Wendelken@dartmouth.edu*

<sup>3</sup>*Department of Mathematics, Tufts University, Medford, MA 02155, USA; mfaube01@emerald.tufts.edu*

## ABSTRACT

We present studies of meteor head echo statistics at UHF frequencies using the megawatt-class Millstone Hill incoherent scatter radar facility during the November 1999 and November 2000 Leonid meteor shower periods. The majority of meteoroid particles observed have approximate radar cross-sections of  $10^{-5} - 10^{-4} m^2$  and masses in the 70 mg range. Diurnal count rates show expected sporadic meteor peaks at local dawn and minimum at local dusk during both shower periods. However, the lack of a significant increase in counts during periods when the Leonid radiant is visible implies that Leonid showers do not possess significant enhancement in milligram-class meteoroid particles. Altitude distributions from November 2000 show significant unusual enhancements in count rates at 118 km in addition to normal 105-110 km altitude peaks. We also describe upcoming enhancements to the Millstone Hill system which will allow improved statistics as well as advanced trajectory determinations.

Key words: meteors; head echoes; incoherent scatter radar.

## 1. INTRODUCTION

Studies of the properties of meteors using radiowave techniques have been conducted since the mid 1940's by numerous scientific groups. Beginning with the seminal work of Evans [1] and continuing through the present day [2, 3, 4, 5, 6], a unique data set has been gathered using large-aperture, high-power radars whose primary purpose is making ionospheric measurements using the technique of incoherent scatter [7]. These megawatt-class radars are capable of detecting weak -170 dBW signals reradiated from the background ionosphere, and this level of sen-

sitivity allows them to study so-called radar head echoes arising from scattering in the region immediately surrounding the meteoroid. In particular, these radars are sensitive to the properties of micrometeoroids with approximate mass on the order of micrograms, equivalent visual magnitudes smaller than 12th order, and radar scattering cross-section (RCS) values below  $10^{-6} m^2$ .

Recently, the mid-latitude U. S.-run Millstone Hill ionospheric observatory, first used for meteor investigations in the work of Evans [1], has seen a reactivation of meteor experiments prompted by the results reported at the EISCAT, ALTAIR, and Arecibo radar facilities in Europe, the Pacific, and Puerto Rico respectively. Whereas these facilities initially discovered meteor echoes within experimental results aimed at E region ionospheric diagnostics, the contemporary Millstone observations have been specifically targeted from the outset at observing meteor head echo characteristics at the radar operating frequency of 440 MHz (67 cm wavelength). Because the meteoroid itself enters the atmosphere at high speed and the radar antenna beam is of small angular size, high-resolution data capturing techniques capable of recording individual meteor echoes are crucial in obtaining good statistical determinations of micrometeor characteristics.

We report in this paper on observations made at Millstone Hill during the Leonid meteor shower periods in November of 1999 and 2000. We focus here on statistical distributions of UHF meteor head echoes with respect to altitude, RCS, and time. Doppler characteristics will be covered in a future work. In addition to the results already obtained, we describe future enhancements in meteor observations which will be made possible by upgrades to the Millstone Hill MIDAS data acquisition system.

Table 1. Millstone Hill Radar Meteor Experiment: System Parameters

Antenna diameter	68 m
One-way antenna gain	~ 45 dB
Antenna beamwidth (FWHM)	0.6°
Beam diameter at 100 km altitude	1.1 km
Receiver system temperature	~ 120 K
Transmitter power	1 - 2 × 10 <sup>6</sup> W
Transmitter frequency	440 MHz
Transmitter wavelength	67 cm
Transmitter waveform	13 baud
	Barker code
Waveform baud	4 μs
Receiver bandwidth	500 kHz
Maximum observable velocity	85.5 km/s

## 2. OBSERVATIONAL TECHNIQUE

The observations reported here were made using the Millstone Hill incoherent scatter radar, located on the U. S. mainland at 42.6° N latitude and 288.5° E longitude in suburban Massachusetts. Relevant radar system parameters are listed in Table 1. Meteor head echo data was collected on several occasions, but we concentrate here on experiments during the Leonid meteor shower periods on November 17 - 19, 1999 and November 17 - 18, 2000. The Millstone Hill radar has two available large antennas, but for the experiments to date, the fixed 68 meter zenith antenna was employed to ensure maximum signal-to-noise ratio (SNR). As outlined in [8], the narrow 0.6° FWHM field of view of this antenna, coupled with the high velocity of the meteor target, means that meteor head echoes are visible only for < 0.1 sec and may be Doppler shifted by up to 200 kHz from the 440 MHz center frequency. Since these experiments were exploratory and the nature of the meteor selection algorithms was not known apriori, a wideband recording mode capable of saving power profiles from individual radar pulses (a "raw data" mode) was applied. This mode of operation yielded large data quantities (74 GB over 44 hours for the 1999 experiments) for later postprocessing.

Table 1 also describes the transmitter and receiver parameters. The transmitted waveform selected is a standard 13-baud Barker code [9] first applied to meteor observations at EISCAT [10]. On reception, the observed signal is passed through a matched digital decoding filter, and the decompressed echo exhibits Doppler decorrelation patterns which are a function of the instantaneous Doppler velocity of the meteor head echo. It is then possible to apply a least-squares fitting technique to derive not only the mean altitude and total RCS, but the Doppler velocity of each meteor echo observed. A future work will describe the results of this Doppler decorrelation analysis as applied to the 1999 and 2000 data. Here,

we concentrate on postprocessed measurements of the mean meteor head echo altitude and RCS. Altitude is derived by estimating the middle range of the Doppler decorrelation signature, and RCS is estimated by integrating the total received signal power under the decorrelation envelope since this quantity is conserved regardless of the actual Doppler velocity [10]. The received signal is sampled at twice the transmitted waveform baud rate in order to avoid appreciable loss of signal power which would occur if the meteor Doppler shift placed the received echo outside the analog filter passband. The experiment parameters selected ensure that all meteors with velocities up to 85.5 km/s are visible, a figure beyond the Leonid shower radiant velocity of 72 km/s.

An important step in the signal processing of the recorded data is separation of valid meteor echoes from other impulsive events such as in-band radiofrequency interference and momentary receiver noise. We accomplish this by first identifying those recorded echoes with a SNR threshold of 9 dB, and then further filtering the results by assembling them into time sequences. A final filtering criterion rejects short impulses as well as long-duration satellite echoes by asserting that the meteor echo sequence be contiguous over a minimum of 10 msec and a maximum of 123 msec. The SNR threshold used, combined with the system sensitivity and antenna gain from Table 1, sets the hard-target minimum detectable RCS at approximately -60 dBsm. The upper limit of observability before reaching receiver saturation is in excess of -10 dBsm.

## 3. LEONID SHOWER RESULTS

### 3.1. SNR, RCS Statistics

For the November 2000 observations, we present meteor head echo statistics ordered by SNR and RCS in Figure 1; results for the November 1999 experiments are similar. The RCS values were calculated from the SNR statistics by assuming the meteor head echo is a point target and employing the hard-target radar equation

$$RCS = \frac{P_N (4\pi)^3 R^4}{P_T \lambda^2 G^2} SNR \quad (1)$$

where  $P_N = k_B T_{sys} BW$ ,  $T_{sys}$  is the system noise temperature,  $k_B$  is Boltzmann's constant,  $BW$  is the receiver bandwidth in Hz,  $R$  is the meteor echo range in meters,  $\lambda$  is the transmitter wavelength in meters, and  $G$  is the one-way antenna gain; parameters are taken from Table 1. The results show that at the 440 MHz frequency of Millstone Hill, the radar observes micrometeoroids with cross-sections between  $3 \times 10^{-5}$  and  $10^{-3} m^2$ . Employing the methods of Mathews [5] where the RCS is assumed to be (very roughly) equivalent to the geometric area around the

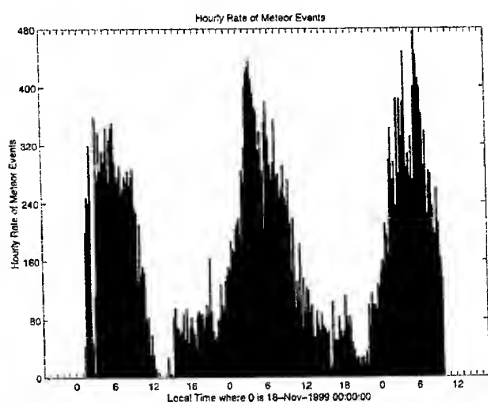


Figure 2. Millstone Hill meteor head echo count statistics as a function of local time for the November 1999 Leonid shower observations.

meteor's plasma head, we estimate this corresponds to particles with average mass of approximately 70 mg assuming a density of  $3 \text{ g/cm}^3$ .

### 3.2. Diurnal Statistics

We present meteor head echo count statistics, expressed in effective number of meteor counts per hour as a function of time, in Figure 2 for the November 1999 and Figure 3 for the November 2000 Leonid shower periods. The diurnal variation of the two observations peaks during local dawn at rates of 150 - 300 meteors/hour when the relative earth-meteor velocity is greatest, and becomes a minimum near dusk, in good agreement with other meteor head echo and classical trail echo results (e.g. [3]). However, observed counts do not significantly deviate from those characteristic of non-shower periods (e.g. November 10, 1998; not shown here), and no significant short-duration enhanced count rates are seen.

### 3.3. Altitude Statistics

We plot meteor head echo count statistics versus mean altitude in Figure 4 for November 1999 and Figure 5 for November 2000; due to an oversight in experiment setup, the receiver sampling altitudes for the latter experiment begin at 100 km. The November 19, 1999 day shown is typical of the entire data set for 1999 and shows a distribution centered near 105 - 110 km altitude, typical of meteor head echoes at UHF frequencies, as the electron density in front of the impacting meteoroid rapidly increases creating an overdense target [11]. The results from November 2000 in contrast exhibit a somewhat variable distribution, which we illustrate in Figure 5 by separating the echoes into three time periods from November 17

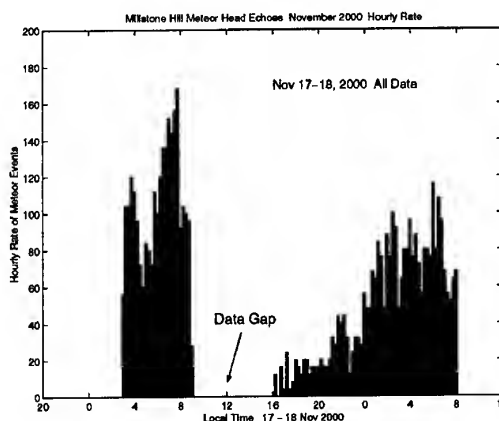


Figure 3. Millstone Hill meteor head echo count statistics as a function of local time for the November 2000 Leonid shower observations.

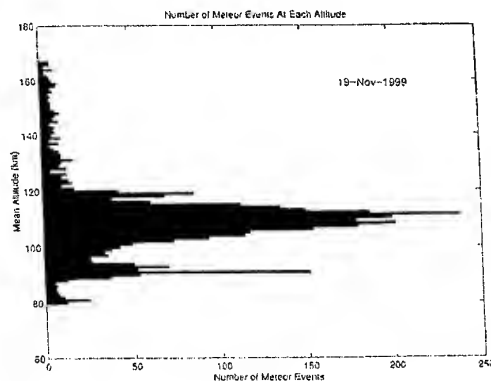


Figure 4. Millstone Hill meteor head echo count statistics as a function of altitude for the November 1999 Leonid shower observations. Sampling extends from 85 to 165 km altitude.

03 - 09 LT, November 17 16 - 22 LT, and November 17 22 - 08 LT. The first nighttime period and the intervening daytime observations show a primary peak centered on  $\sim 105$  km as in 1999, but a significant secondary peak exists at approximately 118 km. By the second evening of November 17-18 the 118 km peak has become the dominant mean center altitude for meteor head echoes, with the lower peak still visible. The upper peak cannot be ascribed to meteor echoes entering a sidelobe, as the strongest sidelobe of the Millstone zenith antenna is  $\sim 2 - 3^\circ$  off bore-sight and no significant antenna response exists at a  $27.1^\circ$  degree offset which would be implied by assuming the 118 km mean altitudes were actually 105 km echoes in a sidelobe. No other unusual systematic differences were uncovered that might lead to exclusion of the upper peak as an instrumental artifact.

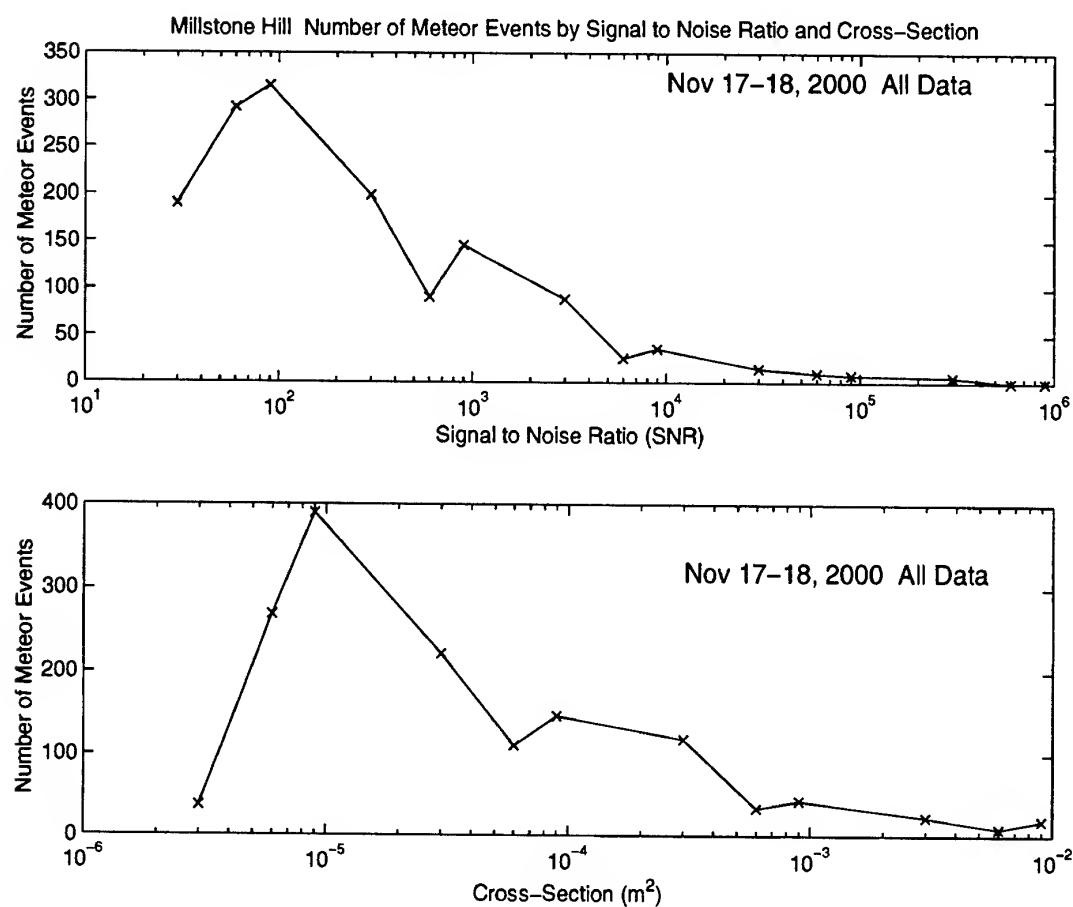


Figure 1. Millstone Hill meteor head echo count statistical distribution in SNR and RCS for the November 2000 Leonid shower observations. The data were binned in SNR before computing RCS; overall standard deviation was less than 10 percent.

### 3.4. Discussion

The 105–110 km altitude distribution presented in section 3.3 for a majority of the Millstone Hill observations is in good agreement with results from Arecibo [3] and EISCAT [2]. However, the 118 km mean altitude peak in meteor head echo counts observed on the evenings of November 17 and 18, 2000 is a very high altitude for meteor head echo observations, and does not agree with theories proposed to explain the observed upper altitude cutoff for conventional meteor radar distributions [12] or meteor head echo distributions [2, 11]. The mechanism postulated by these studies predicts that the upper cutoff is due to the electrons within either the plasma cloud (for head echoes) or trail (for conventional meteor radars) cancelling one another's scattering contributions. The resulting predicted upper limit on UHF head echo observation is  $\sim 110$  km, and complete cancellation of the reflected wave should occur at 118 km, as the atmospheric mean free path there is much larger than the 67 cm wavelength used at Millstone Hill. Future studies will attempt to further confirm and quantify this upper altitude peak.

We note that temporal count statistics presented in section 3.2 do not exceed those observed on typical days when only sporadic meteor populations are present. However, significant Leonid shower activity has been reported during both the November 1999 (maximum at November 18, 2202 LT) and 2000 (maximum at November 18, 0312 LT) Leonid showers by optical observations [13, 14] and lower-frequency radiowave observations (e.g. the Ondrejov backscatter radar in the Czech Republic - cf. <http://sunk1.asu.cas.cz/~koten/radar.html>). Furthermore, the Leonid radiant point was visible at Millstone Hill's location from approximately 2200 to 1300 LT during each November day, reaching a maximum altitude of  $69^\circ$ . The Millstone Hill observations strongly suggest, therefore, that the Leonid streams encountered by the earth during these showers do not possess significant enhancements in meteoroid particles at the milligram level.

### 4. MIDAS-W: ENHANCED CAPABILITIES FOR METEOR RESEARCH

The results from the 1999 and 2000 Leonid meteor periods demonstrate the capability at Millstone Hill for dedicated meteor observation experiments. Since 1992, the radar has employed MIDAS (Millstone Incoherent Scatter Data Acquisition System), a hierarchical hardware/software system based on an abstract model of a general incoherent scatter radar, for its experiment management and data acquisition needs. The MIDAS system has proved to be a versatile and robust datataking system, but is currently limited to a single-processor configuration in which

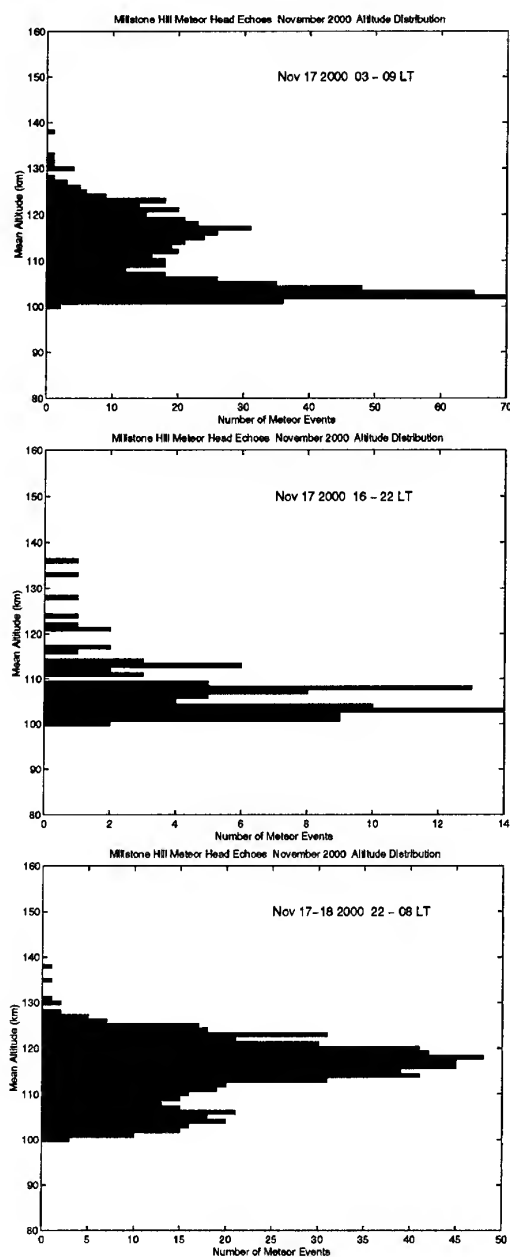


Figure 5. Millstone Hill meteor head echo count statistics as a function of altitude for three periods during the November 2000 Leonid shower observations: (a) between 03–09 LT November 17; (b) between 16–22 LT November 18; (c) between 22–08 LT November 18/19. Sampling extends from 100 to 140 km altitude.

each incoming radar pulse is associated one-to-one with a corresponding analysis algorithm tailored to a specific scientific goal.

The system is currently undergoing an upgrade to the MIDAS-W software radar system [8] where all signal processing functions are performed in the digital domain on general purpose computers. The observations presented in this work from November 2000 were in fact made with a prototype version of the MIDAS-W system. A fundamental goal of MIDAS-W is to flexibly extend the kinds of processing that can be done on radar signals by providing raw voltage samples across a multicast high-speed Ethernet backbone. This allows multiple attached clients to independently analyze received echoes in different ways through simultaneous access to the incoming data. Receiver system performance will also improve, and the library of accessible transmitter modulations will be greatly expanded to utilize the full  $\sim 1$  MHz bandwidth of the klystron-based transmitter.

This system upgrade will have significant implications for meteor observation statistics. The modern revival of interest in high-frequency meteor head echoes at the EISCAT facility [2] arose in fact as a result of anomalous echoes, generated by incoming meteors, appearing in experimental data aimed instead at measuring neutral and ionized parameters in the ionospheric E region near 100 km altitude. In a similar manner, normal ionospheric observing programs at Millstone Hill also have meteor echoes embedded in data intended for other purposes. We intend in the future to construct a software meteor detection module, always present in the signal processing chain, which takes advantage of the multicast MIDAS-W received data to automatically log and classify strong point-scatter targets independently of other more ionosphere-specific analysis modes. Since Millstone Hill operates over 2000 hours per year in various coordinated and site-specific experiments, statistics of micrometeoroids will be vastly improved over reliance on dedicated meteor experiments alone, although some transmitted waveforms will by their nature produce more accurate head echo results. The improved receiver bandwidth and enhanced transmitter waveform library will also allow the meteor module to routinely process head echoes in both range and Doppler shift in real-time.

In addition to the 68 meter zenith antenna used in this work, Millstone Hill also has available a 46 meter fully steerable antenna, and the transmitter can be switched between the two antennas in approximately 1.5 seconds. Furthermore, the 46 meter steerable antenna has a four horn monopulse feed which provides two azimuth and two elevation error channels in addition to the central sum channel. We plan to instrument all four error channels and the main sum channel with high dynamic range receivers, and we will si-

multaneously sample these channels, using their data to construct a more sophisticated meteor orbit determination system. This technique will combine the interferometric phase information provided by the error channels to allow unambiguous trajectory angle and orbit determination on each observed meteor head echo target. Such phase angle information has already been employed successfully at the ALTAIR Pacific UHF/VHF radar [15] in dedicated experiments, but the design of the Millstone Hill/MIDAS-W software radar system combined with the large number of potential observation times will greatly increase the number of orbital determinations possible.

## 5. SUMMARY

We have begun to explore the characteristics of meteor head echoes at UHF frequencies from Millstone Hill using a new set of experimental modes as the micrometeors pass through the narrow-beam, high-power incoherent scatter radar. Diurnal distributions during the 1999 and 2000 Leonid meteor showers do not show significant count enhancements over normal sporadic meteor patterns, leading to the conclusion that meteoroids in the cross-section range of  $10^{-5} - 10^{-4} m^2$  and estimated masses of  $\sim 10 - 100$  milligrams are not a significant population within the Leonid interplanetary debris streams. Altitude distributions, particularly during the November 2000 observations, show evidence of very high-altitude meteor echoes which disagree with conventional theories predicting upper altitude cutoffs at 110 km for UHF radar frequencies. Future studies will be able to more completely explore these features and map out Doppler velocities with greatly enhanced statistics as the MIDAS-W software radar system is brought online.

## ACKNOWLEDGMENTS

We wish to thank A. Pellinen-Wannberg for helpful discussions concerning the Doppler decorrelation method. Two of the authors (SMW, MAF) were supported under the U. S. National Science Foundation's Research Experiences for Undergraduates program at MIT Haystack Observatory under grant AST-9619444.

## REFERENCES

1. J. V. Evans. Radio-echo studies of meteors at 68-centimeter wavelength. *J. Geophys. Res.*, 70:5395-5416, 1965.

2. A. Pellinen-Wannberg and G. Wannberg. Meteor observations with the European incoherent scatter UHF radar. *J. Geophys. Res.*, 99:11379–11390, 1994.
3. Q. H. Zhou, C. A. Tepley, and M. P. Sulzer. Meteor observations by the Arecibo 430 Mhz incoherent scatter radar: 1. Results from time-integrated observations. *J. Atmos. Terr. Phys.*, 57:421–431, 1995.
4. Q. H. Zhou and M. C. Kelley. Meteor observations by the Arecibo 430 MHz incoherent scatter radar. II. Results from time-resolved observations. *J. Atmos. Solar Terr. Phys.*, 59:739–752, 1997.
5. J. D. Mathews, D. D. Meisel, K. P. Hunter, V. S. Getman, and Q. Zhou. Very high resolution studies of micrometeors using the Arecibo 430 MHz radar. *Icarus*, 126:157–169, 1997.
6. D. Janches, J. D. Mathews, D. D. Meisel, and Q.-H. Zhou. Micrometeor observations using the Arecibo 430 MHz radar - I. Determination of the ballistic parameter from measured Doppler velocity and deceleration results. *Icarus*, 145:53–63, 2000.
7. J. P. Dougherty and D. T. Farley. A theory of incoherent scattering of radio waves by a plasma. *Proc. Roy. Soc. A*, 259:79, 1960.
8. J. M. Holt, P. J. Erickson, A. M. Gorczyca, and T. Grydeland. MIDAS-W: a workstation-based incoherent scatter radar data acquisition system. *Ann. Geophys.*, 18:1231–1241, 2000.
9. R. H. Barker. Group synchronizing of binary digital systems. In W. Jackson, editor, *Communications Theory*, pages 273–287. Academic, New York, 1953.
10. G. Wannberg, A. Pellinen-Wannberg, and A. Westman. An ambiguity-function-based method for analysis of Doppler decompressed radar signals applied to EISCAT measurements of oblique UHF-VHF meteor echoes. *Radio Sci.*, 31(3):497–518, 1996.
11. A. Westman. Development of high resolution radar measurement techniques for studies of transient phenomena in the ionospheric E and F layers. Scientific report 246, Swedish Institute for Space Physics, Kiruna, Sweden, 1997.
12. D. Olsson-Steel and W. G. Elford. The height distribution of radar meteors: Observations at 2 MHz. *J. Atmos. Terr. Phys.*, 49:243–258, 1987.
13. R. Arlt, L. B. Rubio, P. Brown, and M. Gyssens. Bulletin 15 of the International Leonid Watch: first global analysis of the 1999 Leonid storm. *WGN, the Journal of the International Meteor Organization*, 27(6):286–295, 1999.
14. R. Arlt and M. Gyssens. Bulletin 16 of the International Leonid Watch: results of the 2000 Leonid meteor shower. *WGN, the Journal of the International Meteor Organization*, 28(6):191–204, 2000.
15. S. Close, M. Oppenheim, S. Hunt, and L. Dyrud. Scattering characteristics of meteor head echoes detected at ALTAIR. to be submitted to *J. Geophys. Res.*, 2001.

# INTERPRETATION OF NON-SPECULAR RADAR METEOR TRAILS

Lars P. Dyrud, Meers M. Oppenheim, Sigrid Close, and Stephen Hunt

Center for Space Physics, Boston U., 725 Comm. Ave., Boston, MA 02215 U.S.A., Email ldyrud@bu.edu

## ABSTRACT

We present comparisons between plasma theory and radar observations to explain why radars only measure non-specular echoes of meteor trails within a limited altitude range. While large-aperture radars detect meteor head echos between 85 km and 135 km, non-specular trail reflections typically arrive from between 95 km and 105 km. Plasma simulations have demonstrated that meteor trails are often unstable to the growth of Farley-Buneman/gradient-drift (FBGD) waves. These waves frequently become turbulent and generate large field aligned irregularities (FAI)'s which allow radars to measure reflections. We present analysis of the meteor trail FBGD instability to show that trails are only unstable within a limited altitude range. To demonstrate this effect, we evaluate a number of radar observations obtained during the Leonid 1998 shower with the ALTAIR radar on the Kwajalein atoll. Using these analysis techniques, we show that the narrow condition for meteor trail instability leads to a non-specular trail dependency on meteor velocity. Finally, future work may provide new and exciting diagnostic tools for other meteor parameters, such as size, composition, and trail initial radius.

## 1. INTRODUCTION

The Earth is continuously bombarded by extraterrestrial material in meteoric form. Since most of this mass flux is comprised of very small meteors ( $< 10^{-5}$  kg), they are either undetected or measured only by radars. This difficulty in directly detecting meteor entry has led to poorly constrained global estimates of both meteoric mass flux and composition (Cziczko et al. 2001). This paper presents techniques that may prove useful in using large aperture radars to more effectively monitor the meteor mass flux and composition.

Recent observations demonstrate that sensitive radars, such as Jicamarca, ALTAIR, Arecibo, MU, and EISCAT are capable of detecting a "new" type meteor phenomena (Wannberg et al. 1996; Close et al. 2000; Janches et al. 2000; Chapin & Kudeki

1994; Zhou et al. 2001). Traditional low power meteor radars require specular echos or trails perpendicular to the radar beam to ensure a large enough cross-section for reflection (See Cepelcha et al. (1998) for a review of traditional meteor physics). However, these sensitive, large aperture radars detect plasma generated from direct meteor entry (head echo) which is often followed by trail reflections, despite the fact that many trails are roughly aligned with the radar beam. These "new" trail echos have been attributed to coherent radio scatter from field aligned irregularities (FAI) in electron density that have been generated from plasma turbulence. Various names for this type of meteor trail observation have been used, and we chose to call them "non-specular echos" to emphasize their observational distinction, and we shall refer to head echos followed by non-specular trails as head-trail pairs.

McKinley (1961) was perhaps the first author to present observations of head-trail pairs. However, as written by Zhou et al. (2001) the head echos were likely misinterpreted as overdense trails, and the trails were suggested as caused by roughness in the ionization distribution of the trail, or by wind shears. Chapin & Kudeki (1994) was the first to present observations and interpretation of non-specular trails that suggested plasma instability as the cause for radio reflection. Their observations were coincident with electrojet backscatter and were interpreted as a two-stream or Farley-Buneman instability driven by the presence of the electrojet  $\mathbf{E}$ -field. This interpretation was confirmed by the plasma simulations of Oppenheim et al. (2000), who also demonstrated that meteor trails will not initially track neutral winds but instead follow the electron  $\mathbf{E} \times \mathbf{B}$  drift. Dyrud et al. (2001) showed that meteor trails were inherently unstable without a background  $\mathbf{E}$ -field, and that the resulting instability and turbulence was responsible for an anomalous cross-field diffusion of meteor trails that can be up to an order of magnitude faster than the rate expected from ambipolar diffusion. Recently, using the steerable MU radar Zhou et al. (2001) demonstrated that non-specular trails were easily detectable when the radar pointed perpendicular to  $\mathbf{B}$ , while none were detected in the parallel to  $\mathbf{B}$  direction. These observations provide dramatic support for the idea that non-specular trails are radio scatter from FAI, and were made at

mid-latitudes where strong E-fields are rare, thereby demonstrating meteor trail's inherent instability.

Using analysis of the results shown by previous plasma simulations we provide an explanation for one of the most obvious features of head echo and non-specular trail pairs observed by the Kwajelele VHF and UHF radar. This paper will demonstrate that the altitude range for meteor trail FBGD instability is colocated with the observed altitude range of non-secular trails. Additionally, since the conditions for trail FBGD instability are highly sensitive to several meteor properties, this new understanding of meteor trails may provide for exciting diagnostic tools for monitoring meteor properties.

## 2. NON-SPECULAR TRAIL OBSERVATIONS AND ANALYSIS

Fig. 1 shows altitude time intensity (ATI) images of a head echo and non-specular trail from the ALTAIR radar at both UHF and VHF frequencies. The ALTAIR system is a highly sensitive 46 m dish with both VHF (160 MHz) and UHF (422 MHz) transmitters and receivers, located on the Kwajelele Atoll (see Close et al. (2000) and Hunt et al. (This Volume) regarding information about this data set, or the facilities). In addition to high sensitivity, the system operates at unprecedented range resolutions of 30 m at VHF and 2.5 m at UHF. The first obvious feature in both panels is the diagonal line that extends from 107 to 92 km (VHF) and 102-93 (UHF) km in altitude. This is the head echo, which is presumed to be the instantaneous reflection from meteor generated ionization (Wannberg et al. 1996; Janches et al. 2001). The reflection is designated a head echo by the clear range rate of the reflector, for this case, 60 km/s. The precise radio scattering mechanism from head echos is a currently debated topic, and is not the focus of this paper. However, we assume that it signals the generation of a meteor trail at given altitude. After the appearance of the head echo the next clear feature is the non-specular trail itself. From 96 km altitude and above there is a near constant delay time (25 ms) between head echo and trail formation. We discuss the cause for this delay time in an upcoming paper, while we focus on the altitude range of trail observations here.

We have closely examined 16 non-specular head echo and trail pair observations. While this is a small subset of the ALTAIR meteor data set, it represents all the high resolution data made public at this time. However, we feel comfortable presenting statistics, because all the available examples demonstrate consistent features, with little variation, leading us to believe that even this small data set is statistically significant. The VHF image in Fig. 1 shows head echo scatter between 107-92 km altitude, while trail scatter is observed over the more narrow range of 102-95 km. The remainder of the paper will focus on explaining this feature and introducing possible

meteor diagnostic tools based upon the non-specular trail altitude range.

### 2.1. Instability threshold

Dyrud et al. (2001) used a simple calculation predicts the minimum altitude of meteor trail instabilities and anomalous diffusion. This criterion, shown in figure 4 of that paper, was based upon the Fejer et al. (1984) demonstration that the FBGD instability is driven when  $\mathbf{E}_\perp \cdot \nabla n > 0$ . Therefore, it was presumed that the FBGD waves would not exist when the driving electric field, in this case the ambipolar field, was reversed. Ambipolar fields reverse sign with respect to  $\nabla n$  at approximately 96 km because electron cross-field mobility begins to exceed the ion mobility at this altitude. However, we have now conducted a detailed analysis of the FBGD as applied to meteor trails and have discovered that the problem is more complex. Oppenheim et al. (This volume) presents the detailed derivation of meteor trail FBGD instability, and we merely summarize those results in a simple 1-D formulation.

In order to solve for meteor instability we must first solve for the equilibrium electron drift velocity. Eq. (1) describes this including the diamagnetic drift and assumes that E-fields are entirely ambipolar,

$$\mathbf{v}_{de} = \frac{\nabla n \times \hat{\mathbf{B}}}{n} C_s^2 \left( \frac{1/\Omega_i}{1 + \Psi} \right), \quad (1)$$

where  $\hat{\mathbf{B}} \equiv \mathbf{B}/|B|$  is a unit vector pointing in the direction of the magnetic field,  $L_n = (\nabla n/n)^{-1}$ ,  $\Omega_i$  and  $\Omega_e$  are the ion and electron cyclotron frequencies,  $\nu_i$  is the ion-neutral collision frequency,  $\Psi_0 \equiv \frac{\nu_e \nu_i}{\Omega_e \Omega_i}$ , and  $C_s$  is the ion acoustic velocity. Replacing Eq. (1) into the complete fluid dispersion relation (Eq. 5) published by Fejer et al. (1984), yields the 1-D dispersion relation,

$$\omega^2 \left( \frac{i\Psi}{\nu_i} + \frac{1}{k L_n \Omega_i} \right) + \omega \left( 1 + \Psi - \frac{i\nu_i}{k L_n \Omega_i} \right) + \frac{k C_s^2}{L_n \Omega_i} \left( \frac{\Psi}{1 + \Psi} \right) + \frac{i k^2 C_s^2 \Psi}{\nu_i} = 0, \quad (2)$$

where  $\omega = \omega_r + i\gamma$  is the complex wave frequency, and  $k$  is the 1-D wave number and points in the same direction as the electron drift. This equation includes some important effects that are not included in the simple  $\mathbf{E}_\perp \cdot \nabla n > 0$  criterion (Dyrud et al. 2001). First, we include the diamagnetic drift in the electron drift. This is important, because the steep density gradients present in meteor trails generate diamagnetic drift as large as several km/s.

In order to simplify the dispersion relation several FBGD terms are usually neglected based upon  $\gamma < \omega_r < \nu_{in}$ . Due to the high frequency waves that form on meteor trails the relation above is not valid and all terms in Eq. (2) must be included. Including these assumptions in the criterion for meteor

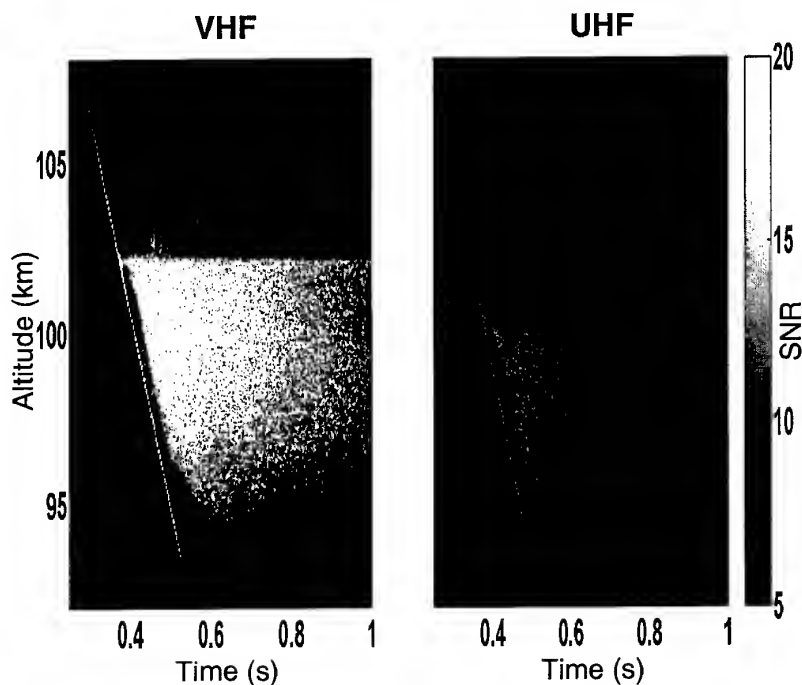


Figure 1. Altitude-time-intensity plots of head and non-specular echos over extended range from ALTAIR VHF/UHF Radar obtained on 2242 UT, November 17, 1998.

trail instability vs altitude has two important effects. The lower altitude limit of meteor trail instability is not necessarily predicted by the reversal of the meteor trail ambipolar electric field, but by increased damping from the previously neglected terms. For example, the new dispersion relation predicts no growth even at altitudes when the electron drift far exceeds both the ion acoustic speed and the modified FBGD speed published in Fejer et al. (1984). However, the inclusion of the diamagnetic drift offsets the influence from damping, so the lower altitude limit for meteor trail instability is little changed from that predicted by Dyrud et al. (2001), and for most conditions remains approximately 96 km. Conversely, the inclusion of these assumptions has a profound effect on meteor trail instability at higher altitudes. The growth rate for this dispersion relation is highly dependent on the gradient length scale,  $L_n = (\nabla n/n)^{-1}$ , which leads to several important dependencies on meteor properties. Most notably, a strong dependence on meteor trail initial radius,  $r_i$ , which is defined as the average distance ablated meteor particles travel during thermalization. Initial radius increases with altitude, due to the decrease in neutral density, because ablated meteor ions will random walk a greater distance during their thermalization in a less dense atmosphere than in greater density Ceplecha et al. (1998). Clearly, a larger initial radius results in weaker density gradients leading to more weakly driven instability processes.

Fig. 2 shows the growth rate of the meteor trail FBGD as a function of altitude and meteor veloc-

ity. Meteor velocity becomes a criterion for instability due to the dependency of initial radius on meteor velocity. First, this plot demonstrates that weakening density gradients with altitude results in meteor trail instability over a limited altitude range between ~96-105 km. Second, this plot demonstrates that the actual altitude range for instability is dependent on meteor trail velocity. There should be an observable difference in the altitude range of non-specular trail generated by ~60 and ~20 km/s meteors. Several simplifying assumptions, discussed in the following paragraph, were made in producing Fig. 2. However, even with these assumptions we manage to predict the altitude range for observed non-specular trails within a 1-2 km. Here we discuss the assumptions made in generating Fig. 2 and the steps required for future improvement and use of this model for non-specular trail observations. The initial radius has the following dependence on velocity and atmospheric mass density  $r_i \propto \rho^{-1} v^{0.8}$  (Bronshten 1983). Oppenheim et al. (This volume) has examined the important dependency on initial radius and shown that, of the current models, the Bronshten (1983) formula best characterizes  $r_i$  as a function of altitude. We assumed that meteor trails consist of a gaussian distribution of increased density with  $\sigma = r_i$ . The velocity is assumed to be constant at all altitudes, which is a not completely accurate. Also, for this particular plot the trails are assumed to be 100 times more dense than the surrounding ionosphere at all altitudes. This assumption is also not entirely correct, but still demonstrates the necessary point that the strongest dependence on growth lies with initial radius and atmospheric density. In order to make

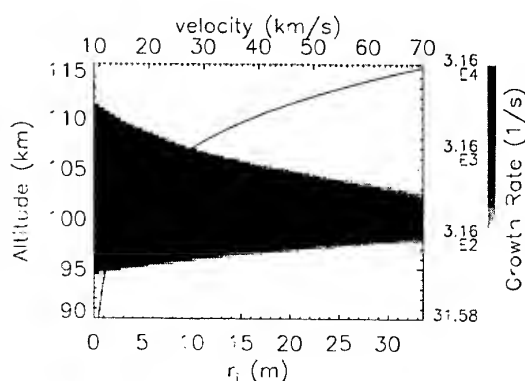


Figure 2. Plot of instability growth rate for the FBGD instability as a function meteor velocity. The function for initial radius,  $r_i \propto \rho^{-1} v^{0.8}$  based upon Bronshten (1983) is also plotted.

a more accurate plot, an ablation model should be incorporated to calculate the deposition of mass at a given altitude range for a particular meteor mass and velocity. While the variation with velocity shown here is important, the clearest point shown by this figure is that regardless of velocity or the line density of the trail, the plasma comprising a meteor trail is only unstable to the FBGD under a limited altitude range. For example a trail that is created over a 10 km altitude range may only be unstable within 4-5 km centered around 98 km altitude.

Fig. 1 demonstrated that the head echo reflections occur over a broader range in altitude than do the trail echos. This indicates that even though there is a sufficient column of ionization at certain altitudes, there are no trail reflections. Fig. 3 demonstrates this observational fact on a statistical basis as well. The figure is a plot of the altitude range of all currently available head echo and trail pairs observed by the ALTAIR VHF radar, and shows that head echo scattering occurs at both higher and lower altitudes than the non-specular trails, and that all non-specular trail observations are confined within the 95-105 km altitude range. These data are strong evidence that the scenario predicted in Fig. 2 of meteor trail instability over a limited altitude range is correct on both an individual and a statistical basis.

### 3. SUMMARY

We presented data showing that the ALTAIR radar observes meteor head echos over a broader range in altitude than non-specular trails, on both an individual and statistical basis. A detailed fluid analysis of the condition for growth of FBGD waves on meteor trails demonstrates that trails are unstable within a limited altitude range. This altitude range is between ~95-104 km and predicts the observed overall altitude range of non-specular meteor trails to within

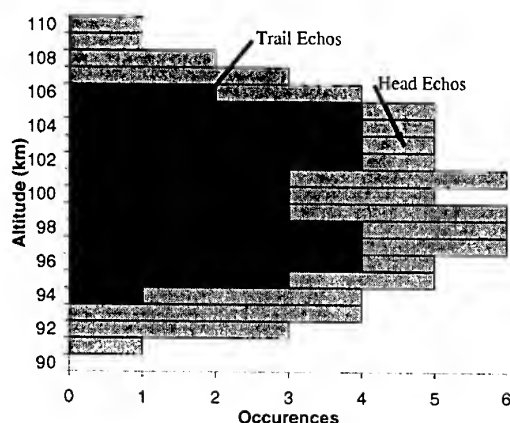


Figure 3. Occurrence of head echos and non-specular trails demonstrating that trails are confined to a narrower altitude range than head echos.

1-3 km. Since this altitude range depends on a number of meteoric properties including velocity, trail expansion radius and ion composition, it may provide a new diagnostic tool for studying the properties of micro-meteors.

**Acknowledgments:** The authors would like to thank Kelly McMillon and Licia Ray for producing many of the figures. This research was supported by NASA (S00-GSRP-092) and NSF (ATM 9988976).

### REFERENCES

- Bronshten V.A., 1983, Physics of Meteor Phenomena, D. Reidel Publ. Co.
- Cepelcha Z., Borovicka J., Elford W.G., et al., 1998, Space Science Reviews, 84, 327
- Chapin E., Kudeki E., 1994, Geophys. Res. Lett., 21, 2433
- Close S., Hunt S.M., Minardi M.J., McKeen F.M., Sep. 2000, Radio Science, 35, 1233
- Cziczo D.J., Thomson D.S., Murphy D.M., Mar. 2001, Science, 291, 1772
- Dyrud L.P., Oppenheim M.M., vom Endt A.F., 2001, Geophysics Research Letters, 28, 2775
- Fejer B.G., Providakes J., Farley D.T., 1984, J. Geophys. Res., 89, 7487
- Janches D., Mathews J.D., Meisel D.D., Zhou Q.H., May 2000, Icarus, 145, 53
- Janches D., Meisel D.D., Mathews J.D., Apr. 2001, Icarus, 150, 206
- McKinley D.W.R., 1961, Meteor Science and Engineering, McGraw-Hill, New York
- Oppenheim M.M., vom Endt A.F., Dyrud L.P., 2000, Geophysics Research Letters, 27, 3173
- Wannberg G., Pellinen-Wannberg A., Westman A., May 1996, Radio Science, 31, 497
- Zhou Q.H., Mathews J.D., Nakamura, Takuji, 2001, Geophysics Research Letters, 28, 1399

# ASTRONOMICAL AND PHYSICAL DATA FOR METEOROIDS RECORDED BY THE ALTAIR RADAR

P. Brown<sup>1</sup>, S. Hunt<sup>2</sup>, and S. Close<sup>2</sup>

<sup>1</sup>Los Alamos National Laboratory, MS J577, Los Alamos, NM 87545 USA email: pbrown@lanl.gov

<sup>2</sup>MIT Lincoln Labs, 244 Wood Street, Lexington, MA 02420 USA email: hunt@ll.mit.edu

## ABSTRACT

We present preliminary results of orbital and physical measurements of a small selection of meteoroids observed at UHF frequencies by the ALTAIR radar on Kwajalein island on November 17, 1998. The head echoes observed by ALTAIR allowed precise determination of velocities and decelerations from which orbits and masses of individual meteoroids derived from numerical modelling have been measured. During these observations, the ALTAIR radar detected average head echo rates of 1665 per hour. The effective system limiting magnitude is found to be between magnitude +10.5 and +11 corresponding to masses near  $6 \times 10^{-10}$  kg using an observed mean velocity of our analyzed sample of  $56 \text{ km s}^{-1}$ . This compares favorably to a mean modelled initial mass from the observed decelerations of the largest events of near  $2 \times 10^{-9}$  kg. All observations were made with the antenna beam pointing very near the center of the north apex sporadic source. The resulting orbits determined from modelling are largely consistent with the orbital characteristics of that source derived from other radar orbital surveys. Despite these observations occurring near the time of the expected Leonid maximum in 1998, no definite Leonids were detected in our analyzed sample.

## 1. INTRODUCTION AND EQUIPMENT

The observation of meteor head-echoes with large aperture radars offers several advantages over other radar meteor observations. Due to the nature of the scattering (cf. Jones and Webster, 1991), the radar return actually reflects off a small region of plasma in the vicinity of the meteoroid and hence can precisely follow the path of the ablating meteoroid. This affords very precise measurements of velocities and may also yield useful decelerations of the impinging meteoroid. This information may be used to compute a pre-atmospheric orbit for the meteoroid and also provide an estimate of the mass of the meteoroid. The meteoroid masses accessible by these large radars are typically intermediate between nor-

mal VHF backscatter meteor radars and spacecraft dust measurements.

One such large aperture radar is the Advanced Research Projects Agency Long-Range Tracking and Instrumentation Radar (ALTAIR) located on the island of Roi-Namur in the Kwajalein Atoll which is part of the Republic of the Marshall Islands (9°N, 167°E). The principle function of ALTAIR is as a contributing sensor to the US Space Command satellite-tracking network. ALTAIR is a dual-frequency, high-power (6 Mw peak at both frequencies), narrow beam (half-power beamwidths are 2.8° at 160 MHz and 1.1° at 422 MHz) system using a 46-m diameter mechanically steered dish. ALTAIR transmits right circular polarized energy and records left circular with a range resolution of 15 m at VHF and 7.5 m at UHF. The 46-m diameter antenna employs a focal point VHF feed and multi-mode Cassengrain UHF feed in conjunction with a frequency selective sub-reflector (5.5 m diameter), giving a monopulse angle tracking capability at either frequency. This allows precise azimuth and elevation angle measurements which together with range contribute to the accurate determination of target position in three dimensions. The aforementioned characteristics allow ALTAIR to reliably detect a -62 dBsm target in VHF and a -81 dBsm target at UHF at a range of 100 km.

For these interferometric measurements, the ALTAIR receivers are offset from the focus of the dish, and their signal energies are differenced to produce two additional channels of data, including the left circular azimuth difference (ALC) and left-circular elevation difference (ELC). ALC and ELC are combined in a process known as amplitude comparison monopulse (a form of phase interferometry) to measure the angle of arrival of the radar return (for each pulse) to a small fraction of the beam width. The average angular measurement accuracy (standard deviation) of the ALTAIR system is 11.2 mdeg in azimuth and elevation at UHF as determined from control measurements of radar calibration spheres. More information on the ALTAIR system is given in Close et al. (2000).

Here we examine the basic astronomical and physical characteristics from a short sequence of data collected at UHF by ALTAIR on November 17, 1998. This data collection interval was originally designed to detect Leonid meteoroids.

## 2. DATA COLLECTION

Head echo data were collected from 15 - 21 UT on 17 November, 1998 to coincide with expected heightened activity from the Leonid meteor shower. The ALTAIR beam was pointed at the Leonid radiant as well as off-radiant (by about 20 degrees). Although data were gathered at a total of five frequencies (UHF and VHF from ALTAIR, plus TRADEX, which operates at 1320 and 2951 MHz and ALCOR, which operates at 5664 MHz) only UHF ALTAIR data are analyzed here. Table 1 contains the pointing directions in elevation and azimuth, in sun-centred coordinates, the total head echo rate plus main beam rate, estimated collecting area and equivalent limiting magnitude. Each data collection lasted a total of two minutes from the stated time. Note that some echoes have significant portions of their paths in sidelobes rather than the main beam and these are generally removed from our more detailed physical analysis.

Only echoes more than 10 dB above the noise-floor were examined. For each echo, the range, amplitude, polarization and position in the beam were measured every  $3 \times 10^{-3}$  s and these data saved for later analysis.

## 3. DETERMINATION OF LIMITING SENSITIVITY

The absolute limiting sensitivity for ALTAIR UHF observations is of considerable interest from the standpoint of physical modelling. Here we have taken two approaches to the problem. The first is to model the velocity vs. height curve for each meteoroid using the gross-fragmentation model of Ceplecha et al. (1993), to provide an approximate minimum mass for the larger events (which have the best SNR and show clear deceleration). The second approach relies on the high head echo rate for ALTAIR to compute flux from the observed rates and calculated collecting areas. Many of the head echoes detected by ALTAIR intersect the main radar beam at considerable angles; as a result the effective beam collecting area is not just the top of the beam cylinder, but includes much of the sides as well.

### 3.1. Using the observed radar rate to determine limiting mass

For the sporadic sources sampled by ALTAIR for this data collection (mainly the north apex source), most

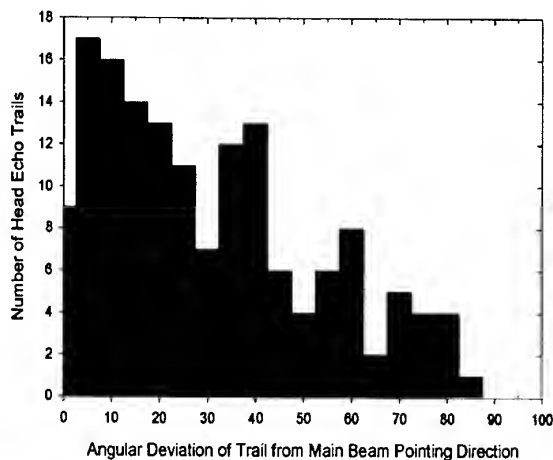


Figure 1. Angular deviation (in  $5^\circ$  bins) of individual trails from the beam pointing direction for all head echoes with measured trail orientations. From this figure it is apparent that few meteor head echoes travel directly down-the-beam; this is an expected result based solely on the very small solid-angle subtended by the beam at UHF.

radiants are within  $30^\circ$  of the pointing direction of the beam. The physical collecting area of the beam cylinder (top+sides) is approximately  $130 \text{ km}^2$  for our observations, most of this area belonging to the sides of the beam. Figure 1 shows the distribution of trail orientations relative to the beam direction.

To verify that these measurements of trail orientation are physically reasonable (and hence that the monopulse measurements of the azimuth and altitude for the head-echoes in the beam are believable) we also examine the variation in trail length with trail orientation. We expect a priori that those trails coming closest to down the main beam will have the longest trails. For trails intersecting the beam at larger angles we expect nearly constant trail lengths reflecting the beam width only. For our average range (near 110 km), the beam has an approximate linear width (to the 3 dB points) of 2 km. In general we expect those trails at large angles to the main beam to have lengths of  $\leq 2 \text{ km}$ . Figure 2 shows the measured distribution of trail lengths versus trail orientation. The basic distribution is as expected, verifying our monopulse angle measurements as essentially correct. The scatter at lower angles begins to reflect growing numbers of head echoes which actually end in the main beam and hence the population of smaller trail lengths.

As a first approximation we take the average radiant deviation as the mean angle between meteoroids impinging on the beam and the cylinder sides and derive an equivalent collecting area of  $67 \text{ km}^2$ . As ALTAIR sees effectively ( $\geq 90\%$  of all head echoes) only the highest velocity meteor component ( $\geq 40 \text{ km s}^{-1}$ ) as head echoes, the sporadic population sampled for our pointing directions is almost exclusively that of

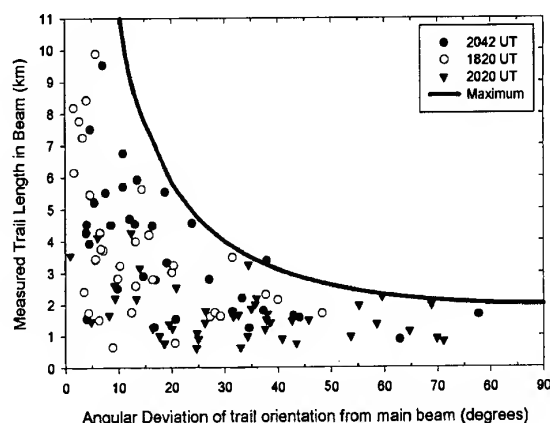


Figure 2. Measured trail length as a function of trail orientation relative to the main beam. The echoes recorded for all three measurement intervals are labelled. The solid curve shows the expected maximum trail length at a range of 110 km to the 3 dB points of the beam as a function of trail orientation.

the apex source. To a constant mass threshold, Taylor and McBride (1997) show the north apex source to represent 4% of the total integrated flux and covering the velocity interval from 40–70 km s<sup>-1</sup>. Using a mean velocity of 60 km s<sup>-1</sup> for ALTAIR head echo observations and scaling the Grün et al (1985) total interplanetary flux to this velocity we derive the curve shown in Figure 3. Using the observed average ALTAIR head echo flux of 18 km<sup>-2</sup> hour<sup>-1</sup> and scaling to the interplanetary flux curve for the total meteoroid population we get an equivalent total flux of 443 km<sup>-2</sup> hour<sup>-1</sup>, which from the curve is appropriate to a limiting magnitude near +11. Given all the uncertainties, the total integrated flux from the north apex source to a constant limiting mass could be a factor of two different from this 4% value, implying an uncertainty in the determination of the limiting magnitude of one stellar magnitude.

### 3.2. Numerical modelling applied to the question of limiting mass

The second approach to estimating masses for the ALTAIR head echo population is to model the deceleration curves for individual meteoroids. For each meteoroid we need  $v_{\text{inf}}$ , the ablation coefficient ( $\sigma$ ), initial mass and density (assuming a known shape factor), as well as the orientation of the trajectory to fully characterize the particle physically and compute an orbit. ALTAIR data only provides a small segment of the trail showing velocity as a function of height as well as providing the trail orientation. Hence we need to compute  $v_{\text{inf}}$ ,  $m_{\text{inf}}$ , density and the ablation coefficient. There are insufficient data from each head echo to compute all of these quantities uniquely. We therefore choose a very low ablation coefficient (0.0015 s<sup>2</sup> km<sup>-2</sup>) to provide a lower limit on the minimum mass and a maximum for the initial velocity for each echo. This is done using the gross

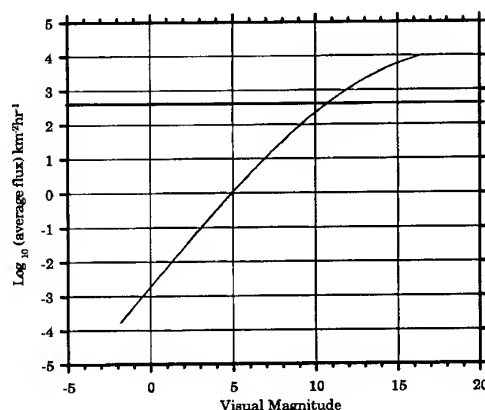


Figure 3. Comparison of the equivalent total flux from the interplanetary flux model of Grün et al. (1985) normalized to an encounter velocity of 60 km s<sup>-1</sup> with the corrected flux (assumed to be that of the apex source only) measured by ALTAIR. The bold horizontal line shows the overlap near +11 as the equivalent sensitivity of the system.

fragmentation model of Ceplecha et al. (1993), which provides model output in the form of velocity as a function of height. As well, we assume a density appropriate to the observed apex population, which is almost certainly cometary, of 800 kg m<sup>-3</sup>. We then iteratively match the observed velocity vs. height profile to provide an estimate of the minimum initial mass and upper limit for the velocity. We also determine the ballistic parameter (surface area/mass) defined as (Evans, 1965)

$$\eta = 2v\rho\cos\theta\left\{\frac{dv}{dh}\right\}^{-1} \quad (1)$$

where  $\eta$  is the ballistic parameter,  $v$  is the velocity as a function of time,  $\rho$  is the air density (determined from the MSIS-E model),  $\theta$  is the elevation of the radiant and  $h$  is the height. In Eq (1) we have assumed the meteoroid to be spherical and hence  $\eta$  is equivalent to the product of the meteoroid radius and density. An example of an echo with a modelled fit is shown in Figure 4. For echoes showing largely linear decelerations, the modelled ballistic parameters range from  $0.03 \leq \eta \leq 0.3$  kg m<sup>-2</sup>, with an average near  $8.5 \times 10^{-2}$  kg m<sup>-2</sup>. The range of minimum masses measured for our small sample of 18 UHF echoes vary from  $2 \times 10^{-11}$  kg to  $1 \times 10^{-8}$  kg with an average value of  $1.8 \times 10^{-9}$  kg based on this modelling approach.

## 4. ORBITS

The orbits found for our small subset (18) of UHF head echoes are similar to the orbital distribution of north apex source sporadic meteoroids as given in

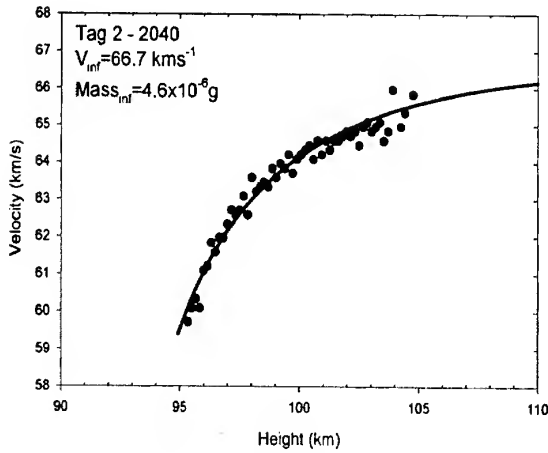


Figure 4. An example of the observed measurements of head-echo velocity as a function of height (black dots) and the numerical entry model fit following Cepveda et al. (1993) (line).

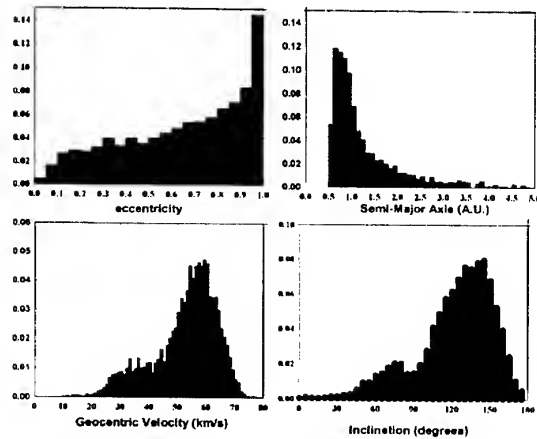


Figure 5. The normalized distribution of orbital elements for meteoroids from the north apex source taken from Jones and Brown (1993).

Jones and Brown (1993). Figure 5 shows the distribution of north apex meteoroids from orbital surveys taken from Jones and Brown (1993), while figure 6 is from our small ALTAIR orbital dataset. Table 2 shows all orbital data derived from our ALTAIR measurements.

The dominance of small number statistics in the ALTAIR data is apparent, but there exists gross similarities in semi-major axis and inclination between these data. The eccentricity is less comparable between these datasets and might reflect a true difference between the source character of the smaller ALTAIR population. One meteoroid orbit was interstellar and examination of the original monopulse data in detail does not show any unusual features (such as measurements which might indicate the echo occurred in a sidelobe). Based on the modelled initial velocity this meteoroid was  $7.4 \text{ km s}^{-1}$  beyond the interstellar velocity limit for its computed radiant. Indeed, the actual measured velocity is fully  $2 \text{ km s}^{-1}$  beyond the interstellar limit for the measured radiant. We

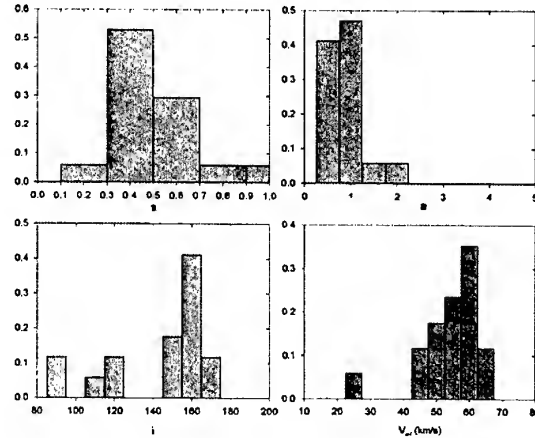


Figure 6. Normalized orbital element distributions for the population of ALTAIR observed meteoroids taken with the beam directed toward the north apex source. Compare to figure 5.

believe this to be a true interstellar meteoroid detection.

The original intent of the observation campaign, namely to record Leonid head echoes, has proven an elusive goal. In none of the orbits yet analyzed has any evidence of Leonid meteoroids been detected. This is perhaps in part due to the main beam being pointed within a few degrees of the nominal Leonid radiant. Such a geometry provides only a very small (of order a few  $\text{km}^2$ ) effective collecting area through the top of the beam for detection of Leonids. Indeed, using the measured Leonid flux in 1998 as given by Brown and Arlt (1998) of  $0.03 \text{ Leonids km}^{-2} \text{ hour}^{-1}$  and extrapolating directly using a mass-index value of 1.75 to our estimated limiting magnitude of +11, the equivalent Leonid flux at the time of our observations in 1998 corresponded to a Leonid rate coming down the main beam of 2 Leonids per hour.

Given that a total of only 17 minutes of UHF Leonid data have been analyzed to date, the lack of Leonids is not surprising. We also note that this computed Leonid rate is really an upper limit; in fact the effects of radiation pressure will completely remove Leonid meteoroids with a ratio of radiation pressure to gravitational force ( $\beta$ ) greater than 0.05. This represents a spherical Leonid of approximate magnitude +13, but the roll-off in number will certainly begin several magnitudes higher than this value due to non-spherical shapes for some meteoroids. Sato et al. (2000) also undertook observations of the Leonids on the same date as our ALTAIR data collection using the MU-radar in Japan and from 235 determined orbits also found no evidence for a signature from the Leonids.

## 5. CONCLUSIONS

Observations using the ALTAIR radar over a 17-minute period on 18 November, 1998 have been ana-

lyzed for orbital determination and mass of observed head-echoes. From the observed rates and an estimate of the collecting area in the main beam, a limiting magnitude sensitivity at UHF frequencies for the ALTAIR system of  $+11 \pm 1$  has been computed. The mean velocity of meteor head echoes recorded by ALTAIR was found to be  $56 \text{ km s}^{-1}$ . At this velocity, the flux-determined limiting sensitivity corresponds to  $3.6 \pm_{2.3}^{6.4} \times 10^{-10} \text{ kg}$ . The distribution of head echo trail orientations with respect to the main beam was found to average  $30^\circ$ , with no head echoes coming closer than  $2^\circ$  to the main beam pointing direction.

Applying the model of Ceplecha et al. (1993) to the velocity and height data we were able to determine lower bounds for the initial mass and upper limits for the velocity of a subset of the observed head echoes outside the sidelobes of the radar and with the best signal-to-noise ratios. These largest 18 echoes were found to have minimum modelled masses of  $1.8 \pm 2.8 \times 10^{-9} \text{ kg}$  in reasonable agreement with the absolute detection limit mass found independently from flux considerations.

The orbital distribution for the ALTAIR observed population is consistent with that determined from other techniques for larger meteoroids. The population represents a sample of the north apex source and we have found no evidence for any Leonids in the sample analyzed.

#### REFERENCES

- Brown, P. and J. Jones. A Determination of the Strengths of the Sporadic Radio Meteor Source, EARTH, MOON AND PLANETS, Vol. 68, 223, 1995.
- Ceplecha, Z., Spurny, P., Borovica, J., and J. Kečlikova, J. Atmospheric fragmentation of meteoroids, ASTRONOMY AND ASTROPHYSICS, Vol. 279, 615, 1993.
- Close, S. Hunt, S.M., Minardi, M.J., and F.M. McKeen. Analysis of Perseid meteor head echo data collected using the Advanced Research Projects Agency Long-Range Tracking and Instrumentation Radar (ALTAIR), RADIO SCIENCE, Vol. 35, 1233, 2000.
- Evans, J. Radio-echo studies of meteors at 68-centimeter wavelength, JOURNAL OF GEOPHYSICAL RESEARCH, Vol. 70, 5395, 1965.
- Grun, E., Zook, H., Fechtig, H. and R.H. Giese. Collisional Balance of the Meteoritic Complex, ICARUS, Vol. 62, 244; 272, 1985.
- Jones, J. and P. Brown. Sporadic meteor radiant distributions - Orbital survey results, MONTHLY NOTICES OF THE ROYAL ASTRONOMICAL SOCIETY, Vol. 265, 524, 1993.
- Jones, J. and A.R. Webster. Visual and radar studies of meteor head echoes, PLANETARY AND SPACE SCIENCE, Vol. 39, 873, 1991.
- Sato, T., Nakamura, T. and K. Nishimura. Orbit determination of Meteors using the MU radar, Transactions of the Institute of Electronics, Information and Communication Engineers, Vol E83-B(9), 1990, 2000.
- Taylor, A.D. and N. McBride. A radiant-resolve meteoroid model, in Proceedings of the Second European Conference on Space Debris, Eds. Kaldeich-Schurmann, B. and Bob Harris, ESA SP-393, Noordwijk, Netherlands, p. 375, 1997.

Time (UT)	$\theta, \phi$	Sun-centred	Total Rate	Main-beam rate	Collecting Area $\text{km}^2$	Limiting Magnitude
18:20	72, 43	10, 270	0.33	0.31	63	10.8
20:20	68, 357	9, 261	0.50	0.34	68	10.8
20:42	64, 302	9, 268	0.43	0.30	71	10.6

Table 1. Pointing directions for the ALTAIR radar on 17 November, 1998. The time of the start of each two minute data collection is given in the first column. The second and third columns given the pointing direction in local altitude ( $\theta$ ), azimuth ( $\phi$ ) and ecliptic sun-centred coordinates respectively (with the sun at zero degrees and the apex of the Earth's way at 270 degrees). The total measured head echo rate (per second) and the rate in the main beam only are also shown. Finally, the collecting area and equivalent limiting stellar meteor magnitude (see section 3.2) are given in the last two columns.

$V_\infty$	$\phi$	$\theta$	a	e	i	$\omega$	$\Omega$	q	Q	$\alpha_G$	$\delta_G$	$M_\infty$
62.0	300.6	62.4	1.18	0.223	163.9	233.1	235.317	0.9166	1.44	146.17	22.34	8.80E-10
63.6	306.5	66.7	2.03	0.518	160.3	194.2	235.317	0.9784	3.09	149.09	24.08	4.60E-09
62.0	283.6	66.5	1.73	0.446	179.4	204.5	235.302	0.9612	2.50	144.06	14.64	3.20E-09
49.8	278.1	59.1	1.04	0.507	167.6	115.1	55.318	0.5151	1.57	131.11	12.29	9.60E-10
73.3	317.5	63.1	1.37	0.363	156.5	122.9	235.317	0.8684	1.86	160.17	21.49	5.60E-09
63.1	314.5	61.8	1.23	0.213	151.6	207.6	236.326	0.9687	1.50	151.80	27.36	2.50E-10
77.5	303.0	63	1.32	0.423	165.0	102.4	235.316	0.7579	1.87	161.38	16.00	1.10E-08
55.2	285.4	61.6	1.14	0.387	180.0	93.3	55.607	0.6985	1.58	137.06	16.43	5.50E-10
63.5	310.9	25.4	0.52	0.905	33.0	358.7	235.317	0.0500	0.99	148.22	26.30	1.90E-11
32.3	3.8	58.6	-1.59	1.609	91.1	192.7	235.305	0.9738	-	175.31	67.46	6.30E-10
59.7	5.8	50.5	0.96	0.217	111.6	70.1	235.305	0.7523	1.17	171.54	39.95	2.70E-10
68.8	355.7	51.4	0.79	0.366	129.0	31.5	235.304	0.4976	1.07	165.61	30.80	2.70E-10
82.5	68.9	53.3	0.89	0.763	153.6	35.1	235.304	0.2106	1.57	174.78	12.08	3.40E-10
69.5	123.4	47.3	1.04	0.101	98.1	113.8	235.307	0.9343	1.14	173.14	48.76	2.00E-10
71.6	6.3	47.9	0.70	0.565	125.0	24.2	235.304	0.3057	1.10	169.65	27.93	1.30E-10
75.2	25.2	58.5	0.89	0.247	162.8	307.9	235.220	0.6727	1.11	144.37	22.84	2.90E-09
70.4	56.1	56.4	0.79	0.288	160.5	22.5	235.220	0.5636	1.02	155.08	19.92	1.70E-10
75.2	16.9	60.2	1.01	0.284	162.8	281.6	235.220	0.7261	1.30	142.34	23.65	1.20E-10

Table 2. Head echo trail orientation, orbital elements and modelled initial mass.  $\phi$  and  $\theta$  are the radiant local azimuth and altitude respectively;  $V_\infty$  is the computed initial velocity in  $\text{kms}^{-1}$ ; a is the orbital semi-major axis in A.U.; e is the eccentricity; i is the inclination;  $\omega$  is the argument of perihelion;  $\Omega$  is the longitude of the ascending node; q is the perihelion distance in A.U.; Q is the aphelion distance in A.U.;  $\alpha_G$  and  $\delta_G$  is the geocentric location of the radiant and  $M_\infty$  is the modelled initial mass in kilograms.

## **Fireballs, Bolides and Meteorites**

## ON THE RELATIONSHIP BETWEEN ASTEROIDS, FIREBALLS AND METEORITES

A.E. Rosaev<sup>1</sup>

*FGUP NPC Nedra, Svobody 8/38, 150000 Yaroslavl, Russia, rosaev@nedra.ru*

Best of interest searching for parental bodies for meteors, fireballs and meteorites with well determined orbits. There are two ways to study this problem. First way - investigation close orbits by one of number of empirical criteria like criterion Southworth-Hawkins. The second way is to study the orbit intersection statistics.

The fireballs of Prairie network and meteorites with well determined orbits, was took into account. If take the suggestion, that similar objects are form in collisions NEA with each other, possible expect that crossing the orbits of asteroids and fireballs, or meteorites will indicate the most recent events of mutual collisions NEA.

### 1. INTRODUCTION. USED METHODS

There are four known meteorites, orbits which determined on basis photographic observations. This chondrites Phibram (Czechoslovakia, 1959 IV.7.81), Lost City (USA, 1970, I.4.093), Innisfree (Canada, 1977 II.6.0955), Peekskill (USA, (9.X.1992). In addition to this list some meteorites, orbits of which was determined in [1], was added.

Best of interest searching for parental bodies for these meteorites. This problem may be solved by two ways. First way - investigation close orbits by one of number of empirical criterion's like criterion Southworth - Hawkins. The second way is to study the orbits intersections statistics. We apply both methods on this work.

$$D = \left\{ (e_1 - e_2)^2 + (q_1 - q_2)^2 + 4 \left[ \left( \sin \frac{\Delta i}{2} \right)^2 + \sin i_1 \sin i_2 \left( \sin \frac{\Delta \Omega}{2} \right)^2 \right] \right\}^{1/2}$$

$$+ \frac{(e_1 + e_2)^2 \left( \sin \frac{\Delta \omega}{2} \cos \frac{\Delta i}{2} \cos \frac{\Delta \Omega}{2} + \cos \frac{\Delta \omega}{2} \sin \frac{\Delta i}{2} \cos \frac{\Delta \Omega}{2} \right)^2}{1 - \left[ \left( \sin \frac{\Delta i}{2} \right)^2 + \sin i_1 \sin i_2 \sin \frac{\Delta \Omega}{2} \right]^2} \}^{1/2}$$

$$\Delta i = i_1 - i_2, \quad \Delta \omega = \omega_1 - \omega_2, \quad \Delta \Omega = \Omega_1 - \Omega_2$$

where  $\omega_i, \Omega_i, e_i, i_i$  - argument of perihelion, nodal angle, eccentricity and inclination of the first and second objects.

For the simplify feature of vicinity of elements was applying also factor to:

$$K = \left\{ (e_1 - e_2)^2 + (q_1 - q_2)^2 + \frac{(i_1 - i_2)^2 + (\omega_1 - \omega_2)^2 + (\Omega_1 - \Omega_2)^2}{360} \right\}^{1/2} \quad (2)$$

The problem of determination of the minimal distance between elliptic orbits reduced to solving the system of equations:

$$\begin{aligned} \Delta^2 &= (x_1 - x_0)^2 + (y_1 - y_0)^2 + (z_1 - z_0)^2 \\ x_j &= R_j (\cos u_j \cos \Omega_j - \sin u_j \sin \Omega_j \cos i_j) \\ y_j &= R_j (\cos u_j \sin \Omega_j + \sin u_j \cos \Omega_j \cos i_j) \\ z_j &= R_j \sin u_j \sin i_j \end{aligned} \quad (3)$$

$$u_j = \lambda_j - \Omega_j, \quad j = 0, 1$$

We suppose the new method of numeric search of this system, based on a suggestion, that minimal distance reach close to point, determined by conditions:

$$\begin{aligned} \lambda_1 = \vartheta_1 - \omega_1 - \Omega_1 = \lambda_2 = \vartheta_2 - \omega_2 - \Omega_2 = \lambda \\ r_1 = r_2 = r \end{aligned} \quad (4)$$

More, the expressions for minimal distance between orbits determination :

$$\Delta_s^2 = r^2 \sum (a_i \cos \lambda + b_i \sin \lambda)^2 \quad (5)$$

where:

$$\lambda_{\min} = 0.5 \operatorname{atg} \frac{2 \sum a_i b_i}{\sum a_i^2 - b_i^2} \quad (6)$$

$$\begin{aligned} a_1 &= \cos^2 \Omega_1 + \sin^2 \Omega_1 \cos i_1 - \cos^2 \Omega_2 - \sin^2 \Omega_2 \cos i_2 \\ b_2 &= \sin^2 \Omega_1 + \cos^2 \Omega_1 \cos i_1 - \sin^2 \Omega_2 - \cos^2 \Omega_2 \cos i_2 \\ a_2 &= \sin \Omega_1 \cos \Omega_1 (1 - \cos i_1) - \sin \Omega_2 \cos \Omega_2 (1 - \cos i_2) \\ b_1 &= \sin \Omega_1 \cos \Omega_1 (1 - \cos i_1) - \sin \Omega_2 \cos \Omega_2 (1 - \cos i_2) \\ a_3 &= -\sin \Omega_1 \sin i_1 - \sin \Omega_2 \sin i_2 \\ b_3 &= \cos \Omega_1 \sin i_1 - \cos \Omega_2 \sin i_2 \end{aligned}$$

allow us to enter a new criteria for genetic related orbits search:

$$DN = \sum \Delta_i / n$$

where  $\Delta_i$  determined (5)-(6). The similar criteria was supposed by Danielsson [2], but presented consideration have some advantages. First of all - it clear dependence from time.

## 2. NEAR EARTH ASTEROID'S ORBITAL INTERSECTIONS STATISTICS

As followed from our previous work [3], the distribution of intersection of Near Earth Asteroids (NEA) significantly non-homogenous. It is seems most easy for cases triplex quasi-intersections of NEA's orbits (Fig.1-2, table 1).

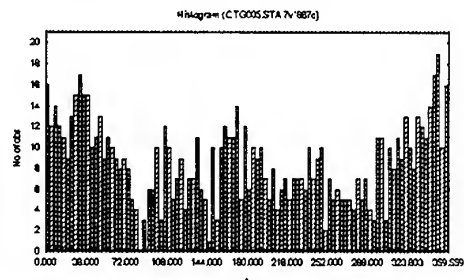


Fig.1. Distribution of main orbital intersections NEA-NEA ( $d < 0.005$  a.u)

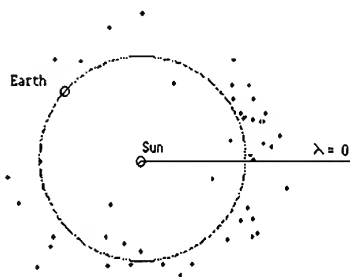


Fig.2. Distribution of main orbital intersections NEA-NEA ( $d < 0.005$  a.u)

In table the information about possible related fireballs of Prairie Network, calculated by orbital elements [4-5], is given (last column).

Table 1  
The location of some possible cases NEA's triplex orbits intersections

N	Name of minor planet	Heliocentric distance, a.u.	Longitude, degree	Possible related meteorites	Possible related fireball
1	Geographos	1.05	338	Peace River	48,159,160
	1986 PA	$\pm 0.02$	$\pm 4.0$		81
	Florence				
	Khufu				
	Pan				
	Wilson-Hilton				
2	Magellan	1.27	344	Homestead	23,59,63
	Pele	$\pm 0.04$	$\pm 2.0$	Tzarev	91,129,165
	Nefertiti				86,182,193
	Don Quixot				167(?)
	Ubasty				
	Mithra				
3	Midas	1.08	0	Kainsaz	17,90,166
	1980 PA	$\pm 0.01$	$\pm 3.0$		171,164
	Cuyo				167
	Verenia				
	Toutatis				
4	Alinda	1.10	112	Bruderhaim	73,53(?) 289
	Aten	$\pm 0.05$	$\pm 5.0$		
5	Geographos			Pultusk	74,75,85(?)
	Amor				186
	Seneca				

## 3. PRAIRIE NETWORK FIREBALLS ORBITAL INTERSECTIONS

Obviously, that fireballs and meteorites - an essence of bodies, having potentially unstable orbits and, as an effect, small time life's. If take sufficiently natural suggestion on that, that similar objects are form in collisions NEA with each other and with comets. possible expect that crossing the orbits of asteroids and fireballs, or meteorites will indicate us on the most close on a time-nor events of mutual collisions NEA. Really, the distribution nearly intersected orbits in the system NEA-fireball and fireball-fireball show significant non-homogenous. However, as would be expected, distribution data are not same that such for the system NEA-NEA. Possible select about 10 areas to concentrations the cross points of orbits of fireballs and NEA. Probably, they correspond to events the most close on a time of disastrous events.

The longitude distribution of orbital intersections is given at the Fig 3-5.

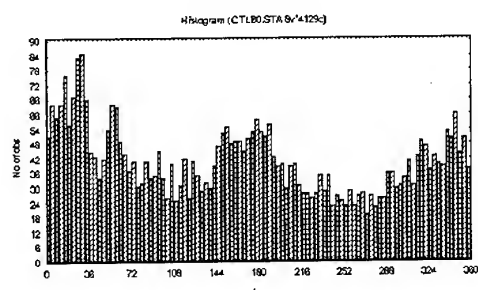


Fig 3. Distribution of orbital intersections NEA-fireballs ( $d < 0.035$  a.u., 350 NEA, 379 fireballs)

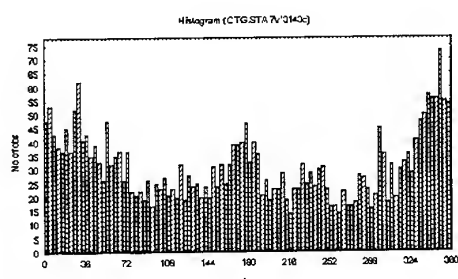


Fig 4. Distribution of orbital intersections NEA-NEA ( $d < 0.035$  a.u., 350 NEA)

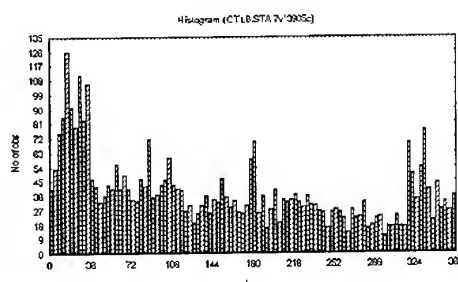


Fig 5. Distribution of orbital intersections fireball-fireball ( $d < 0.035$  a.u., 379 fireballs)

It seems, that distribution of fireball-fireball orbits intersections significantly differ from another two distributions. It may be easy explained. Some of fireballs may appear at impacts of small bodies on asteroid's surface and not related with a large collisions. In additions, number of fireballs may be related with comets.

#### 4. POSSIBLE ORIGINS OF THE FEW METEORITES

In our previous work we consider possible origin of meteorites with photographic registered orbits - Prhram (Czechoslovakia, 1959 IV.7.81), Lost City (USA, 1970, I.4.093), Innisfree (Canada, 1977 II.6.0955), Peekskill, mainly by using Southwork - Hawkins criterion (1). The main conclusions of these investigations[6] - most possible genetic related body for Prhram is minor planet Mithra, in according with result [7].

In table 2 we give minimal distances between orbit of Peekskill and orbits of Near Earth Asteroids (NEA).

Table 2

Possible genetic related asteroids for Peekskill meteorit

	$\Delta_{min}$	Longitude
Orthos	0.012175	-5.98
** 1980PA	0.038614	34.54
** Wilson-H'ton	0.032776	41.13
Toutatis	0.001068	12.82
Rees	0.014019	183.90
Betulia	0.000438	245.33
* Bacchus	0.000815	228.89
* Mera	0.012151	228.69

Below we apply method of minimal distance between orbits for meteorites, orbits of which determined by craters distributions [1], table 3.

Table 3

Orbital elements of few meteorites, reconstructed by craters position [1]

NAME	Type	a	e	i	$\Omega$	$\omega$
Pultusk	H5	2.53	0.619	2	310	161
Mocz	L6	0.82	0.24	33	314	26
Home-stead	L5	1.36	0.355	9	144	306
Tzarev	L5	1.7	0.434	2	254	158
Lowicz	MS	0.66	0.805	76	351	18
Kainsaz	CO3	3.41	0.704	0.1	170	0
Crymka	LL3	1.44	0.314	20	301	167
Sykhote-alin	OGG	1.41	0.303	6	322	1.71
Kuna-shak	L6	10.4	0.903	20	80	178
Brudre-heim	L6	2.81	0.647	2	343	176
Peace river	L6	1.00	0.11	1	190	262
Allende	CV3	1.25	0.215	13	140	346
Dhajala	H3-4	1.37	0.418	20	308	111
Kirin	H5	1.78	0.474	7	168	328

The main results of our investigation are given in tables 4-5. In the first of them we determine for each meteorite groups of most possible genetic related objects, in mutual collision of which it can appear, and according heliocentric distance  $R$  and longitude. In the table 5 we present a most possible parent objects.

Table 4  
Possible genetic related asteroids for few meteorites with known orbits

Meteorite	Related asteroids	$R$ , a.u.	Longitude, rad	Mean minimal distance, a.u.
Peace River,	Geographos,	1.03	5.8	0.035
	Florence, Toutatis			
	Khufu, Castalia,	1.04	5.7	0.006
	Toro, Orpheus	0.88	1.7	0.008
	Midas, Aristaeus, Asclepius	0.98	3.1	0.005
Pultusk	Icarus, Anteros	1.10	4.5	0.005
	1980PA, Sisyphus,	1.08	1.1	0.034
	Toutatis, Nereus,	1.00	1.4	0.010
	Phaethon			
	Amor, Geographos, Seneca	1.12	2.8	0.004
Tzarev	1986LA, 1980WF, Ganymed, Cerberus	1.30	0.5	0.020
	Cuyo, Midas, 1980PA	1.07	0.0	0.007
	Ra-Shalom, Pele, Krok, Nefertiti,	1.20	5.9	0.020
	1982RB, Magellan			
	Alinda, Aten	1.10	1.9	0.005
Allende	1982RB Magellan	1.33	0.0	0.020
	Toro Hathor Nereus	0.98	2.1	0.020
Dhajala	Ra-Shalom, Krok, Verenia, 1986PA, Beltrivata	1.22	5.5	0.005
	Nereus Quctzalcoatl	1.00	2.35	0.020
Kainsaz	Midas Asclepius Bacchus Mera	1.01	3.12	0.015
Kunashak	Oljato Dionysus 1990MU	1.01	4.4	0.035
Bruderhaim	Eros, Alinda, Aten, Bacchus Mera	1.10	2.0	0.017
		1.33	3.9	0.022
Homestead	Antinous, 1982RB, Don Quixote, Eric	1.30	5.9	0.020
	Ra-Shalom	1.06	0.3	0.0003
Kirin	Midas, Asclepius	1.05	3.2	0.024
	Poseidon, Ninkasi	1.65	4.3	0.021
	Mithra	1.85	0.2	0.0005
SIH-AL	(?) Cerberus, 1980WF	1.48	0.3	0.025

## CONCLUSIONS

The main results of this work are in following:

1. The minimal distances between orbits of minor bodies  $d$  is a important criterion of genetic relation determination. The longitude distribution of minimal distance points coordinates significantly non-homogeneous. The method of the fast calculation  $d$  is given;
2. Some of known meteorites and fireballs have NEA as a most possible parent bodies. Based on used criteria, the most possible parent asteroids for some meteorites are given;
3. The longitude distributions of minimal distances between orbits NEA-NEA and fireballs-fireballs are significantly differ;

In case of a general conclusion of this work, the hypothesis of an very close relation studied meteorites with NEA put forward.

Table 5  
Orbital elements for possible genetic related asteroids and meteorites

Object	$\Delta_{min}$	$e$	$a$	$i$ (rad)	$w$ , rad	Node (rad)
1 Prhigram	-	0.674	2.42	0.182	0.30	4.22
Mithra	0.04	0.662	2.19	0.053	1.44	2.94
2 Tzarev	0.005	0.434	1.70	0.035	2.75	4.43
1980PA		0.459	1.93	0.038	2.20	4.57
3 Pultusk	0.006	0.619	2.53	0.035	2.81	5.41
Seneca		0.581	2.49	0.267	0.59	2.95
4 Bruderhaim	0.01	0.647	2.81	0.035	3.07	5.99
Alinda		0.563	2.49	0.162	6.10	1.93
5 Peace River	0.001	0.11	1.00	0.017	4.57	3.31
Castalia		0.483	1.06	0.155	2.11	5.68
6 Peekskill		0.410	1.49	0.080	5.37	0.30
1980PA	0.038	0.459	1.93	0.038	2.20	4.57
Bacchus	0.001	0.349	1.07	0.16	0.96	0.58
7 Allende	0.005	0.215	1.25	0.226	6.03	2.44
Nereus		0.361	1.49	0.025	2.75	5.49

## References:

1. Tevetkov V.I. Atmospheric splitting of large meteor bodies and dispersion fragments of meteorites on Earth's surface // Abstr. Thes., Kazan, 1985, 18 p.
2. Danielsson L. Statistical arguments for asteroidal jet streams. - // *Astroph. Space Sci.* - 5.- P.53-58
3. Rosacv A.E. (1997) Catalogue of semi crossing orbits of the Earth Approach Asteroids // Vologda. 124 p.

4. McCrosky R.E., Shao C.-Y., Posen A. Fireballs of Prairie Network: I. Common informations and orbits. *Meteoritics*, v. 37, 1978, p.44-59.
5. Ceplecha Z. Fireballs of European Network. *Meteoritics*, v. 37, 1978, p.60-68.
6. Rosaev A.E. On possible parent bodies of Innisfry, Lost City and Prhibram meteorites. // *Astron. Vestn.*, V.28, 1994, N 6, P.119-122.
7. Drummond J.D. (1991) Earth-Approaching Asteroid Streams *Icarus*, 89, 14-25

# GLOBAL INFRASONIC MONITORING OF LARGE BOLIDES

D. O. ReVelle

*Los Alamos National Laboratory, P.O. Box 1663, MS J577, Earth and Environmental Sciences Division,  
Atmospheric and Climate Sciences Group, Los Alamos, New Mexico 87545 USA  
Email: dor@vega.lanl.gov*

## ABSTRACT

Using recent infrasonic data (1995-2001) and older infrasonic data recorded by AFTAC (1960-1974), we have refined our estimates of the global influx rate (cumulative influx) of large bolides with sufficient strength to deeply penetrate the atmosphere (below ~ 50 km). The number of bolides arriving as a function of their initial source energy has been estimated from a least-squares curve-fit of our database of 19 bolides (for a source energy > 0.053 kt) with the resulting values and an estimate of the associated statistical counting errors:  $30.3 \pm 6$  bolides at  $\geq 0.1$  kt,  $5.8 \pm 2$  at  $\geq 1$  kt and  $0.84 \pm 0.25$  at  $\geq 15$  kt. In this work we also used these estimates to infer the recurrence interval for energy levels slightly outside the original source energy range, The Tunguska bolide of 1908 (~10 Mt) is a prime example of a previously observed body of great interest. Almost regardless of how we analyze the recent data, the conclusion is that bolides with Tunguska type energy levels should reoccur on the average every  $120 \pm 10$  years.

## 1. INTRODUCTION AND OVERVIEW:

Reliable influx rate estimates come from a large variety of sensors including the Lunar cratering record, Spacewatch telescope and other ground-based CCD systems, ground-based photographic meteor-fireball Networks (USA, Canada, Czech Republic, etc.), infrasonic pressure sensor arrays, US DoD Satellites (optical and infrared sensors) and other space platforms, radar systems, etc. Previous estimates have varied widely (by factors > 100 times), due largely to the uncertainties in properly calibrating various sensors.

In the last 20 years it has become possible to more reliably estimate the infrasonically measured contribution to the total NEO global influx using a better estimates of source energy as a function of readily observable parameters,

estimates of percent coverage of the Earth as a function of source energy and season, a wide distribution of large arrays on global scales with the proper sensor response

## 2. APPROACH

Given the inputs of the bolide source energy (from the AFTAC empirical relationship, etc.), the percent coverage of the Earth as a function of source energy and season, i.e., the relative detection probability of each bolide event and the total time of operation of the infrasonic network, we can make cumulative energy influx predictions for large bolides.

Let:

$\Sigma N$  = Cumulative (integral) number of bolides at any source energy,  $E_S$

$A_E$  = Surface area of the Earth

Percent coverage =  $f(E_S, \text{season}) \cdot A_E$ , where the function,  $f$ , is known (AFTAC network).

$\Delta t_0$  = Time of operation of the infrasonic network

$E_S$  = Bolide source energy

$N(E_S) = \Sigma N \cdot \{1/[f(E_S, \text{season}) \cdot A_E]\} \cdot \{1/\Delta t_0\}$

where

$N(E_S)$  = cumulative number of bolides/(over the Earth per unit time) as a function of the deduced source energy

We have been provided with raw data that have been developed into least-squares curve-fits: (Olmstead and Leies, personal communication, 1978) of the USAF AFTAC empirical estimates for global infrasound array detection probabilities. These empirical results were obtained for a quasi-global network operation that demanded three-station detection and an additional technique for verification of the detection. The original source energy range was from  $0.20 \leq E_S \leq 100$  kt.

i) Winter:

$$P_D(\%) = 11.74 \cdot \{E_s / 2.0\}^{0.375}; r^2 = 0.9928$$

ii) Summer:

$$P_D(\%) = 12.5 \cdot \{E_s / 2.0\}^{0.416}; r^2 = 0.8816$$

$$P_D(\%) = 11.35 + 15.19 \cdot \ln\{E_s / 2.0\}; r^2 = 0.9870$$

The much higher correlation curve-fit for summer systematically produces negative, i.e., unphysical  $P_D$  values at small source energies (< 1 kt) that are consistently positive for the same source energies in winter. To avoid this problem, the lower correlation, curve-fit relation was used instead throughout the summer period.

## 2.1 Available source energy prediction methods

Among the many methods available to predict source energy, we can appeal to the following:

- i) AFTAC semi-empirical, wave period at maximum amplitude approach: Olmstead and Leies (1979)-for the Stratospheric acoustic return (phase)
- ii) Los Alamos wind-corrected amplitude approach: Mutschlechner and Whitaker (1988): For point source-near surface explosions
- iii) Acoustic efficiency approach: Cox (1958): For point source-near surface explosions
- iv) Cylindrical line source amplitude and wave period approach: ReVelle (1976); Source altitude effects included; Also, a separate wave period approach for line sources
- v) Lamb wave mode approach: Pierce-Posey (1971): For point source-near surface explosions-Generally, Lamb waves are only important for very large sources. Previously, ReVelle and Delinger (1981) used this approach to analyze the Lamb waves from bolides compared to the original formulation of Pierce and Posey (1971).
- vi) Combined Lamb/wind-corrected amplitude approach: ReVelle and Whitaker (1996): For point source-near surface explosions

- vii) Point source, multi-modal wave synthesis: Pierce et. al. (1976)- Source altitude explicitly included
- viii) Line source, acoustic-gravity wave results: Golitsyn et al. (1977)

We have decided in our analysis to use the semi-empirical yield-period relation discussed along with our reasoning directly below.

## 2.2 Semi-empirical yield-period relationship: Olmstead and Leies (1978)

This approach was derived from a "quasi-global" network of widely spaced arrays, with a minimum of 3 arrays being required for the detection of infrasonic waves at large ranges. These signals all had propagation in the stratospheric sound channel from large near-surface nuclear explosions (below ~15,000 feet). The nuclear explosion yield,  $Y$  was assumed to be equal to one-half of the source energy,  $E_s$ , where the factor of two accounts in an approximate way for the large amount of electromagnetic energy radiated during the detonation of a nuclear "fireball". The empirical relation developed by the US Air Force can be written as ( $1 \text{ kt} = 4.185 \cdot 10^{12} \text{ J}$ ):

$$E_s = 2 \cdot \{\tau / 5.92\}^{3.34}, E_s / 2 < 100 \text{ kt}$$

$$\log(E_s / 2) = 3.34 \cdot \log(\tau) - 2.58; E_s / 2 < 100 \text{ kt}$$

where

$\tau$  = Observed infrasonic wave period at the maximum signal amplitude (only for wave frequencies  $\gg$  acoustic-cut-off frequency)

Since previous influx estimates have been made using this formula or a variant of it, we decided to continue to use it for the analysis of the new data. In ReVelle and Whitaker (1999), the equations for line source blast waves were used to analyze the bolide event on 11/17/1999. Very good agreement was obtained between infrasonic source estimates and the other techniques. Since all the new events other than this one were at much greater range we decided to use an energy relation that was range independent in order to simplify the analysis.

Also, in order to process these data, we could choose to either average the wave periods from all arrays detecting a specific bolide before computing a source energy or alternatively, we

could compute and evaluate all of the individual values at each array element for a specific bolide. We decided to average the wave periods and produce a single average energy for each event rather than having as many energy estimates as there were array elements detecting a specific bolide. This choice of the data analysis does have a small effect on the results quoted later below.

The source heights were assumed to be relatively low and certainly below the Stratopause (about 50 km). Thus, most of the recorded objects are likely to be deeply penetrating and of "relatively strong" composition, i.e. of bolide group I. or possibly group II.

### 2.3 Line source and modified line source : Observed characteristics

Previously bolide observations have been made over ranges from about 100 to ~14,000 km with the following properties:

- 3 Wave periods: 0.5 s to > 5 min.
- 4 Amplitude: 0.2 to 160  $\mu$ bars: 0.02-16 Pa
- 5 Source energies :  $\sim 10^{-6}$  kt to > ~10 MT

The observed signal characteristics are similar to other explosive manmade and natural impulsive type sources: The signals generally exhibit Lamb waves (for the larger sources), multi-path (multi-phase) arrivals, with geometric and material signal dispersion effects, etc.

Similarly, most seismic signals from bolides have been observed as "forced" air-coupled Rayleigh waves or as "free" direct Earth impact waves (P and S types) and as seismo-acoustic coupled signals.

## 3. GLOBAL INFRASONIC INFLUX ESTIMATES

### 3.1 Previous infrasonic results (cumulative number of bolides per year over the earth)

These analyses were first carried out by Shoemaker and Lowery (1968). It was later discovered that the US Army Signal Corps yield-period relation was not properly calibrated (E.M. Shoemaker, personal communication, 1972). For 9 bolides, including Tunguska, they found the result:

$$N(E \geq E_s) = 2 \cdot 10^2 / E_s$$

Next, Wetherill and ReVelle (1978) and later ReVelle (1980) used a proper source energy-wave period calibration provided by the USAF (AFTAC) and adjusted for the end height effects and initial kinetic energy, rather than simply the kinetic energy at the terminal release height.

For 10 bolides, not including Tunguska:

$$N(E \geq E_s) = 10.4 \cdot E_s^{-0.87}$$

ReVelle (1997) additionally used 4 new bolides that were observed at Los Alamos and elsewhere since the time of the original AFTAC data. For 14 bolides, not including Tunguska, he found that:

$$N(E \geq E_s) = 7.17 \cdot E_s^{-0.731}$$

### 3.2 Recent bolide infrasonic data: 1994-2001

We have again revised our cumulative influx rate estimates, uncertainties and implications using 9 additional bolides (5 new bolides since 1997). We have not included several bolides that were either detected by only one array or which were not enough far away to use the AFTAC energy relation in a reliable manner, etc. The bolides that were specifically omitted included the Kincardine bolide (9/16/66), the Wyoming skip-fireball (8/10/72), the Marshall Islands bolide (2/01/94), the Borneo bolide (2/18/00), the Tagish Lake meteorite fall (1/18/00) and the Moravka meteorite fall (5/06/00). Thus, the inferred influx rate is an absolute minimum.

We tried to analyze the data that are now available in several different ways, only three of which we will report on here. These included using the AFTAC empirical relation for the source energy,  $E_s$ , but only using the newest infrasound data from 1995- 2001. For an observing time of 5.41 years, we determined that:

$$N(E \geq E_s) = 9.53 \cdot E_s^{-0.736}, r^2 = 0.997$$

using the Baja, CA, 4/23/01 bolide = 0.81 k (see below).

Next we combined the AFTAC data and the new infrasound data into a single data set for a total observing time of 19.084 years and we found that:

$$N(E \geq E_s) = 5.84 \cdot E_s^{-0.716}, r^2 = 0.9464$$

using the Baja, CA, 4/23/01 bolide = 11 kt.

For this situation, the total energy flux = 219.07 kt/year on the Earth (for  $0.053 \leq E_s \leq 1000$  kt), with a corresponding total mass flux =  $5.66 \cdot 10^6$  kg/year on the Earth (assuming  $V = 18$  km/s for the initial mass range from  $1369 \leq m_{\infty} \leq 2.84 \cdot 10^7$  kg).

Finally, we repeated the above procedure for all of the available data assuming the Baja, CA bolide of 4/23/01 assuming it to be = 0.81 kt and determined the result:

$$N(E \geq E_s) = 5.66 \cdot E_s^{-0.724}, r^2 = 0.954$$

### 3.3 Comparisons against previous influx estimates (ReVelle, 1997- AFTAC data):

ReVelle (1997) determined that at a source energy of 0.10 kt (1 kt), 38.59 (7.17) bolides per year would occur (on the average over earth). Also, at a source energy of 15 kt, there were ~0.99 bolides per year over earth predicted. Events with a source energy of 10 Mt (similar to that of Tunguska) are predicted to occur once every 117.1 year, but this is clearly an extrapolated value outside the original energy range of the observations. Using the newest infrasound data (observing time = 5.41 years) and using  $E_s = 0.81$  kt, for the 4/23/01 Baja, CA bolide, we found that at 1 kt, 9.52 bolides were predicted per year over the Earth, at 15 kt, we found 1.30 per year, while for Tunguska (~10 Mt), we found a reoccurrence every 92.6 years. Using  $E_s = 11$  kt for the 4/23/01 Baja, CA: bolide, we found 10.98 bolides/year over the Earth and at 15 kt, we found 1.80 /year, while for Tunguska we found a rate of reoccurrence of 42.6 years. When we combined the original AFTAC data with the new data for all bolides whose source energies exceeded 0.053 kt (using  $E_s = 11$  kt for the 4/23/01, Baja, CA bolide), we found that at a source energy of 0.10 kt and 1 kt, there were 30.34 and 5.84 bolides per year predicted over the earth. At a source energy of 15 kt, there were 0.84 bolides per year predicted over the earth and finally at a source energy of 10 Mt (Tunguska) a rate of reoccurrence of every 124.7 year was predicted.

### 3.4 Further comments:

As shown in Cepelcha (1997), there are probably selection effects that are affecting our results since cometary type bolides generally do not penetrate deeply enough to generate a blast wave source. Also, there is a small energy limit of ground-based detection even for chondrites. ReVelle (1976) has shown that there is a minimum blast radius ( $R_0 > \sim 10$  m) for bolides, below which we do not expect signals to reach ground level. This is due to very heavy wave absorption effects above 70 km for small energy sources.

In addition, extended line source effects generally produce ray paths that suffer a smaller amount of refraction and can more easily be detected at ground level. The original AFTAC source energy estimates were expected to be accurate only for the range from  $0.5 \cdot E_s \leq E_s^* \leq 2.0 \cdot E_s$  which was originally derived for low altitude nuclear explosions observed at very great horizontal ranges from the explosion at altitudes below ~4.74 km or ~0.70 pressure scale heights. The combination of possible source altitude effects on the wave period, combined with the fact that the kinetic energy of the bolide at the terminal point is often significantly below that at the top of the atmosphere was previously shown by ReVelle (1980) to be nearly a compensating effect.

We have also estimated statistical counting errors for our results. We have used the following definitions:

Let:

$N$  = number of bolides/year predicted at source energy,  $E_s$ .

$N^*$  = number of bolides with source energy  $\geq E_s$ .

The statistical counting error is given by the standard relationship  $\pm N/\{N^*\}^{0.50}$ . The values of these parameters for the final influx result is given in Table 2. below.

## 4. MINIMUM BOLIDE ENERGY FOR GROUND-BASED INFRASONIC DETECTION

There is a minimum kinetic energy,  $KE_{\min}$  at which bolide infrasound can be detected at the ground, i.e.,  $\sim 1.55 \cdot 10^{-5}$  kt. This is the energy of the bolide that Kraemer and Bartman (1981) detected (US PN42556) at 130 km in range, which had the following entry and recorded infrasonic properties:

- i)  $V = 16.5$  km/s for  $\sim 320$  g bolide (Maximum stellar magnitude brightness,  $\sim 5.1$ )
- ii) 0.21 seconds period at 2.3 microbars amplitude,  $\sim 5$  s signal duration

Subsequent reverse ray tracing missed the photographed (two camera station) trajectory by  $< 410$  m.

As noted earlier, ReVelle (1976) found the minimum ground, detectable blast radius,  $R_0$  ( $\equiv Ma \cdot d$ )  $\approx 10$  m due to atmospheric absorption losses at higher frequency (for bolide sources with smaller  $R_0$ ). Direct manipulation of the expression for the bolide KE can be shown to be proportional to  $R_0^3$  and to  $V^{-1}$ . For a spherical Group IIIA bolide with  $V = 30$  km/s,  $R_0 = 10$  m and a bulk density  $= 1000$  kg/m<sup>3</sup>, a minimum detectable kinetic energy  $= 6.2 \cdot 10^{-5}$  kt is predicted. This value is in quite good agreement with the very small meteor that was detected by Kramer and Bartman and quoted above. Also, bolide sources  $< \sim 10^{-5}$  kt cannot penetrate the atmosphere deeply enough to produce a line source blast wave or even if they could the heavy absorption of the signal would not allow detection at ground level. Since typical shower meteors have kinetic energies  $> \sim 10^8$  times smaller than the minimum source energies quoted above, we certainly do not expect infrasound from typical shower meteors to be detected infrasonically. This was also noted earlier in Opik (1958), i.e., sound waves at these corresponding high frequencies that are launched downward toward the ground from altitudes above  $\sim 80$  km will suffer very large absorption by viscous and heat conduction effects. (For  $R_0 \leq 10$  m, the initial bolide associated wave frequencies are typically  $\geq 10$  Hz at a representative sound speed for this region of the atmosphere of 270 m/s).

## 5. SUMMARY AND CONCLUSIONS

### 5.1 Bolide detection using infrasonic techniques and their interpretations:

We have an independently calibrated, empirical source energy relationship for line and modified line sources (including fragmentation effects), etc. The origin of the waves from such an object can be used to readily locate its position. We can readily derive both the azimuth/elevation angles of the arrival and also the three-dimensional

intersecting bearings from multiple detecting arrays. There has now been detection of at least 25-30 bolides over the energy range from 0.05 kt to 10 Mt, with the minimum bolide energy detection level of  $\sim 8.0 \cdot 10^{-6}$  kt (ReVelle, 1997).

The data can be regarded historically into a period from 1960-1974 with the Tunguska detection of 1908 falling into a separate category for detection of the full range of periods in the acoustic-gravity wave realm. The second period was from about 1991 until the present with  $> 10$  bolides detected at Los Alamos of source energy  $> 0.053$  kt and detection's at IRF in Sweden (Greenland bolide of 12/9/1999), one in Russia detected by the Obukhov Institute of Atmospheric Physics, one at the Australian National University (August 18, 2000) and also one at NOAA in Boulder and an additional recent recording of a very large bolide at an array along the East coast (7/23/2001). In addition there have been acoustic recordings on conventional surveillance camera equipment in Spain (2 detection's) and in Colorado (2 detection's), with the best recording still that of the Boveedy-Sprucefield meteorite fall in 1969.

As a result of our work, there is a minimum expectation of  $\sim 30$  bolides/year at 0.1 kt and  $\sim 1$  bolides/year at 15 kt. The latter value is in very good agreement with the results of satellite systems operating in the optical and in the infrared part of the electromagnetic spectrum (Tagliaferri et. al., 1994).

Data from the future IMS infrasound system (60 arrays with uniform global coverage) will certainly improve upon our bolide influx estimates for energies  $< 1$  kt. Also, synergy is clearly possible with other methods such as satellite systems, seismic, hydroacoustic techniques, etc. The influx we have currently estimated only represents the flux of the most deeply penetrating and "strong" objects.

Recently, we have found order of magnitude discrepancies between the two types of source energy estimates, with the satellite energy  $> 10X$  the infrasonic inferred energy (4/23/2001, Baja, CA and 7/23/2001, Lancaster, PA bolide):

The satellite data has been analyzed by assuming the bolide blast wave radiative source, black body temperature (6000 K) and a 10 % luminous efficiency factor over the wavelength interval of the sensor to derive the integrated source energy over the trail. The luminous efficiency should be highly variable, however and is now being studied intensively by our group at Los Alamos.

Recent and older volume porosity modeling efforts (ReVelle, 1983 and 2001a-this

conference) have shown that significant bolide porosity produces much brighter bolides at the same mass and velocity while using the same luminous efficiency. This may be one way of trying to resolve these recent source energy discrepancies.

## 5.2 Acoustic(Audible) Bolide Recordings

Finally, we would like to summarize the relatively recent high frequency audible (acoustic) detections of bolides made in recent years. With the growing number of security cameras and associated microphone capabilities, the potential now exists for routine monitoring of such high frequency acoustic effect from bolides almost routinely and at very low cost. Listed below are acoustic recordings from bolides that are presently known to the author:

- i) 4/25/1969, Northern Ireland- Boveedy-Sprucefield meteorite (or the Belfast bolide). Audio recorded by Miss Eileen Brown and taken to Dr. Ernst Opik at Armagh Observatory for validation.
- ii) 11/21/1995, Colorado Springs bolide: Video/audio security camera; Also, infrasonic detection at Los Alamos.
- iii) 11/17/1995, 23.59.33 UTC, Spain- H. Betlem (Dutch meteor society): Recorded by video camcorders with microphones and image intensifiers at 2 temporary stations (Zafarraya and Almedinilla)-. There are also data available from 3 cameras of the European fireball network: Stellar magnitude = -15, initial speed = 32.9 km/s, end height = 29.46 km, orbital data, etc.)- Data from P. Spurny, Ondrejov Observatory, The Czech Republic.
- iv) 1/11/1998, Colorado Springs: ~0709 UTC, Video/audio security camera. Also, infrasonic detection (Bedard, NOAA, Boulder, CO).

Instrumentation, Conference Number 3116B, San Diego, CA, pp. 1-10, 1997.

Opik, E.J., Physics of Meteor Flight in the Atmosphere, Interscience Publishers, Inc., New York, 174 pp., 1958.

ReVelle, D.O., Interactions of Large Bodies with the Earth's Atmosphere, IAU Symposium No. 90, Solid Particles in the Solar System, eds. I. Halliday and B.A. McIntosh, D. Reidel Pub. Co., Dordrecht, 185-198, 1980.

ReVelle, D.O., Modeling the Dynamics, Ablation and Luminosity of Fireballs, Meteoritics, 18, 386, 1983.

ReVelle, D.O., Historical Detection of Atmospheric Impacts by Large Bolides Using Acoustic-Gravity Waves, Annals of the New York Academy of Sciences, Near-Earth Objects- The United Nations International Conference, ed. J.L. Remo, The New York Academy of Sciences, New York, New York, 822, 284-302, 1997.

ReVelle, D.O., Bolide Dynamics and Luminosity Modeling: Comparisons between Uniform Bulk Density and Porous Meteoroid Models, Conference Proceedings, Meteoroids2001, Kiruna, Sweden, August 6-10, 2001, 2001a..

ReVelle, D.O. and W.G. Delinger, Passive Acoustic Remote Sensing of Infrasonic of Natural Origin, Proceedings of International Symposium on Acoustic Remote Sensing of the Atmosphere and the Oceans, eds. T. Mathews and R.B. Hicks, pp. V6-V15, Univ. Calgary Press, Calgary Alberta, Canada, 1981.

Shoemaker, E.M and C.J. Lowery, Airwaves Associated with Large Fireballs and the Frequency Distribution of Energy of Large Meteoroids, Meteoritics, 3, 123-4, 1967.

Tagliferri, E. , R. Spalding, C. Jacobs, S.P. Worden and A. Erlich, Detection of Meteoroid Impacts by Optical Sensors in Earth Orbit, Hazards due to Comets and Asteroids, ed. T. Gehrels, Univ. Arizona Press, Tucson, AZ, 199-220, 1994.

## 6. REFERENCES:

- Cox, E. F., Sound Propagation in Air, Handbuch der Physik, vol. XLVIII, pp. 455-478, ed. J. Bartels, Springer-Verlag, Berlin, 1958.
- Ceplecha, Z., Influx of Large Meteoroids onto Earth, SPIE, International Symposium on Optical Science, Engineering and

**Table 1. Recent infrasonic detections of bolides (1994-2001)**

Date	Time-UTC	Lat. (deg)	Long. (deg)	Period (sec)	Energy (kt)
020194	22:38	2.6 N	164 E	-----	50-200
112195	09:18	39 N	105 W	2.0	0.053
100496	03:44	36 N	118 W	4.0-5.0	0.5-1.1
100997	18:47	32 N	106 W	3.33	0.29
120997	08:12	63 N	51 W	2.5	0.11
061398	14:06	34 N	103 W	3.0	0.21
081198	10:18	20 S	134 E	9.4	9.38
111798 (*)	10:05	36 N	106 W	1.4	0.3-1 t
081699	05:18	35 N	107 W	2.5	0.11
082500	01:12	15 N	106 W	4.6-7.2	2.5
042301	06:13	30 N	134 W	3.1-5.1	~1.0
072301	22:19	42 N	76 W	3-3.33	0.29

(\*) Not used in the influx calculations- This is a large and very bright Leonid bolide detected infrasonically at Los Alamos during the night of the Leonid meteor shower and associated storm of 1998.

**Table 2. Bolide Infrasound Data and the Predicted Global Influx Rate (Cumulative number of bolides per year at the Earth whose source energy exceeds  $E_s$ ) as well as standard, statistical counting errors, i.e.,  $\pm N/\{N\}^{1/2}$**

Source Energy, $E_s$ : kt	Number, N, per year at the Earth	Cumulative Number, $N' \geq E_s$	Standard statistical counting errors
1100	0.05	1	$\pm 0.05$
30	0.18	2	$\pm 0.13$
26	0.30	3	$\pm 0.17$
20	0.434	4	$\pm 0.22$
14	0.63	5	$\pm 0.28$
11	1.24	6	$\pm 0.51$
10	1.55	8	$\pm 0.55$
9.86	2.21	9	$\pm 0.74$
8	1.26	10	$\pm 0.40$
6	2.51	11	$\pm 0.76$
2.5	4.58	12	$\pm 1.32$
0.84	8.04	13	$\pm 2.23$
0.29	12.8	14	$\pm 3.43$
0.21	16.2	15	$\pm 4.18$
0.20	32.3	16	$\pm 8.06$
0.112	23.6	17	$\pm 5.74$
0.11	23.7	18	$\pm 5.58$
0.053	33.1	19	$\pm 7.59$

# BOLIDE FRAGMENTATION PROCESSES: SINGLE-BODY MODELING VERSUS THE CATASTROPHIC FRAGMENTATION LIMIT

D. O. ReVelle

*Los Alamos National Laboratory, P.O. Box 1663, MS J577, Earth and Environmental Sciences Division,  
Atmospheric and Climate Sciences Group, Los Alamos, New Mexico 87545, USA  
Email: dor@vega.lanl.gov*

## ABSTRACT

The catastrophic "pancake" fragmentation process, proposed as being generally applicable to very large meteoroid entry in the early 1990's by a number of workers, has been carefully examined. In this effort, the transition from the traditional single-body dynamics and energetics model to a catastrophic "pancake" fragmentation process has been delineated. The key parameters are the  $\mu$  parameter originally proposed by Levin and the fragmentation scale height,  $H_f$ , which we have derived from  $\mu$ . It has been found that this break-up process can only occur for an optimum set of circumstances.

## 1. INTRODUCTION AND OVERVIEW:

### 1.1 Simple ablation theory: A brief summary

Following Bronshten (1983) and ReVelle (1999), we have initially assumed that an analytic solution for hypersonic meteoroid entry, assuming a hydrostatic, isothermal, atmosphere with a constant ablation coefficient,  $\sigma$  and a height variable velocity, while allowing for shape change using a constant  $\mu$  parameter value is adequate to investigate this problem. Additional assumptions associated with this solution of simultaneously including ablation, deceleration, shape change and also the process of catastrophic fragmentation (as defined here) is the neglect of lift, coriolis effects and gravity gradients, non-isothermal and non-steady atmospheric effects, etc. Two fundamental regimes have been identified, namely:

#### i) $|H_p/H_f| \ll 1$ :

Single-body model approximation

$H_f$  = fragmentation scale height

$H_p$  = pressure scale height

Previous investigators have also identified the following behavior within this limit:

- a.  $\mu \approx 2/3$ : Self-similar ablation regime with no shape change.
- b. For  $0 \leq \mu < 2/3$ : Ablation and deceleration, while allowing for simultaneous shape change
- c.  $A(z)$  decreasing with decreasing height with  $|H_p/H_f| \ll 1$

#### ii) If $H_p/H_f \gg 1$ :

Catastrophic "pancake" fragmentation

For  $\mu < 0$ , there is the possibility of simultaneous ablation and deceleration, while allowing shape change, but with  $A(z)$  increasing with decreasing height

It is this latter regime and the transition from the realm of applicability of the single-body approximation that we want to outline in this paper. Independently ReVelle and Cepplecha (2001f) have evaluated the most precise bolide flight data available for sizes up to  $\sim 1$  m across and have found very little support for the process of catastrophic fragmentation.

## 2. PREVIOUS MODERN FRAGMENTATION MODELING

### 2.1 Break-up schemes:

### Uniform and porous limits

Various schemes have been proposed by different workers regarding the drag area and heat transfer areas during entry. In the single-body limit these areas are equal:

$$A_d (\text{drag}) = A_h (\text{heat transfer})$$

if the bodies are homogeneous (uniform in bulk density). For porous bodies, ReVelle (1983, 2001a) has shown that:

$$A_h = A_d (1 + \psi')^{-1}$$

where

$\psi'$  = normalized porosity function ( $0 < \psi' < 1$ )

which is assumed to be zero (or very small compared to unity) in the ordinary chondritic limit (bolide type I.).

### 2.2 Specific types of approaches for modeling fragmentation:

- Increase of the frontal cross-sectional drag area proportional to the number of fragments produced during fragmentation.
- $A_h \gg A_d$  due to turbulent mixing of air/ablated vapor
- Significant porosity effects:  $A_h \gg A_d$
- Progressive fragmentation processes producing a cascade of break-ups starting after the initial triggering process.
- "Pancake" break-up without ablation: Rapid lateral growth of the body
- "Pancake" break-up with ablation included

Most of the recent "pancake" efforts on this subject have been associated with the dramatic entry into Jupiter's atmosphere of Comet Shoemaker-Levy 9, i.e., for very large bodies (hundreds of meters to kilometers across). These pancake models were never expected to work for objects as small as the typical US DoD bolides or for the still smaller bodies photographed by ground-based camera networks (personal communication with J.G. Hills, 2001). In the forthcoming *Icarus* paper a full summary will be given of all of these process types along with the credits due to the authors of these numerous contributions on the fragmentation process.

### 2.3 Possible break-up mechanisms:

The standard break-up mechanisms that have been previously proposed include both thermal and mechanical forcing. The thermal mechanism has been shown to be very unlikely except perhaps for Nickel-iron bodies with very large thermal conductivity. This process is much too inefficient a process because of the long time-scales that are necessary for it to be effective. In this paper we assume that the later mechanism is operative once a triggering has been established. We assume that mechanical effects dominate the break-up process and that pressure loading on the frontal cross-section leads to a "triggering" of break-up if the stagnation pressure  $\geq$  uni-axial tensile/compressive strength of the body. We also assume that any earlier break-up (before this triggering by pressure loading is reached) is due entirely to internal weaknesses in the body, such as fracture planes, from cracks produced during prior space collisions.

An additional mechanism described in ReVelle (1980) suggested that the very rapid shape change process initiated by the large ablation rate at the stagnation point could aid in triggering fragmentation. The gradient in the ablation rate at the stagnation point compared to radial positions far removed from the stagnation point was suggested as a mechanism for allowing additional weaknesses in the integrity of the body to develop so that break-up would be more likely.

## **3. BOLIDE FRAGMENTATION PROCESSES AND THEIR IMPLICATIONS**

### 3.1 Single-body model limit:

$$|H_f| \gg H_p$$

where

The fragmentation scale height,  $H_f$

$$H_f = -f(z)/\partial f/\partial z; f \equiv A(z)/A_\infty$$

$H_f$  = the vertical distance (downward) by which the instantaneous cross-sectional area,  $A(z)$ , increases by  $1/e$ .

The pressure scale height,  $H_p$  is defined as:

$$H_p = -p(z)/\partial p(z)/\partial z = RT/g \text{ (if hydrostatic):}$$

$$H_p \sim 6\text{--}8 \text{ km from } 0 \leq z \leq 120 \text{ km}$$

The full details of all of the concepts and derivations in this paper along with the fundamental single-body and post fragmentation diagnostic indicators regarding a bolide entry trajectory will be submitted to *Icarus* during early 2002. Because of primarily space limitations, only a limited selection of results will be provided here.

Prior to the onset of fragmentation, we assume that only smooth, quasi-continuous break-up processes are occurring. This has been the case used prior to the early 1990's for almost all workers for bolide and meteor modeling efforts. In this regime, ablation, deceleration and quasi-continuous fragmentation all occur simultaneously as the body size decreases at various rates determined by the ablation coefficient and by the changes in the bolide velocity during entry.

### 3.2 Catastrophic "pancake" fragmentation:

$$H_f \ll H_p$$

or:

$$H_p / H_f \gg 1$$

In this regime of flight,  $\mu < 0$  and the frontal cross-sectional area of the body increases with decreasing height. In this development,  $\mu < 0$ , is a necessary condition for the rapid lateral growth of the body, but for the effect to be dynamically or energetically significant, a sufficient condition must also be satisfied, namely that the ratio:  $H_p / H_f \gg 1$ . We have assumed that a sudden onset of catastrophic fragmentation occurs by the triggering process when the stagnation pressure exceeds the strength of the body. We have not yet completed the analysis of  $\mu < 0$  on the emission of light, but only on the dynamics of entry, but we will present evidence below that the same parameters control the light emission process for this break-up limit. In addition there is also an expression originally due to Levin (1962) for the model of light emission presented in Bronshten (1983), including the case  $\mu < 0$ , but this expression was devised for the limit in which  $(\sigma, V, \mu) = \text{constant}$ . This is the standard meteor light curve developed by assuming proportionality to the mass loss rate. In the *Icarus* paper a full derivation for the case where the first two of these quantities are height variable will be presented. Also, an expression for the light curve that was derived by assuming

light emission is proportional to the time rate of change of the kinetic energy will be presented as well. These assumptions are clearly more applicable to the large bolide case.

### 3.3 Scale height ratio implications

#### 3.3.1 General Implications

As a result of our evaluation of the scale height ratio,  $H_p / H_f$ , that will be presented in full detail in *Icarus*, for  $\mu < 0$ , we can say that in both the negligible and large deceleration limit this scale height ratio increases. Similarly, this is also the case for larger  $\sigma$ , for larger  $\sigma V^2(z)$ , for larger  $\mu$  ( $< 0$ ) and for larger initial velocities (for large decelerations). Also, this scale height ratio increases for a smaller initial radius, for smaller radii at lower heights, for smaller bulk density (using a uniform bulk density model) or for a smaller entry angle,  $\theta$ . In the limit of no ablation, the scale height ratio  $\rightarrow 0$  as  $\sigma \rightarrow 0$ . The scale height ratio also  $\rightarrow 0$  as  $\mu \rightarrow 0$ . Thus, severe ablation or large  $\mu$  ( $< 0$ ) promotes catastrophic break-up as the body size decreases with decreasing height. Such behavior is not bounded however. If  $\mu = -3.33$ , a frontal area increase of 500-1000 times and much higher end heights are predicted. Thus, from our analysis, we have found that bolides with an optimum  $\sigma$  or large  $\mu$  (at higher altitudes) or with larger initial speeds are likely to break-up catastrophically as a result. Similarly, If  $\sigma$  is too large, the end height velocity will be quite large and  $\mu$  will be not  $< 0$  and catastrophic break-up is less likely to occur, since the definition of the onset of fragmentation will not be satisfied.

#### 3.3.2. Scale height ratio for the same initial velocity, $\sigma$ , $\theta$ , etc.

Effects of e-folding energetics using the D parameter of ReVelle (1993). For  $D = 2.30$  ( $\rightarrow 10\%$  kinetic energy reduction), smaller decelerations are expected which are more generally consistent with the behavior of bolides of cometary origin. The end height velocity is also larger which makes the largest possible  $\mu$  value less negative. Thus, catastrophic break-up is far less likely to occur, for this case. For  $D = 4.61$  ( $\rightarrow 1\%$  kinetic energy reduction), larger decelerations are expected, which are more generally consistent with meteorite-dropping

fireballs. The end height velocity is also far smaller which makes the largest possible  $\mu$  value more negative. Thus, catastrophic break-up is far more likely to occur for this case.

Both of these limiting  $D$  values also have a nearly linear increase of  $H_p/H_f$  as height decreases, except for progressively smaller  $\mu$ 's. The increase in frontal area for  $\mu < 0$  produces more atmospheric drag and a progressively higher end height. Thus,  $\mu$  can not become too large otherwise the end height will rapidly increase as the frontal cross-section rapidly increases.

### 3.3.3 Implications for Break-up

If the stagnation pressure loading on the frontal cross-section is the fundamental mechanism for break-up, with all other factors the same, direct analysis of the fundamental equations shows that larger bodies will only break-up catastrophically ( $\mu < 0$ ) if they are extremely strong. Conversely, smaller bodies will only break-up catastrophically ( $\mu < 0$ ) if they are extremely weak. Thus, for a necessarily limiting range of body strengths, an optimum size or mass range exists where catastrophic type, "pancake" break-up will occur, corresponding to  $\mu < 0$ . Otherwise, for  $\mu > 0$ , only quasi-continuous fragmentation processes can occur under these assumptions.

## 4. FRAGMENTATION AND LIGHT EMISSION

### 4.1 Previous analytical studies of the effects of fragmentation on light emission

In Bronshten (1983) an analytical expression, originally due to Levin (1962), for the effects of  $\mu$  on the emission of light is presented, namely:

$$I \equiv dm/dt/(dm/dt)|_{\max}$$

$$I = I_{\max} \cdot \{\mu^{-\mu/(1-\mu)}\} \cdot \{\rho(z)/\rho_{\max}\} \cdot [1 - (1-\mu) \cdot \{\rho(z)/\rho_{\max}\}]^{\mu/(1-\mu)}$$

where

$I$  = Assumed isotropic light emission in Joules/s  
 $\rho_{\max}$  = air density at the altitude of maximum light emission

$$\mu \equiv \{\ln(A(z)/A_{\infty})/\ln(m(z)/m_{\infty})\}$$

OR:

$$A(z) \equiv A_{\infty} \{m(z)/m_{\infty}\}^{\mu}$$

where the subscript  $\infty$  refers to values at the top of the atmosphere (initial values) and  $m$  is the instantaneous mass of the bolide and  $A(z)$  is the bolide frontal cross-sectional area.

The light emission formula was derived from classical meteor theory for an isothermal, hydrostatic atmosphere, assuming that  $\{V, \sigma, \mu\}$  were all constants. Its range of applicability should be quite small for large bright bolides where air drag (and consequently very large deceleration) is very significant. Also, for very large negative  $\mu$ , drag is even more important and the formula is even less likely to be very useful. Such large negative  $\mu$  values have the desirable property of increasing the end height of bolides quite dramatically, but to achieve the necessary increase in the end height to explain the bolide behavior for groups IIIA or IIIB, the frontal cross-section of the body must increase  $> 500$  times! This is clearly a very unrealistic possibility. In addition, the general expression of Levin reproduced above produced results, which have an imaginary component below the altitude of maximum light emission for large bodies. Clearly, although of interest because of its dependency on  $\mu$ , we should develop alternative expressions for the effects of fragmentation on the light emission process.

### 4.2 The fragmentation scale height for light emission: The height of maximum light

In order to illustrate the influence of these limiting parameter regimes, we now evaluate the altitude of maximum light emission in an approximate manner. We start from the assumed balance between the light output and the product of the luminous efficiency and the time rate of change of the kinetic energy. The first derivative is then taken and equated it to zero to find the altitude of maximum light emission for a uniform bulk density meteoroid. Slight changes are required for this expression for a porous meteoroid model, as will be summarized below:

$$dI/dt = d/dt \{-\tau \cdot dE_k/dt\}$$

where

$$dE_k/dt = -(V^2/2) \cdot dmdt \cong -0.25\rho \cdot V^5 \cdot C_D \cdot \sigma \cdot A$$

which has been evaluated for  $2/(\sigma \cdot V^2) \ll 1$  (small deceleration limit) with an unchanging body shape and for simplicity with  $\tau$ ,  $\sigma$ ,  $V$ , and  $C_D$  = all constant, where  $C_D$  is the drag coefficient for hypersonic flow:

$$d/dt\{dE_k/dt\} = -0.25(\tau \cdot \sigma \cdot C_D) \cdot d/dt\{\rho \cdot V^5 \cdot A\} = 0$$

which can be simplified further to a height derivative form using the ancillary relations:

$$dz/dt = -V(z) \cdot \sin\theta$$

$$A = A_\infty \exp[\sigma \cdot (\mu-1) \cdot (V_\infty^2 - V^2(z))]$$

Letting:

$$A = A_d = \text{frontal drag area}$$

to the form:

$$\sin\theta \cdot \{-(1/\rho) \cdot \partial\rho/\partial z - (1/A_d) \cdot (\partial A_d/\partial z)\} \\ = (5/2) \cdot \{\rho(z) \cdot A_d \cdot C_D/m\}$$

In an isothermal hydrostatic atmosphere, we also have the results:

where

$$1/H_p = -(1/p(z)) \cdot (\partial p(z)/\partial z)$$

$$1/H_\rho = -(1/\rho(z)) \cdot (\partial \rho(z)/\partial z)$$

$$\rho(z) = \rho_0 \cdot \exp[-z/H_\rho]$$

$$p(z) = p_0 \cdot \exp[-z/H_p]$$

$$H_p = RT/g = \text{constant for an ideal gas}$$

$$H_\rho = \text{density scale height}$$

$$H_p = H_\rho \text{ (only if isothermal conditions exists)}$$

$$p_0 = \text{atmospheric pressure at the surface (z = 0)}$$

$$\rho_0 = \text{atmospheric density at the surface (z = 0)}$$

and similarly:

$$1/H_f(z) = -(1/A_d(z)) \cdot (\partial A_d(z)/\partial z)$$

Turning to pressure as the atmospheric variable and making use of the ideal gas law, we can then solve for  $z$  at maximum light. Thus, we have arrived at the following general expression:

$$z_{\max} = -H_p \cdot \ln\{0.40 \cdot \{p^*(z)/p_0\} [H_p/H_f(z) + 1]\}$$

where

$$p^*(z) = \text{modified ballistic entry parameter}$$

$$" \equiv mg \sin\theta / (C_D \cdot A_d)$$

$$m = \text{instantaneous bolide mass}$$

$$g = \text{acceleration due to gravity}$$

$$p^*(z) = p_\infty^* \cdot \exp[(\sigma/2)(\mu-1) \cdot (V_\infty^2 - V^2(z))]$$

$$p_\infty^* = \text{initial modified ballistic entry parameter}$$

which for single-body behavior ( $H_p/H_f(z) \ll 1$ ) reduces to:

$$z_{\max} = -H_p \cdot \ln\{(0.40)\{p^*(z)/p_0\}\}$$

while for catastrophic fragmentation

( $H_p/H_f \gg 1$ ), this expression becomes:

$$z_{\max} = -H_p \cdot \ln\{(0.40)\{p^*(z)/p_0\} [H_p/H_f(z)]\}$$

The large increase in the height of maximum light for the limiting case in which catastrophic fragmentation dominates the light emission behavior is clearly evident from the latter expression. This is the case since the quantity inside the natural logarithm is so greatly increased by virtue of the small fragmentation scale height. This is directly due to the large increase in the drag that is experienced by a laterally expanding object traveling at a hypersonic velocity.

The expression for the fragmentation scale height can be further modified if a porous meteoroid model is adopted so that  $A_h \neq A_d$ . In this case the definition of  $H_f$  in the expressions above becomes:

$$H_f(z) = -f(z)/\partial f(z)/\partial z; f(z) \equiv A_h(z)/A_{h\infty}$$

or

$$H_f(z) = -(1/A_h(z)) \cdot (\partial A_h(z)/\partial z)$$

i.e., now specifically written in terms of the heat transfer area and with all other terms remaining the same as before. This is very significant since for very porous objects the heat transfer area can increase dramatically compared to the definition of  $H_f$  in terms of  $A_d$  for the uniform density case for objects with negligibly small porosity (such as Group I., etc.).

#### 4. SUMMARY AND CONCLUSIONS

A newly discovered concept, the fragmentation scale height,  $H_f(z)$  needs to be compared against the local pressure scale height,  $H_p(z)$  in order to determine if a single-body approach or a catastrophic fragmentation type approach is evident for a specific problem. We have indicated that if:  $H_f(z) \gg H_p(z)$ , the single-body approximation is valid, whereas if  $H_f(z) \ll H_p(z)$ , catastrophic type "pancake" fragmentation is expected.

We have also independently evaluated these parameters using data from the most precise bolide trajectories that are available (ReVelle and Ceplecha, 2001f). From this work we have independently determined that catastrophic fragmentation behavior is not very likely to occur for most bolides.

Assuming that  $\mu$  is  $\neq f(\text{body size})$  and not too negative ( $|\mu| < \sim 3.33$ ), the start of "pancake" fragmentation occurs for lower density bolides of high initial speed, at shallower entry angles and having a larger ablation coefficient. Larger (smaller) bodies can only break-up by this mechanism if they are exceptionally strong (weak). Thus, there is an optimum range of masses for which this can occur (if  $\mu = \text{constant}$ ). Unfortunately,  $\mu$  is also far from constant as shown by ReVelle and Ceplecha (2001f). Direct observations of the most precise bolides by ReVelle and Ceplecha (2001f) also does not show much support for a catastrophic type break-up process for bodies as large as  $\sim 1$  m across. Only 8 of 22 observed bolides exhibited significantly negative  $\mu$  values. Even fewer cases showed that  $H_f \ll H_p$  over any height region. Thus, many bolides (including the frequently observed bolides recorded on US DoD satellite sensors) can be safely treated using the single-body theory with  $\mu > 0$ . Pancake type break-up is generally not expected to occur.

#### 5. REFERENCES

- Bronshten, V.A., Physics of Meteoric Phenomena, D. Reidel Pub. Co., Dordrecht, 356 pp., 1993.
- Levin, B., Fragmentation of Meteor Bodies, Nature, 196, 527-529, 1962.
- ReVelle, D.O., The Interaction of Large Bodies with the Earth's Atmosphere, IAU Symposium Number 90, Solid Particles in the Solar System, eds. I. Halliday and B.A. McIntosh, D. Reidel Pub. Co, Dordrecht, 185-198, 1980.
- ReVelle, D.O., Modeling the Dynamics, Ablation and Luminosity of Fireballs, Meteoritics, 18, 386, 1983.
- ReVelle, D.O., Bolide Fragmentation Processes: Modeling the Break-up of Very Large Meteors, Presented at the Cornell ACM Conference, Ithaca, New York, July, 1999.
- ReVelle, D.O., Bolide Dynamics and Luminosity Modeling: Comparisons Between Uniform Bulk Density and Porous Meteoroid Models, Conference Proceedings, Meteoroids2001, Kiruna, Sweden, August 6-10, 2001, 2001a
- ReVelle, D.O. and Z. Ceplecha, Calculations of Shape Change and Fragmentation Parameters Using Very Precise Bolide Data, Conference Proceedings, Meteoroids2001, Kiruna, Sweden, August 6-10, 2001, 2001f.

## THE TAGISH LAKE METEORITE FALL : INTERPRETATION OF FIREBALL PHYSICAL CHARACTERISTICS

P. Brown<sup>1</sup>, D.O. ReVelle<sup>1</sup>, and A.R. Hildebrand<sup>2</sup>

<sup>1</sup>Los Alamos National Laboratory, MS J577, Los Alamos, NM 87545 USA email: pbrown@lanl.gov

<sup>2</sup>Department of Geology and Geophysics, University of Calgary, Calgary, Alberta, CANADA

### ABSTRACT

We have analyzed available instrumental and eyewitness records associated with the fireball leading to the fall of the Tagish Lake meteorite. Initial chemical and physical studies of this carbonaceous chondrite have shown it to be unique. It is one of the most primitive meteorites yet recovered and is physically weak. By determining the meteoroid trajectory, velocity, and physical breakup in the atmosphere, we can characterise the fireball as intermediate between Type II and Type IIIa, following the classification of Ceplecha et al. (1998). Modelling suggests an initial porosity for the pre-atmospheric meteoroid in the range 40-60%. The initial fragmentation occurred under less than 0.3 MPa dynamic pressure. Determination of Tagish Lake's orbit suggests a linkage to parent bodies in the main asteroid belt, though association with Encke-type comets cannot be strictly excluded. Tagish Lake may represent an intermediate object between chondritic asteroids and cometary bodies consistent with a linkage to D-class asteroids based on results from reflectance-spectra work.

### 1. INTRODUCTION

The Tagish Lake meteorite fell on January 18, 2000 at 16:43:43 UT (08:43:43 local time). The fireball accompanying the meteorite fall was widely observed over the Yukon Territory, British Columbia, portions of Alaska and the Northwest Territories. The fireball was of unusually long duration; many observers reported it to be visible for 15-20 seconds. That the duration of the event was significant is verified by a security video camera record which shows increased illumination of the local terrain from the fireball for just over ten seconds. The peak brightness of the fireball was enough to illuminate the still dark terrain to near daylight conditions for observers near the endpoint. The final portion of the fireball trajectory was dominated by one short burst followed by a more extended terminal disintegration. Reports from eyewitnesses invariably described these two major detonations as primary features of the event. Substantial

delayed sounds were heard by observers at distances of up to 200 km from the fireball trajectory. In addition to these delayed sounds, several observations of electrophonic sounds (cf. Keay et al., 1980) were also reported. Particularly notable are several reports of unusual smells being detected at nearly the same time, to slightly following, the passage of the fireball proper. Observers uniformly reported these smells to be of a foul metallic, chemical or sulfurous odour.

In addition to these eyewitness records, a total of five video records and 24 still photographs of the associated dust cloud were provided by witnesses. Figure 1 shows an example of the still photos taken shortly after the fireball. In addition to these data, sensors on US Department of Defence satellites detected the event in the infrared (providing positional information) and at optical wavelengths (defining the light curve). The space-based recordings include a fortuitous image of the dust-cloud made by the Defence Meteorological Satellite Program F-13 satellite which scanned the area including the endpoint of the fireball only two minutes after the event. Figure 2 shows this image of the associated dust cloud.

The airwave signal from the fireball was recorded on three local seismic stations, Whitehorse (WHY), Haines Junction (HYT) and Dease Lake (DLBC). These show both direct air-coupled Rayleigh wave arrivals, the airwave itself as well as seismically coupled body waves due to the airblast.

Of great value in constraining interpretation of the fireball data is the recovery of meteorites from the ice surface of the Taku Arm of Tagish Lake over the interval January - May, 2000 (cf. Brown et al., 2000). In total some 410 individual fragments from the fireball were located and more than 200 samples recovered for later analysis, totalling approximately 5 kg of material. Based on the available fall data, the physical characteristics of the recovered samples, and modelling of the event, here we attempt to reconstruct the pre-atmospheric orbit and physical character of the Tagish Lake meteoroid.



Figure 1. Dust cloud remaining after the passage of the Tagish lake fireball. This image was still-framed captured from video of the dust cloud shot by Doug Davidge from Whitehorse, Yukon Territory several minutes after the fireball. The recording was made using a Sony TRV75 Hi-8 camcorder equipped with extended infrared response. The bright portion of the trail near the lower part of the image represents that segment of the trail where the sun is within a few degrees of rising above the local horizon. This fact coupled with the enhanced dust deposition near the end of the trail is the probable reason this portion appears so much brighter than the rest of the trail.

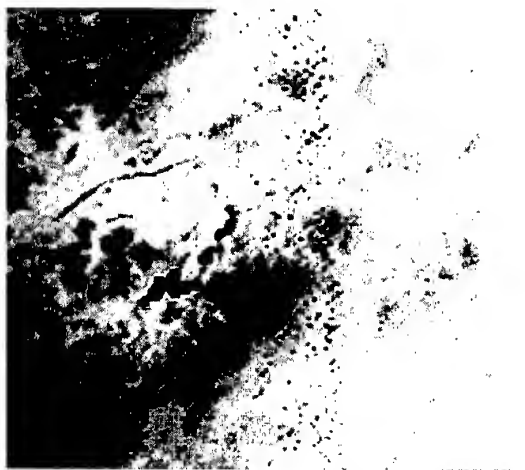


Figure 2. Visible light detection of the fireball dust cloud from space. This image was captured by the Defence Meteorological Satellite Program F-13 satellite. The satellite scanned through the dust trail (dark cloud left of center) approximately two minutes after the passage of the fireball. The image has been inverted for clarity.

## 2. CALCULATION OF THE FIREBALL TRAJECTORY, VELOCITY, INITIAL MASS AND ORBIT

### 2.1. Velocity and Atmospheric path

To compute the fireball trajectory we first make use of eyewitness data. In total over 90 persons were interviewed and measurements made of the observed path of the fireball in the Yukon and British Columbia. These data, however, are widely discordant and do not provide a good estimate for the complete trajectory. In particular, the slope of the fireball path in the atmosphere is particularly uncertain from these data. However, sufficient visual observations exist close to either side of the ground track to strictly constrain the fireball apparent radiant azimuth to be in the range  $327^\circ \leq \phi \leq 334^\circ$ . Using the best eyewitness data and the least-squares solution method of Borovicka (1990), the formal trajectory solution (with formal error) is given in Table 1. Note that this solution does not make use of the observers proximate to the ground track as these were observations of the dust cloud only. The relatively flat trajectory of the fireball is qualitatively reflected in numerous visual observers who (incorrectly) reported following the fireball to the southern horizon. The eyewitness solution should be treated very cautiously as the real errors are much larger than the formal error margins shown. Indeed, solutions with entry values from near zero to  $25^\circ$  and azimuths from  $320^\circ$  to nearly  $350^\circ$  may be accommodated with different (subjectively chosen) subsets of the eyewitness reports using the least-squares technique.

More accurate determination of the trajectory is possible by making use of the photographs and video of the associated dust cloud. In particular, three were made very shortly after the fireball, had good positional references in the fields of view, and were well separated spatially so as to provide a good intersection solution. An example of one of these is given in Figure 3. These observations consist of a video recordings made from Whitehorse ( $60.718^\circ\text{N}$ ;  $135.054^\circ\text{W}$ )(Wheeler) beginning 15 seconds after the fireball, a still photo of the dust cloud from  $60.367^\circ\text{N}$ ;  $134.089^\circ\text{W}$  approximately 120 seconds after the event (Ford) and finally a still digital photo of the dust cloud from Atlin, British Columbia ( $59.572^\circ\text{N}$ ;  $133.703^\circ\text{W}$ ) taken roughly 90 seconds after the fireball (Lenke).

To better resolve the original trajectory, the video record from Whitehorse was used to examine the upper wind motions. By following the dust cloud over a period of several minutes, the local wind vectors may be defined at different points along the trail. To determine the best fits for each observation, the same points on each trail were identified and the approximate wind vectors were inverted to reconstruct the original fireball trail—this iterative process was stopped when the modelled dust trails became nearest to linear at each site. Using the resulting appar-



Figure 3. Dust cloud photo taken from Atlin, British Columbia by Ewald Lemke.

ent trajectories plus the original dust cloud measurements, a best-fit trajectory was determined as shown in Table 1.

To compute the velocity, common features in the optical light curve were compared with the infrared satellite measurements. From this comparison a mean velocity prior to the main burst of  $15.5 \pm 0.6$   $\text{kms}^{-1}$  was found. Comparison of the satellite optical light curve and measured features on the most detailed dust cloud photos (Lemke) yield a velocity of  $15.7$   $\text{kms}^{-1}$  prior to the main burst and velocities approaching  $9$   $\text{kms}^{-1}$  at the end of the visible light curve.

Taking the satellite-determined fireball radiant altitude and azimuth as most accurate and an initial velocity of  $15.8 \pm 0.6$   $\text{kms}^{-1}$  (corrected for early deceleration of the large pre-atmospheric meteoroid as shown in the next section) the orbit solution is shown in Table 2. The orbit is similar to previously measured meteorite orbits, having a Tisserand value of 3.6 and  $1/a=0.5$ . However, these values would not rule out classification as an Encke-type cometary orbit.

## 2.2. Initial Mass

A measure of the initial mass of the meteoroid comes from satellite records of the event. Figure 4 is the lightcurve associated with the fireball recorded by US Department of Defence satellites. Assuming the bolide radiates as a 6000K blackbody, the integrated optical light energy from the fireball is  $1.1 \times 10^{12}$  J. The results of the St. Robert fireball/meteorite fall (Brown et al., 1996; Hildebrand et al., 1997) had both cosmogenic nuclide activities from recovered meteorites (which constrained the entry mass (Herzog et al., 1997)) and satellite data available to yield an apparent luminous efficiency ( $\tau$ ) of 10% in the silicon pass-band of the satellite sensor for this H-chondrite. Using this conversion efficiency as well as the integrated optical energy and the initial veloc-

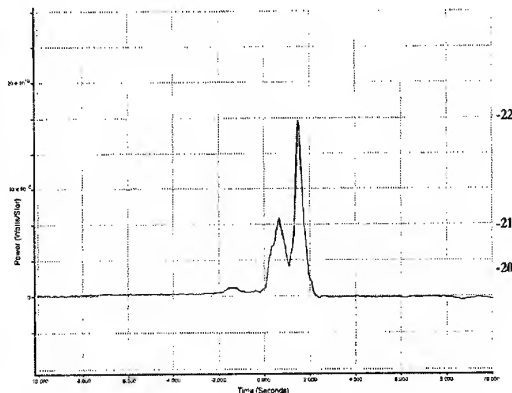


Figure 4. Optical satellite light curve. The right axis shows approximate absolute visual magnitude assuming a 6000K blackbody. Zero time is 16:43:42s UT on 18 January, 2000.

ity determined from the previous section we derive an initial mass estimate near  $9 \times 10^4$  kg. Given the unusual makeup of Tagish Lake as compared to H-chondrites, we anticipate this efficiency will be somewhat different. Taking a range of physically probable efficiencies to be from 5-20%, implies probable mass ranges from  $5 \times 10^4$  to  $1.8 \times 10^5$  kg.

To better estimate this initial mass, we use the entry model employed to interpret the lightcurve and initial mass for the St. Robert fireball (Brown et al., 1996), namely that of the gross fragmentation model of Ceplecha et al. (1993). Here we adopt the entry angle, initial velocity, apparent heights of initial break-up and satellite observed light curve as constraints for the modelling. Our goal is to determine the initial mass, using only a constant ablation coefficient as an assumed input. We note that the light so-produced is referenced to the revision in the panchromatic luminous efficiency scale computed by Ceplecha (1996) from analysis of the Lost City meteorite fall of 5.2%. We expect that for such a fragile body that the value for the ablation coefficient ( $\sigma$ ) will be larger than chondritic values and most likely in the range  $0.04 - 0.20$   $\text{sec}^2 \text{km}^{-2}$ . The implication of this larger  $\sigma$  is that the effective luminous efficiency will be higher than the ordinary stoney value (cf. ReVelle, 1983) and our estimates extreme upper limits (within the constraints of an assumed constant ablation coefficients). In particular, using a  $\sigma=0.02$   $\text{sec}^2 \text{km}^{-2}$  and a shape-density factor,  $K=0.46$  (appropriate to type I fireballs) we compute an upper limit for the initial mass of 115 Tonnes.

To examine the effects of changing  $\sigma$ , particularly to (more realistic) higher values, we use the mean value for type II fireballs (which are believed to be associated with carbonaceous chondrites) as given in Ceplecha et al. (1998). Here we take  $\sigma=0.042$   $\text{sec}^2 \text{km}^{-2}$  and  $K=0.69$  to again fit the light curve. This produces a nominal mass estimate of 97 tonnes. Extending this to higher  $\sigma$  makes matching the light

curve and other observed parameters effectively impossible due to the simplification of using a constant ablation coefficient. However, recognizing the intrinsically higher  $\tau$  values associated with such a porous object as noted by ReVelle (1983) and the higher effective  $\sigma$  associated with the extensive fragmentation, we regard both of the above estimates as upper limits to the true mass.

### 2.3. Seismic Data

In addition to satellite and ground-based photos/videos, the airwaves generated by the passage of the meteoroid were detected at several seismic stations. Other work has demonstrated the utility of deriving parameters for bolide trajectories from seismic data alone (cf. Qamar, 1995) when numerous stations detect the airwave. In the present case, however, only two seismic stations showed strong signals from the fireball and one other a weak probable signal. Fortunately, the entry geometry has been well-defined from satellite data.

The airwave from a meteoroid can be recorded as seismic waves in several ways. First, the airwave itself may force transverse oscillations at the Earth's surface due to the overpressure of the wavefront; these we call air-coupled Rayleigh waves. Secondly, the acoustic wave may match the natural seismic wave velocities in the ground and excite these modes directly; these we term air-coupled body waves, usually p-type seismic (longitudinal) waves.

The seismic station near Whitehorse (WHY) recorded a large impulsive (and relatively long lasting signal) beginning 208s after the main detonation recorded by the satellite (at 16:43:43 UT). Using a high-pass filter on these data (1 Hz and higher) we also note an emergent waveform beginning some 128s after the main detonation time. These phases are shown in Figure 5.

The strongest arrival is associated with the main airwave. We suggest this signal records the first direct arrival of the airwave from the ballistic shock, having started to propagate from the trajectory as a cylindrical blast wave. Rayleigh waves moving at near acoustic velocities in the topmost portion of the soil near the seismic station arrive next. The earliest arrival of the airwave phase is that of an N-wave signature in the vertical component of the seismograph (showing strong downward motion), indicative of that expected of shock loading of the local terrain (cf. Kanamori et al., 1991). The large amplitude of this arrival phase is typical of air-coupled Rayleigh waves which often are the strongest component of seismic records of airbursts due to resonant coupling with loose soil (Ewing et al. 1967).

The earlier P-wave (body wave) arrival is interpreted as resulting from sound coupling near the sub-terminal point of the fireball, where the sound first reaches the earth. Indeed, provided the amplitude of

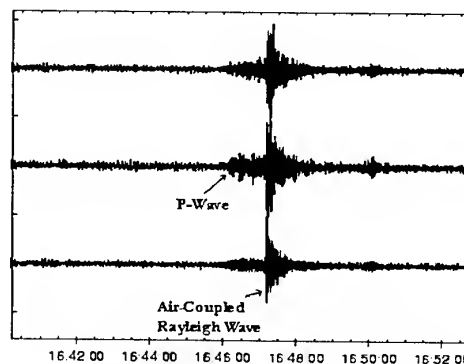


Figure 5. High-pass (1 Hz) filtered seismic record from WHY showing P-wave and Rayleigh wave arrivals. The three components shown are (from top) the E, N and Z-components. Amplitudes are normalized within each component.

the blast is sufficient, we expect the shock to couple directly into the ground very near the locus of points directly under the trajectory where the trace velocity across the ground of the cylindrical blast wave is comparable to the local P-wave velocity (which we adopt as  $6 \text{ km s}^{-1}$ ). Thus, the earliest P-wave signal should be from the region nearest the terminal portion of the fireball where a significant blast wave is still produced. Our final P-wave solution times and heights are relatively insensitive to values for upper crustal P-wave velocity different from the above. The effect of lower P-wave speeds (which would be the expected trend in a mountainous region) will be to push the solution to slightly higher heights.

To further examine the question of the origin of these seismic waves, we have taken the fireball trajectory determined from the satellite data as being most representative of the trajectory and modelled the expected arrival times of waves at WHY. We have used radiosonde data from WHY taken at 12 UT on Jan 18, 2000 as an input atmosphere to an altitude of 30 km and used the MSIS-E NASA atmosphere model above this height to define the acoustic velocity as a function of height. Ignoring wind corrections to this apparent sound velocity, we have computed the airwave arrivals at WHY as a function of height along the fireball path. Similarly, we compute the arrival times for P-waves, using the previously described model of the airblast travelling to ground then the P-waves travelling to the seismic station. A graphical version of the resulting solution is shown in figure 6.

A priori, ignoring fragmentation (which produces quasi-spherical symmetry along the trajectory) we expect the ballistic-weak-shock to propagate approximately normal to the fireball trajectory (cf. Revelle, 1976). As a result, this airwave should have an origin from that portion of the trajectory of the fireball passing closest to the station. In figure 6 this would

be the minimum in the parabolic time propagation curve. In fact, the large-amplitude acoustic arrival occurs almost 20 seconds after this point.

To determine if this discrepancy is due to our ignoring the upper winds in calculation of the sound velocity, we have numerically modelled ray arrivals to the station from along the fireball trajectory. This simulation uses the same atmosphere as described earlier, but explicitly takes into account the wind velocity and ray propagation geometry in computing ray arrival times. As the wind velocity was very high near 30 km altitude (almost 70 m/s), we expect this may produce significant deviations from our nominal curves, making the sound velocity a function of propagation azimuth.

The model results for propagation from various source heights are shown in figure 6 as solid squares. The wind effects are clearly evident and account nicely for the timing difference. Where several rays reach WHY we have shown the extreme range in arrival times for a given height. The numerical results suggest that the beginning of the main seismic signal (and the largest amplitude) is indeed from the ballistic wave propagating nearly normal to the fireball path, with significant modifications from the upper wind.

The main seismic signal beginning 208s after the detonation continues for approximately 84s. This is longer than would be expected if only the portion of the trail near the specular point were contributing the airwave signal where dispersion effects which spread the acoustic signal in time are minimal. Anglin and Haddon, 1987 and Cumming, 1989 both show examples of air-coupled seismic waves from bright fireballs - in both cases the signals persist for  $\leq 10$  seconds. In our records, there are several additional maxima during this 84 second window. While some contribution from the P-wave may be present early in the record, it is unlikely to persist for this entire interval or show such localized maxima. We note that the extended signal could be a consequence of the properties of the soil proximal to the seismograph or the result of sound reflecting off the steep local terrain. No simple means of determining if extended resonance effects are significant due to local ground properties or sound reflection; we can only indicate that these are not seen for fireball airwaves recorded by other seismic instruments at different locations.

One interpretation of this extended signal is that it represents acoustic energy from ongoing gross fragmentation not represented in the cylindrical blast wave model and propagating in a wider suite of directions (ReVelle, 1976) to WHY. Such a model would suggest arrivals at WHY from the terminal portions of the fireball where the satellite light curve shows significant ablation and (by inference) possibly fragmentation. This is similar to the interpretations of Cumming (1989) and Folinsbee et al. (1969) where seismic data were compared to photographically determined fireball trajectories and suggested almost

all the acoustic signal was due to energy generated near the terminal portions of the trajectory. In both cases these locations were significantly different than the closest points along the trajectory relative to the receiving seismic stations.

Examining figure 6 we see that the numerical ray modelling shows acoustically accessible paths from heights along the trajectory restricted to those greater than 37 km altitude. Our numerical modelling reveals that lower heights may produce acoustic signatures, but these are just inside the first acoustic shadow zone of the sound as seen from WHY and would not contribute significantly to the seismic signal. Figure 8 demonstrates this effect.

That the numerical arrival times end within 10 seconds of the cessation of the main seismic signal suggests that fragmentation along the latter portion of the path is a plausible production mechanism for the extended signal. We also note that while heights along the fireball path below 38 km will not contribute significantly to the signal, our ray modelling is a geometrical approximation which ignores scattering and diffraction effects whereby lower portions of the trajectory may contribute to some of the trailing end of the main signal.

On the basis of seismic data from WHY, we suggest that the major portion of the large scale fragmentation for the Tagish Lake fireball ended near 32 km altitude. The seismic solution for station HYT is shown in figure 7 and supports this height determination. The WHY seismic record also suggests that this fragmentation dominated the last 45-60 km (3-4 seconds of travel through the atmosphere) of the path in agreement with the satellite light curve which shows almost 4 seconds of noticeable signal (corresponding to  $\approx 60$  km along the path at the nominal initial entry velocity).

### 3. PHYSICAL INTERPRETATION

#### 3.1. Meteorites

The meteorites recovered from the Tagish Lake fireball have been classified as C2, ungrouped. They represent a primitive form of carbonaceous chondrite, perhaps the most primitive meteorite studied to date (cf. Brown et al., 2000). Recent studies of the reflectance spectra from powdered Tagish Lake material also suggest a linkage with D-class asteroids (Hiroi et al., 2001). This represents the first connection between D-class asteroids and meteoritic material. This also supports the supposition that Tagish Lake material is primitive, given the presumed supercarbonaceous origins for the D-class asteroids (cf. Bell et al., 1989).

To further examine the physical character of the original Tagish Lake object, we have measured the densities and porosities of two Tagish Lake specimens.

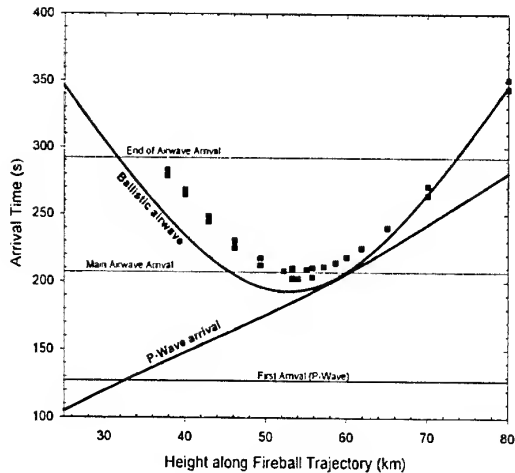


Figure 6. Seismic wave arrival times (labelled horizontal lines) and nominal air wave arrival times at WHY using a mean sound velocity as a function of height along the fireball trajectory (parabolic line). The zero time is the time of the fireball main detonation (16:43:43 UT). Also shown is the solution for P-wave arrivals. Square symbols represent numerical solutions from ray-path modelling (including wind effects) at each height to WHY as described in the text. These model solutions show those heights at which acoustic ray paths to WHY exist - this does not imply actual acoustic signals arrive from such heights as this also depends on the source generation mechanism, i.e. ballistic cylindrical shock vs. fragmentation. All modelled travel times have been corrected for the fireball's velocity.

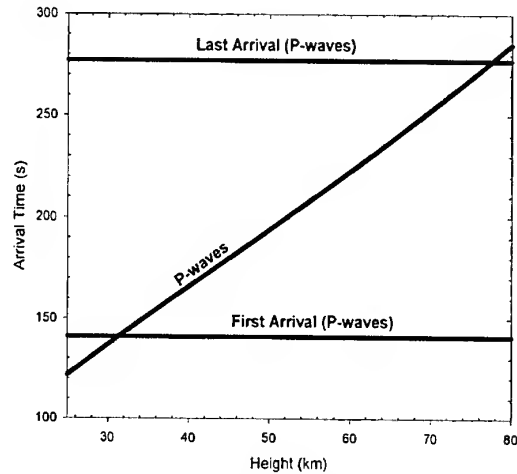


Figure 7. Seismic wave arrival times (labelled horizontal lines) at HYT using a mean sound velocity as a function of height along the fireball trajectory. The zero time is the time of the fireball main detonation (16:43:43 UT). Also shown is the solution for P-wave arrivals. All modelled travel times have been corrected for the fireball's velocity.

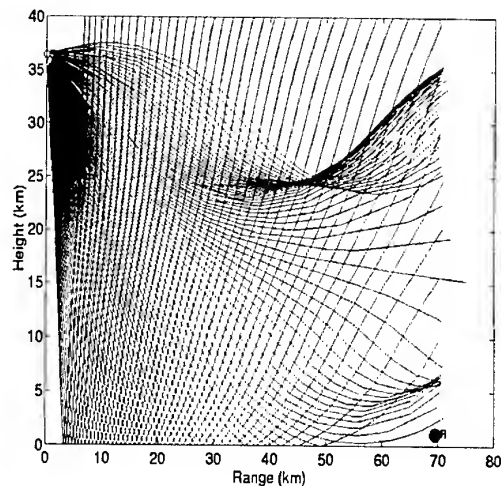


Figure 8. Acoustic ray paths from the location of the main burst to WHY (labelled as R in the lower right-hand corner of the figure). Notice the lack of rays reaching the receiver for this combination of height and range.

The results are shown in Table 2. The porosity and bulk density for Tagish lake are among the lowest yet measured for meteorites. Only the Orgueil CI-chondrite has been reported with comparable porosity and bulk density, though controversy exists as to whether these low values may be due to weathering effects (cf. Corrigan et al., 1997).

We expect that the material recovered from Tagish Lake preferentially represents the strongest portions of the original brecciated body. The implication of these measurements is that the original pre-atmospheric Tagish lake meteoroid had comparable or higher porosities and lower bulk densities to those given in Table 2. This would imply probable porosities of order  $\geq 40\%$ .

### 3.2. The Fireball

To attempt to place the Tagish Lake fireball in the context of physical data available for other fireballs, we make use of the PE-criterion introduced by Ceplecha and McCrosky (1976). This statistical index is a proxy measure for the relative physical strength of the associated meteoroid based on the ability of the associated fireball to penetrate the atmosphere. More specifically, the PE-criterion is given by

$$PE = \log(\rho_E) - 0.42 \log(m_\infty) + 1.49 \log(V_\infty) - 1.29 \log(\cos(Z_R))$$

where  $\rho_E$  is the air density at the fireball end-point,  $m_\infty$  is the initial mass,  $V_\infty$  is the initial velocity and  $Z_R$  is the zenith angle of the trajectory. Ceplecha and McCrosky (1976) suggested four basic physical groupings existed in the fireball record, from the strongest, most penetrating material (Group I) to the weakest material (Group IIIb). These groupings have been associated with (cf. Ceplecha et al., 1998), ordinary chondrites, carbonaceous chondrites, strong cometary material and weak cometary material for groups I, II, IIIa and IIIb respectively. We emphasize that the exact PE values where one group ends and another begins is somewhat uncertain as this is a purely statistical measure. From our best estimate for the initial mass of the Tagish Lake object (65 tonnes), its initial velocity (15.8 km/s), its known zenith angle at entry (72.2°) and the last observed dust cloud "point" from the ground based data of 29 km, we arrive at a  $PE = -5.39$ . This is near the border of the Type II and IIIa groups (which split at  $PE = -5.25$ ). Given the statistical uncertainties in the broader groups, we suggest that Tagish Lake represents the low end of the strength spectrum for carbonaceous chondrites or the very highest end of the cometary strength spectrum. This is consistent with the physical evidence from the meteorites.

## 4. DISCUSSION AND CONCLUSIONS

From the above evidence, we suggest that Tagish Lake represents an object which physically bridges the population of cometary objects and the weakest "asteroidal" material existing in meteorite collections. The high porosity of measured fragments as well as the higher inferred porosity of the initial object all suggest a weakly structured object. That any material reached the surface for collection is almost certainly the result of the large initial mass, low entry angle (and hence lower dynamic pressures) coupled with the region of the fall. We speculate that Tagish Lake-type material landing in warmer and wetter climates would be quickly eroded into chips and dust.

Of particular interest is the spectral connection between Tagish Lake and D-class asteroids (cf. Hiroi et al., 2001). We note that the only probable D-class asteroids to have accurate density determinations are Phobos and Deimos (cf. Britt and Consolmagno, 2000). Currently, the most accurate bulk densities for Phobos are  $1.53 \pm 0.1 \text{ g cm}^{-3}$  and  $1.34 \pm 0.83 \text{ g cm}^{-3}$  for Deimos (Smith et al., 1995). Comparison with Tagish Lake shows that the bulk densities are (within error) the same as the bulk density measurements for Tagish Lake. The high porosity of Tagish Lake samples ( $\approx 40\%$ ) indicates that both Martian moons need not have significant macroporosity and suggests that appeals to large amounts of interior ice or a thick regolith (eg. Smith et al., 1995) to account for the low bulk density of the Martian moons may be unnecessary.

## REFERENCES

- Anglin, F. M. & Haddon, R. A. W. 1987, *Nature*, 328, 607
- Bell, J. F., Davis, D. R., Hartmann, W. K., & Gaffey, M. J. 1989, *Asteroids II*, 921
- Borovicka, J. 1990, *Bulletin of the Astronomical Institutes of Czechoslovakia*, 41, 391
- Britt, D. T. & Consolmagno G. J., 2000, *Icarus*, 146, 213
- Brown, P. G. et al. 2000, *Science*, 290, 320
- Brown, P. et al. 1996, *Meteoritics and Planetary Science*, 31, 502
- Ceplecha, Z. & McCrosky, R. E. 1976, *Journal of Geophysical Research*, 81, 6257
- Ceplecha, Z. 1996, *Astronomy & Astrophysics*, 311, 329
- Ceplecha, Z., Spurný, P., Borovicka, J., & Kecklikova, J. 1993, *Space Science Reviews*, 279, 615
- Ceplecha, Z. ; K., Borovicka, J. ; Í., Elford, W. G., Revelle, D. O., Hawkes, R. L., Porubčan, V. ;, & Šimček, M. ; 1998, *Space Science Reviews*, 84, 327
- Corrigan, C. M., Zolensky, M. E., Dahl, J., Long, M., Weir, J., Sapp, C., & Burkett, P. J. 1997, *Meteoritics and Planetary Science*, 32, 509

- Cumming, G.L., 1989, *Canadian Journal of Earth Science*, 26, 1350
- Ewing, W.M., Jardetsky, W.S., & Press, F., *Elastic Waves in Layered Media*, McGraw-Hill, New York, 1967
- Herzog, G. F. et al. 1997, *Meteoritics & Planetary Science*, vol. 32, page A59, 32, 59
- Hildebrand, A. R. et al. 1997, *JRASC*, 91, 261
- Hiroi, T., Zolensky, M. E., & Pieters, C. M. 2001, *Lunar and Planetary Science Conference*, 32, 1776
- Kanamori, H., Anderson, D. L., Mori, J., & Heaton, T. H. 1991, *Nature*, 349, 781
- Keay, C. S. L. 1980, *Science*, 210, 11
- Qamar, A. 1995, *Seismological Research Letters*, 66, 6
- ReVelle, D.O. 1983, *Meteoritics*, 18, 386
- Revelle, D. O. 1976, *Journal of Geophysics Research*, 81, 1217
- Smith, D. E., Lemoine, F. G., & Zuber, M. T. 1995, *Geophysical Research Letters*, 22, 2171

Table 1. Trajectory solutions for the Tagish lake fireball using eyewitness data, the best three ground-instrumental records and satellite records. Shown are the apparent azimuth( $\phi$ ) and altitude( $\theta$ ) of the apparent radiant; the longitude ( $\lambda$ ) and latitude ( $\delta$ ) of the main burst, and the estimated height of the main burst

Solution	$\phi$	$\theta$	Main Burst ( $\lambda, \delta$ )	Height of main burst (km)
Eyewitness	$319 \pm 2.6^\circ$	$9.1 \pm 3.0^\circ$	$134.630 \pm 0.18^\circ, 59.99 \pm 0.11^\circ$	$31.4 \pm 2.7$
Video&Photographic	$330.7^\circ \pm 2.4^\circ$	$14.5^\circ \pm 1.6^\circ$	$134.645^\circ, 60.040^\circ$	$37.6 \pm 1.7$
Satellite	$330.7^\circ$	$17.8^\circ$	$134.6^\circ, 60.02^\circ$	35

Table 2. Orbit for the Tagish Lake fireball using the satellite recorded trajectory solution. All angular coordinates are J2000.0

$V_\infty$	$15.8 \pm 0.6 \text{ kms}^{-1}$
$\alpha_G$	$89.9 \pm 2.2^\circ$
$\delta_G$	$29.8 \pm 2.4^\circ$
a	$2.0 \pm 0.2 \text{ A.U.}$
c	$0.56 \pm 0.04$
q	$0.885 \pm 0.010 \text{ A.U.}$
$\omega$	$223.9 \pm 2.2^\circ$
$\Omega$	$297.901 \pm 0.001^\circ$
i	$2.0 \pm 0.9^\circ$
Q	$3.2 \pm 0.4 \text{ A.U.}$

Table 3. Densities and porosities of two Tagish Lake meteorites.  $M(g)$  is the measured mass in grams while mineral  $\rho$  is the grain density of the specimen ( $\text{gcm}^{-3}$ ) as measured by a helium pycnometer. The bulk  $\rho$  is the bulk density computed from the mass and volume (measured using glass beads). The porosity is a measure of the void space in the object and is computed from the grain density and mass. Data for Orgueil (CI chondrite) and other meteorite class averages are taken from Britt and Consolmagno (2000).

Sample	$M(g)$	Mineral $\rho$	Bulk $\rho$	Porosity (%)
Tagish Lake (RB)	30.44	2.74	$1.65 \pm 0.15$	$40 \pm 10$
Tagish Lake (ET-06)	77.19	2.56	$1.61 \pm 0.10$	$37 \pm 6$
Orgueil	47.2	2.43	$1.58 \pm 0.03$	$35 \pm 7$
H-Chon (Av.)	-	3.70	3.46	5
CM-Chon (Av.)	-	2.71	2.21	12

# BOLIDE PHYSICAL THEORY WITH APPLICATION TO PN AND EN FIREBALLS

D. O. ReVelle<sup>(1)</sup> and Z. Ceplecha<sup>(2)</sup>

<sup>(1)</sup>Los Alamos National Laboratory, P.O. Box 1663, MS J577, Earth and Environmental Sciences Division, EES-8, Atmospheric and Climate Science Group, Los Alamos, NM 87545, USA, Email: dor@vega.lanl.gov

<sup>(2)</sup>*Emeritus: Academy of Sciences, Astronomical Institute, Observatory, 25165 Ondřejov*

## ABSTRACT

Using data on 22 “precise bolides” with up to 882 individual points on their trajectories [4], [5], and using data on 29 “bright bolides” and on 10 artificial meteors [6], [8], [9], [10], we tried to derive the dependence of the ablation and shape-density coefficients, and of the luminous efficiency on various time dependent parameters. The only significant dependence we found was that on  $v_{\infty} - v$  (the difference of the initial and instantaneous velocities). We present the results as Eq's 3, 4 and 8, with coefficients  $a_1, a_2, a_3, a_4, b_1, b_2, b_3, c_1, c_2$  have been computed for a number of different bolide types. Also, the average values of the ablation, and shape-density coefficients as well as the average luminous efficiencies for individual bolide types are given.

## 1. BASIC DIFFERENTIAL EQUATIONS

Basic differential equations of meteor motion, ablation and radiation are given in [1]. The geometrical conditions of a bolide trajectory are described as a straight line over the local spherical Earth's surface. The shape-density coefficient,  $K$ , the ablation coefficient,  $\sigma$ , and the luminosity coefficient,  $\tau$ , are defined also in [1] (page 349).

## 2. SOLUTION WITH CONSTANT COEFFICIENTS

Solutions with constant coefficients  $K$  and  $\sigma$  ([1], [2], [3]) applied to sufficiently precise data (better than  $\pm 30$  m for one observed distance along the trajectory) on photographic multistation bolides yielded solutions without any gross-fragmentation (about 40%), and additional solutions with one gross-fragmentation point (about 40%). The remainder are either events with multi-fragmentation or with coefficients  $K$  and  $\sigma$  variable with time. Thus, we need to proceed to a solution of the basic differential equations with  $K$  and  $\sigma$  being variable with time.

## 3. SOLUTIONS WITH VARIABLE COEFFICIENTS

Solution of the basic equations with  $K$  and  $\sigma$  being a general function of time is given in [4]. This solution was applied to 22 bolides (PN and Ondřejov) with precision mostly around  $\pm 10$  m for one measured distance along trajectory (extremes were between  $\pm 4$  m and  $\pm 15$  m). For shortness we will refer to these 22 bolides as “precise bolides”. The results on precise bolides are given in [4], and in details in [5] (267 individual plots of different parameters for “precise bolides” as a function of time).

## 4. DEPENDENCE OF THE ABLATION COEFFICIENT, $\sigma$ , ON PARAMETERS

A suitable analysis of precise bolides could yield the dependence of  $\sigma$  on time dependent parameters. We performed the analysis for type-I and for type-II bolides separately. We do have not enough data to analyze the type-IIIA and type-IIIB bolides. Thus, for these latter two groups only the average, constant coefficient  $\sigma$ -values are available.

The data on  $\sigma$  for “precise bolides” in [4] were used to derive the change of  $\sigma$  with various parameters. We limited ourselves to search for the coefficients of logarithmic additive dependences, which is equivalent to multiplication of parameters, each put on an unknown power. This procedure of deriving the dependence of  $\sigma$  on any chosen parameter,  $P$ , can be described by Eq. 1. If any chosen parameter is denoted  $P$ , then we can define the relation of  $\ln P$  to  $\ln \sigma$  (where  $\ln$  is the natural logarithm) as

$$\ln \sigma_i = a_1 \ln P + a_{(i+1)}, \quad i = 1, 2, \dots, n \quad (1)$$

where  $n$  is the number of different bolides we used for the computation. Because we have many values available for each of the  $i$ -th bolide, we can use the least squares solution of Eq. 1. Then  $a_1$  defines the

average slope in the  $\ln \sigma$  over  $\ln P$  for all bolides used, while the values of  $a_2$  until  $a_{(n+1)}$  are shifts of individual dependences according to the average  $\ln \sigma$  value. We have available 391 individual values of  $\sigma$  for 15 type-II bolides. Results derived from these data:  $\sigma$  does not

depend on  $m, \frac{dm}{dt}, h$ . However,  $\sigma$  depends on

$v, \frac{dv}{dt}$  as:

$$\sigma \propto v^{-0.63 \pm 0.12} \left( -\frac{dv}{dt} \right)^{-0.32 \pm 0.05} \quad (2)$$

The proportionality constant in (2) resulted from (1) with a standard deviation larger than its value. Inspecting the reasons we came to the conclusion that relation (2) originates in the dependence of  $\sigma$  on  $v_x - v$  (where  $v_x$  is the initial velocity). The relation between  $\sigma$  and  $v_x - v$  was the strongest dependence we were able to determine and also with the smallest residuals. Individual values of  $\ln \sigma$  for each bolide were corrected to the same level of the average  $\sigma = 0.042 \text{ s}^2 \text{ km}^{-2}$  using the values  $a_2$  until  $a_{(1+n)}$ . The resulting average values of  $\ln \sigma$  for type-II bolides and for different intervals of  $\ln(v_x - v)$  are summarized in Table 1 and plotted in Fig. 1. The interval limits applied were 0, 0.5, 0.8, 0.9, 1.1, 1.25, 1.55, 1.90, which define 9 intervals. The smooth curve in Fig. 1 is the best fit to the average values by using a function defined as

$$\ln \sigma = a_1 \exp\{a_2 [\ln(v_x - v) + a_3]^2\} + a_4 \quad (3)$$

The best fit for the type-II bolides corresponds to

$$a_1 = -0.84, a_2 = -4.67, a_3 = -0.88, a_4 = -2.86$$

Standard deviation of the fit for one point is  $\pm 0.08$  in  $\ln \sigma$ .

There is not nearly as much data available on the „exact bolides“ of type I so that the same analysis as for type-II bolides could be carried out. We have only 56 individual values of  $\ln \sigma$  belonging to 4 different bolides available. Again, we used corrections of  $\ln \sigma$  to the same average level (type-I, i.e.  $\sigma = 0.014 \text{ s}^2 \text{ km}^{-2}$ ), and again no other significant dependence other than that on  $\ln(v_x - v)$  was found. The resulting average values of  $\ln \sigma$  for type-I bolides and for different intervals of  $\ln(v_x - v)$  are summarized in Table 2 and plotted in Fig. 1. The interval limits applied were 0.72, 1.04, 1.50, 1.78, defining five intervals. Because we have only 56 points divided into 5 intervals, it was not possible to determine all 4 unknown parameters of Eq. (3) just

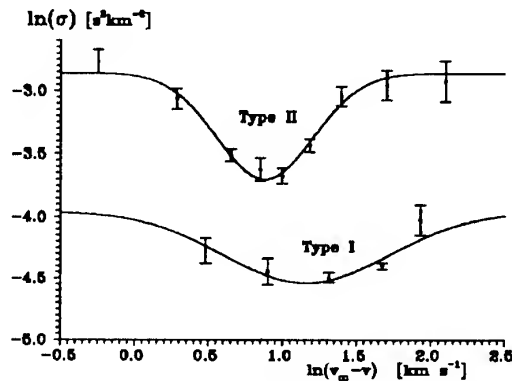


Fig. 1.

from these data alone. We used an additional condition that  $\ln \sigma$  for very large and very small values of  $\ln(v_x - v)$  have to be  $-3.96$ , i.e. a value that keeps the average difference of  $\ln \sigma$  between type-I and type-II bolides equal to  $1.10$ , which corresponds to a  $\sigma$ -ratio of  $1$  to  $3$  ( $0.014$  to  $0.042$ ). The smooth curve in Fig. 1 for the type-I bolides is the best fit of Eq. 3 to values in Table 1 and corresponds to

$$a_1 = -0.58, a_2 = -1.60, a_3 = -1.16, a_4 = -3.96.$$

The standard deviation for one point is  $\pm 0.03$  in  $\ln \sigma$ . This reflects the situation that we determined only 3 unknowns (the fourth one was fixed at  $-3.96$ ).

Table 1. Type-II bolides  
n ... is number of individual values

$\ln(\sigma)$	$\ln(v_x - v)$	n
$-2.767 \pm 0.094$	$-0.247 \pm 0.030$	38
$-3.062 \pm 0.081$	$0.287 \pm 0.021$	52
$-3.512 \pm 0.048$	$0.651 \pm 0.010$	68
$-3.623 \pm 0.092$	$0.850 \pm 0.006$	23
$-3.675 \pm 0.059$	$0.998 \pm 0.009$	45
$-3.432 \pm 0.052$	$1.184 \pm 0.008$	32
$-3.043 \pm 0.077$	$1.396 \pm 0.012$	52
$-2.954 \pm 0.120$	$1.703 \pm 0.015$	54
$-2.925 \pm 0.162$	$2.100 \pm 0.035$	27

Table 2. Type-I bolides  
n ... is number of individual values

$\ln(\sigma)$	$\ln(v_x - v)$	n
$-4.278 \pm 0.103$	$0.482 \pm 0.049$	12
$-4.446 \pm 0.107$	$0.901 \pm 0.029$	10
$-4.494 \pm 0.042$	$1.315 \pm 0.043$	10
$-4.400 \pm 0.026$	$1.674 \pm 0.023$	9
$-4.024 \pm 0.123$	$1.931 \pm 0.024$	15

## 5. DEPENDENCE OF THE SHAPE-DENSITY COEFFICIENT, $K$ , ON PARAMETERS

The 22 „precise bolides“ were used to derive the change of  $K$  with various parameters. The procedure of doing this was the same as described for  $\sigma$  using Eq. (1). We also corrected individual  $K$  values for the average  $K$  of the corresponding type (type I: average  $K=0.46$ , type II: average  $K=0.69$ ). We have available substantially more individual values of  $K$  than those of  $\sigma$ , that we used for determining the average dependence of  $\sigma$  on different parameters. This situation reflects the fact that  $\sigma$  cannot be determined during the early parts of trajectories, and  $K$  moreover does not depend on the average  $\sigma$  used at these early parts of trajectories. Thus we have available 882 individual values of  $K$  for type-II bolides. We tested the dependence of these 882 values of  $K$  on  $v$ ,  $dv/dt$ ,  $m$ ,  $dm/dt$  and  $h$ . No significant dependence (i.e. exceeding one standard deviation) was found. Particularly,  $K$  proved to be independent of height  $h$  (i.e. of the air density).

We also added the difference of  $v_\infty - v$  to possible parameters, because  $K$  shows a well defined and rather strong dependence on this parameter. Applying Eq. (5) (the least-squares) to all 15 bolides available for type-II „precise bolides“, we found a strong correlation to  $v_\infty - v$ . Using the 882 values mentioned above, we computed averages of  $\ln(v_\infty - v)$  and  $\ln K$  for consecutive intervals of  $\ln(v_\infty - v)$  chosen so that the standard deviations of average values of  $\ln K$  were kept within reasonable limits. The interval limits we applied were  $-3.5, -1.5, -1.0, -0.5, -0.1, 0.3, 0.7, 1.1, 1.5$ , defining 9 intervals (we omitted 3 points with  $\ln(v_\infty - v) < -3.5$ , because of a very large spread due to the large standard deviations of individual values). The results are given in Table 3 and Fig. 2. The smooth curve in Fig. 2 is the best fit of a function defined as:

$$\ln K = b_1 + b_2 \tanh(b_3 \ln(v_\infty - v)) \quad (4)$$

The fit for type-II bolides corresponds to  $b_1 = -0.3$ ,  $b_2 = 2.5$ ,  $b_3 = -0.2$ .

The standard deviation for one point is  $\pm 0.11$  in  $\ln K$ . This value has already been corrected for the average value of  $\ln K$ . The average value of  $\ln K$  computed from Eq. (4) with the above values of  $b_1, b_2, b_3$ , and computed inside an interval of  $\ln(v_\infty - v)$  from  $-2.3$  to  $2.6$  resulted in  $\ln K = -0.37$ , i.e.  $K = 0.69$  (c.g.s.).

There is not much data available on the „precise bolides“ of type I, but it is again more than for determining average dependence of  $\sigma$  on parameters.

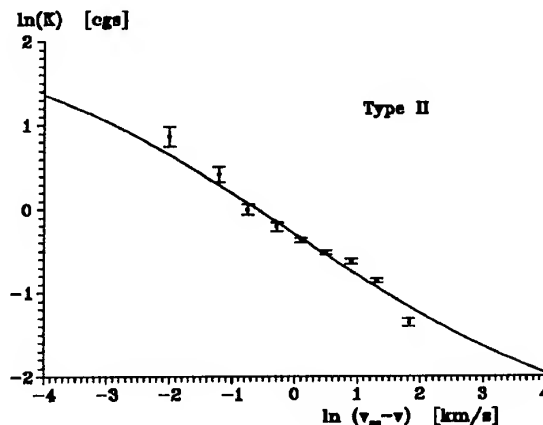


Fig. 2.

The variability of  $\ln K$  with different time dependent parameters was tested by means of all 4 „precise bolides“ of type I. Altogether we have available 124 values of  $K$  for type I. Using these 124 values, we computed averages of  $\ln(v_\infty - v)$  and  $\ln K$  for consecutive intervals of  $\ln(v_\infty - v)$  chosen so that the standard deviations of the average values of  $\ln K$  were kept within reasonable limits. The interval limits we applied were  $-0.5, 0.5, 1.5$ , defining 4 intervals. The results are given in Table 4. These values are very close to the smooth curve in Fig. 2 (derived for type-II bolides). The average  $\ln K = -0.776$ , i.e.  $K = 0.46$  (c.g.s.), i.e. exactly the average value for all PN bolides. This corresponds to an interval from  $-1.6$  to  $3.6$  in  $\ln(v_\infty - v)$ , if equation (4) is used with the same values of  $b_1, b_2, b_3$ , as were derived for type-II bolides. Because of insufficient precision, our conclusion is simple. There is no significant (one standard deviation) difference of  $\ln K$  as a function of  $\ln(v_\infty - v)$  from the dependence derived for type-II bolides. Thus, we will assume that this function is the same for type-I as well as for type-II bolides.

Table 3. Type-II bolides  
n ... is number of individual values

$\ln K$	$\ln(v_\infty - v)$	n
$0.865 \pm 0.113$	$-2.005 \pm 0.041$	75
$0.426 \pm 0.088$	$-1.213 \pm 0.017$	77
$-0.002 \pm 0.061$	$-0.752 \pm 0.015$	107
$-0.211 \pm 0.051$	$-0.289 \pm 0.012$	96
$-0.379 \pm 0.029$	$0.099 \pm 0.012$	93
$-0.520 \pm 0.026$	$0.496 \pm 0.012$	95
$-0.628 \pm 0.028$	$0.901 \pm 0.012$	98
$-0.858 \pm 0.024$	$1.307 \pm 0.010$	126
$-1.358 \pm 0.049$	$1.821 \pm 0.024$	112

Table 4. Type-I bolides  
n ... is number of individual values

$\ln K$	$\ln(v_\infty - v)$	n
$-0.122 \pm 0.115$	$-0.888 \pm 0.063$	26
$-0.830 \pm 0.071$	$0.048 \pm 0.054$	29
$-0.831 \pm 0.045$	$0.975 \pm 0.051$	32
$-1.192 \pm 0.029$	$1.924 \pm 0.036$	33

## 6. DEPENDENCE OF THE LUMINOUS EFFICIENCY, $\tau$ , ON PARAMETERS

The entire section on luminous efficiency will deal exclusively with the *differential* luminous efficiency,  $\tau$ , as defined in [1] (page 362, eq. (29)). The average values of  $\tau$  for individual bolide types can be derived from a previous study on "bright bolides" in [6], where all the necessary data are listed in Table 2. Also, the entire procedure of computing and correcting one average value of  $\tau$  for each bolide is described on pages 48 to 50 in [6]. The results, based on 29 individual "bright bolides", are given in Table 5 together with the average values of  $K$  and  $\sigma$  ( $\tau$  is given in percent of the total kinetic energy,  $E$ ). There was insufficient data available for obtaining independent values of  $\tau$  for type IIIA and IIIB separately, and they were therefore treated as one group.

Table 5: Average values of  $K$ ,  $\sigma$  and  $\tau$  for different bolide types:  
( $\tau$  is in percent of total kinetic energy,  $E$ )

type	I	II	IIIA	IIIB
$\rho_d$ g cm <sup>-3</sup>	3.7	2.0	0.75	0.27
$\sigma$ s <sup>2</sup> km <sup>-2</sup>	0.014	0.042	0.10	0.21
$K$ cgs ( $\Gamma A=1.1$ )	0.46	0.69	1.33	2.63
$\tau$ % of $E$	5.57	1.35	0.242	

### 6.1 Luminous Efficiency as Function of Velocity and Mass

Since the very beginning of meteor physics, it was recognized that luminous efficiency depends on velocity. We start the present analysis with a function

given in [7] (Fig.1 and equation (40)). Below 16 km/s the cited relation took into account experimental results (artificial meteors produced in the atmosphere by man-made bodies fired down from high altitude rockets) given in [8]. The results given in [7] are also based on detailed study of the motion of individual recovered fragments of the Innisfree meteorite in [9] (where photographic records are available). The relation can be written as an interpolation formula (already in a form using natural logarithms):

for  $v < 25.372$  km/s:

$$\ln \tau = k_1 - 10.307 \ln v + 9.781 (\ln v)^2 - 3.0414 (\ln v)^3 + 0.3213 (\ln v)^4 \quad (5)$$

for  $v \geq 25.372$  km/s:

$$\ln \tau = \ln v + k_2$$

where values of  $k_1 = -1.494$  and  $k_2 = -3.488$  correspond to the values in [7]. However, we will leave  $k_1$  and  $k_2$  as free parameters, and determine their numerical values for individual bolide types after we increase the complexity of expression (5) by additional terms for mass,  $m$ , and eventually by additional terms for other possible parameters.

What remains to be done first is the dependence of  $\tau$  on mass, which became possible after the analysis of the Lost City bolide and meteorite fall that was published in [10]. Well-documented meteorite falls (multistation photographic records) form a reliable way to obtain realistic values of  $\tau$ , because the dynamical mass computations can be calibrated by the terminal mass (recovered meteorites). Such results seem to be equivalent to the results of the rocket experiments in [8], and moreover yield data on much larger bodies and also for those at somewhat higher entry speeds. We used the following expression for the  $\tau$ -dependence on mass as an additive term to the velocity dependence:

$$\ln \tau(m) = k_3 + k_4 \tanh(k_4 \ln m) \quad (6)$$

If Eq. (6) is used as an additive term to Eq. (5), the advantage of having a smooth change of  $\tau$  with  $m$  between two extreme values (one for very small masses and the other for very large masses) is evident. The form of Eq. (6) assumes that the largest change of  $\tau$  with  $m$  takes place at masses of 1 kg, which corresponds to the situation that experimental values for smaller masses of several grams in [8] are about 10 times smaller than the values derived for the Lost City

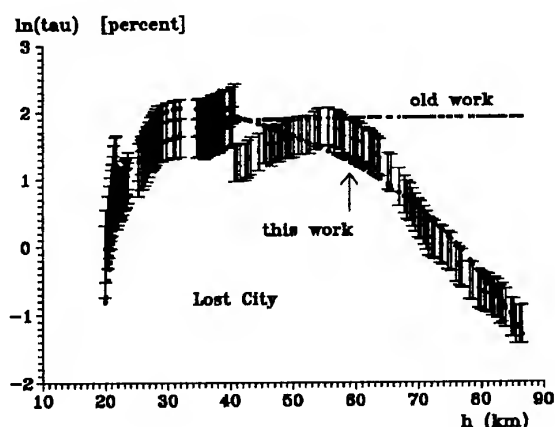


Fig. 3.

meteoroid (initial mass of 163 kg). These two sets of  $\tau$  values, the Innisfree bolide  $\tau$ -values for different fragments, and the „bright bolide“  $\tau$ -values were normalized to the same velocity by Eq. (5). Then Eq. (6) applied to them yielded  $k_3 = 1.15 \pm 0.16$ , and  $k_4 = 0.38 \pm 0.12$ .

## 6.2 Luminous Efficiency as Function of Other Parameters

Data on 15 „precise bolides“ (those for which photometric data are available) can be used in the same way as we already have used data on all 22 „precise bolides“ for determining the dependence of  $\sigma$  and  $K$  on different parameters. A similar procedure as described by Eq. (1) was adopted for the residuals

$$\ln \tau (\text{obs}) - \ln \tau (\text{com}),$$

where the computed values of  $\ln \tau$  included the sum of both  $\ln \tau$  values computed from equation (5) and (6). The individual values of  $\ln \tau$  at all 791 observed points of 15 „precise bolides“ were used as the observed values of  $\ln \tau$ . No significant dependence on different parameters were found except for  $\ln(v_\infty - v)$  (this is analogous to the previous  $\sigma$  and  $K$  results). The resulting dependence of the above defined residuals on  $\ln(v_\infty - v)$  was found as

$$\ln \tau = k_5 + k_6 \ln(v_\infty - v) + k_7 (\ln(v_\infty - v))^3 \quad (7)$$

where the fit to 791 values of residuals yielded  $k_6 = 0.26 \pm 0.02$  and  $k_7 = 0.0042 \pm 0.0005$ , while  $k_5$  for individual bolides differed so much that its standard deviation is also well outside its average value.

## 6.3 Resulting Expression for Computing Luminous Efficiency for Different Bolide Types

If we add all the terms (5), (6), and (7), we determined only two constants,  $c_1$  and  $c_2$ , valid for two different velocity intervals defined by (5):  $c_1 = k_1 + k_3 + k_5$  and  $c_2 = k_2 + k_3 + k_5$ . These two constants differ for different bolide types and were determined using equation (8) so that the average difference of  $\ln \tau$  follows the differences given in Table 5. The resulting expression for computing  $\ln \tau$  is given as follows

for  $v < 25.372$  km/s

$$\begin{aligned} \ln \tau = & c_1 - 10.307 \ln v + 9.781 (\ln v)^2 - \\ & - 3.0414 (\ln v)^3 + 0.3213 (\ln v)^4 + \\ & + 1.15 \tanh(0.38 \ln m) + 0.26 \ln(v_\infty - v) + \\ & + 0.0042 (\ln(v_\infty - v))^3 \end{aligned} \quad (8)$$

for  $v \geq 25.372$  km/s

$$\begin{aligned} \ln \tau = & c_2 + \ln v + 1.15 \tanh(0.38 \ln m) + \\ & + 0.26 \ln(v_\infty - v) + 0.0042 (\ln(v_\infty - v))^3 \end{aligned}$$

where

$$\text{for type-I bolides} \quad c_1 = +0.466, \quad c_2 = -1.538$$

$$\text{for type-II bolides} \quad c_1 = -0.955, \quad c_2 = -2.959$$

$$\text{for type-IIIA, IIIB} \quad c_1 = -2.670, \quad c_2 = -4.674$$

When the resulting Eq. (8) was used for the Lost City bolide, and the computed values of  $\ln \tau$  compared to those values previously derived in [10], a significant improvement was evident. The luminous efficiencies determined for the early parts of the Lost City trajectory were not readily explainable using the previous analysis of  $\tau$  (and where we did not have the „precise bolide“ data available then). However, the present analysis for  $\ln \tau$  fits the observed values of  $\ln \tau$  for the early parts of the Lost City bolide quite well. This improvement was shaped into the final expression (8) by the analysis of the „precise bolides“. A comparison of the old and the new values of  $\ln \tau$  for the Lost City bolide is presented in Fig. 3 and forms independent evidence that the present analysis of  $\ln \tau$  is principally correct.

#### 6.4 Radiation Pass-Band of the Derived Luminous Efficiency

For deriving  $\tau$  in this section, we made use of data on luminosity obtained from photographic observations with panchromatic emulsions. Thus the derived  $\tau$ -values correspond to panchromatic pass-band, i.e. approximately between 360 and 650 nm. However, most of the bolide energy, especially for slower meteoroids, is radiated just in this pass-band with a characteristic temperature of 4500 K for the main spectral component (in [1], page 362–366). Spectral data on radiation in other pass-bands are almost non-existent. If we had such data available, we could derive spectral (temperature) corrections for the values of Eq. (8), which would allow the transformation of  $\tau$  to other spectral pass-bands.

#### 6.5 Comparison to Earlier Theoretical Work

In [11], the panchromatic luminous efficiency was also explicitly calculated for the three photographed and recovered meteorites at that time, Lost City, Innisfree and Pribram using the entry model in [12] and utilizing the luminous efficiency equation expressed in terms of the full kinetic energy depletion process. The calculations for all three meteorites all indicated a nearly Gaussian shaped pulse of the luminous efficiency versus height whose peak value was ~ 1-2 %, with the exception of the more uncertain case of Pribram which was not observed photographically over all altitudes. The degree to which the current approach agrees with these earlier results is far better than we could have expected, especially since the new results were done totally independently from the earlier work. It is especially of interest that these two approaches agree so well, both in shape and in the magnitude of the differential luminous efficiency since the two approaches are so different. The approach in [11] and in [12] produces results based on the observed bolide flight data and very detailed physically based convective and radiative heat transfer calculations (with the latter being the dominant heat transfer mechanism for the larger bodies). The current approach has only flight data at its disposal, including the historically difficult to measure parameter, the bolide deceleration. This parameter depends on a first time derivative of the directly observed velocity. The excellent agreement between these two approaches for the differential luminous efficiency is clearly a topic that should be more fully investigated.

#### 7. REFERENCES

1. Ceplecha Z., Borovička J., Elford W.G., ReVelle D.O., Hawkes R.L., Porubčan V., and Šimek M., Meteor Phenomena and Bodies, *Space Science Reviews*, Vol. 84, 327–471, 1998
2. Ceplecha Z., Spurný P., Borovička J., and Keckliková J., Atmospheric Fragmentation of Meteoroids. *Astron. Astrophys.*, Vol. 279, 615–626, 1993.
3. Ceplecha Z., Meteoroid Properties from photographic Records of Meteors and Fireballs, Asteroids, Comets, Meteors 1993, *IAU Symp.* 160, 343–356, 1994.
4. Ceplecha Z., Borovička J., and Spurný P., Dynamical Behavior of Meteoroids in the Atmosphere Derived from Very Precise Photographic Records, *Astron. Astrophys.* Vol. 367, 1115–1122, 2000.
5. Ceplecha Z., Borovička J., and Spurný P., Dynamical Behavior of Meteoroids in the Atmosphere Derived from Very Precise Photographic Records, Plots for Results, <http://www.asu.cas.cz/~ceplecha/prechol.html>, 2000.
6. Ceplecha Z., Spalding R.E., Jacobs C. and Tagliaferri E., Luminous Efficiencies of Bolides. *Proc. SPIE*, Vol. 2813, 46–56, 1996.
7. Pecina P. and Ceplecha Z., New Aspects in Single-Body Meteor Physics, *Bull. Astron. Inst. Czech.*, Vol. 34, 120–121, 1983.
8. Ayers W.G., McCrosky R.E., and Shao C.-Y., Photographic Observations of 10 Artificial Meteors, *Smithsonian Astrophys. Obs. Spec. Rep.*, Vol. 317, 1–40, 1970.
9. Halliday I., Griffin A.A., and Blackwell A.T., The Innisfree Meteorite Fall, *Meteoritics* Vol. 16, 153–170, 1981.
10. Ceplecha Z., Luminous Efficiency Based on Photographic Observations of the Lost City Fireball and Implication for the Influx of Interplanetary Bodies onto Earth, *Astron. Astrophys.* Vol. 311, 329–332, 1996.
11. ReVelle, D.O. and Rajan R.S. (1979). On the Luminous Efficiency of Meteoritic Fireballs, *J. Geophysical Research*, Vol. 84, 6255–6262, 1979.
12. ReVelle, D.O., A Quasi-simple Ablation Model for Large Meteorite Entry: Theory versus Observations, *J. Atmosph. Terr. Physics.*, Vol. 41, 453–473, 1979.

# BOLIDE DYNAMICS AND LUMINOSITY MODELING: COMPARISONS BETWEEN UNIFORM BULK DENSITY AND POROUS METEOROID MODELS

D. O. ReVelle

*Los Alamos National Laboratory, P.O. Box 1663, MS J577, Earth and Environmental Sciences Division,  
Atmospheric and Climate Sciences Group, Los Alamos, New Mexico, 87545 USA  
Email: dor@vega.lanl.gov*

## ABSTRACT

We compare predictions of bolide behavior using basic meteoroid models, first assuming a uniform bulk density throughout the body and secondly assuming a uniform chondritic composition throughout, but with varying amounts of porosity (assumed to be filled with either water-ice or open space). The second model is based on the uniformity of spectral observations over many years from shower meteors from the extremes of the Geminids to the dustball-like Draconids. The first model utilized is due to ReVelle (1979, 1993) and the second is based upon the porous meteoroid model of ReVelle (1983, 1993). The standard, uniform bulk density model assumes that the drag and heat transfer area are equivalent in the positive, shape change factor limit. For porous meteoroids however, the heat transfer area can exceed the drag area by increasingly larger amounts as the body's porosity increases. ReVelle (1983) used this approach to show that the bulk density and ablation parameter compositional group identifications of Ceplecha and McCrosky (1976) were essentially correct. When these factors are introduced into the relevant model equations, a set of nearly self-consistent predictive relations are developed which readily allows comparisons to be made of the end-height variations and of the normalized luminous output of the two basic meteoroid models.

## 1. INTRODUCTION AND OVERVIEW

### 1.1 Uniform versus porous meteoroids:

Spectral measurements of shower meteors taken over many years indicate nearly chondritic

abundances for all showers from the Geminids to the Draconids regardless of their inferred bulk density or overall strength. This indicates that one way of accounting for atmospheric behavioral differences, i.e., bolide types, is to assume varying degrees of porosity (but are the pore spaces filled with water-ice or something else or just empty?) In this paper, we will model bolides both ways and determine which approach best agrees with the observed data (dynamics and luminosity).

### 1.2 Normalized or un-normalized light curves:

We have separated the light emission into the product of a unit normalized light curve as a function of either height or of time and a height, velocity, mass and wavelength dependent luminous efficiency. The emission is un-normalized by taking the product of these two quantities and the maximum time rate of change of the kinetic energy over a specified electromagnetic wavelength band. We have not completed this part of the work yet so here we will only summarize previous work that has already been done on this topic. We will report on this separately later next year at the Berlin ACM Conference (July, 2002).

## 2. FUNDAMENTAL METEOROID MODELING

### 2.1 Uniform bulk density models versus porous meteoroid models:

Uniform bulk density models arise from the definition,  $\rho_m \equiv m/V_o$ , with the shape factor,  $S_f \equiv A_d/V_o^{2/3}$ , where  $A_d$  is the drag area (of the frontal cross-section) and  $V_o$  is the total volume.

Porous, meteoroid modeling can be summarized by noting that the heat transfer area,  $A_h$ , increases in direct proportion to the relative degree of porosity,  $\psi' = \text{porous volume/total volume}$  ( $0 \leq \psi' \leq 1$ ), with the result (ReVelle, 1983) for porous meteoroids:

$$A_h = A_d \cdot (1 - \psi')^{-1}$$

$$\rho_m^* = (1 - \psi') \rho_{mo} + \psi' \rho_m^*$$

$A_h = A_d$  if  $\psi' = 0$ : Uniform bulk density limit

where

$\rho_{mo}$  = bulk density of nonporous chondritic materials  
 $\rho_m^*$  = bulk density of porous materials with the constraint that:

$$0 \leq \rho_m^* \leq 1.0 \text{ g/cm}^3$$

using the water-ice density and empty space (vacuum) as upper and lower limits of the pore space density respectively.

$$\sigma^* = \sigma \cdot \{A_h/A_d\}$$

$$\sigma^* \rho_m = \sigma \rho_{mo} = \text{constant} = 7.4 \cdot 10^{-12} \text{ (CGS units)}$$

At  $V_\infty = 20 \text{ km/s}$  for porous meteoroids:

$$\log(\sigma^* \rho_m) = -11.13$$

## 2.2 Interpretation of bolide groups

From Cepplecha et al. (1998) using a uniform bulk density bolide model and averaging over all bolide groups (with  $\pm 1$  std. dev. term included):

$$\log(\sigma^* \rho_m) = -11.183 \pm 9.91 \cdot 10^{-2}$$

This can be compared directly to the result above for porous meteoroids. The excellent agreement between these two independent evaluations makes porosity a very viable explanation of most bolide behavior if bolides are actually both porous and chondritic. The advantage of this approach is that as porosity  $\rightarrow 0$ , the two models produce identical results.

## 3. LUMINOSITY MODELING OF BOLIDES

### 3.1 Normalized and un-normalized bolide light curves

Assuming that the light emission,  $I$  over an electromagnetic wavelength band is proportional to the time rate of change of the kinetic energy,  $dE_k/dt$ , of the body (where the proportionality constant is  $\tau$ , the luminous efficiency of a chondritic substance of uniform bulk density) over that wavelength band.

$$I = -\tau \cdot dE_k/dt$$

$$dE_k/dt = -0.50 \cdot V^2 \cdot dm/dt \cdot \{1 + \Delta(z)\}$$

$$dm/dt = \sigma V \cdot dV/dt = -0.50 \cdot \rho V^3 \sigma (A_h/m)$$

$$\Delta(z) = 2/(\sigma V^2)$$

" = inverse dimensionless ablation efficiency at any height

Assume  $\tau = \text{constant}$  and normalizing the light by  $I_{\max}$  to have unit amplitude, where  $I_{\max}$  is the value of the maximum theoretical light emission. In our approach, we have allowed  $\rho$ ,  $V$  and  $\sigma$  to vary with time/height unlike the classical approach (Bronshten, 1983) that has only allowed  $\rho$  as a variable.

$$\therefore I_L / I_{\max} = \Psi(t) \cdot \tau_c$$

$$I_{\max} \propto \rho_{\max} \cdot V_{\max}^5 \cdot \sigma_{\max} \cdot \{1 + \Delta_{\max}(z_{\max})\}$$

where

$$\Psi(t) = -dE_k/dt / I_{\max}$$

" = the theoretical light curve shape versus time.

To obtain the actual light emission in absolute power units over a specific wavelength interval, we must calculate  $\tau_L$  from first principles. It is expected that  $\tau_L = f(\rho(z), V, \text{composition, body size, Knudsen number, etc.})$ .

### 3.2 Effects of $\mu < 0$ on the emission of light:

An expression due to Levin and presented in Bronshten (1983) for the standard light curve as a function of the  $\mu$  parameter (for details see ReVelle, 2001d):

$$I \equiv dm/dt / (dm/dt)_{\max}$$

$$I = I_{\max} \cdot \{\mu^{-\mu/(1-\mu)}\} \cdot \{\rho/\rho_{\max}\} \cdot [1 - (1-\mu) \cdot \{\rho/\rho_{\max}\}]^{\mu/(1-\mu)}$$

This formula was derived from classical meteor theory for an isothermal, hydrostatic atmosphere, assuming that:

$$V = V = \text{constant}, \sigma = \text{constant}, \mu = \text{constant}$$

Its range of applicability should be small for large, bright bolides where air drag is significant. Also, for large negative  $\mu$ , drag is even more important and the formula is even less likely to be useful. Its solutions become imaginary, however if  $\rho/\rho_{\max} < 1$ .

We have also derived a new, generalized light curve model with "gross-fragmentation" break-up (used below) with  $\rho$ ,  $V$ , and  $\sigma$  as variables (to be submitted shortly). Details will be presented at the Berlin ACM Conference in July of 2002.

As shown by ReVelle (1999, ACM, and 2001d-this conference), it is not a sufficient condition for  $\mu$  to be  $< 0$  to have significant effects that would invalidate the single-body approximation. It is also necessary that  $H_f \ll H_p$ . After fragmentation starts, the effective  $Q_i$  will also decrease (and  $\sigma$  will become larger) which will also influence this progression of events.

#### 4. APPLICATIONS: THE TAGISH LAKE METEORITE FALL: JANUARY 18, 2000- SOME PRELIMINARY RESULTS

Below we summarize some of our preliminary results for the Tagish Lake bolide. This is given below for the case of  $\mu = 0.10 = \text{constant}$ . We also present results in Table 2 at the end of this paper for the case of  $\mu = 2/3$  (no shape change).

##### 4.1 Fixed bolide entry parameters:

1.  $V_{\infty} = 15.8 \text{ km/s}$ ,  $\theta = 18^\circ$ ,  $S_f = 1.209$  (sphere initially),  $Q_{\text{vap}} = 7.98 \cdot 10^6 \text{ J/kg}$ ,  $Q_{\text{melt}} = 1.884 \cdot 10^6 \text{ J/kg}$
2.  $k_1 = 5$ ,  $k_2 = 25$ ,  $Re_{\text{trans}} = 9 \cdot 10^5$  (at the turbulent boundary layer transition)
3.  $8.0 \cdot 10^4 \text{ Pa} \leq S_{\text{tensile}} \leq 3.0 \cdot 10^5 \text{ Pa}$ : Fragmentation triggering if  $p_{\text{stag}} \geq S_{\text{tensile}}$
4.  $D = 4.605$  (99 % kinetic energy depletion at the end height)
5.  $C_D (Kn \geq 10) = 2.0$ ,  $C_D (Kn \leq 0.1) = 0.92$
6.  $\mu_{\text{init}} = 0.10$  (shape change allowed during entry-mean value from ReVelle and Ceplecha, 2001-this conference).

##### 4.2 Varied parameters:

1. Uniform bulk density model (measured values):  $1600 \text{ kg/m}^3 \leq \rho_m \leq 1670 \text{ kg/m}^3$
2. Porous meteoroid model: Volume porosity:  $0 \leq \psi \leq 70 \%$
3. Initial body radius:  $1.0 \leq r \leq 2.5 \text{ m}$
4. Fundamental atmospheric model parameters:  $p_{\text{surf}} = 1.01325 \cdot 10^5 \text{ Pa}$ ,  $\lambda_{\text{surf}} = 5.49 \cdot 10^{-8} \text{ m}$ ,  $g = 9.80665 \text{ m/s}^2$ ,  $M_{\text{surf}} = 28.966 \text{ kg/kmole}$

##### 4.3 Uniform meteoroid modeling results: $\mu = 0.10$ (Significant shape change)

- i)  $m_{\text{initial}} = 3.70 \cdot 10^4 \text{ kg}$ ,  $m_{\text{final}} = 6.4 \cdot 10^3 \text{ kg}$  (Brown et. al., 2000 estimate 200 kg)
- ii)  $r_{\text{initial}} = 1.75 \text{ m}$  with predicted ablation = 83 %
- iii)  $z_{\text{end}} = 25.0 \text{ km}$  (= 33.95 km with variable  $\sigma$  and break up).
- iv)  $z_{\text{break}} = 37\text{--}52 \text{ km}$  for  $6.9 \cdot 10^5 \leq p_s \leq 10^5 \text{ Pa}$ .
- v)  $V_{\text{end}} = 9.33 \text{ km/s}$
- vi)  $R_o = 178.6$  to  $2.2 \text{ m}$ , which corresponds to  $\tau_{\text{wave}} = 1.62$  to  $0.02 \text{ s}$  (line source blast wave at 10 scaled radii (~1.79 km from the trail)).

##### 4.4 Porous meteoroid modeling results: 50 % $\mu = 0.10$ (Significant shape change)

- i)  $m_{\text{initial}} = 6.20 \cdot 10^4 \text{ kg}$ ,  $m_{\text{final}} = 1675 \text{ kg}$
- ii)  $r_{\text{initial}} = 2 \text{ m}$  with predicted ablation = 97 %
- iii)  $z_{\text{end}} = 22.3 \text{ km}$  (or 35.7 km with variable  $\sigma$  and break up).
- iv)  $z_{\text{break}} = 37\text{--}51 \text{ km}$  for  $6.7 \cdot 10^5 \leq p_s \leq 10^5 \text{ Pa}$ .
- v)  $V_{\text{end}} = 8.62 \text{ km/s}$
- vi)  $R_o = 204.2$  to  $0.43 \text{ m}$ , which corresponds to  $\tau_{\text{wave}} = 1.85$  to  $0.0039 \text{ s}$  (at 10 scaled radii).

#### 5. GENERALIZED RESULTS: Dynamics and light curves

##### 5.1 Generalized dynamical results

Group I bolides are well explained with bodies of chondritic elemental abundance and nearly zero porosity. This is the limit of a uniform chondritic body where the two theories converge in their predictive properties. Groups II, IIIA and IIIB, need progressively larger amounts of porosity to be readily explainable. The degree of porosity necessary must extend from ~ 50 % (group II) to as much as 91 % (group IIIB) to explain their atmospheric dynamical behavior. These results,

as summarized in Table I at the end of this paper, are given at an entry velocity = 20 km/s, since they are slightly entry velocity dependent.

If the pore spaces are filled with water-ice or other substances, the degree of dynamical agreement rapidly degrades unless the substances themselves are of very low bulk density. For the emission of light we also find agreement with the deduced bolide types with an assumed luminous efficiency factor (constant at all heights). For the progression from I  $\rightarrow$  II  $\rightarrow$  IIIA for an entry mass of 100 kg at 20 km/s, we find the peak luminosity increasing progressively from -14.3 to -15.1. This porous meteoroid model result stems from the increased surface area for heat transfer processes compared to that for air drag.

#### 4.2 Generalized light emission: Porous meteoroids

We will now generalize the standard light curve expression (Bronshten, 1983) for a homogeneous meteoroid so that we can predict the expected behavior for a porous meteoroid model under similar conditions:

Starting from the relation for a uniform meteoroid:

$$I = -\tau \cdot dE_k / dt$$

where

$$dE_k / dt \equiv (V^2/2) dm/dt = +0.25 \rho V^5 \sigma C_D A$$

(assuming that  $\Delta(z) \ll 1$  for simplicity)

$\tau$  = the differential luminous efficiency for a chondritic meteoroid (uniform in bulk density) and with a specific volume fraction of iron. (This is important since iron dominates many of the lines that have previously been observed spectroscopically for almost all meteors).

We will generalize this expression for a porous meteoroid, first assuming that the luminous efficiency of both types of meteoroids are equal, since their cosmic abundances are nearly the same (iron content, etc.)

Thus, we can write the expression for the light from a porous meteoroid:

$$I^* = -\tau_c \cdot dE_k / dt \mid^*$$

Now, we can also write that:

$$dE_k / dt \mid^* / dE_k / dt = (\sigma^* A) / (\sigma A_d)$$

and using the relation for  $\sigma^*$  found earlier, we can write the above ratio in the form:

$$dE_k / dt \mid^* / dE_k / dt \mid_c = \{A_h/A_d\}^2$$

Thus, we can now write the ratio of the light output from a porous meteoroid to that for a chondritic uniform density meteoroid in the identical form (since we have assumed that the luminous efficiencies of both types of models have the same numerical value):

$$I^*/I = \{A_h/A_d\}^2 = \{\sigma^*/\sigma\}^2$$

which is generally much larger than unity if the luminous efficiencies are identical as expected. This clearly explains why the light curves that were determined in ReVelle (1983) continued to become more luminous with all other factors held constant. We explicitly compare this ratio as the final entry in Table I at the end of this paper using the uniform and the porous ratios of the values of square of the ablation coefficient. In the limit as the porosity disappears, this expression becomes unity as expected.

This method also gives a physical explanation of why the  $(I/I) \cdot dI/dt$  method of Ceplecha et al. (1997) works for the identification of bolide types. Porous (lower density) bodies have inherently larger light curve intensity variations than do nonporous bodies so their  $(I/I) \cdot dI/dt$  values should also be inherently greater.

## 6. SUMMARY AND CONCLUSIONS

We have found very good entry modeling agreement with other approaches (Brown et al., 2000) that have also determined detailed parameters associated with the fall of the Tagish Lake meteorites (January 18, 2000).

Porous meteoroid modeling is superior to uniform bulk density modeling when simultaneously considering the dynamics, energetics and light curve data of bolides, but especially for this bolide, since it is so porous. For ordinary chondrites, on the other hand, we have the limit of near-zero porosity and the fundamental differences in the two models disappear. Larger ablation coefficients for the porous meteoroid model produces higher end

heights in comparison to uniform bulk density models (ReVelle, 1983). For Tagish Lake this is an end height difference of ~5-10 km. These larger ablation coefficient produces larger luminosity, at the same mass and velocity, even with the same luminous efficiency factor (ReVelle, 1983). The addition of substances such as water-ice, etc. to the pores degrades the improvement that is gained using a porous meteoroid model.

## 7. REFERENCES

- Bronshten, V.A., Physics of Meteoric Phenomena, D. Reidel Pub. Co., Dordrecht, 356 pp, 1983.
- Brown, P., A.R. Hildebrand, M.E. Zolensky, M. Grady, R.N. Clayton, T.K. Mayeda, E. Tagliaferri, R. Spalding, N.D. MacRae, E.L. Hoffman, D.W. Mittlefehldt, J.F. Wacker, J. A. Bird, M.D. Campbell, R. Carpenter, H. Gingerich, M. Glatiotis, E. Greiner, M. Mazur, P. J.A. McCausland, H. Plotkin and T. R. Mazur, The Fall, Recovery, Orbit and Composition of the Tagish Lake Meteorite, A New Type of Carbonaceous Chondrite, Science, **290**, 320-325, 2000.
- Ceplecha, Z. and R.E. McCrosky, Fireball End-heights: A Diagnostic for the Structure of Meteoric Material, J. Geophys. Res., **81**, 6257-6275, 1976.
- Ceplecha, Z., C. Jacobs and C. Zaffery, Correlation of Ground- and Space-based Bolides, in Near-Earth Objects, Annals of the New York Academy of Sciences, Ed. J. Remo, **822**, 145-154, 1997.
- Ceplecha, Z., J. Borovicka, W.G. Elford, D.O. ReVelle, R.L. Hawkes and M. Simek, Meteor Phenomena and Bodies, Space Science Reviews, **84**, 327-471, 1998.
- ReVelle, D.O., Modeling the Dynamics, Ablation and Luminosity of Fireballs, Meteoritics, **18**, 386, 1983.
- ReVelle, D.O., A Quasi-Simple Ablation Theory Model for Large Meteorite Entry: Theory versus Observations, J. Atmos. Terr. Physics, **41**, 453-473, 1979.
- ReVelle, D.O., The Meteoroid-Atmosphere Interaction Spectrum, in Meteoroids and Their Parent Bodies, eds. J. Stohl and I.P. Williams, Bratislava, Slovakia, Slovak Academy of Sciences, pp. 343-346, 1993.
- ReVelle, D.O., Bolide Fragmentation Processes: Modeling the Break-up of Very Large Meteors, Presented at the Cornell ACM Conference,

Ithaca, New York, July, 1999.

ReVelle, D.O., Bolide Fragmentation Processes: Single-body Modeling versus the Catastrophic Fragmentation Limit, Conference Proceedings, Meteoroids2001, Kiruna, Sweden, August 6-10, 2001, 2001.

**Table 1. Comparisons between meteoroid parameters for US PN bolide data using a uniform bulk density model (Ceplecha et. al., 1998) or an inhomogeneous, porous meteoroid model (following ReVelle, 1983).**

Type	I.	II.	IIIA.	IIIB.
Uniform model				
$\rho_m$ : g/cm <sup>3</sup>	3.7	2.0	0.75	0.27
$\sigma$ : s <sup>2</sup> /km <sup>2</sup>	0.014	0.042	0.10	0.21
Porous model	$\psi = 0\%$	$\psi = 50\%$	$\psi = 75\%$	$\psi = 91\%$
$\rho_m$ : g/cm <sup>3</sup>	3.7	1.85	0.93	0.34
$\sigma$ : s <sup>2</sup> /km <sup>2</sup>	0.02	0.04	0.08	0.22
$\Gamma/I$ : Uniform $\sigma$ values	1.0	9.0	51.0	225.0
$\Gamma/I$ : Porous $\sigma$ values	1.0	4.0	16.0	121.0

**Table 2. Preliminary Tagish Lake results**

Model type:	Uniform:	Porous : 60 %
$\mu = 2/3$ : Constant $\sigma$ solutions	$m_{\text{initial}} = 3.70 \cdot 10^4$ kg, $r_{\text{initial}} = 1.75$ m	$m_{\text{initial}} = 4.96 \cdot 10^4$ kg, $r_{\text{initial}} = 2.00$ m
Starting height	67.50	67.33
V at max. light	12.05	12.34
Height of max. light: km	32.76	33.24
Height where $p_{\text{stag}} > T_s$ : km	35-51 for $p_s$ : $10^5$ to $8 \cdot 10^5$ Pa	34-52 for $p_s$ : $10^5$ to $6 \cdot 10^5$ Pa
Height of max. $m \cdot dV/dt$ : km	29.43	30.49
End height velocity: km/s	9.33	9.93
End height: km	19.3 (31.1 for variable $\sigma$ with break up)	20.0 (33.9 for variable $\sigma$ with break up)
Predicted Ablation	82 %	98 %
Terminal mass	$m_{\text{final}} = 6,794$ kg	$m_{\text{final}} = 979.4$ kg

# EN310800 VIMPERK FIREBALL: PROBABLE METEORITE FALL OF AN ATEN TYPE METEOROID

Pavel Spurný and Jiří Borovička

*Astronomical Institute, Ondřejov Observatory, 251 65 Ondřejov, Czech Republic,  
Email: spurny@asu.cas.cz*

## ABSTRACT

We report a detection of an unique fireball photographed at two Czech stations of the European Fireball Network (EN). This slow-moving fireball with initial velocity of only 15 km/s reached the maximum absolute brightness  $-13.8$  magnitude and penetrated down to almost 20 km. The meteorite fall of several pieces of the total mass of several kilograms is highly probable. However, no meteorite has been recovered yet. From one very rough spectral record and also from its behavior in the atmosphere we found that it was stony meteoroid, probably ordinary chondrite. The main exceptionality of this fireball is in its heliocentric orbit, with semimajor axis only 0.8 AU, eccentricity 0.3, aphelion 1.03 AU and inclination 17 degrees. This rare Aten type orbit is only third one in the history of decades-long operation of the EN.

## 1. INTRODUCTION

The very bright fireball with a peak absolute magnitude  $-13.8$  was photographed on August 31, 2000 at 22<sup>h</sup>51<sup>m</sup>56.0<sup>s</sup> UT (the beginning of the photographed trajectory). It was named Vimperk after a town in SW part of Bohemia, which was lying below the terminal point of the luminous trajectory.

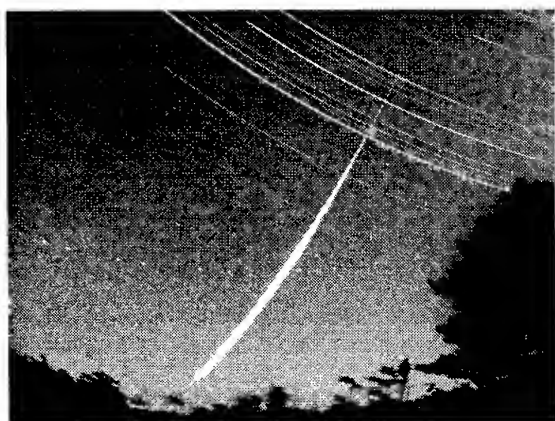


Fig. 1. Detailed view of the EN310800 Vimperk

The fireball was recorded at two stations of the Czech part of the European Fireball Network (EN) – stations Ondřejov (Fig.1) and Svratouch. Both stations are equipped with all-sky cameras (fish-eye objective Zeiss Distagon 3.5/30mm) operated in fixed regime. Moreover one additional camera of the same type at Ondřejov is also operated in guided regime to obtain precise time of the fireball passage. Only these two stations in the central part of the Czech network had a clear sky during the fireball flight. Unfortunately all our western stations, which would have recorded this fireball from a substantially lower distance, had a cloudy sky. Nevertheless, in spite of the lack of close stations, all geophysical, dynamic and orbital data presented below are determined with a good accuracy. All these values are collected to the tables and figures below.

## 2. ATMOSPHERIC TRAJECTORY

After successful reduction of all available records, atmospheric trajectory data have been computed by means of our standard procedures [1,2]. All these data are presented in Table 1.

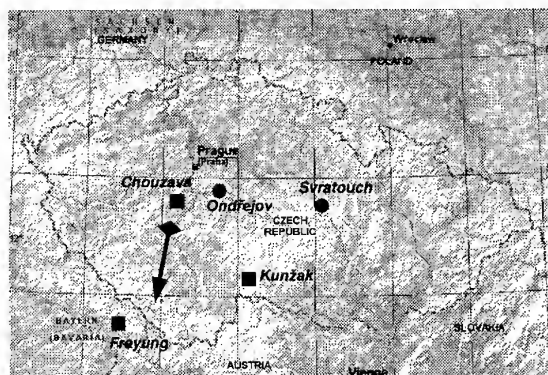


Fig. 2. Schematic display of the places where the Vimperk fireball was recorded and projection of the photographed fireball atmospheric trajectory on the map of the Czech Republic. Direct photographic detections are labeled by dark circles and other detections by dark squares.

	Beginning	Maximum light	Terminal
Velocity (km/s)	$14.915 \pm 0.004$	9.89	$6.4 \pm 0.2$
Height (km)	$81.82 \pm 0.01$	25.88	$21.46 \pm 0.01$
Longitude ( $^{\circ}$ E)	$14.0843 \pm 0.0002$	13.844	$13.8251 \pm 0.0002$
Latitude ( $^{\circ}$ N)	$49.5048 \pm 0.0001$	48.983	$48.9407 \pm 0.0001$
Dynamic mass (kg)	105.	65.	5.
Absolute magnitude	-3.5	-13.8	-4.
Slope ( $^{\circ}$ )	$42.71 \pm 0.02$	-	$42.12 \pm 0.02$
Total length (km)/Duration (s)	89.47 / 6.68		
Ablation coefficient ( $s^2 km^{-2}$ )	$0.0076 \pm 0.0008$		
PE coefficient / Fireball type	-4.29 / I		
EN stations No.	20 Ondřejov, 9 Svratouch		

Table 1. Atmospheric trajectory data

Very precise time of the fireball passage was determined from the DCF controlled radiometric record from the Kunžak station. The precision of this method is of the order of 0.1 s. This time is in a very good agreement with the time determined from the combination of the records from fixed and guided cameras at Ondřejov. However the precision of this method is more than 10 times worse. This time also very well corresponds to many visual observations. This fireball started its almost 90 km luminous trajectory at an altitude of 81.8 km with the low entry velocity of 14.92 km/s and terminated its flight at a height of only 21.5 km after 6.7 seconds. The average slope of the atmospheric trajectory to the Earth's surface was 42.4 degrees. The projection of the trajectory on the Earth's surface along with the position of all those places from which the Vimperk fireball was recorded is schematically displayed in Fig. 2. Dark circles represent positions of two EN stations where the fireball was photographed, dark squares represent positions of places where another different kind of fireball registrations were taken – the spectral record at Chouzavá, the radiometric record at Kunžak and finally the infrasound record at Freyung, Germany [3]. All these registrations except the infrasound record will be discussed below.

### 2.1. Light curve

The photometry of all-sky pictures taken by our fish-eye cameras is usually determined by a standard method described in [2]. However, this method is reliable for

fireballs which are photographed everywhere on the sky from the zenith down to a zenith distance of 70 degrees. Unfortunately, it was not the case of the Vimperk fireball, because practically whole second half of the luminous trajectory was behind this limitation even for the closest station Ondřejov. Moreover, the biggest flare near the terminal was only about 10 degrees above horizon. Therefore we were not able to use this method for determination of the lightcurve and correct photometry at all.

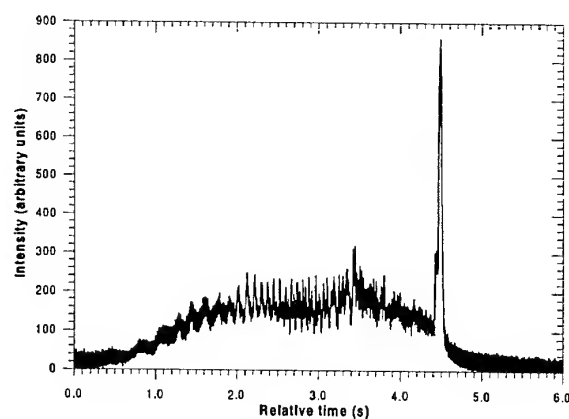


Fig. 3. The lightcurve of the EN310800 Vimperk fireball in intensities as a function of time from the radiometric system at Kunžak station. The absolute time of the maximum intensity was 22<sup>h</sup>52<sup>m</sup>1.49<sup>s</sup> UT.

Nevertheless since August 1999, we operate two radiometric systems, which were developed and constructed at Sandia National Laboratories [4]. The radiometer is a PC based hardware and software system that is used to monitor the whole sky for nighttime optical events with a very high time resolution  $1200 \text{ s}^{-1}$ . These instruments enable us to obtain very detailed lightcurves for all brighter fireballs over the Czech Fireball Network. The Vimperk fireball was bright enough to be recorded by radiometer. Its very detailed lightcurve from radiometer placed at Kunžak station is presented in Fig. 3. The intensity is given in linear scale in arbitrary units. By a calibration performed on another fireball well observed both photographically and radiometrically, the relation between the intensity  $I$  and apparent magnitude  $m$  was found:

$$m = -2.5 \log I - 5.75 \quad (1)$$

This relation is valid only for slow fireballs [5]. Taking into account its range from the Kunžak station and average atmospheric extinction for the zenith distance of the main flare, the peak absolute magnitude of the Vimperk fireball was computed to be  $-13.8$ . From the dynamic behavior and also from the deep atmospheric penetration the Vimperk fireball is a typical member of the type I fireballs with a very high probability of producing meteorites with a significant

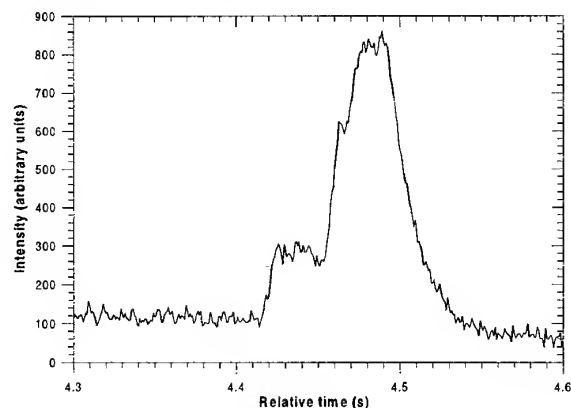


Fig. 4. Detailed plot of the terminal flare of the Vimperk fireball ( $T_0 = 22^{\text{h}}51^{\text{m}}57.0^{\text{s}}$  UT).

terminal mass in the order of kilograms. There are also indications that the initial meteoroid was fragmented very high, at altitudes above 50 km, which means that the initial dynamic mass presented in Table 1 could be significantly higher, probably up to mass of about 500 kg. For the type I fireballs it is typical that their lightcurves are relatively smooth without significant terminal flare. Typical type I fireball becomes steadily brighter as it penetrates deeper into the atmosphere, passes through a maximum, and then fades as the velocity decreases as a consequence of atmospheric

drag [6]. However it is not completely the case of the Vimperk fireball. Its lightcurve exhibits several interesting features.

First, there is a big terminal flare of amplitude of 2.3 magnitudes observed at a height of 26 km and lasting only 0.1 seconds. The detail of this part of the lightcurve is plotted in Fig. 4. The maximum is reached within two steps and after a very short plateau, intensity is

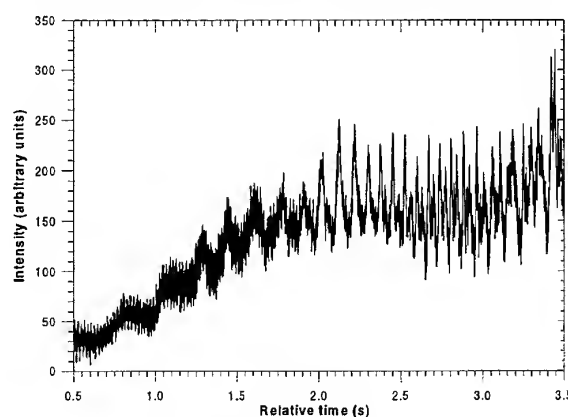


Fig. 5. Periodic variations in brightness in the first part of the lightcurve.

fading very smoothly at the terminal. The flare was caused by a severe fragmentation of the body. Nevertheless a relatively big piece survived the break-up and continued the flight (see Fig. 1).

Second interesting and quite unusual feature is observed in the first half part of the lightcurve. As it is shown in Fig. 5, significant periodic fluctuations in brightness are observed shortly after beginning. It is possible to distinguish two overlapping fluctuations with changing frequencies as it is presented in Fig. 6. The first period started to be recognizable at a height of 59 km ( $H_{B1}$ ) with a low frequency of 3 Hz and the second period

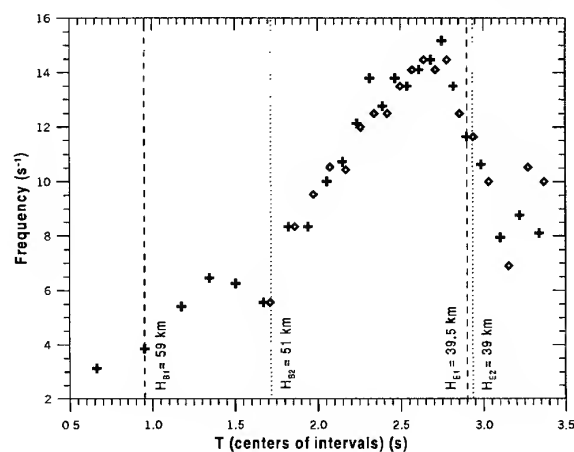


Fig. 6. Change of the frequency of two periods observed for the first half part of the Vimperk fireball trajectory.

started about 8 km lower at a height of 51 km ( $H_{B2}$ ) with slightly higher frequency of 5.5 Hz. At the same height have both periods very similar frequencies with a significant growing trend. Both reach the maximum about 15 Hz around 40 km altitude and after a short decrease both periods disappear at a height around 39 km. This effect is not very common, during two years of operation and more than 20 fireball registrations it was recorded only for this fireball. Such periodic variation in brightness could be possibly explained by rotation of two fragments, which were separated relatively high, at a height above 50 km.

## 2.2. Spectral data

In addition to above-mentioned direct photographic records one low-resolution prism spectrum of the fireball beginning was obtained by our fellow-worker

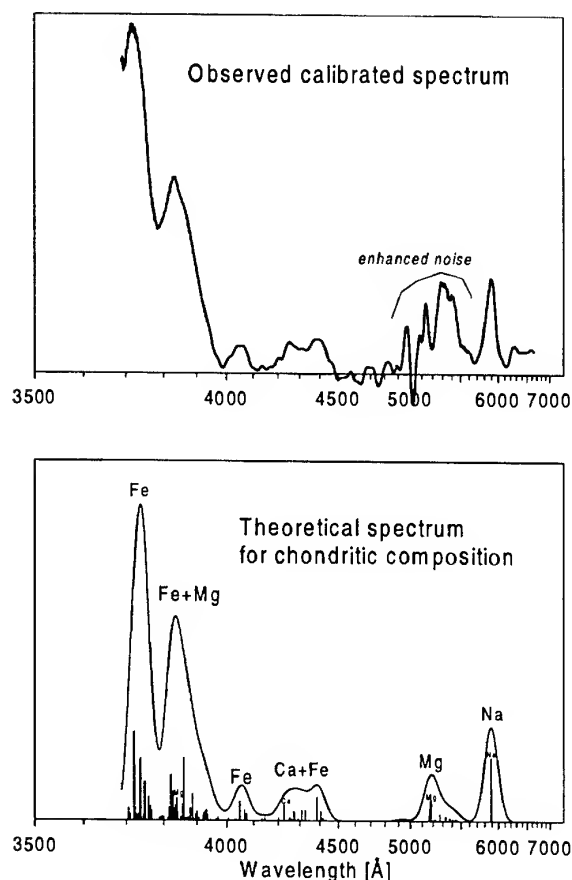


Fig. 7. The spectrum of the Vimperk fireball. The upper plot shows the observed spectrum after calibration, the lower plot shows the theoretical spectrum.

M. Weber at station Chouzavá (Fig. 2). This spectrum was taken by the spectral camera equipped with objective Tessar (1/4.5,  $f = 165$  mm) and  $45^\circ$  prism. Though the spectrum is very weak and its quality is not very high we were able to get basic information about the meteoroid composition (Fig. 7). The upper panel in Fig. 7 shows the spectrum after a calibration to spectral sensitivity (film sensitivity is low at 5000-5500 Å, thus the noise is enhanced in that region). The lower panel shows the theoretical spectrum computed for chondritic composition and temperature 4500 K. Individual spectral lines are given as vertical lines. The summary spectrum is drawn to the same resolution as the observed spectrum. The agreement with the observed spectrum is good. Though the majority of lines in the spectrum are due to iron, the clear presence of the sodium line rules out the possibility that the meteoroid was of iron composition. Most probably it was a chondrite. It well corresponds with the classification of this fireball. According to several criteria used for fireball classification as a low value of ablation coefficient (Table 1) or high penetration ability are, the Vimperk fireball belongs to the type I fireballs, which represents the most compact interplanetary bodies.

## 2.3. Dark flight and impact area

The Vimperk fireball was extraordinary also in its deep penetration into the atmosphere, considerable brightness and a relatively high terminal dynamic mass of the order of kilograms. For these reasons it was a typical meteorite-producing fireball. The geographical coordinates of the most probable impact point for meteorite with terminal mass of 5 kg are:  $\varphi = 48.8694$  deg N,  $\lambda = 13.8082$  deg E. The predicted impact area has a shape of rectangle about 2 km long and 500 m wide. Unfortunately all this impact area lies in the hilly, marshy and heavily forested Sumava Mountains region. Therefore the systematic search for meteorites was very difficult. Nevertheless about 60% of the impact area was thoroughly searched (and most of the other part less thoroughly) in September and October 2000. No meteorites have been recovered yet.

## 3. RADIANT AND HELIOCENTRIC ORBIT

The last exceptionality of the Vimperk fireball is in its rare type of the heliocentric orbit. From the orbital elements listed in Table 2 and from Fig. 8 it is clearly visible that this meteoroid orbited the Sun on a very short orbit with semimajor axis significantly smaller

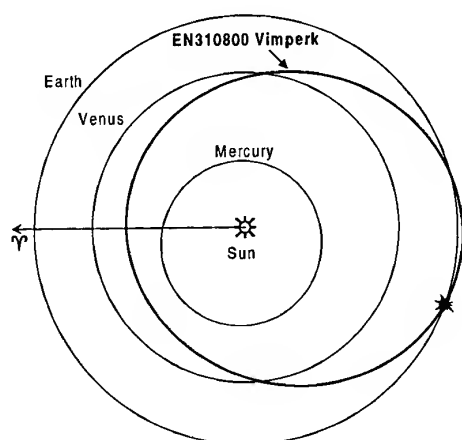


Fig. 8. Schematic display of the Vimperk fireball orbit projected into the ecliptic plane.

than 1 AU – only 0.80 AU. The meteoroid hit the Earth practically in the aphelion while the perihelion was between Venus and Mercury orbits. It was a typical Aten type orbit and only third one in the history of the decades long operation of the European Fireball Network. The US Prairie Network (PN) detected 11 fireballs on similar orbits [7] and the Canadian MORP Network detected 4 such cases [8]. ReVelle and Ceplecha [9] concluded that three of the PN Atens were likely of iron composition. For the Vimperk fireball we positively know that it was stony.

$\alpha_R$ (deg)	$91.33 \pm 0.07$
$\delta_R$ (deg)	$76.54 \pm 0.03$
$v_\infty$ (km/s)	$14.915 \pm 0.004$
$\alpha_G$ (deg)	$117.79 \pm 0.07$
$\delta_G$ (deg)	$69.69 \pm 0.03$
$v_G$ (km/s)	$9.816 \pm 0.006$
$v_H$ (km/s)	$25.394 \pm 0.005$
$a$ (A.U.)	$0.7969 \pm 0.0002$
$e$	$0.2958 \pm 0.0003$
$q$ (A.U.)	$0.5612 \pm 0.0004$
$Q$ (A.U.)	$1.03263 \pm 0.00005$
$\omega$ (deg)	$19.13 \pm 0.03$
$\Omega$ (deg)	$158.81694 \pm 0.00001$
$i$ (deg)	$16.74 \pm 0.02$

Table 2. Radiant and orbital elements (J2000.0) of the Vimperk fireball

All important data concerning radiant and orbit are collected in Table 2. The individual entries accompanied with their standard deviations have the following meaning:  $\alpha_R$ ,  $\delta_R$  are the right ascension and declination of the observed radiant,  $v_\infty$  is the initial velocity,  $\alpha_G$ ,  $\delta_G$  are the right ascension and declination of the geocentric radiant (corrected for the Earth's rotation and for zenith attraction),  $v_G$  is the geocentric velocity,  $v_H$  is the heliocentric velocity, and  $a$ ,  $e$ ,  $q$ ,  $Q$ ,  $\omega$ ,  $\Omega$ ,  $i$  are the orbital elements using the normalized symbols. The angular orbital elements as well as all the right ascensions and declinations are given in the J2000.0 coordinate system.

### Acknowledgements

We are very much indebted to A. Kolář and F. Košák for their perfect service at the fireball stations at the time of the Vimperk fireball. Similarly, we very much appreciate the systematic work of M. Weber, which photographed the Vimperk fireball by his spectral camera and which very kindly gave us this record for analysis. Our special thanks are due to J. Keclřková, who measured all photographic records and to J. Boček who is systematically taking care of the Czech fireball stations.

We are also very grateful to Dr. R. E. Spalding and his team at Sandia National Laboratories, NM, USA, who initiated to develop and construct the radiometric systems and who kindly made possible to use these instruments within the Czech Fireball Network.

We thank several groups of students and young people led by P. Suchan, J. Verfl, M. Prouza and J. Větráček for their careful search for meteorites in the impact area. This work has been partly supported by project No. K1-003-601 of the Czech Academy of Sciences and by grants of the Grant Agency of the Czech Republic Nos. 205-00-1727 and 205-99-0146.

### 4. REFERENCES

1. Borovička J., et al. A New Positional Astrometric Method for All-sky Cameras. *Astronomy & Astrophys. Suppl. Ser.*, Vol. 112, 173 – 178, 1995.
2. Ceplecha Z., Geometric, Dynamic, Orbital and Photometric Data on Meteoroids from Photographic Fireball Networks. *Bull. Astron. Inst. Czechosl.*, Vol. 38, 222 – 234, 1987.
3. Hartmann G., *private communication*, 2001

4. Spalding R. E. et al., Radiometer System - Users Manual. Sandia National Laboratories, Albuquerque, NM, USA, 1998.
5. Spurný et al., Common Ground-based Optical and Radiometric Detections within Czech Fireball Network. *This volume*. In print.
6. Wetherill G. and ReVelle D. O., Which Fireballs are Meteorites? A Study of the Prairie Network Photographic Meteor Data. *ICARUS*, Vol. 48, 308 – 328, 1981.
7. McCrosky R.E. et al., Prairie Network Fireball Data. I. Summary and Orbits. *Preprint Series No. 665*, Smithsonian Astrophysical Observatory, 13 pp, 1976.
8. Halliday I. Et al., Detailed Data for 259 Fireballs from the Canadian Camera Network and Inferences Concerning the Influx of Large Meteoroids. *Meteoritics & Planetary Science*, Vol. 31, 185 – 217, 1996.
9. ReVelle D. O. and Ceplecha Z., Analysis of Identified Iron Meteoroids: Possible Relations with M-type Earth-crossing Asteroids?, *Astronomy & Astrophysics*, Vol. 292, 330 – 336, 1994.

## MODELING THE DYNAMICAL AND PHOTOMETRIC BEHAVIOR OF FAINT METEORS IN THE EARTH'S ATMOSPHERE

Luis R. Bellot Rubio<sup>1</sup>, María Jesús Martínez González<sup>2</sup>, Lola Ruiz Herrera<sup>2</sup>,  
Javier Licandro<sup>3</sup>, David Martínez Delgado<sup>1</sup>, Pablo Rodríguez Gil<sup>1</sup>, and Miquel Serra-Ricart<sup>1</sup>

<sup>1</sup>Instituto de Astrofísica de Canarias, E-38200, La Laguna, Tenerife, Spain

<sup>2</sup>Dept. de Astrofísica, Universidad de La Laguna, La Laguna, Tenerife, Spain

<sup>3</sup>Centro Galileo Galileo and Telescopio Nazionale Galileo, La Palma, Spain

### ABSTRACT

Faint meteors observed with Super-Schmidt cameras are re-examined in order to assess whether their dynamical and photometric behavior can be described by means of the single body theory. Velocities, decelerations and magnitudes are fitted simultaneously to synthetic curves resulting from integration of the appropriate set of differential equations. The parameters determined by this procedure are the ablation coefficient, the shape-density coefficient and the preatmospheric mass of the meteoroids. It turns out that 64% of the meteors analyzed here are reasonably well described by this theory, suggesting that they did not undergo significant fragmentation during their atmospheric flight. We identify some systematic differences between observed and theoretical light curves of meteors for which the fit is good. From the retrieved shape-density coefficients we derive meteoroid bulk densities. The average density turns out to be  $1.0 \text{ g cm}^{-3}$ , with individual values ranging from  $0.2 \text{ g cm}^{-3}$  to  $1.4 \text{ g cm}^{-3}$ . This work represent a first step toward the analysis of low-light level video observations of very small meteoroids.

Key words: meteoroids; light curves; densities; numerical modeling.

### 1. INTRODUCTION

Our capability to model the interaction between the atmosphere and meteoroids is rather limited. As a consequence, the physical properties of the meteoroids remain uncertain. This is especially true for some important quantities, such as bulk densities. According to Jacchia et al. (1967), the mean density of the faint meteors photographed by Super-Schmidt cameras is  $0.26 \text{ g cm}^{-3}$ . More recent investigations, however, suggest significantly larger values. The discrepancy is due to the different models used to describe the behavior of meteoroids in the Earth's

atmosphere. According to current views, low densities result if meteoroids are assumed to be compact, non-fragmenting particles, while the opposite is true if meteoroids undergo some kind of fragmentation during their atmospheric flight.

Early in the 1950s it was recognized that instantaneous dynamical masses determined from very precise measurements of deceleration are much smaller than photometric masses estimated from the observed light curves. The difference was explained in terms of fragmentation effects. Since then, analyses of the behavior of meteoroids in the atmosphere have concentrated on the modeling of either dynamical (velocity and deceleration) data or photometric measurements. To our knowledge, studies considering both kind of data have not been performed so far.

In this work we try to improve this situation by attempting a simultaneous modeling of the dynamic and photometric behavior of faint meteoroids. The aim is to assess whether the same simple theory can reproduce the observed velocities and decelerations along with the light curve. Clearly, using all information available will help better determine the physical properties of the meteoroids. To this end, very precise measurements are necessary. Among the various sources available, the catalog of Super-Schmidt photographic meteoroids of Jacchia et al. (1967) is generally regarded as being the most accurate. Another advantage of this catalog is that it has been employed in many investigations. Therefore, our use of it will allow direct comparisons with previously published results.

### 2. THE MODEL

In order to determine the physical properties of meteoroids one needs a suitable model for describing their interaction with the Earth's atmosphere. The single body theory (e.g. Bronshten

1983) assumes that meteoroids are compact, non-fragmenting particles. Models incorporating fragmentation include the dustball treatment proposed by Hawkes & Jones (1975) and the quasi-continuous fragmentation model (Novikov, Pecina & Konovalova 1998). The basic assumption in these models is that meteoroids lose mass through the detachment of small fragments which further ablate as non-fragmenting particles.

The single body model has been successfully applied to fireballs and bright meteors. For fainter meteors, this treatment may not be appropriate if they undergo fragmentation. Flares, wakes, and terminal blendings recorded by photographic and video systems are clear signatures of fragmentation. However, since many faint meteors do not show any of these phenomena, the question arises whether they can be described by the simple single body theory, especially when both dynamical and photometric data are taken into account simultaneously.

Given the simplicity of this model and its success in describing the behavior of large meteoroids, we will examine its validity for faint meteors before trying more complex fragmentation models. This is the purpose of the present work.

The motion and ablation of a single nonfragmenting particle in the Earth's atmosphere can be expressed by the drag and mass-loss equations

$$\frac{dv}{dt} = -K \rho m^{-1/3} v^2, \quad (1)$$

$$\frac{dm}{dt} = -\sigma K \rho m^{2/3} v^3, \quad (2)$$

where  $t$  is time,  $v$  the instantaneous velocity,  $m$  the instantaneous mass,  $\rho$  the air density,  $\sigma$  the ablation coefficient, and  $K$  the shape-density coefficient. The height in the atmosphere  $h$  is related to  $t$  by the geometrical relationship  $dh/dt = \cos z v$ , where  $z$  is the inclination of the trajectory with respect to the vertical. Finally, the luminosity equation reads

$$\frac{dI}{dt} = \tau \frac{1}{2} \left( -\frac{dm}{dt} \right) v^2, \quad (3)$$

with  $I$  the radiation intensity and  $\tau$  the so-called luminous efficiency. We adopt model A for  $\tau$ , hence  $\tau = \tau_0 v$ , with  $\tau_0 = 6.46 \times 10^{-19}$  in units of a 0 mag star (Jacchia et al. 1967).

### 3. NUMERICAL PROCEDURE

Equations (1) and (2) form a system of ordinary differential equations. Synthetic curves  $v = v(h)$ ,  $dv/dt = dv/dt(h)$  and  $I = I(h)$  are constructed by integrating them for given initial values of  $v$  and  $m$  and parameters  $\sigma$  and  $K$ . These curves are then compared with the observed velocities, decelerations, and magnitudes in order to determine the best-fitting  $\sigma$  and  $K$  parameters.

For the integration of (1) and (2) we use a fourth-order Runge-Kutta method with stepsize  $\Delta h = 100$  m.  $\sigma$  and  $K$  are assumed to be constant during the atmospheric flight. The air density at  $h$  is computed by interpolation of the US Standard Atmosphere 1976. The preatmospheric velocity and mass are taken from the Jacchia et al. catalog. The initial mass is photometric (obtained by integration of the light curve), and therefore not very reliable given the uncertainties in  $\tau$ .

The synthetic curves are fitted to the experimental data ( $v$ ,  $dv/dt$ , and magnitude as a function of  $h$ ) by means of a non-linear, least-squares Marquardt algorithm (Press et al. 1987). The free parameters determined from the inversion are  $\sigma$ ,  $K$ , and the initial mass  $m_0$ . The partial derivatives of  $v$ ,  $dv/dt$ , and magnitude with respect to the free parameters are computed numerically. During the inversion, the relative weights assigned to velocity, deceleration, and photometric data are 2, 0.5, and 1, respectively. Therefore, in case of a bad fit velocities will be reproduced better than magnitudes and decelerations. This seems appropriate given the much lower quality of the later.

### 4. RESULTS

Figure 1 shows three examples of meteors for which the single body theory provides an excellent description of their dynamical and photometric behavior. 85 out of the 133 meteors examined (i.e., 64%) are reasonably well described by this model. This suggests that they did not undergo significant fragmentation during their atmospheric passage. The behavior of the remaining meteors cannot be reproduced in terms of the ablation of nonfragmenting particles with constant  $\sigma$  and  $K$ . For these meteors, the theoretical light curves differ significantly from the observed ones, and sometimes the dynamical data are also badly fitted.

Even in the case of good fits, the photometric behavior is somewhat difficult to reproduce. In particular, we find the following general trends:

- The brightest magnitude is usually 0.2–0.5 mag *fainter* than observed
- The predicted height of maximum light is *higher* than the observed one by 2–5 km
- The magnitude at the beginning point is usually *brighter* than observed

From the dynamical data alone we are able to determine  $\sigma$  and the product  $K m_0^{-1/3}$  only. The exact value of  $m_0$  (hence of  $K$ ) is obtained from the shape of the light curve. Therefore, with the precision and quantity of the present data, use of the photometric information is mandatory for reliable determinations of the shape-density coefficient. The fits shown in

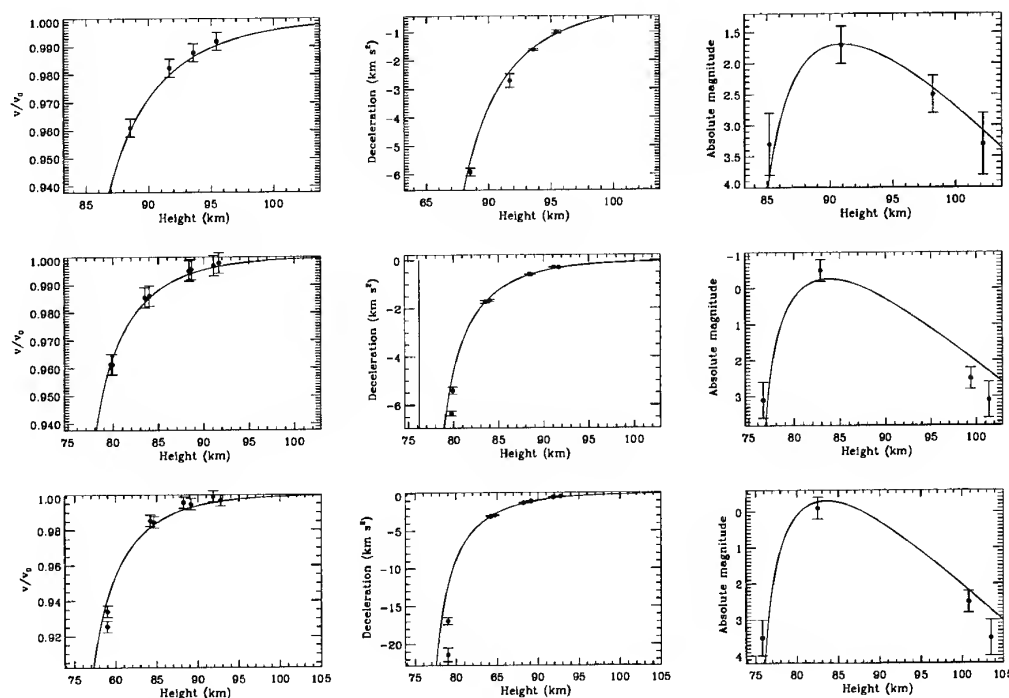


Figure 1. Example of the application of the single body theory to faint Super-Schmidt photographic meteors. Experimental velocities, decelerations, and magnitudes (dots) are plotted in the left, central, and right panels, respectively, for meteors 8945 (top), 6949 (middle), and 9015 (bottom) in the Jacchia et al. catalog. The solid lines show the best-fit curves resulting from the inversion of the observed quantities. The bulk densities of these meteoroids are found to be 0.5, 1.8, and 1.2 g cm<sup>-3</sup>, respectively.

Figure 1 demonstrate that the single body theory is capable of reproducing the observed light curves, at least for a significant fraction of the cases examined.

For 43 out of the 85 meteors for which the model seems to be appropriate (i.e., 50%), the retrieved initial mass differs from the photometric mass. Only for 17 meteors (20%) the two values are clearly different, the tendency being to obtain lower initial masses. These smaller masses ensure much better fits to the early part of the light curve, although the quality of the fit to the brightest magnitude becomes somewhat poorer.

Figure 2 shows an histogram of the ablation coefficients determined from the observations. The values of  $\sigma$  are in excellent accordance with those found in other analyses (see Ceplecha et al. 1998).

## 5. BULK DENSITIES

From the inferred values of  $K$  it is possible to determine the bulk density as  $\delta = (\Gamma A/K)^{2/3}$ , where  $\Gamma$  is the drag coefficient and  $A$  the shape factor. For small meteoroids as the ones we consider here, it is reasonable to take  $\Gamma = 1$  because no significant shielding or evaporation occurs. Regarding the shape factor, we adopt  $A = 1.21$  assuming that meteoroids are spherical bodies.

Figure 3 shows an histogram of bulk densities for the 85 meteoroids whose dynamical and photometric behavior is well described by the single body theory. In interpreting these results it is necessary to bear in mind that the reliability of the derived densities is strongly dependent on the correctness of  $K$ . As pointed out before, the separation of  $K$  and  $m_0$  is achieved by fitting the light curve shape, so there might be some residual crosstalk between  $K$  and  $m_0$  capable of producing unreliable  $K$  values. Because of the same reason, uncertainties in the luminous efficiency may introduce a strong bias in the derived densities. Model A has been used here for consistency with the results of Jacchia et al. (1967), but it is clear that much better values are to be preferred as, for example, the experimental luminous efficiencies determined by ReVelle & Ceplecha (2001).

Keeping in mind these limitations, the average bulk density turns out to be 1.0 g cm<sup>-3</sup>, with individual values ranging from 0.2 to 4 g cm<sup>-3</sup>. Most meteoroids, however, are characterized by densities in the range 0.3–1.4 g cm<sup>-3</sup>. There is a clear difference between shower and sporadic meteoroids, the former being denser on average. An extreme case is that of Geminids. The mean density of 10 Geminids included in the sample is 3.0 g cm<sup>-3</sup>, with a standard deviation of 0.9 g cm<sup>-3</sup>. It is important to note here that our results do not confirm the extremely large densities found by application of the

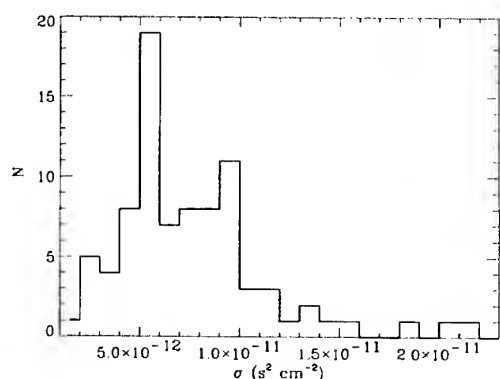


Figure 2. Histogram of ablation coefficients  $\sigma$  from the fitting of experimental data of 85 meteoroids.

quasi-continuous fragmentation (QCF) model. The work of Babadzhanyan (1994), for example, suggests an average density of  $3.3 \text{ g cm}^{-3}$ , with individual values ranging from  $0.1$  to  $8 \text{ g cm}^{-3}$ . Light curves are the basic observational material in studies making use of the QCF theory. Since the dynamical behavior is not considered, the resulting densities might be in error if the meteoroids do not fragment during their atmospheric flight. This could explain, at least in part, the unrealistically large densities determined from QCF models.

## 6. CONCLUSIONS

A numerical procedure implementing the single body theory has been developed to fit the dynamical and photometric behavior of meteoroids in the Earth's atmosphere. By applying it to 133 faint Super-Schmidt meteors we have determined their ablation coefficients, shape-density coefficients and initial masses. Eighty five of them are described reasonably well by this theory. In general, velocities and decelerations are almost perfectly reproduced. Matching the light curve is somewhat more difficult, but very important for constraining the value of the initial mass (hence of  $K$ , since from dynamical data alone we are able to determine precise values for  $K m_0^{-1/3}$  only).

From the inferred values of  $K$  we have estimated meteoroid bulk densities, although they may be strongly biased by uncertainties in the luminous efficiency. The average density for 85 meteors (mostly shower members) is  $1.0 \text{ g cm}^{-3}$ , with individual values ranging from  $0.3$  to  $4.0 \text{ g cm}^{-3}$ . Geminid meteoroids are much denser ( $3.0 \text{ g cm}^{-3}$ ) than the other particles.

Only meteors with excellent dynamical data were included in the catalog of Jacchia et al. (1967). Since long trajectory meteors yield the best dynamical data, the material in Jacchia et al. (1967) is biased. According to Ceplecha (1988), 32% of the Super-Schmidt meteors of this catalog are A-type bodies and 62% are C-type particles. Because of their dif-

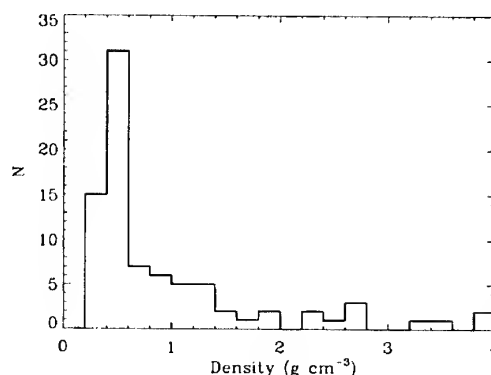


Figure 3. Histogram of bulk densities from the fitting of experimental data of 85 meteoroids. These are mostly shower meteoroids. For a discussion of the bias in this histogram see text

ferent origin and structure, the later are less dense than the former (mean density of  $0.75 \text{ g cm}^{-3}$  vs  $2.0 \text{ g cm}^{-3}$ ). Thus, the density distribution shown in Figure 3 is biased toward small values as it is dominated by C-type particles. The uneven sampling of the different meteoroid populations should be kept in mind in interpreting Figure 3.

The most important result of this work is that the single body theory is capable of explaining the behavior of a significant fraction (64%) of faint Super-Schmidt meteors. Apparently, these meteors did not undergo severe fragmentation processes as this would have caused the single body theory to fail. The smoothness of the light curves of these meteors in the original plates is another proof that fragmentation did not play a dominant role. For the remaining 36% of the sample, however, more complex fragmentation models could be necessary.

For practical purposes, the fact that more than half of the Super-Schmidt meteors are well described by the single body theory suggests that it might also be applicable to the smaller meteors recorded by intensified video systems. This is very important, as no appreciable deceleration is measured for such small meteors with the instrumentation currently available and the determination of their physical properties completely relies upon analysis of the observed light curves. If the single body theory applies, one can use analytical expressions (e.g., Bronshten 1983) for estimating meteoroid bulk densities from the light curve alone, thus simplifying the analysis to a large extent.

## ACKNOWLEDGMENTS

We wish to express our gratitude to Dr. Z. Ceplecha and Dr. O. Popova for very valuable suggestions and comments on this work.

## REFERENCES

- Babadzhanov, P.B., 1994. In: Milani, A., Di Martino, M., Cellino, A. (eds), Proc. IAU Symp. 160. Asteroids, Comets, Meteors 1993, Kluwer (Dordrecht), 45
- Bronshten, V.A., 1983, Physics of Meteoric Phenomena, D. Reidel Publishing Company (Dordrecht)
- Ceplecha, Z., 1988, Bull. Astron. Inst. Czechosl. 39, 221
- Ceplecha, Z., Borovicka, J., Elford, W.G., ReVelle, D.O., Hawkes, R.L., Porubcan, V., & Simek, M., 1998, Space Science Reviews 84, 327
- Hawkes, R.L., Jones, J., 1975, MNRAS 173, 339
- Jacchia, L.G., Verniani, F., & Briggs, R.E., 1967, Smithson. Contr. Astrophys. 10, 1
- Novikov, G.G., Pecina, P., & Konovalova, N.A., 1998, A&A 329, 769
- Press, W.H., Flannery, B.P., Teukolsky, S.A., Vetterling, W.T., 1989, Numerical Recipes, Cambridge University Press (Cambridge)
- ReVelle, D., Ceplecha, Z., 2001, these proceedings

# **Hypervelocity Impact Effects on Spacecraft**

# HYPERVELOCITY IMPACT EFFECTS ON SPACECRAFT

Gerhard Drolshagen

ESA/ESTEC, NL-2200 AG Noordwijk, The Netherlands, Email: [Gerhard.Drolshagen@esa.int](mailto:Gerhard.Drolshagen@esa.int)

## ABSTRACT

Every spacecraft in orbit is exposed to a certain flux of impacting meteoroid and space debris particles. These impacts occur at typical velocities between a few and some tens of kilometers per second. Sub-micron and micron sized particles can lead to degradation of sensitive spacecraft surfaces and equipment, like mirrors, optical sensors and thermal control surfaces. Somewhat larger particles with diameters in the size range tens to hundreds of microns can penetrate outer spacecraft coatings and foils as well as solar cells. Millimeter sized particles can penetrate exposed tanks and seriously damage certain equipment. Impactors of cm size or larger will typically lead to complete destruction of the impacted spacecraft part. In addition to these mechanical effects, every hypervelocity impact creates plasma. Such impact-generated plasma can lead to electromagnetic interference with spacecraft systems and payloads. This paper gives an overview of hypervelocity impact effects on spacecraft and also briefly addresses some common protection measures.

## 1. INTRODUCTION

Hypervelocity impacts can affect spacecraft in orbit in many different ways. Sub-micron and micron sized particles can degrade sensitive spacecraft surfaces and equipment, like mirrors, optical sensors and thermal control surfaces. Somewhat larger particles with diameters in the size range tens to hundreds of microns can penetrate outer spacecraft coatings and foils as well as solar cells. Millimeter sized particles can penetrate exposed tanks and seriously damage certain equipment. Even larger particles will typically lead to complete destruction of the impacted spacecraft part. In addition to such structural damage every hypervelocity impact creates plasma that can result in electromagnetic interference. If spacecraft surfaces are already charged by the ambient plasma discharges can be triggered. Other effects include impact generated light flashes and attitude changes. Effects from impacts of natural meteoroids and man made space debris objects are very similar and all effects described apply to both types of particles.

In the following first an overview of hypervelocity impact effects is given. Next, the general cratering and ejecta process is described. Crater sizes and structural damages

from smaller and larger particles are then discussed, followed by a brief section on shielding concepts. Then effects from impact plasma are addressed. In the last 2 sections the relative abundance of meteoroids and space debris in near Earth space and the added risk from meteoroid streams and storms are discussed.

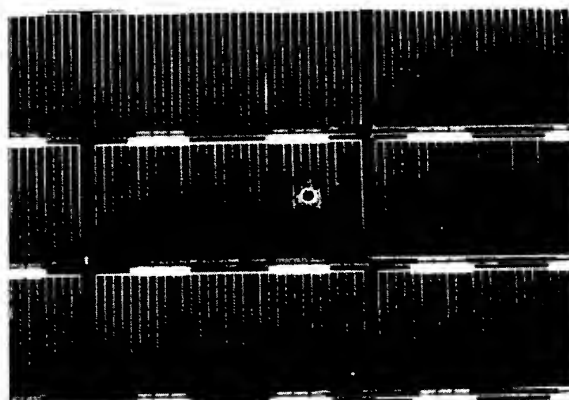


Fig. 1 Impact crater on HST solar cell. Solar cell dimension: 2 cm x 4 cm.

## 2. OVERVIEW OF IMPACT EFFECTS

Fig. 1 shows a typical impact on a solar cell of the Hubble Space Telescope (HST). Effects of hypervelocity impacts depend on many parameters of the impactor and target. Most important impact parameters are the size of the incident object and the impact velocity. The impact angle, shape and material density of the impactor can also be important. The damage of a given impact will also depend on the sensitivity of the target. Relevant parameters are the target structure, thickness and material but equally important the sensitivity to certain failure criteria. For example a small crater might have no noticeable effect on the outer spacecraft structural wall or solar array but could degrade a sensor, mirror or window and lead to sealing problems. Low intensity impact plasma might normally have no effect but could trigger a much larger electrostatic discharge if the spacecraft surface was already previously charged by high-energy plasma from the magnetosphere. The list below gives an overview of potential effects from hypervelocity impacts:

### Cratering and ejecta

- Surface erosion and degradation leading to a change

- in thermal, optical or electrical properties.
- Degradation of sensors and mirrors, including impacts on internal instruments by secondary ejecta.
- Degradation of windows (even relatively small craters require the exchange of Space Shuttle windows).
- Sealing problems if e.g. exposed hatches have to be closed.

#### *Structural damage*

- Penetration of spacecraft walls, leading to structural damage of inner subsystems.
- Penetration of pressurised vessels (tanks, manned modules, coolant loops).
- Cutting of cable or tether.
- Short circuits.
- Complete destruction of impacted spacecraft or spacecraft subsystem by larger object.

#### *Plasma effects*

- Electrical interference
- Current flow
- Triggering of electrostatic discharges
- Light flashes

#### *Momentum transfer (attitude change)*

While these effects are usually detrimental to spacecraft they have been exploited in a positive sense as detection methods for in-situ impact detectors. Past detectors have e.g. been based on impact ionisation, momentum transfer, capacitor breakdown triggered by impact, penetration of pressurised cans, etc.

It is obvious that any hypervelocity impact on a spacecraft creates new space debris particles in the process.

### 3. IMPACT CRATERS AND EJECTA

#### 3.1 Basic Processes

Hypervelocity impacts create a shock wave in the target material and lead to very high pressures ( $>100$  GPa) and temperatures ( $>10000$  K). The maximum pressures and temperatures are a strong function of the impact velocity. The high pressures and temperatures lead to structural failure of a certain target volume that is ejected from the impact site leaving a crater surrounded by an area of damaged target material. The main impact process lasts only a few microseconds.

The impacting object and the target material are fragmented, molten or vaporised. The ratio depends on the impact velocity and materials. For impacts with velocities up to about 5 km/s most of the ejected material

are solid fragments. Above 20-25 km/s the ejecta is completely vaporised. Ejecta from impacts in the velocity range 5-20 km/s are a mixture of solid fragments, molten droplets and vapour.

A small fraction of the ejected material is ionised. This fraction is a strong function of the impact velocity but does not exceed about 1 % for even the fastest meteoroids.

The ejected mass can be much larger (factor 10-1000) than the mass of the original impactor. Most of the impact energy ends up in the ejecta. Ejecta can be very numerous. For solid ejecta, the largest particles are comparable to the size of the impactor and the maximum ejection velocity is similar to the impact velocity. A small portion can even be ejected at higher velocities (jetting effect). For brittle materials (e.g. glass) larger spall fragments can be ejected at lower velocities around the main crater. This leads to a much-enlarged damaged area.

More details of the basic impact process can e.g. be found in [1]. A detailed description of a recent ejecta model is given in [2].

A schematic view of the main cratering and ejection features resulting from a hypervelocity impact is presented in Fig. 2 (taken from [3]).

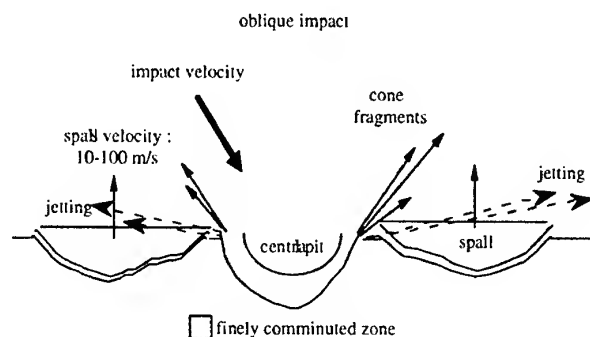


Fig. 2 Sketch of main impact crater features.

#### 3.2 Crater Sizes and Shapes

Most craters are roughly hemispherical. In ductile materials, like metals, crater diameters are typically 2-5 times larger than the diameter of the impactor. In brittle material a zone of shattered material often surrounds a central crater. The visible crater size can be 10-20 times the size of the impactor. If the target is thin relative to the impactor (foils) the hole size approaches the size of the impactor. Fig. 3 gives an enlarged view of an impact crater on a solar cell of the Eureka spacecraft. The total

percentage of cratered area is relatively small. Even for brittle glasses it is usually less than 0.1 % per year of space exposure.

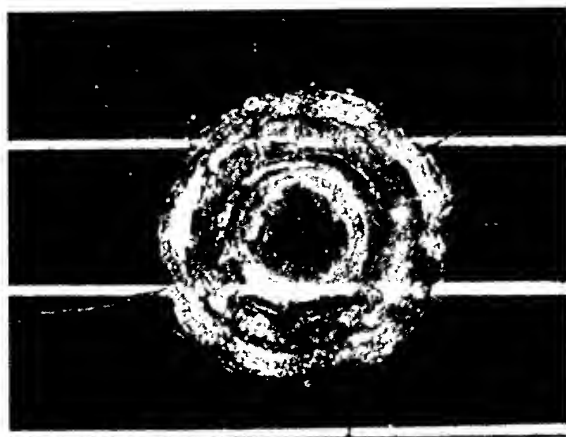


Fig. 3 Enlarged view of impact crater on Eureka solar cell. The bright lines are spaced by 1.25 mm.

Most craters have spherical shape even if the impact occurred at some angle from the surface normal. Only for incidence angles larger than about 60 degrees (from the surface normal) the crater shape becomes non-spherical. Fig. 4 gives an example of a crater on a HST solar cell from an oblique impact. This characteristic shape is called a 'butterfly'.

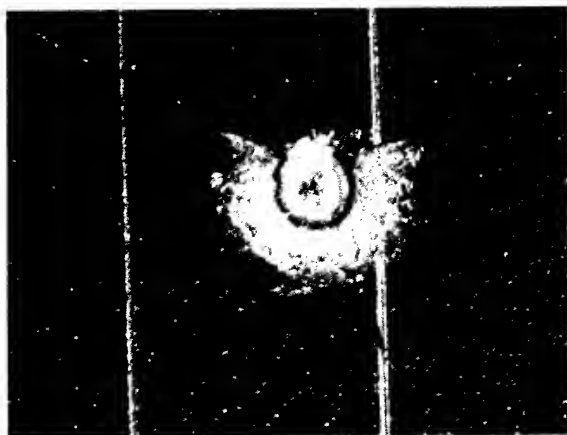


Fig. 4 Crater from oblique impact on HST solar cell. The bright lines are spaced by 1.25 mm.

The material ejected during the impact process can lead to numerous small secondary craters in the vicinity of a primary impact. An example is shown in Fig. 5 for secondary craters in an Aluminium foil. This foil was part of the TICCE experiment on EURECA which was retrieved after 11 months in space. The primary impact had a diameter of 70 microns and was a few mm away

from the shown field of high density cratering (photo taken from [3]).

Impact ejecta could have detrimental effects on sensitive instruments like mirrors, sensors and CCD detectors. While ejecta are usually small they can be very numerous within a certain cone around the primary impact site. Ejecta from impacts on side walls or baffles near sensitive equipment could well be more damaging than a direct hit by the primary projectile would have been.

For a quantitative description of crater sizes so called damage equations have been developed. These equations relate parameters of the impacting particles, like diameter, velocity, impact angle, etc to features of the resulting crater, like penetration depth or crater diameter. These equations have usually been obtained empirically. Many different damage equations have been derived for specific target configurations and materials. A recent overview is given in [4]. One of the most widely used equations for single metal walls is given in Eq. 1 [5]. It expresses the penetration depth in the target as function of a target material parameter and of the mass, density and velocity of the impactor.

$$p = k m^{0.352} \rho^{1.167} (v \cos \theta)^{0.667} \quad (1)$$

Where

$p$ : penetration depth [cm]

$k$ : target material constant [e.g. 0.42 for Alu]

$m$ : mass of projectile [g]

$\rho$ : material density of projectile [g/cm<sup>3</sup>]

$v$ : impact velocity [km/s]

$\theta$ : impact angle from normal

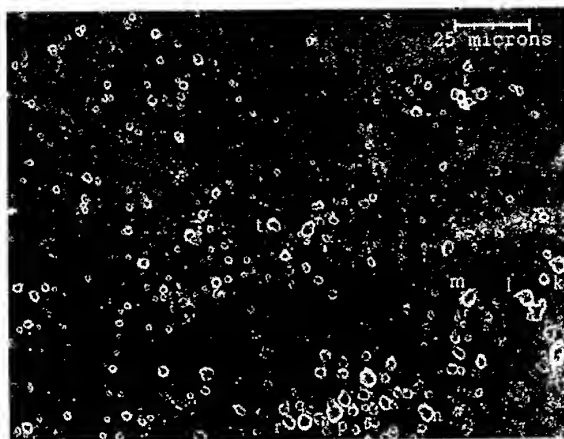


Fig. 5 Area with high density of craters in Aluminium foil resulting from secondary ejecta (from [3]).

Paul and Berthoud derived Eq. 2 for the conchoidal or spall crater size,  $D_{co}$ , in semi-infinite glass targets [6]. This equation describes the visible crater diameter in thick glass (relative to the impactor).

$$D_{co} = 5 \times 10^{-4} d^{1.076} \rho_t^{-0.5} \rho^{0.784} v^{0.727} (\cos \theta)^{0.601} \quad (2)$$

Where all units are in cgs ( $v$  is in cm/s) and

$D_{co}$ : conchoidal damage diameter [cm]

$\rho_t$ : material density of target [g/cm<sup>3</sup>]

$d$ : projectile diameter [cm]

Other variables are as in Fig. 1.

### 3.3 Target Penetration

If the penetration depth reaches about 1/2 of the target thickness, spall detaches from the rear wall. If the kinetic energy of the projectile is further increased the wall will be completely penetrated, leaving a hole. Fig. 6 shows a complete penetration of a HST solar cell. The complete HST solar cell compound is only 0.77 mm thick.



Fig. 6 Complete penetration of HST solar cell by hypervelocity impact. The central hole is about 0.9 mm in diameter.

Penetration of a single metal wall can be quantitatively described by multiplying Eq. 1 with a factor specifying the failure criterion:

$$t = c p,$$

where,  $t$ , is the threshold thickness for failure,  $p$ , is the penetration depth from Eq. 1 and,  $c$ , specifies the failure mode:

- $c \geq 3$  : crater generation without spallation
- $2.2 \leq c < 3$  : spallation of the plate
- $1.8 \leq c < 2.2$  : spall breaks away
- $c < 1.8$  : perforation of the plate

Fig. 7 shows an example of the penetration of a single plate by an Aluminium sphere with a diameter similar to the plate thickness. The projectile impacted with 6.6 km/s at an angle of 45 degrees. Experimental tests and hydrocode (AUTODYN) simulations are compared with good agreement [7].

Damage equations for penetration often give the ballistic limit for a given target thickness, i.e. the threshold conditions for marginal penetration. Other equations aim to determine the hole size resulting from an impact. If the projectile diameter is much larger than the target thickness, the hole size does approach the projectile size. For very thin foils even the shape of the projectile can be mirrored in the shape of the hole.

An overview of damage equations for crater sizes, ballistic limit and hole sizes in different targets is given in [4,8,9]. An advanced hole size equation covering the range from marginal perforation to big holes is given in [10].

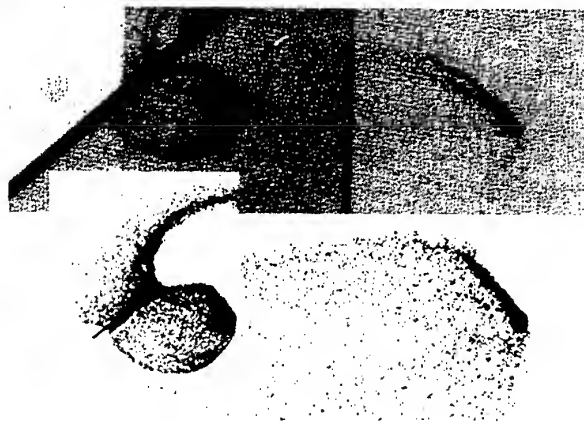


Fig. 7 Penetration of a single metal plate. Comparison of experiment (top) and hydrocode simulation (bottom) after 6.6  $\mu$ s and 22.6  $\mu$ s (from [7]).

A few special cases for penetration should be mentioned:

- For pressurised modules (tanks etc.) penetration of more than 1/3 of the wall thickness can lead to burst.
- Tethers or cables can be cut by a particle with a diameter of 1/3 of the tether thickness. This can reduce the lifetimes of long single strand tethers to the order of only weeks or months.

- Penetration of solar cells can create conducting paths that can lead to a short circuit.

Fig. 8 shows a burn mark observed on the EURECA solar array after retrieval. This burn was caused by a short circuit and arc discharge sustained by the solar array itself. While impacts could trigger such an effect it should be pointed out that in this case no obvious signs for an impact were found at the damaged site.

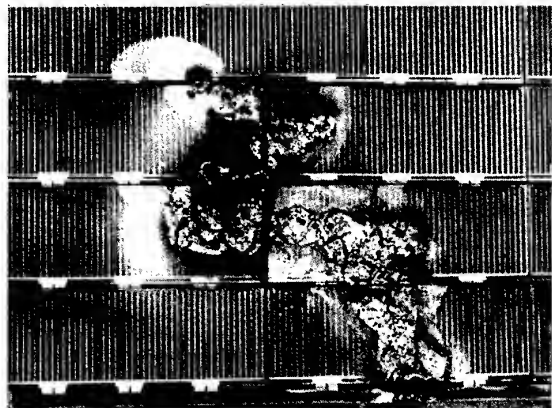


Fig. 8 Burn mark on Eureka solar array after retrieval from space. Picture area is 12 cm x 8 cm.

#### 4. SHIELDING AGAINST IMPACTS

Single walls are not very effective as protection against hypervelocity impacts. A combination of several walls with spacing in between offers a much better shielding capability for the same mass. In the case of double walls the outer wall or bumper breaks up the projectile. The fragment cloud spreads while crossing the spacing. When the fragments hit the rear wall the impact load is distributed over a wider area, resulting in many small craters rather than one deep penetration. For highest efficiency a double wall impact shield has to be designed properly. The bumper should have a thickness of about 0.15 -- 0.2 times the diameter of the largest projectile, which the shield aims to defeat. Thinner bumpers will not completely break up the projectile and thicker bumpers are unnecessary heavy. The protection capability increases rapidly with the separation distance of bumper and rear wall. This holds true up to a distance where the individual cloud fragments no longer overlap on the rear wall. In practise this distance is about 30 - 40 cm. A minimum spacing of 1-2 cm is required before the double wall effect sets in.

Fig. 9 shows x-ray flash photographs of a hypervelocity impact on a multiple wall target. These tests were performed at the Ernst-Mach Institut (EMI) in Germany. A 4 mm Aluminium sphere impacts with 7.2 km/s at 45

degrees angle. The ejecta clouds on both sides of the 1.2 mm bumper are clearly visible. The rear wall that is 3.3 mm thick and 49.5 mm behind the bumper stops the expanded cloud of fragments. It is also visible that the cloud inside the bumper is composed of a mixture of solid or molten fragments and of vapour or very small dust. Two witness plates were not damaged.

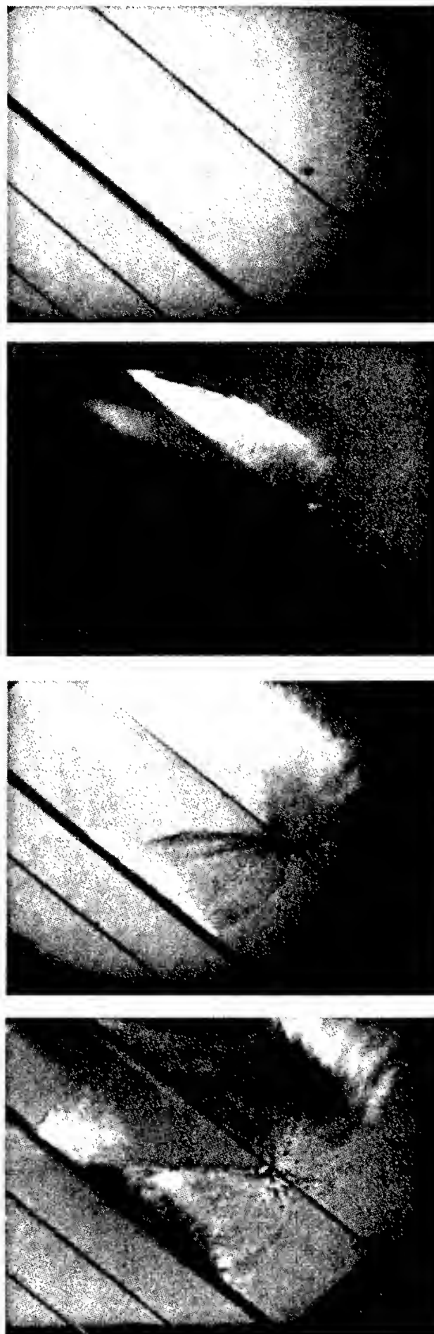


Fig. 9 X-ray flash photographs of a hypervelocity impact on a multiple wall target (test and photos by EMI).

Even a properly designed bumper is only effective if the impact velocity of the projectile is sufficiently high to lead to complete fragmentation and vaporisation. One can distinguish several regimes: for impact velocities up to 3-4 km/s a double wall is not really effective and its protection capability is only similar to a single wall with the combined thickness of the two walls. Above 7-8 km/s the projectile is properly fragmented and a double wall provides much enhanced protection. In Earth orbit most impacts from meteoroids and space debris particles do occur at velocities above 8 km/s. For a more detailed description of damage equations for modern multiple wall shielding designs see e.g. [8,9].

Ground based tests and analysis of material retrieved from space have shown that even Multi Layers Insulation (MLI) which is frequently used for the thermal design of spacecraft offers considerably enhanced protection, especially if it is separated somewhat (1 cm or more) from the main structure.

Adding additional layers of e.g. Kevlar or Nextel between the bumper and rear wall, leading to a multiple wall shielding, can further enhance a shield against hypervelocity impacts. Such a multiple wall shielding is used for most parts of manned modules of the International Space Station (ISS). Most parts of the European Columbus module of the ISS have a shielding protection design composed of: An Aluminium bumper of 2.5 mm, a combination of several Nextel/Kevlar layers with a combined thickness equivalent to about 4mm Aluminium, and a rear wall made of 4.8 mm Aluminium. The total spacing from bumper to rear wall is 13 cm. Tests and simulations have shown that this shield should be able to prevent penetration of the rear wall from all particles smaller than 1.2 -- 1.5 cm at 10 km/s.

## 5. IMPACT PLASMA

The extreme conditions during a hypervelocity impact partially ionise the projectile and target material and create plasma [1]. Near the impact site this plasma can be very dense ( $> 10^{12}$  ions/cm<sup>3</sup>). The initial plasma expansion velocity is similar to the bulk ejection velocity, corresponding to a plasma energy of a few eV. The rise time of a plasma signal is a few  $\mu$ s over some tens of cm distance.

Plasma generation during impact depends strongly on the impact parameters, especially on the impact velocity.

An empirically derived equation for impact-generated plasma is given in Eq. 3 (from [11]):

$$Q = 0.1 \, m \, (m/10^{-11})^{0.02} (v/5)^{3.48} \quad (3)$$

where

Q: plasma charge [Coulombs]

m: mass of projectile [g]

v: impact velocity [km/s]

This equation was obtained during extensive calibration tests of an impact ionisation detector. Projectile masses ranged from sub-micron to a few microns, impact velocities ranged from a few km/s up to around 70 km/s. It is believed that this equation remains valid for larger masses as well.

According to Eq. 3 an impact from a Leonid meteoroid stream particle with mass  $m=10^{-6}$  g at 72 km/s will generate a plasma charge of  $10^{-3}$  Coulomb.

### 5.1 Plasma Effects

The impact-generated plasma will normally recombine quickly. If some electrical fields are present the positive and negative charges can be separated and a current pulse into neighbouring spacecraft wires or components could be generated.

The plasma can lead to electromagnetic interference with spacecraft sub-systems and noise in scientific instruments.

It is suspected that plasma oscillations of the dense and expanding impact plasma can lead to radiated interference with sensitive equipment [12].

The impact plasma can also trigger a discharge of electrostatically charged dielectric surfaces or bulk material, releasing a current that is much larger than would be possible by the impact alone. This discharge current can reach Ampere levels. Such a triggering of discharges by impact-generated plasma has been experimentally verified [13]. The threshold (projectile size, generated plasma quantity, pre-impact charging level, etc) for the triggering of discharges is largely still unknown and requires further investigation. However it is already clear that even relatively small particles in the sub-millimeter size range could trigger discharges. These small size particles are much more abundant than bigger particles which could inflict structural damage.

Triggering of discharges on pre-charged spacecraft parts could well be the biggest risk from meteoroid and debris impacts in Earth orbit.

Every hypervelocity impact will also produce a flash of light.

## 6. METEORIODS AND SPACE DEBRIS

Natural meteoroids are present throughout space. Man-made space debris is mainly found in LEO (Low Earth Orbits, below 2000 km) and in the GEO ring around 36000 km. Average impact velocities on spacecraft in LEO are 10 km/s for space debris and 20 km/s for meteoroids. The average material density for debris is around the value for Aluminium alloys (2.8 g/cm<sup>3</sup>). For meteoroids the density is more variable, ranging from 0.15 g/cm<sup>3</sup> to 8 g/cm<sup>3</sup> with an average around 2 g/cm<sup>3</sup>.

Fig. 10 shows a comparison of predicted and measured fluxes to the front side of the HST solar array as function of the incident particle diameter [3]. The solid line is the prediction from the meteoroid reference model [14], the dashed line is for the debris model given in [15]. The lines with error bars give the result of the measurements after careful data reduction. The flux models predict a domination of natural meteoroids for particle sizes in the range 5-500  $\mu$ m. Space debris is predicted to exceed the meteoroid flux at smaller and larger sizes. The measurements include both, meteoroids and debris. They are in very good agreement with the total predicted flux, except for the smallest and largest sizes measured. This gives confidence in the models but still does not allow a distinction between meteoroids and debris.

Direct information on the relative abundance of meteoroids and space debris in LEO can be obtained by either measuring the orbit of the meteoroids or meteors or by a chemical analysis of impact residues.

Modern measurements of meteors in the Earth atmosphere allow the determination of the orbits of the originating particles. However, the creation of an ionised path in the atmosphere, the meteor, is strongly increasing with the velocity of the incident particle ( $\propto v^{3.5}$ , similar to the dependence in Eq. 3). This leads to a strong bias towards faster particles. Almost all observed meteors are from natural meteoroids and not from debris which enters the atmosphere with a velocity of only around 8 km/s. In-situ measurements of particle trajectories in orbit is possible but costly and has rarely been attempted.

The analysis of impact craters in retrieved hardware has proved very successful. Crater production is not much biased by the projectile velocity (see Eq. 1) and meteoroids and debris have similar efficiency. Experience has shown that meteoroids and debris usually cannot be distinguished from the crater shape alone. However they can be separated by a chemical analysis of impact residues left in the craters. Refined chemical analysis techniques have allowed determining the origin of about 80 % of analysed craters in HST solar cells [3,16]. For the HST orbit (600 km altitude) the results confirm the

predictions of the flux models as shown in Fig. 10: for particle sizes between about 5 microns and 500 microns the flux is dominated by natural meteoroids. Space debris dominates for larger and smaller sizes.

The residue study did also show that most of the small craters from debris were caused by Aluminium and Aluminium-oxide droplets that are the exhaust product from the firing of solid rocket motors [16]. More details on the chemical analysis of impact craters in HST solar cells are given in [3,16].

Fig. 10 gives the situation during the 1990s when the analysed HST solar array had been exposed in space. While meteoroid fluxes are on average constant with time, all space debris has been created during the last 40 years and the future debris population will depend on future space activities and on the success of measures to prevent the further increase of debris.

## 7. METEOROID STREAMS AND STORMS

Meteor streams and storms, like the Leonids in 1999, can be spectacular events for an Earth based observer. But how big is the additional impact risk from these stream particles to a spacecraft in orbit? It is probably fair to state that the extra risk depends on the failure mode under consideration but it is usually not very high.

Meteors are clearly biased towards fast particles by the strong dependence of their intensity on the incident velocity of the particle. Most meteor streams only appear as such because of their high velocity that makes much smaller particles visible or detectable than for background meteoroids. Fluxes at given mass and damage relevant effects like penetration of a given plate thickness or formation of a crater of given size increase far less than the ZHR during a stream event.

Even for a Leonid storm with a ZHR of 10000 over a period of 1 hour the additional risk for spacecraft amounts to only the equivalent of a few days or maximum weeks of exposure to background meteoroids [11].

The velocity effect is also prominent if only the background meteoroids are considered. These meteoroids have a velocity distribution, relative to Earth, ranging from about 3 - 72 km/s. In [11] the velocity weighted means for different impact effects are given. The true mean velocity at constant mass is 17.9 km/s. The velocity weighted mean for penetration of a single wall is calculated at 25.8 km/s. For the generation of plasma charge the weighted mean is 31 km/s. That implies as well that the average velocity of observed sporadic meteors that are caused by the creation of plasma charge should be around 31 km/s.

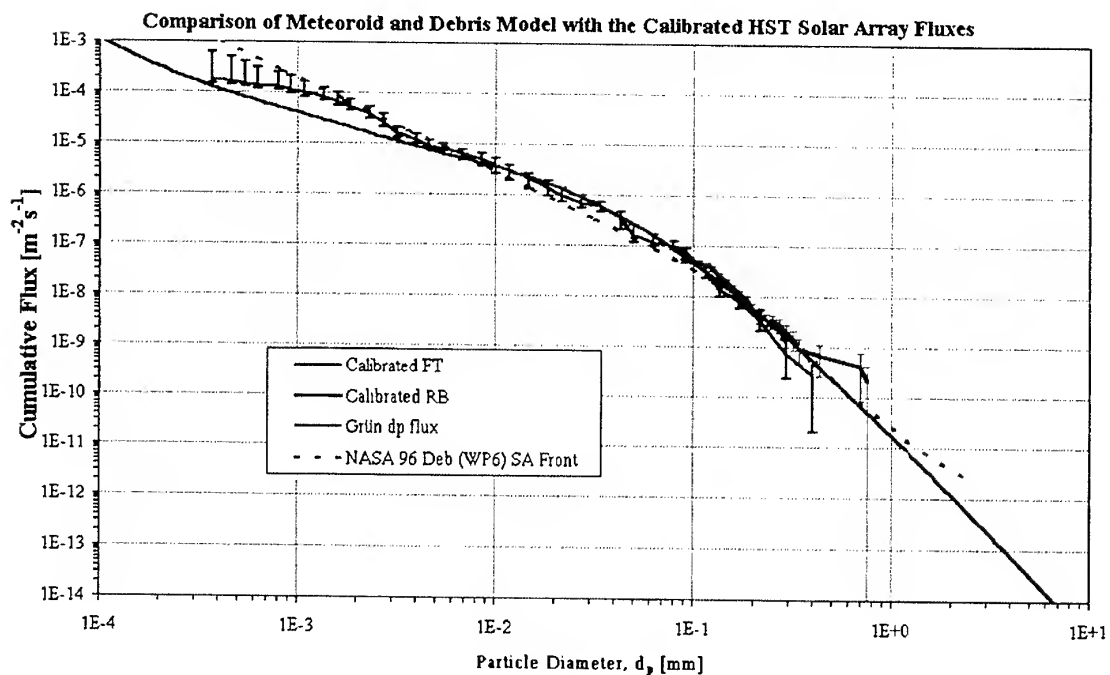


Fig. 10 Predicted and measured fluxes to the front side of the HST solar array as function of the incident particle diameter. The lines with error bars give the measurements. The solid and dashed lines give the predictions of meteoroid and space debris flux models, respectively (from [3]).

The only impact effect that increases like the ZHR during a stream is the generation of impact plasma. It was noted in Section 5 that this could well be the most dangerous effect to spacecraft via the triggering of electrostatic discharges of pre-charged surfaces. Such discharges could be triggered by relatively small particles that are usually the most abundant. However in meteoroid streams particles smaller than about  $10^{-6}$  g are rare as perturbing forces are quickly removing them. That implies that the absolute additional risk even for this damage mode remains small during meteoroid streams. Most likely the background flux of small particles will dominate this risk even during a major meteor storm.

The Olympus telecommunications satellite in GEO is often cited as a spacecraft damaged in orbit by a Perseid stream particle. On August 11, 1993 at 23:32 UT, Olympus lost attitude control leading to a chain of events which ultimately led to the end of its mission [17]. The anomaly occurred just 4 hours before the peak of the Perseid meteor stream. At the time of the anomaly the ZHR was about 100 and still rising to its later maximum around 400. An on-board micro-accelerometer was operating before and during the anomaly. It should have been able to record impacts on the main spacecraft body

but did not detect any. During the week before the anomaly increased fluxes of penetrating electrons in GEO were observed. It is possible that spacecraft dielectric parts were charged up internally and an electrostatic discharge led to a current pulse and then to the anomaly.

Such a discharge could have been triggered by an impact (see discussion in section 5). However, the extra risk from the Perseids was rather small. If a particle that was too small to be detected by the acoustic sensor triggered a discharge chances are that it was a sporadic meteoroid rather than a Perseid. A larger projectile could also have impacted a solar array near the main body, without being detected by the micro-accelerometer. While it cannot be ruled out there is no direct evidence that a meteoroid (or debris) impact ended the life of Olympus.

Of course, during a meteor stream or storm the impact risk to spacecraft is increased, although the increase may be small. Precautionary measures like delay of a launch by a few days or alerting spacecraft operators of an upcoming event are recommended. But overall it can be said that meteor storms are exciting to watch and study but not very dangerous to spacecraft.

## 8. CONCLUSIONS

An overview of effects of hypervelocity impacts on spacecraft was given. Effects from natural meteoroids and man-made space debris are similar. In near Earth space natural meteoroids are dominating in the size range 5-500  $\mu\text{m}$ . For larger sizes man-made space debris is already more numerous.

Micron size particulates can degrade surfaces and sensitive sensors, mirrors and detectors. As instruments get ever smaller and more sensitive and sophisticated the risk from these small particles will likely increase in future. Secondary ejecta from impacts on sidewalls and baffles could be more damaging than direct hits.

Certain structures like solar cells are very robust against impacts. Normally even complete penetration of a solar cell causes no functional problems. In special cases a conductive path and short circuit could be created. Multiple walls against impacts should protect sensitive equipment, like electronics and tanks.

Impact generated plasma can lead to electrical interference and triggering of discharges. This effect needs further study but could well be the biggest impact risk to spacecraft in Earth orbit.

The additional impact risk from meteor streams is relatively small, even if the ZHR reaches storm conditions.

The risk from hypervelocity impacts should be considered for any spacecraft design. Protective measures include additional shielding or placing of sensitive equipment at safe locations inside the spacecraft. If functional reasons prevent such options (e.g. for mirrors and sensors) a proper margin for degradation from impacts has to be allowed for.

## 9. REFERENCES

- McDonnell, J.A.M., editor, *Cosmic Dust*, Wiley, 1987.
- Rival, M. and Mandeville, J.-C., Modeling of Ejecta Produced upon Hypervelocity Impacts, *Space Debris*, Vol. 1, pp. 45-57, 1999.
- McDonnell, J.A.M., editor, Meteoroid and Debris Flux and Ejecta Models, Final and Summary Reports of ESA contr. 11887/96/NL/JG, 1998.
- Berthoud, L. and Mandeville, J.-C., Empirical Impact Equations and Marginal Perforation, Proceed. First Europ. Conf. Space Debris, Darmstadt, 5-7 April 1993, *ESA SD-01*, pp. 459-464, 1993.
- NASA SP-8042, Meteoroid Damage Assessment, 1970.
- Paul, K.G., and Berthoud, L., Empirical scaling laws for crater dimensions for impacts into solar cells, in *Physics, Chemistry and Dynamics of Interplanetary Dust*, Proc. IAU Colloq. No 150, Gainesville, Florida, 1995.
- Hayhurst, C. Livingstone, I., Advanced Numerical Simulations for Hypervelocity Impacts, ESA CR(P) 4218, 1998.
- Lambert, M., Hypervelocity Impacts and Damage Laws, *Adv. Space Res.* Vol. 19, No. 2, pp. 369-378, 1997.
- Christiansen, E., Design and Performance Equations for Advanced Meteoroid and Debris Shields, *Int. J. Impact Engng.*, Vol. 14, pp. 145-156, 1993.
- Gardner, D.J., McDonnell, J.A.M., and Collier, I., Hole growth characterisation for hypervelocity impacts in thin targets, *Int. J. Impact Engng.*, 19, pp. 589-602, 1997.
- McBride, N., McDonnell, J.A.M., Meteoroid impacts on spacecraft: sporadics, streams, and the 1999 Leonids, *Planet. Space Sci.*, 47, pp 1005-1013, 1999.
- Foschini, L., Electromagnetic Interference from Plasmas Generated in Meteoroids Impacts, *Europhys. Lett.* 43 (2), pp. 226-229, 1998.
- Soubeyran, A., editor, Combined Environmental Interaction of Solar Arrays, Final Report of ESA contr. 9989/92/NL/US(SC), 1995.
- Grün, E. et al., Collisional Balance of the Meteoritic Complex, *Icarus*, 62, pp. 244-277, 1985.
- Kessler, D.J. et al., A Computer-Based Orbital Debris Environment Model for Spacecraft Design and Observation in Low Earth Orbit, *NASA TM 104825*, 1996.
- Graham, G.A. et al., Microparticle Impacts upon HST Solar Cells, COSPAR 2000, *Adv. Space Res.*, 2001.
- Caswell, R.D., McBride, N. and Taylor, A., Olympus End of Life Anomaly -- a Perseid Meteoroid Impact Event?, *Int. J. Impact Engng.*, Vol. 17, pp. 139-150, 1995.

# COMPARISON OF METEOROID AND SPACE DEBRIS FLUXES TO SPACECRAFT IN EARTH ORBIT

Veronika Ekstrand<sup>(1)</sup>, Gerhard Drolshagen<sup>(2)</sup>

<sup>(1)</sup> ESTEC/ESA, Keplerlaan 1, NL - 2201 AZ Noordwijk ZH, e-mail: v.ekstrand@spray.se

<sup>(2)</sup> ESTEC/ESA, Keplerlaan 1, NL - 2201 AZ Noordwijk ZH, e-mail: Gerhard.Drolshagen@esa.int

## ABSTRACT

Spacecraft in Earth orbit will be impacted by natural meteoroids and man made space debris particles. The relative ratio depends mainly on the particle size, the spacecraft orbit and attitude. Predicted numbers of impacts from different flux models are presented for particle sizes ranging from microns to cm. For low Earth orbits, meteoroid fluxes dominate for sizes between some 10 microns and about 1 mm while space debris is more abundant for smaller and larger sizes. The most recent flux models show generally a good agreement. The model differences for a given population indicate the present level of uncertainty.

## 1. INTRODUCTION

In this study the latest meteoroid and space debris models are compared for a set of test cases. The importance of these kind of test is to evaluate the advantages and disadvantages of the different models in different stages of a prediction. Some of the models are preferred for a preliminary fast prediction when a rough estimation about the environmental flux is sufficient. In other instances, a more sophisticated impact risk assessment is required and it is more important to have all the latest sources of debris and meteoroids included in the model.

As the debris environment is changing the models have to be periodically validated and improved. The models that are used today have a built in prediction parameter about the future development of the debris in space and any abrupt changes in the space environment can cause the model to not be reliable any more. This is well known and it is one of the reasons why improved and more advanced models regularly appear. The second reason for more advanced models are the increased power of computers which make it possible to process larger amounts of data and equations in shorter time. When several new models have appeared, it is important to make an independent evaluation of them and to test all models with the same test parameters.

To keep the available debris information for the different models updated, different kinds of measurements are done. Larger particles can be observed and tracked by ground-based instruments like different kinds of radar and optical telescopes. From Earth it is though not possible to track all the small particles that are orbiting Earth. For information about

those, space based measurements and simulations are needed.

In Low Earth Orbit (LEO), objects larger than about 10 cm in diameter are regularly tracked by radar and catalogued. Objects down to about 1 cm in size are occasionally monitored by radar or optical telescopes. The best source of information on particles in the size range 10 $\mu$ m -- 1mm is the analysis of the retrieved hardware. Recent examples include: the Long Duration Exposure Facility (LDEF), the EUREKA spacecraft, a solar array from the Hubble Space Telescope (HST), hardware from MIR and shuttle windows.

Even smaller particles can be monitored by in-situ detectors like dust monitors on Ulysses, Galileo and Cassini in interplanetary space or the GORID detector in the geostationary orbit or the planned DEBIE in-situ detectors. DEBIE will be flown in a polar orbit and later on the International Space Station (ISS). Between the ground based measurement techniques existing and the space-based techniques is a gap in particle size from about 1mm up to a few cm. The different measurements are combined with numerical simulations to produce comprehensive flux models for natural meteoroids and man made space debris.

Recently several new population models for natural meteoroids and man made space debris particles have been developed. These models are applied to different test cases and compared to each other. The numbers of impacts to ESA's DEBIE impact detectors are predicted. DEBIE-1 is planned for launch in 2001 into a polar orbit, DEBIE-2 will be launched in 2005 to the ISS.

## 2. BACKGROUND AND SCOPE

### 2.1 Meteoroids

The investigation on Meteoroids are conducted down to 0.1 micrometer because meteoroids have a very high speed up to 72 km/s and this gives even very small particles high damage potential because of their kinetic energy. The meteoroid environment can be considered to be static in the long term. However there is short-term variation and annually recurring seasonal stream events can vary the activity during the year.

Various populations of meteoroids can interact with satellites orbiting Earth. Because of the movement of

Earth around the sun, impacting meteoroids have different speed [1]. The velocity is highest if the meteoroids encounter Earth (and the orbiting satellites) head on. This is called the Apex direction. The lowest speeds of the meteoroids are found at the trailing side of Earth, because here the meteoroids have to catch up with the Earth and overcome Earth's initial speed. This gives these incoming meteoroids a lower velocity relative to Earth.

## 2.2 Debris

The definition of space debris as discussed in this paper is: any man made Earth orbiting object which is non-functional with no reasonable expectation of assuming or resuming its intended function, or any other function for which it is or can be expected to be authorised, including fragments and parts thereof [2].

Objects included in man made orbital debris are rocket-bodies, non-operational spacecraft and fragments generated by collision and explosions of upper stages and satellites. Other sources are:

- Launch related objects
- Coolant release from nuclear reactors in space (NaK)
- Surface degradation particles (paint flakes)
- Ejecta generated by impacts of small man-made objects and meteoroids.
- Exhaust particles from Solid Rocket Motor firings.

The main hazard of space debris is unintended collision between debris and operational spacecraft. When the debris cannot be controlled and traced, the risk could eventually be too high to launch a new satellite that could be destroyed by debris and result in a severely shortened planned lifetime of the mission. The fact that debris are man made and are fragments that come from different space missions makes them accumulate into orbits with high space activity [3].

Some of the populations mentioned are traced from ground-based sensors, but this is only true for particles bigger than a few centimetres. The United States Space Command's USSPACECOM Space Surveillance Network (SSN) catalogue consists of particles larger than 10cm. The roughly 9000 objects in this catalogue (status 2001) are estimated to be only 5% of the number of particles at 1 cm.

For debris particles, impact velocities range from 0 to about 18 km/s. In LEO, atmospheric drag will act to circularise the orbit of the debris and spiral the orbit into the atmosphere. How long this process takes is proportional to the area to mass ratio of the object. Micron sized particles below 500 km altitude will decay in a matter of weeks, while cm sized objects at 1000 km can stay in orbit for hundreds or thousands of years.

## 2.3 DEBIE

The DEBris In orbit Evaluator (DEBIE) [4], is an in-situ impact detector instrument. The detection principle is a combination of impact ionisation, momentum and foil penetration.

The DEBIE instrument is designed as a standard instrument that can be used on many different missions. The information received from the instrument provides information about the mass and velocity of the incoming particles. The main information is on micron size particles and the main purpose of this instrument is to provide data to validate and improve the meteoroid and debris population models.

DEBIE is designed to have up to four sensors with an area of 10 cm x 10 cm each. These can be mounted on different outside walls of a spacecraft. The first flight is planned to be on the PROBA mission in October 2001. This will be into a polar orbit around 600 km and it will have two sensors on the front and one side. The second planned mission is on ISS / EUTEF module with sensors at the front, space and North side. This is planned to be in 2005. Patria Finavitec (Fin) built the DEBIE instrument based on a design by UniSpace Kent (UK)

## 2.4 The models

### 2.4.1 MASTER '99

#### The Meteoroid Background Flux Model

MASTER '99 [5] includes the so called 'Divine-Staubach' model for meteoroids. This model is non-isotropic with flux coming from different populations. It has a built in velocity distribution. Divine's theory of five distinct populations with specific signatures is the base of the MASTER 'meteoroid background flux model'. The specific signatures are in terms of mass spectrum, eccentricity, inclination and perihelion distance in an ecliptic reference system [6]. Peter Staubach modified this model under ESOC contract in 1996 [7]. This updated model takes into account data from the dust detectors flown aboard the Ulysses and Galileo spacecraft.

#### The Meteoroid Stream Flux Model

The MASTER meteoroid model includes seasonal streams with their time dependency and flux directionality. The Cour-Palais and Jenniskens-McBride models have been implemented for this reason. The Cour-Palais model [8] describes 18 streams given by their stream activity in terms of a flux enhancement factor, that describes the ratio of the cumulative flux of each stream with respect to the average cumulative sporadic flux. Gravitational focussing and Earth shielding effects are not considered in this model. The Jenniskens-McBride model describes the default meteoroid stream model based on data

compiled by P. Jenniskens [9] and a count rate/flux conversion proposed by N. McBride [10]. The meteoroid stream model is not applied in this study.

### Debris model

The MASTER '99 space debris model uses a semi-deterministic approach. The data from the USSPACECOM catalogue, as explained above, are implemented deterministically into the debris model. Simulations supply untraceable smaller particles. In MASTER all the debris creations events are simulated individually. A deterministic approach is used for the SRM firings and a statistically approach is used for the paint flakes and the ejecta. Paint flakes are the main source in LEO for particles around 10 micrometer. Exhaust particles from SRM firings dominate the 1  $\mu\text{m}$  size regime.

### 2.4.2 ORDEM 2000

ORDEM2000 [11] is an update of ORDEM96 for the debris in Low Earth Orbit. It is valid between 200 km and 2000 km altitude. The two main reasons for updating ORDEM 96 are the changing environment and new measurements. This update makes the model more reliable. The ORDEM2000 model is based on a more rigorous mathematical approach. For more detailed information see [12].

To test and validate the model output, 11 different data sources were used. The major data sources are used to build the debris environment. These are the Space Surveillance Network (SSN) catalogue, the Long Range Imaging Radar (LRIR), Haystack, radar, the Long Duration Exposure Facility (LDEF), and the Hubble Telescope Solar Array. The remaining sources of data are used to adjust the debris population. The debris populations are derived from different data sources, i.e. the 10 cm and bigger are from the SSN catalogue and the Haystack radar is used for the 1 cm and higher. The LDEF are used for particles smaller than 100 micrometer. The remaining gap is closed with the Goldstone radar data. The Goldstone radar data are used for verifying the cubic spline interpolation used in the output for debris of arbitrary sizes, and especially to verify the interpolation for the 1mm size debris output.

### 2.4.3 ORDEM 96 (NASA 96)

This is a computer-based orbital debris engineering model. It is based on empirical considerations and defines orbits in six different inclination domains. Instead of expressing the flux and velocity distribution as a function of orbital parameters, it derives the debris populations from available observational data and measurement data. ORDEM96 simplifies the data into six inclination bands and two eccentricity families. The inclination bands used are  $7^\circ$ ,  $28^\circ$ ,  $51^\circ$ ,  $65^\circ$ ,  $82^\circ$ ,  $98^\circ$ . It also assumes that the particles have a random distribution between  $0^\circ$  and  $360^\circ$  degrees on the

longitude of the ascending node ( $\Omega$ ) and argument of perigee ( $\omega$ ). For more information about the formulas see [13]. This model is included in ESABASE [14].

One major upgrade from NASA90 is the possibility of including eccentric debris orbits, which was previously not possible. The debris population is divided into two eccentricity families, the circular orbit family that include debris up to an eccentricity of 0.2 and the eccentric family group which include all debris with an eccentricity of more than 0.2. These elliptical orbits will have a fixed apogee height at 20 000 km. Contributions from circular orbits are a function of altitude, particle size, mission time and solar activity. Contributions from eccentric orbits are a function of perigee altitude, particle size and mission time. Debris in circular orbits will not have any contribution to the top or bottom surfaces of spacecraft. For debris in eccentric orbits, an impact probability exists on these surfaces. Fluxes are obtained by calculating the spatial debris density along the target orbit. When looking into the collision analysis, one can see that fluxes are averaged over one spacecraft revolution. Therefore no flux variation will be seen along the orbital path.

### 2.4.4 NASA 90

The NASA 90 [15] debris model is older and simpler than the ORDEM models. Its flux and velocity distributions are given in analytical form. A major simplification of the model is the assumption that all debris moves in circular orbits. This model is limited to below 1000 km altitude.

For more extent information about NASA90 flux model see [15]. The velocity distribution and debris fluxes of the model are defined by functions that depend on the diameter of debris, on the altitude, on the epoch and on the inclination.

### 2.4.5 Grün et al. Meteoroid model

The Interplanetary flux model for a position at 1 AU distance from the sun and in the ecliptic plane was established in 1985 by Grün et al [16] and is today the de facto standard for the sporadic meteoroid environment. This model is an omni-directional flux model. It has no velocity distribution of its own, but can be combined (e.g. within ESABASE) with either the NASA90 velocity distribution, a constant velocity or the Taylor HRMP velocity/flux function. The model assumes an isotropic flux with respect to the Earth surface. A directional dependence is introduced by the orbital velocity of the satellite. The model represents the total meteoroid influx at Earth position. The focusing effect of the gravitational field and the shielding effect of the atmosphere are taken into consideration with extra corrections.

The Grün model expresses the average flux in terms of the integral flux  $F$  ( $1/\text{m}^2/\text{yr}$ ) from a meteoroid with given minimum mass and larger, that impact from one side on a randomly tumbling plate at 1 AU in the ecliptic plane. The velocity distribution used ranges from 11 km/s to 72 km/s.

### 3. CASES ANALYSED

The models described above were compared for a number of different orbits and size ranges. All simulations were made for the date of 1<sup>st</sup> of August 2002. The first orbit used for this was the orbit of the International Space Station (ISS), which is a circular orbit with a semimajor axis of 6778 km and an inclination of 51.6 degrees. The second orbit was a circular Polar orbit with a semimajor axis of 7078 km and an inclination of 98 degrees. The last orbit used was the circular Geostationary orbit (GEO) which had a semimajor axis of 42164 km and an inclination of 0.01 degrees.

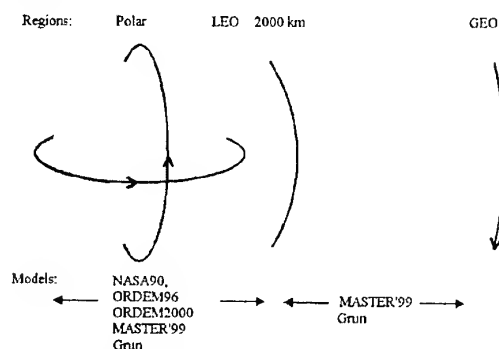


Fig.1. Explanation of the range of the models (modified figure from [17])

Simulations were performed to predict the number of particle impacts per  $\text{m}^2$  per year. This was done for different minimum sizes of the particles, with the start at 0.1 micrometer and increasing the minimum size with the power of ten until the minimum size was 1 cm. First simulations were made for a randomly tumbling plate and then for an oriented box. The oriented box had one side towards Earth and one side towards the velocity vector. (see Fig. 2).

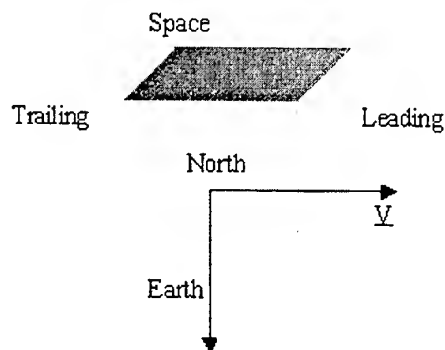


Fig. 2. Oriented box used as a test case.

The box sides were defined with azimuth and elevation angles, as shown in Tab. 1 below.

Side	Azimuth	Elevation
Leading	0	0
Space	0	90
Trailing	0	180
Earth	0	-90
North	90	0
South	-90	0

Tab.1 Box orientation

The reason for simulating an oriented box is to study the directional dependence of the impacting particles. Most of the incoming particles will hit the body with an azimuth angle between 30 and 70 degrees from the velocity vector because debris fluxes are normally parallel to the Earth's surface. Spacecraft orientation and geometry needs to be considered, for example, for the International Space Station, which has a fixed orientation with respect to the velocity vector.

For all the simulations, an eccentricity of 0.001 degrees was used. Solar activity was 140 ( $F_{10.7}$  cm), the right ascension of ascending node was 120 degrees and the argument of perigee was 150 degrees (this is only relevant for some models).

#### 3.1 MASTER'99/ Divine-Staubach

The first model that was investigated was MASTER'99, the Meteoroid And Space Debris Terrestrial Environment Reference Model. This model was used for all orbits and for both a randomly tumbling plate and an oriented box. This was done by altering the surface description in the program. The constellation traffic file used 9 different constellations. It had a range of particle sizes from 1 micrometer up to 1 cm for debris simulations and for meteoroids the range was from 1 micrometer up to 0.3 cm. For the Meteoroid simulations the Divine-Staubach model was used. In MASTER'99 the analyst model was used which made it possible to perform more extended simulations.

When debris was simulated, all the sources of debris were selected. The start and end period of the analysis interval was set to the same date and the 'annual population growth rate' was set to 2.5 %. Depending on whether it was a simulation for debris or meteoroids, the size interval was set to either mass for debris or kg for meteoroids. When meteoroids were simulated, the source was set to meteoroids and then it was possible to edit the population between core-, asteroid-, A-, B- and C populations. In this window, all the populations were entered and the seasonal meteoroid stream was set to 'no seasonal'. If seasonal streams are used, it is possible to choose between Jenniskens-McBride and Cour-Palais. When all the preparations for the simulation were completed, it was also possible to choose what set

of graphs were preferred. The 2D-spectrum definition has a variety of 15 different types of graphs, which can be displayed in linear or logarithmical mode and several other display functions. The types of graphs chosen in the 2D choice can be combined in various 3D graphs.

### 3.2 ORDEM2000

The next program evaluated was ORDEM 2000 (Orbital Debris Engineering Model) from NASA. In this model, a sphere was used as object in the simulations. Since the results were given in cross sectional flux, the results were divided by 4, which made the results comparable with a randomly tumbling plate. For this model, the ISS and polar orbits were evaluated. The size range was 10 micrometer up to 1 cm. The investigated orbit was divided into 18 different orbit segments.

When working with this model, the first choice was to decide whether the spacecraft assessment or the radar/telescope assessment was to be used. For this investigation, the spacecraft assessment was chosen. The following level of the program defines the input for the spacecraft to be analysed. Here the orbit was specified by either selecting 'semimajor axis (km) and eccentricity (0 or 1)' or by choosing 'apogee/perigee (km)'. Here also the inclination and year of observation could be given. In this program, the user names the output files himself and it is mandatory to choose the directory of the output files.

After the program has computed the results, the original inputs were displayed for confirmation that the right values had been calculated. Here it was possible to choose between displaying the graph as 'flux verses size' or as 'flux over orbit path'. With the graphical display of the result, it was also possible to calculate the flux for any value of minimum particle diameter within the range of the program. The results, as a graph or as data, can be saved, printed or transferred to clipboard. If the advanced display control was used the graphical display could be altered by changing the axis, the title, the plot style, the grid style or the tic marks.

### 3.3 ESABASE

Since the three models ORDEM 96, NASA90 and Grün et al. were included in the ESABASE analytic tool, the operating procedure of ESABASE will be explained here. Some extra specific comments on the models are presented in their separate section.

When starting the ESABASE tool, first the terminal type was chosen. When the program was open, the main menu was visible with six different entries: 'prepare orbit' 'translate input' 'applications' 'display tools' 'gateway' and 'management'. In the 'prepare input' menu the main input file for the analysis was selected. Note that in this program it is only possible to chose a

file from the current directory. In the 'translate input' entry, the files used for the simulation had to be selected. The ones used were the system file the command file and the orbit file. In the 'applications' entry, it was possible to decide the type of the simulation. The one used in this paper was Debris/Meteoroids. The 'display tools' was an entry to decide which kind of geometrical display tools was to be used. With the 'gateway', it was possible to transfer configuration data to external software for further processing. Finally, the 'management' entry was for choosing the way to handle the results. It could convert the results into ASCII or binary form as well as display of models and results.

When 'Debris/Meteoroids' was chosen, the input of the simulation could be changed. When the randomly tumbling plate was simulated, the non geometric model was used, and when the oriented box was simulated, the geometric version was used. The post processor is an interactive program to access results at element level. After the geometric model or the non-geometric model was entered, a number of files were selected from the directory for the analysis. The execution type menu options were 'Interactive', 'Normal batch', 'Fast Batch' and 'Slow Batch' and for these kinds of simulations the interactive option was used. The final step is that the program executes the simulation and a result file is created.

#### 3.3.1 ORDEM96 (NASA96)

This debris model included in ESABASE is used to predict debris for the ISS and polar orbits. It is used to simulate both a randomly tumbling plate and an oriented box. The polar orbit is simulated with an inclination of 98.1 degrees. The particle minimum size range is from 0.1 micrometer up to 1 cm. The actual collision analysis is performed for four orbital points.

#### 3.3.2 NASA90

This debris model included in ESABASE is also used for the ISS and polar orbits. It can simulate both orientation modes, and the particle minimum size range is 0.1 micrometer up to 1 cm. This is an analytical model that requires two additional parameters when running the simulation, namely mass growth per year ( $p=0.05$ ) and fragment growth per year ( $q=0.02$ ).

#### 3.3.3 Grün et al.

This meteoroid model included in ESABASE can simulate all three orbits and both orientation modes. The particle minimum diameter range is from 0.1 micrometer up to 1 cm.

#### 4. RESULTS OF THE STUDY

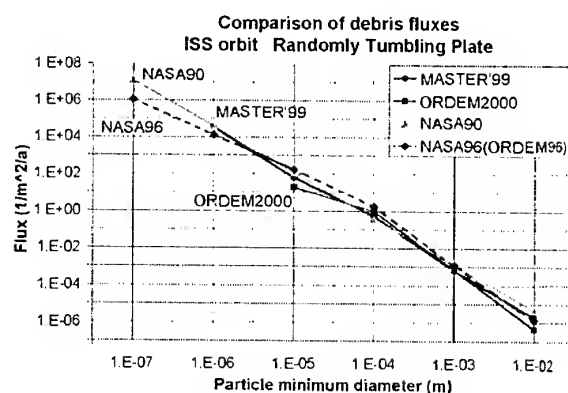


Fig. 3 Comparison of debris fluxes for the ISS orbit.

Fig. 3 shows a comparison of all 4 debris models studied for the ISS orbit and a randomly tumbling plate. The models generally agree quite well for most parts of the size range analysed. A noticeable exception is the NASA 90 model which predicts higher fluxes for the smallest ( $\leq 1\mu\text{m}$ ) and largest ( $1\text{cm}$ ) sizes. NASA90 is the oldest model and the difference can be explained by new measurements and data that are considered by newer models. The ORDEM 2000 model predicts the smallest fluxes at  $10\mu\text{m}$ , the minimum size for which it is applicable.

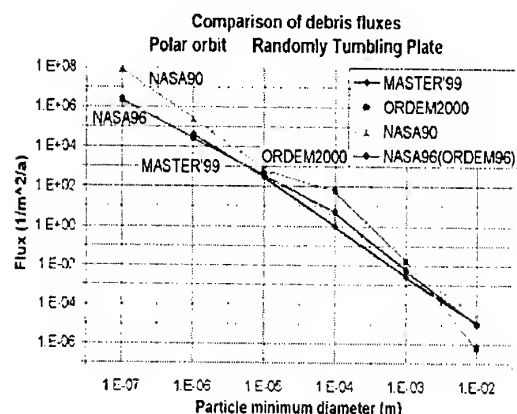


Fig. 4. Comparison of debris fluxes in Polar orbit

Fig. 4 shows the comparison in polar orbit and for a randomly tumbling plate. In this comparison all four debris models were applied. Here a noticeable difference can be seen for the ORDEM2000 model. When compared to the other models the predicted fluxes are higher at  $100\mu\text{m}$  and lower at  $1\text{cm}$ . Main sources of debris at these sizes are surface degradation, NaK droplets, and fragmentation debris. The ORDEM2000 is the newest model compared, and the difference can be explained by new measurements and data that are considered.

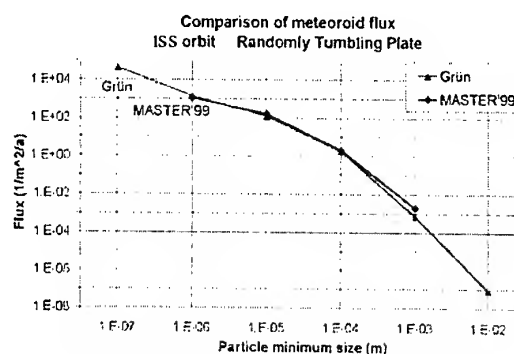


Fig. 5. Comparison of meteoroid fluxes, ISS orbit.

Fig. 5 shows the results from the Grün and MASTER'99 models for meteoroids. The comparison is for the ISS orbit and for a randomly tumbling plate. The model results agree very well with each other. Note that the MASTER'99 has a smaller size range

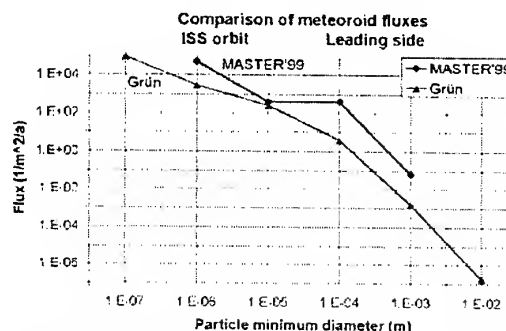


Fig.6 Comparison of meteoroid fluxes for a forward facing surface in the ISS orbit.

Fig. 6 shows the comparison of the Grün and MASTER'99 meteoroid models. The comparison is for the ISS orbit with an oriented box. Here the leading side has been used for comparison. It is noticeable that the two models are no longer comparable. The results of the MASTER'99 model appear strange and not consistent with the values for the randomly tumbling plate (Fig. 5). The most likely explanation is that the meteoroid data in MASTER 99 are stored too coarsely for such a detailed analysis. This deficiency should be easy to overcome in future updates.

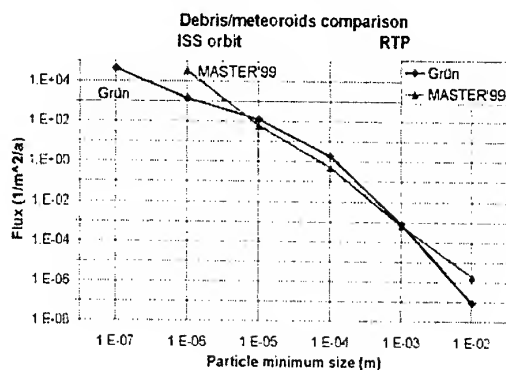


Fig. 7. Debris/ meteoroid comparison, ISS orbit.

Fig. 7 shows the comparison between the Grün meteoroid model and the MASTER'99 debris model. The results are for the ISS orbit and for a randomly tumbling plate. The MASTER'99 model shows a higher value of space debris at particle minimum size larger than 1mm and smaller than 10  $\mu\text{m}$ .

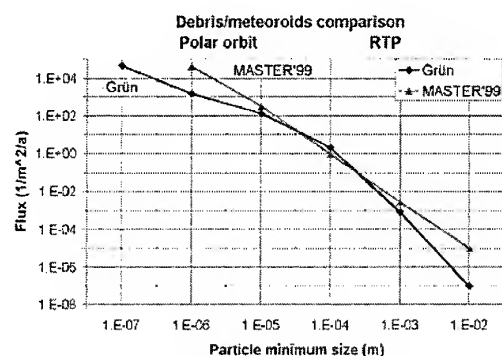


Fig. 8. Debris/meteoroid comparison, Polar orbit.

Fig. 8 shows the comparison between the Grün meteoroid model and the MASTER'99 debris model. The comparison is for the Polar orbit and a randomly tumbling plate. The MASTER'99 model shows a higher value of space debris at particle minimum sizes larger than 500  $\mu\text{m}$  and smaller than 50  $\mu\text{m}$ .

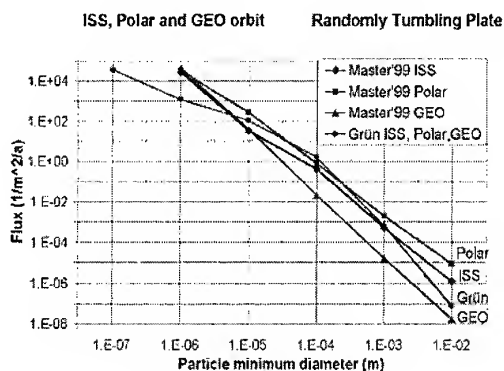


Fig. 9. Debris /Meteoroid comparison, ISS, Polar and GEO orbit.

Fig. 9 shows the comparison between the Grün meteoroid model and the MASTER'99 debris model. The comparison is made for all three orbits and for a randomly tumbling plate. The meteoroid values are nearly the same for all three orbits.

For the three orbits compared the debris fluxes are nearly identical for the smallest size particles. As the particle minimum size is increased so is the difference of the debris flux in the different orbits. At one cm diameter, the difference between GEO and polar debris fluxes becomes very large.

The debris results for a randomly tumbling plate show that the fluxes are different depending on the orbit analysed. A significant difference is found between the

GEO orbit (triangle) and the orbits closer to Earth. The highest fluxes are predicted for the polar orbit. This is the preferred orbit for Earth observation missions and debris in this orbit has a much higher lifetime than in lower orbits.

PROBA	Leading		Side		Space	
Polar	Meteoroids	Debris	Meteoroids	Debris	Meteoroids	Debris
0.1 $\mu\text{m}$	966.00		467.10		N/A	N/A
1 $\mu\text{m}$	31.77	308	15.36	106.40	N/A	N/A
10 $\mu\text{m}$	2.78	2.59	1.34	0.62	N/A	N/A

ISS	Leading		Side		Space	
	Meteoroids	Debris	Meteoroids	Debris	Meteoroids	Debris
0.1 $\mu\text{m}$	908.40		429.20		643.80	
1 $\mu\text{m}$	29.88	245.60	14.12	68.36	21.17	21.99
10 $\mu\text{m}$	2.61	0.37	1.23	0.24	1.85	0.02

Tab. 2. Predicted number of impacts per year for each of the planned DEBIE sensors for different minimum particle sizes. Each DEBIE sensor has a sensitive area of 0.01  $\text{m}^2$ .

For the planned two missions of the DEBIE in-situ detectors, calculations were performed for the actual orientations and aperture sizes of the sensors. The Grün model was used for meteoroids and MASTER 99 for debris. The results are presented in Tab.2. Given is the predicted number of impacts per year for each of the sensors. DEBIE should be able to detect particles down to about  $10^{-15}$  g ( $\sim 0.1$   $\mu\text{m}$ ) if they are sufficiently fast.

Almost all impacts from particles  $>1$   $\mu\text{m}$  should be detected. Tab.2. shows that a few impacts per day can be expected on average by the DEBIE detectors. For a minimum size of 0.1  $\mu\text{m}$ , only predictions for meteoroids are reported as the debris models are considered too unreliable at these small sizes. The measurements by the DEBIE detectors should help to validate or improve the present population models.

More results of the model comparisons are presented in a comprehensive study report [18].

## 5. CONCLUSIONS

The most popular recent meteoroid and space debris flux models were compared for different Earth orbits. In general, the models, especially the most recent once, show good agreement. Some noticeable differences were found for fluxes on oriented surfaces. These model differences give an indication about inherent uncertainties.

In LEO natural meteoroids still dominate the particulate population for particles in the size range 5 --500 microns. At larger and smaller sizes man made space debris is already more abundant.

Comparisons as presented in this paper are important for the future evolution of debris and meteoroid models. Planned measurements from ground and by in-situ detectors will further enhance the flux models and lead to more accurate and reliable impact risk assessments of spacecraft in orbit.

## 6. REFERENCES

- 1 Norton, R., *Rocks from space*, Mountain Press Publishing Company, Missoula, Montana, 1994.
- 2 Position Paper on Orbital Debris, *International Academy of Astronautics*, 2001.
- 3 ECSS, *Space engineering/ Space environment standard*, ECSS-E-10-04A, 2000.
- 4 Kuitunen, J., et al., DEBIE -- First Standard In-Situ Debris Monitoring Instrument, Proceedings of 3<sup>rd</sup> European Conference of Space Debris, Darmstadt, Germany, 19-21 March 2001.
- 5 Wegener, P., et al., Upgrade of the ESA MASTER model, *Final report of ESA contract 12318/97/D/IM*, 2000.
- 6 Divine, N., Grün, E., Staubach, P., Modeling the Meteoroid Distributions in Interplanetary Space and Near Earth, Proceedings of 1<sup>st</sup> European Conference on Space Debris, Darmstadt, Germany, 5-7 April 1993, *ESA SD-01*, pp.245-250,
- 7 Staubach, P., Numerische Modellierung von Mikrometeoroiden und ihre Bedeutung für interplanetare Raumsonden und geozentrische Satelliten, *Thesis at the University of Heidelberg*, April 1996.
- 8 Cour-Palais, B.G, Meteoroid Environment model 1969, *NASA SP-8013*, NASA JSC, Houston TX 1969.
- 9 Jenniskens, P., Meteor Stream Activity -1. The Annual Meteor Streams, *Journal of Astron. And Astrophys.*, Vol. 287, pp990-1013, 1994.
- 10 McBride, N., The Importance of Annual Meteoroid Streams to Spacecraft and their Detectors, *Advances in Space Research* 20, 1513-1516, 1997.
- 11 Liou, J-C., et al., The new NASA orbital debris engineering model ORDEM2000. Proceedings of 3<sup>rd</sup> European Conference of Space Debris, Darmstadt, Germany, 19-21 March 2001.
- 12 Liou, J-C., et al., Updating the NASA LEO orbital debris engineering model with recent radar and optical observations and in situ measurements, *IAA-00-IAA.6.4.08*, 2000.
- 13 Kessler, D.J et al., A Computer Based Orbital Debris Environment Model for Spacecraft Design and Observations in low Earth orbit, *NASA Technical memorandum 104825*, NASA JSC, March 1996.
- 14 Lemcke, C., et al., Enhanced debris / micrometeoroid environment models and 3D software tools, *Software User Manual*, S-50/95-SUM-HTS, August 1998.
- 15 Anderson, B.J., editor, Review of Meteoroids/Orbital Debris environment, *NASA SSP 30425*, Revision A, 1991.
- 16 Grün E., et al., Collisional Balance of the Meteoritic Complex, *Icarus* 62, pp244-272, 1985.
- 17 McDonnell, J.A.M. et al., Update of Statistical Meteoroid / Debris Models for GEO, ESA Contract 13145/98 /NL/WK, *Final Report*, Unispace Kent, Dec 2000.
- 18 Ekstrand, V., Comparison of meteoroid and space debris fluxes to spacecraft in Earth orbit, Umeå University, Space physics dept. Kiruna Sweden, *Study Report*, 2001.

# CALCULATIONS OF SHAPE CHANGE AND FRAGMENTATION PARAMETERS USING VERY PRECISE BOLIDE DATA

D. O. ReVelle<sup>1</sup> and Z. Ceplecha<sup>2</sup>

(1) Los Alamos National Laboratory, P.O. Box 1663, MS J577, Earth and Environmental Sciences  
Division, Atmospheric and Climate Sciences Group, Los Alamos, New Mexico 87545 USA  
Email: dor@vega.lanl.gov

(2) Emeritus: Academy of Sciences, Astronomical Institute  
Observatory 25165 Ondrejov, The Czech Republic

## ABSTRACT

Using the theoretical formalism of ReVelle (2001d), we have analyzed 22 European (EN) and US Prairie Network fireballs (PN) with the most precise trajectory information available for shape change and fragmentation effects. For 14 bolides the shape change parameter,  $\mu$ , was always  $> 0$  and for the other 8 cases there were instances of  $\mu < 0$ , but with large oscillations in its sign with height or time. When the shape change parameter,  $\mu$ , was  $< 0$ , the fragmentation scale height was  $> 0$  and in a few instances was briefly even smaller than the pressure scale height. This is the necessary condition in addition to the sufficient condition of  $\mu < 0$  for the onset of the catastrophic fragmentation process ("pancake" break-up). A histogram of all computed  $\mu$  values indicates that an average value was  $\langle \mu \rangle \approx 0.10$ , indicating that substantial shape change has taken place during entry for these bolides. This is fully consistent with the recent analyses of ReVelle and Ceplecha (2001g) of the changes in the shape-density coefficient,  $K$ , with time as well. Thus, the use of the  $\mu = 2/3$  (self-similar solution with no shape change) is not recommended for bolide modeling efforts. From our results we can conclude that most of the US DoD bolides can be successfully modeled using single-body theory without resorting to the "pancake" catastrophic fragmentation model that was "rediscovered" in the early 1990's by a number of workers. These researchers included Hills and Goda, Chyba, Thomas and Zahnle, etc. who specifically developed this break-up model for studying the impact into Jupiter of the huge Shoemaker Levy-9 comet.

## 1. INTRODUCTION AND OVERVIEW:

### 1.1 Previous modern fragmentation modeling

Various break-up schemes have been devised in order to correct the conventional single-body model for the effects of fragmentation processes. These include modifications of the drag and heat transfer areas in a systematic manner as described in ReVelle (2001d) for both homogeneous and porous meteoroids.

Several possible break-up mechanisms have been previously proposed including thermal break-up due to heating effects, but this is very inefficient, especially for the typical chondritic materials with very low thermal conductivity. On the other hand, mechanical break-up effects due to pressure loading which are triggered by stagnation pressure exceeding the uni-axial tensile or compressive strength of the body seem very plausible. The observed premature, early break-up at very low stagnation pressures are presumably due to additional weaknesses in the body from cracks due to prior space collisions.

### 1.2 Analyses of bolide behavior in the atmosphere

In our analysis we have used what are now standard bolide analysis techniques (Ceplecha et al., 1998) for determining the altitude behavior of various meteoroid flight parameters, including the velocity,  $V$  and its derivatives, the ablation parameter,  $\sigma$ , the shape-density coefficient,  $K$  and the shape change parameter,  $\mu$ , etc. The reference model atmosphere used is the monthly mean value as a function of height and month for the CIRA 1977 standard atmosphere. These fireballs have also previously been analyzed for their possible gross-fragmentation behavior as well.

## 2. MODELING OF BOLIDE FRAGMENTATION PROCESSES: LIMITING BEHAVIOR

In this paper we will only analyze the fragmentation possibilities in two distinct limits, namely:

- i) Single-body model limit
- ii) Catastrophic "pancake" type fragmentation limit

The definitions of these regimes are as follows:

### 2.1 Single-body model limit:

$$\text{Criterion: } |H_f| \gg H_p$$

where

$H_f$  = Fragmentation scale height

$$H_f = -f(z)/\partial f/\partial z; f \equiv A(z)/A_\infty$$

$H_p$  = Pressure scale height

$H_p = -p(z)/\partial p/\partial z = RT/g$  (if the atmosphere is in exact hydrostatic balance)

$H_p \sim 6-8$  km from  $0 \leq z \leq 120$  km for the "real" atmosphere

### 2.2 Catastrophic "pancake" fragmentation:

$$\text{Criterion: } H_f \ll H_p$$

Physically,  $H_f$  is the downward vertical distance scale by which the bolide frontal cross-sectional area increases by  $1/e$ . This parameter can be determined directly from the approach originally due to Levin and developed in Bronshten (1983). This is readily evident from the definition of the  $\mu$  parameter when it is  $< 0$ . The definition of  $\mu$  is:

$$\mu = d(\ln(K))/d(\ln(m)) \equiv \Delta(\ln(K))/\Delta(\ln(m))$$

where

$K$  = Shape-density coefficient

$m$  = instantaneous dynamic mass

If stagnation pressure loading on the frontal cross-section is the fundamental mechanism for break-up,

Otherwise, for  $\mu > 0$ , only quasi-continuous fragmentation processes can occur under these assumptions.

We have not yet evaluated the effects of  $< 0$  on the light emitted during the bolide-atmosphere interaction process. Such details will appear in a forthcoming paper.

## 3. ANALYSIS OF 22 VERY PRECISE PN AND EN BOLIDES (assuming a uniform bulk density model)

Following ReVelle and Cepplecha (2001g), we have analyzed 22 of the best-observed PN and EN bolides with very precise trajectory data in order to evaluate the fragmentation possibilities. A list of the bolides analyzed are as follows (PN designates US Prairie network fireballs and O designates Ondrejov observatory fireballs which is a part of the European fireball network (EN):

- i) PN38737, PN38768
- ii) PN38827 (\*), PN39122
- iii) PN39154, PN39197 (\*)
- iv) PN39424B, PN39476
- v) PN39499, PN39509C (\*)
- vi) PN39608, PN39820B (\*)
- vii) PN39828, PN39938B (\*)
- viii) PN40379A, PN41280,
- ix) PN41432, PN41593 (\*),
- x) PN41827
- xi) O24421, O27471 (\*)
- xii) O32202 (\*)

(\*) Bolides with very significant negative  $\mu$  and positive  $H_f$ .

### 3.1 Cases with $\mu > 0$

From our analyses of these data, we have found that 14 bolides have  $\mu$  entirely positive. Also, there are no systematic  $\mu$  values  $> 0$  as a function of height smaller than 0.10. The equation used to evaluate the fragmentation scale height,  $H_f$  evaluated from individual values of  $\mu(z)$ ,  $\sigma(z)$  and of  $V(z)$  and of  $dV(z)/dt$ :

$$H_f(z) = \sin\theta / \{\mu(z) \cdot \sigma(z) \cdot dV(z)/dt\}$$

where

$$\sin\theta = \cos(Z_R)$$

$Z_R$  = Zenith angle of the radiant

In our analysis  $\theta$  was assumed to be constant which is an excellent approximation over most of the trajectory. The following variables were explicitly determined along the trajectory:

- i)  $V(z)$  and  $dV(z)/dt$
- ii)  $\sigma(z)$

The  $\mu$  parameter was computed from a finite difference height derivative indicated earlier generally over a few km height interval along the trajectory (smaller height differences were attempted, but they did yield reliable results). We can readily conclude from our work that  $\mu$  is definitely not a constant with either height or time as assumed in the original theory of Levin.

A histogram of  $\mu$  versus the total number of bolides in our sample indicates that the  $\langle \mu \rangle \cong 0.10$  (see Table 1. below). Since the classical value for self-similar behavior with no shape change is  $2/3$ , (Bronshten, 1983) we are left with the very reasonable conclusion that most bolides also experience significant shape change due to ablation during their entry into the atmosphere.

**Table 1: Histogram of Results**

$\mu$	Number of cases (*)
< -2.0	4
-1.0 to -2.0	2
-0.67 to -1.0	2
-0.33 to -0.67	1
0 to -0.33	7
0 to 0.33	23
0.33 to 0.67	10
0.67 to 1.0	7
1.0 to 2.0	6
> 2.0	9

(\*) 71 values of  $\mu$  with standard deviations exceeding the value by > 3 times for 22 bolides

Thus, the mean value for all cases is about 0.10. This indicates that a large amount of shape change is taking place during entry for these bolides.

In Table 2. below we have indicated a representative summary of the altitude profile of the cases for  $\mu > 0$ . In this table we have also indicated each of the starting and ending height intervals ( $h_1$  and  $h_2$ ) for the evaluations of  $\mu$  as well as the individual  $\mu$  values and their

computed standard deviations inside each of these intervals. Although there is one case with  $\mu$  slightly > 0, if we consider the computed formal standard deviation of  $\mu$ , this value is clearly not significant.

### 3.2 Cases with $\mu < 0$

From our analyses of these data, we have found that 8 cases with  $\mu < 0$ , i.e., with "pancake" type catastrophic fragmentation. In our analysis, we have found that if  $\mu$  is negative, the position(s) where this occurs along the trajectory can generally occur either quite early during entry or quite close to the terminal point.

The latter behavior is consistent with the concept that fragmentation being triggered by stagnation pressure loading, but what is happening very early during entry is still quite puzzling. Also,  $\mu$  is clearly not constant along the trajectory in regions where it is negative. Although systematic values of  $\mu$  that have been identified can exceed -10 (PN41593), most calculated negative  $\mu$  values are much smaller. Very rarely are  $|\mu|$  values larger than 2 to 4 and most  $\langle |\mu| \rangle$  are < 0.35. Also, we have found that  $\mu$  values can alternate between positive and negative for an individual bolide case. We have also found that there is no clearly observed dependence of  $\mu$  on mass, deceleration, velocity or altitude.

Regarding the fragmentation scale height,  $H_f$ , it was found to be positive in regions where  $\mu < 0$  and varies between the limits of very small values (somewhat less than the pressure scale height,  $H_p$ ) to very large values. For conditions near the terminal point,  $H_f$  is slightly <  $H_p$  for the following bolides:

- i) O32202, PN39509C, PN39820B, PN39938B

and earlier in the trajectory for:

- ii) O27471, PN39938B

In Table 3. below we have indicated a representative summary of the altitude profile of the cases for  $\mu < 0$ . Three of these five cases have  $\mu < 0$  near to the start of the visible trajectory which is not readily understandable unless break-up is occurring due to weaknesses in the bodies (from pre-existing cracks) which lower the effective strength at which stagnation pressure loading can trigger fragmentation.

There is one such case presented with a very large negative  $\mu$  (PN41593). Even allowing for deviations as large as three standard deviations about the mean, this  $\mu$  value is clearly  $< 0$  and very significant. Obviously such cases require much more detailed study. Finally, we have the PN39938B case for which  $\mu < 0$  at two different heights along the trajectory, both of which are statistically significant at the three standard deviation level.

#### 4. SUMMARY AND CONCLUSIONS

Using a newly discovered concept, the Fragmentation scale height,  $H_f(z)$  and the  $\mu$  parameter originally devised by Levin, we have systematically analyzed the flight trajectory data of 22 of the most precise US Prairie Network and European network bolides. For these cases we have found that 14 cases satisfy the standard single-body model that follows the criterion:

$$i) H_f(z) \gg H_p(z)$$

We have also found that 8 cases which have  $\mu < 0$  in some altitude interval such that catastrophic "pancake" break-up behavior is possible over some small height interval if:

$$ii) H_f(z) \ll H_p(z)$$

Assuming that  $\mu$  is  $\neq f(\text{body size})$  and not too negative ( $|\mu| < 3.33$ ), ReVelle (2001d) has concluded that for  $\mu = \text{constant}$ , the start of "pancake" fragmentation occurs for lower density bolides of higher initial speed, at shallower entry angles and having a relatively large ablation coefficient. From the analysis of ReVelle (2001d), we can conclude that larger (smaller) bodies can only break-up if they are exceptionally strong (weak). Still larger negative  $\mu$  values require increases in the frontal cross-section of the body that are not defensible in this authors' opinion unless the process of the tearing of the body laterally is intrinsically unstable. This in fact seems to be demonstrated both by the observed extreme variations of  $\mu$  with height and with its rapid change in sign across relatively small altitude intervals.

From the work of ReVelle (2001d), there appears to be an optimum range of masses for which this type of fragmentation can occur (if  $\mu = \text{constant}$ ). Recall however that all of the catastrophic fragmentation "pancake" models

were originally developed for the study of very very large bodies (hundreds of meters to kilometers across). This is a puzzle however given the work of ReVelle (2001d) and its conclusions regarding the relative sizes needed for this process to be viable (again for  $\mu = \text{constant}$ ). The range of applicability of the original pancake models is thought to be extremely limited for the small bodies of the size typically observed by ground-based camera networks (J. G. Hills, personal communication, 2001). Clearly this difference of the relevant body size for this process needs to be more fully understood. We still conclude that many bolides (including the frequently observed US DoD bolides) can be safely treated using the single-body theory with  $\mu > 0$ . "Pancake" type break-up is generally not expected.

Direct observations of 22 of the most precise bolides does not show much support for a catastrophic type break-up for bodies up to  $\sim 1$  m across. Only 8 of 22 bolides exhibited any significantly negative  $\mu$  values.

#### 5. REFERENCES:

- Bronshten, V. A., Physics of Meteoric Phenomena, D. Reidel Publishing Co., Dordrecht, 356 pp., 1983.
- Ceplecha, Z., J. Borovicka, W.G. Elford, D.O. ReVelle, R.L. Hawkes, V. Porubcan and M. Simek, Meteor Phenomena and Bodies, Space Science Reviews, **84**, 327-471, 1998.
- ReVelle, D.O., Bolide Fragmentation Processes: Single-body Modeling versus the Catastrophic Fragmentation Limit, Conference Proceedings, Meteoroids2001, August 6-10, 2001, Kiruna, Sweden, 2001d.
- ReVelle, D.O. and Z. Ceplecha, Bolide Physical Theory with Application to PN and EN Fireballs, Conference Proceedings, Meteoroids2001, Kiruna, Sweden, August 6-10, 2001, 2001g.

**Table 2. Representative summary of individual bolide data: With  $\mu > 0$ .**

Number	$h_1$	$h_2$	$\mu$	Std. dev. of $\mu$
O24421	72.7	62.5	1.0	$\pm 0.40$
O24421	62.5	59.0	-0.06	$\pm 0.03$
O24421	59.0	55.3	0.32	$\pm 0.03$
O24421	55.3	50.7	0.42	$\pm 0.08$
PN39154	67.0	58.0	4.0	$\pm 1.4$
PN39154	58.0	46.6	1.1	$\pm 0.30$
PN39154	46.6	41.2	0.0	$\pm 0.10$
PN39499	65.7	41.0	0.76	$\pm 0.07$
PN39499	41.0	38.6	0.19	$\pm 0.04$
PN39499	38.6	37.0	0.37	$\pm 0.02$
PN39608	67.4	57.8	2.0	$\pm 0.20$
PN39608	57.8	54.3	0.0	$\pm 0.04$
PN39608	54.3	50.3	0.34	$\pm 0.03$
PN39608	50.3	48.3	1.0	$\pm 0.20$

**Table 3. Representative summary of individual bolide data: With  $\mu < 0$ .**

Number	$h_1$	$h_2$	$\mu$	Std. dev. of $\mu$
O27471	60.7	56.9	-3.9	$\pm 0.30$
O27471	56.9	54.1	2.0	$\pm 0.70$
O27471	54.1	52.1	-1.4	$\pm 0.20$
O27471	52.1	41.6	-0.02	$\pm 0.01$
O32202	76.4	68.0	-0.03	$\pm 0.02$
O32202	68.0	66.0	1.1	$\pm 0.10$
O32202	66.0	64.9	-0.80	$\pm 0.20$
PN38827	78.3	56.8	4.8	$\pm 0.50$
PN38827	56.8	52.0	-0.68	$\pm 0.23$
PN38827	52.0	48.0	0.11	$\pm 0.05$
PN38827	48.0	45.3	0.71	$\pm 0.20$
PN39938	60.6	55.2	8.1	$\pm 0.70$ (*)
PN39938	55.2	50.0	0.7	$\pm 0.70$
PN39938	50.0	43.9	-0.38	$\pm 0.09$
PN39938	43.9	42.3	2.7	$\pm 0.30$
PN39938	42.3	40.6	-3.1	$\pm 0.70$
PN41593	62.8	58.3	-12.0	$\pm 2.0$
PN41593	58.3	34.9	0.36	$\pm 0.01$
PN41593	34.9	33.3	0.05	$\pm 0.01$

(\*) All entries for this case are for PN39938B.

# ON THE VERY HIGH VELOCITY METEORS

A. Hajduk

Astronomical Institute Slovak Academy of Sciences, 842 28 Bratislava, Slovakia

## ABSTRACT

The reexamination of radar methods used in the AMOR meteor project for the determination of meteor velocities leads to the conclusion that the sets of highly hyperbolic velocities in the range 100-500 km s<sup>-1</sup>, based on the time-lag method and its combinations, cannot be accepted, until the approval of this dataset by means of suggested tests of meteor astronomy is not made. Therefore, also the conclusions based on these highly hyperbolic orbits, derived from AMOR system needs some revision.

Key words: meteor, radar echo, velocity, AMOR, hyperbolic meteors, interstellar meteors.

## 1. INTRODUCTION

A number of papers occurred in the last decade proposing the identification or even evidence of huge interstellar meteor populations, based mainly on the measured meteor velocities. Especially the results from AMOR (radar) system (see Baggaley et al. 1993 a, b and 1998, Taylor et al. 1994 and 1996) presents meteor velocities up to 500 km s<sup>-1</sup>. The number distribution of 1508 meteors with geocentric velocities higher than 100 km s<sup>-1</sup> (Fig. 2 in Baggaley 1993 a) shows tens of cases with velocities over 300 km s<sup>-1</sup> and hundreds over 200 km s<sup>-1</sup>. These shocking results (apart from their consequences on the interstellar populations) have been silently accepted by the scientific community or even supported (Hughes 1996) or used as confirmation of results from space probes (Baguhl et al. 1996 and others) without any comments or questions concerning the velocity measurements. This can be partly explained by the fairly complicated way in which these high velocity meteors were deduced from the original data. Moreover, the particular steps in obtaining the final distribution of meteors with 100 km s<sup>-1</sup> < v < 500 km s<sup>-1</sup> are spread in more papers on AMOR data, and finally the observational data (of at least 1508 cases) are still unpublished.

This short paper would like to fill-up, at least partly, this shortcoming and to break that silence.

## 2. ON THE SENSITIVITY OF RADAR METHODS OF THE VELOCITY DETERMINATION

It was shown by many authors, that in general, the proportion of hyperbolic meteors in the examined samples decreases considerably with the quality of data (see e. g. Štohl 1971) where radar data usually belong to the much less precise in comparison with the photographic ones. However the data from AMOR system are well beyond the photographic limits, concerning incomparably fainter meteors and the authors of AMOR papers have chosen 1508 cases well beyond the reasonable measurement error (3  $\sigma$ ). What could be then wrong?

Three methods are mentioned as applied to the AMOR velocity data. The method of Fresnel zones, the time-lag method and the Verniani's ionization relation.

The first of them, the Fresnel method, generally applied in radar velocity determinations, was used only for small velocities ( $v_g < 50$  km s<sup>-1</sup>) and hence not applied directly to the sample of 1508 high velocity meteors.

The time-lag method was described in paper by Baggaley et al. 1993a in Fig. 1 of that paper. It shows an example of the echo, lasting about 0.7 s (more than 250 radar pulses), and demonstrates the procedure of the time-lag determination (in that case of about 15 pulses). This procedure applied to the same echo from all three receiver sites, together with other echo data recorded, give then observational basis for the velocity components of the meteor. Naturally, the authors recognized that the same procedure as in this particular case cannot be applied to meteors, creating time-lags lasting 1 or few radar pulses, which is by the AMOR system puls repetition frequency prf = 379 s<sup>-1</sup> according to paper Taylor et al. (1994, p. 136) the case of high altitude and high velocity meteors. The AMOR group uses therefore a statistical approach for the improvement of high velocities of highly hyperbolic meteors or HHMs, as called by the authors. They have made a comparison of results of both, Fresnel and time-lag determination, for the sample of meteors, for which both methods were ap-

plied, and comparing the error distribution of two methods they conclude that the discrepancy is between the limits of  $\pm 20 \text{ km s}^{-1}$  (Taylor et al. 1994 Fig. 4). For the velocities over, say  $200 \text{ km s}^{-1}$ , it would represent a wonderful precision. However:

1. this result was obtained for velocities  $v < 50 \text{ km s}^{-1}$ ;
2. Fresnel velocities in HHM meteors represent only about 1% of cases of the sample of 9 777 HHM meteors analyzed;
3. Here is no check of individual velocity pairs of the common 115 HHM meteors;
4. finally the only example shown in the paper (Taylor et al. 1994, Fig.3) show tremendous difference in determined Fresnel velocity  $v_{\text{Fresnel}} = 18.3 \text{ km s}^{-1}$  and the three station time-lag velocity  $v_{\text{timelag}} = 246 \text{ km s}^{-1}$  for the same meteor.

The authors recognize this contradiction; in spite of this they believe in time-lag horrible velocities, arguing with a statistical comparison of the atmospheric height distribution (the maximum of which is 7 km higher for HHMs), then with the inclination distribution (Baggaley et al. 1998 a) (giving much broader distribution for HHMs towards the retrograde orbits), - what should be the case anywhere, or further, with the  $3\sigma$  test, which cannot, of course exclude meteor velocities of hundreds of  $\text{km s}^{-1}$  (Taylor et al. 1996). In this case the authors refer to their own test result applied to the Eta Aquarid shower meteors with  $v_{\text{geoc}} = 65 \text{ km s}^{-1}$ , for which they derived  $1\sigma$  error =  $6 \text{ km s}^{-1}$  and, hence  $3\sigma < 20 \text{ km s}^{-1}$ . Well, but how to believe principally to a method by which "about one half of more than 500 Aquarid meteors (it is meteors belonging to well known Halley comet showers) observed with AMOR have  $e > 1$  and we might expect extreme values up to  $e \approx 1.5$ " (Taylor et al. 1994).

The Vermiani ionization relation has been mentioned in the Nature article (Taylor et al. 1996) as giving support to the derived sample of 1 508 meteors with measured speeds  $v > 100 \text{ km s}^{-1}$ . Vermiani's empirical relation  $q = 0.0509 \text{ m}^{0.92} v^{3.91}$  (where  $q$  is the electron line density of the ionized trail in  $\text{m}^{-1}$ ,  $m$  - mass of a meteoroid body in grams and  $v$  - the velocity of a meteor in  $\text{m s}^{-1}$ ) was here demonstrated as a dependence from which velocity of a meteor may be obtained by measuring the line density (with some assumption on the limiting sensitivity of radar and the beam function) and assuming the mass of a meteoroid and using constants and exponents derived by Verniani (1973) for a quite different set of data and using entirely different equipment. My opinion is that better could be not to mention such support, even when it was not shown, how it had to be applied.

### 3. COMMENT TO THE ATMOSPHERIC HEIGHTS OF HIGHLY HYPERBOLIC METEORS (HHM)

The atmospheric heights of HHM have been deduced from the relation  $h = 92.5 + 18.6 \log_{10} (v_{\text{atm}}/30)$ , which was obtained for meteors with velocities between  $20 - 70 \text{ km s}^{-1}$  and heights between  $90 - 99 \text{ km}$  (Taylor et al. 1994). This equation was then extrapolated for heights obtained from time-lag method for HHMs, yielding 7 km higher maximum for the atmospheric height distribution of HHMs (for the mean velocity  $v_{\text{HHM}} = 140 \text{ km s}^{-1}$ ). But such a height distribution (7 km higher) derived by using HHM velocities, has been used as an argument in Nature paper (Taylor et al. 1996) supporting the reality of HHM extremely high velocities, stating that "the mean speed for this data  $v \approx 164 \text{ km s}^{-1}$  with an uncertainty of  $\pm 30 \text{ km s}^{-1}$ , is in agreement with a crude estimate of  $v = 140 \text{ km s}^{-1}$  derived solely from their mean ionization height<sup>(7)</sup>" where reference (7) is back to paper Taylor et al. (1994).

### 4. COMMENTS TO THE INCLINATION DISTRIBUTION OF HHMS AND OTHER ORBITAL ELEMENTS

Until the orbital data and the observational data, from which they were deduced will not be published, or given to the Meteor Data Center, there is no possibility for the independent confirmation of the results suggested by the AMOR team. As it can be seen from sections 2 and 3 of this paper, the crucial point - the velocity determination of HHM in AMOR data is more than problematic. The inclination determination, after applying a series of corrections, partly with probability functions (Baggaley et al. 1993 b, Baggaley 1998) and without the possibility to check the individual HHM cases, does not give high confidence to the derived main results concerning the interstellar sources of HHM meteors. Moreover, the lack of simple comparison of the effectivity of such sources in their diurnal variation (e.g. for the same set of 1 508 meteors), or in the periodicity of their occurrence in consecutive years, or during the major shower periods (as applied by Hajduková (1993 and 1994) on the photographic meteor data), leads to the conclusion that some approval of the AMOR results is badly needed.

I would like to stress that other parts of AMOR results with their enormous contribution to meteor science (except very high velocities and their applications) were outside the scope of this paper and remain untouched.

### ACKNOWLEDGEMENTS

This work was supported by VEGA the Slovak Grant Agency for Science (grant No 7151).

## REFERENCES

- Baggaley, W.J., Taylor, A.D., Steel, D.I., 1993a, The influx of meteoroids with hyperbolic heliocentric orbits. In: *Meteoroids and their Parent Bodies*, eds. J. Štohl and I.P. Williams, Astron. Inst. Slovak Acad. Sci., Bratislava, 53-56
- Baggaley, W.J., Taylor, A.D., Steel, D.I., 1993 b, The southern hemisphere meteor orbit radar facility. AMOR. In *Meteoroids and their Parent Bodies*, eds. J. Štohl and I.P. Williams, Astron. Inst. Slovak Acad. Sci., Bratislava, 245-248
- Baggaley, W.J., 1998, The interstellar particle component measured by AMOR. In: *Meteoroids 1998*, eds. W.J. Baggaley and V. Porubčan, Astron. Inst. Slovak Acad. Sci., Bratislava 1999, 265-273
- Baguhl, M., Grün, E., Landgraf, M., 1996, In situ measurements of interstellar dust with the Ulysses and Galileo space probes. *Space Sci. Rev.* 78, 165-172
- Hajduková, M., 1993, On the hyperbolic and interstellar meteor orbits. In: *Meteoroids and their Parent Bodies*, eds. J. Štohl and I.P. Williams, Astron. Inst. Slovak Acad. Sci., Bratislava, 61-64
- Hajduková, M., 1994, On the frequency of interstellar meteoroids. *Astro. Astrophys.* 288, 330-334
- Hughes, D.W., 1996, Dust from beyond the Solar System. *Nature* 380, 283
- Štohl, J., 1971, On the problem of hyperbolic meteors. *Bull. Astron. Inst. Czechosl.* 21, 10-27
- Taylor, A.D., Baggaley, W.J., Bennet, R.G.T., Steel, D.I., 1994, Radar measurements of very high velocity meteors. *Planet Space Sci.* 42, 135-140
- Taylor, A.D., Baggaley, W.J., Steel, D.I., 1996, Discovery of interstellar dust entering the Earth's atmosphere. *Nature* 380, 323-325
- Verniani, F., 1973, *J. Geophys. Res.* 78, 8429-8462

# **Physical Properties of Interplanetary Dust**

# IS THE PROBLEM OF SPORADIC METEOROID SPACE DISTRIBUTION SOLVING CORRECT?

O.I. Belkovich

Branch of Kazan State University in Zelenodolsk, Saidashego st., 4, Zelenodolsk, Tatarstan, Russia, Email: oleg@green.kcn.ru

## ABSTRACT

Flux density over the celestial sphere and meteoroid orbital element distributions are discussed. Corrected for selections of observations methods distributions has been compared. Sporadic meteoroid velocity distributions do not depend on minimum registered mass of meteoroids in mass interval  $1-10^{-4}$  g and depend only on radiant elongation from the Earth's apex. Now there are not reliable sporadic distributions of flux densities over the celestial sphere or distributions of orbital elements confirmed by comparison of results obtained even two different method of observations

## 1. INTRODUCTION

Up to now we have got a lot of sporadic meteoroid data observed by photographic, radar and TV methods. Every method has its own mass range of observed meteoroids and its selectivity. Interpretations of observed data are rather complicated and many selectivity factors have to be taking into account. So, there can be some uncertainty: whether we obtained results are different due to the wrong processing of observations or the difference is real and corresponds to the different mass range of observed meteoroids. One problem is the form of results presentation.

## 2. PRESENTATION OF RESULTS

As a physicist I can say that the best form presentation particle distributions is the phase density, i.e. density of particles in the 6-dimensional space of co-ordinates and velocities  $NP(r, V)$  as a function of their masses. What corresponds now in the meteor astronomy to this definition? T.Kaiser [1] the first has introduced the term "the flux density of sporadic meteor bodies" as a number of meteor particles with masses greater then some value, crossing in the unit of time the unit of area normal to the velocity vector and coming from the unit of solid angle of the celestial sphere. Comparing this definition with the definition of the phase density one can find what missed: "in the unit of the velocity range" Now the sporadic meteoroid flux density in the point of space shown by the vector  $r$  can be presented as:

$$Q(r, \lambda, \delta, V) = Q(r) \cdot P_r(\lambda, \delta) \cdot P_{r, \lambda, \delta}(V), \quad (1)$$

where  $\lambda, \delta$  are the meteor radiant co-ordinates at the celestial sphere,  $V$  is the meteoroid velocity,  $Q(r)$  is the meteoroid flux density from the whole celestial sphere in the point  $r$ ,  $P_r(\lambda, \delta)$  is the meteor radiant distribution over the celestial sphere and  $P_{r, \lambda, \delta}(V)$  is the meteoroid velocity distribution in the point of the space  $r$  and the radiant co-ordinates  $\lambda, \delta$ . Now the relation between the phase density and meteoroid flux density can be derived by the simple transition from the Decart frame of references to the spherical one:

$$NP(r, V) = Q(r, \lambda, \delta, V) \cdot V^3. \quad (2)$$

It is known from the Leuwill's theorem that the phase density of the particles is constant along their trajectories, so, if the points  $r_1$  and  $r_2$  belong to the same trajectory then

$$Q(r_2, \lambda_2, \delta_2, V_2) = (V_2/V_1)^3 Q(r_1, \lambda_1, \delta_1, V_1). \quad (3)$$

It is the formula of transformation of the sporadic meteor flux density not only along the particle trajectory, but from one frame of references to another.

Another one way of the presentation of meteoroid distribution in the space corresponding to the phase density could be a distribution of the 6 meteoroid orbital elements. But for the point of  $r$  there are 3 elements: major semi-axes  $a$ , eccentricity  $e$  and inclination of orbit  $i$ .

## 3. ASTRONOMICAL SELECTION

The selection of meteor observations is caused by the fact that ground based observations are made on the moving and attracting Earth what introduced a distortion in the observed meteoroid flux. E.Opik [2] has shown that the probability  $P$  of a meteoroid encounter with the Earth depends on  $a, e, i$  as

$$P = \frac{R^2 V_\infty^2}{\pi V_g \sin i} [2 - a^{-1} - a(1 - e^2)]^{\frac{1}{2}} \quad (4)$$

Or, after some evaluations

$$P = \frac{\tau^2 V_g}{V_h \cos \alpha \sin i}, \quad (5)$$

where  $\alpha$  is the angle between the vectors from the Sun to the Earth and the heliocentric meteoroid velocity  $V_h$ ,  $V_g$  is the geocentric velocity and  $\tau = \sigma_\alpha / \sigma_E$  is the ratio of the Earth's cross section out of gravitation field to the Earth's cross section. F. Whipple [3] has used the Opik's formula  $1/P$  as «the cosmic weight» for the correction of the photographic orbit distributions due to astronomical selection. Nevertheless there are some questions:

- 1) Opik has considered the whole Earth but in observations we have a collecting area much less than the Earth's cross section, have we to correct it?
- 2) what are the meanings of the special points  $\alpha = \pi/2$ ,  $i = 0$  and  $i = \pi$ ?
- 3) what area of the space correspond the corrected orbit distribution to?

To answer these questions I have solved the problem of correction of observed orbital element distributions to the bulk of meteoroids crossing the sphere with the center in the Sun and with the radius of 1 a.u. [4]. The next formula was obtained:

$$P = \frac{\tau^2 V_g}{a^{3/2} V_h \cos \alpha \sin i}, \quad (6)$$

and in this case  $\tau = d\sigma_\alpha / d\sigma_g$  - ratio of the collected area out of gravitation field of the Earth to one in the Earth's atmosphere.  $\tau \approx V_g / V_\infty$  for  $V_\infty \geq 20 \text{ km s}^{-1}$ . The second difference this formula with Opik's one is the factor  $a^{3/2}$  actually proportional to  $T$  - the period of a meteoroid evolution around the orbit. One can understand now the meanings of the special points:  $\alpha = \pi/2$  - the orbit is tangent to the sphere,  $i = 0$  and  $i = \pi$  - the area  $S$  of meteor radiants at the celestial sphere in the interval of nodes of observation

$\Omega_1 - \Omega_2$  for given  $i$  is equal to zero ( $S = 2(\Omega_1 - \Omega_2) \sin i$ ).

The derivations of the formula have been made in the assumption that the distribution of perihelion arguments  $\omega$  of sporadic meteoroid orbits with given values of  $a$ ,  $e$ ,  $i$  is uniform. The assumption has been confirmed when the symmetry of radiant relative the plane normal to the ecliptic one and crossing the Earth's apex and antapex was found [5]. There was found also that velocity distributions of sporadic meteoroids depend on one angle  $\varepsilon$  on the celestial sphere only. This angle is the meteoroid radiant elongation off the Earth's apex. That fact is the reason to choose another one polar frame of references on the celestial sphere for meteor studies with the pole in the Earth's apex, the polar angle  $\varepsilon$  and the other angle  $\psi$ ,  $0 \leq \varepsilon \leq \pi$ ,  $0 \leq \psi \leq 2\pi$ ,  $\psi = 0$  in the ecliptic plane in the direction to outside of the Earth's orbit.

So, now for ground based observations of sporadic meteoroids we have the two three-dimensional forms of presentation:

- 1) meteoroid flux in the vicinity of the point of observations  $r$  in form of

$$Q(r, \varepsilon, \psi, V) = Q(r) \cdot P_r(\varepsilon, \psi) \cdot P_{r,v}(V), \quad (7)$$

- 2) Distribution of the three orbital elements of meteoroids intersecting the sphere of the radius 1 a.u. with the Sun in the center:

$$P(\Omega, a, e, i) = P(\Omega) \cdot P_\Omega(a, e, i). \quad (8)$$

The last two formulae can be transformed one in another.

Everybody knows that results of observations are reliable only in a case they have confirmed by another method of observations or by another equipment. But before the comparison data have to be reduced to one minimal mass of meteoroids. Even data obtained by any one equipment belong to the different minimal masses because of physical and equipment selectivity. The formula of a flux reduction from  $Q_1$  to  $Q_2$  with corresponding minimal masses  $m_1$  and  $m_2$  is  $Q_2/Q_1 = (m_1/m_2)S-1$ , where  $S$  is the mass distribution index. If  $\sigma(s)$  and  $\sigma(Q_2/Q_1)$  are the r.m.s. values of  $S$  and  $Q_2/Q_1$  correspondingly and taking into account the mean value of  $S \approx 2$  so

$$\sigma(Q_2/Q_1) = 0.7 (m_1/m_2) \cdot \sigma(s), \quad (9)$$

and for example  $\alpha(s) = 0.1$  and  $(m_1/m_2) = 100$  then  $\sigma(Q/Q_1) = 7$ . Now you can see what the accuracy we have to know the S value. We do not analyze the selection functions here but we have to point out only that they are the functions of the meteoroid velocity, radiant coordinates and equipment parameters. One way to check the accuracy of data reduction methods is the comparison of results of meteor shower observations made by a radar and optical equipment: in this case meteoroid velocity is fixed.

#### 4. METEOROID VELOCITIES

In Fig 1 sporadic meteoroid velocity distributions in some intervals of elongation angles  $\varepsilon$  are shown. The distributions obtained from observations by 5 different radars [6] and corrected for selectivity. There are no significant differences in the results though sensitivities, wavelength and other parameters of equipments were rather different.

The comparison corrected velocity distributions from radar observations in Obninsk and from TV observations in Canada (Fig.2) shows also the coincidence of the result the both radar and optical observations. Now we came to two next conclusions:

- 1) coincidence of meteoroid velocity distributions obtained by different methods of observation confirms the accuracy our method of observation reduction;
- 1) meteoroid velocity distributions does not depend on the minimal observed mass of meteoroids.

#### 5. RADIANT DISTRIBUTIONS

Sporadic meteoroid radiant distributions over the celestial hemisphere by radar observations can be obtained by two methods: the first one is an equipment measuring of individual meteor orbits, the second method is tomographic one [7]. The first method can be realized directly in the observational process. It is impossible to obtain that kind of distributions from meteoroid orbit catalogues because the last ones do not contain the whole information to correct them for equipment selectivity. The defect of the method is the fact that 30 - 40 per cent meteors only have all measured parameters to calculate orbits.

Tomographic method used measurements two parameters only - the two arrivals angles and therefore it has a minimal selectivity. It is impossible practically to obtain sporadic radiant distributions from optical observations because of the lack of data.

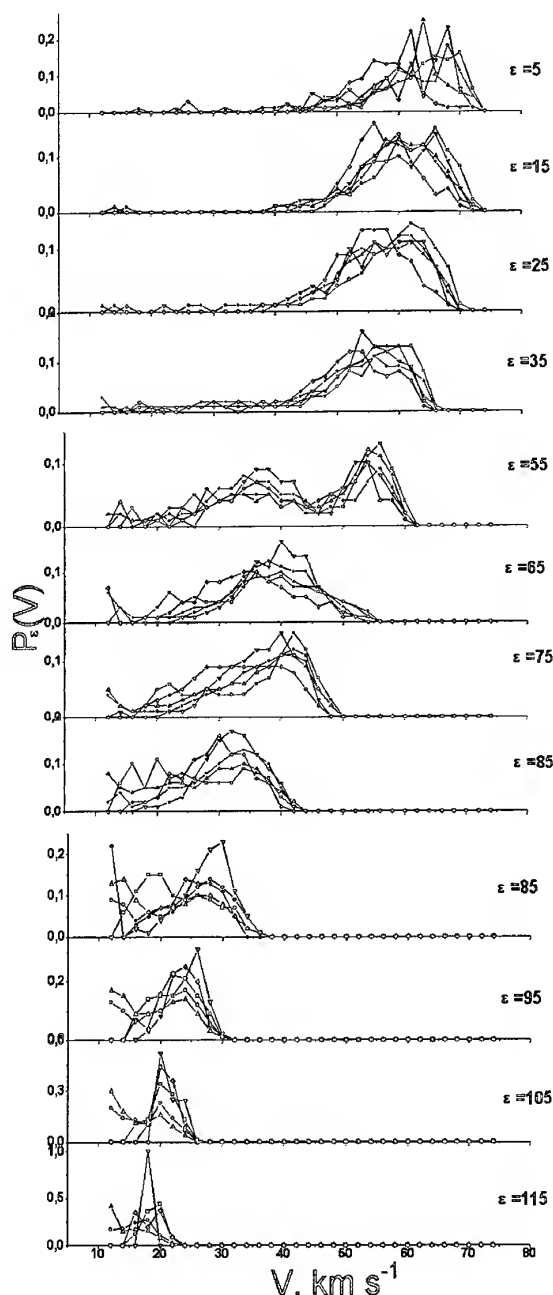


Fig. 1. Reduced velocity distributions of sporadic meteoroids from radar observations

We have tried to avoid the difficulty and to consider one-dimension distribution  $P(\varepsilon)$  but there are some additional factors that complicate the problem. The main of them is the condition that observations are to carry out even not simultaneously but in the same time interval of a day or a season to avoid temporal differences in distributions.

Distributions corrected for the selectivity factors do not coincide each other in contrast to velocity distributions. So it can be supposed that they depend on the minimal observed mass of meteoroids i.e. the mass index  $S$  has no uniform distribution over the celestial sphere. One has to have got the mass index  $S$  as a function of celestial coordinates to reduce radiant distribution to one minimal mass.

The attempt was made to find the distribution by different methods from radar and optical observations. It was found  $S$  variation as a function of the angle  $\varepsilon$  [5]. Application of the function to reductions of data to coincidences of radiant distributions obtained by radar and TV methods, but there are the difference with photographic data (Fig 3). May be reduction for selection of photographic method was not complete.

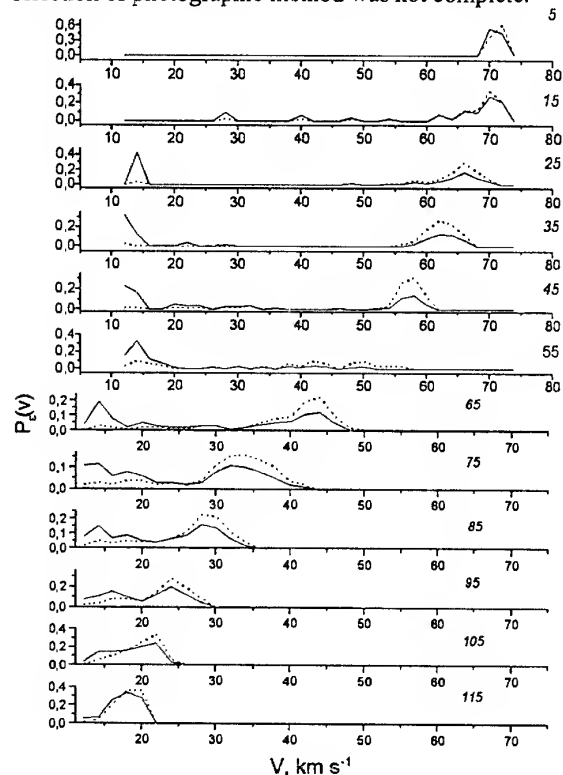


Fig. 2. Reduced velocity distributions of sporadic meteoroids from radar and TV observations

## 6. ORBITAL DISTRIBUTIONS

Analyses of sporadic meteoroid orbital elements distributions encounter with the same problems as flux density distributions. V. Lebedinets [8] has found out that distributions of orbits observed by small cameras, by Super-Schmidt ones and by radars with middle and high sensitivities reduced for selectivities are coincide. On that basis he came to the conclusion that the orbit

distribution does not change in the meteoroid mass range  $1 - 10^{-5}$  g.

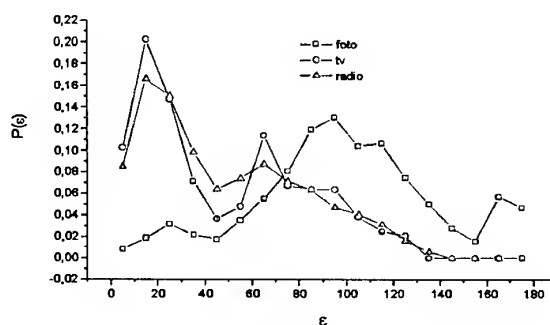


Fig. 3. Sporadic meteoroid flux density distribution as a function of elongation  $\varepsilon$  from photographic, TV and radar observations.

We have derived the distribution  $P(a, e, i)$  from  $Q(\varepsilon, \psi, V)$  taking into account the astronomical selection. It was found the reduction of meteoroid orbital perihelia near the Mercury orbit. (Fig. 4)

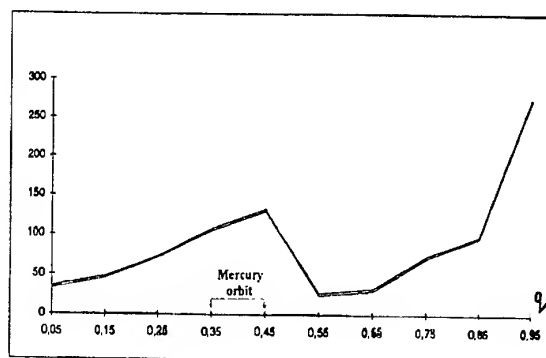


Fig. 4. Distribution of Sporadic Meteoroid Perihelions

Also meteoroid bulk densities over the sphere with the radius 1 a.u. and the Solar in the center were found. They are shown in Fig. 5 in the polar co-ordinates.

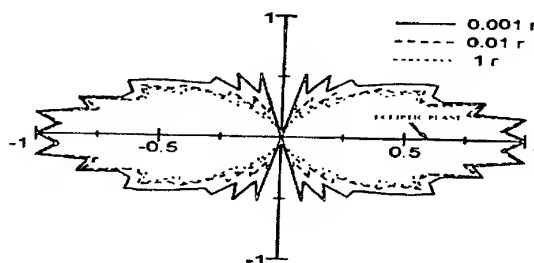


Fig. 5. Meteoroid bulk densities radius 1 a.u.

## 7. CONCLUSION

- 1) Comparison results of observations can be made only by comparison of flux densities or orbital distributions corrected for selections of observation methods and for astronomical selection.
- 2) Sporadic meteoroid velocity distributions do not depend on minimum registered mass of meteoroids in mass interval  $1-10^{-4}$  g and depend only on radiant elongation from the Earth's apex..
- 3) Comparison of flux density distributions over the celestial sphere orbital distributions is possible if observations are carried out simultaneously or in the same time interval of a day or a season to avoid temporal differences of distributions.
- 4) Now there are not reliable sporadic distributions of flux densities over the celestial sphere or distributions of orbital elements confirmed by comparison of results obtained even two different method of observations.

## 8. REFERENCES

1. Kaiser T.R., *The Interpretation of Radio Echoes from Meteor Trails*, Spec. Suppl. J. Atm. Terr. Phys., Vol. 2, 119 – 130, 1955.
2. Opik E., *Collision Probabilities with the Planet and the Distribution of Interplanetary Matter*, Proc. Roy. Irish. Acad, No. 12, 165 – 169, 1951.
3. Whipple F., *Photographic Meteor Orbits and their Distribution in Space*, Astron. J. Vol. 59, No. 6. .201 – 217, 1954.
4. Belkovich O.I., *Astronomical Selection and ...*, Solar System Res, Vol. 17, No. 2, 1983.
5. Andreev V.V., et al, *Some Peculiarities of Mass, Velocity and Radiant Distributions of Sporadic Meteoroids*, Planet. Space Sci., Vol. 42, No. 9, 785 – 790, 1994.
6. Lindblad B.A., *Documentation Of Meteor Data Available at the IAU Meteor Data Center*, 1992.
7. Belkovich O.I. et al, *Structure of Sporadic Meteor Radiant Distributions from Radar Observations*, Earth, Moon and Planets, Vol. 68, 207 – 215, 1995.
8. Lebedinets V.N., *Aerosol in the Upper Atmosphere and interplanetary Dust*, Hidrometizdat, Leningrad, 1981

# PROBING THE STRUCTURE OF THE INTERPLANETARY DUST CLOUD USING THE AMOR METEOROID ORBIT RADAR

D. P. Galligan and W. J. Baggaley

Dept. of Physics and Astronomy, University of Canterbury, Christchurch, New Zealand

## ABSTRACT

The Advanced Meteor Orbit Radar (AMOR) routinely determines the heliocentric orbits of Earth-impacting dust particles. Radar meteoroid orbital distributions have a number of inherent biases. This paper details a work in progress whose aim is to determine and correct these biases on the data set of  $\sim 5 \times 10^5$  meteoroid orbits provided by AMOR between 1995–1999. Interim orbital distributions corrected for some of the identified biases are presented. These illustrate the importance of careful correction of the data set.

Key words: Radar Meteors; Zodiacal Light; Interplanetary Dust.

## 1. INTRODUCTION

Knowledge of the solar system dust population is important. From it we can detect traces of the passages of past comets and asteroids; we can gain understandings of the dynamical evolution of different sized particles under the influences which affect them; this knowledge is also important for the planning of long term space missions to develop an understanding of the environment in which they must survive.

There are a range of methods which are used for the detection of interplanetary dust. In-situ methods using detectors mounted on spacecraft provide information on dust  $< 1\mu\text{m}$  in size (Grün et al. 1995a,b). Study of the zodiacal light intensity allows one to estimate the spatial density of dust (Staubach & Grün 1995). The long-term exposure of surfaces in space and the study of lunar craters can also contribute to our knowledge of the spatial density and meteoroid size distributions at 1 AU (McDonnell 1991; Man-ville 1976).

The other major detection method involves the use of the Earth's atmosphere as a very large area detector. Here, the ablation of Earth-impacting dust produces an ionisation train in the upper atmosphere

at heights of between 70 and 120 km. Particularly bright visible trains allow the detection by optical techniques which yield accurate orbits upon reduction.

Radar detection of ionisation trains is possible due to the density of electrons therein. Much larger numbers of meteors are detected by radar due to the fainter magnitude to which they are sensitive, however the quality of the individual orbital parameter measurements is lower. Radar methods, as with the other methods, of meteoroid orbital distribution determination have inherent biases. This paper reports on progress in the correction of the data set provided by the AMOR facility for these biases. The main biasing factors under consideration are detailed and interim results of the distributions produced by accounting for some of these identified biases are discussed.

## 2. THE AMOR FACILITY

The AMOR facility, located near Christchurch in New Zealand, has been in operation since 1990 (Baggaley et al. 1994; Baggaley 1995; Baggaley & Bennett 1996; Baggaley et al. 2001). It routinely catalogues the population of incoming meteoroid dust with  $\sim 10^6$  high quality orbits currently secured. AMOR comprises three receiver stations, in conjunction with a dual-spacing interferometer and a narrow azimuthal beam shape ( $\sim 2^\circ$  FWHM), allowing the determination of a meteoroid's velocity.

The data set obtained between 1995 and 1999 was particularly homogeneous; this was also the period of greatest sensitivity for the radar with a limiting size of  $40\mu\text{m}$  (mass  $\sim 3 \times 10^{-10}$  kg) being achieved. In the 1995–1999 data set currently under consideration the azimuthal beam was orientated along the North-South meridian; an upgrade has now added an identical East-West array in order to increase sky coverage. Baggaley et al. (2001) provides further information on the current AMOR system configuration.

### 3. BIAS EFFECTS

A radar meteoroid orbit data set is strongly affected by a number of biasing effects. The observed orbital distributions differ dramatically from those which have undergone correction for these biases.

The data set provided by the Harvard radar system was the first to be systematically corrected for detection biases (Southworth & Sekanina 1973). It has since been found by Taylor & Elford (1998) that several important corrections were ignored in the original Harvard work in addition to a numeric error made in the entry of the mass distribution index which had a large effect on the end result.

The response of a radar system to meteors appearing from a particular radiant point in the sky was determined by Elford (1964). This "radar response function", taking into account the geometry and the antenna beam gain patterns of the system, provides a measure of the number of meteors expected for any given radiant in the alt-azimuth reference frame relative to an isotropic distribution of meteors over all radiants. A mass distribution assumption is required to calculate the radar response. The number of meteoroids ( $N$ ) with masses greater than a limiting mass ( $m_0$ ) is given by

$$N(m > m_0) \propto m_0^{-\alpha}, \quad (1)$$

where  $\alpha$  is the cumulative mass distribution index.

Based upon laboratory experiments on the expected constituent elements of a meteoroid, Bronshten (1983) finds that

$$q \propto mV^{3.42}, \quad (2)$$

where  $q$  is the electron line density,  $m$  the meteoroid's mass and  $V$  the speed.

By weighting each meteor by  $V^{-3.42\alpha}$  we can correct for the "ionisation efficiency" and hence obtain, similarly to the mass distribution in Equation 1, the zenithal electron density ( $q_z = q_{\max}/\cos \chi$ ) cumulative distribution given by

$$N(q > q_z) \propto q_{z0}^{-\alpha}. \quad (3)$$

A cumulative mass distribution index of  $\alpha = 1.0$ , is often used for the meteor population detectable by radar. This value was experimentally verified for the Harvard system, a facility which was almost as sensitive as AMOR (Elford 1964). This mass distribution is consistent with a predominantly collisional formation process for the current meteoroid complex sampled by AMOR. Grun et al. (1985) shows that AMOR's mass sensitivity places many of the meteoroids detected within a cross over region from collisional to Poynting-Robertson dominance in the formation process. Dikarev (2001) notes that a mixture of meteoroids whose orbital evolution has been dominated by these two different modes of formation may

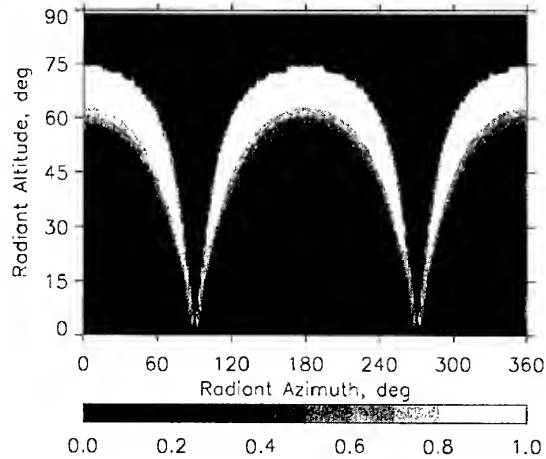


Figure 1. The relative response of the central AMOR receiver site to meteors at 97 km.

therefore be present. This scenario is currently under investigation; however for the purposes of this paper, a collisional formation process with  $\alpha = 1.0$  will be assumed from here on.

By inserting the appropriate gain functions for AMOR, making allowances for the three station detection requirement for orbit determination, and by accounting for other intrinsic features of the system, the radar response function is derived. The function for a single station detection at AMOR's central site (see system layout in Baggaley et al. 2001), for meteors having an average height of 97 km and detected on the North-South transmitting beam, is shown in Figure 1.

While the response function provides a measure of the probability of detecting a meteor at a particular position in the sky, we must also take into account the probability of detecting meteors from a given geocentric radiant position over time (declination response). Currently the change in the region of the response function at which a radiant of a given declination sits during a daily revolution of the Earth is accounted for by summing the alt-azimuth response for a given radiant over that day. The effects of radar down-time or daytime interference surrounding the detection of a particular meteor are accounted for by removing corresponding response values from the cumulative daily response. A correction for the annual detectability of a particular orbit, in addition to this diurnal detectability, is also under consideration.

A number of effects were identified by Taylor & Elford (1998) as having been missing from the original Harvard corrections of Southworth & Sekanina (1973) and Sekanina & Southworth (1975). These effects are related to attenuation of the radio signal returned from the meteor train for underdense trains only—note that AMOR orbits used in this study have been selected to only derive from underdense meteors. Ceplecha et al. (1998) provide a summary of the attenuation factors which must be accounted

for. These may be listed as:

- *Initial Radius Factor:* If the initial radius of a meteor train is close to the wavelength,  $\lambda$ , of the radar then destructive interference will reduce the received signal level. Cepplecha et al. (1998) note a relationship between the initial radius and the atmospheric density and the meteoroid speed:

$$r_0 \propto \rho^{-0.25} V^{0.6}. \quad (4)$$

Other exponents in this expression are possible from other studies. For example, Baggaley (1980) determines  $r_0 \propto \rho^{-0.42 \pm 0.07} V^{1.0 \pm 0.3}$  while Baggaley (1981) finds  $r_0 \propto \rho^{0.26}$ .

The attenuation factor due to initial radius is

$$A = \exp\left(\frac{-4\pi^2 r_0^2}{\lambda^2}\right). \quad (5)$$

- *Train Diffusion:* Reflection coefficients of earlier parts of the meteoroid train diminish by diffusion while the later part is still forming. Peregrin (1958) determines this attenuation factor as

$$A = \frac{1 - \exp(-\Delta)}{\Delta}, \quad (6)$$

where

$$\Delta = \frac{2k^2 D \sqrt{2R\lambda}}{V}. \quad (7)$$

Here  $D$  is the diffusion coefficient,  $R$  is the range to the train, and  $V$  the in-atmosphere speed.

- *PRF Factor:* A meteoroid train must exist for several radar pulses in order to be determined as a meteor detection as opposed to some form of sporadic noise. For a radar system with a pulse repetition frequency ( $p$ ) and a level in the atmosphere with a diffusion coefficient ( $D$ ), Cepplecha et al. (1998) quote an attenuation due to this effect of

$$A = \frac{1 - \exp(-w)}{w \exp(n-1)}, \quad (8)$$

where

$$w = \frac{4k^2 D}{p}. \quad (9)$$

- *Faraday Rotation:* At AMOR's frequency of 26 MHz the phase difference between the ordinary and extraordinary wave components in the daytime ionosphere produces Faraday rotation. Cepplecha et al. (1998) summarize this effect with an approximate attenuation expression given by

$$A = \cos(2\Omega), \quad (10)$$

where

$$\Omega = 2.36 \times 10^4 f^{-2} \int_{path} B \cos \chi N(s) ds. \quad (11)$$

Here  $f$  is the radio frequency,  $B$  the geomagnetic field,  $\chi$  the angle between the wave propagation direction and  $\mathbf{B}$ , and  $N$  the electron density.

By using attenuation factors in conjunction with the expected electron line density profiles for meteors with a particular speed and zenith angle, the radar response function is modified to predict the attenuated response (Taylor & Elford 1998).

Once all in-atmosphere effects have been accounted for, the probability of the collision of a meteoroid on a particular orbit with the Earth must be determined. Öpik (1951) developed a formulation for this problem. Assuming a circular orbit for the Earth this can be written

$$P \sim \frac{1}{\sin i} \sqrt{\frac{3 - a^{-1} - 2\sqrt{a(1-e^2)} \cos i}{2 - a^{-1} - a(1-e^2)}}. \quad (12)$$

The effect of a speed dependent flux enhancement due to time spent in the gravitational field of the Earth must also be considered. The increase in flux expected due to this effect (e.g. Divine 1993) is proportional to

$$\left(\frac{V_A}{V_G}\right)^2. \quad (13)$$

#### 4. ORBITAL DISTRIBUTIONS

As mentioned previously, not all of the known bias factors have yet been included in the correction of the AMOR data set. The orbital distributions resulting from correction for radar response function, declination response, ionisation efficiency, collision probability with the Earth and gravitational flux enhancement are presented here. Atmospheric attenuation effects are currently being added to the correction process and are thus not represented here. An assumption of a cumulative mass distribution index,  $\alpha = 1.0$ , is made in all of the corrections below.

Other preparations of the data set include the removal of the (minor) meteoroid shower component as identified in Galligan (2000) and the removal of overdense persistent meteors. The showers are removed as we are interested in the background dust distribution and strong coherent sources will affect this objective. The overdense meteors are removed due to the lack of attenuation experienced by these trains—such meteors may be included in the future, but as a separate population whose correction bypasses the attenuation corrections and with a different mass distribution assumption.

Figure 2 shows the change in the inclination distribution from its original form to that with the biases removed. The directly observed distribution shows a large density of dust close to the ecliptic plane ( $i \lesssim 20^\circ$ ). The amount of dust very close to the ecliptic ( $i \lesssim 10^\circ$ ) is substantially reduced upon correction which is to be expected as the orbit on the Earth upon the ecliptic will substantially increase the dust distribution perceived to orbit close to that plane—this is the reason for the  $(\sin i)^{-1}$  dependence in Equation 12. Other features of note in Figure 2

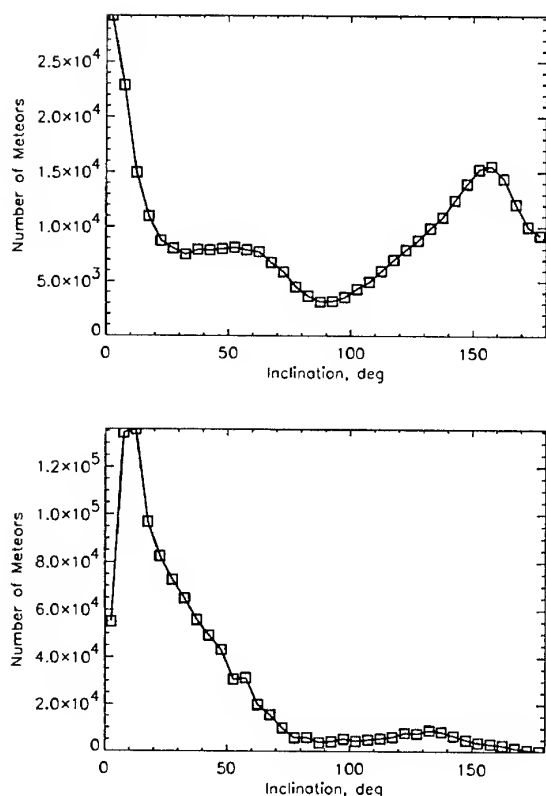


Figure 2. The directly observed inclination distribution (above) and that obtained after correction for the bias conditions presently accounted for (below). The corrected distribution is normalised to contain  $10^6$  meteoroids.

are the almost equal numbers of prograde and retrograde meteoroid orbits observed changing to a population dominated by prograde orbits upon correction. There is undoubtedly a significant population of retrograde orbiting particles as evidenced by the observed graph however this population is very much overstated due to the increased probability of detection of these high speed meteors as clearly stated by the ionisation efficiency factor (Equation 2). The correction process leaves us with an almost linear decrease in the number of meteors with inclinations from  $20^\circ$  to  $90^\circ$ . If we change our assumption of a higher cumulative mass distribution index (e.g.  $\alpha = 1.3$ ) then we find a much smaller number of retrograde meteoroids and also a lower number of higher inclination prograde meteoroids relative to those at lower inclinations. Conversely a decrease in this index (e.g.  $\alpha = 0.7$ ) raises both of these populations relative to lower inclinations. It is important, therefore, to determine as carefully as possible the most appropriate mass distribution index.

The perihelion distance ( $q$ ) and eccentricity ( $e$ ) distributions are also important to consider. These are partitioned according to orbital direction, prograde and retrograde, in the following diagrams as there are vast differences between these two populations—

the latter are essentially a distribution formed by the bias conditions while the former contain some astronomically real underlying structure which we hope to observe.

Study of the  $q$ -distribution, shown in Figure 3, reveals a strong peak at  $\sim 1$  AU for both prograde and retrograde partitions. This peak is due to the increased probability of detection of meteoroids at their perihelion points when they are on steeply inclined orbits. The radial component in the meteoroid's velocity at its intersection with the Earth is zero at its perihelion or aphelion points thus increasing the chance of detection. While the retrograde  $q$ -distribution is flat aside from this peak, the prograde distribution exhibits a much larger and broader peak at low to mid  $q$ . In fact if one ignores the region below  $q \simeq 0.2$  AU then a linear fall off in the number of meteors up to the  $q \simeq 1$  AU peak is evident. The unpartitioned corrected distribution follows this same trend with a general decrease from about 0.2 AU onwards. The  $q \simeq 1$  AU peak has been completely removed in this corrected figure showing it to be an artifact solely introduced by the inherent biases.

The eccentricity distribution is shown in Figure 4. The uncorrected prograde and retrograde eccentricity partitions show strong differences. The prograde partition is characterised by mostly high eccentricity ( $e \gtrsim 0.7$ ) meteoroids while the retrograde partition has meteoroids spread relatively uniformly down to low eccentricity values. The corrected distribution is similar to the directly observed prograde partition, however low- to mid- ( $e \lesssim 0.5$ ) and near parabolic-eccentricities ( $e \gtrsim 0.9$ ) have been substantially removed. The removal of the latter is due to the increased detection probability driven by the high meteoroid speeds while the removal of the former is due to the increased probability of detecting a meteoroid as its eccentricity approaches circular. If one studies an extended graph which includes hyperbolic meteoroids one finds a very swift cut off in the eccentricity distribution for  $e$  only just above 1 (the start of this decline can be seen in the uncorrected curves for  $e \gtrsim 0.95$ ). Many of these slightly hyperbolic meteoroid orbits will have been mistakenly assigned due to their high uncertainties and therefore they really belong strictly below the parabolic limit—this measurement uncertainty issue explains well this sharp decrease after the parabolic limit.

## 5. CONCLUSIONS

The presence of a number of inherent biases present in a radar detected meteoroid data set have been discussed. The effect of correction for some of these factors on  $\sim 10^5$  meteoroid orbits determined by the AMOR facility has been shown to be very significant. Due to the number of corrections identified, very careful inspection of the weighting formulations used for this work must be made.

Work is currently under way to include the atmo-

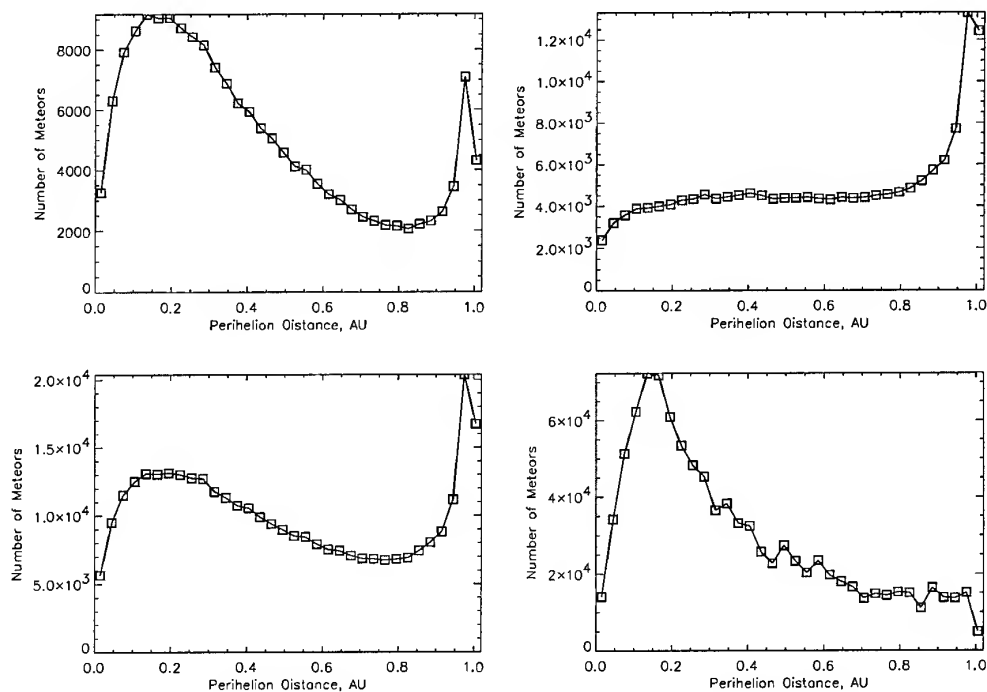


Figure 3. Directly observed prograde (left,top), retrograde (right,top) and combined (left,bottom) perihelion distributions are presented. Correction for the (currently accounted for) bias conditions yields the graph on the bottom right. The latter is normalised to contain  $10^6$  meteoroids.

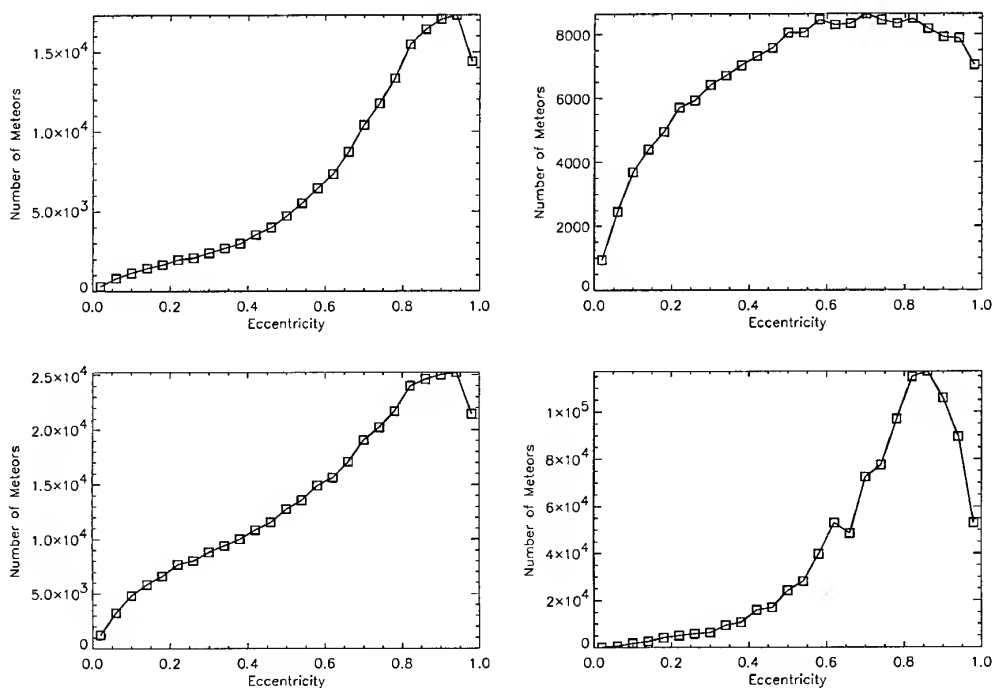


Figure 4. Directly observed prograde (left,top), retrograde (right,top) and combined (left,bottom) eccentricity distributions are presented. Correction for the (currently accounted for) bias conditions yields the graph on the bottom right. The latter is normalised to contain  $10^6$  meteoroids.

spheric attenuation effects in this continuing study. These effects tend to reduce the number of higher speed meteoroids as these ablate in the upper meteor region. Therefore the corrections are expected to raise the number of higher inclination prograde and all retrograde meteoroid orbits in the data set due to the higher speeds of meteoroids on such orbits.

A correction for the annual detectability of a particular orbit is also under consideration.

### ACKNOWLEDGMENTS

This routine monitoring is being undertaken as part of the ESOC "Upgrade of Meteoroid Model to Predict Impacts on Spacecraft" contract: ESOC RFQ/3-9528/99/D/CS and under contract: UOC911 to the Marsden Fund of New Zealand. Financial support from these sources is gratefully acknowledged. Valuable discussions particularly with Valeri Dikarev, Steven Marsh and Bob Bennett, are gratefully acknowledged.

### REFERENCES

- Baggaley W.J., 1980, *Bull. Astron. Inst. Czechosl.*, 31, 308
- Baggaley W.J., 1981, *Bull. Astron. Inst. Czechosl.*, 32, 345
- Baggaley W.J., 1995, *Earth, Moon and Planets*, 68, 127
- Baggaley W.J., Bennett R.G.T., 1996, In: *Physics, Chemistry and Dynamics of Interplanetary Dust*, vol. 104, 65–70
- Baggaley W.J., Bennett R.G.T., Steel D.I., Taylor A.D., 1994, *QJRAS*, 35, 293
- Baggaley W.J., Marsh S.H., Bennett R.G.T., Galligan D.P., 2001, In: Warmbein B. (ed.) *Meteoroids 2001*
- Bronshten V.A., 1983, *Physics of Meteoroid Phenomena*, D. Reidel Publishing Company, Dordrecht, Holland
- Cepkecha Z.K., Borovička J.I., Elford W.G., et al., Apr. 1998, *Space Science Reviews*, 84, 327
- Dikarev V., 2001, personal communication
- Divine N., Sep. 1993, *JGR*, 98, 17029
- Elford W.G., 1964, Calculation of the response function of the Harvard Radio Meteor Project radar system, no. 8 in *Harvard Radio Meteor Project Research Report*, Smithsonian Astrophysical Observatory
- Galligan D.P., 2000, In: *Proceedings of the IAU/COSPAR Colloquium 181 on Dust in the Solar System and Other Planetary Systems*, Canterbury, UK, submitted
- Grün E., Zook H.A., Fechtig H., Giese R.H., May 1985, *Icarus*, 62, 244
- Grün E., Baguhl M., Divine N., et al., 1995a, *Planet. Space Sci.*, 43, 971
- Grün E., Baguhl M., Divine N., et al., 1995b, *Planet. Space Sci.*, 43, 953
- Mandeville J.C., 1976, In: *Proc. Lunar Sci. Conf.* (7th), 1031–1038
- McDonnell J.A.M., 1991, In: *Lunar and Planetary Science Conference*, vol. 22, 185–193
- Öpik E.J., 1951, In: *Proc. Roy. Irish Acad. Sect. A*, vol. 54, 165–199
- Peregudov F.I., Dec. 1958, *Soviet Astronomy*, 2, 833
- Sekanina Z., Southworth R.B., 1975, *Physical and dynamical studies of meteors*, NASA CR-2615, Smithsonian Institution, Cambridge, MA, USA
- Southworth R.B., Sekanina Z., 1973, *Physical and dynamical studies of meteors*, NASA CR-2316, Smithsonian Institution, Cambridge, MA, USA
- Staubach P., Grün E., 1995, *Advances in Space Research*, 16, 103
- Taylor A.D., Elford W.G., 1998, *Earth Planets Space*, 50, 569

## MODELLING OF THE SPORADIC METEORID SOURCES (ESA SP-495)

J. Jones, M. Campbell, S. Nikolova

*University of Western Ontario, London, Ontario, CANADA, N6A 3K7, Email: jimeteor@uwo.ca*

### ABSTRACT

We have modelled the sporadic meteoroid distribution assuming (i) long and short-period comets to be the sole sources of particles and (ii) the Poynting-Robertson effect to be the only depletion mechanism. We find the steady-state distribution of the orbits of meteoroids released from these sources and calculated the radiant and velocity distributions of these particles as they would be observed by an Earth-based meteor radar. The method predicts the Helion/Antihelion and the Apex sources and also provides an explanation for the North and South Toroidal sources. Agreement of the theoretical predictions and the observations obtained from the Harvard Radio Meteor Project is excellent.

### 1. BACKGROUND

Meteoroids can be conveniently divided into two classes: stream and sporadic. Stream meteoroids travel in highly collimated orbits that result in greatly enhanced localized particle fluxes that may be also time-dependent. When the Earth passes through such a stream, a meteor shower or even a storm is observed. Sporadic meteors on the other hand can be thought of as a diffuse background of meteoroid activity. In this report we will be concerned with modelling the sporadic meteoroid complex. The reason for this is simple – sporadic meteoroids constitute the greater impact hazard to space vehicles. Although the mean sporadic meteoroid activity is low compared with that of stream meteoroids at the peak of a shower, it is present continuously throughout the year and as a result the integrated number of sporadic meteoroids far outweighs that of shower meteoroids. The mean rate of shower meteors is probably an order of magnitude less than that of sporadics.

Although the detailed calculation of the orbits of meteor stream particles is an extremely time-consuming task, for sporadic meteoroids we can start, at least initially, by making a number of simplifying assumptions.

If our model is to be considered reliable it must predict distributions of radiants and velocities similar to those

of sporadic meteors observed from the Earth. This paper describes our model of the sporadic meteoroid complex model and compares its predictions with Earth-based radar meteor data.

### 2. OVERALL STRATEGY

In this report we consider long and short-period comets as the sources of sporadic meteoroids. We first calculate steady-state orbital distribution of the meteoroids released from these sources and then convert these orbital distributions to meteoroid fluxes as would be measured by a meteor-radar on the Earth.

As a first step we take the cometary orbits to be distributed symmetrically about the ecliptic pole so that the important orbital parameters  $a$ ,  $e$  and  $i$  – the semi-major axis, the eccentricity and the inclination are the important parameters. The ascending nodes and the arguments of perihelion are taken to be uniformly distributed so that the orbital distributions are azimuthally symmetric. This azimuthal symmetry property can be relaxed in subsequent studies.

Although we acknowledge that comets come in a range of sizes, for simplicity we take all our model comets to be of equal size so that the rate at which the cometary material is sublimated by solar radiation depends only on the orbital elements.

Because this model is essentially based on simulation, we need to consider a large number of simulated meteoroids to ensure that random variations arising from the stochastic nature of the simulation are kept to acceptable level. One possible source of correlations in the orbital elements could arise if we were to consider multiple particles ejected from a given comet. We have avoided these correlations by letting each “comet” eject one “meteoroid”.

In these simulations we have chosen to ignore planetary perturbations since the computational burden for the very long time scales involved would be beyond our capability. But this can be justified to some extent on physical grounds. Over the long term, the mean gravitational perturbing force on meteoroids that do not make a very close encounter with a planet is

azimuthally symmetric since we can regard the planet's mass as being smeared out into a ring. In such cases the meteoroid orbit is changed only slightly, since the planet's mass is small relative to that of the sun and the main perturbation is a precession of perihelion which will not change an initially azimuthally symmetric orbital distribution. We will ignore the effects of both very close encounters and mean motion resonances both of which we anticipate will affect only a relatively small fraction of the meteoroid population.

A given comet will eject many meteoroids in closely similar orbits and these correlations are seen from the Earth as either as meteor showers or storms. From simulations which have included planetary perturbations, we have found that meteor storms become greatly attenuated after a few hundred years indicating that such perturbations tend to get averaged out in the long term. We plan to consider this aspect in greater detail in subsequent studies in which we will estimate the relative time scales of the various processes that are active.

After release from the comet, the meteoroid orbits change with time, the major force being the Poynting - Robertson (PR) effect [1] - a radiation force that acts very much like viscous drag on the meteoroid. As a result of the PR drag, the meteoroid orbits shrink at a rate determined by the dimensions of the orbit. One of our tasks will be to estimate the steady-state orbital distribution of these meteoroids.

The final step in the simulation is to convert the orbital distribution of "meteoroids" to a flux of meteoroids that would be observed from the Earth. This is complicated by the fact that it matters how the meteoroids are observed. In most cases they are not observed directly but rather by their interactions with the atmosphere where they ablate and appear as visual and radio-meteors. In the case of optical observations, one needs to know how efficiently the kinetic energy of the meteoroid is transformed into luminosity while for radio-meteors ionization efficiency is the crucial quantity. Neither of these parameters nor their variation with velocity is well-known so our model will be uncertain to that extent. We have calculated the relative fluxes as would be seen by a meteor radar and have taken the electron line density along the train,  $q$ , to vary with the meteoroid mass  $m$  as

$$q \sim m (v-v_0)^n \quad (1)$$

if  $v > v_0$  else  $q = 0$ . The value of  $n$  is thought to be close to 4 [2] but this is by no means certain. Jones [3] has argued that it might be as low as 2.8. The  $v_0$  term arises because at low speeds, meteoric atoms do not have sufficient kinetic energy to cause ionization and

Jones suggests that for typical metallic meteor atoms,  $v_0$  is close to 10 km/s.

### 3. THE LONG-PERIOD COMET SOURCE

From Marsden's comet catalogue [4], we extracted the long-period comet orbits which are defined as those having periods in excess of 200 years. Their inclination distribution is essentially isotropic and their orbits are generally almost parabolic with eccentricities very close to unity.

In order to generate a set of orbits with a distribution similar to that of long-period comets easily, we seek a set of parameters that are essentially independent of each other in order to avoid artifacts arising from correlations. We found that the perihelion distance,  $q$ , and the reciprocal semi-major axis fulfilled this condition. Because of the almost complete lack of correlation between  $q$  and  $1/a$  we can generate these quantities separately knowing that the choice of one does not affect the other. We generated values of  $q$  and  $1/a$  using the distribution functions

$$p_q \sim 2.045 q e^{-1.43 q} \quad (2)$$

where  $p_q$  is the probability of  $q$  being in the interval  $q$  to  $q + dq$ , and

$$p_b \sim -0.55 + 0.163 b^{-0.891} \quad (3)$$

where  $p_b$  is the probability of  $b$  being in the interval  $b$  to  $b+db$  and where

$$b = 1/a \quad (4)$$

As the result of sublimation due to solar radiation, the meteoroids are released from the cometary ices and are ejected from the comet with fairly low velocities. Initially we considered the orbital changes resulting from this ejection but later calculations showed that the omission of these changes does not alter the final results appreciably. The meteoroids experience planetary perturbations as well as the viscous-like drag due to the PR effect. They also suffer collisions with other interplanetary particles which cause space erosion and which are sometimes catastrophic. We have considered the PR effect to be the dominant force and have ignored all the others. Future studies will investigate how well this is justified

Wyatt and Whipple [1] give the following formulae for the rates of change of  $a$  and  $e$  due to the PR effect:

$$\frac{da}{dt} = -\frac{\alpha (2 + 3e^2)}{a (1 - e^2)^{3/2}} \quad (5)$$

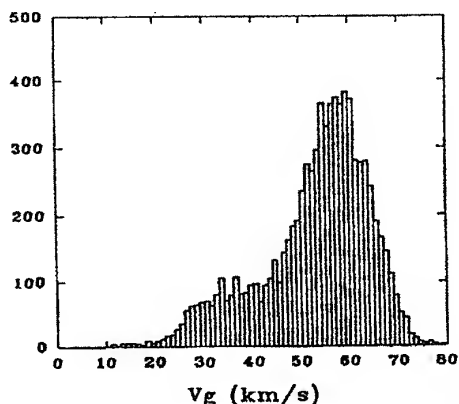


Fig. 3. Speed distribution of radar meteors from the Apex source as determined by Harvard Radio Meteor Project [8].

The obvious close similarity of the predicted and observed speed distributions shown in Figs. 2 and 3 is also very encouraging.

#### 4. THE SHORT-PERIOD COMET SOURCE

In contrast to long-period comets, short-period comet orbits are close to the ecliptic and we have found a Gaussian distribution of accessible inclinations with a RMS width of  $11.8^\circ$  to be a fairly good fit to observations.

For the  $a-e$  distribution we have taken the orbital elements to be uniformly distributed in the region  $a < 2.3/(1-e)$  and  $a > 5.2/(1+e)$ . The first condition ensures that the perihelion of the comet is close enough to the Sun for significant sublimation to occur while the second condition puts the aphelion of the comet orbit beyond that of Jupiter. Together with the small inclination distribution, the two conditions ensure that there is the possibility of a close approach to Jupiter which is important since most short-period comets belong to the Jupiter family. We have tried other distributions but the results seem to be fairly insensitive to the precise details of the source distribution.

Using essentially the same procedure as for the long-period source we have obtained the radiant and speed distributions shown in Figs. 4 – 6.

Again the agreement of the predicted and observed radiant sources is excellent – the predicted sources being within  $2^\circ$  of the observed. The radii of the predicted sources are also very close to the widths of the observed sources [8].

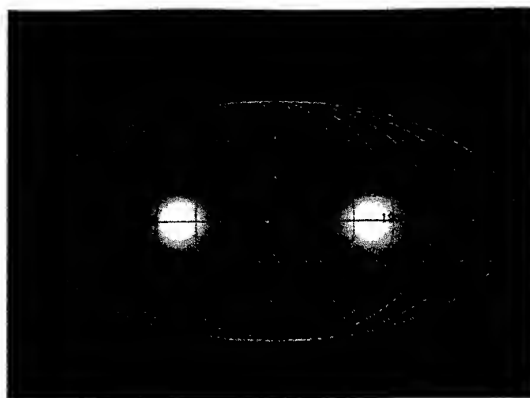


Fig. 4. Predicted radiant distribution of particles released from the short-period comet source as would be observed by meteor radar.

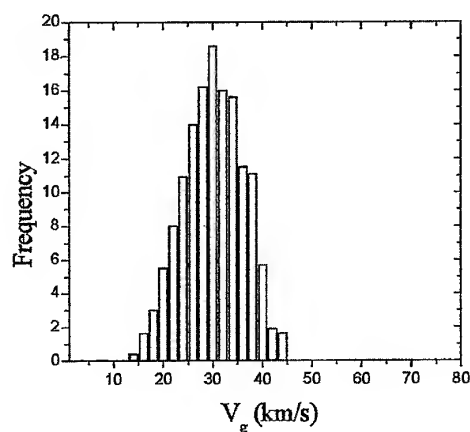


Fig. 5. Predicted speed distribution for particles released from the short-period comet source as observed from an Earth-based meteor radar.

Not only are the predicted positions and sizes of the Helion/Antihelion sources in excellent agreement with observation, the speed distributions also agree very well.

#### 5. THE TOROIDAL SOURCE

Soon after the identification of the Apex and the Helion/Antihelion sources, a concentration of sporadic radiants at high latitudes was found in the Jodrell Bank radar meteor data that was also found in the Harvard Radio Meteor Project observations. This concentration came to be known as the Toroidal Source. A correspond southern source was later found in the Adelaide data [8]. The origin of these sources however remained an even greater mystery than that of their

$$\frac{de}{dt} = -\frac{5\alpha e}{2a^2 (1-e^2)^{1/2}} \quad (6)$$

and also showed that there exists a constant of motion,  $C_{PR}$  for the PR effect:

$$C_{PR} = a e^{-4/5} (1-e^2) \quad (7)$$

The use of Eq. 7 greatly speeds the calculation of the evolution of the orbital elements of a particle moving under the influence of the PR effect.

Using Eqs. 5-7 we can find the steady state distribution of orbital elements of the meteoroids released from the comets. We make the assumption that the rate of release is constant so that at any given time there will be a uniform distribution of residence times from zero to the times required for all the particles to spiral into the Sun. By a process of trial and error we found  $3 \times 10^8$  years to be an adequate upper limit for particles of mass 1 g. Throughout this simulation we took each source to release  $10^5$  particles.

Our next task was to convert our distributions of orbital elements to particle densities and velocities at any point in space. Fortunately the equations for this transformation are available in the literature [5] - [7]:

$$S(R) \sim \frac{R a}{\sqrt{(R-q)(Q-R)}} \quad (8)$$

$$B(\beta) \sim \frac{f(i)}{\sqrt{\sin(i)^2 - \sin(\beta)^2}} \quad (9)$$

$S(R)$  is the density of particles at distance  $R$  from the Sun, and  $Q$  and  $q$  are the aphelion and perihelion distances of the orbit respectively.  $B(\beta)$  is the probability of an observer at ecliptic latitude  $\beta$  detecting a particle moving in a orbit of inclination  $i$  if the differential inclination distribution is  $f(i)$ . For an Earth-based observer  $\beta = 0$ .

The final step in the calculation is to sum the contributions from all the particles taking into account the relative velocities as seen from the Earth-based observer as well as the  $S(R)$  and  $B(\beta)$  weightings and also taking into account the dependency of the ionization efficiency on the geocentric speed as described by Eq. 1. We did not attempt to include the effects of initial radius attenuation or zenithal attraction.

The results of the long-period source calculations are shown in Figs. 1-3.



Fig. 1. Predicted radiant distribution of particles released from long-period comet source as would be observed by meteor radar. The centre of the diagram corresponds to the apex of the Earth's way and the Sun is at (0,0).

The radiant distribution shown in Fig. 1 is in excellent agreement with that of meteors from the Apex source Jones and Brown, [8]. There is however no splitting of the Apex source into North and South components and the suggested splitting probably arises from geographic factors rendering simultaneous observation of the whole region very difficult.

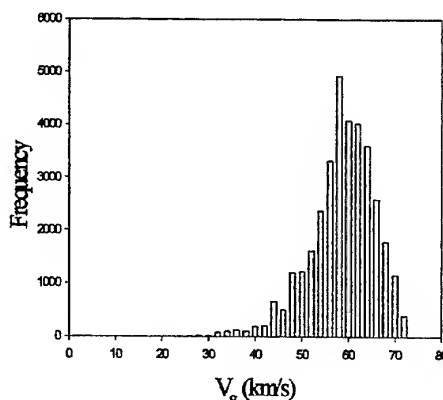


Fig. 2. Predicted speed distribution for particles released from long-period source as observed from an Earth-based meteor radar.

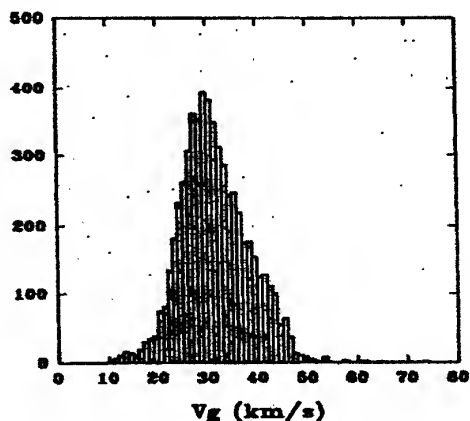


Fig. 5. Speed distribution of radar meteors from the Helion/Antihelion sources as observed by Harvard Radio Meteor Project [8].

equatorial cousins. We, too, were at a loss how to explain it.

It was clear that if the short-period comet orbits had an inclination distribution similar to that of long-period comets, they too would appear to have a radiant distribution close to the Apex of the Earth's way because the velocity dependence of the ionisation efficiency favours those meteors with high relative velocities. We therefore examined the effect of increasing the scatter of the inclinations of the short-period "comets" and found that after we increased the RMS scatter of the accessible inclinations from  $11.8^\circ$  to  $28^\circ$ , a Toroidal-like concentration of radiants did in fact appear as shown in Fig. 6.

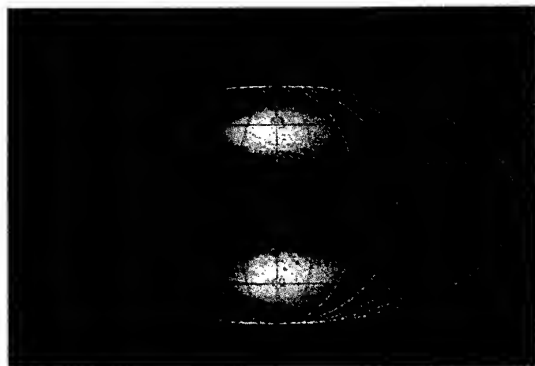


Fig. 6. Predicted radiant distribution of particles released from the short-period comet source with increased scatter in accessible inclinations as would be observed by meteor radar.

On reflection it became clear that this source is the product of the competing factors of increased likelihood of detection as the result of increased relative velocity combined with the decreasing numbers of meteors as the latitude increases.

In Figs. 7 and 8 we present the predicted and observed speed distributions of meteoroids from these Toroidal sources. Again the agreement is excellent both in peak values and widths.

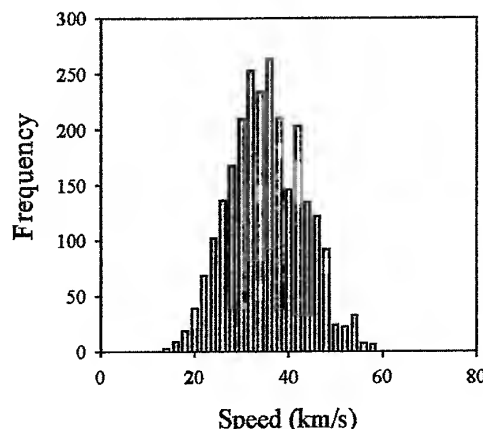


Fig. 7. Predicted speed distribution for particles released from the short-period source with increased scatter in accessible inclinations as observed from an Earth-based meteor radar.

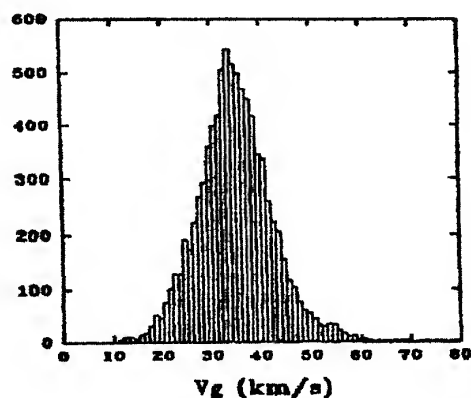


Fig. 8. Speed distribution of radar meteors from the Toroidal sources as observed by Harvard Radio Meteor Project [8].

## 6. CONCLUSIONS

We are amazed that a model built with such few simple assumptions is able to yield predictions which agree so well with observations. The model has neglected

particle depletion due to both collisional erosion and annihilation arising from catastrophic collisions. On the other hand, it is difficult to include such effects since the structure of the meteoric material is unknown and laboratory measurements of the erosional parameters still show a scatter of several orders of magnitude.

We should note that the observations are more representative of average values since they were collected over a period of several years. In fact we know that our assumption that the meteoroid complex is azimuthally symmetric about the ecliptic pole is incorrect because there are marked variations in the sporadic flux throughout the year. In future models this might be included by introducing non-uniform distributions of the ascending nodes and arguments of perihelion. But for the present we lack sufficient information to implement such improvements and are forced to use average values.

The model has also ignored the effects of planetary gravitational perturbations. As mentioned previously if the meteoroid orbits do not make a close approach with Jupiter such perturbations such cause the orbits to precess which would go largely unnoticed if the sporadic meteoroid complex were azimuthally symmetric. If the azimuthal symmetry were not present then such perturbations would make it more so. We might therefore conclude that the marked annual variations in the sporadic meteoroid flux indicate that planetary perturbations have not been large enough to erase them and may be small enough to be neglected.

On the observational side we have ignored the underdense echo ceiling which is known to cause increased attenuation of radar echoes with height. Since classical meteor ablation classical theory and observations indicate that faster meteors ablate at greater heights we expect the fraction of meteors going undetected to increase with speed. In this case the observed speed distributions would be biased towards the low values and we might expect the peak values to be shifted downwards. In fact there is no indication of this – the predicted and observed peaks of the speed distributions are in excellent agreement even for the high speed Apex source. Possibly the answer lies in the fragmentation – if the meteoroids fragment high enough in the atmosphere, the effective width of the train is determined by fragmentation rather than by mean-free-path considerations. This is a puzzle in need of a solution.

Finally we should note once more how well the model that has so few assumptions predicts the observed distributions of sporadic radiants and speeds. This agreement is most encouraging and the possibility of a useful physical model of the sporadic meteoroid

complex is that much closer to reality. We willingly acknowledge that the model needs more work – in particular with regard to inter-particle collisions and planetary perturbations. It would seem however that these will prove to be more second order effects and that the core structure of the sporadic complex in this size range is determined by the action of the PR effect on particles released from the long and short-period comet sources.

## ACKNOWLEDGEMENTS

The authors gratefully acknowledge both NASA and the NSERC of Canada for funding the program of which this project forms a part.

## REFERENCES

1. Wyatt, S.P. and Whipple, F.L. The Poynting-Robertson effect on meteor orbits, *Astrophys. J.* **111**, 134, (1950)
2. Verniani, F. and Hawkins, G.S. On the Ionizing Efficiency of Meteors, *Astrophys. J.* **140**, 1590
3. Jones, W. The Poynting-Robertson effect on Meteor Orbits, *MNRAS*, **288**, 995, (1997)
4. Marsden, B. *A Catalog of Cometary Orbits* Cambridge, Massachusetts: Smithsonian Astrophysical Observatory. (1989)
5. Opik, E.J. Collisional probabilities with the planets and the distribution of interplanetary matter. *Proc. Roy. Irish Acad.* **54**, 165, (1951)
6. Kessler, D.J. Derivation of the Collision Probability between Orbiting Objects: The Lifetimes of Jupiter's Outer Moons. *Icarus*, **48**, 39, (1981)
7. Steel, D.I. and Elford, W.G. Collisions in the Solar System – III. Meteoroid survival times *MNRAS* **218**, 185, (1986)
8. Jones, J. and Brown, P. Sporadic Meteor Radiant Distributions - Orbital Survey Results, *MNRAS* **265**, 530, (1993)

# LIFETIMES OF METEOROIDS IN INTERPLANETARY SPACE: THE EFFECT OF EROSIVE COLLISIONS AND PLANETARY PERTURBATIONS

Simona Nikolova<sup>(1)</sup>, James Jones<sup>(1)</sup>

<sup>(1)</sup> *Department of Physics and Astronomy, University of Western Ontario, London, Ontario, N6A 3K7 Canada, Email: [srnikolo@uwo.ca](mailto:srnikolo@uwo.ca)*

<sup>(1)</sup> *Department of Physics and Astronomy, University of Western Ontario, London, Ontario, N6A 3K7 Canada, Email: [srnikolo@uwo.ca](mailto:srnikolo@uwo.ca)*

## ABSTRACT

A number of factors affect the life times of meteoroids in interplanetary space. These include Poynting-Robertson effect (PR), radiation pressure, electromagnetic forces, collisions and gravitational perturbations. A physical model of the sporadic meteoroid complex was recently developed by Jones, J. and Nikolova, S [1]. It considers short and long period comets as primary sources of meteoritic material and PR effect as a dominant mechanism of orbital change. The model agrees well with observations and it predicts the observed distributions of meteor radiant. However, it ignores the effects of collisions and gravitational perturbations. A further improvement to this model involves the addition of the above as secondary effects.

This paper investigates the life times of meteoroids against erosive collisions and gravitational perturbations in relation to the PR life times.

## 1. THEORY

### 1.1 Collisions: catastrophic and erosive

The effect of erosion of meteoroids in interplanetary space has been of interest for many years. Erosion rates were calculated from measurements of short-lived radioactive elements produced by cosmic ray spallation. The method was introduced by Whipple [2]. Spallation produces stable isotopes, and their total accumulation leads to an estimate of an erosion rate. Whipple quotes erosion rates of a micron per year in radius. However the erosion rates thus obtained are only a crude approximation because they are based on data for iron meteorites. Stones would exhibit different erosion rates than irons because they are more friable and brittle. The erosion rates therefore would greatly depend on the composition of the meteorites and the latter is not well known, and therefore, a different approach to calculation of more accurate erosion rates is needed.

### 1.2 The Gamma Factor ( $\Gamma_0$ )

The conditions that determine whether a collision is catastrophic or erosive are as follows:

A catastrophic collision will occur if the mass of the projectile ( $m_1$ ) is less than or equal to a constant times the mass of the target ( $m_2$ ) as indicated below:

$$m_1 \leq \Gamma_0 m_2 \quad (1)$$

If, on the other hand, the mass of the target is greater than the mass of the projectile by the same factor an erosive collision will occur:

$$m_1 > \Gamma_0 m_2 \quad (2)$$

The gamma factor depends on the composition of the particles and their relative velocity and can be expressed as follows [3]:

$$\Gamma_0 = 9.76 \times 10^2 S_c^{-0.45} \left( \frac{m_1}{\rho_1} \right)^{0.075} v^2 \quad (3)$$

where  $S_c$  is the unconfined compressive strength of the material,  $m_1$  and  $\rho$  are the mass and density of the target and  $v$  is the encounter velocity.

It can be seen from Eq. 3 that this factor is proportional to the square of the relative velocity of the two particles. Dohnanyi quotes a value of  $250v^2$  [4]. In order to obtain an accurate value for meteoroids we need relative velocities of the order or 20 km/s. Experimental techniques in the laboratory however can only reach velocities of 10 km/s (Fig. 1).

Table 1. Experimental Techniques

Accelerating Technique	Operating Velocities (m/s)	References
Single-stage gas gun	~1000	Curtis J.S [5]
Powder gun	~1000	Mizutani et al. Matsui et al. [6],[7]
Two stage light gas gun	3000 - 5000	Seigel [8]
Modified explosive shaped charge	6000 - 10,000	Martelli and Newton [9]

Higher velocities are obtained by extrapolations based on the results from these experiments [10].

An extensive literature search yielded the values shown in the graph below.

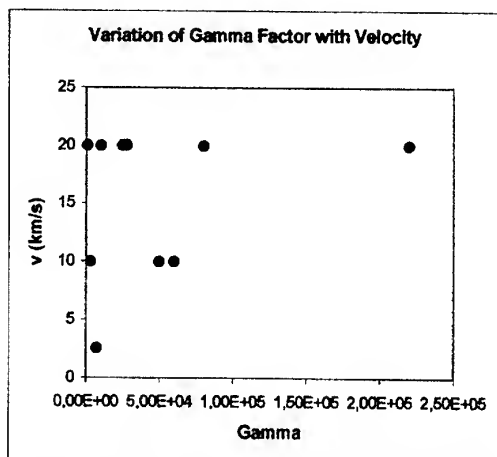


Fig. 1 Variation of Gamma Coefficient with Velocity

It can be seen from Fig. 2 that the gamma values vary over a wide range of about 50 to 200,000. The values are obtained for materials such as glass, mortar cement, granite and basalt, which are not representative of the meteoroidal particles in interplanetary space. The latter are more fluffy and porous. We do not have a good estimate for what  $\Gamma_0$  is for meteoroids. Therefore a range of values will be considered.

### 1.3 Collision Probability Calculations

The collision probability calculations are based on Kessler's approach [11]. The positions of the objects in a unit volume are assumed to be random, and the objects moving in straight line. The model is similar to a model of kinetic theory of gasses. One can calculate flux for one object by

$$F = S \cdot v \quad (4)$$

where  $S$  is the spatial density of the object considered within a unit volume and  $v$  is the velocity of the object.

The collision rate for two moving objects with spatial densities of  $S_1$  and  $S_2$  in a volume  $\Delta U$  can thus be represented by

$$R = S_1 S_2 \sigma V_{rel} \Delta U \quad (5)$$

Where  $V_{rel}$  is their relative velocity and  $\sigma$  is their mutual collision cross-section. The total collision probability is calculated by summing over all the collision rates. The sum is carried over volume elements accessible to both objects:

$$P = \int_{Volume} S_1 S_2 v_{rel} \sigma dU \quad (6)$$

In order to solve Eq. 6 numerically we sum over all volume elements making sure that the spatial densities do not vary significantly within those elements.

#### 1.3.1 Spatial Density

The spatial densities are calculated using 10,000 generated test particles [1]. The spatial density consists of a radial and latitudinal components, which can be considered separately. The equations used in calculating the spatial densities are available in literature [12,13].

$$S(R, \beta) = S(R)S(\beta) \quad (7)$$

$$S(R) \propto [(R - q)(q' - R)]^{-1/2} \quad (8)$$

$$S(\beta) \propto [(\sin^2 \iota - \sin^2 \beta)^{-1/2}] \quad (9)$$

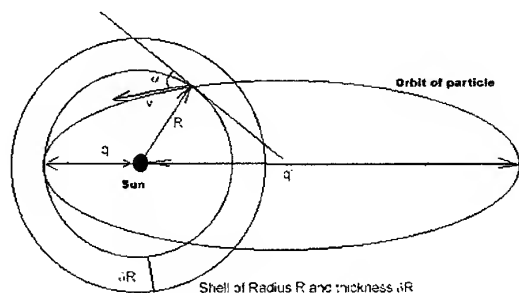


Fig.2. Spatial Density

### 1.3.2 Relative Velocity

The method of calculation of relative velocity is based on Kessler's collisional model and later implemented by Steel and Baggaley [12] and Steel and Elford [13].

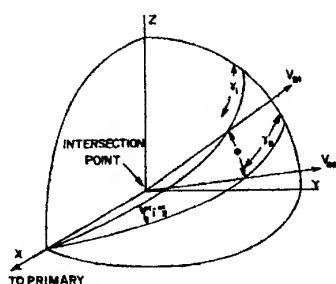


Fig.3. Relative Velocity

In order to calculate the relative velocities of the colliding particles we first calculate the individual velocities. The individual velocities can be found by

$$V = \sqrt{\frac{2}{r} - \frac{1}{a}} \quad (10)$$

The relative velocity is obtained once the individual velocities and the encounter angle  $\phi$  are known.

$$V^2 = V_{B1}^2 + V_{B2}^2 - 2V_{B1}V_{B2}\cos\phi \quad (11)$$

The encounter angle can be calculated from the geometry on Fig. 3 using Eq.12 below:

$$\cos\phi = \pm[\sin\gamma_1\sin\gamma_2] + [\cos\gamma_1\cos\gamma_2\cos(\alpha_1 \pm \alpha_2)] \quad (12)$$

where  $\gamma_1$  and  $\gamma_2$  the angles the velocity vectors of the two particles form with the tangent to the shell. The angles  $\alpha_1$  and  $\alpha_2$  are the calculated from the inclination and latitude of the particles as follows:

$$\cos i = \cos\alpha\cos\beta \quad (13)$$

Since there are four possible values for the intersection angle  $\phi$  there are four possible velocities that should be considered. Since the likelihood of obtaining each is not equal we consider, as a first approximation the average of the four.

### 1.3.3 The Method

The life-times against collision are calculated using Eq. 6, with the integral replaced by a sum and integration carried out over volume element  $dU$  where

$$dU = 2\pi R^2 \cos\beta \Delta R \Delta\beta \quad (14)$$

Integrations are first carried out in the plane of the ecliptic. Collision probabilities are obtained for a range of heliocentric distances. The model is later extended to perform integrations over ecliptic latitude thus covering all possible value for the particle inclinations.

### 1.3.4 Results and Discussion

First we consider the simple approximation of meteoroids in the ecliptic plane, at a perihelion distance of 1 AU and relative velocity of 20 km/s. The erosion lifetimes obtained by us are listed in the table below together with values obtained by Dohnanyi [14] and Giese and Grün [15]. The sizes of particles considered in our model are in the mm to cm range. As a first approximation gamma factor of 1000 was used.

Table 2. Life Times for mm Sized Particles

	Relative Velocity (km/s)	Gamma Factor	Life-time against erosive collisions (years)
Dohnanyi [14]	20	1000	3,000
Giese and Grün [15]	20	1000	40,000
Nikolova, Jones, present work	20	1000	62,000

Table 3. Life-Times for cm Sized Particles

	Relative Velocity (km/s)	Gamma Factor	Life-time against erosive collisions (years)
Dohnanyi [14]	20	1000	100,000
Giese and Grün [15]	20	1000	800,000
Nikolova, Jones, present work	20	1000	200,000

It can be seen from the tables above that our values agree with erosion rates obtained by previous models.

This model is only good to a first approximation. We know that the relative velocities of the impacting bodies change with heliocentric distance. Therefore we can improve the results by using Eqs. 10, 11 and 12 above to calculate the relative velocities of the colliding particles. We can then obtain new erosion rates. We use a wider range of heliocentric distances and a gamma factor of 1000. The relative velocities range from 18 km/s to 26 km/s at perihelion to 5 km/s to 15 km/s near aphelion.

## 2. GRAVITATIONAL PERTURBATIONS

### 2.1 Theory

Gravitational perturbations over large time scales could have a significant effect on the life times of meteoroids in interplanetary space.

Gravitational perturbations affect the motion of meteoroids away from Jupiter's region but this effect is one of rotation of the orbital plane due to precession. The precession will lead to a more symmetrical distribution. Since we have assumed azimuthal symmetry of the distribution such perturbations will not be of great importance. We are however interested in perturbations in regions of space where the likelihood of interparticle collisions is greater.

We investigate the life times against gravitational perturbation of particles ejected from short period comets. The integration times vary from a few thousand to a million years. Preliminary results are shown and discussed below.

### 2.2 The Integration Package

For our integrations we used Mercury 5.0 - a package for N-body integrations designed to calculate the evolution of objects in a gravitational field of a

central body [16]. It consists of the following five N-body algorithms:

- MVS (mixed variable symplectic)
- General Bulirsch Stoer
- Conservative Bulirsch-Stoer
- RA15 (RADAU)
- Hybrid Symplectic/ Bulirsch-Stoer

The most appropriate integrator for our purposes was the HYBRID algorithm. It is a combination of a conventional integrator and a symplectic component. The conventional integrator is used for close encounters only. It is much faster than all the other algorithms and therefore well suited for integrations over millions of years.

## 2.3 RESULTS

Integrations over a few thousand to a million years were performed on short period comets using the Hybrid Symplectic/Bulirsch Stoer algorithm. The resulting motion of the comets was followed and recorded every hundred years. The figures below show the initial distribution and the final evolution of the comets. Integration times are two thousand and five hundred thousand years.

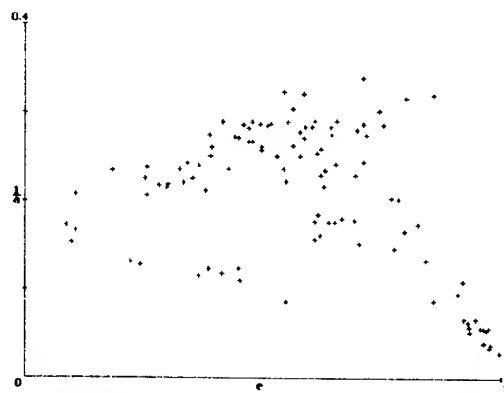


Fig.4. Initial Orbital Distribution of Short Period Comets

Fig. 4 shows the initial distribution of all catalogued short period comets, with inverse semi-major axes plotted on the y-axis and eccentricity on the x-axis. The comets are confined within a region in space centered on Jupiter's orbit (5AU) and extending to 2.5 AU and 40 AU. The effect of planetary perturbations is to increase the eccentricity and semi-major axis orbits thus making the orbits more unstable until they are ejected from the Solar System. The comets however tend to stay confined in that region. We do not see material being brought to smaller heliocentric distances.



Fig.5. Two Thousand Year Integration on Short Period Comets

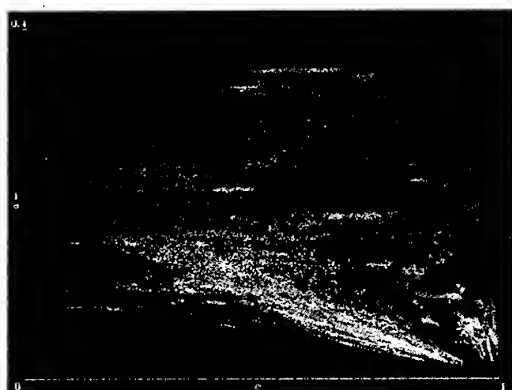


Fig.6. Five Hundred Thousand Year Integration on Short Period Comets

Fig.5 and Fig.6 show that no significant changes in the orbital distribution of short period comets occur over the time intervals shown above. Comets tend to move down to higher eccentricities and semi-major axes but there is no change in the boundaries of the distribution. Integrations over a million years show similar results. However, the amount of objects ejected from the solar system increases with increasing integration times. These preliminary results are indicative of the fact that gravitational perturbations do not in fact influence the life times of objects in interplanetary space in comparison to the PR times and it is therefore safe to consider them as a secondary effect.

## 2. REFERENCES

1. Jones J., et al. Modelling of the Sporadic Meteoroid Sources, ESA SP-495, 2001.
2. Whipple F. On Maintaining the Meteoritic Complex, *The Zodiacal Light and the Interplanetary Medium*, NASA SP-150, 1967.
3. Grün E., et al. Collisional Balance of the Meteoritic Complex, *ICARUS*, Vol.62, 244-272, 1985.
4. Dohnanyi J.S. On the Origin and Distribution of Meteoroids, *Journal of Geophysical Research*, Vol. 75, No. 17, 3468-3493, 1970.
5. Curtis J.S. An Accelerated Reservoir Light-Gas Gun, NASA TN D-1144, 1962.
6. Mizutani H., et al. A performance Test of the Low Velocity Shock Gun with a Novel Sabot Stopper, *Proc. ISAS Lunar Planet. Symp.* Vol.14, 267-277, 1981.
7. Matsui T., et al. Destruction of Rocks by Low Velocity Impact and its Implications for Accretion and Fragmentation Processes of Planetesimals. *Proc. Lunar Planet. Sci. Conference J. Geophys. Res. Suppl.* Vol.89 B700-706, 1984.
8. Seigel A.E., The Theory of High Speed Guns, *AGARDograph 91*, 1965.
9. Martelli G. and Newton G., Hypervelocity cratering and Impact Magnetization of Basalt, *Nature*, Vol. 269, 478-480, 1977.
10. Fujiwara A., et al. Experiments and Scaling Laws for Catastrophic Collisions, in *Asteroids II*; Proceedings of the Conference, Tucson, AZ, Mar. 8-11, 1988 Tucson, AZ, University of Arizona Press, 240-265, 1989.
11. Kessler D., Derivation of the Collision Probability between Orbiting Objects: the Lifetimes of Jupiter's Outer Moons, *ICARUS*, Vol. 48, 39-48, 1981.
12. Steel D. and Baggaley W. J. Collisions in the Solar System – I. Impacts of the Apollo-Amor – Aten Asteroids upon the Terrestrial Planets, *Mon. Not. R. Astr. Soc.* Vol. 218, 185 - 199, 1986.
13. Steel D. and Elford W. Collisions in the Solar System – III. Meteoroid Survival Times, *Mon. Not. R. Astr. Soc.* Vol. 212, 817-836, 1985.
14. Dohnanyi J.S. *Cosmic Dust*, 1978, p.527 ed. McDonnell J.A.M, Wiley, Chichester.
15. Giese R.H. and Grün E. *Lecture Notes in Physics*, Vol. 48, 135, 1976.
16. Chambers J. E. A Hybrid Symplectic Integrator that Permits Close Encounters Between Massive Bodies, *Mon. Not. R. Astron. Soc.*, Vol.304, 793-799, 1999.

## CLUES TO THE STRUCTURE OF METEORIODS, FROM DUST LIGHT SCATTERING PROPERTIES

A. Chantal Levasseur-Regourd<sup>(1)</sup> and Edith Hadamcik<sup>(2)</sup>

<sup>(1)</sup>Univ. Paris VI / Aéronomie CNRS/IPSL, BP 3, 91371, Verrières, France, [aclr@aerov.jussieu.fr](mailto:aclr@aerov.jussieu.fr)

<sup>(2)</sup>Aéronomie CNRS/IPSL, BP 3, 91371, Verrières, France, [edith.hadamcik@aerov.jussieu.fr](mailto:edith.hadamcik@aerov.jussieu.fr)

### ABSTRACT

Clues to the structure (compact or fluffy) of dust particles in meteor streams are provided through observations of solar light scattered by cometary and interplanetary dust particles. While their phase curves are mostly similar, and indeed characteristic of irregular particles, differences are noticed (both from remote and in-situ observations), mainly in terms of polarization levels and polarization colour. These differences suggest different formation regions, as well as an evolution of the dust morphological properties, linked to fragmentation and evaporation processes.

Recent results, mainly from laboratory measurements, are presented. Significant polarization phase curves, obtained with the PROGRA<sup>2</sup> experiment, are presented for samples of terrestrial and meteoritic origin. Some results of the CODAG experiment, launched from Esrange in May 1999, are discussed. The significance of microgravity for light scattering measurements on low-density clouds is emphasized, together with the differences in polarization colour effects for compact particles and fluffy aggregates.

### 1. INTRODUCTION

Knowing the physical properties (size distribution, shape, porosity, albedo) of dust particles in meteor streams is of major interest to understand their interaction with the atmosphere and their impacts effects on spacecraft.

Information about the physical properties of dust particles in meteor streams has mainly been provided by through collection of IDPs in the near-Earth environment. The IDPs are likely to have been altered during their atmospheric entry. It is thus of interest to accurately assess the physical properties of meteoroids, (i.e. dust particles belonging to cometary comae and tails, or to the interplanetary dust cloud that is continuously replenished by cometary or asteroidal

dust), through observations of the light they scatter, or emit in the infrared domain.

This paper first summarizes the main results of light scattering observations by cometary and interplanetary dust, and secondly presents some information provided by models and laboratory measurements, with emphasis on new measurements performed under microgravity conditions.

### 2. LIGHT SCATTERING OBSERVATIONS

#### 2.1. Brightness and polarization

The solar light scattered by optically thin media is linearly polarized. Polarization measurements are of major interest since: (i) they do not required any normalization to be compared to one another, (ii) they enhance changes in the physical properties, as demonstrated by the polarization images of the inner coma of Comet Hale-Bopp, in which jets and arcs structures are quite conspicuous (see e.g. Fig. 1, adapted from [1]).

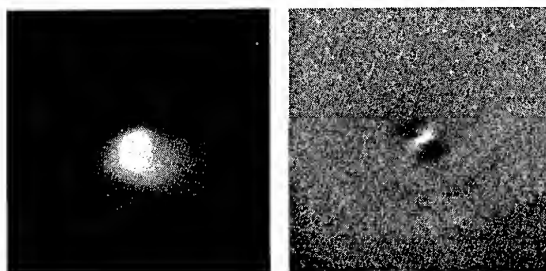


Fig. 1. Brightness (left) and polarization (right) images of the coma of Comet C/1995 O1 Hale-Bopp.

The images correspond to observations performed on 9 April 1997 from Haute-Provence Observatory (France). Field of view is of about 80000 x 80000 km<sup>2</sup>.

The brightness  $Z$  and the linear polarization  $P$  are derived from measurements of the two polarized components of the brightness (corresponding to the electric vector respectively perpendicular and parallel to the scattering plane),  $Z_{\perp}$  and  $Z_{\parallel}$ , where:

$$Z = (Z_{\perp} + Z_{\parallel})$$

$$P = (Z_{\perp} - Z_{\parallel}) / (Z_{\perp} + Z_{\parallel})$$

The polarization values mainly depend upon the phase angle ( $\alpha$ ), which is the angle between the direction of the Sun and the direction of the observer, as seen from the scattering object. They also depend upon the wavelength of the scattered light.

### 2.1. Cometary dust

Systematic observations of the polarization of cometary comae have begun with the return of Comet 1P/Halley in 1985-1986 [2]. Polarization phase curves have now been obtained for numerous comets [3]. As can be noticed in Fig. 2, updated from [1, 3], all polarization data points correspond to similar trends, at least in the  $2^{\circ}$  to  $120^{\circ}$  phase angle range where observations are available.

To be more specific, a faint negative branch, with a minimum of about  $-1\%$  near  $10^{\circ}$ , is noticed for small phase angles. The inversion region occurs near  $21^{\circ}$ , and corresponds to a slope of about  $-0.2\%$  per degree. The curve presents a wide positive branch, with a peak in the  $90^{\circ}$  to  $100^{\circ}$  range.

Phase curves allow to point out, not only similarities, but also differences between comets [3]. Actually, three classes of comets are noticed: (i) comets with a low maximum, of 10 to 15%, (ii) comets with a higher maximum, of 25 to 30%, and Comet Hale-Bopp, whose polarization at a given wavelength is always the highest. It may be of interest to notice that a comparison between different regions of Hale-Bopp on the one hand, and between Halley and Hale-Bopp on the other hand, suggests that a higher polarization is correlated to a higher albedo [4].

Observations of scattered light are always performed through filters, which cut off the gaseous cometary emissions. Fig. 2 actually gathers all observations performed on various comets from various instruments, through green filters for the upper part, and through red filters for the lower part. The comparison immediately indicates that, for ( $\alpha$ ) greater than about  $30^{\circ}$  to  $40^{\circ}$ , the polarization at a given phase angle increases with the

wavelength. This so-called polarization colour effect could be less important in the inner coma [see e.g. 5], and possibly opposite in the vicinity of the nucleus, as revealed by in-situ observations of Comet Halley [6].

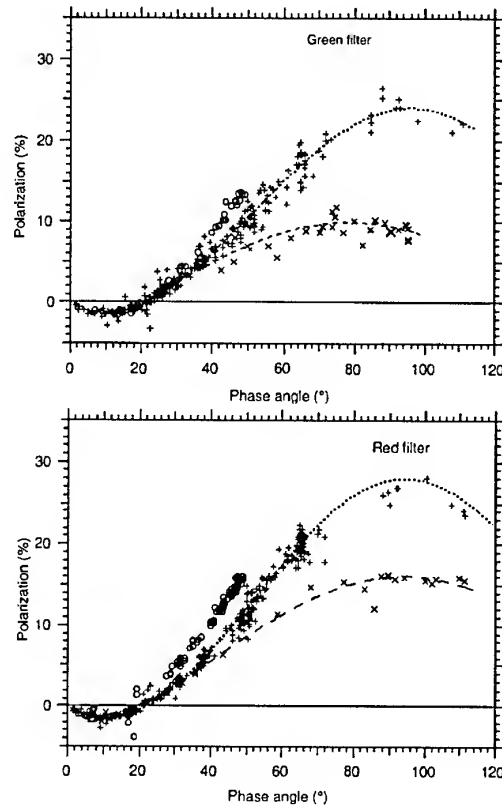


Fig. 2. Polarization of light scattered by cometary dust, as a function of phase angle, for all observations performed through narrow-band green filters for the upper part, and through red filters for the lower part. (X) Comets with low maximum, (+) Comets with high maximum, (O) Comet Hale-Bopp.

### 2.2. Interplanetary dust

Zodiacal light observations, i.e. observations of solar light scattered by interplanetary dust, do not immediately provide clues to the dust scattering properties. The brightness is extended all along the line-of-sight, which extends from the observer to (at least) the outer fringe of the asteroid belt. Since both the scattering angle and the physical properties of the dust vary along the line-of-sight, an inversion is required to retrieve local information and to derive polarization phase curves.

Results have been obtained in the vicinity of the ecliptic plane by two different approaches, the nodes of uncertainty method [7] and the kernel of Volterra

method [8], as summarized in [9]. The results derived from different data sets agree fairly well. The shapes of the interplanetary dust phase curves are similar to those of cometary dust.

For large enough phase angles, the local polarization depends upon the distance to the Sun. For solar distances  $R$  in the 0.3 AU to 1.5 AU range, it can be described in the green domain through:

$$P(90^\circ) = (0.30 \pm 0.03) R^{+0.5 \pm 0.1}.$$

The local albedo is found to simultaneously decrease with increasing solar distance, with a  $(-0.34 \pm 0.05)$  power law exponent [9]. A higher polarization seems to be correlated to a lower albedo, i.e. an effect opposite to what is noticed for cometary dust. The study of the wavelength dependence reveals an other discrepancy, since the polarization at a given phase angle possibly decreases with the wavelength [10].

### 2.3. Interpretation in terms of properties of the micrometeoroids

The smooth phase curves of cometary and interplanetary dust have similar shapes, as already discussed in e.g. [11]. The phase curves obtained for asteroidal regoliths also present the same trend, with a polarization colour opposite to that of cometary dust [12]. All these curves may be described by trigonometric functions such as:

$$P(\alpha) = C (\sin \alpha)^a (\cos \alpha/2)^b \sin(\alpha - \alpha_0)$$

Such smooth phase curves are typical of irregular particles. Relatively large grains (e.g. of asteroidal origin) that have suffered numerous collisions are indeed irregular. Tiny grains (e.g. interstellar or cometary) that have aggregated, leading to fractal type structures, also build up irregular particles.

Indeed, some IDPs collected in the stratosphere, although they have been heated during their crossing of dense atmospheric layers, are still aggregates. Their size is in a 1  $\mu\text{m}$  to 1 mm size range, and they are built up of a mixture of smaller grains of clear and absorbing material [13].

The differences noticed in polarization levels for a fixed phase angle ( $>35^\circ$ ) and for a fixed wavelength need also to be understood. Different comets actually exhibit different phase curves, in good agreement with the fact that their formation region expanded over tens of astronomical units, leading to a significant variety of physical properties. Their nuclei actually condensed at

the origin of the solar system, either in the giant planets region, from where they were expelled to build up the Oort cloud, or in the Kuiper belt region.

A given extended object (i.e. cometary coma, interplanetary dust cloud) may also present different scattering properties between its different regions. It is indeed expected that some dust particles originating from the same source exhibit some dynamical segregation. Besides, it is likely that these particles evolve with time, while they suffer fragmentation or evaporation. Cometary dust particles observed in the inner coma have been ejected more recently than those observed further away; with a longer timescale, interplanetary dust particles observed at large heliocentric distances are younger than those observed closer to the Sun, since they spiral under Poynting-Robertson effect.

Finally, differences are pointed out between the variation of the polarization with the wavelength, and also possibly with the albedo. Such important discrepancies in light scattering properties suggest differences in morphological properties. The physical parameters, which define the shape, the porosity and the structure of these irregular dust particles, are certainly highly variable. It is necessary, in order of knowing how each of them influences the scattering properties, to perform simulations and/or laboratory measurements on a large number of "virtual" or real particles.

## 3. INFORMATION PROVIDED BY MODELS AND LABORATORY MEASUREMENTS

### 3.1. Computational approaches

Computations of light scattered by some irregular particles and some fractal aggregates, formed through growth processes that remain invariant over a given range of sizes, are relatively easy. The results suggest that smooth phase curves could be obtained by compact gaussian particles. They can also be obtained by aggregates, with a fractal dimension below 2.5 and/or with a high complex refractive index [see e.g. 11, 14].

However, it is difficult to obtain unique and converged solution for complex particles. Besides, some methods only apply to a specific geometry and/or size interval. Laboratory measurements are thus required [15], to provide a ground truth with realistic dust particles and aggregates.

### 3.2. Laboratory measurements

Multiple scattering on gravity packed layers is avoided through elaborate techniques, such as microwave analogue measurements, as well as levitation techniques and measurements under microgravity conditions. The microwave approach is an efficient tool, which requires assumptions about the properties of the artificial particles that are built up [16]. The latter approach allows to perform measurements on any type of real particles, including aggregates that have been formed under realistic conditions.

The results presented here are limited to some measurements obtained with the PROGRA<sup>2</sup> and CODAG experiments, with particles in the 1  $\mu\text{m}$  to 1 mm size range. Fig. 3 shows an example of such particles. Both experiments are performed with nephelometer type instruments, and are calibrated through comparisons between measurements on documented spheres and results of Mie theory computations.

### 3.3. PROGRA<sup>2</sup> and polarization colour

PROGRA<sup>2</sup> provides polarization values and images of the light scattered by dust particles at a given phase angle, which can vary from 8° to 165°. Measurements are performed during parabolic flight campaigns that allow multiple reduced gravity sequences, of about 25 s duration each, with a sample levitating inside a vial.

Various campaigns, on CNES Caravelle, NASA KC-135 and CNES A300 have already allowed a detailed database to be built. Detailed information about the instrument can be found in [17, 18]. Some significant results have been published in [19, 20].

The experiment has validated the concept of light scattering measurements in microgravity conditions. Besides, the important role of the packing density, i.e. of multiple scattering between particles and inside aggregates, has been pointed out.

The light scattered by the samples is illuminated either by a green or by a red laser. The polarization colour can thus be measured, both on deposited particles in the laboratory and on levitating particles during parabolic flights, as shown respectively on Fig. 4 and 5.

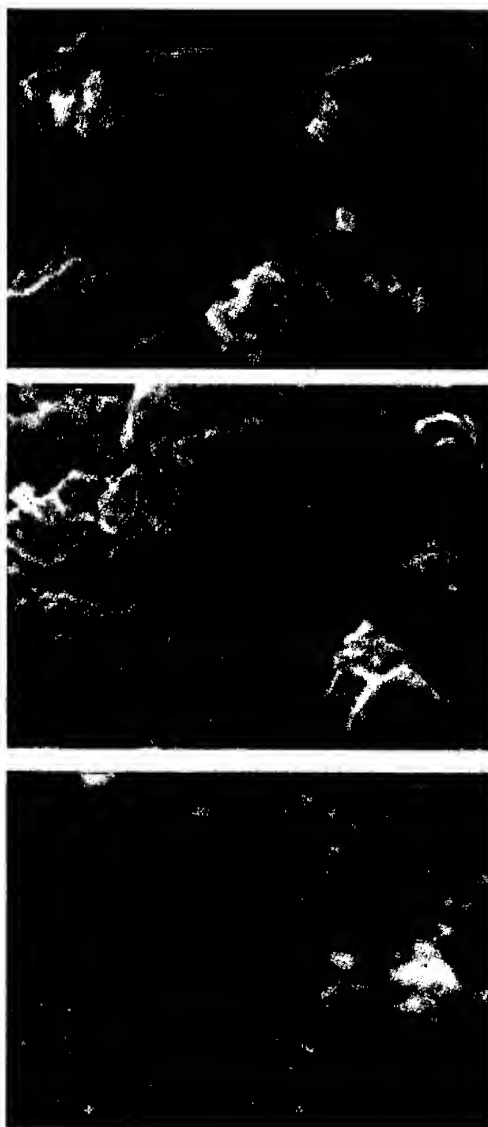


Fig. 3. SEM images (5 mm x 3,6 mm) of some samples used for light scattering laboratory measurements with particles and aggregates. From top to bottom:  
 Particles from Allegan meteorite  
 Aggregates from Orgueil meteorite,  
 Fluffy industrial aggregates of alumina  
 (see also on [www.esf.org/progra2](http://www.esf.org/progra2))

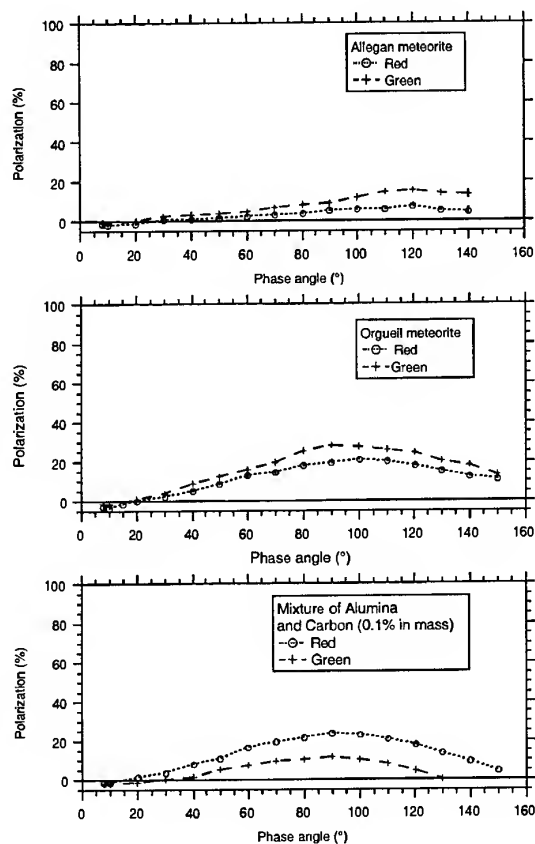


Fig. 4. Wavelength dependence of polarization, measured with PROGRA<sup>2</sup> experiment on deposited particles. Top: Allegan, middle: Orgueil, bottom: mixture of alumina, with 0.1% carbon, leading to the same albedo than for Allegan.

Fewer particles are necessarily in the field of view, when they are floating in a low-density cloud, than when they are deposited on a surface. The signal to noise ratio is thus lower, and the error bars are bigger. It may be noticed that the polarization levels are usually higher and the values of the maximum angle may be lower for measurements performed in reduced gravity conditions.

An important result, obtained both for deposited and for levitating particles, is that the polarization decreases with increasing wavelength for the particles of meteoritic origin that are actually quite compact. On the opposite, the polarization increases with increasing wavelength for extremely porous and fluffy aggregates, whose albedos are similar.

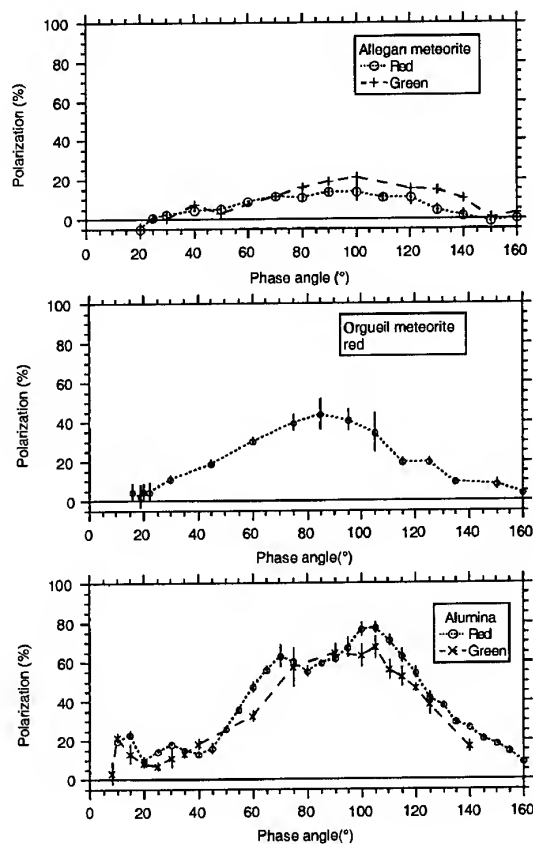


Fig. 5. Typical polarization phase curves, as measured with PROGRA<sup>2</sup> experiment on levitating particles, with samples similar to those used for deposited particles measurements

It makes sense to infer, from the analysis of such polarization colour effects, that the particles of asteroidal origin are more compact than the particles found in the outer comae regions. The latter, as well as most particles in meteor streams, could indeed be quite fluffy.

### 3.4. CODAG and aggregates formation

The CODAG experiment investigates the ballistic aggregation in a cloud of particles enclosed in a low-pressure chamber. The process, which requires the absence of gravitational sedimentation, can be studied under longer microgravity conditions, on board a rocket or a satellite [21].

The CODAG - Light Scattering Unit (LSU) is a polar nephelometer, which continuously monitors the brightness and polarization of the light scattered by dust particles, simultaneously in 22 phase angles, from  $10^\circ$  to  $165^\circ$ . Information about CODAG - LSU instrument can be found in [14, 22]. Results have already been presented in [23, 24].

The light emitted by a near infrared laser diode illuminates through a vacuum tight window the particles injected in the low-pressure chamber. Analysers, mounted on a ring around the chamber, measure the polarized brightness components of the scattered light for the 22 phase angles. A total of 44 optical fibres, plus 2 fibres connected to the laser diode and to a light trap opposite to it, are used to link the analysers to the detecting unit.

The functioning of the LSU, together with pre- and post-flight calibrations, has been ensured during parabolic flight campaigns on board the CNES A300 aircraft (see e.g. Fig. 6). Various samples of micron-sized  $\text{SiO}_2$  and latex spheres, with different sizes, concentrations and complex refractive indices, had been prepared (see e.g. Fig. 7). A given sample, sealed in a conical glass vial, was positioned at the centre of the ring before a reduced gravity sequence.

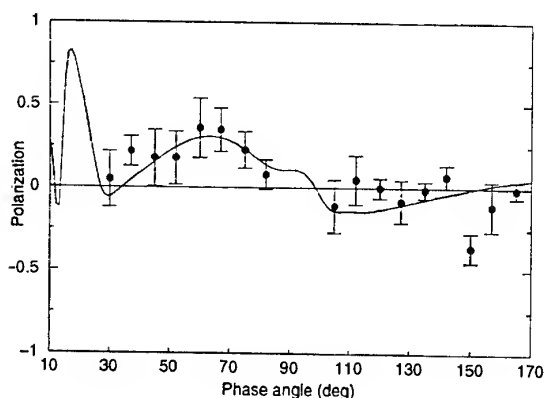


Fig. 6. Typical polarization degrees obtained during one parabola and computed for a given sample (radius  $6.25 \mu\text{m}$ , log normal distribution  $s = 0.18$ , index  $= 1.52 + 0.001i$ ). The discrepancies between the measurements and the Mie curve are attributed to surface heterogeneities and to uncertainty in the value of the imaginary part of the complex refractive index

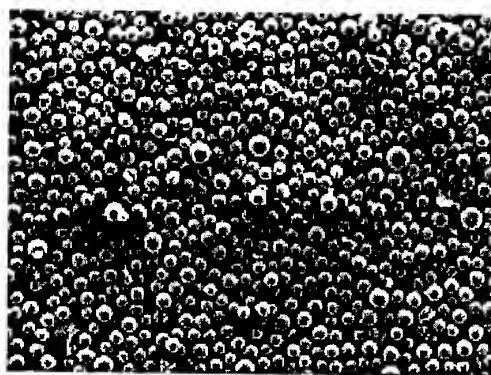


Fig. 7. Example of spheres used for the calibration

For the rocket experiment, micron-sized  $\text{SiO}_2$  spheres, assumed to be representative of interstellar grains, had been chosen to simulate the preplanetary aggregation processes. The CODAG experiment with its LSU was successfully flown from Esrange (Kiruna, Sweden) on board the ESA / MASER 8 rocket flight on 14 May 1999. An apogee of 268 km was reached, leading to a microgravity duration of 378 s.

Up to 310 s after injection, a perfect agreement is found between the measured phase curves and those computed for individual particles with characteristics [mean radius  $(0.502 \pm 0.025) \mu\text{m}$ , complex refractive index  $(1.388 + 0.0001 i)$ ] comparable with those that had been specified. In the interval corresponding to 310 s - 378 s after injection, the intensities were continuously increasing, while the shape of the phase curves was getting significantly smoother.

This evolution, interpreted as a transition from individual grains to aggregates of a few grains (2 to 8), actually took place after about 310 s. A detailed analysis shows that it is consistent with a growth process corresponding mainly to Ballistic Cluster Aggregation.

The CODAG experiment has thus validated the concept of dust particles aggregation under microgravity conditions. The LSU has demonstrated that it is possible to monitor the evolution of the scattering properties of the aggregates that are progressively formed. The instrument is now being upgraded, with a second laser, tuneable analysers, and new samples.

#### 4. CONCLUSION AND PROSPECTIVE

The results reported here emphasize the significance of light scattering measurements to provide information about the structure of the micrometeoroids. It is quite likely that the particles of cometary origin are fluffy and porous, at least as long as they have not been suffering too much heating and fragmentation.

They also demonstrate that it is possible to measure the scattering properties of naturally formed micrometeoroids under microgravity conditions. They are most encouraging for the ICAPS project, Interactions in Cosmic and Atmospheric Particle Systems, selected for the International Space Station. This seven year scientific program is now under phase A at ESA. The results of the Research Topic 5, devoted to the optical and morphological properties of aggregates, will be of major interest to accurately assess the physical properties of the cometary and interplanetary dust particles.

#### REFERENCES

1. Hadamcik, E., Levasseur-Regourd, A.C., and Renard, J.B., CCD imaging polarimetry of Comet Hale-Bopp, *Earth Moon Planets*, Vol. 78, 365 - 371, 1999.
2. Dollfus, A., Bastien, P., Le Borgne, J.M., Levasseur-Regourd, A.C., and Mukai, T., Optical polarimetry of P/Halley, *Astron. Astrophys.*, Vol. 206, 348 - 356, 1988.
3. Levasseur-Regourd, A.C., Hadamcik, E., and Renard, J.B., Evidence for two classes of comets from their polarimetric properties at large phase angles, *Astron. Astrophys.*, Vol. 313, 327 - 333, 1998.
4. Mason C.G., Gehrz, R.D., Jones, T.J., Hanner, M.S., Williams, D.M., and Woodward, C.E., Observations of unusually small dust grains in the coma of comet Hale-Bopp C/1995 O1, *Astrophys. J.*, Vol. 549, 635 - 646, 2001.
5. Levasseur-Regourd, A.C., Polarization of light scattered by cometary dust particles: observations and tentative interpretations, *Space Science Rev.*, Vol. 90, 163 - 168, 1999.
6. Hadamcik, E., Contribution à une classification des comètes à partir d'observations et de simulations en laboratoire, Thesis, Université Paris VI, 1999.
7. Dumont, R., and Levasseur-Regourd, A.C., Properties of interplanetary dust from infrared and optical observations, *Astron. Astrophys.*, Vol. 191, 154 - 160, 1988.
8. Lumme, K., Scattering properties of interplanetary dust particles, *Light scattering by non spherical dust particles*, M.I. Mishchenko, J.W. Hovenier and L.D. Travis eds., Academic Press, 555 - 583, 2000.
9. Levasseur-Regourd, A.C., Mann, I., Dumont, R., and Hanner, M.S., Optical and thermal properties of interplanetary dust, *Interplanetary dust*, E. Grun, B. Gustafson, S. Dermott, and H. Fechtig eds., Springer-Verlag, 57 - 94, 2001.
10. Leinert, C., Bowyer, S., Haikala, L.K., Hanner, M.S., Hauser, M.G., Levasseur-Regourd, A.C., Mann, I., Mattila, K., Reach, W.T., Schlosser, W., Staude, H.J., Toller, G.N., Weiland, J.L., Weinberg, J.L., and Witt, A.N., The 1997 reference of diffuse night sky brightness, *Astron. Astrophys. Suppl. Ser.*, Vol. 127, 1 - 99, 1998.
11. Levasseur-Regourd, A.C., Cabane, M., and Haubebourg, V., Observational evidence for the scattering properties of interplanetary and cometary dust clouds: an update, *JQSRT*, Vol. 63, 631 - 641, 1999.
12. Goidet-Devel, B., Renard, J.B., and Levasseur-Regourd, A.C., Polarization of asteroids: Synthetic curves and characteristic parameters, *Planet. Space Sci.*, Vol. 43, 6, 779 - 786, 1995.
13. Jessberger, E.K., Stephan, T., Rost, D., Arndt, P., Maetz, M., Stadermann, F.J., Brownlee, D.E., Bradley, J.P., and Kurat, G., Properties of interplanetary dust: information from collected samples, *Interplanetary dust*, E. Grun, B. Gustafson, S. Dermott, and H. Fechtig eds., Springer-Verlag, 253 - 294, 2001.
14. Levasseur-Regourd, A.C., Cabane, M., Worms, J.C., and Haubebourg, V., Physical properties of dust in the solar system: relevance of a computational approach and of measurements under microgravity conditions, *Adv. Space Res.*, Vol. 20, 8, 1585 - 1594, 1997.
15. Levasseur-Regourd, A.C., Cabane, M., Haubebourg, V., and Worms, J.C., Light scattering experiments under microgravity conditions, *Earth, Moon, Planets*, Vol. 80, 343 - 368, 1998.
16. Gustafson, B.A.S., Microwave analog to light scattering measurements, *Light scattering by non spherical dust particles*, M.I. Mishchenko, J.W. Hovenier and L.D. Travis eds., Academic Press, 367 - 390, 2000.

17. Worms, J.C., Renard, J.B., Hadamcik, E., Brun-Huret, N., and Levasseur-Regourd, A.C., The PROGRA<sup>2</sup> light scattering instrument, *Planet. Space Sci.*, Vol. 48, 493 - 505, 2000.

18. Renard, J.C., Worms, J.C., Lemaire, T., Hadamcik, E., and Huret, N., Light scattering by dust particles in microgravity: polarization and brightness imaging with the new version of the PROGRA<sup>2</sup> instrument, *Applied Optics*, in press, 2001.

19. Worms, J.C., Renard, V., Hadamcik, E., Levasseur-Regourd, A.C., and Gayet, J.F., Results of the PROGRA<sup>2</sup> experiment: an experimental study in microgravity of scattered polarised light by dust particles with large size parameter, *Icarus*, Vol. 142, 1, 281 - 297.

20. Hadamcik, E., Renard, J.B., Worms, J.C., Levasseur-Regourd, A.C., and Masson, M., Polarization of light scattered by fluffy particles, *Icarus*, in press, 2001.

21. Blum, J., Wurm, G., Poppe, T., The CODAG sounding rocket experiment to study aggregation of thermally diffusing dust particles, *Adv. Space Res.*, Vol. 23, 7, 1267 - 1270, 1999.

22. Levasseur-Regourd, A.C., Cabane, M., Chassefière, E., Haubebourg, V., and Worms, J.C., The CODAG Light Scattering Experiment for light scattering measurements by dust particles and their aggregates, *Adv. Space Res.*, Vol. 23, 7, 1271 - 1277, 1999.

23. Haubebourg, V., Propriétés de diffusion lumineuse de particules en suspension: transition du régime de Mie à celui d'agrégats. Thesis, Université Paris VI, 2000.

24. Levasseur-Regourd, A.C., Haubebourg, V., Cabane, M., and Worms, J.C., Light scattering measurements on dust aggregates, from MASER 8 to ISS, *First international symposium on microgravity research and applications*, ESA SP-454, 797 - 802, 2001.

## INTERPLANETARY DUST OBSERVATION IN THE EARTH – MARS REGION BY MARS DUST COUNTER (MDC) ON BOARD NOZOMI: THREE-YEAR RESULTS

S. Sasaki<sup>1</sup>, E. Igenbergs<sup>2</sup>, H. Ohashi<sup>3</sup>, G. Hofschuster<sup>2</sup>, R. Münzenmayer<sup>2§</sup>, W. Naumann<sup>2#</sup>, R. Senger<sup>2</sup>, F. Fischer<sup>4</sup>, A. Fujiwara<sup>5</sup>, E. Grün<sup>6</sup>, Y. Hamabe<sup>1</sup>, T. Kawamura<sup>7</sup>, I. Mann<sup>8</sup>, H. Miyamoto<sup>1\*</sup>, K. Nogami<sup>7</sup>, H. Svedhem<sup>8</sup>

<sup>1</sup> *Department of Earth and Planetary Science, The University of Tokyo, Tokyo 113-0033, Japan*

<sup>2</sup> *LRT, Technische Universität München, 85748 Garching, Germany*

<sup>3</sup> *Department of Ocean Sciences, Tokyo University of Fishery, Minato-ku, Tokyo 108-0075, Japan*

<sup>4</sup> *RTSG, Technische Universität München, 80333 München, Germany*

<sup>5</sup> *Institute of Space and Astronautical Sciences, Sagami-hara, 229-8510, Japan*

<sup>6</sup> *Max Planck Institut für Kernphysik, Saupfercheckweg 1, 69117 Heidelberg, Germany*

<sup>7</sup> *Dokkyo University School of Medicine, Mibu, Tochigi 312-0207, Japan*

<sup>8</sup> *Space Science Department, ESA-ESTEC, PO Box 299, 2200 AG Noordwijk, The Netherlands*

<sup>§</sup> *Now at Astrium Space, Postfach 1420, 88039 Friedrichshafen, Germany*

<sup>#</sup> *Now at Kayser-Threde GmbH, Wolfratshauser Str. 48, 81379 München, Germany*

<sup>\*</sup> *Now at Department of Geosystem Engineering, The University of Tokyo, Tokyo 113-8656, Japan*

### ABSTRACT

Mars Dust Counter (MDC) is a light-weight impact-ionization dust detector on board Japanese Mars mission NOZOMI, which was launched on July 4th 1998. The main aim of MDC is to detect dust particles around Mars and reveal the distribution of the martian ring or torus of dust from Phobos and Deimos. In three years between July 1998 and June 2001, MDC has detected more than 90 dust impacts. In November 1998, NOZOMI encountered the Leonid meteoroid stream. Although MDC detected two dust impacts, directional analysis showed that those probably did not belong to the Leonid particles. In the interplanetary observation from 1999, NOZOMI has detected about 60 interplanetary particles moving around the sun and several particles of interstellar origin.

### 1. INTRODUCTION

Mars Dust Counter (MDC) is a dust detector of impact ionization type on board Japanese Mars mission NOZOMI. Although its weight is as light as 730g, MDC can determine mass, velocity, and direction of a dust particle using rise time of impact-induced charge signals [1]. NOZOMI was launched on July 4th (3rd at UT) 1998. NOZOMI with various plasma instruments will investigate the martian upper atmosphere, especially its interaction with the solar wind [2]. For this purpose, NOZOMI will take a very elliptical orbit around Mars, where the periapsis altitude is 150km and apoapsis distance is 15 Mars radii, beyond Deimos orbit. The main objective of MDC is to discover the predicted martian dust ring or torus [3-10]. Significant

dust abundance detectable by NOZOMI-MDC was predicted under the self-sustaining mechanism, where satellite-dust collisions are the main source of dust particles [5, 6, 8, 9, 11]

After leaving the circumterrestrial orbit in December 1998, NOZOMI should have started observation around Mars in October 1999. However, due to a problem at the powered fly-by with the Earth on 20th December 1998, NOZOMI orbital plan was changed largely. From December 1998 to December 2002 for four years, NOZOMI will take an eccentric orbit whose perihelion and aphelion are at the Earth's orbit and at the Mars' orbit, respectively. Then, after two flybys with the Earth in December 2002 and June 2003, NOZOMI will enter circummartian orbits at the beginning of 2004. During this extended cruising interplanetary phase as long as five years, MDC can continuously observe interplanetary dust. In the present study, we show our data by the end of June 2001. So far MDC has detected more than 90 doubtless dust impacts.

### 2. MDC-NOZOMI

MDC is an improved version of HITEN and BREMSAT dust detectors which were developed at the Technical University of Munich [1]. Previous similar detectors had already successfully measured dust particles around the Earth [12]. The weight of MDC is 730g, its dimensions are 136 x 127 x 181mm<sup>3</sup>, and the area of its sensor aperture is 124 x 115mm<sup>2</sup>, which is 1.5 times as large as the previous versions. NOZOMI is a spin-stabilized satellite with a high-gain antenna on its top. Its spin axis is pointing to the Earth to keep high telemetry rate basically during the interplanetary

cruising phase. The sensor aperture axis is 135 degrees from the spin axis of NOZOMI (Fig. 1). FOV (field-of-view) of MDC aperture is close to 180 degree on the plane parallel to the side panel of NOZOMI, and 135 degree on the plane vertical to the side panel of NOZOMI. Since the solar direction angle (Sun – NOZOMI – Earth) is always less than 45 degree, MDC sensor box can thus avoid direct sunlight which would increase noise signals due to photoelectrons.

Measurement principle of MDC was described elsewhere [1, 13]. From the total charge and rise time of the signal, mass and velocity of impacted particle can be estimated in comparison with laboratory calibration data obtained using a dust accelerator. At 10km/s impact speed, MDC can determine mass of particles approximately between  $5 \times 10^{-15}$  and  $10^{-10}$  g (between 0.1 and 10  $\mu\text{m}$  in diameter under density  $1\text{g/cm}^3$ ).

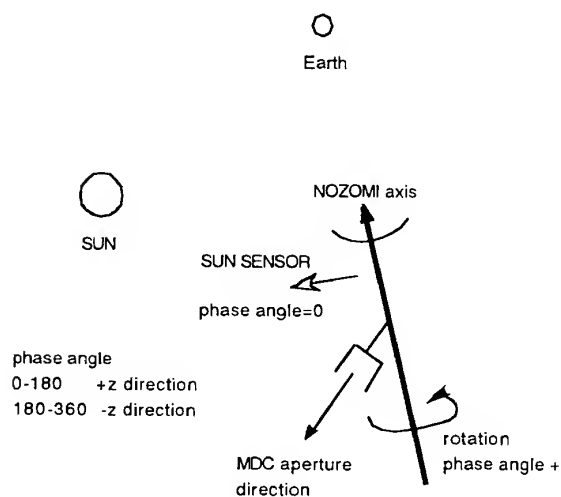


Fig. 1 A schematic image of MDC sensor direction. In NOZOMI, both MDC and the sun sensor determining phase angle are on the same side panel. During the interplanetary phase from March 1999, NOZOMI spin axis is parallel to the ecliptic plane. Then MDC aperture is looking at the northern (+z) celestial sphere when the phase angle is between 0 and 180 degrees and at the southern (-z) celestial sphere when the phase angle is between 180 and 360 degrees.

### 3. OBSERVATION AROUND THE EARTH

On July 10th after the launch on 4th, MDC was first switched on and on the same day it detected the first impact signal. NOZOMI was on eccentric parking orbits around the Earth for 5 months performing two fly-bys with the Moon. MDC has detected more than 20 impact signals during this circumterrestrial phase.

Mass and velocity of particles detected during the circumterrestrial phase in 1998 are shown in Figure 2. On 18th November 1998, NOZOMI encountered the Leonid meteoroid stream which was formed by particles emitted by Comet 55P/Tempel-Tuttle. The relative velocity between NOZOMI and the Leonid dust stream was 70km/s. MDC high voltage was put off (at 4:00UT on 18th) during the predicted peak encounter event to avoid damage on the sensor. Before the high voltage off, MDC detected two distinct impact signals with preliminarily estimated velocity 19 and 13km/s, respectively. Since NOZOMI is a spin-stabilized satellite, MDC sensor direction is described by the phase angle from the solar direction. Although predicted phase angle of the Leonid particles was 280 degree, the phase angles of those events were 75 and 154 degrees in the anti-Leonid directions (10-190 degree). Moreover, their velocities are lower than the relative impact velocity of Leonid meteor stream. Thus, they would not be dust particles in the Leonid stream. However, we should note that detected dust number was apparently significantly high in November although distance between NOZOMI and the Earth is large ( $>10^6\text{km}$ ). The Leonid meteoroid stream would have increased the dust population around the Earth. One possibility is that dust ejection from collisions of stream particles with the Moon, which could be suggested from the enhancement of lunar sodium tail following Leonid meteor stream [14, 15].

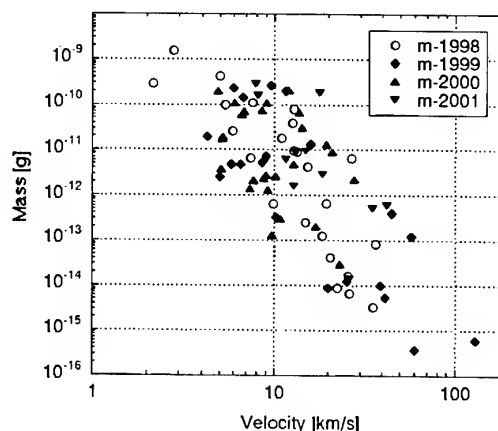


Fig. 2 Mass – velocity range of detected particles based on the preliminary analysis in 1998, 1999, and 2000-2001. Each velocity value has an error factor of 1.5 and each mass value has an error factor of 5 according to calibration experiments [18]. Numbers of impact events compiled in this figure are 24 (1998), 20 (1999), 26 (2000), and 12 (2001 between January and June). About 10 impact data where velocity and mass have not been estimated are not included.

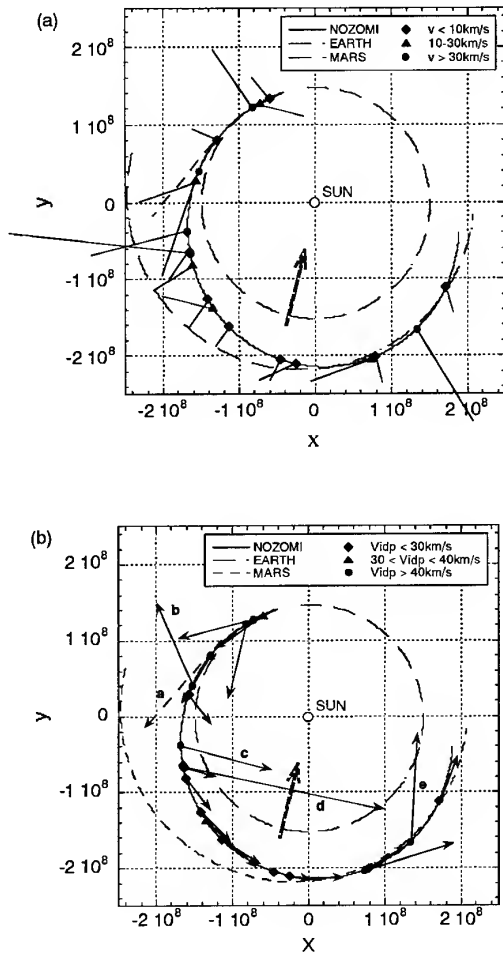


Fig. 3 Dust impacts detected by MDC in 1999. Orbits of NOZOMI, the Earth, and Mars are shown in the ecliptic plane. The  $+x$  direction is the direction of the Sun at vernal equinox. The big arrow denotes the direction of interstellar gas flow into the solar system. (a) Direction of MDC sensor aperture and impact velocity (i.e. relative velocity between NOZOMI and a dust particle). For each impact, the direction is expressed by a line from the impact mark. The length of each line corresponds to velocity of the impacted particle. One event with a broken line denotes a fast impact with a large vertical velocity component. (b) Velocity of dust in the interplanetary space calculated from impact velocity and orbital velocity. Dust particles with high velocity ( $>40\text{km/s}$ ) are denoted by attached characters (a, b, c, d, e).

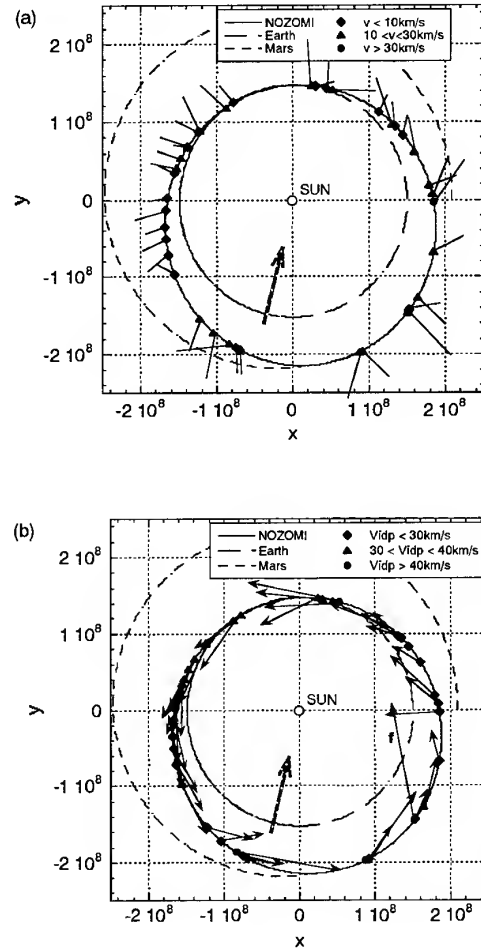


Fig. 4 Dust impacts detected by MDC in 2000 and 2001. Orbits of NOZOMI, the Earth, and Mars are shown in the ecliptic plane. The  $+x$  direction is the direction of the Sun at vernal equinox. The big arrow denotes the direction of interstellar gas flow into the solar system. (a) Direction of MDC sensor aperture and impact velocity. For each impact, the direction is expressed by a line from the impact mark. The length of each line corresponds to velocity of the impacted particle. (b) Velocity of dust in the interplanetary space calculated from impact velocity and orbital velocity. A dust particle with high velocity is denoted by attached characters (f).

#### 4. OBSERVATION OF INTERPLANETARY AND INTERSTELLAR DUST

As explained in INTRODUCTION, from December 1998 to December 2002 for four years, NOZOMI takes an elliptical orbit whose perihelion and aphelion are at the Earth's orbit (1.0AU) and at the Mars' orbit (1.5AU), respectively. From March 10, 1999, the spin axis of NOZOMI has been pointing to the Earth on the ecliptic plane. We have compiled impact event data by June 2001. The velocity and mass of those data are shown in Fig. 2. Although velocity-mass distribution of impact data of 1999-2001 is overlapped with that of 1998, several differences are observed in Fig. 2. Particles with impact velocities smaller than 4km/s have not been detected in the cruising phase. On the contrary, high velocity particles ( $v > 40\text{km/s}$ ) are detected only during the cruising phase, especially in 1999.

Impact events in 1999 are shown in Fig. 3. Since MDC sensor is not looking at the solar direction (Fig. 1), dust impact direction is usually inward as seen in Fig. 3(a). There are several particles whose velocity is higher than 30km/s. Figure 3(b) shows velocities of dust particles in the interplanetary space. They are calculated from dust impact velocity and orbital velocity of NOZOMI. Most of particles are Keplerian dust particles moving around the sun. There are several high velocity particles which are apparently different from such Keplerian particles, although there is direction ambiguity of  $\pm$  several tens degree because of the large aperture of MDC sensor. In Fig. 3(b), direction of two dust particles (b, e) corresponds to that of typical interstellar particles, which should correspond to the direction of the solar system moving against the surrounding interstellar gas cloud with a relative velocity 26km/s [16]. Particle a has a large vertical component. Other high-velocity particles c, d would have different origin but the component with this direction has not been reported in the interstellar dust source [17].

In 2000-2001 season, MDC detected similar number of dust particles but fewer high velocity particles (Fig. 4(a)). Figure 4(b) show that there is only one candidate f of interstellar dust. Most of particles are typical interplanetary dust particles moving around the sun. The difference between 1999 data and 2000-2001 data does not necessarily mean the change of interstellar dust flow. It could be rather explained by the change of dust detection efficiency according to NOZOMI spin axis direction (V. Dikarev, private communication).

#### 5. CONCLUSION

MDC-NOZOMI has detected more than 90 dust particles in three years operation between July 1998 and June 2001. In the interplanetary space, most of detected particles are interplanetary dust moving around the sun but MDC has detected several particles of interstellar origin.

Acknowledgements: The authors thank support of ISAS and NOZOMI-operation team members for continuous operation of MDC.

#### REFERENCES:

1. Igenbergs, E., S. Sasaki, R. Münzenmayer, H. Ohashi, G. Fäber, F. Fischer, A. Fujiwara, Y. Hamabe, H. Iglseider, D. Klinge, H. Miyamoto, A. Glasmachers, E. Grün, T. Mukai, W. Naumann, K. Nogami, G. Schwehm, H. Svedhem, and K. Yamakoshi, Mars Dust Counter, *Earth Planets Space* 50, 241-245, 1998.
2. Yamamoto, T. and K. Tsuruda. The PLANET-B Mission, *Earth Planets Space* 50, 175-181, 1998.
3. Soter, S., The dust belts of Mars. Rep. *Center for Radiophys. Space Res.* 462, Cornell Univ. Ithaca, 1971.
4. Horányi, M., J. A. Burns, M. Tótrallyay, and J. G. Luhmann, Toward understanding the fate of dust lost from the Martian satellites. *Geophys. Res. Lett.* 17, 853-856, 1990.
5. Sasaki, S., Martian dust tori formation: Ejecta at collision of torus particles with the satellite can sustain dust abundance. In *Proc. 27th ISAS Lunar Planet. Symp.* (eds. M. Shimizu and H. Mizutani), 47-50, 1994.
6. Sasaki, S., Dust ring/torus around Mars, waiting for detection by NOZOMI. *Adv. in Space Res.* 23, 1907-1910, 1999.
7. Ishimoto, H. and T. Mukai, Phobos dust rings. *Planet. Space Sci.* 42, 691-697, 1994.
8. Hamilton, D. P., The asymmetric time-variable rings of Mars. *Icarus* 119, 153-172, 1996.
9. Ishimoto, H., Formation of Phobos/Deimos dust rings. *Icarus* 122, 153-165, 1996.

10. Krivov, A. V. and D. P. Hamilton, Martian dust belts: waiting for discovery. *Icarus* 128, 335-353, 1997.
11. Sasaki, S., Martian self-sustaining dust torus. *In Physics, Chemistry, and Dynamics of Interplanetary Dust*, (eds. B. A. S. Gustafson and M. S. Hanner), ASP Conf. Ser. 104, 187-190, 1996.
12. Igenbergs, E., A. Hildepohl, K. Uesugi, T. Hayashi, H. Svedhem, H. Iglseider, G. Koller, A. Glasmachers, E. Grün, G. Schwehm, H. Mizutani, T. Yamamoto, A. Fujimura, N. Ishii, H. Araki, K. Yamakoshi, and K. Nogami, The present status of the Munich Dust Counter experiment on board of the HITEN spacecraft. *In Origin and Evolution of Interplanetary Dust*, (eds. A. C. Levasseur-Regourd and H. Hasegawa), Kluwer, 15-20, 1991.
13. Sasaki, S., Igenbergs, E., Ohashi, H., Mnzenmayer, R., Naumann, W., Hofschuster, G., Born, M., Fber, G., Fischer, F., Fujiwara, A., Glasmachers, A., Grm, E., Hamabe, Y., Iglseider, H., Kawamura, T., Miyamoto, H., Morishige, K., Mukai, T., Naoi, T., Nogami, K., Schwehm, G., Svedhem, H., Observation of interplanetary and interstellar dust particles by Mars Dust Counter (MDC) on board NOZOMI, *Adv. in Space Res.*, in press, 2001.
14. Smith, S. M., J. K. Wilson, J. Baumgardner, M. Mendillo, Discovery of the distant lunar sodium tail and its enhancement following the Leonid meteor shower of 1998. *Geophys. Res. Lett.* 26, 1649-1652, 1999.
15. Shiokawa, K., M. K. Ejiri, T. Ogawa, T. Nakamura, Distant lunar sodium tail observed in the Japanese local-time sector during the Leonid meteor shower of 1998, *J. Geophys. Res.* 105, 24621-24626, 2000.
16. Grün, E., B. Gustafson, I. Mann, M. Baguhl, G. E. Morfill, P. Staubach, A. Taylor, and H. A. Zook, Interstellar dust in the heliosphere. *Astron. Astrophys.* 286, 915-924, 1994.
17. Taylor, A., Baggaley, W. J., and Steel, D. I., Discovery of interstellar dust entering the Earth's atmosphere, *Nature* 380, 323-325, 1996.
18. Naumann, W., Computerized automation of an experiment in the interplanetary space, Doctoral dissertation, Technical University of Munich, 2000.

## IO REVEALED IN THE JOVIAN DUST STREAMS

Amara Graps<sup>1</sup>, Eberhard Grün<sup>1</sup>, Harald Krüger<sup>1</sup>, Mihály Horányi<sup>2</sup>, and Håkan Svedhem<sup>3</sup>

<sup>1</sup>Max-Planck-Institut für Kernphysik, Heidelberg, Germany

<sup>2</sup>LASP, Boulder, USA

<sup>3</sup>ESTEC, Noordwijk, Netherlands

### ABSTRACT

The Jovian dust streams are high-speed bursts of submicron-sized particles traveling in the same direction from a source in the Jovian system. Since their discovery in 1992, they have been observed by three spacecraft: Ulysses, Galileo and Cassini. The source of the Jovian dust streams is dust from Io's volcanoes. The charged and traveling dust stream particles have particular signatures in frequency space and in real space. The frequency-transformed Galileo dust stream measurements show different signatures, varying orbit-to-orbit during Galileo's first 29 orbits around Jupiter. Time-frequency analysis demonstrates that Io is a localized source of charged dust particles. Aspects of the particles' dynamics can be seen in the December 2000 joint Galileo-Cassini dust stream measurements. To match the travel times, the smallest dust particles could have the following range of parameters: radius: 6 nm, density: 1.35–1.75 g/cm<sup>3</sup>, sulfur charging conditions, which produce dust stream speeds: 220\450 km s<sup>-1</sup> (Galileo\Cassini) and charge potentials: 5.5\6.3 V (Galileo\Cassini).

Key words: Jovian dust streams, frequency analysis, Cassini-Galileo dust measurements, Io's volcanoes.

### 1. OVERVIEW

The Jovian dust streams are high-speed collimated streams of submicron-sized particles traveling in the same direction from a source in the Jovian system. They were discovered in March 1992 by the cosmic dust detector instrument onboard the Ulysses spacecraft, when the spacecraft was just past its closest approach to Jupiter. Observations of the Jovian dust stream phenomena continued in the next nine years. A second spacecraft, Galileo, now in orbit around Jupiter, is equipped with an identical dust detector instrument to Ulysses' dust instrument. Before and since the Galileo spacecraft's arrival in the Jupiter system in December 1995, investigators recorded more dust stream observations. In July and August 2000, a third spacecraft with a dust detector (combined with a chemical analyzer), Cassini, traveling

on its way to Saturn, recorded more high-speed streams of submicron-sized particles from the Jovian system. The many years-long successful Jovian dust streams observations reached a pinnacle on December 30, 2000, when both the Cassini and Galileo dust detectors accomplished a coordinated set of measurements of the Jovian dust streams inside and outside of Jupiter's magnetosphere.

Indirect methods applied by previous researchers have pointed to Io being the simplest explanation for the question of the origin of the Jovian dust streams. We first show by direct methods that Io is the source of the Jovian dust streams. To address the issue of identifying Io directly in the Galileo dust detector data, we apply time-frequency analysis, in particular, Fourier methods, to the Galileo dust data. Additional frequency signatures, such as amplitude modulation, also emerge from the time-frequency analysis.

The second part of this paper focuses on the dust streams dynamics. Here, we apply a detailed Jovian particles and fields model to simulate a dust stream particle's trajectory as the particle moves from Io's orbit through Jupiter's magnetosphere and beyond. Through the model, we show one possible set of parameters that match the travel times seen in the December 30, 2000 Galileo-Cassini joint dust stream measurements.

### 2. IO'S FREQUENCY FINGERPRINT

In order to find Io's frequency 'fingerprint' in the Galileo dust detector data, we followed the following steps: 1) we transformed the Galileo dust detector data into frequency space via periodograms, 2) we noted frequency patterns such as amplitude modulations, 3) we compared the frequency-transformed Galileo data with synthetic data, and, 4) we noted spacecraft effects such as Doppler shifts.

#### 2.1. Time-Frequency Analysis via Periodograms

The "classic" or Schuster periodogram (Bretthorst 1988) is conventionally defined as the modulus-squared of the

discrete Fourier transform. If the input time series contains a periodic feature, then the periodogram can be calculated for any frequency and it displays the presence of a sinusoid near one frequency value as a distinct peak in the spectrum. The Lomb-Scargle periodogram applied here is a slightly modified version of the classic periodogram giving a simpler statistical behavior (Scargle 1982).

Our best Galileo dust dataset for detecting Io's frequency fingerprint emerged from the earlier Galileo orbits around Jupiter, because the spacecraft orbital geometry of the first years of the Galileo mission favored higher fluxes of dust stream particles. Therefore, by combining two years of the early data, we gained a higher signal-to-noise dataset. In Fig. 1, we show a Lomb-Scargle periodogram for the first two years, 1996-1997, of Galileo dust impact rate data. This particular periodogram is the best example from the Galileo dust detector data showing, with high confidence: Io's frequency signature, Jupiter's frequency signatures, and amplitude modulation effects. The periodogram shows the following frequency signatures.

#### Frequency Summary of Fig. 1

1. A strong peak near the origin,
2. An asymmetric peak: maximum at  $0.6 \text{ day}^{-1}$ , center at  $0.7 \pm 0.2 \text{ day}^{-1}$ ,
3. An asymmetric peak: center at  $1.7 \pm 0.2 \text{ day}^{-1}$ ,
4. A tall peak: center at  $2.4 \pm 0.1 \text{ day}^{-1}$ ,
5. A peak: center at  $3.1 \pm 0.1 \text{ day}^{-1}$ ,
6. Harmonics of the previous three peaks, and
7. Progressively smaller and less-defined peaks.

#### 2.2. Amplitude Modulation in Frequency Space

Frequencies in frequency space can interact in numerous ways. We interpret the frequency peaks, seen in Fig. 1, to be the result of Io's frequency of orbital rotation, Jupiter's magnetic field frequency of rotation, and an interaction between these two frequencies called amplitude modulation (AM). The simplest case of AM is a sinusoid modulating the amplitude of a carrier signal, which is itself a sinusoid. Then the carrier signal is broken down in frequency space into several sinusoidal oscillations:  $x \approx \sin(\omega_0 t) + \sin(\omega_0 t) \sin(\Omega t)$ , which can be converted to sums of frequencies using a trigonometric identity for sine products. The result is a signature in frequency space that displays a carrier frequency:  $\omega_0$  with side frequencies ("modulation products"):  $(\omega_0 + \Omega)$  and  $(\omega_0 - \Omega)$ .

The process of amplitude modulation applies to Io's orbital and Jupiter's rotational frequencies in the following way. Jupiter's rotation period is 9.8 hours corresponding to a frequency of 2.4 rotations per day. Io's orbital period (and rotation period) is 1.8 days, corresponding to a frequency of 0.6 rotations per day. If the dust originates from Io, and the dust flux is modulated by Jupiter,

then the spectrum in frequency space would appear like the spectrum in Fig. 1, where the modulation products (sidelobes) at Jupiter's frequency at full and half-rotations are due to Jupiter's frequency modulating Io's frequency of orbital rotation. The frequency difference between Jupiter's rotational frequency and each of the sidelobes is the same frequency as Io's frequency of orbital rotation. In addition, if one or both of the original signals have broad spectra, then the spectrum of the modulation products will be broadened to the same extent (since the modulation process is linear). Therefore, the spread of Io's peak is repeated in the same way for the sidelobes of Jupiter's frequency peaks (full and half-rotation).

Modulation products appeared in about 20% of the first 29 frequency-transformed Galileo orbits. Galileo's orbit E4 was the first orbit for which a hint of the amplitude modulation appeared, then in orbit G8, the signature was unmistakable. Other Galileo spacecraft orbits for which one can clearly see the modulation products are: C10, E18, and G29. Periodograms of each of the individual orbits can be seen in Graps (2001).

#### 2.3. Synthesizing the Frequency-transformed Dust Stream Data

The main physical processes behind the frequency-transformed data can become clearer when one synthesizes data and compares the synthesized data to the real data. We have synthesized a spectrum, using typical periods from Galileo's dust impact rate data, a Jupiter rotation and half rotation period, and an Io orbital rotational period, which show in the real data. We added some Gaussian-distributed noise, and after transforming the synthesized data into frequency space with an FFT, frequency peaks appear with their modulation products, which are in the same locations as those in the 1996-1997 Galileo dust detector periodogram. Figures of the synthesized time series and frequency-transformed data can be seen in Fig. 2.

#### 2.4. Spacecraft Effects in Frequency Space

Several Galileo spacecraft orbital characteristics can be identified in the frequency-transformed data. The first effect is at the origin. For each orbit, the dust instrument receives more dust impacts while in the inner Jovian system than while in the outer Jovian system, which in frequency space, results in a peak at the origin. The second spacecraft effect is a Doppler effect between Galileo and Io, as the "observer" and the "source." In frequency space, the result is that both the Io and the Jupiter peaks can be smeared by Doppler shifts. The Io frequency peak Doppler shift is to shorter periods. This asymmetry appears in the modulation products, as well. A table of the Doppler shift trends can be seen in Graps (2001).

## 2.5. August-September 2000 Dust Storm

In August and September 2000, both Cassini (travelling by at  $\sim 1$  A.U. from Jupiter), and Galileo (in an orbit carried to  $\sim 250 R_J$  from Jupiter, where  $R_J = 7.134 \cdot 10^9$  cm is the equatorial radius of Jupiter) detected increases in the rate of dust impacts, which were approximately 100 times their nominal impact rates. In the frequency-transformed data from both spacecraft, Io's frequency signature swamped all other frequency signatures in the Galileo data, which was noteworthy, because both spacecraft were located far from Jupiter, outside of Jupiter's magnetosphere. Galileo detected the 'dust storm' earlier during the perijove portion of its G28 orbit, during Days  $\sim 218$ –240. After Day 240, Galileo's impact rate decreased, however, Cassini observed high impact rates particularly on  $\sim$ Day 251 and  $\sim$ Day 266. (See the periodogram of the dust impact rate in Fig. 3). Cassini's dust detector's observational geometry is very different from Galileo's, however, by accident, Cassini captured the dust storm approximately 1–2 weeks after Galileo detected the dust storm.

## 2.6. Conclusions of Io's Frequency Fingerprint

Frequency analysis via Fourier techniques of the Galileo dust data provides our first direct evidence of an Io dust source. The presence of Io's rotation frequency argues that Io is a localized source of charged dust particles because charged dust from diffuse sources would couple to Jupiter's magnetic field and appear in frequency space with Jupiter's rotation frequency and its harmonics. A confirmation of Io's role as a localized charged dust source arises through the modulation effects.

The Galileo dust detector periodogram data shows variabilities, orbit-to-orbit, even for some orbits which share similar orbital geometry. This orbit-to-orbit variability is a clue that, either the intervening medium or Io itself, i.e. its volcanoes, is a source of the variability.

## 3. JOVIAN DUST STREAM DYNAMICS

To describe the dynamics of the dust streams, we apply a detailed Jovian particles and fields model to simulate a dust stream particle's trajectory as the particle moves from Io's orbit through Jupiter's magnetosphere and beyond. For the model, one needs to assume approximations for the following: 1) Jupiter's magnetic field, 2) Jupiter's plasma, 3) dust particle density, 4) dust particle optical property, 5) charging processes, and 6) forces.

### 3.1. Jovian Dust Stream Model Details

We approximate Jupiter's magnetic field by implementing Connerney's  $O_4$  or  $O_6$  model (Connerney 1981, 1993), which is a quadrupole expansion of the planet's

internal field. Additionally, we hinge Connerney's current sheet described in Connerney et al. (1981), to approximate Jupiter's magnetodisk. Connerney's sheet implementation considers the magnetodisk as a perturbation to Jupiter's internal field.

Jupiter's plasma is approximated using a plasma model which is a fit to the Voyager 1 and 2 cold plasma measurements, described in Bagenal (1989). We assumed a constant mixing ratio of 50% between single ionized oxygen and sulfur ions.

For the dust particle density, we use density values  $1.35$ – $2.0$  g/cm<sup>3</sup>. The dust particle's optical properties are manifested via  $Q_{pr}$ , which affects the particle's dynamics through the radiation pressure force. For this work, a  $Q_{pr}$  value for the dust particle is calculated based on the particle's size, and following the curve in Burns et al.'s classic paper: Burns et al. (1979).

The charge of the dust particles is approximated by summing over the currents: photoelectron emission, ion and electron collection, and secondary electron emission. The charge of the particle, which varies in time, is integrated simultaneously with the particle's acceleration. Here, we model the acceleration by considering the following forces: Jupiter's gravitational force, the light pressure force, the Lorentz force, and the solar gravitational force (Horányi et al. 1997). We have neglected the neutral gas and plasma (Coulomb) drag forces on the dust particle because the time-scales used in these runs are short (hours to a day), compared to the time-scales over which those forces have an effect.

More details of the Jovian dust stream model can be found in M. Horányi's papers, such as Horányi et al. (1997), and in Graps (2001).

### 3.2. Dynamics Results

A window of particle sizes exists for which dust particles can escape from traveling in Keplerian orbits in Jupiter's magnetosphere. For small dust particles, their motion is as plasma ions and electrons, which gyrate about Jupiter's magnetic field lines. For large dust particles, their motion is governed by gravity. From Io's orbital location, the window of dust particle sizes for escaping particles is approximately radius 5 nm to 35 nm. This particle size is strongly dependent on the charging assumptions, especially the secondary electron emission material assumption. In our numerical experiments thus far, we found that smaller dust particles can be ejected when the impacting ion or electron energy is lower than the energy of other impacting ions or electrons in the secondary electron emission process. For example, a particle with sulfur properties can be ejected from Io's location with a minimum size 4 nm, versus a particle with silicate material properties, which can be ejected from Io's location with a minimum size 6 nm.

As the dust stream particle moves through the Jovian magnetosphere, equilibrium potential is rarely reached. Therefore, as the particle moves outward, it continues

to collect charges, which further accelerate the particle. We now think that the Jovian dust stream particles move faster (at least 400 km/sec) than previously assumed in the earlier work presented by Zook et al. (1996), which suggested dust speeds, at least 200 km/sec.

### 3.3. Joint Measurements: December 2000 from Galileo & Cassini

On December 30, 2000, the Cassini spacecraft closely flew by Jupiter, providing a simultaneous two-spacecraft measurement (Cassini-Galileo) of particles from one collimated stream from the Jovian dust streams. Particles in a stream were detected by Galileo, as the spacecraft was orbiting inside of the Jovian magnetosphere close to Ganymede (8–12 Jovian radii), and then particles in the stream traveled to Cassini, as Cassini flew by Jupiter at approximately 140 Jovian radii. Figure 4 shows the dust impact rate data for the dual dust stream measurements, the gold line denotes the Galileo rates and the green line indicates the Cassini rates. We assumed that the same dust stream at each spacecraft began where the black horizontal line marks the midpoint of the peak rise in impact rate. The travel time between the two black-marked peaks is approximately 7 hours. One goal of the dynamical modeling was to match this travel time. From preliminary modeling, Fig. 5 shows the result of one possible trajectory of a Jovian dust streams particle released near Io's orbit. Here, the smallest dust particles could have the following range of parameters: size: 6 nanometers, density: 1.35–1.75 g/cm<sup>3</sup>, initial charge potential: 1–4 V, secondary electron emission yield: 3.0, dependent on a maximum electron energy 300 eV, and a photoelectron emission yield: 0.1–1.0, which produce dust particle speeds: 220\450 km s<sup>-1</sup> (Galileo\Cassini) and charge potentials: 5.5\6.3 V (Galileo\Cassini). Smaller and larger particles than 6 nanometers result in the wrong direction towards Cassini, and with travel times that are either too fast or too slow.

## 4. SYNOPSIS

Our work from frequency analysis shows Io as the dominant source of the Jovian dust streams. The variability seen in the frequency analysis shows that we might be able to use dust stream measurements to monitor Io's volcanoes' plume activity.

Our charging and dynamics modeling, (more details in Graps (2001)), shows that the dust streams' equilibrium potential is rarely reached in the Jovian magnetosphere, and that the Jovian dust stream particles travel faster than found previously in Zook et al. (1996). In our preliminary analysis and modeling of the Galileo-Cassini dust stream measurements, we show that one set of conditions, which can match the travel times, gives a dust streams speed at Galileo of 220 km s<sup>-1</sup>, with a charge potential: 5.5 V, and a dust streams speed at Cassini of 450 km s<sup>-1</sup>, with a charge potential: 6.3 V.

## ACKNOWLEDGEMENTS

The authors gratefully acknowledge the hard work of the Galileo and Cassini Dust Science Teams. Funding provided by the Deutsches Zentrum für Luft-und Raumfahrt E.V. (DLR), and the Deutsche Forschungsgemeinschaft (DFG).

## REFERENCES

- Bagenal F., 1989, In: Belton M., West R.A., Rahe J. (eds.) *Time-Variable phenomena in the Jovian system*, SP-494, 1–403
- Bretthorst G., 1988, *Bayesian Spectrum Analysis and Parameter Estimation*, Springer-Verlag
- Burns J.A., Lamy P.L., Soter S., 1979, *Icarus*, 40, 1
- Connerney J.E.P., Sep. 1981, *J. Geophys. Res.*, 86, 7679
- Connerney J.E.P., Oct. 1993, *J. Geophys. Res.*, 98, 18,659
- Connerney J.E.P., Acuna M.H., Ness N.F., 1981, *J. Geophys. Res.*, 86, 8360
- Graps A.L., Jul. 2001, *Io Revealed in the Jovian Dust Streams*, Ph.D. thesis, Ruprecht-Karls-Universität Heidelberg
- Horányi M., Grün E., Heck A., 1997, *Geophys. Res. Letters*, 24, 2175
- Scargle J.D., 1982, *Ap. J.*, 263, 835
- Zook H.A., Grün E., Hamilton D.P., et al., 1996, *Science*, 274, 1501

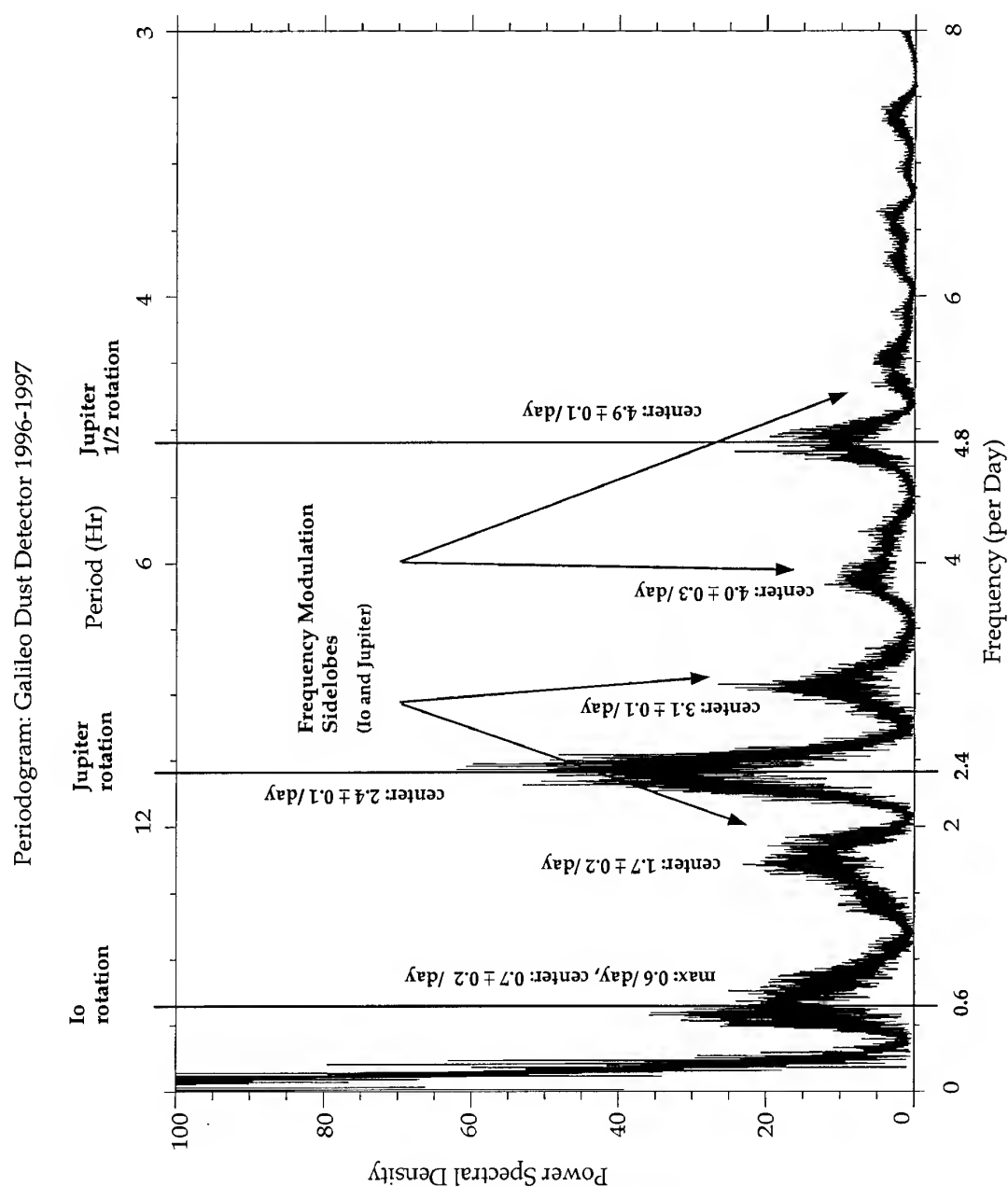


Figure 1. A Lomb-Scargle periodogram for the first two years, 1996-1997, of Galileo dust impact rate data, with the specific signatures described in the text. Io's frequency of orbital rotation, in particular, can be seen here in frequency space, which provides our first direct evidence that Io is a source of the Jovian dust streams. A confirmation of Io's role as a localized charged dust source arises through the modulation effects. The vertical solid lines mark Io's orbital and Jupiter's rotational periods, and the arrows point to Jupiter's modulation products with Io straddling Jupiter's frequency. The first harmonic of Jupiter's rotation frequency is visible at ( $\omega_1 = 4.8 \text{ day}^{-1}$ ) and Jupiter's modulation products with Io, which are straddling that first harmonic peak, can be seen, as well. The strong frequency peak near the origin at 1 over Galileo's orbital period is due to the Galileo spacecraft orbital geometry.

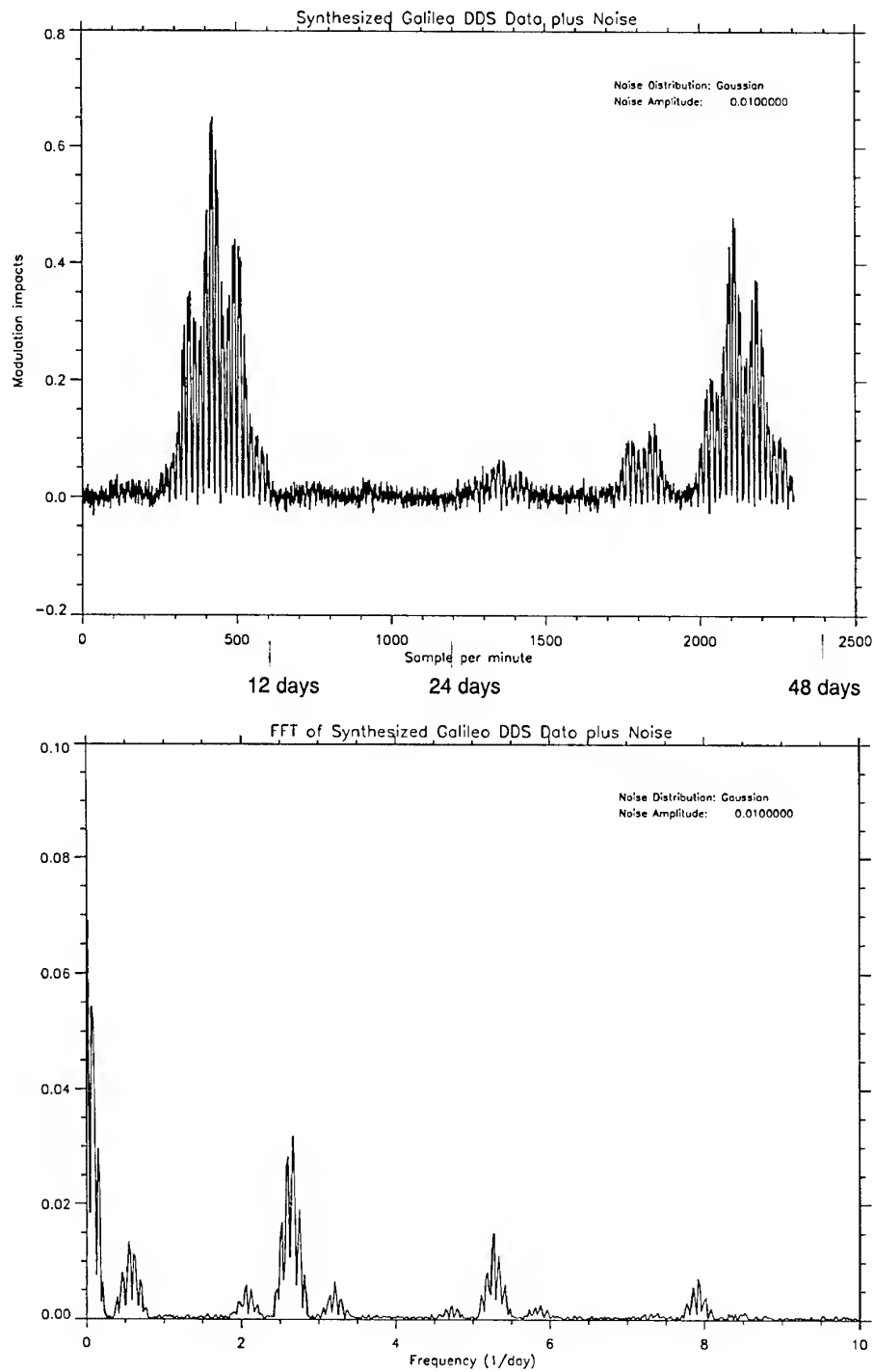


Figure 2. Top: A synthetic impact rate dataset, with added Gaussian noise, which includes the following periods: 48 days for Galileo's orbit, 9 and 17 days for smaller data blocks, a Jupiter rotation and half rotation period, and an Io rotation period. Bottom: An FFT of the synthetic rate dataset. Galileo's motion (at the origin), Io's frequency of orbital rotation ( $0.6 \text{ d}^{-1}$ ), Jupiter's full frequency ( $2.4 \text{ d}^{-1}$ ) and half-frequency ( $4.8 \text{ d}^{-1}$ ) of rotation can be seen, as well as the Io-Jupiter amplitude modulation products (sidelobes around Jupiter's frequencies).

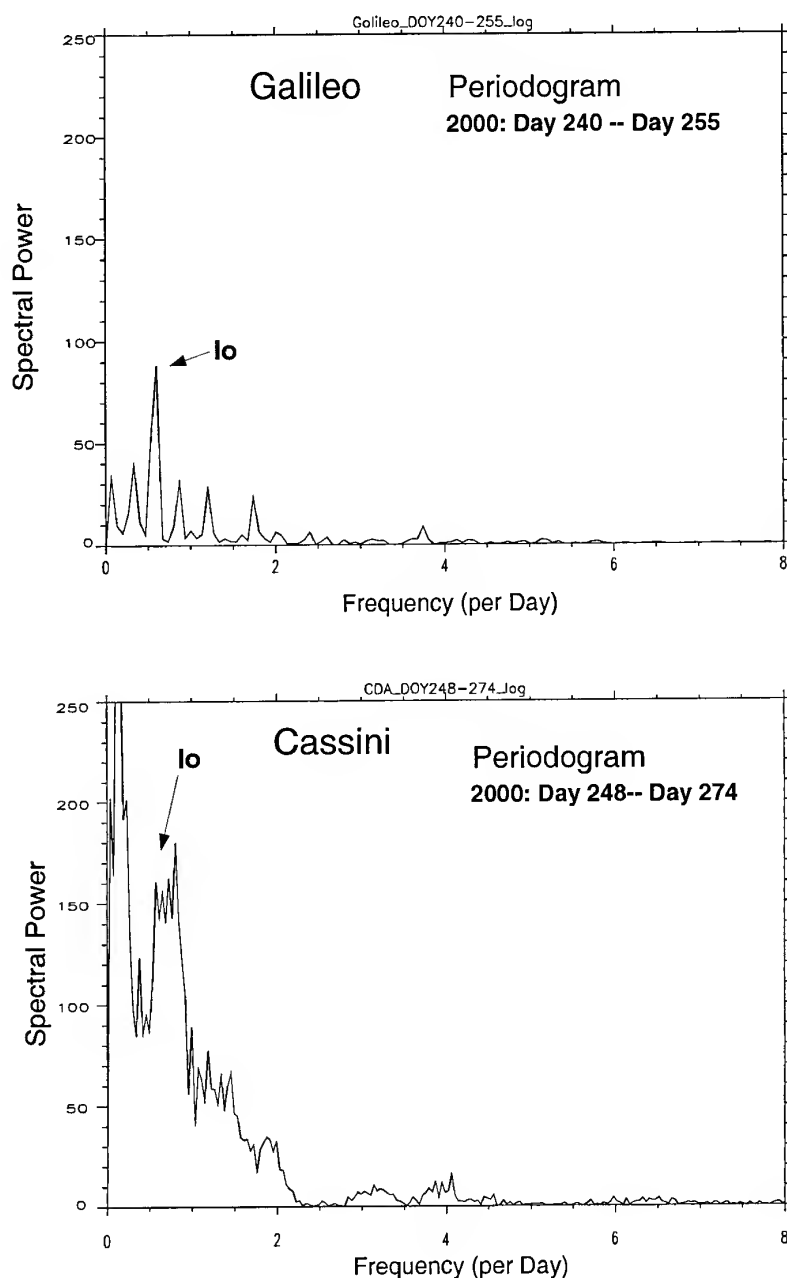


Figure 3. A Lomb-Scargle periodogram of dust impact rate data from Galileo (top) and Cassini (bottom) during selected days in July and August 2000. The Galileo data occurred during Galileo's G28 orbit, when the spacecraft was located outside of Jupiter's magnetosphere at  $\sim 250 R_J$  (where  $R_J = 7.134 \cdot 10^9$  cm is the equatorial radius of Jupiter). This Io dust streams storm detected in interplanetary space was stronger in the earlier portion of this orbit close to perijove on Days 218–240 than in the later days, when Cassini detected the storm. Cassini observed high impact rates particularly on  $\sim$ Day 251 and  $\sim$ Day 266, when the spacecraft was traveling far outside of Jupiter's magnetosphere at  $\sim 1$  A.U.

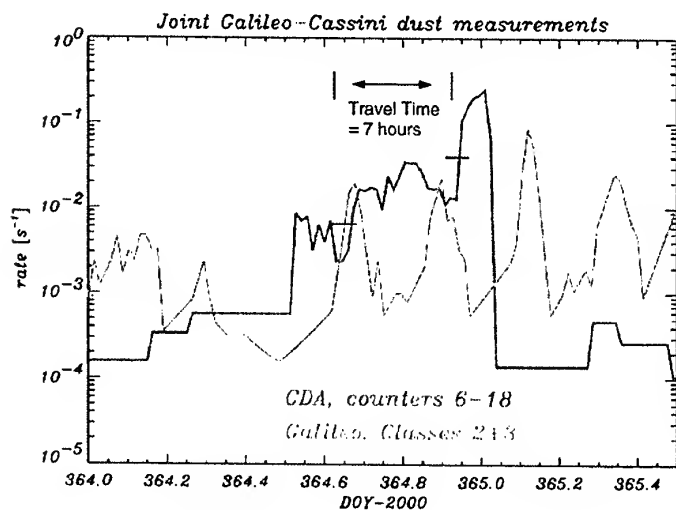


Figure 4. Dust impact rates from the Cassini-Galileo dual dust stream measurements performed on December 30, 2000. The marked travel time, 7 hours, is the time for a dust particle in a collimated dust stream to travel from Galileo to Cassini.

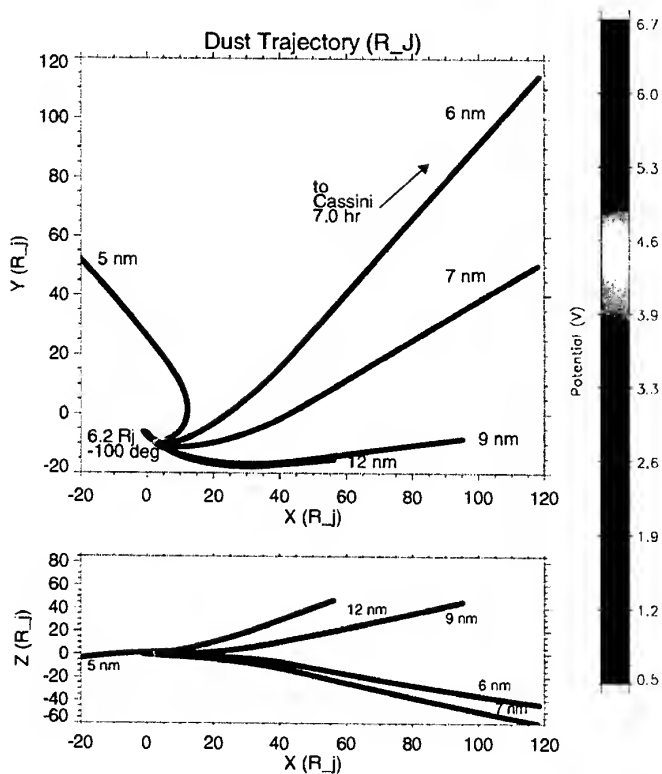


Figure 5. Dust particle trajectories in x-y (top) and x-z (bottom) Jupiter-centered coordinates for different sized particles released from a near-Io Keplerian orbit at 6.2 Jovian radii. The colors indicate the values of the particle's charge potentials. The trajectory with the arrow indicates a reasonable trajectory which would bring the particle near to the Cassini spacecraft.

## INTERPLANETARY DUST MODEL: FROM MICRON-SIZED DUST TO METEORS

Valeri Dikarev<sup>1,2</sup>, Eberhard Grün<sup>1</sup>, Markus Landgraf<sup>3</sup>, W. Jack Baggaley<sup>4</sup>, and David P. Galligan<sup>4</sup>

<sup>1</sup>Max-Planck-Institut für Kernphysik, Heidelberg, Germany

<sup>2</sup>Astronomical Institute of St. Petersburg State University, Russia

<sup>3</sup>European Space Agency, ESOC, Darmstadt, Germany

<sup>4</sup>University of Canterbury, Christchurch, New Zealand

### ABSTRACT

New populations of interplanetary dust are proposed for the ESA meteoroid model. Formulation of the new model extends earlier meteoroid models and is now tied to orbital evolution of the interplanetary dust. To validate the new model, infrared emission observations with COBE DIRBE instrument, impact counts with the dust detectors aboard Galileo and Ulysses spacecraft, and the radar meteors monitored with AMOR are used. Incorporation of meteor data in the model is discussed.

### 1. INTRODUCTION

Divine (1993) constructed an empirical model of the interplanetary meteoroids which attempted to match variety of data available by that time. The model was used by NASA to estimate fluxes of meteoroids on spacecraft in the Solar system. Its version METEM by Garrett et al. (1999) is currently applied in meteoroid hazard studies by NASA, while ESA had developed an advanced version of the Divine model with useful extensions (Staubach & Grün 1995; Grün et al. 1997).

In all the above-listed models, the interplanetary dust particles were assumed to move along Keplerian orbits with uniform distributions in mean anomaly and argument and longitude of perihelion. The distributions in perihelion distance, eccentricity and inclinations were separated, each represented by a table of values at appropriate abscissas, and interpolation was applied between the abscissas. The distribution in mass was separated from the distributions in orbital elements as well.

Such a formulation of the model allows to calculate fluxes, spatial number densities, and line-of-sight brightness integrals in wide variety of observation conditions, making a basis for synthesis of data obtained by various methods. This is also the way to suppress observational biases through statistical inference of the model parameters from series of observations subject to random noise.

Divine (1993) incorporated in the model results of a radar

meteor survey, several in-situ dust experiments, zodiacal light observations and lunar microcrater data. He began with radar meteor data and already had to introduce two populations since the data did not support mathematical separability of the distribution function in orbital elements he assumed. Three more populations were introduced in order to reproduce in-situ flux measurements with dust experiments on Pioneer 10 and 11, Helios-1, Galileo and Ulysses, and zodiacal light observations.

New data have now become available which can be used to improve the model. Firstly, the infrared observations made by the COBE satellite, which cover a large area of the sky, are highly homogeneous and quite accurate. Ten bands cover the infrared spectrum from 1.25  $\mu\text{m}$  to 240  $\mu\text{m}$  with the dust thermal emission being dominant in the 4.9, 12.5, 25 and 60  $\mu\text{m}$  wavelength bands. Next, there are impact counts from Ulysses processed up to the end of 1999. Finally, the advanced meteor radar AMOR in New Zealand (Baggaley et al. 1994) is currently monitoring the upper atmosphere counting  $\sim 10^3$  meteors each day. The radar data is analysed to determine heliocentric orbital elements of the dust particles and is expected to produce a database of about  $10^6$  orbit determinations by the end of 2001. We replace Sekanina and Southworth radar meteors because some doubts were raised by Taylor (1995) about processing of that data.

In addition to incorporation of the new data, we extend the formulation of the model beyond Keplerian dynamics and account for the orbital evolution of dust particles.

### 2. INVENTORY OF ZODIACAL CLOUD

Since 1993 when Divine introduced his empirical approach, new theoretical results have become available, and older ones have been approved. Ishimoto (2000) suggested a semianalytical description of the interplanetary dust cloud which describes the effects of different orbital evolution for different size ranges. He stated the problem in the form of continuity equation for the number density  $n(m, r)$  as a function of particle mass  $m$  and distance from the Sun  $r$ . Although orbital eccentricities

of dust particles were disregarded in the model, making the description of the radial transport of dust rather approximate, the model is still able to explain the shape of the mass distribution at 1 AU (Grün et al. 1985). Following (Ishimoto 2000), we introduce the mass parameter  $m_0$  that separates the two regimes of particle evolution: Poynting-Robertson drag and collisional destruction.

Small particles ( $m \ll m_0$ ) evolving under the Poynting-Robertson drag. They have a small probability of colliding with other particles and their lifetime is determined solely by the rate of the drag which is inversely proportional to the solar radiation pressure-to-gravity ratio  $\beta \propto m^{-1/3}$ . The fragment size distribution in impact ejecta or collisional fragmentation is  $\propto m^{-\gamma}$ , where  $\gamma \approx 5/3$  can be assumed (see Ishimoto 2000). This results in the mass distribution

$$n(m) \propto m^{-\gamma+1/3}. \quad (1)$$

Large particles ( $m \gg m_0$ ) are destroyed by collisions before their semi-major axes can change noticeably under the Poynting-Robertson drag and their lifetimes are constrained by collisions which have a frequency proportional to the inverse cross-sectional area ( $\propto m^{-2/3}$ ). This yields, for the regions of continuous replenishment of the dust,

$$n(m) \propto m^{-\gamma-2/3}. \quad (2)$$

Large particles cannot be supplied by other regions, unless distant encounters with planets are taken into account.

At 1 AU the critical mass  $m_0$  is about  $10^{-6}$  g.

The two mass ranges allow for two distinct types of dynamical behavior. Small grains mainly drift under the Poynting-Robertson drag, while large grains stay on the orbits of their parent bodies or get pulled into different orbits due to gravitational scattering by major planets.

The evolution of grains under the Poynting-Robertson drag is well understood. Since this effect does not alter the inclination, it is reasonable to consider the distribution of particles only in semimajor axis  $a$  and eccentricity  $e$  in order to construct a comprehensive picture of the spatial distribution of particles. This was done by Leinert et al. (1983) who solved the continuity equation for the distribution function  $f(a, e)$  determined by the Poynting-Robertson drag and (in a rough approximation) by collisions, with the collisional term being omitted here, for an arbitrary source distribution function  $f_0(a, e)$ :

$$f(a, e) \propto \frac{2}{5\sqrt{1-e^2}e^{1/5}} \times \int_{\tilde{e}=e}^1 f_0(\tilde{a}, \tilde{e}) \tilde{a}^2 \tilde{e}^{-4/5} (1-\tilde{e}^2) d\tilde{e}, \quad (3)$$

where  $\tilde{a}$  is calculated according to the integral of motion under the Poynting-Robertson drag (Wyatt & Whipple 1950)

$$\tilde{a} \frac{1-\tilde{e}^2}{\tilde{e}^{4/5}} = a \frac{1-e^2}{e^{4/5}}. \quad (4)$$

Recently a similar idea was presented by Gor'kavyi et al. (1998) who were able to derive a "reference model" of the zodiacal dust distribution in orbital elements. Gor'kavyi et al. (1997), Ozernoy et al. (2000) pointed to gravitational scattering by the giant planets as well, the effect previously discussed very scarcely or hidden in the "black box" of numerical integrators in favour of resonances (Liou et al. 1995, 1996, 1999; Grogan et al. 2001). Gravitational scattering obviously shapes the distribution of short-period comets, and Ozernoy et al. (2000) predicted belts of millions of comet-sized bodies along the orbits of giant planets. These bodies, as well as large meteoroids and boulders spalled from asteroids and undergone distant encounters with Jupiter, serve as sources of small dust observed at 1 AU as well.

An inventory of zodiacal dust populations is presented in Fig. 1 and 2. Fig. 1 features one-dimensional distributions of dust in orbital elements, after the integration over the other dimensions. Asteroids and comets already reveal the orbits of large particles spalled from or erupted by the parent bodies. Since there is a limited number of known comet orbits only, distributions of comets are not so smooth as those of asteroids. Asteroids and comets, as well as large asteroidal and cometary debris, generate small dust that evolves under the Poynting-Robertson drag. The large debris from comets and asteroids might be scattered by planets, as long as the orbits intersect. Those scattered debris particles constitute a population and generate small dust through collisions. Fig. 2 illustrates same populations of dust in two dimensions.

### 3. NEW MODEL DESIGN

New model design admits many — a number well above Divine's five — populations with the distribution functions defined a-priori. Each population is constructed in order to represent a possible structure of the interplanetary dust cloud in accordance with long-term evolution of dust grain orbits. For example, the orbits of dust particles of sizes from 1 to 100 microns should evolve under P-R drag. Consequently, distribution of these particles in semimajor axis and eccentricity should look analogous to the distributions of small cometary or asteroidal particles in Fig. 1 and 2.

As follows from the above example, distribution functions of the new populations are not separable in the form suggested by Divine (1993). The distributions are rather complicated, but since their relative profiles have been fixed, each of them add only one unknown parameter to the model — a normalisation factor. Each prediction  $C_j$  for the observation  $O_j$  is described as a linear combination of the normalisation factors  $x_i$

$$O_j \approx C_j = \sum_{i=1}^N w_{ij} \cdot x_i, \quad j = 1, \dots, M. \quad (5)$$

where  $w_{ij}$  is the contribution of  $i$ -th population to  $j$ -th observation, i.e. prediction of the observed value (brightness, flux, number of craters on a surface exposed to meteoroids) of  $i$ -th population assuming the normalisation factor equals one.

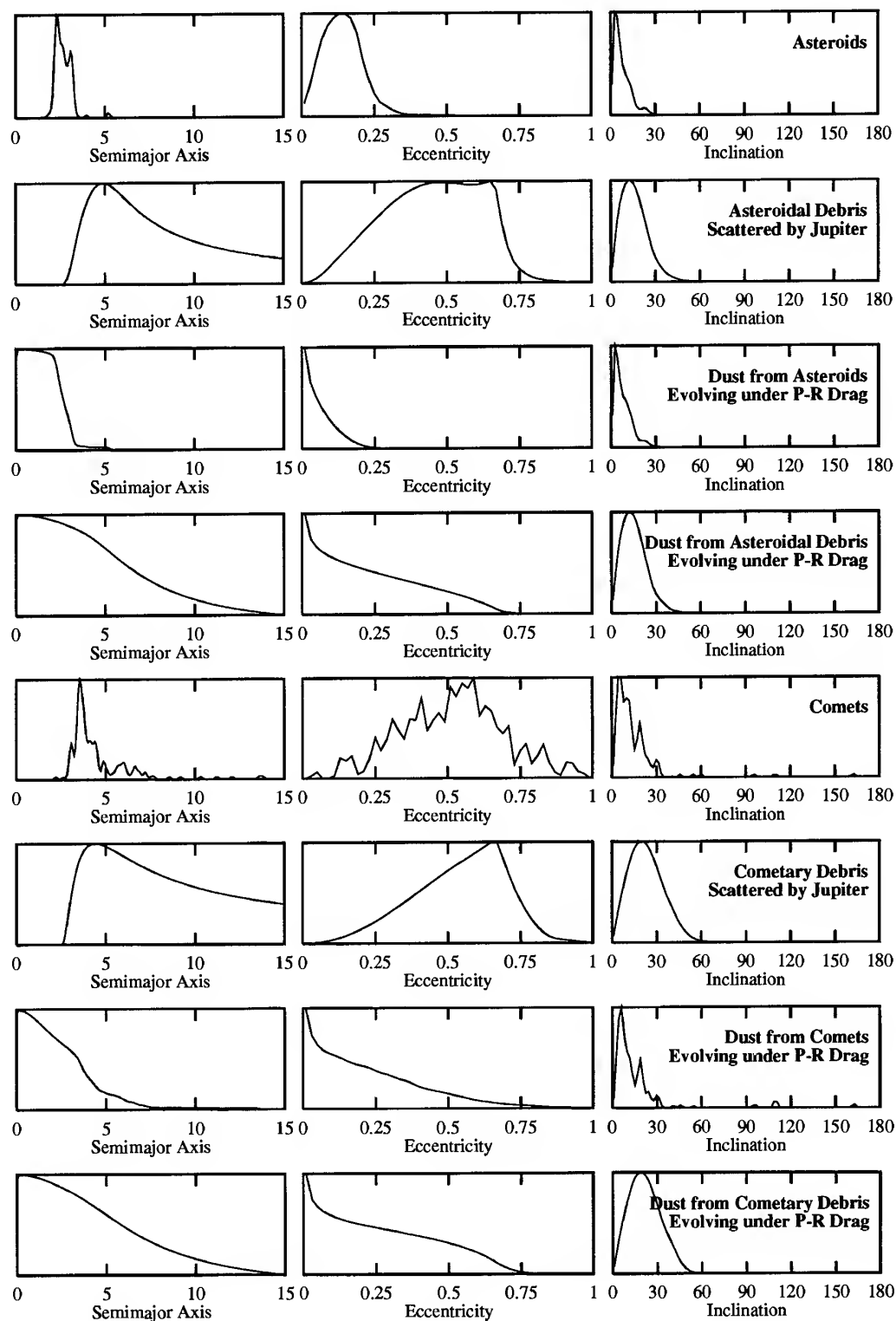


Figure 1. Inventory of zodiacal cloud. Plotted are the distributions in orbital elements for different populations of dust expected in the cloud. Asteroids, comets and debris derived from them and scattered by Jupiter represent the populations of big particles not subject to the Poynting-Robertson drag.

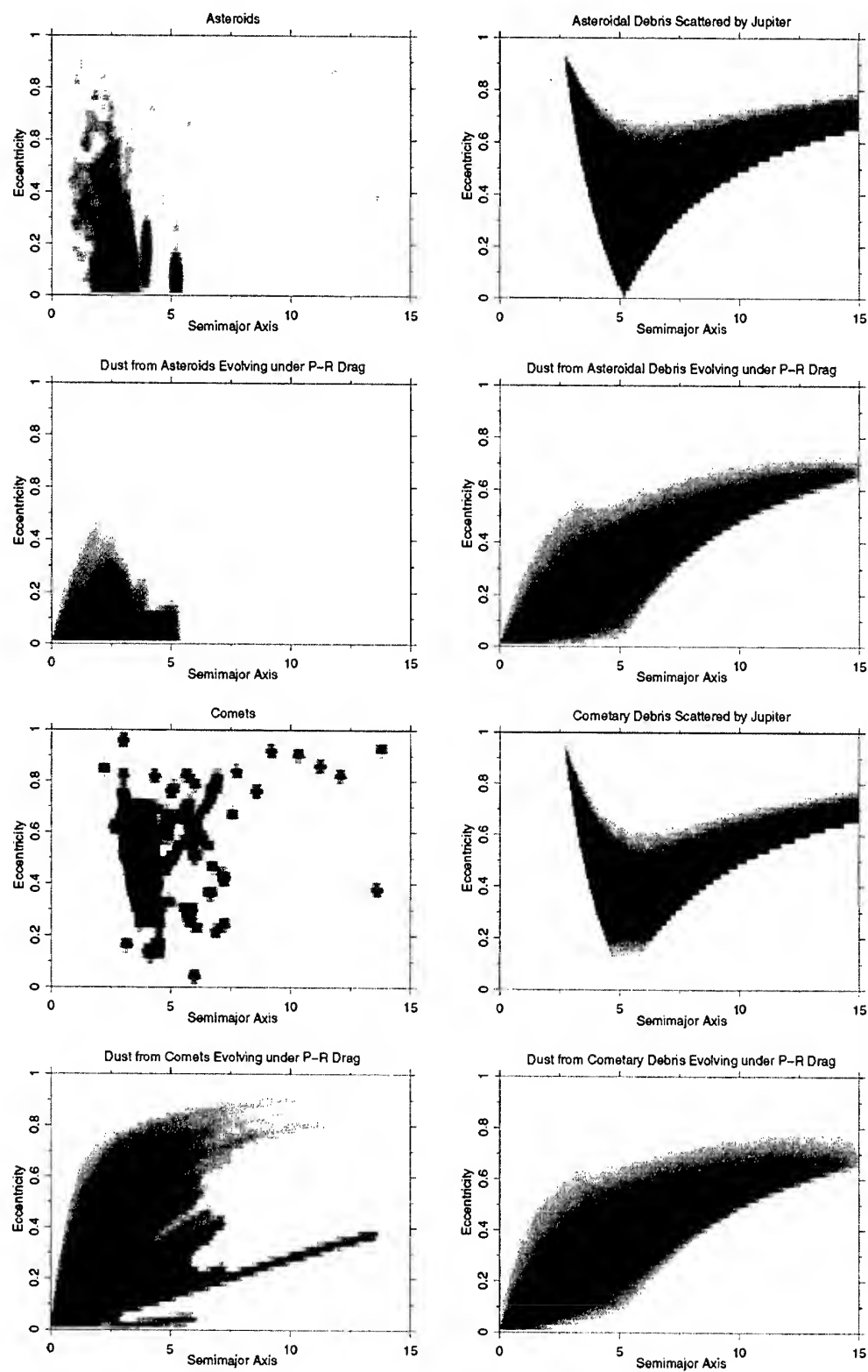


Figure 2. Inventory of zodiacal cloud. Plotted are the 2-D distributions in semimajor axis and eccentricity for the populations of dust introduced in Fig. 1. The gray scale intensity is proportional to the logarithm of the distribution function value.

In order to determine the normalisation factors  $x_i$ , a linear inverse problem has to be solved. For both Gaussian and Poisson noises relevant to typical line-of-sight observations and in-situ impact counts, respectively, procedures exist to find the maximum likelihood estimates of  $x_i$  given the biased observations  $O_j$ .

The new model design has several advantages over the previous one. The amount of computations needed to adjust the model to the observations is decreased substantially since the observables are in linear relationships with the normalisation factors. Each individual observation — no matter whether it is a line-of-sight brightness measurement or in-situ impact count — may be expanded in a weighted sum of individual population contributions (5). This is done once only when a new population is introduced or a new observation is incorporated in the model, and then standard procedures can be applied to solve the inverse problem. In the Divine model one had to recalculate all predictions each time any parameter is changed. This is especially cumbersome when the inverse problem is solved through trial-and-error iterations.

The new design allows for an easy and comprehensive extension of the model: To add a new population or to modify an old definition, it is sufficient to expand observations in sums of weighted population contributions, and to re-adjust each population's norm. It is also straightforward to add new data sets. The procedure is to properly describe the response function  $w_{ij}$  of the instrument and the conditions of the observations, to calculate population contributions to the observed values and to re-adjust the normalisation factors.

Employment of orbital evolution gives credibility to the model predictions where no observation data is available, i.e. the model-based extrapolations of existing measurements should, in general, be more reliable than in the Divine model which extrapolated measurements in an arbitrary way.

#### 4. MODEL FIT TO REMOTE OBSERVATIONS

The COBE DIRBE instrument accomplished a survey of the sky confined to the solar elongations larger than  $60^\circ$  and smaller than  $135^\circ$ . Based on this survey, weekly averaged sky maps were produced which we processed as follows. All southern and northern ecliptic latitudes were mapped onto one hemisphere and averaged, thereby removing the slight asymmetry of the zodiacal cloud with respect to the ecliptic plane which is seen in the data but which is not present in the formulation of the model<sup>1</sup>. Ecliptic longitudes of the Earth at each observation were subtracted from the ecliptic longitudes of the observation directions so that all observations were reduced to a single location of the Earth. Multiple observations of the

<sup>1</sup>The deviation of the model from the real asymmetrical dust cloud is negligible given the purpose of the model — prediction of fluxes on spacecraft with the accuracy of a factor of two being fairly acceptable — and can be effectively reduced by assuming that the dust cloud has a symmetry plane different from the ecliptic plane. See Dermott et al. (2001) for details about the symmetry surface of the zodiacal cloud.

same positions on celestial sphere were averaged. Figure 3A shows the emission of the dust particles in  $12\ \mu\text{m}$  waveband.

Calculation of the population contributions  $w_j$  demanded assumptions on the optical properties of the dust grains. Indeed, the temperature and emissivity of dust particles is necessary to convert the number densities given by the model into the infrared emission intensities that are observed. Mie theory was used with the refractory indexes for astrosilicate and graphite particles (Draine 1985; Reach 1988).

Normalisation factors for all populations were then iterated using the L-BFGS-B algorithm (Byrd et al. 1995) to fit the model to the data, with the Gaussian function describing the distribution of errors of measurements

$$\text{Residual} = \sum_j \frac{(O_j - C_j)^2}{\sigma_j^2} \quad (6)$$

where  $C_j$  are weighted sums of all population contributions to the  $j$ -th observation each corresponding to a line of sight from the map on Fig. 3A,  $\sigma_j$  is the error of measurement. The results are shown in Fig. 3B for the  $12\ \mu\text{m}$  waveband. Agreement with the observations in the other wavebands at  $4.9$ ,  $25$  and  $60\ \mu\text{m}$  was good as well, so that both the spatial number densities and the spectrum of interplanetary dust were well matched by the model.

#### 5. MODEL FIT TO IN-SITU MEASUREMENTS

The spatial distribution of dust derived from the zodiacal light and infrared emission observations as well as by the in-situ flux measurements was principally explained by the action of the Poynting-Robertson drag on small particles. Dikarev et al. (2001) compared the prediction of a simple dynamical model taking into account the Poynting-Robertson drag, with the impact counts by the Galileo and Ulysses dust detectors. Since the impacts by interstellar grains compose a significant fraction of the impact events, they used the corresponding population from the ESA meteoroid model.

Dust experiments on-board spacecraft usually yield a sequence of impact events accompanied by inferred grain properties, spacecraft locations and velocities, as well as detector orientations. Based on similarity of observation conditions at the time of impacts (e.g. orientation of the detector, heliocentric distance, spacecraft velocity) the impacts can be sorted in bins to resolve fluxes of particles moving on different orbits. Description of the instrument response function is necessary to reproduce the impact counts in the model. In an ideal situation when the instrument response function is precisely known, Poisson statistics (coming from the well-known Poissonian distribution) can be applied to adjust the model to the observed impact counts:

$$\text{Residual} = \sum_j (C_j - O_j \ln C_j). \quad (7)$$

Application of the Poisson statistics to dust experiment data yields only moderately successful results. Dikarev

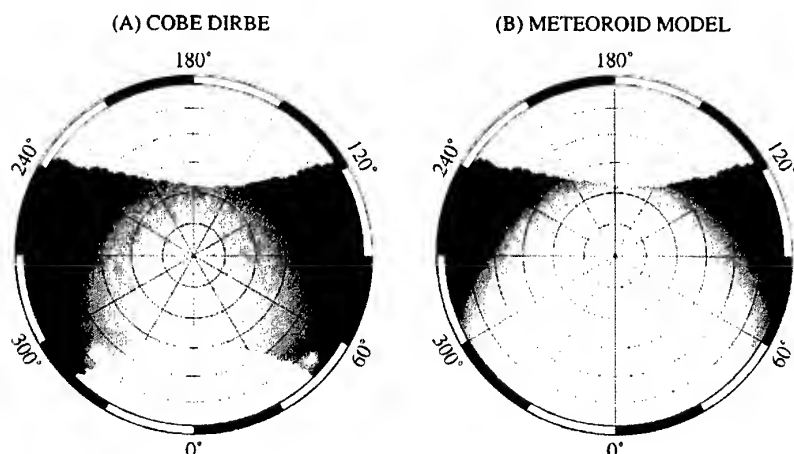


Figure 3. Thermal emission map at  $12\ \mu\text{m}$  as seen by COBE DIRBE (a) and predicted by the interplanetary meteoroid model (b). DIRBE's observations obtained in ecliptic southern and northern hemispheres were mapped onto one hemisphere and averaged. Reference frame is rotating synchronous to Earth's orbital motion. The centre shows thermal emission in the direction of the ecliptic North (or South) pole,  $0^\circ$  corresponds to anti-Sun direction.

et al. (2001) construct a model and show that Galileo and Ulysses data can be reproduced reasonably well. Our more recent analyses suggest that the agreement can be improved if "poor" impact events are excluded from the Galileo data set, i.e. impacts of classes 0 and 1. This may be an indication of incompleteness of our current model or biases in the data set itself.

Note that calibration of dust detectors usually leaves large uncertainty factors. For example, the accuracy of mass determination with the dust detector system (DDS) installed on Galileo and Ulysses, according to ground calibration, is one order of magnitude. Impact velocities are believed to be known within a factor of 2 only.

## 6. METEOR DATA

Construction of a meteoroid model is impossible without a knowledge of the distributions of big particles ( $m \gg m_0 = 10^{-6}\text{ g}$ ). These are the most harmful impactors, despite they are sparse compared to the abundances of small grains. In addition, big particles serve as sources of small grains through collisional destruction.

However, their sizes and number densities make them difficult to track. They are too small and cannot be observed individually from remote site, they are too scarce and slip past the low-area in-situ dust detectors, and both their number densities and sizes do not allow for observable collective effects, such as scattered light. The only way their orbital distributions can be determined is a meteor orbit survey.

As a part of the ESA meteoroid model upgrade, advanced meteor radar AMOR in New Zealand (see e.g. Baggaley et al., 1994) is currently monitoring the upper atmosphere counting about 1,500 meteors each day, 300 to 600 of which can be used for orbit determination, depending on

the time of year. The radar data is analysed to determine orbital elements of the dust particles and is expected to produce a database of about 1,000,000 orbit determinations by the end of 2001. It is due to replace Sekanina and Southworth radar meteors regarding which some doubts were raised by Taylor (1995).

This meteor orbit survey is naturally confined to a certain subset of the Solar system's meteoroid orbits, and modeling is required to extrapolate the orbital statistics beyond the observed region. Yet even more crucial problem is to correct for observational biases properly, since orbit restoration from the radar data is not the end of the reduction process. One needs to know the meteor detection probability in order to convert the orbital distributions instantaneously given in the radar measurements into the true distributions outside the attraction sphere of the Earth. The detection probability is composed of several factors, such as Earth collision probability determined by the orbit of the meteoroid, orbit visibility conditions varying due to Earth rotation and revolution about the Sun, ionisation in meteor trail dependent on the meteoroid mass and speed, etc<sup>2</sup>.

A search for meteor radiants or clusters of meteor orbits is possible without all above-listed corrections, as the detection probability is believed to change a little only for the orbits and radiants confined to a small neighbourhood. In contrast, to portray the global structure of the zodiacal cloud, all corrections are important.

AMOR team will produce corrected orbital distributions for the region of  $(a, e, i)$ -space available to Earth-bound survey, and the populations of meteoroid model will be used to extrapolate the radar data. It is obvious that the model and correction procedure should be based on identical assumptions. Working on the meteoroid model and

<sup>2</sup>More details can be found in the paper by Galligan and Baggaley, these proceedings.

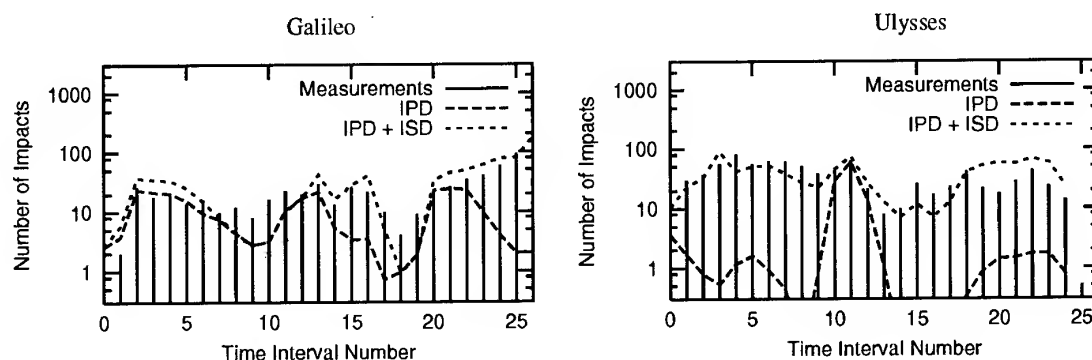


Figure 4. Comparison between the impact counts reported by Galileo (left) and Ulysses (right) and the rates predicted on the base of the model. The time is split into intervals of variable length so that within each interval the changes in the spacecraft coordinates, velocity and spin axis direction are small. Shown are the measured impact counts (vertical lines), the counts predicted by the interplanetary dust (IPD) model described in the text and the predicted counts taking into account the interstellar dust (ISD) population defined by Staubach (1996). Theoretical distributions of the IPD model were adjusted to fit the data using a multiplication factor.

the corrected orbital distributions, we have noticed that correction procedure might disagree about the mass distribution slope of the meteoroids. Previous meteoroid orbit surveys were not so sensitive and detected meteoroids of the masses well above  $m_0 = 10^{-6}$  g, where the mass distribution slope was  $-\gamma - 2/3 \approx -2.3$ . However, AMOR advanced into the region of the Poynting-Robertson dynamics, it observes the meteoroids as small as  $3 \cdot 10^{-7}$  g, where the slope already undergoes flattening from  $-2.3$  to  $-\gamma + 1/3 \approx -1.3$ . This transition is strongly supported by the lunar microcrater counts Grün et al. (1985) and by more recent inspection of retrieved LDEF surfaces. The transition between slopes starts at  $m \sim 10 m_0$  and ends at  $m \sim 10^{-1} m_0$ .

In addition to the radar meteors, other kinds of observations should also be converted into the true orbital distributions, or the model of distributions should be tested against the data in case the data do not admit the full conversion. There are ongoing projects routinely archiving video meteors, including synchronous recording with two cameras that allow to determine all orbital elements of the meteoroids. However, the goal of these projects is a search for meteor streams only. Understanding biases inherent in those observations would permit to use more data in construction of the models of sporadic meteoroid background.

## REFERENCES

- Baggaley W.J., Bennett R.G.T., Steel D.I., Taylor A.D., 1994, In: *Proceedings ASA*, vol. 11(2), 151–156
- Byrd R.H., Lu P., Nocedal J., Zhu C., 1995, *SIAM Journal on Scientific Computing*, 16
- Dermott S.F., Grogan K., Durda D.D., et al., 2001, In: *Interplanetary Dust*, 569–639, Springer Verlag, Berlin Heidelberg New York
- Dikarev V., Jehn R., Grün E., 2001, *Adv. in Space Research*, in press
- Divine N., 1993, *Journal of Geophys. Research*, 98, E9, 17029
- Draine B.T., 1985, *ApJ Suppl.*, 57, 587
- Garrett B. H., Drouilhet S., Oliver J.P., W. E.R., 1999, *Journal of Spacecraft and Rockets*, 36, 124
- Gor'kavyi N., Ozernoy L., Mather J., Taidakova T., 1998, *Earth, Planets and Space*, 50, 539
- Gor'kavyi N.N., Ozernoy L.M., Mather J.C., 1997, *ApJ*, 474, 496
- Grogan K., Dermott S.F., Durda D.D., 2001, *Icarus*, 152, 251
- Grün E., Zook H.A., Fechtig H., Giese R., 1985, *Icarus*, 62, 244
- Grün E., Staubach P., Baguhl M., et al., 1997, *Icarus*, 129, 270
- Ishimoto H., 2000, *A&A*, 362, 1158
- Leinert C., Roser S., Buitrago J., 1983, *ApJ*, 118, 345
- Liou J., Zook H.A., Jackson A.A., 1999, *Icarus*, 141, 13
- Liou J.C., Zook H.A., Jackson A.A., 1995, *Icarus*, 116, 186
- Liou J.C., Zook H.A., Dermott S.F., 1996, *Icarus*, 124, 429
- Ozernoy L.M., Gorkavyi N.N., Taidakova T., 2000, *PSS*, 48, 993
- Reach W.T., 1988, *ApJ*, 335, 468
- Staubach P., Grün E., 1995, *Adv. Space Res.*, 16, (11)103
- Taylor A.D., 1995, *Icarus*, 116, 154
- Wyatt S.P., Whipple F.L., 1950, *ApJ*, 111, 134

## MICROSWARM STRUCTURE OF A METEORIC COMPLEX BEYOND AN ECLIPTIC PLANE

Sergey Kalabanov<sup>(1)</sup>, Vladimir Sidorov<sup>(1)</sup>, Tamara Filimonova<sup>(1)</sup>

<sup>(1)</sup>Kazan State University, Russia, 420008, Kremlevskaya, 18, Physic Department, Email: Sergei.Kalabanov@ksu.ru

### ABSTRACT

The purpose of this work is to determine maximum allowed numbers of measurements used in the discrete solution, at which probability to detect a false microshower will be rather small, and to find out how this number is connected to the solution accuracy and how it corresponds with productivity of the meteoric radar. We have advanced a quasi-thomography method in the solution of a problem of determination of meteor radiant distributions on a celestial sphere based on the data of radar goniometer measurements. We have tried to find out, how the stable structures of radiants prolated along an elongation angle from apex in the course of the year vary, how they are correlated in time and whether they will be repeated from one year to other year.

### 1. METHOD OF SOLUTION

To evaluate a sensitivity level for weak showers and to evaluate probabilities of obtaining of the false solutions in discrete quasy thomography problem, the simplified model experiment was conducted. Instead of a spherical problem on a celestial orb we have considered a flat problem with smaller dimension. On an area 40X40 of discrete segments we generated points with random coordinates, which imitated radiants of separate meteors. The lines passing through these points with random angles, imitated position lines these meteors, which determined their angular coordinates. The section lengths of these lines intersecting an elementary site imitated belonging probability of the given meteor to each section. In the model an every new section length intersecting the given site was summarized, and, thereby, the model posteriori cumulative distribution function was imitated indicating that some of meteors is registered in some site. Radar sensitivity and atmospheric entrance angle of a meteor were taken into account in actual spherical algorithm. In model we have simplified a problem, supposing equable radar sensitivity for meteors from any segment of a celestial orb. An example of distribution imitation of a posterior probability of sporadic meteor detection on elementary sites of a simulated segment of a celestial orb is presented in Fig.1.

Scale on an abscissas axis is selected in a way to map probable number of meteors in an elementary site. In this example we imitated one determined radiant, with 8 meteors ( $X=10.5$ ,  $Y=10.5$  - peak of greatest height) and 32 random radiants. The model shown in Fig.1 was received for 40 generated radiants, with 1600 elementary platforms in model. In figure it is visible, that simulated radiant is precisely selected with probable number 9. Let's mark, that near to a maximum there is a more broad support - peak looks like eroded at the basis. Besides there is a second maximum with probable number 7, which can be accepted for a microshower radiant. The false peaks with intensity 6 are observed also; 5 and the vast number of peaks with intensity 4 and less. If not knowing, that there is only one microshower, with incorrect level selection we risk to accept false peak of a posterior probability for a microshower. This very uncertainty has induced us to search for the discrete solution.

### 2. SIMULATION OF THE DISCRETE SOLUTION

Let's apply now to the data submitted in a Fig. 1.

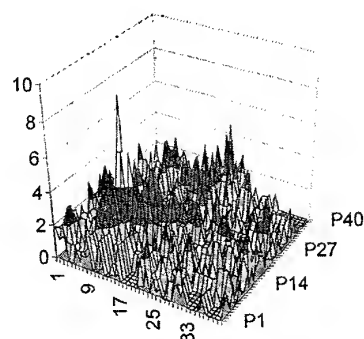


Fig.1. Posterior probability of meteor radiant distribution.

This is our developed version of the discrete solution, which is oriented only on allocation of microshowers.

Briefly essence of a method consists of the following. The experimental data are broken into three independent groups. On a celestial orb it is made the search of coordinates of cross points of meteor position lines inside one group. It is supposed, that among obtained coordinates there are coordinates of microshower radiant, if not less than two meteors from one radiant are in an analyzable data set. It is supposed, that the angular sizes of shower radiant are less than the sizes of a selected elementary site on a celestial orb with coordinates which determine fixed coordinates in this site of radiant. If we take other pair of measurements, again a cross point coordinate of position lines will belong or belong to radiant of a meteoric shower, or will be random. If the second pair of reflections belongs to the same meteoric shower, then coordinate of its radiant will be measured twice and will be in the same elementary site. The line cross points of sporadic meteors and meteors, belonging to different flows, will give accidentally located coordinates.

The problem is how to distinguish data-flow radiants from random position line intersections. The complexity of this problem is that with growth of number of measurements a number of random points on a celestial orb grows as number of combinations of two measurements, but the number of true radiant flow grows linearly.

If there are shower meteors in the second group of the data, the coordinates of intersection of their position lines will be same as in the first group, while the appropriate coordinates of sporadic meteors again will be random. The logic association "AND" of two tables with cross point coordinates of position lines allows to select coordinates of flow radiants and considerably to reduce number of false coordinates. If there are not two meteors in the second group, belonging to the given flow, then there is probability, that such two meteors will be in the third group. Integrating three versions of the possible solutions with logic operation "OR", we will receive coordinates of desirable radiants. This is only essence of the solution, which is presented in details in [5].

### 3. OUTCOMES OF SIMULATION

The data of simulation of the discrete solution for a model situation adduced in Fig.1, is adduced in Fig.2. We can see that radiant with determined coordinates was selected, while random "false" radiants, as well as sporadic, it is not revealed. "Fuzzying" of peak of radiant is not revealed in model solution also, though its intensity increase is observed.

The increase is connected to a fact that the sporadic meteors precisely intersect with "true" radiants. This method can not distinguish them. Having this fact the

intensity of detected radiant ts appear increased. The model allows to detect such "components" and to evaluate them statistically. These "components" complicate a problem of identification of belonging of particular meteors to a chosen microshower and evaluation its intensity. However it is a new problem, which we will discuss in the next article.

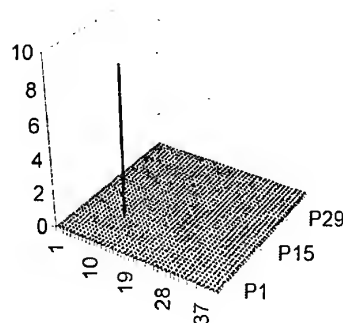


Fig.2. The discrete solution for a data set in Fig.1

The number of random points on a celestial orb grows as a number of combinations of two measurements, and the number of true shower radiants will grow linearly. So that, if we rely on sensitivity level then it can be made only with the limited number of the registered reflections. When we increased a number of used reflections on 20%, a discrete method started to give additional false solutions. The simulation has shown, that for number of elementary platforms  $n=1600$  numbers of meteors treated by this method should not exceed 40. In this case with majority of tests for 8 shower meteors and 32 sporadic at a minimum threshold of detection of a flow - 4 meteors, we in 90 % cases had not false flows, and no cases, when the model shower was not found.

It was revealed, that the higher resolution, the higher this limit of number. So for the resolution  $90^\circ \times 180^\circ$  of elementary cells, what corresponds to an elementary cell  $2^\circ \times 2^\circ$ , we can use simultaneously no more than 120 meteors at equal radiant distribution on a celestial orb. Although so equal distribution is not really observed, we have accepted a little bit more rigid limitation - 60 meteors, though it would be possible to receive a precise evaluation, by complicating model, by finishing it up to the sizes of the full scale simulation model.

We simulated a problem of allocation of one flow on a hum noise of sporadic meteors. It would be interesting to know what happens to several simultaneously operational flows. We assume, that at maximum number

40 meteors and threshold of radiant allocation 4 meteors, it is possible to select 10 meteoric flows, but in this case it is necessary to take into account, that under a random partition in three groups it is possible to lose some combinations, and do not register some model radiants. Therefore we will assume, that 5 meteoric flows act simultaneously, in which are registered 4, 6, 8, 10 and 12 meteors accordingly.

Applying to such model the discrete solution, we will receive distribution of chosen radiants, shown in a Fig.3. We see, that model radiants were selected according to intensities 5, 7, 9, 9, 12, however we have not avoided the false solution with intensity 4. As we see, the intensity of smaller peaks was increased on 1, the intensity of 10 has decreased on 2 and the intensity of 12 was saved. This example shows, that the discrete method well selects some simultaneously operational flows, however it can in some cases give false radiant. As a rule, this false radiant is threshold radiant and this number can be reduced, rejecting threshold radiant.

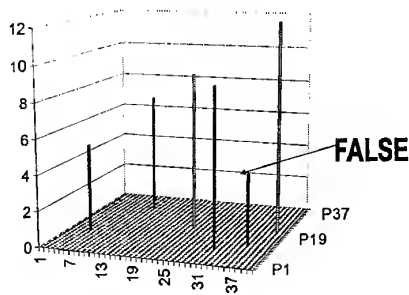


Fig.3. An example of simulation of the discrete solution in picking out of 5 model showers of different intensity

In Fig. 4, the result of the discrete solution for model with 4 showers is added.

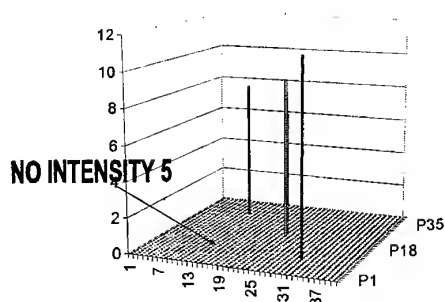


Fig.4. An example illustrating the discrete solution with loss one of four simulated meteoric showers.

We can see that the flows with intensities 9 and 11 were selected without distortions, the flow with intensity 7 has received additional 1, and the flow with intensity 5 was not detected. Cases with no detection of flows is the outcome of a random partition in three groups. At other realization of the same model situation all 4 flows were selected.

#### 4. COMPARISON OF RESULTS

Here we compare the results of method of posterior probability and results of the discrete method. The data almost of continuous radar observations of the meteors in January-April and June-December 1993 and during 3 different years in April (1987, 1988, 1993) and December (1986-1988) in Kazan were analyzed by a quasi-thomography method with angular measurement accuracy -  $10^\circ \times 10^\circ$ . In Fig. 5, 6 we submitted results for different months during one year (1993). We have detected, that the toroid structure precisely finds out in February and April. In August-October on the contrary is observed the stable minimum in a neighborhood  $90^\circ$  to ecliptic plane. The data of December were analyzed additionally by discrete quasy-thomography method with the  $2^\circ \times 2^\circ$  degrees.

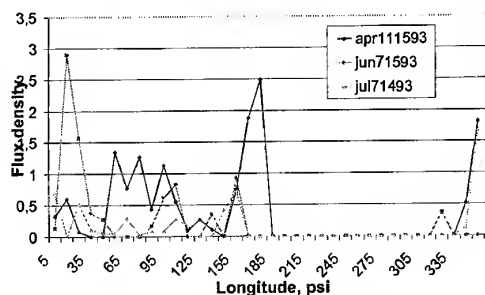


Fig. 5 Distribution of flow density of meteors by latitude in April, June, July

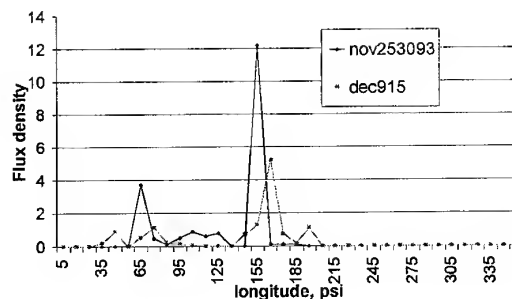


Fig.6 Distribution of flow density of meteors by latitude in November, December

In Fig.7. we can see distribution of radiant density of microshowers by latitude.

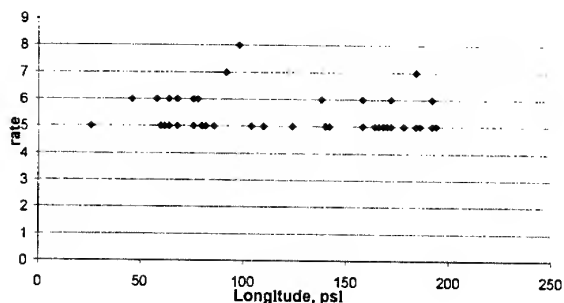


Fig.7 Distribution of rate microshowers on its longitude (without Geminid)

It is evident that in the distribution of radiant density of microshowers and distribution which is obtained from quasy tomography analysis both have two maximums: near  $60^\circ - 75^\circ$  and  $70^\circ - 85^\circ$  by longitude. They vary only in results of Geminid absence in discrete solution. We could not exclude Geminid shower in tomography solution. It is evident that maximums in distribution of radiant density by longitude in tomography results are results of adding to sporadic background showers and microshowers.

## 5. CONCLUSION

It was developed the computer model for the analysis of methods in the solution of quasy-tomography problem of definition of distribution of meteors on a celestial orb with goniometer data of the meteoric radar. It was made the comparison of two methods of the solution – the statistical method [1] and the discrete one [5]. It is shown that, both ways result in success at the limited maximum number of the used data in one cycle of calculation.

It is shown, that for the resolution  $2^\circ \times 2^\circ$ , the number of meteors of microshowers, simultaneously used for detection, should be no more than 60. The increase of this number even on 10 % results in sharp increase of number of detection of "false" microshowers.

The computer simulation shows, that the large part of errors, as a rule, is connected to a threshold situation, as well as in any other problem of an optimum decision making of detection.

This situation can be described by probabilities not to detect an existing flow or to detect not existing. The developed model allows these probabilities to evaluate.

The radiation intensity distributions of meteors on different angels to ecliptic plane for different years are very close. There is a preferable concentration maximum of radiant density near  $30^\circ$ ,  $70^\circ$ ,  $90^\circ$ ,  $115^\circ$  and  $150^\circ$  degrees.

It is possible that maximums in distribution of radiant density by longitude in tomography results are results of adding to sporadic background showers and microshowers.

## 6. ACKNOWLEDGEMENTS

This work has been supported by Russian Fund of Fundamental Investigations (No 00-02-16845) and by American Meteor Society.

## 7. REFERENCES

1. Sidorov V.V., Filimonova T.K., Rassim Amer Ali, Ganin V.A. *Research of the thin structure of meteor falling flux in locality of Earth by radar tomographic method*, Astronomical Society of the Pacific conference series, 390 Ashton Avenue, San Francisco, California 94112, Vol.3, 154-160, 1994.
2. Sidorov V.V., Rassim Amer Ali. *Distribution of speeds of meteors on a celestial orb on observations on one radar station with goniometer*, Astronomical bulletin, Vol. 28 - N1, 81-92, 1994.
3. Belkovich O.I., Filimonova T.K., Sidorov V.V., *Structure of sporadic meteor radiant distributions from radar observations*, Kluwer Academic Publishers, Dordrecht, J. Earth, Moon and Planetes, Vol. 68, 1995.
4. Evdokimov O.I., Filimonova T.K., Sidorov V.V., Rasim Amer Ali, *Investigation of micro streams and associations by the data of radar meteor observations in Kazan*, Kluwer Academic Publishers, Dordrecht, J. Earth, Moon and Planetes, Vol. 68, 1995.
5. Sidorov V.V., Kalabanov S.A., *The discrete solution of quasy-tomography problem of definition of radiant distribution of shower meteors on a celestial sphere*, (in this issue)

## DEVELOPMENT OF A NEW REFLECTRON TYPE TOF MASS SPECTROMETER FOR DUST ANALYSIS IN SPACE

Yoshimi Hamabe<sup>(1)</sup>, Sho Sasaki<sup>(1)</sup>, Hideo Ohashi<sup>(2)</sup>, Tohru Kawamura<sup>(3)</sup>, Ken-ichi Nogami<sup>(3)</sup>,  
Hajime Yano<sup>(4)</sup>, Sunao Hasegawa<sup>(4)</sup>, and Hiromi Shibata<sup>(5)</sup>

<sup>(1)</sup>*Earth and Planetary Science, University of Tokyo, Tokyo 113-0033, Japan, hamabe@space.eps.s.u-tokyo.ac.jp*

<sup>(2)</sup>*Department of Ocean Science, Tokyo University of Fisheries, Tokyo 108-8477, Japan*

<sup>(3)</sup>*Department of Physics, Dokkyo University School of Medicine, Tochigi 321-0293, Japan*

<sup>(4)</sup>*Institute of Space and Astronautical Science, Kanagawa 229-0022, Japan*

<sup>(5)</sup>*Research Center for Nuclear science and Technology, University of Tokyo, Tokyo 113-0032, Japan*

### ABSTRACT

In order to analyse the elements of dust particles in space, we have been developing a reflectron-type dust TOF-MS (Time-Of-Flight Mass Spectrometer) with a curved electric field. Now we have done performance experiments of our device by impacting hypervelocity microparticles with a Van de Graaff accelerator at HIT (High Fluence Irradiation Facility, University of Tokyo), where carbon particles of 0.3-2.0  $\mu\text{m}$  in diameter are accelerated up to 5-20 km/s which are comparable with the velocity of dust particles in space. The results showed the device has higher mass resolution than the system with a parallel reflecting region under the same experiment situation by factor 2 or 3. Moreover the TOF spectra showed the higher detection efficiency, and the value was 10 times higher compared to the parallel reflectron TOF-MS. These effective results are considered to be caused by a curved electric field in a reflecting region.

### 1. INTRODUCTION

Dust analysers on board spacecraft such as Vega [1], Giotto [2], Galileo [3], Ulysses [4], Nozomi [5], Cassini, and Stardust have carried out in-situ measurements of microparticles. These analysers are roughly divided into two analysers; one is a dust detector to measure the velocity, the mass and the direction of microparticles. The other is a dust analyser, which provides the chemical composition of microparticles as well as the physical elements such as the velocity, the mass and the direction. Information on the chemical composition is required to constrain the properties, histories and origins of these microparticles. Microparticles in the solar system are divided into two types; interplanetary dust, which come from interplanetary space such as comets, asteroids, EKBs (EdgeWorth Kuiper Belt Objects) and dust rings of planets, and interstellar dust particles, which may come from interstellar clouds.

We have been developing a reflectron-type TOF-MS to analyse the chemical composition of microparticles as well as the physical elements in space. In following chapter, we will report our new dust analyser and results of impact experiments of microparticles.

### 2. EXPERIMENTAL CONFIGURATION

#### 2.1 Dust Accelerator

The Van de Graaff accelerator has been improved at HIT (High Fluence Irradiation Facility, University of Tokyo) in Japan to simulate the hypervelocity impacts of microparticles in space [6] (Fig.1). A dust reservoir which are filled with microparticles of carbon or silver is mounted in the accelerator which runs at up to 3.75 MV. Microparticles are charged on the top of a needle which is at a potential of 10 kV against the terminal, and are accelerated up to by the potential difference of 2 or 3 MV. The velocity of microparticles is decided by the charge and the accelerating potential as following equation,

$$\frac{1}{2}mv^2 = qU \quad (1)$$

where  $m$ ,  $v$  and  $q$  are respectively the mass, the velocity, and the charge of microparticle, and  $U$  is the accelerating potential of Van de Graaff. The distribution of microparticle mass and velocity is shown in Fig.2. The velocity more than 5 km/s is required for the vaporization of impactor [7, 8]. So we used carbon microparticles as impactor although two materials, carbon and silver, were accelerated. Carbon particles around 0.3-2.0  $\mu\text{m}$  in diameter (mass is about  $10^{-14}$ - $10^{-16}$  kg) have the velocity range from 5 km/s to 20 km/s. The carbon microparticles impact with the incident angle of 45 degrees onto the target which are set at the end of the beam line

## 2.2 TOF-MS Configuration

We made a prototype of reflectron type TOF-MS, which was already produced by Mamyrin [9] and has been on board spacecrafts such as Giotto and Vega. These previous analyzers were large and heavy, although they had high mass resolution ( $m/\Delta m \sim 100$ ). However, these analyzers have low ion detection efficiency, which means they could hardly detect ions extended at the target. The efficient extracted angle, which is defined as an angle from the perpendicular of the target, was about 2 degrees.

Our developing device has a high resolution in time and space as well as small-sized body. The reflectron type (Fig. 3) consists of four parts; an ion source, a field-free drift region of length 120 mm, a reflecting region, and a detector. Ion source consists of a metal target and a front mesh. The target materials were gold, silver or carbon, which were 20 mm square and 0.2 mm thick, and the target was maintained at a positive potential. A tungsten mesh of which wire was 0.2 mm in diameter and 50 mesh/inch was mounted 6 mm in front of the target. This mesh was electrically isolated from the target and was earthed. An accelerating region was constructed between the target and the mesh. The target surface was inclined at an angle of 45 degrees to the incident microparticles. Impacting microparticles are vaporized by their own kinetic energies and ions are produced. There is no difference in ion yield or energy and angular distributions for impacts at an angle

of 45 degrees [10]. For reflectron type, as can be seen in Fig. 3, microparticles impact with a larger incident angle of 52.5 degrees because the target was mounted with inclination of 7.5 degrees with respect to the horizontal direction of the device. Positive ions are accelerated by the planar electric field, and are extracted in the direction of the target normal. Negative ions and electrons, on the other hand, are collected on the target. The detector part consists of MSP (Micro Sphere Plate) and a tungsten mesh which was mounted 8 mm in front of MSP surface. The detector part also constructs an accelerating region where MSP surface and the front mesh were applied  $-2700$  V and  $0$  V, respectively. And this part also is mounted with the inclination of 7.5 degrees.

Reflecting region consists of 10 potential rings of 140 mm in inner diameter and 1 mm thick. Two types potential electric fields are formed; a planar electric field of decreasing trend with which this device can focus ions in time but in space. This type had been on board spacecraft such as Giotto and Vega, and the mass resolution ( $m/\Delta m$ ) achieved about 100. The other electric field, a curved electric field, is also constructed by changing the potential difference between the mesh and the first potential ring. Ions are focused in space as well as in time with the curved electric field. Simulation of ion optics also suggested that the curved electric field was capable of focusing ions with the extracted angle from  $+80$  to  $-80$  degrees (Fig. 4), and that the mass resolution could achieve 1000.

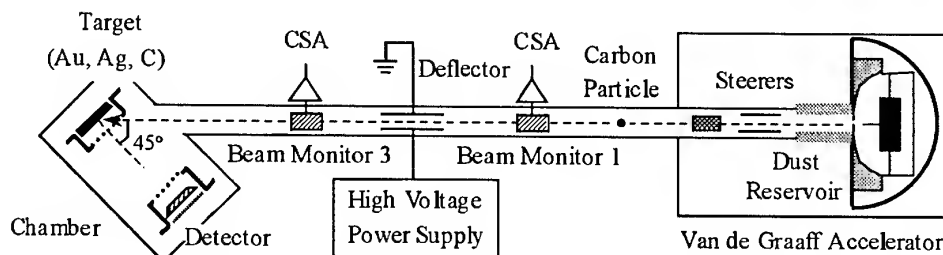


Fig. 1. Configuration of Van de Graaff dust accelerator

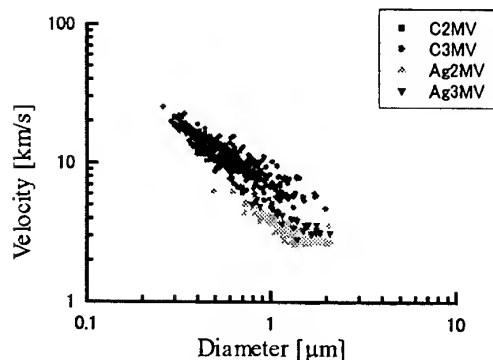


Fig. 2. Particle velocity versus diameter

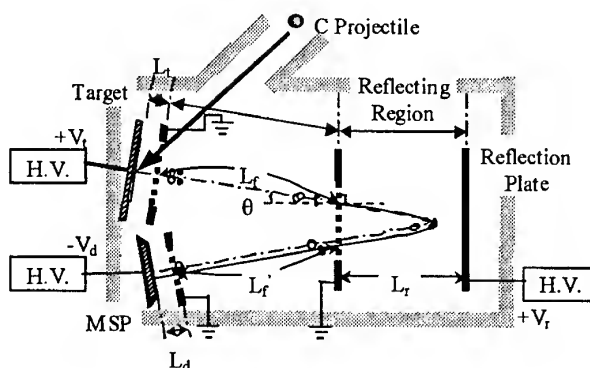


Fig. 3. Configuration of reflectron type TOF-MS

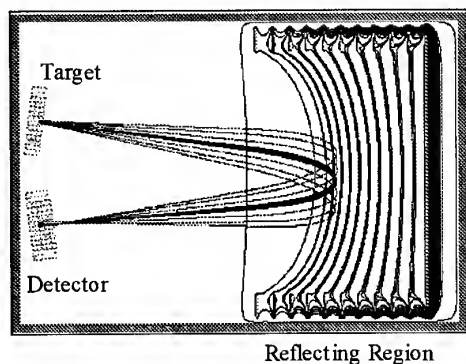


Fig. 4. Ion's tracks in a curved equipotential field when ions are extracted with an angle from +80 to -80 degrees. It is noticed that ions are focused in space although they have initial energies of 10 eV.

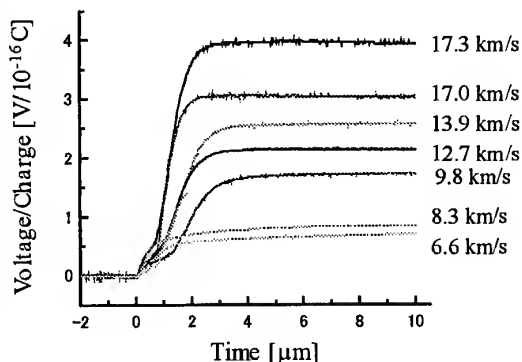


Fig. 5. Target Signals.

The horizontal axis is time passed after the impacts of microparticles. Impact time is 0  $\mu\text{m}$ .

### 3. EXPERIMENTAL RESULTS

#### 3.1 Target Signal

Target signal provides the total ion yield, the velocity and the mass of impacting microparticles. Fig.5 shows the target signals when microparticles impacted with the velocity range from 6.6 km/s to 17.3 km/s. The signal has two distinct components: a fast-rising component and a slow one. A fast-rising component indicates the plasma produced in the primary impact, and the time constant is determined by the strength of the accelerating field. A slow component due to plasma produced by ejecta hitting the accelerating mesh, and the time constant is determined by the time of flight of ejecta particles between the target and the front mesh and is thus a function of the impact velocity [5, 10, 11].

In evaluating the target signal, amplitude and rise time of charge are the most important values, which give mass  $m$  and velocity  $v$  of an impacting particle. There are empirical relations:

$$t = c_g v^\alpha \quad (2)$$

$$Q/m = c_r v^\beta \quad (3)$$

where  $Q$  is the maximum charge and  $t$  is rise time of a charge signal. Both  $Q$  and  $t$  can be estimated directly from the target signal. In the above,  $c_g$ ,  $c_r$ ,  $\alpha$ , and  $\beta$  are constants which should be determined by calibration. In our experiment where carbon particles impacted on gold target, the values derived for the constant  $c_g$ ,  $c_r$ ,  $\alpha$ , and  $\beta$  were  $6 \times 10^{-5}$ ,  $7 \times 10^{-3}$ , -1.1, 3.4, respectively. We have confirmed that there might be some other methods to determine velocity e.g., using the ratio of charges due to primary impact and secondary ejecta, although further calibration experiments are necessary for establishing these methods.

#### 3.2 TOF-MS Spectra

Analysis with TOF-MS starts to ionize the impacting projectile, and measures the total flight time of ions from the target to the detector, which depends on mass/charge ratios of ions. Ions are produced by hypervelocity impacts of microparticles and accelerated within the ion source. After ions are extracted from the ion source, they are turned to the reverse directions in a reflecting region, and arrive at the detector through a drift region. The total flight time from the target to the detector gives us the mass/charge ratios, which help us to distinguish the ions.

Fig. 6 shows the spectrum obtained by carbon particles impacted on a gold target with a curved equipotential field. This spectrum indicates the average of 20 spectra under the same condition for a target voltage and an electric field of a reflecting region, although the velocity ranges from 5 to 20 km/s. The horizontal axis is the time passed from an impact time which is indicated by 0  $\mu\text{s}$ . The vertical axis is the voltage, which means the average of 20 spectra. The numbers in Fig.6 indicate mass/charge ratios.

Ions from a carbon particle and a target metal,  $\text{C}_n^+$  and  $\text{Au}^+$ , were expected to be detected. However, alkali metal sodium and potassium were dominant, especially in lower velocity impacts. Alkali metals such as  $\text{Na}^+$  and  $\text{K}^+$  are almost impossible to eradicate as contaminants in the system and are highly visible in spectra due to their low ionization energy. This result has been reported previously [12]. This implies that the alkali metals may be produced by a different process than the target and projectile material, and may reflect the change from surface processes to bulk ionization of the projectile and the target [11].

Carbon ions were also detected except  $\text{C}^+$ .  $\text{C}^+$  is rarely seen in impacts below 20 km/s. Hence  $\text{C}^+$  is expected to be not ionized at lower velocity because

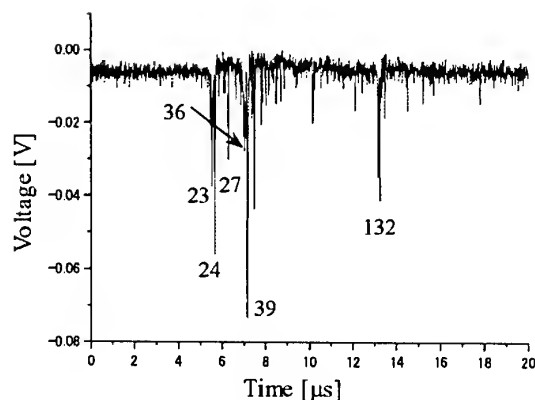


Fig. 6. TOF spectrum for impacting of carbon particles on a gold target.

the energy is not enough to ionize. Cluster ions of carbon,  $C_2^+$  and  $C_3^+$ , were always detected even at lower velocity. And heavier cluster ions of carbon  $C_n^+$  are sometimes detected in impacts above 15 km/s.

Gold ions were rarely seen at these velocity ranges. Detection of gold ions probably requires hypervelocity impacts. Observations of metal targets showed that the surface was sputtered by impacting particles. Hence, there is an assumption that sputtered gold was not ionized and came out as neutral atoms.

### 3.2 Mass Resolution

Mass resolution is the most important factor for a mass spectrometer in order to measure the chemical composition of dust particles. Mass resolution is expressed as follow,

$$R = \frac{M}{\Delta M} = \frac{t}{2\Delta t} \quad (4)$$

where  $M$  and  $t$  are mass and flight time of ion, respectively.

The mass resolution of this device was derived from spectrum in Fig. 6, which consists of 20 spectra for impacting of carbon particles onto gold target. In this situation, the mass resolution ( $M/\Delta M$ ) achieved 600. In our previous experiments using a reflectron type TOF-MS with a parallel equipotential surface, the mass resolution was about 100. A reflectron type TOF-MS with a parallel equipotential surface is not capable of focusing ions in space. However, TOF-MS with a curved equipotential surface can focus ions in space and time. Therefore, the mass resolution could achieve such a high value. In other words, to enhance the mass resolution, focusing ions in space as well as in time is required.

## 4. CONCLUSIONS

We performed impact experiments with a new type reflectron TOF-MS with an optical focusing of ions. Comparing the mass resolution of conventional reflectron type TOF-MS with those of a new type TOF-MS, the latter achieved higher value than the former. This is the effect of a curved equipotential surface, where ions are focused in time and space. However, the carbon ions  $C^+$  cannot be detected at the velocity ranged from 5 to 20 km/s. It is necessary to detect ions from impacting particles. Further study is required to confirm the performance of this device.

### Acknowledgments

We are grateful to Dr. T. Iwai and Mr. T. Omata for operating an accelerator. This work was supported by a Research Fellowship of the Japan Society for the Promotion of Science for Young Scientists.

### References

1. Kissel J., Composition of comet Halley dust particles from Vega observations, *Nature* 321, 280-282 (1986).
2. Kissel J., et al., Composition of comet Halley dust particles from Giotto observations, *Nature* 321, 336-337 (1986).
3. Gruen E., et al., Constraints from Galileo observations on the origin of jovian dust streams, *Nature* 381, 395-398 (1996).
4. Gruen E., et al., Discovery of jovian dust streams and interstellar grains by the Ulysses spacecraft, *Nature* 362, 428-430 (1993).
5. Icenbergs E. et al., Mars Dust Counter, *Earth Planets Space*, 50, 241-245, (1998).
6. Hasegawa S., et al., Design of electrostatic accelerators for the development of microparticle detectors in Japan, *Adv. Space Res.*, 23, No.1 (1999).
7. Knabe W. and Krueger F.R., Z., Ion formation from Alkali Iodide Solids by Swift Dust Particle Impact, *Z. Naturforsch* 371, 1335-1340 (1982).
8. Kissel J. and Krueger F.R., Ion Formation by Impact of Fast Dust Particles and Comparison with Related Techniques, *Appl. Phys. A* 42, 69-85 (1987).
9. Mamyrin B. A. et al., The mass-reflectron, a new nonmagnetic time-of-flight mass spectrometer with high resolution, *Sov. Phys. -JETP*, 37, 45-48, (1973).
10. Krueger F. R., Ion emission on solid surfaces: comparison of dust impact with other excitations, *ESA SP-224*, 49-54 (1984).
11. Ratcliff P. R. et al., Experimental measurements of hypervelocity impact plasma yield and energetic, *Int. J. Impact Engineering*, 20, 663-674, (1997).
12. Dalmann B. K. The ion-composition of the plasma produced by impacts of fast dust particles, *Planet. Space Sci.*, 25, et al., 35-147 (1977).

## **Interstellar Meteors and Dust**

# CONTEMPORARY INTERSTELLAR METEOROIDS IN THE SOLAR SYSTEM - IN SITU MEASUREMENTS AND CLUES ON COMPOSITION

M. Landgraf

ESA/ESOC, 64293 Darmstadt

## ABSTRACT

Meteoroids originating from the local interstellar medium traverse the solar system. This has been proven by in situ measurements by interplanetary spacecraft as well as highly sensitive radar measurements. Early attempts to detect interstellar meteoroids using the instruments on board the Pioneer 8 and 9 spacecraft failed. More sensitive detectors on board the joint ESA/NASA mission Ulysses as well as on board the NASA spacecraft Galileo, however, unambiguously detected meteoroids of interstellar origin. This discovery has started efforts to compare the results from the in situ measurements with highly sophisticated models of interstellar dust properties derived from astronomical absorption and extinction measurements. It was found that, at least locally, is more mass locked up in meteoroids than expected from the astronomical measurements. So far the in situ measurements only allow to derive composition information indirectly via the meteoroid's dynamics.

Key words: dust; interstellar; in-situ measurements.

## 1. SOURCES OF METEOROIDS IN INTERPLANETARY SPACE

Our Solar System is filled with small solid fragments, meteoroids, that originate mainly from larger objects [1]. Asteroids collide with each other and produce large amounts of meteoroids [e.g., 2]. Existing meteoroids impact larger bodies and create more meteoroids. Comets disintegrate due to solar heating, releasing gas as well as solid fragments [e.g., 3]. But not only Solar System objects are sources of solid particles in the vicinity of the Sun. Meteoroids, that are known to exist in our galaxy [4], enter the Solar System from its local interstellar environment, and traverse it on unbound trajectories [5]. Depending on their size, they interact differently with the gravity and electromagnetic fields of the heliosphere. Table 1 gives an overview of the sources of meteoroids in interplanetary space.

In this work an overview is given of the in situ measurements of meteoroids originating from the interstellar

Table 1. Sources of meteoroids in interplanetary space.

source	characteristics	
	orbit	particle
Asteroids	low eccentricity, low inclination	silicate-type, compact
Comets	high eccentricity, random inclination	carbonaceous, fluffy
Edgeworth-Kuiper belt	low eccentricity, low inclination	unknown
Interstellar medium	hyperbolic	unknown

medium. Also, first hints regarding their composition are discussed. The advantage of in situ measurements using detectors on board interplanetary spacecraft is that the object is analysed without the contaminating effects of the Earth. The meteoroids' orbits are preserved until just before impact, and can, theoretically, be determined with infinite precision. There are no changes to the shape or chemistry of the meteoroid due to an entry into an atmosphere. However, because of the limited size and mass of in situ detectors, so far only rough orbit determination has been possible and the area of chemical analysis by mass spectroscopy has just started [6, 7]. While the comparison of the in situ results with isotopically anomalous meteoritic inclusion is interesting, a full discussion on the latter is out of the scope of this work. Also, the solid matter that is observed by astronomical means in cold molecular clouds of our and other galaxies is not discussed in detail here, despite the fact that it is obviously connected to the local interstellar meteoroid population.

## 2. DUST IN THE LOCAL INTERSTELLAR MEDIUM

The local interstellar medium (LISM) is immersed in a bubble of very hot ( $10^6$  K) and very tenuous ( $10^{-3}$  atoms  $\text{cm}^{-3}$ ) galactic matter [8, 9]. Numerous clouds are present in this bubble, one of which is the local interstellar cloud [LIC, 10] that surrounds the Sun. Another example is the G-cloud in which the nearby star  $\alpha$  Cen is located. It is believed [11] that the Sun will soon leave the LIC and enter the G-cloud. Figure 1 shows the

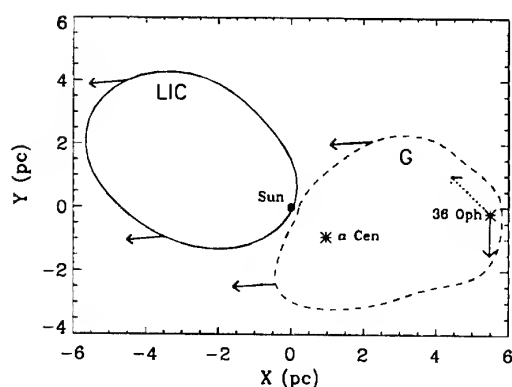


Figure 1. Sketch of clouds in the local interstellar medium as shown by Wood et al. [11] in their figure 2. A  $10 \times 10$  AU region of the galactic plane is shown with arrows indicating the heliocentric velocities of the clouds. The local interstellar cloud (LIC), at the edge of which the Sun is located, is indicated by the solid line boundary. According to the Wood et al. model, the Sun will leave the LIC in the near future and will enter the G-cloud (indicated by the dashed line). The nearby star 36 Oph has a proper motion such that its velocity vector relative to the G-cloud (dotted line), and thus its astrosphere, has an angle with the line of sight towards the Sun.

situation.

All material that reaches the Solar System from interstellar space is per definition part of the LIC. The properties of the LIC are summarised in table 2. The LIC is a typical warm, partially ionised diffuse cloud [12]. In the diffuse clouds solid material is normally subject to destruction processes, returning condensable elements like carbon, oxygen, nitrogen, as well as silicate, iron, magnesium etc. to the gas phase [13]. The analysis of the elementary composition of the LIC [14] shows that the mass fraction of solid to gaseous material should be between 1 : 500 and 1 : 400 [15].

Table 2. Properties of the Local Interstellar Cloud (LIC) according to Frisch et al. [15].

neutral Hydrogen density	$0.22 \text{ cm}^{-3}$
ionised Hydrogen density	$0.10 \text{ cm}^{-3}$
motion relative to the Sun	$\lambda = 74.7^\circ$
(ecliptic coordinates)	$\beta = -4.6^\circ$
temperature	6900 K
magnetic field	few $\mu\text{G}$
average mass density	$2 \times 10^{-25} \text{ g cm}^{-3}$

The dust content of more remote interstellar clouds can be determined by measurements of the extinction of starlight passing through the cloud [4]. Typically a wavelength-dependent extinction is observed, caused by solid particles smaller than the wavelengths of the optical band. The concentration of larger grains can however not be determined this way, because they absorb and reflect light in-

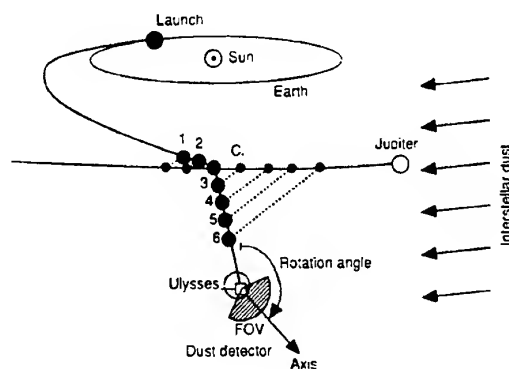


Figure 2. Ulysses measurements of the stream of interstellar meteoroids (entering from the right). A view from above the ecliptic plane is shown with the orbits of the Earth, Jupiter, and the Ulysses spacecraft. The big labelled dots indicate the positions of Ulysses during measurements of dust streams emanating from the Jovian system before and after the fly-by. The field of view (FOV) of the meteoroid sensor on board Ulysses is indicated by the hashed area. The instrument rotates about the spacecraft's spin axis and thus the impact rotation angle for each detected meteoroid can be measured. Most impacts after Jupiter fly-by (disregarding Jovian dust streams) have been detected at rotation angles around  $90^\circ$ . Figure taken from Grün et al. [16].

dependent of the wavelength. The lines of sight through the LIC are too short to exhibit significant extinction. The emission of infrared radiation is also below any instrument's sensitivity. It is therefore impossible to observe solid particles in the LIC directly using remote sensing.

### 3. THE EXISTENCE OF LOCAL INTERSTELLAR METEORIODS

Whether or not local interstellar meteoroids exist and whether they penetrate the solar system was extensively discussed in the 1970ies and 1980ies. The Earth orbiting Pioneer 8 and 9 spacecraft that carried instruments for the detection of impacts by meteoroids did not find any unambiguously interstellar impactors. It was concluded [18] that less than 4% of the meteoroids found at 1 AU can be of interstellar origin. This was explained by modelling efforts [19, 20] that showed that the heliospheric magnetic field was able to divert solid particles, as long as their are not larger than  $0.1 \mu\text{m}$ , which was then believed to be the upper size limit of interstellar meteoroids [21] in the diffuse interstellar medium. At that point it seemed to be clear that no interstellar meteoroids can make it into the Solar System.

An argument derived from a work by Holzer [12] revived the discussion about the existence of solid interstellar matter in the Solar System: On average 1% of the mass of the interstellar medium is contained in dust. If that is true for the LIC, with its average mass density of

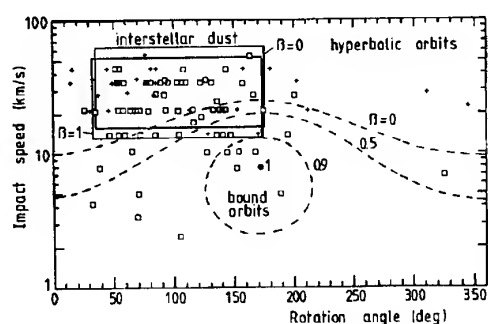


Figure 3. Impact speed and rotation angle of meteoroids detected by Ulysses after Jupiter fly-by. Crosses mark impact speed and rotation angle of meteoroids with masses below  $10^{-13}$  g, squares represent meteoroids with masses above  $10^{-13}$  g. The two boxes indicate the uncertainties in the measurement of the impact direction and velocity around the expected values for interstellar meteoroids of  $26 \text{ km s}^{-1}$  and  $100^\circ$  for two values of radiation pressure coefficient  $\beta$ , where  $\beta = 0$  means no radiation pressure, and  $\beta = 1$  means radiation pressure equals gravity. Figure taken from Grün et al. [17].

$2 \times 10^{-25} \text{ g cm}^{-3}$  and its relative velocity of  $26 \text{ km s}^{-1}$  with respect to the Sun, an interstellar meteoroid flux density of  $10^{-3} \text{ m}^{-2} \text{ s}^{-1}$  can be expected. However, the flux at Earth of meteoroids with masses greater than  $10^{-13} \text{ g}$  was found to be  $1 \times 10^{-4} \text{ m}^{-2} \text{ s}^{-1}$  [22], one order of magnitude lower than the value derived from the theoretical mass density of the LIC. The discussion on the existence of interstellar meteoroids was settled by the unambiguous detection of small interstellar particles (masses if typically  $10^{-13} \text{ g}$ ) by an instrument on board the Ulysses spacecraft after its fly-by of Jupiter [16].

The evidence of the interstellar origin of the meteoroids detected by Ulysses comes from three independent observations: (a) The majority of impacts after Jupiter fly-by came from a retrograde direction, opposite to the direction of motion of meteoroids from Asteroids and short-period comets, (b) the impact velocity of particles from the retrograde direction was higher than the local solar system escape velocity, even if radiation pressure effects are neglected, and (c) the rate of impacts from that direction stayed nearly constant over a range of ecliptic latitude from  $0^\circ$  to  $79^\circ$ . Observation (a) is illustrated in figure 2, showing the geometry of the measurements after the fly-by of Jupiter. Most meteoroids were detected at rotation angles around  $90^\circ$ . This means that the observed meteoroids can only be of Solar System origin if a majority of them moves on retrograde orbits, which contradicts meteor observations. Observation (b) shows that the orbits of the detected meteoroids have to be hyperbolic. Due to the uncertainty in the measurement of the impact velocity, this statement does not hold for individual impacts, but for the statistic ensemble of impacts measured from the retrograde direction after Jupiter fly-by (see figure 3).

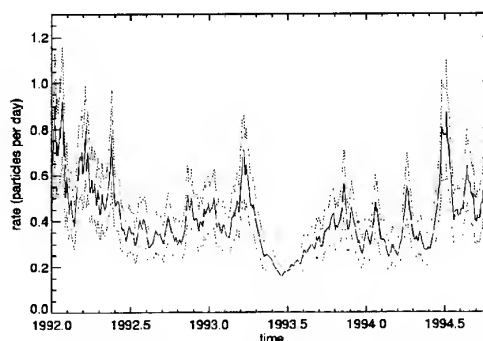


Figure 4. Impact rate of meteoroids measured by the detector on board the Ulysses spacecraft from 1992 to end-1994. A sliding mean average over 4 impacts is shown (solid line), together with  $1\sigma$  uncertainties (dotted lines). Ulysses left the ecliptic plane at 1992.2 towards increasing ecliptic latitudes until end-1994. Figure taken from Baguhl et al. [23]

A stream of interstellar meteoroids penetrates the whole Solar System and must thus be detectable independent of ecliptic latitude. Observation (c) shows that this is true for the Ulysses observations. The impact rate from all impacts (interstellar plus interplanetary) is shown in figure 4. While it is true that the rate decreases by less than a factor of 3 after the spacecraft leaves the ecliptic plane (February 1992), it levels off above 0.3 impacts per day. If only meteoroids of Solar System origin were detected, the decrease in impact rate would have decreased by more than an order of magnitude. In combination, observations (a), (b), and (c) are considered evidence for the existence of interstellar meteoroids in the Solar System.

#### 4. CHARACTERISTICS OF THE LOCAL INTERSTELLAR DUST POPULATION

The Ulysses spacecraft continues to monitor the stream of interstellar meteoroids. From these observations three discoveries have been made: (1) the particle mass distribution is not cut off at  $10^{-13} \text{ g}$  as expected from extinction measurements [24], which leads to an apparent excess in dust mass and thus the dust-to gas ratio of the LIC by at least a factor of 2, (2) solar radiation pressure does affect the stream inside 4 AU [25], and (3) the flux of small interstellar meteoroids is modulated with the solar cycle [26]. In what follows the three phenomena and their consequences are discussed.

The mass density-mass distribution of the interstellar meteoroids measured by the Ulysses detector as well as an identical instrument on board the Galileo spacecraft is shown in figure 5. The comparison of this local distribution with the average distribution derived from extinction measurements [21] over long interstellar lines of sight contains three interesting observations. First, the mass density contained small interstellar meteoroids is lower in the local distribution than in the average inter-

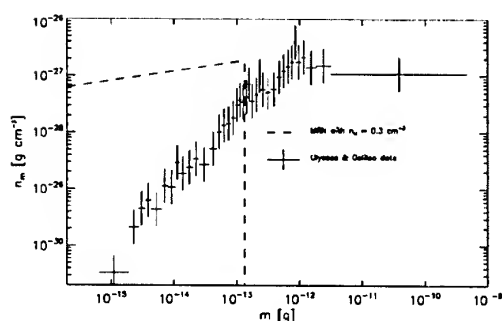


Figure 5. Mass density-mass distribution of interstellar meteoroids. The crosses represent the combined in situ measurements by the detectors on board the Ulysses and Galileo spacecraft. The dashed line shows the particle mass distribution of an model of the interstellar particle population derived from extinction measurements as well as cosmic abundance considerations [MRN, 21]. For this model it is assumed that the average gas density in the LIC is  $0.3 \text{ cm}^{-3}$ .

stellar distribution. This was attributed to the effect of the solar wind magnetic field that deflects small interstellar meteoroids from the solar system [26]. Second, the mass range of interstellar meteoroids detected locally extends almost 4 orders of magnitude to higher masses than was expected from the average extinction measurements [27]. Since large particles with masses above  $10^{-13} \text{ g}$  do not cause a strong wavelength dependent extinction in the optical and UV bands, the observation of these grains does not directly contradict the extinction measurements. However, current models of the interstellar particle population [28, 29] feature a cut-off to large masses in the interstellar particle mass distribution, because they are constrained by the amount of condensable elements available in interstellar space. This leads to the third observation in figure 5. The total mass, which is given by the area beneath the curves in figure 5 locked up in local interstellar meteoroids is by about a factor of 2 bigger than expected from cosmic abundance considerations [15]. Thus, the in situ detection of relatively large ( $m > 10^{-13} \text{ g}$ ) local interstellar meteoroids apparently violates the cosmic abundance of condensable elements. It can be speculated that the local interstellar meteoroids are injected into the LIC by some mechanism and thus do not contribute to the budget of chemical elements in the LIC. In that case the original source of local interstellar meteoroid population is still unknown.

The Ulysses measurements of the mass distribution of local interstellar meteoroids at different heliocentric distances shows that there is an interaction of the interstellar meteoroid stream with the solar radiation. Figure 6 shows the particle mass distribution of interstellar meteoroids measured by Ulysses at two different heliocentric distances. Meteoroids in the mass range between  $10^{-17}$  and  $10^{-16} \text{ kg}$  are less abundant in the measurements closer to the sun (2 to 4 AU) than they are in the measurements more far away from the Sun (outside 4 AU). Starting with the assumption that the meteoroid mass distribution

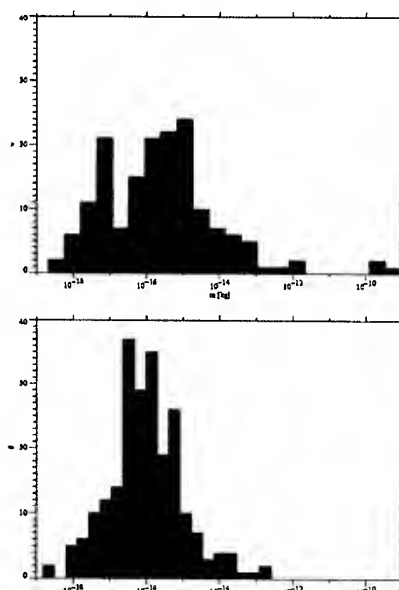


Figure 6. Histograms of the particle mass distribution measured by the Ulysses detector between 2 and 4 AU (upper panel), and outside 4 AU (lower panel). In the upper panel a lack of particles between  $10^{-17}$  and  $10^{-16} \text{ kg}$  can be seen compared to the distribution in the lower panel.

measured outside 4 AU is a better representation of the distribution in the LIC, it can be concluded that some mass-selective mechanism that is more efficient closer to the Sun removes the meteoroids in this mass region. The only mechanism that specifically affects meteoroids in the mass region between  $10^{-16}$  and  $10^{-17} \text{ kg}$  is solar radiation pressure that is most effective for meteoroids that have sizes in the order of the maximum wavelength of the solar spectrum ( $\lambda_{\text{max}} = 450 \text{ nm}$ ). While this observation depends on uncertain micro-physical properties of the meteoroids such as the bulk mass density and optical properties, it can be concluded that the material of which the local interstellar meteoroids consist can neither be too absorbent (like pure graphite) nor transparent (like pure quartz) [25, see also the paper by H. Kimura in this issue].

Another aspect of the Ulysses in situ measurements of interstellar meteoroids is the time variability of the interstellar stream. After Jupiter fly-by February 1992 until mid-1996 the interstellar particle flux appeared to be constant at  $1 \times 10^{-4} \text{ m}^{-2} \text{ s}^{-1}$ . Then the flux decreased significantly to  $4 \times 10^{-5} \text{ m}^{-2} \text{ s}^{-1}$ , about a factor of 3 below its former value (see figure 7). While it can not be ruled out that the reason for this decrease is a change in the local interstellar meteoroid concentration in the LIC, it is more likely due to the change in the phase of the solar cycle and thus in the heliocentric magnetic field configuration [30]. Modelling of the interaction of a constant stream of meteoroids, that acquire an electrostatic charge in interplanetary space, with the heliocentric magnetic field can account for this decrease of meteoroid flux in the Solar

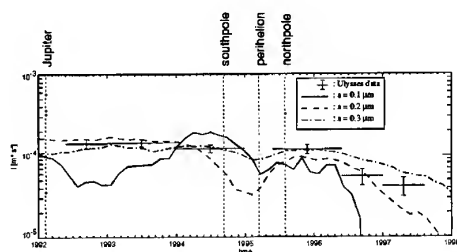


Figure 7. Time variability of interstellar meteoroid flux. The error-bars show the flux measured by the Ulysses detector and the lines indicate the flux predicted by the magnetic interaction model for various particle radii. Vertical lines indicate special events of the Ulysses mission. Figure taken from Landgraf [26].

System. The picture drawn by the model is the following: the magnetic field polarity between the solar maxima in 1980 and 1991 was favourable for focusing the interstellar meteoroid stream towards low heliographic latitudes, i.e. towards the magnetic equator of the Sun. Starting at the maximum in 1991, the magnetic field polarity was reversed, causing a deflecting action of the magnetic field. The average magnetic field strength at the beginning of a new cycle is not very strong, so the deflection started to be effective in 1995. Ulysses then consequently observed a decreasing flux in mid-1996 more than 1 year later due to the lag caused by the meteoroid's dynamics. The model curves in figure 7 fit reasonably well the measured flux values for spherical particles with radii of 0.2  $\mu\text{m}$ , corresponding to masses of  $10^{-16}$  kg, the maximum in the particle mass distribution.

## 5. FUTURE MEASUREMENTS

After Ulysses and Galileo a new generation of meteoroid detectors was launched, one aboard the Cassini spacecraft [6] towards Saturn, and one aboard Stardust, a mission to collect cometary as well as interstellar meteoroids in situ [7]. While the Cassini detector is not expected to find many interstellar meteoroids due to the orientation of its trajectory downstream of the Sun, Stardust is specifically designed to collect and measure in situ interstellar particles. The collected particles will be available for analysis to the scientific community after the capsule returns to the Earth in 2006. The Cometary and Interstellar Dust Analyser (CIDA) instrument on board Stardust has detected few interstellar meteoroids so far, due to its small sensitive area of 80  $\text{cm}^2$  and the reduced interstellar dust flux, as predicted [31]. The information content of these impacts is however high, because CIDA is capable of determining the elementary composition of the impactors.

The discussion in this paper shows that important information about our galactic neighbourhood is contained in the stream of interstellar meteoroids through the Solar System. From what we have learned so far new questions arise: what is the precise stream direction, and how close is it to the flow direction of gas from the LIC? Are there other interstellar meteoroid streams that also pass through

the Solar System, but have lower flux densities so that the Ulysses detector can not identify them? What is the composition of local interstellar meteoroids and how does it compare to isotopically anomalous components of IDPs [32–34]? In order to find an answer to these questions new measurements have to be performed, because the Ulysses dust detector has a limited sensitive area (0.1  $\text{m}^2$ ) and limited direction, velocity and mass measurement accuracy. An ideal instrument for these measurements is a large-area, direction sensing, limited field of view detector as proposed by Grün et al. [35, see also the paper by Grün in this issue].

## REFERENCES

- [1] F. L. Whipple. On maintaining the meteoritic complex. In *Zodiacal Light and the Interplanetary Medium*, number 150 in NASA-SP, pages 409–426, 1967.
- [2] K. Grogan, S. F. Dermott, and T. J. J. Kehoe. The Distribution of Asteroidal Dust in the Inner Solar System. In *IAU Symposium*, volume 202, pages E71–E72, 2000.
- [3] G. Cremonese, M. Fulle, F. Marzari, and V. Vanzani. Orbital evolution of meteoroids from short period comets. *Astronomy and Astrophysics*, 324:770–777, 1997.
- [4] J. S. Mathis. Interstellar dust and extinction. *Annual Review of Astronomy and Astrophysics*, 28:37–70, 1990.
- [5] H. A. Zook and O. E. Berg. A source for hyperbolic cosmic dust particles. *Planetary and Space Science*, 23:183–203, 1975.
- [6] R. Srama and E. Grün. The dust sensor for CASSINI. *Advances in Space Research*, 20:1467–1470, 1997.
- [7] D. E. Brownlee, P. Tsou, B. Clark, M. S. Hanner, F. Hörz, J. Kissel, J. A. M. McDonnell, R. L. Newburn, S. Sandford, Z. Sekanina, A. J. Tuzzolino, and M. Zolensky. Stardust: A Comet Sample Return Mission. *Meteoritics & Planetary Science*, 35:35–36, 2000.
- [8] P. C. Frisch. Characteristics of nearby interstellar matter. *Space Science Reviews*, 72:499–592, 1995.
- [9] P. C. Frisch. LISM structure – fragmented super-bubble shell? In R. von Steiger, R. Lallement, and M. A. Lee, editors, *The Heliosphere in the Local Interstellar Medium*, volume 78 of *Space Science Reviews*, pages 213–222. Kluwer Academic Publishers, 1996.
- [10] R. Lallement and P. Bertin. Northern-hemisphere observations of nearby interstellar gas – possible detection of the local cloud. *Astronomy and Astrophysics*, 266:479–485, 1992.
- [11] B. E. Wood, J. L. Linsky, and G. P. Zank. Heliospheric, astrospheric, and interstellar  $\text{Ly}\alpha$ ; absorption toward 36 ophiuchi. *Astrophysical Journal*, 537:304–311, 2000.

- [12] T. E. Holzer. Interaction between the solar wind and the interstellar medium. *Annual Review of Astronomy and Astrophysics*, 27:199–234, 1989.
- [13] A. P. Jones, A. G. G. M. Tielens, D. J. Hollenbach, and C. F. McKee. Grain destruction in shocks in the interstellar medium. *Astrophysical Journal*, 433: 797–810, 1994.
- [14] C. Gry, L. Lemonon, A. Vidal-Madjar, M. Lemoine, and R. Ferlet. The interstellar void in the direction to  $\epsilon$  Cma: local clouds and hot gas. *Astronomy and Astrophysics*, 302:497+, 1995.
- [15] P. C. Frisch, J. Dorschner, J. Geiß, J. M. Greenberg, E. Grün, M. Landgraf, P. Hoppe, A. P. Jones, W. Krätschmer, T. J. Linde, G. E. Morfill, W. T. Reach, J. Slavin, J. Svestka, A. Witt, and G. P. Zank. Dust in the local interstellar wind. *Astrophysical Journal*, 525:492–516, 1999.
- [16] E. Grün, H. A. Zook, M. Baguhl, A. Balogh, S. J. Bame, H. Fechtig, R. Forsyth, M. S. Hanner, M. Horanyi, J. Kissel, B.-A. Lindblad, D. Linkert, G. Linkert, I. Mann, J. A. M. McDonnell, G. E. Morfill, J. L. Phillips, C. Polanskey, G. Schwehm, N. Siddique, P. Staubach, J. Svestka, and A. Taylor. Discovery of jovian dust streams and interstellar grains by the Ulysses spacecraft. *Nature*, 362: 428–430, 1993.
- [17] E. Grün, B. Å. S. Gustafson, I. Mann, M. Baguhl, G. E. Morfill, P. Staubach, A. Taylor, and H. A. Zook. Interstellar dust in the heliosphere. *Astronomy and Astrophysics*, 286:915–924, 1994.
- [18] J. A. M. McDonnell and O. E. Berg. Bounds for the interstellar to solar system microparticle flux ratio over the mass range  $10^{-11}$  –  $10^{-13}$  g. In *Space Research XV*, pages 555–563. Akademie-Verlag, Berlin, 1975.
- [19] G. E. Morfill and E. Grün. The motion of charged dust particles in interplanetary space – ii. interstellar grains. *Planetary and Space Science*, 27:1283–1292, 1979.
- [20] B. Å. S. Gustafson and N. Y. Misconi. Streaming of interstellar grains in the solar system. *Nature*, 282: 276–278, 1979.
- [21] J. S. Mathis, W. Rumpl, and K. H. Nordsieck. The size distribution of interstellar grains. *Astrophysical Journal*, 280:425–433, 1977.
- [22] E. Grün, H. A. Zook, H. Fechtig, and R. H. Giese. Collisional balance of the meteoritic complex. *Icarus*, 62:244–272, 1985.
- [23] M. Baguhl, E. Grün, and M. Landgraf. In situ measurements of interstellar dust with the Ulysses and Galileo spaceprobes. In R. von Steiger, R. Lallement, and M. A. Lee, editors, *The Heliosphere in the Local Interstellar Medium*, volume 78 of *Space Science Reviews*, pages 165–172. Kluwer Academic Publishers, 1996.
- [24] M. Landgraf, W. J. Baggaley, E. Grün, H. Krüger, and G. Linkert. Aspects of the mass distribution of interstellar dust grains in the solar system from in-situ measurements. *Journal of Geophysical Research*, 105(A5):10343–10352, 2000.
- [25] M. Landgraf, K. Augustsson, E. Grün, and B. Å. S. Gustafson. Deflection of the local interstellar dust flow by solar radiation pressure. *Science*, 286: 2319–2322, 1999.
- [26] M. Landgraf. Modeling the motion and distribution of interstellar dust inside the heliosphere. *Journal of Geophysical Research*, 105(A5):10303–10316, 2000.
- [27] E. Grün and M. Landgraf. Collisional consequences of big interstellar grains. *Journal of Geophysical Research*, 105(A5):10291–10298, 2000.
- [28] J. S. Mathis. Dust models with tight abundance constraints. *Astrophysical Journal*, 472:643, 1996.
- [29] A. Li and J. M. Greenberg. A unified model of interstellar dust. *Astronomy and Astrophysics*, 323: 566–584, 1997.
- [30] B. Å. S. Gustafson and S. M. Lederer. Interstellar grain flow through the solar wind cavity around 1992. In B. Å. S. Gustafson and M. S. Hanner, editors, *Physics, Chemistry and Dynamics of Interplanetary Dust*, volume 104 of *Astronomical Society of the Pacific Conference Series*, pages 35–39, 1996.
- [31] M. Landgraf, M. Müller, and E. Grün. Prediction of the in-situ dust measurements of the Stardust mission to comet 81P/Wild 2. *Planetary and Space Science*, 47:1029–1050, 1999.
- [32] J. P. Bradley. Chemically anomalous preaccretionally irradiated grains in interplanetary dust from comets. *Science*, 265:925, 1994.
- [33] J. P. Bradley, L. P. Keller, T. P. Snow, M. S. Hanner, G. J. Flynn, J. C. Gezo, S. J. Clemett, D. E. Brownlee, and J. E. Bowey. An infrared spectral match between GEMS and interstellar grains. *Science*, 285: 1716–1718, 1999.
- [34] L. P. Keller, S. Messenger, and J. P. Bradley. Analysis of deuterium-rich interplanetary dust particle (IDP) and implications for presolar material in IDPs. *Journal of Geophysical Research*, 105(A5): 10397–10402, 2000.
- [35] E. Grün, M. Landgraf, M. Horanyi, J. Kissel, H. Krüger, R. Srama, H. Svedhem, and P. Withnell. Techniques for galactic dust measurements in the heliosphere. *Journal of Geophysical Research*, 105 (A5):10403–10410, 2000.

# PROPERTIES OF LOCAL INTERSTELLAR DUST DERIVED FROM REMOTE ASTRONOMICAL OBSERVATIONS, LABORATORY ANALYSES, AND IN SITU MEASUREMENTS

Hiroshi Kimura<sup>1</sup>, Ingrid Mann<sup>1,2</sup>, and Elmar K. Jessberger<sup>1</sup>

<sup>1</sup>Institut für Planetologie, Westfälische Wilhelms-Universität, Wilhelm-Klemm-Straße 10, D-48149 Münster, Germany

<sup>2</sup>Solar System Division, ESA-ESTEC, P.O. Box 299, 2200 AG Noordwijk, The Netherlands

## ABSTRACT

This paper reviews the current knowledge of properties of dust in the local interstellar cloud (LIC), in which the solar system is currently embedded. The chemical composition of dust in the LIC can be inferred from measured gas-phase abundances in the LIC and the reference elemental abundances. The spatial variation in the mass distribution of the local interstellar dust measured with spacecraft puts further constraints on the properties of dust in the LIC.

The interstellar extinction curve and the dust-phase elemental abundances have been applied to model the average properties of dust in the interstellar medium (ISM). Presolar grains and pristine cometary dust may act as real samples of ancient interstellar dust in the early stage of the solar system formation. Recently the local structure of the ISM has become accessible to remote astronomical observations and in situ measurements. Comparison of available information on average, ancient, and local interstellar dust reveals common properties of interstellar dust at different points in space and time.

## 1. INTRODUCTION

Dust grains are condensed from gas mainly in the latest stages of stellar evolution and then injected into the interstellar medium (ISM) with gas. Interstellar dust plays an important role in cooling and heating of interstellar gas and catalyzing certain molecules in cold dense clouds (Ostriker & Silk, 1973; Watson, 1972; Watson & Salpeter, 1972). While traveling through the ISM, physical and chemical processes in the ISM alter the properties of interstellar dust (Sandford, 1996). Dust grains may be disrupted by mutual collisions and sputtering in shocks, but they grow by accretion of gas and coagulation processes in molecular clouds where star formation takes place (Draine, 1985). In the early stages of planetary system formation, interstellar dust is incorporated into comets and asteroids. Therefore, young long-period comets and primitive asteroids within the solar system may still contain pristine interstellar dust. Dust grains released from comets and asteroids either spiral into the sun

and eventually sublime into gas or leave the solar system and enter the ISM. The study of the properties of interstellar dust and the comparison to the pristine dust in the solar system improve our understanding of the evolution of matter from the ISM to planetary systems.

There are three different methods to measure the properties of interstellar dust: remote astronomical observations of phenomena associated with interactions of interstellar dust with radiation or gas, laboratory analyses of presolar grains and pristine matter in cometary dust, and finally in situ measurements of interstellar and cometary dust. Remote astronomical observations have provided information on the properties of interstellar dust averaged over the line of sight (Mathis, 1990; Dorschner, 2001). Laboratory analyses are possible for presolar grains extracted from primitive meteorites and pristine cometary dust collected in the earth's stratosphere (Anders & Zinner, 1993; Jessberger et al., 2001). In situ measurements of cometary dust have improved our knowledge of pristine matter preserved in comets (Sekanina et al., 2001). They represent samples or remnants of ancient interstellar dust that existed in the molecular cloud when the solar system formed (Bernatowicz & Walker, 1997; Messenger, 2000). In contrast, in situ measurements of interstellar dust from spacecraft in the solar system provide information on the properties of dust in the local interstellar cloud (LIC), in which the sun is currently embedded (Mann & Kimura, 2000; Grün et al., 2001). The study of dust in the LIC becomes recently possible with remote astronomical observations that have revealed the properties of the LIC (Frisch et al., 1999). In this context, we review our current knowledge of physical and chemical properties of dust in the LIC along with the properties of average interstellar dust, presolar grains, and pristine cometary dust.

## 2. AVERAGE INTERSTELLAR DUST

### 2.1. Extinction Curve and Emission Features

Interstellar dust scatters and absorbs electromagnetic radiation and reradiates absorbed energy as thermal radiation. The extinction of stellar radiation has long been rec-

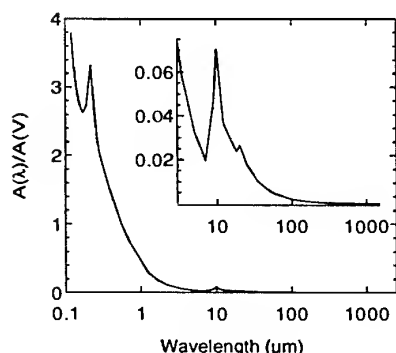


Figure 1. The observed extinction for the average ISM with the optical parameter of 3.02 as a function of wavelength. The values are normalized to the visual extinction at a wavelength of 550 nm.

ognized by astronomers even before Trumpler (1930a,b) explained it by the presence of dust in the ISM. The polarization of initially unpolarized light from distant stars is also attributed to dust grains that are aligned in the ISM (Hall & Mikesell, 1949; Hiltner, 1949). The spectral variation of the interstellar extinction has given clues about the average mineralogical properties of interstellar dust. Fig. 1 shows the interstellar extinction curve normalized to the visual extinction at a wavelength  $\lambda$  of 550 nm with  $R_V = 3.02$  where  $R_V$  is the ratio of the visual extinction to the color excess (Mathis & Whiffen, 1989). The observed interstellar extinction shows a prominent feature at  $\lambda = 217.5$  nm, which was primarily attributed to graphite grains (Stecher, 1965; Stecher & Donn, 1965). Although the identification of the 217.5 nm feature is still in debate, it is most likely due to small carbonaceous particles such as graphite grains with radii  $a \leq 20$  nm and polycyclic aromatic hydrocarbons (PAHs) (Duley & Seahra, 1998). The observed interstellar features at 9.7 and 18  $\mu\text{m}$  are discussed as evidence for the presence of amorphous silicate (Day, 1974; Ney, 1977). Among amorphous silicates, amorphous olivine has been suggested to be a candidate material for the broad 10  $\mu\text{m}$  feature (Stephens & Russell, 1979).

Recent observations have shown extended red emission (ERE) in the diffuse ISM, which is a broad emission feature of 100 nm width around  $\lambda = 600$  nm (Szomoru & Guhathakurta, 1998). The ERE seemingly arises from photoluminescence by either carbon nanoparticles such as hydrogenated amorphous carbon and PAHs or silicon nanoparticles (Duley, 2001; Ledoux et al., 2001). Observations of the ERE indicate that the carrier of the ERE is an abundant and ubiquitous component of interstellar dust (Seahra & Duley, 1999; Witt, 2000). Carbon and silicon nanoparticles might be responsible to the observed 217.5 nm and 10  $\mu\text{m}$  features, respectively.

## 2.2. Elemental Abundances

The determination of dust-phase elemental abundances in the ISM puts constraints on the mineralogical properties of interstellar dust. The spatial distribution of dust

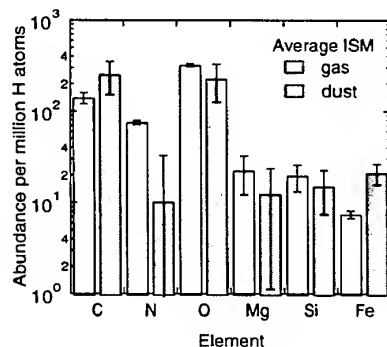


Figure 2. The abundances of C, N, O, Mg, Si, and Fe per million H atoms in the average ISM. The solar abundance is assumed to be a reference.

is correlated with that of gas with a gas-to-dust mass ratio of 100 on average (Lilley, 1955; Savage & Jenkins, 1972). Measurements of the elemental abundances in the gas phase, therefore, allow to indirectly determine the elemental abundances in the dust phase if compared to standard abundances. Namely, the dust-phase abundances of elements can be inferred by subtracting measured gas-phase abundances from the standard abundances.

The definition of the standard abundances for the ISM in our Galaxy or the so-called "cosmic" abundances is not trivial. Solar photospheric abundances have widely been assumed, but were questioned when Greenberg (1974) pointed out that they yield too large abundances of C, N, and O in the dust phase. New spectrographic measurements of interstellar absorption lines with the Goddard High Resolution Spectrograph (GHRS) on the *Hubble Space Telescope* (HST) have recalled the assumption into question (Sofia et al., 1994). The problem of the large oxygen abundance for the dust phase could be solved if the cosmic abundances of elements relative to hydrogen are assumed to be sub-solar rather than solar (Mathis, 1996). A compilation of data on the composition of young stars in the solar neighborhood has also supported sub-solar abundances as a standard (Snow & Witt, 1996). Because of their sub-solar abundances and young ages, B stars have been proposed as a plausible standard (Sofia et al., 1994; Cardelli et al., 1996; Sofia, 1997). Recent studies on the composition of interstellar dust have utilized multiple standard references (Sembach & Savage, 1996; Jones, 2000).

The solar photospheric abundances have very recently been revised with new photospheric data, taking effects of the deviation from the local thermodynamic equilibrium in the photosphere and photospheric granulation into account (Holweger, 2001). In particular, the solar photospheric oxygen abundance has greatly been reduced and therefore the solar photospheric abundances seem again to be a reasonable reference for the average ISM (Holweger, 2001; Sofia & Meyer, 2001). Young ( $\leq 2$  Gyr) F and G stars may be an alternate candidate for providing standard abundance information, but uncertainties in the measured abundances are still larger than those for the solar abundances. On the other hand, a new com-

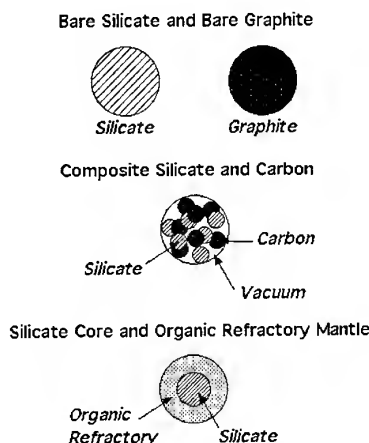


Figure 3. Illustration of the selected dust models; Two populations of silicate grains and graphite grains, composite grains consisting of silicate, carbon, and vacuum, and grains with a silicate core and an organic refractory mantle.

pilation of B stars shows large variations in elemental abundances that exceed the uncertainties of the measurements and yields negative N and Si abundances in the dust phase within the large variations (Sofia & Meyer, 2001). Even taking into account the uncertainties, the B star abundances are no longer an appropriate standard because the dust-phase Si abundance is too low to account for the silicate features in the extinction curve. We hereafter assume the revised values of the solar photospheric abundance as standard for the total (gas plus dust) abundance in the ISM, but the uncertainties of these assumptions have to be kept in mind. Fig. 2 shows the elemental abundances of C, N, O, Mg, Si, and Fe per million H atoms for the average ISM (Sofia & Meyer, 2001). The silicate mineralogy of interstellar dust may be inferred from the ratio  $(\text{Mg} + \text{Fe})/\text{Si}$  in the dust phase. The ratio  $(\text{Mg} + \text{Fe})/\text{Si} = 2.2 \pm 1.4$  for dust in the average ISM implies that the average interstellar dust has olivine-type stoichiometry, although the uncertainty in the ratio is large. This is consistent with common understanding that the broad  $10\ \mu\text{m}$  feature in the extinction curve originates from amorphous olivine.

### 2.3. Dust Models

Numerous models of interstellar dust have been proposed to explain the spectral variation of the interstellar extinction, taking into account the elemental abundances and, in some cases, the emission features. We here concentrate on three models as we illustrate them in Fig. 3 assuming interstellar dust to be spherical. Note that this is an oversimplified view of morphology because observations of interstellar polarization indicate the presence of non-spherical dust particles (Davis & Greenstein, 1951; Spitzer & Tukey, 1951; Gold, 1952). Fig. 4 shows the cumulative mass distributions for the selected dust mod-

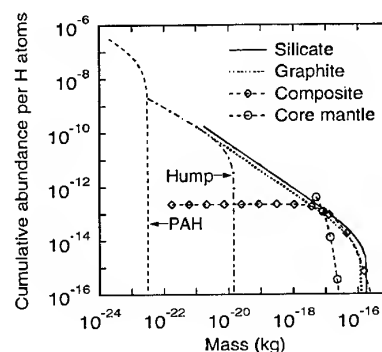


Figure 4. The cumulative number density modeled for dust in the average ISM. The values are normalized to the hydrogen number density.

els normalized to the number density of hydrogen atoms.

The interstellar extinction curve is reasonably well fitted with a superposition of extinctions by silicate grains and graphite grains (Mathis et al., 1977). The size distribution of the grains is described by a power law for radii from 5 to 250 nm (Draine & Lee, 1984). The power-law spectrum can be explained by the fragmentation process due to grain-grain collisions in the ISM (Biermann & Harwit, 1980). For homogeneous spherical grains, the size range covers the mass  $m$  from  $2 \times 10^{-21}$  to  $2 \times 10^{-16}$  kg for amorphous olivine and  $m = 1 \times 10^{-21}$ – $1 \times 10^{-16}$  kg for graphite. The mass distributions are shown in Fig. 3 as solid and dotted curves for bare silicate grains and bare graphite grains, respectively.

Mathis & Whiffen (1989) assume loosely bounded agglomerations of silicate, amorphous carbon, and graphite, claiming that silicate and carbon do not exist separately, but are mixed in molecular clouds. In this model, composite dust grains contain 80 % of vacuum and the single constituents are nanometer sized. In addition, the extinction feature at  $\lambda = 217.5$  nm is attributed to bare graphite grains of nanometer size without any specific size distribution. The mass distribution of the composite grains for  $R_V = 3.02$  follows a power law in the radius range of 30–900 nm, that is, the mass range of  $6 \times 10^{-20}$ – $2 \times 10^{-15}$  kg. Mathis (1996) has refined the model of composite grains to consist of silicate, amorphous carbon, and 45 % of vacuum, the distribution of which is shown in Fig. 3 as diamonds with dashed lines. The suggested size distribution of the composite grains no longer obeys a power law, but has a peak at  $a \approx 100$  nm distributed mostly in the range  $30 \leq a \leq 300$  nm (Dwek, 1997). The mass distribution, therefore, shows a peak around  $m = 2$ – $3 \times 10^{-18}$  kg in the range  $10^{-19} \leq m \leq 10^{-16}$  kg. Small graphite grains and small silicate grains are responsible for the extinction hump at  $\lambda = 217.5$  nm and a steep rise in the extinction at  $\lambda < 170$  nm, respectively. The size distributions of these small grains are not specified because their sizes do not affect the extinction.

On the basis of interaction between dust and gas in molecular clouds, Greenberg (1973, 1998) has proposed interstellar dust to have a core-mantle structure. These

Table 1. The abundances of C, N, O, Mg, Si, and Fe per million H atoms required for the selected models of dust in the average ISM.

Model	C	N	O	Mg	Si	Fe
silicate+graphite	282	0	131	36	33	29
composite	160	0	128	32	32	32
core-mantle	194	4	103	20	20	20

core-mantle grains form as a result of the accretion of ice onto the surface of silicate grains in molecular clouds. Subsequent photochemical processing of ice under ultraviolet radiation in the ISM transforms the ice into organic refractories (Greenberg & Hage, 1990; Sandford, 1996). The grains with a silicate core and an organic refractory mantle are assumed to have a Gaussian size distribution with a peak at the core radius of 70 nm (Li & Greenberg, 1997). The majority of the core-mantle grains lies in the mass range  $6 \times 10^{-18} \leq m \leq 2 \times 10^{-17}$  kg. Spherical core-mantle grains can be as massive as  $8 \times 10^{-16}$  kg when the organic refractory mantle reaches the maximum thickness of 400 nm (Greenberg, 1980). This model requires an additional population of small carbonaceous grains to explain the 217.5 nm hump feature in the extinction curve. Moreover, PAHs are required to produce the steep rise of the extinction curve in the far ultraviolet wavelength range. Both the hump particles and the PAHs are assumed to follow power-law size distributions in the mass ranges of  $3 \times 10^{-23}$ – $2 \times 10^{-20}$  kg and  $2 \times 10^{-24}$ – $3 \times 10^{-23}$  kg, respectively. Open circles with dashed lines in Fig. 3 display the distribution for the grains with a silicate-core and an organic refractory mantle, while the additional population for the 217.5 nm extinction hump is also included as a dash-dotted curve and the population of PAHs as a dashed curve.

Table 1 gives the abundances of C, N, O, Mg, Si, and Fe per million H atoms necessary for the selected models of dust in the average ISM. The model with bare silicate and bare graphite grains requires C, N, and O within the available dust-phase abundances. However, the dust-phase abundances of Mg, Si, and Fe in the average ISM are insufficient for this model. Composite grains of silicate and amorphous carbon with 45 % of vacuum also contain Mg, Si, and Fe more than their available dust-phase abundances in the average ISM, while the required C, N, and O are within the dust-phase abundances. Grains with a silicate core and an organic refractory mantle well satisfy the constraints on the elemental abundances in the dust phase derived from remote astronomical observations.

### 3. ANCIENT INTERSTELLAR DUST

#### 3.1. Presolar Grains in Meteorites

Presolar grains are not necessarily representative of dust in the LIC because of the difference in the present and

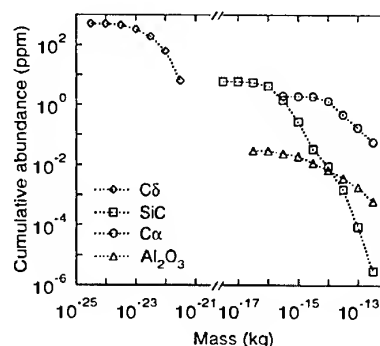


Figure 5. The cumulative bulk abundances of presolar grains in primitive meteorites as a function of grain mass.

past environments surrounding the sun. In addition, presolar grains are mostly acid insoluble residues that survive chemical treatments of isolation from meteorites. Nevertheless it is worth to study presolar grains because they give clues about the properties of dust in the ancient ISM: Presolar grains are extracted from primitive meteorites that have a chemistry and mineralogy indicative of little alteration since their formation (Bernatowicz & Walker, 1997).

Presolar grains found in meteorites are diamond (C $\delta$ ), silicon carbide (SiC), graphite (C $\alpha$ ), corundum (Al $_2$ O $_3$ ), silicon nitride (Si $_3$ N $_4$ ), spinel (MgAl $_2$ O $_4$ ), titanium oxide (TiO $_2$ ), and hibonite (CaAl $_2$ O $_7$ ) (Lewis et al., 1987; Bernatowicz et al., 1987; Amari et al., 1990; Hutcheon et al., 1994; Nittler et al., 1995, 1997; Nittler & Alexander, 1999; Choi et al., 1999). Within presolar graphite grains, carbides of Ti, Zr, and Mo, kamacite (FeNi), and cohenite ([FeNi] $_3$ C) were found as nanometer to tens of nanometer sized crystals (Bernatowicz et al., 1991, 1996, 1999). Choi et al. (1999) propose even the presence of presolar perovskite (CaTiO $_3$ ) and melilite (Ca $_2$ [Al,Mg,Si] $_2$ O $_7$ ) grains in meteorites, but these grains are not expected to survive the separation. The presolar grains have been identified by their isotopic anomalies and an attempt for searching presolar silicates has failed (Messenger & Bernatowicz, 2000; Alexander et al., 2001). Note that the isolated grains may represent only a minor component of the ancient interstellar dust: Silicates are dissolved and organic components are destroyed during the process of isolating presolar grains from meteorites.

The size distributions of presolar diamond, silicon carbide, and graphite grains can be fit with a log-normal rather than a power-law (Lewis et al., 1989; Amari et al., 1994). Fig. 5 displays the cumulative mass distributions of presolar grains in primitive meteorites. Open diamonds, squares, circles, and triangles indicate the distributions of presolar diamond, silicon carbide, graphite, and corundum grains, respectively. Presolar diamond grains are nanometer sized in the mass range from  $5 \times 10^{-25}$  to  $5 \times 10^{-22}$  kg (Lewis et al., 1989). In contrast, the other presolar grains are micron sized: The mass of corundum grains ranges from  $3 \times 10^{-17}$  to  $3 \times 10^{-13}$  kg (Nittler et al., 1997). Silicon carbide grains cover the mass range from  $8 \times 10^{-18}$  to  $5 \times 10^{-13}$  kg and graphite

grains from  $9 \times 10^{-16}$  to  $5 \times 10^{-13}$  kg (Amari et al., 1994).

Presolar SiC grains show various morphological structures from euhedral shapes with crystalline feature to aggregates of submicron crystallites (Hoppe et al., 1994). The majority of presolar graphite grains appears to be either cauliflower-like aggregates of submicron grains or onion-like concentric layers of well crystallized grains (Zinner et al., 1995). Lee et al. (1992) have reported needle-shaped  $\text{Si}_3\text{N}_4$  of possibly presolar origin, but presolar  $\text{Si}_3\text{N}_4$  grains found by Nittler et al. (1995) are blocky in shape. Two hibonite grains of presolar origin found in an ordinary chondrite show plate-like structure and crystal faces on each plate (Choi et al., 1999).

### 3.2. Pristine Matter in Interplanetary Dust Particles

Comets are believed to be formed as an agglomeration of pristine interstellar dust through the collapse of a molecular cloud. Young comets may still preserve pristine interstellar dust even though the radioactive elements might modify the nature of volatile components. Comets are also a major source of interplanetary dust particles (IDPs) that have been collected in the earth's stratosphere (Leinert & Grün, 1990). Therefore, their analyses may reveal information on pristine interstellar materials preserved in comets. In particular, porous aggregate IDPs with chondritic bulk compositions and high carbon contents are anhydrous and certainly primitive (Jessberger et al., 2001). They are supposed to originate from comets, but primitive asteroids cannot be ruled out as the source (Schramm et al., 1989).

The majority of chondritic porous IDPs contains glass with embedded metal and sulfides (GEMS) that is supposedly interstellar amorphous silicate (Bradley, 1994). The radii of GEMS range from 50 to 250 nm while the metal and sulfide inclusions are nanometer-sized. The infrared spectral profile of GEMS matches that of amorphous silicate grains in molecular clouds and the Si-O stretch bands near  $10 \mu\text{m}$  for a GEMS-rich IDP are shown to resemble those for comets and Herbig Ae/Be stars (Bradley et al., 1999). The presence of tiny metal inclusions in GEMS might also be relevant for the grain alignment and thus the interstellar linear polarization (Martin, 1995).

Deuterium-rich IDPs may well preserve pristine properties, since the high deuterium content is an indicator for the most primitive materials (Jessberger et al., 2001). Large deuterium enrichments are common among cluster IDPs that were fragmented by impact with the stratospheric collector (Messenger et al., 1996; Messenger, 2000). Analysis of one cluster D-rich IDP shows that GEMS are the major constituent and are surrounded by carbonaceous material (Keller et al., 2000). This D-rich IDP also contains Mg-rich pyroxene and olivine, and Fe-Ni sulfides, while organic molecules within the carbonaceous material are the possible host for the D enrichment. It is worth noting that PAHs are observed only in D-rich IDPs and Raman spectra of these IDPs show similarity to interstellar infrared emission features attributed to PAHs

(Clemett et al., 1993; Messenger et al., 1995; Allamandola et al., 1987).

### 3.3. Pristine Matter in Cometary Dust

A search for pristine interstellar materials in comets was directly carried out by mass spectrometers on space missions to comet Halley. The elemental composition of dust in the coma of comet Halley was measured in situ with PUMA-1 on VeGa 1, PUMA-2 on VeGa 2, and PIA (Particle Impact Analyzer) on *Giotto*. The mass spectra of impact-generated ions from PUMA-1 have been explained with a lack of both Fe-rich pyroxenes and Fe-rich olivines in the dust (Jessberger et al., 1988). Mg-rich and Fe-poor silicates comprise the majority of the Halley's inorganic component while Fe-Ni sulfides are approximately 10 % of the component and Fe oxides are a minor component (Jessberger, 1999). The ratio of Mg to Fe greatly differs from particle to particle, but the Si/Mg ratios are nearly constant. Although the ratio  $(\text{Mg} + \text{Fe})/\text{Si} = 0.8 \pm 0.1$  for Halley's dust might agree with pyroxene-type stoichiometry, the uncertainty in the abundance determinations by a factor of two prevents us from concluding the mineralogical properties. In fact, spectroscopic observations of Halley's coma in the infrared wavelength range have shown that crystalline olivine is abundant in the comet (Campins & Ryan, 1989). The data analyses of PUMA-1, PUMA-2, and PIA have shown that most of the Halley's grains are rich in H, C, N, and O, indicating the presence of organic refractory materials (Kissel et al., 1986a,b; Fomenkova, 1999). Further analyses of PUMA-1 data have revealed that the volume ratio of inorganic to organic component ranges from two to five (Schulze et al., 1997).

It may be worth mentioning that the mass spectrometers measured spectra of positive ions generated by hypervelocity impact of Halley's dust. Ionization efficiencies for each element are required for the determination of chemical compositions from mass spectra, although such hypervelocity impact phenomena have not been simulated in a laboratory. Nevertheless, a recent application of a hydrodynamic model to mean PUMA-1 spectra has yielded chemical compositions of Halley's dust roughly in accord with those previously derived from empirical methods (Hornung & Kissel, 1994).

In situ data analysis with the time-of-flight mass spectrometer CIDA (Cometary and Interstellar Dust Analyzer) onboard the current mission *Stardust* will reveal information on the chemical compositions of dust from comet Wild 2 (Brownlee et al., 1996, 2000). *Stardust* measures not only the composition of cometary dust in situ with CIDA but also the flux and mass distribution of cometary grains with the dust detector DFMI (Dust Flux Monitoring Instrument) (Brownlee et al., 2000). Furthermore cometary dust grains will be collected with low-density silica aerogel SRC (Sample Return Capsule) to bring them back to the earth. Laboratory analyses of the collected grains will greatly improve our knowledge of their physical and chemical properties. The upcoming *Rosetta* mission will rendezvous comet 46P/Wirtanen and will provide a whole set of measurements of pristine

cometary dust with GIADA (Grain Impact Analyser and Dust Accumulator), MIDAS (Micro-Imaging Dust Analysis System), and COSIMA (Cometary Secondary Ion Mass Analyser) (Schwehm & Schulz, 1999). COSIMA is a time-of-flight secondary ion mass spectrometer that measures elemental and isotopic composition of dust particles (Zscheeg et al., 1992). GIADA is designed to monitor the dust environment in the cometary coma and allows the determination of the mass and speed of single grains and of the dust mass flux (Bussoletti et al., 1999). MIDAS will provide microtopographic images and a statistical distribution of dust particles based on an atomic force microscope (AFM) (Riedler et al., 1999). The CONTOUR (Comet Nucleus Tour) mission will investigate cometary dust with CIDA visiting the two comets Encke and Schwassmann-Wachmann 3 (Bell et al., 2000).

#### 4. LOCAL INTERSTELLAR DUST

##### 4.1. Dust Composition in the LIC

The sun is located near the edge of the LIC with a dimension of a few parsecs, which contains partially ionized and warm rarefied gas (Redfield & Linsky, 2000). Although there are no extinction measurements towards stars in the LIC, recent measurements of interstellar absorption lines could provide the gas-phase elemental abundances in the LIC. Frisch et al. (1999) have derived the elemental abundances in the LIC from the absorption spectra in the direction to  $\epsilon$  Canis Majoris ( $\epsilon$ CMa). They have suggested the local interstellar dust to be core-mantle grains consisting of olivine and metal oxides in the core and pyroxene in the mantle. This model implies that properties of dust in the LIC bear no resemblance to dust models for the average ISM. The estimated elemental abundances give the ratio  $(\text{Mg} + \text{Fe})/\text{Si} = 5$  for the dust in the LIC. The elemental abundances in the LIC are not necessarily identical to the elemental abundances for the average ISM. It is, however, worthwhile noting that the authors derive carbon abundances in the gas phase that exceed the solar abundance even if the error bars are taken into account. This implies carbon abundances in the dust phase to be negative, which is physically impossible and therefore needs to be re-investigated.

Recent measurements with GHRS/HST and the Interstellar Medium Absorption Profile Spectrograph (IMAPS) on the ORFEUS-SPAS II mission provide new data of gas column densities in the LIC towards  $\epsilon$ CMa (Gry & Jenkins, 2001). We can, therefore, improve the gas-phase abundances of element in the LIC with these data and the hydrogen column density. The hydrogen column density in the LIC toward  $\epsilon$ CMa was derived to amount to  $4.7 \times 10^{21} \text{ m}^{-2}$  when assuming that the dust contains no sulfur. Note that the hydrogen column density in the LIC would be underestimated if local interstellar dust contains sulfur. The presence of sulfur in dust will therefore decrease gas-phase abundances and consequently we may underestimate the depletion of elements in the LIC. If GEMS found in chondritic porous IDPs are proved to be interstellar silicate, the depletion of sulfur would become evident from the sulfur inclusions in GEMS.

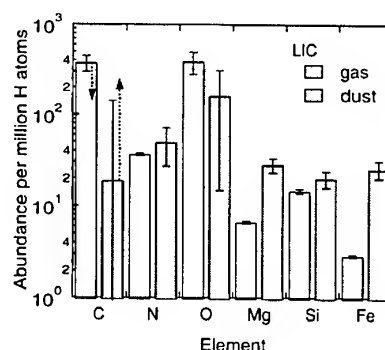


Figure 6. The abundances of C, N, O, Mg, Si, and Fe per million H atoms in the LIC. For the carbon abundances in the gas and dust phases, respectively, the upper and lower limits are given.

The gas-phase abundances in the LIC can also be derived from observations of interstellar pickup ions. Interstellar pickup ions are produced when interstellar neutral gas is ionized at the inner part of the solar system and instantaneously carried with the solar wind. Pickup helium ions of interstellar origin have been discovered with the time-of-flight spectrometer SULEICA (Suprathermal Energy Ionic Charge Analyzer) on AMPTE/IRM (Möbius et al., 1995). Interstellar proton, oxygen, nitrogen, and neon pickup ions have been identified with the time-of-flight spectrometer SWICS (Solar Wind Ion Composition Spectrometer) on *Ulysses* (Gloeckler et al., 1993; Geiss et al., 1994). Gloeckler & Geiss (1998) and Kallenbach et al. (2000) have recently provided the density of H, He, N, O, Ne in the LIC based on the SWICS measurements. The LIC gas-phase abundances derived from these measurements agree with those from observations of gas column densities within the uncertainties in the measurements. Pickup ion measurements especially provide the abundance of oxygen ions, which has not been determined from absorption spectra.

Fig. 6 shows the elemental abundances in the LIC while the carbon abundances in the gas and dust respectively are the upper and lower limit. It is worthwhile noting that the carbon abundance is no longer negative as opposed to the result by Frisch et al. (1999). We suppose olivine-type stoichiometry for the local interstellar dust from the ratio  $(\text{Mg} + \text{Fe})/\text{Si} = 2.7 \pm 0.6$ . This is in agreement with the silicate mineralogy of dust in the average ISM although a lack of extinction measurements in the LIC prevents us from confirming this hypothesis.

##### 4.2. Interstellar Dust in the Solar System

Interstellar dust is an essential constituent of the LIC and can partly enter the interplanetary medium. The local interstellar dust can be identified in the solar system on the basis of the difference in the dynamical behavior of interstellar and interplanetary dust. In consequence of the solar motion through the LIC, the mono-directional flow of the local interstellar dust could be observed in the solar system. The multi-coincidence microparticle sensing

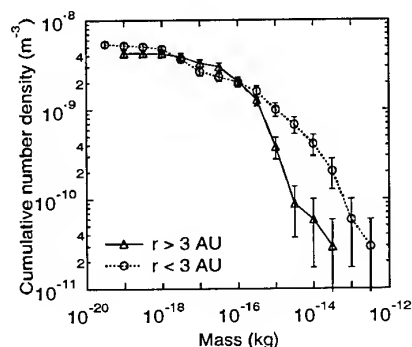


Figure 7. The cumulative number density of the local interstellar grains as a function of grain mass, derived from the *Ulysses* data between Oct. 1990 and Dec. 1995.

system on *Pioneer* 8 and 9, however, failed to provide clear evidence within the detection limit for the stream of interstellar dust in the heliocentric distance range of 0.75–1.25 AU from the sun (McDonnell & Berg, 1975). In contrast, Bertaux & Blamont (1976) identified the gravitational focussing of the local interstellar dust at the earth's orbit in data from two impact detectors of metal-oxide-silicon capacitor type onboard *Meteoroid Technology Satellite* (Alvarez, 1976). The stream of interstellar dust into the solar system has been confirmed on the basis of measurements with impact ionization detectors on *Ulysses*, *Hiten*, and *Galileo* (Grün et al., 1994; Svedhem et al., 1996; Grün et al., 1997).

Recent state-of-the-art dust detectors enable deducing the mass and impact speed of dust grains with uncertainties of factors of 6 and 1.6 respectively (Göller & Grün, 1989). Fig. 7 shows the cumulative number density derived from the *Ulysses* data between Oct. 1990 and Dec. 1995 (Mann & Kimura, 2000). Open circles indicate the data between 1 and 3 AU from the sun, and open triangles the data between 3 and 5.4 AU. The mass distribution ranges from  $3 \times 10^{-20}$  to  $3 \times 10^{-13}$  kg and a power law can reasonably well reproduce the mass distribution for  $m > 3 \times 10^{-16}$  kg (Kimura et al., 1999). Note that the mass ranges of dust models are distinct from the mass distribution of interstellar dust derived from in situ measurements in the solar system. Small grains with  $m \leq 10^{-18}$  kg may be deflected in the interstellar and interplanetary magnetic fields and the detector has a low sensitivity in this mass range (Kimura & Mann, 1998a,b; Linde & Gombosi, 2000). The data since 1996 need to be analyzed in order to decrease the statistical errors and to investigate a possible temporal variation in the mass distribution.

As the heliocentric distance of measurements decreases, a gap in the distribution appears in the mass range between  $10^{-17}$  and  $10^{-16}$  kg. The *Galileo* measurements near the ecliptic plane have confirmed the depletion of interstellar grains in the same mass range as they approach the sun. This has been interpreted as the dynamical deflection of grains by the solar radiation pressure (Landgraf et al., 1999).

Gloeckler & Geiss (1998) have derived a hydrogen number density of  $2.4 \times 10^5 \text{ m}^{-3}$  from the SWICS pickup ion measurements. This value implies the total mass density of local interstellar dust to be  $4 \times 10^{-24} \text{ kg m}^{-3}$  if a gas-to-dust mass ratio of 100 is assumed. In contrast, the total mass density of local interstellar dust estimated from the *Ulysses* in situ dust data amounts to  $0.75\text{--}2.8 \times 10^{-23} \text{ kg m}^{-3}$  resulting in the gas-to-dust mass ratio of 15–54 (Frisch et al., 1999; Kimura et al., 1999). The low value of the gas-to-dust mass ratio in the LIC might arise from an overestimate of the dust density in the LIC. Heavy grains in the data largely contribute to the dust mass density, regardless of their small amount. In addition, the spatial concentration of heavy grains focussed by solar gravity in the inner solar system leads to the overestimate. In fact, the gravitational focussing effect can be seen in Fig. 6 as high density for dust with  $m \geq 10^{-15}$  kg for  $r < 3$  AU compared to the data for  $r > 3$  AU. On the other hand, the upper limit of the gas-to-dust mass ratio in the LIC can be estimated from Fig. 6 to be 165. Improved analysis of a larger data set of interstellar dust and more accurate measurements of the gas absorption features will give a better estimate of the gas-to-dust mass ratio in the LIC in future.

The impact speed data and information on the orientation and velocity of spacecraft in the reference frame of the sun can be used for determining the heliocentric velocity of detected interstellar grains. The distribution of speed scatters around  $26 \text{ km s}^{-1}$  with dispersion of  $5 \text{ km s}^{-1}$  but the interpretation of the dispersion is controversial (Grün et al., 1994). Further analyses of in situ data may yet show the spatial variation in the velocity distribution, which contains information on the dynamics of dust in the LIC.

A study of the properties of interstellar dust certainly benefits from ongoing and upcoming space missions. *Stardust* measures in situ chemical compositions of dust streaming from the LIC as well as dust from comet Wild 2 (Kissel, 1999). Moreover, local interstellar grains will be captured and be brought back to the earth for future laboratory analyses. The preliminary in situ analysis has identified five impacts of supposedly LIC origin around 1–2 AU from the sun (Krueger & Kissel, 2000). Because of their complexity, however, interpretation of the spectra is far from straightforward and needs confirmation by further analyses. The proposed *Cosmic DUNE* mission, if selected, will perform in situ measurements of local interstellar dust at the earth's orbit (Grün et al., 2000). The in situ dust telescope on *Cosmic DUNE* consists of CIDA, CDA (Cosmic Dust Analyzer), and D2S (Dust Detector System), which includes ISIDE (Impact Sensor for Interstellar Dust Exploration). While CIDA will measure the composition of dust with a high-resolution mass spectrometer, CDA will be used to determine the mass, impact velocity, electric charge, and coarse composition of single grains (Srama et al., 1996; Srama & Grün, 1997). D2S consists of the electrostatic charge-sensing dust detectors and the polyvinylidene fluoride (PVDF) dust detector for determination of the mass, velocity, and charge of dust grains (Auer, 1996; Tuzzolino, 1996). In order to retrieve the properties of dust in the LIC, however, one needs to take into account the selection effect on the dust during

Table 2. The maximum  $\beta$  ratio for the selected dust models and the mass at which the  $\beta$  ratio is maximized. The local interstellar dust satisfies  $1.4 < \beta < 3.1$  in the mass range from  $10^{-17}$  to  $10^{-16}$  kg.

Model	$\beta$	Mass (kg)
bare silicate	0.9	$8 \times 10^{-17}$
bare graphite	5.0	$5 \times 10^{-18}$
composite ( $P = 80\%$ )	1.4	$1 \times 10^{-16}$
composite ( $P = 45\%$ )	1.6	$3 \times 10^{-16}$
core-mantle	2.7	$3 \times 10^{-16}$

entry into the solar system (Mann & Kimura, 2000). A suggested *Interstellar Probe* mission would travel more than 200 AU within 15 years towards the incoming interstellar flux (Mewaldt et al., 1995). The composition of local interstellar dust is expected to be measured in situ with an impact ionization mass spectrometer. The success of this mission would provide direct information on the composition of dust in the LIC.

#### 4.3. Dust Properties Inferred From Radiation Pressure

The spatial variation in the mass distribution of the local interstellar dust can be used to constrain the properties of the dust (Mann & Kimura, 2000). The maximum ratio  $\beta$  of solar radiation pressure to solar gravity must be in the mass range from  $10^{-17}$  to  $10^{-16}$  kg in order to explain the gap in the mass distribution of interstellar dust. Furthermore the maximum value of the  $\beta$  ratio can be specified in the range of  $1.4 < \beta < 3.1$  for the gap to be absent outwards from 5.4 AU.

We shall here investigate the previously discussed dust models in terms of the  $\beta$  ratio, since the models for dust in the average ISM seem to match the dust-phase abundances in the LIC, regardless of the discrepancy in the size distribution. Applying the models of dust in the average ISM, Table 2 gives numerical results for the maximum  $\beta$  ratio and the mass at which the  $\beta$  ratio is peaked.

The maximum  $\beta$  ratio for amorphous olivine grains never exceeds unity while graphite grains have  $\beta \approx 5$  at maximum (Kimura & Mann, 2000). Consequently, the model of interstellar dust with bare-silicate and bare-graphite fails to explain the gap in the mass distribution. The composite grains of silicate, amorphous carbon, and graphite with porosity of 80 % have the maximum  $\beta$  ratio of 1.4 at  $m \approx 1 \times 10^{-16}$  kg while the relatively compact composite grains of silicate and amorphous carbon have a higher  $\beta$  ratio of 1.6 at  $m \approx 3 \times 10^{-16}$  kg. Spherical grains with a silicate core and an organic refractory mantle attain a maximum  $\beta$  ratio of 2.7 around  $m \approx 3 \times 10^{-16}$  kg when the radius of the core is 70 nm (Mann & Kimura, 2001). While the  $\beta$  ratio for the core-mantle grains satisfies both the maximum value and the mass at which the  $\beta$  ratio is peaked, large grains of  $m \geq 10^{-15}$  kg cannot be spheri-

cal with a silicate core and an organic refractory mantle. Therefore aggregates of a silicate core and an organic refractory mantle are a candidate for the majority of the interstellar dust entering the solar system.

## 5. CONCLUDING REMARKS

Observational data show similarities in the physical and chemical properties among average interstellar dust, ancient interstellar dust in primitive meteorites, cometary IDPs, and cometary dust, and the local interstellar dust. Dust-phase elemental abundances in the LIC show no obvious discrepancies with those in the average ISM. Certain minerals inferred from the interstellar extinction curve agree with pristine materials in cometary dust. The extinction feature at 217.5 nm, which is often attributed to graphite, may even arise from carbon nanoparticles comparable to the presolar diamonds found in meteorites (Sandford, 1996). Furthermore the size range of the local interstellar dust agrees with that of presolar grains. Unfortunately none of the currently available dust models well describes these global properties of interstellar dust. Aggregates of grains with a silicate core and an organic refractory mantle may be a promising model of interstellar dust, but need to be proven in the future (Greenberg & Gustafson, 1981). This presumption might be justified by the coagulation process, in which mutual collisions of grains in molecular clouds form fluffy dust aggregates (Ossenkopf, 1993). An appropriate non-sphericity and all major features of interstellar linear polarization can be explained with dust grains grown in cluster-cluster aggregation processes (Wurm & Blum, 2000; Wurm & Schnaiter, 2001). We expect that a further comparison between dust in the LIC and dust in the average ISM will improve our knowledge of the properties of interstellar dust and, in turn, the evolution of the ISM.

## ACKNOWLEDGMENTS

We are grateful to Chiyoe Koike, Hiroki Chihara, Tadashi Mukai, Ulysses J. Sofia, Iris Weber, and Martin Lewelling for useful communications. This research has been supported by the German Aerospace Center DLR (Deutsches Zentrum für Luft- und Raumfahrt) under the project "Kosmischer Staub: Der Kreislauf interstellarer und interplanetarer Materie".

## REFERENCES

- Allamandola L.J., Sandford S.A., Wopenka B., 1987, *Science* 237, 56
- Alvarez J. M., 1976, in *Interplanetary Dust and Zodiacal Light* (H. Elsässer, H. Fechtig, eds.), pp. 181, Springer-Verlag, New York.
- Alexander C.M.O'D., Nittler L., Tera F., 2001, *Lunar Planet. Sci.* 32, 2191
- Anders E., Zinner E., 1993, *Meteoritics* 28, 490

- Amari S., Anders E., Virag A., Zinner E., 1990, *Nature* 345, 238
- Amari S., Lewis R.S., Anders E., 1994, *Geochim. Cosmochim. Acta* 58, 459
- Auer S., 1996, in *Physics, Chemistry, and Dynamics of Interplanetary Dust* (B.Å.S. Gustafson, M.S. Hanner, eds.) pp. 251, Astron. Soc. of the Pac., San Francisco
- Bell III J.F., Veverka J., Belton M., et al., 2000, *Meteoritics Planet. Sci.* 35, A23
- Bernatowicz T.J., Walker R.M., 1997, *Phys. Today* 50, 26
- Bernatowicz T., Fraundorf G., Ming T., et al., 1987, *Nature* 330, 728
- Bernatowicz T.J., Amari S., Zinner E.K., Lewis R.S., 1991, *ApJ* 373, L73
- Bernatowicz T.J., Cowsik R., Gibbons P.C., et al., 1996, *ApJ* 472, 760
- Bernatowicz T., Bradley J., Amari S., Messenger S., Lewis R., 1999, *Lunar Planet. Sci.* 30, 1392
- Bertaux J.L., Blamont J.E., 1976, *Nature* 262, 263
- Biermann P., Harwit M., 1980, *ApJ* 241, L105
- Bradley J.P., 1994, *Science* 265, 925
- Bradley J.P., Keller L.P., Snow, T.P., et al., 1999, *Science* 285, 1716
- Brownlee D.E., Burnett D., Clark B., et al., 1996, in *Physics, Chemistry, and Dynamics of Interplanetary Dust* (B.Å.S. Gustafson, M.S. Hanner, eds.) pp. 223, Astron. Soc. of the Pac., San Francisco
- Brownlee D.E., Tsou P., Clark B., et al., 2000, *Meteoritics Planet. Sci.* 35, A35
- Bussoletti E., Colangeli L., Lopez Moreno J.J., et al., 1999, *Adv. Space Res.* 24(9), 1149
- Campins H., Ryan E.V., 1989, *ApJ* 341, 1059
- Cardelli J.A., Meyer D.M., Jura M., Savage B.D., 1996, *ApJ* 467, 334
- Clemett S.J., Maechling C.R., Zare R.N., Swan P.D., Walker R.M., 1993, *Lunar Planet. Sci.* 24, 309
- Choi B.-G., Wasserburg G.J., Huss G.R., 1999, *ApJ* 522, L133
- Day K.L., 1974, *ApJ* 192, L15
- Davis Jr. L., Greenstein J.L., 1951, *ApJ* 114, 206
- Dorschner J., 2001, in *Interplanetary Dust* (E. Grün, B.Å.S. Gustafson, S.F. Dermott, H. Fechtig, eds.) pp. 728, Springer-Verlag, Heidelberg
- Draine B.T., 1985, in *Protostars & Planets II* (D.C. Black, M.S. Matthews, eds.) pp. 621, Univ. of Arizona Press, Tucson
- Draine B.T., Lee H.M., 1984, *ApJ* 285, 89
- Duley W.W., 2001, *ApJ* 553, 575
- Duley W.W. & Seahra S., 1998, *ApJ* 507, 874
- Dwek E., 1997, *ApJ* 484, 779
- Fomenkova M.N., 1999, *Space Sci. Rev.* 90, 109
- Frisch P.C., Dorschner J.M., Geiss J., et al., 1999, *ApJ* 525, 492
- Geiss J., Gloeckler G., Mall U., et al., 1994, *A&A* 282, 924
- Gloeckler G., Geiss J., 1998, *Space Sci. Rev.* 86, 127
- Gloeckler G., Geiss J., Balsiger H., et al., 1993, *Science* 261, 70
- Göller J.R., Grün E., 1989, *Planet. Space Sci.* 37, 1197
- Gold T., 1952, *MNRAS* 112, 215
- Greenberg J.M., 1973, in *Interstellar Dust and Related Topics* (J.M. Greenberg, H.C. van de Hulst, eds.) pp. 3, D. Reidel, Dordrecht
- Greenberg J.M., 1974, *ApJ* 189, L81
- Greenberg J.M., 1980, in *Solid Particles in the Solar System* (I. Halliday, B.A. McIntosh, eds.) pp. 343, D. Reidel, Dordrecht
- Greenberg J.M., 1998, *A&A* 330, 375
- Greenberg J.M., Gustafson B.Å.S., 1981 *A&A* 93, 35
- Greenberg J.M., Hage J.I., 1990, *ApJ* 361, 260
- Grün E., Gustafson B., Mann I., et al., 1994, *A&A* 286, 915
- Grün E., Staubach P., Baguhl M., et al., 1997, *Icarus* 129, 270
- Grün E., Landgraf M., Horányi M., et al., 2000, *JGR* 105, 10403
- Grün E., Baguhl M., Svedhem H., Zook H.A., 2001, in *Interplanetary Dust* (E. Grün, B.Å.S. Gustafson, S.F. Dermott, H. Fechtig, eds.) pp. 295, Springer-Verlag, Heidelberg
- Gry C., Jenkins E.B., 2001, *A&A* 367, 617
- Hall J.S., Mikesell A.H., 1949, *AJ* 54, 187
- Hiltner W.A., 1949, *ApJ* 109, 471
- Holweger H. 2001, in *Solar and Galactic Composition* (R.F. Wimmer-Schweingruber ed.) in press, Springer-Verlag, New York
- Hoppe P., Amari S., Zinner E., Ireland T., Lewis R.S., 1994, *ApJ* 430, 870
- Hornung K., Kissel J., 1994, *A&A* 291, 324
- Hutcheon I.D., Huss G.R., Fahey A.J., Wasserburg G.J., 1994, *ApJ* 425, L97
- Jessberger E.K., 1999, *Space Sci. Rev.* 90, 91
- Jessberger E.K., Christoforidis A., Kissel J., 1988, *Nature* 332, 691
- Jessberger E.K., Stephan T., Rost D., et al., 2001, in *Interplanetary Dust* (E. Grün, B.Å.S. Gustafson, S.F. Dermott, H. Fechtig, eds.) pp. 253, Springer-Verlag, Heidelberg
- Jones A.P., 2000, *JGR* 105, 10257
- Kallenbach R., Geiss J., Gloeckler G., von Steiger R., *Astrophys. Space Sci.* 274, 97
- Keller L.P., Messenger S., Bradley J.P., 2000, *JGR* 105, 10397
- Kimura H., Mann I., 1998a, *ApJ* 499, 454
- Kimura H., Mann I., 1998b, in *Physics of Dusty Plasmas* (M. Horányi, S. Robertson, B. Walch, eds.) pp. 321, Am. Inst. of Phys., Woodbury
- Kimura H., Mann I., 2000, *Adv. Space. Res.* 25(2), 299
- Kimura H., Mann I., Wehry A., 1999, *Astrophys. Space Sci.* 264, 213

- Kissel J., 1999, in *Formation and Evolution of Solids in Space* (J.M. Greenberg, A. Li., eds.) pp. 427, Kluwer Academic Publ., Dordrecht
- Kissel J., Sagdeev R.Z., Bertaux J.L. et al., 1986a *Nature* 321, 280
- Kissel J., Brownlee D.E., Büchler K. et al., 1986b *Nature* 321, 336
- Krueger F.R., Kissel J., 2000, *Sterne und Weltraum* 39, 326
- Landgraf M., Augustsson K., Grün E., Gustafson B.Å.S., 1999, *Science* 286, 2319
- Ledoux G., Guillois O., Huisken F., et al., 2001, *A&A* 377, 707
- Lee M.R., Russell S.S., Arden J.W., Pillinger C.T., 1992, *Meteoritics* 27, 248
- Leinert C., Grün E., 1990, in *Physics of the Inner Heliosphere I* (R. Schwenn, E. Marsch, eds.) pp. 207, Springer-Verlag, Berlin
- Lewis R.S., Ming T., Wacker J.F., Anders E., Steel E., 1987, *Nature* 326, 160
- Lewis R.S., Anders E., Draine B.T., 1989, *Nature* 339, 117
- Li A., Greenberg J.M., 1997, *A&A* 323, 566
- Lilley A.E., 1955, *ApJ* 121, 559L
- Linde T.J., Gombosi T.I., 2000, *JGR* 105, 104411
- Mann I., Kimura H., 2000, *JGR* 105, 10317
- Mann I., Kimura H., 2001, *Space Sci. Rev.* 97, 389
- Martin P.G., 1995, *ApJ* 445, L63
- Mathis J.S., 1990, *Annu. Rev. Astron. Astrophys.* 28, 37
- Mathis J.S., 1996, *ApJ* 472, 643
- Mathis J.S., Whiffen G., 1989, *ApJ* 341, 808
- Mathis J.S., Rumpl W., Nordsieck K.H., 1977, *ApJ* 217, 425
- McDonnell J.A.M., Berg O.E., 1975, *Space Res.* 15, 555
- Messenger S., 2000, *Nature* 404, 968
- Messenger S., Bernatowicz T.J., 2000, *Meteoritics Planet. Sci.* 35, A109
- Messenger S., Clemett S.J., Keller L.P., et al., 1995, *Meteoritics* 30, 546
- Messenger S., Walker R.M., Clemett S.J., Zare R.N., 1996, *Lunar Planet. Sci.* 27, 867
- Mewaldt R.A., Kangas J., Kerridge S.J., Neugebauer M., 1995, *Acta Astronautica* 35, 267
- Möbius E., Rucinski D., Hovestadt D., Klecker B., 1995, *A&A* 304, 505
- Ney, E.P. 1977, *Science* 195, 541
- Nittler L.R., Alexander C.M.O'D., 1999, *Lunar Planet. Sci.* 30, 2041
- Nittler L.R., Hoppe P., Alexander C.M.O.'D., et al., 1995, *ApJ* 453, L25
- Nittler L.R., Alexander C.M.O'D., Gao X., Walker R.M., Zinner E., 1997, *ApJ* 483, 475
- Ossenkopf V., 1993, *A&A* 280, 617
- Ostriker J.P., Silk J., 1973, *ApJ* 184, L113
- Redfield S., Linsky J.L., 2000, *ApJ* 534, 825
- Riedler W., Torkar K., Rüdener F., et al., 1999, *Adv. Space Res.* 21(11), 1547
- Sandford S.A., 1996, *Meteoritics Planet. Sci.* 31, 449
- Savage B.D., Jenkins E.B., 1972, *ApJ* 172, 491
- Schramm L.S., Brownlee D.E., Wheelock M.M., 1989, *Meteoritics* 24, 99
- Schulze H., Kissel J., Jessberger E.K., 1997, in *From Stardust to Planetesimals* (Y.J. Pendleton, A.G.G.M. Tielens, eds.) pp. 397, Astron. Soc. of the Pac., San Francisco
- Schwehm G., Schulz R., 1999, *Space Sci. Rev.* 90, 313
- Seahra S.S., Duley W.W., 1999 *ApJ* 520, 719
- Sekanina Z., Hanner M.S., Jessberger E.K., Fomenkova M.N., 2001, in *Interplanetary Dust* (E. Grün, B.Å.S. Gustafson, S.F. Dermott, H. Fechtig, eds.) pp. 95, Springer-Verlag, Heidelberg
- Sembach K.R., Savage B.D., 1996, *ApJ* 457, 211
- Snow T.P., Witt A.N., 1996, *ApJ* 468, L65
- Sofia U.J., 1997, in *From Stardust to Planetesimals* (Y.J. Pendleton, A.G.G.M. Tielens, eds.) pp. 77, Astron. Soc. of the Pac., San Francisco
- Sofia U.J., Meyer D.M., 2001, *ApJ* 554, L221 (Erratum 2001, *ApJ* 558, L147)
- Sofia U.J., Cardelli J.A., Savage B.D., 1994, *ApJ* 430, 650
- Spitzer Jr. L., Tukey J.W., 1951, *ApJ* 114, 187
- Srama R., Grün E., 1997, *Adv. Space Res.* 20(8), 1467
- Srama R., Grün E., The CASSINI-Dust-Science Team. 1996, in *Physics, Chemistry, and Dynamics of Interplanetary Dust* (B.Å.S. Gustafson, M.S. Hanner, eds.) pp. 227, Astron. Soc. of the Pac., San Francisco
- Stecher T.P., 1965, *ApJ* 142, 1683
- Stecher T.P., Donn B., 1965, *ApJ* 142, 1681
- Stephens J.R., Russell R.W., 1979, *ApJ* 228, 780
- Svedhem H., Münzenmayer R., Iglöeder H., 1996, in *Physics, Chemistry, and Dynamics of Interplanetary Dust* (B.Å.S. Gustafson, M.S. Hanner, eds.) pp. 27, Astron. Soc. of the Pac., San Francisco
- Szomoru A., Guhathakurta P., 1998, *ApJ* 494, L93
- Trumpler R.J., 1930a, *Publ. Astron. Soc. Pac.* 42, 214
- Trumpler R.J., 1930b, *Publ. Astron. Soc. Pac.* 42, 267
- Tuzzolino A.J., 1996, *Adv. Space Res.* 17(12), 123
- Watson W.D., 1972, *ApJ* 176, 103
- Watson W.D., Salpeter E.E., 1972, *ApJ* 174, 321
- Witt A.N., 2000, *JGR* 105, 10299
- Wurm G., Blum J., 2000, *ApJ* 529, L57
- Wurm G., Schnaiter M., 2001, *ApJ* in press
- Zinner E., Amari S., Wopenka B., Lewis R.S., 1995, *Meteoritics* 30, 209
- Zscheeg H., Kissel J., Natour Gh., Vollmer E., 1992, *As-trophys. Space Sci.* 195, 447

# INTERSTELLAR PARTICLE DETECTION AND SELECTION CRITERIA OF METEOR STREAMS

B.L. Kashcheyev <sup>(1)</sup>, S.V. Kolomiyets <sup>(2)</sup>

<sup>(1,2)</sup> Kharkiv State Technical University of Radioelectronics, 61166, 14 Lenin av. (Ukraine),

<sup>(1)</sup> Email: ort@kture.kharkov.ua,

<sup>(2)</sup> Email: kometa@kture.kharkov.ua

## ABSTRACT/RESUME

There is a hypothesis on possible searching of interstellar particles from kinematics discussions. It is possible the near 75% of interstellar particles, which are observed on the Earth, are distributed in the interval from 1 to 1.1. There are adduced the results of search the orbits of interstellar particles by criterions which are based on analysis of orbital elements and on limitations which associates with conditions of observation such particles on the Earth. The approbation of search was made on the different samples from observation material, which volume is more than 7 thousands hyperbolic and about parabolic orbits of Kharkiv electronic radiometeor catalogue. It is possible that there is a certain number of interstellar meteoroids.

## 1. RADIO METEOR INVESTIGATIONS IN KHARKIV

The Problematic Scientific-Research Laboratory of Radiotechnique of Kharkiv State Technical University of Radioelectronics (Ukraine), whose employees more than thirty years under the guidance of professor B.L. Kashcheyev are occupied with radar researches of meteors, disposes of unique Kharkiv electronic orbit catalogue [1]. This catalogue contains the primary information, speeds, radiants and orbits of near 250000 radiometeoroids with mass from 0.001 g till 0.00001 g. These data was registered during radar observations 1972-1978 [2]. They were got by impulse-diffraction method during base observation (third separated receiving items). Astronomical azimuths of items were: 214° (4,32 km), 270° (main), 290° (8,42 km). The geographical coordinates of the radar installation are 49° 24' 50" S and 36° 51' 30" E. The Meteor Automatic Radar System (MARS) was developed in 1971-1972 at the Kharkiv Institute of Radioelectronics (KhIRE). During 1966-1993 institute's name was the Kharkiv Institute of Radioelectronics (KhIRE). During 1993-2001 its name was the Kharkiv State Technical University of Radioelectronics (KhTURE). More about these you can see on Website:  
<http://www.kture.kharkov.ua/>  
<http://www.kture.edu.ua/>

MARS was the first automatic meteor radio system in Ukraine. The system included two automatic radar subsystems operating in the real time scale. The first one was the subsystem for the study of the number of radiometeors and the influx of meteor matter. The second one was the subsystem of automatic measurement of velocities and radiant coordinates for individual meteors. There were synchronous calculations of individual meteoroid orbital parameters. More than 20 million meteors were detected with this system during 1972-1978, and many thousands of meteor orbits were determined and studied. There are used radio signals that were reflected from meteor underdense ionised trails. The obtain data include orbits of faint meteors to + 12<sup>m</sup>. The radiomagnitude of such meteors correspond electron line density of trails  $\alpha > 10^{11} \text{ e} \cdot \text{m}^{-1}$ . The lower limit of meteoroid mass detection of the orbital subsystem is  $5 \cdot 10^{-6} \text{ g}$ . The nominal parameters of MARS are given on Tab.1.

Tab.1. The nominal parameters of MARS [2,3]

Operating frequency	31,1 MHz
Peak pulse power	till 1 MW
Pulse repetition rate	500 Hz
Transmitted pulse width	30 microseconds
Antenna gain	250
Minimum discernible signal of a receiver	5 $\mu\text{V}$ (for a signal to noise ratio of 2)

The standard deviation of measurement was estimated by using the results of observations of meteor members of known streams (Heminids, Quadrantids, Orionids). The accidental root-mean-square errors of measurement equatorial coordinates of radiants of individual meteors assign as Eqs.1 [4].

$$\begin{aligned} \sigma\delta &= \pm 2.0^\circ; \\ \sigma\alpha &= \pm 2.0^\circ \cdot \sec \delta \end{aligned} \quad (1)$$

The piecewise-linear approximation of a root-mean-square error of no-atmosphere velocity according to [4] is the equation:

$$\sigma v = \begin{cases} 2.5 - 0.05v, v \leq 20 \text{ km/s} \\ 2.5 - 0.05v, v \in (20...30) \text{ km/s} \\ 1.0 \text{ km/s}, v \in (30...40) \text{ km/s} \\ 0.05v - 1.0, v \in (40...50) \text{ km/s} \\ 0.125v - 4.75, v \geq 50 \text{ km/s} \end{cases} \quad (2)$$

But really the accidental root-mean-square errors of measurements of individual sporadic meteoroid velocities by the Kharkiv measurements much less than  $\sigma v$  from Eq.2. The dependence of the estimates of  $\sigma v$  on  $v$  according to the statistical analyse [4] of the results of these measurements is on Tab.2.

Tab.2. The estimates of  $\sigma v$  on  $v$  according the statistical analyse

$V, \text{km} \cdot \text{s}^{-1}$	$\sigma v, \text{km} \cdot \text{s}^{-1}$
19-21	0.5
26-27	0.5
31-33	0.4
37-39	0.3
57-59	0.5
59-61	0.4
63-65	0.7

According to this method the root-mean-square error of a heliocentric velocity of an individual meteor  $\sigma v_h$  not should to exceed 0.2-0.3 km/s.

The errors of radio measurements appreciated on observation of meteoric streams frequently are inflated [4].

Velocities and meteor orbits data obtained by radar method in Kharkiv (1975-1976) were taken for verification of hyperbolic orbits calculation accuracy according to observations results. For calculations it was accepted [5], that errors of measurements are equal to the following values:

$$\sigma v \cdot v^{-1} = 0.02; \sigma \alpha = 2.1^\circ; \sigma \delta = 1.7^\circ. \quad (3)$$

Root-mean-square errors of definition of speed and radiant coordinates, eccentricity:

$$\sigma e = \frac{1}{2ae} \left\{ \sigma^2 p + \frac{\sigma^2 a}{a^2} \right\}^{1/2} \quad (4)$$

and other elements of an orbit were calculated. The root-mean-square errors of photographic and radio measurements are given Tab. 3.

Tab.3: Root-mean-square errors of meteoroid velocities, coordinates of the radiants and orbital elements obtained by different techniques. 1. Photographic in Odessa and Dushanbe [6-7]. 2. Radar in Kharkiv (observations of the Geminids meteor stream) [8]. 3. Radar in Kharkiv (calculation with analytical formulas, average values for elliptic orbits) [4]. 4. Radar in Kharkiv (individual hyperbolic orbits) [5]. 5. Radar in Obninsk [9]. 6. Photographic Perseid meteors [10]. 7. The AMOR radar [11].

	$V_g, \text{km/s}$	$\sigma A$ $^\circ$	$\sigma Z$ $^\circ$	$\sigma \alpha$ $^\circ$	$\sigma \delta$ $^\circ$	$\sigma e$	$\sigma(1/a)$ $\text{AU}^{-1}$	$\sigma i$ $^\circ$	$\sigma \omega$ $^\circ$
1	0.6	-	-	0.5	0.5	0.052	0.054	2.12	2.46
2	2.0	-	-	2.7	2.4	0.028	0.15	5.6	4.3
3	1.4	-	-	-	-	0.25	0.12	6.6	-
4	2.4	1.8	4.2	-	-	0.205	0.253	7.0	7.6
5	1.6	-	-	2.0	2.0	0.04	0.08	3.0	4.0
6	0.6	-	-	0.5	0.05	0.048	0.050	1.78	1.92
7	$5\%(v_h)$							$2^\circ$	$2^\circ$

The values for radio meteors with hyperbolic orbits [5] are averaged taking into consideration the tails of error distribution functions. The accuracy of individual orbits is sometimes better. One can meet such minimal values as follows:  $\sigma V_g < 1.5 \text{ km/s}$ ,  $\sigma Z < 0.5^\circ$ ,  $\sigma A < 0.5^\circ$ ,  $\sigma V_h < 1 \text{ km/s}$ .

It is shown in the papers [4,5,9] that the accuracy of catalogues of the orbits of radio meteors is not worse than that of photographic catalogues and sometimes exceeds it. The accuracy of catalogued orbits in Kharkiv can be improved by increasing the accuracy of computations (if initial parameters are known), i.e. taking better algorithm and constants [4,12].

## 2. DATA ON HYPERBOLIC ORBITS

The most of meteors observed instrumentally belong to the Solar system. Nevertheless, the Solar system is not closed. It is permeable for the particles and even large bodies flying inward and outward. Since a meteoroid with a hyperbolic heliocentric velocity may have an usual geocentric velocity [5,13] then a possibility to record a hyperbolic meteor is no more connected with a great error of determination of its velocity. Presence of interstellar particles in the observation data is not proved till now because the accuracy of measurements and calculations is not good enough to check the reliability of these data. This problem is known as the problem of hyperbolic meteoroids but really it is the problem of hyperbolic orbits of dust grains in the Solar system. No one exact enough orbit of a small body is distinctly classified as really hyperbolic.

Since both interstellar particles and those leaving the Solar system can have hyperbolic orbits it is rather complicated to analyse data on such orbits. The problem of interstellar meteoroids has already become

a component of the problem of hyperbolic orbits. So it is difficult to reveal the peculiar motion of the Sun in distributions of all hyperbolic orbits. According to the theory of capture [14] the captured into the Solar system bodies will have elliptic and near parabolic orbits. It makes the search of interstellar particles more complicated.

The growth of the number of hyperbolic orbits with increasing of the volume of data may be either real or a result of accumulation of erroneous data. Analysis of formation of hyperbolic orbits in the Solar system shows that their number cannot exceed some percent. The less is the mass of a meteoroid the more mechanisms to transform its orbit into a hyperbola exist but it is more difficult to detect such a body.

According to the Vsekhsvyatsky's estimates [15] an interstellar meteor must be observed practically every day. In this case the meteoroids with  $e \gg 1$  must be present among the observed bodies. According to other estimates [16-17], on the contrary, the eccentricities of gravitationally focused interstellar meteor orbits must be concentrated around unity. The orbits, which became hyperbolic due to perturbations from the nearest planets [18-19], are expected to have eccentricities  $e \sim 1$  as well. A possible mechanism of the origin of hyperbolic meteoroids with  $V_h > 57$  km/s is a collision of two asteroids [20].

There are different mechanisms [21], which can change an orbit of a meteor body (especially of a small mass  $M \ll 1$ g) in the Solar system: non-gravitational effects (e.g. light pressure), perturbations from the Sun and the Moon within the sphere of the Earth attraction.

Recent astronomical discoveries qualitatively confirmed the hypothesis [15] on origin hyperbolic meteoroids by volcanic eruption on satellites of planets as well as elsewhere in the Galaxy. Data available on Geminid show a direct connection between the materials released during the Supernova explosion and discovered micrometeoroid streams of the Arecibo particles [22] and the Ulysses ones. [23-24].

The dust experiments on board of the Ulysses and other spacecrafts detected a significant flux of the  $\beta$ -meteoroids with interstellar hyperbolic orbits in the mass range  $10^{-16}$ – $10^{-8}$  g [24-25]. Meteor investigation with Arecibo radar system in 1997 confirmed the existence of hyperbolic meteoroids with masses  $10^{-11}$ – $10^{-6}$  g. The radar system AMOR is working daily in the Southern Hemisphere and gives a possibility to study the characteristics of groups of non-bound particles with mass  $\geq 10^{-7}$ g in the inner Solar system [11].

The percentage of the hyperbolic orbits under investigation shows the dependence on measurements accuracy [13,18]. It occurs that there are 1-2% of hyperbolas in precise photographic data [26] and up to 10% in less precise ones as well as in radio meteor

catalogues [27-28], once at 2 to 24 % [5, 29]. There are also observed data on hyperbola determined by photographic and radio techniques in Kiev, Kazan and Kharkiv. Radar surveillances yield to the best photographic observations in measurement accuracy, but they surpass them considerably in statistic provision with results and they allow to register fainter meteors. An increase in the relative number of hyperbolic orbits in radio catalogues versus photographic ones can be the consequence not only of the measurement errors but also of more favourable conditions for registration of meteor bodies with hyperbolic orbits. At the same time the upper boundary of feasibility to observe the real hyperbolic orbits in radio measurements cannot exceed theoretical estimations of the probability of the Earth meeting with such orbits.

There are hyperbolic orbits in television meteor catalogues [30]: almost 15% in the Japanese one that includes the observations in 1990–1994 and 12% in the Canadian catalogue.

According to Öpik the Pultusk famous meteorite is a single body with confidently determined hyperbolic velocity [31]. It is also worthy to mention 98 hyperbolic comets of the Marsden's catalogue and hyperbolic orbits in other comet catalogues. Several catalogues of hyperbolic meteoroids have been published. There are among them: the Vsekhsvyatsky's catalogue consisting of 78 orbits [15], the Simakina's catalogue consisting of 38 hyperbolic orbits [32], the Odessa catalogue of the transplanetary radiants of 737 hyperbolic meteors [33].

Having more data one can study the distribution of hyperbolic orbit even each orbit is not very precise. Unfortunately, the accumulated at present time observation data on bodies with hyperbolic orbits are very non-uniform and insufficiently comprehensive to make any ultimate significant conclusions.

### 3. IDENTIFICATION CRITERIA OF HYPERBOLIC ORBITS

There are many criteria to evaluate the efficiency of a hyperbolic orbit formation mechanism in the Solar system. One of the criteria is the number of nodes of the testing orbit [34]. A hyperbolic orbit on the contrary to an elliptic one can cross the ecliptic plane only once. For the hyperbolic meteoroids having two nodes one can find the perturbation forces in the ecliptic plane, which could transform into hyperbola their initial, probably a non-hyperbolic orbit. In Kharkiv it is proposed to use the radius vectors of ascending and descending nodes when applying this criterion. The results of measurements in Kharkiv have been checked in this way. Such suspicious orbits have been found among the data of 1975-1976. They are

transformed by planetary perturbations of Mars (4 orbits), Jupiter (3 orbits) and Saturn (2 orbits): Tab.4.

Tab.4. Orbital parameters of meteor bodies with  $e \geq 1$  formed by planetary perturbations of Mars (1-4), Jupiter (5-7) and Saturn (8-9) on results of radio observation in Kharkiv

N	Date	Time	$V_h$ , km/s	$i^\circ$	$\omega^\circ$	$e$	$p$ , AU	$q$ , AU	$R$ , AU
1	16.08.76	12:23	47	88	99	1.33	1.23	0.55	1.56
2	2.09.76	5:10	45	74	259	1.19	1.22	0.56	1.56
3	7.09.76	3:05	42	13	79	1.04	1.19	0.58	1.51
4	9.09.76	2:15	43	32	260	1.10	1.20	0.57	1.52
5	3.02.75	16:44	44	61	123	1.11	1.59	0.75	4.05
6	7.02.75	1:50	43	9	49	1.06	1.67	0.81	5.59
7	19.03.76	7:51	42	132	227	1.00	1.63	0.84	4.54
8	12.06.75	13:48	57	26	113	2.09	1.82	0.60	8.09
9	19.06.76	13:37	68	53	108	2.02	1.85	0.51	8.99

The idea that any planet of the Solar system is able to transform an orbit into hyperbola is proved in [34] by estimation of the incoming flux of the particles whose hyperbolic orbits are the result of transformation of their initial orbits in spheres of influence of planets.

There is a hypothesis on a possibility to detect the interstellar particles by kinematical considerations. It gives 46.6 km/s as the lowest limit of the heliocentric velocity of interstellar meteoroids. Therefore, if the heliocentric velocity of a meteoroid exceeds the parabolic velocity more than by 10 km/s this body may be of interstellar origin [29]. Moreover, a concentration of meteor radiants to the apex of the Sun ( $\lambda' = 272^\circ$ ,  $\beta' = 57.5^\circ$ ) should be observed for interstellar meteoroids.

If meteoroids from interstellar space were ejected from stellar systems, one would expect the radiants of these meteors to be concentrated in the plane of the Galaxy. Several potential source regions for interstellar meteoroids can be postulated [35].

For a particle entering the Solar system from interstellar space and coming to the Earth (i.e. moving from the apex) the distributions of interstellar meteoroids on the orbital eccentricity and the perihelion distance have been calculated in the paper [17] for different longitudes of the Earth (observation dates). It has turned out that the most convenient observation periods for detection of interstellar meteoroids were in March and September. Eccentricities of such interstellar particles' orbits should not exceed the value 1.1

Computer methods of search meteor streams may be used for search of groups of interstellar particles. Computer stream searching techniques were introduced by Southworth and Hawkins (1963) [36]. Their method

is a cluster analysis search based on a nearest-neighbours searching and linking technique in five dimensional  $(q, e, i, \omega, \Omega)$  space. The authors introduced a generalized distance  $D$  between any two points in five dimensional  $(q, e, i, \omega, \Omega)$  space and computed all possible distances between these points. Next all pairs which satisfied the condition  $D < D_s$ , where  $D_s$  is an in advance stipulated largest permissible distance in phase space, are grouped together either directly or indirectly to form a cluster (meteor stream). The distance algorithm used was

$$D_{AB}^2 = (e_A - e_B)^2 + (q_A - q_B)^2 + \left( 2 \sin \frac{1}{2 \cdot I_{AB}} \right)^2 + (e_A + e_B)^2 \left( \sin \frac{1}{2 \cdot \Pi_{AB}} \right)^2 \quad (5),$$

where A and B are two orbits to be compared and  $I_{AB}$  is the angle between the orbital planes and  $\Pi_{AB}$  is the difference between the longitudes of perihelion measured from the intersection of the orbits. This algorithm is often referred to as the D-criterion. An application of this (Eq.5) and new [1, 4, 37] D criteria is necessary for search of grouping among meteoroid orbits having eccentricity close to unit.

#### 4. THE KHARKIV HYPERBOLIC METEORS ORBITS

More than 7 thousand near parabolic and hyperbolic orbits of the meteoroids with the masses  $> 10^{-6}g$  have been registered in Kharkiv with the Meteor Automatic Radar System (MARS) from January 1972 till December 1978 among 250 thousand of all orbits. The distribution of geocentric velocity  $V_g$  for meteoroids with hyperbolic orbits is only slightly shifted to larger velocities in comparison with the distribution  $V_g$  for elliptic orbits (Fig.1).

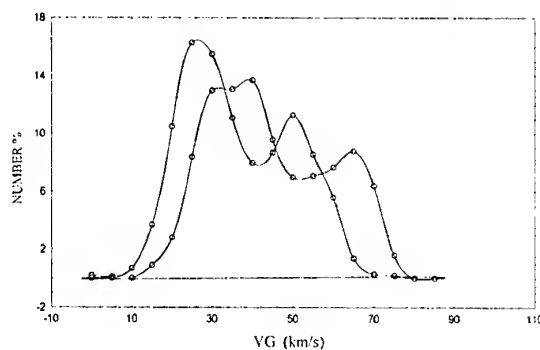


Fig.1. Distribution number of meteors against geocentric velocity  $V_g$  for elliptic (shift left) and hyperbolic (shift right) orbits

The physical factor of noticeability of radio meteors is a function of the observed velocity and the zenith distance of radiant. The geometric form factor is a

function mainly of the radiant inclination in continuous day-and-night observations [8]. The difference between the distributions of hyperbolic and elliptic meteoroids by their azimuth, zenith distance and the radiant inclination is unessential [4, 5]. So, with regard to the stated above analogy of distributions for all the meteors and the meteoroids with hyperbolic orbits, one can conclude that it is possible to use the Kharkiv data to compare different parameters of hyperbolic and elliptic orbits.

When analysing a distribution on heliocentric velocity it is worthy to mention that rather many orbits have errors of individual estimates less than the average value of  $\sigma V_h = 2$  km/s. According to the Kharkiv data the tail of the velocity distribution function extends up to  $V_h \sim 90$  km/s, but the main maximum of distribution of  $V_h$  is in the range from 40 km/s to 50 km/s.

The hyperbolic meteoroid orbits in Kharkiv were studied by samples of different volumes selected of the mentioned multitude by a criterion:  $a < 0$ ,  $e \geq 1$  and  $a > 0$ ,  $0.9 < e < 1$ . A list of 533 elliptical orbits (data of 1975 with  $0.9 \leq e < 1$ ) was used. It was compiled using the Kharkiv elliptical orbit catalogue [3]. All the 7911 hyperbolic selected orbits cover a 7-year period. The number of such orbits changes during a year approximately as the total number of orbits with a minimum in the first half of the year. The percentage of hyperbolic orbits changes during a year from 1.2 to 4.8 (in 1975). The averaged annual percentage of hyperbolic orbits is 2.8% of the total number of orbits. The distributions of all different samples hyperbolic meteor orbits on the eccentricity are investigated. Among 7911 orbits 28 ones are the eccentricity above 5 and 2303 orbits are  $1 < e < 2$ , fifteen orbits (1975) have  $5 < e < 7$  [11]. The distribution on  $e$  of all the hyperbolic meteoroids as well as that of the hyperbolic orbits with  $1 < e < 2$  have the main maximum at  $e = 1.0$  to 1.1.

The distribution of elongation of the radiant from the Sun is a weighty argument in favour of reality of hyperbolic orbits in the Kharkiv data. These distributions for hyperbolas and ellipses with  $0.9 < e < 1.0$  are essentially different [13].

The distribution of radiant coordinates ( $\lambda'$ ,  $\beta'$ ) of hyperbolic orbits in the ecliptic heliocentric coordinate system can testify for the conclusion about the concentration of meteor radiants to the apex of the Solar peculiar motion and to the several another potential source regions (Fig.2) [38]. A possibility to locate interstellar meteoroids according to [17] has been studied as well. It is possible that there are certain number of interstellar meteoroids among those observed periods: 20 days before and 20 days after March 21; June 22; September 23; December 22 (Fig. 3). During a seven years interval 1972–1978 1102 meteoroids with the hyperbolic orbits having  $1 < e < 1.1$

has been found. Distribution of their parameters is given in Fig. 4.

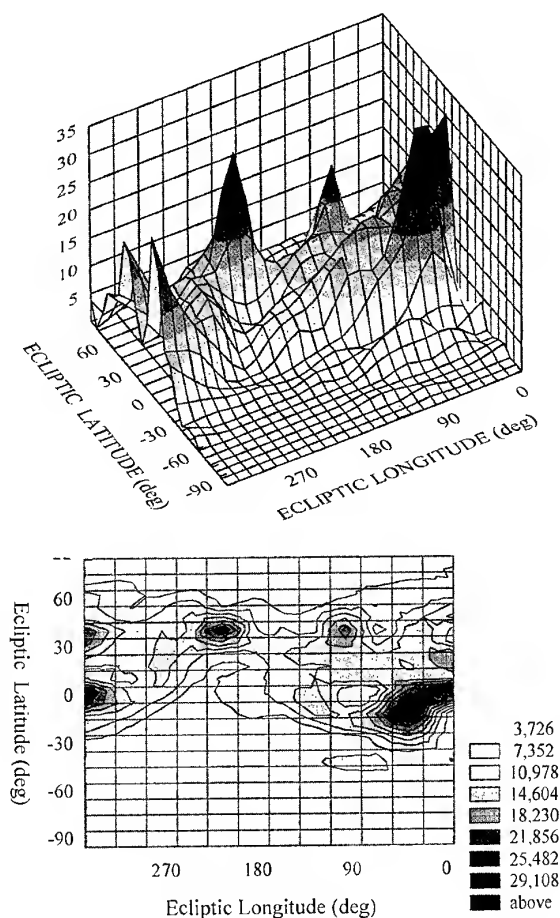


Fig. 2.  $N=N(\beta', \lambda')$  of 1102 hyperbolic orbits with  $1 < e < 1.1$  (1972–1978) in Kharkiv

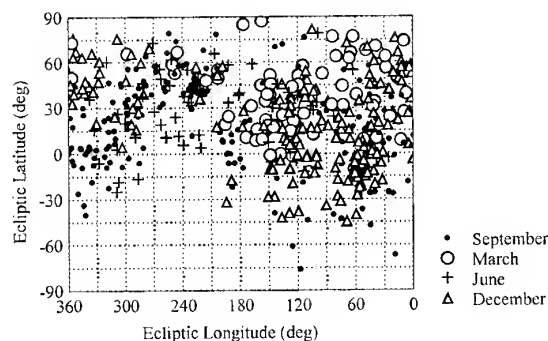


Fig.3. Contribution of radiants ( $\beta'$ ,  $\lambda'$ ) of the hyperbolic orbits ( $1 < e < 1.1$ ) from four seasons

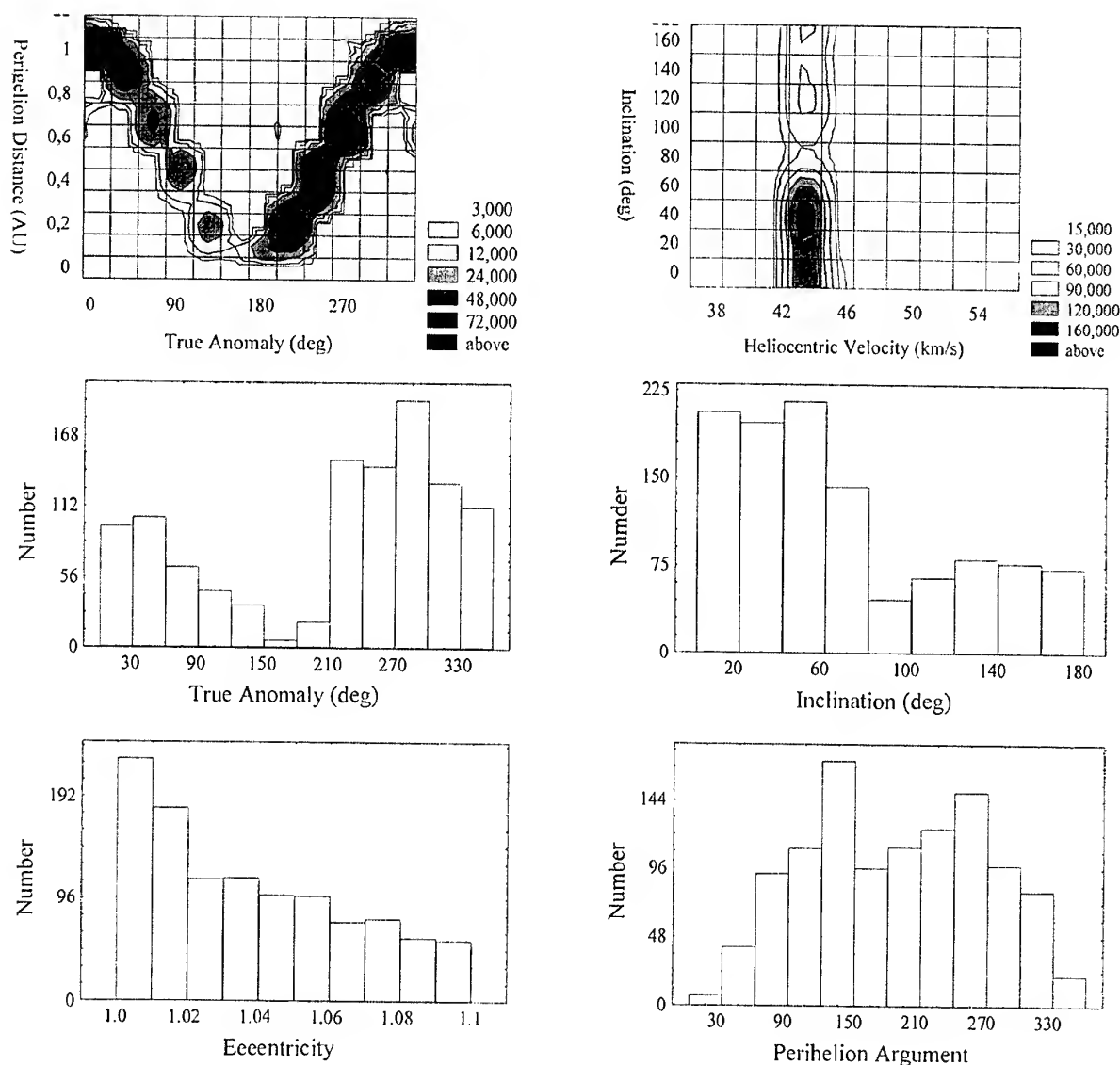


Fig. 4. Distribution of 1102 hyperbolic meteor orbits ( $1 < e < 1.1$ ) on heliocentric velocity and on orbits elements

## 5. CONCLUSIONS

The research carried out in Kharkiv gave many evidences of existence of real hyperbolic orbits. They stimulate us to search for interstellar meteoroids in future. This search today has much more prospects because increasing volume of data but as well as before it is limited by accuracy of meteoroid data. New criteria of choice of interstellar meteoroids are necessary and the problem of such criteria has not been solved yet. The hyperbolic meteors problem remaining unsolved at present sets new task. Meteor bodies with orbits

$$e \rightarrow 1, \quad 1/a \rightarrow 0$$

give much more statistical material than long period comets. The properties of the complex of such meteors orbits may serve as the tests both for selection of the interstellar particles and for the searching of parent bodies on a boundary of the Solar system.

## 6. REFERENCES

1. Voloshehuk Yu.I., et al. A Meteor Complex Near Earth's Orbit: Sporadic Background, Streams, and Associations. I. The Technique for Selection of Streams and Associations from a Large Sample of Individual Meteor Orbits. SOLAR SYSTEM RESEARCH, Vol.29, N 5, 382-391, 1995.

2. Kashcheyev B.L., et al. Meteoric Automatic Radar System, METEORNYE ISSLED., N.4, 11-61, 1976.
3. Kashcheyev B.L. and Tkachuk A.A., *Results of Radar Observations of Faint Meteors Catalogue of Meteor Orbits to +12<sup>m</sup>*, Materials of the Worlds Data Centre B, Moscow, 1980.
4. Voloshchuk Yu. I., et al., *Meteors and a Meteoric Substance*, Naukova dumka, Kiev, 1989.
5. Kashcheyev B.L., et al. On the Problem of Hyperbolic Meteors, SPACE PHYSIC PROBLEM, Rel. 17, 3-15, 1982.
6. Babadzanov P.B. and Kramer Y.N. Some Results of Investigations of Instantaneous Meteor Photographs, PHYSICS AND DYNAMICS OF METEORS, 128-142, 1968
7. Katasev L.A. *Research of Meteors in an Atmosphere of the Earth a Photographic Method*, Leningrad, 1966.
8. Kashcheyev B.L., et al. *Meteoric Phenomena in the Earth's Atmosphere. Investigation Meteor*, N2, Nauka, Moskva, 1967.
9. Lebedinets V.N., *Dust in the Upper Atmosphere and Space. The Meteors*, IEM, Leningrad, 1980.
10. Babadzhanov P.B. Photographic observation of Perseids, THE BULLETIN OF INSTITUTE OF ASTROPHYSICS, N 26, 13-20, 1958.
11. Baggley W.J. The Interstellar Particle Component measured by AMOR, METEORIDS 1998, 265-273, 1999.
12. Kolomiyets S.V. Change of The Calculated Shape of Meteoric Bodies Orbits as Dependent upon Accuracy of Calculations, METEOR STUDIES, N12, 75-86, 1986.
13. Andreyev G.V., et al. Contradictions in the Problem of Hyperbolic Meteors, METEOR STUDIES., N13, P.93-104, 1987.
14. Radzievsky V.V. and Tomanov V.P. To the Question About the Origin Nearly Parabolic Comets, ASTRON. JOURNAL, MOSKVA, Vol. 47, N5, P.1094-1099, 1980.
15. Vsekhsvyatsky S.K. Eruptive Processes in Galaxy and Hyperbolic Meteors, SPACE PHYSICS PROBLEMS, Rel. 13, 141-146, 1978.
16. Belkovich O.I., Potapov I.N. Expected Distribution of Some of the Orbits Elements of Interstellar Particles in the solar System, ASTRON. VESTNIK, Vol. 19, N3, 206-210, 1985.
17. Kazantsev A.M. The Possibility to Detect Interstellar Meteoroids, KINEMATICS AND PHYSICS OF CELESTIAL BODIES, 82-88, 1998.
18. Stohl J. On the Problem of Hyperbolic Meteors, BULL. ASTRON. INST. CZECHOSL., Vol. 21, 10-17, 1970.
19. Kazantsev A.M., Sherbaum L.M. Hyperbolic meteors and Jupiter, BULL. KIEV. UNIV. ASTRONOMY, Vol.24, 72-74, 1982.
20. Kazantsev A.M., Sherbaum L.M. Search of The Mechanism of an Origin of Strongly Pronounced Hyperbolic Orbits of Meteors, ASTRON. VESTNIK, MOSCKOW, Vol. 24, N1, 72-78, 1990.
21. Kramer Y.N. Dust particles, dust aggregates and other interstellar meteoroids, ABSTRACTS BOOK. INTERNATIONAL CONFERENCE METEORIDS, TATRANSKA LOMNICA 17-21 AUGUST, 1998.
22. Mathews J.D. and al. Possible Origins of Low Inclination Antapex Micrometeors Observed Using The Arecibo UHF Radar, METEORIDS 1998, 79-82, 1999.
23. Grun E. Dust Detection From Space Vehicles, METEORIDS AND THEIR PARENT BODIES, 349-356, 1992.
24. Wehry A. and Mann I. Analysis of In-situ Measurements of Dust Particles Onboard the Ulysses Spacecraft, METEORIDS 1998, 287-290, 1999.
25. Mann I. The Out of Ecliptic Distribution of Interplanetary Dust and its Relation to Other Bodies in the Solar System, EARTH, MOON AND PLANETS, Vol.68, N1-3, 419-426, 1995.
26. Jaccia L.G., Whipple F.L. Precision Orbits of 413 Photographic Meteors, SMITHSONIAN. CONTRIB. ASTROPHYSICS, Vol. 4, N4, 97-129, 1961.
27. Davies J.G., Gill J. C. Radio Echo Measurement of the Orbits of Faint Sporadic Meteors, MON. NOT. ROY. ASTRON. SOC., Vol. 121, N5, 437-462, 1960.
28. Elford W.G., Cervera M.A. Meteor Velocities: a New Look at on Old Problem, EARTH, MOON AND PLANETS, Vol. 68, N1-3, 257-266, 1995.

29. Hajdukova. M.Jr. On the Hyperbolic and Interstellar Meteoror orbits, METEORIDS 1998, 61-64, 1999.
30. Sarma T., Jones J. Double -station Observations of 454 TU Meteors, BULL. ASTRON. INST. CZECHOSL., Vol. 36, N9, 103-115, 1985.
31. McKinley D. W. R. *Meteors science and engineering*, McGraw-Hill Book Company, Inc, New York Toronto London, 1961.
32. Simakina E.G. About Hyperbolic Meteor Orbits, ASTRON. VESTNIC, Vol. 11, N3, 153-157, 1968.
33. Kramer E.N., et al. *Meteor Orbits from Photographic Observation 1957-1983. Catalogue*. Materials of the Worlds Data Centre B, Moscow, 1986.
34. Andreyev G.V., et al. Hyperbolic Meteoroid Flux Near Earth Orbit, ABSTRACTS FOR IAU SYMPOSIUM 160: ASTEROIDS, COMETS, AND METEORS, BELGIRATE (NOVARA), ITALY, JUNE 14-18 1993, 12, 1993.
35. Hawkes R. and et al. Meteoroids from Outside the Solar System, METEORIDS 1998, 257-264, 1999.
36. Southworth R.B. and Hawkins G. S. Statistics of Meteor Streams, SMITHS. CONTR. ASTROPHYS., N 7, 261-265, 1963.
37. Jopek T.J., et al. Meteor Stream Identification: a New Approach. Application to 3675 Radio Meteors, METEORIDS 1998, 307-310, 1999.
38. Kashcheyev B.L. and Kolomiyets S.V. Statistics of Perihelion Directions of Nearly Parabolic and Hyperbolic Orbits of Meteor Bodies, METEOR STUDIES, N11, 81-89, 1984.

## DUST ASTRONOMY: A NEW APPROACH TO THE STUDY OF INTERSTELLAR DUST (ESA SP-495)

Eberhard Grün<sup>(1,2)</sup>, Sascha Kempf<sup>(1)</sup>, Harald Krüger<sup>(1)</sup>, Markus Landgraf<sup>(3)</sup>, Ralf Srama<sup>(1)</sup>

<sup>(1)</sup> *MPI Kernphysik, Saupfercheckweg 1, 69117 Heidelberg, (Germany), Email: "first"."last name"@mpi-hd.mpg.de*

<sup>(2)</sup> *Univ. Hawaii, HIGP, 1680 East West Road Honolulu, HI 96822 (USA), Email: gruen@higp.hawaii.edu*

<sup>(3)</sup> *ESA-ESOC, Robert Boschstr. 5, 64293 Darmstadt, Germany, Email: markus.landgraf@esa.int*

### ABSTRACT/RESUME

Dust particles, like photons, are born at remote sites in space and time. From knowledge of the dust particles' birthplace and their bulk properties, we can learn about the remote environment out of which the particles were formed. This approach is called dust astronomy which is carried out by means of a dust telescope on a dust observatory in space. It can provide valuable information about the particles' birthplace which may not be accessible by other techniques. Targets for a dust telescope are interstellar, cometary, and asteroidal dust. Interstellar and interplanetary dust particles are separated by in-situ dust detectors with narrow apertures and by the measurements of the electric charge signals that are induced when the charged grains fly through the detector. Modern in-situ dust detectors are capable of providing mass, speed, physical and chemical information of dust grains in space.

### 1. ASTRONOMICAL OBSERVATIONS OF INTERSTELLAR DUST

Interstellar dust (ISD) research began around 1930, when the observed reddening of starlight was attributed to the presence of dust in interstellar space. Models of the size distribution could explain the observed extinction. Later, infrared spectroscopy allowed the analysis of molecular features and thus gave insight into the chemical composition of ISD. Prominent silicate (Si-O) features near 10 and 20  $\mu\text{m}$  were detected. The infrared spectra also contained features at 3.3, 6.2, 7.7, and 11.3  $\mu\text{m}$  which were tentatively attributed to polycyclic aromatic hydrocarbons (PAHs). More recently, the European Infrared Space Observatory (ISO) provided for the first time, high resolution spectra in the wavelength range 2 to 200  $\mu\text{m}$ . With the ISO data it was possible to obtain an inventory of molecular ice features of  $\text{H}_2\text{O}$ ,  $\text{CO}$ ,  $\text{CO}_2$ , and  $\text{CH}_3\text{OH}$ . The grain model by Mathis [1] suggests three grain types: small graphite grains, silicate grains, composite grains containing carbon (amorphous, hydrogenated, or graphitic), silicates, and oxides. On the basis of the same elementary composition, Li and Greenberg [2] proposed three different grain types:

large grains consisting of a silicate core and an organic refractory mantle; small carbonaceous grains; very small grains (or large molecules) of PAHs.

Evolved stars continuously lose mass. About 90% of the stellar mass loss is provided by cool, high-luminosity stars, in particular by asymptotic giant branch (AGB) and post-AGB stars. As the ejected gas cools in expanding stellar winds, and also in supernova remnants [3], solid particles condense out of the gas phase [4]. This so-called "stardust" provides the seeds for ISD grains that grow in cool interstellar clouds by accretion of atoms and molecules and by agglomeration. Interstellar shock waves provide an effective destruction mechanism for ISD grains as small grains are caught in the shock and collide with bigger grains that don't follow the shock's motion due to their larger inertia [5]. In diffuse interstellar clouds, the grains lose their volatile constituents due to ultraviolet irradiation [6] and thermal sputtering in interstellar shock fronts. Ultimately, an ISD grain can be incorporated (and destroyed) in a newly forming star, or else, it can become part of a planetary system. In this way, ISD grains are repeatedly recycled through the galactic evolution process [7]. More locally, dust is contained in the interstellar clouds surrounding the solar system. Fig. 1 shows the local interstellar environment of the Sun. The local interstellar cloud (LIC) is a small-scale (1 pc) part of the warm medium shown as the local finger reaching into the hot local bubble.

### 2. INTERSTELLAR GRAINS IN THE SOLAR SYSTEM

Solid material that makes up the Earth and other planets has resided in galactic interstellar dust grains 5  $10^9$  years ago before it was mixed and altered during the planetary formation process. Composition information on galactic dust has been extracted by laboratory analysis of collected interplanetary dust particles (IDPs) and of presolar dust grains found in meteorites. While the most abundant of them (diamonds) are too small (only 2.6 nm on average) for individual grain analysis, many other grains, primarily

grains of graphite, silicon carbide, aluminium oxide and silicon nitride, have been individually analyzed. The isotopic composition of a variety of elements that have been studied, e.g. C, N, Mg, Si, Ca, Ti, Sr, Zr, Mo, noble gases, strongly deviates from the solar system composition and provides evidence for their presolar origin [9].

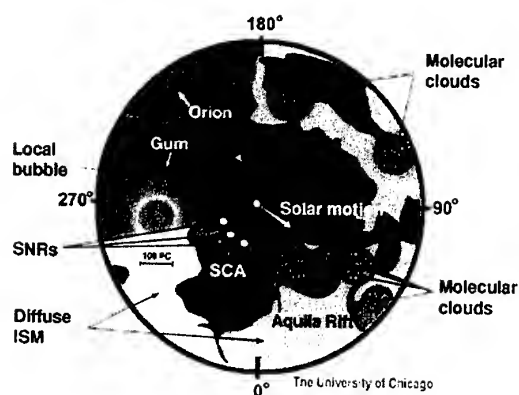


Fig. 1. Morphology of the local galactic environment of the Sun (at the centre), projected onto the galactic plane [8]. The radius of the figure is 500 pc. The arrows in the center show the motion of the Sun and of the local finger of warm partially ionized material of the local interstellar cloud (LIC), respectively. In the local standard of rest frame, the LIC moves with, 19 km/s towards galactic coordinates  $l=145^\circ$ ,  $b=0^\circ$  and the Sun moves with 15.4 km/s towards  $l=51^\circ$ ,  $b=+23^\circ$ . Nearby molecular clouds and the diffuse interstellar medium (ISM) which reddens starlight are indicated. The interior of the hot local bubble is shown by the dark wedge-like feature. The gray region within 50 pc of the Sun between galactic longitudes,  $20^\circ$  and  $90^\circ$  represents diffuse interstellar gas ablated from the parent molecular cloud complex when impacted by the combined stellar winds and supernova shock fronts from star formation and destruction in the Scorpius-Centaurus association (SCA). Courtesy of Priscilla Frisch.

IDPs, after their collection in the stratosphere, are first classified on the basis of Secondary Electron Microscope and X-ray analysis, which allows to differentiate these particles from terrestrial particles, either natural (mainly volcano dust) or artificial (aluminum oxide from solid rocket exhaust). The most direct evidence for the interstellar origin of constituents of IDPs comes from their infrared spectrum. Bradley et al. [10] have been able to match the spectra of silicate phases in IDPs with spectra of circumstellar and interstellar material. The physical properties of these

silicate phases that are dubbed GEMS (Glass with Embedded Metal and Sulfides) are exotic (e.g., they contain superparamagnetic metal inclusions) but similar to those found throughout interstellar and circumstellar space [11]. Isotopic anomalies of H, N, O in IDPs indicate a presolar or interstellar origin of constituents of IDPs [12]. In some IDPs hotspots of extreme isotopic anomalies up to a factor of 50 have been found [13].

How do these presolar interstellar grains compare with contemporary local ISD? Although those particles identified in meteorites are only minor constituents and are probably not representative of all dust in the interstellar medium (ISM) 5  $10^9$  years ago, the same types of grains are likely to be present as a dust component of the ISM today. Presolar silicates and sulfides, which are expected to be present in the ISM, have not been identified in meteorites yet, although they may have been found in IDPs in the form of the GEMS mentioned above [10, 11].

Less than ten years ago ISD grains were unambiguously detected in the solar system with in-situ instruments. After its flyby of Jupiter, the highly sensitive dust instrument on board the Ulysses spacecraft detected impacts predominantly from a direction opposite to that expected for interplanetary dust grains having low-inclination and low-eccentricity orbits [14]. It was found that on average, the impact velocities exceeded the local solar system escape velocity [15]. Further evidence for an interstellar origin of these grains was the fact that their flux was the same above the sun's poles as in the ecliptic plane. An identical dust detector on board the Galileo spacecraft, which was en route to Jupiter at that time, confirmed Ulysses' findings [16].

Once it became evident that galactic ISD is accessible to in-situ detection and even sample return to Earth, NASA selected the Stardust mission to analyze and return, samples of ISD acquired at asteroid belt distances [17]. Since early, 1999 Stardust has been on its way to the outer solar system where it will undergo a fast fly-by of comet Wild 2. En route to the comet, and on the return path to Earth, Stardust will collect interstellar dust and analyze it with the state-of-the-art Cometary and Interstellar Dust Analyzer, CIDA. Thus, the prospect of results from the Stardust mission will vitalize interstellar dust research. Estimates by Landgraf [18] suggest that CIDA will record and analyze only 10 to 30 interstellar grains. These authors also predict that the impact velocities of larger ISD grains (masses  $m > 10^{-12}$  g) onto the Stardust aerogel collector are above, 20 km/s. At such high impact speeds, collection in aerogel might be impossible [19] due to grain destruction during impact.

Recent in-situ measurements show that ISD can be measured at Earth's distance from the Sun (1 AU). Data obtained by the dust detector on board the Hiten satellite [20], which is on a highly eccentric orbit about the Earth, indicate that micron and sub-micron sized ISD grains indeed reach 1 AU. Measurements by the Cosmic Dust Analyzer (CDA) on board the Cassini spacecraft also suggest the presence of ISD in the inner solar system. Furthermore, modeling of the Ulysses and Galileo data implies that up to 30% of the flux at 1 AU of cosmic dust grains of  $10^{-13}$  g and larger is of interstellar origin [21]. Radar observation of meteors with speeds above the heliocentric escape speed [22] shows that ISD grains with sizes larger than 40  $\mu\text{m}$  are present at 1 AU.

### 3. DUST OBSERVATORY

Dust astronomy is carried out by means of a dust observatory in space. A dust observatory for interstellar dust must be designed to allow the distinction between interstellar and interplanetary dust, to measure the chemical and isotopic composition of local ISD, and to determine the trajectories of ISD grains through the solar system by monitoring the mass dependent ISD flux direction over the duration of the mission. To minimize the contamination by artificial solid particles near Earth, the observatory's trajectory should lie outside the debris belts at the distance of geosynchronous orbit. Possible trajectories are high Earth orbits or orbits about the libration points of the Earth-Sun system (Fig. 2). The dust observatory exploits the effect of Earth's motion ( $v_E \sim 30$  km/s) on the local ISD velocity ( $v_{ISD} \sim 26$  km/s) and flux. This can be used to confirm the interstellar origin of the measured dust population. During the Earth's upwind motion, the velocities add up to 56 km/s, and during the downwind motion the relative velocity is low (-4 km/s).

#### 3.1 Mission Scenario

In Fig. 3 we suggest an observation strategy for the dust telescope, for which we have assumed that the interstellar upstream direction is ecliptic longitude  $\lambda_e = 259^\circ$ , and latitude  $\beta_e = 8^\circ$ . When the dust telescope points into this direction, the flux of ISD grains is almost an order of magnitude larger than the flux of interplanetary grains.

During the first two years of the mission the interstellar dust flux along the Earth's orbit around the Sun, as well as the interplanetary dust background flux, will be determined. In order to provide statistically meaningful data, the dust telescope will perform blocks of observations, each of duration 4 weeks, with a fixed

instrument pointing in inertial space. The observations will be linked by maintenance periods of about two days.

The observation strategy for the second year can be modified depending on the findings from the first year. In particular, deviations of the flux direction of big interstellar grains from the nominal direction are important to characterize the coupling of big galactic grains to the LIC, or larger structures, and to identify potential sources of these particles.

Observations during later years could be open to proposals from the scientific community. Potential targets are interplanetary phenomena, e.g. dust in meteoroid streams, cometary dust, asteroidal dust, dust from the Moon or other collimated sources of dust.

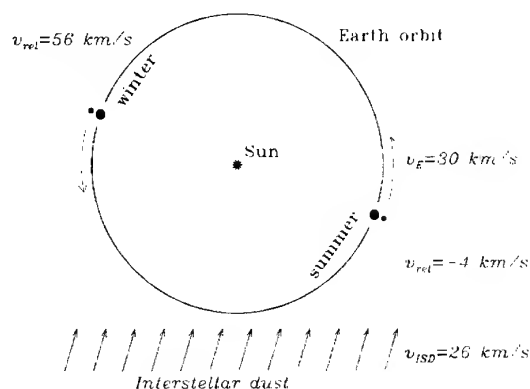


Fig. 2. Dust observatory mission. Earth's orbit around the Sun ( $v_E = 30$  km/s), and the direction of the interstellar gas and dust flow at speed  $v_{ISD} = 26$  km/s are shown. Two positions of the Earth (big dot) and the satellite (small dot) are shown (right: late summer, and left: late winter). We have assumed that radiation pressure and solar gravity for ISD grains cancel each other, therefore ISD traverses the solar system on straight trajectories.

#### 3.2 Dust Telescope

The payload of a dust observatory is a dust telescope which combines the characteristics of several present dust instrument. It consists of instruments [24] having narrow fields-of-view and a plasma monitor. The relatively narrow aperture of the dust telescope of only  $25^\circ$  half-width allows pointed observations of the interstellar dust flow. The instruments share a common impact plane of  $1 \text{ m}^2$  in size which is a ten times larger collection area than current instruments have. Potential instruments (cf. Table 1) are, a high resolution impact mass spectrometer (Stardust's CIDA), a dust analyzer

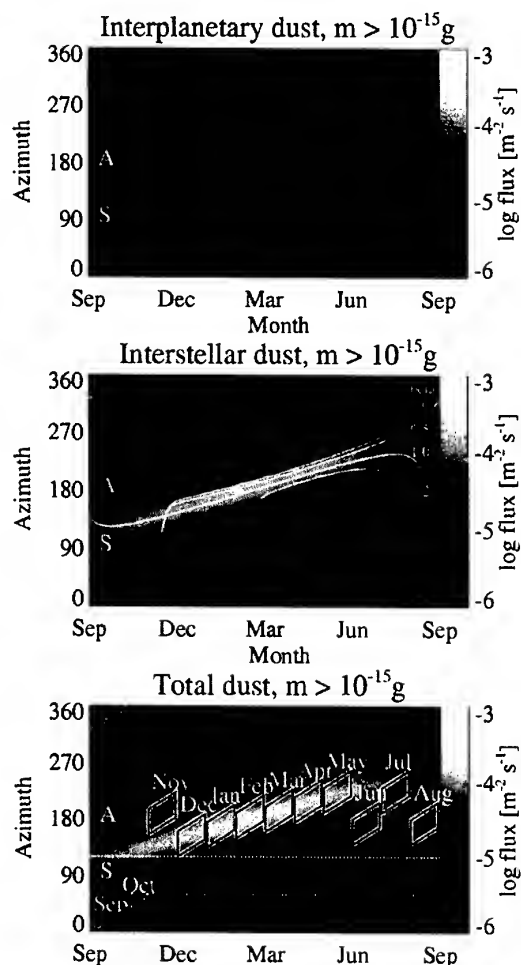


Fig. 3. Model dust fluxes and observation strategy. The top panel shows the gray coded interplanetary dust flux as derived from the interplanetary dust flux model [23].

The assumed spacecraft orbit is a circular orbit about the Sun at 1 AU with the spacecraft position characterized by its ecliptic longitude. The assumed detector sensitivity is  $10^{-15}$  g and the detector has a  $50^\circ$  wide aperture. Azimuth  $90^\circ$  corresponds to the solar direction (S) and  $180^\circ$  is the apex direction of the Earth's motion (A). The middle panel shows the flux of ISD grains with an assumed  $\beta$ -value of 1 (white lines for  $\beta = 0, 0.5, 1$ , and  $1.2$ ). The bottom figure displays the combined fluxes. Overlain is a sample of possible observations represented by the diamonds. Individual observations last about a month (the months indicated represent the start of an observation at about the 20th day of the month). The azimuth range corresponds to  $50^\circ$ . It is assumed that during each observation the spacecraft with the dust telescope points to a fixed direction in inertial space. Within  $30^\circ$  from the solar direction is the Sun avoidance zone.

for the determination of physical and chemical dust properties (Cosmic Dust Analyzer, CDA), a large area impact detector with trajectory analysis (Dust Detector System, D2S), the momentum sensor ISIDE (Impact Sensor for Interstellar Dust Exploration) and a plasma monitor, PLASMON.

The instruments employ various detection techniques and have different sensitivities. CIDA and CDA have the highest sensitivity for fast particles. The D2S detectors have a somewhat lower sensitivity. The momentum sensor has about the same sensitivity as the D2S sensor. Of course, bigger particles above the measurement range can be detected, but their derived mass will represent a lower limit. The sensitivity of the charge sensors of D2S has been assumed to be the same ( $10^{-15}$  C) as that of the charge sensors on Cassini CDA.

CDA, ISIDE and seven elements of D2S are combined in the interior of the dust telescope, CIDA is mounted to the side. Fig. 4 shows the impact plane of the dust telescope. Seven segmented polyvinylidene fluoride (PVDF) targets of D2S surround the central opening for CDA. ISIDE is mounted in one corner. In front of the seven segments of D2S, of CDA and of ISIDE are collimators that include the charge sensing grids of the trajectory sensors. Fig. 5 is a side view of the dust telescope with CIDA attached to the baffle of the D2S dust collimators (0.7 m height) and CDA and ISIDE below. PLASMON monitors the plasma environment and thus supports the interpretation of the dust charge measurements. The total mass of the dust telescope is 62.8 kg and the total power consumption is 53.3 W.

## 4. MEASUREMENT GOALS

### 4.1 Distinction of Interstellar from Interplanetary Dust

ISD grains are distinct from interplanetary grains by their kinematic, and probably by their compositional, properties. One major goal, therefore, is to distinguish interstellar from interplanetary dust grains by their kinematic properties. The kinematics of interstellar dust (ISD) is determined by the solar motion through the local interstellar cloud, which thus defines the encounter velocity of ISD in the heliocentric frame and its dynamics in the immediate solar vicinity.

From the in-situ measurements of the Ulysses and Galileo dust instruments, the upstream direction of ISD particles was found to be close to ecliptic coordinates  $\lambda_c = 259^\circ$ ,  $\beta_c = 8^\circ$  [25]. This direction is approximately the upstream direction of interstellar gas as measured by the Ulysses GAS experiment [26]. The initial

Table 1. Instrument characteristics of the model payload. sensitive areas, mass, and power. The mass for each instrument includes the mass for the electronics box.

Instrument	Measurements	Sensitive Area [m <sup>2</sup> ]	Sensitivity at, 20 km/s [g]	Mass [kg]	Power [W]	Heritage
CDA	Mass, speed, composition	0.1	10 <sup>-14</sup>	13,1	7,1	Cassini
D2S	Trajectory, mass	7 x 0.11	10 <sup>-12</sup>	32,2	14,7	VeGa, Cassini
CIDA	Composition	0.009	10 <sup>-14</sup>	10,3	15	Stardust
ISIDE	Mass	4 x 0.015	10 <sup>-12</sup>	5,9	15	Rosetta
PLASMON	Plasma	./.	./.	1,3	1,5	Rosetta

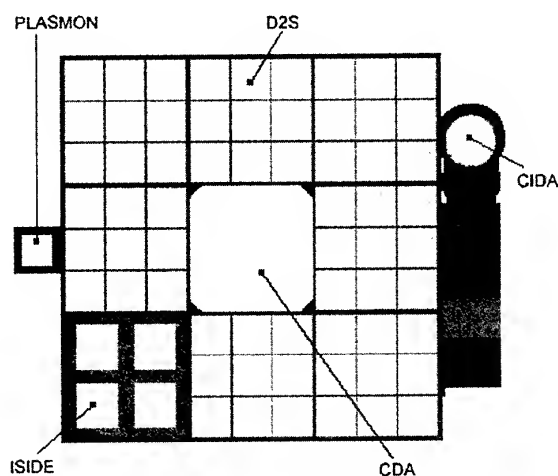


Fig. 4 Impact plane of the dust telescope. In the centre and in one corner of the 1 m<sup>2</sup> impact plane, are the holes for CDA and ISIDE, respectively, which are mounted directly underneath. Seven segmented D2S targets surround CDA and ISIDE. CIDA and PLASMON are attached to the baffles of D2S.

velocity of ISD grains with respect to the Sun is compatible with 26 km/s, which is the initial velocity of the gas. Close to the Sun, the motion of ISD grains is changed by their interaction with solar gravity, radiation pressure, and the solar electromagnetic field. A dust telescope will use two different, complementary strategies to establish the interstellar origin of small ( $m < 10^{-11}$  g), and big ( $m > 10^{-11}$  g) dust grains. For big ISD grains, the primary electrostatic charge is sufficient to determine the impact velocity and direction, by use of a large area charge and trajectory sensing instrument [24]. ISD grains can then easily be distinguished from interplanetary grains, because their velocity exceeds the local solar system escape velocity. Furthermore, their initial direction of motion can be determined by integrating backwards along their trajectory. This way the direction and angular width of the flow big ISD grains can be determined.

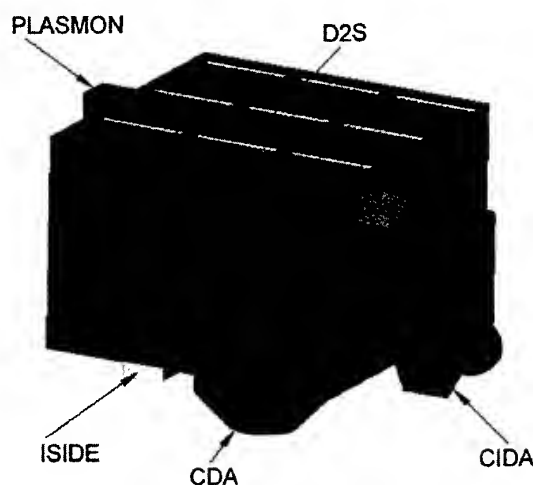


Fig. 5 Dust telescope. On top are 9 dust collimators containing the charge sensing grids, seven of which belong to D2S. CDA is mounted below the central collimator, whereas ISIDE is mounted underneath a corner collimator. CDA is embedded within the spacecraft with the impact plane being at one spacecraft wall. CIDA and PLASMON are attached to the side.

An ensemble of small ISD grains can be distinguished from the interplanetary dust population by statistical arguments, even if the exact trajectories of the individual particles are not known. This method has been demonstrated by the identification of an interstellar subset of the Ulysses and Galileo dust impacts [16]. The Galileo and Ulysses instruments can only determine the impact direction of the dust particles with an accuracy of  $\pm 70^\circ$ . However, the statistical analysis of the distribution of impact directions of a large set of impacts, gives the interstellar upstream direction within  $\pm 10^\circ$  in ecliptic latitude and  $\pm 20^\circ$  in ecliptic longitude [25]. Compared to the Ulysses and Galileo measurements, a dust observatory will provide an improved identification capability of small ISD grains. This can be achieved by instruments with a narrow field of view of  $25^\circ$  half-width.

## 4.2 Chemical and Isotopic Analysis of Interstellar Dust

One of the outstanding scientific issues today is the origin of the elements and the chemical evolution of the Galaxy and the Universe. The evolution of ISD follows the evolution of the metallicity in the galaxy. Dwek [27] has found that the dust mass is linearly proportional to the interstellar metallicity, and contains about 40 % of the total mass of heavy elements in the Galaxy. The factory producing heavy elements in our Galaxy consists of nucleosynthesis in stars, and in supernovae. ISD [28, 29] grains carry most of the mass of refractory elements in the ISM (e.g. Fe, Mg, Si) as well as C and O. In principle, the metallicity of both disk stars and the interstellar medium, including ISD, increases with time. However, recent studies of heavy elements in nearby cool field stars (F and G disc dwarfs) failed to find clear evidence for this increase [30], and the intrinsic metallicity of the ISM is poorly understood.

In stars, the general marker for metallicity is the ratio  $[\text{Fe}/\text{H}]$ , since iron is formed in supernova nucleosynthesis. However, in the interstellar medium, typically more than 90% of the iron is inside ISD grains. The lifetime of iron in dust grains indicates that iron is present in a robust grain core that defies destruction in interstellar shocks [28, 29]. Although constituents of ISD grains are partially known, there are no direct measurements of the full grain composition.

The probable identification of interstellar minerals not seen in meteorites is closely related to the question of dust survival in the solar system and this may give new insights into the early solar system history as well as into the interstellar medium at the present time. Because the isotopic compositions of certain elements (e.g., Si) in dust grains from cool stars are expected to be largely unaffected by the nucleosynthesis inside the grains' parent stars, it should be possible to trace the evolution of the isotopic composition of such elements in our galaxy during the past  $5 \cdot 10^9$  years. This is of high scientific interest because the concept of galactic chemical evolution is closely related to the question of dust and gas injection from different types of stars into the ISM, thus providing important information on the history of the local ISM.

## 4.3 Measurement of the Interstellar Dust Flux near Earth

At large heliocentric distances, the Ulysses and Galileo dust instruments measured an average ISD flux for  $10^{-15}$  g particles of  $1.5 \cdot 10^{-4} \text{ m}^{-2} \text{ s}^{-1}$  [14]. The local ISD

flux for a satellite moving with the Earth around the Sun exhibits an annual variation. Assuming a constant ISD flux of  $1.5 \cdot 10^{-4} \text{ m}^{-2} \text{ s}^{-1}$  and a velocity of 26 km/s from a direction of  $\lambda_{\text{ecl}} = 259^\circ$ ,  $\beta_{\text{ecl}} = 8^\circ$ , the maximum interstellar flux of  $3 \cdot 10^{-4} \text{ m}^{-2} \text{ s}^{-1}$  occurs in February and remains more than 4 times larger than the interplanetary flux during 6 months around this time.

The dynamics of ISD grains in the solar system is governed by solar gravity, radiation pressure, and the Lorentz force induced by the radially expanding solar wind magnetic field. These forces shape the trajectory of an individual grain and determine the ISD flux distribution at any given location in the solar system.

If gravity dominates radiation pressure ( $\beta < 1$ ), ISD is concentrated in a wake downstream of the Sun. In the case  $\beta > 1$ , an ISD-free cavity around the Sun forms [31]. The influence of the solar wind magnetic field on the dynamics of ISD grains is important for grains smaller than  $0.4 \mu\text{m}$  in diameter. It was shown numerically [32] and confirmed by the in-situ measurements of Ulysses [18] that the flux of small ISD grains varies with the 22-year polarity cycle of the solar magnetic field. According to this simulation, the best time to measure a large number of ISD grains will be between, 2004 and, 2012, when the flux, and thus the impact rate, of  $10^{-14}$  g grains at 1 AU will be enhanced by up to a factor of 10 compared to the currently (2000) observed flux. The flux of large ( $m > 10^{-11}$  g) grains is permanently increased at 1 AU by gravitational focusing. More than 1,000 interstellar grains will be recorded within two years of operation by a dust telescope described above, 60 of which with high resolution mass spectra.

The measurements of local ISD by Ulysses and Galileo have already shown that the local ISD population contains more large grains than predicted by models based on astronomical observations [25]. However, because of their limited target area of  $0.1 \text{ m}^2$ , Ulysses and Galileo detected only a few ISD grains with masses above  $10^{-11}$  g, which corresponds to a diameter of  $\sim 2 \mu\text{m}$  [33]. Information about the abundance of ISD particles with masses  $m > 10^{-6}$  g was obtained by the Advanced Meteor Orbit Radar (AMOR) facility in New Zealand [22]. Fig. 6 shows the cumulative flux mass distribution measured by Ulysses, Galileo, and AMOR.

The extrapolation of the local ISD mass distribution to masses  $m > 10^{-11}$  g over five orders of magnitude, shown in Fig. 4, is highly speculative. However, recent observations by Arecibo meteor radar (Meisel, private communication) indicated an extension of the Ulysses mass flux to higher masses. Because large grains are the dominant contributors to the overall mass of the

dust population, we can only understand the heavy element content of the LIC if we fill this gap. Grains with  $m > 10^{-11}$  g are also a candidate for the source that replenishes the interstellar medium with smaller fragments [34].

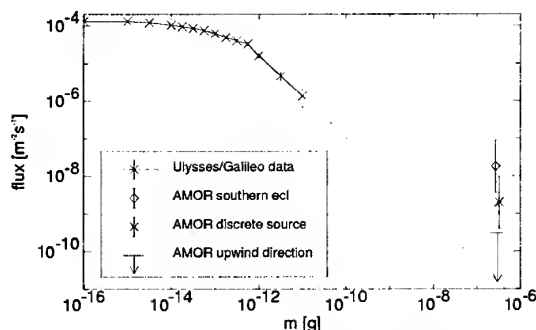


Fig. 6. Cumulative flux mass distribution derived from Ulysses and Galileo data compared to the flux of interstellar radar meteors detected by AMOR. Dotted line: extrapolation of Ulysses and Galileo data by a power-law with exponent -1.1. The radar data are distinguished for different source directions; diamond: influx from southern ecliptic hemisphere, asterix: influx from discrete source located in southern ecliptic hemisphere, horizontal bar: upper limit of influx from ISD upstream direction.

## 5. ENABLING TECHNOLOGIES

### 5.1 Flux and Trajectory Measurements

The flux of sub-micron to millimeter sized dust in interplanetary space has been determined by dust detectors, and by crater counts on satellite surfaces and on lunar samples. The expected impact rate on dust detectors at 1 AU is given in Table 2.

Because of the low dust flux expected in interplanetary space the dust detectors on the Galileo and Ulysses missions have sensitive areas of  $0.1 \text{ m}^2$  and a wide aperture (of  $140^\circ$  opening angle corresponding to  $1.4 \text{ sr}$  field-of-view). These dust detectors provided a coarse determination of the mass, speed, and impact direction of the recorded dust particles. From these measurements it was possible to identify by statistical means several different populations of dust (interplanetary, interstellar, and Jupiter dust) in interplanetary space. At 1 AU the flux of interstellar dust particles is estimated to be about 30% of the total flux of  $10^{-13}$  g particles [21]. Narrowing the aperture of a dust detector to a cone of only  $50^\circ$  is a means to obtain better trajectory analysis. However, for a dust

detector with narrow aperture it is mandatory to further increase the sensitive area to about  $1 \text{ m}^2$ .

One of the primary objectives is to measure the local ISD size distribution over the widest possible range. In order to obtain information about the flux of ISD grains with  $m > 10^{-11}$  g, the sensitive areas of the dust telescope instruments have to be as large as possible. With an area of  $1 \text{ m}^2$  it takes 2 years to detect 2 to 5 very large grains with masses of approx.  $10^{-9}$  g which represents the upper limit of the ISD mass range accessible by such a dust observatory.

Table 2. Dust charges, cumulative fluxes and count rates of particles of a given mass or radius on a dust detector at 1 AU from the sun [35]. It is assumed that the detector has a sensitive area of  $0.1 \text{ m}^2$ ,  $\pi \text{ sr}$  field-of-view, and is mounted to a spinning platform with the spin axis perpendicular to and the sensor axis scanning in the ecliptic plane. Spherical particles of density  $2.5 \text{ g/cm}^3$  have been assumed. A surface potential of 5 V has been assumed to calculate the dust charges.

Mass (g)	Radius ( $\mu\text{m}$ )	Dust Charge (C)	Flux ( $\text{m}^{-2} \text{s}^{-1}$ )	Count Rate (per day)
$10^{-14}$	0.1	$5.6 \cdot 10^{-17}$	$2.5 \cdot 10^{-4}$	2.2
$10^{-13}$	0.21	$1.2 \cdot 10^{-16}$	$8.3 \cdot 10^{-5}$	0.7
$10^{-12}$	0.46	$2.6 \cdot 10^{-16}$	$3.4 \cdot 10^{-5}$	0.3
$10^{-11}$	1	$5.6 \cdot 10^{-16}$	$1.5 \cdot 10^{-5}$	0.13
$10^{-10}$	2.1	$1.2 \cdot 10^{-15}$	$6.4 \cdot 10^{-6}$	0.06
$10^{-9}$	4.6	$2.6 \cdot 10^{-15}$	$3.0 \cdot 10^{-6}$	0.03

Any meteoroid in interplanetary space is electrically charged. Because of the predominance of the photoelectric effect in interplanetary space, meteoroids are usually charged positively at a potential of a few Volts. The charge  $q$  of a dust particle of mass  $m$  at a surface potential  $U$  is

$$q = \epsilon_0 \eta U m^{1/3} \quad (1)$$

where  $\epsilon_0 = 1.1 \cdot 10^{-12} \text{ Vm/C}$  is the permittivity, and  $\eta$  is a constant of order one describing the shape, structure, and density of the particle,  $U \approx +5\text{V}$  due to the photoelectric effect. It was Cassini's CDA that reliably identified this charge on several interplanetary dust grains for the first time (Fig. 7). The dust charge measurements were obtained by monitoring the induced charge on an assembly of four grids that are mounted in front of the impact detector. From the signal the speed and impact direction could be determined. The charge sensitivity of CDA is about  $10^{-15} \text{ C}$ , which corresponds approximately to a particle of  $6 \cdot 10^{-11} \text{ g}$  ( $\sim 1.6 \mu\text{m}$  radius) at a potential of  $+5 \text{ V}$ .

For the proposed 3-dimensional system, consisting of two CDA stages, the accuracy of the trajectory measurement of is a few degrees and the accuracy of the speed measurement a few percent at a signal-to-noise ratio of 3.

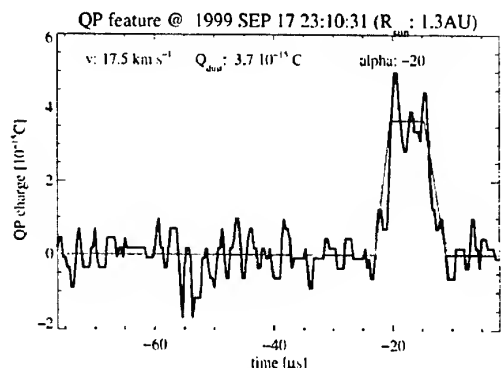


Fig. 7. Signal of a charged dust particle passing through the four charge sensor grids of Cassini CDA that are mounted in front of the impact detector. The first and fourth grid are electrically grounded whereas the two middle grids are connected to a single charge sensitive amplifier. The two middle grids are inclined by  $9^\circ$  with respect to the outer grids. A trapezoidal signal resulted when a charged dust particle passed through the grid array. The edges of the trapezoid correspond to the times when the particle passed closest to a grid. By measuring these times the speed of the particle and the angle at which the particle passed through the grid assembly could be determined.

## 5.2 Compositional measurements

A dust telescope will use techniques for the chemical analysis of ISD which have previously successfully been applied to cometary dust. It will use a time-of-flight mass spectrometer to analyze the chemical and isotopic composition of ISD. The method of in-situ mass spectrometry was demonstrated by the PUMA, and PIA instruments that took data close to the nucleus of comet 1P/Halley on board the spacecraft Vega 1, Vega 2, and Giotto respectively. The data collected by PIA/PUMA demonstrate that each individual event detected by the mass spectrometer on board of a dust observatory, will contain a wealth of scientific information. Fig. 8 shows two atomic mass spectra measured by the PUMA instrument onboard the Vega spacecraft [36]. Spectrum #53499, shows an example of a presolar cometary constituent. This particle consists of 99% C and exhibits an extreme  $^{12}\text{C}/^{13}\text{C}$  ratio of 5,000. A typical H, C, N, and O-rich particle with a nearly solar  $^{12}\text{C}/^{13}\text{C}$  ratio of 100 was recorded as

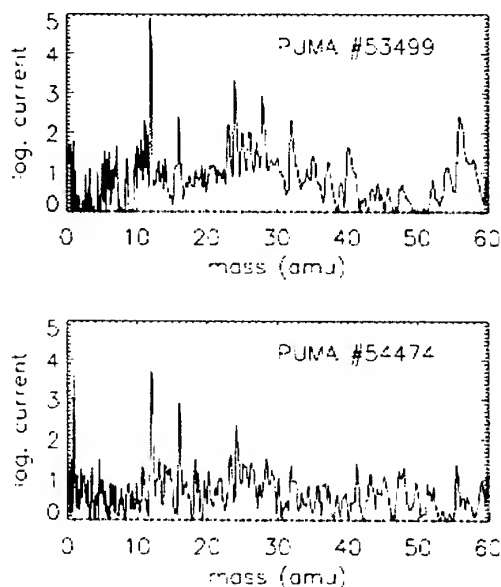


Fig. 8. Time of flight mass spectra of cometary dust particles measured by the PUMA1 experiment on board the Vega 1 spacecraft near comet 1P/Halley. The mass is given in atomic mass units (amu).

PUMA spectrum #54474. The elements of Mg, Al, Si and Fe in both spectra shows the typical composition of the rock-forming elements. The isotopic ratio of  $^{24}\text{Mg}$ : $^{25}\text{Mg}$ : $^{26}\text{Mg}$  of 8:1:1, is close to the solar value.

The statistical analysis of spectra obtained from many individual dust particles gives information about the composition of their source. In the case of Halley, it was found that the abundances of elements more refractory than O resemble solar composition and the composition of CI chondrites alike (see Fig. 9). H, C and N on the other hand, are less depleted than in CI chondrites, indicating the even more primitive (unequilibrated) character of Halley's dust than CI. For C and N, the composition of dust from comet Halley is nearly solar. The organic component of Halley dust has been inferred from coincidence analysis of molecular lines [37]. The organic component consists mainly of highly unsaturated hydrocarbon polymers containing C-H and C-N-H compounds.

A medium resolution ( $M/\Delta M$ , 20 to 50) impact mass spectrometer of  $100\text{ cm}^2$  sensitive area is part of the Cassini CDA instrument which totals a sensitive area of  $0.1\text{ m}^2$ . On its way to Saturn it has measured several impact spectra of interplanetary or interstellar dust particles and of Jupiter stream particles (Fig. 10).

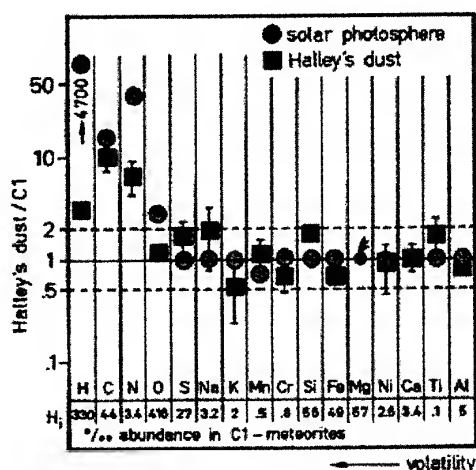


Fig. 9. Average abundance of elements (with increasing refractivity from left to right) in dust from comet 1P/Halley (squares) compared to element abundances in the solar photosphere (circles). All abundances are normalized to the elementary abundances in C1 chondrites. The error bars indicate the variability of the measured dust grains.

### 5.3 Dust Accelerators

A prerequisite for the development of advanced space dust detectors that will be employed in a dust telescope is the availability of appropriate simulation techniques. In order to simulate impact and collision phenomena in space, it is necessary to have accelerators that provide projectiles in the speed range at and above 10 km/s [38]. The work horse of accelerators for millimeter and bigger projectiles is the light gas gun. However, light gas guns operate economically only up to speeds of about 7 km/s and the blast problem for experiments requiring high vacuum is not solved. But on the other side a wide range of projectile materials can be accelerated by this method.

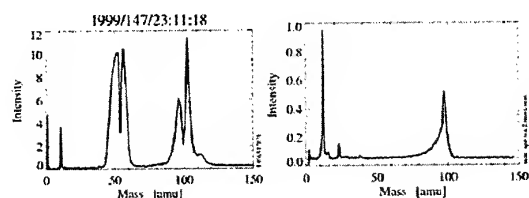


Fig. 10. Impact mass spectra obtained by Cassini's CDA instrument en route to Saturn. The left spectrum was obtained at about 1 AU distance when the interstellar dust flux was within the field-of-view of the instrument. The right spectrum was obtained when Cassini was within 1 AU from Jupiter and CDA pointed towards the planet.

For smaller (0.1-mm-sized) projectiles the Plasma Drag Gun has been developed by Igenbergs and Kucera [39]. In this gun an electric discharge accelerates a plasma to speeds of several 10 km/s. 100 micron-sized dust grains are accelerated by plasma drag. Projectile speeds of up to, 20 km/s can be reached. Because of the enormous thermal stress during the interaction with the plasma only transparent glass beads (glass efficiently radiates excess heat away) can be successfully accelerated and used for dust detector calibrations [40].

Micron-sized and smaller particles are accelerated by electrostatic accelerators that were developed by [41] Joe Friichtenicht (see also [38]). Voltages of several MV are obtained by van-de-Graaff generators. In an electrostatic dust accelerator the ion source is replaced by a dust source in which dust is electrically charged. In a 2 MV accelerator micron-sized iron particles reach speeds of 12 km/s, and 0.1 micron-sized particles reach speeds of 35 km/s. Speeds as high as 70 km/s have been observed for very small grains. Because of the charging process only conducting particles can be accelerated. Up to now, particles consisting of iron, carbon, aluminum, and metallic coated glass and plastic spheres have been used in these accelerators.

Another type of an electrostatic dust accelerator was developed by Vedder [42]. It used a quadrupole trap to charge dust particles by an ion beam. The particles were accelerated by a multiple stage linear accelerator. However, a range of non-conducting projectile materials like aluminum oxide, quartz, kaolin, soda-lime glass, and polystyrene were accelerated [43].

### 6. CONCLUSIONS

A dust observatory mission provides the next logical step to a full-fledged galactic dust analysis and sample return program. It implements the following large improvements over Stardust: greatly improved separation of interstellar from interplanetary dust; a much larger sensitive area; dramatically improved directionality measurements; speed and charge measurements; much wider mass range; a more accessible orbit and small (<10 km/s) capture velocities for follow-up sample return missions. The presence of ISD in Earth's vicinity gives us the opportunity to obtain information about stellar evolution processes in our galaxy that is otherwise inaccessible with today's technology.

A dust observatory near Earth shall characterize interstellar and interplanetary dust in-situ, in order to provide crucial information not achievable with remote astronomical methods. Galactic interstellar dust

constitutes the solid phase of matter from which stars and planetary systems form. Cometary and asteroidal material are remainders from the early stages of our solar system. Thus, studies of interstellar, cometary and asteroidal dust by means of a dust observatory in Earth orbit will provide insights into the physical conditions during planetary system formation. Their genetic connection is highly important for planetary science and astrophysics alike.

The dust observatory mission provides major advancements in cosmic dust research:

- Analysis of the chemical and isotopic composition of cosmic dust grains
- Characterization of the interstellar dust flow through the planetary system
- Measurement of the size distribution of interstellar dust
- Analysis of interplanetary dust of cometary and asteroidal origin

The science payload is a dust telescope consisting of instruments that use various dust detection techniques (having heritage from instruments on Giotto, VeGa, Cassini, Stardust, Rosetta and other missions). They are optimized for 1) large area impact detection and trajectory analysis of micron sized and larger dust grains, 2) determination of physical properties of submicron-sized grains, like flux, mass, speed, electrical charge, and coarse chemical composition, and 3) high resolution chemical analysis of cosmic dust. Previous measurements at Halley's comet have shown that the heavy element and isotopic composition of dust grains can be measured. A plasma monitor supports the dust charge measurements. The viewing directions of all dust instruments shall be co-aligned with narrow fields of view. About 1000 grains are expected to be recorded by this payload every year, with 100 or more providing high resolution mass spectra.

## 7. REFERENCES

- [1] Mathis, J.S., Dust Models with Tight Abundance Constraints. *Astrophysical Journal*, 472, 643, 1996.
- [2] Li, A., and Greenberg, J. M., A unified model of interstellar dust. *Astronomy and Astrophysics*, 323, 566-584, 1997.
- [3] Tuffs, R. J., et al., Spectrophotometry of Dust and Gas in Cassiopeia and the Cygnus Loop. in: The first ISO workshop on Analytical Spectroscopy. ESA SP, no. 419, 177-187, 1997.
- [4] Whittet, D. C. B., The Composition of Dust in Stellar Ejects. Page 455 of: *Interstellar Dust. Proceedings of the IAU Colloquium*, no. 135, 1989.
- [5] Jones, A.P., et al., Grain destruction in shocks in the interstellar medium. *Astrophysical Journal*, 433, 797-810, 1994.
- [6] Greenberg, J. M., et al., Approaching the Interstellar Grain Organic Refractory Component. *Astrophysical Journal Letters*, 455, L177, 1995.
- [7] Dorschner, J., and Henning, T., Dust metamorphosis in the galaxy. *The Astron. Astrophs. Rev.*, 6, 271-333, 1995.
- [8] Frisch, P. C., The Local Bubble, Local Fluff, and Heliosphere, *Lecture Notes in Physics*, vol. 506. Springer, Berlin, 269-278, 1998.
- [9] Zinner, E., Stellar Nucleosynthesis and the Isotopic Composition of Presolar Grains from Primitive Meteorites. *Annual Review of Earth and Planetary Sciences*, 26, 147-188, 1998.
- [10] Bradley, J. P., et al., An Infrared Spectral Match Between GEMS and Interstellar Grains. *Science*, 285, 1716-1718, 1999.
- [11] Bradley, J. P., Chemically Anomalous Preaccretionally Irradiated Grains in Interplanetary Dust from Comets. *Science*, 265, 925, 1994.
- [12] Tielens, A. G. G. M., Deuterium and interstellar chemical processes. in: Bernatowicz, T. J., and Zinner, E. (eds), *Astrophysical implications of the laboratory study of presolar materials*, vol. CP402. New York: Amer. Inst. Physics, 523-544, 1997.
- [13] Messenger, S., and Walker, R. M., Evidence for molecular cloud material in meteorites and interplanetary dust. in: Bernatowicz, T. J., and Zinner, E. (eds), *Astrophysical implications of the laboratory study of presolar materials*, vol. CP402. New York: Amer. Inst. Physics, 523-544, 1997.
- [14] Grün, E., et al., Discovery of jovian dust streams and interstellar grains by the Ulysses spacecraft. *Nature*, 362, 428-430, 1993.
- [15] Grün, E., et al., Interstellar Dust in the Heliosphere. *Astronomy and Astrophysics*, 286, 915-924, 1994.

- [16] Baguhl, M. et al., The flux of interstellar dust observed by Ulysses and Galileo. *Space Science Reviews*, 72, 471-476, 1995.
- [17] Brownlee, D. E., et al., The STARDUST Mission: Returning Comet Samples to Earth. *Meteoritics and Planetary Science*, 32, A22, 1997.
- [18] Landgraf, M., et al., Prediction of the In-Situ Dust Measurements of the Stardust mission to Comet 81P/Wild 2. *Planetary and Space Science*, 47, 1029-1050, 1999.
- [19] Hörz, F., et al., ODC: Aerogel Particle Capture During 18 Months Exposure on MIR. Page 1773 of: *Proceedings of the 30th Lunar and Planetary Science Conference*, vol. 29, 1998.
- [20] Svedhem, H., et al., Detection of Possible Interstellar Particles by the HITEN Spacecraft. in: *Physics, Chemistry, and Dynamics of Interplanetary Dust*. ASP Conference Series, no. 104., 27-30, 1996.
- [21] Grün, E., et al., South-North and Radial Traverses Through the Zodiacal Cloud. *Icarus*, 129, 270-289, 1997.
- [22] Baggaley, W. J., AMOR Radar Measurements of Interstellar Meteoroids. *Journal of Geophysical Research*. 10353-10362, 2000.
- [23] Divine, N., Five populations of interplanetary meteoroids. *Journal Geophys. Res.*, 98, 17029-17048, 1993.
- [24] Grün, E. et al., Techniques for Galactic Dust Measurements in the Heliosphere, *Journal of Geophysical Research*, 105, 10403-10410, 2000.
- [25] Frisch, P. C., et al., Dust in the Local Interstellar Wind. *Astrophysical Journal*, 525, 492- 516, 1999.
- [26] Witte, M., et al., Recent Results on the Parameters of Interstellar Helium from the Ulysses/GAS Experiment. in: von Steiger, R., Lallement, R., and Lee, M. A. (eds), *The Heliosphere in the Local Interstellar Medium*. *Space Science Reviews*, vol. 78. Kluwer Academic Publishers, 289-296, 1996.
- [27] Dwek, E., The Evolution of the Elemental Abundances in the Gas and Dust Phases of the Galaxy. *Astrophysical Journal*, 501(July), 643, 1998.
- [28] Tielens, A. G. G. M., Interstellar Depletions and the Life Cycle of Interstellar Dust. *Astrophysical Journal*, 499, 267, 1998.
- [29] Lagage, P. O., et al., Dust formation in the Cassiopeia A supernova. *Astronomy and Astrophysics*, 315, L273-L276, 1996.
- [30] Edvardsson, B., et al., The Chemical Evolution of the Galactic Disk - Part One - Analysis and Results. *Astronomy and Astrophysics*, 275, 101, 1993.
- [31] Landgraf, M., Modeling the Motion and Distribution of Interstellar Dust inside the Heliosphere. *Journal of Geophysical Research*. 105,10303-10316, 2000.
- [32] Landgraf, M., et al., Deflection of the Local Interstellar Dust Flow by Solar Radiation Pressure. *Science*, 286, 2319- 2322, 2000.
- [33] Landgraf, M., et al., Aspects of the Mass Distribution of Interstellar Dust Grains in the Solar System from In-Situ Measurements. *Journal of Geophysical Research*. 105, 10343- 10352, 2000.
- [34] Grün, E., and Landgraf, M., Collisional Consequences of Big Interstellar Grains. *Journal of Geophysical Research*. 105, 10,291-10,297, 2000.
- [35] Grün, E., et al., Collisional balance of the meteoritic complex. *Icarus*, 62, 244-272, 1985.
- [36] Jeßberger, E. K., and Kissel, J., Chemical properties of cometary dust and a note on carbon isotopes. In: *Comets in the post-Halley era*. Kluwer. 1075-1092, 1991.
- [37] Kissel, J., and Krüger, F. R., The organic component in dust from comet Halley as measured by the PUMA mass spectrometer onboard Vega 1. *Nature*, 326, 755-760, 1987.
- [38] Auer S., Instrumentation, in "Interplanetary Dust", E. Grün, B.A.S. Gustafson, S.F. Dermott, and H.Fechtig, eds., Springer, Berlin, 385-444, 2001.
- [39] Igenbergs E., Kuczera H, Micrometeoroid and Dust Simulation, *Proc of the Comet Halley Micrometeoroid Hazard Workshop*, ESTEC, 18-19 April, 1979, ESA SP-153, 109-114, 1979.
- [40] Göller et al., Calibration of the DIDSY-IPM dust detector and application to other impact ionization detectors on board the P/Halley probes, *Astron. Astrophys.* 187, 693-698, 1987.
- [41] Friichtenicht, J. F., Two-million-volt electrostatic accelerator for hypervelocity research, *Rev Sci. Instr.* 33:209-212, 1962.

[42] Vedder J.F., Charging and acceleration of microparticles, Rev. Sci. Instrum., 34, 1175-1183, 1963.

[43] Dalmann B.K. et al., The Ion Composition of the Plasma Produced by Impact of Fast Particles. Planet. Space Sci., 25, 135-147, 1977.

# MAPPING THE INTERSTELLAR DUST FLOW INTO THE SOLAR SYSTEM

W. J. Baggaley and D. P. Galligan

*Department of Physics and Astronomy, University of Canterbury, Christchurch, New Zealand*

## ABSTRACT

The Advanced Meteor Orbit Radar facility (AMOR) monitors the dynamical properties of meteoroids of sizes down to about  $40\ \mu\text{m}$ . The orbital data set secured to date contains about  $10^6$  orbits. The population of inner Solar System meteoroids sampled contains a significant proportion of particles that are moving in unbound solar orbits. Maps the far-sun inflow directions of this extra-Solar System population show the presence of both a broad interstellar inflow and discrete sources.

Key words: meteor radar; interstellar dust.

## 1. INTRODUCTION

The Solar System is immersed in a low density region of diffuse dust and gas – the local interstellar cloud (LIC). Indirect information about the dust can be obtained using methods that rely on various screening effects caused by the dust on the radiation from distant stars. Sources of dust seeding the interstellar medium are expected to be red giants, Post AGB stars, dust-rich carbon stars and supernovae. Interstellar particles (ISPs) of size  $< 1\ \mu\text{m}$  have been detected by the Pioneer, Galileo and Ulysses spacecraft ([1]) while much larger grains on extra-solar orbits have been measured by radar ([2]). In both types of observations only rather limited information could be gained about the dust particle inflow direction into the Solar System. The question of the presence of extra-solar grains in the Solar System has been a controversial topic and for many decades attempts to provide unequivocal evidence of ISPs in interplanetary space by meteor observations have been unable to provide a definitive solution (e.g. [3].)

Here we report measurements of the upstream directions and far-Sun speeds of radar-detected ISPs. These are the first directional data for a large population of particles. There are two separate types of signature for confirming ISPs – geometry and energy.

## 2. RADAR DATA

The AMOR facility ([4], [5]) is a continuously operating multi-site system measuring the heliocentric orbits of earth-impacting meteoroids. The detection limit of the particles sampled corresponds to radii of  $40\ \mu\text{m}$  (mass  $> 3 \times 10^{-7}\ \text{gm}$ ). The uncertainties for individual orbits are  $\sim 2^\circ$  in angular elements  $i$  and  $\omega$  and  $\sim 5\%$  in size elements  $a$ ,  $q$ , and  $e$ . The system has been in operation from 1990 to date securing dynamical data for  $\sim 10^6$  inner Solar System particles. Astronomical calibration of the archived orbits is secured via correlations with the orbital parameters available from other ground-based multi-site techniques – photographic, TV, image-intensifier video.

## 3. EXTRA-SOLAR ORBITS

Unbound ISPs have heliocentric speeds at Earth impact that are greater than the parabolic limit at  $\approx 1$  AU of  $41.8$  to  $42.5\ \text{km s}^{-1}$  (the value depending on the Earth's longitude and hence date). Such particles can be recognised by their hyperbolic orbit eccentricity values greater than unity. It is recognised that a small proportion of dust may possess hyperbolic properties as a result of Solar System internal process such as ejection from near-parabolic comets or as a consequence of being perturbed into such an orbit from inter-particle collisions or near-planetary encounters. Radiation pressure on micron-sized dust can lead to a solar outflow ( $\beta$  meteoroids).

For truly extra-Solar System material the up-stream inflow direction would be expected to reflect the source direction. For a near-parabolic closed orbit we identify the inflow direction as coincident with the orbital apse line so that the far-Sun approach direction is situated at the heliocentric longitude and latitude of aphelion. For a particle on a hyperbolic orbit the corresponding direction is identified as the asymptote to the hyperbola – a line which deviates from the apse line by an angle which depends on the eccentricity. In this work the far-Sun approach directions are determined for a large sample of Earth-impacting dust to map their locations in space. The particles measured by radar here are insignificantly

affected by non-gravitational forces like solar-wind interaction, solar radiation pressure or deviation due to Lorenz forces: Keplerian dynamics are well sufficient to describe the fate of radar-detected meteoroids.

#### 4. INFLOW DIRECTIONS

To permit a reliable description of any ISPs it is necessary to consider the uncertainties in the measured near-parabolic orbits. Indeed it is the difficulty in assigning a confident value to the heliocentric speed in the presence of measurement uncertainties that has hampered any firm recognition of extra-solar particles in many surveys ([3]). For a heliocentric speed  $V_h \approx 42 \text{ km s}^{-1}$  the corresponding atmospheric speed depends on the elongation from the earth's apex and is in the range  $\sim 50$  to  $73 \text{ km s}^{-1}$ . The corresponding uncertainty is  $\sim 3 \text{ km s}^{-1}$ . Therefore meteoroid orbital data here are considered in two velocity bins: a narrow energy bin  $38 < V_h < 39$  (being  $1\sigma <$  parabolic limit) contrasted with  $45 < V_h < 50$  (lower bound  $1\sigma >$  parabolic limit). The higher velocity bin will be expected to contain a proportion of truly bound orbits and the lower one a proportion of unbound. For all orbits the upstream direction as defined above can be calculated for each. Plots can be made of the heliocentric longitude and latitude of the far-sun directions (by analogy with meteor directions as seen by an earth-bound observer - 'the solar apparent radiant'). The total number of orbits to probe this question of extra-solar sources is much larger ( $> 10^5$ ) than has been available from previous surveys. The results of such plots of the angular density of radiants for an observer situated on the Sun have a preponderance of sources in the ecliptic plane with some high latitude structure.

By taking the ratio of the angular densities of the two plots sources of un-bound particles can be sensed. This mapping procedure is a sensitive indicator of the presence of ISPs. There are two significant aspects ([6]): there is a general inflow of extra-solar particles from southern ecliptic latitudes and also the presence of discrete streams, the dominant of which are at heliocentric ecliptic coordinates  $(\lambda, \beta)$   $260^\circ$ ,  $-57^\circ$  and  $70^\circ$ ,  $+45^\circ$ . The uncertainties in the positions of these discrete radiants is  $\sim 5^\circ$  and the  $1\sigma$  dispersion  $\sim 15^\circ$ . These localized features are present all year: the former is predominant and has greatest influx in the period December through April. This characteristic is in contrast to interplanetary cometary streams which produce earth-detected meteoroids for a limited period ( $\sim$  several days) as the earth intersects the stream of dust.

#### 5. DYNAMICAL MODEL

To interpret the characteristics of such a discrete feature, a model ([7]) has been developed to examine the annual variation of the heliocentric orbital

elements of meteoroids that would be produced by earth-impacting particles due to a collinear stream of ISPs flowing into the Solar System. The dust particles of such a stream (of size comparable or larger than the Solar System) can impact the Earth on two possible trajectories. Thus with  $\beta$  negative (the latitude of the dominant source examined here) impacts can occur at the particle's ascending node (termed here type 1 collisions) so that the observed radiants are south of the ecliptic or at the particle's descending node (type 2 collisions) impacting with radiants north of the ecliptic. Since ISPs follow hyperbolic orbits it is possible for only one node to exist. The time variations in the heliocentric orbital elements registered at the Earth have a seasonal modulation, the characteristics of which allow the fixing (in addition to the mapping signature above) of the far-Sun inflow direction and the far-Sun inflow speed  $V_\infty$ . For example for  $\beta$  negative and type 1 geometry the observed inclination  $i$  will equal  $90^\circ$  if the heliocentric longitudes of the earth and source  $D = (\lambda_E - \lambda)$  differ by  $0^\circ$  or  $180^\circ$ ;  $i = \beta$  for  $D = 90^\circ$  and  $i = 180 - \beta$  for  $D = 270^\circ$ . Similar seasonal modulations occur in the other elements - perihelion distance  $q$  and argument of ascending node  $\omega$ . Fig. 1 shows the modeled behaviour of the elements as a function of  $D$  for  $V_\infty = 10 \text{ km s}^{-1}$  and a range of values of ecliptic latitude  $\beta$ .

In addition to these geometrical effects, the geocentric velocity  $V_g$  and flux will undergo similar modulations.  $V_g$  will be greatest when  $D = 270^\circ$  and least when  $D = 90^\circ$  while the detected flux will have a maximum when  $D$  lies between  $180^\circ$  and  $270^\circ$  (the exact value depending on  $V_\infty$ ), the upper limit occurring when  $V_g$  maximizes and the lower limit corresponding to the maximum dust concentration on the ecliptic plane caused by the gravitational focusing of the ISPs ([8]). Clearly, such a behaviour is quite unlike that expected of a closed Solar System dust stream.

#### 6. THE OBSERVED ORBITAL CHARACTERISTICS

The seasonal changes of the orbital distributions (in  $i, \omega, q, V_g$  and flux) of all meteoroids (archived data 1996-1999) having heliocentric upstream directions within  $15^\circ$  of the major source at  $(\lambda, \beta)$   $260^\circ$ ,  $-57^\circ$  were examined. All elements show a seasonal modulation (see [6]) in agreement with the model and behaving in a way quite distinct from that due to an interplanetary cometary or asteroid stream. This is strong evidence for the presence of a collinear stream influx into the Solar System.

#### 7. ENERGY DISTRIBUTION

Following the early surveys carried out on determining the velocity characteristics of the circum-solar

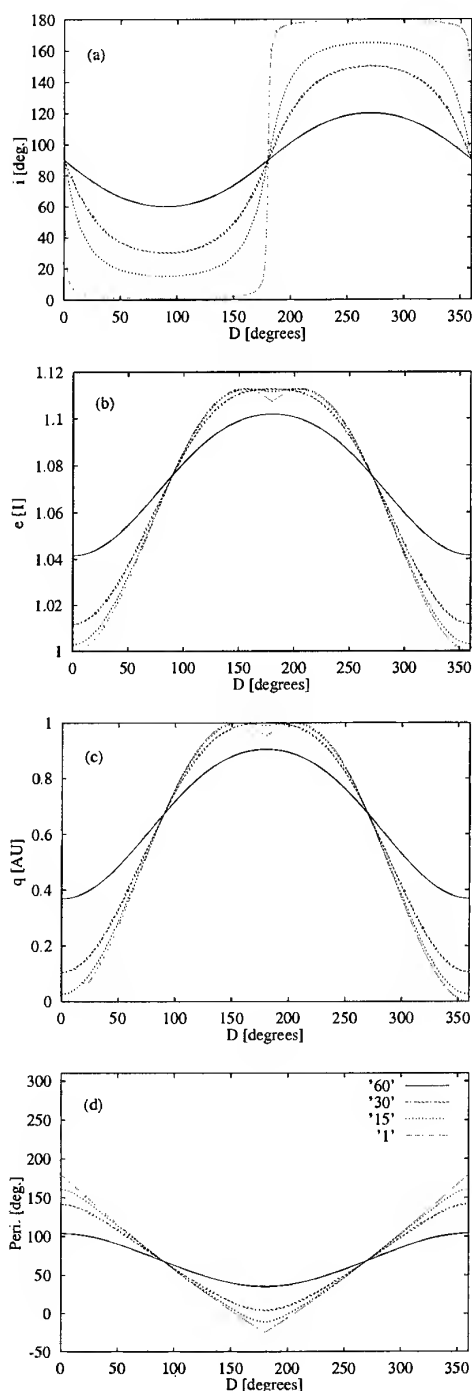


Figure 1. The seasonal variations in the orbital elements (a)  $i$ , (b)  $e$ , (c)  $q$ , and (d)  $\omega$  for  $V_{\infty} = 10 \text{ km s}^{-1}$  as a function of  $D = (\lambda_E - \lambda)$  with  $\lambda_E$  and  $\lambda$  the heliocentric longitudes of the Earth and source respectively. For illustration, source latitudes of  $\beta = -60^\circ, -30^\circ, -15^\circ, -1^\circ$  are displayed.

dust – e.g. the visual work using rocking mirror cameras in the 1930s – one component of evidence for the presence of extra-solar dust in the inner Solar System has hinged on the identification of a real particle population having speeds  $V_h > 42 \text{ km s}^{-1}$ . The presence of some such reported hyperbolic populations have been attributed to uncertainties in orbit measurement. In this paper we examined the heliocentric speed distributions for all meteoroids outside the earth's orbit ( $V_h > 30 \text{ km s}^{-1}$ ) for two populations: one group having source directions within  $10^\circ$  of the ecliptic (and therefore essentially of Solar System origin); the other within  $15^\circ$  of the discrete feature (coordinates  $(\lambda, \beta) 260^\circ, -57^\circ$ ). The ecliptic population beyond 1 AU contains 10% of orbits  $>$  the parabolic limit – a value consistent with the orbital mis-measurement as expected from the system uncertainty. In contrast, for the discrete source meteoroids, 40% exceed the open-orbit limit and have a clear peak at  $46 \text{ km s}^{-1}$ . This is important because the presence of a clear enhancement in the velocity distribution – rather than simply a distribution fall-off – is strong evidence for the presence of a distinct population of particles.

## 8. UPSTREAMING DIRECTION

Allowing for the solar gravitational acceleration, an ISP speed at 1 AU of  $\sim 46 \text{ km s}^{-1}$  corresponds to an asymptotic heliocentric inflow speed  $V_{\infty}$  of  $\sim 13 \text{ km s}^{-1}$ . The observed angular dispersion of  $\sim 15^\circ$  suggests a near-collinear particle stream. The collision distance for  $40 \mu\text{m}$  particles interacting with the ambient interstellar dust is  $< 10^3 \text{ pc}$  ([9]) placing an upper limit on the source distance. In attempting to identify any interstellar source with an observed discrete feature two approaches can be followed. One route is to work with the relative space speeds of the sun and any hypothetical (stellar) source – such stellar motions relative to the Sun are available directly from the Hipparchus catalogue and the more recent U.S. Naval Observatory data base: such a route would involve the individual comparisons many Sun-star pairs. Alternatively, a measure of the space motion of any dust stream with respect to the Local Standard of Rest (LSR) provides a useful picture of the dynamics of such dust flow in the solar neighbourhood so yielding the dust motion in relation to features such as the Local Interstellar Bubble. Using the latter method and a solar peculiar motion of  $16.5 \text{ km s}^{-1}$  with apex galactic  $l = 53^\circ, b = +25^\circ$  the ISP stream motion with respect to the LSR is upstream  $l = 263^\circ, b = -28^\circ$  with  $V_{LSR} = 25 \text{ km s}^{-1}$ .

To seek a corresponding source for such a dust flow it is necessary to consider stellar dynamics: during the dust travel time both the source and sun will have moved thus complicating the search for any association. The observed (LSR) flow direction at the present epoch depends on the dust ejection speed from the star, the star's space speed and space location. However we note the close approximation

(within  $\sim 5^\circ$ ) of the LSR upstream direction to that of the present position of the dust debris main sequence A5 star  $\beta$  Pictoris. This well studied star distance 19.5 pc possesses an edge-on planetary disk and with a small space speed has moved little ( $\sim 3^\circ$ ) over the dust travel time of  $\sim 0.8$  My.

## 9. CONCLUSIONS

Radar meteoroid-orbit data collected over several years in the AMOR programme containing a very large sample ( $> 10^5$  orbits) has produced unequivocal evidence for the presence of a near-collinear stream of interstellar particles crossing the Solar System together with a general southern ecliptic inflow. The geometrical behaviour and the energy characteristics of the particles of the discrete feature point strongly to the extra-solar nature of this localized stream. The source direction matches that of a dust-debris star in the solar neighbourhood known to be surrounded by and ejecting dust. Models for the mechanism of the high-speed ejection of dust from such systems has recently been considered ([10]) while cataclysmic events have been modeled to produce a non-equilibrium material ejection process ([11]).

## ACKNOWLEDGMENTS

This work was supported by the New Zealand Marsden Fund UoC 911-2000.

## REFERENCES

1. Taylor A. D., Baggaley W. J., Steel D. I., 1996, Discovery of interstellar dust entering the Earth's atmosphere. *Nature* 380, 323.
2. Grün E., et al., 1993, Discovery of Jovian dust streams and interstellar grains by the *Ulysses* spacecraft. *Nature* 362, 428.
3. Hawkes R., Close T., Woodworth S., 1999, In: *Meteoroids 1998*, eds. W. J. Baggaley and V. Porubčan, Inst. Slovak Acad. Sci., Bratislava, p. 257.
4. Baggaley W. J., Bennett R. G. T., Steel D. I. and Taylor A. D., 1994, The Advanced Meteor Orbit Radar: AMOR. *Q. J. Roy. Astr. Soc.* 35, 293-320.
5. Baggaley W. J., Marsh S. H., Bennett R. G. T., Galligan D. P. 2001, Features of the enhanced AMOR facility: the Advanced Meteor Orbit Radar. *Proceedings Meteoroids 2001 Conference*. (ESA SP-495)
6. Baggaley W. J., 2000, Advanced Meteor Orbit Radar observations of interstellar meteoroids. *J. Geophys. Res.* 105, 10, 353.
7. Baggaley W. J., Neslušan L., 2001, A model of the heliocentric orbits of a stream of Earth-impacting interstellar meteoroids. *A & A* (submitted).
8. Neslušan L., Baggaley W. J., 2001, (in preparation).
9. Grün E., Landgraf M., 2000, Collisional consequences of big interstellar grains. *J. Geophys. Res.* 104, 10291.
10. Krivova N., 2001, (unpublished).
11. Larwood J. D., Kalas P. G., 2001, Close stellar encounters with planetesimal discs: the dynamics of asymmetry in the  $\beta$  Pictoris system. *Mon. Not. R. Astron. Soc.* 323, 402.

# EXPECTED DISTRIBUTION OF INTERSTELLAR METEOROIDS IN THE VICINITY OF THE EARTH'S ORBIT.

A.R. Bagautdinova<sup>(1)</sup>, O.I. Belkovich<sup>(2)</sup>

<sup>(1)</sup> Branch of Kazan State University in Zelenodolsk, Saidashego st., 4, Zelenodolsk, Tatarstan, Russia, Email: albina@green.kcn.ru

<sup>(2)</sup> Branch of Kazan State University in Zelenodolsk, Saidashego st., 4, Zelenodolsk, Tatarstan, Russia, Email: oleg@green.kcn.ru

## ABSTRACT

Hypothesis that the sources of interstellar particles are planet systems of late class stars is discussed. It was supposed that the planet systems have something like the Oort cloud in our planet system on the boundary the Sun gravitation field. Some particles leave a cloud due to perturbations of nearest stars. The most probable leaving velocity relative to the parent star is the minimal one. So one can expect the velocity distribution of interstellar particles relative the local centroid of stars is similar to the velocity distribution of stars. The interstellar meteoroids flux is distorted by gravitational field of the Sun and its moving relative meteoroid cloud. The transformation of interstellar meteoroid flux density in the gravitational field of the Sun lead to the appearance of some areas at the celestial sphere with high concentrations of their radiant. It is the coincidence of the observed and the calculated radiant concentrations of interstellar meteoroids at the celestial sphere.

## 1. INTRODUCTION

The interest to interstellar meteoroids is growing from year to year. Baggaley [1] has analyzed some orbital characteristics of interstellar particles and pointed out to some radiant concentrations at the celestial sphere. But the problem what is the source of interstellar meteoroids does not solved yet.

One can expect that meteoroid flux reduction with the distance off a source must be comparable with the reduction of a starlight so if a source ore even several sources are placed near some stars the probability of an interstellar particle encounter with the Earth is extremely low.

We have put forward the hypothesis that the sources of interstellar particles are planet systems of late class stars. We have supposed that the planet systems have something like the Oort cloud in our planet system on the boundary the Sun gravitation field. Some particles leave a cloud due to perturbations of nearest stars. The most probable leaving velocity relative to the parent star is the minimal one. So one can expect the velocity dis-

tribution of interstellar particles relative the local centroid of stars is similar to the velocity distribution of stars.

We observe interstellar meteoroids in the vicinity of the Earth's orbit where the interstellar meteoroids flux is distorted by gravitational field of the Sun and its moving relative interstellar meteoroid cloud. One can expect the transformation of interstellar meteoroid flux density in the gravitational field of the Sun lead to the appearance of some areas at the celestial sphere with high concentrations of their radiant.

## 2. DISTRIBUTION OF INTERSTELLAR PARTICLE VELOCITIES RELATIVE TO THE SUN

The velocity distribution of the interstellar particles relative the local centroid of stars is similar to the Maxwell's distribution. That means the distribution projections of velocities at any direction is the normal distribution. To find parameters of this distribution the Strasburg's catalogue of radial velocities of stars has been used. Stars of classes F and G were selected. The method of straight line diagram has been used to minimized action of spherical component of stars. (Figs.1-2)

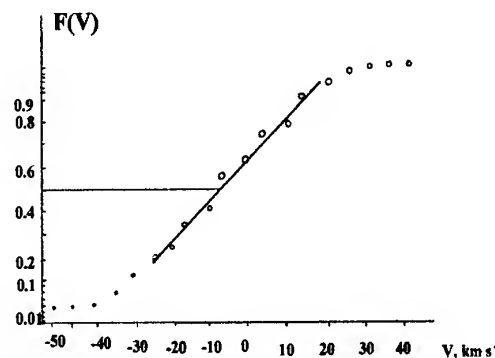


Fig. 1. The method of straight line diagram to minimized spherical component stars action

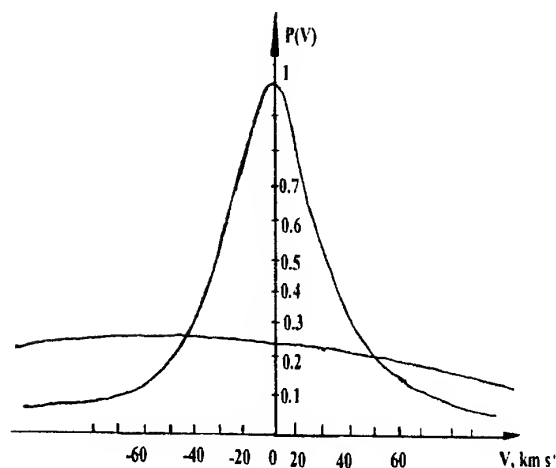


Fig. 2. Two components velocity distribution of stars.

Whole of the celestial sphere has been divided by areas  $10^\circ \times 10^\circ$ . Mean value of the radial star velocity  $V$  and the standard deviation  $\sigma(V)$  were found for every area. Then the coordinates of the Sun's apex, velocity of the Sun relative to the local centroid of stars of F and G classes and the mean value of  $\sigma(V)$  has been found using this data. (Table 1)

Tab. 1. Coordinates of apex of the Sun, Sun's velocity and standard deviation  $\sigma(V)$  of interstellar meteoroid distribution.

Galactic coordinates of apex	$l=58.30^\circ$ $b=19.19^\circ$
Heliocentric Coordinates of apex	$\lambda=334.78^\circ$ $\beta=78.43^\circ$
Sun's velocities $V$	$21.01 \text{ km s}^{-1}$
Standard deviation $\sigma(V)$	$20.04 \text{ km s}^{-1}$

### 3. TRANSFORMATION OF METEOROID FLUX DENSITY

The Sun's motion relative to the interstellar meteoroid cloud and gravitational field of the Sun lead to the appearance of meteoroid flux density irregularities on the celestial sphere. Comparison of calculated irregularities with observed ones would give a chance to accept or reject our hypothesis on the origins of interstellar particles.

The transformation of the meteoroid flux density from the galactic frame of references to heliocentric one has been made by the next formula [1]:

$$\gamma = \frac{Q_h}{Q_g} = \frac{V_h^3}{V_g^3}, \quad (1)$$

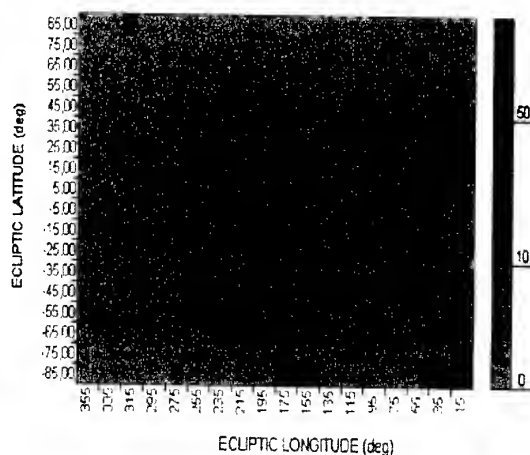


Fig. 3. Distribution of  $\gamma$ -value over the celestial sphere. March.

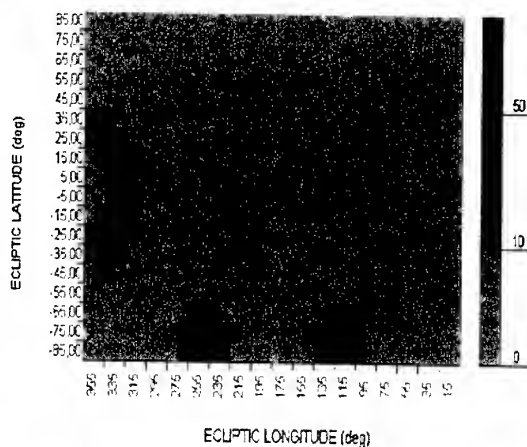


Fig. 4. Distribution of  $\gamma$ -value over the celestial sphere. June.

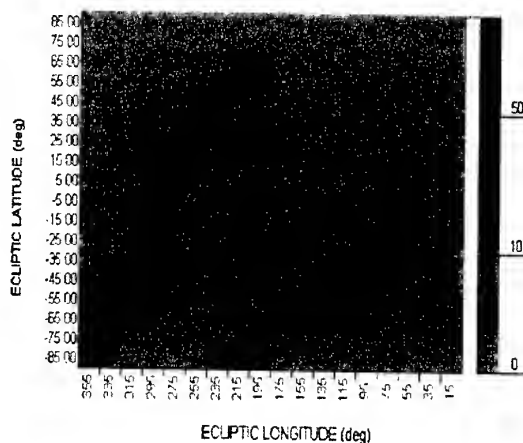


Fig. 5. Distribution of  $\gamma$ -value over the celestial sphere. August.

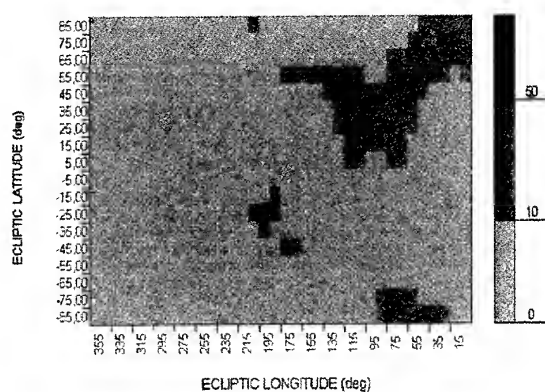


Fig. 6. Distribution of  $\gamma$ -value over the celestial sphere. January.

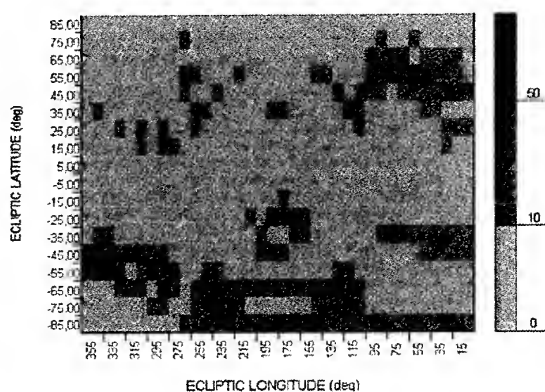


Fig. 7. Distribution of  $\gamma$ -value over the celestial sphere. Averaged for the year.

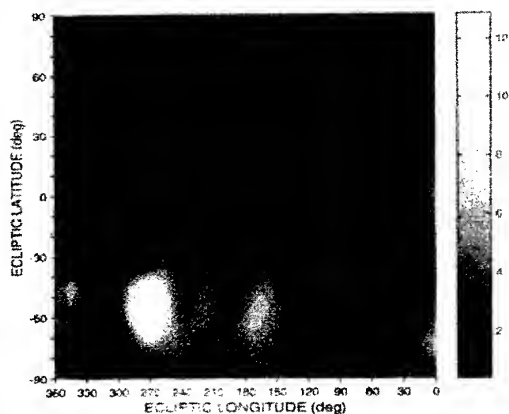


Fig. 8. The ratio in angular densities of the heliocentric source directions. Ratio of  $V_h \geq 44 \text{ km s}^{-1}$  to  $38 < V_h < 39$ .

where  $Q_h$  and  $Q_g$ ,  $V_h$  and  $V_g$  are the flux densities and meteoroids velocities in heliocentric and galactic coordinates respectively. Again whole of the celestial sphere has been divided by areas  $10^0 \times 10^0$ . The value of  $\gamma$  has been calculated by meteoroid velocity integration for every area at the celestial sphere and for every month. Distributions of  $\gamma$ -values for some months are shown in Figs. 3-6.

The distribution of  $\gamma$ -values averaged for the year is shown in Fig. 7. Observed results [1] are given in Fig. 8.

One can see the rather good coincidence of the observed and the calculated radiant concentrations of interstellar meteoroids at the celestial sphere.

## 2. CONCLUSION

The coincidence of the observed distribution of interstellar meteoroid radiant density over the celestial sphere with calculated one confirms the hypothesis of interstellar meteoroid origin in the late class star systems.

## 3. REFERENCE

1. Baggaley W.J., *The Interstellar Particle Component measured by AMOR*, Meteoroids 1998, Astron. Inst., Slovak Acad. Sci., Bratislava, 265-273, 1999.
2. Belkovich O.I., *Astronomical selection of meteoric observations and methods of its calculated*, Solar System Res., Vol. 17, No. 2., 1985.

## Possibility of Meteor Path Determination by Records in Ancient Chinese Local Gazetteers

Nagatoshi NOGAMI

*Sumitomo Chemical Co.,LTD 3-1-98 Kasugade-naka Konohana-ku Osaka , 554-8558 Japan*  
*e-mail:nogamin@sumitomo-chem.co.jp*

### ABSTRACT

It is well known that many meteor observations were described ancient Chinese historical records.

Especially in Ch'ing dynasty period (1644-1912), many of them in local gazetteers were recorded with event time, path direction and observation location. By precise searching these factors, possibility of meteor path determination were examined. Four probable examples in 1891, 1873, 1672 and 1661 are shown and discussed their characteristics. Only projected paths on the ground were determined by lack of height information in records.

### Collecting of the Events

Records of original text were collected from the libraries of the Documentation Center for Oriental Studies belonging to the Institute for Research in Humanities in Kyoto University and "General Compilation of Ancient Chinese Astronomical Records": Beijing Observatory, 1988.

Many meteor records were described in authorized historical books edited by every dynasties, local historical geographic books by local governments and private books. But in order to avoid rewrite error of event date which sometimes can be seen in dynasty's edited books, and to fix observation place records are collected from local gazetteers in Ch'ing dynasty.

Records of events which were on the same date and location distance less than 200km from potential meteor path were collected.

### Characteristics of Events and Discussion

Following four events' records were listed as candidates. (See Table.1) Solar longitude (2000.0), projected location of emitting point and disappearing point on the ground in longitude and latitude of each meteor are listed in Table.2. These projected location points have roughly  $\pm 20$ km error at smallest. It

comes from relation of observed places and observed meteor directions. In addition because of no observed height description in all records, no accurate path was gained as a result.

#### --Event I --

Direction were determined to locate just between two observations' place. But calculated low elevating angle of the path cause of so far distance as about 200km to the meteor from each places, possibility may be thought lower. Calculated elevating angle of emitting point is  $33^\circ$  from supposed 130km height

#### --Event II --

Path direction still have low accuracy cause of two observation sites didn't had the path between them.

And one can seem to exist time lag in these two records, "at dawn" for "From 7 to 9 a.m."

#### --Event III--

Direction is thought as mentioned cases III or III+III'. In case III path length can be thought less than 100km from considering location of three observed places. In case III+III' the path can be thought about 100km shifted to the east of case III and elongated more than 100km. Even four observation places were considered the path can be determined as located in the west of  $119^\circ\text{E}$  at most. The reason is more than 200km distance from meteor will make less chance to observe it by its low elevating angle.

#### --Event IV--

Direction can be determined as listed in Table.2. But it is difficult to determine its emitting point and disappearing point from each records because relation of observed directions and places are puzzled. It makes gained direction less accurate than expected.

### Conclusion

By examining ancient Chinese meteor records from

local gazetteers, four meteor path directions were roughly determined. But all their paths cannot be fixed accurately because of lack of their height description and relation of observed places and unclear observed meteor direction.

#### Reference

(1) "General Compilation of Ancient Chinese Astronomical Records": Beijing Observatory, 1988

**Table.1 List of the Records**

	Date	Time	Observed Direction	Location	Long.	Lat.
I	18.Jun. 1891	At night	to the north	Zhu-cheng	119°.23'E	36°.02'N
I	18.Jun. 1891	At night	in the south-west	Chang-li	119°.14'E	39°.44'N
II	12.Feb.1873	At dawn	in the north	Huang-mei	115°.53'E	30°.05'N
II	12.Feb.1873	7-9 a.m.	from the east to the north	Luo-tian	115°.20'E	30°.48'N
III	12.May1672	At dawn	from the east to the south	Wang-jiang	116°.43'E	30°.18'N
III	12.May1672	At dawn	in the east	Huai-ning	116°.39'E	30°.29'N
III	12.May1672	At dawn	from the east	Dong-liu	116°.57'E	30°.21'N
III'	12.May1672	3-5 a.m.	from the north-east to the south	Shi-dai	118°.12'E	30°.27'N
IV	2.Sept.1661	3-5 p.m.	from the west to the east	Xin-ning	111°.52'E	26°.35'N
IV	2.Sept.1661	3-5 p.m.	from the south-west to the north	Ling-ling	111°.57'E	26°.17'N
IV	2.Sept.1661	3-5 p.m.	from the south-west to the north	Heng-zhou	112°.30'E	26°.06'N

**Table.2 Factors of meteors**

	SolarL. (2000.0)	emitting point	disappearing point
I	86.9	119°.5'E 38°.0'N	117°.0'E 38°.0'N
II	323.4	116°.0'E 30°.5'N	115°.5'E 31°.5'N
III	54.3	117°.4'E 30°.7'N	117°.3'E 30°.0'N
III+III'	54.3	118°.5'E 31°.0'N	118°.3'E 29°.8'N
IV	164.1	110°.3'E 26°.0'N	110°.0'E 27°.5'N

## **Participants**

## Meteoroids 2001 Participants list

Abe, Shinsuke  
Institute of Space and Astronautical  
Science  
3-1-1 Yoshinodai,  
Sagamihara  
Kanagawa, 229-8510, Japan  
E.mail: avell@planeta.sci.isas.ac.jp

Asher, David  
Armagh Observatory  
College Hill  
Armagh BT61 9DG, UK  
E.mail: dja@star.arm.ac.uk

Baffur, Awuah Eric Ntim  
Princelay Ghana Ltd  
PO Box AE 20 Atomic Energy  
Accra, Ghana  
E.mail: nanakofi30@hotmail.com

Bagautdinova, Albina  
Zelenodolsk branch of the Kazan State  
University  
24-10, Ivan Zaikin street,  
Zelenodolsk, Tatarstan Republic, 422542,  
Russia  
E.mail: albina@green.kcn.ru,  
albagautd@estart.ru

Baggaley, Jack  
Department Physics & Astronomy  
University Canterbury  
Private Bag 4800  
Christchurch 8020. New Zealand  
E.mail: PHYS051@it.canterbury.ac.nz

Belkovich, Oleg  
Prof Oleg Belkovich  
Zelenodolsk branch of the Kazan State  
University  
5 - 1, Engelhardt Astronomical  
Observatory,  
Oktyabrsky, Zelenodolsk reg., 422526,  
Russia  
E-mail: oleg@green.kcn.ru

Bellot Rubio, Luis R.  
Instituto de Astrofisica de Canarias  
C/Via Lactea s/n, E-38200 La Laguna,  
Tenerife  
Spain  
Fax: 34 922 605 210  
E-mail: lbellot@iac.es

Borovicka, Jiri  
Ondrejov Observatory  
Astronomical Institute  
25165 Ondrejov, Czech Republic  
E.mail: borovic@asu.cas.cz

Brändström, Urban  
Swedish Institute of Space Physics  
PO Box 812  
SE-981 28 Kiruna. Sweden  
E.mail: urban.brandstrom@irf.se

Brosch, Noah  
Wise Observatory  
Tel Aviv University  
Tel Aviv 69978, Israel  
E.mail: noah@wise1.tau.ac.il

Brown, Peter  
Los Alamos National Laboratory  
EES-8 MS J577  
Los Alamos, NM 87545, USA  
E.mail: pbrown@lanl.gov

Burns, David  
EOARD  
223/231 Old marylebone Road  
London NW1 5TH  
United Kingdom  
e-mail: David.Burns@London.AF.MIL

Campbell, Margaret  
University of Western Ontario  
Department of Physics and Astronomy  
London, ON N6A 3K7, Canada  
E.mail: mdcampbe@uwo.ca

Cepkecha, Zdenek  
Astronomical Observatory  
25165 Ondrejov, Czech Republic  
E.mail: cepkecha@asu.cas.cz

Despois, Didier  
Observatoire de Bordeaux  
BP 89,  
F- 33270 Floirac, France  
E.mail: despois@observ.u-bordeaux.fr

Dikarev, Valeri  
Max-Planck-Institut fuer Kernphysik  
Saupfercheckweg 1  
Heidelberg, Germany  
E.mail: dikarev@galileo.mpi-hd.mpg.de

Drolshagen, Gerhard  
ESA/ESTEC  
Keplerlaan 1  
2201 AZ Noordwijk, The Netherlands  
E.mail: Gerhard.Drolshagen@esa.int

Drummond, Jack  
Starfire Optical Range  
Air Force Research Laboratory  
Directed Energy Directorate  
3550 Aberdeen Av SE  
Kirtland AFB, NM 87117-5776, USA  
E.mail: Jack.Drummond@kirtland.af.mil

Dyrud, Lars  
Boston University  
Center for Space Physics  
725 Commonwealth Avenue  
Boston, MA 02215, USA  
E.mail: ldyrud@bu.edu

Ekstrand, Veronica  
Kyrkogatan 12B  
SE-981 38 Kiruna, Sweden  
E.mail: 97ve@ryp.umu.se

Elford, Graham  
Department of Physics and Mathematical  
Physics  
University of Adelaide  
Adelaide, SA 5005, Australia  
E.mail: gelford@physics.adelaide.edu.au,  
Wgelford@aol.com

Elst, Erik  
Royal Observatory Uccle  
Ringlaan 3  
B-1180 Uccle, Belgium  
E.mail: ericelst@oma.be

Emel'vanenko Vacheslav  
Department of Theoretical Mechanics  
South Ural University  
Lenina 76  
Chelyabinsk 454080, Russia  
E.mail: emel@termeh.tu-chel.ac.ru

Erickson, Philip  
Phil Erickson  
Atmospheric Sciences Group  
MIT Haystack Observatory  
Off Rte, 40  
Westford, MA 01886, USA  
E.mail: pje@haystack.mit.edu

Fischer, Daniel  
Meteor Working Group Germany  
Im Kottsiepen 10  
DE-53639 Koenigswinter, Germany  
E.mail: dfischer@astro.uni-bonn.de

Foschini, Luigi  
Institute TeSRE-CNR  
Via Gobetti 101  
I-40129 Bologna, Italy  
E.mail: luifosc@tin.it

Fujiwara, Yasunori  
2-16-8 Mikanuhonmachi  
Yodogawa-ku  
Osaka 532-0005, Japan  
E.mail: DHB15312@biglobe.ne.jp

Galligan, David  
Dept of Physics and Astronomy  
University of Canterbury  
Private Bag 4800  
Christchurch, New Zealand  
E.mail: d.galligan@phys.canterbury.ac.nz

Graps, Amanda  
 Max-Planck-Institut fuer Kerphysik  
 Saupfercheckweg 1,  
 D-69117 Heidelberg, Germany  
 E-mail: Amara.Graps@mpi-hd.mpg.de

Grün, Eberhard  
 Max-Planck-Institut für Kernphysik  
 Saupfercheckweg 1  
 69117 Heidelberg, Germany  
 E-mail: eberhard.gruen@mpi-hd.mpg.de

Gustafson, Bo  
 Laboratory for Astrophysics  
 Department of Astronomy  
 University of Florida, USA  
 E-mail: gustaf@astro.ufl.edu

Hajduk, Anton  
 Astronomical Institute of the Slovak  
 Academy of Sciences  
 Dubravská cest 9  
 SK-84228 Bratislava, Slovakia  
 E-mail: astrohaj@savba.sk

Hamabe, Yoshima  
 University of Tokyo  
 7-3-1 Hongo,  
 Bunkyo-ku  
 Tokyo 113-0033, Japan  
 E-mail: hamabe@space.eps.s.u-tokyo.ac.jp

Hasegawa, Hitoshi  
 ASTEC, Inc.  
 1-3-11 Koishikawa  
 Bunkyo-ku  
 Tokyo 112-0002, Japan  
 E-mail: kin@seed.pro.or.jp  
 E-mail: hh@astec.co.jp

Hasegawa, Ichiro  
 Otemae University  
 4-18-5 Fujivaradaikita  
 Kata-ku  
 Kobe 651-1301, Japan  
 E-mail: hasegawa@otemae.ac.jp

Hawkes, Bob  
 Mount Allison University  
 Physics Department  
 67 York st.  
 Sackville, NB, E4L 1E6 Canada  
 E-mail: rhawkes@mta.ca

Heinselman, Craig  
 SRI International  
 333 Ravenswood Ave  
 Menlo Park, CA 94025, USA  
 E-mail: craig.heinselman@sri.com

Hunt, Stephen  
 MIT Lincoln Laboratory  
 Wood St. Lexington, MA, USA  
 E-mail: shunt10460@yahoo.com;  
 sorion@bu.edu

Janches, Diego  
 Swedish Institute of Space Physics  
 PO Box 812,  
 SE-981 28 Kiruna, Sweden  
 E-mail: diego.janches@irf.se

Jenniskens, Peter  
 SETI Institute  
 NASA Ames Research Center  
 Mail Stop 239-4  
 Moffett Field, CA 94035-1000, USA  
 E-mail: pjenniskens@mail.arc.nasa.gov

Jones, James  
 Department of Physics and Astronomy  
 University of Western Ontario  
 London, ON, N6A 3K7 Canada.  
 E-mail: jimeteor@julian.uwo.ca

Kalabanov, Sergei  
 Radiophysics Department of Kazan  
 university  
 Kazan university  
 Kremlevskaia str 18  
 Kazan 420008, Russia  
 E-mail: sergei.kalabanov@ksu.ru

Karpov, Arkadia  
Kazan university  
Kremlevskaia str 18  
Kazan 420008, Russia  
E.mail: arkadi.karpov@ksu.ru

Khavroshkin, Oleg  
Schmidt United Institute of Physics of the  
Earth  
B. Gruzinskaya 10  
GPS-5  
123995 Moscow D-242, Russia  
E.mail: khavole@uipe-ras.scgis.ru

Kimura, Hiroshi  
Institute of Planetology  
University of Münster  
Wilhelm-Klemm-Str. 10  
D-481 49 Münster, Germany  
E.mail: kimura@uni-muenster.de

Kolomiyets, Svetlana  
Kharkiv State Technical University of  
Radioelectronics (KhTURE)  
Lenina av 14  
Kharkiv, 611667 Ukraine  
E.mail: kometa@kture.kharkov.ua

Koten, Pavel  
Astronomical Institute  
251 65 Ondrejov, Czech Republic  
E.mail: koten@asu.cas.cz

Kozak, Pavlo  
Astronomical Observatory  
Kyiv Shevchenko National University  
3, Observatorna Str.  
Kyiv, Ukraine  
E.mail: kozak@observ.univ.kiev.ua

Kruchynenko, Vitalij  
Astronomical Observatory  
Kiev Natinal University  
Kiev, Ukraine  
E.mail: kruch@observ.univ.kiev.ua

Kuznetsov, Valery  
Department of Theoretical and  
Mathematical Physics  
Novgorod State University  
St.-Petersburgskayua st., 41  
173003 Novgorod the Great, Russia  
E.mail: kv1@nrofsirf.natm.ru

Landgraf, Markus  
ESA7ESOC  
Robert-Bosch-Str 5  
64233 Darmstadt, Germany  
E.mail: [Markus.Landgraf@esa.int](mailto:Markus.Landgraf@esa.int)

Levasseur-Regourd, Anny-Chantal  
Universite Paris VI and Service  
d'Aeronomie CNRS-IPSL  
Aeronomie, BP 3  
F-91371 Verrieres, France.  
E.mail:  
[Chantal.Levasseur@aerov.jussieu.fr](mailto:Chantal.Levasseur@aerov.jussieu.fr)

Lindblad, B.A.  
Storskolevagen 17  
SE 22467 Lund, Sweden  
E.mail: LINASU@gemini ldc.lu.se

Mann, Ingrid  
Space Science Department ESTEC SCI-  
SO  
PO Bus 299  
220 AG Noordwijk, The Netherlands  
E.mail: imann@so.estec.esa.nl

Mathews, John  
Communications and Space Science  
Laboratory (CSSL)  
The Pennsylvania State University  
323 A EE East  
University Park, PA 16802-2707, USA  
E.mail: JDMathews@psu.edu

Molau, Sirko  
RWTH Aachen  
Lehrstuhl für Informatik VI  
Ahrnstr 55  
D-52056 Aachen, Germany  
E.mail: sirko@molau.de

Müller, Michael  
Planetary Sciences and Space Research  
Institute  
The Open University  
Walton Hall  
Milton Keynes, MK7 6AA, UK  
E.mail: m.mueller@open.ac.uk

Murad, Edmond  
Air Force Research Lab  
AFRL/VSBX  
Hanscom AFB, MA 01731, USA  
E.mail: Ed.Murad@hanscom.af.mil

Nakamura, Takuji  
Radio Science Center for Space and  
Atmosphere  
Kyoto University  
Uji, Kyoto 611, Japan  
E.mail: nakamura@kurasc.kyoto-u.ac.jp

Nikolova, Simona  
University of Western Ontario  
33 Duke St  
London, Ontario, N6T 2X3 Canada  
E.mail: srnikolo@julian.uwo.ca

Nissinen, Markku  
URSA Astronomical Association  
Naavakuja 9B8  
F-78870 Varkaus, Finland  
E.mail: markku.nissinen@pp.inet.fi

Nogami, Nagatoshi  
Fine Chemicals Research Laboratory in  
Sumitomo  
Chemical Co., LTD.  
4-13-22 Sakamoto Ohrsu  
Shiga 520-0113, Japan  
E.mail: nogamin@sc.sumitomo-  
chem.co.jp

Novikov, GG  
Department of Theoretical and  
Mathematical Physics  
Novgorod State University  
St.-Petersburgskaya st, 41  
173003 Novgorod the Great, Russia  
E.mail: ngg@inf.novsu.ac.ru

Ogawa, Hiroshi  
Institute of Geoscience  
University of Tsukuba  
D-201 Yokota-Haitsu  
2-11-4 Amakubo  
Tsukuba, Ibaraki 305-0005, Japan  
E.mail: HZH02257@nifty.ne.jp

Ohnishi, Kouji  
Nagano National College of Technology  
391 Tokuma Nagano 389-8550, Japan  
E.mail: ohnishi@ge.nagano-nct.ac.jp

Ohtsuka, Katsuhito  
Tokyo Meteor Network  
1-27-5 Daisawa  
Stagaya-ku, Tokyo 155-0032, Japan  
E.mail: ohtsuka@jb3.so-net.ne.jp

Oppenheim, Meers  
Boston University  
725 Commonwealth Ave  
Boston, MA 02215, USA  
E.mail: meerso@bu.edu

Owumere-Onyekwelu Henry  
Chukwuemeka PPT# A0983273  
Imon -Ozy General Merchant Nig LTD  
61 Ikare Road  
Owo, Ondo State  
Nigeria  
E.mail: sukiltd@yahoo.com

Pecina, Petr  
Astron. Institute  
251 65 Ondresov, Czech Republic  
E.mail: ppecina@asu.cas.cz

Pellinen-Wannberg, Asta  
Swedish Institute of Space Physics  
PO Box 812  
SE-981 28 Kiruna, Sweden  
E.mail: asta.pellinen-wannberg@irf.se

Plane, John  
School of Environmental Sciences  
University of East Anglia  
Norwich NR4 7TJ, UK  
E.mail: J.Plane@uea.ac.uk

Ponomarjov, Maxim  
 State Academy of Aviation Technology  
 Promyshlennaya Str 1 (box 22)  
 152300 Tutaev  
 Yaroslavl region, Russian Federation  
 E.mail: pmg@univ.uniyar.ac.ru  
 E.mail: ponomarjov\_maxim@mail.ru

Popova, Olga  
 Institute for Dynamics of Geospheres  
 Russian Academy of Science  
 Leninsky prospekt 38, bld 6  
 Moscow, Russia 117334  
 E.mail: olga\_idg@rambler.ru,  
 E.mail: olga\_idg.chph.ras.ru

Porubcan, Vladimir  
 Astronomical Institute  
 Slovak Academy of Sciences  
 Astronomical Institute SAV  
 Dubravska 9  
 84228 Bratislava, Slovakia  
 E.mail: astropor@savba.sk

Rendtel, Jurgen  
 International Meteor Organization  
 PF 000118  
 14401 Potsdam, Germany  
 E.mail: jrendtel@aip.de

ReVelle, Douglas  
 Technical Staff Member  
 Los Alamos national Laboratory  
 P.O. Box 1663, MS J577  
 Earth and Environmental Sciences  
 Division  
 EES-8, Atmospheric and Climate Sciences  
 group  
 Los Alamos, New Mexico 87545, USA  
 E.mail: dor@vega.lanl.gov  
 revelle@lanl.gov

Rickman, Hans  
 Astronomiska observatoriet  
 Inst f'r astronomi och rymdfysik  
 Box 515  
 SE-751 20 Uppsala, Sweden  
 E.mail: hans@astro.uu.se

Rosaev, Alexey  
 FGUP NPC Nedra  
 Svoboda Str., 8/38  
 150000 Yaroslavl, Russia  
 E.mail: rosaev@nedra.ru

Ryabova, Galina  
 Research Institute of Applied Mathematics  
 and Mechanics of the Tomsk State  
 University  
 Department of Astrometry and Celestial  
 Mechanics  
 Lenin pr. 36  
 634050 Tomsk-50, Russia  
 E.mail: astrodep@niipmm.tsu.ru

Sasaki, Sho  
 Dept Earth and Planetary Sci.  
 University of Tokyo  
 Hongo, Tokyo 113-0033, Japan  
 E.mail: sho@eps.s.u-tokyo.ac.jp

Selvamurugan R.  
 Research Associate  
 National MST Radar Facility  
 Department of Space  
 Govt. of India, Gadanki-517 112  
 Pakala Mandal, Andhra Pradesh, India  
 E.mail: selvastella@yahoo.com

Serizawa, Hirotaka  
 The Nippon Meteor Society  
 Saitama University  
 173-3-201 Ohkubo-Ryoke  
 Saitama 338-0826, Japan  
 E.mail: aaf80100@pop17.odn.ne.jp

Shibata, Hiromi  
 Research Center for Nuclear Science and  
 Technology  
 University of Tokyo  
 2-22 Shirakata-shirane  
 Tokai-mura, Ibaraki, Japan  
 E.mail: shibata@tokai.t.u-tokyo.ac.jp

Sidorov, Vladimir  
Sibirskiy trakt 5 appart. 7  
Post 420029  
Kaxan, Russia  
E.mail: Vladimir.Sidorov@ksu.ru

Singer, Werner  
Leibniz-Institute of Atmospheric Physics  
Schloss-str. 6  
D-1825 Kuehlungsborn, Germany  
E.mail: singer@iap-kborn.de

Spurny, Pavel  
Ondrejov Observatory  
Astronomical Institute  
Fricova 1  
251 65 Ondrejov, The Czech Republic  
E.mail: spurny@asu.cas.cz

Stork, Rostislav  
Ondrejov Observatory  
Astronomical Institute  
Fricova 1  
251 65 Ondrejov, The Czech Republic  
E.mail: stork@asu.cas.cz

Su, Yang  
Beijing Astronomical Observatory  
A20 Dutun Road  
Chaoyang District  
Beijingh 100012, P.R. China  
E.mail: ysu@bao.ac.cn

Svedhem, Håkan  
ESA/ESTEC,  
PB 299,  
NL-2200AG Noordwijk, The Netherlands,  
E.mail: H.Svedhem@Esa.int

Svoren, Jan  
Astronomical Institute  
Skalnate Pleso Observatory  
SK-059 60 Tatranska Lomnica, The  
Slovak Republic  
E.mail: astrsven@auriga.ta3.sk

Takaaki Iwasa  
Deputy Director, Mr  
Japan Society for the Promotion of  
Science

Tomtebodavägen 19A  
S-171 77 Stockholm  
Sweden  
Tel 08-50 88 4561  
Fax 08-31 38 86  
E-mail: t-iwasa@jsps-sto.co

Toyomasu, Shinji  
Misato Observatory  
180 Matsugamine  
Misato  
Wakayama 640-1366, Japan  
E.mail:  
toyomasu@obs.misato.wakayama.jp

Tsukamoto, Toshio  
Nagoya University  
National Astronomical Observatory  
2-21-1 Osawa Mitaka  
Tokyo 181-8588, Japan  
E.mail: tsukmtts@cc.nao.ac.jp

Ueda, Masayoshi  
43-2 Asuka Habino-shi  
Osaka 583-0842, Japan  
E.mail: m-ueda@mua.biglobe.ne.jp

Ulich, Thomas  
Sodankyla Geophysical Observatory,  
Finland  
Tahtelantie 112  
FIN-99600 Sodankyla, Finland  
E.mail: thu@sgo.fi

Valsecchi, Giovanni  
I.A.S.-C.N.R.  
Via Fosso del Cavaliere 100  
I-00133 Roma, Italy  
E-mail: giovanni@ias.rm.cnr.it

Voloshchuk, Yuri  
Kharkiv State Technical University of  
Radioelectronics  
Lenina av. 14  
Kharkiv, 61166 Ukraine  
E.mail: kometa@kture.kharkov.ua

von Zahn, Ulf  
Inst. of Atmospheric Physics  
Schloss-Str 6  
DE-182 25 Kühlungsborn, Germany  
E.mail: vonzahn@iap-kborn.de

Watanabe, Junichi  
National Astronomical Observatory  
2-21-1 Osawa, Mitaka  
181-8588 Tokyo, Japan  
E.mail: jun.watanabe@nao.ac.jp

Webster, Alan  
University Western Ontario  
Richmond St.,  
London ONT. N6LK 2A1, Canada  
E.mail: awebster@fes.engga.uwo.ca

Welch, Philip  
Astronomy Unit  
Queen Mary and Westfield College  
Maths Department  
Mile End Rd  
London E1 4AH, UK  
E.mail: p.g.welch@qmw.ac.uk

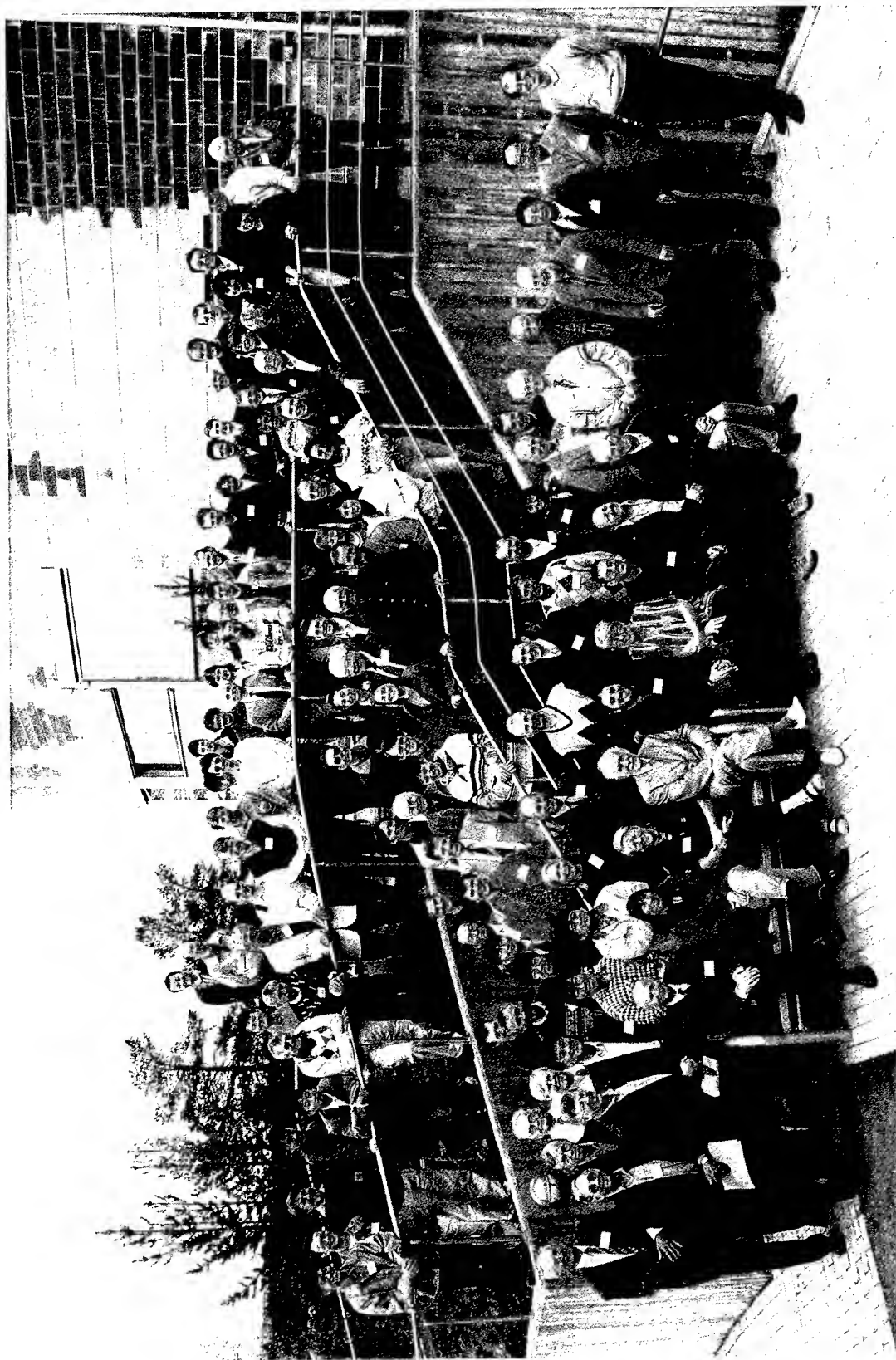
Widell Ola  
SSC, Erange  
Box 802,  
SE-981 28 Kiruna, Sweden  
E.mail: ola.widell@esrange.ssc.se

Williams, Iwan  
Astronomy Unit  
Queen Mary  
London E1 4NS, UK  
E.mail: i.p.williams@qmw.ac.uk

Wu, Guang-Jie  
Yunnan Observatory  
Chinese Academy of Sciences  
PO Box 110  
Kunming, Peoples Republic of China  
E.mail: ynaowugj@public.km.yn.cn

Yrjölä, Ilkka  
Jukolantie 16  
FIN-45740 Kuusankoski, Finland  
E.mail: oh5iy@sci.fi

Zhou, Qihou  
Arecibo Observatory  
HC3 Box 53995  
Arecibo, PR 00612  
Puerto Rico, USA  
E.mail: zhou@naic.edu



**European Space Agency**  
**Agence spatiale européenne**

*Contact: ESA Publications Division*

c/o ESTEC, PO Box 299, 2200 AG Noordwijk, The Netherlands

Tel (31) 71 565 3400 - Fax (31) 71 565 5433